THE UNIVERSITY OF TEXAS AT AUSTIN
CENTER FOR TRANSPORTATION RESEARCH

TECHNICAL REPORT 0-6829-1
TxDOT PROJECT NUMBER 0-6829

Fatigue Resistance and Reliability of High Mast Illumination Poles (HMIPs) with Pre-Existing Cracks: Final Report

Mohammed A. Morovat
Ying-Chuan Chen
Mark T. Eason
Michael D. Engelhardt
Lance Manuel
Todd A. Helwig
Eric B. Williamson
Patricia M. Clayton

March 2018; Revised and Published November 2018

http://library.ctr.utexas.edu/ctr-publications/0-6829-1.pdf

Technical Report Documentation Page

1. Report No. FHWA/TX-18/0-6829-1	2. Government Accession No.	3. Recipient's Catalog No.
4. Title and Subtitle Fatigue Resistance and Reliability of High Mast Illumination Poles (HMIPs) with Pre-Existing Cracks: Final Report		5. Report Date March 2018; Revised and Published November 2018 6. Performing Organization Code
7. Author(s) Mohammed A. Morovat, Ying-Chuan Chen, Mark T. Eason, Michael D. Engelhardt, Lance Manuel, Todd A. Helwig, Eric B. Williamson, Patricia M. Clayton		8. Performing Organization Report No. 0-6829-1
9. Performing Organization Name and Address Center for Transportation Research The University of Texas at Austin 3925 W. Braker Lane Austin, TX 78759		10. Work Unit No. (TRAIS) 11. Contract or Grant No. 0-6829
12. Sponsoring Agency Name and Address Texas Department of Transportation Research and Technology Implementation Office P.O. Box 5080 Austin, TX 78763-5080		13. Type of Report and Period Covered Technical Report (8/14-3/18) 14. Sponsoring Agency Code

15. Supplementary Notes
Project performed in cooperation with the Texas Department of Transportation and the Federal Highway Administration.

16. Abstract

High mast illumination poles (HMIPs) are used throughout Texas and the U.S. to provide lighting along highways and at interchanges. Texas currently has about 5000 HMIPs, varying in height from 100 to 175 ft. Failures of HMIPs have been reported in several states, attributed to failures at the shaft-to-base plate connection.

No collapses of HMIPs have been reported in Texas. However, recent studies have shown that many galvanized HMIPs in Texas have pre-existing cracks at their shaft-to-base plate connection, most likely caused by the galvanization process before the poles were placed in service. Previous research has also shown that pre-existing cracks may significantly reduce the fatigue life of galvanized HMIPs.

TxDOT has identified three major issues/concerns with respect to HMIPs with pre-existing cracks: the lack of reliable experimental data about the fatigue life of pre-cracked HMIP base-connection details; the significant uncertainty regarding the natural wind response of HMIPs to the various major wind environments in Texas (much of this uncertainty is related to the lack of measured data from comprehensive field studies); and, due to this lack of data, the 'safe/serviceable' life of in-service TxDOT HMIPs with pre-existing cracks cannot be reliably predicted.

The main goal of this research project was to generate data and information to support a probabilistic-based assessment of the remaining life of HMIPs with pre-existing cracks. The research included extensive laboratory fatigue testing of HMIPs with pre-existing cracks, field monitoring of in-service HMIPs ate five locations across Texas, and the development of a reliability based framework to assess the safety of in-service HMIPs with pre-existing cracks.

The results of this study show a wide range in the predicted lives of HMIPs with pre-existing cracks at different locations throughout the state. Based on a probability of failure of 5-percent, the predicted fatigue life at a number of locations analyzed throughout the state showed predicted lives varying from approximately 30 years to over 300 years. The variation in predicted lives is mainly affected by differing wind characteristics at each location.

17. Key Words	18. Distribution Statement
High mast illumination poles, galvanized, pre-existing cracks, fatigue life	No restrictions. This document is available to the public through the National Technical Information Service, Springfield, Virginia 22161; www.ntis.gov.

19. Security Classif. (of report)	20. Security Classif. (of this page)	21. No. of pages	22. Price
Unclassified	Unclassified	548	

Form DOT F 1700.7 (8-72) Reproduction of completed page authorized

THE UNIVERSITY OF TEXAS AT AUSTIN
CENTER FOR TRANSPORTATION RESEARCH

Fatigue Resistance and Reliability of High Mast Illumination Poles (HMIPs) with Pre-Existing Cracks: Final Report

Mohammed A. Morovat
Ying-Chuan Chen
Mark T. Eason
Michael D. Engelhardt
Lance Manuel
Todd A. Helwig
Eric B. Williamson
Patricia M. Clayton

CTR Technical Report:	0-6829-1
Report Date:	March 2018; Revised and Published November 2018
Project:	0-6829
Project Title:	Fatigue Resistance and Reliability of High Mast Illumination Poles (HMIPs) with Pre-Existing Cracks
Sponsoring Agency:	Texas Department of Transportation
Performing Agency:	Center for Transportation Research at The University of Texas at Austin

Project performed in cooperation with the Texas Department of Transportation and the Federal Highway Administration.

Center for Transportation Research
The University of Texas at Austin
3925 W. Braker Lane
Austin, TX 78759

http://ctr.utexas.edu/

Disclaimers

Author's Disclaimer: The contents of this report reflect the views of the authors, who are responsible for the facts and the accuracy of the data presented herein. The contents do not necessarily reflect the official view or policies of the Federal Highway Administration or the Texas Department of Transportation (TxDOT). This report does not constitute a standard, specification, or regulation.

Patent Disclaimer: There was no invention or discovery conceived or first actually reduced to practice in the course of or under this contract, including any art, method, process, machine manufacture, design or composition of matter, or any new useful improvement thereof, or any variety of plant, which is or may be patentable under the patent laws of the United States of America or any foreign country.

Notice: The United States Government and the State of Texas do not endorse products or manufacturers. If trade or manufacturers' names appear herein, it is solely because they are considered essential to the object of this report.

Engineering Disclaimer

NOT INTENDED FOR CONSTRUCTION, BIDDING, OR PERMIT PURPOSES.

Project Engineer: Michael D. Engelhardt
Professional Engineer License State and Number: Texas No. 88934
P. E. Designation: Research Supervisor

Acknowledgments

The authors extend their appreciation to the Texas Department of Transportation for providing the funding for this research. The authors thank Tim Bradberry, Jim Yang, Michael Smith, and the entire project monitoring committee for their assistance and guidance. The authors also thank the Project Manager, Wade Odell, for oversight and coordination of this project.

Table of Contents

List of Figures

List of Tables

Chapter 1. Introduction

1.1 Overview

High Mast Illumination Poles (HMIPs) are used throughout Texas and the U.S. to provide lighting along highways and at interchanges. HMIPs are also referred to as High Level Illumination Poles by AASHTO. Texas currently has about 5000 HMIPs, varying in height from 100 to 175 ft. Failures of galvanized HMIPs have been reported in several states. These collapses have been attributed to failures at the shaft-to-base plate connection.

No such collapses of HMIPs have been reported in Texas. However, recent studies have shown that many galvanized HMIPs in Texas have pre-existing cracks at their shaft-to-base plate connection, most likely caused by the galvanization process used when the poles were first manufactured. Previous research has also shown that these pre-existing cracks may significantly reduce the fatigue life of galvanized HMIPs.

TxDOT has identified three major issues/concerns with respect to HMIPs with pre-existing cracks. First, there is a lack of reliable experimental data about the fatigue life of pre-cracked HMIP base-connection details. Second, there is significant uncertainty regarding the natural wind response of HMIPs to the various major wind environments in Texas. Much of this uncertainty is related to the lack of measured data from comprehensive field studies. Third, due to this lack of data, the 'safe/serviceable' life of in-service TxDOT HMIPs with pre-existing cracks cannot be reliably predicted.

1.2 Project Motivation

The remaining fatigue life of in-service galvanized HMIPs in Texas is an important issue with safety and cost implications. Past research has shown that many in-service galvanized HMIPs likely have a significant degree of pre-existing cracks at the connection of the shaft to the base plate; cracks that likely formed during the galvanizing process before the poles were placed in service. Research has also shown that these pre-existing cracks may substantially reduce the fatigue life of these poles. Considering the large TxDOT inventory of HMIPs, approximately 5000 across the state, better information and methods to predict the remaining life of these poles are needed to help guide decisions on the use of resources for inspection, monitoring, repair or replacement of HMIPs.

Past research has also developed a reliability-based framework that allows an assessment of the probability of failure of an HMIP with pre-existing cracks as a function of years of service. However, additional data are needed to make this probabilistic-based approach a useful tool for TxDOT. Test data are needed on the fatigue performance of HMIPs with pre-existing cracks, at low stress ranges. Additional studies and data are also needed to better assess the effects of vortex shedding on HMIPs, as this appears to be the dominant mechanism that produces stress cycles and therefore fatigue damage in HMIPs. Finally, additional information is needed for TxDOT on options for mitigating risk associated with cracked HMIPs, such as increased inspection and monitoring and repair techniques.

1.3 Project Objectives and Report Outline

The Project 0-6829 was funded by TxDOT to address the concerns outlined above. The main goal of this research project was to generate data and information to support a probabilistic-based assessment of the remaining life of pre-cracked HMIPs. Laboratory fatigue tests were conducted on pre-cracked galvanized HMIPs. In addition, field data were collected and additional analyses were performed to characterize wind response of Texas HMIPs. Field and laboratory studies were supplemented by finite element studies simulating the global and local response of pre-cracked HMIPs. The results of the laboratory data, field studies, and analytical studies were combined in a reliability-based framework to provide a probabilistic assessment of the fatigue life of in-service pre-cracked HMIPs. Finally, additional information was developed in this project on options for mitigating risk associated with cracked HMIPs, such as increased inspection and monitoring, and repair/retrofit techniques.

The following major tasks, each discussed in a separate chapter in this report, were included in Project 0-6829:

- Perform a comprehensive literature review that includes the topics of designs of TxDOT HMIPs, experimental investigation of fatigue behavior of HMIPs with pre-existing cracks, wind-induced response of in-service HMIPs with pre-existing cracks, and probabilistic assessment of fatigue life and inspection scheduling (Chapter 2).
- Complete a survey to collect data on in-service HMIPs in the state of Texas to determine the HMIP designs of most interest and their locations in the state of Texas (Chapter 3).
- Collect historical wind data in the state of Texas for the HMIP design types and locations of interest identified in the survey and for locations representative of major wind environments in Texas (Chapter 4).
- Generate experimental data on the fatigue life of pre-cracked galvanized HMIP shaft-to baseplate connections at low stress ranges representative of wind-induced stresses experienced by the HMIPs in service (Chapter 5).
- Perform field monitoring of in-service HMIPs to obtain data on fatigue-load history and to characterize wind response of Texas HMIPs (Chapter 6).
- Conduct computational studies to extend the information collected in the laboratory test and the field monitoring programs, and to evaluate the capability of available computational tools to study the fatigue behavior of cracked HMIPs (Chapter 7).
- Develop and test a weld-repair procedure to extend the fatigue life of cracked HMIPs in service (Chapter 8).
- Develop a reliability-based framework to extend the information collected in the laboratory test and during the field monitoring tasks to assess the safety of in-service HMIPs with pre-existing cracks (Chapter 9).

Chapter 2. Background and Literature Review

2.1 Overview

High Mast Illumination Poles (HMIPs) are used throughout the U.S. to provide lighting along highways and at interchanges. HMIPs in Texas are typically tapered steel poles that are fabricated in segments and are galvanized for corrosion protection. There are currently about 5000 HMIPs in Texas that consist of 8 or 12 sided cross-sections, with heights varying from 100 to 175 ft. Figure 2.1 shows an example of a typical high mast illumination pole. At its base, the HMIP shaft is welded to a steel base plate, which in turn is attached to a concrete foundation through a series of anchor bolts.

Figure 2.1: Typical High Mast Illumination Pole (Rios 2007)

A number of collapses of HMIPs have been reported in other states, including the collapse of a 140 ft. HMIP along Interstate 29 in Sioux City, Iowa in 2003 and the collapse of a 150 ft. HMIP in Rapid City, South Dakota in 2005. These collapses have occurred by fracture at the shaft-to-base plate joint. Collapses have also been reported for HMIPs used at schools and at outdoor stadiums, including an incident of an HMIP falling through the roof of a school gymnasium (Magenes 2011). These collapses have been attributed to fatigue failures at the shaft-to-base plate connection (Rios 2007).

No such collapses of HMIPs have been reported in Texas. However, recent studies have shown that many galvanized HMIPs in Texas have pre-existing cracks at their shaft-to-base plate connection, most likely caused by the galvanization process (Kleineck 2011). Research has also shown that pre-existing cracks may significantly reduce the fatigue life of galvanized HMIPs (Rios 2007, Stam 2009, Pool 2010). The potentially poor performance of galvanized HMIPs with pre-existing cracks in Texas is a significant concern. Collapse of an HMIP can cause fatalities or serious injuries. In addition, inspection, monitoring, repair and replacement of HMIPs may be a significant cost, particularly in light of the large number of HMIPs in Texas. The cost of repairing a single HMIP has been estimated at approximately $6400 and the cost of replacing an HMIP at $35,000 (Goyal et al 2012). Because of the serious safety and cost concerns, better methods are needed to identify the remaining fatigue life of in-service TxDOT HMIPs with pre-existing cracks. This information is needed to guide decisions on the use of TxDOT resources for inspection, monitoring, repair, or replacement of HMIPs.

A comprehensive literature review was conducted over several topics pertaining to the research conducted in this project. These topics include an overview of TxDOT HMIPs, experimental investigation of fatigue behavior of HMIPs with pre-existing cracks, wind-induced response of in-service HMIPs with pre-existing cracks, and probabilistic assessment of fatigue life and inspection scheduling. The following sections of this chapter summarize the findings of the literature review.

2.2 TxDOT HMIPs

Details of the inventory of the Texas HMIPs of concern are specified on TxDOT Standard Drawing HMIP-98. Texas HMIPs have heights of 100 ft, 125 ft, 150 ft, or 175 ft. and are designed for a fastest mile wind speed of either 80 mph or 100 mph. The HMIPs consist of 8- or 12-sided shafts with a bottom diameter ranging from 24-5/8 in. to 37-3/8 in. Shaft thickness at the base varies from 5/16-in. to 9/16-in. The shafts are tapered, reducing in diameter with height. The taper varies from 0.16 in/ft to 0.19 in/ft. The shaft is welded to an annular base plate with holes for anchor bolts. Details for welds connecting the shaft to the base plate are specified on TxDOT Standard Drawing HMIP-98, and are shown in Figure 2.2.

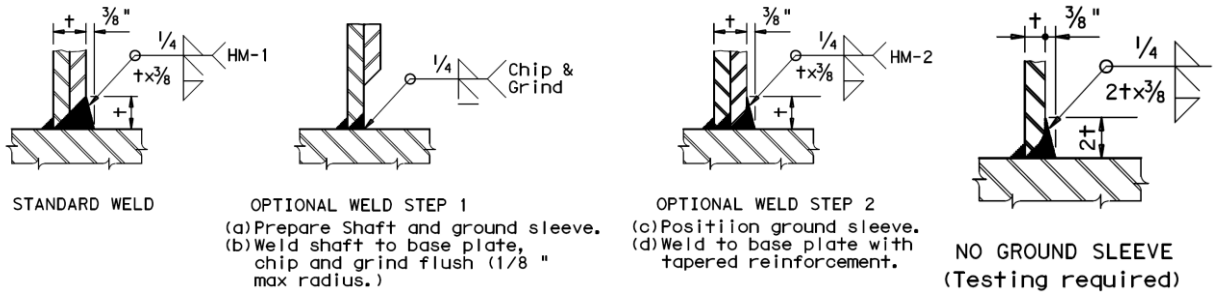

Figure 2.2: Shaft-to-Base Plate Weld Details for Texas HMIPs (TxDOT Standard Drawing HMIP-98)

The connection of the shaft to the base plate can be done either with or without an external steel collar known as a *ground sleeve*. When no ground sleeve is provided, the required weld detail is shown in the right-most drawing in Figure 2.2. The shaft is connected to the base plate using a complete joint penetration (CJP) groove weld, made from the outside without a backing bar. When a ground sleeve is provided, two alternative details are specified. For one detail (left-most drawing in Figure 2.2), a single CJP groove weld is used to connect the combined shaft and ground sleeve to the base plate. In the alternative detail (center drawings in Figure 2.2), the shaft is first welded to the base plate with a CJP groove weld. The ground sleeve is then welded to the base plate with a second CJP groove weld. For all weld details shown in Figure 2.2, a 1/4-in. reinforcing fillet weld is provided on the inside of the shaft to function as a backing bar to prevent burn through of the grove weld, and the outer edge of the CJP groove weld is provided with tapered reinforcement. After fabrication, HMIPs are galvanized. As part of this process, the HMIP segments are cleaned, pickled, fluxed, and then finally dipped into a molten zinc bath with a temperature in the range of 815 °F to 850 °F. Further details of the galvanizing process are described by Kleineck (2011).

2.3 Fatigue Behavior of HMIPs

A significant amount of work has been completed in Texas and elsewhere on the fatigue performance of HMIPs. Representative and pertinent experimental and analytical studies are reviewed in this section. Particular emphasis is placed on past studies on the fatigue performance of galvanized HMIPs and on HMIPs known to have pre-existing cracks. Further, the focus of this review is on HMIPs that use shaft-to-base plate connection details that are representative of Texas HMIPs.

2.3.1 Concept of Fatigue

As conceived by Schutz (1996), fatigue is the process of the weakening of a metal when subjected to cyclic variations in the applied stress (i.e. repeated vibrations or strains). The magnitudes of applied stresses are usually below the yield stress of the metal. Therefore, under the condition of small stresses, weakening in the form of crack growth takes place due to stress concentrations resulting from the presence of defects or micro-cracks in the metal. Consequently, in what it terms "high-cycle fatigue", a crack grows to a critical size and brittle fracture occurs only after number of cycles in the range of several hundred thousand to several million are achieved (Barsom and Rolfe 1999).

2.3.2 Brief History of Fatigue

In 1829, W.A.J. Albert, a German mining engineer, was most probably the first to note the concept of fatigue observing the in-service failure of conveyer chains (Schutz 1996). Poncelet, in 1839, used the word "fatigue" to describe the worn out of metal components. In 1844, Rankine contributed further to the topic of fatigue through his study of the stress concentration effect on the failure of railroad axles. The concept of S-N curves were first introduced by Wohler in 1860 to represent the fatigue problem of railway axles. Spangenberg, however, was the first who actually plotted S-N curves, and called them Wohler curves. Spangenberg specifically referred to the problem of fatigue by concluding that "materials can be induced to fail by many repetitions of stresses, all of which are lower than the static strength…." (Brooks and Choudhury 2002). Basquin was the first who introduced the idea of an endurance limit (Basquin Law) through the representation of the finite life region of the "Wohler curve" in the LogS-LogN format (Basquin 1910). In his view, the S-N curve was the mean curve drawn to represent survival of 50 percent of the data points. Early in the twentieth century, Baushinger defined what is called the cyclic behavior of materials or the cyclic stress strain curve (Bauschinger 1886). In 1903, Ewing and Humphries developed the idea of fatigue crack initiation using cyclic deformation. The linear damage rule for variable amplitude loading was first proposed by Palmgren in 1924 and was further developed by Miner in 1945. Today the method is commonly referred to as Miner's Rule (Miner 1945). As presented later in this chapter, Palmgren-Miner rule states that the damage done by each cycle is assumed to be proportional from the first to the last cycle. In 1954, Coffin and Manson observed that, in the low cycle regime, there existed a nominal plastic strain in each cycle that caused the accumulation of "fatigue damage" (Bannantine, et al. 1990).

2.3.3 Characterizing Fatigue Resistance

There are two common approaches for characterizing the fatigue resistance of a particular joint or a given detail. The resistance can be determined experimentally following a stress-based

approach (S-N curves) or numerically from a fracture-mechanics model. Both methods result in considerable uncertainty in the fatigue resistance, partly because fatigue is a complex process that involves localized damage accumulation. In addition, the actual nature of the applied loads and the extent of imperfections are not known.

Stress-Based Approach

The classical experimental method to characterize fatigue resistance is to test a given detail in tension at a constant-amplitude stress range and count the number of cycles to failure. Nominally identical details are tested at different constant-amplitude stress ranges until failure. The stress range is defined as the difference between the highest and lowest values in a stress history (Figure 2.3).

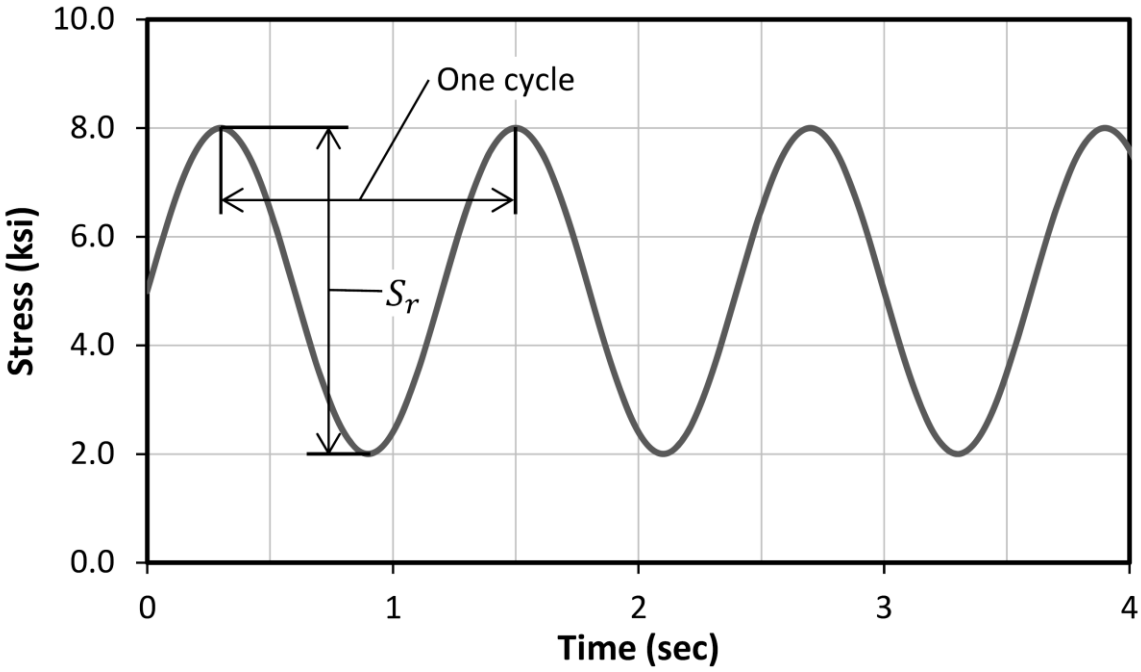

Figure 2.3: Definition of a Stress Cycle (Fasl 2013)

After testing a specific weld detail at various stress ranges, the data can be plotted on a graph of number of cycles to failure N_f for various cyclic stress ranges (S_r). The data are typically plotted on a log-log plot, as demonstrated in Figure 2.4. It was determined empirically that stress range and type of detail are the primary variables affecting fatigue resistance. It is important to note that the stress range is typically the nominal stress range. The flow of stresses at discontinuities and/or welds creates locations of stress concentrations that lead to higher magnitudes than calculated from engineering mechanics (bending stress, axial stress, etc.). Because the stress concentrations vary with the detail, the nominal stress (stress calculated away from the discontinuities and/or welds) is typically used to characterize the S-N curves.

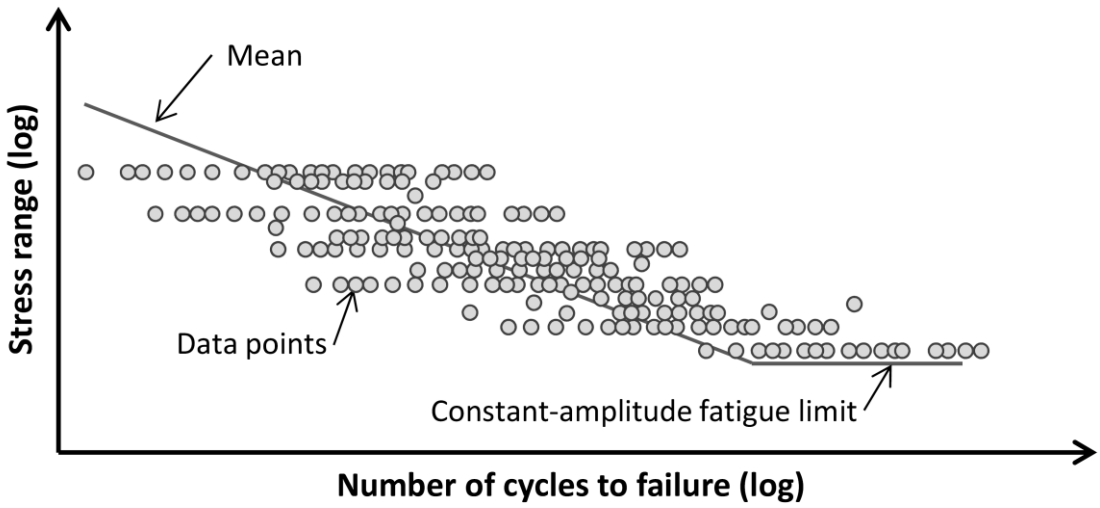

Figure 2.4: Sample Data from a Representative Fatigue Test (Fasl 2013)

Considering a single type of weld detail, the fatigue resistance can be described by Equation 2.1. The constants B and C are determined empirically using fatigue test data.

$$N_f = C \cdot {S_R}^B \qquad \textbf{Equation 2.1}$$

where,
N_f = number of cycles until failure at S_R
C = empirical constant for a specific weld detail from fatigue data (ksi^{-B})
S_r = nominal constant-amplitude stress range (ksi)
B = slope of the S-N curve

To determine the fatigue resistance, regression techniques are used to define the line that goes through the mean of the data. For most metals, the slope of the S-N curve (B) will vary between -2 to -4. The code value is determined by moving the mean failure line approximately two standard deviations to the left (Figure 2.5). The code value in the AASHTO Load and Resistance Factor Design (LRFD) Bridge Design Specifications (AASHTO 2010) typically corresponds to a 95% confidence interval of a 95% probability of survival (probability of failure of approximately 5%) (Keating and Fisher 1986).

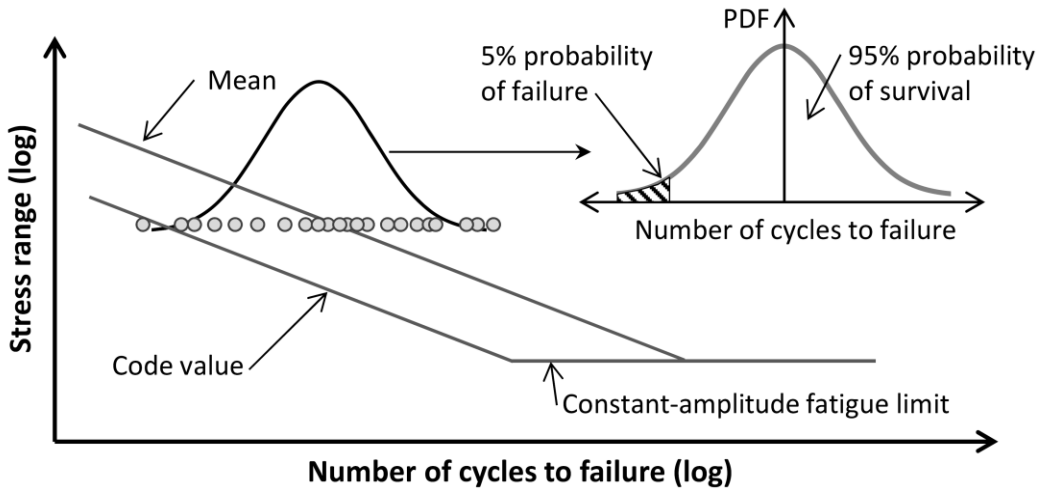

Figure 2.5: Regression Lines from a Representative Fatigue Test (Fasl 2013)

As shown in Figure 2.4, there is a stress range at which the weld detail is assumed to have an infinite fatigue life for a given constant-amplitude stress range. This horizontal line corresponds to the constant-amplitude fatigue limit (CAFL). The determination of the CAFL historically corresponded to two million cycles, at which point the specimen would be declared a "run-out" test. The two-million cycle limit was based upon equipment limitations during the period of testing (1970s-1980s) (Munse 1964). With modern testing facilities, specimens can be and are often tested to much higher cycle counts.

The equation currently used in the AASHTO LRFD Specifications (AASHTO 2010) is shown in Equation 2.2. As expected, the form closely follows that in Equation 2.1, with the exception that all detail categories are assumed to have a value of B equal to -3. Because Equation 2.2 is used for design, the fatigue constant (A) for each fatigue category reported in Table 2.1 are lower-bound values (approximately 5% probability of failure).

$$N_f = \frac{A}{S_R{}^3} \qquad \textbf{Equation 2.2}$$

where,
N_f = number of cycles until failure at S_R
A = fatigue constant for each detail category, defined by AASHTO LRFD Specification (AASHTO 2010) (ksi^3)
S_r = constant-amplitude stress range (ksi)

Table 2.1: Fatigue Constant (A) and Constant-Amplitude Fatigue Limit (CAFL) for Each Fatigue Detail Category (AASHTO 2010)

Mode	Fatigue Constant, A (ksi^3)	CAFL (ksi)
A	250×10^8	24.0
B	120×10^8	16.0
B′	61×10^8	12.0
C	44×10^8	10.0
C′	44×10^8	12.0
D	22×10^8	7.0
E	11×10^8	4.5
E′	3.9×10^8	2.6

The AASHTO fatigue categories for design are best understood by graphing the expressions in the form of S-N curves as shown in Figure 2.6 (AASHTO 2010). The AASHTO LRFD Specifications (AASHTO 2010) provide examples of typical weld details that fit into each of the eight fatigue categories.

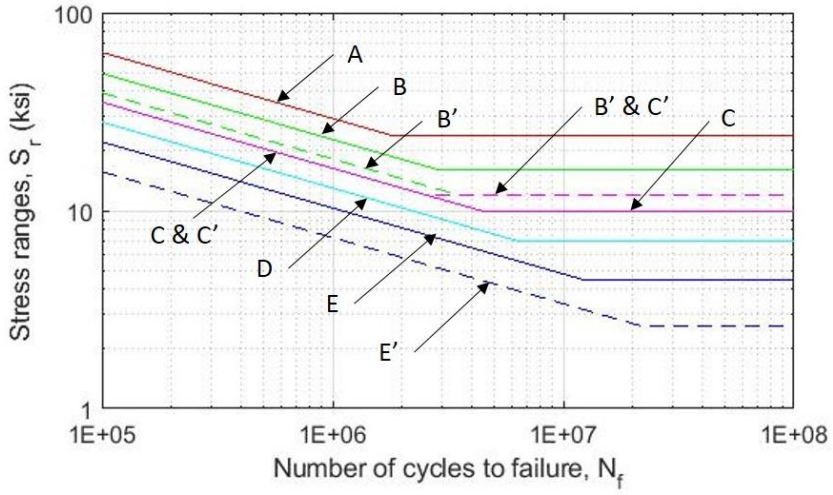

Figure 2.6: AASHTO S-N Curves for the Fatigue Design of Steel Bridges (AASHTO 2010)

Palmgren-Miner's Rule

Although fatigue tests have historically been performed using a constant-amplitude stress range, real structures are subjected to varying-amplitude stress ranges. For bridges, the amplitudes vary with the weight and length of the crossing vehicles. For offshore structures, the amplitudes depend on the wave height and frequency. Though one event may generate a 5-ksi cycle and the next event produces a 3-ksi cycle, each will contribute to the fatigue damage.

A cumulative damage theory is needed to relate the varying-amplitude cycles to the constant-amplitude fatigue data. Palmgren-Miner's rule is the most commonly used cumulative damage theory because it is simple and agrees well with historic fatigue data. The rule follows a linear-damage hypothesis and is expressed by Equations 2.3 and 2.4 (Miner 1945).

$$D_j = \frac{n_j}{N_{f,j}} \qquad \textit{Equation 2.3}$$

$$D = \sum_{j=1}^{k} D_j \qquad \textit{Equation 2.4}$$

where, $D_j =$ contribution of cycles n_j to Palmgren-Miner's damage accumulation index
$D =$ Palmgren-Miner's damage accumulation index
$n_j =$ number of cycles measured at $S_{R,j}$
$k =$ number of different stress ranges

In Palmgren-Miner's rule, each cycle causes damage; however, the damage induced is proportional to the number of cycles corresponding to failure for the actual stress range. The total damage in an element subjected to multiple stress ranges can be determined by simply summing the damage that accumulates at each stress range.

2.3.4 Experimental Investigation of Fatigue of HMIPs

Due to the collapse of several High Level Illumination Poles in the U.S. in recent years, a considerable amount of research has been conducted to better understand the fatigue behavior of the shaft-to-base plate connections. A great deal of research has been conducted in Texas (Anderson 2007, Goyal et al 2012, Koenings 2003, Kleineck 2011, Magenes 2011, Pool 2010, Richman 2009, Rios 2007, Stam 2009) and elsewhere (Foley et al 2004, Ocel, Chang et al 2009, Dexter and Ricker 2002, Krishna et al 2004, Suksawang et al 2009, Connor et al 2012, Roy et al 2012).

Fatigue Tests on HMIP Specimens at the University of Texas at Austin

An extensive series of tests and computational studies on the fatigue performance of HMIPs was conducted at the University of Texas at Austin starting in 2005, in a multi-state pooled fund study. The study was conducted in three phases. In Phases I and II (Rios 2007, Stam 2009), fatigue tests were conducted on several shaft-to-base plate details, including a Texas detail and a Wyoming detail, both of which used CJP groove welds, as well as a fillet welded detail called the "socket connection." The fatigue tests included in these studies used the test setup illustrated in Figure 2.7. Two specimens were tested simultaneously, in a back-to-back configuration with a stiff reaction box in the middle. Fatigue loading was applied by a single actuator working in displacement control. The applied displacements were chosen to produce a target stress range at the base of the HMIP specimens, typically chosen to be 12 ksi to 15 ksi. The test results showed very poor performance of the fillet welded socket detail, falling well below AASHTO fatigue category E′ (It is important to note that the Texas HMIP detail considered in this study utilizes full penetration welds and therefore the poor fatigue performance of socket detail is not necessarily an indication of poor performance of full penetration detail). The Texas detail (with no ground sleeve) and the Wyoming detail showed better performance, satisfying fatigue category E′ requirements. The Texas detail with a ground

sleeve showed even better performance, satisfying fatigue category C requirements. Tests also showed fatigue performance improved with thicker base plates and a reduction in base plate inner diameter.

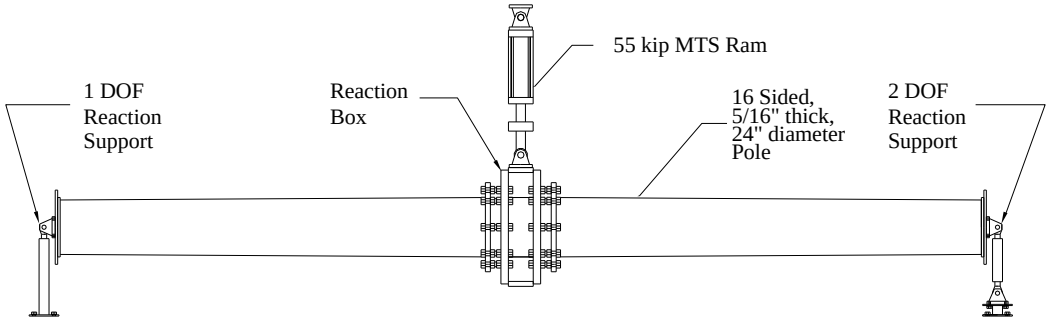

Figure 2.7: Setup for Fatigue Testing of HMIPs at the University of Texas at Austin (Rios 2007)

In Phase III of the pool-funded study, additional fatigue tests were conducted on the Texas detail, both with and without ground sleeves. Further, whereas in Phases I and II only 24-inch diameter shafts were tested, 33-in. diameter shafts were tested in Phase III. Finally, in Phase III, the fatigue performance of galvanized HMIPs was compared to black (ungalvanized) specimens. The tests showed that the 33-inch diameter specimens had significantly worse fatigue performance than the 24-inch diameter specimens. The tests also showed that the galvanized specimens had significantly worse fatigue performance than the black specimens. Prior to testing, TxDOT personnel conducted ultrasonic tests (UT) of the specimens. The UT showed that the galvanized specimens had a large number of pre-existing internal cracks in the shaft at the shaft-to-base plate weld, whereas the black specimens had no pre-existing cracks (Pool 2010). Subsequent investigation showed that many of the galvanized specimens had pre-existing cracks, but that the presence, location and severity of initial cracking were highly variable from specimen to specimen. Subsequent work (Kleineck 2011) showed that the initial cracks were the result of the galvanization process. The most important observation, however, is that the fatigue performance of the 33-inch diameter galvanized poles could be substantially reduced by these pre-existing cracks. This was a particularly worrisome discovery, since TxDOT has quite a large inventory of 33-inch diameter galvanized HMIPs.

The results of fatigue tests on galvanized poles (Stam 2009, Pool 2010, Magenes 2011) is shown in Figure 2.8. The specimen designations are shown in the key. The first number in the designation (24 or 33) is the shaft diameter in inches, the second number is the base plate thickness (3-in. for each specimen), next is the number of anchor rods (12 anchor rods for each specimen). Following is a designation for the shaft-to-base plate detail (TX = Texas detail without ground sleeve; TXEC = Texas detail with ground sleeve), a designation for the manufacturer, and the finish (G = galvanized).

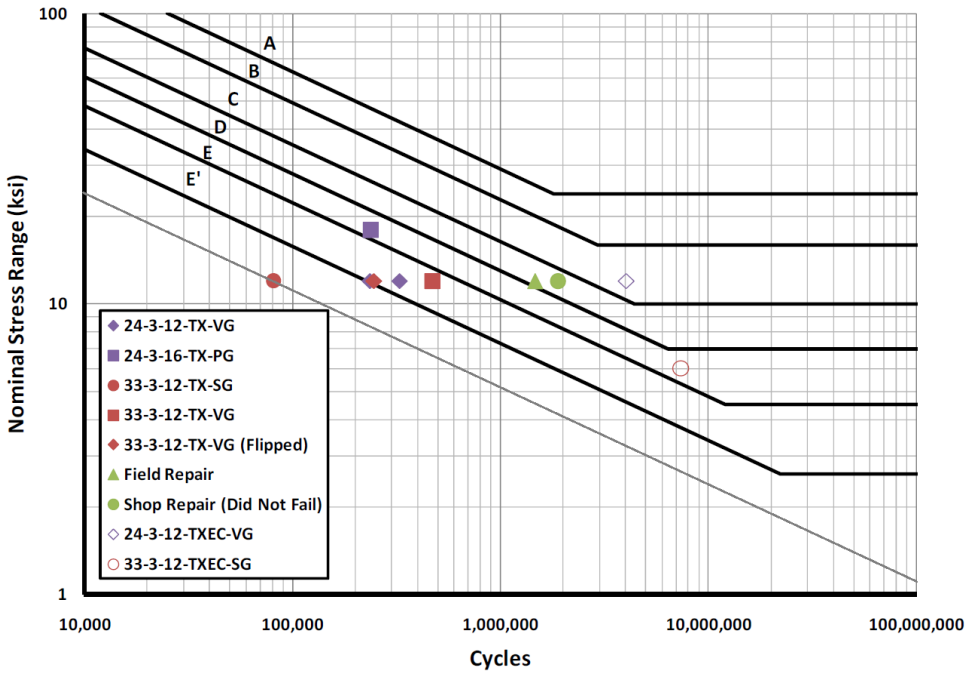

Figure 2.8: Fatigue Test Data on Galvanized HMIPs (Magenes 2011)

Similar data are shown in Table 2.2, which also shows the results of UT inspections of the poles conducted prior to fatigue testing. Listed in the table is the percentage of bends in the 12-sided poles that showed pre-existing cracks, and the total crack length. The number of cycles to failure at a 12 ksi stress range is also listed.

Table 2.2: Fatigue Test Results on Galvanized HMIPs

HMIP Designation	External Collar	Galvanized	% of Bends Cracked	Total Crack Length (in)	Cycles to Failure @ 12 ksi
33-3-12-TXEC-SG-A	Yes	Yes	17	5.00	No failure
33-3-12-TXEC-SG-B	Yes	Yes	25	8.00	No failure
33-3-12-TX-SG-A	**No**	**Yes**	**83**	**11.00**	**81326**
33-3-12-TX-VG-A	No	Yes	25	5.00	358228
33-3-12-TX-VG-B	No	Yes	33	4.63	358228
33-3-12-TX-SG-B	No	No	0	0	No failure

An important observation is that galvanized HMIPs may have significantly reduced fatigue life (worse than the AASHTO fatigue category E′) because of the presence of pre-existing cracks. However, the amount of fatigue test data on galvanized HMIPs with pre-existing cracks is currently insufficient to quantify their fatigue performance. More recently, limited additional fatigue testing was conducted at a 5-ksi stress range on an HMIP taken out of service from along IH-10 in El Paso due to the discovery of a large number of cracks (Belivanis 2013). Test results showed the fatigue performance barely made the category E′. However, considering

the large amount of initial cracking, this was actually a promising result, but suggests further fatigue testing is needed on HMIPs with pre-existing cracks.

Following the discovery that galvanized HMIPs can have pre-existing cracks, TxDOT conducted UT evaluation of cracks for a number of in-service 12-sided poles at various locations across the state. Results are listed in Table 2.3. The HMIPs were divided into two groups: 80 mph and 100 mph designs. The row labeled #UT is the number of inspected HMIPs, whereas the row labeled #CR is the number of HMIPs that were found with cracks. The row labeled %CR is the percentage of inspected HMIPs with cracks. It is important to note that a large percentage of in-service galvanized HMIPs were found to have internal cracks at the shaft-to-base plate weld.

Table 2.3: Cracked In-Service HMIPs in Texas (Identified through Ultrasonic Testing)

12-Sided HMIPs

	80 mph								**100 mph**							
	100 ft		**125 ft**		**150 ft**		**175 ft**		**100 ft**		**125 ft**		**150 ft**		**175 ft**	
	TX	EC	TX	EC	TX	EC	TX	EC	TX	EC	TX	EC	TX	EC	TX	EC
#UT	7	3	1	3	3	36	8	17	9	0	3	26	4	17	8	23
#CR	4	2	1	1	3	36	3	9	2	0	0	0	1	5	6	2
%CR	57	67	100	33	100	100	38	53	22	0	0	0	25	29	75	9
D/t	79	79	90	90	104	104	97	97	68	68	66	66	77	77	75	75

Also listed in Table 2.3 is the ratio of shaft diameter to thickness (*D/t*). A possible correlation between *D/t* and amount of cracking became evident in this data. Figure 2.9 shows a plot of the percentage of cracked poles versus *D/t* of the shaft for the in-service poles evaluated by TxDOT. The *D/t* ratio of the shaft appears to be a useful indicator of the potential for cracks within in-service HMIPs. However, the impact of this cracking on the remaining fatigue life of the HMIP is still unclear.

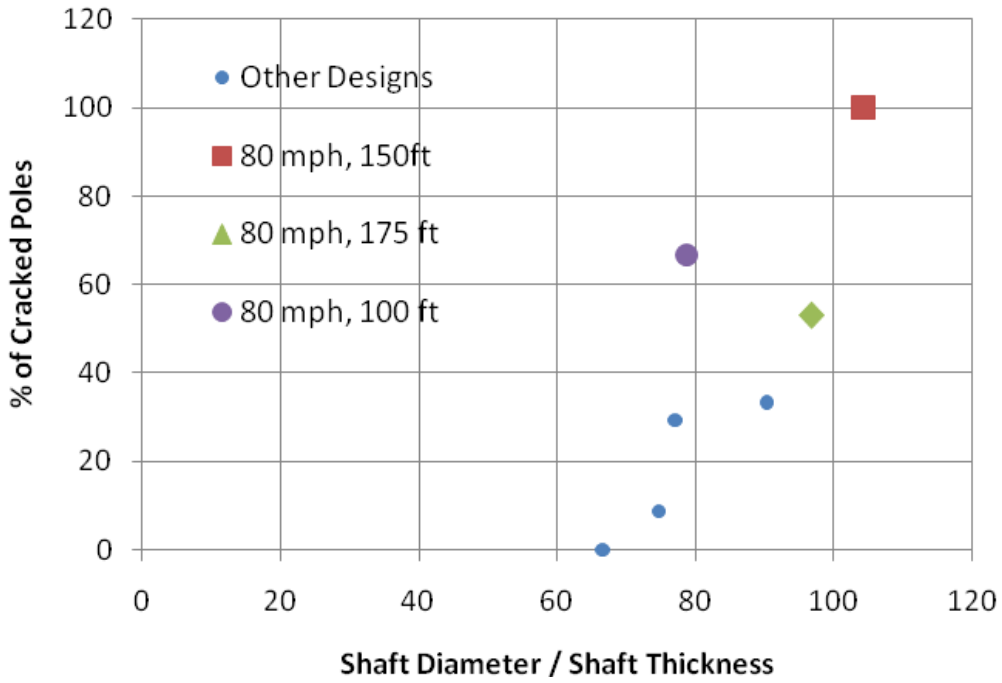

Figure 2.9: Percentage of Cracked In-Service HMIPs versus Shaft D/t Ratio (Magenes 2011)

2.4 Wind-Induced Response of HMIPs

2.4.1 Introduction

Previous studies on predicting wind-induced response of HMIPs, including gust effects and vortex shedding, are reviewed in this part. Included in the review are analytical and computational approaches for computing wind response, as well as the results of field studies and measurements on the wind response of HMIPs. Methods to reduce vortex shedding, such as the use of vortex spoilers, strakes, fins, and other suppression devices and on optimal placement of these devices to mitigate vortex-induced vibrations are also reviewed.

2.4.2 Dynamic Properties of HMIPs

Drag Coefficient

According to AASHTO (AASHTO 2013), the wind load effect is a function of projected area and static wind pressure. The projected area is the area on the plane, perpendicular to the wind direction that the structure projects upon. The area of the pole is calculated using the geometric dimensions, whereas the area of the luminaire is typically given in terms of effective projected area (EPA). The static wind pressure is a function of wind velocity, drag coefficient, and other factors. Drag coefficient changes with varying geometric shapes and Reynolds number.

The EPA of the luminaires varies with the number of lights attached. In NCHRP Report No. 718 (Connor et al. 2012), a mathematical model using a parabolic curve is proposed to estimate EPA of the luminaires based on the number of lights (Figure 2.10). Note that the drag coefficient can be neglected or set to one if the EPA of the luminaire is provided by the manufacturer (AASHTO 2013).

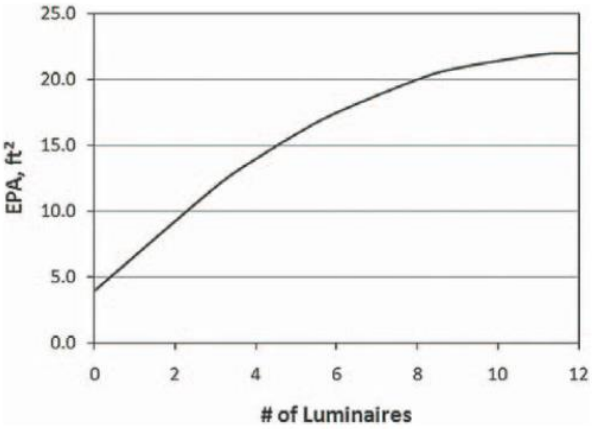

Figure 2.10: Estimated Effective Projected Area (EPA) of Luminaires (Connor et al. 2012)

The drag coefficient of the pole varies with wind velocities and geometric shape of the pole. NHCRP Report No. 718 (Connor et al. 2012) provides graphical information on how the drag coefficient varies with wind velocities for different pole geometries. These plots, shown in Figure 2.11, are based on the most conservative values of corner radius. The maximum value of the drag coefficient could be used as a conservative value for all wind velocities. AASHTO (AASHTO 2013) states that the drag coefficient should be based on the yearly mean wind velocity at the location of the pole.

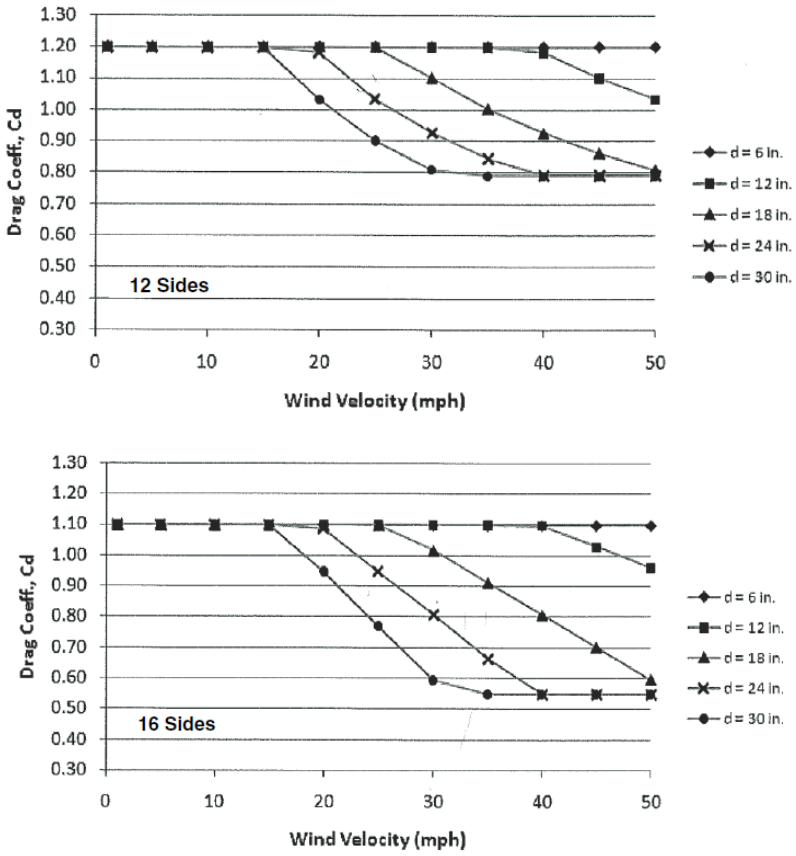

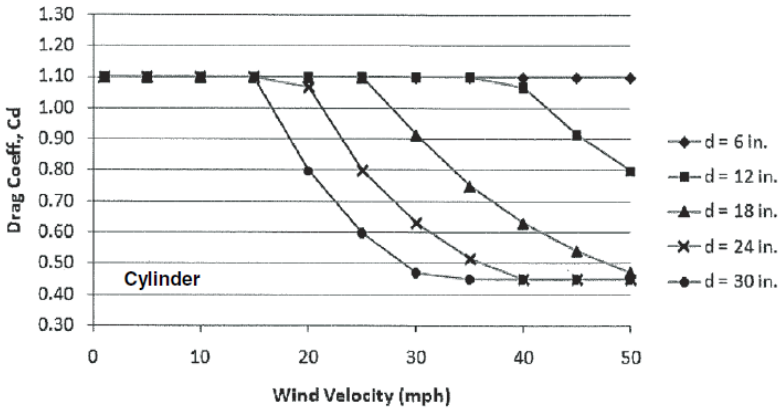

Figure 2.11: Drag Coefficient as a Function of Wind Velocity and Geometric Shape of HMIPs (Connor et al. 2012)

Modal Frequencies

Two methods have been commonly used to evaluate the modal frequencies of the HMIPs. The first method has incorporated Finite Element Analysis (FEA) using commercial software packages like ANSYS, Abaqus, and SAP2000 to conduct an eigenvalue modal analysis in order to obtain the natural frequencies or periods corresponding to different modes of vibration. In the second method, modal frequencies have been extracted from field-measured data using cycle counting in the time domain or peak picking in the frequency domain. These two methods were implemented in previous studies conducted by Chung (2007), Ahearn and Puckett (2010), and Magenes (2011), and reported in the NHCRP Report No. 718 (Connor et al. 2012).

The HMIP studied in Iowa (Chang 2007) was a 150 foot long, 12-sided pole with 0.14 inches per foot taper; the one considered in Wyoming (Ahearn and Puckett 2010) was a 120 foot long, 16-sided pole with 0.14 inches per foot taper; and the one analyzed in Texas (Magenes 2011) was a 150 foot long, 12-sided pole with 0.17 inches per foot taper.

The HMIP in Iowa was analyzed using ANSYS whereas the other two poles in Texas and Wyoming were simulated using SAP2000. Tapered (non-prismatic) beam elements were used to model the poles. Additional masses were lumped at the top to represent the effect of luminaries on dynamic characteristics of the poles. The results of these FEA for different pole designs are listed in Table 2.4. The first four mode shapes obtained using FEA in Iowa study (Chang 2007) are also shown in Figure 2.12. As seen from the results summarized in Table 2.4, despite the differences in the geometry of the HMIPs in different studies, similar frequencies for the first couple of modes have been calculated. Further, note that all these previous research studies have indicated that the first three modes are sufficient to fully characterize the dynamic behavior of HMIPs in a wind environment.

Table 2.4: Modal Frequencies Resulted from FEA (Chang 2007, Ahearn and Puckett 2010, Magenes 2011)

Mode	Chang	Ahearn et al.	Magenes
1	0.338 Hz	0.385 Hz	0.28 Hz
2	1.337 Hz	1.64 Hz	1.2 Hz
3	3.407 Hz	4.22 Hz	3.57 Hz

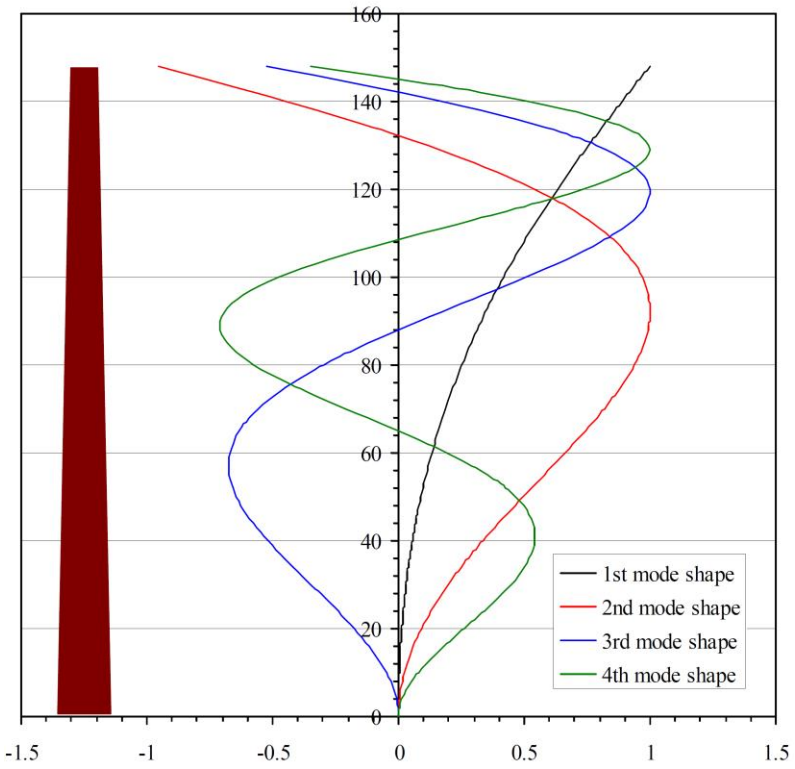

Figure 2.12: The First Four Mode Shapes of a Representative HMIP Obtained in FEA (Chang 2007)

As mentioned above, the natural frequencies of the HMIPs can also be extracted from field-measured data such as acceleration data or strain data. Pluck test data and ambient test data can both be used for extracting natural frequencies. However, in most of the previous studies (Chang 2007, Ahearn and Puckett 2010, Magenes 2011, and Connor et al. 2012), peak picking in the frequency domain using pluck test data was utilized to evaluate natural frequencies of the poles. More specifically, higher frequencies are more accurately obtained using accelerometer data whereas lower frequencies are more precisely evaluated using strain gage data (Connor et al. 2012). Cycle counting is further used to verify the natural frequencies extracted from field-measured data through peak picking process. Filtering the original time-domain signals using a band about the frequencies determined from peak picking gives the approximate number of cycles in a specific time period. The number of cycles divided by the time duration should match the frequencies used to filter the data.

Natural frequencies determined from field-measured data have been shown to agree reasonably well with FEA results. A representative of such agreement is indicated in Table 2.5 (Chang 2007).

Table 2.5: Comparison between Frequencies Evaluated Using Field Data and FEA (Chang 2007)

Mode	FEA	FFT	Difference
1	0.338 Hz	0.305 Hz	10.82 %
2	1.337 Hz	1.294 Hz	3.32 %
3	3.407 Hz	3.333 Hz	2.22 %
4	6.702 Hz	6.396 Hz	4.78 %

Damping Ratios

Three common methods to extract damping ratios in each mode were found in previous literature (Ahearn and Puckett 2010, Connor et al. 2012). These methods include: (1) the log-decrement in the time domain, (2) the half-power bandwidth in the frequency domain, and (3) the Prony method.

Log-decrement in the time domain method is usually used when pluck test data are available. Each individual mode must be first isolated from other modes and the surrounding noise when using log-decrement method. This is done by applying a filter to remove frequencies outside of the modal frequency passbands (Connor et al. 2012). After filtering the data, the steady decay profile of each mode of interest can be used to obtain the damping ratio. The log decrement, δ, is equal to the log of the ratio of two consecutive peaks as shown in Equation 2.5.

$$\delta = ln\left(\frac{v_n}{v_{n+1}}\right) \qquad \textit{Equation 2.5}$$

In Equation 2.5, v_n and v_{n+1} are the values of two consecutive peaks in the steady decay profile of the mode in consideration. The damping ratio, ξ, can then be calculated using Equation 2.6.

$$\xi = \frac{\delta}{\sqrt{4\pi^2 + \delta^2}} \qquad \textit{Equation 2.6}$$

Half-power bandwidth method is applied to the ambient test data in the frequency domain. The ambient test data are usually converted from the time domain to the frequency domain using Fast Fourier Transform (FFT) algorithm, and the resulting curve is commonly referred to as the frequency response curve. In order to calculate the damping ratios, first, a modal frequency is selected from the frequency response curve and its peak value is established. Second, the half-power frequencies corresponding to the modal peak amplitude divided by the root of 2 (f_1 and f_2 in Figure 2.13) are determined on each side of the peak frequency.

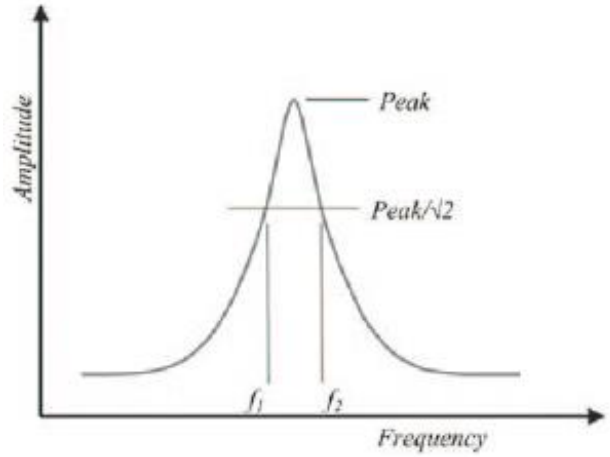

Figure 2.13: Definition of Half-Power Points used in the Half-Power Bandwidth Method (Connor et al. 2012)

The damping ratios can then be calculated using Equation 2.7.

$$\xi = \frac{f_2 - f_1}{f_1 + f_2} \qquad \textbf{Equation 2.7}$$

The half-power bandwidth method can reflect more truly the inherent damping of HMIPs since ambient data streams longer and has more data points than data from a pluck test. Also, the ambient excitations due to natural effects such as wind gusts and vortex shedding are more representative of the true source of cyclic stress causing fatigue damage. This method is also a standard method to calculate damping ratios according to ASTM E756 – Standard Test Method for Measuring Vibration-Damping Properties of Materials (ASTM 2010).

Finally, in the Prony analysis, a sum of damped sinusoids is utilized to approximate real data from a uniformly sampled signal (Ahearn and Puckett 2010). If the sampled signal is approximated as a single damped sinusoid, the signal can be expressed as

$$f(t) = Ae^{\sigma t}\cos(\omega t + \theta) = \frac{A}{2}e^{j\theta}e^{(\sigma + j\omega)t} + \frac{A}{2}e^{-j\theta}e^{(\sigma - j\omega)t} \qquad \textbf{Equation 2.8}$$

By setting $s_1 = \sigma + j\omega$, $s_2 = \sigma - j\omega$, $C_1 = \frac{A}{2}e^{j\theta}$, $C_2 = \frac{A}{2}e^{-j\theta}$, and $\mu_i = e^{S_i T}$ where T is the sampling period, Equation 2.8 can be rewritten as

$$f(k) = C_1{\mu_1}^k + C_2{\mu_2}^k \qquad \textbf{Equation 2.9}$$

Three major steps need to be taken in the Prony analysis to estimate the frequency, phase, and damping of the signal presented in Equation 2.9. First, the least squares problem demonstrated in Equation 2.10 needs to be solved to evaluate parameters a_1 and a_2.

$$\begin{bmatrix} f(2) \\ f(3) \\ \vdots \\ f(N-1) \end{bmatrix} = \begin{bmatrix} f(1) & f(0) \\ f(2) & f(1) \\ \vdots & \vdots \\ f(N-2) & f(N-3) \end{bmatrix} \begin{bmatrix} a_1 \\ a_2 \end{bmatrix} \qquad \textbf{Equation 2.10}$$

Second, the characteristic polynomial in Equation 2.11 will be solved for μ_1 and μ_2, with a_1 and a_2 as coefficients.

$$\mu^2 - a_1\mu - a_2 = (\mu - \mu_1)(\mu - \mu_2) \qquad \textbf{Equation 2.11}$$

Third, C_1 and C_2 are calculated by solving the least squares problem in Equation 2.12.

$$\begin{bmatrix} f(0) \\ f(1) \\ f(2) \\ \vdots \\ f(N-1) \end{bmatrix} = \begin{bmatrix} 1 & 1 \\ \mu_1 & \mu_2 \\ {\mu_1}^2 & {\mu_2}^2 \\ \vdots & \vdots \\ {\mu_1}^{(N-1)} & {\mu_2}^{(N-1)} \end{bmatrix} \begin{bmatrix} C_1 \\ C_2 \end{bmatrix} \qquad \textbf{Equation 2.12}$$

The estimates of parameters A, σ, ω, and θ are then provided using the values of μ_1, μ_2, C_1, and C_2 calculated in Equation 2.13 through Equation 2.16.

$$A = 2|C_1| \qquad \textbf{Equation 2.13}$$

$$s = \frac{1}{T}\ln(\mu) \qquad \textbf{Equation 2.14}$$

$$\sigma = real\{s\}, \qquad \omega = imag\{s\} \qquad \textbf{Equation 2.15}$$

$$\theta = angle(C_1) \qquad \textbf{Equation 2.16}$$

The damping ratio is finally calculated using the formula in Equation 2.17,

$$\xi = \frac{-\sigma}{\sqrt{\sigma^2 + \omega^2}} \qquad \textbf{Equation 2.17}$$

2.4.3 Wind Characteristics of Interest

Four aerodynamic phenomena are often considered in wind-induced vibration analyses of HMIPs: vortex shedding, buffeting, galloping, and flutter. Previous research studies (Chang 2006, NCHRP 2012) have identified the vortex shedding and buffeting as the two major wind loadings affecting the fatigue damage of slender pole structures.

Vortex Shedding

Vortex-induced vibrations (VIV) occur when vortices on each side of an object sheds alternately at a specific frequency, forming a sinusoidal pattern flow wake known as Von Karman Street (Dyrbye and Hansen 1997). The pressure difference caused by the vortices around the object drives the object back and forth creating sinusoidal loads on the object in the direction perpendicular to the wind. In order for VIV to occur, certain parameters including Reynolds number and Strouhal number must be met with certain criteria. Based on previous literature (Connor et al. 2012, Connor and Hodgson 2006), vortex shedding phenomenon is found to mostly affect the pole vibrations in the second and the third modes.

Reynolds Number:

The Reynolds number is defined as the ratio of the inertial force and the viscous force on an object. The Reynolds number is used to identify dynamic similarity for different cross sectional dimensions. Large Reynolds number indicates that inertial forces control the fluid force balance. Small Reynolds number indicates that viscous forces control the fluid force balance. The Reynolds number is generally expressed in the format shown in Equation 2.18.

$$R_e = \frac{\rho \cdot U \cdot D}{\mu} = \frac{U \cdot D}{\nu} \qquad \textbf{\textit{Equation 2.18}}$$

where U is the fluid velocity, ρ is the flow density, μ is the coefficient of fluid viscosity, D is the cross-wind dimension of the cross section, and ν is the coefficient of kinematic fluid viscosity.

Strouhal Number:

The Strouhal number is a dimensionless constant, which relates the vortex shedding frequency, the cross-wind dimension, and the wind velocity as shown in Equation 2.19.

$$S_t = \frac{f_s\, D}{U} \qquad \textbf{\textit{Equation 2.19}}$$

In Equation 2.19, S_t is the Strouhal number, f_s is the vortex shedding frequency, D is the cross-wind dimension, and U is the wind velocity. Reynolds number ranging from 300 to 30000 is where vortex shedding is found to be significant. Strouhal number is approximately 0.21 for a smooth circular cylinder (Figure 2.14). It has also been indicated that the roundness of the section affects the Strouhal number (Connor et al. 2012). In addition, as the number of sides of the pole decreases, the Strouhal number also decreases. The typical Strouhal number for multi-sided HMIPs is reported to be 0.15 to 0.18 (Connor et al. 2012).

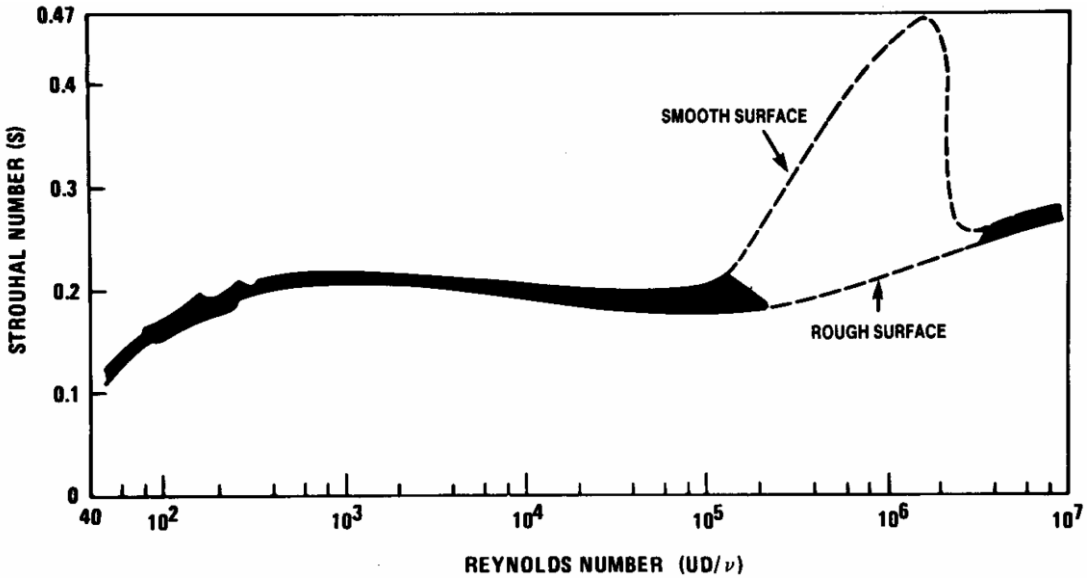

Figure 2.14: Strouhal Number for a Smooth Cylinder (Chang 2007)

Lock-in Phenomenon:

When the frequency of a structure coincides with the vortex shedding frequency, the vortex strength increases which amplifies the induced displacements and stresses of the pole. This resonance behavior is known as the lock-in phenomenon. The lock-in velocity can be calculated using Equation 2.20.

$$U_{lock-in} = \frac{f_n D}{S_t} \qquad \textbf{Equation 2.20}$$

In Equation 2.20, f_n is the natural frequency, D is the cross-wind dimension, and S_t is the Strouhal number. As shown in Figure 2.15, lock-in phenomenon occurs in a range of velocities indicating small variation of wind velocities or pole diameter may still have constant vortex shedding frequency. This allows a certain length of a tapered pole to lock-in at the same frequency.

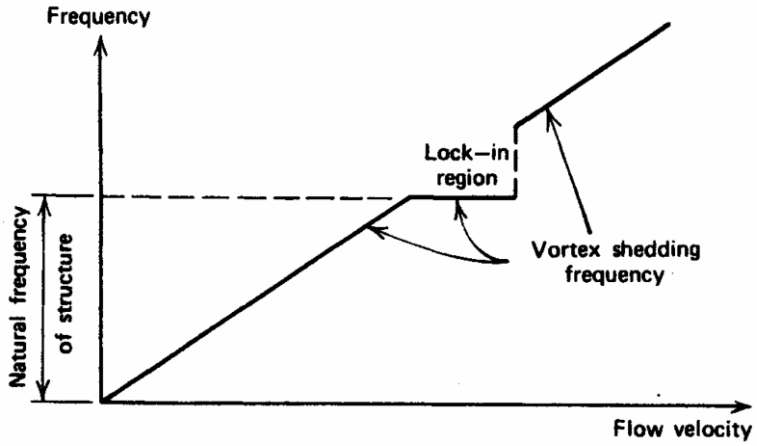

Figure 2.15: Lock-in Phenomenon during the Vortex Shedding Vibrations (Chang 2007)

Scruton Number:

The amplitude of across wind displacement is related to the Scruton number, S_c. The Scruton number is determined using several parameters, as shown in Equation 2.21,

$$S_c = \frac{m\xi}{\rho D^2} \qquad \textbf{Equation 2.21}$$

where m is mass per unit length, ξ is the damping ratio, ρ is the flow density, and D is the cross-wind dimension.

Buffeting

Buffeting is an unsteady loading of a structure caused by fluctuations in wind velocity in the incoming flow. As a result, buffeting induces vibrations in the pole in the direction parallel to the wind direction. In general, large buffeting effect can occur whenever there is high wind turbulence intensity. Wind turbulence intensity is high if the mean speed of wind is high, structural damping is low, and the natural frequencies of the structure are below 1 Hz. Although buffeting is not limited to high wind speeds, the dynamic excitation is normally more significant under high wind speed.

According to the Iowa study (Chang 2007), the relationship between the fluctuating wind loads and the upstream turbulent wind in frequency domain can be defined through aerodynamic admittance function. However, due to the complex turbulent wind flow around a structure, the aerodynamic admittance function can only be obtained through wind tunnel experiments. An approximate expression of the admittance function (Equation 2.22) for an airfoil was experimented and verified by Jancauskas and Melbourne (1986)

$$\chi^2_{aero}(k) = \frac{1}{1+5k} \qquad \textbf{Equation 2.22}$$

where k is the reduced frequency defined as,

$$k = \frac{n\pi c}{U} \qquad \textit{Equation 2.23}$$

In Equation 2.23, n is the frequency, c is the chord length of an airfoil, and U is the wind velocity.

2.4.4 Wind Behavior of In-Service HMIPs

This section reviews several field studies conducted in the past (Chang 2007, Ahearn and Puckett 2010, Magenes 2011, and Connor et al. 2012) to quantify the wind behavior of in-service HMIPs. For each study, the monitoring campaign is reviewed, and the field data are presented and discussed. In general, field monitoring of HMIPs is separated into two parts: pluck test and long-term monitoring. Pluck test is done by exciting the pole by pulling and releasing a cable that is connected to the pole at a certain height. As mentioned previously, the frequency content of the vibration gives the basic modal frequencies while the decrement of the amplitude gives the damping information. Long-term monitoring usually consists of wind speed and wind direction along with the vibration-induced stresses at the bottom of the pole. Raw data may be collected under certain triggering events such as a critical wind velocity that results vortex-induced vibrations. Long-term stress records are usually saved as histograms using rain-flow counting algorithm. Long-term wind data may be saved as one-minute or-three minute averages.

Chang 2007

In the field study reported by Chang (2007), two HMIPs were monitored near Mason City in Iowa from October 2004 to January 2006 (Figure 2.16). Two poles (12 sided, 148 ft. high, having three discrete sections and a taper ratio of 0.14 in./ft) were located two miles apart in an open terrain. Pole 1 and the auxiliary wooden pole near it were instrumented to monitor and record wind-induced vibrations of pole 1. Pole 2 was instrumented to capture the wind profile using anemometers distributed along its height. Strain gages were also installed on both poles to record the vibration-induced stresses.

(a) Pole 1 (b) Pole 2

Figure 2.16: The Two High Mast Poles Monitored in Mason City, Iowa (Chang 2007)

a. Setup and Instrumentation

The general setup of the monitoring system used in the Iowa study is shown in Figure 2.17. The instruments used in the field monitoring included data acquisition system, strain gages, accelerometers, anemometers, and video equipment. Pole 1 had no crack and no retrofit prior to the field monitoring whereas Pole 2 was retrofitted with steel jacket at the base (Figure 2.18).

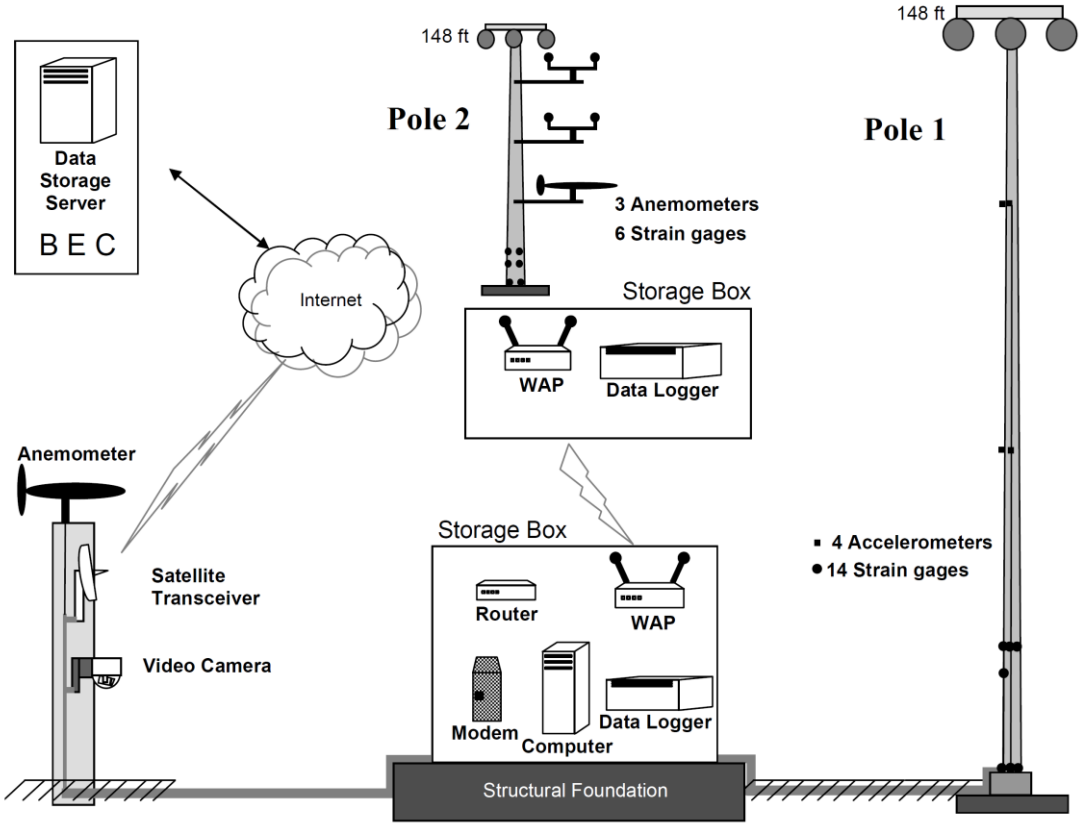

Figure 2.17: General Setup of the Long-Term Monitoring System in the Iowa Study (Chang 2007)

(a) Pole 1 (b) Pole 2

Figure 2.18: Retrofitted and Un-Retrofitted Poles Monitored in the Iowa Study (Chang 2007)

Fourteen strain gages (Model LWK-06-W250B-350) and four single axis accelerometers (Model 3701G3FA50G) with a peak acceleration of 50 g were installed on pole 1 (Figure 2.19) to monitor vibrations and stresses of the pole. Strain gages were attached on the pole at 3 in. and 5.75 ft above the base. The accelerometers were located at 43.25 ft and 120 ft above the base on orthogonal faces of the pole. A propeller anemometer (Model Young 5103) was installed on the top of a 33 ft-tall wooden pole located near pole 1 to record the wind speeds and directions. A data acquisition system (Campbell Scientific CR9000) was used to record strains for one minute when wind velocity was at a specific speed and to record 3-min wind velocity and direction. A camera was installed on the wooden pole to record vibrations of pole 1.

Six strain gages (Model LWK-06-W250B-350) were installed on pole 2 (Figure 2.19) at 3 in., 4 ft, and 4.92 ft above the base to observe the effect of the steel jacket reinforcement. To obtain the wind profile, one propeller anemometer (Model Young 5103) and two cup anemometers (Model Young 3101) were installed on pole 2 at 33 ft, 86.5 ft, and 140 ft, respectively. The data acquisition system (Campbell Scientific CR5000) was used to record strains for one minute when wind velocity was at a specific speed and to record 1-min wind velocity and direction.

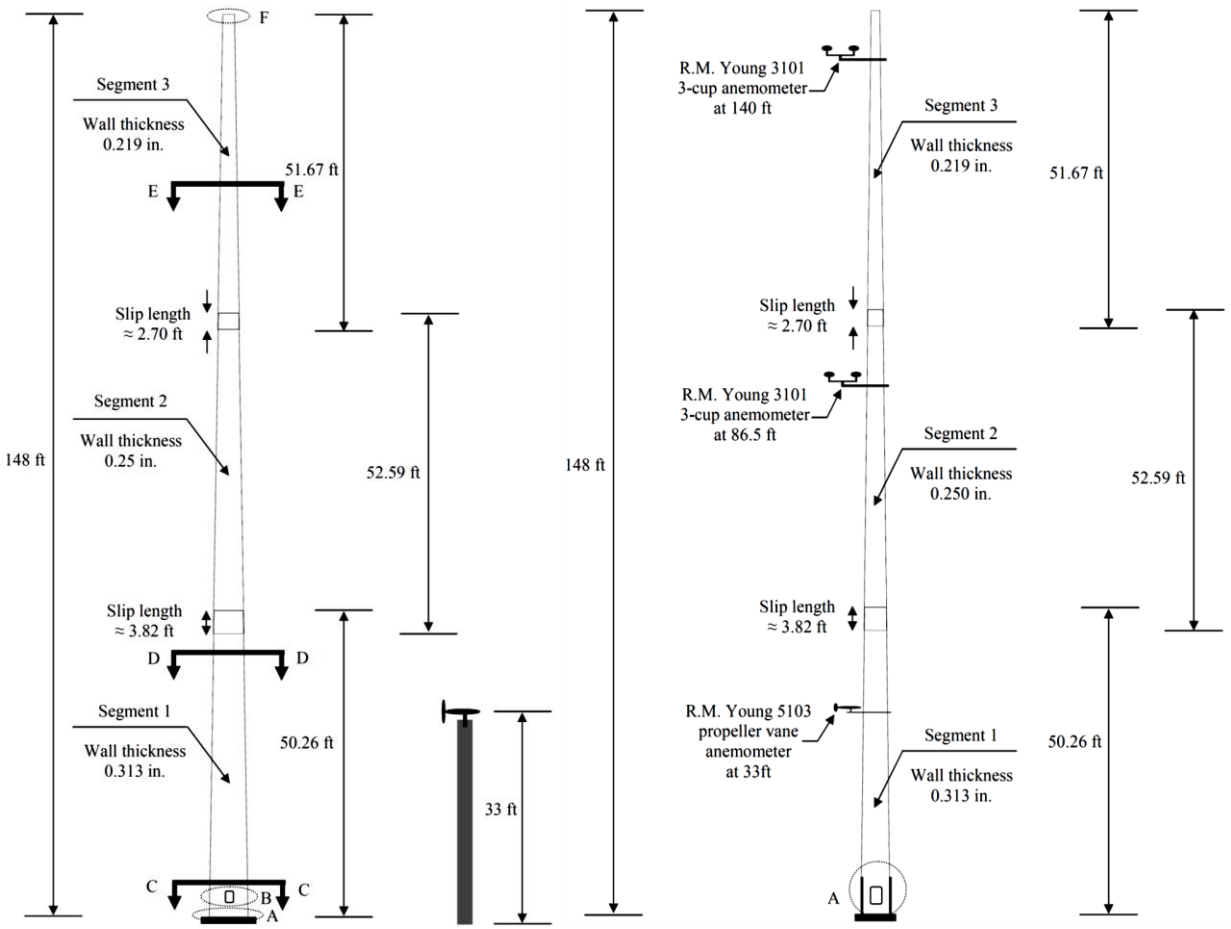

Figure 2.19: Details of the Instrumentation Schemes in the Iowa Study (Chang 2007)

b. Analysis of Field Data

Pluck Test:

Fast Fourier Transform (FFT) analyses were conducted on the pluck test data to evaluate the basic four vibration frequencies. The modal frequencies evaluated from the test data were further compared to the ones calculated using the Finite Element software ANSYS. Results from this comparison are summarized in Table 2.6. Following the procedure of log-decrement described in Section 2.3.2, modal damping ratios were also calculated using the pluck test data. Calculated values for modal damping ratios are presented in Table 2.6.

Table 2.6: Modal Frequencies and Damping Ratios for the Poles Monitored in the Iowa Study (Chang 2007)

Mode	FEA	FFT	Difference	Damping Ratio
1	0.338 Hz	0.305 Hz	10.82 %	0.60 %
2	1.337 Hz	1.294 Hz	3.32 %	0.17 %
3	3.407 Hz	3.333 Hz	2.22 %	0.27 %
4	6.702 Hz	6.396 Hz	4.78 %	0.30 %

Long-Term Monitoring:

The average wind speeds and directions were obtained using the propeller anemometers installed on both poles. As shown in Figure 2.20, wind roses generated from the field data clearly indicate the prevailing wind directions and the magnitude of the prevailing winds.

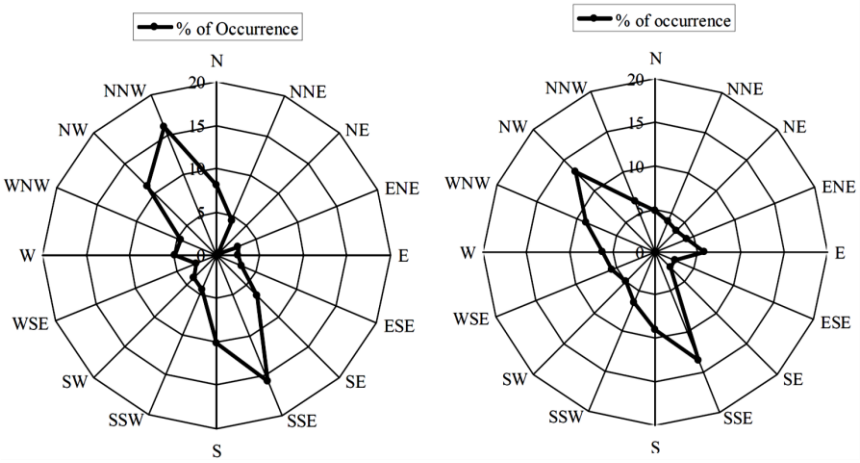

(a) Pole 1 (b) Pole 2

Figure 2.20: Wind Rose Generated for the Two Poles Monitored in the Iowa Study (Chang 2007)

To better represent the most dominant wind speed ranges, probability density graphs are also generated from the wind data. Figure 2.21 plots representative of such graphs showing the wind speed distribution for 3-min wind velocity data from pole 1. The probability density graph in Figure 2.21 clearly shows that the wind speeds in the range of 5 mph to 8 mph are the most dominant wind speeds observed for the pole 1 monitored in the Iowa study.

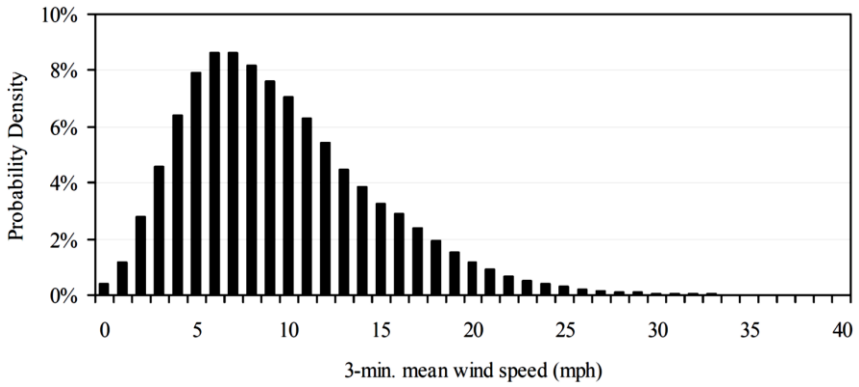

Figure 2.21: Probability Density Graph for the Wind Velocity Data from Pole 1 in the Iowa Study (Chang 2007)

Utilizing the wind speed data collected by the three anemometers installed on pole 2, the wind profile and the roughness length are further evaluated following Equation 2.24 and Equation 2.25, respectively.

$$\frac{U(z_1)}{U(z_2)} = \left(\frac{z_1}{z_2}\right)^{\alpha} \qquad \textbf{Equation 2.24}$$

where $U(z)$ is the mean wind velocity at height z above the ground and α is the terrain factor.

$$U(z_g, z_0) = 2.5u_*(lnz_g - lnz_0) \qquad \textbf{Equation 2.25}$$

where $U(z_g, z_0)$ is the mean wind velocity at height z_g, z_g is the height above z_0, z_0 is the roughness length, and u_* is the shear friction velocity of the flow.

Turbulence intensities for along-wind and across-wind directions are determined using Equation 2.26.

$$I_{\bar{z}} = c \cdot \left(\frac{33}{\bar{z}}\right)^{1/6} \qquad \textbf{Equation 2.26}$$

where $I_{\bar{z}}$ is the turbulence intensity at height $\bar{z}$, and c is the exposure coefficient. As seen in Table 2.7, good agreement can be observed between the values for the wind parameters calculated in the Iowa study (Chang 2007) and the values reported in the literature (e.g. Simiu and Scanlan 1996).

Table 2.7: Wind Parameters Determined from the Long-Term Monitoring Campaign in the Iowa Study (Chang 2007)

Parameter	Field	Reference Values (Simiu and Scanlan 1996)
z_0	0.213 ft (6.5 cm)	2 ~ 7 cm
α	0.145	0.12 ~ 0.15
I_u	14 %	20 %
I_w	14 %	0.8 I_u

The significance of buffeting wind loads is observed in the steady increase of stress ranges with wind speeds in both along-wind and across-wind directions when the wind speed is above 10 mph (Figure 2.22). The largest stress-range time history is observed under 35 mph wind at which the pole vibrates in the first mode. The large stress ranges are therefore assumed to result from the natural wind gust. The lock-in speed of the vortex shedding is determined using the cross dimension at peak normalized mode (anti-node) for each vibration mode. Vortex-shedding vibration in the first three modes are estimated to occur at wind speed of 0.6 mph, 5.11 mph, and 9.97 mph respectively at 33 ft above the ground. The accelerations recorded at a mean wind speed of 5.5 mph also shows the pole vibrating in the second mode at the frequency of 1.3 Hz (Figure 2.23). Although vortex shedding induced vibrations in the third mode are also observed in a wind speed ranging from 8 mph to 20 mph, the second mode vibrations are found to be the most common. The stress ranges recorded under second mode vibrations are observed to exceed the Constant Amplitude Fatigue Limit (CAFL) for Category E′ in AASHTO (AASHTO 2013).

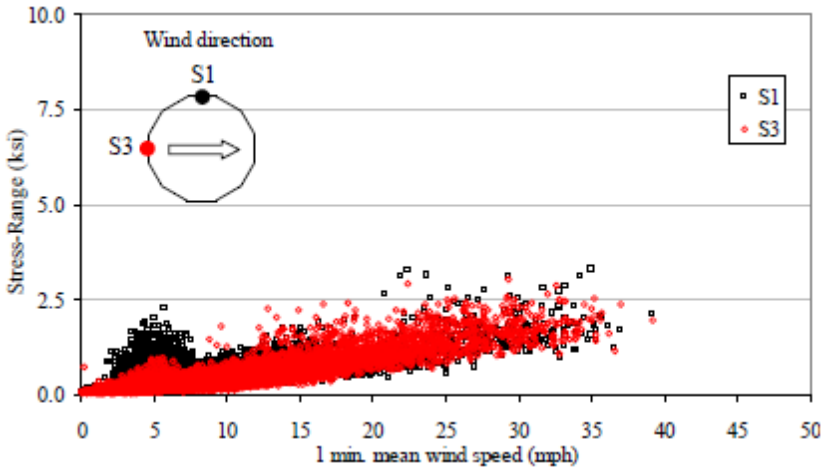

Figure 2.22: Stress Range versus Wind Speed Data Measured for Both Along-Wind and Across-Wind Directions in the Iowa Study (Chang 2007)

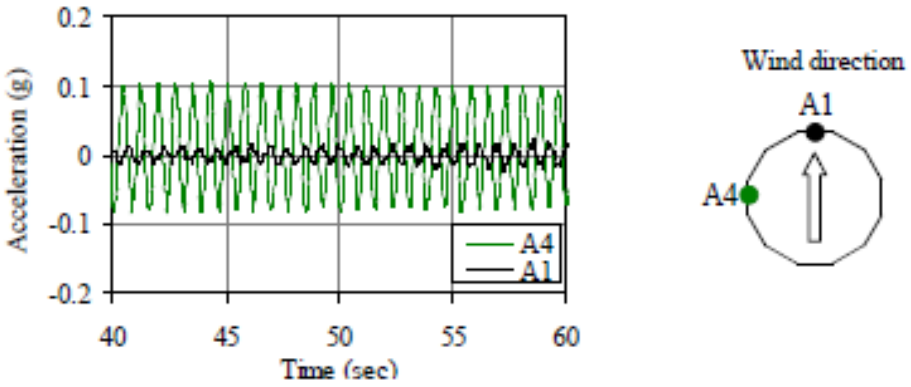

Figure 2.23: Lock-in Vibrations in Second Mode (1.3 Hz) for a 5.5 mph Wind as Observed in the Iowa Study (Chang 2007)

The stress range histogram was developed based on the rain-flow cycle counting algorithm (Miner 1945). The stress cycles smaller than 0.5 ksi were discarded to eliminate errors resulted from data acquisition noise. Figure 2.24 shows a stress range histogram where S1 and S12 are on the dominating wind direction while S10 and S12 are on the orthogonal direction.

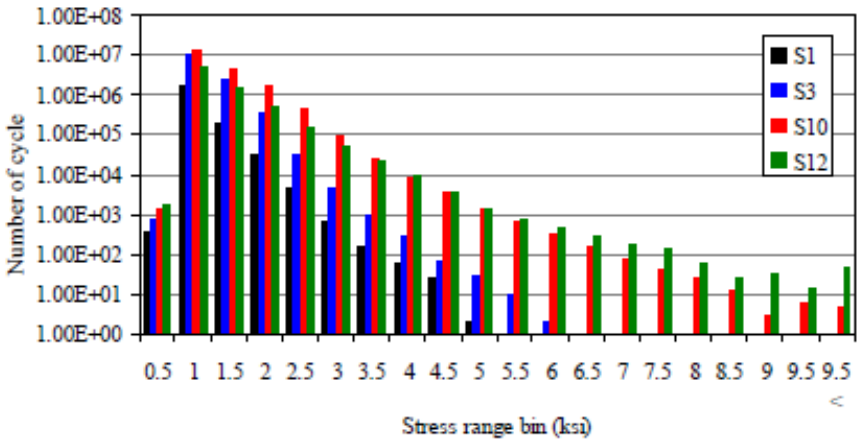

Figure 2.24: Stress Range Distribution for Across-Wind and Along-Wind Directions as Observed in the Iowa Study (Chang 2007)

Ahearn and Puckett 2010

a. Setup and Instrumentation

In the field study reported by Ahearn and Puckett (2010), two HMIPs, referred herein as pole 3 and pole 4, were monitored near Laramie in Wyoming (Figure 2.25). These two poles (16 sided, 120 ft. high, having three discrete sections and a taper ratio of 0.14 in./ft) were located 550 ft apart from each other and at the I-80/US287 interchange in an open terrain. Strain gages and accelerometers were installed on both poles to monitor the stresses and the vibrations. Only one anemometer was installed on pole 3 since two poles were in close proximity. The influence of moving vehicles on the highway was observed in the difference of induced-vibrations between the two poles since pole 4 was relatively closer to the highway than was the pole 3.

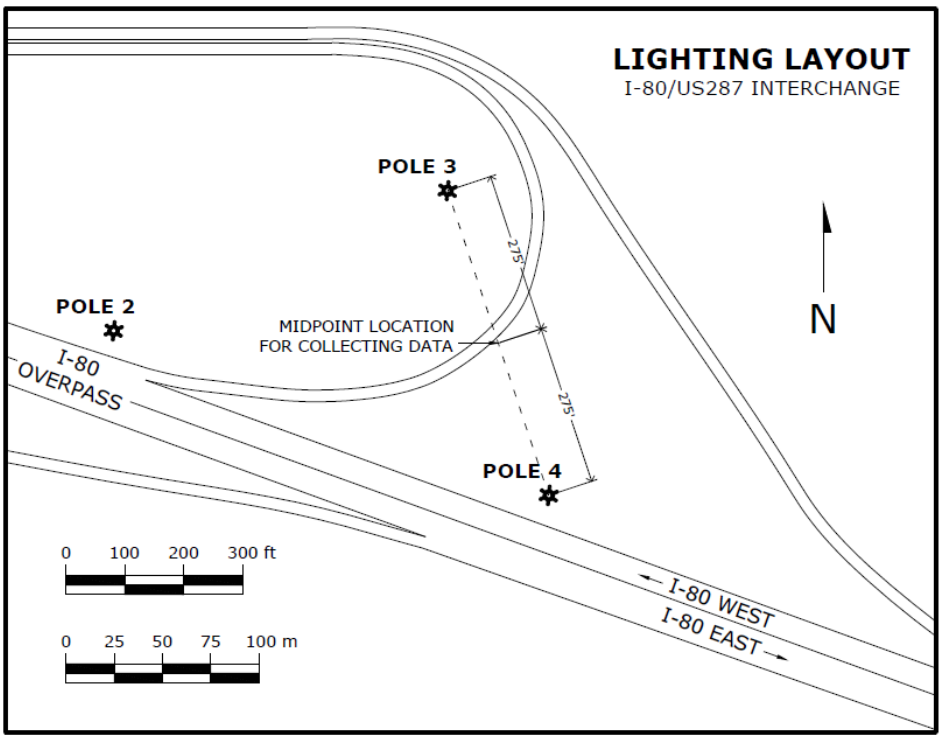

Figure 2.25: Locations of the Poles 3 and 4 Monitored in the Wyoming Study (Ahearn and Puckett 2010)

Four strain gages (Model C2A-06-250LW-350) were instrumented individually on both poles at 60 in. above the ground (15 in. above the hand hole). Four wireless tri-axial accelerometers (MicroStrain G-Link) were located at 41 ft. and 56 ft. on each pole respectively. A propeller anemometer (Model Young 05103VP) was installed on pole 3 at 33 ft. to record the wind speeds and directions. A USB base station (Agile-Link 2.4 GHz) was used to trigger the wireless nodes to retrieve data when critical wind speed was recorded. An additional accelerometer was also installed at the base of pole 4 and nearby concrete slab to measure vertical and lateral vibrations induced by vehicle traffic. Pole 3 was later monitored following the application of several vortex-shedding mitigation methods. These methods consisted of installing ribbons, helical strakes, perforated shroud, and the increase in surface roughness. More information on the mitigation methods adopted by Ahearn and Puckett (2010) is provided in Section 2.4.6.

b. Analysis of Field Data

Pluck Test:

Fast Fourier Transform (FFT) analyses were conducted on the pluck test data to determine the first four modal frequencies. Modal frequencies were also calculated using a series of Finite Element Analyses (FEA) on SAP2000. A comparison between modal frequencies determined using pluck test data and those calculated using SAP2000 simulations are presented in Table 2.8. The differences in the modal frequencies evaluated from pluck tests and simulations are attributed to the assumption of fixed-base condition in the SAP model of the poles (Ahearn and Puckett 2010).

Table 2.8: Natural Frequencies for the First Four Vibration Modes of the Poles Monitored in the Wyoming Study (Ahearn and Puckett 2010)

Mode	FEA (SAP)	FFT	Difference
1	0.385 Hz	0.350 Hz	9.0 %
2	1.640 Hz	1.500 Hz	8.6 %
3	4.220 Hz	3.800 Hz	9.9 %
4	8.270 Hz	7.500 Hz	9.3 %

Long-Term Monitoring:

The main emphasis of the long-term monitoring in the study conducted by Ahearn and Puckett (2010) was on Mode 3 vibrations since the mean wind speed in Laramie was close to the critical wind velocity causing the vortex shedding. The wind speed causing Mode 3 lock-in vibrations was determined to be in the range of 10.4 mph to 18.8 mph (the theoretical critical wind velocity at 33 ft. above the ground was calculated as 11.8 mph). Figure 2.26 shows the vibrations in Mode 3 under a mean wind speed of 18.7 mph.

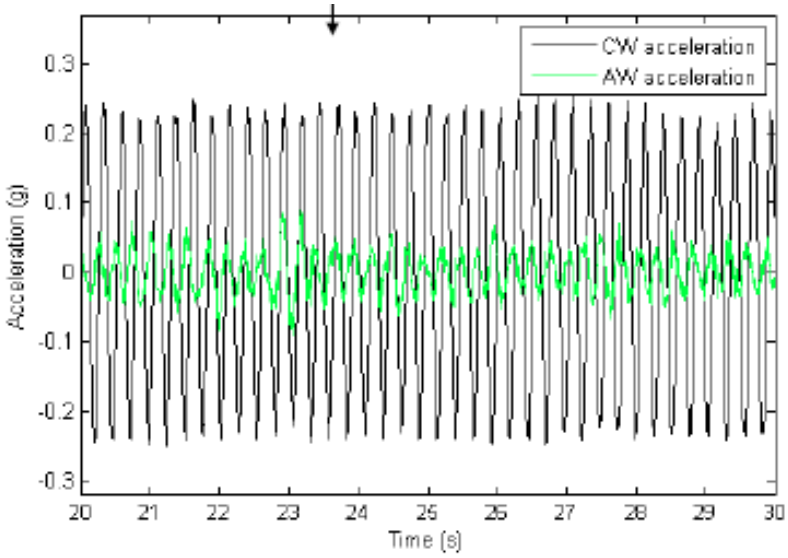

Figure 2.26: Mode 3 Vibrations at 3.8 Hz for Both Along-wind and Across-wind Directions (Ahearn and Puckett 2010)

Magenes 2011

a. Setup and Instrumentation

In the study conducted by Magenes (2011), five HMIPs were instrumented and monitored at four different locations across Texas (Austin, El Paso, Corpus Christi, and Lubbock) (Figure 2.27). These five poles (12 sided, 150 ft high, having three discrete sections and a taper ratio of 0.17 in./ft) had basically the same geometry and slightly different connection details (unlike the other poles, the pole in Corpus Christi had ground sleeves, refer to Section 2.1.1 for details of TxDOT HMIPs). These five different regions were selected to represent different wind environments throughout Texas. More specifically, El Paso was selected as a representative of wind conditions near the deserted mountains; Corpus Christi was selected as a representative of Texas coast; and Lubbock was selected as a representative of Texas high plains.

Each pole was instrumented with an anemometer and four strain gages to monitor the wind environment as well as the induced stresses at the shaft-to-base plate of the poles.

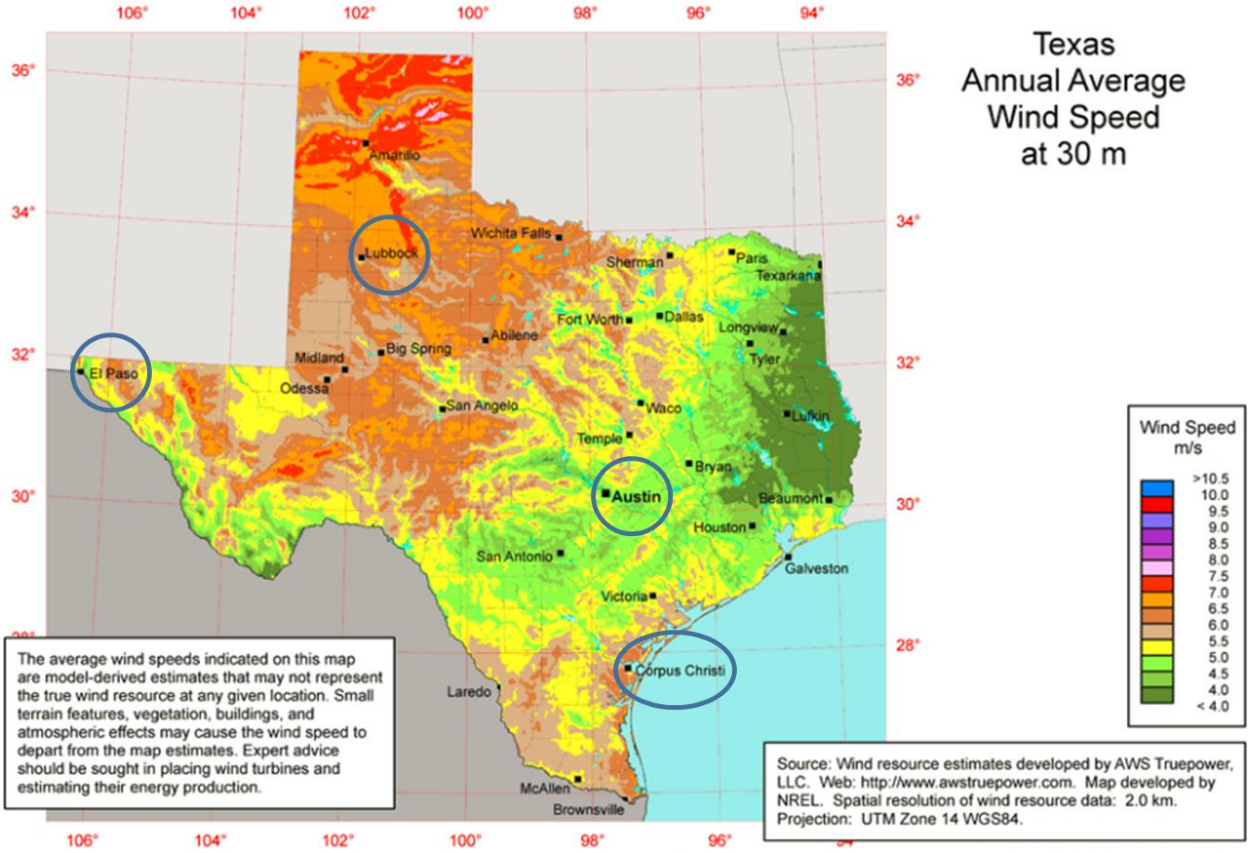

Figure 2.27: Locations of the Monitored Poles in the Texas Study on a Map of Average Wind Speed Distribution in Texas (windexchange.energy.gov)

In the Texas study reported by Magenes (2011), four strain gages were installed on each orthogonal face of the poles at 76 in. above the base. A propeller anemometer (Model Young 05103) was installed at 35 ft. above the ground on a 66 in. extended arm attached to the pole to measure the wind speed and direction. The data acquisition system (CompactRIO 9024 from National Instruments) was used to collect raw data (at 50 Hz) and to perform stress rainflow analysis on the data. A cellular modem (Airlink Raven X) was used for remote access to the CompactRIO through GPRS/EDGE wireless network. A charge controller (Morningstar Sunsaver 6) was employed to supply the power from a 130 Ah battery (Deep cycle by Trojan) connected with a 50 W nominal solar panel (BP Solar BP350J) to the compactRIO data acquisition system. Voltage of the battery was also monitored with CompactRIO to make sure the power was sufficient during the monitoring period.

b. Analysis of Field Data

The data were only recorded for wind speeds in the range of 7 mph to 20 mph (i.e. for the wind speed range causing vortex shedding) (Magenes 2011). Figure 2.28 shows the across-wind

vibrations in the second mode resulted from a 7 mph wind. The period of vibrations in Figure 2.28 is 0.87 seconds, and the resulting stress range is 0.2 ksi. Figure 2.29 further shows that, under a 25 mph wind, a mixed mode across-wind vibrations consisting of the first and third modes is observed. The smaller than 0.2 ksi amplitudes of stress range indicate the small contribution from the third mode. Figure 2.30 shows the along-wind vibrations at a high wind velocity around 50 mph resulting first-mode vibrations with a 7 ksi stress range. This high stress range along the wind direction is mainly due to the buffeting effect.

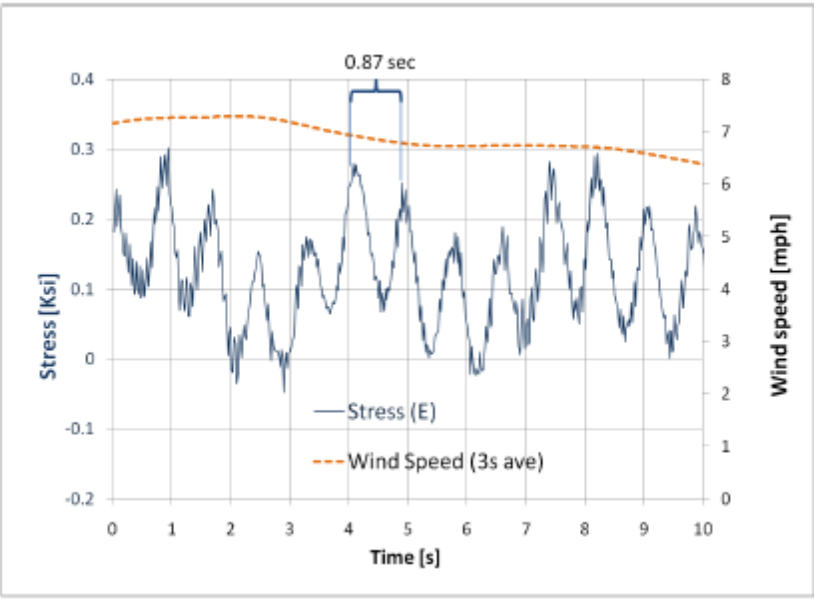

Figure 2.28: Second-Mode Across-Wind Vibrations for a 7 mph Wind as Observed in the Texas Study (Magenes 2011)

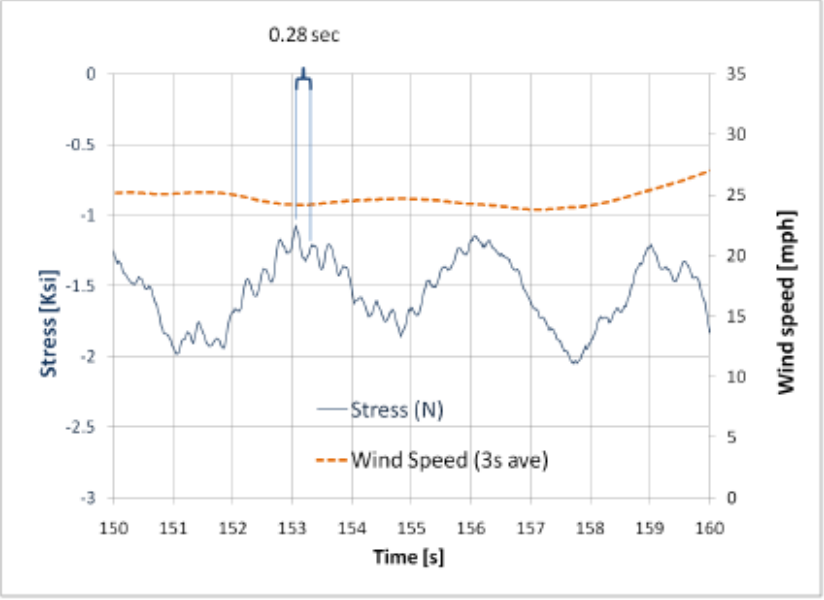

Figure 2.29: First and Third Mode Across-Wind Vibrations for a 25 mph Wind as Observed in the Texas Study (Magenes 2011)

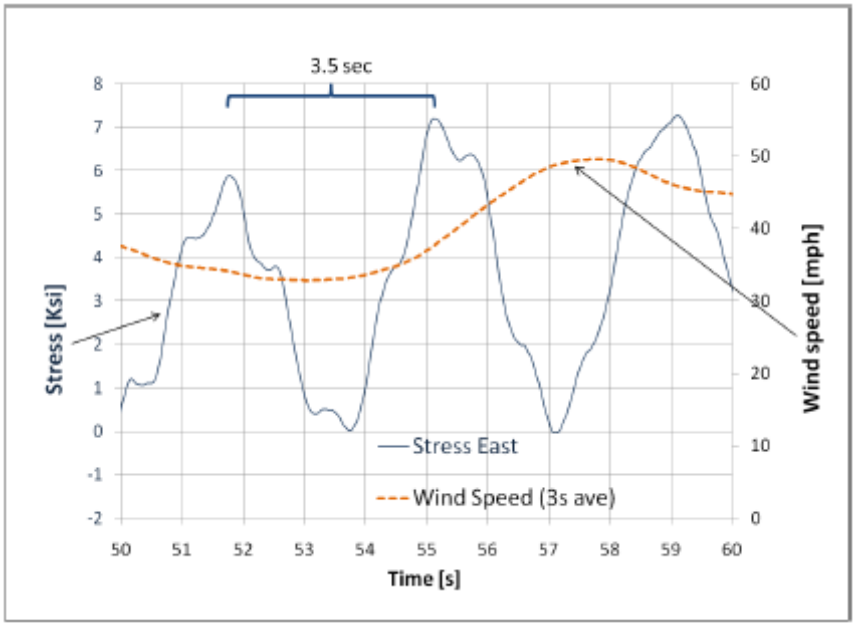

Figure 2.30: First Mode Along-Wind Vibrations for a 50 mph Wind as Observed in the Texas Study (Magenes 2011)

The stress ranges and their corresponding average wind speeds measured in both the Texas study (Magenes 2011) and the Iowa study (Chang 2007) are shown and compared in Figure 2.31. The reason for the smaller stress ranges corresponding to the wind speeds below 10 mph in the study by Magenes (2011) is believed to be the higher taper ratio (0.17 in./ft) and larger cross section at the base (33 in.) of the instrumented poles. The constant amplitude fatigue limit (CAFL) of 0.5 ksi was proposed since no sudden change of fatigue life would occur for the stresses smaller than 0.5 ksi.

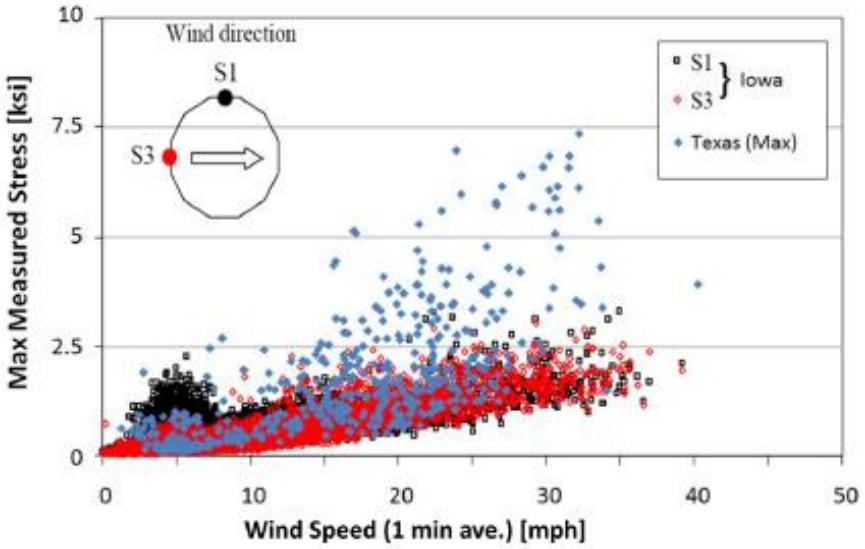

Figure 2.31: Stress Range distribution Measured in both the Texas and Iowa Studies (Magenes 2011, Chang 2007)

2.4.5 Wind Tunnel Studies of HMIPs

Several researchers performed wind tunnel tests on HMIP specimens to quantify wind- and geometry-related parameters required to study the vortex shedding and buffeting phenomena (Section 2.4.3). These wind tunnel studies are briefly presented and discussed in this section.

Chang 2007

In the study conducted by Chang (2007), the wind tunnel tests were designed to obtain the six major wind- and geometry-related parameters for dodecagonal (12 sided) cylinders, which were not well defined in the AASHTO code. The drag coefficient and the slope of lift coefficient were determined through static wind tunnel tests. The Strouhal number, Lock-in velocity range, and Scruton number were determined in dynamic wind tunnel tests. Finally, the aerodynamic admittance function was obtained from buffeting wind tunnel tests requiring gust generator to produce harmonic gust oscillations. The test specimen was a wooden dodecagonal (12 sided) cylinder with a diameter of 4 inches and a length of 20 inches. The specimen was installed inside a suction type wind tunnel of size 3 feet by 2.5 feet by 8 feet with a maximum speed of 180 mph.

The static wind tunnel test demonstrates how the drag coefficient varies with Reynolds and how the lift coefficient varies with wind attacking angles. As seen in Figure 2.32, for Reynolds number exceeding 1.5×10^6, the drag coefficient converges approximately to 1.45 and 1.56 for corner and flat orientations, respectively. Figure 2.32 also indicates that flat orientation has a slightly higher Reynolds number than that of a corner orientation. In addition, the slope of the lift coefficient, defined as the ratio of lift coefficient and wind attacking angle, was observed to be approximately -0.7π and 0.5π for flat and corner orientations, respectively.

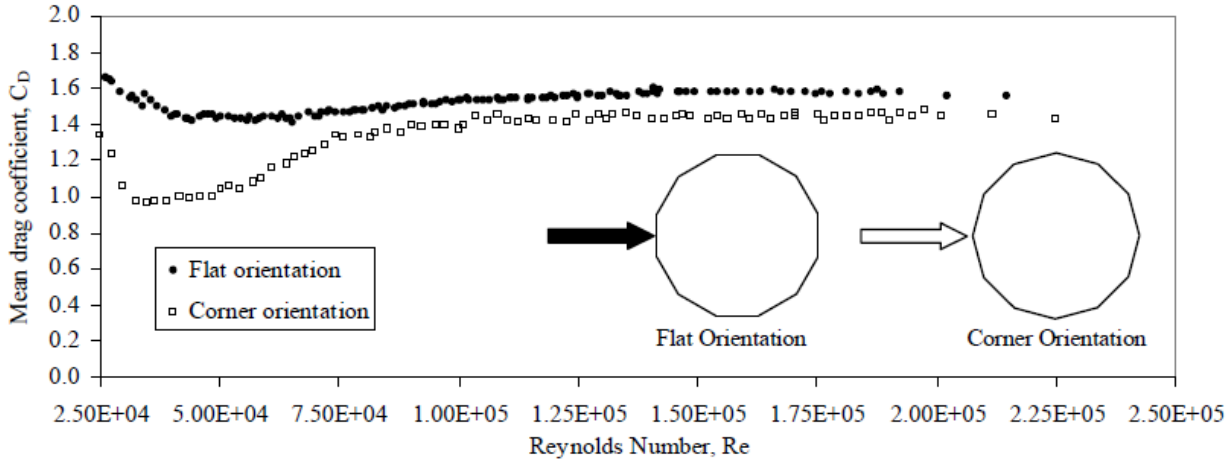

Figure 2.32: The Drag Coefficient of the 12 Sided Cylinder Obtained in Static Wind Tunnel Tests (Chang 2007)

The dynamic wind tunnel tests were performed to evaluate the Strouhal number, the lock-in range, and the Scruton number. The lock-in range of the reduced velocity (U/nD) and normalized frequency (f_s/f_n) is plotted and shown in Figure 2.33. As indicated in Figure 2.33, the Strouhal number was found to be approximately 0.2, and the lock-in occurred for reduced velocities between 5 and 7. Further, the relation between Scruton number, S_c, and the reduced amplitude, y_0/D, from the experiments conducted by Chang (2007) is plotted in Figure 2.34. For

the sake of comparison, the data from wind tunnel tests on circular cylinders are presented in Figure 2.34 as well.

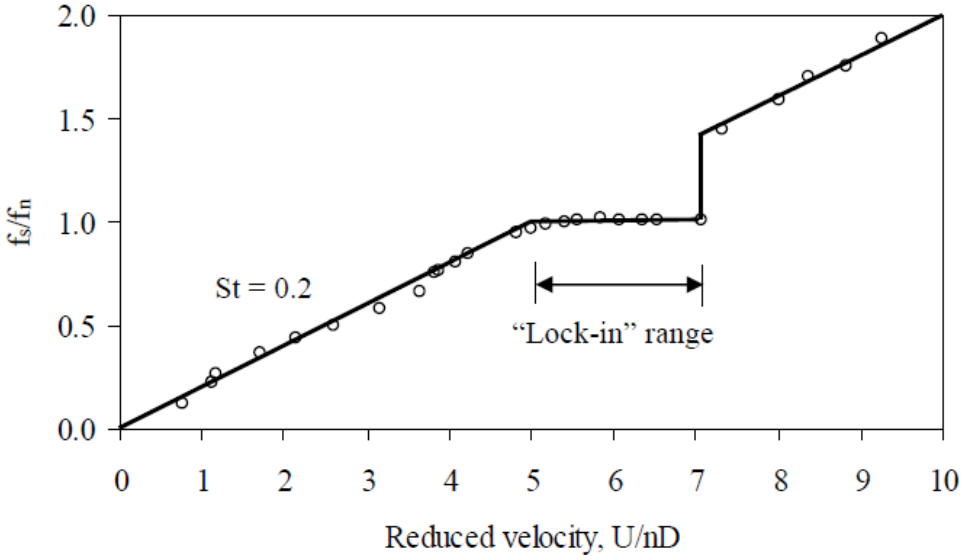

Figure 2.33: The Lock-in Range for the 12 Sided Cylinder Obtained in Dynamic Wind Tunnel Tests (Chang 2007)

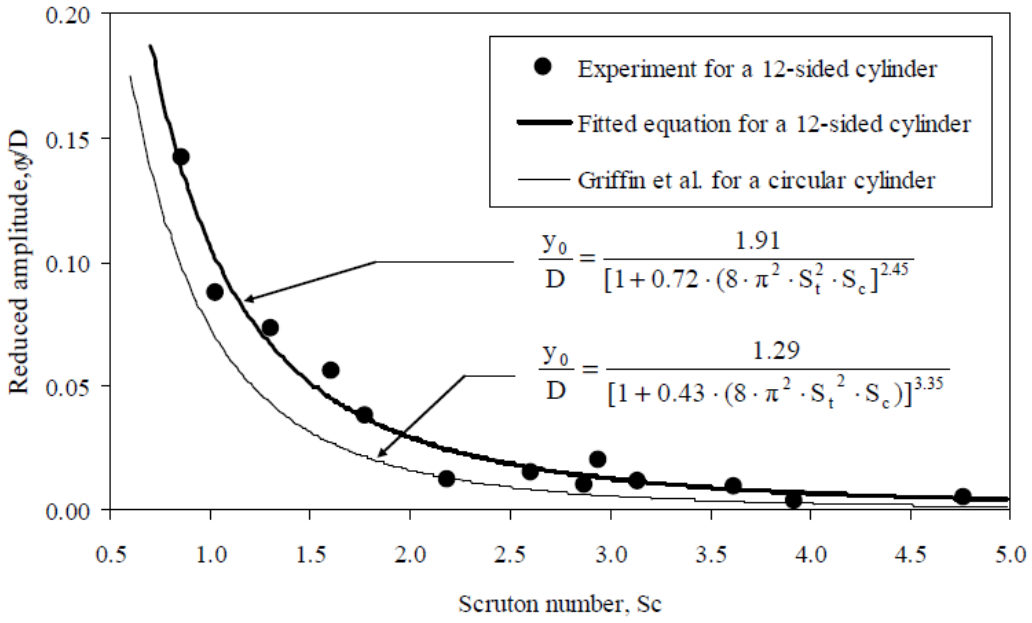

Figure 2.34: Reduced Amplitude as a Function of Scruton Number for a 12 Sided Cylinder Obtained in Dynamic Wind Tunnel Tests (Chang 2007)

In the buffeting wind tunnel tests, the aerodynamic admittance functions for along-wind and across-wind directions, $\chi_u^2(n)$ and $\chi_w^2(n)$, were obtained in the frequency domain using power spectral density function for buffeting forces, $S_{F_b^x F_b^x}(n)$ and $S_{F_b^y F_b^y}(n)$, and power spectral density functions for across-wind velocity fluctuations, $S_{uu}(n)$ and $S_{ww}(n)$. The power spectral

density function are reported in literature and presented in Equation 2.27 and Equation 2.28 (Dyrbye and Hanson 1997):

$$S_{F_b^x F_b^x}(n) = \left(\frac{1}{2}\cdot\rho\cdot U^2\cdot A\cdot C_D\right)^2\cdot\frac{4\cdot S_{uu}(n)}{U^2}\cdot\chi_u^2(n) \qquad \textbf{Equation 2.27}$$

$$S_{F_b^y F_b^y}(n) = \left[\frac{1}{2}\cdot\rho\cdot U^2\cdot A\cdot\left(C_D+\frac{dC_L}{d\alpha}\right)\right]^2\cdot\frac{4\cdot S_{ww}(n)}{U^2}\cdot\chi_w^2(n) \qquad \textbf{Equation 2.28}$$

The aerodynamic function resulted from the experiment for both along-wind and across-wind directions are plotted in Figures 2.35 and 2.36 in comparison with flat plate and airfoil experimental data from previous literature, respectively. The fitted curves to the experimental data presented in Figures 2.35 and 2.36 are needed in modeling of the pole vibrations under buffeting wind loads.

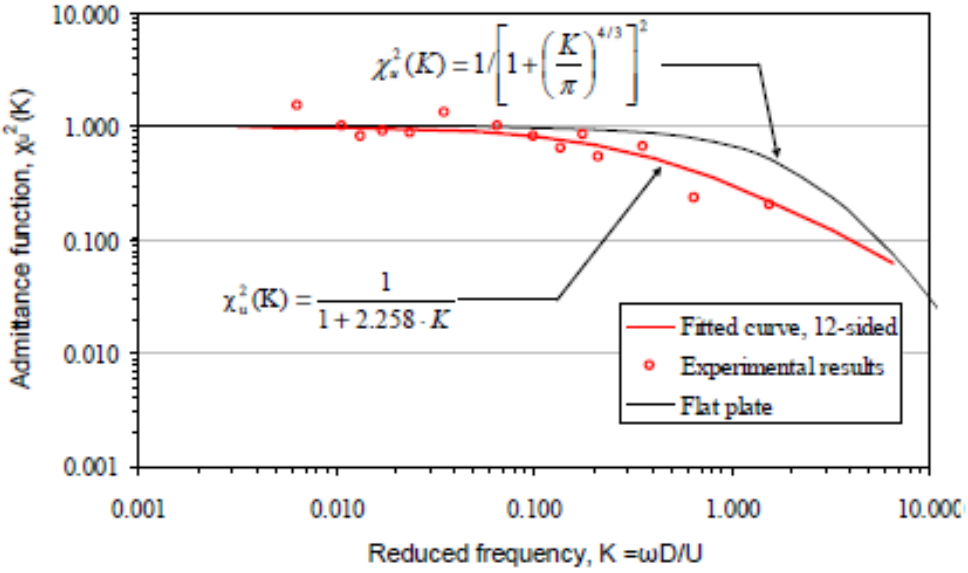

Figure 2.35: Along-Wind Admittance Function for a 12 Sided Cylinder Obtained in Buffeting Wind Tunnel Tests (Chang 2007)

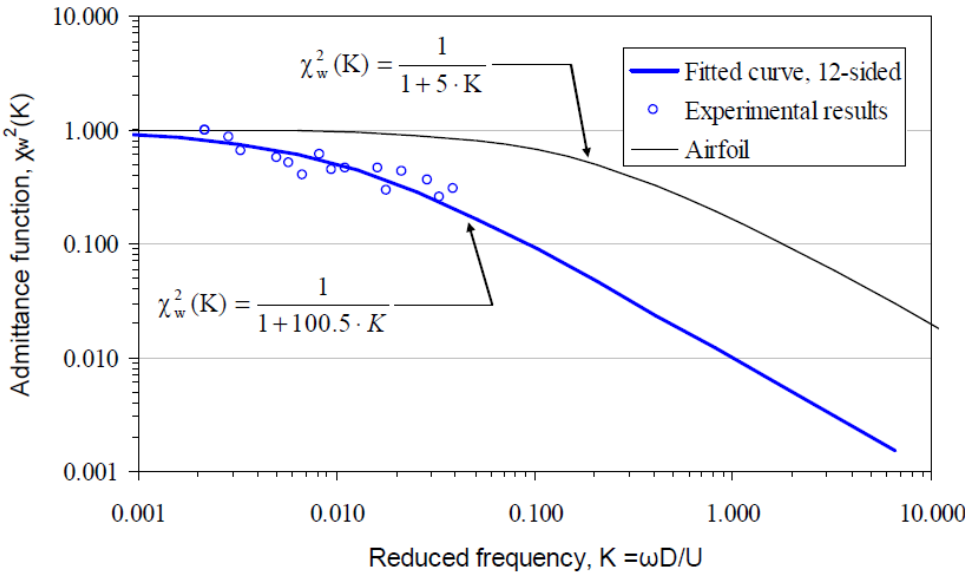

Figure 2.36: Across Wind Admittance Function for a 12 Sided Cylinder Obtained in Buffeting Wind Tunnel Tests (Chang 2007)

Connor et al. 2012

Connor et al. (2012) designed and performed wind tunnel tests to study the pressure and the velocity field around an HMIP model. Several 8-sided, 12-sided, and 16-sided tapered models were used to examine the surface and the near wake behavior of the models in a wind environment. The results at the surface and the associated force were used for quantifying the design loads in future design of poles. Oscillation forcing rig was instrumented to imitate the movement of the specimens. Certain locations were probed with hot-wire anemometry to measure wind velocity. Pressure scanner was used for measuring pressure fluctuations on the surface of the pole. Smoke wand was installed to identify the location of separated shear layer.

Test results from the pressure scanner found that due to the sharp edges of 12 sided cylinder, separation of the shear layer was farther upstream than that expected for a circular cylinder. The results from the instrumented hot-wire anemometry further showed that the corner upwind configuration was more susceptible to lock-in phenomenon than face upwind configuration. Frequency of the flow behind the specimen locks-in together at different diameter location behind the tapered pole indicating lock-in phenomenon still had an effect on tapered poles.

2.4.6 Simulation of Wind-Induced Response of HMIPs

Simulation of Wind Tunnel Tests (Connor et al. 2012)

In their study of wind behavior of HMIPs, Connor et al. (2012) compared the results from the wind tunnel tests conducted at Purdue University with the ones from computational fluid dynamics models obtained using Fluent (ANSYS and Cfdesign software packages from Blue Ridge Numerics/Autodesks). The 2-D model from ANSYS was implemented to find the preliminary separation point to place the probes used in wind tunnel experiments. Location of pressure taps were also based on the ANSYS analysis results. Smoke wand results were used to compare observations from the ANSYS model and the experiment.

In the Fluent model, the separation point of the shear layer was more downstream than that found in experiments. The Cfdesign software was used to model and simulate the 3-D flow around the tapered structure of the poles. The results indicated different point of separation of the shear layer when compared to the experimental results. However, the simulations using the Cfdesign software indicated certain pressure areas conforming to the experimental findings. Large eddy simulation (LES) was proposed for future studies since it resulted in greater accuracies in modeling turbulence.

Simulation of Wind-Induced Forces (Chang 2007)

a. Buffeting-Induced Forces

In order to determine the forces induced by buffeting, the turbulent wind velocity and the relationship between the turbulent wind velocity and the induced-forces must be determined. The turbulent wind velocity is simulated through wind turbulence power spectral density functions. The relationship between the turbulent wind velocity and the induced-forces is established using data from the wind tunnel experiment.

Simulation of Turbulent Wind Velocity:

Turbulent wind velocity for along-wind (u) and across-wind (w) directions and at m number of locations along the height of the pole are simulated using wind velocity spectral density functions, $S(n)$, as indicated in Equation 2.29.

$$u_i(t) \text{ or } w_i(t) = \sum_{l=1}^{m}\sum_{k=1}^{N} |H_{il}(\omega_k)|\sqrt{2\Delta\omega_k} \cdot \cos[\omega_k t + \theta_{il}(\omega_k) + \phi_{lk}] \qquad \textit{Equation 2.29}$$

$$\text{for} \quad i = 1,2,\cdots,m$$

where, $H_{il} =$ the (i,l) entry of the matrx H which satisfies wind velocity spectral density functions, $S(n) = H \cdot \bar{H}^T$

$\bar{H}^T =$ the matrix transposition of the complex conjugate of H

$\Delta\omega_k =$ the chosen frequency interval

$\theta_{il}(\omega_k) = \tan^{-1}[Im\{H_{il}(\omega_k)\}/Re\{H_{il}(\omega_k)\}]$

$Im\{H_{il}(\omega_k)\} =$ the imaginary component of $H_{il}(\omega_k)$

$Re\{H_{il}(\omega_k) =$ the real component of $H_{il}(\omega_k)$

$\phi_{lk} =$ the random phase angles from its unit uniform distribution between 0 and 2π

$N =$ the number of discrete frequencies, over the range of wind velocity spectrum

The wind velocity spectral density functions are defined using an empirical equation (Equation 2.30) as specified by Simiu and Scanlan (1996).

$$\frac{n \cdot S_{uu}(z,n)}{u_*^2} = \frac{200f}{(1+50f)^{5/3}} \qquad \textit{Equation 2.30}$$

$$\frac{n \cdot S_{ww}(z,n)}{u_*^2} = \frac{15f}{(1+9.5f)^{5/3}}$$

where $n =$ frequency

$S_{uu}(z,n)$ and $S_{ww}(z,n) =$ wind turbulence power spectral density functions in along-wind and across-wind directions, respectively

$u_*^2 =$ square of friction velocity ($\frac{I^2 \cdot U(z)^2}{\beta}$)

$I =$ turbulence intensity

$U(z) =$ mean wind velocity

$\beta =$ independent wind parameter; approximately equal to 6 for open terrain

$f =$ reduced frequency ($\frac{n \cdot z}{U(z)}$)

$z =$ elevation from the ground

The mean wind velocity along the height of the pole is determined from the wind profile equation (Equation 2.29) using the parameter, α, obtained from field monitoring data. The turbulence intensity factor is also determined from the field monitoring data. The cross-spectral power density function between two heights i and j, $S_{ij}(n)$, are represented with the square root of the coherence function and wind turbulence spectral density function at heights i and j (Equation 2.31).

$$S_{ij}(n) = \sqrt{S_i(n) \cdot S_j(n)} \cdot Coh_{ij}(n) \qquad \textbf{Equation 2.31}$$

where $S_i(n)$ and $S_j(n) =$ the wind turbulence power density spectra at heights i and j, calculated in Equation 2.30.

$Coh_{ij}(n) =$ square root of the coherence function, $e^{-\hat{f}}$

$\hat{f} =$ decay variable ($\frac{n \cdot C_z \cdot |z_1 - z_2|}{\frac{1}{2}[U(Z_1) - U(Z_2)]}$)

$C_z =$ exponential decay coefficient

The exponential decay coefficient, C_z, for along-wind and across-wind directions are suggested to be 10 and 6.67, respectively (Chang 2007, Simiu and Scanlan 1996).

Buffeting Indicial Function:

The wind tunnel experiment conducted by Chang (2007) determined the aerodynamic admittance function, $\chi^2(K)$, which is the relationship in frequency domain between the power spectral density of turbulent wind velocity in the upstream flow and the power spectral density of fluctuating wind load. Similar relationship in the time domain, known as buffeting indicial function (relation between the upwind turbulent wind velocity and the induced-wind load), can also be found using Sears' function. The result of $\chi^2(K)$ from the wind tunnel test and the relationship with the Sears' function is shown in Equation 2.32.

$$\chi_u^2(K) = \frac{1}{1 + 2.258 \cdot K} = |\Phi_u(K)|^2$$

$$\chi_w^2(K) = \frac{1}{1 + 100.5 \cdot K} = |\Phi_w(K)|^2 \qquad \textbf{Equation 2.32}$$

In Equation 2.32, K is the reduced frequency ($n \cdot \pi \cdot D/U$), n is the frequency, D is the across-wind dimension of the cross section, U is the mean wind velocity, and $\Phi(K)$ is the Sears'

function. The derivative of the buffeting indicial function, $\phi'(s)$, defined in Equation 2.33, and the Sears' function are Fourier Transform pairs as expressed in Equation 2.34.

$$\phi'(s) = A_1 \cdot e^{-A_2 \cdot s} + A_3 \cdot e^{-A_4 \cdot s} \qquad \textbf{Equation 2.33}$$

$$\Phi(K) = \int_0^\infty \phi'(\sigma) \cdot e^{-i \cdot K \cdot \sigma} \, d\sigma \qquad \textbf{Equation 2.34}$$

The aerodynamic admittance function, $\chi^2(K)$, can therefore be obtained by combining Equation 2.33 and Equation 2.34 as expressed as,

$$\chi^2(K) = |\Phi(K)|^2 = \left(\frac{A_1 \cdot K}{A_2^2 + K^2} + \frac{A_3 \cdot K}{A_4^2 + K^2}\right)^2 + \left(\frac{A_1 \cdot A_2}{A_2^2 + K^2} + \frac{A_3 \cdot A_4}{A_4^2 + K^2}\right)^2 \qquad \textbf{Equation 2.35}$$

The constants A_1 to A_4 are calculated through commercial software, Origin, for both along-wind and across-wind buffeting indicial function derivatives. The derivative of buffeting indicial function for a dodecagonal cross section is then expressed in Equation 2.36.

$$\phi'_u(s) = 0.060 \cdot e^{-0.183 \cdot s} + 0.850 \cdot e^{-1.309 \cdot s}$$
$$\phi'_w(s) = 0.009 \cdot e^{-0.012 \cdot s} + 0.069 \cdot e^{-0.256 \cdot s} \qquad \textbf{Equation 2.36}$$

Induced Forces:

According to Chang (2007), the buffeting-induced forces can be obtained using simulated turbulent wind velocity, $u(s)$, and the derivative of buffeting indicial function, $\phi'(s)$, as shown in Equation 2.37.

$$F_b^x(s) = \rho \cdot U \cdot D \cdot C_D \cdot \int_0^s \left[u(\sigma) \cdot \phi'_u(s - \sigma)\right] \cdot d\sigma$$
$$F_b^y(s) = -\frac{1}{2} \cdot \rho \cdot U \cdot D \cdot (C_D + C'_L) \cdot \int_0^s \left[w(\sigma) \cdot \phi'_w(s - \sigma)\right] \cdot d\sigma \qquad \textbf{Equation 2.37}$$

b. Vortex-Induced Forces

The research conducted by Chang (2007) proposed the Scanlan's Van-der Pole Oscillator model (Simiu and Scanlan 1996) for calculating the forces caused by vortex shedding (Equation 2.38).

$$F_v^y(t) = \frac{1}{2} \cdot \rho \cdot U^2 \cdot D \cdot \left[Y_1 \cdot \left(1 - \varepsilon \cdot \frac{y^2}{D^2}\right) \cdot \frac{\dot{y}}{U} + Y_2 \cdot \frac{y}{D} + \widetilde{C_L} \cdot \sin(\omega_n \cdot t + \phi)\right] \qquad \textbf{Equation 2.38}$$

where Y_1 and $\varepsilon =$ self-excited damping parameters
$Y_2 =$ linear aeroelastic stiffness parameter
$\widetilde{C_L} =$ root mean square of lift coefficient
$\dot{(\,)} =$ derivative with respect to time

Y_2 and $\widetilde{C_L}$ are ignored according to Simiu and Scanlan (1996) due to negligible effects. Y_1 and ε are functions of Scruton number during lock-in effect and are determined from the wind tunnel test.

c. Pole Vibrations

The time-dependent forces for both the along-wind and across-wind directions contain a self-excited component (se), mainly calculated from the mean wind speed of the incoming flow. Chang (2007) used the flutter derivative to express the self-excited force as represented in Equation 2.39,

$$F_{se}^{x}(t) = \frac{1}{2} \cdot \rho \cdot U^2 \cdot D \cdot \left[K \cdot P_1^* \cdot \frac{\dot{y}}{U} \right] \qquad \textit{Equation 2.39}$$

where $K =$ reduced frequency $(\omega \cdot D/U)$
$P_1^* =$ flutter derivative in quasi-steady form ($-2C_D/K$ for the along-wind direction and $-(C_D + C_L{}')/K$ for the across-wind direction)

The along-wind force can then be expressed with self-excited force and along-wind buffeting force as in Equation 2.40. The across-wind force can also be expressed with self-excited force, across-wind buffeting force, and vortex-shedding force as in Equation 2.40.

$$F^x = F_{se}^x + F_b^x$$
$$F^y = F_{se}^y + F_b^y + F_v^y \qquad \textit{Equation 2.40}$$

The generalized motion response of the pole for both along-wind and across-wind directions are then determined using the generalized Equation 2.41

$$\ddot{q}_i(t) + 2\xi_i\omega_i\dot{q}_i(t) + {\omega_i}^2 q_i(t) = \frac{\int_0^L \phi_i(z) \cdot F(z,t) \cdot dz}{M_i} \qquad \textit{Equation 2.41}$$

where $i =$ vibration mode
$q_i =$ generalized coordinate in ith mode
$\xi_i =$ damping ratio in ith mode
$\omega_i =$ circular frequency in ith mode
$\phi_i(z) =$ normalized shape of ith mode
$M_i =$ generalized mass in ith mode
$F(z,t) =$ force along the length of the pole

The pole motion, $x(z,t)$, can then be calculated using the generalized coordinates and the normalized mode shapes as shown in Equation 2.42.

$$x(z,t) = \sum_{i=1}^{N} \phi_i(z) \cdot q_i(t)$$ ***Equation 2.42***

2.4.7 Mitigation of Vortex-Induced Vibrations for In-Service HMIPs

A variety of methods to reduce vortex-induced vibrations (VIVs) have been developed in several past studies. The introduction of aerodynamic damping by modifying the surface and geometry of the structure can significantly suppress the motion caused by vortex shedding. Installing Tuned-Mass Dampers (TMD) can also mitigate VIV response by attaching a small vibrating system that vibrates in opposite direction to the motions of the structure. The motion of the TMD, if tuned to the right frequency, cancels the excited vibrations of the HMIP structure.

There are several ways to implement aerodynamic damping. The most common ways are installing helical strakes, fixing perforated shrouds around the structure, attaching ribbons to the structure, or increasing surface roughness of the structure. Helical strakes (Figure 2.37a) are installed using flexible rope to wrap around the structure in a helical fashion. Strakes are widely used in industry and have been proved to reduce VIV for tall and slender structures. However, there are studies indicating helical strakes tend to increase the drag coefficient of the structure. Perforated shroud is a thin metal cylinder surrounded with holes (Figure 2.37b). Structures enclosed with the perforated shroud can decrease a great amount of VIV as well as drag (Kumar, Sohn, and Gowda 2008). Attaching ribbons, as shown in Figure 2.37c, was also found to have significant effect in suppressing both VIV and drag force (Kumar, Sohn, and Gowda 2008). The ribbons are relatively easy to install and are more cost effective. However, the optimal ribbon length to reduce drag force can only be determined through experiments. Increasing surface roughness is also found to have the ability to reduce drag and vortex shedding (Durgesh 2006). Increasing surface roughness also has the advantage of becoming a part of the manufacturing process. Beside the aforementioned methods, there are many additional means such as installing axial slates, spoiler plates and hemispherical bumps that can also mitigate the VIV responses.

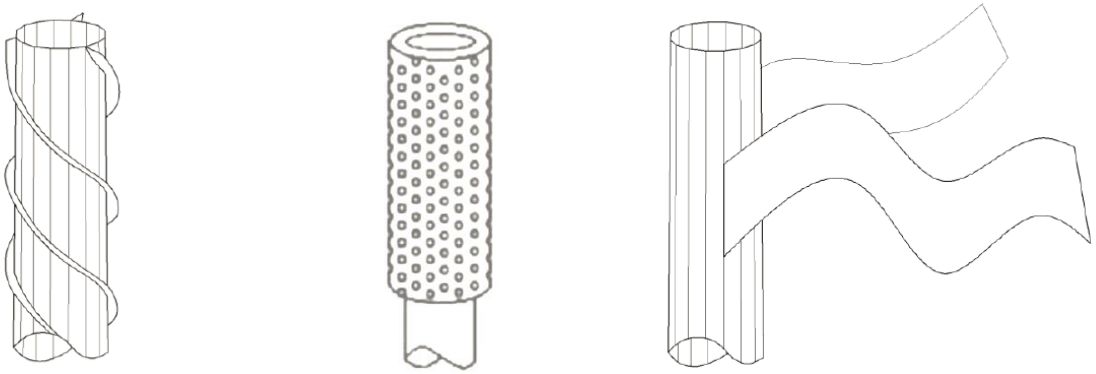

(a) Helical Strakes ***(b) Perforated*** ***(c) Ribbons***

Figure 2.37: Different Vortex-Shedding Mitigation Methods (Kumar, Sohn, and Gowda 2008)

Ahearn and Puckett 2010

The study conducted at Wyoming implemented four different aerodynamic damping methods on high-mast illumination poles to evaluate the significance of each method in reducing vortex-shedding vibrations (Ahern and Puckett 2010). The four different methods included, installing ribbons, installing helical strakes, installing perforated shrouds, and increasing the surface roughness of the poles. The length and the location of the installment of mitigating devices were similar in that they all were 16-feet long, and were installed at 89 feet to 105 feet from the ground.

Five feet long and 11 inch wide woven plastic ribbons were installed at a 3 feet spacing on the poles. The design was based on the guidelines provided in previous literature (Kumar, Sohn, and Gowda 2008). The results indicated that mode-three vortex shedding could still be observed at a mean wind speed of approximately 10 mph and vibrating at a frequency 3.8 Hz.

Helical strakes were also tested and yielded similar results compared to ribbon-retrofitted and un-retrofitted poles. Helical strakes were installed wrapping 1-inch diameter rubber hoses around the poles in a spiral pattern. The mode-three lock-in was still observed at 12.8 mph mean wind speed vibrating at a frequency of 3.8 Hz (Figure 2.38).

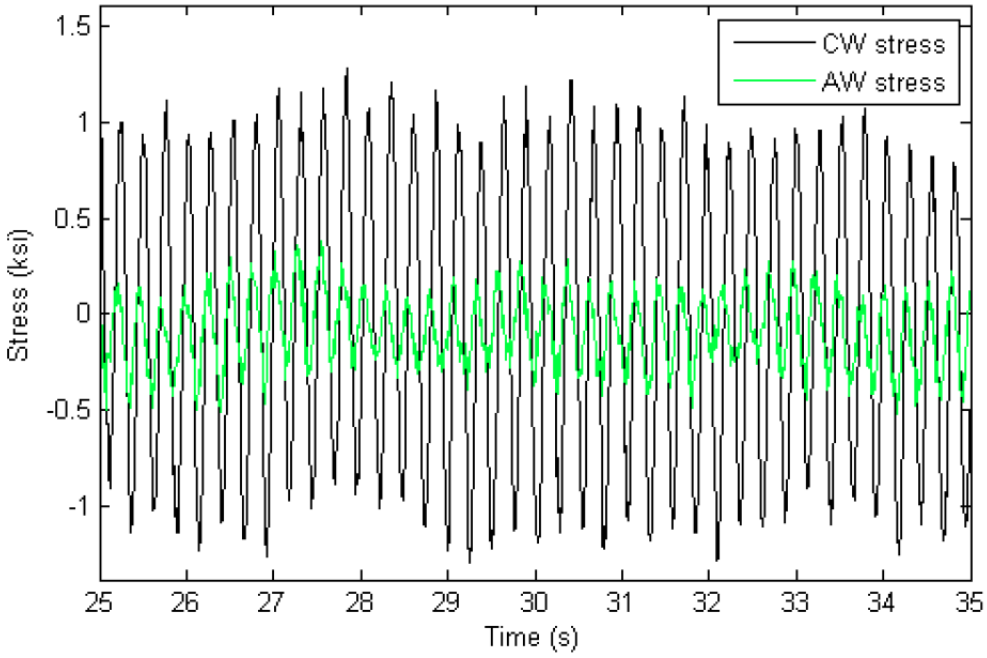

Figure 2.38: Lock-in Vibration at 3.8 Hz under 12.8 Mean Wind Speed Observed for a Pole with Helical Strakes in the Wyoming Study (Ahearn and Puckett 2010)

The perforated shroud was found to be the most effective method among the four methods adopted in diminishing VIV response of the poles in the Wyoming study (Ahern and Puckett 2010). The perforated shroud is made of rigid, high-density polyethylene net with 0.275 inch square holes. The speed range that was monitored varied from 6.7 mph to 18 mph where no lock-in at any mode was observed from the collected data. Figure 2.39 shows the large reduction of acceleration response when perforated shroud is installed.

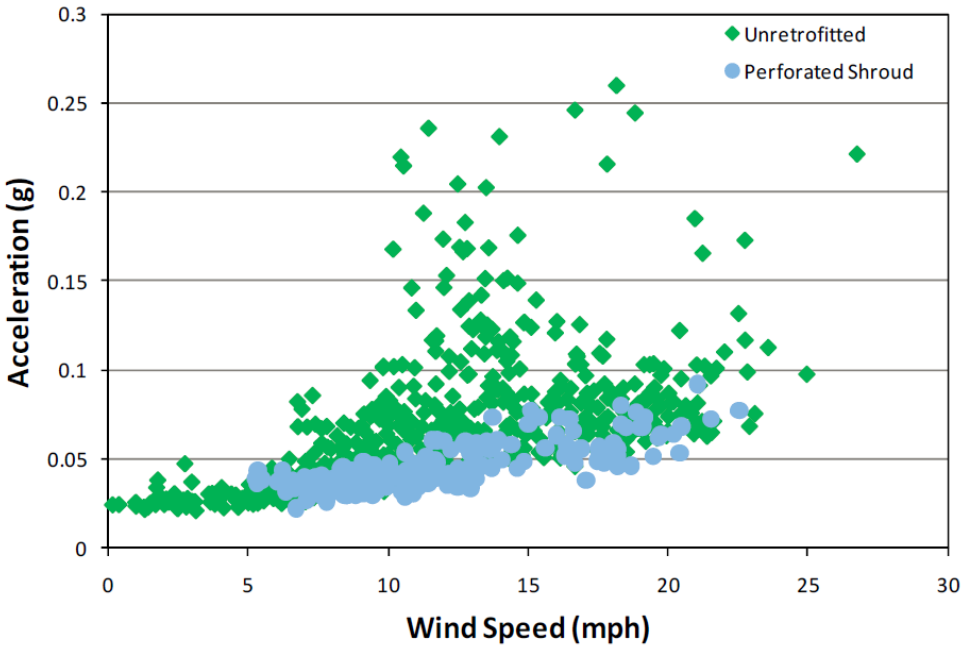

Figure 2.39: Wind-Induced Response of a Pole with and without Perforated Shrouds as Observed in the Wyoming Study (Ahearn and Puckett 2010)

Surface roughness was found to be the least effective method to limit the VIV response of the HMIPs in the Wyoming study (Ahern and Puckett 2010). 0.125 inch thick rubber floor covering was attached to the pole with double-sided tape to increase the surface roughness of the pole. Figure 2.40 shows little difference in acceleration response between the retrofitted and un-retrofitted poles. The third mode lock-in was still observed from recorded data for wind speeds ranging from 9.9 mph to 15.4 mph.

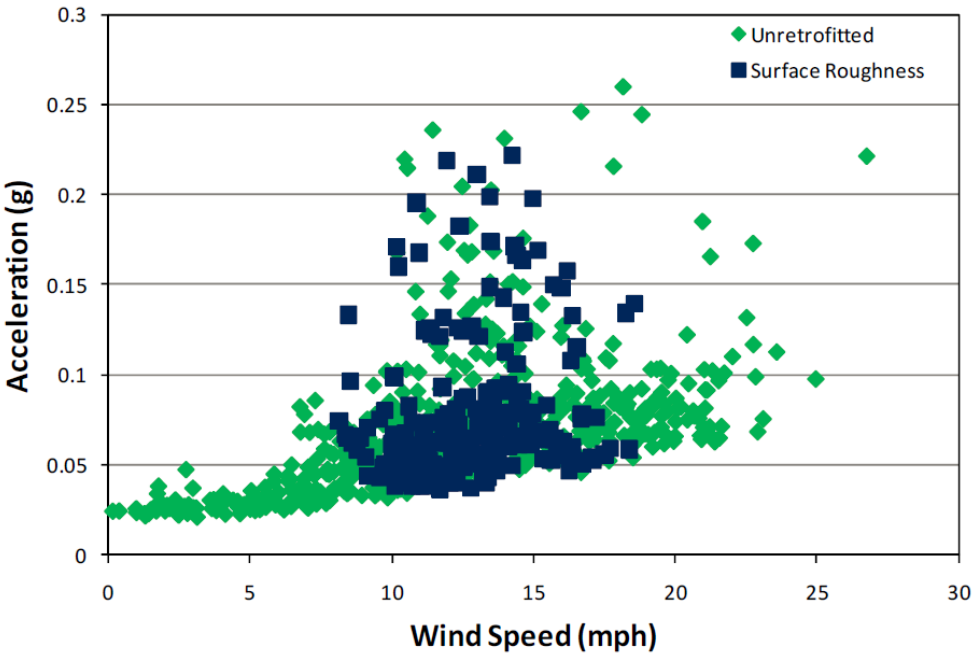

Figure 2.40: Wind-Induced Response of a Pole with and without the Application of Surface Roughness Methods as Observed in the Wyoming Study (Ahearn and Puckett 2010)

Connor et al. 2012

Due to the convenience of wrapping poles with ropes, helical strakes were selected to mitigate the vortex-induced vibrations in the study summarized in the NCHRP Reported No. 718 (Connor et al. 2012). The first test was designed to investigate the difference in response between poles retrofitted with single strakes and double strakes on the entire length of the pole. The second test was designed to observe the difference in behavior between one pole fully retrofitted with double strakes and the other with only the top one third being retrofitted.

The results of the first test indicated that the pole retrofitted with the full-length double strakes experienced significant reductions in number of fatigue cycles and smaller stress amplitudes during vibrations. Figure 2.41 shows that the number of wind-induced cycles per day has drastically dropped after either single or double strakes were installed. The channels in Figure 2.41 indicate different locations around the circumference at the same height at the bottom of the pole. Although the pole with full-length single strakes experienced fewer number of cycles in general, the decrease in number of cycles are mostly seen in certain directions whereas the decrease in number of cycles for the pole with double strakes happened in all directions. The reason for this is that double strakes disrupt the wind vortices in all directions including disrupting the flow that causes vortex shedding. Another concern that was examined was the increased drag force caused by the increased area from the additional strakes. The report indicated that according to the fatigue analysis, there was no evidence to support the notion that installing additional strakes caused larger stress ranges. Furthermore, as shown in Figure 2.42, the stresses in the across-wind direction for the poles with strake mitigation (MT) are significantly smaller than stresses in the pole without mitigation (FT). The small stresses observed in retrofitted poles indicate that mitigation has significant impact in reducing vortex-induced vibrations.

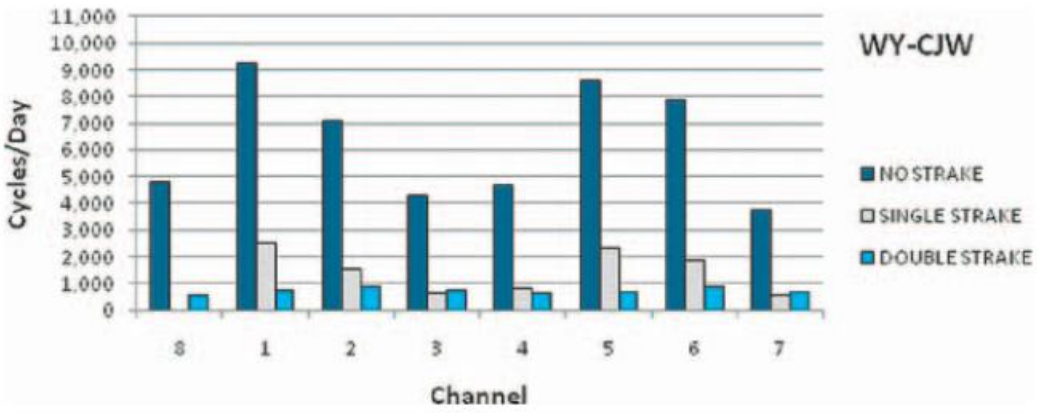

Figure 2.41: Number of Sustained Cycles/Day with No/Single/Double Strakes Installed on a pole in the Iowa Study (Connor et al. 2012)

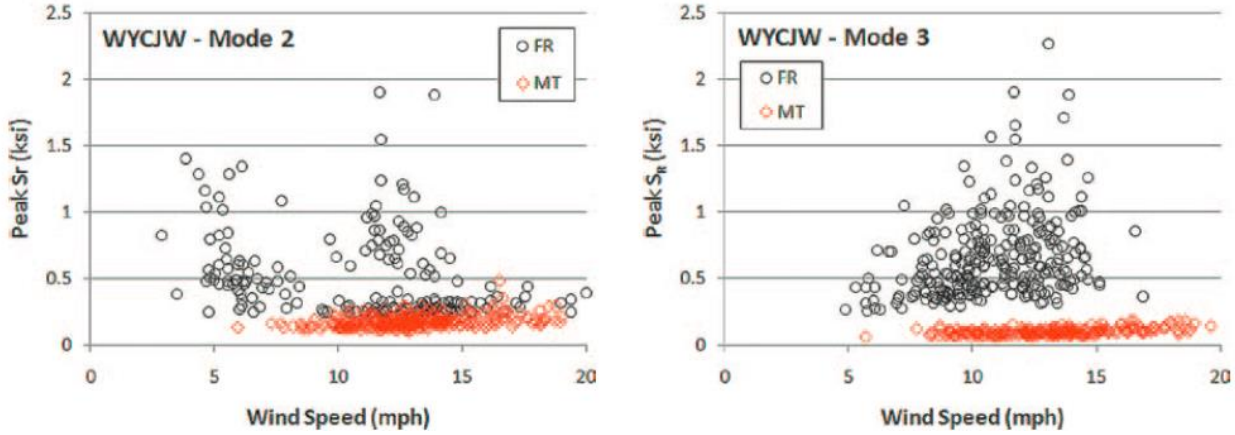

Figure 2.42: Stress Ranges Before and After Installment of Strakes as observed in the Iowa Study (Connor et al. 2012)

The second test results indicate that installing the strakes over only one-third of the pole length was not as effective as installing strakes over the full length. Figure 2.43 compares the difference in stress ranges observed for a pole with the full-length strakes versus the top one-third strakes configurations.

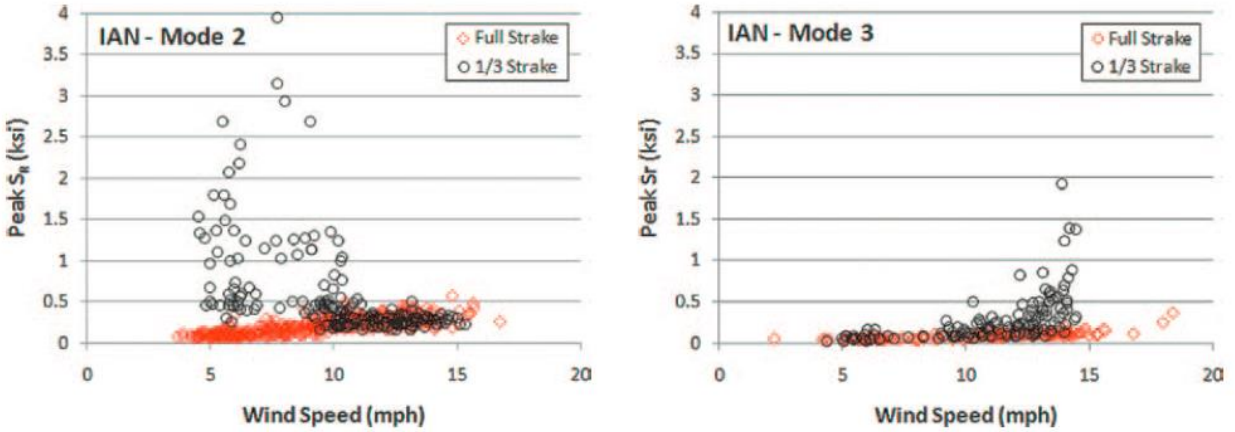

Figure 2.43: Stress Ranges Following the Application of Strakes over the Full Length and over the Top 1/3 Length of the Poles as observed in the Iowa Study (Connor et al 2012)

2.5 Probabilistic Assessment of Fatigue Life and Development of Guidelines for Inspection of In-Service HMIPs

This section reviews the literature on probabilistic methods for predicting fatigue failure of steel structures, and on reliability-based inspection scheduling. Brief reviews are also provided on literature generated in previous TxDOT Projects 0-6650 (Fatigue Failure and Cracking in High Mast Poles) and 0-2135 (Guidelines for Inspection of Fracture-Critical Steel Trapezoidal Girders), as well as other relevant literature on similar issues related to aircraft, pressure vessels, pipelines, and offshore oil and gas platforms.

2.5.1 Review of the TxDOT Project 0-2135 (Chung 2003)

Stress Range Distribution Analysis for Steel Material

The two major parameters needed in fatigue reliability analysis are the number of stress cycles and the corresponding effective stress ranges. The three most common ways described in TxDOT report 0-2135 (Chung 2003) to obtain the effective stress ranges are: Stress spectrum Analysis, Rayleigh Distribution Analysis, and Fatigue Truck Analysis.

The Stress Spectrum Analysis method is used when sufficient stress data on specific details are provided. The effective stress range can be determined from the collected stress data using Equation 2.43 proposed by Schilling et al. (1987).

$$S_{RE} = \left\{ \sum_{i=1}^{n} \gamma_i \cdot S_{R,i}^3 \right\}^{1/3} \qquad \textit{Equation 2.43}$$

where γ_i is the ratio of the number of cycles in $S_{R,i}$ stress range to the total number of cycles that can be sustained. The need for the collection of numerous data points and the use limitation for a specific detail are the two major disadvantages of this method.

To avoid collecting enormous amounts of data, the Rayleigh Distribution Analysis method proposed by Schilling et al. (1987) can be utilized to provide a reasonable estimate for the stress range spectrum for different design details in steel bridges. The distribution of stress range is expressed using Rayleigh probability distribution as shown in Equation 2.44.

$$f_{S_{RE}}(S_{RE}) = \left(\frac{S_{RE}}{{S_{R0}}^2} \right) \cdot exp\left[-\frac{1}{2} \left(\frac{S_{RE}}{S_{R0}} \right)^2 \right] \qquad \textit{Equation 2.44}$$

In Equation 2.44, S_{R0} is

$$S_{R0} = \sqrt{\frac{2}{\pi}} E(S_{RE}) \qquad \textit{Equation 2.45}$$

The mean stress range effect of $(S_R)^B$ can be determined from Equation 2.46, which can be used corresponding to miner's rule.

$$E[S_R^B] = \sum_{i=1}^{n} \gamma_i \cdot S_{R,i}^B = \left(\sqrt{2} S_{R0}\right)^B \cdot \Gamma\left(\frac{B}{2} + 1\right) = {S_{RE}}^B \qquad \textit{Equation 2.46}$$

Another method to obtain the effective stress range is the Fatigue Truck method where an "effective" fatigue truck is considered to mimic the fatigue caused by actual trucks on bridges. This method curtails the data collecting duration, and therefore can be more feasible than methods requiring long term monitoring.

Fatigue reliability analysis

Target Reliability Index, β_{target}

The minimum safety level approved for a specific application is often defined by the target reliability index, β_{target}. The target reliability index is related to the target probability of failure, P_F, through cumulative distribution function of a standard Gaussian random variable, Φ, as shown in Equation 2.47.

$$\beta_{target} = \Phi^{-1}(1 - P_F) \qquad \textit{Equation 2.47}$$

As observed in Equation 2.47, the probability of failure decreases with increasing target reliability index. The determination of target reliability index is suggested based on the different failure consequences proposed by Onoufriou (1999), and shown in Table 2.9. Onoufriou (1999) selected the target reliability index of 3.7 for the reliability study of steel offshore structures This target reliability index was associated with "serious" failure consequences and probability of occurrence of 1/10000.

Table 2.9: Target Reliability Index Values for North Sea Jacket Structures (Onoufriou 1999)

Failure Consequence	Target Reliability Index (β_{target})	Failure Probability (P_F)
Very Serious	4.27	10^{-5}
Serious	3.72	10^{-4}
Not Serious	3.09	10^{-3}
Local Effect	2.33	10^{-2}
Negligible Effect	1.28	10^{-1}

AASHTO Fatigue Reliability Approach

The AASHTO S-N curves are representing the fatigue categories for 8 different details common in steel bridges. These fatigue categories were mainly obtained through fatigue tests conducted in 1970s. These S-N curves have a general form expressed in Equation 2.48

$$N = A \cdot {S_R}^{-3} \qquad \textit{Equation 2.48}$$

In Equation 2.48, N is the number of constant-amplitude stress cycles or stress ranges, S_R, and A are the parameters for different categories associated with different design details specified in AASHTO (AASHTO 2014). The S-N curves provide an estimate of expected number of cycles to fatigue failure under a constant amplitude stress range, or an estimate of a maximum stress range for a given minimum number of cycles. However, most of the sustained stress ranges caused by actual traffic loadings are not constant amplitude. The Miner's rule and effective stress range are then introduced to consider the effect of variations in stress ranges.

Miner's rule (Equation 2.49) was proposed to evaluate the fatigue damage resulting from variable-amplitude stress ranges.

$$D = \sum \frac{n_i}{N_i} \geq \Delta \qquad \textit{Equation 2.49}$$

In Equation 2.49, D is the Miner's accumulation damage index, n_i is the number of cycles under specific stress range amplitude, N_i is the number of cycles that a design detail can sustain under the same specified stress range amplitude, and Δ is the Miner's critical damage accumulation index, which is observed to be approximately equal to 1.0 for metallic materials. Fatigue damage for any specific detail (represented through the constant A), is expected to occur when D exceeds Δ.

The S-N curve can be combined with the Miner's rule, as indicated in Equation 2.50.

$$D = \sum \frac{n_i}{N_i} = \sum \frac{\gamma_i \cdot N}{A \cdot {S_{R,i}}^{-3}} = \frac{N}{A} \sum \left[\gamma_i \cdot {S_{R,i}}^{3}\right] = \frac{N}{A} {S_{RE}}^{3} \geq \Delta \qquad \textit{Equation 2.50}$$

where N is the total number of stress cycles regardless of the stress levels, γ_i is the ratio of n_i to N, and S_{RE} is the effective stress range introduced in Equation 2.43. The critical number of cycles, N_c, can then be determined when D equals Δ as shown in Equation 2.51.

$$N_c = \frac{A \cdot \Delta}{{S_{RE}}^{3}} \qquad \textit{Equation 2.51}$$

The parameter A was analyzed by Moses el al. (1987) and was found to fit a lognormal random variable using extensive fatigue data from steel bridges reported by Keating and Fisher (1985). The mean value and coefficient of variable for the five different categories in AASHTO are listed in Table 2.10. The parameter Δ was also found to fit a lognormal random variable with a mean value of 1.0, and coefficient of variable of 0.30 (Wirsching and Chen 1988, Miner 1945).

Table 2.10: Mean and Coefficient of Variance of the Fatigue Parameter *A*

AASHTO Category	μ_A (Mean Value)	δ_A (COV)
A	1.50×10^{11}	0.54
B	7.85×10^{10}	0.35
C	1.10×10^{10}	0.15
D	4.76×10^{9}	0.25
E	2.01×10^{9}	0.26

The number of sustained cycles regardless of the sustained stress range, N, and the critical number of cycles, N_c, are employed in the AASHTO fatigue reliability approach as shown in Equation 2.52.

$$g(\boldsymbol{X}) = N_c - N \qquad \textit{Equation 2.52}$$

where $g(\boldsymbol{X})$ is the limit state function and indicates failure when it is smaller than zero. Thus, the probability of fatigue failure and the probability of the limit state function smaller than zero are the same, and can be expressed in terms of the reliability index, β, as shown in Equation 2.53.

$$P_f = P(g(\boldsymbol{X}) \leq 0) = \Phi(-\beta) \qquad \textbf{Equation 2.53}$$

The reliability index can be calculated directly using Equation 2.54 since the parameters A and Δ in the limit state function follow a lognormal distribution with known mean value and coefficient of variance (as shown in previous research described above).

$$\beta = \frac{(\lambda_\Delta + \lambda_\mathrm{A}) - 3\ln S_{RE} - \ln(N)}{\sqrt{\zeta_\Delta^2 + \zeta_\mathrm{A}^2}} \qquad \textbf{Equation 2.54}$$

where $\lambda_\Delta, \lambda_\mathrm{A}, \zeta_\Delta, \zeta_\mathrm{A}$ are obtained using Equation 2.55.

$$\lambda_\mathrm{A} = \ln(\mu_A) - \frac{\zeta_A^2}{2}$$

$$\lambda_\Delta = \ln(\mu_\Delta) - \frac{\zeta_\Delta^2}{2}$$

$$\zeta_A = \sqrt{\ln(1 + \delta_A^2)} \qquad \textbf{Equation 2.55}$$

$$\zeta_\Delta = \sqrt{\ln(1 + \delta_\Delta^2)}$$

where μ_A and μ_Δ are the means of parameters A and Δ, and δ_A and δ_Δ are the coefficient of variance of parameters A and Δ, respectively. The S_{RE} in Equation 2.54 can be obtained from the stress range distribution from Stress Spectrum Analysis, or a Rayleigh Distribution Analysis. Alternatively, the number of stress cycles regardless of stress range is computed in Equation 2.56 from the number of stress cycles per truck passage, C_s, the Average Daily Truck Traffic, $ADTT$, and the number of service years, Y.

$$N = 365 \cdot C_s \cdot ADTT \cdot Y \qquad \textbf{Equation 2.56}$$

A graph for fatigue reliability index, β, for the AASHTO category E detail under various stress ranges, is shown in Figure 2.44. The target reliability index in Figure 2.44 is 3.7, which corresponds to a probability of failure of 10^{-4}.

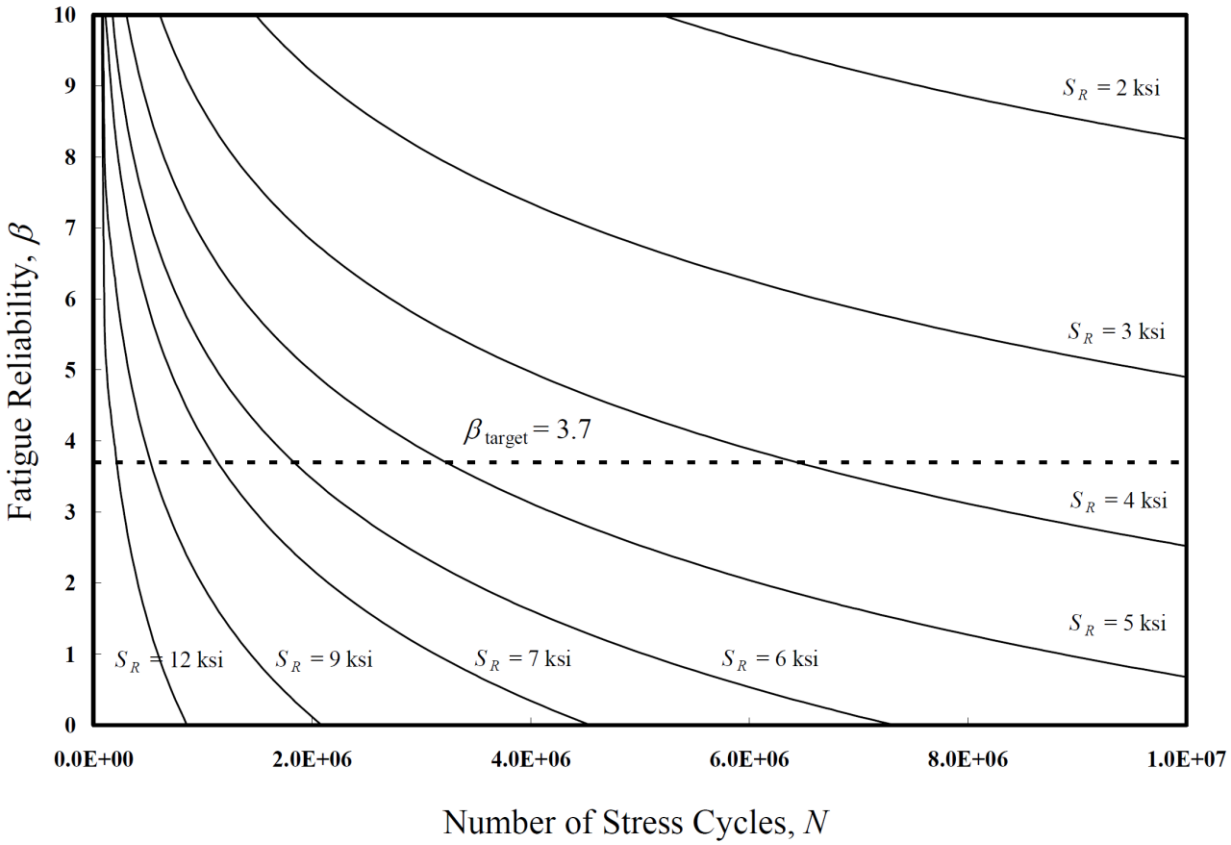

Figure 2.44: **Fatigue Reliability for the AASHTO Category E Detail under Various Stress Range Levels (Chung 2004)**

LEFM Fatigue Reliability Approach

Linear elastic fracture mechanics (LEFM) reliability analysis method takes the sizes of existing cracks into account to overcome the variability of details not included in the eight fatigue categories specified by AASHTO. The Paris' law commonly used in linear elastic fracture analysis is employed to determine the fatigue reliability. The limit state function and the prime parameters such as crack geometry functions, initial and critical crack sizes, and the fatigue crack growth parameters are needed to successfully employ this fatigue reliability analysis approach.

A limit state function, $g(\boldsymbol{X})$, which uses Paris Law in LEFM was proposed by Madsen et al. (1985). The Paris Law proposed by Paris and Erdogan (1963) is a relationship between the crack growth rate and the stress intensity factor shown in Equation 2.57.

$$\frac{da}{dN} = C \cdot (\Delta K)^m \qquad \textbf{\textit{Equation 2.57}}$$

In Equation 2.57, a is the crack size, N is the number of cycles, C and m are material parameters, and ΔK is the stress intensity range. The stress intensity range can be expressed by stress range, crack geometry function, and crack size as shown in Equation 2.58.

$$\Delta K = F(a) \cdot S_{RE} \cdot \sqrt{\pi a} \qquad \textbf{Equation 2.58}$$

Equation 2.58 can then be arranged into Equation 2.59, where the number of sustained cycles, $N = N_f - N_0$, are related to the final crack length, a_f.

$$\int_{a_0}^{a_f} \frac{da}{\left[F(a) \cdot \sqrt{\pi a}\right]^m} = C \cdot S_{RE}^m \cdot \left(N_f - N_0\right) \qquad \textbf{Equation 2.59}$$

Madsen et al. (1985) introduced a damage function, $\psi(a_1, a_2)$, to represent the accumulated fatigue damage under crack length propagation from a_1 to a_2 (Equation 2.60). The capacity side of the fatigue strength can then be expressed as $\psi(a_0, a_c)$ whereas the demand side can be expressed as $\psi(a_0, a_N)$. The crack size, a_0, a_c, and a_N represents the initial crack size, the critical crack size, and the crack size associated with the sustained N number of cycles.

$$\psi(a_1, a_2) = \int_{a_1}^{a_2} \frac{da}{\left[F(a) \cdot \sqrt{\pi a}\right]^m} \qquad \textbf{Equation 2.60}$$

The limit state function, $g(\boldsymbol{X})$, for the LEFM fatigue reliability approach can then be expressed as indicated in Equation 2.61 where failure occurs when $g(\boldsymbol{X})$ is smaller than zero.

$$g(\boldsymbol{X}) = \psi(a_0, a_c) - \psi(a_0, a_N) = \int_{a_0}^{a_c} \frac{da}{\left[F(a) \cdot \sqrt{\pi a}\right]^m} - C \cdot S_{RE}^m \cdot \left(N_f - N_0\right) \qquad \textbf{Equation 2.61}$$

The geometry function, $F(a)$, is a function that takes into account the crack shape. The geometry function can be obtained through intensity factors, K, associated with different crack geometries documented in numerous handbooks and specifications (Equation 2.62). The geometry function can also be determined using advanced finite element methods.

$$K = F(a) \cdot \sigma\sqrt{\pi a} \qquad \textbf{Equation 2.62}$$

Initial crack size, a_0, can be obtained through Non-Destructive Evaluation (NDE) methods or the Equivalent Initial Flaw Size (EIFS) methods. NDE methods can detect crack size without damaging the target object. However, there are numerous ways to apply NDE methods, which may result in different outcomes. In addition, every NDE method has a limit on the minimum detectable flaw size. Therefore, alternative methods like EIFS methods, are proposed to capture the initial crack sizes. The initial crack size is also obtained by back-solving the Equation 2.61. As an example, the statistical distribution of initial crack size for AASHTO fatigue categories were analyzed and documented by Yazdani (1984).

Critical crack size, a_c, can be determined through Charpy V-notch Impact (CVN) tests. Rippling and Crosley (1983) proposed that the fracture toughness, which is directly related to the critical crack size, can be fitted to a truncated normal distribution model for different steel materials. Table 2.11 shows the fracture toughness statistics for ASTM A36, A588, and A514 steels (Albrecht et al., 1986).

Table 2.11: Fracture Toughness Statistics for ASTM A36, A588, A514 Steels (Albrecht et al., 1986)

Steel Type	Mean (ksi$\sqrt{\text{in}}$)	COV
A36	40.0	0.18
A588	45.1	0.19
A514	70.1	0.24

The two parameters in Paris Law (C and m) can be determined through regression analysis using fatigue test data. The statistical characteristics of these two parameters for different steels and environmental conditions are summarized by Yazdani and Albrehct (1989).

The probability of failure, P_f, and reliability index, β, are related through the same equation used in AASHTO fatigue reliability approach (Equation 2.52) where $g(\boldsymbol{X})$ in the LEFM approach is calculated according to Equation 2.61. Note that the closed-form expression for the reliability index, β, used in AASHTO approach is not feasible due to the limit state function. However, a Monte Carlo simulation method or the First Order Reliability Method (FORM) can be used to calculate P_f or β.

Reliability-Based Inspection Scheduling

An optimal inspection scheduling for steel bridges based on the reliability theory, and taking into account both economy and safety, was also proposed in the TxDOT 0-2135 research project (Chung 2003). The main goal was to adjust the inspection times within appropriate time intervals to minimize cost without compromising safety of steel bridges against fatigue failure. The proposed scheduling involved an event tree analysis, which simulated all possible inspection and repair scenarios. Specifically, the likelihood of needed repair following each inspection was derived using the AASHTO and the LEFM fatigue reliability approaches. The cost function based on inspection, repair, and structural failure was then formulated to optimize the number of inspections during the assumed service life.

As mentioned above, in the study performed by Chung (2003; 2004; 2006), an event tree analysis (Figure 2.45) was employed to develop an optimal inspection scheduling by simulating all possible decision scenarios at the time of each inspection. In Figure 2.45, T1 and T2 are the time of inspections divided in two branches of "Repair" and "No Repair". This branching process will result in 2^n branches (scenarios) if n inspections are performed. The probability of occurrence for each branch is determined based on the AASHTO and the LEFM fatigue reliability approaches. The welded detail was assumed to be as good as new after each repair. If sufficient data are provided, the "good as new" assumption can be modified based on repair details for a more comprehensive analysis.

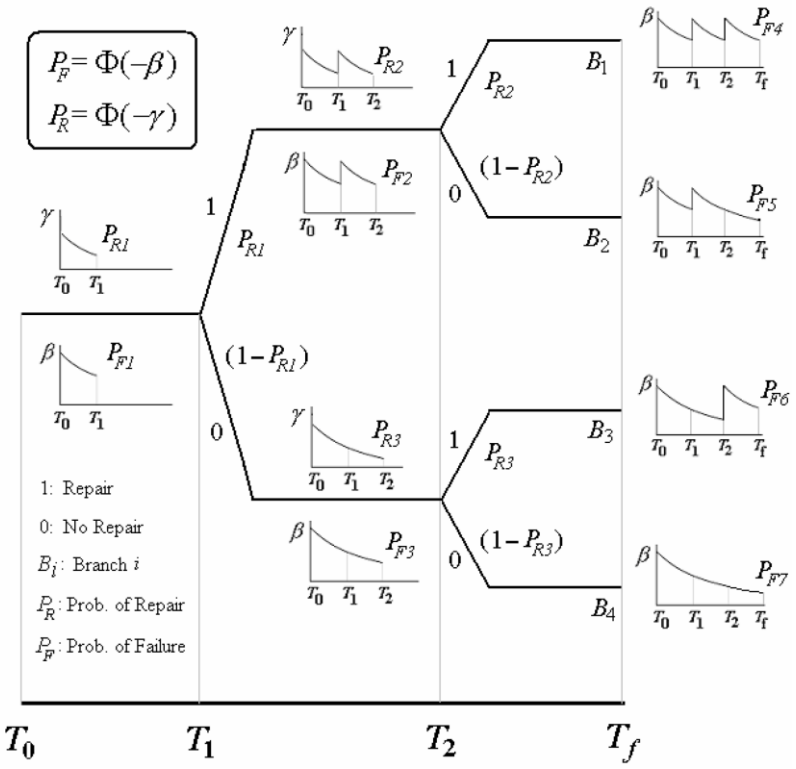

Figure 2.45: Representative Event Tree Showing Inspection and Repair Realizations (Chung 2003)

The likelihood of repair, P_R, following each inspection is used to calculate the probability of occurrence for each branch. This likelihood is determined as the probability of a crack size larger than that prompting repair. Both the AASHTO and the LEFM fatigue reliability approaches can be implemented to obtain P_R. For the AASHTO approach, a limit state function, $H(\boldsymbol{X})$, similar to the limit state function, $g(\boldsymbol{X})$, presented in Equation 2.52 for the AASHTO approach for fatigue failure, is proposed and shown in Equation 2.63

$$H(\boldsymbol{X}) = 0.75N_c - N = \frac{0.75A \cdot \Delta}{S_{RE}^3} - N \qquad \textbf{Equation 2.63}$$

In Equation 2.63, N is the number of cycles that is sustained, and N_c is the critical number of cycles to fatigue failure. For the LEFM approach, a limit state function, $H(\boldsymbol{X})$, similar to the limit state function, $g(\boldsymbol{X})$, presented in Equation 2.61 for the LEFM approach for fatigue failure, is proposed and shown in Equation 2.64.

$$H(\boldsymbol{X}) = \psi(a_0, a_R) - \psi(a_0, a_N) = \int_{a_0}^{a_R} \frac{da}{\left[F(a) \cdot \sqrt{\pi a}\right]^m} - C \cdot S_{RE}^m \cdot N \qquad \textbf{Equation 2.64}$$

In Equation 2.64, N is the number of cycles that is sustained, and a_R is the maximum permissible crack size before repair is required. The likelihood of repair for both approaches can then be obtained with Equation 2.65.

$$P_R = P(H(\boldsymbol{X}) \leq 0) \qquad \textbf{Equation 2.65}$$

The expected cost within the service period can be determined using the event tree analysis, which provides not only the probability of each branch, but also the fatigue reliability associated with each inspection. The expected cost consists of inspection cost, repair cost, and failure cost. The cost of inspections, C_I, can be expressed as the summation of the cost for each single inspection, K_I, (Equation 2.66).

$$C_I = \sum_{i=1}^{n} K_I \qquad \textbf{Equation 2.66}$$

The cost of repairs, C_R, is represented by the cost of single repair, K_R, and the expected number of repairs, $E[R_i]$, at T_i. The expected number of repairs is the summation of the probability of repair at each branch (Equation 2.67).

$$E[R_i] = \sum_{j=1}^{2^{i-1}} P\left(R_i \cap B_j^i\right) \qquad \textbf{Equation 2.67}$$

In Equation 2.67, R_i denotes the repair event at T_i, and B_j^i denotes branch j of the event tree at T_i. The cost of repair is then expressed in Equation 2.68

$$C_R = \sum_{i=1}^{n} K_R \cdot E[R_i] \qquad \textbf{Equation 2.68}$$

The cost of failure, C_F, represents the expected cost resulting from a failure. C_F is represented by the cost of failure, K_F, and the expected probability of failure within the service life for each scenarios in the event tree (Equation 2.69).

$$C_F = \sum_{i=1}^{2^n} \left\{ \frac{1}{T_f - T_0} \int_{T_0}^{T_f} K_F \cdot P(F \cap B_i) dT \right\} \qquad \textbf{Equation 2.69}$$

Substituting the summation of probability of failure in each branch with the expected reliability index, $E[\beta]$, Equation 2.69 is then expressed as in Equation 2.70

$$C_F = \frac{1}{T_f - T_0} \int_{T_0}^{T_f} K_F \cdot \Phi(-E[\beta]) dT \qquad \textbf{Equation 2.70}$$

The total cost is the summation of inspection cost, repair cost, and failure cost as shown in Equation 2.71.

$$C_T = C_I + C_R + C_F \qquad \textit{Equation 2.71}$$

After the event tree and the total cost is formulated, the fatigue inspection scheduling problem becomes a mathematical optimization problem (Equation 2.72) that yields the optimal variables such as the number of inspections, n, and the corresponding inspection time, $T_1, T_2, \dots T_n$. The optimization is based on finding the optimal variables that minimize the cost under acceptable fatigue reliability over its service life.

$$\min_{n, T_1, \dots T_n} C_T = \left\{\sum_{i=1}^{n} K_I\right\} + \left\{\sum_{i=1}^{n} K_R \cdot E[R_i]\right\} + \left\{\frac{1}{T_f - T_0}\int_{T_0}^{T_f} K_F \cdot \Phi(-E[\beta])dT\right\} \qquad \textit{Equation 2.72}$$

where $T_1, T_2, \dots T_n$ should lie in the time period between T_0 and T_f, and $E[\beta]$ should be larger than the reliability index, β_{min}, which corresponds to the minimum acceptable safety level of the specified welded detail.

2.5.2 Review of the TxDOT Project 0-6650 (Dawood et al. 2012)

Dawood et al. (2012, 2014) conducted a research on the fatigue failure and cracking of High Mast Poles in Texas. The focus of their study was on the nature of galvanized cracking, the structural response of HMIPs under wind loading, and the different repair methods and their associated costs. The analytical procedure developed by Dawood et al. (2012, 2014) to predict fatigue life of cracked HMIPs is reviewed in the following.

Stress Range Distribution Analysis for Steel Material

Dawood et al. (2012, 2014) proposed a comprehensive analytical method that consisted of twelve individual steps shown as a flow chart in Figure 2.46. This method was used to analyze the wind-induced response of poles, and to provide an assessment of failure probability using AASHTO fatigue reliability approach (Chung et al. 2003, 2004).

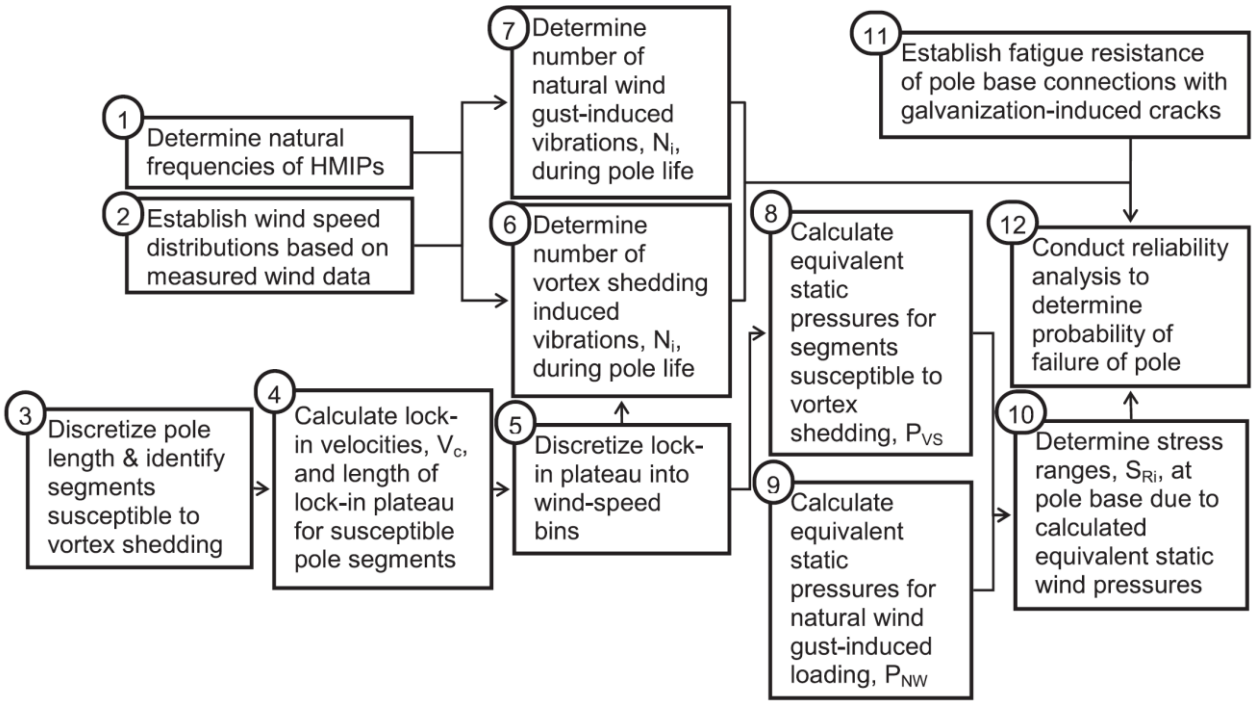

Figure 2.46: An Analysis Approach for Predicting Fatigue Behavior of In-Service HMIPs in Texas (Dawood et al. 2014)

The natural frequencies of studied poles were obtained using the modal analysis in finite element analysis program SAP 2000. In these analyses, the slip joint section was not modeled and the pole base was modeled as a fixed-end to represent the thick base plate (Foley et al. 2004). The illumination on the top of the pole was simulated using a lumped mass of 910 lb equally distributed on the top segment of the modeled pole. The analysis of the first four modes showed similar results to the numerical predictions conducted in Wisconsin (Foley et al. 2004) and the actual pole response in Iowa (Chang et al. 2009).

Due to the difficulty in modeling the vortex-shedding response of a pole with varying diameter and wind velocity along the height, this study proposed to separate the pole into segments that could be individually analyzed as prismatic cylinder. This approach is based on the Canadian Highway Bridge Design Code (CSA 2006), which suggests that a tapered pole can be reasonably assumed to behave in the same manner as a prismatic pole when the diameter of the pole are within ±10 percent of the critical diameter (the diameter in the middle of the pole). The poles in this study were then discretized into six to eight segments based on pole heights.

After the pole segments were determined, the lock-in velocity range due to vortex-shedding was calculated for each segment. The lock-in velocity range was based on a previous research (Chung et al. 2009), in which a vortex-shedding frequency plateau was observed for wind velocities between the so-called critical, V_c, and limiting, V_e, velocities (Equation 2.73). This phenomenon indicates that the synchronization of the pole and the wind vortices can be observed under a range of velocities. This study then calculated the velocity range for each segments based on the critical diameter (the diameter in the middle of the segment) and the first three modes of vibration.

$$V_c = 0.68\frac{f_n \cdot D}{S_n}$$

$$V_e = 1.22V_c$$

Equation 2.73

In Equation 2.73, f_n is the natural frequency of the pole, D is the width of the cross section, and S_n is the Strouhal number. The wind speed range between V_c and V_e was then divided equally into three bins due to the large difference in base stress calculations.

The equivalent static wind pressure ranges for vortex-shedding induced vibrations, P_{VS}, and natural wind gust induced vibrations, P_{NW}, were calculated based on the AASHTO guideline (AASHTO 2009) shown in Equation 2.74.

$$P_{VS} = \frac{0.00256V_c^2 C_d I_F}{2\beta} \qquad (psf)$$

$$P_{NW} = 5.2C_d I_F \qquad (psf)$$

Equation 2.74

In Equation 2.74, V_c is the lock-in velocity, C_d is the drag coefficient taken as 1.2, I_F is the importance factor taken as 1, and β is the damping ratio of the poles taken as 0.005 (AASHTO 2009). It is important to note that the natural wind gust equivalent pressure ranges are independent of wind speed and pole diameter.

The stress ranges were further calculated using finite element analysis with the equivalent static pressure applied on pole segments susceptible to vortex-shedding or natural wind gust. The segments susceptible to vortex-shedding were determined according to the lock-in speed ranges and the Reynolds number for each segment. All segments of the pole were susceptible to natural wind gust due to the equivalent static forces independent of the wind speed and pole diameter. This method was applied for all three modes.

Poles at five different locations in Texas: Dallas/Fort Worth (DFW), San Antonio (SAT), Austin (RMMA), Houston (IAH), and El Paso (ELP) were selected to be analyzed using historical wind data obtained from the National Oceanographic and Atmospheric Administration (NOAA). The dominant wind direction observed from the data was in north-south direction, indicating vortex-shedding induced vibrations in the east-west direction. The east-west direction was then selected as the prime direction for analysis. The analysis also considered the natural gust wind in the east-west direction as they would also induce vibration in the same direction. The wind speed data organized in N-S direction and E-W direction were fitted to a log-normal distribution. The probability of occurrence of each wind speed in N-S or E-W direction was then used to calculate the number of induced vibrations.

The number of vortex-shedding induced vibrations in the nth mode was calculated using Equation 2.75.

$$N = [\Phi(V_{i+1}) - \Phi(V_i)](f_n)(P_{N-S})(t)$$

Equation 2.75

where $\Phi()$ is the cumulative log-normal distribution function for the wind in N-S direction, f_n is the natural frequency of the nth mode, t is the time period of interest in seconds, and P_{N-S} is the probability of wind blowing in the N-S direction obtained from the collected wind data. The

difference between the two cumulative functions of different wind speed represents the probability of wind speed occurring in that range. The lock-in wind speeds were used to generate the wind speed range to calculate the probability of vortex-shedding induced vibration. The number of natural wind gust induced vibration in the 1st mode was calculated using Equation 2.76

$$N = (P_{gust})(f_{n,1})(P_{E-W})(t) \qquad \textbf{\textit{Equation 2.76}}$$

In Equation 2.76, P_{gust} is the probability of wind gust, $f_{n,1}$ is the natural frequency of the 1st mode, t is the time period of interest in seconds, and P_{E-W} is the probability of wind blowing in E-W direction obtained from the collected wind data. The vibration caused by the wind gust is normally felt in the first mode.

The fatigue resistance of pole base with cracks caused by galvanization was proposed to feature an 80 percent reduction in the A parameter in the S-N curve (Equation 2.77).

$$N = A \cdot S^{-m} \qquad \textbf{\textit{Equation 2.77}}$$

In Equation 2.77, N is the number of cycles, and A and m are empirical coefficients. The reduction proposed in this study is based on previous experiments conducted by Stam et al. (2011). The detail of groove-welded design without a ground sleeve is classified as AASHTO Category E fatigue detail (AASHTO 2009) whereas the detail with ground sleeve and without galvanization is tested to have similar behavior to AASHTO Category C fatigue detail (Stam et al., 2011). The dashed line in Figure 2.47 indicates the 80 percent reduction in parameter A for category C and E; the square and circular markers indicate with and without ground sleeve details respectively; the solid and hollow markers indicate non-galvanized and galvanized details respectively.

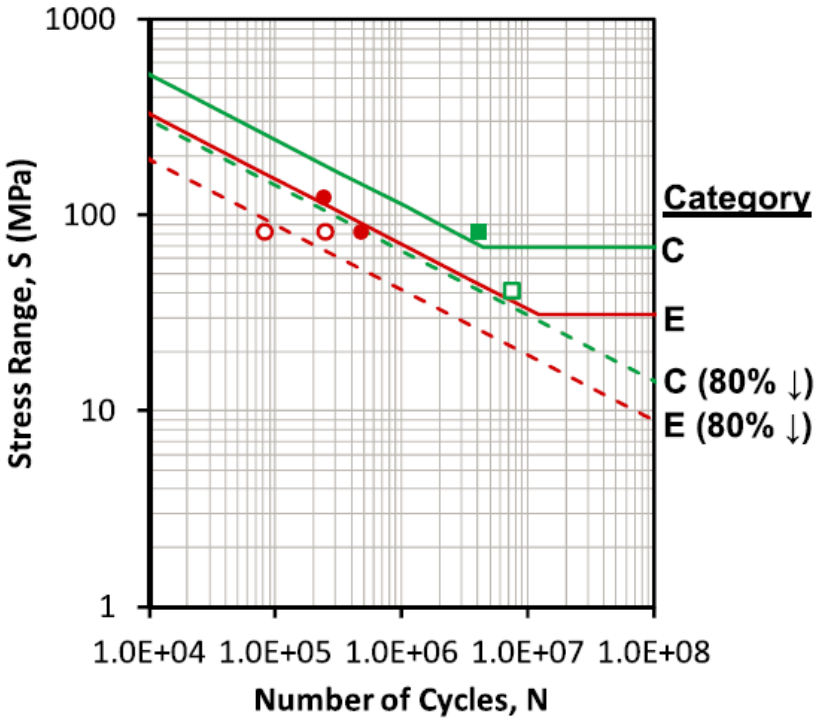

Figure 2.47: Experimental Fatigue Behavior of Various Pole-Base Details (Dawood et al. 2014)

The reliability analysis was based on the basic framework presented by Chung et al. (2003) used for reliability analysis of fracture-critical steel trapezoidal girders. The probability of failure, P_f, is given by a reliability index, β (Equation 2.78).

$$P_f = \Phi(-\beta) \qquad \textit{Equation 2.78}$$

where $\Phi()$ is a cumulative distribution function of a standard normal random variable. The reliability index is then calculated with the function (Equation 2.78) proposed by Chung et al. (2003). The values of μ_A and δ_A were determined from Chung et al. (2003) and shown in Table 2.10 whereas the values of μ_Δ and δ_Δ were considered as 1.0 and 0.30, respectively (as suggested by Chung et al. 2003). The effective stress range, S_{RE}, can be calculated from Equation 2.43 where the induced stress range and the associated number of cycles for a given wind speed can be determined from the proposed step: equivalent static pressure range and the number of vibration induced by vortex-shedding and wind gust.

Major Findings of the TxDOT Project 0-6650 (Dawood et al. 2012)

The natural frequencies determined from finite-element program SAP2000 agree reasonably well with previous results from monitoring data and analytical data (Chung et al., 2003). The dynamic properties of poles with ground sleeve detail are also found to have negligible effect compared to poles with no ground sleeve detail. The results in the form of number of stress cycles indicate that the poles in urban or suburban terrains experience more stress cycles than those in open terrain due to the wind speed in urban or suburban closer to the critical wind speed that induces vortex-shedding. Vortex-shedding induced vibrations are found to occur mostly in second and

third modes. The effective stress ranges, S_{RE}, is found to be higher in open terrain than in urban or suburban terrain. The higher S_{RE} is contributed by the higher wind speed and the resulted higher equivalent pressure. Ground sleeve detail is observed to reduce the S_{RE} to approximately half compared to the same pole without ground sleeve.

The results from reliability indices indicated a trend in higher probabilities of failure for shorter poles or lower design wind speeds (Figure 2.48). The acceptable reliability index, β, of 3.5, which corresponds to a probability of failure of 0.02%, was proposed since it is a widely accepted number in many modern North American structural design codes and specifications (AASHTO 2010; ASCE 2010; AISC 2011). A 50% increase in safe service years when the acceptable probability of failure is increased from 0.02 to 0.6% is also observed in this study. The assumptions for the values of the fatigue life coefficient, A, is found to play a crucial role in the safe service life predictions. A decrease of 80% to 50% in the assumed values for the coefficient, A, results in a 2.67 times longer service life.

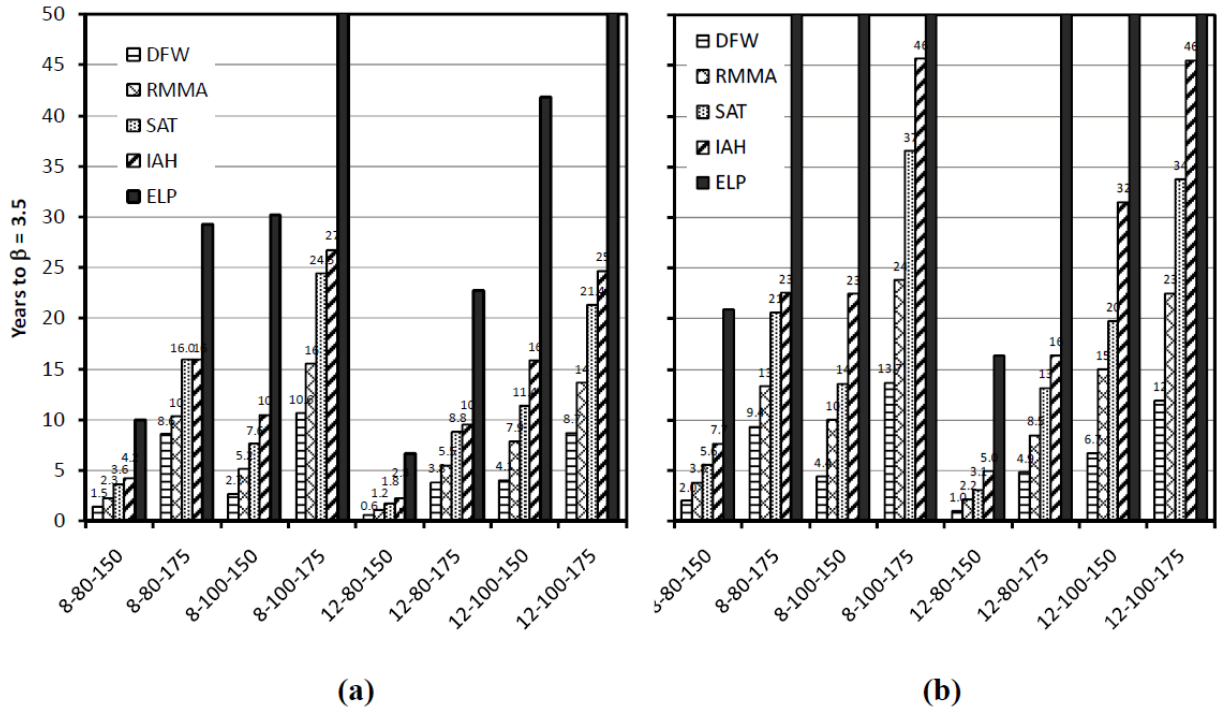

Figure 2.48: Safe Service Life Predicted for Different Pole Designs (Assuming the Acceptable Reliability Index of 3.5) Located in (a) Urban/Suburban, and (b) Open Terrain in Texas (Dawood et al. 2012)

The higher probabilities of failure for shorter poles and poles with lower design wind speeds are mainly due to the induced stresses based on the geometry of the poles. Although the number of fatigue cycles are higher for the 150 feet, 80 mph design wind velocity pole, the effective stress ranges, S_{RE}, is found to be more influential in predicting the service life. The ground sleeve detail was found to improve the service life above 50 years of all but one case analyzed in this study. The probability of failure of poles at each location is contributed mainly by the wind characteristics. Higher probability for the wind to blow in N-S direction and higher mean wind speed in N-S direction will result in higher probability of failure. The higher

probability of failure for poles in open terrain is due to the higher mean wind speed. In other words, the wind-induced stresses were found to play a more important role in predicting the service life of the poles in open terrain.

The main limitation of the study conducted by Dawood et al. (2012; 2014) is the assumption of the 80 percent reduction in fatigue coefficient, A, and no constant amplitude fatigue threshold (CAFT). The simplified approach to calculate the pole response under wind loads is another limitation to this study. The reduction of the fatigue coefficient, A, and the constant amplitude fatigue threshold can be obtained from more comprehensive data from extensive tests on the weld details with pre-existing cracks caused by galvanization. A more advanced non-linear dynamic time history analysis would also result in a more accurate prediction of the wind-induced loads.

2.6 Summary

This chapter has presented a review of the literature on the fatigue behavior of HMIPs including topics of experimental investigation of fatigue behavior of HMIPs with pre-existing cracks, wind-induced response of in-service HMIPs with pre-existing cracks, and probabilistic assessment of fatigue life and inspection scheduling.

The remaining fatigue life of in-service galvanized HMIPs in Texas is an important issue with safety and cost implications. Past research has shown that many in-service galvanized HMIPs likely have a significant degree of pre-existing cracks at the connection of the shaft to the base plate; cracks that likely formed during the galvanizing process before the poles were placed in-service. Research has also shown that these pre-existing cracks may substantially reduce the fatigue life of these poles. Considering the large TxDOT inventory of HMIPs, approximately 5000 across the state, better information and methods to predict the remaining life of these poles are needed to help guide decisions on the use of resources for inspection, monitoring, repair or replacement of HMIPs.

Past research has also developed a reliability-based framework that allows an assessment of the probability of failure of an HMIP with pre-existing cracks as a function of years of service. However, additional data are needed to make this probabilistic based approach a useful tool for TxDOT. Test data are needed on the fatigue performance of HMIPs with pre-existing cracks, at low stress ranges. Additional studies and data are also needed to better assess the effects of vortex shedding on HMIPs, as this appears to be the dominant mechanism that produces stress cycles and therefore fatigue damage in HMIPs. Finally, additional information is needed for TxDOT on options for mitigating risk associated with cracked HMIPs, such as increased inspection and monitoring, and repair techniques. These issues are addressed in the remainder of this report.

Chapter 3. Survey of Texas HMIPs

3.1 Overview

This chapter describes a survey undertaken to collect data on in-service HMIPs in the state of Texas, and to determine the HMIP designs of most interest and their locations in the state of Texas. An overview is provided of the data gathered on the inventory of Texas HMIPs. Representative results of ultrasonic tests (UT) performed by TxDOT CST (construction division) on the various HMIP designs in service are further provided. Based on the results of this study, the HMIP designs of most interest and their locations in Texas are identified and summarized.

3.2 Inventory of HMIPs in Texas

In this section, information provided in an Excel file on the inventory of Texas HMIPs are presented and explained (an electronic version of this modified Excel file will be provided to TxDOT). It should be noted that the research team received the original Excel file on the inventory of HMIPs in Texas from TxDOT. They further reorganized the information to have more consistent inventory data among districts.

3.2.1 Inventory of Texas HMIPs: An Overview of the Excel File

The most complete and updated inventory of Texas HMIPs is presented in an Excel file that will be provided to TxDOT. There are couple of important things to note about information included in this Excel file.

1. The inventory includes information about in-service poles up to 2009. In addition, most of the poles included in the inventory were the ones maintained by TxDOT. Therefore, the inventory was not complete in that it was missing information about poles maintained by the cities, especially those located in Dallas district. Research team worked with TxDOT engineers to include information on the poles in-service by the cities to have a more complete inventory.
2. The inventory of Texas HMIPs has been done by District. For reference, the District-County map of Texas is shown in Figure 3.1. Please note that the "Bridge Project Management Areas" on this map are not germane to the HMIP; it is just the only map available to the researchers.

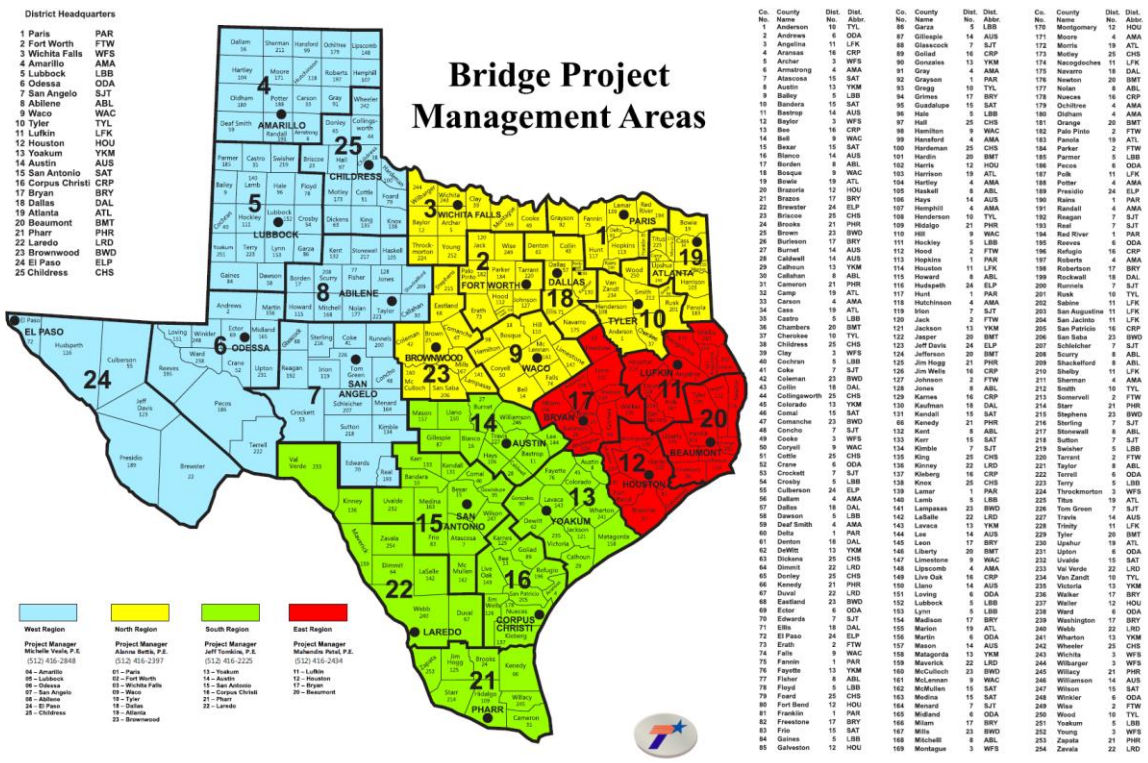

Figure 3.1: District-County Map of Texas

3. Besides information about the county in which poles are located, data on the GPS location of the poles and their design are also provided.

For the sake of completeness, details on the inventory of Texas HMIPs are also provided in the following in Figures 3.20 to 3.61. It should be note that there are no HMIPs in San Angelo, Yoakum, and Childress districts. In addition, data provided in Figures 3.20 to 3.61, indicate that there are approximately 3,228 HMIPs in Texas, which are maintained by TxDOT.

County	Highway(s)	Control & Section	HQ Pole Number	GPS		Wind Speed Rating (mph)	Pole Height (ft)	# Sides	Ground Sleeve
				Latitude	Longitude				
Lamar	US 271 @ BU271B NE (southern most)	0221-01-032	D	33.646	-95.502	70	150	8	yes
Lamar	US 271 @ S.E. Interchange (middle pole)	0221-01-032	E	33.648	-95.504	70	150	8	yes
Lamar	US 271 @ S.E. Interchange (northern most)	0221-01-032	F	33.650	-95.505	70	150	8	yes
Grayson	SH 91 @ SP 503 (west on SP 503)	0047-02-101	A2	33.720	-96.562	80	150	12	yes
Hunt	IH 30 @ BU 67 NW	0009-13-027	AAH1	33.134	-96.077	80	150	12	no
Hunt	IH 30 @ SH 34 SW	0009-13-027	AH2	33.095	-96.112	80	150	12	no
Grayson	SH 91 @ SP 503 (north on SH 91)	0047-02-101	B5	33.721	-96.558	80	150	12	yes
Hunt	IH 30 @ BU 67 SW	0009-13-027	BBH1	33.135	-96.074	80	150	12	no
Hunt	IH 30 @ SH 34 SE	0009-13-027	BH1	33.096	-96.109	80	150	12	no
Hunt	IH 30 @ SH 34 SW	0009-13-027	BH2	33.096	-96.110	80	150	12	no
Grayson	SH 91 @ SP 503 (south on SH 91)	0047-02-101	C1	33.720	-96.559	80	150	12	yes
Hunt	IH 30 @ BU 67 SE	0009-13-027	CCH1	33.135	-96.069	80	150	12	no
Hunt	IH 30 @ BU 67 SE	0009-13-027	CCH2	33.135	-96.072	80	150	12	no
Hunt	IH 30 East of BU 67 SFR	0009-13-027	DDH1	33.135	-96.067	80	150	12	no
Hunt	IH 30 @ SH 34 NW	0009-13-027	DH1	33.097	-96.110	80	150	12	no
Hunt	IH 30 @ SH 34 NE	0009-13-027	DH2	33.098	-96.109	80	150	12	no
Hunt	IH 30 East of BU 67 NFR	0009-13-027	EEH1	33.134	-96.062	80	150	12	no
Hunt	IH 30 East of BU 67 NFR	0009-13-027	EEH2	33.135	-96.064	80	150	12	no
Hunt	IH 30 @ SH 34 NE	0009-13-027	EH4	33.098	-96.107	80	150	12	no
Hunt	IH 30 West of US 69 NFR	0009-13-027	FH1	33.107	-96.103	80	150	12	no
Hunt	IH 30 West of US 69 NFR	0009-13-027	GH1	33.109	-96.102	80	150	12	no
Grayson	US 75 @ Washington (Sbd exit)	0047-01-047	H-1	33.646	-96.613	80	150	12	yes
Lamar	US 82 @ Pine Mill (by intersection)	1690-01-097	HM1	33.666	-95.512	80	150	12	yes
Lamar	US 82 @ Pine Mill (by church parking lot)	1690-01-097	HM2	33.664	-95.511	80	150	12	yes
Lamar	US 82 @ BU 82 (at shopping center)	1690-01-097	HM4	33.659	-95.509	80	150	12	yes
Lamar	US 82 @ Pine Mill (by Ford Dealership)	1690-01-097	HM5	33.669	-95.512	80	150	12	yes
Hunt	IH 30 West of US 69 NFR	0009-13-027	IH1	33.112	-96.102	80	150	12	no
Hunt	IH 30 @ SH 24 SW	0009-13-027	IIH1	33.129	-95.995	80	150	12	no
Grayson	US 75 @ SH 91 (Nbd exit)	0047-01-047	J-1	33.648	-96.612	80	150	12	yes
Hunt	IH 30 West of US 69 NFR	0009-13-027	JH1	33.114	-96.101	80	150	12	no
Hunt	IH 30 @ SH 24 NW	0009-13-027	JJH1	33.131	-95.991	80	150	12	no
Hunt	IH 30 @ SH 24 NW	0009-13-027	JJH2	33.130	-95.992	80	150	12	no
Grayson	US 75 @ SH 91 (on SH 91)	0047-01-047	K-1	33.650	-96.611	80	150	12	yes
Grayson	US 75 @ SH 91 (N of Sbd turn around)	0047-01-047	K-2	33.651	-96.611	80	150	12	yes
Hunt	IH 30 @ US 69 NW	0009-13-027	KH1	33.118	-96.103	80	150	12	no
Hunt	IH 30 @ US 69 NW	0009-13-027	KH2	33.116	-96.101	80	150	12	no
Hunt	IH 30 @ SH 24 NE	0009-13-027	KKH1	33.132	-95.989	80	150	12	no
Hunt	IH 30 @ US 69 SW	0009-13-027	LH1	33.115	-96.098	80	150	12	no
Hunt	IH 30 @ SH 24 NE	0009-13-027	LLH1	33.130	-95.989	80	150	12	no
Hunt	IH 30 @ US 69 SE	0009-13-027	MH1	33.114	-96.096	80	150	12	no
Hunt	IH 30 @ SH 24 SW	0009-13-027	MMH1	33.129	-95.996	80	150	12	no
Hunt	IH 30 @ US 69 NE	0009-13-027	NH1	33.117	-96.100	80	150	12	no
Hunt	IH 30 @ SH 24 SE	0009-13-027	NNH1	33.129	-95.993	80	150	12	no
Hunt	IH 30 @ US 69 NE	0009-13-027	OH1	33.118	-96.099	80	150	12	no
Hunt	IH 30 @ US 69 NE	0009-13-027	OH2	33.119	-96.097	80	150	12	no
Hunt	IH 30 East of SH 24 NFR	0009-13-027	OOH1	33.130	-95.987	80	150	12	no
Hunt	IH 30 @ BU 69D NE	0009-13-027	PH1	33.121	-96.096	80	150	12	no
Hunt	IH 30 East of SH 24 NFR	0009-13-027	PPH1	33.129	-95.984	80	150	12	no
Hunt	IH 30 @ BU 69D NFR	0009-13-027	QH1	33.122	-96.093	80	150	12	no
Hunt	IH 30 East of SH 24 NFR	0009-13-027	QQH1	33.129	-95.980	80	150	12	no
Hunt	IH 30 @ BU 67 NE	0009-13-027	XH1	33.138	-96.076	80	150	12	no
Hunt	IH 30 @ BU 67 NE	0009-13-027	YH1	33.053	-96.169	80	150	12	no
Hunt	IH 30 @ BU 67 NE	0009-13-027	ZH1	33.136	-96.071	80	150	12	no
Hunt	IH 30 @ BU 67 NW	0009-13-027	AAH2	33.136	-96.075	80	175	12	yes
Lamar	US 82 @ BU 82 (at intersection)	1690-01-097	HM3	33.661	-95.510	80	175	12	yes

Figure 3.2: TxDOT HMIP Inventory - Paris District

County	Highway(s)	Control & Section	HQ Pole Number	GPS		Wind Speed Rating (mph)	Pole Height (ft)	# Sides	Ground Sleeve
				Latitude	Longitude				
Tarrant	IH20 E/B @ 157 EXIT	02-78-03-220-742-IH20-13	Tower 010-63	32.674	97.141	80	150	8	yes
Tarrant	IH20 E/B @ EXIT 157	02-78-03-220-742-IH20-13	Tower 010-64	32.675	97.139	80	150	8	yes
Tarrant	E/B 20 SR @ 157	02-78-03-220-742-IH20-13	Tower 010-65	32.675	97.137	80	150	8	yes
Tarrant	E/B 20 @ 157 SW CLOVERLEAF	02-78-03-220-742-IH20-13	Tower 010-66	32.675	97.135	80	150	8	yes
Tarrant	E/B 20 @ 157 SE CLOVERLEAF	02-78-03-220-742-IH20-13	Tower 010-67	32.675	97.134	80	150	8	yes
Tarrant	E/B 20 @ ON RAMP FROM 157	02-78-03-220-742-IH20-13	Tower 010-68	32.675	97.132	80	150	8	yes
Tarrant	W/B 20 SR @ EXIT TO 157	02-78-03-220-742-IH20-13	Tower 010-69	32.677	97.148	80	150	8	yes
Tarrant	W/B 20 SR @ 157	02-78-03-220-742-IH20-13	Tower 010-70	32.676	97.150	80	150	8	yes
Tarrant	I 20 @ 157 NE CLOVER LEAF	02-78-03-220-742-IH20-13	Tower 010-71	32.681	97.134	80	150	8	yes
Tarrant	W/B I 20 @ 157 NW CLOVER LEAF	02-78-03-220-742-IH20-13	Tower 010-72	32.676	97.136	80	150	8	yes
Tarrant	W/B I 20 @ ON RAMP FOR 157	02-78-03-220-742-IH20-13	Tower 010-73	32.676	97.138	80	150	8	yes
Tarrant	N/B IH 820 @ IH 30 E/B EXIT	02-78-03-742-220-IH820-13	Tower 02-09	32.734	97.481	80	150	8	yes
Tarrant	N/B 820 @ EB IH30	02-78-03-742-220-IH820-13	Tower 02-10	32.738	97.481	80	150	8	yes
Tarrant	IH30 EAST OF 820	02-78-03-742-220-IH30-13	Tower 02-11	32.738	97.479	80	150	8	yes
Tarrant	IH30 @ IH820 N/B	02-78-03-742-220-IH30-13	Tower 02-12	32.739	97.480	80	150	8	yes
Tarrant	S/B IH820 @ EXIT IH30 W/B	02-78-03-742-220-IH820-13	Tower 02-13	32.740	97.482	80	150	8	yes
Tarrant	S/B IH820 @ W/B IH 30	02-78-03-742-220-IH820-13	Tower 02-14	32.739	97.482	80	150	8	yes
Tarrant	IH 30 W/B @ ALEMEDA	02-78-03-742-220-IH30-13	Tower 02-15	32.738	97.484	80	150	8	yes
Tarrant	E/B IH 30 @ IH820 S/B EXIT	02-78-03-742-220-IH30-13	Tower 02-16	32.737	97.483	80	150	8	yes
Tarrant	IH30E/B @ 580 EXIT	02-78-03-742-220-IH30-13	Tower 03-17	32.721	97.522	80	150	8	no
Tarrant	IH30E/B @ RAMP FROM SPUR 580	02-78-03-742-220-IH30-13	Tower 03-18	32.721	97.521	80	150	8	no
Tarrant	IH30E/B @ MARY'S CREEK	02-78-03-742-220-IH30-13	Tower 03-19	32.722	97.519	80	150	8	no
Tarrant	N/B SH121 @ CARSON	02-78-10-220-742-SH121-13	Tower 04-20	32.789	97.256	80	150	8	yes
Tarrant	IH 20 E/B @ 360	02-78-03-220-742-IH20-13	Tower 09-59	32.677	97.060	80	150	8	yes
Tarrant	E/B IH20 @ RAMP FROM 360	02-78-03-220-742-IH20-13	Tower 09-60	32.677	97.056	80	150	8	yes
Tarrant	W/B IH 20 @ 360 S/B RAMP	02-78-03-220-742-IH20-13	Tower 09-61	32.678	97.058	80	150	8	yes
Tarrant	IH20 W/B @ N/B RAMP 360	02-78-03-220-742-IH20-13	Tower 09-62	32.678	97.060	80	150	8	yes
Tarrant	I 20 W/B @ EXIT TO US 287	02-78-03-220-742-IH20-13	Tower 11-74	32.672	97.205	80	150	8	yes
Tarrant	I 20 W/B @ US 287	02-78-03-220-742-IH20-13	Tower 11-75	32.671	97.208	80	150	8	yes
Tarrant	I 20 W/B WEST OF US 287 BRIDGE	02-78-03-220-742-IH20-13	Tower 11-76	32.671	97.210	80	150	8	yes
Tarrant	I 20 W/B @ BOWMAN SPRINGS	02-78-03-220-742-IH20-13	Tower 11-77	32.669	97.216	80	150	8	yes
Tarrant	I 20 E/B @ US 287 SPLIT	02-78-03-220-742-IH20-13	Tower 11-78	32.669	97.214	80	150	8	yes
Tarrant	I 20 E/B @ US 287	02-78-03-220-742-IH20-13	Tower 11-79	32.669	97.212	80	150	8	yes
Tarrant	I 20 E/B @ 287 BRIDGE	02-78-03-220-742-IH20-13	Tower 11-80	32.670	97.210	80	150	8	yes
Tarrant	S/B US 287 EXIT RAMP	02-78-03-220-742-US287-13	Tower 11-81	32.669	97.208	80	150	8	yes
Tarrant	S/B US 287 @ LITTLE RD. SPLIT	02-78-03-220-742-US287-13	Tower 11-82	32.668	97.207	80	150	8	yes
Tarrant	S/B US 287 @ LITTLE RD.	02-78-03-220-742-US287-13	Tower 11-83	32.668	97.205	80	150	8	yes
Tarrant	I 20 E/B @ RAMP TO DALLAS	02-78-03-220-742-IH20-13	Tower 11-84	32.670	97.206	80	150	8	yes
Tarrant	I 20 E/B BEFORE US 287 ON RAMP	02-78-03-220-742-IH20-13	Tower 11-85	32.671	97.206	80	150	8	yes
Wise	US 380 & US 81 NE CLOVERLEAF	02-78-02-742-249-US380-01	Tower 12-86	33.241	97.583	80	150	8	yes
Wise	US 380 & US 81 NW CLOVERLEAF	02-78-02-742-249-US380-01	Tower 12-87	33.240	97.601	80	150	8	yes

Figure 3.3: TxDOT HMIP Inventory – Fort Worth District

County	Highway(s)	Control & Section	HQ Pole Number	GPS		Wind Speed Rating (mph)	Pole Height (ft)	# Sides	Ground Sleeve
				Latitude	Longitude				
Tarrant	I-20 & WINSCOTT	02-78-03-742-220-IH-0020-13	Tower 01-01	32.684	97.454	80	150	12	yes
Tarrant	I-20 & WINSCOTT	02-78-03-742-220-IH-0020-13	Tower 01-02	32.684	97.455	80	150	12	yes
Tarrant	I-20 & WINSCOTT	02-78-03-742-220-IH-0020-13	Tower 01-03	32.684	97.457	80	150	12	yes
Tarrant	I-20W/B JUST PASS US 377	02-78-03-742-220-IH-0020-13	Tower 01-04	32.685	97.462	80	150	12	yes
Tarrant	I-20 @US 377 SW CLOVERLEAF	02-78-03-742-220-IH-0020-13	Tower 01-05	32.684	97.461	80	150	12	yes
Tarrant	I-20 @ US 377 SE CLOVERLEAF	02-78-03-742-220-IH-0020-13	Tower 01-06	32.684	97.459	80	150	12	yes
Tarrant	I-20 @ US 377 NW CLOVERLEAF	02-78-03-742-220-IH-0020-13	Tower 01-07	32.685	97.460	80	150	12	yes
Tarrant	I-20&US 377 NE CLOVERLEAF	02-78-03-742-220-IH-0020-13	Tower 01-08	32.685	97.459	80	150	12	yes
Tarrant	N/B SH121 @ IH 820 S/B EXIT	02-78-10-220-742-SH121-13	Tower 05-21	32.804	97.212	80	150	12	yes
Tarrant	S/B 820 @ SH 10	02-78-10-220-742-IH820-13	Tower 05-22	32.810	97.210	80	150	12	yes
Tarrant	IH 820 JUST PASS SH 10	02-78-10-220-742-IH820-13	Tower 05-23	32.808	97.211	80	150	12	yes
Tarrant	IH 820 PAST SH 10 @ SH 121	02-78-10-220-742-IH820-13	Tower 05-24	32.807	97.211	80	150	12	yes
Tarrant	N/B S/R IH820 @ ONRAMP TO 820	02-78-10-220-742-IH820-13	Tower 06-25	32.826	97.205	80	150	12	yes
Tarrant	IH 820 N/B EXIT TO SH 26	02-78-10-220-742-IH820-13	Tower 06-26	32.828	97.205	80	150	12	yes
Tarrant	NB IH 820 @ AIRPORT FRWY	02-78-10-220-742-IH820-13	Tower 06-27	32.829	97.205	80	150	12	yes
Tarrant	AIRPORT FRWY @ BEDFORD-EULESS RD	02-78-10-220-742-SH183-13	Tower 06-28	32.834	97.201	80	150	12	yes
Tarrant	W/B SH 183 JUST PASS BEDFORD-EULESS RD	02-78-10-220-742-SH183-13	Tower 06-29	32.833	97.202	80	150	12	yes
Tarrant	ON RAMP FROM BEDFORD-EULESS TO IH 820	02-78-10-220-742-SH183-13	Tower 06-30	32.832	97.204	80	150	12	yes
Tarrant	N/B IH 820 CENTER MEDIAN @ AIRPORT FRWY	02-78-10-220-742-IH820-13	Tower 06-31	32.831	97.205	80	150	12	yes
Tarrant	W/B SH 183 @ IH 820 S/B & 820 W/B	02-78-10-220-742-SH183-13	Tower 06-32	32.833	97.205	80	150	12	yes
Tarrant	SH 183 @ W/B 820 CENTER MEDIAN	02-78-10-220-742-SH183-13	Tower 06-33	32.833	97.207	80	150	12	yes
Tarrant	W/B 183 SR @ GRAPEVINE HWY	02-78-10-220-742-IH820-13	Tower 06-34	32.834	97.214	80	150	12	yes
Tarrant	E/B SR IH 820 BEFORE DAVIS ST	02-78-10-220-742-IH820-13	Tower 06-35	32.833	97.218	80	150	12	yes
Tarrant	E/B IH820 CENTER MEDIAN @ DAVIS	02-78-10-220-742-IH820-13	Tower 06-36	32.832	97.217	80	150	12	yes
Tarrant	E/B IH820 SR @ CORNER OF DAVIS ST.	02-78-10-220-742-IH820-13	Tower 06-37	32.833	97.215	80	150	12	yes
Tarrant	E/B IH820 @ SH 183 SPLIT	02-78-10-220-742-IH820-13	Tower 06-38	32.833	97.213	80	150	12	yes
Tarrant	E/B IH820 CENTER MEDIAN @ SH 183 SPLIT	02-78-10-220-742-IH820-13	Tower 06-39	32.833	97.210	80	150	12	yes
Tarrant	IH 820 CENTER MEDIAN @ SH 183 SPLIT	02-78-10-220-742-IH820-13	Tower 06-40	32.832	97.208	80	150	12	yes
Tarrant	E/B 183 @ IH 820 S/B	02-78-10-220-742-SH183-13	Tower 06-41	32.831	97.207	80	150	12	yes
Tarrant	S/B IH 820 @ ON RAMP FROM SH 183	02-78-10-220-742-IH820-13	Tower 06-42	32.829	97.206	80	150	12	yes
Tarrant	S/B IH 820 @ PIPELINE RD.	02-78-10-220-742-IH820-13	Tower 06-43	32.823	97.206	80	150	12	yes
Tarrant	W/B SH 183 @ SH 10 EXIT	02-78-10-220-742-SH183-13	Tower 07-44	32.838	97.073	80	150	12	yes
Tarrant	W/B SH 183 ON WEST SIDE OF SH 10	02-78-10-220-742-SH183-13	Tower 07-45	32.838	97.076	80	150	12	yes
Tarrant	E/B SH 183 @ SH 10 BRIDGE	02-78-10-220-742-SH183-13	Tower 07-46	32.838	97.077	80	150	12	yes
Tarrant	E/B 183 SR @ DICKEY DR	02-78-10-220-742-SH183-13	Tower 07-47	32.837	97.075	80	150	12	yes
Tarrant	E/B I83 SR @ AMERICAN BLVD	02-78-10-220-742-SH183-13	Tower 07-48	32.837	97.072	80	150	12	yes
Tarrant	N/B 360 IN CENTER MEDIAN	02-78-10-220-742-SH360-13	Tower 08-49	32.903	97.097	80	150	12	yes
Tarrant	N/B 360/ NORTH OF STONE MEYERS	02-78-10-220-742-SH360-13	Tower 08-50	32.904	97.098	80	150	12	yes
Tarrant	SH 121 @ 360 N/B SPLIT	02-78-10-220-742-SH121-13	Tower 08-51	32.905	97.099	80	150	12	yes
Tarrant	SH 121 W/B @ WILLIAM D. TATE	02-78-10-220-742-SH121-13	Tower 08-52	32.909	97.099	80	150	12	yes
Tarrant	SH 121 S/B @ 360 S/B EXIT	02-78-10-220-742-SH121-13	Tower 08-53	32.911	97.099	80	150	12	yes
Tarrant	SH 121 S/B PAST 360 EXIT	02-78-10-220-742-SH121-13	Tower 08-54	32.908	97.099	80	150	12	yes
Tarrant	SH 121 S/B @ 360 OVERPASS	02-78-10-220-742-SH121-13	Tower 08-55	32.907	97.100	80	150	12	yes
Tarrant	SH 121 S/B @ STONE MEYERS	02-78-10-220-742-SH121-13	Tower 08-56	32.904	97.100	80	150	12	yes
Tarrant	SH 121 S/B SR @ STONE MEYERS	02-78-10-220-742-SH121-13	Tower 08-57	32.903	97.099	80	150	12	yes
Tarrant	S/B 360 SR PAST STONE MEYERS	02-78-10-220-742-SH360-13	Tower 08-58	32.902	97.096	80	150	12	yes
Hood	S/B US 377 @ BU 377	02-78-05-742-112-US377-02	Tower 13-88	32.440	97.760	80	150	12	yes
Hood	US 377 N/B AFTER BU 377 ON RAMP	02-78-05-742-112-US377-02	Tower 13-89	32.440	97.761	80	150	12	yes
Hood	US 377 @ BU 377	02-78-05-742-112-US377-02	Tower 13-90	32.440	97.763	80	150	12	yes
Hood	US 377 N/B CENTER MEDIAN	02-78-05-742-112-US377-02	Tower 13-91	32.439	97.763	80	150	12	yes
Hood	US 377 N/B @ BU 377 SPLIT	02-78-05-742-112-US377-02	Tower 13-92	32.438	97.765	80	150	12	yes

Figure 3.4: TxDOT HMIP Inventory – Fort Worth District - Cont'd

County	Highway(s)	Control & Section	HQ Pole Number	GPS		Wind Speed Rating (mph)	Pole Height (ft)	# Sides	Ground Sleeve
				Latitude	Longitude				
Wichita	US287	0044-01	1	33.889	98.484	80	150	8	yes
Wichita	US287	0044-01	2	33.886	98.453	80	150	8	yes
Wichita	SH79 & US281	0249-01	3	33.882	98.478	80	150	8	yes
Wichita	US287	0044-01	4	33.882	98.478	80	150	8	yes
Wichita	US287	0044-01	5	33.884	98.477	80	150	8	yes
Wichita	US287	0249-01	6	33.885	98.473	80	150	8	yes
Wichita	US287	0044-01	7	33.885	98.476	80	150	8	yes
Wichita	US287	0044-01	8	33.886	98.448	80	150	8	yes
Wichita	US287	0044-01	9	33.886	98.471	80	150	8	yes
Wichita	US287	0044-01	10	33.886	98.451	80	150	8	yes
Wichita	US287	0044-01	11	33.886	98.480	80	150	8	yes
Wichita	SH79	0044-11	12	33.887	98.447	80	150	8	yes
Wichita	US287	0044-01	13	33.887	98.482	80	150	8	yes
Cooke	US82 & IH35	0044-08	14	33.641	97.155	80	150	12	yes
Cooke	US82 & IH35	0044-08	15	33.640	97.155	80	150	12	yes
Cooke	US82 & IH35	0044-08	16	33.640	97.157	80	150	12	yes
Cooke	US82 & IH35	0044-08	17	33.641	97.155	80	150	12	yes
Cooke	US82 & IH35	0044-08	18	33.641	97.157	80	150	12	yes
Wichita	US287 & US281	0044-01	19	33.890	98.486	80	150	12	no
Wichita	Kellwest (Interchange)	0044-01	20	33.893	98.489	80	150	12	yes
Wichita	US82 & US287	0044-01	21	33.895	98.490	80	150	12	no
Wichita	Kellwest (Interchange)	0044-01	22	33.896	98.498	80	150	12	no
Wichita	Kellwest (Interchange)	0044-01	23	33.897	98.496	80	150	12	no
Wichita	Kellwest (Interchange)	0044-01	24	33.899	98.492	80	150	12	no
Clay	BU 287 (Wilson Overpass)	0044-12	25	33.881	98.411	80	150	12	no
Wichita	US287	0044-01	26	33.896	98.492	100	175	12	yes
Wichita	Kellwest (Interchange)	0044-01	27	33.897	98.494	100	175	12	yes
Wichita	Kellwest (Interchange)	0044-01	28	33.898	98.494	100	175	12	yes

Figure 3.5: TxDOT HMIP Inventory – Wichita Falls District

County	Highway(s)	Control & Section	HQ Pole Number	GPS		Wind Speed Rating (mph)	Pole Height (ft)	# Sides	Ground Sleeve
				Latitude	Longitude				
Potter	I-40 Interchange	none given	V-1	35.192	101.835	100	150	12	yes
Potter	I-40 Interchange	none given	D-1	35.193	101.835	100	150	12	yes
Potter	I-40 Interchange	none given	S-2	35.193	101.840	100	150	12	yes
Potter	I-40 Interchange	none given	U-1	35.192	101.838	100	150	12	yes
Potter	I-40 Interchange	none given	U-2	35.193	101.838	100	150	12	yes
Potter	I-40 Interchange	none given	E-1	35.194	101.837	100	150	12	yes
Potter	I-40 Interchange	none given	B-1	35.195	101.836	100	150	12	yes
Randall	I-40 Interchange	none given	D-2	35.193	101.850	100	150	12	yes
Potter	I-40 Interchange	none given	B-2	35.194	101.839	100	150	12	yes
Potter	I-40 Interchange	none given	S-1	35.192	101.839	100	150	12	yes
Potter	I-40 Interchange	none given	E-2	35.193	101.836	100	150	12	yes
Randall	US 60 Split	none given	Canyon 1	34.987	101.920	100	150	8	yes
Randall	US 60 Split	none given	Canyon 2	34.989	101.919	100	150	8	yes
Randall	US 60 Split	none given	Canyon 3	34.991	101.919	100	150	8	yes
Randall	I-27	none given	I-27-1	35.019	101.919	100	150	8	yes
Randall	I-27	none given	I-27-2	35.020	101.917	100	150	8	yes
Randall	I-27	none given	I-27-3	35.021	101.918	100	150	8	yes
Randall	I-27	none given	I-27-4	35.023	101.918	100	150	8	yes
Randall	I-27	none given	I-27-5	35.025	101.918	100	150	8	yes
Randall	I-27	none given	I-27-6	35.027	101.919	100	150	8	yes

Figure 3.6: TxDOT HMIP Inventory – Amarillo District

County	Highway(s)	Control & Section	HQ Pole Number	GPS		Wind Speed Rating (mph)	Pole Height (ft)	# Sides	Ground Sleeve
				Latitude	Longitude				
Lubbock	South I-27 & flyover	none given	HT11	33.53	-101.84	80	125	8	yes
Lubbock	I-27 & flyover	none given	HT12	33.53	-101.84	80	125	8	yes
Lubbock	LP289 & Crosbyton Hwy	none given	LT1	33.60	-101.79	80	125	8	no
Lubbock	LP289	none given	LT11	33.53	-101.84	80	125	8	yes
Lubbock	LP289 & flyover	none given	LT12	33.53	-101.85	80	125	8	yes
Lubbock	LP289	none given	LT13	33.53	-101.85	80	125	8	yes
Lubbock	LP289 & 19th	none given	LT14	33.58	-101.94	80	125	8	yes
Lubbock	LP289 & 19th	none given	LT15	33.58	-101.94	80	125	8	yes
Lubbock	LP289 & 19th	none given	LT16	33.58	-101.94	80	125	8	yes
Lubbock	LP289 & 19th	none given	LT17	33.58	-101.94	80	125	8	yes
Lubbock	LP289 & Crosbyton Hwy	none given	LT2	33.60	-101.79	80	125	8	no
Lubbock	LP289 & Crosbyton Hwy	none given	LT3	33.60	-101.79	80	125	8	no
Lubbock	LP289 & MLK	none given	LT4	33.53	-101.82	80	125	8	yes
Lubbock	LP289 & MLK	none given	LT5	33.53	-101.82	80	125	8	no
Lubbock	LP289 & MLK	none given	LT6	33.53	-101.82	80	125	8	no
Lubbock	Loop 289 & I 27	none given	LT7	33.53	-101.84	80	125	8	yes
Lubbock	Loop 289 & I 27	none given	LT8	33.53	-101.84	80	125	8	yes
Lubbock	Loop 289 & I 27	none given	LT9	33.53	-101.85	80	125	8	yes
Lubbock	Loop 289 & I 27	none given	LT 10	33.53	-101.85	80	125	12	yes
Lubbock	I-27 & 19th	none given	HT10	33.58	-101.84	100	125	12	yes
Lubbock	I-27 & 19th	none given	HT4	33.58	-101.84	100	125	12	yes
Lubbock	I-27 & 19th	none given	HT5	33.58	-101.84	100	125	12	yes
Lubbock	I-27 & 19th	none given	HT6	33.58	-101.84	100	125	12	yes
Lubbock	I-27 & 19th	none given	HT7	33.58	-101.84	100	125	12	yes
Lubbock	I-27 & 19th	none given	HT8	33.58	-101.84	100	125	12	yes
Lubbock	I-27 & 19th	none given	HT9	33.58	-101.84	100	125	12	yes
Lubbock	LP289 (#1)	none given	1	33.54	-101.93	100	150	12	yes
Lubbock	LP289 (#2)	none given	2	33.54	-101.93	100	150	12	no
Lubbock	LP289 (#3)	none given	3	33.54	-101.93	100	150	12	no
Lubbock	LP289 (#4)	none given	4	33.54	-101.93	100	150	12	no
Lubbock	LP289 (#5)	none given	5	33.54	-101.93	100	150	12	no
Lubbock	LP289 (#6)	none given	6	33.54	-101.94	100	150	12	no
Lubbock	LP289 (#7)	none given	7	33.54	-101.94	100	150	12	yes
Lubbock	LP289 (#8)	none given	8	33.55	-101.94	100	150	12	yes
Lubbock	LP289 (#9)	none given	9	33.55	-101.94	100	150	12	no
Lubbock	LP289 (#10)	none given	10	33.55	-101.94	100	150	12	no
Lubbock	LP289 (#11)	none given	11	33.55	-101.94	100	150	12	no
Lubbock	MS (#12)	none given	12	33.55	-101.94	100	150	12	no
Lubbock	LP289/MSF (#13)	none given	13	33.55	-101.94	100	150	12	no
Lubbock	LP289/MSF (#14)	none given	14	33.55	-101.94	100	150	12	no
Lubbock	LP289 (#15)	none given	15	33.56	-101.94	100	150	12	yes
Lubbock	LP289 (#16)	none given	16	33.56	-101.94	100	150	12	no
Lubbock	MSF (#17)	none given	17	33.55	-101.94	100	150	12	no
Lubbock	MSF (#18)	none given	18	33.55	-101.94	100	150	12	no
Lubbock	MSF (#19)	none given	19	33.56	-101.94	100	150	12	yes
Lubbock	MSF (#20)	none given	20	33.56	-101.93	100	150	12	yes
Lubbock	MSF (#21)	none given	21	33.58	-101.90	100	150	12	yes
Lubbock	MSF (#22)	none given	22	33.58	-101.90	100	150	12	yes
Lubbock	MSF (#23)	none given	23	33.59	-101.88	100	150	12	yes
Lubbock	MSF (#24)	none given	24	33.59	-101.88	100	150	12	yes
Lubbock	MSF (#25)	none given	25	33.59	-101.88	100	150	12	yes
Lubbock	MSF (#26)	none given	26	33.59	-101.88	100	150	12	yes
Lubbock	US 62/82	none given	Wolforth	33.52	-101.99	100	150	12	yes
Lubbock		none given	HT1	33.61	-101.84		125	8 sided 14 bolts	yes
Lubbock	I-27 & N LP 289	none given	HT2	33.61	101.85		125	8 sided 14 bolts	yes
Lubbock	I-27 & N LP 289	none given	HT3	33.61	101.85		125	8 sided 14 bolts	yes

Figure 3.7: TxDOT HMIP Inventory – Lubbock District

County	Highway(s)	Control & Section	HQ Pole Number	GPS		Wind Speed Rating (mph)	Pole Height (ft)	# Sides	Ground Sleeve
				Latitude	Longitude				
Ector	US 385 & SH 158	0463-01-020	1.TXC1	32.023222	-102.4322	80	150	12	no
Ector	US 385 & SH 158	0463-01-020	2.TXC2	32.025611	-102.4306	80	150	12	no
Ector	US 385 & SH 158	0463-01-020	3.TXC3	32.024472	-102.4291	80	150	12	no
Ector	US 385 & IH 20	0463-01-041	1.TXB1	31.826556	-102.3597	80	150	12	no
Ector	US 385 & IH 20	0463-01-041	2.TXB2	31.827972	-102.358	80	150	12	no
Ector	US 385 & IH 20	0463-01-041	3.TXB3	31.827639	-102.3562	80	150	12	no
Ector	US 385 & IH 20	0463-01-041	4.TXB4	31.828167	-102.3543	80	150	12	no
Ector	US 385 & IH 20	0463-01-041	5.TXB5	31.829	-102.3535	80	150	12	no
Ector	US 385 & IH 20	0463-01-041	6.TXB6	31.828806	-102.3511	80	150	12	no
Ector	IH 20 & LP 338	0463-01-041	1.TXD1	31.864083	-102.3054	80	150	12	no
Ector	IH 20 & LP 338	0463-01-041	2.TXD2	31.865889	-102.3036	80	150	12	no
Ector	IH 20 & LP 338	0463-01-041	3.TXD3	31.865528	-102.3023	80	150	12	no
Ector	IH 20 & LP 338	0463-01-041	5.TXD5	31.86725	-102.3009	80	150	12	no
Ector	IH 20 & LP 338	0463-01-041	4.TXD4	31.8665	-102.3007	80	150	12	no
Ector	IH 20 & LP 338	0463-01-041	6.TXD6	31.8685	-102.2985	80	150	12	no
Ector	IH 20 & Parkway	0005-13-043	8.TXA8	31.860056	-102.3115	80	150	12	no
Ector	IH 20 & Parkway	0005-13-043	6.TXA6	31.857194	-102.3146	80	150	12	no
Ector	IH 20 & Parkway	0005-13-043	5.TXA5	31.855472	-102.3157	80	150	12	no
Ector	IH 20 & Parkway	0005-13-043	7.TXA7	31.858194	-102.3127	80	150	12	no
Ector	IH 20 & Parkway	0005-13-043	4.TXA4	31.8545	-102.3176	80	150	12	no
Ector	IH 20 & Parkway	0005-13-043	2.TXA2	31.851806	-102.3206	80	150	12	no
Ector	IH 20 & Parkway	0005-13-043	1.TXA1	31.850167	-102.3216	80	150	12	no
Ector	IH 20 & Parkway	0005-13-043	3.TXA3	31.852722	-102.3188	80	150	12	no
Midland	IH 20 & LP 250	0005-14-060	1.TXE1	31.945722	-102.1488	80	150	12	no
Midland	IH 20 & LP 250	0005-14-060	2.TXE2	31.947	-102.1462	80	150	12	no
Midland	IH 20 & LP 250	0005-14-060	3.TXE3	31.948611	-102.1451	80	150	12	no
Midland	IH 20 & LP 250	0005-14-060	4.TXE4	31.947778	-102.1443	80	150	12	no
Midland	BI 20 & LP 250	0005-02-091	1.TXG1	31.960833	-102.1437	80	150	12	yes
Midland	IH 20 & LP 250	0005-14-060	5.TXE5	31.949083	-102.1433	80	150	12	no
Midland	BI 20 & LP 250	0005-02-091	2.TXG2	31.961917	-102.1426	80	150	12	yes
Midland	IH 20 & LP 250	0005-14-060	7.TXE7	31.949944	-102.1423	80	150	12	no
Midland	IH 20 & LP 250	0005-14-060	6.TXE6	31.948889	-102.142	80	150	12	no
Midland	BI 20 & LP 250	0005-02-091	3.TXG3	31.958778	-102.1413	80	150	12	yes
Midland	IH 20 & LP 250	0005-14-060	8.TXE8	31.949833	-102.1405	80	150	12	no
Midland	BI 20 & LP 250	0005-02-091	1.C1	31.962778	-102.1391	80	150	12	yes
Midland	IH 20 & LP 250	0005-14-060	9.TXE9	31.951361	-102.1388	80	150	12	no
Midland	BI 20 & LP 250	0005-02-091	2.C2	31.963778	-102.1373	80	150	12	yes
Midland	BI 20 & LP 250	0005-02-091	3.C3	31.964944	-102.1349	80	150	12	yes
Midland	IH 20 & SH 349	0005-14-060	6.TXF6	31.9725	-102.072	80	150	12	no
Midland	IH 20 & SH 349	0005-14-060	7.TXF7	31.973722	-102.0693	80	150	12	no
Midland	IH 20 & SH 349	0005-14-060	5.TXF5	31.973	-102.0728	80	150	12	no
Midland	IH 20 & SH 349	0005-14-060	4.TXF4	31.971861	-102.0743	80	150	12	no
Midland	IH 20 & SH 349	0005-14-060	3.TXF3	31.972528	-102.0752	80	150	12	no
Midland	IH 20 & SH 349	0005-14-060	2.TXF2	31.971472	-102.0766	80	150	12	no
Midland	IH 20 & SH 349	0005-14-060	1.TXF1	31.970778	-102.0797	80	150	12	no
Midland	BI 20 & LP 250	0005-02-091	9.C9	31.972167	-102.1209	80	150	12	yes
Midland	BI 20 & LP 250	0005-02-091	8.C8	31.970861	-102.1233	80	150	12	yes
Midland	BI 20 & LP 250	0005-02-091	7.C7	31.969667	-102.1256	80	150	12	yes
Midland	BI 20 & LP 250	0005-02-091	5.C5	31.967278	-102.1303	80	150	12	yes
Midland	BI 20 & LP 250	0005-02-091	4.C4	31.966	-102.1327	80	150	12	yes
Midland	BI 20 & LP 250	0005-02-091	5.TXG5	31.961389	-102.141	80	150	12	yes
Midland	BI 20 & LP 250	0005-02-091	6.TXG6	31.962806	-102.1415	80	150	12	yes
Midland	BI 20 & LP 250	0005-02-091	4.TXG4	31.960389	-102.1417	80	150	12	yes
Midland	BI 20 & LP 250	0005-02-091	6.C6	31.968611	-102.1278	80	150	12	yes

Figure 3.8: TxDOT HMIP Inventory – Odessa District

County	Highway(s)	Control & Section	HQ Pole Number	GPS		Wind Speed Rating (mph)	Pole Height (ft)	# Sides	Ground Sleeve
				Latitude	Longitude				
Haskell	US 380 & FM 2407	360-3	6	33.18	-99.81	100	125	12	yes
Shackelford	SH 6 & US 180	296-6	11	32.77	-99.59	100	125	12	yes
Callahan	SH36 & US283	437-4	20	32.23	-99.40	100	125	12	yes
Shackelford	SH 351 & FM 604	974-7	21	32.55	-99.57	100	125	12	yes
Taylor	US83 at BI20	6--18	10	32.45	-99.73	100	150	8	yes
Mitchell	IH-20 at Loraine	6--1	1	32.41	-100.71	100	150	12	yes
Taylor	US83/84 at Loop 322	2398-1	2	32.39	-99.74	100	150	12	yes
Taylor	US83/84 at Loop 322	2398-1	3	32.39	-99.74	100	150	12	yes
Taylor	US83/84 at Loop 322	2398-1	4	32.39	-99.74	100	150	12	yes
Taylor	US83/84 at Loop 322	2398-1	5	32.39	-99.74	100	150	12	yes
Taylor	US83/84 at Loop 322	2398-1	7	32.39	-99.74	100	150	12	yes
Taylor	US83/84 at Loop 322	2398-1	8	32.38	-99.74	100	150	12	yes
Taylor	US83/84 at Loop 322	2398-1	9	32.39	-99.74	100	150	12	yes
Nolan	BI20	6--15	12	32.45	-100.46	100	150	12	yes
Jones	US 277 & US 83	157-5	13	32.78	-99.90	100	150	12	no
Taylor	US83 at I-20	33-6	14	32.48	-99.77	100	150	12	yes
Taylor	US83 at I-20	33-6	15	32.48	-99.77	100	150	12	yes
Taylor	US83 at I-20	33-6	16	32.48	-99.77	100	150	12	yes
Taylor	US83 at I-20	33-6	17	32.48	-99.77	100	150	12	yes
Taylor	US83 at I-20	33-6	18	32.48	-99.77	100	150	12	yes
Taylor	US83 at I-20	33-6	19	32.48	-99.77	100	150	12	yes
Mitchell	IH-20 at Loraine	6--1	22	32.41	-100.70	100	150	12	yes

Figure 3.9: TxDOT HMIP Inventory – Abilene District

County	Highway(s)	Control & Section	HQ Pole Number	GPS		Wind Speed Rating (mph)	Pole Height (ft)	# Sides	Ground Sleeve
				Latitude	Longitude				
Bell	IH 35 & US 190	15-6	HM1.TX1	31.05	-97.47	80	125	8	yes
Bell	IH 35 & US 190	15-6	HM2.TX2	31.05	-97.47	80	125	8	yes
Bell	IH 35 & SH 53	15-4	HM3.TX3	31.10	-97.36	80	150	12	yes
Bell	IH 35 & SH 53	15-4	HM4.TX4	31.10	-97.36	80	150	12	yes
Bell	SH 36 & SH 317	184-2	HM1.TX5	31.16	-97.42	80	150	12	yes
Bell	SH 36 & SH 317	184-2	HM2.TX6	31.16	-97.42	80	150	12	yes
Bell	SH 36 & SH 317	184-2	HM3.TX7	31.16	-97.42	80	150	12	yes
Bell	SH 36 & SH 317	184-2	HM4.TX8	31.16	-97.42	80	150	12	yes
Bell	SH 36 & SH 317	184-2	HM5.TX9	31.16	-97.42	80	150	12	yes
Bell	SH 36 & SH 317	184-2	HM6.TX10	31.16	-97.42	80	150	12	yes
Bell	US 190 & Clear Creek	0231-03	HM1.TX11	31.12	-97.79	80	150	12	yes
Bell	US 190 & Clear Creek	0231-03	HM2.TX12	31.12	-97.79	80	150	12	yes
Bell	US 190 & Clear Creek	0231-03	HM3.TX13	31.12	-97.80	80	150	12	yes
Bell	US 190 & Clear Creek	0231-03	HM4.TX14	31.12	-97.80	80	150	12	yes
Bell	US 190 & Clear Creek	0231-03	HM5.TX15	31.12	-97.80	80	150	12	yes
Bell	US 190 & Clear Creek	0231-03	HM6.TX16	31.12	-97.80	80	150	12	yes
Bell	US 190 & Clear Creek	0231-03	HM7.TX17	31.12	-97.80	80	150	12	yes
Bell	US 190 & Clear Creek	0231-03	HM8.TX18	31.12	-97.79	80	150	12	yes
Bell	IH 35 & SH 53	15-4	HM1.TX19	31.10	-97.36	80	175	12	yes
Bell	IH 35 & SH 53	15-4	HM2.TX20	31.10	-97.36	80	175	12	yes
Hill	SH81	0014-07	HM4.TX21	31.97	97.12	80	150	12	yes
Hill	SH81	0014-07	HM5.TX22	31.97	97.12	80	150	12	yes
Hill	SH81	0014-07	HM6.TX23	31.97	97.12	80	150	12	yes
Hill	SH81	0014-07	HM7.TX24	31.97	97.12	80	150	12	yes
Hill	IH 35	0048-09	HM1.TX25	32.04	97.10	80	150	12	yes
Hill	IH 35	0048-09	HM2.TX26	32.04	97.09	80	150	12	yes
Hill	IH 35	0048-09	HM5.TX27	32.47	97.09	80	150	12	yes
Hill	IH 35	0048-09	HM6.TX28	32.05	97.09	80	150	12	yes
Hill	IH 35	0048-09	HM7.TX29	32.05	97.09	80	150	12	yes
Hill	IH 35	0048-09	HM8.TX30	32.05	97.09	80	150	12	yes
Hill	IH 35	0048-09	HM10.TX31	32.06	97.09	80	150	12	yes
Hill	IH 35	0048-09	HM11.TX32	32.06	97.10	80	150	12	yes
Hill	IH 35	0048-09	HM3.TX33	32.04	97.10	80	175	12	no
Hill	IH 35	0048-09	HM4.TX34	32.05	97.09	80	175	12	no
Hill	IH 35	0048-09	HM9.TX35	32.06	97.09	80	175	12	yes
McLennan	IH 35	0015-01	DOHM1.TX36	31.58	97.11	80	125	8	yes
McLennan	IH 35	0015-01	DOHM2.TX37	31.58	97.11	80	125	8	yes
McLennan	IH 35	0015-01	HM2-A1.TX38	31.50	97.15	80	150	12	no
McLennan	IH 35	0015-01	HM2-A2.TX39	31.49	97.15	80	150	12	no
McLennan	IH 35	0015-01	HM2-C1.TX40	31.49	97.15	80	150	12	no
McLennan	IH 35	0015-01	HM2-C2.TX41	31.50	97.15	80	150	12	no
McLennan	IH 35	0015-01	HM3-B1.TX42	31.49	97.15	80	150	12	no
McLennan	IH 35	0015-01	HM3-A2.TX43	31.49	97.15	80	150	12	no
McLennan	IH 35	0015-01	HM3-A1.TX44	31.49	97.15	80	150	12	no
McLennan	IH 35	0015-01	HM4-A1.TX45	31.49	97.15	80	150	12	no
McLennan	IH 35	0015-01	HM4-A2.TX46	31.49	97.15	80	150	12	no
McLennan	IH 35	0015-01	HM4-B2.TX47	31.49	97.15	80	150	12	no
McLennan	IH 35	0015-01	HM4-B1.TX48	31.49	97.15	80	150	12	no
McLennan	IH 35	0015-01	HM4-C1.TX49	31.49	97.15	80	150	12	no
McLennan	SH6 & US 77	0209-01	HMA.TX50	31.50	97.13	80	150	12	yes
McLennan	SH6 & US 77	0209-01	HMB.TX51	31.50	97.13	80	150	12	yes
McLennan	SH6 & US 77	0209-01	HMC.TX52	31.50	97.12	80	150	12	yes
McLennan	SH6 & US 77	0209-01	HMD.TX53	31.50	97.12	80	150	12	yes
McLennan	SH6 & US 77	0209-01	HME.TX54	31.50	97.13	80	150	12	yes

Figure 3.10: TxDOT HMIP Inventory – Waco District

County	Highway(s)	Control & Section	HQ Pole Number	GPS		Wind Speed Rating (mph)	Pole Height (ft)	# Sides	Ground Sleeve
				Latitude	Longitude				
Gregg	IH 20	0393-01-074	P3.C1	32.45	-94.71	80	150	8	no
Gregg	IH 20	0393-01-074	P4.C1	32.45	-94.71	80	175	8	no
Gregg	IH 20	0393-01-074	P2.C1	32.45	-94.71	80	150	8	no
Gregg	IH 20	0393-01-074	P1.C1	32.45	-94.72	80	150	8	no
Gregg	IH 20	0393-01-074	P8.C1	32.45	-94.72	80	150	8	no
Gregg	IH 20	0393-01-074	P5.C1	32.45	-94.72	80	150	8	no
Gregg	IH 20	0393-01-074	P7.C1	32.45	-94.72	80	150	8	no
Gregg	IH 20	0393-01-074	P6.C1	32.45	-94.72	80	150	8	no
Gregg	IH 20 @ FM 42	0495-03-057	P5.TX5	32.43	-94.86	80	150	8	no
Gregg	IH 20 @ FM 42	0495-03-057	P4.TX5	32.43	-94.86	80	175	8	no
Gregg	IH 20 @ FM 42	0495-03-057	P3.TX5	32.43	-94.86	80	150	8	no
Gregg	IH 20 @ FM 42	0495-03-057	P2.TX5	32.43	-94.86	80	150	8	no
Gregg	IH 20 @ FM 42	0495-03-057	P1.TX5	32.43	-94.87	80	150	8	no
Gregg	IH 20 @ SH 135	0495-03-057	P5.TX6	32.43	-94.92	80	175	8	yes
Gregg	IH 20 @ SH 135	0495-03-057	P4.TX6	32.43	-94.92	80	175	8	yes
Smith	IH 20 @ SH 135	0495-03-057	P3.TX6	32.43	-94.93	80	175	8	yes
Gregg	IH 20 @ SH 135	0495-03-057	P2.TX6	32.43	-94.93	80	175	8	yes
Gregg	IH 20 @ SH 135	0495-03-057	P1.TX6	32.43	-94.93	80	175	8	yes
Gregg	IH 20 @ FM 3053	0495-03-057	P5.TX3	32.43	-94.94	80	150	8	no
Smith	IH 20 @ FM 3053	0495-03-057	P4.TX3	32.43	-94.94	80	150	8	no
Gregg	IH 20 @ FM 3053	0495-03-057	P3.TX3	32.43	-94.94	80	150	8	no
Gregg	IH 20 @ FM 3053	0495-03-057	P2.TX3	32.43	-94.95	80	150	8	no
Gregg	IH 20 @ FM 3053	0495-03-057	P1.TX3	32.43	-94.95	80	150	8	no
Smith	IH 20 @ US 271	0495-03-057	P6.TX7	32.44	-95.13	80	150	8	no
Smith	IH 20 @ US 271	0495-03-057	P5.TX7	32.44	-95.13	80	175	8	yes
Smith	IH 20 @ US 271	0495-03-057	P4.TX7	32.44	-95.13	80	175	8	yes
Smith	IH 20 @ US 271	0495-03-057	P3.TX7	32.44	-95.13	80	175	8	yes
Smith	IH 20 @ US 271	0495-03-057	P2.TX7	32.44	-95.14	80	150	8	no
Smith	IH 20 @ US 271	0495-03-057	P1.TX7	32.44	-95.14	80	150	8	no
Smith	IH 20 @ FM 14	0495-03-057	P7.TX2	32.45	-95.28	80	150	8	no
Smith	IH 20 @ FM 14	0495-03-057	P6.TX2	32.45	-95.28	80	150	8	no
Smith	IH 20 @ FM 14	0495-03-057	P4.TX2	32.45	-95.28	80	150	8	no
Smith	IH 20 @ FM 14	0495-03-057	P5.TX2	32.45	-95.28	80	150	8	no
Smith	IH 20 @ FM 14	0495-03-057	P3.TX2	32.45	-95.29	80	150	8	no
Smith	IH 20 @ FM 14	0495-03-057	P2.TX2	32.45	-95.29	80	150	8	no
Smith	IH 20 @ FM 14	0495-03-057	P1.TX2	32.45	-95.29	80	150	8	no
Smith	IH 20 @ US 69	0495-03-057	P5.TX8	32.47	-95.38	80	150	8	no
Smith	IH 20 @ US 69	0495-03-057	P4.TX8	32.47	-95.39	80	150	8	no
Smith	IH 20 @ US 69	0495-03-057	P3.TX8	32.47	-95.39	80	175	8	yes
Smith	IH 20 @ US 69	0495-03-057	P2.TX8	32.47	-95.39	80	150	8	no
Smith	IH 20 @ US 69	0495-03-057	P1.TX8	32.47	-95.39	80	150	8	no
Smith	IH 20 @ FM 110	0495-03-057	P5.TX1	32.48	-95.52	80	150	8	no
Smith	IH 20 @ FM 110	0495-03-057	P4.TX1	32.48	-95.52	80	150	8	no
Smith	IH 20 @ FM 110	0495-03-057	P3.TX1	32.48	-95.52	80	175	8	yes
Smith	IH 20 @ FM 110	0495-03-057	P2.TX1	32.48	-95.52	80	150	8	no
Smith	IH 20 @ FM 110	0495-03-057	P1.TX1	32.48	-95.53	80	150	8	no
Van Zandt	IH 20 @ FM 314	0495-03-057	P6.TX4	32.51	-95.64	80	175	8	yes
Van Zandt	IH 20 @ FM 314	0495-03-057	P5.TX4	32.51	-95.64	80	175	8	yes
Van Zandt	IH 20 @ FM 314	0495-03-057	P4.TX4	32.51	-95.64	80	175	8	yes
Van Zandt	IH 20 @ FM 314	0495-03-057	P3.TX4	32.51	-95.64	80	175	8	yes
Van Zandt	IH 20 @ FM 314	0495-03-057	P2.TX4	32.51	-95.65	80	175	8	yes
Van Zandt	IH 20 @ FM 314	0495-03-057	P1.TX4	32.51	-95.65	80	175	8	yes

Figure 3.11: TxDOT HMIP Inventory – Tyler District

County	Highway(s)	Control & Section	HQ Pole Number	GPS		Wind Speed Rating (mph)	Pole Height (ft)	# Sides	Ground Sleeve
				Latitude	Longitude				
San Jacinto	US 59	0177-02-059	HM16	30.49	-94.99	80	175	12	no
San Jacinto	US 59	0177-02-059	HM17	30.49	-94.99	80	175	12	no
San Jacinto	US 59	0177-02-059	HM15	30.49	-94.99	80	175	12	no
San Jacinto	US 59	0177-02-059	HM18	30.50	-94.99	80	175	12	no
San Jacinto	US 59	0177-02-059	HM14	30.50	-94.98	80	175	12	no
San Jacinto	US 59	0177-02-059	HM19	30.50	-94.99	80	175	12	no
San Jacinto	US 59	0177-02-059	HM20	30.50	-94.99	80	175	12	no
San Jacinto	US 59	0177-02-059	HM12	30.50	-94.99	80	175	12	no
San Jacinto	US 59	0177-02-059	HM13	30.50	-94.99	80	175	12	no
San Jacinto	US 59	0177-02-059	HM21	30.50	-94.99	80	175	12	no
San Jacinto	US 59	0177-02-059	HM11A (Shepherd)	30.51	-94.99	80	175	12	no
Angelina	US 59	0176-03-115	HM22	31.30	-94.73	80	175	12	yes
Angelina	US 59	0176-03-115	HM23	31.30	-94.73	80	175	12	yes
Angelina	US 59	0176-03-115	HM24	31.30	-94.73	80	175	12	yes
Angelina	US 59	0176-03-115	HM25	31.31	-94.73	80	175	12	yes
Angelina	US 59	0176-03-115	HM26	31.31	-94.73	80	175	12	yes
Angelina	US 59/LP 287	0176-03-115	HM27	31.31	-94.72	80	175	12	yes
Angelina	US 59/LP 287	0176-03-115	HM28	31.31	-94.72	80	175	12	yes
Angelina	SH 94/LP 287	2553-01-045	HM11	31.33	-94.76	80	175	12	yes
Angelina	SH 94/LP 287	2553-01-045	HM10	31.33	-94.76	80	175	12	yes
Angelina	US 69	0199-04-005	HM7	31.37	-94.75	100	175	12	yes
Angelina	US 69	0199-04-005	HM8	31.37	-94.75	80	175	12	yes
Angelina	US 69	0199-04-005	HM3	31.37	-94.75	100	175	12	yes
Angelina	US 69	0199-04-005	HM6	31.37	-94.76	80	175	12	yes
Angelina	US 59	0176-02-052	HM1	31.37	-94.71	70	150	12	no
Angelina	US 69	0199-04-005	HM2	31.37	-94.75	100	175	12	yes
Angelina	US 69	0199-04-005	HM5	31.37	-94.76	80	175	12	yes
Angelina	US 69	0199-04-005	HM9	31.37	-94.74	80	175	12	yes
Angelina	US 69	0199-04-005	HM4	31.37	-94.76	100	175	12	yes

Figure 3.12: TxDOT HMIP Inventory – Lufkin District

County	Highway(s)	Control & Section	HQ Pole Number	GPS		Wind Speed Rating (mph)	Pole Height (ft)	# Sides	Ground Sleeve
				Latitude	Longitude				
HARRIS	IH 45	0500-03-313	1634	29.74	95.35	100	100	8	Y
HARRIS	IH 45	0110-05-070	445	29.98	95.42	100	100	12	Y
HARRIS	IH 45	0110-05-070	446	29.99	95.42	100	100	12	Y
HARRIS	IH 45	0110-05-070	447	29.99	95.42	100	100	12	Y
HARRIS	IH 45	0110-05-063	480	29.99	95.42	100	100	12	Y
HARRIS	IH 45	0110-05-063	481	29.99	95.42	100	100	12	Y
HARRIS	IH 45	0110-05-063	482	29.99	95.42	100	100	12	Y
HARRIS	IH 45	0110-05-063	483	29.99	95.42	100	100	12	Y
HARRIS	IH 45	0110-05-063	484	30.00	95.42	100	100	12	Y
HARRIS	IH 45	0110-05-063	485	30.00	95.43	100	100	12	Y
HARRIS	IH 45	0110-05-063	486	30.00	95.43	100	100	12	Y
HARRIS	IH 45	0110-05-063	487	30.00	95.43	100	100	12	Y
HARRIS	US 59	0177-07-080	863	29.97	95.28	100	100	12	Y
HARRIS	US 59	0177-07-080	864	29.97	95.28	100	100	12	Y
HARRIS	US 59	0177-07-080	865	29.97	95.28	100	100	12	Y
HARRIS	US 59	0177-07-080	866	29.97	95.28	100	100	12	Y
HARRIS	US 59	0177-07-080	867	29.97	95.28	100	100	12	Y
HARRIS	US 59	0177-07-080	868	29.97	95.28	100	100	12	Y
HARRIS	US 59	0177-07-080	869	29.98	95.28	100	100	12	Y
HARRIS	US 59	0177-07-080	870	29.98	95.28	100	100	12	Y
HARRIS	US 59	0177-07-080	871	29.98	95.28	100	100	12	Y
HARRIS	US 59	0177-07-080	872	29.98	95.28	100	100	12	Y
HARRIS	US 59	0177-07-080	873	29.98	95.28	100	100	12	Y
HARRIS	US 59	0177-07-080	874	29.98	95.28	100	100	12	Y
HARRIS	US 59	0177-07-080	875	29.99	95.28	100	100	12	Y
HARRIS	US 59	0177-07-080	876	29.99	95.28	100	100	12	Y
HARRIS	US 59	0177-07-080	877	29.99	95.27	100	100	12	Y
HARRIS	US 59	0177-07-080	878	29.99	95.27	100	100	12	Y
HARRIS	US 59	0177-07-080	879	29.99	95.27	100	100	12	Y
FORT BEND	US 59	0027-12-062	940	29.58	95.65	100	100	12	Y
FORT BEND	US 59	0027-12-062	941	29.58	95.64	100	100	12	Y
FORT BEND	US 59	0027-12-062	942	29.58	95.64	100	100	12	Y
HARRIS	SH 225	0502-01-204	1041	29.71	95.26	100	100	12	Y
HARRIS	SH 225	0502-01-204	1044	29.71	95.25	100	100	12	Y
HARRIS	SH 225	0502-01-204	1045	29.71	95.25	100	100	12	Y
HARRIS	SH 225	0502-01-204	1046	29.71	95.25	100	100	12	Y
HARRIS	SH 225	0502-01-204	1047	29.71	95.24	100	100	12	Y
HARRIS	SH 225	0502-01-204	1048	29.71	95.24	100	100	12	Y
HARRIS	SH 225	0502-01-204	1049	29.71	95.24	100	100	12	Y
HARRIS	SH 225	0502-01-204	1050	29.71	95.24	100	100	12	Y
HARRIS	SH 225	0502-01-204	1051	29.71	95.23	100	100	12	Y
HARRIS	SH 225	0502-01-204	1052	29.71	95.23	100	100	12	Y
HARRIS	SH 225	0502-01-204	1053	29.71	95.23	100	100	12	Y
HARRIS	SH 225	0502-01-204	1054	29.71	95.23	100	100	12	Y
HARRIS	SH 225	0502-01-204	1055	29.71	95.23	100	100	12	Y
HARRIS	SH 225	0502-01-204	1056	29.71	95.22	100	100	12	Y
HARRIS	IH 610	0271-15-011	1330	29.71	95.26	100	125	8	N
HARRIS	IH 610	0271-15-011	1331	29.71	95.27	100	125	8	N
HARRIS	IH 610	0271-15-011	1332	29.71	95.27	100	125	8	N
HARRIS	IH 610	0271-15-011	1333	29.71	95.27	100	125	8	N
HARRIS	IH 610	0271-15-011	1336	29.71	95.27	100	125	8	N
HARRIS	IH 610	0271-15-011	1337	29.71	95.27	100	125	8	N
HARRIS	IH 610	0271-15-011	1338	29.71	95.27	100	125	8	N
HARRIS	IH 610	0271-15-011	1339	29.71	95.27	100	125	8	N
HARRIS	IH 610	0271-15-011	1340	29.71	95.27	100	125	8	N
HARRIS	BW 8	3256-01-028	4	29.67	95.56	100	125	8	Y
HARRIS	BW 8	3256-02-037	5	29.94	95.43	100	125	8	Y
HARRIS	BW 8	3256-01-055	11	29.66	95.56	100	125	8	Y

Figure 3.13: TxDOT HMIP Inventory – Houston District

County	Highway(s)	Control & Section	HQ Pole Number	GPS		Wind Speed Rating (mph)	Pole Height (ft)	# Sides	Ground Sleeve
				Latitude	Longitude				
C. HARRIS	BW 8	3256-02-062	15	29.94	95.39	100	125	8	Y
C. HARRIS	BW 8	3256-02-062	16	29.94	95.39	100	125	8	Y
C. HARRIS	BW 8	3256-02-062	17	29.94	95.39	100	125	8	Y
C. HARRIS	BW 8	3256-02-062	20	29.94	95.38	100	125	8	Y
C. HARRIS	BW 8	3256-02-062	21	29.94	95.38	100	125	8	Y
C. HARRIS	BW 8	3256-02-062	22	29.94	95.37	100	125	8	Y
C. HARRIS	BW 8	3256-02-062	23	29.94	95.37	100	125	8	Y
C. HARRIS	BW 8	3256-02-062	24	29.94	95.37	100	125	8	Y
C. HARRIS	BW 8	3256-02-062	25	29.94	95.37	100	125	8	Y
C. HARRIS	BW 8	3256-02-062	26	29.94	95.36	100	125	8	Y
C. HARRIS	BW 8	3256-02-062	27	29.94	95.36	100	125	8	Y
C. HARRIS	BW 8	3256-02-062	28	29.94	95.36	100	125	8	Y
C. HARRIS	BW 8	3256-02-062	29	29.94	95.36	100	125	8	Y
C. HARRIS	BW 8	3256-02-062	30	29.94	95.35	100	125	8	Y
HARRIS	IH 10	0508-01-209	36	29.78	95.29	100	125	8	Y
HARRIS	IH 10	0508-01-209	37	29.78	95.29	100	125	8	Y
HARRIS	IH 10	0508-01-209	38	29.78	95.29	100	125	8	Y
HARRIS	IH 10	0508-01-209	39	29.78	95.28	100	125	8	Y
HARRIS	IH 10	0508-01-209	41	29.78	95.28	100	125	8	Y
HARRIS	IH 10	0508-01-209	42	29.78	95.28	100	125	8	Y
HARRIS	IH 10	0508-01-209	43	29.78	95.27	100	125	8	Y
HARRIS	IH 10	0508-01-209	46	29.78	95.27	100	125	8	Y
HARRIS	IH 10	0508-01-209	47	29.78	95.27	100	125	8	Y
HARRIS	IH 10	0508-01-209	48	29.78	95.27	100	125	8	Y
C. HARRIS	IH 10	0508-01-209	58	29.77	95.25	100	125	8	Y
C. HARRIS	IH 10	0508-01-209	59	29.78	95.26	100	125	8	Y
C. HARRIS	IH 10	0508-01-209	60	29.78	95.26	100	125	8	Y
C. HARRIS	IH 10	0508-01-209	61	29.78	95.26	100	125	8	Y
C. HARRIS	IH 10	0508-01-209	62	29.78	95.26	100	125	8	Y
C. HARRIS	IH 10	0508-01-209	68	29.77	95.26	100	125	8	Y
HARRIS	IH 10	0508-01-230	69	29.77	95.17	100	125	8	Y
HARRIS	IH 10	0508-01-230	70	29.77	95.16	100	125	8	Y
HARRIS	IH 10	0508-01-230	71	29.77	95.16	100	125	8	Y
HARRIS	IH 10	0508-01-230	77	29.77	95.15	100	125	8	Y
HARRIS	IH 10	0508-01-230	78	29.77	95.15	100	125	8	Y
HARRIS	IH 10	0508-01-230	79	29.77	95.14	100	125	8	Y
HARRIS	IH 10	0508-01-230	82	29.77	95.15	100	125	8	Y
HARRIS	IH 10	0508-01-230	83	29.77	95.15	100	125	8	Y
HARRIS	IH 10	0508-01-236	87	29.78	95.16	100	125	8	Y
N. HARRIS	IH 45	0110-06-089	355	29.88	95.41	100	125	8	Y
N. HARRIS	IH 45	0110-06-089	356	29.88	95.41	100	125	8	Y
N. HARRIS	IH 45	0110-06-089	357	29.89	95.41	100	125	8	Y
N. HARRIS	IH 45	0110-06-089	359	29.89	95.41	100	125	8	Y
N. HARRIS	IH 45	0110-06-089	360	29.89	95.41	100	125	8	Y
N. HARRIS	IH 45	0110-06-089	361	29.89	95.41	100	125	8	Y
N. HARRIS	IH 45	0110-06-089	362	29.90	95.41	100	125	8	Y
N. HARRIS	IH 45	0110-06-089	364	29.90	95.41	100	125	8	Y
N. HARRIS	IH 45	0110-06-089	365	29.90	95.41	100	125	8	Y
N. HARRIS	IH 45	0110-06-089	366	29.90	95.41	100	125	8	Y
N. HARRIS	IH 45	0110-06-089	367	29.91	95.41	100	125	8	Y
N. HARRIS	IH 45	0110-06-089	368	29.91	95.41	100	125	8	Y
N. HARRIS	IH 45	0110-06-089	369	29.91	95.41	100	125	8	Y
N. HARRIS	IH 45	0110-06-089	370	29.91	95.41	100	125	8	Y
N. HARRIS	IH 45	0110-06-089	371	29.91	95.41	100	125	8	Y
N. HARRIS	IH 45	0110-06-089	373	29.92	95.41	100	125	8	Y
N. HARRIS	IH 45	0110-06-089	374	29.92	95.41	100	125	8	Y
N. HARRIS	IH 45	0110-06-089	375	29.92	95.41	100	125	8	Y
N. HARRIS	IH 45	0110-06-089	376	29.92	95.41	100	125	8	Y

Figure 3.14: TxDOT HMIP Inventory – Houston District - Cont'd

County	Highway(s)	Control & Section	HQ Pole Number	GPS		Wind Speed Rating (mph)	Pole Height (ft)	# Sides	Ground Sleeve
				Latitude	Longitude				
N. HARRIS	IH 45	0110-06-089	377	29.92	95.41	100	125	8	Y
N. HARRIS	IH 45	0110-06-089	378	29.93	95.41	100	125	8	Y
N. HARRIS	IH 45	0110-06-089	379	29.93	95.41	100	125	8	Y
N. HARRIS	IH 45	0110-06-089	380	29.93	95.41	100	125	8	Y
N. HARRIS	IH 45	0110-06-089	382	29.93	95.41	100	125	8	Y
N. HARRIS	IH 45		383			100	125	8	Y
N. HARRIS	IH 45	0110-06-089	384	29.94	95.41	100	125	8	Y
	IH 45		386			100	125	8	Y
	IH 45		387			100	125	8	Y
	IH 45		388			100	125	8	Y
	IH 45		389			100	125	8	Y
N. HARRIS	IH 45	0110-06-104	390	29.94	95.42	100	125	8	Y
HARRIS	IH 45	0500-03-382	396	29.62	95.22	100	125	8	Y
HARRIS	IH 45	0500-03-382	397	29.62	95.22	100	125	8	Y
HARRIS	IH 45	0500-03-382	398	29.62	95.22	100	125	8	Y
HARRIS	IH 45	0500-03-382	399	29.62	95.22	100	125	8	Y
HARRIS	IH 45	0500-03-382	400	29.62	95.22	100	125	8	Y
HARRIS	IH 45	0500-03-382	401	29.62	95.22	100	125	8	Y
HARRIS	IH 45	0500-03-382	404	29.62	95.21	100	125	8	Y
HARRIS	IH 45	0500-03-382	405	29.61	95.21	100	125	8	Y
HARRIS	IH 45	0500-03-382	406	29.61	95.21	100	125	8	Y
HARRIS	IH 45	0500-03-382	407	29.61	95.21	100	125	8	Y
HARRIS	IH 45	0500-03-382	416	29.60	95.20	100	125	8	Y
HARRIS	IH 45	0500-03-382	421	29.60	95.20	100	125	8	Y
HARRIS	IH 45	0500-03-382	422	29.60	95.19	100	125	8	Y
HARRIS	IH 45	0500-03-382	423	29.59	95.19	100	125	8	Y
HARRIS	IH 45	0500-03-382	424	29.59	95.19	100	125	8	Y
HARRIS	IH 45	0500-03-382	425	29.59	95.19	100	125	8	Y
HARRIS	IH 45	0500-03-382	426	29.59	95.19	100	125	8	Y
HARRIS	IH 45	0500-03-382	427	29.59	95.19	100	125	8	Y
HARRIS	IH 45	0500-03-382	428	29.59	95.19	100	125	8	Y
HARRIS	IH 45	0500-03-382	429	29.59	95.19	100	125	8	Y
GALVESTON	IH 45	0500-04-066	607	29.41	95.04	100	125	8	Y
GALVESTON	IH 45	0500-04-066	613	29.40	94.04	100	125	8	Y
HARRIS	US 59	0027-13-117	654	29.66	95.56	100	125	8	Y
HARRIS	US 59	0027-13-117	656	29.66	95.56	100	125	8	Y
HARRIS	US 59	0027-13-117	663	29.67	95.55	100	125	8	Y
HARRIS	US 59	0027-13-117	664	29.67	95.55	100	125	8	Y
HARRIS	US 59	0027-13-117	665	29.67	95.55	100	125	8	Y
HARRIS	US 59	0027-13-123	669	29.73	95.49	100	125	8	Y
HARRIS	US 59	0027-13-123	673	29.73	95.48	100	125	8	Y
HARRIS	US 59	0027-13-123	677	29.73	95.47	100	125	8	Y
HARRIS	US 59	0027-13-123	678	29.73	95.47	100	125	8	Y
HARRIS	US 59	0027-13-123	680	29.73	95.47	100	125	8	Y
HARRIS	US 59	0027-13-123	684	29.73	95.46	100	125	8	Y
HARRIS	US 59	0027-13-123	685	29.73	95.46	100	125	8	Y
HARRIS	US 59	0027-13-123	686	29.73	95.45	100	125	8	Y
HARRIS	US 59	0027-13-123	687	29.72	95.46	100	125	8	Y
HARRIS	US 59	0027-13-126	693	29.69	95.52	100	125	8	Y
HARRIS	US 59	0027-13-126	694	29.70	95.52	100	125	8	Y
HARRIS	US 59	0027-13-126	695	29.70	95.52	100	125	8	Y
HARRIS	US 59	0027-13-126	696	29.70	95.52	100	125	8	Y
HARRIS	US 59	0027-13-126	699	29.70	95.52	100	125	8	Y
HARRIS	US 59	0027-13-126	701	29.71	95.51	100	125	8	Y
HARRIS	US 59	0027-13-126	702	29.71	95.51	100	125	8	Y
HARRIS	US 59	0027-13-126	703	29.71	95.51	100	125	8	Y
HARRIS	US 59	0027-13-126	704	29.71	95.51	100	125	8	Y
HARRIS	US 59	0027-13-126	705	29.71	95.51	100	125	8	Y

Figure 3.15: TxDOT HMIP Inventory – Houston District - Cont'd

County	Highway(s)	Control & Section	HQ Pole Number	GPS		Wind Speed Rating (mph)	Pole Height (ft)	# Sides	Ground Sleeve
				Latitude	Longitude				
HARRIS	US 59	0027-13-126	706	29.71	95.51	100	125	8	Y
HARRIS	US 59	0027-13-126	707	29.71	95.50	100	125	8	Y
HARRIS	US 59	0027-13-126	708	29.71	95.50	100	125	8	Y
HARRIS	US 59	0027-13-126	709	29.72	95.50	100	125	8	Y
HARRIS	US 59	0027-13-100	722	29.68	95.54	100	125	8	Y
HARRIS	US 59	0027-13-100	723	29.68	95.54	100	125	8	Y
HARRIS	US 59	0027-13-100	724	29.68	95.54	100	125	8	Y
HARRIS	US 59	0027-13-100	725	29.68	95.53	100	125	8	Y
HARRIS	US 59	0027-13-133	734	29.73	95.45	100	125	8	Y
HARRIS	US 59	0027-13-133	736	29.73	95.44	100	125	8	Y
HARRIS	US 59	0027-13-133	737	29.73	95.44	100	125	8	Y
HARRIS	US 59	0027-13-133	739	29.73	95.44	100	125	8	Y
HARRIS	US 59	0027-13-133	740	29.73	95.44	100	125	8	Y
HARRIS	US 59	0027-13-133	741	29.73	95.43	100	125	8	Y
HARRIS	US 59	0027-13-133	742	29.73	95.43	100	125	8	Y
HARRIS	US 59	0027-13-133	743	29.73	95.43	100	125	8	Y
HARRIS	US 59	0027-13-133	745	29.73	95.43	100	125	8	Y
HARRIS	US 59	0027-13-133	746	29.73	95.42	100	125	8	Y
HARRIS	US 59	0027-13-133	747	29.73	95.42	100	125	8	Y
HARRIS	US 59	0027-13-133	749	29.73	95.42	100	125	8	Y
HARRIS	US 59	0027-13-133	750	29.73	95.41	100	125	8	Y
HARRIS	US 59	0177-11-066	753	29.81	95.33	100	125	8	Y
HARRIS	US 59	0177-11-066	763	29.83	95.33	100	125	8	Y
HARRIS	US 59	0177-11-066	764	29.83	95.33	100	125	8	Y
HARRIS	US 59	0177-11-066	765	29.84	95.33	100	125	8	Y
HARRIS	US 59	0177-07-074	789	29.90	95.31	100	125	8	Y
HARRIS	US 59	0177-07-074	790	29.90	95.31	100	125	8	Y
HARRIS	US 59	0177-07-074	791	29.90	95.31	100	125	8	Y
HARRIS	US 59	0177-07-074	792	29.91	95.31	100	125	8	Y
HARRIS	US 59	0177-07-074	793	29.91	95.31	100	125	8	Y
HARRIS	US 59	0177-07-074	794	29.91	95.31	100	125	8	Y
HARRIS	US 59	0177-07-074	795	29.91	95.31	100	125	8	Y
HARRIS	US 59	0177-07-074	796	29.91	95.31	100	125	8	Y
HARRIS	US 59	0177-07-074	797	29.91	95.31	100	125	8	Y
HARRIS	US 59	0177-07-074	798	29.92	95.31	100	125	8	Y
HARRIS	US 59	0177-07-074	799	29.92	95.31	100	125	8	Y
HARRIS	US 59	0177-07-074	800	29.92	95.30	100	125	8	Y
BRAZORIA	SH 288	0598-02-013	1129	29.59	95.39	100	125	8	Y
BRAZORIA	SH 288	0598-02-013	1130	29.58	95.39	100	125	8	Y
BRAZORIA	SH 288	0598-02-013	1137	29.58	95.39	100	125	8	Y
BRAZORIA	SH 288	0598-02-013	1138	29.57	95.39	100	125	8	Y
BRAZORIA	SH 288	0598-02-013	1139	29.56	95.39	100	125	8	Y
BRAZORIA	SH 288	0598-02-013	1140	29.56	95.39	100	125	8	Y
BRAZORIA	SH 288	0598-02-013	1147	29.55	95.39	100	125	8	Y
BRAZORIA	SH 288	0598-02-013	1148	29.55	95.39	100	125	8	Y
HARRIS	SH 288	0598-01-021	1150	29.72	95.38	100	125	8	Y
HARRIS	SH 288	0598-01-021	1151	29.73	95.37	100	125	8	Y
HARRIS	SH 288	0598-01-021	1152	29.73	95.37	100	125	8	Y
HARRIS	SH 288	0598-01-021	1153	29.73	95.37	100	125	8	Y
HARRIS	SH 288	0598-01-045	1155	29.66	95.38	100	125	8	Y
HARRIS	SH 288	0598-01-045	1156	29.66	95.39	100	125	8	Y
HARRIS	SH 288	0598-01-045	1157	29.66	95.39	100	125	8	Y
HARRIS	SH 288	0598-01-045	1161	29.65	95.39	100	125	8	Y
HARRIS	SH 288	0598-01-045	1162	29.65	95.39	100	125	8	Y
HARRIS	SH 288	0598-01-045	1163	29.65	95.39	100	125	8	Y
HARRIS	SH 288	0598-01-045	1164	29.65	95.39	100	125	8	Y
HARRIS	SH 288	0598-01-045	1168	29.64	95.39	100	125	8	Y
HARRIS	SH 288	0598-01-045	1169	29.64	95.39	100	125	8	Y

Figure 3.16: TxDOT HMIP Inventory – Houston District - Cont'd

County	Highway(s)	Control & Section	HQ Pole Number	GPS		Wind Speed Rating (mph)	Pole Height (ft)	# Sides	Ground Sleeve
				Latitude	Longitude				
HARRIS	SH 288	0598-01-045	1170	29.64	95.39	100	125	8	Y
HARRIS	SH 288	0598-01-045	1171	29.63	95.39	100	125	8	Y
HARRIS	SH 288	0598-01-045	1172	29.63	95.39	100	125	8	Y
HARRIS	SH 288	0598-01-045	1177	29.62	95.39	100	125	8	Y
HARRIS	SH 288	0598-01-045	1178	29.62	95.39	100	125	8	Y
HARRIS	SH 288	0598-01-045	1179	29.62	95.39	100	125	8	Y
HARRIS	SH 288	0598-01-045	1184	29.61	95.39	100	125	8	Y
HARRIS	SH 288	0598-01-045	1185	29.61	95.39	100	125	8	Y
HARRIS	SH 288	0598-01-045	1186	29.61	95.39	100	125	8	Y
	SH 288	0271-16-031	1192	29.68	95.38	100	125	8	Y
	SH 288	0271-16-031	1200	29.68	95.38	100	125	8	Y
	SH 288	0271-16-031	1203	29.69	95.38	100	125	8	Y
	SH 288	0271-16-031	1204	29.69	95.38	100	125	8	Y
	SH 288	0271-16-031	1205	29.69	95.38	100	125	8	Y
	SH 288	0271-16-031	1206	29.69	95.38	100	125	8	Y
	SH 288	0271-16-031	1207	29.69	95.38	100	125	8	Y
	SH 288	0271-16-031	1208	29.68	95.38	100	125	8	Y
HARRIS	SPUR 548	2483-01-003	1219	29.82	95.36	100	125	8	Y
HARRIS	SPUR 548	2483-01-003	1220	29.82	95.36	100	125	8	Y
HARRIS	SPUR 548	2483-01-003	1221	29.83	95.35	100	125	8	Y
HARRIS	SPUR 548	2483-01-003	1222	29.82	95.36	100	125	8	Y
HARRIS	SPUR 548	2483-01-003	1223	29.83	95.35	100	125	8	Y
HARRIS	IH 610	0271-14-145	1232	29.81	95.35	100	125	8	Y
HARRIS	IH 610	0271-14-145	1233	29.81	95.35	100	125	8	Y
HARRIS	IH 610	0271-14-145	1234	29.81	95.34	100	125	8	Y
HARRIS	IH 610	0271-14-145	1235	29.81	95.34	100	125	8	Y
HARRIS	IH 610	0271-14-159	1238	29.81	95.37	100	125	8	Y
HARRIS	IH 610	0271-14-159	1239	29.81	95.36	100	125	8	Y
HARRIS	IH 610	0271-14-159	1241	29.81	95.36	100	125	8	Y
HARRIS	IH 610	0271-14-159	1242	29.81	95.36	100	125	8	Y
HARRIS	IH 610	0271-14-105	1245	29.79	95.45	100	125	8	Y
HARRIS	IH 610	0271-14-105	1246	29.79	95.45	100	125	8	Y
HARRIS	IH 610	0271-14-105	1247	29.79	95.45	100	125	8	Y
HARRIS	IH 610	0271-14-105	1248	29.79	95.45	100	125	8	Y
HARRIS	IH 610	0271-14-105	1249	29.79	95.45	100	125	8	Y
HARRIS	IH 610	0271-14-105	1250	29.79	95.45	100	125	8	Y
HARRIS	IH 610	0271-14-105	1251	29.80	95.45	100	125	8	Y
HARRIS	IH 610	0271-14-105	1252	29.80	95.45	100	125	8	Y
HARRIS	IH 610	0271-14-105	1261	29.80	95.45	100	125	8	Y
HARRIS	IH 610	0271-14-105	1262	29.81	95.45	100	125	8	Y
HARRIS	IH 610	0271-14-105	1263	29.81	95.44	100	125	8	Y
HARRIS	IH 610	0271-14-105	1264	29.81	95.44	100	125	8	Y
HARRIS	IH 610	0271-16-064	1266	29.68	95.45	100	125	8	Y
HARRIS	IH 610	0271-16-064	1267	29.68	95.45	100	125	8	Y
HARRIS	IH 610	0271-16-064	1268	29.68	95.45	100	125	8	Y
HARRIS	IH 610	0271-16-064	1271	29.68	95.44	100	125	8	Y
HARRIS	IH 610	0271-16-064	1272	29.68	95.44	100	125	8	Y
HARRIS	IH 610	0271-16-064	1274	29.68	95.44	100	125	8	Y
HARRIS	IH 610	0271-16-064	1275	29.68	95.44	100	125	8	Y
HARRIS	IH 610	0271-16-064	1276	29.68	95.43	100	125	8	Y
HARRIS	IH 610	0271-16-064	1277	29.68	95.43	100	125	8	Y
HARRIS	IH 610	0271-16-064	1278	29.68	95.43	100	125	8	Y
HARRIS	IH 610	0271-16-064	1281	29.68	95.42	100	125	8	Y
HARRIS	IH 610	0271-16-064	1282	29.68	95.42	100	125	8	Y
HARRIS	IH 610	0271-16-064	1283	29.68	95.42	100	125	8	Y
HARRIS	IH 610	0271-16-064	1284	29.68	95.42	100	125	8	Y
HARRIS	IH 610	0271-16-064	1285	29.68	95.41	100	125	8	Y
HARRIS	IH 610	0271-16-064	1287	29.68	95.41	100	125	8	Y

Figure 3.17: TxDOT HMIP Inventory – Houston District - Cont'd

County	Highway(s)	Control & Section	HQ Pole Number	GPS		Wind Speed Rating (mph)	Pole Height (ft)	# Sides	Ground Sleeve
				Latitude	Longitude				
HARRIS	IH 610	0271-16-064	1288	29.68	95.41	100	125	8	Y
HARRIS	IH 610	0271-16-064	1289	29.68	95.41	100	125	8	Y
HARRIS	IH 610	0271-16-064	1290	29.68	95.40	100	125	8	Y
HARRIS	IH 610	0271-16-064	1292	29.68	95.40	100	125	8	Y
HARRIS	IH 610	0271-16-064	1293	29.68	95.40	100	125	8	Y
HARRIS	IH 610	0271-16-064	1294	29.68	95.40	100	125	8	Y
HARRIS	IH 610	0271-16-064	1297	29.68	95.39	100	125	8	Y
HARRIS	IH 610	0271-16-064	1298	29.68	95.39	100	125	8	Y
HARRIS	IH 610	0271-16-064	1299	29.68	95.39	100	125	8	Y
HARRIS	US 290	0050-08-069	1398	29.92	95.63	100	125	8	Y
HARRIS	US 290	0050-08-069	1400	29.92	95.63	100	125	8	Y
HARRIS	US 290	0050-08-069	1401	29.92	95.62	100	125	8	Y
HARRIS	US 290	0050-08-069	1402	29.92	95.62	100	125	8	Y
HARRIS	US 290	0050-08-069	1403	29.92	95.62	100	125	8	Y
HARRIS	US 290	0050-08-069	1404	29.92	95.62	100	125	8	Y
HARRIS	US 290	0050-08-069	1405	29.92	95.62	100	125	8	Y
HARRIS	US 290	0050-08-069	1407	29.91	95.62	100	125	8	Y
HARRIS	US 290	0050-08-069	1408	29.91	95.61	100	125	8	Y
HARRIS	US 290	0050-08-069	1409	29.91	95.61	100	125	8	Y
HARRIS	US 290	0050-08-069	1410	29.91	95.61	100	125	8	Y
HARRIS	US 290	0050-08-069	1411	29.91	95.61	100	125	8	Y
HARRIS	US 290	0050-08-069	1412	29.91	95.61	100	125	8	Y
HARRIS	US 290	0050-08-069	1413	29.91	95.61	100	125	8	Y
HARRIS	US 290	0050-08-069	1414	29.90	95.60	100	125	8	Y
HARRIS	US 290	0050-08-069	1419	29.90	95.60	100	125	8	Y
HARRIS	US 290	0050-08-069	1420	29.90	95.59	100	125	8	Y
HARRIS	US 290	0050-08-069	1421	29.90	95.59	100	125	8	Y
HARRIS	US 290	0050-08-069	1422	29.90	95.59	100	125	8	Y
HARRIS	US 290	0050-08-069	1423	29.89	95.59	100	125	8	Y
HARRIS	US 290	0050-08-069	1424	29.89	95.59	100	125	8	Y
HARRIS	US 290	0050-08-069	1425	29.89	95.59	100	125	8	Y
HARRIS	US 290	0050-08-069	1427	29.89	95.58	100	125	8	Y
HARRIS	US 290	0050-08-069	1428	29.89	95.58	100	125	8	Y
HARRIS	US 290	0050-08-069	1429	29.89	95.58	100	125	8	Y
HARRIS	US 290	0050-08-069	1430	29.89	95.58	100	125	8	Y
HARRIS	US 290	0050-08-069	1431	29.88	95.58	100	125	8	Y
HARRIS	US 290	0050-08-069	1432	29.88	95.57	100	125	8	Y
HARRIS	US 290	0050-08-069	1433	29.88	95.57	100	125	8	Y
HARRIS	US 290	0050-08-069	1434	29.88	95.57	100	125	8	Y
HARRIS	US 290	0050-09-049	1437	29.88	95.57	100	125	8	Y
HARRIS	US 290	0050-09-049	1446	29.87	95.55	100	125	8	Y
HARRIS	US 290	0050-09-049	1449	29.87	95.55	100	125	8	Y
HARRIS	US 290	0050-09-049	1450	29.87	95.55	100	125	8	Y
HARRIS	US 290	0050-09-049	1451	29.87	95.54	100	125	8	Y
HARRIS	US 290	0050-09-049	1452	29.87	95.54	100	125	8	Y
HARRIS	US 290	0271-14-158	1453	29.87	95.54	100	125	8	Y
HARRIS	US 290	0271-14-158	1454	29.87	95.54	100	125	8	Y
HARRIS	US 290	0271-14-158	1455	29.86	95.54	100	125	8	Y
HARRIS	US 290	0271-14-158	1456	29.86	95.53	100	125	8	Y
HARRIS	US 290	0271-14-158	1457	29.86	95.53	100	125	8	Y
HARRIS	US 290	0271-14-158	1458	29.86	95.53	100	125	8	Y
HARRIS	US 290	0271-14-158	1459	29.86	95.53	100	125	8	Y
HARRIS	US 290	0271-14-158	1460	29.86	95.53	100	125	8	Y
HARRIS	US 290	0271-14-158	1463	29.86	95.52	100	125	8	Y
HARRIS	US 290	0271-14-158	1464	29.86	95.52	100	125	8	Y
HARRIS	US 290	0271-14-158	1465	29.86	95.52	100	125	8	Y
HARRIS	US 290	0271-14-158	1466	29.85	95.52	100	125	8	Y
HARRIS	US 290	0271-14-158	1467	29.85	95.51	100	125	8	Y

Figure 3.18: TxDOT HMIP Inventory – Houston District - Cont'd

County	Highway(s)	Control & Section	HQ Pole Number	GPS		Wind Speed Rating (mph)	Pole Height (ft)	# Sides	Ground Sleeve
				Latitude	Longitude				
HARRIS	US 290	0271-14-158	1468	29.85	95.51	100	125	8	Y
HARRIS	US 290	0271-14-158	1471	29.85	95.51	100	125	8	Y
HARRIS	US 290	0271-14-158	1474	29.85	95.50	100	125	8	Y
HARRIS	US 290	0271-14-158	1475	29.85	95.50	100	125	8	Y
HARRIS	US 290	0271-14-158	1476	29.84	95.50	100	125	8	Y
HARRIS	US 290	0271-14-158	1477	29.84	95.50	100	125	8	Y
HARRIS	US 290	0271-14-158	1478	29.84	95.50	100	125	8	Y
HARRIS	US 290	0271-14-158	1481	29.84	95.49	100	125	8	Y
HARRIS	US 290	0271-14-158	1488	29.83	95.48	100	125	8	Y
HARRIS	US 290	0271-14-158	1489	29.83	95.48	100	125	8	Y
HARRIS	US 290	0271-14-158	1490	29.83	95.48	100	125	8	Y
HARRIS	US 290	0271-14-158	1491	29.83	95.48	100	125	8	Y
HARRIS	US 290	0271-14-158	1492	29.83	95.48	100	125	8	Y
HARRIS	US 290	0271-14-158	1495	29.82	95.47	100	125	8	Y
HARRIS	US 290	0271-14-158	1498	29.82	95.47	100	125	8	Y
HARRIS	US 290	0271-14-158	1499	29.82	95.47	100	125	8	Y
HARRIS	US 290	0271-14-158	1500	29.81	95.46	100	125	8	Y
HARRIS	US 290	0271-14-158	1501	29.81	95.46	100	125	8	Y
HARRIS	US 290	0271-14-158	1502	29.81	95.46	100	125	8	Y
HARRIS	US 290	0271-14-158	1505	29.81	95.46	100	125	8	Y
GALVESTON	FM 2004	1607-01-025	1511	29.40	95.03	100	125	8	Y
HARRIS	IH 45	0500-03-337				100	125	8	Y
HARRIS	IH 45	0500-03-337				100	125	8	Y
HARRIS	IH 45	0500-03-337				100	125	8	Y
HARRIS	IH 45	0500-03-337				100	125	8	Y
HARRIS	IH 45	0500-03-337				100	125	8	Y
HARRIS	IH 45	0500-03-337				100	125	8	Y
HARRIS	IH 45	0500-03-323		29.94	95.25	100	125	8	Y
HARRIS	IH 45	0500-03-323		29.65	95.25	100	125	8	Y
HARRIS	IH 45	0500-03-323		29.65	95.25	100	125	8	Y
HARRIS	IH 45	0500-03-323		29.65	95.25	100	125	8	Y
HARRIS	IH 45	0500-03-323		29.65	95.25	100	125	8	Y
HARRIS	IH 45	0500-03-323		29.64	95.25	100	125	8	Y
HARRIS	IH 45	0500-03-323		29.64	95.25	100	125	8	Y
HARRIS	IH 45	0500-03-323		29.64	95.24	100	125	8	Y
HARRIS	IH 45	0500-03-323		29.64	95.24	100	125	8	Y
HARRIS	IH 45	0500-03-323		29.64	95.24	100	125	8	Y
HARRIS	IH 45	0500-03-323		29.64	95.24	100	125	8	Y
HARRIS	IH 45	0500-03-323		29.64	95.24	100	125	8	Y
HARRIS	IH 45	0500-03-323		29.63	95.23	100	125	8	Y
HARRIS	IH 45	0500-03-323		29.62	95.23	100	125	8	Y
HARRIS	IH 45	0500-03-323		29.62	95.22	100	125	8	Y
HARRIS	IH 45	0500-03-231				100	125	8	Y
HARRIS	IH 45	0500-03-231				100	125	8	Y
HARRIS	IH 45	0500-03-231				100	125	8	Y
HARRIS	IH 45	0500-03-231	1516	29.69	95.28	100	125	8	Y
HARRIS	IH 45	0500-03-231				100	125	8	Y
HARRIS	IH 45	0500-03-231	1517	29.68	95.28	100	125	8	Y
HARRIS	IH 45	0500-03-231				100	125	8	Y
HARRIS	IH 45	0500-03-231				100	125	8	Y
HARRIS	IH 45	0500-03-231				100	125	8	Y
HARRIS	IH 45	0500-03-231				100	125	8	Y
HARRIS	IH 45	0500-03-231				100	125	8	Y
HARRIS	IH 45	0500-03-231				100	125	8	Y
HARRIS	IH 45	0500-03-231				100	125	8	Y
HARRIS	IH 45	0500-03-452	1520			100	125	8	Y
HARRIS	IH 45	0500-03-452	1521			100	125	8	Y
HARRIS	IH 45	0500-03-452	1522			100	125	8	Y

Figure 3.19: TxDOT HMIP Inventory – Houston District - Cont'd

County	Highway(s)	Control & Section	HQ Pole Number	GPS		Wind Speed Rating (mph)	Pole Height (ft)	# Sides	Ground Sleeve
				Latitude	Longitude				
HARRIS	IH 45	0500-03-452	1523			100	125	8	Y
HARRIS	IH 45	0500-03-452	1524			100	125	8	Y
HARRIS	IH 45	0500-03-452	1525			100	125	8	Y
HARRIS	IH 45	0500-03-452	1526			100	125	8	Y
HARRIS	IH 45	0500-03-452	1527			100	125	8	Y
HARRIS	IH 45	0500-03-452	1528			100	125	8	Y
HARRIS	IH 45	0500-03-452	1529			100	125	8	Y
HARRIS	IH 45	0500-03-452	1530			100	125	8	Y
HARRIS	IH 45	0500-03-452	1531			100	125	8	Y
HARRIS	IH 45	0500-03-452	1532			100	125	8	Y
HARRIS	IH 45	0500-03-452	1533			100	125	8	Y
HARRIS	IH 45	0500-03-452	1534			100	125	8	Y
HARRIS	IH 45	0500-03-452	1535			100	125	8	Y
HARRIS	IH 45	0500-03-452	1536			100	125	8	Y
HARRIS	IH 45	0500-03-452	1537			100	125	8	Y
HARRIS	IH 45	0500-03-452	1538			100	125	8	Y
HARRIS	IH 45	0500-03-452	1539			100	125	8	Y
HARRIS	IH 45	0500-03-452	1540			100	125	8	Y
HARRIS	IH 45	0500-03-452	1541			100	125	8	Y
HARRIS	IH 45	0500-03-452	1542			100	125	8	Y
HARRIS	IH 45	0500-03-452	1543			100	125	8	Y
HARRIS	IH 45	0500-03-452	1544			100	125	8	Y
HARRIS	IH 45	0500-03-452	1545			100	125	8	Y
HARRIS	IH 45	0500-03-452	1546			100	125	8	Y
HARRIS	IH 45	0500-03-452	1547			100	125	8	Y
HARRIS	IH 45	0500-03-452	1548			100	125	8	Y
HARRIS	IH 45	0500-03-452	1549			100	125	8	Y
HARRIS	IH 45	0500-03-452	1550			100	125	8	Y
HARRIS	IH 45	0500-03-452	1551			100	125	8	Y
HARRIS	IH 45	0500-03-452	1552			100	125	8	Y
HARRIS	IH 45	0500-03-452	1553			100	125	8	Y
HARRIS	IH 45	0500-03-452	1554			100	125	8	Y
HARRIS	IH 45	0500-03-452	1555			100	125	8	Y
HARRIS	IH 45	0500-03-452	1556			100	125	8	Y
HARRIS	IH 45	0500-03-452	1557			100	125	8	Y
HARRIS	IH 45	0500-03-452	1558			100	125	8	Y
HARRIS	IH 45	0500-03-452	1559	29.81	95.37	100	125	8	Y
HARRIS	IH 45	0500-03-452	1560	29.81	95.37	100	125	8	Y
HARRIS	IH 45	0500-03-452	1561	95.37	95.37	100	125	8	Y
HARRIS	IH 45	0500-03-452	1562	29.80	95.37	100	125	8	Y
HARRIS	IH 45	0500-03-452	1563		95.37	100	125	8	Y
HARRIS	IH 45	0500-03-452	1564	29.80	95.37	100	125	8	Y
HARRIS	IH 45	0500-03-452	1565	29.80	95.37	100	125	8	Y
HARRIS	IH 45	0500-03-452	1566	29.80	95.37	100	125	8	Y
HARRIS	IH 45	0500-03-452	1567	29.79	95.37	100	125	8	Y
HARRIS	IH 45	0500-03-452	1568	29.79	95.37	100	125	8	Y
HARRIS	IH 45	0500-03-452	1569	29.79	95.37	100	125	8	Y
HARRIS	IH 45	0500-03-452	1570	29.79	95.37	100	125	8	Y
HARRIS	IH 45	0500-03-452	1571	29.79	95.37	100	125	8	Y
HARRIS	IH 45	0500-03-452	1572	29.78	95.37	100	125	8	Y
HARRIS	IH 45	0500-03-452	1573	29.78	95.37	100	125	8	Y
HARRIS	IH 45	0500-03-452	1574	29.78	95.37	100	125	8	Y
HARRIS	IH 45	0500-03-452	1575	29.78	95.37	100	125	8	Y
HARRIS	IH 45	0500-03-313	1634	29.74	95.36	100	125	8	Y
HARRIS	IH 45	0500-03-220	1634	29.70	95.29	100	125	8	Y
HARRIS	IH 45	0500-03-220	1634	29.70	95.30	100	125	8	Y
HARRIS	IH 45	0500-03-220	1634	29.70	95.30	100	125	8	Y
HARRIS	IH 45	0500-03-220	1634	29.71	95.30	100	125	8	Y

Figure 3.20: TxDOT HMIP Inventory – Houston District - Cont'd

County	Highway(s)	Control & Section	HQ Pole Number	GPS		Wind Speed Rating (mph)	Pole Height (ft)	# Sides	Ground Sleeve
				Latitude	Longitude				
HARRIS	IH 45	0500-03-220	1634	29.71	95.30	100	125	8	Y
HARRIS	IH 45	0500-03-220	1634	29.71	95.30	100	125	8	Y
HARRIS	IH 45	0500-03-220	1634	29.71	95.30	100	125	8	Y
HARRIS	IH 45	0500-03-220	1634	29.71	95.31	100	125	8	Y
HARRIS	IH 45	0500-03-220	1634	29.71	95.31	100	125	8	Y
HARRIS	IH 45	0500-03-278		29.82	95.37	100	125	8	Y
HARRIS	IH 45	0500-03-278		29.82	95.38	100	125	8	Y
HARRIS	IH 45	0500-03-278		29.81	95.37	100	125	8	Y
N. HARRIS	IH 45	0110-06-089				100	125	8	Y
GALVESTON	IH 45	0500-01-117	598	29.31	94.90	100	125	12	N
GALVESTON	IH 45	0500-01-117	599	29.30	94.90	100	125	12	N
GALVESTON	IH 45	0500-01-117	600	29.30	94.90	100	125	12	N
HARRIS	IH 45	0500-03-323		29.63	95.24	100	125	12	N
HARRIS	IH 45	0500-03-323		29.63	95.23	100	125	12	N
HARRIS	IH 45	0500-03-323		29.63	95.23	100	125	12	N
HARRIS	IH 45	0500-03-323	1515	29.63	95.23	100	125	12	N
GALVESTON	IH 45	0500-01-117	601	29.31	94.91	100	125	12	Y
GALVESTON	IH 45	0500-01-117	602	29.31	94.91	100	125	12	Y
GALVESTON	IH 45	0500-01-117	603	29.31	94.91	100	125	12	Y
HARRIS	US 59	0027-13-171	904	29.74	95.38	100	125	12	Y
HARRIS	US 59	0027-13-171	905	29.74	95.38	100	125	12	Y
HARRIS	US 59	0027-13-171	906	29.74	95.38	100	125	12	Y
FORT BEND	US 59	0027-12-110	1009	29.57	95.66	100	125	12	Y
FORT BEND	US 59	0027-12-110	1010	29.57	95.66	100	125	12	Y
FORT BEND	US 59	0027-12-110	1011	29.57	95.66	100	125	12	Y
FORT BEND	US 59	0027-12-110	1012	29.58	95.66	100	125	12	Y
FORT BEND	US 59	0027-12-110	1013	29.58	95.65	100	125	12	Y
HARRIS	SH 249	0720-03-084	1100	30.07	95.63	100	125	12	Y
HARRIS	SH 249	0720-03-084	1101	30.07	95.63	100	125	12	Y
HARRIS	IH 45	0500-03-337				100	125	12	Y
HARRIS	IH 45	0500-03-337				100	125	12	Y
HARRIS	IH 45	0500-03-337				100	125	12	Y
HARRIS	IH 45	0500-03-337				100	125	12	Y
HARRIS	IH 45	0500-03-337				100	125	12	Y
HARRIS	IH 45	0500-03-337				100	125	12	Y
HARRIS	IH 45	0500-03-337	1514	29.66	95.26	100	125	12	Y
HARRIS	IH 10	0271-07-187	31			100	125		
HARRIS	IH 10	0271-07-187	32			100	125		
HARRIS	IH 10	0271-07-187	33			100	125		
N. HARRIS	IH 45	0110-06-089	385				125		
HARRIS	IH 45	0110-06-102	430	29.94	95.41		125		
HARRIS	IH 45	0110-06-102	431	29.94	95.41		125		
HARRIS	IH 45	0110-06-102	432	29.95	95.42		125		
HARRIS	IH 45	0110-06-102	433	29.95	95.42		125		
HARRIS	US 59	0027-13-171	897				125		
	SH 288	0271-16-031	1210				125		
HARRIS	IH 610	0271-15-011	1334	29.71	95.27	100	150	8	N
HARRIS	IH 610	0271-15-011	1335	29.71	95.27	100	150	8	N
HARRIS	BW 8	3256-01-028	1	29.66	95.56	100	150	8	Y
HARRIS	BW 8	3256-01-028	2	29.66	95.56	100	150	8	Y
HARRIS	BW 8	3256-01-028	3	29.67	95.56	100	150	8	Y
HARRIS	BW 8	3256-01-055	6	29.65	95.55	100	150	8	Y
HARRIS	BW 8	3256-01-055	7	29.65	95.55	100	150	8	Y
HARRIS	BW 8	3256-01-055	8	29.66	95.55	100	150	8	Y
HARRIS	BW 8	3256-01-055	9	29.66	95.55	100	150	8	Y
C. HARRIS	BW 8	3256-02-062	18	29.94	95.38	100	150	8	Y
C. HARRIS	BW 8	3256-02-062	19	29.94	95.38	100	150	8	Y

Figure 3.21: TxDOT HMIP Inventory – Houston District - Cont'd

County	Highway(s)	Control & Section	HQ Pole Number	GPS		Wind Speed Rating (mph)	Pole Height (ft)	# Sides	Ground Sleeve
				Latitude	Longitude				
HARRIS	IH 10	0508-01-209	40	29.78	95.28	100	150	8	Y
HARRIS	IH 10	0508-01-209	44	29.78	95.27	100	150	8	Y
HARRIS	IH 10	0508-01-209	45	29.78	95.27	100	150	8	Y
C. HARRIS	IH 10	0508-01-209	66	29.77	95.27	100	150	8	Y
C. HARRIS	IH 10	0508-01-209	67	29.77	95.27	100	150	8	Y
HARRIS	IH 10	0508-01-230	72	29.77	95.16	100	150	8	Y
HARRIS	IH 10	0508-01-230	73	29.77	95.16	100	150	8	Y
HARRIS	IH 10	0508-01-230	74	29.77	95.16	100	150	8	Y
HARRIS	IH 10	0508-01-230	76	29.77	95.15	100	150	8	Y
HARRIS	IH 10	0508-01-230	80	29.77	95.15	100	150	8	Y
HARRIS	IH 10	0508-01-230	81	29.77	95.15	100	150	8	Y
HARRIS	IH 10	0508-01-236	85	29.77	95.16	100	150	8	Y
HARRIS	IH 10	0508-01-236	86	29.78	95.16	100	150	8	Y
N. HARRIS	IH 45	0110-06-089	358	29.89	95.41	100	150	8	Y
N. HARRIS	IH 45	0110-06-089	363	29.90	95.41	100	150	8	Y
N. HARRIS	IH 45	0110-06-089	372	29.91	95.41	100	150	8	Y
N. HARRIS	IH 45	0110-06-089	381	29.93	95.41	100	150	8	Y
N. HARRIS	IH 45	0110-06-104	392	29.94	95.41	100	150	8	Y
N. HARRIS	IH 45	0110-06-104	393	29.94	95.41	100	150	8	Y
N. HARRIS	IH 45	0110-06-104	394	29.94	95.41	100	150	8	Y
N. HARRIS	IH 45	0110-06-104	395	29.94	95.41	100	150	8	Y
HARRIS	IH 45	0500-03-382	408	29.61	95.21	100	150	8	Y
HARRIS	IH 45	0500-03-382	410	29.61	95.21	100	150	8	Y
HARRIS	IH 45	0500-03-382	413	29.60	95.20	100	150	8	Y
HARRIS	IH 45	0500-03-382	415	29.60	95.20	100	150	8	Y
HARRIS	IH 45	0500-03-382	417	29.60	95.20	100	150	8	Y
HARRIS	IH 45	0500-03-382	418	29.60	95.20	100	150	8	Y
HARRIS	IH 45	0500-03-382	419	29.60	95.20	100	150	8	Y
HARRIS	IH 45	0500-03-382	420	29.60	95.20	100	150	8	Y
HARRIS	IH 45	0110-06-102	434	29.95	95.42	100	150	8	Y
HARRIS	IH 45	0110-06-102	435	29.95	95.42	100	150	8	Y
HARRIS	IH 45	0110-06-102	436	29.95	95.42	100	150	8	Y
HARRIS	IH 45	0110-06-102	437	29.95	95.42	100	150	8	Y
HARRIS	IH 45	0110-06-102	438	29.96	95.42	100	150	8	Y
HARRIS	IH 45	0110-06-102	439	29.96	95.42	100	150	8	Y
HARRIS	IH 45	0110-06-102	440	29.96	95.42	100	150	8	Y
HARRIS	IH 45	0110-06-102	441	29.96	95.42	100	150	8	Y
GALVESTON	IH 45	0500-04-066	608	29.41	95.04	100	150	8	Y
GALVESTON	IH 45	0500-04-066	609	29.41	95.04	100	150	8	Y
GALVESTON	IH 45	0500-04-066	610	29.41	95.04	100	150	8	Y
GALVESTON	IH 45	0500-04-066	611	29.41	95.04	100	150	8	Y
GALVESTON	IH 45	0500-04-066	612	29.41	95.03	100	150	8	Y
GALVESTON	IH 45	0500-04-066	614	29.41	95.04	100	150	8	Y
HARRIS	US 59	0027-13-117	655	29.66	95.56	100	150	8	Y
HARRIS	US 59	0027-13-117	660	29.66	95.56	100	150	8	Y
HARRIS	US 59	0027-13-117	661	29.66	95.56	100	150	8	Y
HARRIS	US 59	0027-13-117	662	29.66	95.55	100	150	8	Y
HARRIS	US 59	0027-13-123	666	29.72	95.49	100	150	8	Y
HARRIS	US 59	0027-13-123	667	29.72	95.49	100	150	8	Y
HARRIS	US 59	0027-13-123	668	29.73	95.49	100	150	8	Y
HARRIS	US 59	0027-13-123	670	29.73	95.49	100	150	8	Y
HARRIS	US 59	0027-13-123	671	29.73	95.48	100	150	8	Y
HARRIS	US 59	0027-13-123	672	29.73	95.48	100	150	8	Y
HARRIS	US 59	0027-13-123	674	29.73	95.48	100	150	8	Y
HARRIS	US 59	0027-13-123	675	29.73	95.48	100	150	8	Y
HARRIS	US 59	0027-13-123	676	29.73	95.47	100	150	8	Y
HARRIS	US 59	0027-13-123	679	29.73	95.47	100	150	8	Y
HARRIS	US 59	0027-13-123	681	29.73	95.46	100	150	8	Y

Figure 3.22: TxDOT HMIP Inventory – Houston District - Cont'd

County	Highway(s)	Control & Section	HQ Pole Number	GPS		Wind Speed Rating (mph)	Pole Height (ft)	# Sides	Ground Sleeve
				Latitude	Longitude				
HARRIS	US 59	0027-13-126	697	29.70	95.52	100	150	8	Y
HARRIS	US 59	0027-13-126	698	29.70	95.52	100	150	8	Y
HARRIS	US 59	0027-13-126	700	29.70	95.51	100	150	8	Y
HARRIS	US 59	0027-13-126	710	29.72	95.50	100	150	8	Y
HARRIS	US 59	0027-13-126	711	29.72	95.50	100	150	8	Y
HARRIS	US 59	0027-13-126	712	29.72	95.50	100	150	8	Y
HARRIS	US 59	0027-13-126	713	29.72	95.50	100	150	8	Y
HARRIS	US 59	0027-13-126	714			100	150	8	Y
HARRIS	US 59	0027-13-100	715	29.67	95.55	100	150	8	Y
HARRIS	US 59	0027-13-100	716	29.67	95.55	100	150	8	Y
HARRIS	US 59	0027-13-100	717	29.67	95.55	100	150	8	Y
HARRIS	US 59	0027-13-100	718	29.67	95.54	100	150	8	Y
HARRIS	US 59	0027-13-100	719	29.68	95.54	100	150	8	Y
HARRIS	US 59	0027-13-100	720	29.68	95.54	100	150	8	Y
HARRIS	US 59	0027-13-100	721	29.68	95.54	100	150	8	Y
HARRIS	US 59	0027-13-100	726	29.68	95.53	100	150	8	Y
HARRIS	US 59	0027-13-100	727	29.69	95.53	100	150	8	Y
HARRIS	US 59	0027-13-100	728	29.69	95.53	100	150	8	Y
HARRIS	US 59	0027-13-100	729	29.69	95.53	100	150	8	Y
HARRIS	US 59	0027-13-100	730	29.69	95.53	100	150	8	Y
HARRIS	US 59	0027-13-100	732	29.69	95.53	100	150	8	Y
HARRIS	US 59	0027-13-133	733	29.73	95.45	100	150	8	Y
HARRIS	US 59	0027-13-133	735	29.73	95.45	100	150	8	Y
HARRIS	US 59	0027-13-133	738	29.73	95.44	100	150	8	Y
HARRIS	US 59	0027-13-133	744	29.73	95.43	100	150	8	Y
HARRIS	US 59	0027-13-133	748	29.73	95.42	100	150	8	Y
HARRIS	US 59	0027-13-133	751	29.73	95.41	100	150	8	Y
HARRIS	US 59	0027-13-133	752	29.73	95.41	100	150	8	Y
HARRIS	US 59	0177-11-066	754	29.82	95.33	100	150	8	Y
HARRIS	US 59	0177-11-066	755	29.82	95.34	100	150	8	Y
HARRIS	US 59	0177-11-066	756	29.82	95.33	100	150	8	Y
HARRIS	US 59	0177-11-066	757	29.82	95.34	100	150	8	Y
HARRIS	US 59	0177-11-066	758	29.82	95.33	100	150	8	Y
HARRIS	US 59	0177-11-066	759	29.83	95.34	100	150	8	Y
HARRIS	US 59	0177-11-066	760	29.83	95.33	100	150	8	Y
HARRIS	US 59	0177-11-066	761	29.83	95.33	100	150	8	Y
HARRIS	US 59	0177-11-066	762	29.83	95.33	100	150	8	Y
HARRIS	US 59	0177-11-083	766	29.84	95.33	100	150	8	Y
HARRIS	US 59	0177-11-083	767	29.84	95.33	100	150	8	Y
HARRIS	US 59	0177-11-083	768	29.84	95.33	100	150	8	Y
HARRIS	US 59	0177-11-083	769	29.84	95.33	100	150	8	Y
HARRIS	US 59	0177-11-083	770	29.84	95.33	100	150	8	Y
HARRIS	US 59	0177-11-083	771	29.85	95.33	100	150	8	Y
HARRIS	US 59	0177-11-083	772	29.85	95.33	100	150	8	Y
HARRIS	US 59	0177-11-083	773	29.85	95.33	100	150	8	Y
HARRIS	US 59	0177-11-083	774	29.85	95.33	100	150	8	Y
HARRIS	US 59	0177-11-083	775	29.85	95.33	100	150	8	Y
HARRIS	US 59	0177-11-083	776	29.85	95.33	100	150	8	Y
HARRIS	US 59	0177-11-083	777	29.86	95.33	100	150	8	Y
HARRIS	US 59	0177-11-083	778	29.86	95.33	100	150	8	Y
HARRIS	US 59	0177-11-083	779	29.86	95.33	100	150	8	Y
HARRIS	US 59	0177-11-083	780	29.86	95.33	100	150	8	Y
HARRIS	US 59	0177-11-084	781	29.86	95.33	100	150	8	Y
HARRIS	US 59	0177-11-084	782	29.86	95.33	100	150	8	Y
HARRIS	US 59	0177-11-084	783	29.87	95.33	100	150	8	Y
HARRIS	US 59	0177-11-084	784	29.87	95.33	100	150	8	Y
HARRIS	US 59	0177-11-084	785	29.87	95.33	100	150	8	Y
HARRIS	US 59	0177-11-084	786	29.87	95.33	100	150	8	Y

Figure 3.23: TxDOT HMIP Inventory – Houston District - Cont'd

County	Highway(s)	Control & Section	HQ Pole Number	GPS		Wind Speed Rating (mph)	Pole Height (ft)	# Sides	Ground Sleeve
				Latitude	Longitude				
HARRIS	US 59	0177-11-084	787	29.87	95.33	100	150	8	Y
HARRIS	US 59	0177-11-084	788	29.87	95.33	100	150	8	Y
HARRIS	US 59	0177-07-077	801	29.94	95.30	100	150	8	Y
HARRIS	US 59	0177-07-077	802	29.94	95.30	100	150	8	Y
HARRIS	US 59	0177-07-077	803	29.94	95.30	100	150	8	Y
HARRIS	US 59	0177-07-077	808	29.94	95.29	100	150	8	Y
HARRIS	US 59	0177-07-077	809	29.94	95.29	100	150	8	Y
HARRIS	US 59	0177-07-077	810	29.95	95.29	100	150	8	Y
HARRIS	US 59	0177-07-077	811	29.95	95.29	100	150	8	Y
HARRIS	US 59	0177-07-057	819	29.88	95.33	100	150	8	Y
HARRIS	US 59	0177-07-057	820	29.88	95.33	100	150	8	Y
HARRIS	US 59	0177-07-057	821	29.88	95.32	100	150	8	Y
HARRIS	US 59	0177-07-057	822	29.88	95.32	100	150	8	Y
HARRIS	US 59	0177-07-057	823	29.88	95.32	100	150	8	Y
HARRIS	US 59	0177-07-057	824	29.89	95.32	100	150	8	Y
HARRIS	US 59	0177-07-057	825	29.89	95.32	100	150	8	Y
HARRIS	US 59	0177-07-057	826	29.89	95.32	100	150	8	Y
HARRIS	US 59	0177-07-057	827	29.89	95.32	100	150	8	Y
HARRIS	US 59	0177-07-057	828	29.89	95.32	100	150	8	Y
HARRIS	US 59	0177-07-057	829	29.89	95.32	100	150	8	Y
HARRIS	US 59	0177-07-057	830	29.90	95.32	100	150	8	Y
HARRIS	US 59	0177-07-057	831	29.90	95.31	100	150	8	Y
GALVESTON	SH 146	0389-06-074	1018	29.40	94.95	100	150	8	Y
GALVESTON	SH 146	0389-07-031	1031	29.35	94.94	100	150	8	Y
GALVESTON	SH 146	0389-07-031	1032	29.35	94.94	100	150	8	Y
GALVESTON	SH 146	0389-07-031	1033	29.35	94.94	100	150	8	Y
GALVESTON	SH 146	0389-07-031	1034	29.34	94.94	100	150	8	Y
GALVESTON	SH 146	0389-07-031	1035	29.34	94.94	100	150	8	Y
GALVESTON	SH 146	0389-07-031	1036	29.34	94.94	100	150	8	Y
BRAZORIA	SH 288	0598-02-013	1131	29.58	95.39	100	150	8	Y
BRAZORIA	SH 288	0598-02-013	1133	29.58	95.39	100	150	8	Y
BRAZORIA	SH 288	0598-02-013	1134	29.58	95.38	100	150	8	Y
BRAZORIA	SH 288	0598-02-013	1136	29.58	95.39	100	150	8	Y
BRAZORIA	SH 288	0598-02-013	1141	29.56	95.39	100	150	8	Y
BRAZORIA	SH 288	0598-02-013	1143	29.56	95.39	100	150	8	Y
BRAZORIA	SH 288	0598-02-013	1144	29.56	95.39	100	150	8	Y
BRAZORIA	SH 288	0598-02-013	1146	29.55	95.39	100	150	8	Y
HARRIS	SH 288	0598-01-021	1149	29.73	95.37	100	150	8	Y
HARRIS	SH 288	0598-01-026	1187	29.67	95.38	100	150	8	Y
HARRIS	SH 288	0598-01-026	1188	29.67	95.38	100	150	8	Y
HARRIS	SPUR 548	2483-01-003	1224	29.83	95.35	100	150	8	Y
HARRIS	SPUR 548	2483-01-004	1226	29.82	95.35	100	150	8	Y
HARRIS	SPUR 548	2483-01-004	1227	29.82	95.36	100	150	8	Y
HARRIS	IH 610	0271-14-145	1231	29.81	95.35	100	150	8	Y
HARRIS	IH 610	0271-14-159	1236	29.81	95.37	100	150	8	Y
HARRIS	IH 610	0271-14-159	1237	29.81	95.37	100	150	8	Y
HARRIS	IH 610	0271-14-159	1240	29.81	95.36	100	150	8	Y
HARRIS	IH 610	0271-14-159	1243	29.81	95.36	100	150	8	Y
HARRIS	IH 610	0271-14-105	1253	29.80	95.45	100	150	8	Y
HARRIS	IH 610	0271-14-105	1255	29.80	95.45	100	150	8	Y
HARRIS	IH 610	0271-14-105	1256	29.80	95.45	100	150	8	Y
HARRIS	IH 610	0271-14-105	1258	29.80	95.45	100	150	8	Y
HARRIS	IH 610	0271-14-105	1259	29.80	95.45	100	150	8	Y
HARRIS	IH 610	0271-14-105	1260	29.80	95.45	100	150	8	Y
HARRIS	IH 610	0271-14-105	1265	29.81	95.44	100	150	8	Y
HARRIS	IH 610	0271-16-064	1269	29.68	95.45	100	150	8	Y
HARRIS	IH 610	0271-16-064	1270	29.68	95.45	100	150	8	Y
HARRIS	IH 610	0271-16-064	1273	29.68	95.44	100	150	8	Y

Figure 3.24: TxDOT HMIP Inventory – Houston District - Cont'd

County	Highway(s)	Control & Section	HQ Pole Number	GPS		Wind Speed Rating (mph)	Pole Height (ft)	# Sides	Ground Sleeve
				Latitude	Longitude				
HARRIS	IH 610	0271-16-064	1279	29.68	95.43	100	150	8	Y
HARRIS	IH 610	0271-16-064	1286	29.68	95.41	100	150	8	Y
HARRIS	IH 610	0271-16-064	1291	29.68	95.40	100	150	8	Y
HARRIS	IH 610	0271-16-064	1295	29.68	95.39	100	150	8	Y
HARRIS	IH 610	0271-16-064	1296	29.68	95.39	100	150	8	Y
HARRIS	US 290	0050-08-069	1399	29.92	95.63	100	150	8	Y
HARRIS	US 290	0050-08-069	1406	29.92	95.62	100	150	8	Y
HARRIS	US 290	0050-08-069	1415	29.90	95.60	100	150	8	Y
HARRIS	US 290	0050-08-069	1416	29.90	95.60	100	150	8	Y
HARRIS	US 290	0050-08-069	1417	29.90	95.60	100	150	8	Y
HARRIS	US 290	0050-08-069	1418	29.90	95.60	100	150	8	Y
HARRIS	US 290	0050-08-069	1426	29.89	95.58	100	150	8	Y
HARRIS	US 290	0050-08-069	1435	29.88	95.57	100	150	8	Y
HARRIS	US 290	0050-09-049	1436	29.88	95.57	100	150	8	Y
HARRIS	US 290	0050-09-049	1438	29.88	95.56	100	150	8	Y
HARRIS	US 290	0050-09-049	1439	29.88	95.56	100	150	8	Y
HARRIS	US 290	0050-09-049	1440	29.88	95.56	100	150	8	Y
HARRIS	US 290	0050-09-049	1445	29.87	95.55	100	150	8	Y
HARRIS	US 290	0050-09-049	1447	29.87	95.55	100	150	8	Y
HARRIS	US 290	0050-09-049	1448	29.87	95.55	100	150	8	Y
HARRIS	IH 10	0508-01-209		29.78	95.29	100	150	8	Y
HARRIS	US 290	0271-14-158	1461	29.86	95.53	100	150	8	Y
HARRIS	US 290	0271-14-158	1462	29.86	95.52	100	150	8	Y
HARRIS	US 290	0271-14-158	1469	29.85	95.51	100	150	8	Y
HARRIS	US 290	0271-14-158	1470	29.85	95.51	100	150	8	Y
HARRIS	US 290	0271-14-158	1472	29.85	95.51	100	150	8	Y
HARRIS	US 290	0271-14-158	1473	29.85	95.50	100	150	8	Y
HARRIS	US 290	0271-14-158	1479	29.84	95.49	100	150	8	Y
HARRIS	US 290	0271-14-158	1480	29.84	95.49	100	150	8	Y
HARRIS	US 290	0271-14-158	1482	29.84	95.49	100	150	8	Y
HARRIS	US 290	0271-14-158	1483	29.84	95.49	100	150	8	Y
HARRIS	US 290	0271-14-158	1484	29.84	95.49	100	150	8	Y
HARRIS	US 290	0271-14-158	1485	29.84	95.49	100	150	8	Y
HARRIS	US 290	0271-14-158	1486	29.83	95.48	100	150	8	Y
HARRIS	US 290	0271-14-158	1487	29.83	95.48	100	150	8	Y
HARRIS	US 290	0271-14-158	1493	29.82	95.47	100	150	8	Y
HARRIS	US 290	0271-14-158	1494	29.82	95.47	100	150	8	Y
HARRIS	US 290	0271-14-158	1496	29.82	95.47	100	150	8	Y
HARRIS	US 290	0271-14-158	1497	29.82	95.47	100	150	8	Y
HARRIS	US 290	0271-14-158	1503	29.81	95.46	100	150	8	Y
HARRIS	US 290	0271-14-158	1504	29.81	95.46	100	150	8	Y
HARRIS	US 290	0271-14-158	1506	29.81	95.46	100	150	8	Y
GALVESTON	FM 2004	1607-01-025	1508	29.41	95.03	100	150	8	Y
GALVESTON	FM 2004	1607-01-025	1509	29.40	95.03	100	150	8	Y
GALVESTON	FM 2004	1607-01-025	1510	29.40	95.03	100	150	8	Y
HARRIS	IH 45	0500-03-323		29.65	95.25	100	150	8	Y
HARRIS	IH 45	0500-03-323		29.63	95.23	100	150	8	Y
HARRIS	IH 45	0500-03-323		29.63	95.23	100	150	8	Y
HARRIS	IH 45	0500-03-313	1634	29.73	95.34	100	150	8	Y
HARRIS	IH 45	0500-03-313	1634	29.73	95.34	100	150	8	Y
HARRIS	IH 45	0500-03-313	1634	29.74	95.35	100	150	8	Y
HARRIS	IH 45	0500-03-313	1634	29.74	95.35	100	150	8	Y
HARRIS	IH 45	0500-03-313	1634	29.74	95.35	100	150	8	Y
HARRIS	IH 45	0500-03-313	1634	29.74	95.35	100	150	8	Y
E. HARRIS	IH 10	0508-01-218	127	29.79	95.06	100	150	12	N
E. HARRIS	IH 10	0508-01-218	128	29.79	95.05	100	150	12	N
E. HARRIS	IH 10	0508-01-218	129	29.79	95.05	100	150	12	N
E. HARRIS	IH 10	0508-01-218	130	29.79	95.05	100	150	12	N

Figure 3.25: TxDOT HMIP Inventory – Houston District - Cont'd

County	Highway(s)	Control & Section	HQ Pole Number	GPS		Wind Speed Rating (mph)	Pole Height (ft)	# Sides	Ground Sleeve
				Latitude	Longitude				
E. HARRIS	IH 10	0508-01-218	131	29.79	95.05	100	150	12	N
C. HARRIS	SH 35	0178-09-025	351	29.73	95.34	100	150	12	N
C. HARRIS	SH 35	0178-09-025	352	29.73	95.34	100	150	12	N
C. HARRIS	SH 35	0178-09-025	353	29.72	95.34	100	150	12	N
C. HARRIS	SH 35	0178-09-025	354	29.72	95.34	100	150	12	N
MONTGOMERY	IH 45	0110-04-141	515	30.24	95.46	100	150	12	N
MONTGOMERY	IH 45	0110-04-141	519	30.23	95.46	100	150	12	N
MONTGOMERY	IH 45	0110-04-141	520	30.23	95.46	100	150	12	N
MONTGOMERY	IH 45	0110-04-141	521	30.22	95.46	100	150	12	N
MONTGOMERY	IH 45	0110-04-141	522	30.22	95.46	100	150	12	N
MONTGOMERY	IH 45	0110-04-141	523	30.22	95.46	100	150	12	N
MONTGOMERY	IH 45	0110-04-141	524	30.22	95.46	100	150	12	N
MONTGOMERY	IH 45	0110-04-141	525	30.21	95.46	100	150	12	N
MONTGOMERY	IH 45	0110-04-141	526	30.21	95.46	100	150	12	N
MONTGOMERY	IH 45	0110-04-141	527	30.21	95.46	100	150	12	N
MONTGOMERY	IH 45	0110-04-141	528	30.21	95.46	100	150	12	N
MONTGOMERY	IH 45	0110-04-141	529	30.21	95.46	100	150	12	N
MONTGOMERY	IH 45	0110-04-141	530	30.20	95.46	100	150	12	N
MONTGOMERY	IH 45	0110-04-141	531	30.20	95.46	100	150	12	N
MONTGOMERY	IH 45	0110-04-141	532	30.20	95.45	100	150	12	N
MONTGOMERY	IH 45	0110-04-141	533	30.20	95.45	100	150	12	N
MONTGOMERY	IH 45	0110-04-141	534	30.19	95.45	100	150	12	N
MONTGOMERY	IH 45	0110-04-141	536	30.19	95.45	100	150	12	N
MONTGOMERY	IH 45	0110-04-141	537	30.19	95.45	100	150	12	N
MONTGOMERY	IH 45	0110-04-141	538	30.18	95.45	100	150	12	N
MONTGOMERY	IH 45	0110-04-141	539	30.18	95.45	100	150	12	N
MONTGOMERY	IH 45	0110-04-141	540	30.18	95.45	100	150	12	N
MONTGOMERY	IH 45	0110-04-141	541	30.18	95.45	100	150	12	N
MONTGOMERY	IH 45	0110-04-141	542	30.18	95.45	100	150	12	N
MONTGOMERY	IH 45	0110-04-141	543	30.24	95.46	100	150	12	N
MONTGOMERY	IH 45	0110-04-141	544	30.24	95.46	100	150	12	N
MONTGOMERY	IH 45	0110-04-141	545	30.24	95.46	100	150	12	N
HARRIS	IH 45	0110-05-064	550	30.06	95.43	100	150	12	N
HARRIS	IH 45	0110-05-064	551	30.06	95.43	100	150	12	N
HARRIS	IH 45	0110-05-064	552	30.06	95.43	100	150	12	N
HARRIS	IH 45	0110-05-064	553	30.06	95.43	100	150	12	N
HARRIS	IH 45	0110-05-064	554	30.07	95.43	100	150	12	N
HARRIS	IH 45	0110-05-064	555	30.07	95.43	100	150	12	N
HARRIS	IH 45	0110-05-064	556	30.07	95.44	100	150	12	N
HARRIS	IH 45	0110-05-064	557		95.44	100	150	12	N
HARRIS	IH 45	0110-05-064	558	30.07	95.44	100	150	12	N
HARRIS	IH 45	0110-05-064	559	30.08	95.44	100	150	12	N
HARRIS	IH 45	0110-05-064	560	30.08	95.44	100	150	12	N
HARRIS	IH 45	0110-05-064	561	30.08	95.44	100	150	12	N
HARRIS	IH 45	0110-05-064	565	30.09	95.44	100	150	12	N
HARRIS	IH 45	0110-05-064	566	30.09	95.44	100	150	12	N
HARRIS	IH 45	0110-05-064	567	30.09	95.44	100	150	12	N
HARRIS	IH 45	0110-05-064	568	30.10	95.44	100	150	12	N
HARRIS	IH 45	0110-05-064	569	30.10	95.44	100	150	12	N
HARRIS	IH 45	0110-05-064	570	30.10	95.44	100	150	12	N
HARRIS	IH 45	0110-05-064	571	30.10	95.44	100	150	12	N
HARRIS	IH 45	0110-05-064	572	30.10	95.44	100	150	12	N
MONTGOMERY	IH 45	0110-04-122	590			100	150	12	N
MONTGOMERY	IH 45	0110-04-122				100	150	12	N
MONTGOMERY	IH 45	0110-04-122				100	150	12	N
GALVESTON	IH 45	0912-73-075	591	29.33	94.93	100	150	12	N
GALVESTON	IH 45	0912-73-075	592	29.33	94.93	100	150	12	N
GALVESTON	IH 45	0912-73-075	593	29.33	94.94	100	150	12	N

Figure 3.26: TxDOT HMIP Inventory – Houston District - Cont'd

County	Highway(s)	Control & Section	HQ Pole Number	GPS		Wind Speed Rating (mph)	Pole Height (ft)	# Sides	Ground Sleeve
				Latitude	Longitude				
GALVESTON	IH 45	0912-73-075	594	29.33	94.94	100	150	12	N
GALVESTON	IH 45	0912-73-075	596	29.33	94.93	100	150	12	N
GALVESTON	IH 45	0912-73-075	597	29.33	94.93	100	150	12	N
HARRIS	IH 45	0500-03-449	648	29.54	95.14	100	150	12	N
HARRIS	IH 45	0500-03-449	649	29.54	95.14	100	150	12	N
HARRIS	IH 45	0500-03-449	650	29.54	95.14	100	150	12	N
HARRIS	IH 45	0500-03-449	651	29.54	95.14	100	150	12	N
HARRIS	IH 45	0500-03-449	652	29.54	95.14	100	150	12	N
HARRIS	IH 45	0500-03-449	653	29.54	95.14	100	150	12	N
HARRIS	US 59	0027-13-171	902	29.73	95.39	100	150	12	N
HARRIS	US 59	0027-13-171	903	29.73	95.38	100	150	12	N
FORT BEND	US 59	0027-12-063	951	29.64	95.59	100	150	12	N
FORT BEND	US 59	0027-12-063	952	29.64	95.58	100	150	12	N
FORT BEND	US 59	0027-12-063	953	29.64	95.58	100	150	12	N
FORT BEND	US 59	0027-12-063	954	29.64	95.58	100	150	12	N
FORT BEND	US 59	0027-12-063	955	29.64	95.58	100	150	12	N
FORT BEND	US 59	0027-12-063	956	29.64	95.58	100	150	12	N
FORT BEND	US 59	0027-12-063	957	29.64	95.57	100	150	12	N
FORT BEND	US 59	0027-12-063	958	29.65	95.57	100	150	12	N
FORT BEND	US 59	0027-12-060	972	29.61	95.61	100	150	12	N
FORT BEND	US 59	0027-12-060	973	29.62	95.61	100	150	12	N
FORT BEND	US 59	0027-12-060	974	29.62	95.61	100	150	12	N
FORT BEND	US 59	0027-12-060	975	29.62	95.60	100	150	12	N
FORT BEND	US 59	0027-12-060	976	29.62	95.60	100	150	12	N
FORT BEND	US 59	0027-12-095	977	29.60	95.63	100	150	12	N
FORT BEND	US 59	0027-12-095	978	29.60	95.62	100	150	12	N
FORT BEND	US 59	0027-12-095	980	29.60	95.62	100	150	12	N
FORT BEND	US 59	0027-12-095	981	29.60	95.62	100	150	12	N
FORT BEND	US 59	0027-12-095	982	29.60	95.62	100	150	12	N
FORT BEND	US 59	0027-12-095	983	29.61	95.62	100	150	12	N
FORT BEND	US 59	0027-12-095	985	29.61	95.61	100	150	12	N
FORT BEND	US 59	0027-12-095	986	29.61	95.61	100	150	12	N
HARRIS	US 59	0027-13-165	987	29.73	95.41	100	150	12	N
FORT BEND	US 59	0027-12-059	988	29.62	95.60	100	150	12	N
FORT BEND	US 59	0027-12-059	989	29.62	95.60	100	150	12	N
FORT BEND	US 59	0027-12-059	990	29.62	95.60	100	150	12	N
FORT BEND	US 59	0027-12-059	993	29.63	95.59	100	150	12	N
FORT BEND	US 59	0027-12-059	997	29.63	95.59	100	150	12	N
FORT BEND	US 59	0027-12-059	998		95.59	100	150	12	N
FORT BEND	US 90A	0027-08-148	1014	29.63	95.59	100	150	12	N
FORT BEND	US 90A	0027-08-148	1017	29.63	95.59	100	150	12	N
HARRIS	SH 146	0389-12-064	1020	29.68	95.03	100	150	12	N
HARRIS	SH 146	0389-12-064	1021	29.68	95.03	100	150	12	N
HARRIS	SH 146	0389-12-064	1027	29.69	95.03	100	150	12	N
HARRIS	SH 225	0502-01-159	1038	29.69	95.04	100	150	12	N
HARRIS	SH 225	0502-01-159	1039	29.69	95.03	100	150	12	N
HARRIS	SH 225	0502-01-159	1040	29.69	95.03	100	150	12	N
HARRIS	SH 225	0502-01-204	1057	29.71	95.22	100	150	12	N
HARRIS	SH 225	0502-01-204	1058	29.71	95.22	100	150	12	N
HARRIS	IH 610	0271-17-129	1301	29.69	95.46	100	150	12	N
HARRIS	IH 610	0271-17-129	1302	29.69	95.46	100	150	12	N
HARRIS	IH 610	0271-17-129	1303	29.69	95.46	100	150	12	N
HARRIS	IH 610	0271-17-129	1304	29.69	95.46	100	150	12	N
HARRIS	IH 610	0271-17-129	1305	29.69	95.46	100	150	12	N
HARRIS	IH 610	0271-17-129	1306	29.70	95.46	100	150	12	N
HARRIS	IH 610	0271-17-129	1307	29.70	95.46	100	150	12	N
HARRIS	IH 610	0271-17-129	1308	29.70	95.46	100	150	12	N
HARRIS	IH 610	0271-17-129	1309	29.70	95.46	100	150	12	N

Figure 3.27: TxDOT HMIP Inventory – Houston District - Cont'd

County	Highway(s)	Control & Section	HQ Pole Number	GPS		Wind Speed Rating (mph)	Pole Height (ft)	# Sides	Ground Sleeve
				Latitude	Longitude				
BRAZORIA	SH 332	0586-01-059	1603	29.01	95.40	100	150	12	N
BRAZORIA	SH 332	0586-01-059	1604	29.01	95.39	100	150	12	N
BRAZORIA	SH 332	0586-01-059	1608	29.01	95.39	100	150	12	N
BRAZORIA	SH 332	0586-01-059	1609	29.00	95.39	100	150	12	N
BRAZORIA	SH 332	0586-01-059	1610	29.00	95.39	100	150	12	N
HARRIS	IH 610	0271-17-139	1611	29.70	95.46	100	150	12	N
HARRIS	IH 610	0271-17-139	1614	29.71	95.46	100	150	12	N
HARRIS	IH 610	0271-17-139	1615	29.72	95.46	100	150	12	N
HARRIS	IH 610	0271-17-139	1616	29.72	95.46	100	150	12	N
HARRIS	IH 610	0271-17-139	1617	29.72	95.46	100	150	12	N
HARRIS	IH 610	0271-17-139	1618	29.72	95.46	100	150	12	N
MONTGOMERY	IH 45	0110-04-123	496	30.17	95.45	100	150	12	N
MONTGOMERY	IH 45	0110-04-123	497	30.17	95.45	100	150	12	N
MONTGOMERY	IH 45	0110-04-123	498	30.17	95.45	100	150	12	N
MONTGOMERY	IH 45	0110-04-123	499	30.17	95.45	100	150	12	N
MONTGOMERY	IH 45	0110-04-123	500	30.16	95.45	100	150	12	N
MONTGOMERY	IH 45	0110-04-123	501	30.16	95.45	100	150	12	N
MONTGOMERY	IH 45	0110-04-123	502	30.16	95.45	100	150	12	N
MONTGOMERY	IH 45	0110-04-123	503	30.16	95.45	100	150	12	N
MONTGOMERY	IH 45	0110-04-123	504	30.15	95.45	100	150	12	N
MONTGOMERY	IH 45	0110-04-123	505	30.15	95.45	100	150	12	N
MONTGOMERY	IH 45	0110-04-123	506	30.15	95.45	100	150	12	N
MONTGOMERY	IH 45	0110-04-123	507	30.15	95.45	100	150	12	N
MONTGOMERY	IH 45	0110-04-123	508	30.15	95.45	100	150	12	N
MONTGOMERY	IH 45	0110-04-123	509	30.14	95.45	100	150	12	N
MONTGOMERY	IH 45	0110-04-123	510	30.14	95.45	100	150	12	N
MONTGOMERY	IH 45	0110-04-123	511	30.14	95.45	100	150	12	N
MONTGOMERY	IH 45	0110-04-123	512	30.14	95.44	100	150	12	N
MONTGOMERY	IH 45	0110-04-123	513	30.13	95.44	100	150	12	N
MONTGOMERY	IH 45	0110-04-123	514	30.13	95.44	100	150	12	N
C. HARRIS	BW 8	3256-04-020	12	29.60	95.21	100	150	12	Y
C. HARRIS	BW 8	3256-04-020	13	29.60	95.22	100	150	12	Y
C. HARRIS	BW 8	3256-03-037	14	29.60	95.21	100	150	12	Y
HARRIS	IH 10	0912-71-402	88	29.78	95.38	100	150	12	Y
HARRIS	IH 10	0912-71-402	89	29.78	95.38	100	150	12	Y
HARRIS	IH 10	0912-71-402	90	29.78	95.38	100	150	12	Y
HARRIS	IH 10	0912-71-402	91	29.78	95.38	100	150	12	Y
HARRIS	IH 10	0912-71-402	92	29.78	95.38	100	150	12	Y
HARRIS	IH 10	0912-71-402	93	29.78	95.38	100	150	12	Y
HARRIS	IH 10	0912-71-402	94	29.78	95.38	100	150	12	Y
HARRIS	IH 10	0912-71-402	95	29.78	95.37	100	150	12	Y
HARRIS	IH 10	0912-71-402	96	29.78	95.37	100	150	12	Y
HARRIS	IH 10	0912-71-402	97	29.78	95.37	100	150	12	Y
HARRIS	IH 10	0912-71-402	98	29.78	95.37	100	150	12	Y
HARRIS	IH 10	0912-71-402	99	29.78	95.37	100	150	12	Y
HARRIS	IH 10	0912-71-402	100	29.78	95.37	100	150	12	Y
HARRIS	IH 10	0912-71-402	101	29.78	95.37	100	150	12	Y
HARRIS	IH 10	0912-71-402	102	29.77	95.37	100	150	12	Y
HARRIS	IH 10	0912-71-402	103	29.77	95.37	100	150	12	Y
HARRIS	IH 10	0912-71-402	104	29.77	95.37	100	150	12	Y
HARRIS	IH 10	0912-71-402	105	29.77	95.37	100	150	12	Y
C. HARRIS	IH 10	0271-07-210	106	29.78	95.44	100	150	12	Y
C. HARRIS	IH 10	0271-07-210	107	29.78	95.44	100	150	12	Y
C. HARRIS	IH 10	0271-07-210	108	29.78	95.43	100	150	12	Y
C. HARRIS	IH 10	0271-07-210	109	29.78	95.43	100	150	12	Y
C. HARRIS	IH 10	0271-07-210	110	29.78	95.43	100	150	12	Y
C. HARRIS	IH 10	0271-07-210	111	29.78	95.43	100	150	12	Y
C. HARRIS	IH 10	0271-07-210	112	29.78	95.42	100	150	12	Y

Figure 3.28: TxDOT HMIP Inventory – Houston District - Cont'd

County	Highway(s)	Control & Section	HQ Pole Number	GPS		Wind Speed Rating (mph)	Pole Height (ft)	# Sides	Ground Sleeve
				Latitude	Longitude				
C. HARRIS	IH 10	0271-07-210	113	29.78	95.42	100	150	12	Y
C. HARRIS	IH 10	0271-07-210	114	29.78	95.42	100	150	12	Y
C. HARRIS	IH 10	0271-07-210	115	29.78	95.41	100	150	12	Y
C. HARRIS	IH 10	0271-07-210	116	29.78	95.41	100	150	12	Y
C. HARRIS	IH 10	0271-07-210	117	29.78	95.41	100	150	12	Y
C. HARRIS	IH 10	0271-07-210	118	29.78	95.41	100	150	12	Y
C. HARRIS	IH 10	0271-07-210	119	29.78	95.40	100	150	12	Y
C. HARRIS	IH 10	0271-07-210	120	29.78	95.40	100	150	12	Y
C. HARRIS	IH 10	0271-07-210	121	29.78	95.40	100	150	12	Y
C. HARRIS	IH 10	0271-07-210	122	29.78	95.40	100	150	12	Y
C. HARRIS	IH 10	0271-07-210	123	29.78	95.39	100	150	12	Y
C. HARRIS	IH 10	0271-07-210	124	29.78	95.39	100	150	12	Y
C. HARRIS	IH 10	0271-07-210	125	29.78	95.39	100	150	12	Y
C. HARRIS	IH 10	0271-07-210	126	29.78	95.39	100	150	12	Y
E. HARRIS	IH 10	0508-01-292	153	29.78	95.09	100	150	12	Y
E. HARRIS	IH 10	0508-01-292	154	29.78	95.09	100	150	12	Y
E. HARRIS	IH 10	0508-01-292	155	29.78	95.08	100	150	12	Y
E. HARRIS	IH 10	0508-01-292	156	29.78	95.08	100	150	12	Y
E. HARRIS	IH 10	0508-01-292	157	29.78	95.08	100	150	12	Y
E. HARRIS	IH 10	0508-01-292	158	29.78	95.08	100	150	12	Y
E. HARRIS	IH 10	0508-01-292	159	29.78	95.08	100	150	12	Y
E. HARRIS	IH 10	0508-01-292	160	29.78	95.07	100	150	12	Y
E. HARRIS	IH 10	0508-01-292	161	29.78	95.07	100	150	12	Y
E. HARRIS	IH 10	0508-01-292	162	29.78	95.07	100	150	12	Y
E. HARRIS	IH 10	0508-01-292	163	29.78	95.07	100	150	12	Y
E. HARRIS	IH 10	0508-01-292	164	29.78	95.06	100	150	12	Y
E. HARRIS	IH 10	0508-01-292	165	29.78	95.06	100	150	12	Y
E. HARRIS	IH 10	0508-01-292	166	29.78	95.06	100	150	12	Y
	IH 10	0271-07-274		29.79	95.44	100	150	12	Y
HARRIS	IH 45	0110-05-070	442	29.98	95.42	100	150	12	Y
HARRIS	IH 45	0110-05-070	443	29.98	95.42	100	150	12	Y
HARRIS	IH 45	0110-05-070	444	29.98	95.42	100	150	12	Y
HARRIS	IH 45	0110-06-107	448	29.96	95.42	100	150	12	Y
HARRIS	IH 45	0110-06-107	449	29.96	95.42	100	150	12	Y
HARRIS	IH 45	0110-06-107	450	29.97	95.42	100	150	12	Y
HARRIS	IH 45	0110-06-107	451	29.97	95.42	100	150	12	Y
HARRIS	IH 45	0110-06-107	452	29.97	95.42	100	150	12	Y
HARRIS	IH 45	0110-06-107	453	29.97	95.42	100	150	12	Y
HARRIS	IH 45	0110-06-107	454	29.97	95.42	100	150	12	Y
HARRIS	IH 45	0110-06-107	455	29.97	95.42	100	150	12	Y
HARRIS	IH 45	See 0110-06-071				100		12	Y
HARRIS	IH 45	0110-05-069	457	30.02	95.43	100	150	12	Y
HARRIS	IH 45	0110-05-069	458	30.02	95.43	100	150	12	Y
HARRIS	IH 45	0110-05-069	459	30.02	95.43	100	150	12	Y
HARRIS	IH 45	0110-05-069	460	30.02	95.43	100	150	12	Y
HARRIS	IH 45	0110-05-069	461	30.03	95.43	100	150	12	Y
HARRIS	IH 45	0110-05-069	462	30.03	95.43	100	150	12	Y
HARRIS	IH 45	0110-05-069	463	30.03	95.43	100	150	12	Y
HARRIS	IH 45	0110-05-069	464	30.03	95.43	100	150	12	Y
HARRIS	IH 45	0110-05-069	465	30.04	95.43	100	150	12	Y
HARRIS	IH 45	0110-05-069	466	30.04	95.43	100	150	12	Y
HARRIS	IH 45	0110-05-069	467	30.04	95.43	100	150	12	Y
HARRIS	IH 45	0110-05-069	468	30.04	95.43	100	150	12	Y
HARRIS	IH 45	0110-05-069	469	30.05	95.43	100	150	12	Y
HARRIS	IH 45	0110-05-069	470	30.05	95.43	100	150	12	Y
HARRIS	IH 45	0500-03-427	473	29.61	95.20	100	150	12	Y
HARRIS	IH 45	0500-03-427	474	29.61	95.20	100	150	12	Y
HARRIS	IH 45	0500-03-427	475	29.61	95.20	100	150	12	Y

Figure 3.29: TxDOT HMIP Inventory – Houston District - Cont'd

County	Highway(s)	Control & Section	HQ Pole Number	GPS		Wind Speed Rating (mph)	Pole Height (ft)	# Sides	Ground Sleeve
				Latitude	Longitude				
HARRIS	IH 45	0110-05-077	477	30.05	95.43	100	150	12	Y
HARRIS	IH 45	0110-05-077	478	30.05	95.43	100	150	12	Y
HARRIS	IH 45	0110-05-077	479	30.05	95.43	100	150	12	Y
HARRIS	IH 45	0110-05-063	488	30.00	95.43	100	150	12	Y
HARRIS	IH 45	0110-05-063	489	30.01	95.43	100	150	12	Y
HARRIS	IH 45	0110-05-063	490	30.01	95.43	100	150	12	Y
HARRIS	IH 45	0110-05-063	491	30.01	95.43	100	150	12	Y
HARRIS	IH 45	0110-05-063	492	30.01	95.43	100	150	12	Y
HARRIS	IH 45	0110-05-063	493	30.01	95.43	100	150	12	Y
HARRIS	IH 45	0500-03-429	494	29.60	95.21	100	150	12	Y
MONTGOMERY	IH 45	0110-04-164	615	30.28	95.46	100	150	12	Y
MONTGOMERY	IH 45	0110-04-164	616	30.27	95.46	100	150	12	Y
MONTGOMERY	IH 45	0110-04-164	617	30.27	95.46	100	150	12	Y
MONTGOMERY	IH 45	0110-04-164	618	30.27	95.46	100	150	12	Y
MONTGOMERY	IH 45	0110-04-164	621	30.26	95.46	100	150	12	Y
HARRIS	IH 45	0912-00-300	622	30.11	95.44	100	150	12	Y
HARRIS	IH 45	0912-00-300	623	30.11	95.44	100	150	12	Y
HARRIS	IH 45	0912-00-300	624	30.11	95.44	100	150	12	Y
HARRIS	IH 45	0912-00-300	625	30.11	95.44	100	150	12	Y
HARRIS	IH 45	0912-00-300	626	30.12	95.44	100	150	12	Y
HARRIS	IH 45	0912-00-300	627	30.12	95.44	100	150	12	Y
HARRIS	IH 45	0912-00-300	628	30.12	95.44	100	150	12	Y
HARRIS	IH 45	0912-00-300	629	30.12	95.44	100	150	12	Y
HARRIS	IH 45	0912-00-300	630	30.12	95.44	100	150	12	Y
HARRIS	IH 45	0912-00-300	631	30.13	95.44	100	150	12	Y
HARRIS	IH 45	0912-00-300	632	30.13	95.44	100	150	12	Y
HARRIS	US 59	0027-13-138	832	29.65	95.57	100	150	12	Y
HARRIS	US 59	0027-13-138	833	29.65	95.57	100	150	12	Y
HARRIS	US 59	0027-13-138	834	29.65	95.57	100	150	12	Y
HARRIS	US 59	0027-13-138	835	29.65	95.57	100	150	12	Y
HARRIS	US 59	0027-13-138	836	29.65	95.57	100	150	12	Y
HARRIS	US 59	0027-13-138	837	29.65	95.56	100	150	12	Y
HARRIS	US 59	0027-13-138	838	29.66	95.56	100	150	12	Y
HARRIS	US 59	0177-11-118	841	29.77	95.34	100	150	12	Y
HARRIS	US 59	0177-11-118	842	29.77	95.34	100	150	12	Y
HARRIS	US 59	0177-11-118	843	29.78	95.34	100	150	12	Y
HARRIS	US 59	0177-11-118	844	29.78	95.34	100	150	12	Y
HARRIS	US 59	0177-11-118	845	29.78	95.34	100	150	12	Y
HARRIS	US 59	0177-11-118	846	29.78	95.34	100	150	12	Y
HARRIS	US 59	0177-11-118	847	29.78	95.34	100	150	12	Y
HARRIS	US 59	0177-11-118	848	29.79	95.34	100	150	12	Y
HARRIS	US 59	0177-11-118	849	29.79	95.34	100	150	12	Y
HARRIS	US 59	0177-11-118	850	29.79	95.34	100	150	12	Y
HARRIS	US 59	0177-11-118	851	29.79	95.34	100	150	12	Y
HARRIS	US 59	0177-11-118	852	29.79	95.34	100	150	12	Y
HARRIS	US 59	0177-11-118	853	29.80	95.34	100	150	12	Y
HARRIS	US 59	0177-11-118	854	29.80	95.34	100	150	12	Y
HARRIS	US 59	0177-07-080	855	29.95	95.29	100	150	12	Y
HARRIS	US 59	0177-07-080	856	29.95	95.29	100	150	12	Y
HARRIS	US 59	0177-07-080	857	29.95	95.29	100	150	12	Y
HARRIS	US 59	0177-07-080	858	29.96	95.29	100	150	12	Y
HARRIS	US 59	0177-07-080	859	29.96	95.29	100	150	12	Y
HARRIS	US 59	0177-07-080	860	29.96	95.29	100	150	12	Y
HARRIS	US 59	0177-07-080	861	29.96	95.29	100	150	12	Y
HARRIS	US 59	0177-07-080	862	29.96	95.28	100	150	12	Y
HARRIS	US 59	0177-11-105	880	29.80	95.34	100	150	12	Y
HARRIS	US 59	0177-11-105	881	29.80	95.34	100	150	12	Y
HARRIS	US 59	0177-11-105	882	29.80	95.34	100	150	12	Y

Figure 3.30: TxDOT HMIP Inventory – Houston District - Cont'd

County	Highway(s)	Control & Section	HQ Pole Number	GPS		Wind Speed Rating (mph)	Pole Height (ft)	# Sides	Ground Sleeve
				Latitude	Longitude				
HARRIS	US 59	0177-11-105	883			100	150	12	Y
HARRIS	US 59	0177-07-067	884	29.99	95.27	100	150	12	Y
HARRIS	US 59	0177-07-067	885	30.00	95.27	100	150	12	Y
HARRIS	US 59	0177-07-067	886	30.00	95.27	100	150	12	Y
HARRIS	US 59	0177-07-067	887	30.00	95.27	100	150	12	Y
HARRIS	US 59	0177-07-067	888	30.00	95.27	100	150	12	Y
HARRIS	US 59	0177-07-067	889	30.01	95.27	100	150	12	Y
HARRIS	US 59	0177-07-067	890	30.01	95.27	100	150	12	Y
HARRIS	US 59	0177-07-067	891	30.01	95.26	100	150	12	Y
HARRIS	US 59	0177-06-045	892	30.00	95.27	100	150	12	Y
HARRIS	US 59	0177-06-045	893	30.01	95.27	100	150	12	Y
HARRIS	US 59	0177-06-045	894	30.00	95.27	100	150	12	Y
HARRIS	US 59	0177-06-045	895	30.01	95.27	100	150	12	Y
HARRIS	US 59	0177-11-119	938	29.77	95.34	100	150	12	Y
FORT BEND	US 59	0027-12-062	943	29.59	95.64	100	150	12	Y
FORT BEND	US 59	0027-12-062	944	29.59	95.64	100	150	12	Y
FORT BEND	US 59	0027-12-062	945			100	150	12	Y
FORT BEND	US 59	0027-12-062	946	29.59	95.64	100	150	12	Y
FORT BEND	US 59	0027-12-062	947	29.59	95.63	100	150	12	Y
FORT BEND	US 59	0027-12-062	948			100	150	12	Y
FORT BEND	US 59	0027-12-062	949			100	150	12	Y
FORT BEND	US 59	0027-12-062	950			100	150	12	Y
HARRIS	US 59	0177-06-044	959	30.01	95.26	100	150	12	Y
HARRIS	US 59	0177-06-044	960	30.02	95.26	100	150	12	Y
HARRIS	US 59	0177-06-044	961	30.02	95.26	100	150	12	Y
HARRIS	US 59	0177-06-044	962	30.02	95.26	100	150	12	Y
HARRIS	US 59	0177-06-044	963	30.02	95.26	100	150	12	Y
HARRIS	US 59	0177-06-044	964	30.02	95.26	100	150	12	Y
HARRIS	US 59	0177-06-044	965	30.03	95.26	100	150	12	Y
HARRIS	US 59	0177-06-044	966	30.03	95.26	100	150	12	Y
HARRIS	US 59	0177-06-044	967	30.03	95.26	100	150	12	Y
HARRIS	US 59	0177-06-044	968	30.04	95.26	100	150	12	Y
HARRIS	US 59	0177-06-044	969	30.04	95.26	100	150	12	Y
MONTGOMERY	US 59	0177-05-086	970	30.04	95.25	100	150	12	Y
MONTGOMERY	US 59	0177-05-086	971	30.04	95.25	100	150	12	Y
HARRIS	US 59	0177-07-089	1002	29.94	95.30	100	150	12	Y
FORT BEND	US 59	0027-12-110	1003			100	150	12	Y
FORT BEND	US 59	0027-12-110	1004			100	150	12	Y
FORT BEND	US 59	0027-12-110	1005			100	150	12	Y
FORT BEND	US 59	0027-12-110	1006			100	150	12	Y
FORT BEND	US 59	0027-12-110	1007			100	150	12	Y
FORT BEND	US 59	0027-12-110	1008	29.57	95.66	100	150	12	Y
GALVESTON	SH 146	0389-06-074	1019	29.39	94.95	100	150	12	Y
HARRIS	SH 146	0389-12-064	1028	29.69	95.03	100	150	12	Y
HARRIS	SH 249	0720-03-073	1060	29.95	95.53	100	150	12	Y
HARRIS	SH 249	0720-03-073	1061	29.95	95.53	100	150	12	Y
HARRIS	SH 249	0720-03-073	1062	29.95	95.53	100	150	12	Y
HARRIS	SH 249	0720-03-073	1063	29.95	95.54	100	150	12	Y
HARRIS	SH 249	0720-03-073	1064	29.95	95.54	100	150	12	Y
HARRIS	SH 249	0720-03-073	1065	29.96	95.54	100	150	12	Y
HARRIS	SH 249	0720-03-073	1066	29.96	95.54	100	150	12	Y
HARRIS	SH 249	0720-03-073	1067	29.96	95.54	100	150	12	Y
HARRIS	SH 249	0720-03-073	1068	29.96	95.54	100	150	12	Y
HARRIS	SH 249	0720-03-073	1069	29.96	95.55	100	150	12	Y
HARRIS	SH 249	0720-03-073	1070	29.96	95.55	100	150	12	Y
HARRIS	SH 249	0720-03-073	1071	29.96	95.55	100	150	12	Y
HARRIS	SH 249	0720-03-073	1072	29.96	95.55	100	150	12	Y
HARRIS	SH 249	0720-03-073	1073	29.97	95.55	100	150	12	Y

Figure 3.31: TxDOT HMIP Inventory – Houston District - Cont'd

County	Highway(s)	Control & Section	HQ Pole Number	GPS		Wind Speed Rating (mph)	Pole Height (ft)	# Sides	Ground Sleeve
				Latitude	Longitude				
HARRIS	SH 249	0720-03-073	1074	29.97	95.56	100	150	12	Y
HARRIS	SH 249	0720-03-073	1075	29.97	95.56	100	150	12	Y
HARRIS	SH 249	0720-03-073	1076	29.97	95.56	100	150	12	Y
HARRIS	SH 249	0720-03-081	1077	29.97	95.56	100	150	12	Y
HARRIS	SH 249	0720-03-081	1078	29.97	95.56	100	150	12	Y
HARRIS	SH 249	0720-03-081	1079	29.97	95.56	100	150	12	Y
HARRIS	SH 249	0720-03-081	1080	29.98	95.56	100	150	12	Y
HARRIS	SH 249	0720-03-081	1081	29.98	95.57	100	150	12	Y
HARRIS	SH 249	0720-03-081	1082	29.98	95.57	100	150	12	Y
HARRIS	SH 249	0720-03-081	1083	29.98	95.57	100	150	12	Y
HARRIS	SH 249	0720-03-081	1084	29.98	95.57	100	150	12	Y
HARRIS	SH 249	0720-03-081	1085	29.99	95.57	100	150	12	Y
HARRIS	SH 249	0720-03-081	1086	29.99	95.57	100	150	12	Y
HARRIS	SH 249	0720-03-081	1087	29.99	95.57	100	150	12	Y
HARRIS	SH 249	0720-03-081	1088	29.99	95.57	100	150	12	Y
HARRIS	SH 249	0720-03-081	1089	29.99	95.58	100	150	12	Y
HARRIS	SH 249	0720-03-081	1090	30.00	95.58	100	150	12	Y
HARRIS	SH 249	0720-03-081	1091	30.00	95.58	100	150	12	Y
HARRIS	SH 249	0720-03-081	1092	30.00	95.58	100	150	12	Y
HARRIS	SH 249	0720-03-081	1093	30.00	95.58	100	150	12	Y
HARRIS	SH 249	0720-03-081	1094	30.00	95.58	100	150	12	Y
HARRIS	SH 249	0720-03-081	1095	30.00	95.59	100	150	12	Y
HARRIS	SH 249	0720-03-084	1096	30.06	95.62	100	150	12	Y
HARRIS	SH 249	0720-03-084	1097	30.07	95.62	100	150	12	Y
HARRIS	SH 249	0720-03-084	1099	30.07	95.63	100	150	12	Y
HARRIS	SH 249	0720-03-084	1102	30.07	95.63	100	150	12	Y
HARRIS	SH 249	0720-03-084	1103	30.08	95.63	100	150	12	Y
HARRIS	SH 249	0720-03-084	1104	30.08	95.63	100	150	12	Y
HARRIS	SH 249	0720-03-084	1105	30.08	95.63	100	150	12	Y
HARRIS	SH 249	0720-03-084	1106	30.09	95.64	100	150	12	Y
HARRIS	SH 249	0720-03-084	1107	30.09	95.64	100	150	12	Y
HARRIS	SH 249	0720-03-084	1108	30.09	95.64	100	150	12	Y
HARRIS	SH 249	0720-03-084	1109	30.09	95.64	100	150	12	Y
HARRIS	SH 249	0720-03-084	1110	30.10	95.64	100	150	12	Y
HARRIS	SH 249	0720-03-084	1111	30.10	95.64	100	150	12	Y
HARRIS	SH 249	0720-03-084	1112	30.10	95.64	100	150	12	Y
HARRIS	SH 249	0720-03-084	1113	30.10	95.64	100	150	12	Y
HARRIS	SH 288	0598-01-033	1121	29.60	95.39	100	150	12	Y
HARRIS	SH 288	0598-01-033	1123	29.60	95.39	100	150	12	Y
HARRIS	SH 288	0598-01-033	1124	29.60	95.39	100	150	12	Y
HARRIS	SH 288	0598-01-033	1125	29.59	95.39	100	150	12	Y
HARRIS	SH 288	0598-01-033	1126	29.59	95.39	100	150	12	Y
HARRIS	SH 288	0598-01-033	1127	29.59	95.39	100	150	12	Y
HARRIS	SH 288	0598-01-033	1128	29.59	95.39	100	150	12	Y
HARRIS	SPUR 330	0508-07-278	1211			100	150	12	Y
HARRIS	SPUR 330	0508-07-278	1212			100	150	12	Y
HARRIS	SPUR 330	0508-07-278	1213			100	150	12	Y
HARRIS	SPUR 330	0508-07-278	1218			100	150	12	Y
HARRIS	FM 1960	1685-01-070	1512	29.96	95.55	100	150	12	Y
HARRIS	FM 1960	1685-01-070	1513	29.96	95.55	100	150	12	Y
HARRIS	FM 1960	1685-01-070	1518	29.96	95.55	100	150	12	Y
HARRIS	FM 1960	1685-01-070	1519	29.96	95.54	100	150	12	Y
HARRIS	IH 45	0110-06-107	456	29.98	95.42		150		
MONTGOMERY	IH 45	0110-04-141	535	30.19	95.45		150		
MONTGOMERY	IH 46	0110-04-122					150		
HARRIS	US 59	0027-13-100	731	29.69	95.53	100	150		
HARRIS	US 59	0177-11-119	936	29.77	95.34		150		
HARRIS	US 59	0177-11-119	937	29.77	95.34		150		

Figure 3.32: TxDOT HMIP Inventory – Houston District - Cont'd

County	Highway(s)	Control & Section	HQ Pole Number	GPS		Wind Speed Rating (mph)	Pole Height (ft)	# Sides	Ground Sleeve
				Latitude	Longitude				
HARRIS	SH 146	0389-12-064	1024	29.69	95.04	100	150		
HARRIS	SH 146	0389-12-064	1029	29.69	95.03		150		
HARRIS	SH 146	0389-12-064	1030	29.69	95.03		150		
HARRIS	IH 610	0271-14-105	1244	29.78	95.45	100	150	8	Y
HARRIS	IH 610	0271-16-064	1280	29.68	95.43		150		
HARRIS	BW 8	3256-01-055	10	29.66	95.56	100	175	8	Y
HARRIS	IH 10	0508-01-209	49	29.78	95.26	100	175	8	Y
HARRIS	IH 10	0508-01-209	50	29.78	95.26	100	175	8	Y
HARRIS	IH 10	0508-01-209	51	29.77	95.26	100	175	8	Y
HARRIS	IH 10	0508-01-209	52	29.78	95.26	100	175	8	Y
HARRIS	IH 10	0508-01-209	53	29.78	95.26	100	175	8	Y
HARRIS	IH 10	0508-01-209	54	29.78	95.26	100	175	8	Y
HARRIS	IH 10	0508-01-209	55	29.77	95.26	100	175	8	Y
HARRIS	IH 10	0508-01-209	56	29.77	95.26	100	175	8	Y
C. HARRIS	IH 10	0508-01-209	57	29.77	95.26	100	175	8	Y
C. HARRIS	IH 10	0508-01-209	63	29.77	95.26	100	175	8	Y
C. HARRIS	IH 10	0508-01-209	64	29.77	95.26	100	175	8	Y
C. HARRIS	IH 10	0508-01-209	65	29.77	95.27	100	175	8	Y
HARRIS	IH 10	0508-01-230	75	29.77	95.16	100	175	8	Y
HARRIS	IH 10	0508-01-236	84	29.77	95.16	100	175	8	Y
N. HARRIS	IH 45	0110-06-104	391	29.94	95.42	100	175	8	Y
HARRIS	IH 45	0500-03-382	402	29.62	95.22	100	175	8	Y
HARRIS	IH 45	0500-03-382	403	29.62	95.22	100	175	8	Y
HARRIS	IH 45	0500-03-382	409	29.61	95.21	100	175	8	Y
HARRIS	IH 45	0500-03-382	411	29.61	95.21	100	175	8	Y
HARRIS	IH 45	0500-03-382	412			100	175	8	Y
HARRIS	IH 45	0500-03-382	414	29.60	95.20	100	175	8	Y
MONTGOMERY	IH 45	0110-04-141	516	30.24	95.46	100	175	8	Y
HARRIS	IH 45	0110-06-105	573	29.94	95.41	100	175	8	Y
HARRIS	US 59	0027-13-117	657			100	175	8	Y
HARRIS	US 59	0027-13-117	658	29.66	95.56	100	175	8	Y
HARRIS	US 59	0027-13-117	659	29.66	95.56	100	175	8	Y
HARRIS	US 59	0027-13-123	682	29.73	95.46	100	175	8	Y
HARRIS	US 59	0027-13-123	683	29.73	95.46	100	175	8	Y
HARRIS	US 59	0027-13-123	688	29.73	95.46	100	175	8	Y
HARRIS	US 59	0027-13-123	689	29.73	95.46	100	175	8	Y
HARRIS	US 59	0027-13-123	690	29.73	95.46	100	175	8	Y
HARRIS	US 59	0027-13-123	691	29.73	95.46	100	175	8	Y
HARRIS	US 59	0027-13-123	692	29.73	95.46	100	175	8	Y
HARRIS	US 59	0177-07-077	804	29.94	95.30	100	175	8	Y
HARRIS	US 59	0177-07-077	805	29.94	95.30	100	175	8	Y
HARRIS	US 59	0177-07-077	806	29.94	95.30	100	175	8	Y
HARRIS	US 59	0177-07-077	807	29.94	95.29	100	175	8	Y
HARRIS	US 59	0177-07-088	812	29.92	95.30	100	175	8	Y
HARRIS	US 59	0177-07-088	813	29.92	95.30	100	175	8	Y
HARRIS	US 59	0177-07-088	816	29.93	95.30	100	175	8	Y
HARRIS	US 59	0177-07-088	817	29.93	95.30	100	175	8	Y
HARRIS	US 59	0177-07-088	818	29.93	95.30	100	175	8	Y
BRAZORIA	SH 288	0598-02-013	1132	29.58	95.39	100	175	8	Y
BRAZORIA	SH 288	0598-02-013	1135	29.58	95.39	100	175	8	Y
BRAZORIA	SH 288	0598-02-013	1142	29.56	95.39	100	175	8	Y
BRAZORIA	SH 288	0598-02-013	1145	29.56	95.39	100	175	8	Y
HARRIS	SH 288	0598-01-045	1154	29.67	95.38	100	175	8	Y
HARRIS	SH 288	0598-01-045	1158	29.66	95.39	100	175	8	Y
HARRIS	SH 288	0598-01-045	1159	29.66	95.39	100	175	8	Y
HARRIS	SH 288	0598-01-045	1160	29.66	95.39	100	175	8	Y
HARRIS	SH 288	0598-01-045	1165	29.65	95.39	100	175	8	Y
HARRIS	SH 288	0598-01-045	1166	29.64	95.39	100	175	8	Y

Figure 3.33: TxDOT HMIP Inventory – Houston District - Cont'd

County	Highway(s)	Control & Section	HQ Pole Number	GPS		Wind Speed Rating (mph)	Pole Height (ft)	# Sides	Ground Sleeve
				Latitude	Longitude				
HARRIS	SH 288	0598-01-045	1167	29.64	95.39	100	175	8	Y
HARRIS	SH 288	0598-01-045	1173	29.63	95.39	100	175	8	Y
HARRIS	SH 288	0598-01-045	1174	29.63	95.39	100	175	8	Y
HARRIS	SH 288	0598-01-045	1175	29.63	95.39	100	175	8	Y
HARRIS	SH 288	0598-01-045	1176	29.62	95.39	100	175	8	Y
HARRIS	SH 288	0598-01-045	1180	29.62	95.39	100	175	8	Y
HARRIS	SH 288	0598-01-045	1181	29.62	95.39	100	175	8	Y
HARRIS	SH 288	0598-01-045	1182	29.61	95.39	100	175	8	Y
HARRIS	SH 288	0598-01-045	1183	29.61	95.39	100	175	8	Y
HARRIS	SH 288	0598-01-026	1189	29.67	95.38	100	175	8	Y
HARRIS	SH 288	0598-01-026	1190	29.67	95.38	100	175	8	Y
HARRIS	SH 288	0598-01-026	1191	29.67	95.38	100	175	8	Y
	SH 288	0271-16-031	1193	29.68	95.38	100	175	8	Y
	SH 288	0271-16-031	1194	29.68	95.38	100	175	8	Y
	SH 288	0271-16-031	1195	29.68	95.38	100	175	8	Y
	SH 288	0271-16-031	1196	29.68	95.38	100	175	8	Y
	SH 288	0271-16-031	1197	29.68	95.38	100	175	8	Y
	SH 288	0271-16-031	1198	29.68	95.38	100	175	8	Y
	SH 288	0271-16-031	1199	29.68	95.38	100	175	8	Y
	SH 288	0271-16-031	1201	29.68	95.38	100	175	8	Y
	SH 288	0271-16-031	1202	29.69	95.38	100	175	8	Y
	SH 288	0271-16-031	1209	29.68	95.38	100	175	8	Y
HARRIS	IH 610	0271-14-105	1254	29.80	95.45	100	175	8	Y
HARRIS	IH 610	0271-14-105	1257	29.80	95.45	100	175	8	Y
HARRIS	US 290	0050-09-049	1441	29.87	95.56	100	175	8	Y
HARRIS	US 290	0050-09-049	1442	29.87	95.55	100	175	8	Y
HARRIS	US 290	0050-09-049	1443	29.87	95.56	100	175	8	Y
HARRIS	US 290	0050-09-049	1444	29.87	95.55	100	175	8	Y
HARRIS	US 290	0271-14-158	1507	29.81	95.45	100	175	8	Y
HARRIS	IH 45	0500-03-313	1634	29.73	95.35	100	175	8	Y
HARRIS	IH 45	0500-03-278		29.81	95.38	100	175	8	Y
HARRIS	IH 45	0500-03-278		29.81	95.38	100	175	8	Y
HARRIS	IH 45	0500-03-278		29.82	95.38	100	175	8	Y
HARRIS	IH 45	0500-03-278		29.81	95.37	100	175	8	Y
HARRIS	IH 45	0500-03-278		29.81	95.37	100	175	8	Y
W. HARRIS	IH 10	0271-07-248	167	29.78	95.58	100	175	12	N
W. HARRIS	IH 10	0271-07-248	168	29.79	95.58	100	175	12	N
W. HARRIS	IH 10	0271-07-248	169	29.78	95.58	100	175	12	N
W. HARRIS	IH 10	0271-07-248	170	29.79	95.58	100	175	12	N
W. HARRIS	IH 10	0271-07-248	171	29.78	95.57	100	175	12	N
W. HARRIS	IH 10	0271-07-248	172	29.79	95.57	100	175	12	N
W. HARRIS	IH 10	0271-07-248	173	29.78	95.57	100	175	12	N
W. HARRIS	IH 10	0271-07-248	174	29.78	95.57	100	175	12	N
W. HARRIS	IH 10	0271-07-248	175			100	175	12	N
W. HARRIS	IH 10	0271-07-248	176			100	175	12	N
W. HARRIS	IH 10	0271-07-248	177			100	175	12	N
W. HARRIS	IH 10	0271-07-248	178			100	175	12	N
W. HARRIS	IH 10	0271-07-248	179	29.78	95.56	100	175	12	N
W. HARRIS	IH 10	0271-07-248	180			100	175	12	N
W. HARRIS	IH 10	0271-07-248	181			100	175	12	N
W. HARRIS	IH 10	0271-07-248	182	29.78	95.55	100	175	12	N
W. HARRIS	IH 10	0271-07-248	183	29.78	95.57	100	175	12	N
W. HARRIS	IH 10	0271-07-248	184			100	175	12	N
W. HARRIS	IH 10	0271-07-248	185	29.78	95.56	100	175	12	N
W. HARRIS	IH 10	0271-07-248	186	29.78	95.56	100	175	12	N
W. HARRIS	IH 10	0271-07-248	187	29.78	95.56	100	175	12	N
W. HARRIS	IH 10	0271-07-248	188	29.79	95.56	100	175	12	N
HARRIS	IH 10	0271-07-254	189			100	175	12	N

Figure 3.34: TxDOT HMIP Inventory – Houston District - Cont'd

County	Highway(s)	Control & Section	HQ Pole Number	GPS		Wind Speed Rating (mph)	Pole Height (ft)	# Sides	Ground Sleeve
				Latitude	Longitude				
HARRIS	IH 10	0271-07-254	190	29.79	95.61	100	175	12	N
HARRIS	IH 10	0271-07-254	191			100	175	12	N
HARRIS	IH 10	0271-07-254	192	29.79	95.60	100	175	12	N
HARRIS	IH 10	0271-07-254	193			100	175	12	N
HARRIS	IH 10	0271-07-254	194			100	175	12	N
HARRIS	IH 10	0271-07-254	195			100	175	12	N
HARRIS	IH 10	0271-07-254	196			100	175	12	N
HARRIS	IH 10	0271-07-254	197			100	175	12	N
HARRIS	IH 10	0271-07-254	198	29.79	95.59	100	175	12	N
HARRIS	IH 10	0271-07-254	199			100	175	12	N
HARRIS	IH 10	0271-07-254	200	29.79	95.59	100	175	12	N
HARRIS	IH 10	0271-07-254	201			100	175	12	N
HARRIS	IH 10	0271-07-254	202			100	175	12	N
HARRIS	IH 10	0271-07-249	203	29.78	95.65	100	175	12	N
HARRIS	IH 10	0271-07-249	204			100	175	12	N
HARRIS	IH 10	0271-07-249	205	29.79	95.64	100	175	12	N
HARRIS	IH 10	0271-07-249	206	29.79	95.64	100	175	12	N
HARRIS	IH 10	0271-07-249	207	29.78	95.64	100	175	12	N
HARRIS	IH 10	0271-07-249	208	29.79	95.64	100	175	12	N
HARRIS	IH 10	0271-07-249	209	29.78	95.64	100	175	12	N
HARRIS	IH 10	0271-07-249	210	29.79	95.63	100	175	12	N
HARRIS	IH 10	0271-07-249	211	29.78	95.63	100	175	12	N
HARRIS	IH 10	0271-07-249	212	29.79	95.63	100	175	12	N
HARRIS	IH 10	0271-07-249	213	29.78	95.63	100	175	12	N
HARRIS	IH 10	0271-07-249	214	29.79	95.63	100	175	12	N
HARRIS	IH 10	0271-07-249	215	29.79	95.63	100	175	12	N
HARRIS	IH 10	0271-07-249	216	29.78	95.62	100	175	12	N
HARRIS	IH 10	0271-07-249	217	29.79	95.62	100	175	12	N
HARRIS	IH 10	0271-07-249	218	29.79	95.62	100	175	12	N
HARRIS	IH 10	0271-07-249	219			100	175	12	N
HARRIS	IH 10	0271-07-249	220			100	175	12	N
HARRIS	IH 10	0271-07-249	221	29.79	95.61	100	175	12	N
HARRIS	IH 10	0271-06-090	222	29.78	95.81	100	175	12	N
HARRIS	IH 10	0271-06-090	223	29.78	95.81	100	175	12	N
HARRIS	IH 10	0271-06-090	224	37.70	95.81	100	175	12	N
HARRIS	IH 10	0271-06-090	225	29.79	95.80	100	175	12	N
HARRIS	IH 10	0271-06-090	226	29.79	95.80	100	175	12	N
HARRIS	IH 10	0271-06-090	227	29.79	95.80	100	175	12	N
HARRIS	IH 10	0271-06-090	228	29.79	95.79	100	175	12	N
HARRIS	IH 10	0271-06-090	229	29.79	95.79	100	175	12	N
HARRIS	IH 10	0271-06-090	230	29.79	95.79	100	175	12	N
HARRIS	IH 10	0271-06-090	231	29.79	95.79	100	175	12	N
HARRIS	IH 10	0271-06-090	232	29.79	95.78	100	175	12	N
HARRIS	IH 10	0271-06-090	233	29.79	95.78	100	175	12	N
HARRIS	IH 10	0271-06-090	234	29.79	95.78	100	175	12	N
HARRIS	IH 10	0271-06-090	235	29.79	95.77	100	175	12	N
HARRIS	IH 10	0271-06-090	236	29.79	95.77	100	175	12	N
HARRIS	IH 10	0271-06-090	237	29.79	95.77	100	175	12	N
C. HARRIS	IH 10	0271-07-274	238	29.78	95.45	100	175	12	N
C. HARRIS	IH 10	0271-07-274	240	29.78	95.44	100	175	12	N
C. HARRIS	IH 10	0271-07-274	241	29.78	95.44	100	175	12	N
HARRIS	IH 10	0271-07-244	243	29.78	95.45	100	175	12	N
HARRIS	IH 10	0271-07-244	244	29.78	95.45	100	175	12	N
HARRIS	IH 10	0271-07-244	245	29.78	95.45	100	175	12	N
HARRIS	IH 10	0271-07-244	246	29.78	95.45	100	175	12	N
HARRIS	IH 10	0271-07-244	248	29.78	95.45	100	175	12	N
HARRIS	IH 10	0271-07-244	249	29.78	95.45	100	175	12	N
HARRIS	IH 10	0271-07-244	250	29.78	95.46	100	175	12	N

Figure 3.35: TxDOT HMIP Inventory – Houston District - Cont'd

County	Highway(s)	Control & Section	HQ Pole Number	GPS		Wind Speed Rating (mph)	Pole Height (ft)	# Sides	Ground Sleeve
				Latitude	Longitude				
HARRIS	IH 10	0271-07-244	251	29.78	95.45	100	175	12	N
HARRIS	IH 10	0271-07-244	252	29.78	95.46	100	175	12	N
HARRIS	IH 10	0271-07-244	253	29.78	95.46	100	175	12	N
HARRIS	IH 10	0271-07-244	254	29.78	95.46	100	175	12	N
HARRIS	IH 10	0271-07-244	256	29.78	95.46	100	175	12	N
HARRIS	IH 10	0271-07-244	257	29.78	95.46	100	175	12	N
HARRIS	IH 10	0271-07-244	259	29.78	95.46	100	175	12	N
HARRIS	IH 10	0271-07-244	260	29.78	95.46	100	175	12	N
HARRIS	IH 10	0271-07-244	261			100	175	12	N
HARRIS	IH 10	0271-07-244	262			100	175	12	N
HARRIS	IH 10	0271-07-244	263			100	175	12	N
HARRIS	IH 10	0271-07-244	264	29.78	95.45	100	175	12	N
HARRIS	IH 10	0271-07-244	265	29.78	95.45	100	175	12	N
W. HARRIS	IH 10	0271-07-247	285	29.78	95.55	100	175	12	N
W. HARRIS	IH 10	0271-07-247	287	29.78	95.54	100	175	12	N
W. HARRIS	IH 10	0271-07-247	288			100	175	12	N
W. HARRIS	IH 10	0271-07-247	289	29.78	95.54	100	175	12	N
W. HARRIS	IH 10	0271-07-247	290			100	175	12	N
W. HARRIS	IH 10	0271-07-247	291	29.78	95.53	100	175	12	N
W. HARRIS	IH 10	0271-07-247	292	29.78	95.53	100	175	12	N
W. HARRIS	IH 10	0271-07-247	293	29.78	95.53	100	175	12	N
W. HARRIS	IH 10	0271-07-247	294	29.78	95.53	100	175	12	N
W. HARRIS	IH 10	0271-07-247	295	29.78	95.53	100	175	12	N
W. HARRIS	IH 10	0271-07-247	296	29.78	95.53	100	175	12	N
W. HARRIS	IH 10	0271-07-247	297			100	175	12	N
W. HARRIS	IH 10	0271-07-247	298			100	175	12	N
W. HARRIS	IH 10	0271-07-247	299	29.78	95.52	100	175	12	N
W. HARRIS	IH 10	0271-07-247	300			100	175	12	N
W. HARRIS	IH 10	0271-07-247	301	29.78	95.52	100	175	12	N
W. HARRIS	IH 10	0271-07-247	302			100	175	12	N
W. HARRIS	IH 10	0271-07-247	303	29.78	95.51	100	175	12	N
W. HARRIS	IH 10	0271-07-247	304	29.78	95.51	100	175	12	N
W. HARRIS	IH 10	0271-07-247	305	29.78	95.51	100	175	12	N
W. HARRIS	IH 10	0271-07-247	306			100	175	12	N
HARRIS	IH 10	0271-06-088	307	29.78	95.71	100	175	12	N
HARRIS	IH 10	0271-06-088	308	29.79	95.71	100	175	12	N
HARRIS	IH 10	0271-06-088	309	29.78	95.71	100	175	12	N
HARRIS	IH 10	0271-06-088	310	29.79	95.70	100	175	12	N
HARRIS	IH 10	0271-06-088	311	29.78	95.70	100	175	12	N
HARRIS	IH 10	0271-06-088	312	29.79	95.70	100	175	12	N
HARRIS	IH 10	0271-06-088	313	29.78	95.69	100	175	12	N
HARRIS	IH 10	0271-06-088	314	29.79	95.69	100	175	12	N
HARRIS	IH 10	0271-06-088	315	29.78	95.69	100	175	12	N
HARRIS	IH 10	0271-06-088	316	29.79	95.68	100	175	12	N
HARRIS	IH 10	0271-06-088	317	29.78	95.68	100	175	12	N
HARRIS	IH 10	0271-06-088	318	29.79	95.68	100	175	12	N
HARRIS	IH 10	0271-06-088	319	29.78	95.67	100	175	12	N
HARRIS	IH 10	0271-06-088	320	29.79	95.67	100	175	12	N
HARRIS	IH 10	0271-06-088	321	29.78	95.67	100	175	12	N
HARRIS	IH 10	0271-06-088	322	29.79	95.67	100	175	12	N
HARRIS	IH 10	0271-06-088	323	29.78	95.67	100	175	12	N
HARRIS	IH 10	0271-06-088	324	29.79	95.66	100	175	12	N
HARRIS	IH 10	0271-06-088	325	29.78	95.66	100	175	12	N
HARRIS	IH 10	0271-06-088	326	29.79	95.66	100	175	12	N
HARRIS	IH 10	0271-06-088	327	29.78	95.66	100	175	12	N
HARRIS	IH 10	0271-06-088	328	29.79	95.65	100	175	12	N
HARRIS	IH 10	0271-06-088	329	29.79	95.65	100	175	12	N
HARRIS	IH 10	0271-06-088	330	29.78	95.65	100	175	12	N

Figure 3.36: TxDOT HMIP Inventory – Houston District - Cont'd

County	Highway(s)	Control & Section	HQ Pole Number	GPS		Wind Speed Rating (mph)	Pole Height (ft)	# Sides	Ground Sleeve
				Latitude	Longitude				
		0271-06-088				100		12	N
HARRIS	IH 10	0271-06-089	332			100	175	12	N
HARRIS	IH 10	0271-06-089	333	29.79	95.76	100	175	12	N
HARRIS	IH 10	0271-06-089	334			100	175	12	N
HARRIS	IH 10	0271-06-089	336			100	175	12	N
HARRIS	IH 10	0271-06-089	337	29.79	95.75	100	175	12	N
HARRIS	IH 10	0271-06-089	338	29.78	95.74	100	175	12	N
HARRIS	IH 10	0271-06-089	339	29.79	95.74	100	175	12	N
HARRIS	IH 10	0271-06-089	340	29.78	95.74	100	175	12	N
HARRIS	IH 10	0271-06-089	341	29.79	95.73	100	175	12	N
HARRIS	IH 10	0271-06-089	342	29.78	95.73	100	175	12	N
HARRIS	IH 10	0271-06-089	343	29.79	95.73	100	175	12	N
HARRIS	IH 10	0271-06-089	344	29.78	95.72	100	175	12	N
HARRIS	IH 10	0271-06-089	345	29.79	95.72	100	175	12	N
HARRIS	IH 10	0271-06-089	346	29.78	95.72	100	175	12	N
HARRIS	IH 10	0271-06-089	347	29.79	95.72	100	175	12	N
HARRIS	IH 45	0110-05-064	562	30.08	95.44	100	175	12	N
HARRIS	IH 45	0110-05-064	563	30.08	95.44	100	175	12	N
HARRIS	IH 45	0110-05-064	564	30.09	95.44	100	175	12	N
MONTGOMERY	IH 45	0110-04-122	582			100	175	12	N
MONTGOMERY	IH 45	0110-04-122	583			100	175	12	N
MONTGOMERY	IH 45	0110-04-122	584			100	175	12	N
MONTGOMERY	IH 45	0110-04-122	585			100	175	12	N
MONTGOMERY	IH 45	0110-04-122	586			100	175	12	N
MONTGOMERY	IH 45	0110-04-122	587			100	175	12	N
MONTGOMERY	IH 45	0110-04-122	588			100	175	12	N
MONTGOMERY	IH 45	0110-04-122	589			100	175	12	N
GALVESTON	IH 45	0912-73-075	595	29.33	94.93	100	175	12	N
MONTGOMERY	IH 45	0110-04-164	620	30.26	95.46	100	175	12	N
HARRIS	IH 45	0500-03-544	642			100	175	12	N
HARRIS	IH 45	0500-03-544	643			100	175	12	N
HARRIS	IH 45	0500-03-544	644			100	175	12	N
HARRIS	IH 45	0912-71-865	645	29.78	95.37	100	175	12	N
HARRIS	US 59	0027-13-171	900	29.73	95.39	100	175	12	N
FORT BEND	US 59	0027-12-095	979	29.60	95.62	100	175	12	N
FORT BEND	US 59	0027-12-095	984	29.61	95.61	100	175	12	N
FORT BEND	US 59	0027-12-059	991	29.63	95.60	100	175	12	N
FORT BEND	US 59	0027-12-059	992	29.63	95.59	100	175	12	N
FORT BEND	US 59	0027-12-059	994	29.63	95.59	100	175	12	N
FORT BEND	US 59	0027-12-059	995	29.63	95.59	100	175	12	N
FORT BEND	US 59	0027-12-059	996	29.63	95.59	100	175	12	N
FORT BEND	US 90A	0027-08-148	1015	29.63	95.60	100	175	12	N
FORT BEND	US 90A	0027-08-148	1016	29.63	95.59	100	175	12	N
HARRIS	SH 225	0502-01-204	1042	29.71	95.26	100	175	12	N
HARRIS	SH 225	0502-01-204	1043	29.71	95.25	100	175	12	N
HARRIS	IH 610	0912-00-300	1366	29.81	95.44	100	175	12	N
HARRIS	IH 610	0912-00-300	1367	29.81	95.44	100	175	12	N
HARRIS	IH 610	0912-00-300	1368	29.81	95.43	100	175	12	N
HARRIS	IH 610	0912-00-300	1369	29.81	95.43	100	175	12	N
HARRIS	IH 610	0912-00-300	1370	29.81	95.43	100	175	12	N
HARRIS	IH 610	0912-00-300	1371	29.81	95.43	100	175	12	N
HARRIS	IH 610	0912-00-300	1372	29.81	95.42	100	175	12	N
HARRIS	IH 610	0912-00-300	1373	29.81	95.42	100	175	12	N
HARRIS	IH 610	0912-00-300	1374	29.81	95.42	100	175	12	N
HARRIS	IH 610	0912-00-300	1375	29.81	95.41	100	175	12	N
HARRIS	IH 610	0912-00-300	1376	29.81	95.41	100	175	12	N
HARRIS	IH 610	0912-00-300	1377	29.81	95.41	100	175	12	N
HARRIS	IH 610	0912-00-300	1378	29.81	95.40	100	175	12	N

Figure 3.37: TxDOT HMIP Inventory – Houston District - Cont'd

County	Highway(s)	Control & Section	HQ Pole Number	GPS		Wind Speed Rating (mph)	Pole Height (ft)	# Sides	Ground Sleeve
				Latitude	Longitude				
HARRIS	IH 610	0912-00-300	1379	29.81	95.40	100	175	12	N
HARRIS	IH 610	0912-00-300	1380	29.81	95.40	100	175	12	N
HARRIS	IH 610	0912-00-300	1381	29.81	95.39	100	175	12	N
HARRIS	IH 610	0912-00-300	1382	29.81	95.39	100	175	12	N
HARRIS	IH 610	0912-00-300	1383	29.81	95.39	100	175	12	N
HARRIS	IH 610	0912-00-300	1384	29.81	95.38	100	175	12	N
HARRIS	IH 610	0912-00-300	1385	29.81	95.38	100	175	12	N
HARRIS	IH 610	0271-17-139	1612	29.71	95.46	100	175	12	N
HARRIS	IH 610	0271-17-139	1613	29.71	95.46	100	175	12	N
HARRIS	IH 610	0271-17-140	1619	29.74	95.46	100	175	12	N
HARRIS	IH 610	0271-17-140	1620	29.74	95.46	100	175	12	N
HARRIS	IH 610	0271-17-140	1621	29.74	95.46	100	175	12	N
HARRIS	IH 610	0271-17-140	1622	29.74	95.46	100	175	12	N
HARRIS	IH 610	0271-17-140	1623	29.75	95.46	100	175	12	N
HARRIS	IH 610	0271-17-140	1624	29.75	95.46	100	175	12	N
HARRIS	IH 610	0271-17-140	1625		95.46	100	175	12	N
HARRIS	IH 610	0271-17-140	1626	29.75	95.46	100	175	12	N
HARRIS	IH 610	0271-17-140	1627	29.76	95.46	100	175	12	N
HARRIS	IH 610	0271-17-140	1628	29.76	95.46	100	175	12	N
HARRIS	IH 610	0271-17-140	1629	29.76	95.46	100	175	12	N
HARRIS	IH 610	0271-17-140	1630	29.76	95.46	100	175	12	N
HARRIS	IH 610	0271-17-140	1631		95.46	100	175	12	N
HARRIS	IH 610	0271-17-140	1632	29.77	95.46	100	175	12	N
HARRIS	IH 610	0271-17-140	1633	29.77	95.46	100	175	12	N
HARRIS	IH 610	0271-17-140	1634	29.78	95.46	100	175	12	N
C. HARRIS	IH 10	0271-07-272	132	29.77	95.36	100	175	12	Y
C. HARRIS	IH 10	0271-07-272	133	29.77	95.36	100	175	12	Y
C. HARRIS	IH 10	0271-07-272	134	29.77	95.36	100	175	12	Y
C. HARRIS	IH 10	0271-07-272	135	29.77	95.36	100	175	12	Y
C. HARRIS	IH 10	0271-07-272	136	29.77	95.36	100	175	12	Y
C. HARRIS	IH 10	0508-01-303	137	29.77	95.35	100	175	12	Y
C. HARRIS	IH 10	0508-01-303	138	29.77	95.35	100	175	12	Y
C. HARRIS	IH 10	0508-01-303	139	29.77	95.33	100	175	12	Y
C. HARRIS	IH 10	0508-01-303	140	29.77	95.33	100	175	12	Y
C. HARRIS	IH 10	0508-01-303	141	29.77	95.33	100	175	12	Y
C. HARRIS	IH 10	0508-01-303	142	29.77	95.33	100	175	12	Y
C. HARRIS	IH 10	0508-01-303	143	29.77	95.32	100	175	12	Y
C. HARRIS	IH 10	0508-01-303	144	29.77	95.32	100	175	12	Y
C. HARRIS	IH 10	0508-01-303	145	29.77	95.32	100	175	12	Y
C. HARRIS	IH 10	0508-01-303	146	29.77	95.31	100	175	12	Y
C. HARRIS	IH 10	0508-01-303	147	29.77	95.31	100	175	12	Y
C. HARRIS	IH 10	0508-01-303	148	29.77	95.31	100	175	12	Y
C. HARRIS	IH 10	0508-01-303	149	29.77	95.30	100	175	12	Y
C. HARRIS	IH 10	0508-01-303	150	29.77	95.30	100	175	12	Y
C. HARRIS	IH 10	0508-01-303	151	29.78	95.30	100	175	12	Y
C. HARRIS	IH 10	0508-01-303	152	29.78	95.29	100	175	12	Y
HARRIS	IH 10	0271-07-245	266	29.78	95.50	100	175	12	Y
HARRIS	IH 10	0271-07-245	267	29.78	95.50	100	175	12	Y
HARRIS	IH 10	0271-07-245	268			100	175	12	Y
HARRIS	IH 10	0271-07-245	269	29.78	95.50	100	175	12	Y
HARRIS	IH 10	0271-07-245	270	29.78	95.50	100	175	12	Y
HARRIS	IH 10	0271-07-245	271	29.78	95.49	100	175	12	Y
HARRIS	IH 10	0271-07-245	272	29.78	95.49	100	175	12	Y
HARRIS	IH 10	0271-07-245	273	29.78	95.49	100	175	12	Y
HARRIS	IH 10	0271-07-245	274	29.78	95.51	100	175	12	Y
HARRIS	IH 10	0271-07-245	275	29.78	95.48	100	175	12	Y
HARRIS	IH 10	0271-07-245	276	29.78	95.48	100	175	12	Y
HARRIS	IH 10	0271-07-245	277	29.78	95.48	100	175	12	Y

Figure 3.38: TxDOT HMIP Inventory – Houston District - Cont'd

County	Highway(s)	Control & Section	HQ Pole Number	GPS		Wind Speed Rating (mph)	Pole Height (ft)	# Sides	Ground Sleeve
				Latitude	Longitude				
HARRIS	IH 10	0271-07-245	278	29.78	95.48	100	175	12	Y
HARRIS	IH 10	0271-07-245	279			100	175	12	Y
HARRIS	IH 10	0271-07-245	280	29.78	95.47	100	175	12	Y
HARRIS	IH 10	0271-07-245	281			100	175	12	Y
HARRIS	IH 10	0271-07-245	282	29.78	95.47	100	175	12	Y
HARRIS	IH 10	0271-07-245	283			100	175	12	Y
HARRIS	IH 45	0500-03-427	471	29.61	95.20	100	175	12	Y
HARRIS	IH 45	0500-03-427	472	29.61	95.20	100	175	12	Y
HARRIS	IH 45	0500-03-429	495	29.61	95.21	100	175	12	Y
MONTGOMERY	IH 45	0110-04-141	517	30.23	95.46	100	175	12	Y
MONTGOMERY	IH 45	0110-04-141	518	30.23	95.46	100	175	12	Y
HARRIS	IH 45	0500-03-494	574	29.76	95.37	100	175	12	Y
HARRIS	IH 45	0500-03-494	575	29.76	95.37	100	175	12	Y
HARRIS	IH 45	0500-03-494	576	29.76	95.37	100	175	12	Y
HARRIS	IH 45	0500-03-494	577	29.76	95.37	100	175	12	Y
HARRIS	IH 45	0500-03-494	578	29.76	95.37	100	175	12	Y
HARRIS	IH 45	0500-03-494	579	29.77	95.37	100	175	12	Y
HARRIS	IH 45	0500-03-494	580	29.77	95.37	100	175	12	Y
HARRIS	IH 45	0500-03-494	581	29.77	95.37	100	175	12	Y
GALVESTON	IH 45	0500-04-118	604			100	175	12	Y
GALVESTON	IH 45	0500-04-118	605			100	175	12	Y
GALVESTON	IH 45	0500-04-118	606			100	175	12	Y
MONTGOMERY	IH 45	0110-04-164	619	30.27	95.46	100	175	12	Y
HARRIS	IH 45	0500-03-475	633	29.53	95.13	100	175	12	Y
HARRIS	IH 45	0500-03-475	634	29.53	95.13	100	175	12	Y
HARRIS	IH 45	0500-03-475	635	29.52	95.13	100	175	12	Y
HARRIS	IH 45	0500-03-475	636	29.52	95.13	100	175	12	Y
HARRIS	IH 45	0500-03-475	637	29.52	95.12	100	175	12	Y
HARRIS	IH 45	0500-03-475	638	29.52	95.12	100	175	12	Y
HARRIS	IH 45	0500-03-475	639	29.52	95.12	100	175	12	Y
HARRIS	IH 45	0500-03-475	640	29.52	95.12	100	175	12	Y
HARRIS	IH 45	0500-03-475	641	29.52	95.12	100	175	12	Y
HARRIS	US 59	0177-11-118	839	29.77	95.34	100	175	12	Y
HARRIS	US 59	0177-11-118	840	29.77	95.34	100	175	12	Y
MONTGOMERY	US 59	0177-05-055	907	30.07	95.25	100	175	12	Y
MONTGOMERY	US 59	0177-05-055	908	30.07	95.25	100	175	12	Y
MONTGOMERY	US 59	0177-05-055	909	30.07	95.25	100	175	12	Y
MONTGOMERY	US 59	0177-05-055	910	30.07	95.25	100	175	12	Y
MONTGOMERY	US 59	0177-05-055	911	30.06	95.25	100	175	12	Y
MONTGOMERY	US 59	0177-05-055	912	30.06	95.25	100	175	12	Y
MONTGOMERY	US 59	0177-05-055	913	30.06	95.25	100	175	12	Y
MONTGOMERY	US 59	0177-05-055	914	30.06	95.25	100	175	12	Y
MONTGOMERY	US 59	0177-05-055	915	30.05	95.25	100	175	12	Y
MONTGOMERY	US 59	0177-05-055	916	30.05	95.25	100	175	12	Y
MONTGOMERY	US 59	0177-05-055	917	30.05	95.25	100	175	12	Y
MONTGOMERY	US 59	0177-05-055	918	30.05	95.25	100	175	12	Y
MONTGOMERY	US 59	0177-05-055	919	30.04	95.25	100	175	12	Y
HARRIS	US 59	0177-11-119	920	29.76	95.35	100	175	12	Y
HARRIS	US 59	0177-11-119	921	29.76	95.35	100	175	12	Y
HARRIS	US 59	0177-11-119	922	29.76	95.35	100	175	12	Y
HARRIS	US 59	0177-11-119	923	29.76	95.35	100	175	12	Y
HARRIS	US 59	0177-11-119	924	29.76	95.35	100	175	12	Y
HARRIS	US 59	0177-11-119	925	29.77	95.35	100	175	12	Y
HARRIS	US 59	0177-11-119	926	29.77	95.35	100	175	12	Y
HARRIS	US 59	0177-11-119	927	29.77	95.35	100	175	12	Y
HARRIS	US 59	0177-11-119	928	29.77	95.35	100	175	12	Y
HARRIS	US 59	0177-11-119	931	29.77	95.34	100	175	12	Y
HARRIS	US 59	0177-11-119	932	29.77	95.34	100	175	12	Y

Figure 3.39: TxDOT HMIP Inventory – Houston District - Cont'd

County	Highway(s)	Control & Section	HQ Pole Number	GPS		Wind Speed Rating (mph)	Pole Height (ft)	# Sides	Ground Sleeve
				Latitude	Longitude				
HARRIS	US 59	0177-11-119	934	29.77	95.34	100	175	12	Y
HARRIS	US 59	0177-11-119	939	29.77	95.34	100	175	12	Y
FORT BEND	US 59	0027-12-121	999			100	175	12	Y
FORT BEND	US 59	0027-12-121	1000			100	175	12	Y
FORT BEND	US 59	0027-12-121	1001			100	175	12	Y
HARRIS	SH 146	0389-12-064	1022	29.69	95.03	100	175	12	Y
HARRIS	SH 146	0389-12-064	1023	29.69	95.03	100	175	12	Y
HARRIS	SH 146	0389-12-064	1025	29.69	95.03	100	175	12	Y
HARRIS	SH 146	0389-12-064	1026	29.69	95.03	100	175	12	Y
HARRIS	SH 249	0720-03-084	1098	30.07	95.62	100	175	12	Y
HARRIS	SH 288	0598-01-033	1114	29.60	95.39	100	175	12	Y
HARRIS	SH 288	0598-01-033	1115	29.60	95.38	100	175	12	Y
HARRIS	SH 288	0598-01-033	1116	29.60	95.38	100	175	12	Y
HARRIS	SH 288	0598-01-033	1117	29.60	95.39	100	175	12	Y
HARRIS	SH 288	0598-01-033	1118	29.60	95.39	100	175	12	Y
HARRIS	SH 288	0598-01-033	1119	29.60	95.39	100	175	12	Y
HARRIS	SH 288	0598-01-033	1120	29.60	95.39	100	175	12	Y
HARRIS	SH 288	0598-01-033	1122	29.60	95.39	100	175	12	Y
HARRIS	SPUR 330	0508-07-278	1214			100	175	12	Y
HARRIS	SPUR 330	0508-07-278	1215			100	175	12	Y
HARRIS	SPUR 330	0508-07-278	1216			100	175	12	Y
HARRIS	SPUR 330	0508-07-278	1217			100	175	12	Y
HARRIS	IH 610	0271-17-129	1300	29.68	95.46	100	175	12	Y
HARRIS	IH 610	0502-01-190	1310	29.70	95.28	100	175	12	Y
HARRIS	IH 610	0502-01-190	1311	29.70	95.28	100	175	12	Y
HARRIS	IH 610	0502-01-190	1312	29.70	95.28	100	175	12	Y
HARRIS	IH 610	0502-01-190	1313	29.70	95.28	100	175	12	Y
HARRIS	IH 610	0502-01-190	1314	29.71	95.27	100	175	12	Y
HARRIS	IH 610	0271-15-076	1315	29.71	95.27	100	175	12	Y
HARRIS	IH 610	0271-15-076	1316	29.72	95.27	100	175	12	Y
HARRIS	IH 610	0271-15-076	1317	29.72	95.27	100	175	12	Y
HARRIS	IH 610	0271-15-076	1318	29.73	95.27	100	175	12	Y
HARRIS	IH 610	0271-15-076	1319	29.73	95.27	100	175	12	Y
HARRIS	IH 610	0271-15-076	1320	29.74	95.27	100	175	12	Y
HARRIS	IH 610	0271-15-076	1321	29.74	95.26	100	175	12	Y
HARRIS	IH 610	0271-15-076	1322	29.74	95.26	100	175	12	Y
HARRIS	IH 610	0271-15-076	1323	29.75	95.26	100	175	12	Y
HARRIS	IH 610	0271-15-076	1324	29.75	95.26	100	175	12	Y
HARRIS	IH 610	0271-15-076	1325	29.75	95.26	100	175	12	Y
HARRIS	IH 610	0271-15-076	1326	29.75	95.26	100	175	12	Y
HARRIS	IH 610	0271-15-076	1327	29.76	95.26	100	175	12	Y
HARRIS	IH 610	0271-15-076	1328	29.76	95.26	100	175	12	Y
HARRIS	IH 610	0271-15-076	1329	29.76	95.26	100	175	12	Y
HARRIS	IH 610	0271-14-202	1341	29.81	95.33	100	175	12	Y
HARRIS	IH 610	0271-14-202	1342	29.81	95.33	100	175	12	Y
HARRIS	IH 610	0271-14-202	1343	29.81	95.32	100	175	12	Y
HARRIS	IH 610	0271-14-202	1344	29.81	95.32	100	175	12	Y
HARRIS	IH 610	0271-14-202	1345	29.81	95.32	100	175	12	Y
HARRIS	IH 610	0271-14-202	1346	29.81	95.31	100	175	12	Y
HARRIS	IH 610	0271-14-202	1347	29.81	95.31	100	175	12	Y
HARRIS	IH 610	0271-14-202	1348	29.81	95.31	100	175	12	Y
HARRIS	IH 610	0271-14-202	1349	29.81	95.30	100	175	12	Y
HARRIS	IH 610	0271-14-202	1350	29.81	95.30	100	175	12	Y
HARRIS	IH 610	0271-14-202	1351	29.81	95.30	100	175	12	Y
HARRIS	IH 610	0271-14-202	1352	29.80	95.30	100	175	12	Y
HARRIS	IH 610	0271-14-202	1353	29.80	95.29	100	175	12	Y
HARRIS	IH 610	0271-14-202	1354	29.80	95.29	100	175	12	Y
HARRIS	IH 610	0271-14-202	1355	29.80	95.29	100	175	12	Y

Figure 3.40: TxDOT HMIP Inventory – Houston District - Cont'd

County	Highway(s)	Control & Section	HQ Pole Number	GPS		Wind Speed Rating (mph)	Pole Height (ft)	# Sides	Ground Sleeve
				Latitude	Longitude				
HARRIS	IH 610	0271-14-202	1356	29.80	95.28	100	175	12	Y
HARRIS	IH 610	0271-14-202	1357	29.80	95.28	100	175	12	Y
HARRIS	IH 610	0271-14-202	1358	29.80	95.28	100	175	12	Y
HARRIS	IH 610	0271-14-202	1359	29.80	95.28	100	175	12	Y
HARRIS	IH 610	0271-14-202	1360	29.80	95.27	100	175	12	Y
HARRIS	IH 610	0271-14-202	1361	29.80	95.27	100	175	12	Y
HARRIS	IH 610	0271-14-202	1362	29.79	95.27	100	175	12	Y
HARRIS	IH 610	0271-14-202	1363	29.79	95.27	100	175	12	Y
HARRIS	IH 610	0271-14-202	1364	29.79	95.27	100	175	12	Y
HARRIS	IH 610	0271-14-202	1365	29.79	95.27	100	175	12	Y
BRAZORIA	SH 332	0586-01-059	1605	29.01	95.39	100	175	12	Y
BRAZORIA	SH 332	0586-01-059	1606	29.00	95.39	100	175	12	Y
BRAZORIA	SH 332	0586-01-059	1607	29.00	95.39	100	175	12	Y
W. HARRIS	IH 10	0271-07-248	188				175		
HARRIS	IH 10	0271-07-254	202				175		
HARRIS	IH 10	0271-07-254	202				175		
C. HARRIS	IH 10	0271-07-274	239	29.78	95.44	100	175		
HARRIS	IH 10	0271-07-244	242	29.78	95.45	100	175		
HARRIS	IH 10	0271-07-244	247	29.78	95.45	100	175		
HARRIS	IH 10	0271-07-244	255	29.78	95.46	100	175		
HARRIS	IH 10	0271-07-244	258	29.78	95.46	100	175		
W. HARRIS	IH 10	0271-07-247	284			100	175		
W. HARRIS	IH 10	0271-07-247	286			100	175		
HARRIS	IH 10	0271-06-089	335	29.79	95.75	100	175		
HARRIS	IH 45	0500-03-427	476	29.61	95.20		175		
HARRIS	US 59	0177-07-088	814	29.93	95.30		175		
HARRIS	US 59	0177-07-088	815	29.93	95.30		175		
HARRIS	US 59	0027-13-171	896				175		
HARRIS	US 59	0027-13-171	898				175		
HARRIS	US 59	0027-13-171	899				175		
HARRIS	US 59	0027-13-171	901	29.73	95.38		175		
HARRIS	US 59	0177-11-119	929	29.77	95.35		175		
HARRIS	US 59	0177-11-119	930	29.77	95.35		175		
HARRIS	US 59	0177-11-119	933	29.77	95.34		175		
HARRIS	US 59	0177-11-119	935	29.77	95.34		175		
HARRIS	SH 225	0502-01-204	1059				175		
HARRIS	IH 610	0271-14-145	1228	29.82	95.35	100	175	8	Y
HARRIS	IH 610	0271-14-145	1229	29.81	95.35	100	175	8	Y
HARRIS	IH 610	0271-14-145	1230	29.81	95.35	100	175	8	Y
HARRIS	SPUR 548	2483-01-003	1225	29.83	95.35	100		8	Y
	IH 610		1389	29.68	95.46			8	Y
	IH 610		1390	29.68	95.46			8	Y
	IH 610		1391	29.68	95.46			8	Y
	IH 610		1392	29.68	95.46			8	Y
	IH 610		1393	29.68	95.46			8	Y
	IH 610		1394	29.67	95.46			8	Y
	IH 610		1395	29.67	95.46			8	Y
	IH 610		1396	29.67	95.46			8	Y
	IH 610		1397	29.67	95.46			8	Y
HARRIS	IH 45		1586	29.73	95.34			8	Y
HARRIS	IH 45		1587	29.73	95.34			8	Y
HARRIS	IH 45		1588	29.73	95.34			8	Y
HARRIS	IH 45		1589	29.73	#VALUE!			8	Y
HARRIS	IH 45		1590	29.73	#VALUE!			8	Y
HARRIS	IH 45		1591	29.72	95.33			8	Y
HARRIS	IH 45		1592	29.72	95.33			8	Y
HARRIS	IH 45		1593	29.72	95.33			8	Y
HARRIS	IH 45		1594	29.72	95.33			8	Y

Figure 3.41: TxDOT HMIP Inventory – Houston District - Cont'd

County	Highway(s)	Control & Section	HQ Pole Number	GPS		Wind Speed Rating (mph)	Pole Height (ft)	# Sides	Ground Sleeve
				Latitude	Longitude				
HARRIS	IH 45		1595	29.72	95.32			8	Y
HARRIS	IH 45		1596	29.72	95.32			8	Y
HARRIS	IH 45		1597	29.72	95.32			8	Y
HARRIS	IH 45		1598	29.72	95.32			8	Y
HARRIS	IH 45		1599	29.72	95.32			8	Y
HARRIS	IH 45		1600	29.72	95.31			8	Y
HARRIS	IH 45		1601	29.71	95.31			8	Y
HARRIS	IH 45		1602	29.71	95.31			8	Y
HARRIS	IH 45		1576	29.76	95.37			12	Y
HARRIS	IH 45		1577	29.75	95.37			12	Y
HARRIS	IH 45		1578	29.75	95.37			12	Y
HARRIS	IH 45		1579	29.75	95.37			12	Y
HARRIS	IH 45		1580	29.75	95.37			12	Y
HARRIS	IH 45		1581	29.75				12	Y
HARRIS	IH 45		1582	29.75	95.37			12	Y
HARRIS	IH 45		1583	29.75	95.36			12	Y
HARRIS	IH 45		1584	29.74	95.36			12	Y
HARRIS	IH 45		1585	29.74	95.36			12	Y
HARRIS	US 59			29.75	95.36	100		12	Y
HARRIS	US 59			29.75	95.36	100		12	Y
HARRIS	US 59			29.75	95.36	100		12	Y
HARRIS	US 59			29.75	95.36	100		12	Y
HARRIS	US 59			29.76	95.35	100		12	Y
HARRIS	US 59			29.76	95.35	100		12	Y
HARRIS	IH 10	0271-07-187	34						
			331						
	IH 10		348						
	IH 10		349						
	IH 10		350						
MONTGOMERY	IH 45	0110-04-142	546						
MONTGOMERY	IH 45	0110-04-142	547						
MONTGOMERY	IH 45	0110-04-142	548						
MONTGOMERY	IH 45	0110-04-142	549						
	IH 45		646						
	IH 45		647						
HARRIS	SH 146	0389-13-052	1037						
HARRIS	IH 610		1386						
HARRIS	IH 610		1387						
HARRIS	IH 610		1388						
HARRIS	IH 10	0508-01-209		29.78	95.26	100	125		

Figure 3.42: TxDOT HMIP Inventory – Houston District - Cont'd

County	Highway(s)	Control & Section	HQ Pole Number	GPS		Wind Speed Rating (mph)	Pole Height (ft)	# Sides	Ground Sleeve
				Latitude	Longitude				
Travis (227)	IH35 SB	0015-13	H400.C	30° 24.202'	97° 40.523'	80	100	12	Y
Travis (227)	IH35 SB	0015-13	H410.C	30° 24.105'	97° 40.503'	80	100	12	Y
Travis (227)	IH35 SB	0015-13	H420.C	30° 24.008'	97° 40.473'	80	100	12	Y
Travis (227)	IH35 SB	0015-13	H430.C	30° 23.811'	97° 40.371'	80	100	12	Y
Travis (227)	IH35 SB	0015-13	H440.C	30° 23.690'	97° 40.327'	80	100	12	Y
Travis (227)	IH35 NB	0015-13	H450.C	30° 23.771'	97° 40.296'	80	100	12	Y
Travis (227)	IH35 NB	0015-13	H460.C	30° 23.907'	97° 40.346'	80	100	12	Y
Williamson (246)	SH45	0683-06	H400.R	30° 28.914'	97° 39.895'	80	125	12	Y
Williamson (246)	SH45	0683-06	H410.R	30° 28.936'	97° 39.792'	80	125	12	Y
Williamson (246)	SH45	0683-06	H420.R	30° 28.962'	97° 39.673'	80	125	12	Y
Travis (227)	US183 SB	0151-06	H210.L	30° 22.769'	97° 44.320'	80	150	8	N
Travis (227)	SL1 NB	3136-01	H100.U	30° 23.316'	97° 44.060'	80	150	8	N
Travis (227)	SL1 SB	3136-01	H110.U	30° 23.208'	97° 44.125'	80	150	8	N
Travis (227)	SL1 SB	3136-01	H120.U	30° 23.102'	97° 44.152'	80	150	8	N
Travis (227)	SL1 NB	3136-01	H130.U	30° 22.996'	97° 44.148'	80	150	8	N
Travis (227)	SL1 NB	3136-01	H140.U	30° 22.890'	97° 44.159'	80	150	8	N
Travis (227)	SL1 SB	3136-01	H150.U	30° 22.914'	97° 44.250'	80	150	8	N
Travis (227)	SL1 SB	3136-01	H160.U	30° 22.838'	97° 44.295'	80	150	8	N
Travis (227)	SL1 NB	3136-01	H170.U	30° 22.787'	97° 44.231'	80	150	8	N
Travis (227)	SL1 NB	3136-01	H180.U	30° 22.694'	97° 44.260'	80	150	8	N
Williamson (246)	IH35 NB	0015-08	H100.A	30° 41.245'	97° 39.420'	80	150	12	Y
Williamson (246)	IH35 NB	0015-08	H110.A	30° 41.326'	97° 39.394'	80	150	12	Y
Williamson (246)	IH35 SB	0015-09	H100.B	30° 29.353'	97° 40.641'	80	150	12	Y
Williamson (246)	IH35 SB	0015-09	H110.B	30° 29.250'	97° 40.594'	80	150	12	Y
Williamson (246)	IH35 SB	0015-09	H120.B	30° 29.143'	97° 40.562'	80	150	12	Y
Williamson (246)	IH35 SB	0015-09	H130.B	30° 29.036'	97° 40.528'	80	150	12	Y
Travis (227)	IH35 NB	0015-10	H100.V	30° 26.354'	97° 40.105'	80	150	12	N
Travis (227)	IH35 NB	0015-10	H110.V	30° 26.200'	97° 40.134'	80	150	12	N
Travis (227)	IH35 NB	0015-10	H120.V	30° 26.037'	97° 40.170'	80	150	12	N
Travis (227)	IH35 NB	0015-13	H100.C	30° 25.884'	97° 40.201'	80	150	12	N
Travis (227)	IH35 NB	0015-13	H100.D	30° 12.439'	97° 45.393'	80	150	12	Y
Travis (227)	IH35 NB	0015-13	H110.C	30° 25.733'	97° 40.227'	80	150	12	N
Travis (227)	IH35 NB	0015-13	H110.D	30° 12.571'	97° 45.310'	80	150	12	Y
Travis (227)	IH35 NB	0015-13	H120.C	30° 25.574'	97° 40.255'	80	150	12	N
Travis (227)	IH35 SB	0015-13	H120.D	30° 12.714'	97° 45.272'	80	150	12	Y
Travis (227)	IH35 NB	0015-13	H130.C	30° 25.421'	97° 40.287'	80	150	12	N
Travis (227)	IH35 NB	0015-13	H130.D	30° 12.798'	97° 45.160'	80	150	12	Y
Travis (227)	IH35 NB	0015-13	H140.C	30° 25.300'	97° 40.310'	80	150	12	N
Travis (227)	IH35 NB	0015-13	H150.C	30° 25.175'	97° 40.331'	80	150	12	N
Travis (227)	IH35 NB	0015-13	H150.D	30° 13.128'	97° 44.967'	80	150	12	Y
Travis (227)	IH35 NB	0015-13	H160.C	30° 25.003'	97° 40.364'	80	150	12	N
Travis (227)	IH35 SB	0015-13	H160.D	30° 13.256'	97° 44.956'	80	150	12	Y
Travis (227)	IH35 NB	0015-13	H170.C	30° 24.858'	97° 40.392'	80	150	12	N
Travis (227)	IH35 SB	0015-13	H170.D	30° 13.385'	97° 44.884'	80	150	12	Y
Travis (227)	IH35 SB	0015-13	H180.C	30° 13.511'	97° 44.809'	80	150	12	Y
Travis (227)	IH35 NB	0015-13	H190.C	30° 24.566'	97° 40.443'	80	150	12	N
Travis (227)	IH35 NB	0015-13	H190.D	30° 13.579'	97° 44.701'	80	150	12	Y
Travis (227)	IH35 SB	0015-13	H300.C	30° 19.731'	97° 42.379'	80	150	12	Y
Travis (227)	IH35 SB	0015-13	H310.C	30° 19.604'	97° 42.402'	80	150	12	Y
Travis (227)	LP343 SB	0113-09	H090.F	30° 14.157'	97° 47.626'	80	150	12	Y
Travis (227)	US290 EB	0113-09	H100.F	30° 13.909'	97° 48.146'	80	150	12	Y
Travis (227)	US290 EB	0113-09	H110.F	30° 13.890'	97° 48.253'	80	150	12	Y
Travis (227)	US290 EB	0113-09	H120.F	30° 13.895'	97° 48.380'	80	150	12	Y
Travis (227)	US290 EB	0113-09	H130.F	30° 13.931'	97° 48.495'	80	150	12	Y
Travis (227)	US290 EB	0113-09	H140.F	30° 13.969'	97° 48.603'	80	150	12	Y
Travis (227)	US290 EB	0113-09	H150.F	30° 13.992'	97° 48.726'	80	150	12	Y

Figure 3.43: TxDOT HMIP Inventory – Austin District

County	Highway(s)	Control & Section	HQ Pole Number	GPS		Wind Speed Rating (mph)	Pole Height (ft)	# Sides	Ground Sleeve
				Latitude	Longitude				
Travis (227)	US290 EB	0113-09	H160.F	30° 13.982'	97° 48.850'	80	150	12	Y
Travis (227)	US290 EB	0113-09	H170.F	30° 13.973'	97° 48.965'	80	150	12	Y
Travis (227)	US290 EB	0113-09	H180.F	30° 13.965'	97° 49.066'	80	150	12	Y
Travis (227)	US290 EB	0113-09	H190.F	30° 13.971'	97° 49.183'	80	150	12	Y
Travis (227)	US290 EB	0113-09	H200.F	30° 14.015'	97° 49.293'	80	150	12	Y
Travis (227)	US290 WB	0113-09	H210.F	30° 14.098'	97° 49.323'	80	150	12	Y
Travis (227)	US290 EB	0113-09	H220.F	30° 14.066'	97° 49.439'	80	150	12	Y
Travis (227)	US290 WB	0113-09	H230.F	30° 14.150'	97° 49.419'	80	150	12	Y
Travis (227)	US290 WB	0113-09	H240.F	30° 14.170'	97° 49.487'	80	150	12	Y
Travis (227)	US290 EB	0113-09	H250.F	30° 14.113'	97° 49.515'	80	150	12	Y
Travis (227)	US290 WB	0113-09	H260.F	30° 14.215'	97° 49.544'	80	150	12	Y
Travis (227)	US290 EB	0113-09	H270.F	30° 14.154'	97° 49.622'	80	150	12	Y
Travis (227)	US290 EB	0113-09	H280.F	30° 14.174'	97° 49.725'	80	150	12	Y
Travis (227)	US290 EB	0113-09	H290.F	30° 14.173'	97° 49.838'	80	150	12	Y
Travis (227)	US290 EB	0113-09	H300.F	30° 14.175'	97° 49.952'	80	150	12	Y
Travis (227)	US290 EB	0113-09	H310.F	30° 14.177'	97° 50.063'	80	150	12	Y
Travis (227)	US290 WB	0113-13	H100.G	30° 12.971'	97° 44.352'	80	150	12	Y
Travis (227)	US290 WB	0113-13	H110.G	30° 12.980'	97° 44.524'	80	150	12	Y
Travis (227)	US290 EB	0113-13	H120.G	30° 12.953'	97° 44.681'	80	150	12	Y
Travis (227)	US290 WB	0113-13	H130.G	30° 13.007'	97° 44.803'	80	150	12	Y
Travis (227)	US290 EB	0113-13	H140.G	30° 12.951'	97° 44.920'	80	150	12	Y
Travis (227)	US290 EB	0113-13	H180.G	30° 13.013'	97° 45.233'	80	150	12	Y
Travis (227)	US290 WB	0113-13	H190.G	30° 13.127'	97° 45.298'	80	150	12	Y
Travis (227)	US290 WB	0113-13	H200.G	30° 13.199'	97° 45.451'	80	150	12	Y
Travis (227)	US290 WB	0113-13	H210.G	30° 13.245'	97° 45.557'	80	150	12	Y
Travis (227)	US290 WB	0113-13	H220.G	30° 13.320'	97° 45.712'	80	150	12	Y
Travis (227)	US290 WB	0113-13	H230.G	30° 13.406'	97° 45.844'	80	150	12	Y
Travis (227)	US290 WB	0113-13	H240.G	30° 13.493'	97° 45.981'	80	150	12	Y
Travis (227)	US290 WB	0113-13	H250.G	30° 13.588'	97° 46.119'	80	150	12	Y
Travis (227)	US290 WB	0113-13	H260.G	30° 13.665'	97° 46.306'	80	150	12	Y
Travis (227)	US290 WB	0113-13	H270.G	30° 13.682'	97° 46.476'	80	150	12	Y
Travis (227)	US290 WB	0113-13	H280.G	30° 13.680'	97° 46.651'	80	150	12	Y
Travis (227)	US290 WB	0113-13	H290.G	30° 13.687'	97° 46.848'	80	150	12	Y
Travis (227)	US290 EB	0113-13	H300.G	30° 13.677'	97° 47.042'	80	150	12	Y
Travis (227)	US290 EB	0113-13	H310.G	30° 13.738'	97° 47.198'	80	150	12	Y
Travis (227)	US290 WB	0113-13	H320.G	30° 13.838'	97° 47.327'	80	150	12	Y
Travis (227)	US290 EB	0113-13	H330.G	30° 13.880'	97° 47.502'	80	150	12	Y
Travis (227)	US290 WB	0113-13	H340.G	30° 13.989'	97° 47.651'	80	150	12	Y
Travis (227)	US290	0113-13	H345.G	30° 14.033'	97° 47.803'	80	150	12	Y
Travis (227)	SL360 SB	0113-13	H350.G	30° 14.071'	97° 47.802'	80	150	12	Y
Travis (227)	SL360 SB	0113-13	H360.G	30° 14.162'	97° 47.880'	80	150	12	Y
Travis (227)	SL360 NB	0113-13	H370.G	30° 14.310'	97° 47.933'	80	150	12	Y
Travis (227)	US290 EB	0113-13	H380.G	30° 13.970'	97° 47.960'	80	150	12	Y
Travis (227)	US71 EB	0113-13	G1	30° 37.492'	97° 37.492'	80	150	12	Y
Travis (227)	US290 WB	0114-01	H120.H	30° 19.307'	97° 41.716'	80	150	12	Y
Travis (227)	US290 EB	0114-01	H130.H	30° 19.274'	97° 41.870'	80	150	12	Y
Travis (227)	US290 WB	0114-01	H140.H	30° 19.336'	97° 42.004'	80	150	12	Y
Travis (227)	US290 WB	0114-01	H150.H	30° 19.349'	97° 42.142'	80	150	12	Y
Travis (227)	US290 WB	0114-01	H170.H	30° 19.295'	97° 42.566'	80	150	12	Y
Travis (227)	US290 WB	0114-01	H180.H	30° 19.253'	97° 42.709'	80	150	12	Y
Travis (227)	US290 EB	0114-01	H190.H	30° 19.204'	97° 42.854'	80	150	12	Y
Travis (227)	US290 EB	0114-02	H200.J	30° 20.263'	97° 35.777'	80	150	12	Y
Travis (227)	US290 EB	0114-02	H210.J	30° 20.305'	97° 35.682'	80	150	12	Y
Travis (227)	US290 WB	0114-02	H220.J	30° 20.383'	97° 35.632'	80	150	12	Y
Williamson (246)	US183 NB	0151-05	H100.K	30° 27.636'	97° 47.606'	80	150	12	N
Williamson (246)	US183 NB	0151-05	H110.K	30° 27.745'	97° 47.655'	80	150	12	N
Williamson (246)	US183 NB	0151-05	H120.K	30° 27.838'	97° 47.695'	80	150	12	N
Williamson (246)	US183 NB	0151-05	H130.K	30° 27.958'	97° 47.740'	80	150	12	N

Figure 3.44: TxDOT HMIP Inventory – Austin District - Cont'd

County	Highway(s)	Control & Section	HQ Pole Number	GPS		Wind Speed Rating (mph)	Pole Height (ft)	# Sides	Ground Sleeve
				Latitude	Longitude				
Williamson (246)	US183 NB	0151-05	H180.K	30° 28.463'	97° 47.933'	80	150	12	Y
Williamson (246)	US183 NB	0151-05	H190.K	30° 28.555'	97° 47.981'	80	150	12	Y
Williamson (246)	US183 NB	0151-05	H200.K	30° 28.649'	97° 48.035'	80	150	12	Y
Travis (227)	US183 SB	0151-06	H100.L	30° 23.403'	97° 44.758'	80	150	12	Y
Travis (227)	US183 NB	0151-06	H110.L	30° 23.347'	97° 44.670'	80	150	12	Y
Travis (227)	US183 NB	0151-06	H120.L	30° 23.254'	97° 44.622'	80	150	12	Y
Travis (227)	US183 NB	0151-06	H130.L	30° 23.155'	97° 44.571'	80	150	12	Y
Travis (227)	US183 SB	0151-06	H140.L	30° 23.041'	97° 44.602'	80	150	12	Y
Travis (227)	US183 NB	0151-06	H150.L	30° 23.075'	97° 44.513'	80	150	12	Y
Travis (227)	US183 SB	0151-06	H160.L	30° 22.956'	97° 44.549'	80	150	12	Y
Travis (227)	US183 NB	0151-06	H170.L	30° 22.979'	97° 44.460'	80	150	12	Y
Travis (227)	US183 SB	0151-06	H180.L	30° 22.881'	97° 44.459'	80	150	12	Y
Travis (227)	US183 NB	0151-06	H190.L	30° 22.902'	97° 44.378'	80	150	12	Y
Travis (227)	US183 SB	0151-06	H200.L	30° 22.793'	97° 44.397'	80	150	12	Y
Travis (227)	US183 SB	0151-09	H100.M	30° 19.684'	97° 40.665'	80	150	12	N
Travis (227)	US183 NB	0151-09	H110.M	30° 19.646'	97° 40.513'	80	150	12	N
Travis (227)	US183 NB	0151-09	H120.M	30° 19.582'	97° 40.429'	80	150	12	N
Travis (227)	US183 NB	0151-09	H130.M	30° 19.451'	97° 40.260'	80	150	12	N
Travis (227)	US183 SB	0151-09	H140.M	30° 19.345'	97° 40.187'	80	150	12	N
Travis (227)	US183 SB	0151-09	H150.M	30° 19.273'	97° 40.100'	80	150	12	N
Travis (227)	US183 NB	0151-09	H160.M	30° 19.221'	97° 39.953'	80	150	12	N
Travis (227)	US71 WB	0265-01	N1	30° 11.797'	97° 37.516'	80	150	12	Y
Travis (227)	US71 EB	0265-01	N2	30° 11.836'	97° 37.731'	80	150	12	Y
Travis (227)	US71 EB	0265-01	N3	30° 11.770'	97° 37.628'	80	150	12	Y
Williamson (246)	SH130 NB	0440-05	H100.O	30° 41.155'	97° 39.417'	80	150	12	Y
Williamson (246)	SH130 NB	0440-05	H110.O	30° 41.073'	97° 39.357'	80	150	12	Y
Travis (227)	SH130 NB	0440-06	H100.P	30° 28.690'	97° 35.299'	80	150	12	Y
Travis (227)	SH130 NB	0440-06	H110.P	30° 28.608'	97° 35.346'	80	150	12	Y
Travis (227)	SH130 SB	0440-06	H120.P	30° 28.552'	97° 35.439'	80	150	12	Y
Travis (227)	SH130 SB	0440-06	H130.P	30° 28.465'	97° 35.505'	80	150	12	Y
Travis (227)	SH130 SB	0440-06	H140.P	30° 28.369'	97° 35.563'	80	150	12	Y
Travis (227)	SH130 SB	0440-06	H150.P	30° 28.299'	97° 35.602'	80	150	12	Y
Travis (227)	SH130 NB	0440-06	H160.P	30° 28.216'	97° 35.565'	80	150	12	Y
Travis (227)	SH130 SB	0440-06	H170.P	30° 28.187'	97° 35.661'	80	150	12	Y
Travis (227)	SH130 NB	0440-06	H180.P	30° 28.139'	97° 35.601'	80	150	12	Y
Travis (227)	SH130 NB	0440-06	H190.P	30° 20.874'	97° 35.597'	80	150	12	Y
Travis (227)	SH130 NB	0440-06	H200.P	30° 20.765'	97° 35.594'	80	150	12	Y
Travis (227)	SH130 NB	0440-06	H210.P	30° 20.665'	97° 35.553'	80	150	12	Y
Travis (227)	SH130 NB	0440-06	H220.P	30° 20.587'	97° 35.515'	80	150	12	Y
Travis (227)	SH130 SB	0440-06	H230.P	30° 20.483'	97° 35.557'	80	150	12	Y
Travis (227)	SH130 NB	0440-06	P1	30° 37.343'	97° 37.343'	80	150	12	Y
Travis (227)	SH130 NB	0440-06	P2	30° 11.892'	97° 37.304'	80	150	12	Y
Travis (227)	SH130 NB	0440-06	P3	30° 12.007'	97° 37.293'	80	150	12	Y
Travis (227)	SH130 SB	0440-06	P4	30° 11.723'	97° 37.450'	80	150	12	Y
Travis (227)	SH130 SB	0440-06	P5	30° 11.834'	97° 37.423'	80	150	12	Y
Williamson (246)	SH45 WB	0683-01	H100.Q	30° 28.261'	97° 47.398'	80	150	12	Y
Williamson (246)	SH45 WB	0683-01	H110.Q	30° 28.185'	97° 47.494'	80	150	12	Y
Williamson (246)	SH45 WB	0683-01	H120.Q	30° 28.151'	97° 47.603'	80	150	12	Y
Williamson (246)	SH45 WB	0683-01	H130.Q	30° 28.131'	97° 47.709'	80	150	12	Y
Williamson (246)	SH45 WB	0683-01	H160.Q	30° 28.117'	97° 47.932'	80	150	12	Y
Williamson (246)	SH45 EB	0683-01	H170.Q	30° 28.041'	97° 47.942'	80	150	12	Y
Williamson (246)	SH45 WB	0683-01	H180.Q	30° 28.055'	97° 48.042'	80	150	12	Y
Williamson (246)	SH45 WB	0683-01	H190.Q	30° 28.032'	97° 48.163'	80	150	12	Y
Williamson (246)	SH45 WB	0683-01	H200.Q	30° 27.990'	97° 48.288'	80	150	12	Y
Williamson (246)	SH45 EB	0683-06	H100.R	30° 28.752'	97° 43.155'	80	150	12	N
Williamson (246)	SH45 EB	0683-06	H110.R	30° 28.770'	97° 43.002'	80	150	12	N
Williamson (246)	SH45 WB	0683-06	H120.R	30° 28.794'	97° 42.856'	80	150	12	N
Williamson (246)	SH45 WB	0683-06	H130.R	30° 28.761'	97° 42.687'	80	150	12	N

Figure 3.45: TxDOT HMIP Inventory – Austin District - Cont'd

County	Highway(s)	Control & Section	HQ Pole Number	GPS		Wind Speed Rating (mph)	Pole Height (ft)	# Sides	Ground Sleeve
				Latitude	Longitude				
Williamson (246)	SH45 WB	0683-06	H140.R	30° 28.713'	97° 42.543'	80	150	12	N
Williamson (246)	SH45 WB	0683-06	H150.R	30° 28.660'	97° 42.385'	80	150	12	N
Williamson (246)	SH45 WB	0683-06	H160.R	30° 28.620'	97° 42.240'	80	150	12	N
Williamson (246)	SH45 WB	0683-06	H170.R	30° 28.616'	97° 42.116'	80	150	12	N
Williamson (246)	SH45 EB	0683-06	H180.R	30° 28.589'	97° 41.947'	80	150	12	N
Williamson (246)	SH45 WB	0683-06	H190.R	30° 28.651'	97° 41.960'	80	150	12	N
Williamson (246)	SH45 EB	0683-06	H200.R	30° 28.614'	97° 41.771'	80	150	12	N
Williamson (246)	SH45 WB	0683-06	H210.R	30° 28.680'	97° 41.786'	80	150	12	N
Williamson (246)	SH45 EB	0683-06	H220.R	30° 28.658'	97° 41.606'	80	150	12	N
Williamson (246)	SH45 EB	0683-06	H230.R	30° 28.683'	97° 41.459'	80	150	12	N
Williamson (246)	SH45 WB	0683-06	H240.R	30° 28.745'	97° 41.324'	80	150	12	Y
Williamson (246)	SH45 WB	0683-06	H250.R	30° 28.768'	97° 41.189'	80	150	12	Y
Williamson (246)	SH45 EB	0683-06	H260.R	30° 28.748'	97° 41.066'	80	150	12	Y
Williamson (246)	SH45 WB	0683-06	H270.R	30° 28.813'	97° 40.992'	80	150	12	Y
Williamson (246)	SH45 EB	0683-06	H280.R	30° 28.754'	97° 40.936'	80	150	12	Y
Williamson (246)	SH45 WB	0683-06	H290.R	30° 28.825'	97° 40.866'	80	150	12	Y
Williamson (246)	SH45 EB	0683-06	H300.R	30° 28.770'	97° 40.795'	80	150	12	Y
Williamson (246)	SH45 WB	0683-06	H310.R	30° 28.833'	97° 40.735'	80	150	12	Y
Williamson (246)	SH45 EB	0683-06	H320.R	30° 28.771'	97° 40.658'	80	150	12	Y
Williamson (246)	SH45 WB	0683-06	H330.R	30° 28.830'	97° 40.603'	80	150	12	Y
Williamson (246)	SH45	0683-06	H370.R	30° 28.842'	97° 40.234'	80	150	12	Y
Williamson (246)	SH45	0683-06	H380.R	30° 28.864'	97° 40.129'	80	150	12	Y
Williamson (246)	SH45	0683-06	H390.R	30° 28.890'	97° 40.005'	80	150	12	Y
Travis (227)	SH45 WB	0683-07	H100.S	30° 28.476'	97° 35.599'	80	150	12	Y
Travis (227)	SH45 EB	0683-07	H110.S	30° 28.418'	97° 35.656'	80	150	12	Y
Travis (227)	SH45 EB	0683-07	H120.S	30° 28.505'	97° 35.722'	80	150	12	Y
Travis (227)	SH45 EB	0683-07	H130.S	30° 28.537'	97° 35.788'	80	150	12	Y
Travis (227)	SL1 SB	3136-01	H190.U	30° 22.698'	97° 44.370'	80	150	12	Y
Travis (227)	SL1 NB	3136-01	H200.U	30° 22.606'	97° 44.301'	80	150	12	Y
Travis (227)	SL1 SB	3136-01	H210.U	30° 22.575'	97° 44.385'	80	150	12	Y
Travis (227)	SL1 SB	3136-01	H500.U	30° 14.237'	97° 49.332'	80	150	12	Y
Travis (227)	SL1 SB	3136-01	H510.U	30° 14.228'	97° 49.432'	80	150	12	Y
Travis (227)	SL1 NB	3136-01	H520.U	30° 14.026'	97° 49.513'	80	150	12	Y
Travis (227)	SL1 NB	3136-01	H530.U	30° 13.890'	97° 49.621'	80	150	12	Y
Travis (227)	SL1 NB	3136-01	H540.U	30° 13.816'	97° 49.643'	80	150	12	Y
Travis (227)	SL1NB	3136-01	U1	30° 25.172'	97° 42.2540	80	150	12	N
Travis (227)	SL1NB	3136-01	U2	30° 25.283'	97° 42.207'	80	150	12	N
Williamson (246)	SL1	3136-02	H100.X	30° 28.330'	97° 42.125'	80	150	12	N
Williamson (246)	SL1	3136-02	H110.X	30° 28.459'	97° 42.162'	80	150	12	N
Williamson (246)	SL1	3136-02	H120.X	30° 28.536'	97° 42.105'	80	150	12	N
Williamson (246)	SL1	3136-02	H130.X	30° 28.541'	97° 42.161'	80	150	12	N
Williamson (246)	SL1	3136-02	H140.X	30° 28.538'	97° 42.225'	80	150	12	N
Williamson (246)	IH35	0015-09	H150.B	30° 28.886'	97° 40.403'	80	175	12	Y
Williamson (246)	IH35	0015-09	H160.B	30° 28.854'	97° 40.501'	80	175	12	Y
Travis (227)	IH35 SB	0015-13	H140.D	30° 12.930'	97° 45.169'	80	175	12	Y
Travis (227)	IH35 SB	0015-13	H320.C	30° 19.367'	97° 42.457'	80	175	12	Y
Travis (227)	IH35 SB	0015-13	H330.C	30° 19.261'	97° 42.480'	80	175	12	Y
Travis (227)	IH35 SB	0015-13	H340.C	30° 19.172'	97° 42.466'	80	175	12	Y
Travis (227)	IH35 NB	0015-13	H350.C	30° 19.274'	97° 42.384'	80	175	12	Y
Travis (227)	IH35 NB	0015-13	H360.C	30° 19.386'	97° 42.349'	80	175	12	Y
Travis (227)	IH35 NB	0015-13	H370.C	30° 19.476'	97° 42.362'	80	175	12	Y
Travis (227)	US290 WB	0113-13	H150.G	30° 13.013'	97° 44.990'	80	175	12	Y
Travis (227)	US290 EB	0113-13	H160.G	30° 12.947'	97° 45.053'	80	175	12	Y
Travis (227)	US290 WB	0113-13	H170.G	30° 13.022'	97° 45.085'	80	175	12	Y
Travis (227)	US290 EB	0114-01	H100.H	30° 19.494'	97° 40.428'	80	175	12	N
Travis (227)	US290 WB	0114-01	H110.H	30° 19.499'	97° 40.560'	80	175	12	N
Travis (227)	US290 WB	0114-01	H160.H	30° 19.345'	97° 42.273'	80	175	12	Y
Travis (227)	US290 WB	0114-02	H100.J	30° 19.598'	97° 40.263'	80	175	12	N

Figure 3.46: TxDOT HMIP Inventory – Austin District - Cont'd

County	Highway(s)	Control & Section	HQ Pole Number	GPS		Wind Speed Rating (mph)	Pole Height (ft)	# Sides	Ground Sleeve
				Latitude	Longitude				
Travis (227)	US290 EB	0114-02	H110.J	30° 19.528'	97° 40.309'	80	175	12	N
Williamson (246)	US183 NB	0151-05	H140.K	30° 28.085'	97° 47.746'	80	175	12	N
Williamson (246)	US183 NB	0151-05	H150.K	30° 28.172'	97° 47.783'	80	175	12	N
Williamson (246)	US183 NB	0151-05	H160.K	30° 28.271'	97° 47.869'	80	175	12	N
Williamson (246)	US183 NB	0151-05	H170.K	30° 28.349'	97° 47.907'	80	175	12	N
Williamson (246)	SH45 WB	0683-01	H140.Q	30° 28.145'	97° 47.879'	80	175	12	N
Williamson (246)	SH45 EB	0683-01	H150.Q	30° 28.053'	97° 47.836'	80	175	12	N
Williamson (246)	SH45	0683-06	H340.R	30° 28.770'	97° 40.474'	80	175	12	Y
Williamson (246)	SH45	0683-06	H350.R	30° 28.782'	97° 40.364'	80	175	12	Y
Williamson (246)	SH45	0683-06	H360.R	30° 28.851'	97° 40.337'	80	175	12	Y
Travis (227)	US183 SB	0151-06	H230.L	30° 22.609'	97° 44.073'	100	125	12	Y
Travis (227)	US183 NB	0151-06	H240.L	30° 22.583'	97° 43.921'	100	125	12	Y
Travis (227)	US183 SB	0151-06	H250.L	30° 22.508'	97° 43.860'	100	125	12	Y
Williamson (246)	IH35 SB	0015-09	H140.B	30° 28.926'	97° 40.520'	100	150	12	Y
Travis (227)	IH35 NB	0015-13	H180.D	30° 24.731'	97° 40.413'	80	150	12	N
Travis (227)	IH35 NB	0016-01	E1	30° 6.612'	97° 48.454'	100	150	12	Y
Travis (227)	IH35 NB	0016-01	E2	30° 6.521'	97° 48.497'	100	150	12	Y
Travis (227)	IH35 NB	0016-01	E3	30° 6.421'	97° 48.550'	100	150	12	Y
Travis (227)	IH35 NB	0016-01	E4	30° 6.323'	97° 48.596'	100	150	12	Y
Travis (227)	IH35 NB	0016-01	E5	30° 6.224'	97° 48.643'	100	150	12	Y
Travis (227)	IH35 NB	0016-01	E6	30° 6.118'	97° 48.690'	100	150	12	Y
Travis (227)	IH35 NB	0016-01	E7	30° 6.017'	97° 48.737'	100	150	12	Y
Travis (227)	IH35 NB	0016-01	E8	30° 5.907'	97° 48.822'	100	150	12	Y
Travis (227)	IH35 NB	0016-01	E9	30° 5.800'	97° 48.844'	100	150	12	Y
Travis (227)	IH35 NB	0016-01	E10	30° 5.683'	97° 48.899'	100	150	12	Y
Travis (227)	IH35 NB	0016-01	E11	30° 6.848'	97° 48.360'	100	150	12	Y
Travis (227)	IH35 NB	0016-01	E12	30° 6.950'	97° 48.321'	100	150	12	Y
Travis (227)	IH35 NB	0016-01	E13	30° 7.049'	97° 48.275'	100	150	12	Y
Travis (227)	IH35 NB	0016-01	E14	30° 7.156'	97° 48.232'	100	150	12	Y
Travis (227)	IH35 NB	0016-01	E15	30° 7.261'	97° 48.187'	100	150	12	Y
Travis (227)	IH35 NB	0016-01	E16	30° 7.373'	97° 48.146'	100	150	12	Y
Travis (227)	IH35 NB	0016-01	E17	30° 7.485'	97° 48.095'	100	150	12	Y
Travis (227)	IH35 NB	0016-01	E18	30° 7.603'	97° 48.053'	100	150	12	Y
Travis (227)	IH35 NB	0016-01	E19	30° 7.721'	97° 48.005'	100	150	12	Y
Travis (227)	IH35 NB	0016-01	E20	30° 7.835'	97° 47.963'	100	150	12	Y
Travis (227)	IH35 NB	0016-01	E21	30° 7.953'	97° 47.915'	100	150	12	Y
Travis (227)	IH35 SB	0016-01	E22	30° 6.734'	97° 48.449'	100	150	12	Y
Travis (227)	US183 NB	0151-06	H220.L	30° 22.722'	97° 44.137'	100	150	12	Y
Travis (227)	SH45SE EB	1200-05	T1	30° 6.655'	97° 47.775'	100	150	12	Y
Travis (227)	SH45SE EB	1200-05	T2	30° 6.694'	97° 47.890'	100	150	12	Y
Travis (227)	SH45SE EB	1200-05	T3	30° 6.707'	97° 48.001'	100	150	12	Y
Travis (227)	SH45SE EB	1200-05	T4	30° 6.704'	97° 48.143'	100	150	12	Y
Travis (227)	SH45SE WB	1200-05	T5	30° 6.726'	97° 48.315'	100	150	12	Y
Travis (227)	SH45SE EB	1200-05	T6	30° 6.670'	97° 48.309'	100	150	12	Y
Travis (227)	SH45SE WB	1200-05	T7	30° 6.777'	97° 48.270'	100	150	12	Y

Figure 3.47: TxDOT HMIP Inventory – Austin District - Cont'd

County	Highway(s)	Control & Section	HQ Pole Number	GPS		Wind Speed Rating (mph)	Pole Height (ft)	# Sides	Ground Sleeve
				Latitude	Longitude				
Bexar	IH 35 NBD	0017-02-089	2	29.57	-98.33	80	150	8	yes
Bexar	IH 35 NBD	0017-02-089	1	29.57	-98.33	80	150	8	yes
Bexar	IH 35 SBD	0017-02-089	4	29.57	-98.33	80	150	8	yes
Bexar	IH 35 NBD	0017-02-089	3	29.57	-98.33	80	150	8	yes
Bexar	IH 10 @ IH 410 (SE corner)	0025-02-141	65	29.44	-98.39	80	100	8	yes
Bexar	IH 10 @ IH 410 (NE corner)	0025-02-141	66	29.44	-98.39	80	100	8	yes
Bexar	IH 10 @ IH 410 (SW corner)	0025-02-141	68	29.43	-98.39	80	100	8	yes
Bexar	IH 10 @ IH 410 (NW corner)	0025-02-141	67	29.44	-98.39	80	100	8	yes
Bexar	IH 35 NBD	0017-10-152	42	29.44	-98.48	80	150	8	no
Bexar	IH 35 SBD	0017-10-152	14	29.44	-98.48	80	150	8	no
Bexar	IH 35 SBD	0017-10-152	15	29.44	-98.49	80	150	8	no
Bexar	IH 35 NBD	0017-10-152	39	29.44	-98.49	80	150	8	no
Bexar	IH 35 NBD	0017-10-152	41	29.44	-98.48	80	150	8	no
Bexar	IH 35 NBD	0017-10-152	38	29.44	-98.49	80	150	8	no
Bexar	IH 35 NBD	0017-10-152	37	29.44	-98.49	80	150	8	no
Bexar	IH 35 NBD	0017-10-152	36	29.44	-98.49	80	150	8	no
Bexar	IH 35 SBD	0017-10-152	16	29.43	-98.49	80	150	8	no
Bexar	IH 35 NBD	0017-10-152	35	29.43	-98.50	80	150	8	no
Bexar	IH 35 SBD	0017-10-152	17	29.43	-98.50	80	150	8	no
Bexar	IH 35 NBD	0017-10-152	34	29.43	-98.50	80	150	8	no
Bexar	IH 35 NBD	0017-10-152	33	29.43	-98.50	80	150	8	no
Bexar	IH 35 NBD	0017-10-152	32	29.43	-98.50	80	150	8	no
Bexar	IH 35 SBD	0017-10-152	18	29.43	-98.50	80	150	8	no
Bexar	IH 10 EBD	0017-10-152	46	29.43	-98.50	80	150	8	no
Bexar	IH 35 NBD	0017-10-152	27	29.42	-98.50	80	150	8	no
Bexar	IH 35 SBD	0017-10-152	23	29.42	-98.50	80	150	8	no
Bexar	IH 10 EBD	0017-10-152	45	29.44	-98.50	80	150	8	no
Bexar	IH 35 SBD	0017-10-152	24	29.41	-98.50	80	150	8	no
Bexar	IH 10 EBD	0017-10-152	44	29.44	-98.50	80	150	8	no
Bexar	IH 10 EBD	0017-10-152	43	29.44	-98.51	80	150	8	no
Bexar	IH 10 WBD	0072-12-124	87	29.44	-98.51	80	150	8	yes
Bexar	IH 35 SBD	0017-10-152	25	29.41	-98.51	80	150	8	no
Bexar	IH 35 NBD	0017-10-152	26	29.41	-98.51	80	150	8	no
Bexar	IH 10 WBD	0072-12-124	88	29.44	-98.51	80	150	8	yes
Bexar	IH 35 SBD	0017-10-150	11	29.41	-98.51	80	150	8	yes
Bexar	IH 35 NBD	0017-10-150	10	29.41	-98.51	80	150	8	yes
Bexar	IH 35 NBD	0017-10-150	9	29.41	-98.51	80	150	8	yes
Bexar	IH 10 WBD	0072-12-124	89	29.44	-98.51	80	150	8	yes
Bexar	IH 35 NBD	0017-10-150	8	29.41	-98.51	80	150	8	yes
Bexar	IH 35 NBD	0017-10-150	7	29.41	-98.51	80	150	8	yes
Bexar	IH 35 NBD	0017-10-150	6	29.41	-98.51	80	150	8	yes
Bexar	IH 35 NBD	0017-10-152	31	29.42	-98.50	80	150	8	no
Bexar	IH 35 SBD	0017-10-152	19	29.43	-98.50	80	150	8	no
Bexar	IH 35 NBD	0017-10-152	30	29.42	-98.50	80	150	8	no
Bexar	IH 10 WBD	0072-12-124	90	29.44	-98.51	80	150	8	yes
Bexar	IH 35 NBD	0017-10-150	5	29.40	-98.51	80	150	8	yes
Bexar	IH 35 SBD	0017-10-150	12	29.40	-98.51	80	150	8	yes
Bexar	IH 35 SBD	0017-10-150	13	29.40	-98.51	80	150	8	yes
Bexar	IH 10 WBD	0072-12-124	91	29.44	-98.51	80	150	8	yes
Bexar	IH 35 SBD	0017-10-152	20	29.43	-98.50	80	150	8	no
Bexar	IH 35 SBD	0017-10-152	21	29.44	-98.50	80	150	8	no
Bexar	IH 10 WBD	0072-12-124	92	29.44	-98.51	80	150	8	yes
Bexar	IH 10 WBD	0072-12-124	93	29.45	-98.51	80	150	8	yes
Bexar	IH 10 WBD	0072-12-125	99	29.46	-98.51	80	150	8	yes
Bexar	IH 10 WBD	0072-12-124	96	29.45	-98.52	80	150	8	yes
Bexar	IH 10 WBD	0072-12-124	94	29.45	-98.52	80	150	8	yes
Bexar	IH 10 WBD	0072-12-125	100	29.46	-98.52	80	150	8	yes
Bexar	IH 10 WBD	0072-12-124	95	29.45	-98.52	80	150	8	yes

Figure 3.48: TxDOT HMIP Inventory – San Antonio District

County	Highway(s)	Control & Section	HQ Pole Number	GPS		Wind Speed Rating (mph)	Pole Height (ft)	# Sides	Ground Sleeve
				Latitude	Longitude				
Bexar	IH 10 WBD	0072-12-125	102	29.46	-98.52	80	150	8	yes
Bexar	IH 10 EBD	0072-12-124	86	29.44	-98.52	80	150	8	yes
Bexar	IH 10 WBD	0072-12-125	103	29.47	-98.52	80	150	8	per pictu
Bexar	IH 10 WBD	0072-12-125	104	29.47	-98.52	80	150	8	yes
Bexar	IH 10 WBD	0072-12-125	101	29.46	-98.52	80	150	8	yes
Bexar	IH 10 EBD	0072-12-124	85	29.45	-98.52	80	150	8	yes
Bexar	IH 10 EBD	0072-12-125	98	29.46	-98.52	80	150	8	yes
Bexar	IH 10 EBD	0072-12-125	97	29.46	-98.52	80	150	8	yes
Bexar	IH 10 EBD	0072-12-124	84	29.45	-98.52	80	150	8	yes
Bexar	IH 35 NBD	0017-10-152	29	29.42	-98.50	80	150	8	no
Bexar	IH 10 EBD	0017-10-152	47	29.43	-98.50	80	150	8	no
Bexar	IH 35 NBD	0017-10-152	28	29.42	-98.50	80	150	8	no
Bexar	IH 35 SBD	0017-10-152	22	29.44	-98.50	80	150	8	no
Bexar	IH 10 WBD	0072-12-159	111	29.49	-98.54	80	150	8	no
Bexar	IH 410E (IH 10/IH 410 interchange)	0072-12-102	77	29.51	-98.55	80	150	8	no
Bexar	IH 10 WBD	0072-12-159	110	29.49	-98.55	80	150	8	no
Bexar	IH 410E (IH 10/IH 410 interchange)	0072-12-102	76	29.50	-98.55	80	150	8	no
Bexar	IH 10 WBD	0072-12-159	109	29.49	-98.55	80	150	8	no
Bexar	IH 410W (IH 10/IH 410 interchange)	0072-12-102	83	29.50	-98.55	80	175	8	no
Bexar	IH 10 WBD	0072-12-159	108	29.50	-98.55	80	150	8	no
Bexar	IH 410W (IH 10/IH 410 interchange)	0072-12-159	113	29.51	-98.55	80	150	8	no
Bexar	IH 10W (IH 10/IH 410 interchange)	0072-12-159	116	29.50	-98.55	80	175	8	no
Bexar	IH 10W (IH 10/IH 410 interchange)	0072-12-159	115	29.50	-98.55	80	175	8	no
Bexar	IH 410W (IH 10/IH 410 interchange)	0072-12-159	114	29.50	-98.55	80	150	8	no
Bexar	IH 10 WBD	0072-12-159	107	29.50	-98.55	80	150	8	no
Bexar	IH 10 EBD	0072-12-159	106	29.50	-98.55	80	150	8	no
Bexar	IH 10W (IH 10/IH 410 interchange)	0072-12-102	73	29.50	-98.55	80	150	8	no
Bexar	IH 410E (IH 10/IH 410 interchange)	0072-12-159	118	29.50	-98.55	80	175	8	no
Bexar	Near Transguide Bldg (IH 10/IH 410 interchange)	0072-12-159	105	29.50	-98.55	80	150	8	no
Bexar	IH 410W (IH 10/IH 410 interchange)	0072-12-159	121	29.50	-98.55	80	175	8	no
Bexar	IH 10W (IH 10/IH 410 interchange)	0072-12-102	72	29.51	-98.55	80	150	8	no
Bexar	IH 410E (IH 10/IH 410 interchange)	0072-12-159	117	29.50	-98.55	80	175	8	no
Bexar	Near Transguide Bldg (IH 10/IH 410 interchange)	0072-12-102	80	29.50	-98.55	80	150	8	no
Bexar	IH 410W (IH 10/IH 410 interchange)	0072-12-159	119	29.50	-98.55	80	175	8	yes
Bexar	IH 410W (IH 10/IH 410 interchange)	0072-12-159	120	29.50	-98.55	80	175	8	no
Bexar	IH 410E (IH 10/IH 410 interchange)	0072-12-159	112	29.50	-98.55	80	150	8	no
Bexar	IH 10E (IH 10/IH 410 interchange)	0072-12-102	81	29.50	-98.55	80	175	8	no
Bexar	IH 10E (IH 10/IH 410 interchange)	0072-12-102	71	29.50	-98.55	80	150	8	no
Bexar	IH 410E (IH 10/IH 410 interchange)	0072-12-102	82	29.50	-98.55	80	175	8	no
Bexar	IH 410E (IH 10/IH 410 interchange)	0072-12-102	75	29.50	-98.55	80	150	8	no
Bexar	US 90 EBD	0024-08-087	58	29.40	-98.55	80	150	8	yes
Bexar	US 90 WBD	0024-08-087	48	29.40	-98.55	80	150	8	yes
Bexar	IH 10E (IH 10/IH 410 interchange)	0072-12-102	70	29.51	-98.55	80	150	8	no
Bexar	IH 410W (IH 10/IH 410 interchange)	0072-12-102	78	29.50	-98.55	80	150	8	no
Bexar	US 90 EBD	0024-08-087	57	29.40	-98.56	80	150	8	yes
Bexar	US 90 WBD	0024-08-087	49	29.41	-98.56	80	150	8	yes
Bexar	US 90 EBD	0024-08-087	56	29.40	-98.56	80	150	8	yes
Bexar	US 90 EBD	0024-08-087	55	29.40	-98.56	80	150	8	yes
Bexar	US 90 WBD	0024-08-087	50	29.41	-98.56	80	150	8	yes
Bexar	US 90 EBD	0024-08-087	54	29.40	-98.56	80	150	8	yes
Bexar	US 90 WBD	0024-08-087	51	29.41	-98.56	80	150	8	yes
Bexar	US 90 EBD	0024-08-087	53	29.40	-98.56	80	150	8	yes
Bexar	IH 10E (IH 10/IH 410 interchange)	0072-12-102	69	29.51	-98.55	80	150	8	no
Bexar	US 90 EBD	0024-08-087	52	29.40	-98.56	80	150	8	yes
Bexar	IH 410W (IH 10/IH 410 interchange)	0072-12-102	79	29.50	-98.55	80	150	8	no
Bexar	IH 410E (IH 10/IH 410 interchange)	0072-12-102	74	29.50	-98.55	80	150	8	no
Bexar	IH 35N @ IH 410 (NE corner)	0521-05-112	124	29.32	-98.61	80	150	8	yes
Bexar	IH 35N @ IH 410 (SE corner)	0521-05-112	123	29.32	-98.61	80	150	8	yes
Bexar	IH 35S @ IH 410 (NW corner)	0521-05-112	125	29.32	-98.61	80	150	8	yes
Bexar	IH 35S @ IH 410 (SW corner)	0521-05-112	126	29.32	-98.61	80	150	8	yes
Bexar	SH 151 WBD	3508-01-019	127	29.43	-98.61	80	150	8	no
Bexar	US 90 WBD	0024-08-128	60	29.40	-98.62	80	100	8	yes
Bexar	US 90 EBD	0024-08-128	64	29.40	-98.62	80	100	8	yes
Bexar	US 90 EBD	0024-08-128	63	29.40	-98.62	80	100	8	yes
Bexar	US 90 EBD	0024-08-128	62	29.40	-98.63	80	100	8	yes
Bexar	US 90 WBD	0024-08-128	59	29.40	-98.62	80	100	8	yes
Bexar	US 90 WBD	0024-08-128	61	29.40	-98.63	80	100	8	yes
Bexar	SH 151 WBD	3508-01-019	128	29.43	-98.65	80	150	8	no
Bexar	IH 410 @ US 90 interchange	0521-05-041	122	29.40	-98.65	70	150	8	yes
Bexar	IH 35 NBD	0017-10-152	40			80	150	8	no

Figure 3.49: TxDOT HMIP Inventory – San Antonio District - Cont'd

County	Highway(s)	Control & Section	HQ Pole Number	GPS		Wind Speed Rating (mph)	Pole Height (ft)	# Sides	Ground Sleeve
				Latitude	Longitude				
Nueces	SH 358 & SH 44	617-1	HM11	27.74	97.43	100	100	8	no
Nueces	SH 358 & SH 44	617-1	HM12	27.78	97.47	100	100	8	no
Nueces	SH 358 & SH 44	none given	HM13	27.78	97.47	100	100	8	no
Nueces	SH 358 & SH 44	none given	HM14	27.78	97.47	100	100	8	no
Nueces	US 77 & IH 37 (S Interchange-Redbird)	none given	HM32	27.86	97.62	100	100	8	yes
Nueces	IH 37	none given	HM34	27.86	97.62	100	100	8	yes
Nueces	IH 37 & US 77 (Sharpsburg)	none given	HM33	27.87	97.62	100	100	8	yes
Nueces	IH 37	none given	HM35	27.86	97.62	100	100	8	yes
Nueces	IH 37	none given	HM36	27.86	97.63	100	100	8	yes
Nueces	IH 37	none given	HM37	27.86	97.62	100	100	8	yes
Nueces	SH 286	326-1	HM01	27.74	97.43	100	100	12	no
Nueces	SH 286	326-1	HM02	27.74	97.43	100	100	12	no
Nueces	SH 286	326-1	HM03	27.74	97.43	100	100	12	no
Nueces	SH 286	326-1	HM04	27.74	97.43	100	100	12	no
Nueces	SH 286	326-1	HM05	27.73	97.43	100	100	12	no
Nueces	SH 286	326-1	HM06	27.74	97.43	100	100	12	no
Nueces	SH 286	326-1	HM07	27.74	97.43	100	100	12	no
Nueces	SH 286	326-1	HM08	27.74	97.43	100	100	12	no
Nueces	SH 286	326-1	HM09	27.74	97.43	100	100	12	no
Nueces	SH 286	326-1	HM10	27.74	97.43	100	100	12	no
Nueces	US 77 & IH 37	none given	HM28	27.91	97.30	100	100	12	yes
Nueces	US 77 & IH 37	none given	HM29	27.91	97.63	100	100	12	yes
Nueces	US 77 & IH 37	none given	HM30	27.90	97.63	100	100	12	yes
Nueces	US 77 & IH 37	none given	HM31	27.90	97.63	100	100	12	yes
San Patricio	US 181	101-4	HM15	27.91	97.30	100	100	12	yes
San Patricio	US 181/FM 35	101-4	HM16	27.91	97.30	100	100	12	yes
Jim Wells	SH 44 (WB)	none given	HM10	27.78	98.02	100	150	12	yes
Jim Wells	SH 44 (1st pole going EB)	none given	HM8	27.78	98.02	100	150	12	yes
	2nd pole going EB	none given	HM9	27.78	98.02	100	150	12	yes
Nueces	SH 358 & SH 44		HM12	27° 46′ 55.0	97° 28′ 09.6	100	100	12	yes
Nueces	SH 44 Robstown	none given	HM38	27.79	97.66	100	100	12	yes

Figure 3.50: TxDOT HMIP Inventory – Corpus Christi District

County	Highway(s)	Control & Section	HQ Pole number	GPS		Wind Speed Rating (mph)	Pole Height (ft)	# Sides	Ground Sleeve
				Latitude	Longitude				
Brazos	SH6	0049-12	1	30.59	-96.29	80	150	12	yes
Brazos	SH6	0049-12	2	30.59	-96.29	80	150	12	yes
Walker	IH45	0675-07	3	30.52	-96.49	80	175	12	yes
Walker	IH45	0675-07	4	30.52	-95.49	80	175	12	yes

Figure 3.51: TxDOT HMIP Inventory – Bryan District

County	Highway(s)	Control & Section	HQ Pole Number	GPS		Wind Speed Rating (mph)	Pole Height (ft)	# Sides	Ground Sleeve
				Latitude	Longitude				
Dallas	IH 635	2374-2	1	32.71	-96.62	70	150	8	yes
Dallas	IH 635	2374-2	2	32.70	-96.63	70	150	8	yes
Dallas	IH 635	2374-2	3	32.70	-96.63	70	150	8	yes
Dallas	IH 20	2374-2	4	32.70	-96.63	70	150	8	yes
Dallas	IH 20	2374-2	5	32.70	-96.63	70	150	8	yes
Dallas	IH 20	2374-2	6	32.70	-96.63	70	150	8	yes
Dallas	IH 635	2374-2	7	32.70	-96.63	70	150	8	yes
Dallas	IH 635	2374-2	8	32.70	-96.63	70	150	8	yes
Dallas	IH 635	2374-2	9	32.70	-96.62	70	150	8	yes
Dallas	IH 20	2374-2	10	32.70	-96.62	70	150	8	yes
Dallas	IH 20	2374-2	11	32.70	-96.62	70	150	8	yes
Dallas	IH 20	2374-2	12	32.70	-96.62	70	150	8	yes
Dallas	IH 635	2374-2	13	32.70	-96.62	70	150	12	yes
Dallas	IH 20	2374-2	14	32.70	-96.62	70	150	12	yes
Dallas	US 175	95-13	15	32.69	-96.63	70	150	12	yes
Dallas	US 175	95-13	16	32.69	-96.63	70	150	12	yes
Dallas	US 175	95-13	17	32.69	-96.64	70	150	12	yes
Dallas	US 175	95-13	18	32.69	-96.63	70	150	12	yes
Dallas	US 175	95-13	19	32.69	-96.63	70	150	12	yes
Dallas	IH 20	2374-3	20	32.69	-96.63	70	150	12	yes
Dallas	IH 20	2374-3	21	32.69	-96.63	70	150	12	yes
Dallas	IH 20	2374-3	22	32.66	-96.72	70	150	12	no
Dallas	IH 20	2374-4	23	32.66	-96.72	70	150	12	no
Denton	SH 121	3088-1	24	32.64	-96.82	100	150	12	no
Denton	SH 121	3088-1	25	32.66	-96.72	100	150	12	no
Denton	SH 121	3088-1	26	33.00	-96.99	100	150	12	yes
Denton	SH 121	3088-1	27	33.01	-96.99	100	150	12	yes
Denton	SH 121	3088-1	28	33.00	-96.99	100	150	12	yes
Denton	SH 121	3088-1	29	33.00	-96.99	100	150	12	yes
Denton	SH 121	3088-1	30	33.00	-96.99	100	150	12	yes
Denton	SH 121	3088-1	31	33.00	-96.99	100	150	12	yes
Denton	SH 121	3088-1	32	33.00	-97.00	100	150	12	yes
Denton	SH 121	3088-1	33	33.00	-96.99	100	150	12	yes

Figure 3.52: TxDOT HMIP Inventory – Dallas District

County	Highway(s)	Control & Section	HQ Pole Number	GPS		Wind Speed Rating (mph)	Pole Height (ft)	# Sides	Ground Sleeve
				Latitude	Longitude				
Bowie	Sta 2416+56	0610-07-085	HM-33			80	100	12	no
Bowie	Sta 2423+06	0610-07-085	HM-65			80	100	12	no
Bowie	Sta 2427+06	0610-07-085	HM-66			80	100	12	no
Bowie	Sta 2435+70	0610-07-085	HM-67	33 28.130	-94 3.716	80	100	12	yes
Bowie	Sta 2213+83	0610-07-085	HM-58	33 27.307	-94 7.816	80	100	12	yes
Bowie	Sta 2215+33	0610-07-085	HM-59	33 27.1825	-94 7.859	80	100	12	yes
Bowie	LP 151 @ 1/4 Mile North FM 558	0945-01	#19	33 23.142	-94 5.996	80	150	12	no
Bowie	LP 151 @ Bishop	2050-03	#21	33 23.535	-94 5.905	80	150	12	no
Bowie	LP 151 @ FM 558	0945-01	#16	33 23.172	-94 4.020	80	150	12	no
Bowie	LP 151 @ FM 558	0945-01	#17	33 23.109	-94 4.099	80	150	12	no
Bowie	LP 151 @ FM 558	0945-01	#18	33 23.161	-94 4.645	80	150	12	no
Bowie	LP 151 @ US 82	0218-02	#5	33 26.742	-94 5.786	80	150	12	no
Bowie	LP 151 @ US 82 EB	0218-02	#6	33 26.584	-94 5.768	80	150	12	no
Bowie	LP 151 NB @ US 67	0218-01	#10	33 25.152	-94 5.797	80	150	12	no
Bowie	LP 151 NB @ Wake Village RD	0218-01	#8	33 25.622	-94 5.942	80	150	12	no
Bowie	LP 151 NB Past FM 3527	0945-01	#15	33 23.420	-94 5.780	80	150	12	no
Bowie	LP 151 NB South IH 30 Exit	0218-02	#4	33 26.775	-94 5.743	80	150	12	no
Bowie	LP 151 SB @ Exit SH 93	2050-03	#12	33 23.892	-94 5.893	80	150	12	no
Bowie	LP 151 SB @ SH 93	2050-03	#13	33 24.021	-94 5.896	80	150	12	no
Bowie	LP 151 SB @ US 67	0218-01	#9	33 25.086	-94 6.203	80	150	12	no
Bowie	LP 151 SB @ US 82 WB	0218-02	#1	33 26.756	-94 5.895	80	150	12	no
Bowie	LP 151 SB @ Wake Village	0218-01	#7	33 25.666	-94 5.739	80	150	12	no
Bowie	LP 151 SB @ Wake Village Exit	0218-01	#2	33 26.301	-94 5.827	80	150	12	no
Bowie	LP 151 SB South of US 82	0218-02	#3	33 26.451	-94 5.810	80	150	12	no
Bowie	Sta 111+85	0610-07-085	HM-51			80	150	12	no
Bowie	Sta 2189+84	0610-07-085	HM-01	33 27.317	-94 8.342	80	150	12	no
Bowie	Sta 2198+94	0610-07-085	HM-02	33 27.298	-94 8.161	80	150	12	no
Bowie	Sta 2213+97	0610-07-085	HM-04	33 27.279	-94 7.816	80	150	12	no
Bowie	Sta 2221+61	0610-07-085	HM-05			80	150	12	no
Bowie	Sta 2229+71	0610-07-085	HM-06	33 27.202	-94 7.569	80	150	12	no
Bowie	Sta 2238+70	0610-07-085	HM-07	33 27.206	-94 7.388	80	150	12	no
Bowie	Sta 2248+13	0610-07-085	HM-08	33 27.160	-94 7.210	80	150	12	no
Bowie	Sta 2256+16	0610-07-085	HM-09			80	150	12	no
Bowie	Sta 2265+31	0610-07-085	HM-10			80	150	12	no
Bowie	Sta 2274+33	0610-07-085	HM-11	33 27.130	-94 6.692	80	150	12	no
Bowie	Sta 2281+31	0610-07-085	HM-12	33 27.184	-94 6.664	80	150	12	no
Bowie	Sta 2283+48	0610-07-085	HM-60	33 27.138	-94 6.518	80	150	12	no
Bowie	Sta 2295	0610-07-085	RHM-01	33 27.124	-94 6.295	80	150	12	yes
Bowie	Sta 2305	0610-07-085	RHM-02			80	150	12	no
Bowie	Sta 2310	0610-07-085	RHM-03	33 27.162	-94 5.987	80	150	12	yes

Figure 3.53: TxDOT HMIP Inventory – Atlanta District

County	Highway(s)	Control & Section	HQ Pole Number	GPS		Wind Speed Rating (mph)	Pole Height (ft)	# Sides	Ground Sleeve
				Latitude	Longitude				
Bowie	Sta 2317	0610-07-085	RHM-04	33 27.143	-94 5.821	80	150	12	yes
Bowie	Sta 2337+90	0610-07-085	HM-23*			80	150	12	no
Bowie	Sta 2347+97	0610-07-085	HM-24*	33 27.279	-94 5.395	80	150	12	yes
Bowie	Sta 2347+98	0610-07-085	HM-61*	33 27.358	-94 5.351	80	150	12	no
Bowie	Sta 2354+00	0610-07-085	HM-25	33 27.360	-94 5.221	80	150	12	yes
Bowie	Sta 2354+50	0610-07-085	HM-62*	33 27.328	-94 5.187	80	150	12	no
Bowie	Sta 2355+90	0610-07-085	HM-63*			80	150	12	no
Bowie	Sta 2362+41	0610-07-085	HM-26	33 27.411	-94 5.062	80	150	12	no
Bowie	Sta 2362+42	0610-07-085	HM-64	33 27.459	-94 5.093	80	150	12	no
Bowie	Sta 2370+85	0610-07-085	HM-27*	33 27.550	-94 5.122	80	150	12	yes
Bowie	Sta 2379+94	0610-07-085	HM-28	33 27.638	-94 4.775	80	150	12	no
Bowie	Sta 2389+32	0610-07-085	HM-29	33 27.678	-94 4.619	80	150	12	no
Bowie	Sta 2396+49	0610-07-085	HM-30	33 27.687	-94 4.480	80	150	12	no
Bowie	Sta 2403+46	0610-07-085	HM-31	33 27.774	-94 4.377	80	150	12	no
Bowie	Sta 2411+32	0610-07-085	HM-32	33 27.783	-94 4.248	80	150	12	yes
Bowie	Sta 2423+23	0610-07-085	HM-34	33 27.893	-94 4.022	80	150	12	yes
Bowie	Sta 2432+20	0610-07-085	HM-35	33 27.966	-94 3.861	80	150	12	no
Bowie	Sta 2441+97	0610-07-085	HM-36*	33 28.071	-94 3.706	80	150	12	yes
Bowie	Sta 2451+04	0610-07-085	HM-37	33 28.128	-94 3.538	80	150	12	no
Bowie	Sta 2460+04	0610-07-085	HM-38			80	150	12	no
Bowie	Sta 2469+38	0610-07-085	HM-39	33 28.1241	-94 2.876	80	150	12	no
Bowie	Sta 2478+94	0610-07-085	HM-40	33 28.199	-94 3.001	80	150	12	no
Bowie	Sta 2484+96	0610-07-085	HM-41	33 28.232	-94 2.845	80	150	12	no
Bowie	Sta 2490+56	0610-07-085	HM-42	33 28.290	-94 2.751	80	150	12	no
Bowie	Sta 2497+91	0610-07-085	HM-43	33 28.234	-94 2.626	80	150	12	no
Bowie	Sta 42+00	0610-07-085	RHM-11			80	150	12	no
Bowie	Sta2206+75	0610-07-085	HM-03			80	150	12	no
Bowie	US 59 @ LP 151	0218-01	#23	33 23.489	-94 6.184	80	150	12	no
Cass	US 59 @ SH 43	218-4	#24	33 08.091	-94 9 826	80	150	12	no
Bowie	US 59 NB @ LP 151 South Side	2050-03	#11	33 23.640	-94 5.944	80	150	12	no
Harrison	US 80 & LP 281 N of US 80	2642-2	#25	32 30.289	94 40.342	80	150	12	yes
Harrison	US 80 & LP 281 S of US 80	2642-2	#26	32 30.165	94 40.377	80	150	12	yes
Bowie	LP 151 North of FM 3527	2050-03	#20	33 23.284	-94 5.721	80	175	12	no
Bowie	SH 93 @ LP 151 NB	2050-03	#14	33 23.753	-94 5.864	80	175	12	no
Bowie	Sta 108+83	0610-07-085	HM-50			80	175	12	no
Bowie	Sta 2292+17	0610-07-085	HM-13			80	175	12	no
Bowie	Sta 2298+39	0610-07-085	HM-14	33 27.127	-94 6.223	80	175	12	no
Bowie	Sta 2305+57	0610-07-085	HM-15	33 27.195	-94 6.094	80	175	12	no
Bowie	Sta 2307+18	0610-07-085	HM-16			80	175	12	no
Bowie	Sta 2311+71	0610-07-085	HM-17			80	175	12	no
Bowie	Sta 2313+64	0610-07-085	HM-18			80	175	12	no
Bowie	Sta 2316+64	0610-07-085	HM-19	33 27.137	-94 5.863	80	175	12	no
Bowie	Sta 2319+27	0610-07-085	HM-20	33 27.102	-94 5.824	80	175	12	no
Bowie	Sta 2324+50	0610-07-085	HM-21			80	175	12	no
Bowie	Sta 2330+83	0610-07-085	HM-22	33 27.199	-94 5.694	80	175	12	no
Bowie	US 59 NB @ LP 151 Exit Ramp	0218-01	#22	33 23.574	-94 6.050	80	175	12	no

Figure 3.54: TxDOT HMIP Inventory – Atlanta District - Cont'd

County	Highway(s)	Control & Section	HQ Pole Number	GPS		Wind Speed Rating (mph)	Pole Height (ft)	# Sides	Ground Sleeve
				Latitude	Longitude				
Jefferson	US 69	200-15	A-D-1	30.02	-94.05	100	125	12	no
Jefferson	US 69	200-15	A-D-2	30.02	-94.05	100	125	12	no
Jefferson	US 69	200-15	A-D-3	30.02	-94.05	100	125	12	no
Jefferson	US 69	200-15	A-D-4	30.02	-94.05	100	125	12	no
Jefferson	US 69	200-15	A-E-1	30.02	-94.05	100	125	12	no
Jefferson	US 69	200-15	A-E-2	30.02	-94.05	100	125	12	no
Jefferson	US 69	200-15	A-E-3	30.02	-94.05	100	125	12	no
Jefferson	US 69	200-15	A-E-4	30.01	-94.05	100	125	12	no
Jefferson	US 69	200-15	A-F-1	30.01	-94.05	100	125	12	no
Jefferson	US 69	200-15	A-F-2	30.01	-94.04	100	125	12	no
Jefferson	US 69	200-15	A-F-3	30.01	-94.04	100	125	12	no
Jefferson	US 69	200-15	A-G-1	30.01	-94.04	100	125	12	no
Jefferson	US 69	200-15	A-G-2	30.01	-94.04	100	125	12	no
Jefferson	US 69	200-15	A-G-3	30.00	-94.04	100	125	12	no
Jefferson	US 69	200-15	A-G-4	30.00	-94.04	100	125	12	no
Jefferson	US 69	200-15	A-H-1	29.98	-94.03	100	125	12	no
Jefferson	US 69	200-15	A-H-2	29.98	-94.03	100	125	12	no
Jefferson	US 69	200-15	A-H-3	29.98	-94.03	100	125	12	no
Jefferson	US 69	200-15	A-H-4	29.98	-94.03	100	125	12	no
Jefferson	US 69	200-15	A-H-5	29.98	-94.03	100	125	12	no
Jefferson	US 69	200-15	A-I-1	29.98	-94.03	100	125	12	no
Jefferson	US 69	200-15	A-I-2	29.97	-94.02	100	125	12	no
Jefferson	US 69	200-15	A-I-3	29.97	-94.02	100	125	12	no
Jefferson	US 69	200-15	A-K-1	30.00	-94.04	100	125	12	no
Jefferson	US 69	200-15	A-K-2	30.00	-94.04	100	125	12	no
Jefferson	US 69	200-15	A-K-3	30.00	-94.04	100	125	12	no
Jefferson	US 69	200-15	A-P-1	29.99	-94.03	100	125	12	no
Jefferson	US 69	200-15	A-P-2	29.99	-94.04	100	125	12	no
Jefferson	US 69	200-15	A-X-1	29.98	-94.03	100	125	12	no
Jefferson	US 69	200-15	A-X-2	29.99	-94.03	100	125	12	no
Chambers	IH 10	508-3	I-B-1	29.83	-94.38	100	150	12	yes
Chambers	IH 10	508-3	I-B-2	29.83	-94.38	100	150	12	yes
Chambers	IH 10	508-3	I-B-3	29.83	-94.39	100	150	12	yes
Chambers	IH 10	508-3	I-C-1	29.83	-94.39	100	150	12	yes
Chambers	IH 10	508-3	I-C-2	29.83	-94.39	100	150	12	yes
Chambers	IH 10	508-3	I-C-3	29.83	-94.39	100	150	12	yes
Chambers	IH 10	508-3	I-C-4	29.83	-94.39	100	150	12	yes
Chambers	IH 10	508-3	I-C-5	29.83	-94.39	100	150	12	yes
Chambers	IH 10	508-3	I-D-1	29.83	-94.40	100	150	12	yes
Chambers	IH 10	508-3	I-D-2	29.83	-94.40	100	150	12	yes
Orange	IH 10	28-14	E-N-1	30.12	-93.83	100	150	12	no
Orange	IH 10	28-14	E-N-2	30.12	-93.82	100	150	12	no
Orange	IH 10	28-14	E-O-1	30.12	-93.82	100	150	12	no
Orange	IH 10	28-14	E-P-1	30.12	-93.82	100	150	12	no
Orange	IH 10	28-14	E-P-2	30.11	-93.82	100	150	12	no
Orange	IH 10	28-14	E-P-3	30.11	-93.81	100	150	12	no
Orange	IH 10	28-14	E-S-1	30.11	-93.81	100	150	12	no
Orange	IH 10	28-14	E-S-2	30.11	-93.81	100	150	12	no
Orange	IH 10	28-14	E-S-3	30.11	-93.81	100	150	12	no
Hardin	US 96	65-4	W-A-1	30.36	-94.07	100	150	12	no
Hardin	US 97	65-4	W-A-2	30.36	-94.07	100	150	12	no
Hardin	US 98	65-4	W-B-1	30.36	-94.08	100	150	12	no
Hardin	US 99	65-4	W-B-2	30.36	-94.08	100	150	12	no
Hardin	US 100	65-4	W-C-1	30.36	-94.07	100	150	12	no
Hardin	US 101	65-4	W-C-2	30.36	-94.07	100	150	12	no
Hardin	US 102	65-4	W-D-1	30.36	-94.07	100	150	12	no
Hardin	US 103	65-4	W-D-2	30.36	-94.07	100	150	12	no
Hardin	US 104	65-4	W-E-1	30.36	-94.07	100	150	12	no
Hardin	US 105	65-4	W-E-2	30.36	-94.06	100	150	12	no

Figure 3.55: TxDOT HMIP Inventory – Beaumont District

County	Highway(s)	Control & Section	HQ Pole Number	GPS		Wind Speed Rating (mph)	Pole Height (ft)	# Sides	Ground Sleeve
				Latitude	Longitude				
Cameron	US 77/83	0039-07	3.D	26.11	-97.60	100	150	12	no
Cameron	US 77/83	0039-07	2.D	26.11	-97.61	100	150	12	no
Cameron	US 77/83	0039-07	1.D	26.11	-97.61	100	150	12	no
Cameron	US 77/83	0039-07/0039-19	16.E	26.18	-97.72	100	150	12	no
Cameron	US 77/83	0039-07/0039-19	9.E	26.19	-97.72	100	150	12	yes
Cameron	US 77/83	0039-07/0039-19	8.E	26.19	-97.72	100	150	12	yes
Cameron	US 77/83	0039-07/0039-19	10.E	26.19	-97.72	100	150	12	yes
Cameron	US 77/83	0039-07/0039-19	12.E	26.19	-97.72	100	150	12	yes
Cameron	US 77/83	0039-07/0039-19	13.E	26.19	-97.72	100	150	12	yes
Cameron	US 77/83	0039-19	7.H	26.19	-97.72	100	150	12	yes
Cameron	US 77/83	0039-07/0039-19	14.E	26.20	-97.72	100	150	12	yes
Cameron	US 77/83	0039-19	11.H	26.19	-97.72	100	150	12	yes
Cameron	US 77/83	0039-07/0039-19	15.E	26.20	-97.72	100	150	12	yes
Cameron	US 77/83	0039-19	6.H	26.19	-97.72	100	150	12	yes
Cameron	US 77/83	0039-19	5.H	26.19	-97.72	100	150	12	yes
Cameron	US 77/83	0039-06 / 0039-19	4.B	26.19	-97.73	100	150	12	yes
Cameron	US 77/83	0039-06 / 0039-19	3.B	26.19	-97.73	100	150	12	yes
Cameron	US 77/83	0039-06 / 0039-19	2.B	26.19	-97.73	100	150	12	yes
Cameron	US 77/83	0039-06 / 0039-19	1.B	26.19	-97.73	100	150	12	yes
Hidalgo	US 281 (SH 186/ FM 1017)	0255-07	43	26.56	-98.12	100	150	12	no
Hidalgo	US 281 (SH 186/ FM 1017)	0255-07	46	26.55	-98.12	100	150	12	no
Hidalgo	US 281 (SH 186/ FM 1017)	0255-07	40	26.57	-98.12	100	150	12	no
Hidalgo	US 281 (SH 186/ FM 1017)	0255-07	49	26.55	-98.12	100	150	12	no
Hidalgo	US 281 (SH 186/ FM 1017)	0255-07	41	26.57	-98.12	100	150	12	no
Hidalgo	US 281 (SH 186/ FM 1017)	0255-07	45	26.56	-98.12	100	150	12	no
Hidalgo	US 281 (SH 186/ FM 1017)	0255-07	44	26.56	-98.12	100	150	12	no
Hidalgo	US 281 (SH 186/ FM 1017)	0255-07	42	26.56	-98.12	100	150	12	no
Hidalgo	US 281 (SH 186/ FM 1017)	0255-07	47	26.55	-98.12	100	150	12	no
Hidalgo	US 281 (SH 186/ FM 1017)	0255-07	48	26.55	-98.12	100	150	12	no
Hidalgo	US 281 (FM 162 / Cibolo)	0255-07	60	26.43	-98.14	100	150	12	no
Hidalgo	US 281 (FM 162 / Cibolo)	0255-07	61	26.42	-98.14	100	150	12	no
Hidalgo	US 281 (FM 162 / Cibolo)	0255-07	63	26.42	-98.14	100	150	12	no
Hidalgo	US 281 (FM 162 / Cibolo)	0255-07	62	26.42	-98.14	100	150	12	no
Hidalgo	US 281 (FM 162 / Cibolo)	0255-07	64	26.42	-98.14	100	150	12	no
Hidalgo	US 281 (FM 162 / Cibolo)	0255-07	65	26.41	-98.14	100	150	12	no
Hidalgo	US 281 (FM 162 / Cibolo)	0255-07	66	26.41	-98.14	100	150	12	no
Hidalgo	US 281 (FM 162 / Cibolo)	0255-07	67	26.41	-98.14	100	150	12	no
Hidalgo	US 83/US 281 Interchange	0039-17	12.G	26.20	-98.17	100	150	12	no
Hidalgo	US 83/US 281 Interchange	0039-17	10.G	26.21	-98.17	100	150	12	yes
Hidalgo	US 83/US 281 Interchange	0039-17	9.G	26.21	-98.17	100	150	12	yes
Hidalgo	US 281	0255-08	1.K	26.25	-98.17	100	150	12	no
Hidalgo	US 281	0255-08	3.K	26.25	-98.17	100	150	12	no
Hidalgo	US 83/US 281 Interchange	0039-17	8.G	26.21	-98.18	100	150	12	yes
Hidalgo	US 281	0255-08	4.K	26.25	-98.18	100	150	12	no
Hidalgo	US 281	0255-08	2.K	26.25	-98.18	100	150	12	no
Hidalgo	US 83/US 281 Interchange	0039-17	7.G	26.21	-98.18	100	150	12	yes
Hidalgo	US 83/US 281 Interchange	0039-17	6.G	26.21	-98.18	100	150	12	yes
Hidalgo	US 83/US 281 Interchange	0039-17	11.G	26.21	-98.18	100	150	12	yes
Hidalgo	US 83/US 281 Interchange	0039-17	4.G	26.21	-98.18	100	150	12	yes
Hidalgo	US 83/US 281 Interchange	0039-17	5.G	26.21	-98.18	100	150	12	yes
Hidalgo	US 83/US 281 Interchange	0039-17	3.G	26.21	-98.19	100	150	12	yes
Hidalgo	US 83/US 281 Interchange	0039-17	2.G	26.21	-98.19	100	150	12	yes
Hidalgo	US 83/US 281 Interchange	0039-17	1.G	26.21	-98.19	100	150	12	yes
Hidalgo	US 281 (Spur 241/ Spur 600) Military	0225-09	6.J	26.09	-98.19	100	150	12	no
Hidalgo	US 83/US 281 Interchange	0039-17	13.G	26.21	-98.20	100	150	12	yes
Hidalgo	US 281 (Spur 241/ Spur 600) Military	0225-09	5.J	26.09	-98.20	100	150	12	no
Hidalgo	US 83/US 281 Interchange	0039-17	14.G	26.20	-98.20	100	150	12	yes
Hidalgo	US 281 (Spur 241/ Spur 600) Military	0225-09	4.J	26.09	-98.20	100	150	12	no
Hidalgo	US 281 (Spur 241/ Spur 600) Military	0225-09	3.J	26.09	-98.20	100	150	12	no
Hidalgo	US 281 (Spur 241/ Spur 600) Military	0225-09	2.J	26.09	-98.20	100	150	12	no
Hidalgo	US 281 (Spur 241/ Spur 600) Military	0255-09	1.J	26.10	-98.21	100	150	12	no
Hidalgo	US 83 and Bicentennial	0039-17	1.F	26.19	-98.24	100	150	12	yes
Hidalgo	Spur 115 and FM 1016	1804-02	1.L	26.16	-98.25	100	150	12	yes
Hidalgo	Spur 115 and FM 1016	1804-02	3.L	26.15	-98.25	100	150	12	yes
Hidalgo	Spur 115 and FM 1016	1804-02	4.L	26.15	-98.25	100	150	12	yes
Hidalgo	Spur 115 and FM 1016	1804-02	2.L	26.15	-98.25	100	150	12	yes
Starr	US 83 and FM 2359	0039-01	1.A	26.31	-98.63	100	150	12	yes
Starr	US 83 and FM 2360	0039-01	2.A	26.31	-98.64	100	150	12	yes
Starr	US 83 and FM 2360	0039-01	3.A	26.31	-98.65	100	150	12	yes
Starr	US 83 and FM 2360	0039-01	4.A	26.31	-98.65	100	150	12	yes

Figure 3.56: TxDOT HMIP Inventory – Pharr District

County	Highway(s)	Control & Section	HQ Pole Number	GPS		Wind Speed Rating (mph)	Pole Height (ft)	# sides	Ground Sleeve
				Latitude	Longitude				
Webb	US 83/SH 359	0038-01-033	1.D	27.50	-99.47	80	150	12	yes
Webb	US 83/SH 359	0038-01-033	2.D	27.50	-99.47	80	150	12	yes
Webb	US 83/SH 359	0038-01-033	3.D	27.50	-99.47	80	150	12	yes
Webb	US 83/SH 359	0038-01-033	4.D	27.50	-99.47	80	150	12	yes
Webb	IH 35	0018-06-104	1	27.51	-99.50	80	150	12	yes
Webb	IH 35	0018-06-104	2	27.51	-99.50	80	150	12	yes
Webb	IH 35	0018-06-104	3	27.52	-99.50	80	150	12	yes
Webb	IH 35	0018-06-104	4	27.52	-99.50	80	150	12	yes
Webb	IH 35	0018-06-104	5	27.52	-99.50	80	150	12	yes
Webb	IH-35 & SH-255	0922-33-014	5.E	27.52	-99.50	80	150	12	no
Webb	IH 35	0018-06-104	6	27.52	-99.55	80	150	12	yes
Webb	IH-35 & SH-255	0922-33-014	6.E	27.52	-99.55	80	150	12	no
Webb	IH 35	0018-06-104	7	27.53	-99.50	80	150	12	yes
Webb	IH-35 & SH-255	0922-33-014	7.E	27.53	-99.50	80	150	12	no
Webb	IH 35	0018-06-104	8	27.53	-99.50	80	150	12	yes
Webb	IH-35 & SH-255	0922-33-014	8.E	27.53	-99.50	80	150	12	no
Webb	IH 35	0018-06-104	9	27.53	-99.50	80	150	12	yes
Webb	IH 35	0018-06-104	10	27.53	-99.50	80	150	12	yes
Webb	IH 35	0018-06-104	11	27.54	-99.50	80	150	12	yes
Webb	IH 35	0018-06-104	12	27.54	-99.50	80	150	12	yes
Webb	IH 35	0018-06-104	13	27.54	-99.50	80	150	12	yes
Webb	IH 35	0018-06-104	14	27.54	-99.50	80	150	12	yes
Webb	IH 35	0018-06-104	15	27.54	-99.50	80	150	12	yes
Webb	IH 35	0018-06-104	16	27.55	-99.50	80	150	12	yes
Webb	IH 35	0018-06-104	17	27.55	-99.50	80	150	12	yes
Webb	IH 35	0018-06-104	18	27.55	-99.50	80	150	12	yes
Webb	IH 35	0018-06-104	19	27.55	-99.50	80	150	12	yes
Webb	IH 35	0018-06-104	20	27.56	-99.50	80	150	12	yes
Webb	IH 35	0018-06-104	21	27.56	-99.50	80	150	12	yes
Webb	IH 35	0018-06-104	22	27.56	-99.50	80	150	12	yes
Webb	IH 35	0018-06-104	23	27.56	-99.50	80	150	12	yes
Webb	IH 35	0018-06-104	25	27.57	-99.50	80	150	12	yes
Webb	IH 35	0018-06-104	26	27.57	-99.50	80	150	12	yes
Webb	IH 35	0018-06-104	27	27.57	-99.50	80	150	12	yes
Webb	IH 35	0018-06-104	28	27.58	-99.50	80	150	12	yes
Webb	IH 35	0018-06-104	29	27.58	-99.50	80	150	12	yes
Webb	IH 35	0018-06-104	30	27.58	-99.50	80	150	12	yes
Webb	IH 35	0018-06-104	31	27.58	-99.50	80	150	12	yes
Webb	IH 35	0018-06-104	32	27.58	-99.50	80	150	12	yes
Webb	IH 35	0018-06-104	33	27.59	-99.50	80	150	12	yes
Webb	IH 35	0018-06-104	34	27.59	-99.50	80	150	12	yes
Webb	IH 35	0018-06-104	35	27.59	-99.50	80	150	12	yes
Webb	IH 35	0018-06-104	36	27.59	-99.49	80	150	12	yes
Webb	IH 35	0018-06-104	37	27.60	-99.49	80	150	12	yes
Webb	Loop 20	3483-01-010	3.G	27.60	-99.52	80	150	12	yes
Webb	Loop 20	3483-01-010	2.G	27.60	-99.52	80	150	12	yes
Webb	Loop 20	3483-01-010	1.G	27.60	-99.53	80	150	12	yes
Webb	Loop 20	3483-01-010	4.G	27.60	-99.52	80	150	12	yes

Figure 3.57: TxDOT HMIP Inventory – Laredo District

County	Highway(s)	Control & Section	HQ Pole Number	GPS		Wind Speed Rating (mph)	Pole Height (ft)	# sides	Ground Sleeve
				Latitude	Longitude				
Webb	IH 35	0018-06-131	46	27.60	-99.50	80	150	12	no
Webb	Loop 20	3483-01-010	5.G	27.60	-99.52	80	150	12	yes
Webb	Loop 20	3483-01-010	6.G	27.60	-99.53	80	150	12	yes
Webb	IH 35	0018-06-131	28.H	27.60	-99.50	80	150	12	no
Webb	Loop 20	3483-01-010	7.G	27.60	-99.51	80	150	12	yes
Webb	Loop 20/IH 35	0018-06-131	19.B	27.60	-99.50	80	150	12	no
Webb	Loop 20	3483-01-010	8.G	27.60	-99.51	80	150	12	yes
Webb	Loop 20	3483-01-010	9.G	27.60	-99.51	80	150	12	yes
Webb	IH 35	0018-06-131	13.H	27.60	-99.49	80	150	12	no
Webb	Loop 20	3483-01-010	10.G	27.61	-99.51	80	150	12	yes
Webb	IH 35	0018-06-131	31.H	27.61	-99.49	80	150	12	no
Webb	Loop 20	0018-06-131	36.A	27.61	-99.49	80	150	12	no
Webb	Loop 20/IH 35	0018-06-131	20.B	27.61	-99.50	80	150	12	no
Webb	Loop 20	0018-06-131	38.A	27.61	-99.49	80	150	12	no
Webb	Loop 20	3483-01-010	11.G	27.61	-99.50	80	150	12	no
Webb	Loop 20	0018-06-131	34.A	27.61	-99.49	80	150	12	no
Webb	Loop 20	0018-06-131	32.A	27.61	-99.49	80	150	12	no
Webb	Loop 20	0018-06-131	40.A	27.61	-99.48	80	150	12	no
Webb	Loop 20/IH 35	0018-06-131	30.B	27.61	-99.49	80	150	12	no
Webb	Loop 20	0018-06-131	37.A	27.61	-99.49	80	150	12	no
Webb	Loop 20	3483-01-010	12.G	27.61	-99.50	80	150	12	no
Webb	Loop 20	0018-06-131	39.A	27.61	-99.49	80	150	12	no
Webb	Loop 20	0018-06-131	35.A	27.61	-99.49	80	150	12	no
Webb	Loop 20	0018-06-131	12.A	27.61	-99.50	80	150	12	no
Webb	Loop 20	0018-06-131	33.A	27.61	-99.49	80	150	12	no
Webb	Loop 20/IH 35	0018-06-131	21.B	27.61	-99.50	80	150	12	no
Webb	Loop 20	0018-06-131	42.A	27.61	-99.48	80	150	12	no
Webb	Loop 20/IH 35	0018-06-131	15.B	27.61	-99.50	80	150	12	no
Webb	Loop 20/IH 35	0018-06-131	18.B	27.61	-99.50	80	150	12	no
Webb	Loop 20	0018-06-131	41.A	27.61	-99.48	80	150	12	no
Webb	Loop 20/IH 35	0018-06-131	29.B	27.61	-99.49	80	150	12	no
Webb	Loop 20	0018-06-131	14.A	27.61	-99.50	80	150	12	no
Webb	IH 35	0018-06-131	22.H	27.61	-99.50	80	150	12	no
Webb	IH 35	0018-06-131	17.H	27.61	-99.50	80	150	12	no
Webb	Loop 20	0018-06-131	44.A	27.61	-99.48	80	150	12	no
Webb	Loop 20	0018-06-131	43.A	27.61	-99.48	80	150	12	no
Webb	Loop 20	0018-06-131	16.A	27.61	-99.50	80	150	12	no
Webb	IH 35	0018-06-131	23.H	27.61	-99.49	80	150	12	no
Webb	Loop 20	0018-06-131	45.A	27.61	-99.48	80	150	12	no
Webb	IH 35	0018-06-131	27.H	27.61	-99.49	80	150	12	no
Webb	IH 35	0018-06-131	24.H	27.61	-99.49	80	150	12	no
Webb	IH 35	0018-06-131	26.H	27.61	-99.49	80	150	12	no
Webb	IH 35	0018-06-131	25.H	27.61	-99.49	80	150	12	no
Webb	IH 35	0018-06-131	48	27.61	-99.49	80	150	12	no
Webb	IH 35	0018-06-131	47	27.62	-99.49	80	150	12	no
Webb	IH 35	0018-06-131	49	27.62	-99.49	80	150	12	no
Webb	SH 255 Transfer yard	0922-33-014	2.F	27.73	-99.70	80	150	12	no
Webb	SH 255 Transfer yard	0922-33-014	3.F	27.73	-99.70	80	150	12	no
Webb	CCTR Transfer yard	0922-33-014	1.F	27.73	-99.70	80	150	12	no
Webb	IH-35 & SH-255	0922-33-014	1.E	27.83	-99.41	80	150	12	no
Webb	IH-35 & SH-255	0922-33-014	2.E	27.83	-99.41	80	150	12	no
Webb	IH-35 & SH-255	0922-33-014	3.E	27.83	-99.41	80	150	12	no
Webb	IH-35 & SH-255	0922-33-014	4.E	27.83	-99.41	80	150	12	no

Figure 3.58: TxDOT HMIP Inventory – Laredo District - Cont'd

County	Highway(s)	Control & Section	HQ Pole Number	GPS		Wind Speed Rating (mph)	Pole Height (ft)	# Sides	Ground Sleeve
				Latitude	Longitude				
Eastland	I 20 / US 183	0923-09-046	183A	32.37	-98.98	80	150	12	no
Eastland	I 20 / US 183	0923-09-046	183B	32.37	-98.97	80	150	12	no
Eastland	I 20 / US 183	0923-09-046	183C	32.37	-98.97	80	150	12	no
Eastland	I 20 / US 183	0923-09-046	183D	32.37	-98.97	80	150	12	no
Eastland	I 20 / US 183	0923-09-046	183E	32.37	-98.97	80	150	12	no
Eastland	I 20 / US 183	0923-09-046	183F	32.37	-98.97	80	150	12	no
Eastland	I 20 / US 570	0923-09-039	570A	32.40	-98.79	80	150	12	no
Eastland	I 20 / US 570	0923-09-039	570B	32.40	-98.79	80	150	12	no
Eastland	I 20 / US 570	0923-09-039	570C	32.40	-98.79	80	150	12	no
Eastland	I 20 / US 570	0923-09-039	570D	32.40	-98.79	80	150	12	no
Eastland	I 20 / US 570	0923-09-039	570E	32.40	-98.79	80	150	12	no
Eastland	I 20 / US 570	0923-09-039	570F	32.40	-98.79	80	150	12	no
Eastland	I 20 / US 570	0923-09-039	570G	32.40	-98.78	80	150	12	no
Eastland	I 20 / FM 2461	0923-09-039	2461A	32.44	-98.70	80	150	12	no
Eastland	I 20 / FM 2461	0923-09-039	2461B	32.44	-98.70	80	150	12	no
Eastland	I 20 / FM 2461	0923-09-039	2461C	32.44	-98.70	80	150	12	no
Eastland	I 20 / FM 2461	0923-09-039	2461D	32.44	-98.70	80	150	12	no
Eastland	I 20 / FM 2461	0923-09-039	2461E	32.44	-98.69	80	150	12	no
Eastland	I 20 / FM 2461	0923-09-039	2461F	32.44	-98.69	80	150	12	no
Eastland	I 20 / FM 2461	0923-09-039	2461G	32.44	-98.69	80	150	12	no

Figure 3.59: TxDOT HMIP Inventory – Brownwood District

County	Highway(s)	Control & Section	HQ Pole Number	GPS		Wind Speed Rating (mph)	Pole Height (ft)	# Sides	Ground Sleeve
				Latitude	Longitude				
El Paso	US-54	0924-00-036	35	31.77	-106.45	80	100	12	no
El Paso	US-54	0924-00-036	36	31.77	-106.45	80	100	12	no
El Paso	US-54	0924-00-036	37	31.77	-106.45	80	100	12	no
El Paso	LP-0375	2552-2	67	31.70	-106.29	80	100	12	no
El Paso	LP-0375	2552-2	68	31.70	-106.29	80	100	12	no
El Paso	LP-0375	2552-2	69	31.70	-106.29	80	100	12	no
El Paso	LP-0375	2552-2	70	31.70	-106.29	80	100	12	no
El Paso	LP-0375	BSIF	71	31.67	-106.33	80	100	12	yes
El Paso	LP-0375	BSIF	72	31.67	-106.33	80	100	12	yes
El Paso	LP-0375	BSIF	73	31.66	-106.33	80	100	12	yes
El Paso	LP-0375	BSIF	74	31.66	-106.33	80	100	12	yes
El Paso	LP-0375	BSIF	75	31.66	-106.33	80	100	12	yes
El Paso	IH-10	2121-02-114	4	31.76	-106.49	80	125	12	no
El Paso	IH-10	2121-02-114	9	31.75	-106.49	80	125	12	no
El Paso	IH-10	2121-02-114	11	31.76	-106.50	80	125	12	no
El Paso	IH-10	2121-02-114	1	31.78	-106.45	80	150	12	no
El Paso	IH-10	2121-02-114	2	31.78	-106.45	80	150	12	no
El Paso	IH-10	2121-02-114	3	31.77	-106.48	80	150	12	no
El Paso	IH-10	2121-02-114	5	31.77	-106.51	80	150	12	no
El Paso	IH-10	2121-02-114	6	31.77	-106.51	80	150	12	no
El Paso	IH-10	2121-02-114	7	31.77	-106.51	80	150	12	no
El Paso	IH-10	2121-02-114	8	31.76	-106.50	80	150	12	no
El Paso	IH-10	2121-02-114	10	31.76	-106.50	80	150	12	no
El Paso	IH-10	2121-02-114	12	31.77	-106.47	80	150	12	no
El Paso	IH-10	2121-02-114	13	31.78	-106.46	80	150	12	no
El Paso	IH-10	2121-02-114	14	31.78	-106.43	80	150	12	no
El Paso	IH-10	2121-02-114	15	31.77	-106.46	80	150	12	no
El Paso	IH-10	2121-02-114	16	31.77	-106.45	80	150	12	no
El Paso	IH-10	2121-02-114	17	31.78	-106.47	80	150	12	no
El Paso	IH-10	2121-02-114	18	31.77	-106.48	80	150	12	no
El Paso	IH-10	2121-02-114	19	31.77	-106.51	80	150	12	no
El Paso	IH-10	2121-02-114	23	31.76	-106.50	80	150	12	no
El Paso	IH-10	2121-02-114	24	31.75	-106.50	80	150	12	no
El Paso	IH-10	2121-02-114	25	31.76	-106.49	80	150	12	no
El Paso	IH-10	2121-02-114	28	31.77	-106.48	80	150	12	no
El Paso	IH-10	2121-02-114	29	31.77	-106.48	80	150	12	no
El Paso	IH-10	2121-02-114	30	31.77	-106.43	80	150	12	yes
El Paso	IH-10	2552-01-029	31	31.91	-106.58	80	150	12	no
El Paso	IH-10	2552-01-029	32	31.91	-106.58	80	150	12	no
El Paso	IH-10	2552-01-029	33	31.91	-106.58	80	150	12	no
El Paso	IH-10	2552-01-029	34	31.91	-106.58	80	150	12	no

Figure 3.60: TxDOT HMIP Inventory – El Paso District

County	Highway(s)	Control & Section	HQ Pole Number	GPS		Wind Speed Rating (mph)	Pole Height (ft)	# Sides	Ground Sleeve
				Latitude	Longitude				
El Paso	US-54	0167-01-082	38	31.77	-106.44	80	150	12	no
El Paso	US-54	0167-01-081	39	31.83	-106.44	80	150	12	no
El Paso	US-54	0167-01-081	40	31.82	-106.44	80	150	12	no
El Paso	US-54	0167-01-081	41	31.82	-106.43	80	150	12	no
El Paso	US-54	0167-01-081	42	31.83	-106.44	80	150	12	no
El Paso	US-54	0167-01-081	43	31.83	-106.44	80	150	12	no
El Paso	US-54	0167-01-081	44	31.83	-106.44	80	150	12	no
El Paso	US-54	0167-01-081	45	31.84	-106.44	80	150	12	no
El Paso	US-54	0167-01-081	46	31.83	-106.44	80	150	12	no
El Paso	US-54	0167-01-081	47	31.84	-106.44	80	150	12	no
El Paso	US-54	0167-01-081	48	31.84	-106.44	80	150	12	no
El Paso	US-54	0167-01-081	49	31.84	-106.44	80	150	12	no
El Paso	US-54	0167-01 081	50	31.85	-106.44	80	150	12	no
El Paso	US-54	0167-01-081	51	31.85	-106.44	80	150	12	no
El Paso	US-54	0167-01-081	52	31.85	-106.44	80	150	12	no
El Paso	US-54	0167-01-081	53	31.85	-106.44	80	150	12	no
El Paso	US-54	0167-01-081	54	31.85	-106.44	80	150	12	no
El Paso	US-54	0167-01-081	55	31.86	-106.44	80	150	12	no
El Paso	US-54	0167-01-081	56	31.85	-106.44	80	150	12	no
El Paso	US-54	0167-01-081	57	31.86	-106.44	80	150	12	no
El Paso	US-54	0167-01-081	58	31.87	-106.44	80	150	12	no
El Paso	US-54	0167-01-081	59	31.81	-106.44	80	150	12	no
El Paso	US-54	0167-01-081	60	31.86	-106.44	80	150	12	no
El Paso	US-54	0167-01-081	61	31.82	-106.44	80	150	12	no
El Paso	US-54	0167-01-081	62	31.87	-106.44	80	150	12	no
El Paso	US-54	0167-01-081	63	31.87	-106.44	80	150	12	no
El Paso	US-54	0167-01-081	64	31.84	-106.44	80	150	12	no
El Paso	US-54	0167-01-081	65	31.82	-106.44	80	150	12	no
El Paso	US-54	0167-01-081	66	31.82	-106.44	80	150	12	no
El Paso	IH-10	2121-02-114	20	31.77	-106.46	80	175	12	no
El Paso	IH-10	2121-02-114	21	31.77	-106.46	80	175	12	no
El Paso	IH-10	2121-02-114	22	31.77	-106.47	80	175	12	no
El Paso	IH-10	2121-02-114	26	31.77	-106.47	80	175	12	no
El Paso	IH-10	2121-02-114	27	31.77	-106.47	80	175	12	no
El Paso	US-54		Tower #4	31.77	-106.45			8	yes
El Paso	IH 10-US 54		Tower #12	31.78	-106.44			8	yes
El Paso	IH 10 EB @ Lincoln Center		76	31.78	-106.44			8	yes
El Paso	IH 10-US 54		Tower #10	31.78	-106.43			12	no
El Paso	US-54		Tower #11	31.78	-106.44			12	no
El Paso	IH 10 EB @ Lincoln Center		Tower #7	31.78	-106.44			12	no
El Paso	IH 10 EB @ Lincoln Center		Tower #6	31.78	-106.44			12	no
El Paso	IH 10 EB @ Lincoln Center		Tower #1	31.78	-106.45			12	no
El Paso	IH 10-US 54		Tower #9	31.78	-106.44			12	no

Figure 3.61: TxDOT HMIP Inventory – El Paso District - Cont'd

3.3 UT Field Study on Texas HMIPs: Survey of Cracked Poles

Following a UT field investigation of NTTA (North Texas Tollway Authority) poles indicating the presence of cracks in the base plate-to-shaft welds, TxDOT CST performed an independent UT field study on the various HMIP designs in service. Due to the relevance of these data to the objectives of the project, results of this UT study are presented and discussed in this section.

TxDOT conducted UT study on selected poles in several districts including, Atlanta, Austin, Brownwood, Dallas, El Paso, Harris, Laredo, Odessa, Paris, Waco, and Wichita Falls. Figure 3.62 shows a sample of ultrasonic test results reported by TxDOT for selected poles in El Paso district. As can be seen in Figure 3.62, in the UT field study conducted by TxDOT, crack lengths and depths were reported at each bent of the selected HMIPs. Data gathered during the UT field study by TxDOT, like those depicted in Figure 3.62, provide very valuable information used in reliability-based predictions of fatigue life of in-service HMIPs with pre-existing cracks.

El Paso District - HMIP UT Test Report - 12 Side, 80 MPH, 150 Feet, No Ground Sleeve

HMIP		Bend Line No.												Total Crack	UT Test		Field
Station	Number	1	2	3	4*	5	6	7	8	9	10*	11	12	Length (in)	Date	Time	Notes
551+50	14																
507+00	1	1.5	√	1.5		1.5	√	√	2	0.7		√	1.5	8.7	8/18/2008		
									2.7	1					4/7/2009		
		1.6	√	1.7		1.9	√	√	3.8	1	1	2	2.7	15.7	6/17/2010		
499+50	2	√	1.3	√	√	√	2.5	0.7	√	√		√	√	4.5	8/18/2008		
			1.6				2.8								4/7/2009		
		√	1.7	√	√	√	3	√	√	√		√	√		6/17/2010		
489+75	16																
480+25	15																
454+50	13	√	√	√		2.2	√	√	0.9				0.9	4	6/17/2010		
448+00	17	1.1	√	√	√	√	1.2	√	0.5	√	√	√	√	2.8	6/18/2010		
439+00	12	1.3	2.6	1.3	√	1	2.8	1.4	√	√	√	√	0.7	11.1	6/19/2010		
410+50	18								0.9	0.7				1.6	4/7/2009		
									1	0.7				1.7	6/17/2010		
397+00	3			2.6		2.3	2.2	2.7	3.2	2.7	2.7	2.7	2.7	23.8	8/18/2008		
				2.9		3.2	3.2	3		3			3.8	19.1	4/7/2009		
		0.8		3.7	1	3.3	3.2	2.7	4	3.3	3	2.9	4	31.9	6/17/2010		
Ferguson lab		0.8	2.9	3.9	1.6	3.3	3.3	2.6	4.8	4	3.3	3.1	4	37.6	7/25/2011		
390+50	29	1.6	√	√	√	0.9	2.2	√	2.4	√	√	√	0.7	7.8	6/17/2010		
383+20	28	1.5	2.3	1.7	√	2	0.8	√	0.7	√	√	√	√	9	6/17/2010		
375+00	25																
327+00	23	1.1	√	√	√	3.4	√	√	√	√	√	√	√	4.5	6/17/2010		
317+90	10	√	√	2	√	2	√	1.4	√	√	√	√	2.3	7.7	6/17/2010		
311+65	8			1.4		1.9		1.3					1.8	6.4	4/7/2009		
		√	1.5	√	√	√	√	√	√	√	√	√	√	1.5	6/17/2010		
296+50	9	√	√	√	√	0.7	√	1.5	√	√	√	√	√	2.2	6/17/2010		
287+25	19	1	1.6	1.5	√	√	√	√	1.3	√	√	1.1	1.3	7.8	6/17/2010		
278+00	6		1.7	1.3			1.7		3.2						4/7/2009		
		√	1.9	1.5	√	3.2	1.9	√	3.3	√	√	√	√	11.8	6/17/2010		
270+00	7	√	2	√	√	√	1.4	1.1	0.9	√	√	√	√	5.4	6/17/2010		
264+00	5																
												Average Crack Length (in)		8.75			

Project	
County	El Paso
CSJ	2121-02-114
Project #	IM 10-1(235)
Location	El Paso
Map	Area 3
Letting Date	Aug-04
Test Report Date	
Fabricator	Valmont
Design	
Height	150
Speed	80
Shaft Thickness	0.3125
Design Notes	
Ground Sleeve	no
Galvanized	yes
LEGEND	
#	indication (reflector)
√	no indication (reflector)
	did not U.T.
°	flats U.T.ed
*	Weld Seam
Crack Depth	1/64
	1/32
	>1/32
	1/16

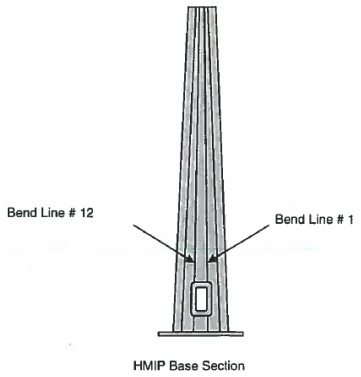

Figure 3.62: Sample UT Results on HMIPs in-Service in El Paso District

3.3.1 Results of UT Field Study on Different HMIP Designs

Results of the UT field study conducted by TxDOT on various HMIP designs throughout Texas are listed in Tables 3.1 to 3.8 (TxDOT 2008). Each table presents results of UT study for poles with a specific number of bends and a specific wind design. Each table further indicates the total number of poles of specific design maintained by TxDOT, the number of poles selected for ultrasonic tests in each category, and the number of poles with detected cracks. Based on the data tabulated in Tables 3.1 to 3.8 (TxDOT 2008), it can be projected that there are approximately 1000 cracked HMIPs currently in-service in the state of Texas (HMIPs maintained by TxDOT).

Table 3.1: UT Field Study: 8-Sided, 80 MPH Designs with Ground Sleeves (TxDOT 2008)

	100 ft.	125 ft.	150 ft.	175 ft.
Total number of poles maintained by TxDOT	10	17	110	18
Number of poles selected in ultrasonic tests	0	11	18	0
Number of poles with observed cracks	0	0	0	0
Observed Crack percentage	-	-	-	-

Table 3.2: UT Field Study: 8-Sided, 80 MPH Designs without Ground Sleeves (TxDOT 2008)

	100 ft.	125 ft.	150 ft.	175 ft.
Total number of poles maintained by TxDOT	0	9	107	11
Number of poles selected in ultrasonic tests	0	9	9	0
Number of poles with observed cracks	0	0	0	0
Observed Crack percentage	-	-	-	-

Table 3.3: UT Field Study: 8-Sided, 100 MPH Designs with Ground Sleeves (TxDOT 2008)

	100 ft.	125 ft.	150 ft.	175 ft.
Total number of poles maintained by TxDOT	7	418	248	91
Number of poles selected in ultrasonic tests	1	9	10	19
Number of poles with observed cracks	0	0	0	1
Observed Crack percentage	-	-	-	5%

Table 3.4: UT Field Study: 8-Sided, 100 MPH Designs without Ground Sleeves (TxDOT 2008)

	100 ft.	125 ft.	150 ft.	175 ft.
Total number of poles maintained by TxDOT	4	10	2	0
Number of poles selected in ultrasonic tests	0	10	2	-
Number of poles with observed cracks	0	0	0	-
Observed Crack percentage	-	-	-	-

Table 3.5: UT Field Study: 12-Sided, 80 MPH Designs with Ground Sleeves (TxDOT 2008)

	100 ft.	125 ft.	150 ft.	175 ft.
Total number of poles maintained by TxDOT	12	4	331	36
Number of poles selected in ultrasonic tests	7	1	2	22
Number of poles with observed cracks	4	1	1	11
Observed Crack percentage	57%	100%	50%	50%

Table 3.6: UT Field Study: 12-Sided, 80 MPH Designs without Ground Sleeves (TxDOT 2008)

	100 ft.	125 ft.	150 ft.	175 ft.
Total number of poles maintained by TxDOT	13	3	379	46
Number of poles selected in ultrasonic tests	3	3	144	32
Number of poles with observed cracks	2	1	144	14
Observed Crack percentage	67%	33%	100%	44%

Table 3.7: UT Field Study: 12-Sided, 100 MPH Designs with Ground Sleeves (TxDOT 2008)

	100 ft.	125 ft.	150 ft.	175 ft.
Total number of poles maintained by TxDOT	51	35	382	165
Number of poles selected in ultrasonic tests	10	8	5	8
Number of poles with observed cracks	2	3	0	5
Observed Crack percentage	20%	38%	-	63%

Table 3.8: UT Field Study: 12-Sided, 100 MPH Designs without Ground Sleeves (TxDOT 2008)

	100 ft.	125 ft.	150 ft.	175 ft.
Total number of poles maintained by TxDOT	10	37	200	221
Number of poles selected in ultrasonic tests	0	12	7	16
Number of poles with observed cracks	0	0	4	2
Observed Crack percentage	-	-	57%	13%

3.4 HMIP Designs of Most Importance to TxDOT and Their Location

3.4.1 Pole Design of most interest: Geometry and Design Wind

Results of the UT field study conducted by TxDOT on HMIPs with various designs, summarized in Tables 3.1 to 3.8 in Section 3.3, indicate that, of all the HMIPs in-service in Texas, poles that are 12-sided, 150 ft tall, with a design wind speed of 80 mph, and without ground sleeves are more prone to cracks in the shaft-to-base plate welds. For this design, of 144 poles examined by ultrasonic testing, all 144 showed the presence of cracks.

To illustrate this observation more clearly, results of the study reported by TxDOT (2008) and summarized in Tables 3.1 to 3.8 in Section 3.3 are summarized in Table 3.9 in terms of the probability of observed cracks for HMIPs with different designs. Note that this table also shows a high probability of cracks in poles that are 12-sided, with a design wind speed of 80 mph, and with ground sleeves. However, for this design, only a very small number of poles have undergone ultrasonic testing. Due to this very small sample size, this pole design was considered to be of secondary interest in this research program.

Table 3.9: Probability of Observed Cracks (in percent) (TxDOT 2008)

		With Ground Sleeve				Without Ground Sleeve			
		100 ft	125 ft	150 ft	175 ft	100 ft	125 ft	150 ft	175 ft
8 sided	80 mph	N/A	0	0	N/A	N/A	0	0	N/A
	100 mph	0	0	0	5	N/A	0	0	N/A
12 sided	80 mph	57	100	50	50	67	33	**100**	44
	100 mph	20	38	0	63	N/A	0	57	13

3.4.2 Pole Design of most interest: Location by District

After indicating the pole design of most interest, it is also helpful to identify districts in Texas where these poles are located. There are seven districts having the largest number of poles of interest. As indicated in Table 3.10, these districts include Austin, Laredo, Atlanta, El Paso, Odessa, Fort Worth, and Paris.

Table 3.10: Total Number of Poles in Districts Having the Largest Number of Poles of Interest

Number of HMIPs		100 ft		125 ft		150 ft		175 ft		Total
		8 sided	12 sided	8 sided	12 sided	8 sided	12 sided	8 sided	12 sided	
Austin District	80 mph	0	7	0	3	10	**195**	0	26	275
	100 mph	0	0	0	3	0	31	0	0	
Laredo District	80 mph	0	0	0	0	0	**101**	0	0	101
	100 mph	0	0	0	0	0	0	0	0	
Atlanta District	80 mph	0	6	0	0	0	**56**	0	14	76
	100 mph	0	0	0	0	0	0	0	0	
El Paso District	80 mph	0	12	0	3	0	**55**	0	5	75
	100 mph	0	0	0	0	0	0	0	0	
Odessa District	80 mph	0	0	0	0	0	**54**	0	0	54
	100 mph	0	0	0	0	0	0	0	0	
Ft. Worth District	80 mph	0	0	0	0	41	**51**	0	0	92
	100 mph	0	0	0	0	0	0	0	0	
Paris District	80 mph	0	0	0	0	0	**50**	0	2	52
	100 mph	0	0	0	0	0	0	0	0	

3.5 Summary

This chapter provided an overview of data gathered on the inventory of Texas HMIPs. The research team worked closely with TxDOT staffs to collect as much data possible on the current inventory of HMIPs in Texas. Representative results of ultrasonic tests (UT) performed by TxDOT CST (construction division) on the various HMIP designs in service were also provided in this chapter. The data collected in this survey showed that, of all the HMIPs in-

service in Texas, poles that are 12-sided, 150 ft tall, with a design wind of 80 mph, and without ground sleeves are more prone to cracks at the shaft-to-base plate welds. The survey also showed that districts that have the largest number of these poles are Austin, Laredo, Atlanta, El Paso, Odessa, Fort Worth, and Paris. This information was used to guide the research efforts on the experimental and field investigations of the fatigue behavior of HMIPs with pre-existing cracks.

Chapter 4. Historical Wind Data for Texas

4.1 Overview

As part of this research project, the research team collected historical wind data for Texas. A summary of these wind data, in various tabular and graphical forms, is provided in this chapter. Specifically, historical wind data were collected for the HMIP design types and locations of interest identified in Chapter 3 of this report. Historical wind data were also provided for locations representative of major wind environments in Texas. Information collected includes daily and monthly average wind speeds and maximum gusts, for various average periods. The number of years of available wind records at each chosen location is also noted.

4.2 Texas Wind Environment

In this section, an overview of the wind environment in Texas is presented and discussed. Different methods of presenting site-specific historical wind data are also explained. A summary of considerations that went into selecting the weather sites is further provided.

4.2.1 Major Wind Environments

Due to geographical differences, wind environments vary throughout Texas. As an example, the variations in the wind environment in Texas are indicated in Figure 4.1, where the annual average wind speed at 100 feet above the ground is shown. In general, the wind speed is high in north Texas, in cities like Amarillo and Lubbock. Corpus Christi and El Paso also experience high wind speeds as a result of proximity to the coast and to the mountains, respectively. East Texas experiences relatively calm wind speeds.

Besides wind speed, wind direction is another important characteristic of the wind environment. Figure 4.2 shows the dominant wind directions in January and July for Texas. The length of the lines in the cardinal directions indicates the rate of occurrence for different wind directions. It is important to note that the difference between the occurrence rates for each direction is caused by seasonal variations. Therefore, at any site, the wind data are collected for at least a period of one year to reflect variations caused by seasonal changes.

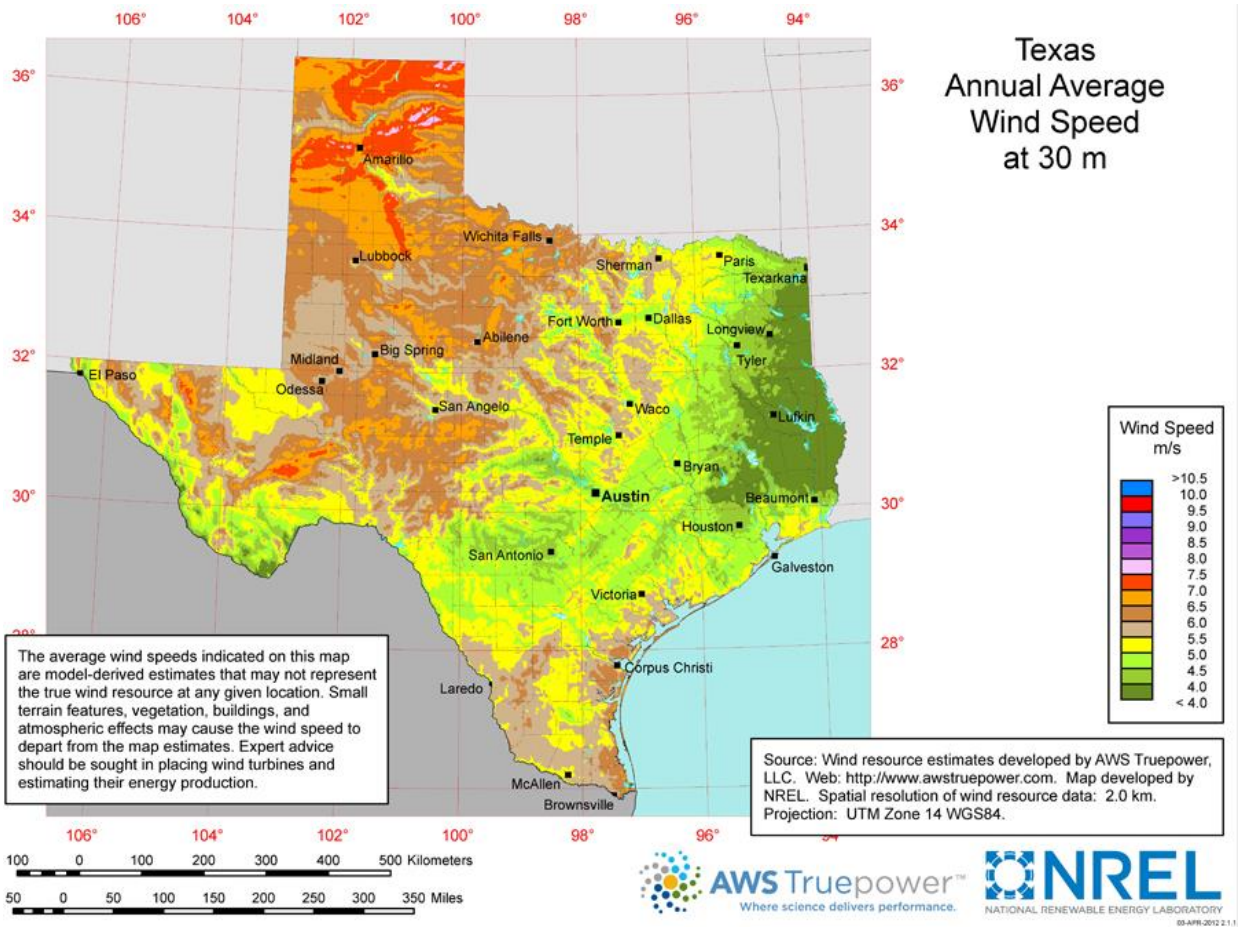

Figure 4.1: Texas Annual Average Wind Speed at 100 Feet above the Ground Level (WINDExchange Website)

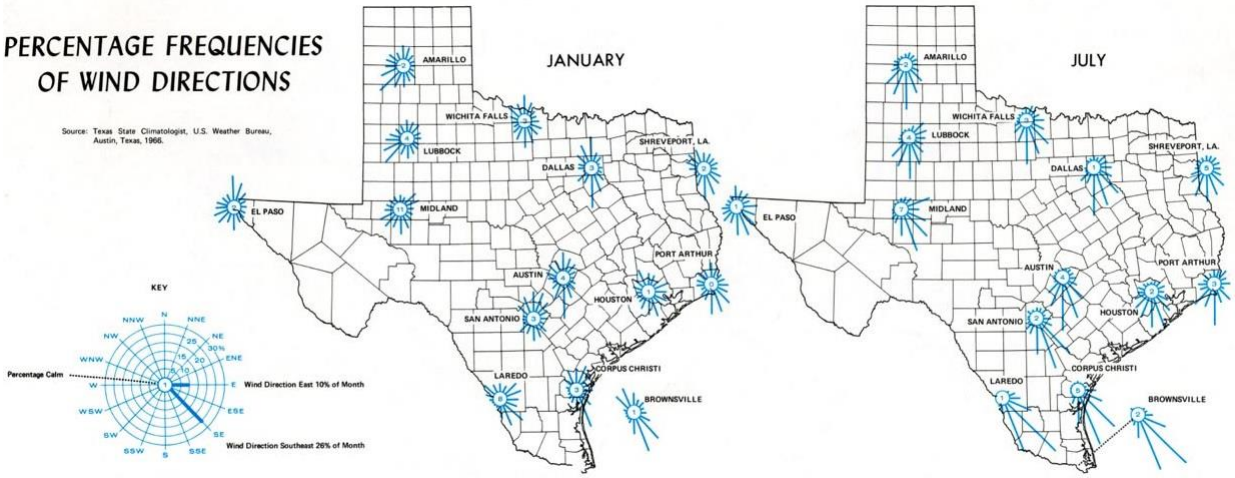

Figure 4.2: Wind Directions in Texas (Atlas of Texas from UT-PCL Map Collection)

4.2.2 Sources of Historical Wind Data

A number of organizations provide archived meteorological data including historical wind data to the public. Numerous historical wind data from various sites can be collected through the following sources:

- National Oceanic and Atmospheric Administration (NOAA), a U.S. scientific agency that offers the world's largest archive of meteorological data
- Weatherunderground, a private company with numerous weather stations across the U.S.
- Texas Commission on Environmental Quality (TCEQ), the environmental agency for the state of Texas.

To collect historical wind data for Texas, the researchers utilized the data archived on NOAA's website since the historical data from this site are more comprehensive compared to other sources. It should also be added that although Weatherunderground reports wind data from a large number of weather stations, the historical data are usually not archived. The datasets collected from NOAA are under the category of quality controlled local climatological data (QCLCD). QCLCD consists of hourly, daily, and monthly data for approximately 1600 locations throughout the U.S., of which 202 locations are stationed in Texas (Figure 4.3).

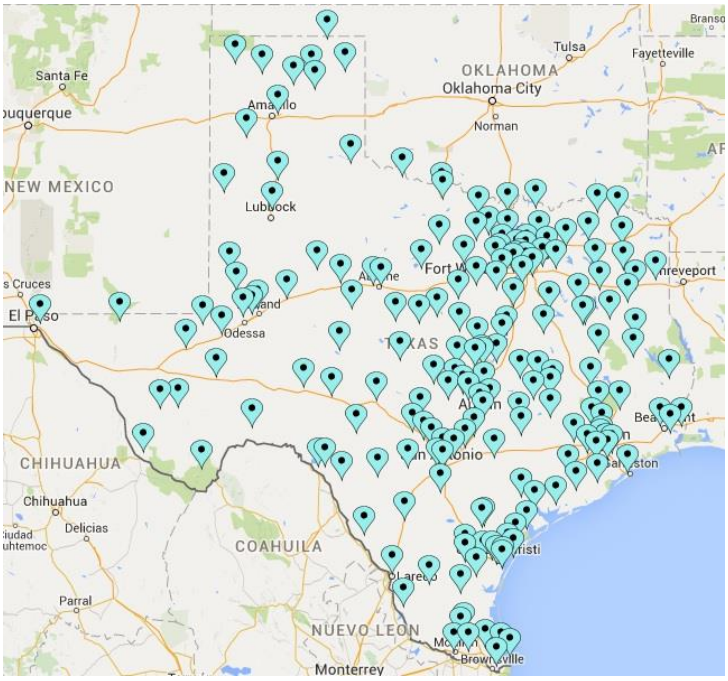

Figure 4.3: Weather Stations in Texas as Listed on NOAA Website (https://www.mapcustomizer.com/#)

Two ASCII type data, hourly and daily, are obtained from NOAA. Hourly wind data consists of 2-minute average wind speed, and wind direction logged every hour. Daily wind data consists of daily average wind speed, maximum 5-second average wind speed, and maximum 2-minute average wind speed. 5-second average wind speed is considered as gust wind in this report.

4.2.3 Graphical Representation of Historical Wind Data

The graphical representation of wind data in this chapter primarily consists of four graphs: wind rose, wind density, rate of occurrence of wind speeds, and monthly/daily average wind speed and maximum gust speed. These graphs are generated using a MATLAB program based on the ASCII type data collected from NOAA.

A wind rose graph (e.g. Figure 4.4) is a traditional representation of wind environment that consists of radial plots indicating the probability of the wind in certain speeds and directions. The length of the radius shows the probability of occurrence, the radial direction represents the wind direction, and the color indicates the wind speed. The script for the wind rose graph is referenced from MATLAB File Exchange (Pereira 2014). A wind density graph (e.g. Figure 4.5) is another representation that also indicates the probability of the wind occurrence with certain speed and in a specific direction. However, the length of the radius represents wind speed where the color indicates the probability of occurrence. The wind density graph particularly represents the highest occurring wind and its speed and direction. Rate of occurrence of wind speed (e.g. Figure 4.6) gives an overall wind speed distribution without considering wind direction. Since vortex-shedding induced vibration (VIV) is triggered in low wind speed, the rate of occurrence is useful in determining whether HMIPs near this site are prone to this type of vibration. Trends of monthly average wind speed and maximum gust (e.g. Figure 4.7) provide the overall wind speed trend and any high gusts recorded near that weather station. Graphs that indicate daily average wind speed can also be generated as shown in Figure 4.8. Since monthly average wind speed better shows the trend in seasonal differences, daily average wind speed is not plotted for collected wind data in this report. However, graphs of daily average wind speed can be easily generated from the collected data if needed.

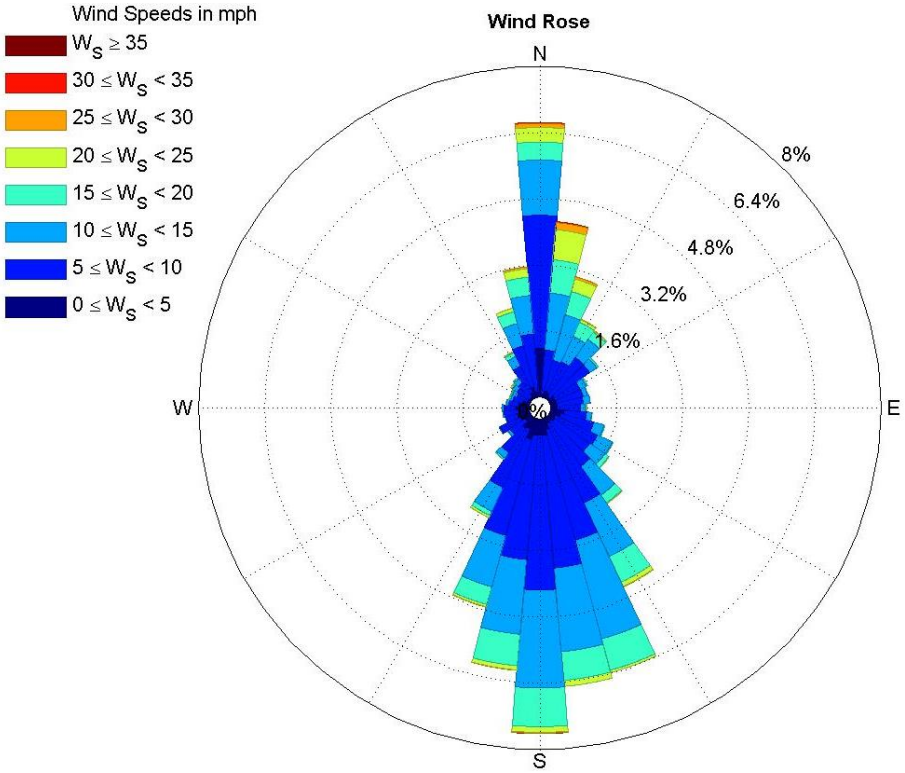

Figure 4.4: A Sample of Wind Rose Graph

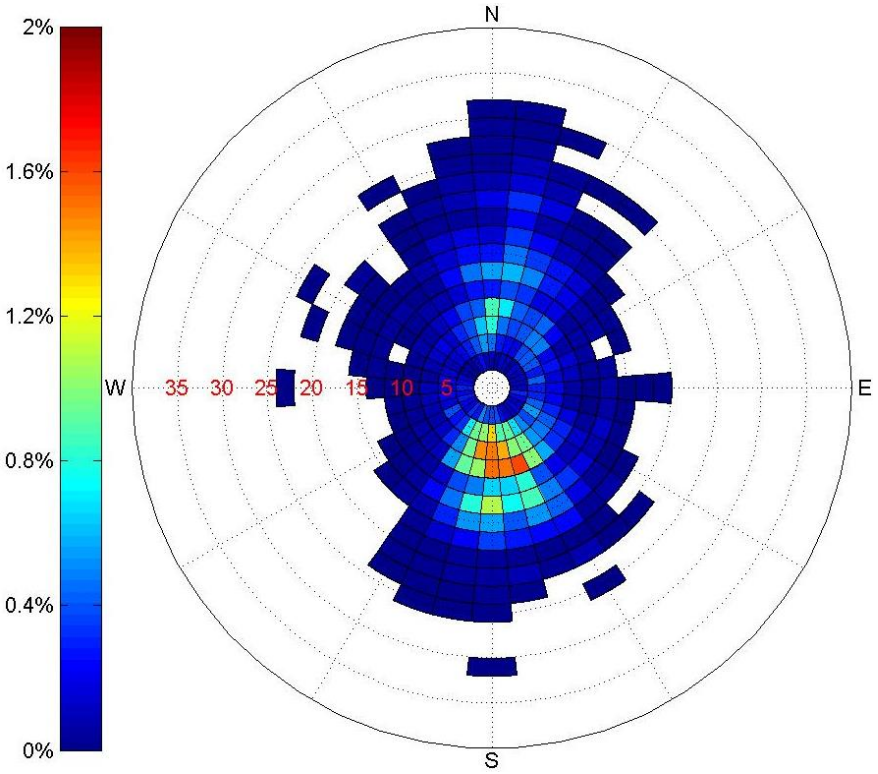

Figure 4.5: A Sample of Wind Density Graph

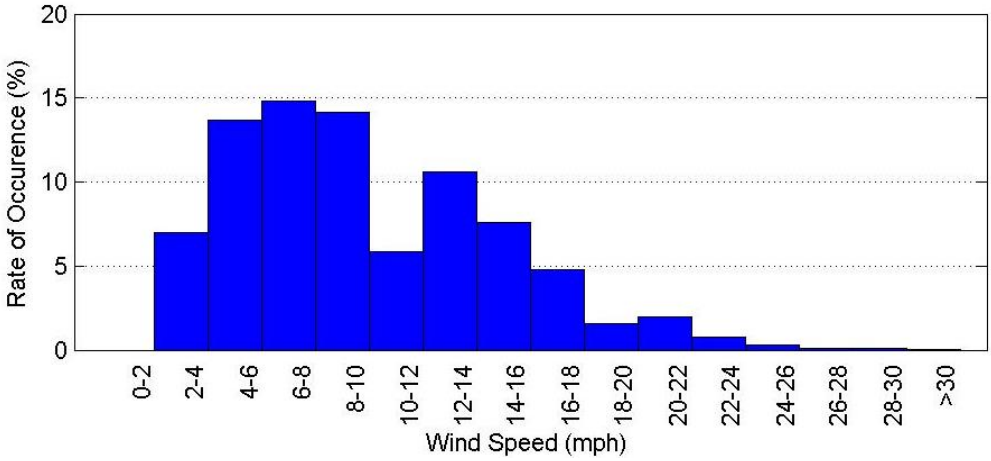

Figure 4.6: A Sample of Wind Speed Rate of Occurrence

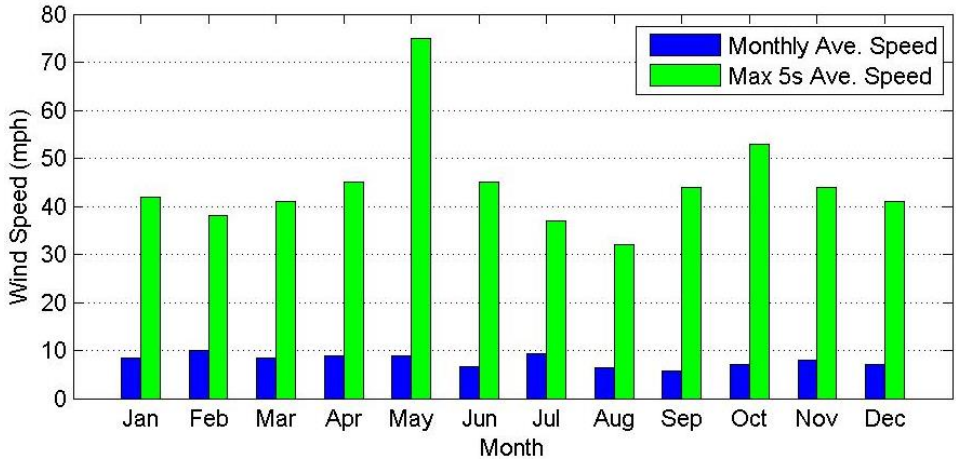

Figure 4.7: A Sample of Monthly Average Wind Speed and Maximum Wind Gust

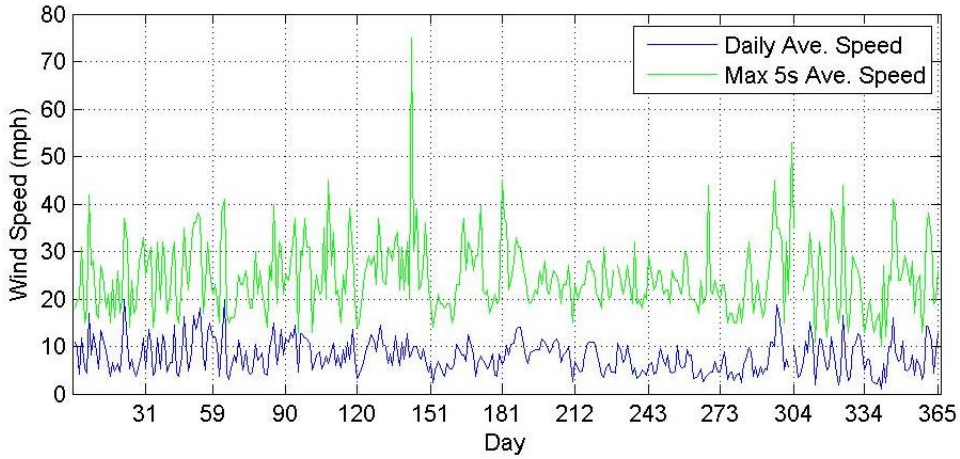

Figure 4.8: A Sample of Daily Average Wind Speed and Maximum Wind Gust

4.2.4 Selection of Wind Stations

As indicated in Chapter 3 of this report, of all the HMIPs in service in Texas, poles having 12-sided, 150 ft-tall shaft without a ground sleeve, and considered design wind of 80 mph are of interest in this research program. This selection is particularly informed by the previous study reported by TxDOT (TxDOT Report) indicating significant cracks in the shaft wall near the shaft-to-base plate welds for HMIPs with this specific design. Therefore, the research team have decided to collect and represent the historical wind data for Texas using mainly the wind stations in the regions/districts where these HMIPs are located. These wind stations are referred to as "primary sites" in this chapter. To better represent major wind environments in Texas, historical wind data from selected stations in districts with no HMIPs with the design of interest are also presented. These additional wind stations are referred to as "secondary sites" in this report.

Primary Sites

Based on the inventory of Texas HMIPs, the districts having HMIPs with the design of interest are listed in Table 4.1. The weather stations, provided by NOAA website, in these districts are listed in Table 4.2. WBAN in Table 4.2 is a weather station identifier originally used by the

Weather Bureau Army Navy (WBAN) and later adopted by NOAA (NOAA has issued more IDs to accommodate new stations). Locations of the selected weather sites (primary sites) in Table 4.2 are further shown as red balloons on Texas map in Figure 4.9.

Table 4.1: Number of HMIPs in the Districts Having HMIPs with the Design of Interest

		100 ft		125 ft		150 ft		175 ft		Total
		8 sided	12 sided	8 sided	12 sided	8 sided	12 sided	8 sided	12 sided	
Austin District	80 mph	0	7	0	3	10	**195**	0	26	275
	100 mph	0	0	0	3	0	31	0	0	
Laredo District	80 mph	0	0	0	0	0	**101**	0	0	101
	100 mph	0	0	0	0	0	0	0	0	
Atlanta District	80 mph	0	6	0	0	0	**56**	0	14	76
	100 mph	0	0	0	0	0	0	0	0	
El Paso District	80 mph	0	12	0	3	0	**55**	0	5	75
	100 mph	0	0	0	0	0	0	0	0	
Odessa District	80 mph	0	0	0	0	0	**54**	0	0	54
	100 mph	0	0	0	0	0	0	0	0	
Ft. Worth District	80 mph	0	0	0	0	41	**51**	0	0	92
	100 mph	0	0	0	0	0	0	0	0	
Paris District	80 mph	0	0	0	0	0	**50**	0	2	52
	100 mph	0	0	0	0	0	0	0	0	
Waco District	80 mph	0	0	4	0	0	**45**	0	5	54
	100 mph	0	0	0	0	0	0	0	0	
Brownwood District	80 mph	0	0	0	0	0	**20**	0	0	20
	100 mph	0	0	0	0	0	0	0	0	
Wichita Falls District	80 mph	0	0	0	0	13	**12**	0	0	28
	100 mph	0	0	0	0	0	0	0	3	
Bryan District	80 mph	0	0	0	0	0	**2**	0	2	4
	100 mph	0	0	0	0	0	0	0	0	

Table 4.2: NOAA Weather Stations Located in the Districts Having HMIPs with the Design of Interest

District	State	Sign	WBAN	Name	Location	Latitude	Longitude
Austin	TX	EDC	230	PFLUGERVILLE	AUSTIN EXECUTIVE AIRPORT	30.395	-97.567
	TX	ATT	13958	AUSTIN/CITY	AUSTIN-CAMP MABRY ARMY NATIONAL GUARD	30.3208	-97.7604
	TX	AUS	13904	AUSTIN/BERGSTROM	AUSTIN-BERGSTROM INTL AIRPORT	30.1831	-97.6799
	TX	GTU	53942	GEORGETOWN	GEORGETOWN MUNICIPAL ARPT	30.67917	-97.67944
Laredo	TX	LRD	12907	LAREDO	LAREDO INTERNATIONAL AIRPORT	27.53333	-99.46667
Atlanta	AR	TXK	13977	TEXARKANA	TEXARKANA REGIONAL AIRPORT-WEBB FIELD	33.4536	-94.0074
	TX	GGG	3901	LONGVIEW	EAST TEXAS REGIONAL ARPT	32.38472	-94.71167
El Paso	TX	ELP	23044	EL PASO	EL PASO INTERNATIONAL AIRPORT	31.81111	-106.37583
Odessa	TX	ODO	3031	ODESSA	ODESSA-SCHLEMEYER FLD ARPT	31.92056	-102.38667
	TX	MAF	23023	MIDLAND	MIDLAND INTERNATIONAL AIRPORT	31.9475	-102.2086
	TX	MDD	3071	MIDLAND	MIDLAND AIRPARK	32.03639	-102.10111
Ft. Worth	TX	DFW	3927	DALLAS-FORT WORTH	DALLAS/FT WORTH INTERNATIONAL AP	32.8978	-97.0189
	TX	FTW	13961	FORT WORTH	FT WORTH MEACHAM INTL ARPT	32.81917	-97.36139
	TX	NFW	13911	FORT WORTH	FORT WORTH NAVAL AIR STATION JRB/CARSWELL FIELD	32.76667	-97.45
	TX	GDJ	53977	GRANBURY	GRANBURY MUNICIPAL ARPT	32.44444	-97.81694
Paris	TX	GVT	13926	GREENVILLE	MAJORS AIRPORT	33.06778	-96.06528
	TX	PRX	93955	PARIS	COX FIELD AIRPORT	33.63333	-95.45
	TX	GYI	53967	SHERMAN/DENISON	GRAYSON COUNTY AIRPORT	33.71417	-96.67361
Waco	TX	INJ	53972	HILLSBORO	HILLSBORO MUNICIPAL ARPT	32.08361	-97.09722
	TX	ACT	13959	WACO	WACO REGIONAL AIRPORT	31.61889	-97.22833
	TX	PWG	53952	WACO	MC GREGOR EXECUTIVE ARPT	31.48472	-97.31639
	TX	TPL	93984	TEMPLE	DRAUGHON-MILLER CNTRL TX RGNL ARPT	31.15	-97.41667
	TX	GRK	3902	FORT HOOD/KILLEEN	ROBERT GRAY AFF AIRPORT	31.06667	-97.83333
	TX	HLR	3933	FORT HOOD (KILLEEN)	HOOD AAF AIRPORT	31.13333	-97.71667
	TX	ILE	3972	KILLEEN	KILLEEN MUNICIPAL AIRPORT	31.08333	-97.68333
Brownwood	TX	BKD	176	BRECKENRIDGE	STEPHENS COUNTY AIRPORT	32.717	-98.892
Wichita Falls	TX	CWC	134	WICHITA FALLS	KICKAPOO DOWNTOWN AIRPORT	33.85	-98.483
	TX	SPS	13966	WICHITA FALLS	SHEPPARD AFB/WICHITA FALLS MUNI AP	33.9786	-98.4928
	TX	GLE	93929	GAINESVILLE	GAINESVILLE MUNICIPAL ARPT	33.65139	-97.19694
Bryan	TX	CLL	3904	COLLEGE STATION	EASTERWOOD FIELD AIRPORT	30.58917	-96.36472
	TX	CFD	438	BRYAN	COULTER FIELD AIRPORT	30.71569	-96.33136

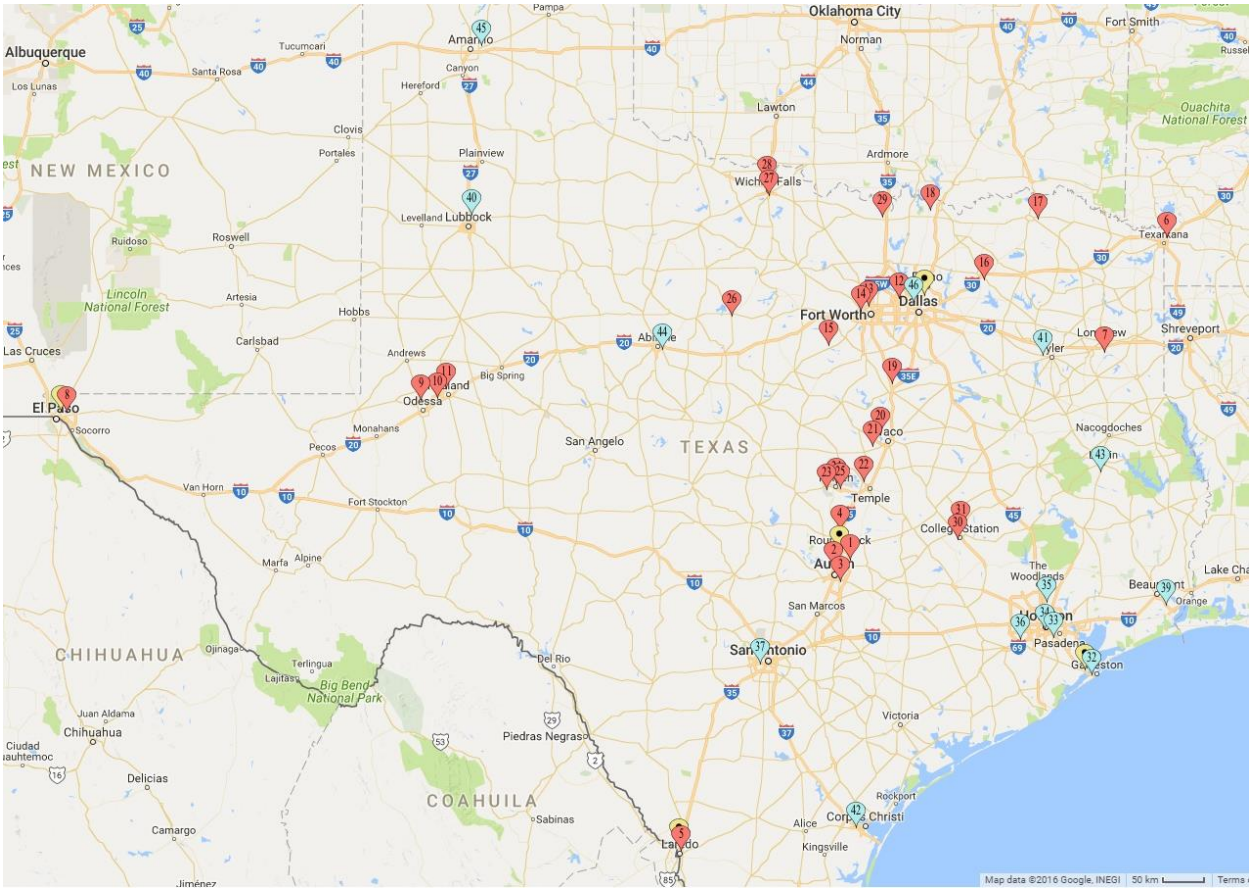

Figure 4.9: Locations of the Weather Stations Selected to Represent Historical Wind Data

Figures 4.10 to 4.21 each shows both the location of HMIPs with the design of interest and the weather stations for individual districts listed in Table 4.1. In Figures 4.10 to 4.21, red-balloons indicate the location of weather stations, while blue balloons indicate the location of HMIPs. It should be noted that the distance between the HMIPs and the weather stations is a useful indicator of how well the collected data represent the actual wind environment at the location of each HMIP.

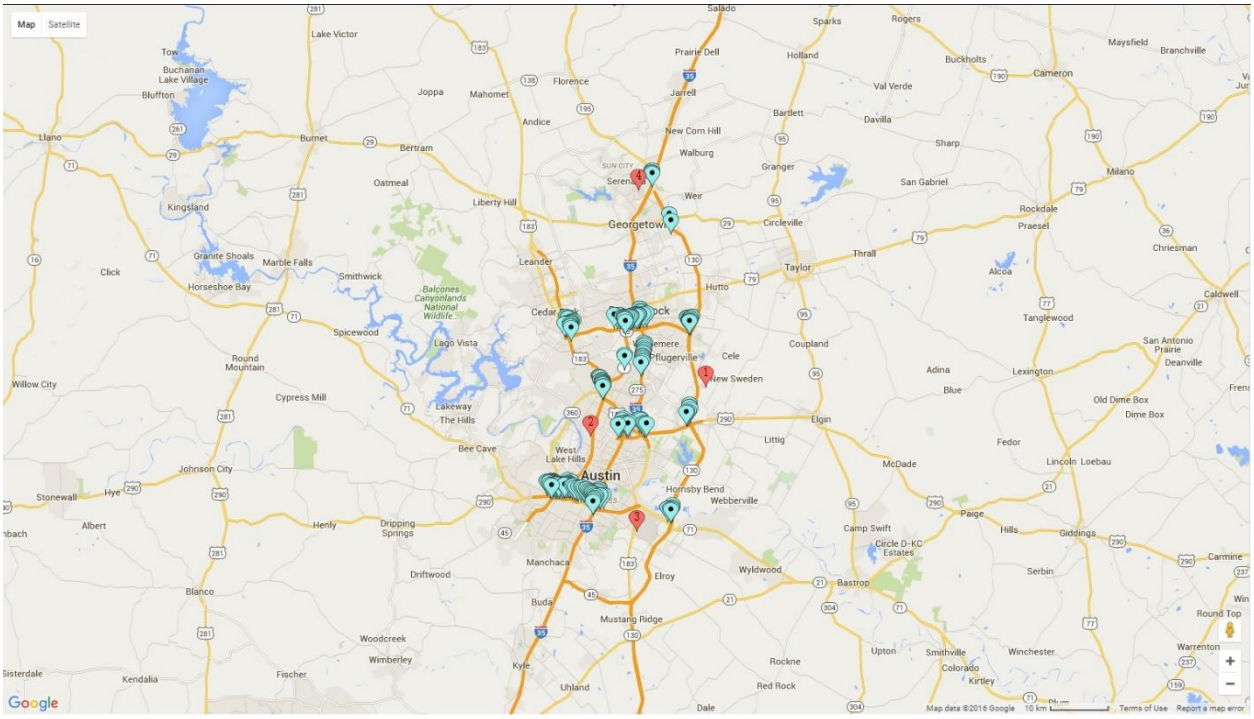

Figure 4.10: Locations of HMIPs and Weather Stations in Austin District

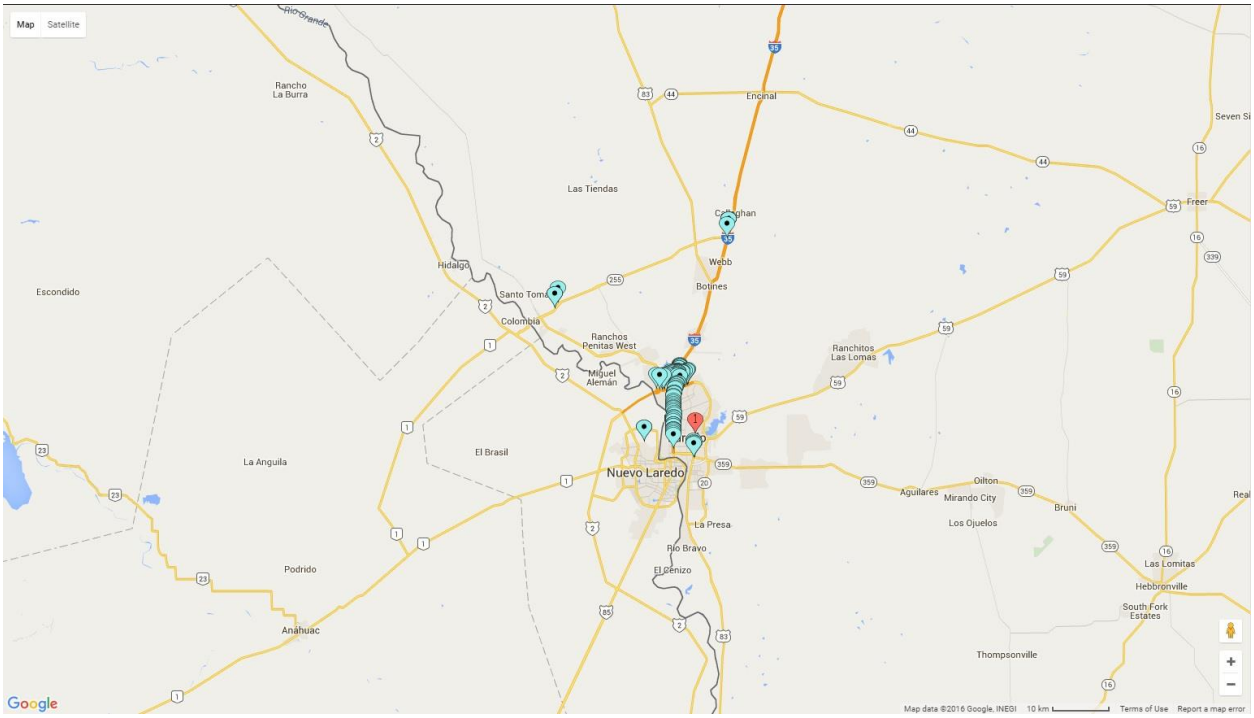

Figure 4.11: Locations of HMIPs and Weather Stations in Laredo District

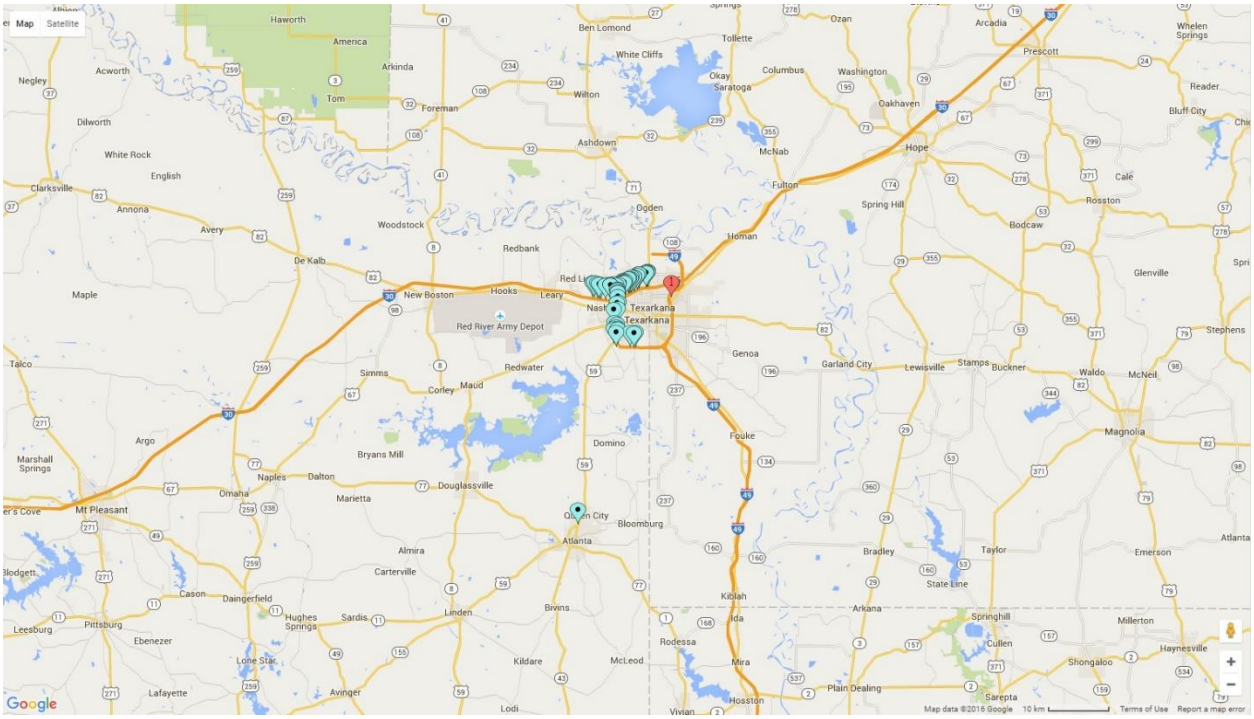

Figure 4.12: Locations of HMIPs and Weather Stations in Atlanta District (North)

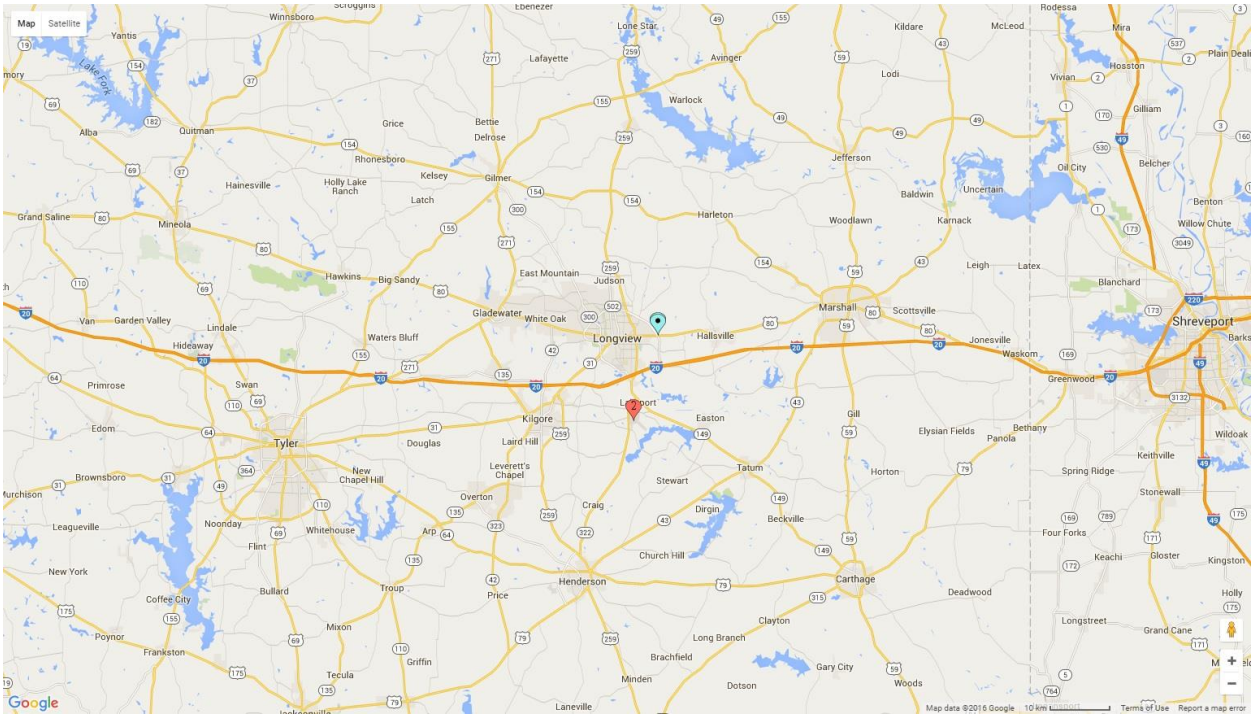

Figure 4.13: Locations of HMIPs and Weather Stations in Atlanta District (South)

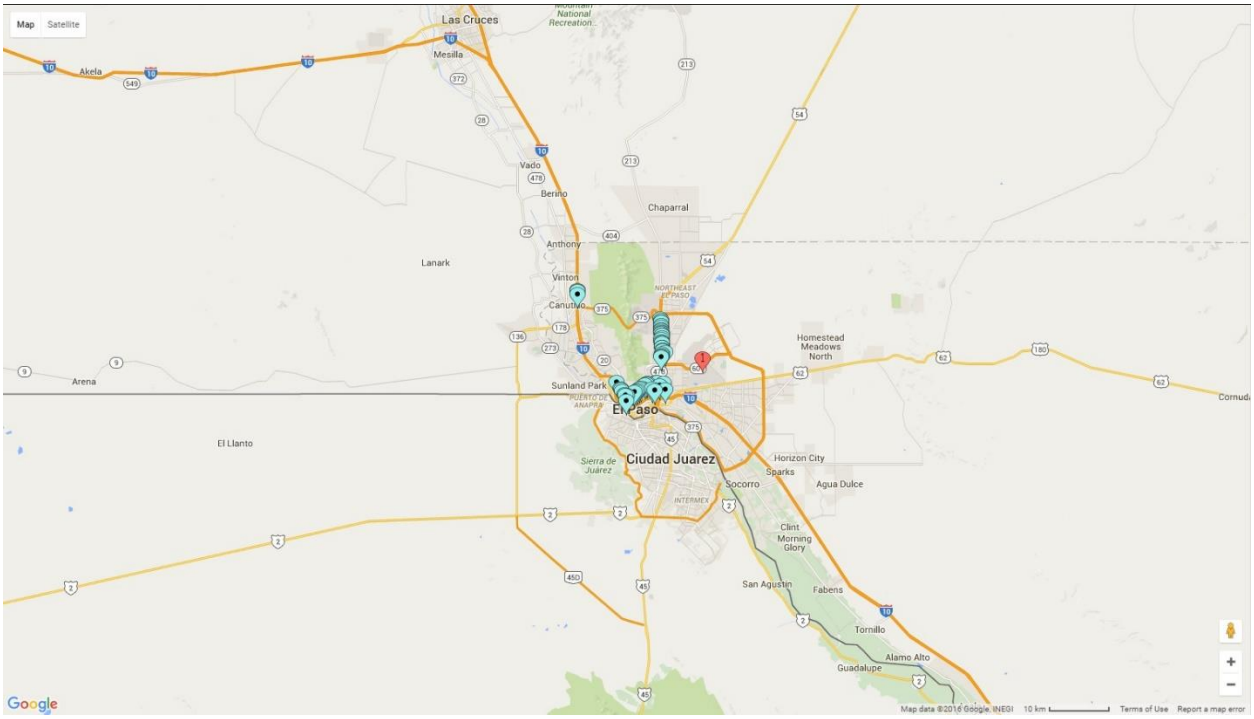

Figure 4.14: Locations of HMIPs and Weather Stations in El Paso District

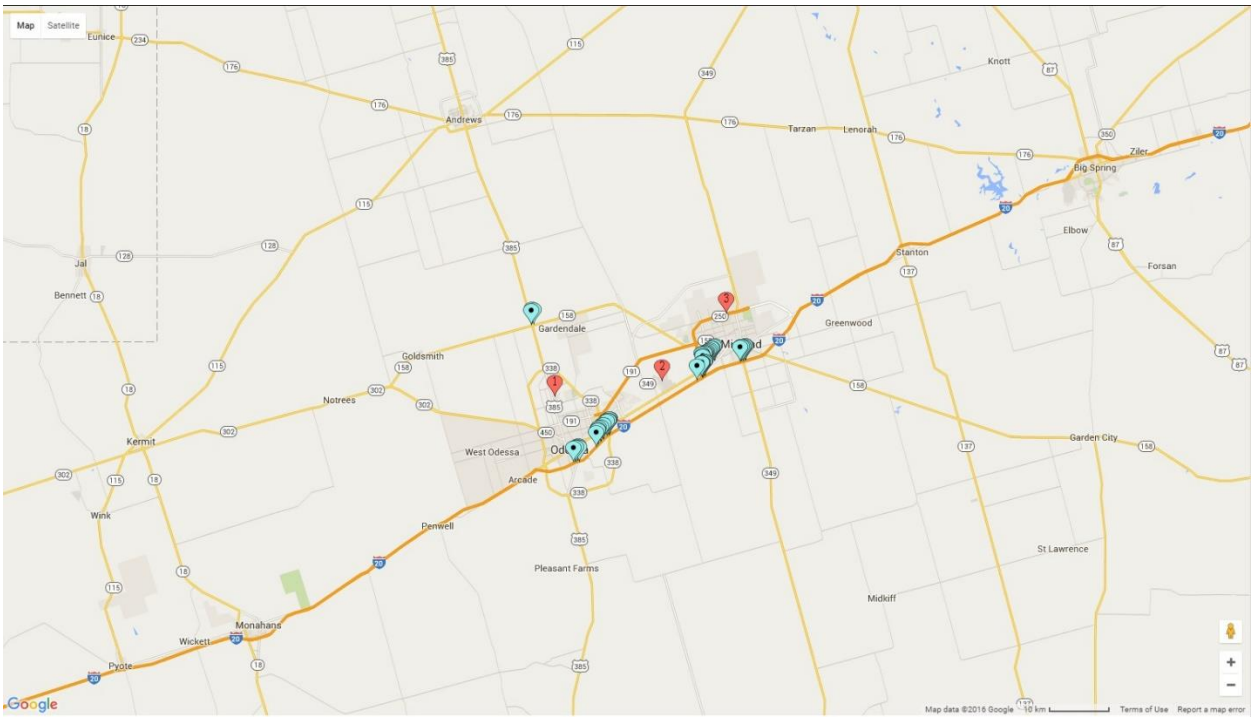

Figure 4.15: Locations of HMIPs and Weather Stations in Odessa District

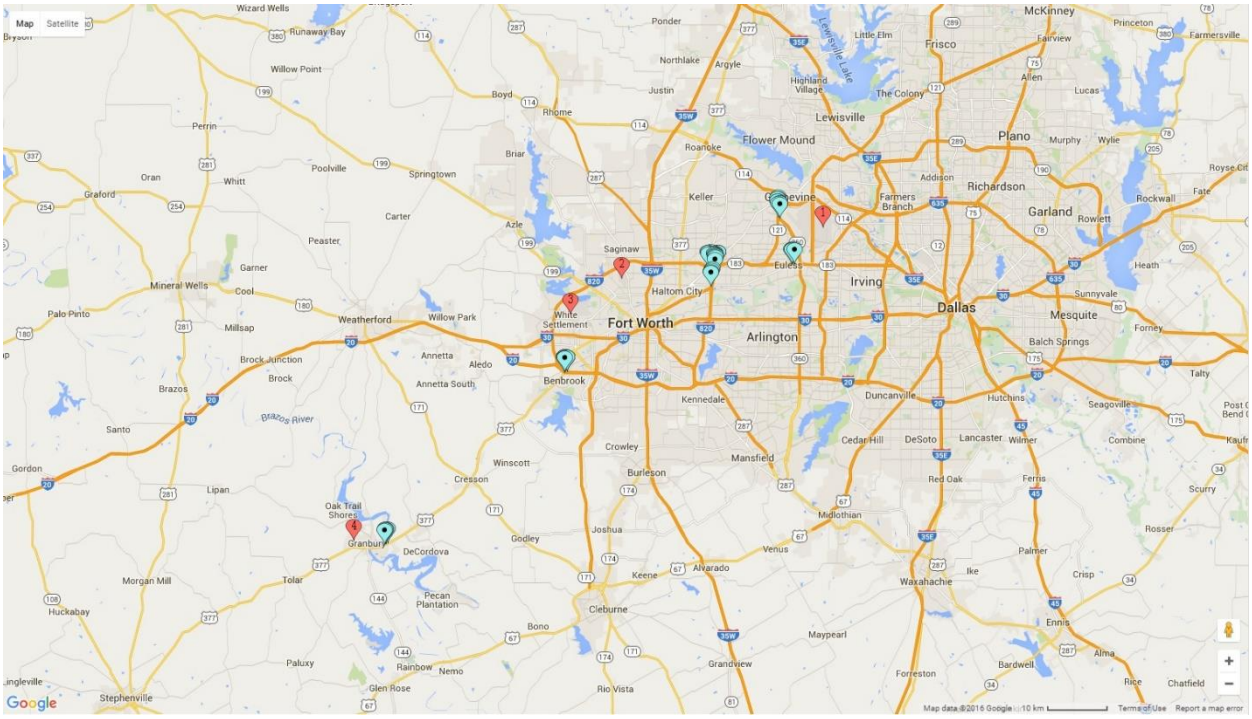

Figure 4.16: Locations of HMIPs and Weather Stations in Ft. Worth District

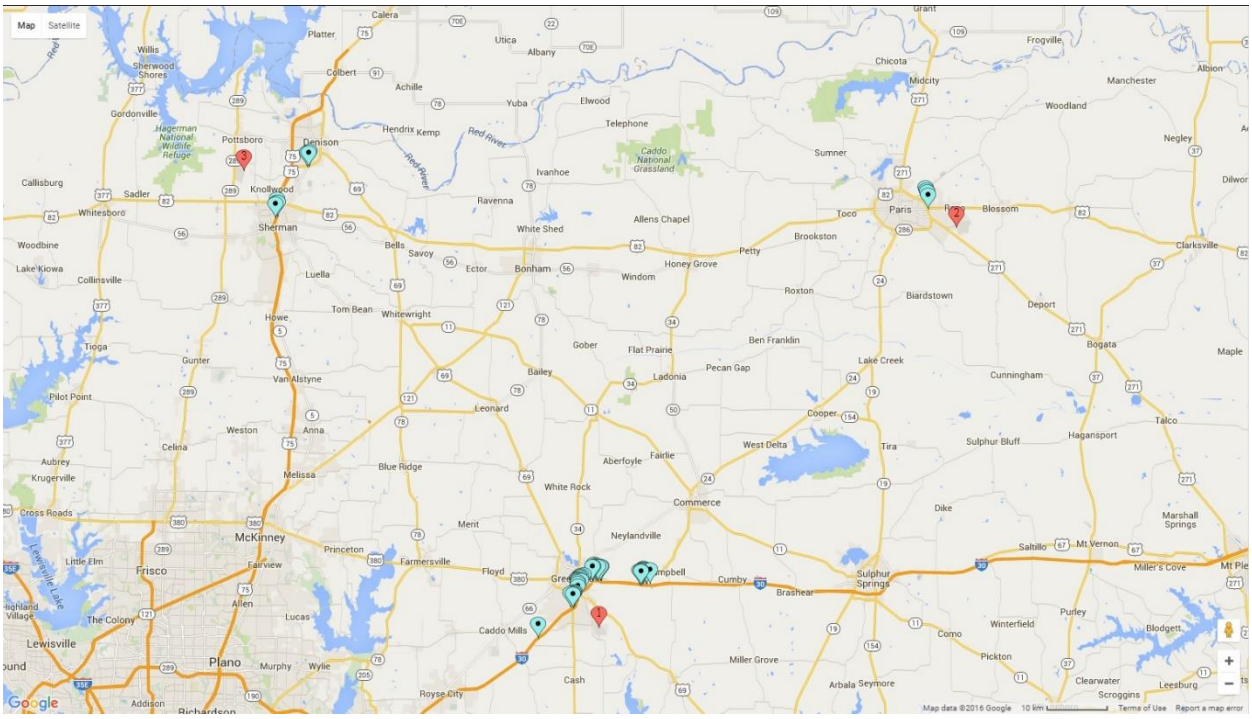

Figure 4.17: Locations of HMIPs and Weather Stations in Paris District

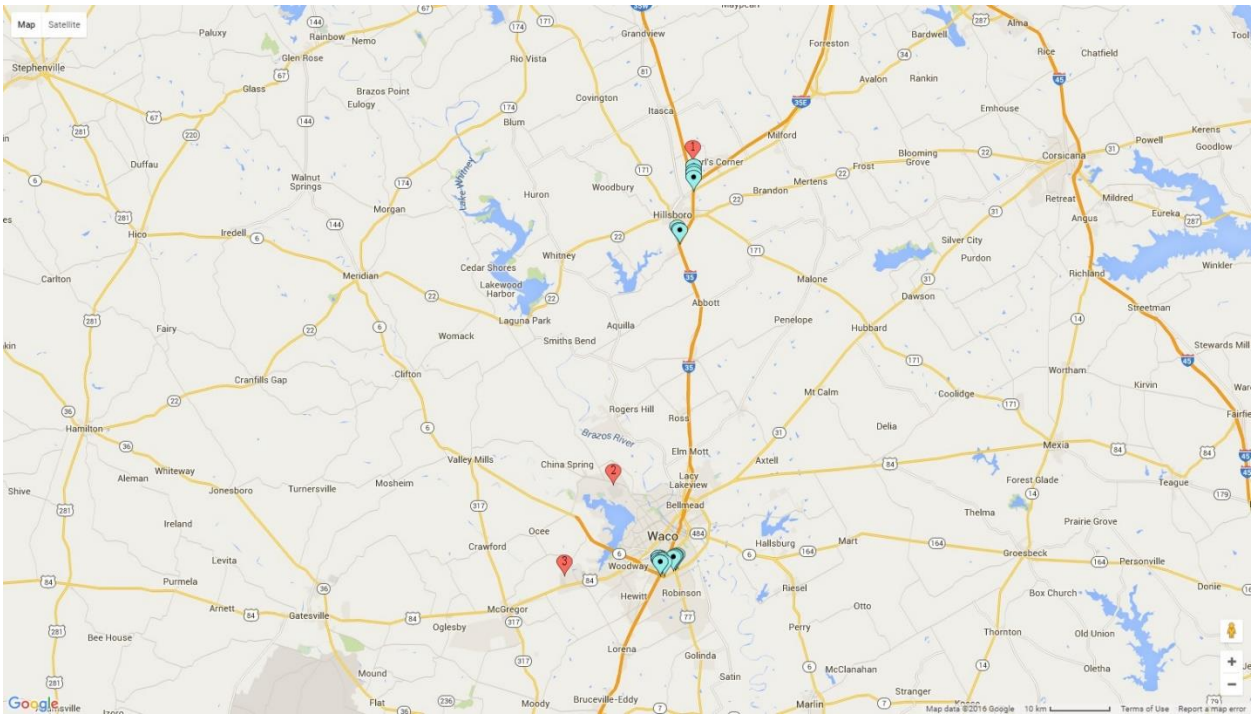

Figure 4.18: Locations of HMIPs and Weather Stations in Waco District (North)

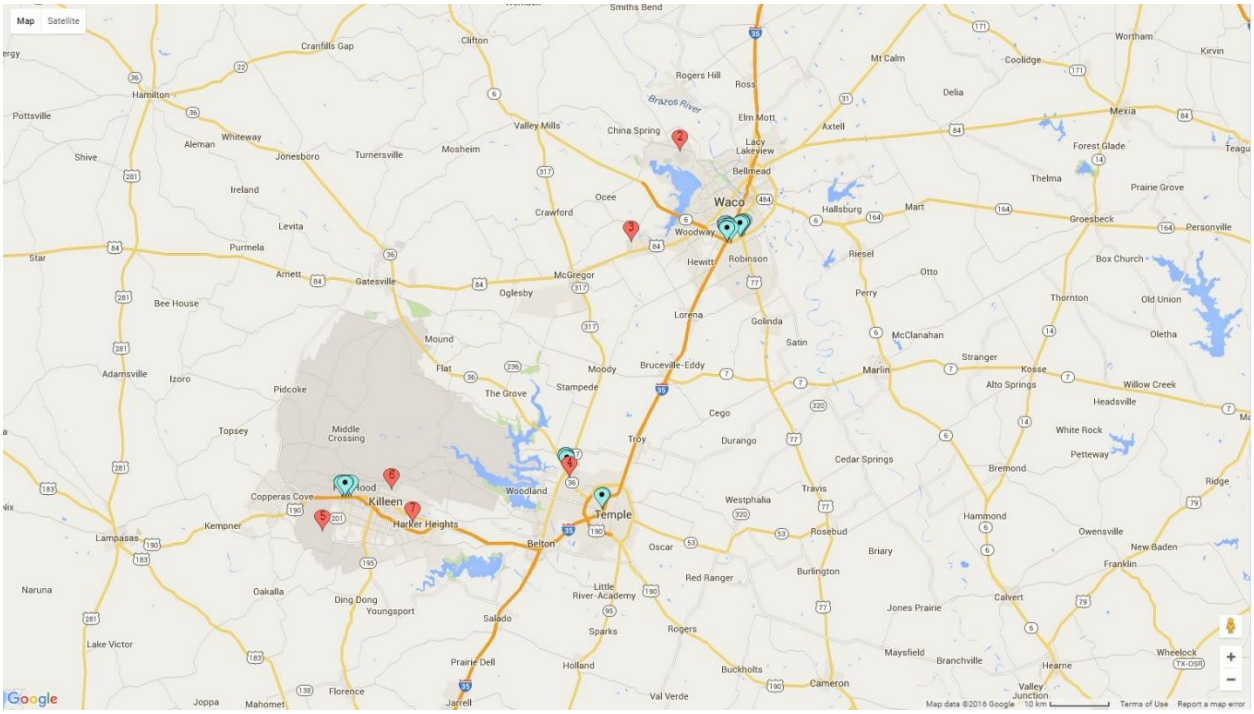

Figure 4.19: Locations of HMIPs and Weather Stations in Waco District (South)

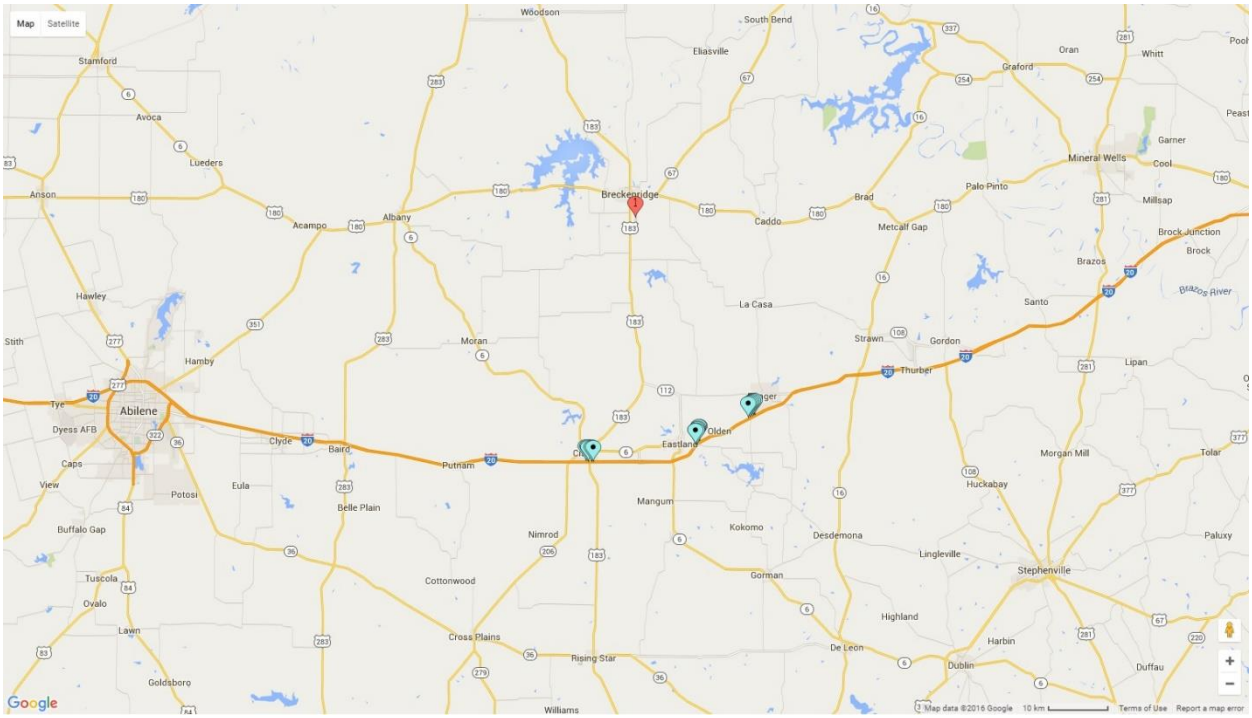

Figure 4.20: Locations of HMIPs and Weather Stations in Brownwood District

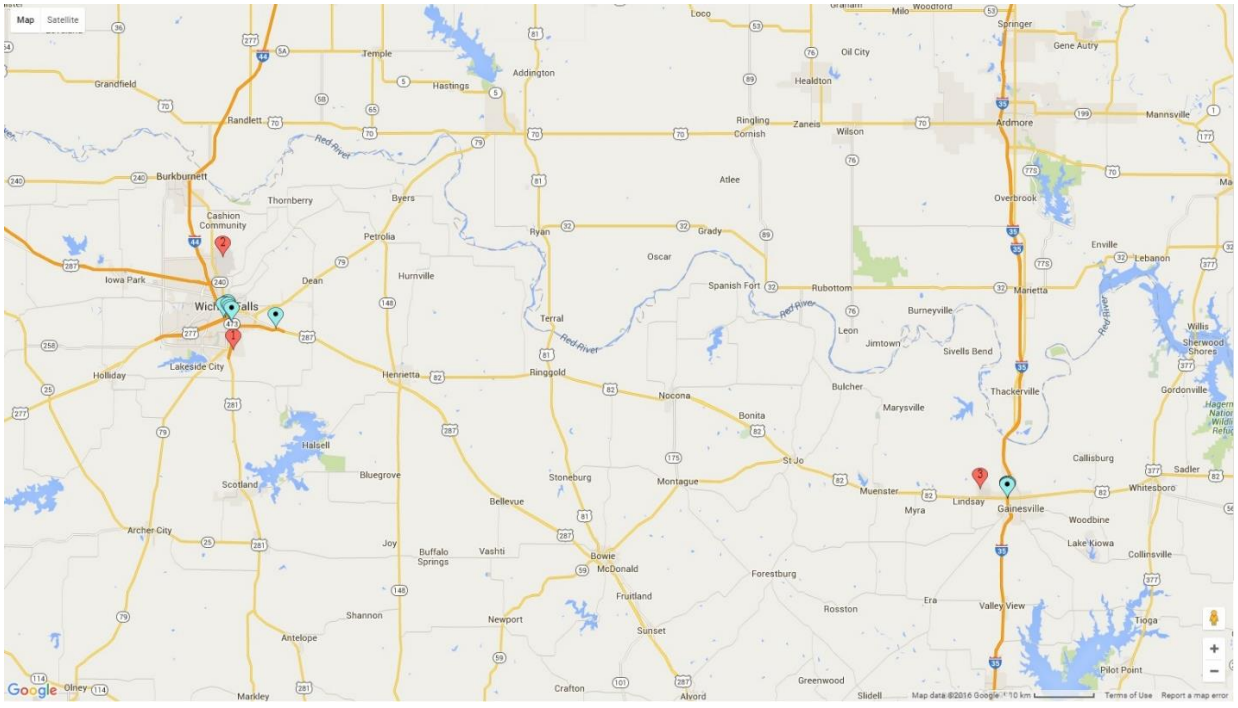

Figure 4.21: Locations of HMIPs and Weather Stations in Wichita Falls District

Secondary Sites

Although other Texas HMIP designs are not of primary concern in this research project, there are considerable number of such HMIPs in districts like Houston and San Antonio. Table 4.3 shows the total number of HMIPs in districts that do not have the HMIPs with the design of interest. It was, therefore, decided to include wind data in these districts to better represent the major wind environments in Texas. As highlighted in Table 4.4, five wind stations in Houston district and one in each remaining district are selected. The selected sites are spread throughout Texas to cover different wind environments. Locations of the selected weather sites (secondary sites) in Table 4.4 are further shown as blue balloons on the Texas map in Figure 4.9.

Table 4.3: Number of HMIPs in the Districts not Having HMIPs with the Design of Interest

		100 ft		125 ft		150 ft		175 ft		Total
		8 sided	12 sided	8 sided	12 sided	8 sided	12 sided	8 sided	12 sided	
Houston District	80 mph	0	0	0	0	0	0	0	0	**1618**
	100 mph	1	45	427	28	240	403	91	383	
San Antonio district	80 mph	10	0	0	0	107	0	10	0	**127**
	100 mph	0	0	0	0	0	0	0	0	
Pharr District	80 mph	0	0	0	0	0	0	0	0	**70**
	100 mph	0	0	0	0	0	70	0	0	
Beaumont District	80 mph	0	0	0	0	0	0	0	0	**59**
	100 mph	0	0	0	30	0	29	0	0	
Lubbock District	80 mph	0	0	18	1	0	0	0	0	**53**
	100 mph	0	0	0	7	0	27	0	0	
Tyler District	80 mph	0	0	0	0	34	0	18	0	**52**
	100 mph	0	0	0	0	0	0	0	0	
Corpus Christi District	80 mph	0	0	0	0	0	0	0	0	**31**
	100 mph	10	18	0	0	0	3	0	0	
Lufkin District	80 mph	0	0	0	0	0	0	0	24	**28**
	100 mph	0	0	0	0	0	0	0	4	
Abilene District	80 mph	0	0	0	0	0	0	0	0	**22**
	100 mph	0	0	0	4	1	17	0	0	
Amarillo District	80 mph	0	0	0	0	0	0	0	0	**20**
	100 mph	0	0	0	0	9	11	0	0	
Dallas District	80 mph	0	0	0	0	0	0	0	0	**10**
	100 mph	0	0	0	0	0	10	0	0	

Table 4.4: NOAA Weather Stations in Districts not Having HMIPs with the Design of Interest

District	State	Sign	WBAN	Name	Location	Latitude	Longitude
Houston	TX	GLS	12923	GALVESTON	SCHOLES INTL AT GLSTON APT	29.2733	-94.8592
	TX	HOU	12918	HOUSTON	WILLIAM P. HOBBY AIRPORT	29.63806	-95.28194
	TX	MCJ	188	HOUSTON	HOUSTON DUNN HELISTOP	29.717	-95.383
	TX	IAH	12960	HOUSTON	G BUSH INTERCONTINENTAL AP/HOUSTON AP	29.98	-95.36
	TX	SGR	12977	HOUSTON	SUGAR LAND REGIONAL ARPT	29.62194	-95.65667
	TX	LVJ	12975	HOUSTON	CLOVER FIELD AIRPORT	29.51889	-95.24167
	TX	DWH	53910	HOUSTON	HOOKS MEMORIAL AIRPT	30.0675	-95.55611
	TX	EFD	12906	HOUSTON	ELLINGTON FIELD AIRPORT	29.61667	-95.16667
	TX	TME	208	BROOKSHIRE	HOUSTON EXECUTIVE AIRPORT	29.8	-95.9
	TX	AXH	223	ARCOLA	HOUSTON SOUTHWEST AIRPORT	29.5	-95.477
San Antonio	TX	SKF	12909	SAN ANTONIO	LACKLAND AIR FORCE BASE (KELLY FIELD ANNEX)	29.38333	-98.58333
	TX	SAT	12921	SAN ANTONIO	SAN ANTONIO INTERNATIONAL AIRPORT	29.5443	-98.4839
	TX	SSF	12970	SAN ANTONIO	STINSON MINICIPAL AIRPORT	29.3389	-98.472
	TX	RND	12911	UNIVERSAL CITY	RANDOLPH AFB AIRPORT	29.5325	-98.2623
Pharr	TX	MFE	12959	MC ALLEN	MC ALLEN MILLER INTL ARPT	26.18389	-98.25389
	TX	EBG	12983	EDINBURG	EDINBURG INTL AIRPORT	26.44194	-98.12944
	TX	8620	12987	EDINBURG	EDINBURG 17 NNE	26.5258	-98.0633
	TX	HRL	12904	HARLINGEN	VALLEY INTERNATIONAL ARPT	26.22806	-97.65417
	TX	T65	12980	WESLACO	MID VALLEY AIRPORT	26.1775	-97.97306
Beaumont	TX	BPT	12917	BEAUMONT/PORT ARTHUR	SOUTHEAST TEXAS REGIONAL AIRPORT	29.95056	-94.02056
	TX	ORG	53998	ORANGE	ORANGE COUNTY AIRPORT	30.06917	-93.80361
	TX	BMT	313	BEAUMONT	BEAUMONT MUNICIPAL AIRPORT	30.071	-94.216
Lubbock	TX	LBB	23042	LUBBOCK	LUBBOCK INTERNATIONAL AIRPORT	33.6656	-101.8231
Tyler	TX	TYR	13972	TYLER	TYLER POUNDS REGIONAL ARPT	32.35417	-95.4025
	TX	GGG	3901	LONGVIEW	EAST TEXAS REGIONAL ARPT	32.38472	-94.71167
Corpus Christi	TX	CRP	12924	CORPUS CHRISTI	CORPUS CHRISTI INTERNATIONAL AIRPORT	27.7742	-97.5122
	TX	NGW	12946	CORPUS CHRISTI	CABANISS FIELD NAVAL OUTLYING FIELD	27.7	-97.43333
	TX	RBO	12984	ROBSTOWN	NUECES COUNTY ARIPORT	27.77861	-97.69056
	TX	ALI	12932	ALICE	ALICE INTERNATIONAL ARPT	27.74111	-98.02472
	TX	TFP	365	ARANSAS PASS	T P MC CAMPBELL AIRPORT	27.917	-97.2
Lufkin	TX	LFK	93987	LUFKIN	ANGELINA COUNTY AIRPORT	31.23611	-94.75444
	TX	6R3	378	CLEVELAND	CLEVELAND MUNICIPAL AIRPORT	30.356	-95.008
Abilene	TX	ABI	13962	ABILENE	ABILENE REGIONAL AIRPORT	32.4105	-99.6822
	TX	DYS	13910	ABILENE	DYESS AIR FORCE BASE	32.43333	-99.85
	TX	SWW	23033	SWEETWATER	AVENGER FIELD AIRPORT	32.47333	-100.46639
Amarillo	TX	AMA	23047	AMARILLO	AMARILLO RICK HUSBAND INTL AIRPORT	35.2295	-101.7042
Dallas	TX	DAL	13960	DALLAS	DALLAS LOVE FIELD AIRPORT	32.8519	-96.8555
	TX	RBD	3971	DALLAS	DALLAS EXECUTIVE AIRPORT	32.68083	-96.86806

	TX	HQZ	53970	MESQUITE	MESQUITE METROPOLITAN ARPT	32.74694	-96.53056
	TX	ADS	3970	DALLAS	ADDISON AIRPORT	32.96861	-96.83639

Figures 4.22 to 4.32 show the locations of HMIPs and the weather stations in each district not having HMIPs with the design of interest. The red and pink balloons indicate the location of weather sites whereas the blue balloons indicate the location of HMIPs in the district. The wind data are considered from the sites indicated with red balloon to represent the wind environment for the entire district. The yellow-marker in Figure 4.32 indicates the location of the HMIP selected for field monitoring in this research (Chapter 6).

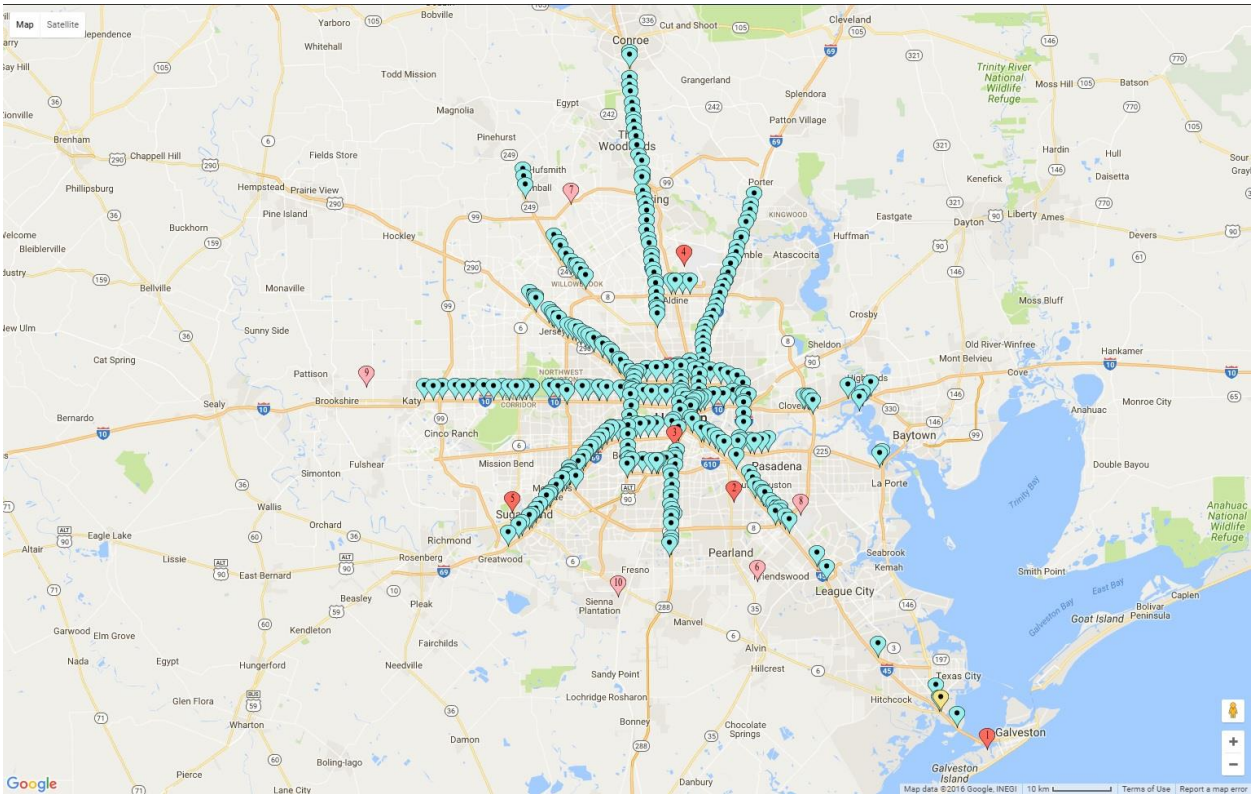

Figure 4.22: Locations of HMIPs and Weather Stations in Houston District

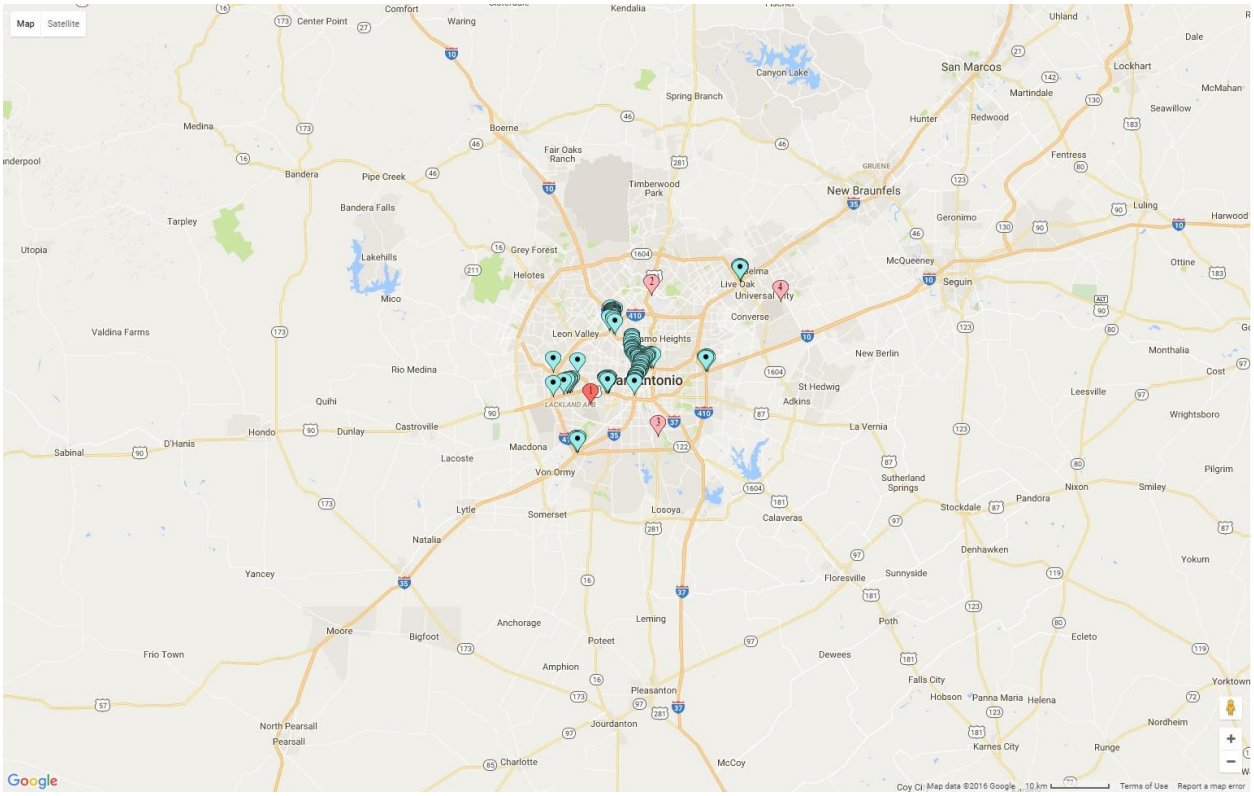

Figure 4.23: Locations of HMIPs and Weather Stations in San Antonio District

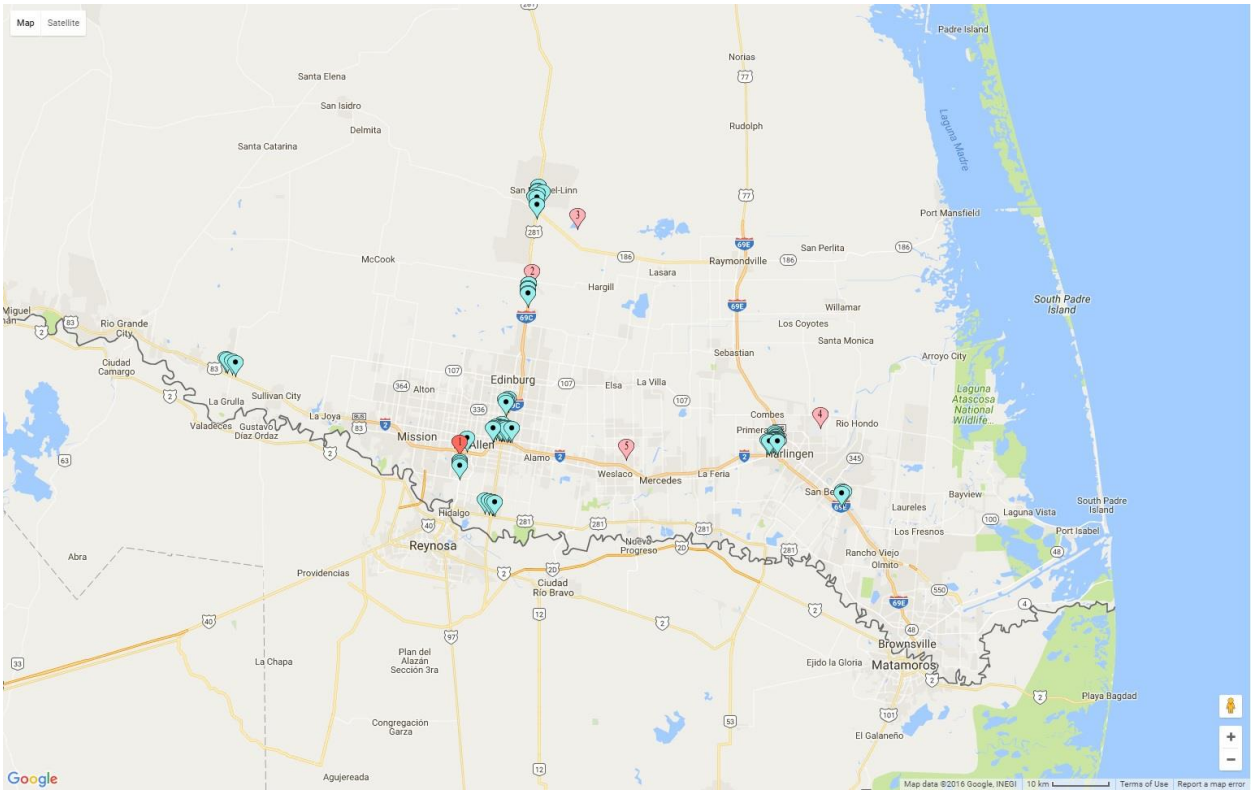

Figure 4.24: Locations of HMIPs and Weather Stations in Pharr District

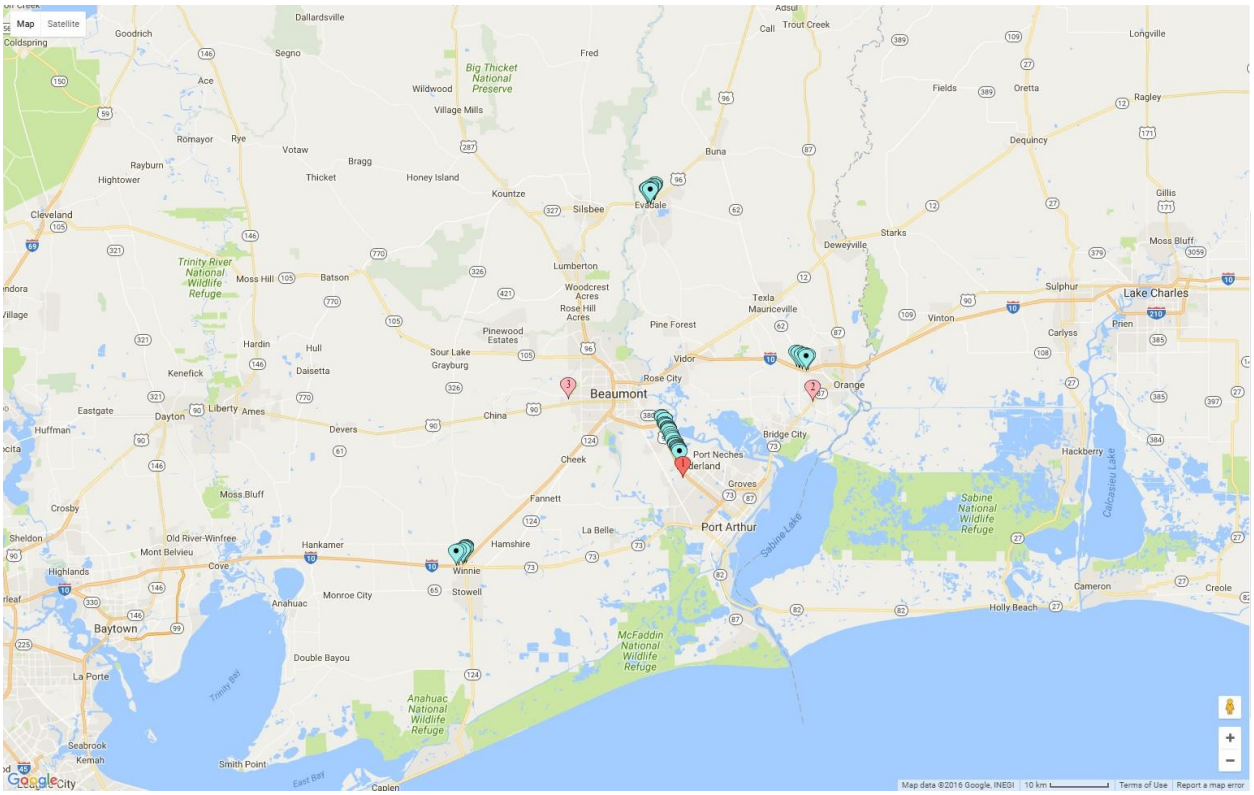

Figure 4.25: Locations of HMIPs and Weather Stations in Beaumont District

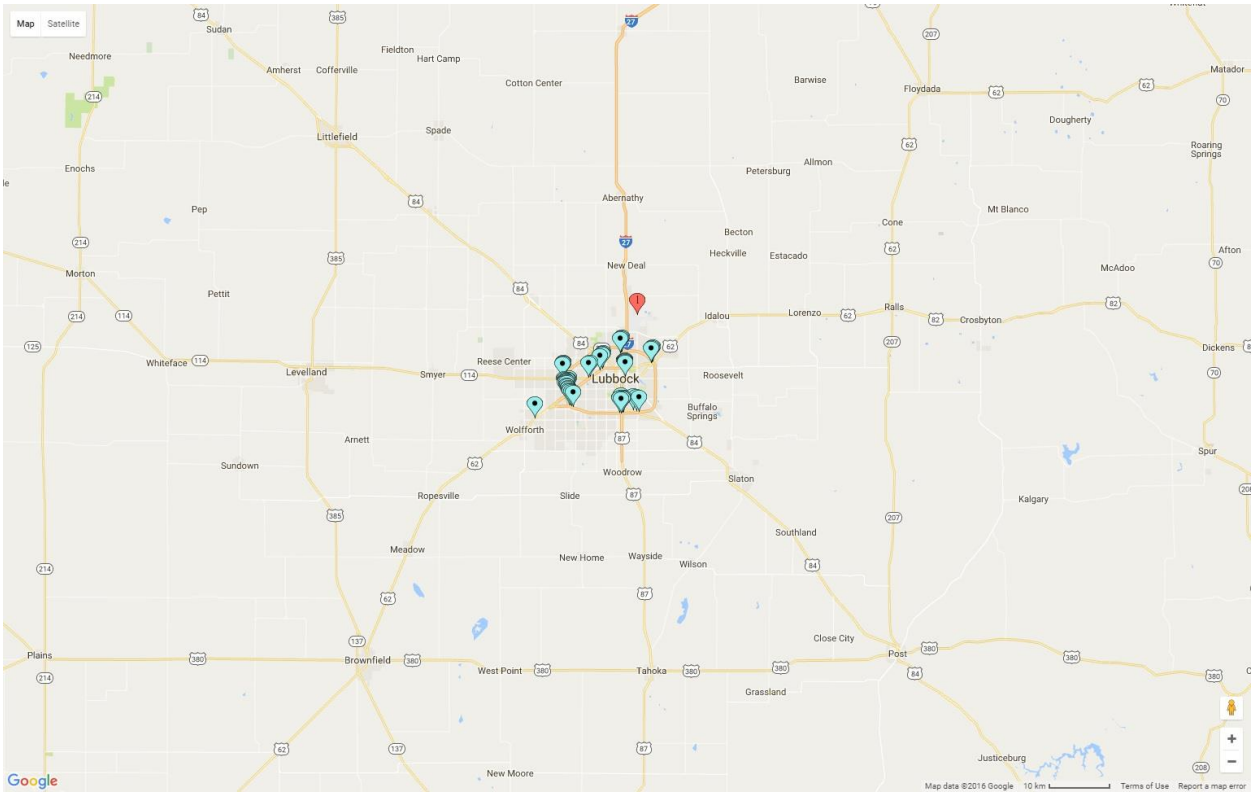

Figure 4.26: Locations of HMIPs and Weather Stations in Lubbock District

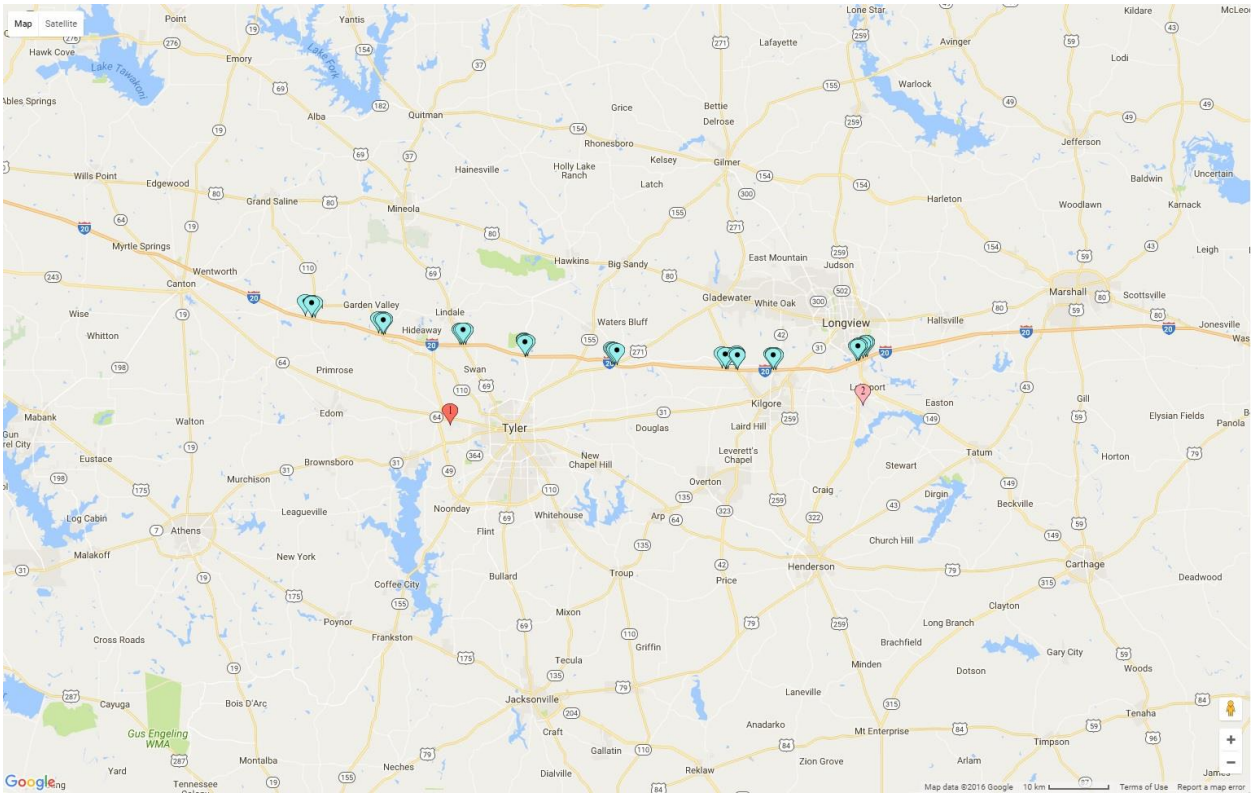

Figure 4.27: Locations of HMIPs and Weather Stations in Tyler District

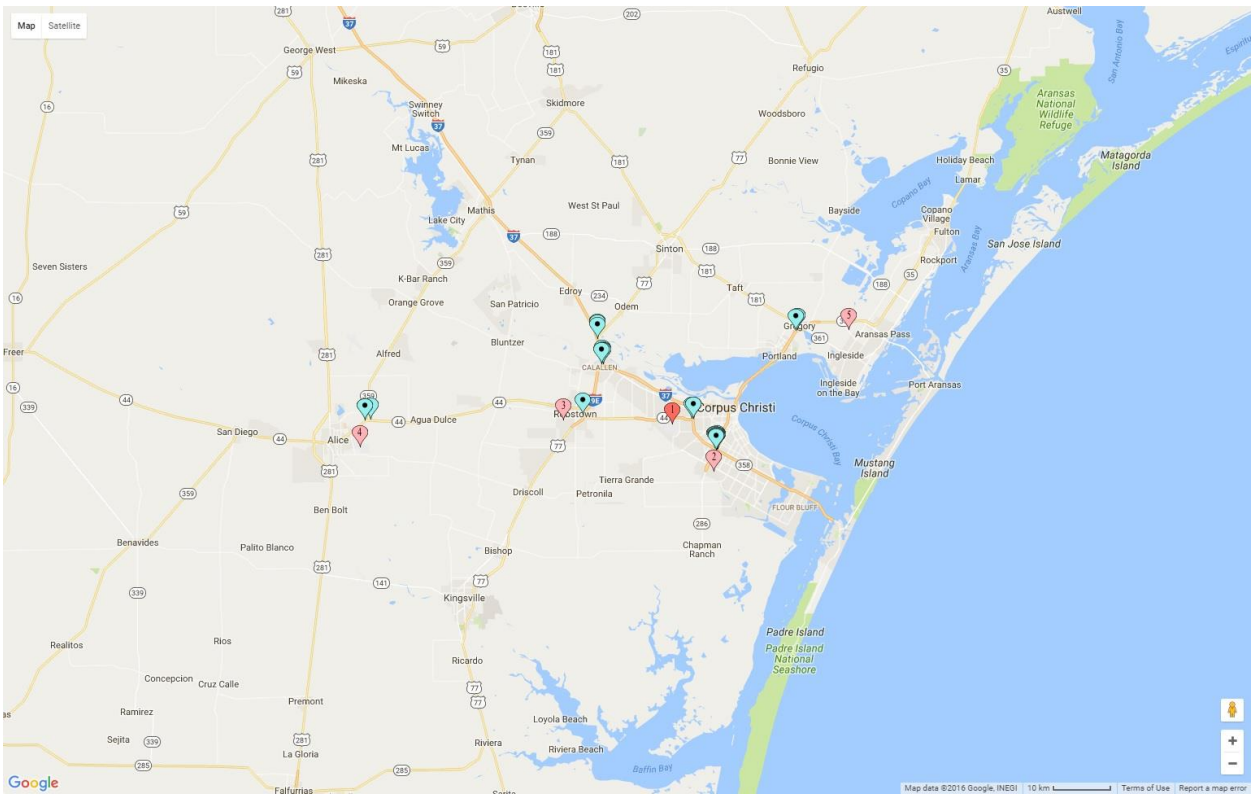

Figure 4.28: Locations of HMIPs and Weather Stations in Corpus Christi District

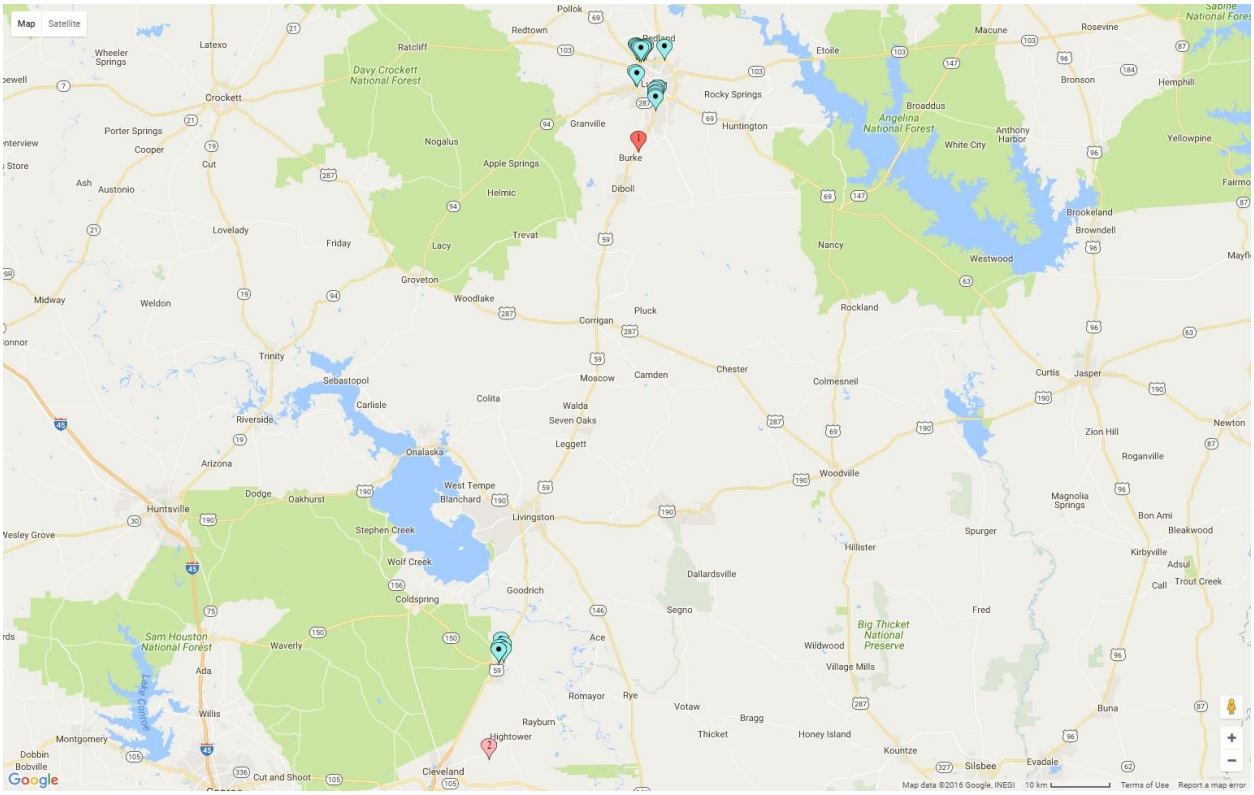

Figure 4.29: Locations of HMIPs and Weather Stations in Lufkin District

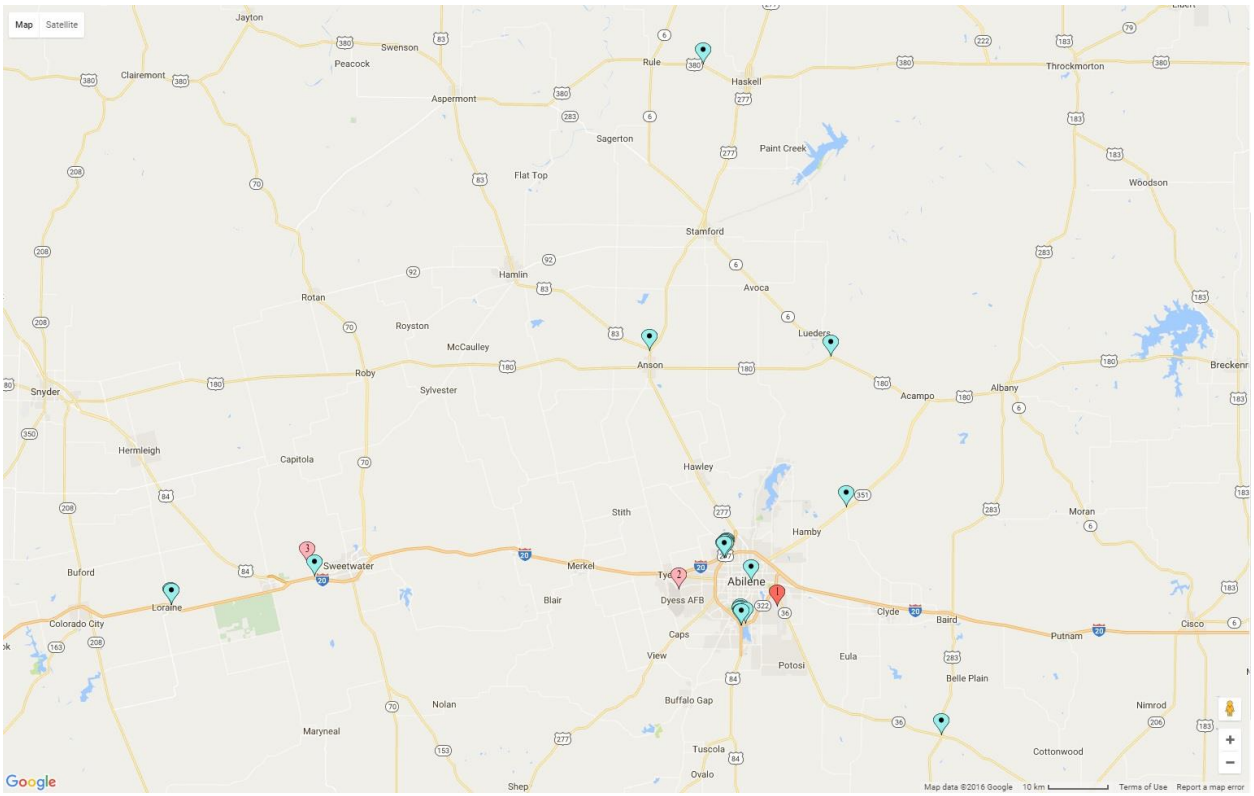

Figure 4.30: Locations of HMIPs and Weather Stations in Abilene District

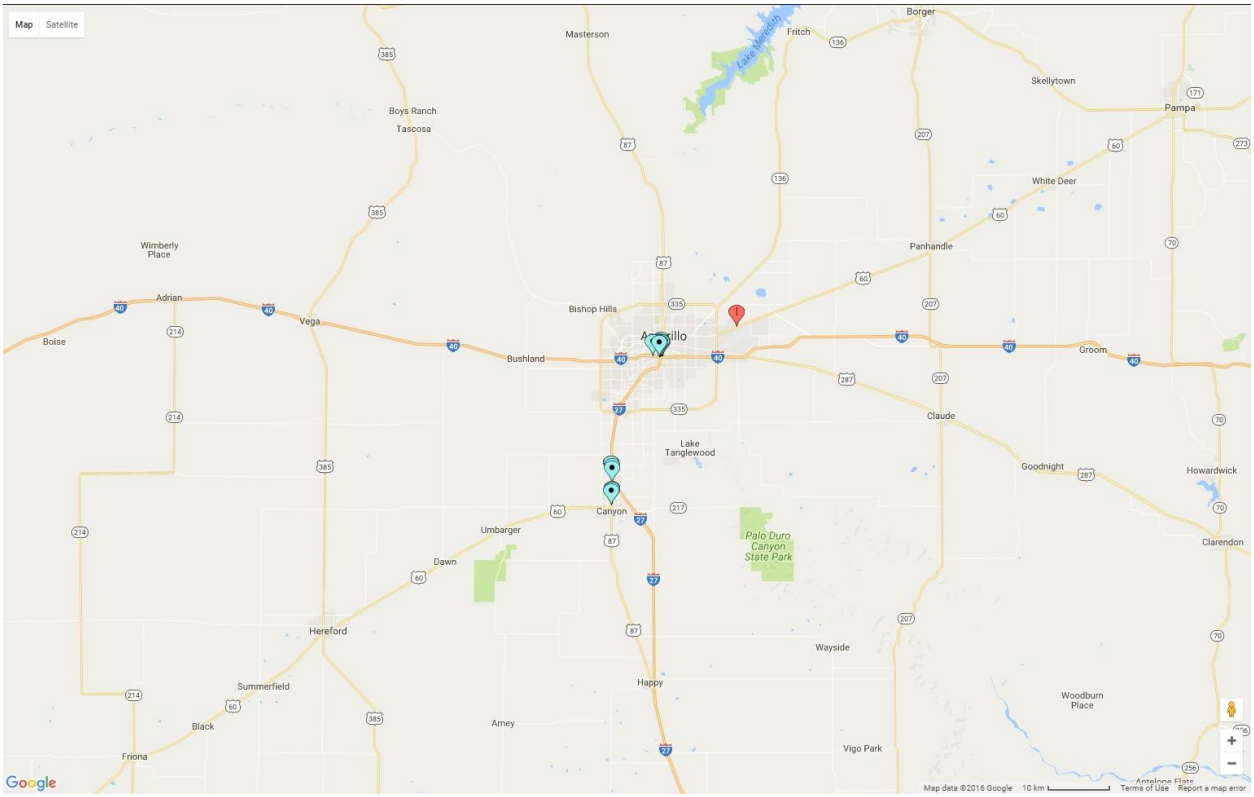

Figure 4.31: Locations of HMIPs and Weather Stations in Amarillo District

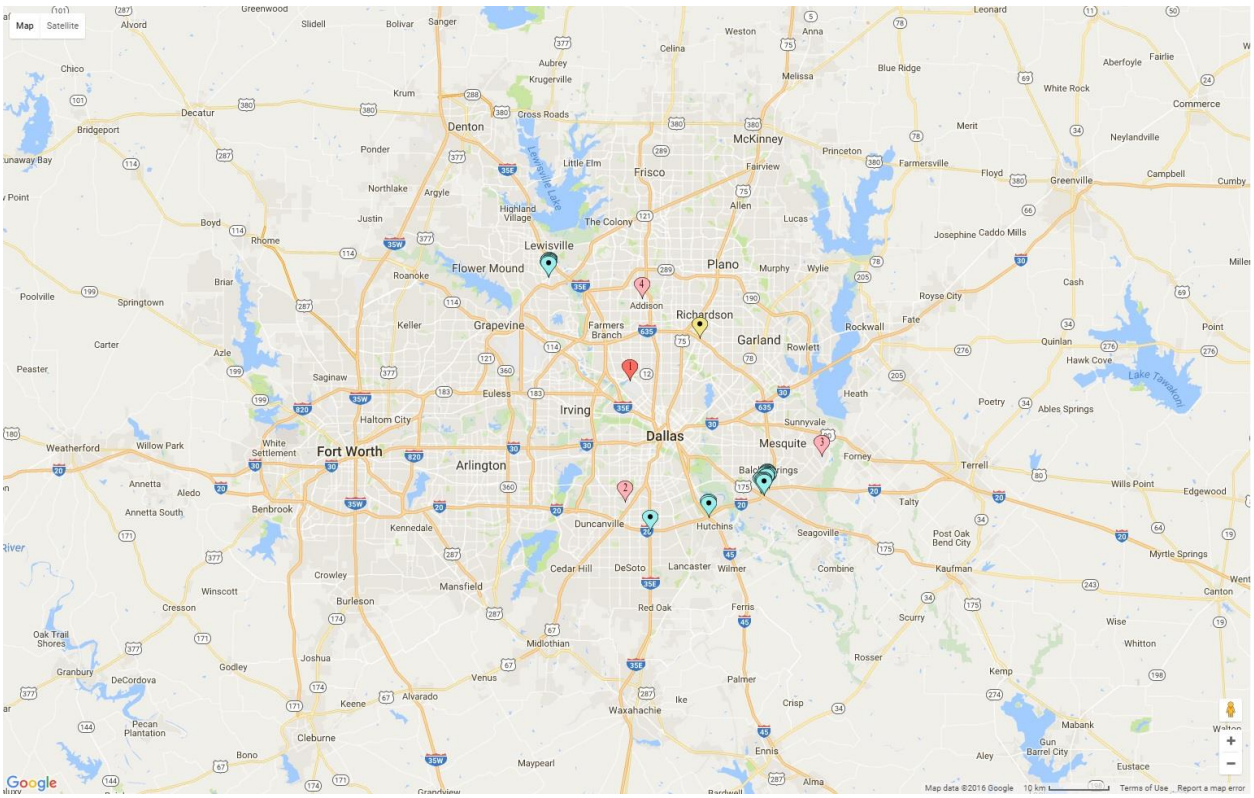

Figure 4.32: Locations of HMIPs and Weather Stations in Dallas District

4.3 Historical Wind Data in Texas - Primary Sites

4.3.1 Yearly Averaged Wind Data

Yearly average wind speeds for primary sites are listed in Table 4.5. Figure 4.33 further indicates if the wind speed at any location has any specific trend over the span of eight years from 2008 to 2015.

Table 4.5: Yearly Average Wind Speed for Primary Sites

District	WBAN	2008	2009	2010	2011	2012	2013	2014	2015	Average
Austin	230	N/A	N/A	N/A	N/A	N/A	N/A	N/A	6.31	6.31
	13958	4.95	4.80	4.65	5.46	4.84	5.14	5.16	4.66	4.96
	13904	8.59	8.09	7.62	9.05	7.43	7.71	8.62	7.84	8.12
	53942	7.91	7.77	7.99	9.33	7.73	7.82	8.44	7.37	8.04
Laredo	12907	9.70	9.70	N/A	N/A	10.41	9.35	9.91	9.45	9.75
Atlanta	13977	6.77	6.48	6.26	6.98	6.58	6.10	6.67	6.47	6.54
	3901	7.60	6.91	6.65	7.76	6.62	6.78	7.02	6.67	7.00
El Paso	23044	8.88	8.18	8.24	8.52	8.12	8.36	8.59	7.92	8.35
Odessa	3031	9.98	9.51	10.20	10.23	9.98	10.33	9.05	10.36	9.96
	23023	10.33	9.63	10.47	10.98	10.63	11.08	11.60	10.43	10.64
	3071	9.43	9.03	9.18	9.67	9.31	8.91	9.58	8.65	9.22
Ft. Worth	3927	11.31	10.56	10.31	11.04	10.18	10.55	11.41	9.99	10.67
	13961	9.97	9.30	8.91	10.20	9.22	9.38	10.30	9.27	9.57
	13911	9.55	9.35	9.07	9.97	9.01	9.00	10.47	9.09	9.44
	53977	7.66	7.13	7.22	8.04	7.30	7.17	7.49	6.36	7.30
Paris	13926	7.55	7.17	7.06	7.81	7.33	6.45	7.26	6.35	7.12
	93955	9.68	9.15	9.06	9.68	9.03	9.09	9.03	7.32	9.01
	53967	10.07	9.42	9.15	10.29	9.45	9.32	9.65	8.55	9.49
Waco	53972	9.73	9.50	8.98	9.72	8.13	9.31	9.78	8.65	9.23
	13959	8.91	9.38	9.35	10.42	9.33	9.08	10.08	9.19	9.47
	53952	9.39	9.32	9.36	10.57	9.06	9.01	9.67	8.61	9.37
	93984	10.39	10.04	10.23	11.37	10.04	9.28	10.50	9.42	10.16
	3902	10.23	9.63	9.90	10.89	10.21	10.14	10.63	9.31	10.12
	3933	8.82	8.22	8.37	9.09	7.95	8.02	8.30	8.77	8.44
	3972	8.97	8.85	8.75	9.81	8.58	8.49	8.99	7.37	8.73
Brownwood	176	N/A	N/A	N/A	N/A	N/A	N/A	N/A	8.14	8.14
Wichita Falls	134	N/A	N/A	N/A	N/A	N/A	N/A	N/A	8.12	8.12
	13966	11.93	10.99	10.68	11.79	10.91	11.13	11.56	10.63	11.20
	93929	9.07	8.75	8.14	8.95	7.94	7.97	8.48	7.66	8.37
Bryan	3904	8.56	8.33	7.81	9.07	7.63	7.98	8.65	7.83	8.23
	438	N/A	N/A	N/A	N/A	N/A	N/A	N/A	6.06	6.06

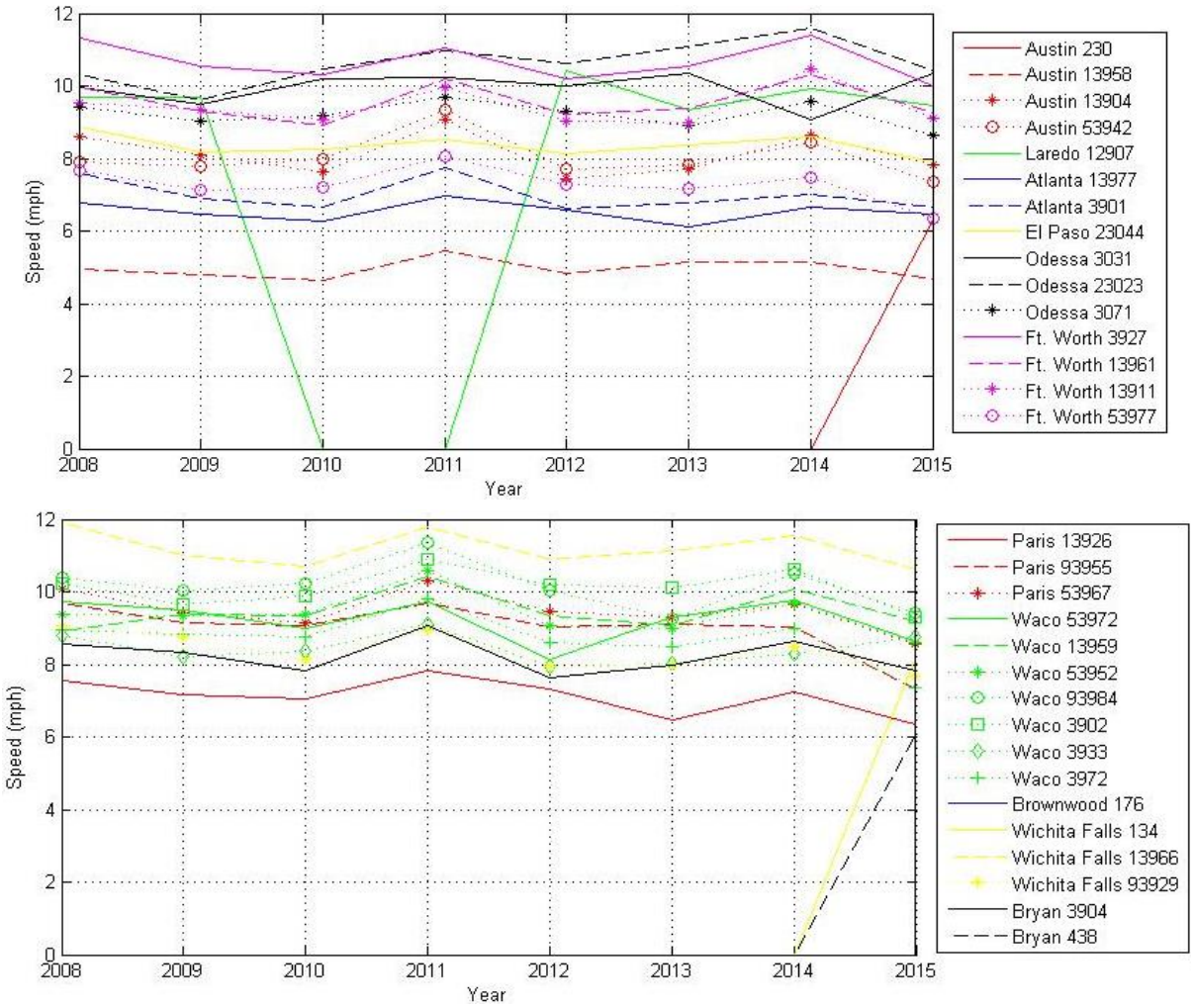

Figure 4.33: Yearly Average Wind Speed for Primary Sites over the Span of 2008 to 2015

Average wind speeds for each month over the period of eight years from 2008 to 2015 are tabulated in Table 4.6 for the primary sites. Seasonal variation can specifically be observed in Figure 4.34.

Table 4.6: Monthly Average Wind Speed from 2008 to 2015 for Primary Sites

District	WBAN	Jan	Feb	Mar	Apr	May	Jun	Jul	Aug	Sep	Oct	Nov	Dec	Ave.
Austin	230	8.22	8.99	8.02	7.70	6.88	2.89	5.71	4.84	4.12	6.91	7.78	7.32	6.61
	13958	4.50	5.45	5.92	6.15	5.87	5.60	4.84	4.46	3.77	4.25	4.38	4.33	4.96
	13904	8.03	9.22	9.41	9.62	9.50	8.72	7.66	7.04	6.15	6.96	7.43	7.79	8.13
	53942	7.78	8.70	9.17	9.40	9.03	9.00	8.05	7.29	6.13	7.06	7.22	7.35	8.01
Laredo	12907	7.83	8.94	10.76	11.23	11.30	12.52	11.98	10.62	7.94	9.00	7.75	7.59	9.79
Atlanta	13977	6.98	7.28	7.81	8.08	7.03	6.31	5.72	5.21	4.92	5.79	6.58	6.80	6.54
	3901	7.38	8.00	8.18	8.88	7.86	6.90	6.11	5.75	5.20	5.96	6.78	7.10	7.01
El Paso	23044	7.11	8.72	9.61	11.51	10.62	9.05	7.84	7.18	6.93	6.92	7.07	7.71	8.36
Odessa	3031	8.73	10.24	10.90	11.58	10.21	11.60	10.51	9.30	8.78	9.41	9.18	9.09	9.96
	23023	9.54	10.89	11.57	12.80	12.29	12.95	10.42	9.34	9.04	9.66	9.63	9.69	10.65
	3071	8.40	9.58	10.23	11.25	10.57	11.29	9.14	7.71	7.70	8.29	8.27	8.27	9.22
Ft. Worth	3927	10.51	11.64	12.50	12.87	11.74	11.50	9.64	8.83	8.37	9.72	10.56	10.25	10.68
	13961	9.00	10.29	11.22	11.66	10.65	10.57	8.79	8.20	7.72	8.43	9.34	9.06	9.58
	13911	8.74	10.00	11.17	11.25	10.78	10.88	8.92	7.89	7.49	8.43	9.28	8.58	9.45
	53977	6.78	7.92	8.62	9.29	8.42	8.46	6.85	5.82	5.50	6.29	6.97	6.68	7.30
Paris	13926	7.29	8.13	8.74	8.89	7.72	7.48	6.13	5.53	5.20	6.14	7.14	7.16	7.13
	93955	9.56	10.15	10.13	9.68	9.28	8.97	7.67	7.56	7.90	8.59	9.31	9.38	9.02
	53967	9.29	10.09	11.06	11.48	10.09	10.12	8.27	7.80	7.55	8.75	9.93	9.29	9.48
Waco	53972	9.13	10.61	11.15	10.99	9.87	9.13	7.81	7.59	7.54	8.47	9.36	9.12	9.23
	13959	9.19	10.34	10.92	11.07	10.36	10.30	8.98	8.28	7.58	8.57	9.07	9.04	9.47
	53952	9.13	10.34	10.78	10.87	9.90	9.81	8.51	8.38	7.69	8.82	9.21	9.09	9.38
	93984	9.68	10.88	11.59	11.85	11.51	11.28	9.47	8.98	8.05	9.18	9.62	9.65	10.14
	3902	10.00	11.14	11.62	12.13	11.31	10.98	9.45	8.40	7.89	9.25	9.70	9.63	10.12
	3933	8.28	9.52	9.80	10.36	9.53	9.12	7.90	6.94	6.52	7.51	7.81	7.95	8.44
	3972	8.28	9.30	9.69	10.61	10.17	9.89	8.37	7.48	6.69	7.95	8.19	8.02	8.72
Brownwood	176	7.42	8.91	6.77	9.43	9.49	7.63	8.54	7.84	7.43	7.70	9.08	8.29	8.21
Wichita Falls	134	8.15	9.06	7.12	9.66	8.93	7.94	8.31	7.38	7.52	7.78	8.82	7.68	8.20
	13966	10.76	11.39	12.60	13.45	12.56	12.64	10.18	9.65	9.43	10.37	11.17	10.31	11.21
	93929	8.31	9.18	10.26	10.58	9.37	8.96	6.96	6.53	6.50	7.12	8.61	8.21	8.38
Bryan	3904	8.22	9.36	9.65	10.09	9.51	8.26	7.20	6.87	6.51	7.15	7.87	8.15	8.24
	438	4.09	7.32	6.30	6.90	7.50	5.21	7.11	5.38	4.32	5.82	6.80	6.41	6.10

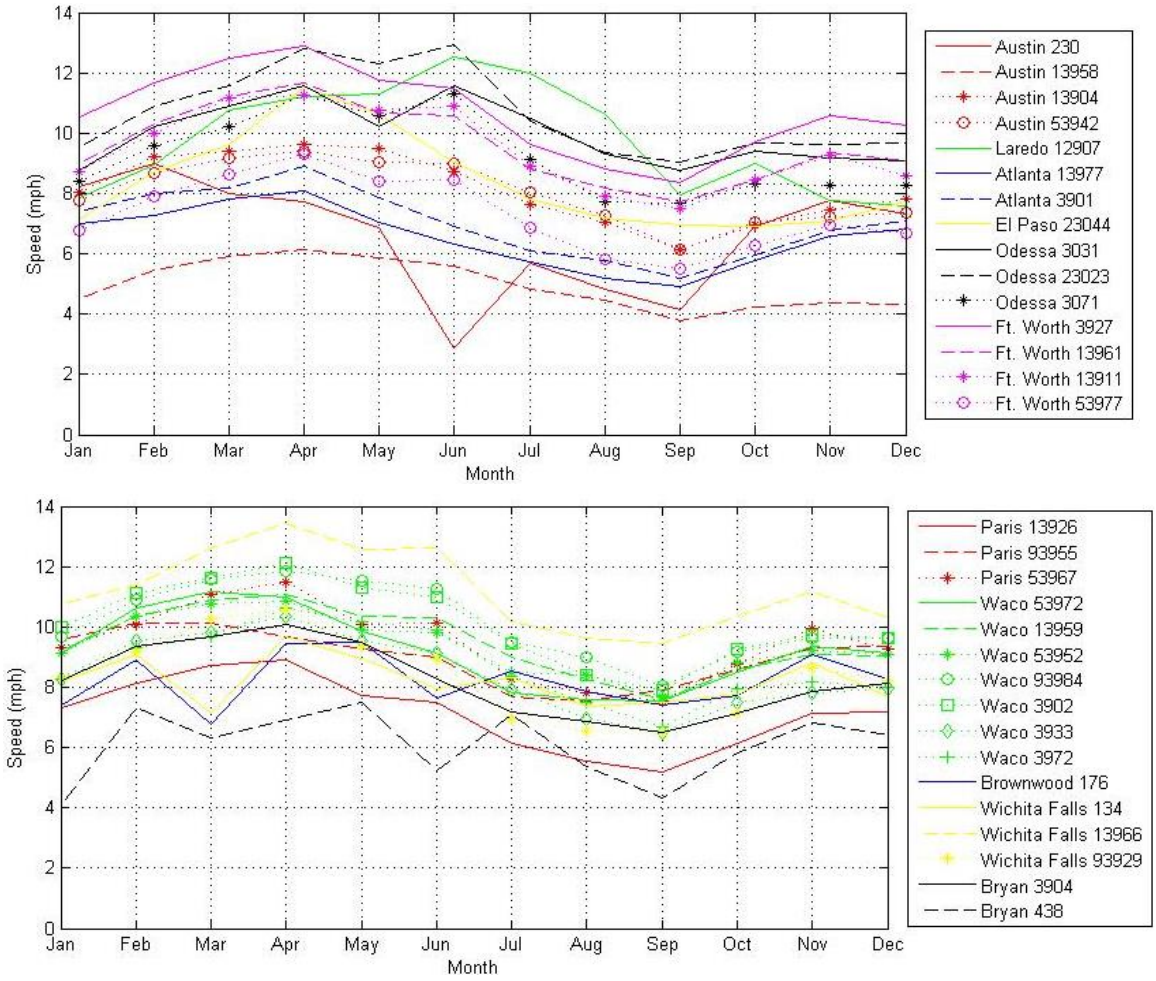

Figure 4.34: Monthly Average Wind Speed for Primary Sites over the Span of 2008 to 2015

4.3.2 Site-Specific Wind Data from Primary Sites

Historical data for the 31 primary sites are presented with four graphs: wind rose graph, wind density graph, wind speed rate of occurrence, and monthly average wind speed and gust wind variation. The graphs of wind roses, wind densities, and wind speed rates of occurrence use the hourly wind data, while the graph of the monthly average wind speed uses the daily wind speed data. Each site is presented with a one-year short term data in 2015 and a long term data covering the span of eight years at most. Data gap may occur in some of the sites. To illustrate this gap, the number of collection days in each year in percent are shown in Table 4.7.

Table 4.7: Days of Collected Wind Data at Primary Sites (in Percent)

District	WBAN	2008	2009	2010	2011	2012	2013	2014	2015
Austin	230	0	0	0	0	0	0	42	100
	13958	100	100	100	100	100	100	100	100
	13904	100	100	100	100	100	100	100	100
	53942	99	100	100	100	100	100	100	100
Laredo	12907	99	99	75	54	100	100	100	100
Atlanta	13977	100	100	100	100	100	100	100	100
	3901	100	100	100	100	100	92	100	100
El Paso	23044	100	100	100	100	100	100	100	100
Odessa	3031	100	100	100	100	100	100	100	100
	23023	100	100	100	100	100	100	100	100
	3071	99	100	100	100	100	100	100	100
Ft. Worth	3927	100	100	100	100	100	92	100	100
	13961	100	100	100	100	100	100	100	100
	13911	98	100	100	100	100	100	100	100
	53977	99	100	100	99	100	100	100	100
Paris	13926	97	100	100	99	100	100	100	100
	93955	98	99	99	100	100	100	100	98
	53967	99	99	100	100	100	100	100	100
Waco	53972	99	100	100	99	100	100	100	100
	13959	100	100	100	100	100	100	100	100
	53952	98	97	100	99	96	100	100	99
	93984	98	100	100	98	100	100	100	97
	3902	99	100	100	100	100	92	100	100
	3933	96	95	100	100	99	95	96	99
	3972	97	99	99	96	100	100	97	94
Brownwood	176	0	0	0	0	0	0	42	100
Wichita Falls	134	0	0	0	0	0	0	44	100
	13966	99	100	100	100	100	100	100	100
	93929	99	100	100	99	100	100	99	96
Bryan	3904	100	100	100	100	100	92	100	100
	438	0	0	0	0	0	0	42	99

%

AUSTIN EXECUTIVE AIRPORT (230)

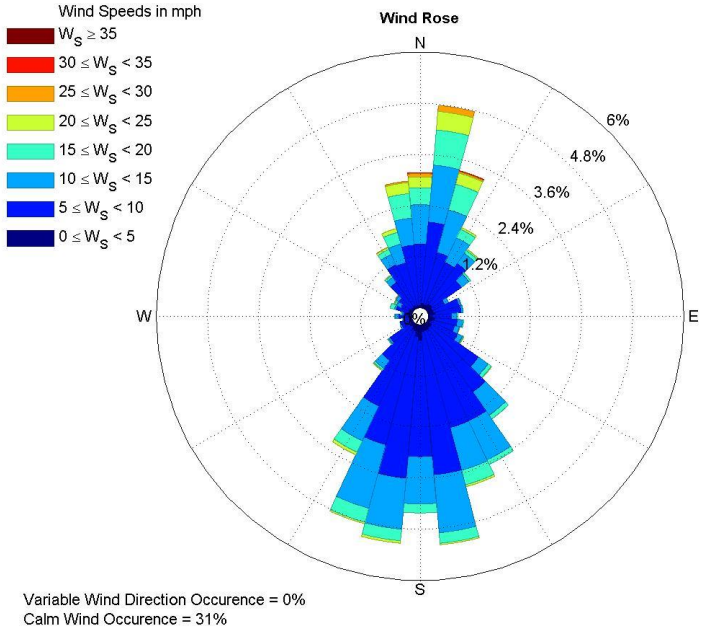

(a) Wind Rose Graph

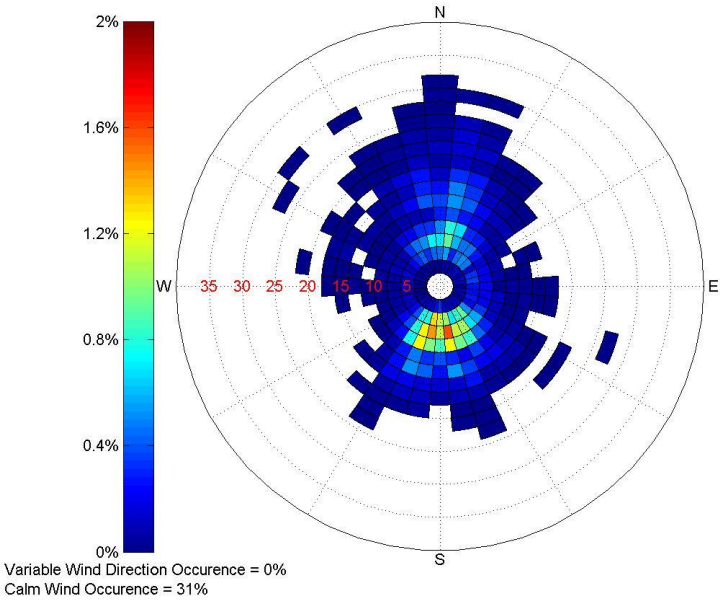

(b) Wind Density Graph

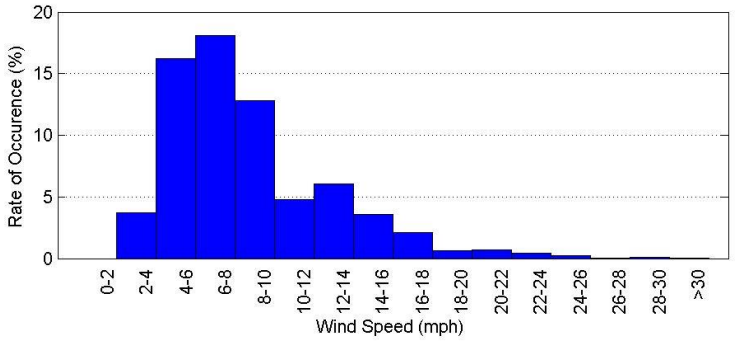

(c) Wind Speed Occurrence Rate

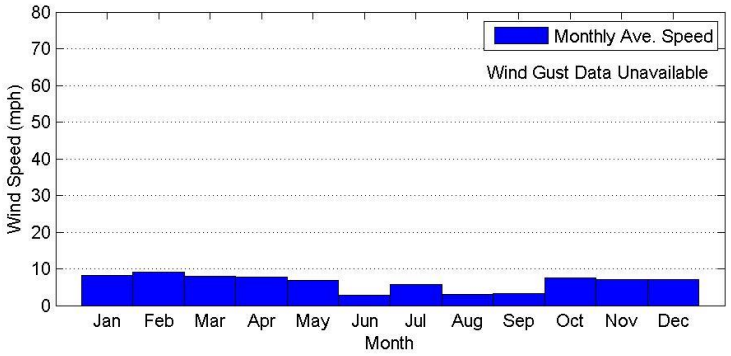

(d) Monthly Average Wind Speed

Figure 4.35: Wind Data Collected at the Austin Executive Airport (230) in the Year 2015

AUSTIN CAMP MABRY ARMY NATIONAL GUARD (13958)

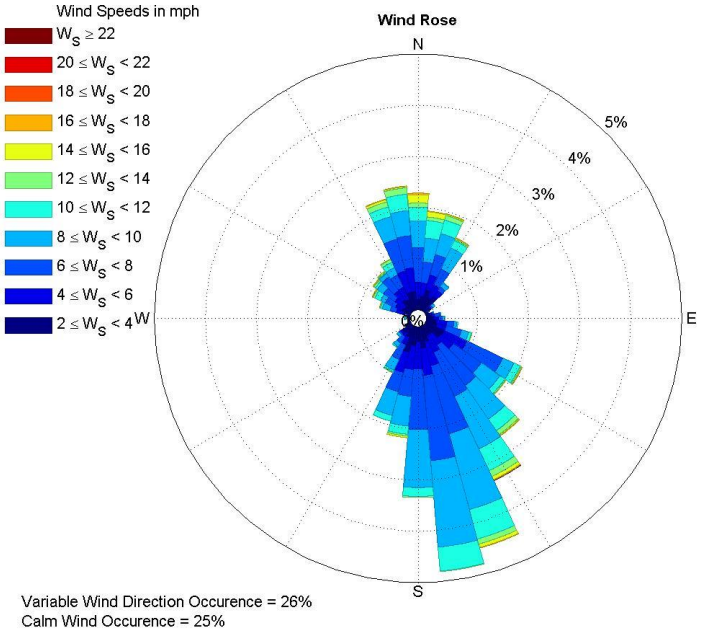

(a) Wind Rose Graph

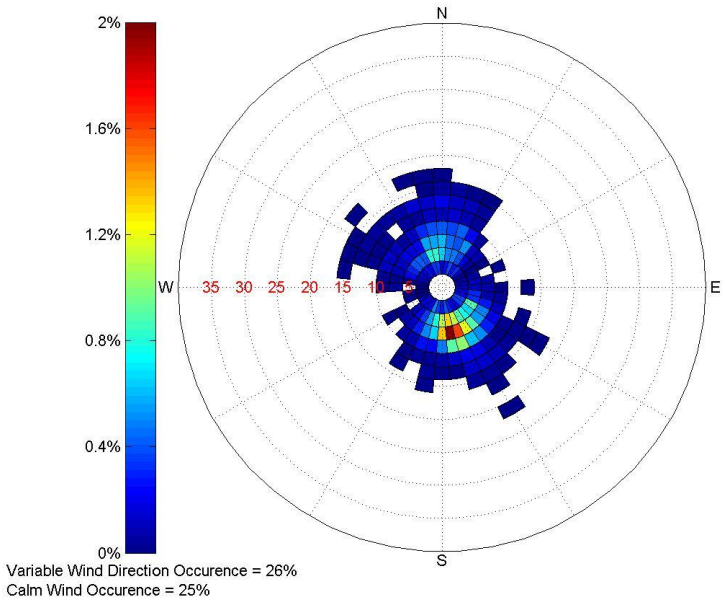

(b) Wind Density Graph

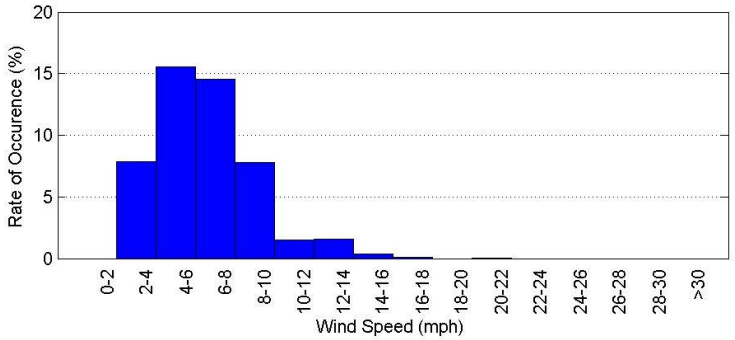

(c) Wind Speed Occurrence Rate

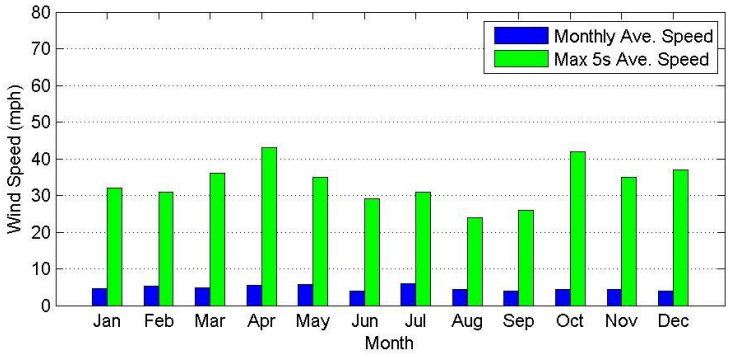

(d) Monthly Average Wind Speed

Figure 4.36: Wind Data Collected at the Austin Camp Mabry Army National Guard (13958) in the Year 2015

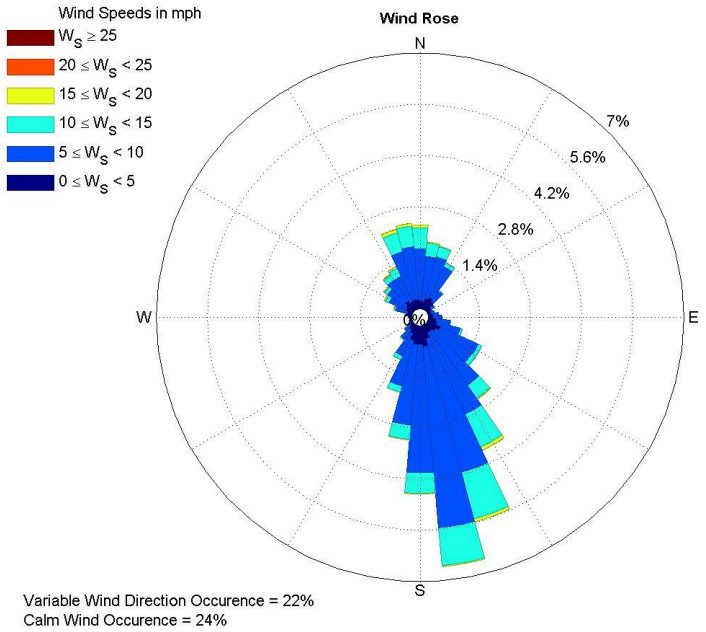

(a) Wind Rose Graph

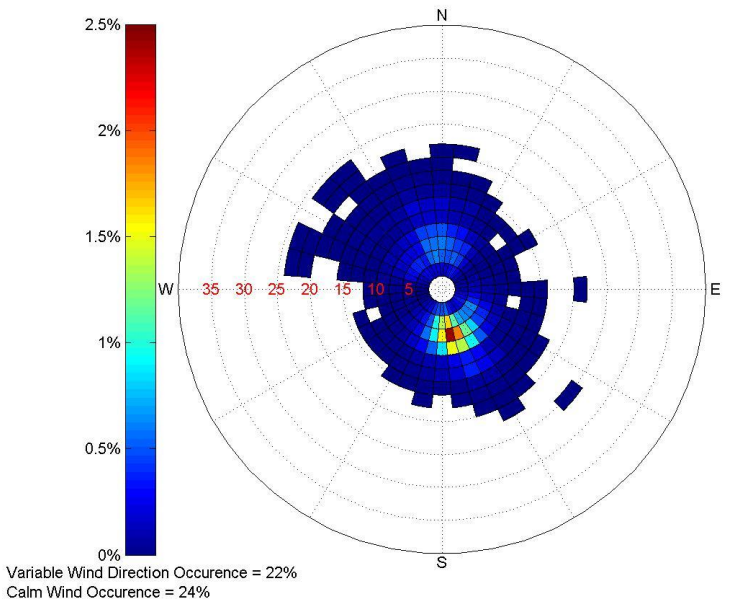

(b) Wind Density Graph

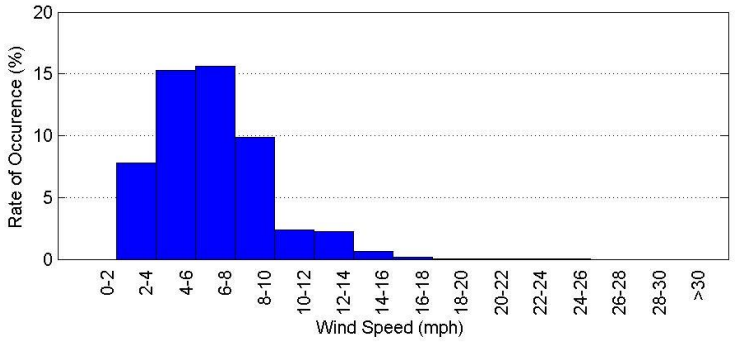

(c) Wind Speed Occurrence Rate

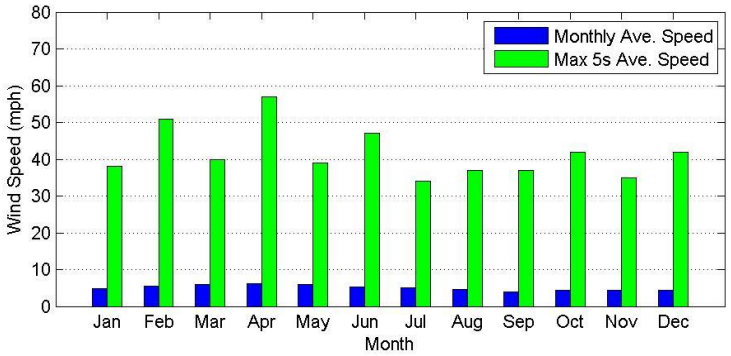

(d) Monthly Average Wind Speed

Figure 4.37: Wind Data Collected at the Austin Camp Mabry Army National Guard (13958) from 2008 to 2015

AUSTIN BERGSTROM INTL AIRPORT (13904)

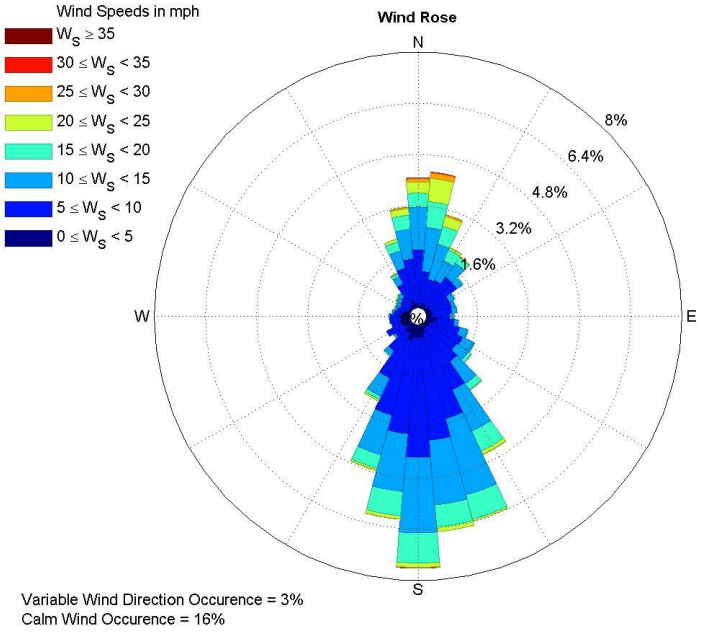

(a) Wind Rose Graph

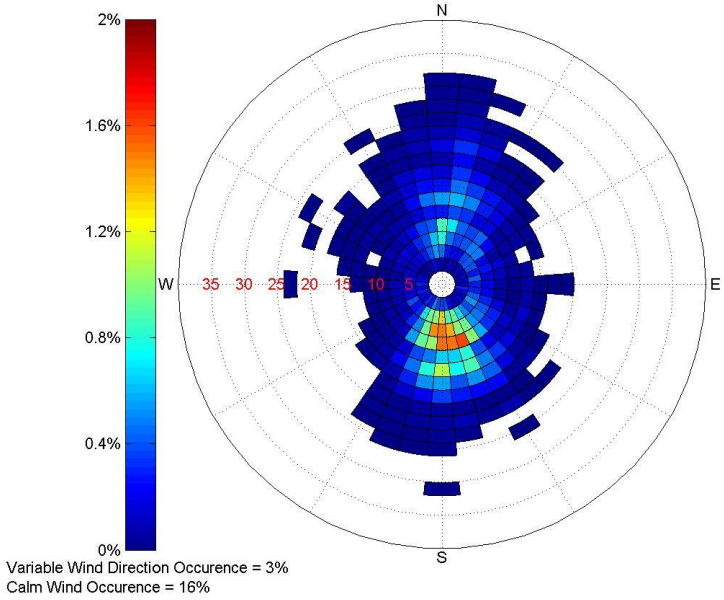

(b) Wind Density Graph

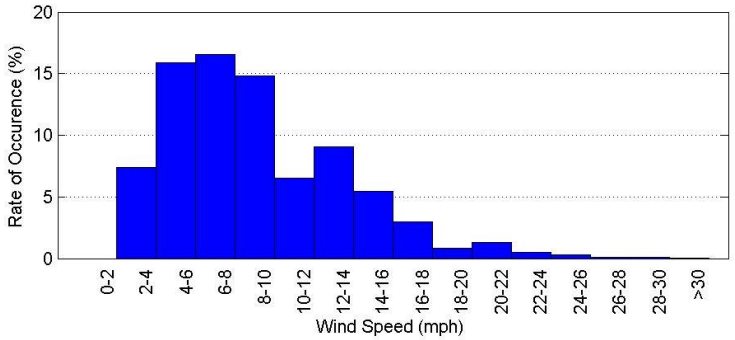

(c) Wind Speed Occurrence Rate

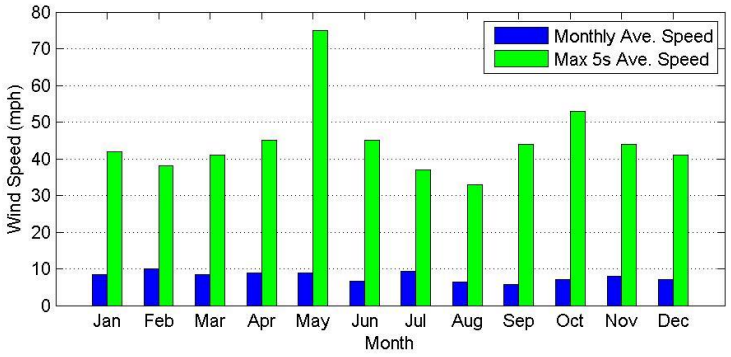

(d) Monthly Average Wind Speed

Figure 4.38: Wind Data Collected at the Austin Bergstrom International Airport (13904) in the Year 2015

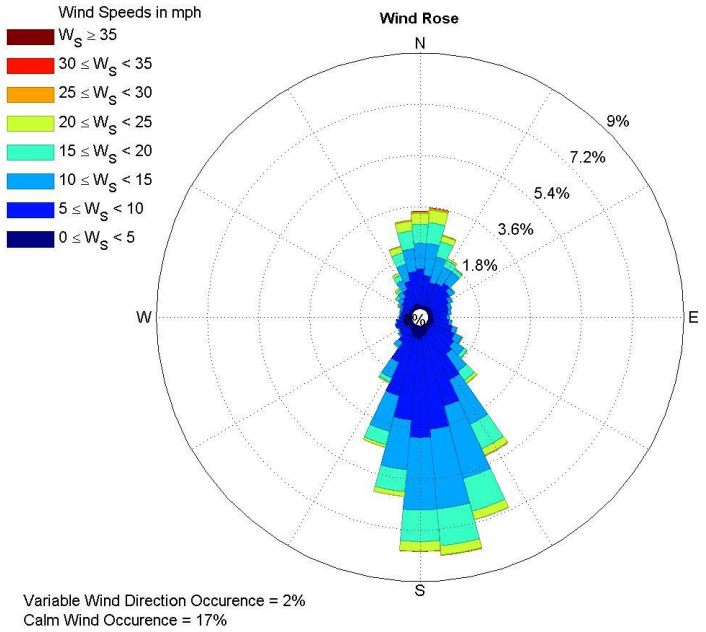

(a) Wind Rose Graph

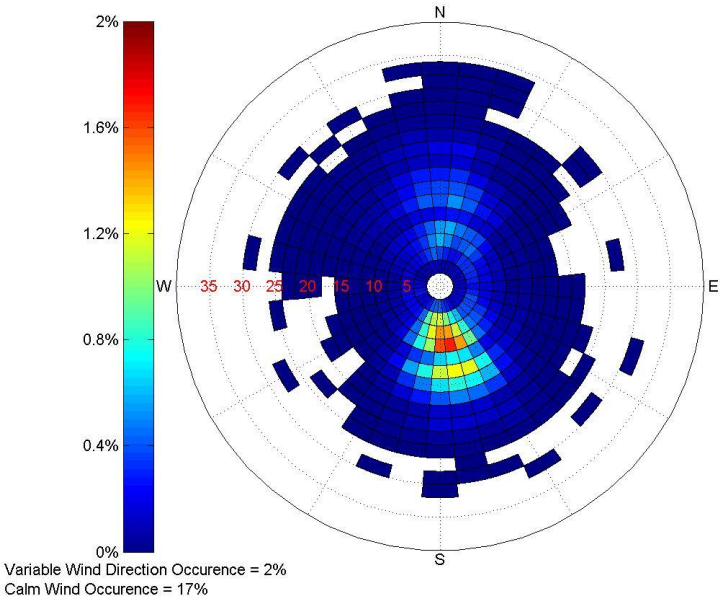

(b) Wind Density Graph

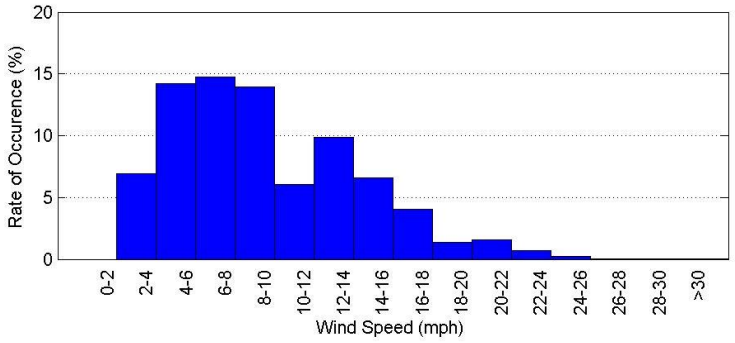

(c) Wind Speed Occurrence Rate

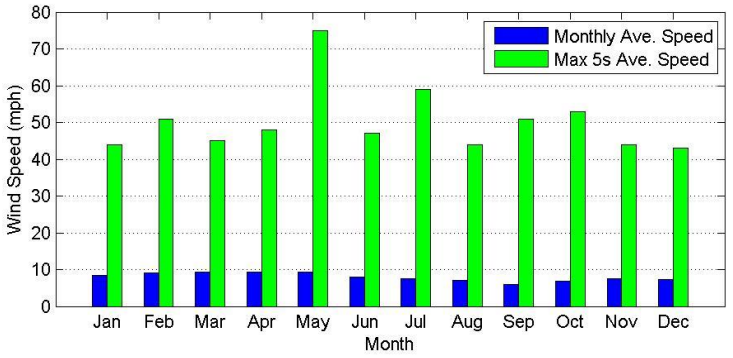

(d) Monthly Average Wind Speed

Figure 4.39: Wind Data Collected at the Austin Bergstrom International Airport (13904) from 2008 to 2015

GEORGETOWN MUNICIPAL ARPT (53942)

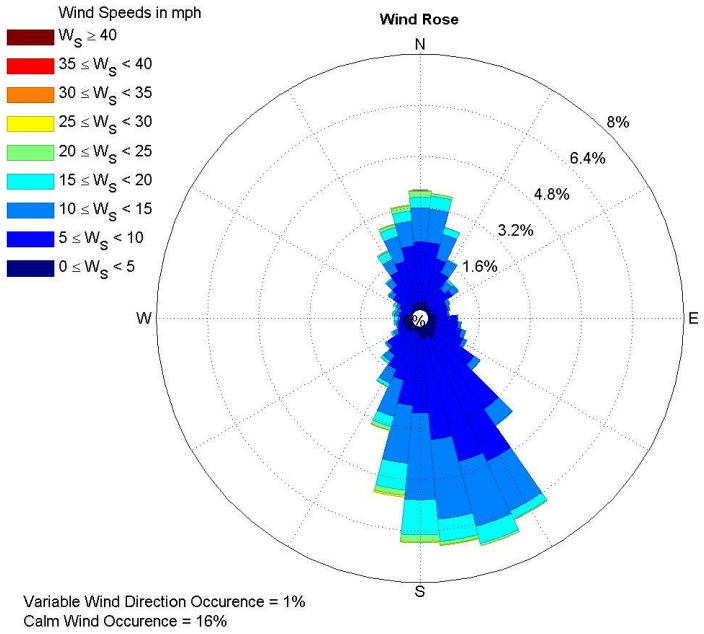

(a) Wind Rose Graph

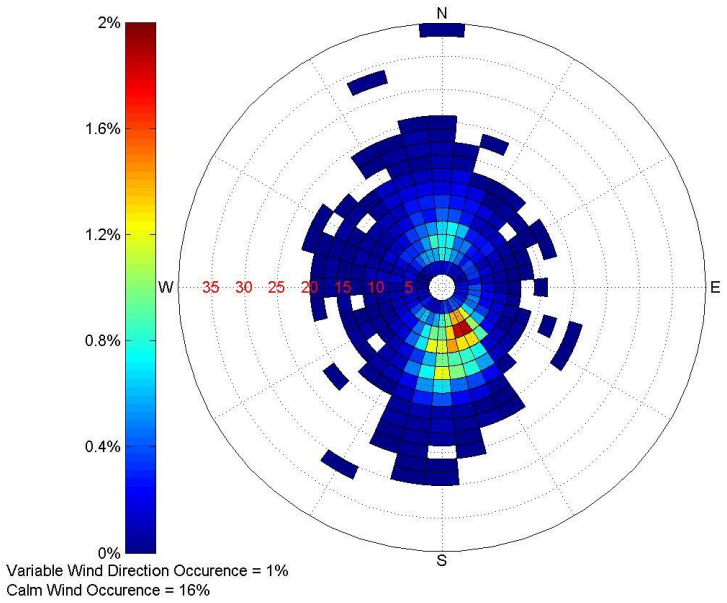

(b) Wind Density Graph

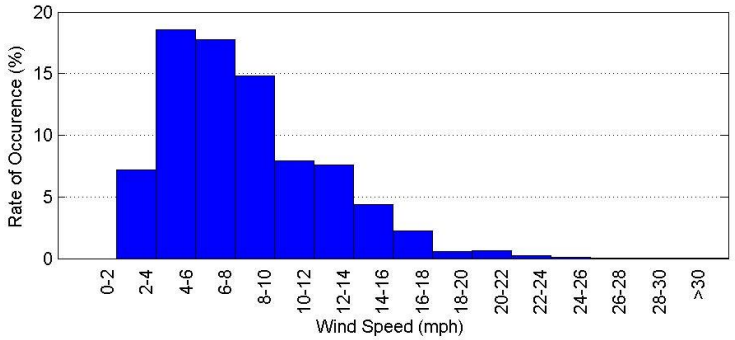

(c) Wind Speed Occurrence Rate

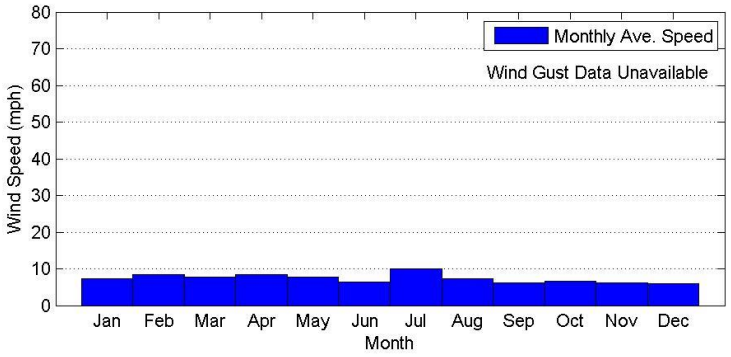

(d) Monthly Average Wind Speed

Figure 4.40: Wind Data Collected at the George Town Municipal Airport (53942) in the Year 2015

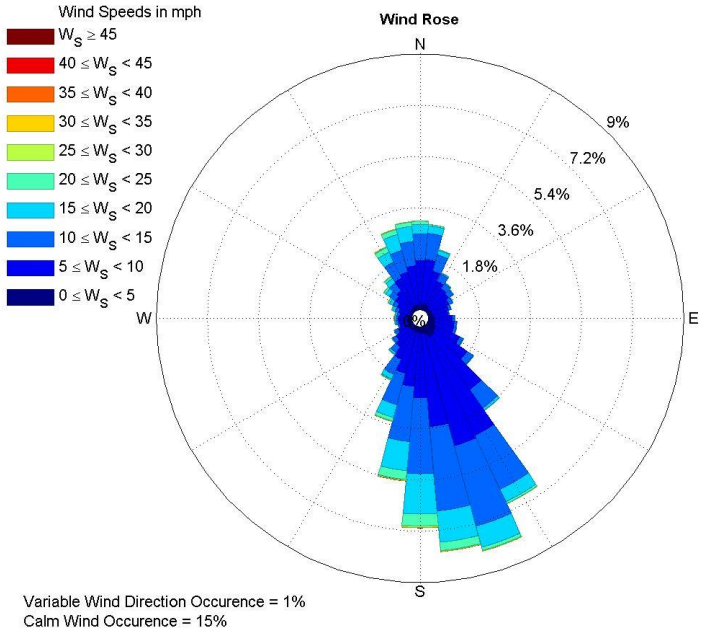

(a) Wind Rose Graph

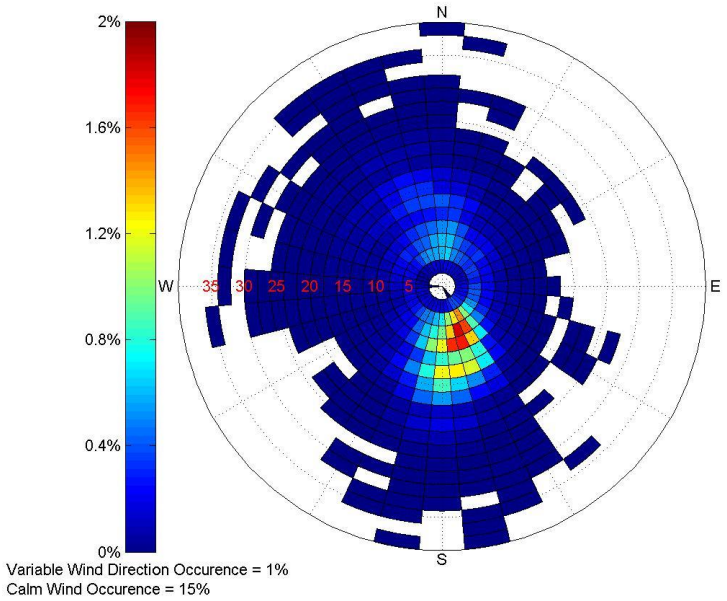

(b) Wind Density Graph

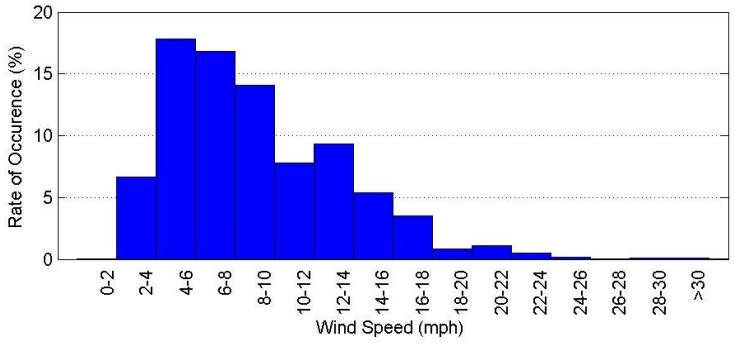

(c) Wind Speed Occurrence Rate

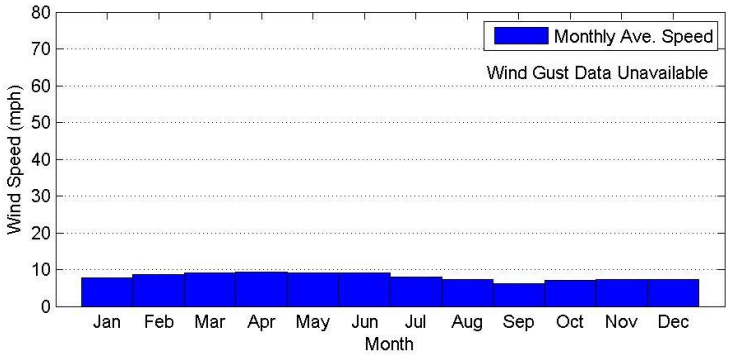

(d) Monthly Average Wind Speed

Figure 4.41: Wind Data Collected at the George Town Municipal Airport (53942) from 2008 to 2015

LAREDO INTERNATIONAL AIRPORT (12907)

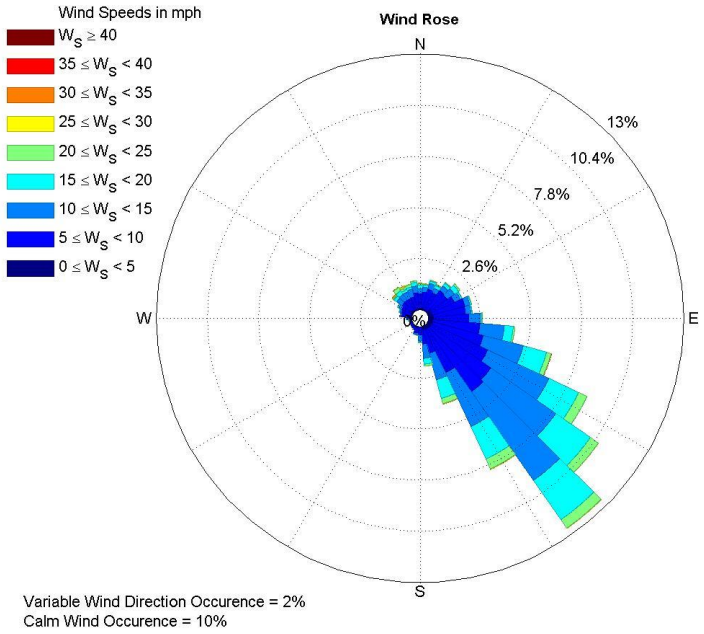

(a) Wind Rose Graph

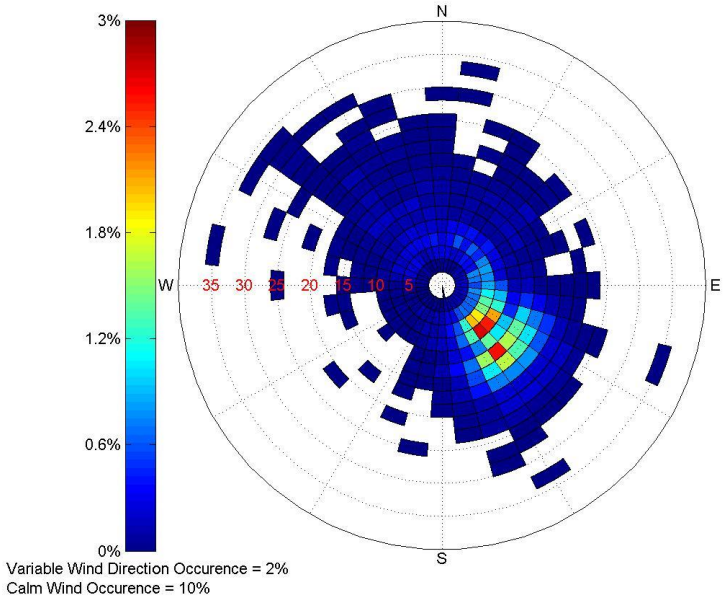

(b) Wind Density Graph

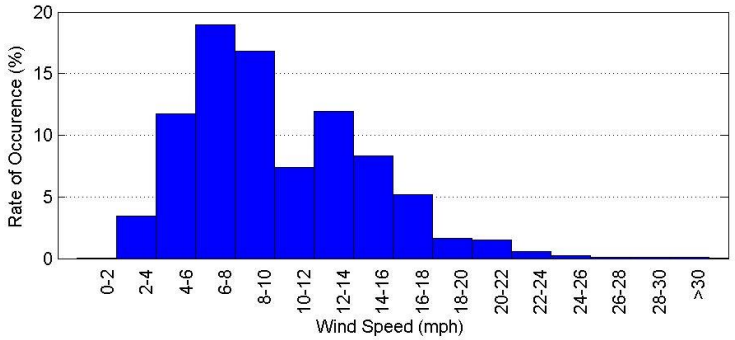

(c) Wind Speed Occurrence Rate

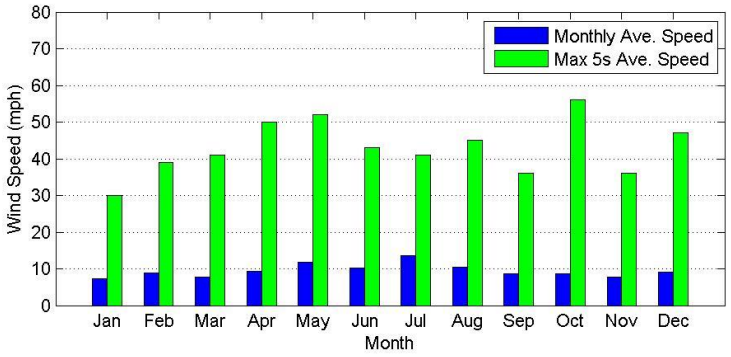

(d) Monthly Average Wind Speed

Figure 4.42: Wind Data Collected at the Laredo International Airport (12907) in the Year 2015

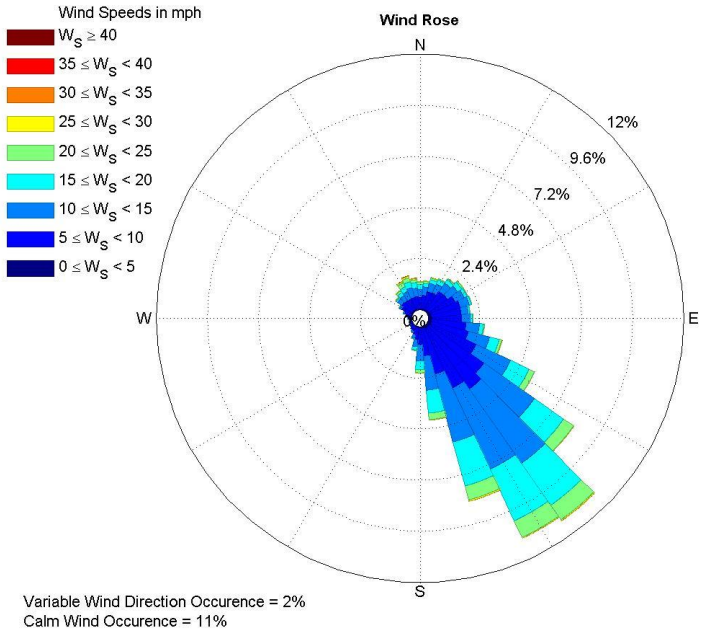

(a) Wind Rose Graph

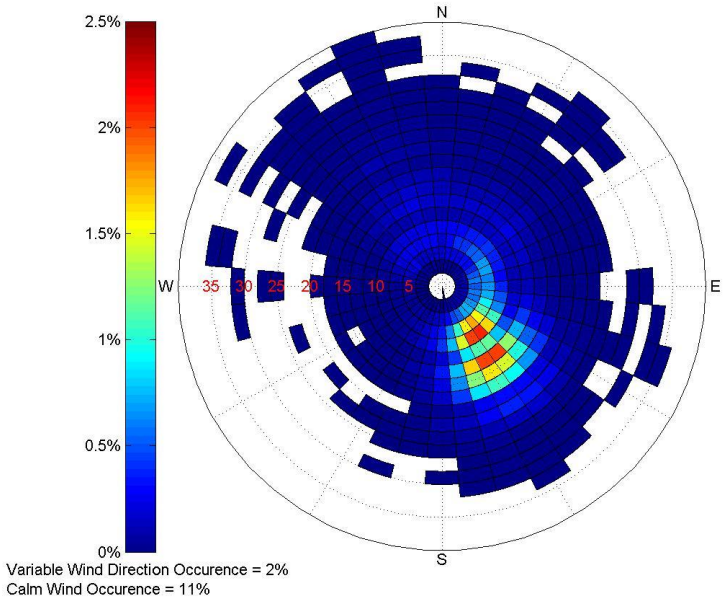

(b) Wind Density Graph

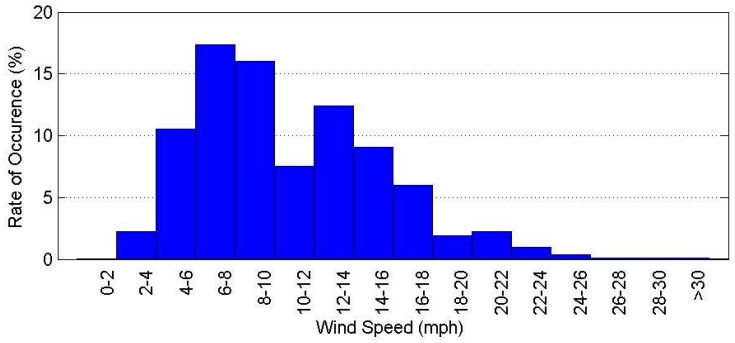

(c) Wind Speed Occurrence Rate

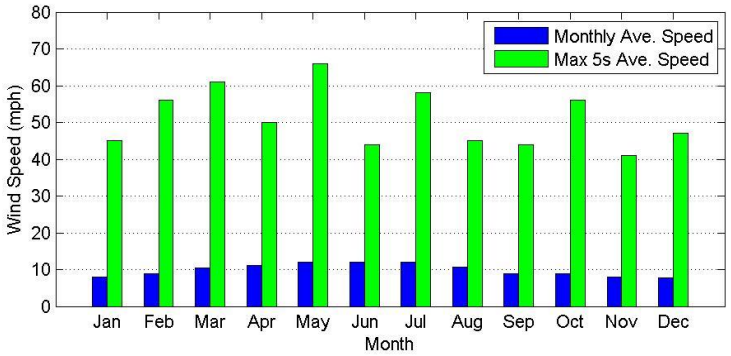

(d) Monthly Average Wind Speed

Figure 4.43: Wind Data Collected at the Laredo International Airport (12907) from 2008 to 2015

TEXARKANA REGIONAL AIRPORT-WEBB FIELD (13977)

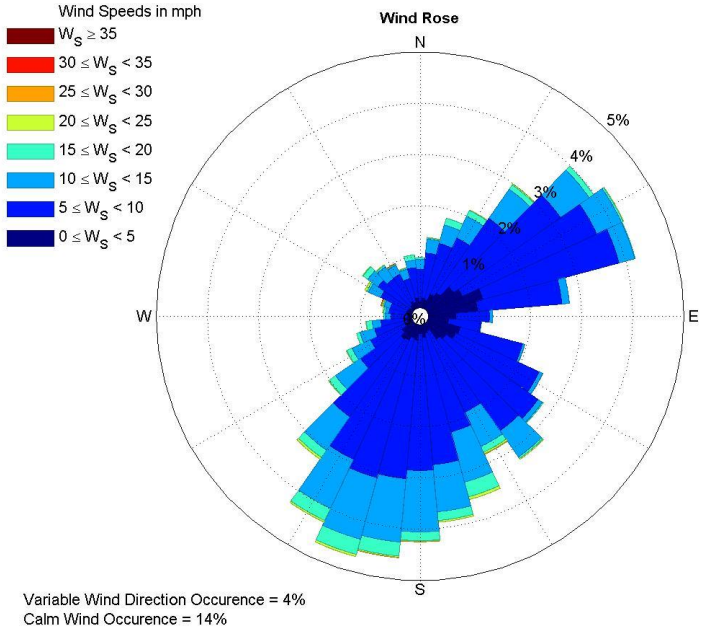

(a) Wind Rose Graph

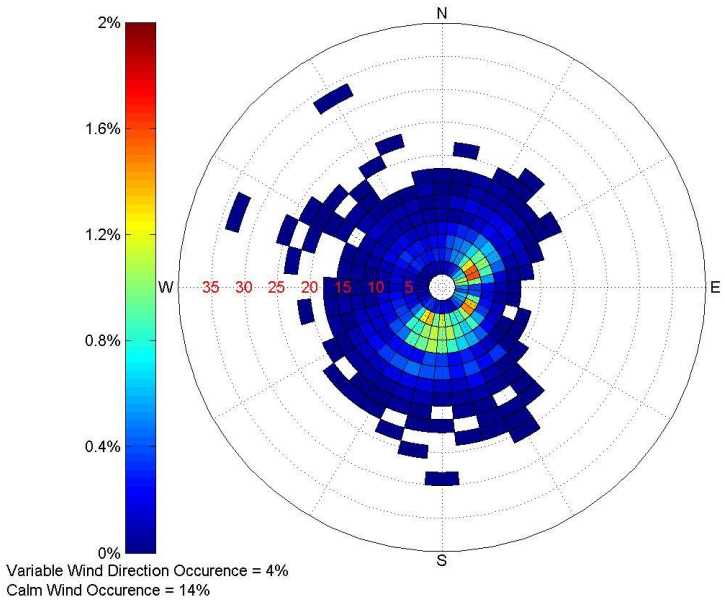

(b) Wind Density Graph

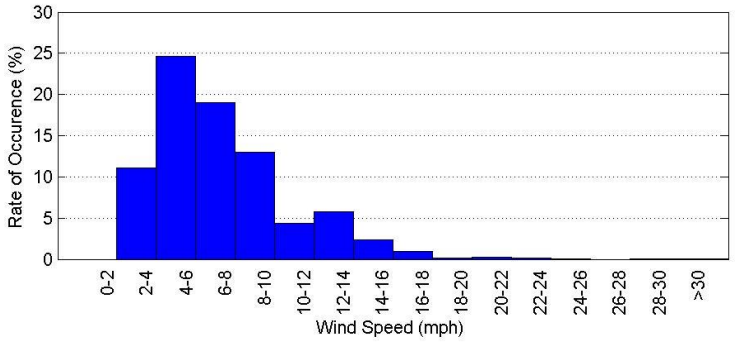

(c) Wind Speed Occurrence Rate

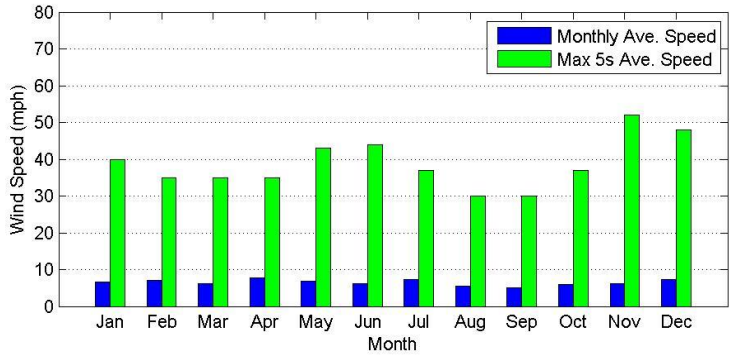

(d) Monthly Average Wind Speed

Figure 4.44: Wind Data Collected at the Texarkana Regional Airport Webb Field (13977) in the Year 2015

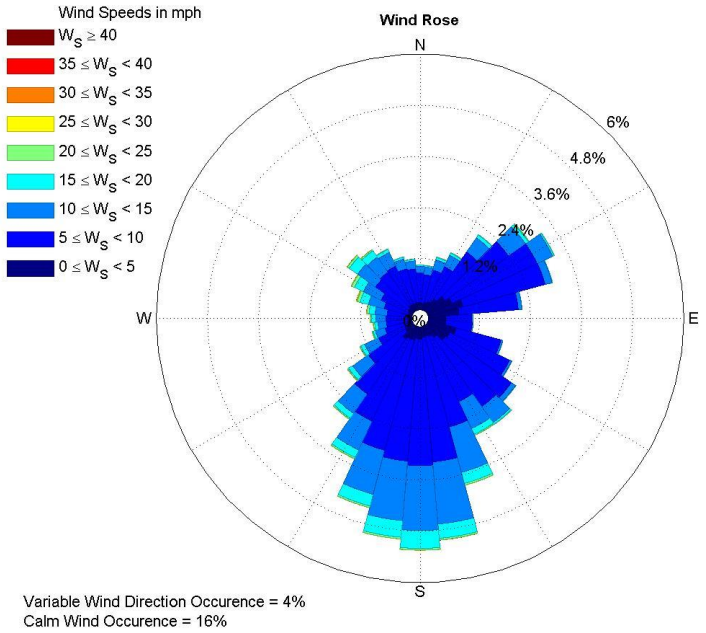

(a) Wind Rose Graph

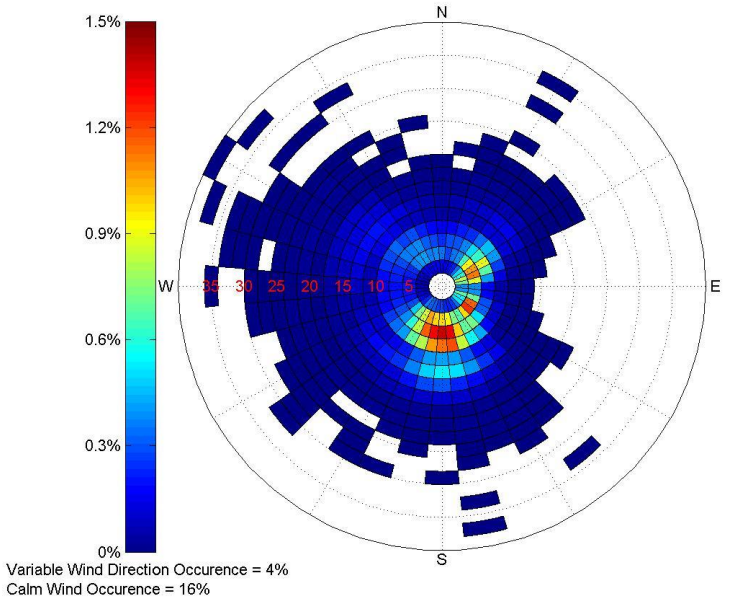

(b) Wind Density Graph

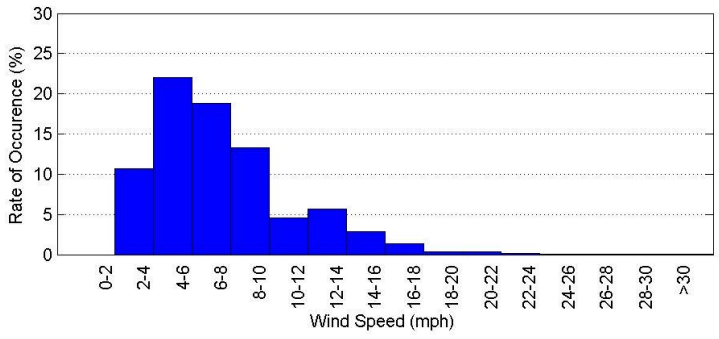

(c) Wind Speed Occurrence Rate

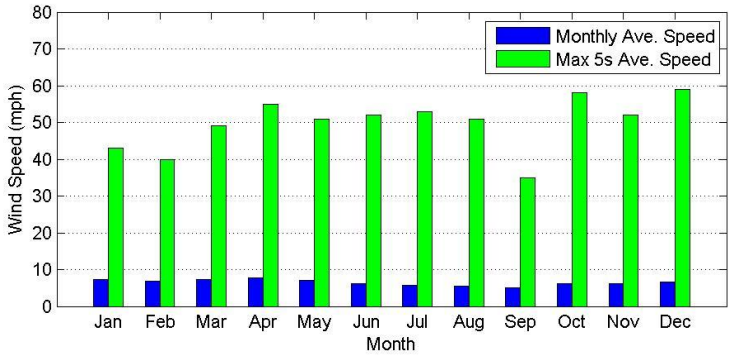

(d) Monthly Average Wind Speed

Figure 4.45: Wind Data Collected at the Texarkana Regional Airport Webb Field (13977) from 2008 to 2015

EAST TEXAS REGIONAL AIRPORT (3901)

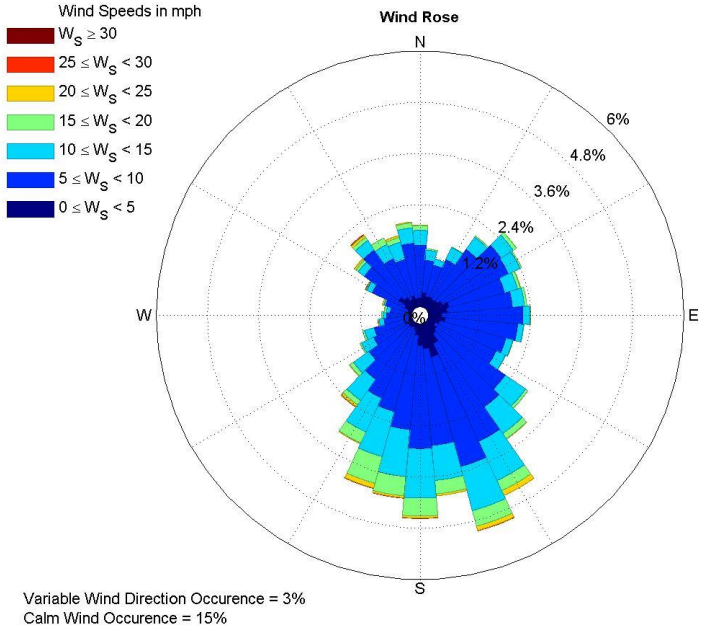

(a) Wind Rose Graph

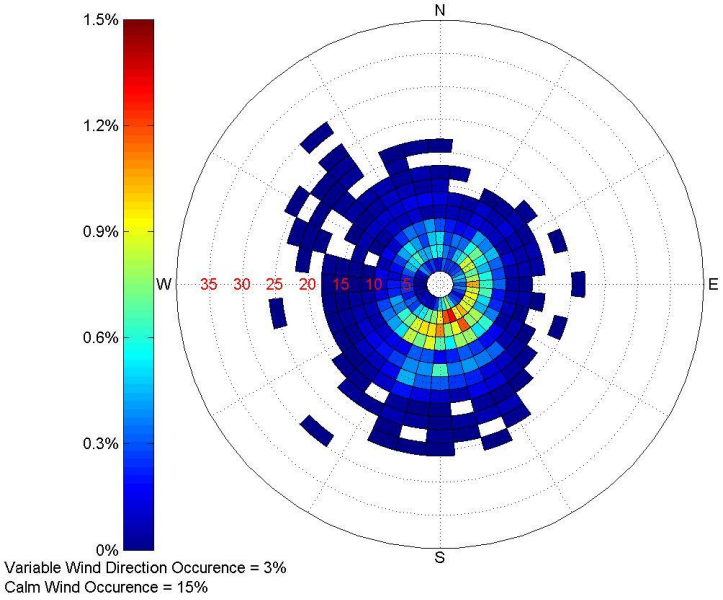

(b) Wind Density Graph

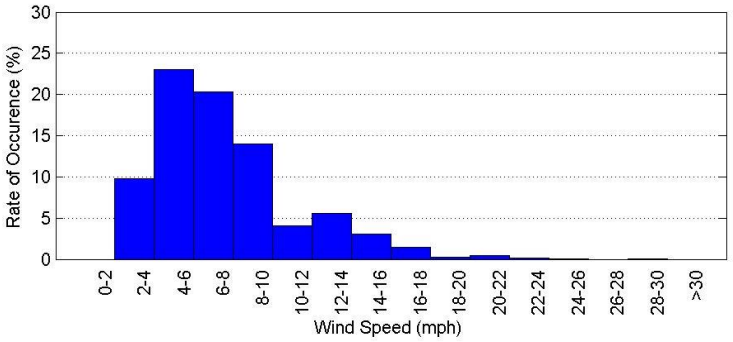

(c) Wind Speed Occurrence Rate

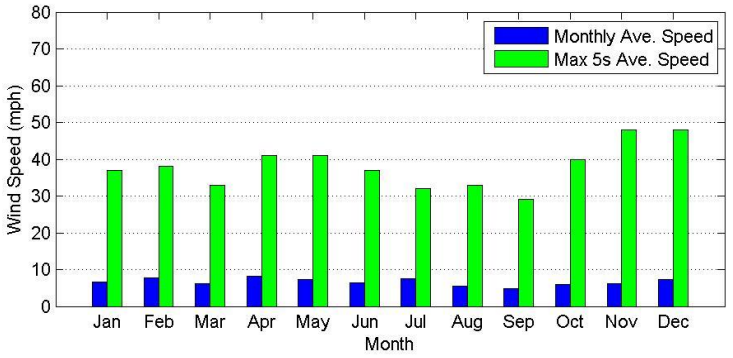

(d) Monthly Average Wind Speed

Figure 4.46: Wind Data Collected at the East Texas Regional Airport (3901) in the Year 2015

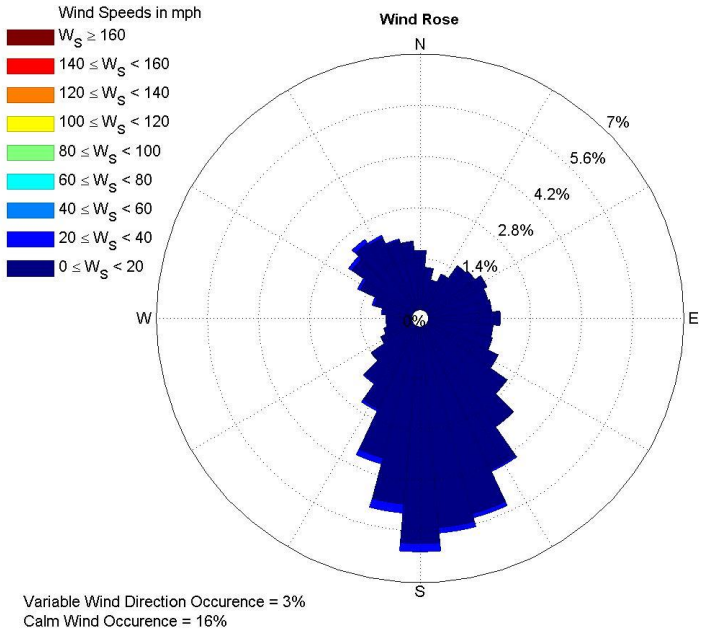

(a) Wind Rose Graph

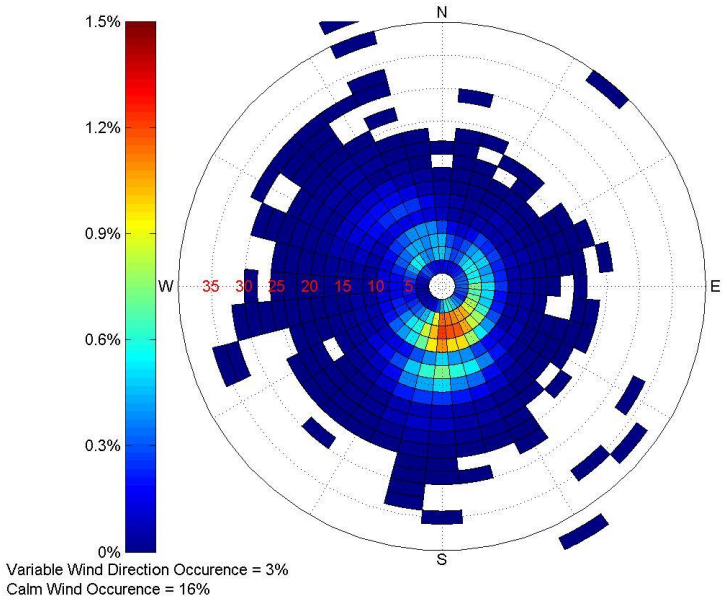

(b) Wind Density Graph

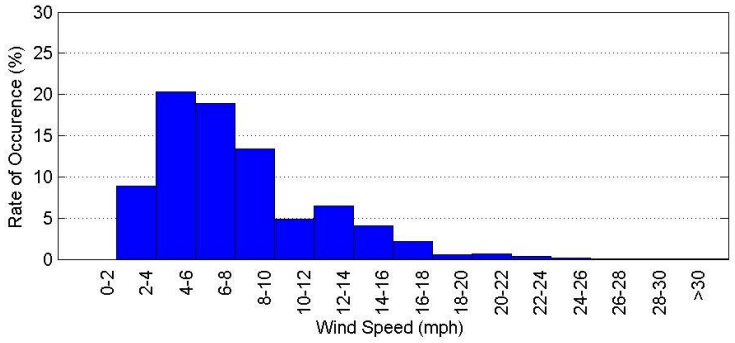

(c) Wind Speed Occurrence Rate

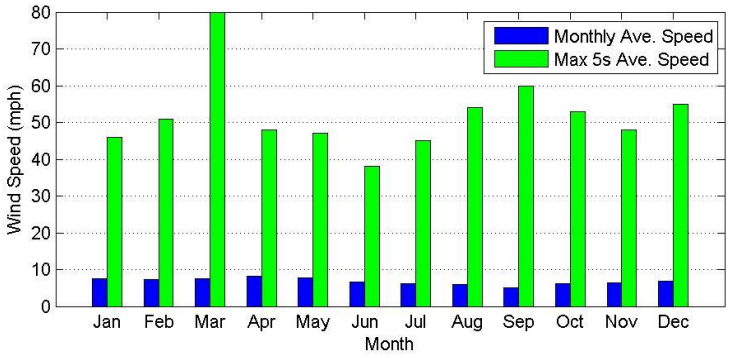

(d) Monthly Average Wind Speed

Figure 4.47: Wind Data Collected at the East Texas Regional Airport (3901) from 2008 to 2015

EL PASO INTERNATIONAL AIRPORT (23044)

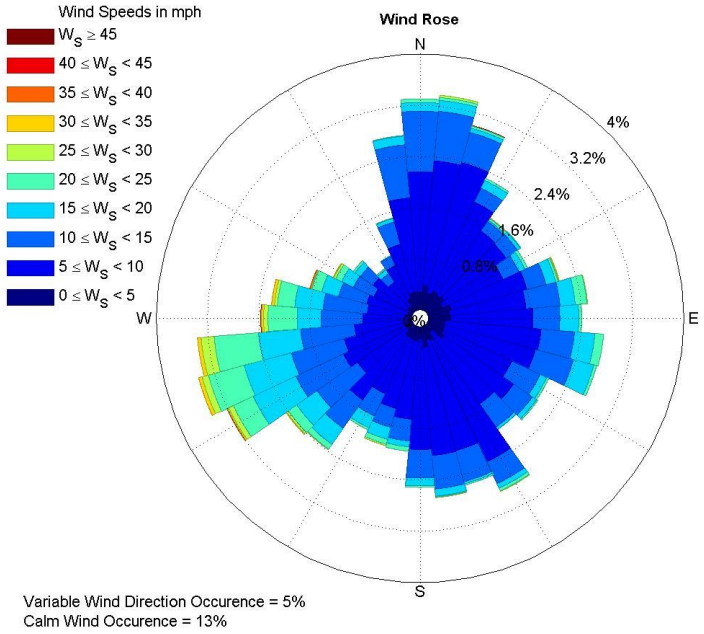

(a) Wind Rose Graph

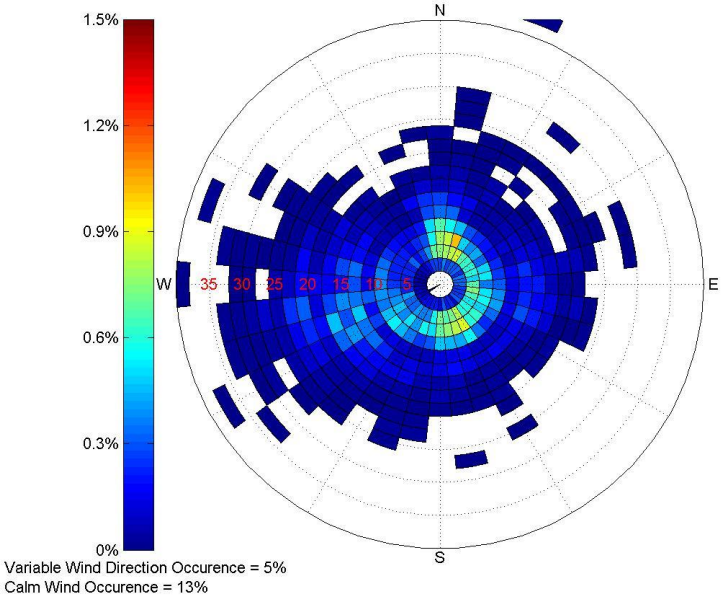

(b) Wind Density Graph

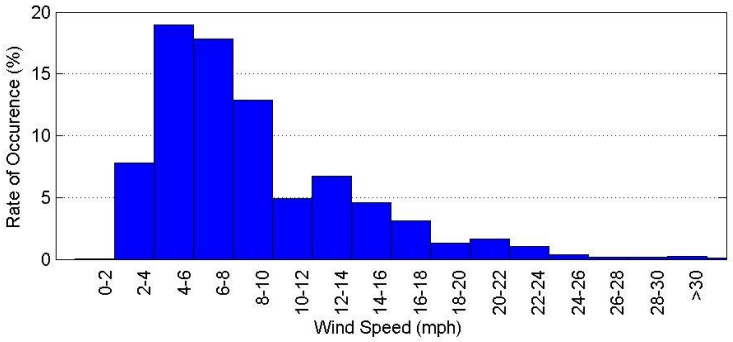

(c) Wind Speed Occurrence Rate

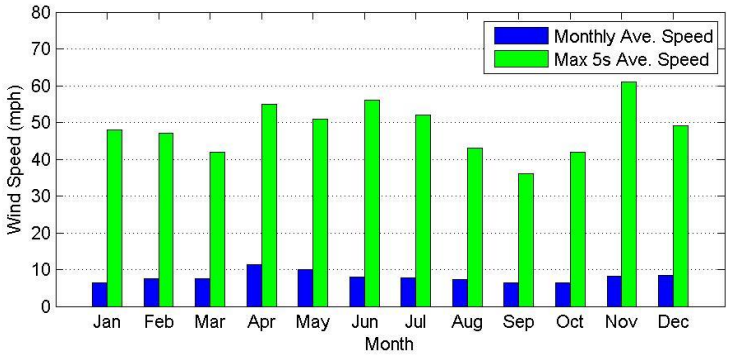

(d) Monthly Average Wind Speed

Figure 4.48: Wind Data Collected at the El Paso International Airport (23044) in the Year 2015

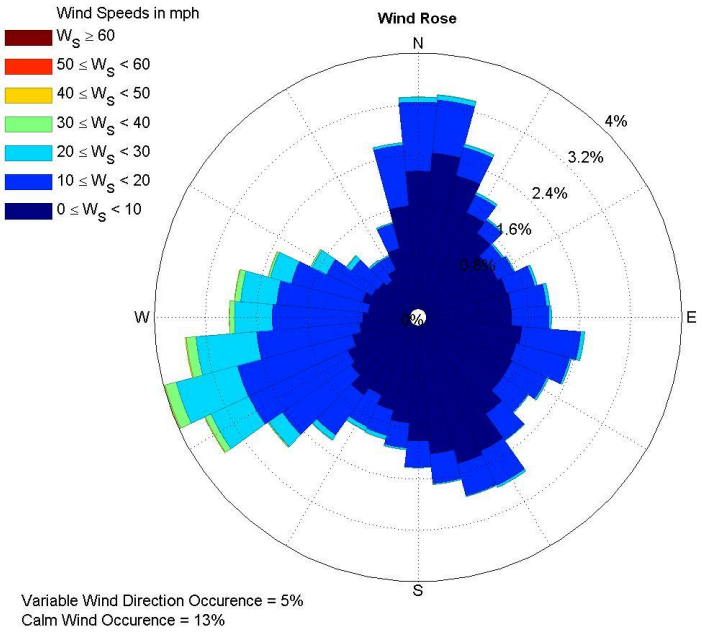

(a) Wind Rose Graph

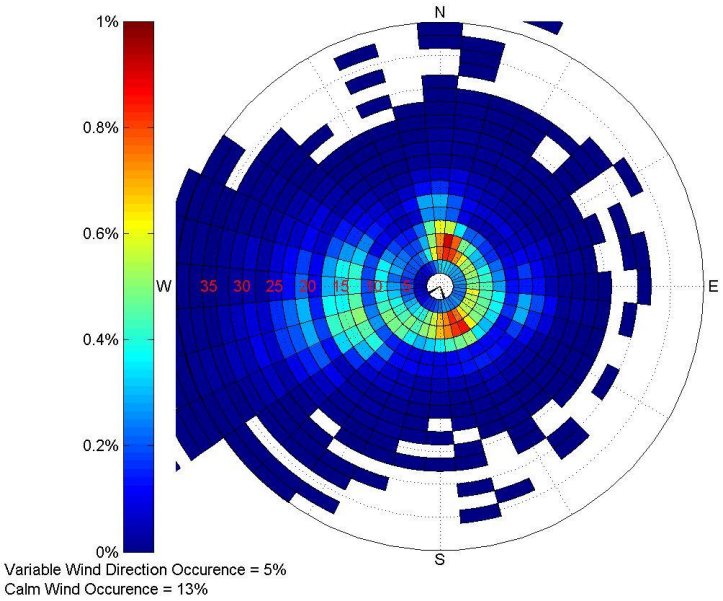

(b) Wind Density Graph

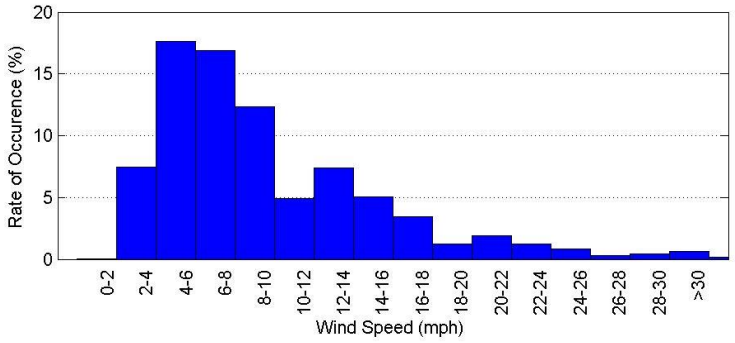

(c) Wind Speed Occurrence Rate

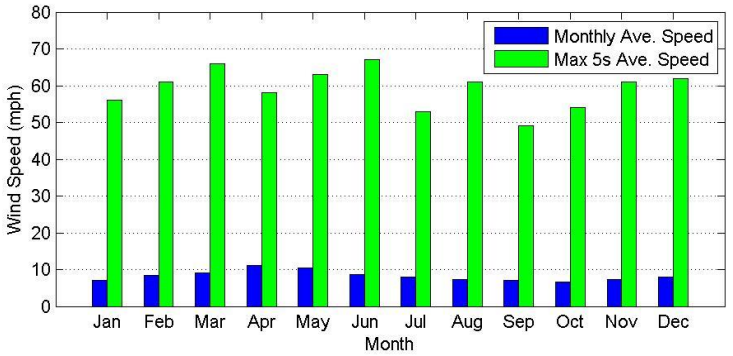

(d) Monthly Average Wind Speed

Figure 4.49: Wind Data Collected at the El Paso International Airport (23044) from 2008 to 2015

ODESSA-SCHLEMEYER FIELD AIRPORT (3031)

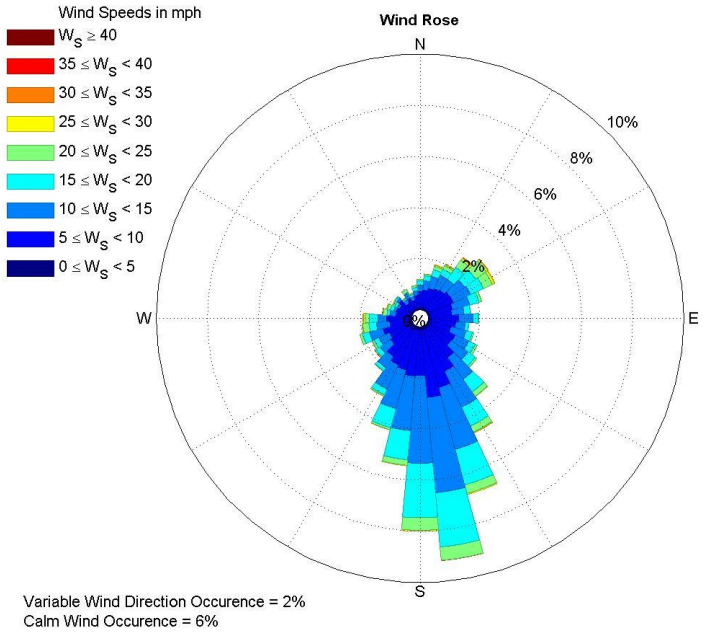

(a) Wind Rose Graph

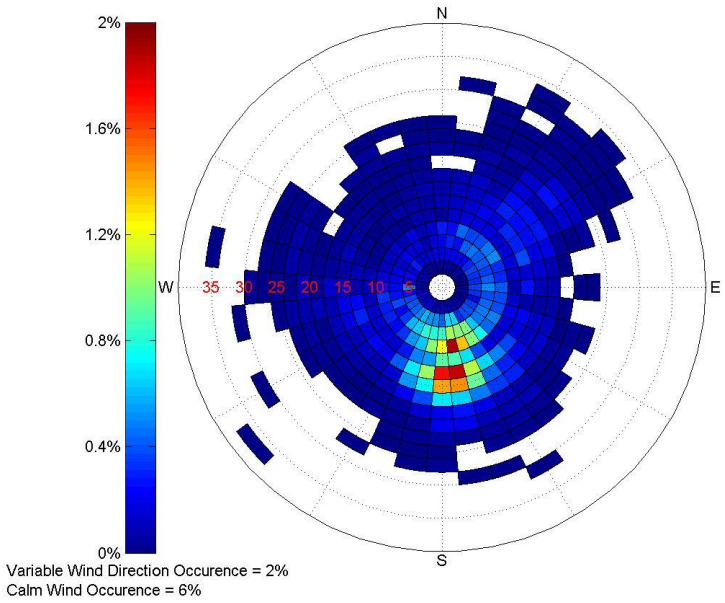

(b) Wind Density Graph

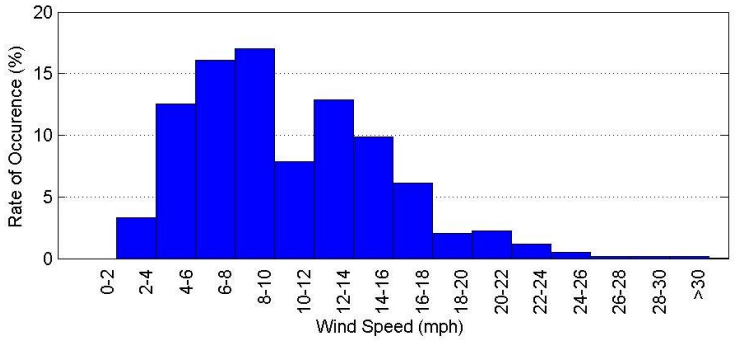

(c) Wind Speed Occurrence Rate

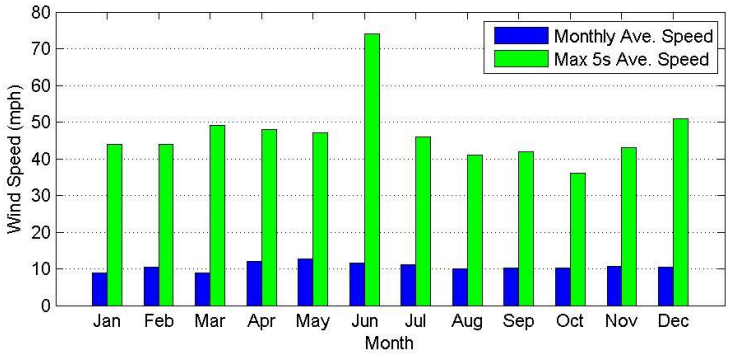

(d) Monthly Average Wind Speed

Figure 4.50: Wind Data Collected at the Odessa Schlemeyer Field Airport (3031) in the Year 2015

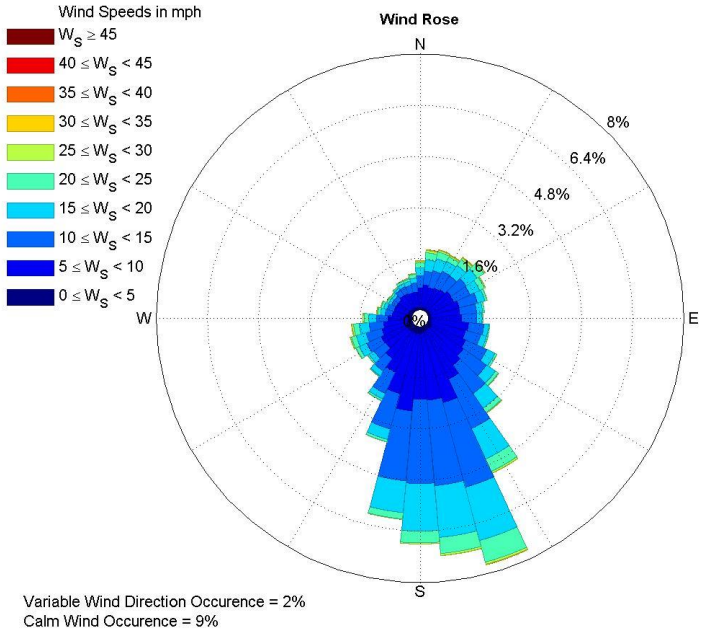

(a) Wind Rose Graph

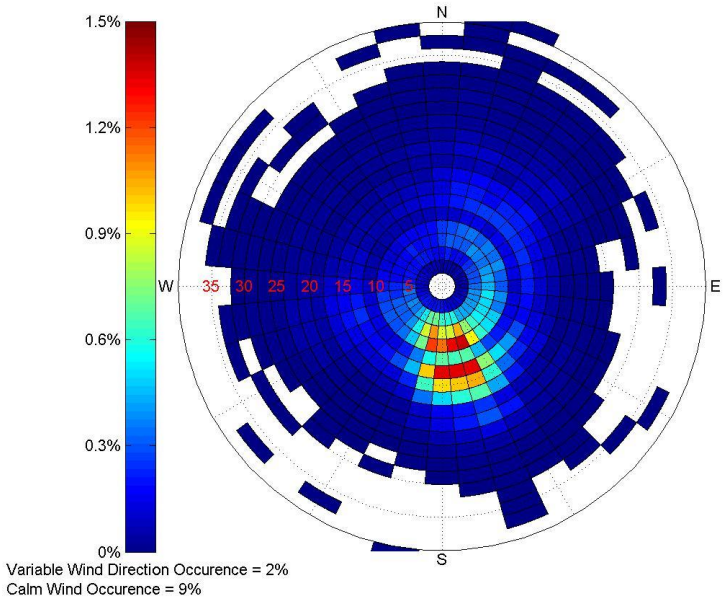

(b) Wind Density Graph

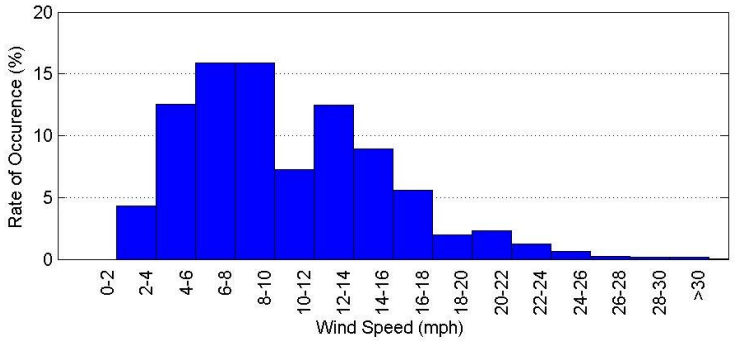

(c) Wind Speed Occurrence Rate

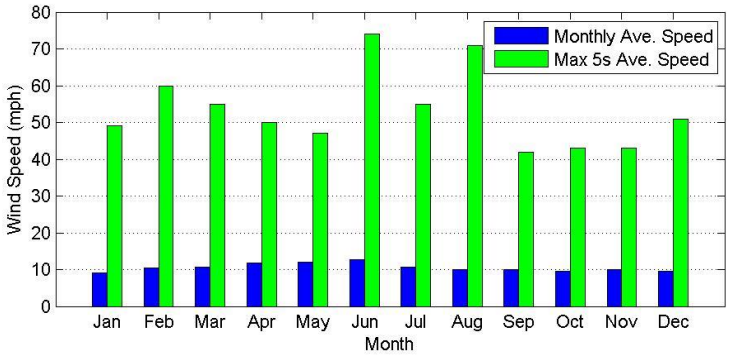

(d) Monthly Average Wind Speed

Figure 4.51: Wind Data Collected at the Odessa Schlemeyer Field Airport (3031) from 2008 to 2015

MIDLAND INTERNATIONAL AIRPORT (23023)

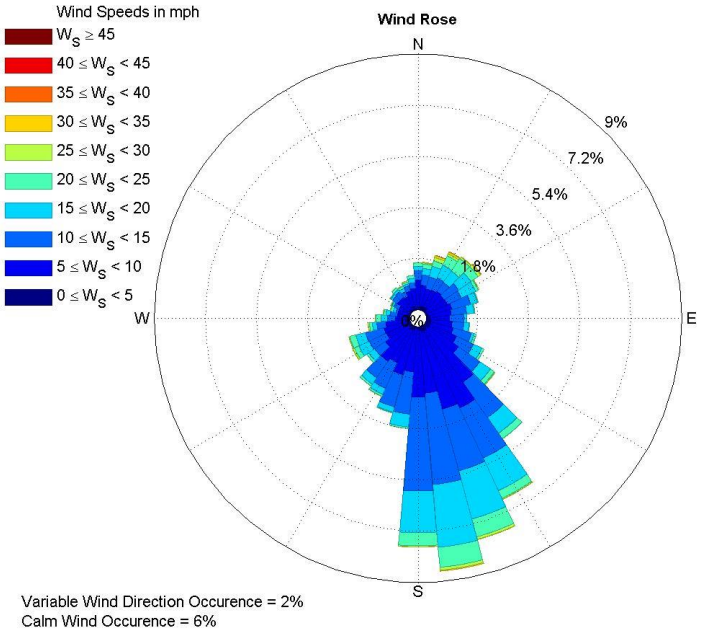

(a) Wind Rose Graph

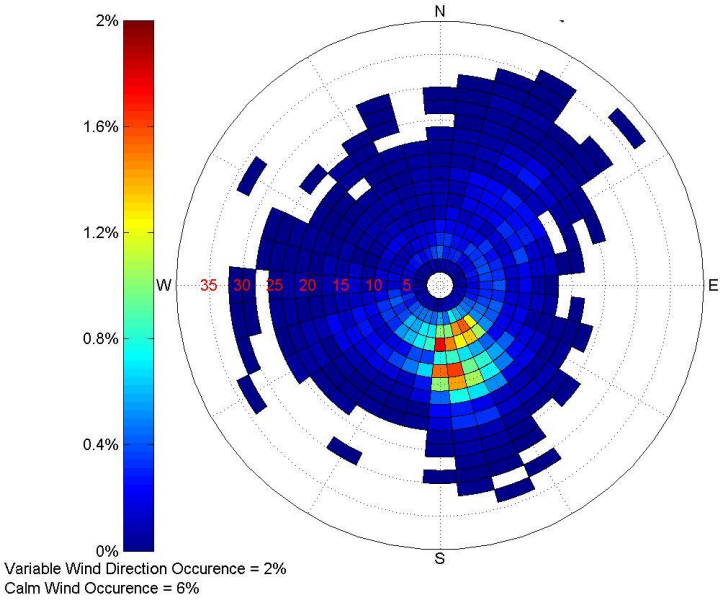

(b) Wind Density Graph

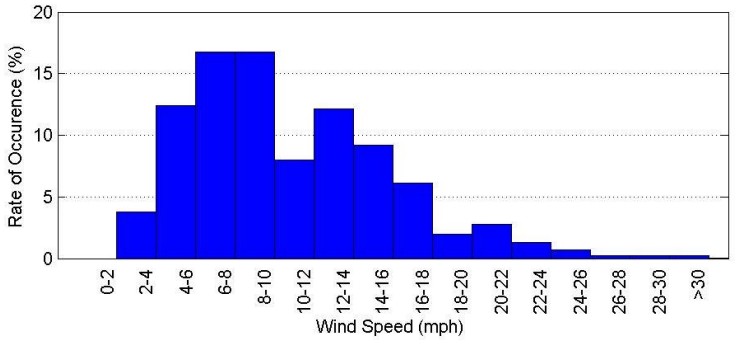

(c) Wind Speed Occurrence Rate

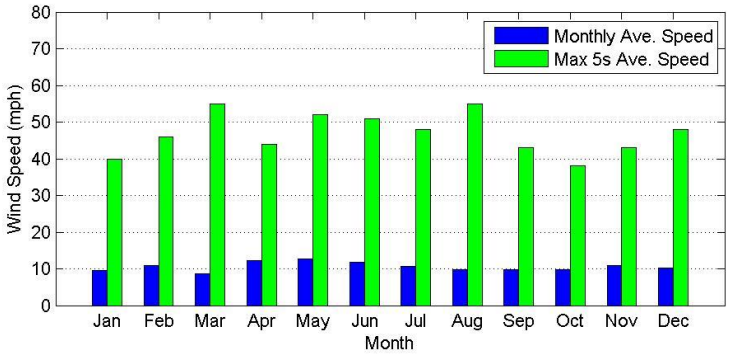

(d) Monthly Average Wind Speed

Figure 4.52: Wind Data Collected at the Midland International Airport (23023) in the Year 2015

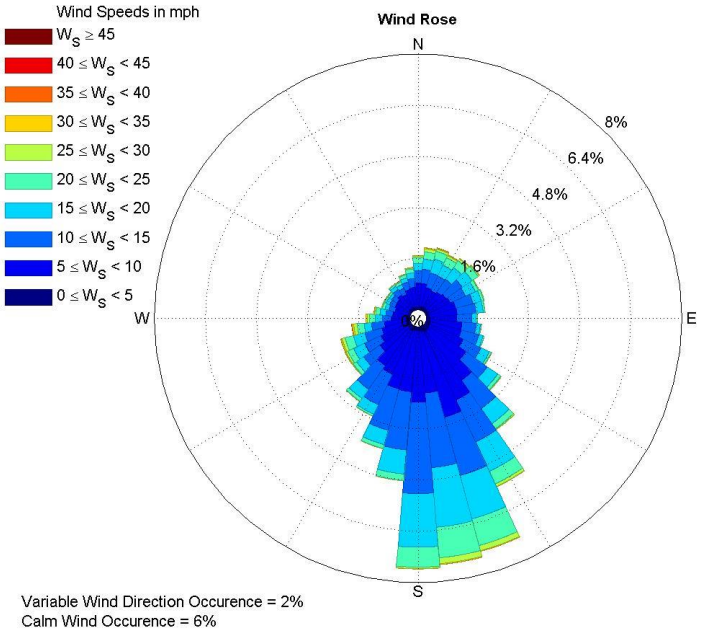

(a) Wind Rose Graph

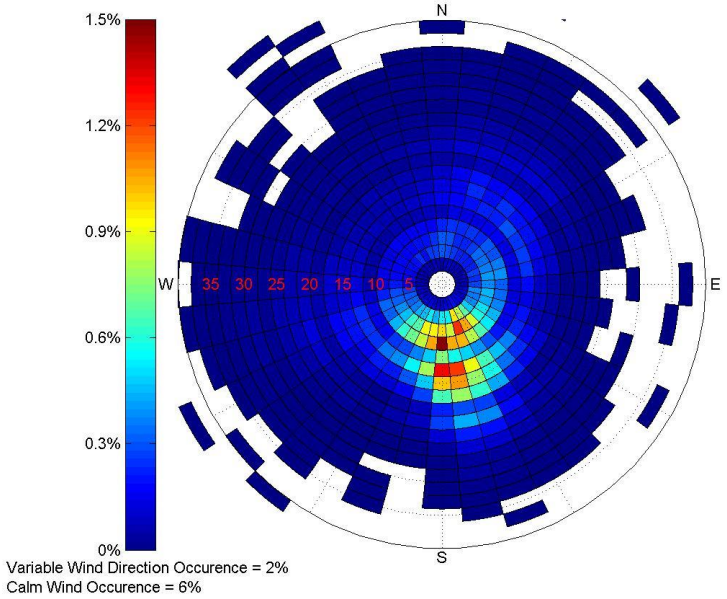

(b) Wind Density Graph

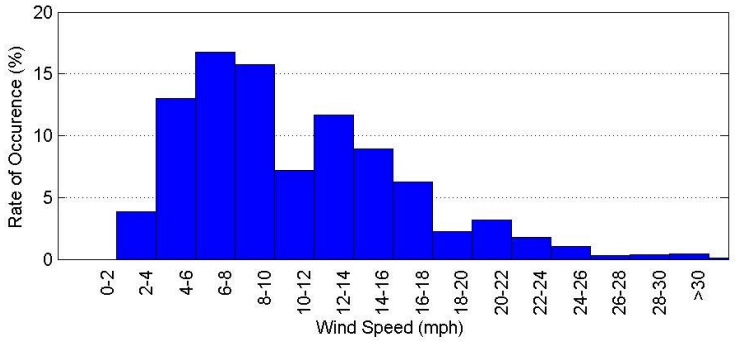

(c) Wind Speed Occurrence Rate

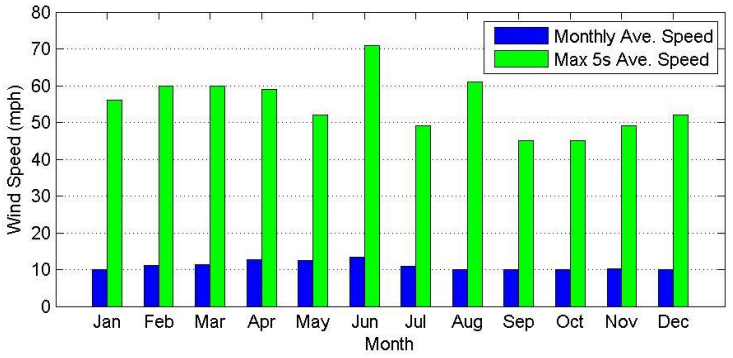

(d) Monthly Average Wind Speed

Figure 4.53: Wind Data Collected at the Midland International Airport (23023) from 2008 to 2015

MIDLAND AIRPARK (3071)

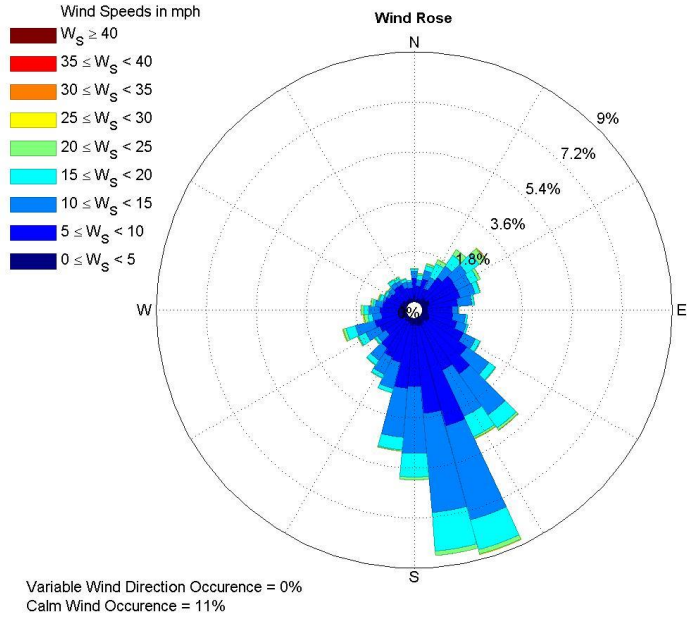

(a) Wind Rose Graph

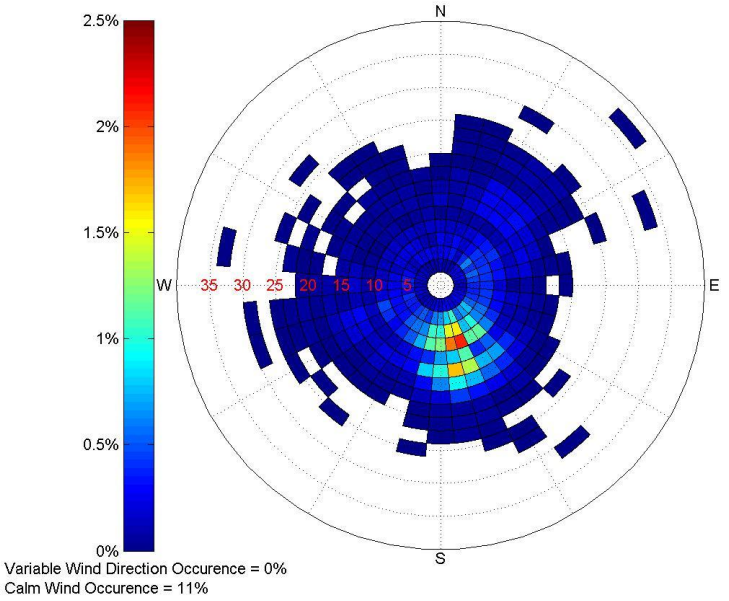

(b) Wind Density Graph

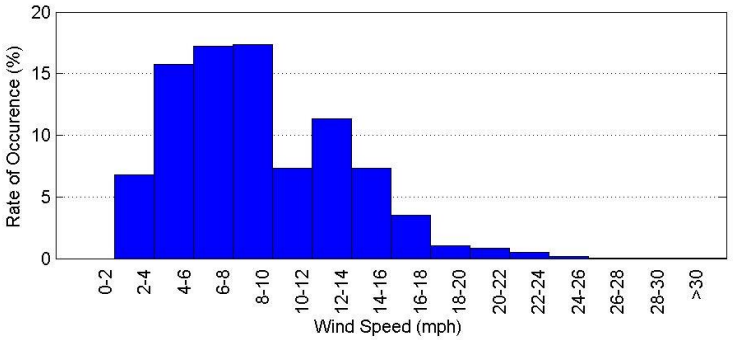

(c) Wind Speed Occurrence Rate

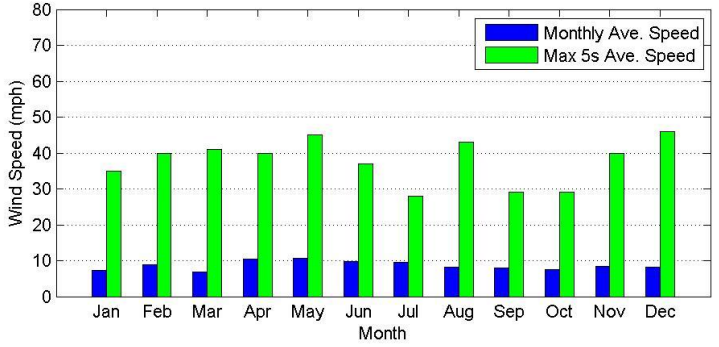

(d) Monthly Average Wind Speed

Figure 4.54: Wind Data Collected at the Midland Airpark (3071) in the Year 2015

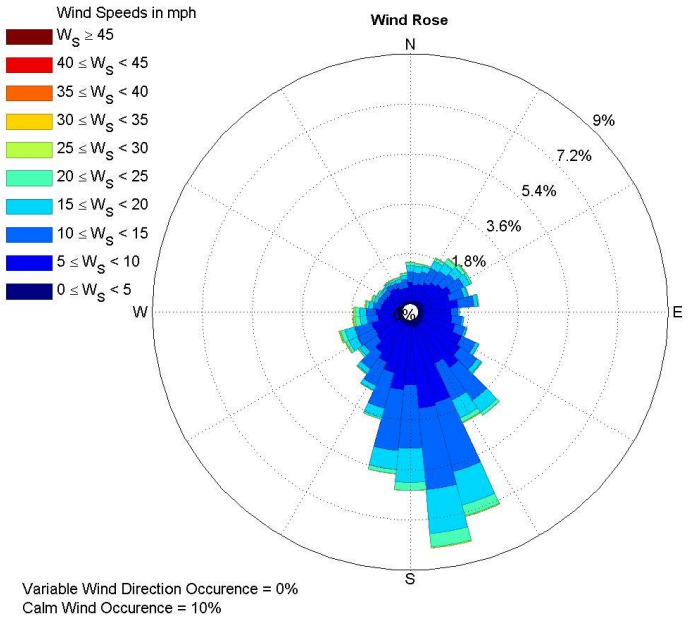

(a) Wind Rose Graph

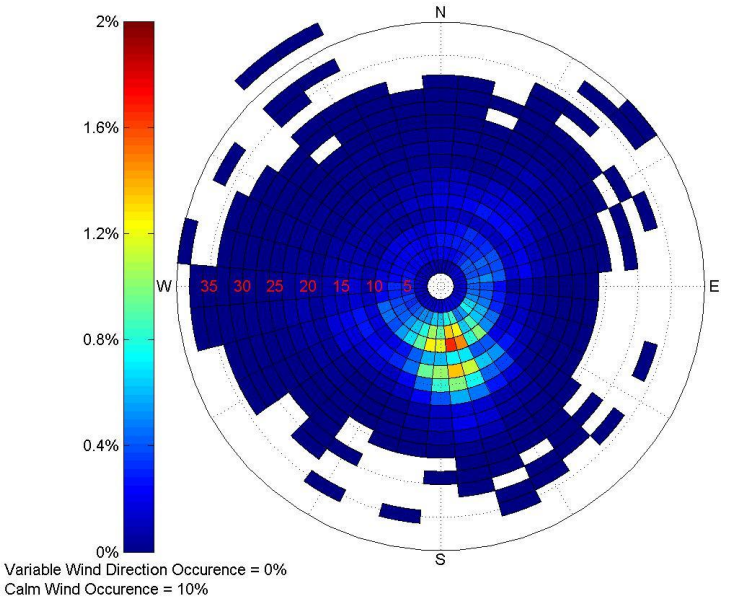

(b) Wind Density Graph

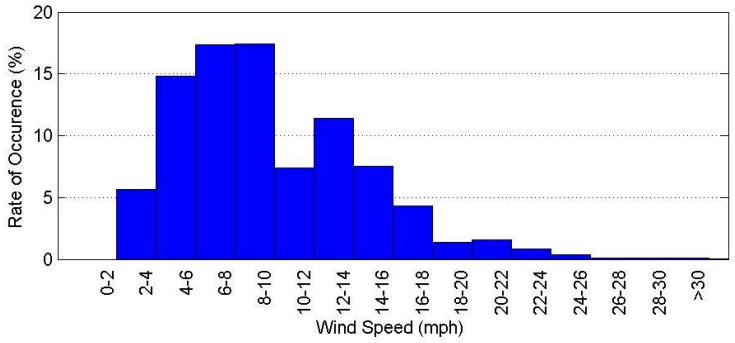

(c) Wind Speed Occurrence Rate

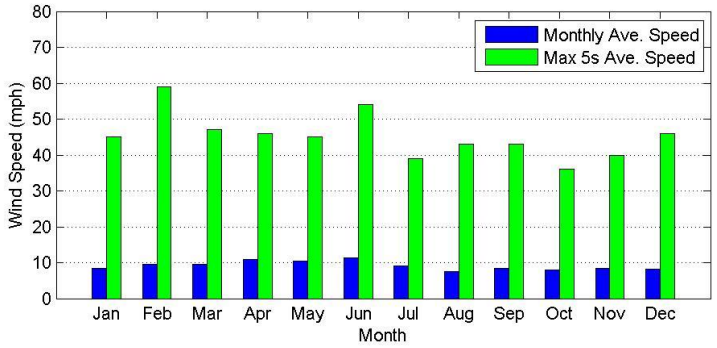

(d) Monthly Average Wind Speed

Figure 4.55: Wind Data Collected at the Midland Airpark (3071) from 2008 to 2015

DALLAS/FT WORTH INTERNATIONAL AP (3927)

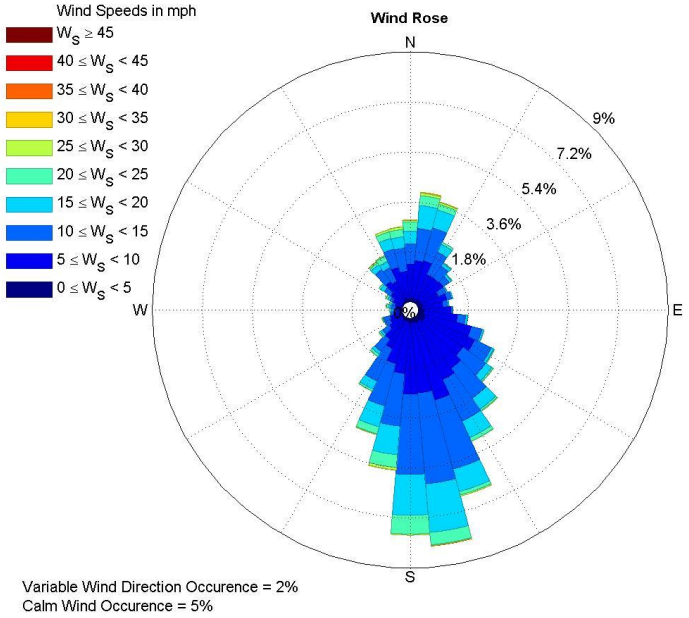

(a) Wind Rose Graph

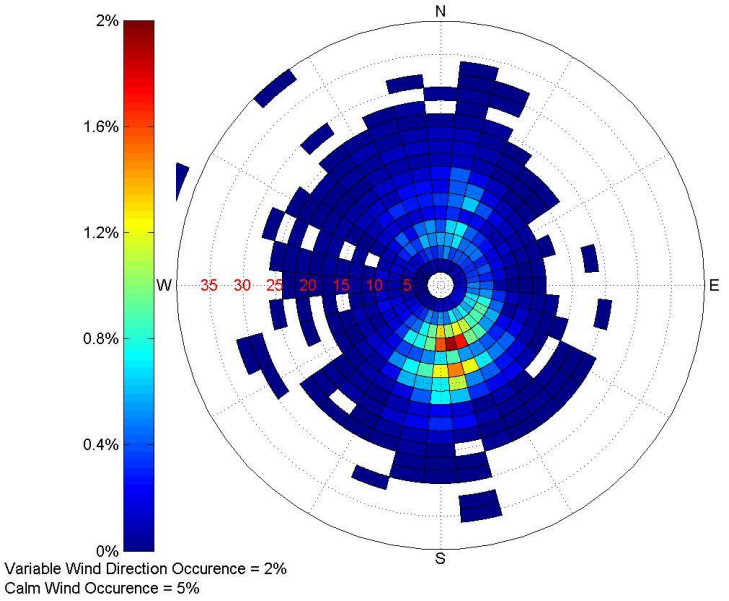

(b) Wind Density Graph

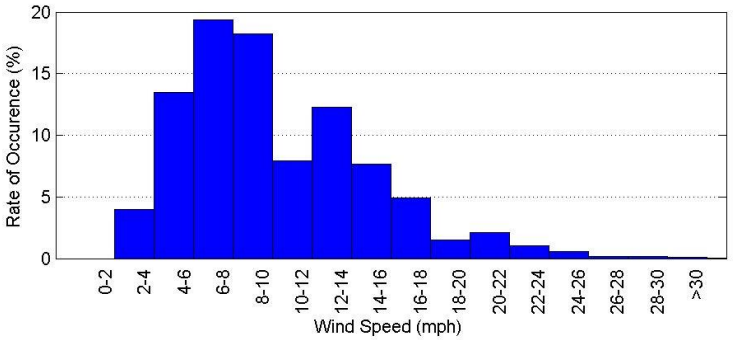

(c) Wind Speed Occurrence Rate

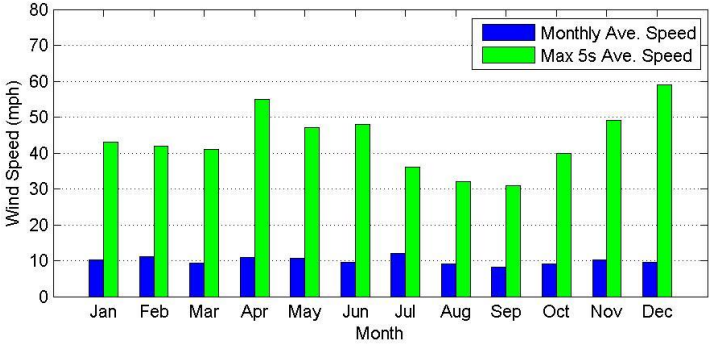

(d) Monthly Average Wind Speed

Figure 4.56: Wind Data Collected at the Dallas Fort Worth International Airport (3927) in the Year 2015

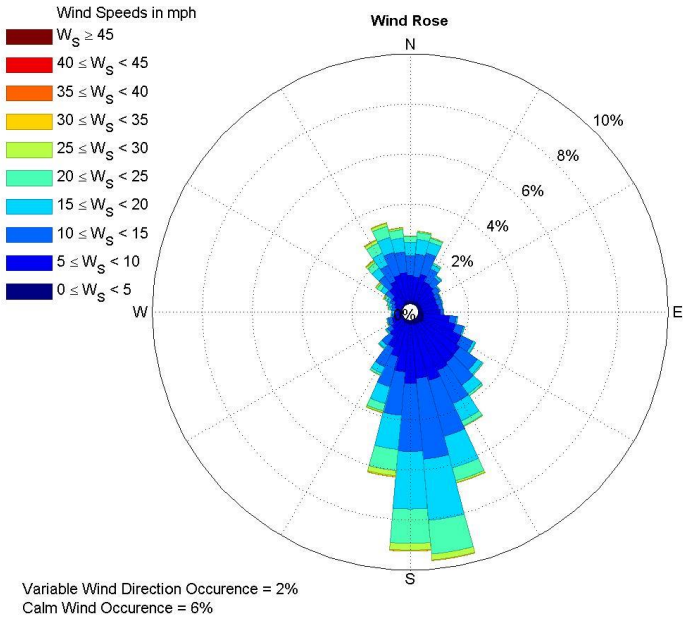

(a) Wind Rose Graph

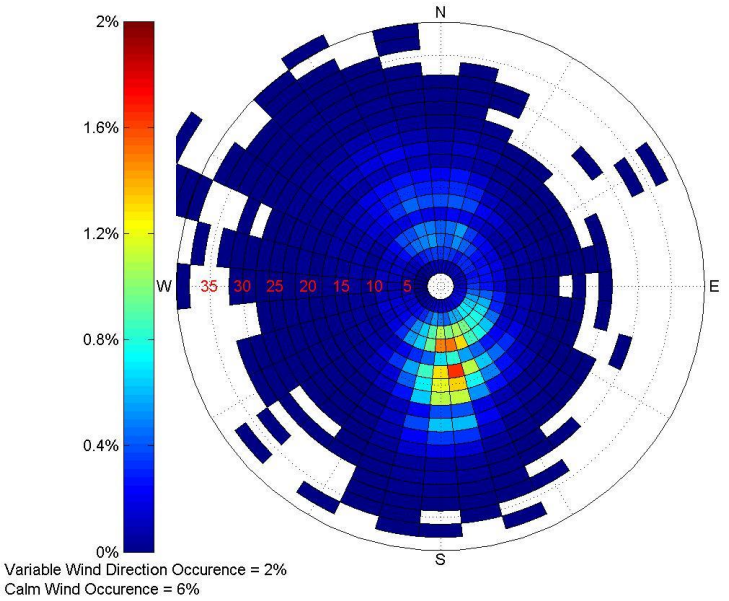

(b) Wind Density Graph

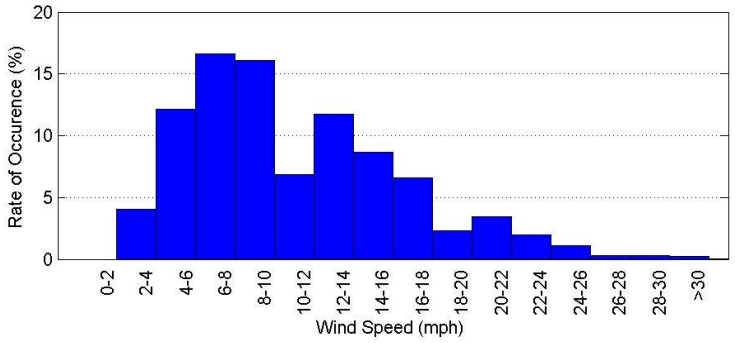

(c) Wind Speed Occurrence Rate

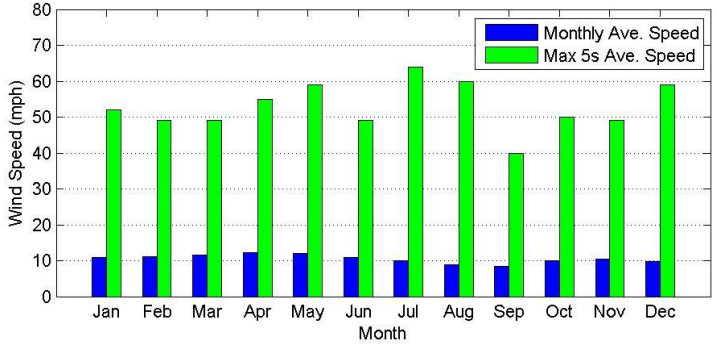

(d) Monthly Average Wind Speed

Figure 4.57: Wind Data Collected at the Dallas Fort Worth International Airport (3927) from 2008 to 2015

FT WORTH MEACHAM INTL ARPT (13961)

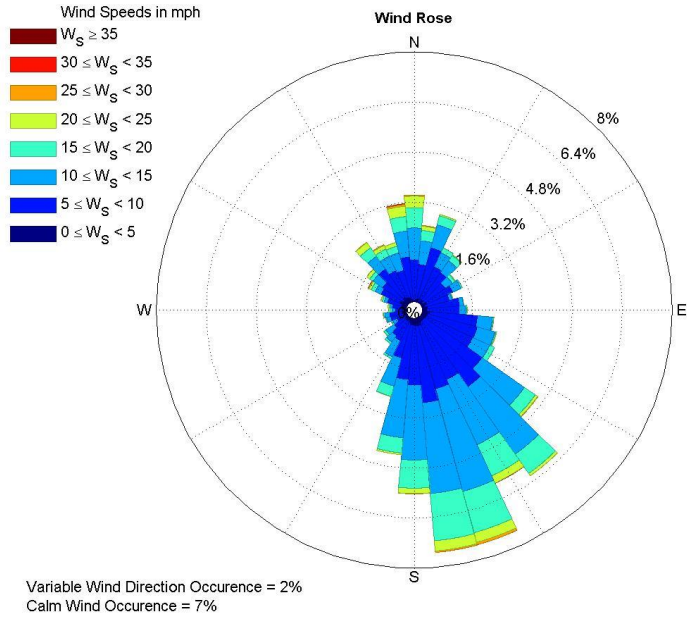

(a) Wind Rose Graph

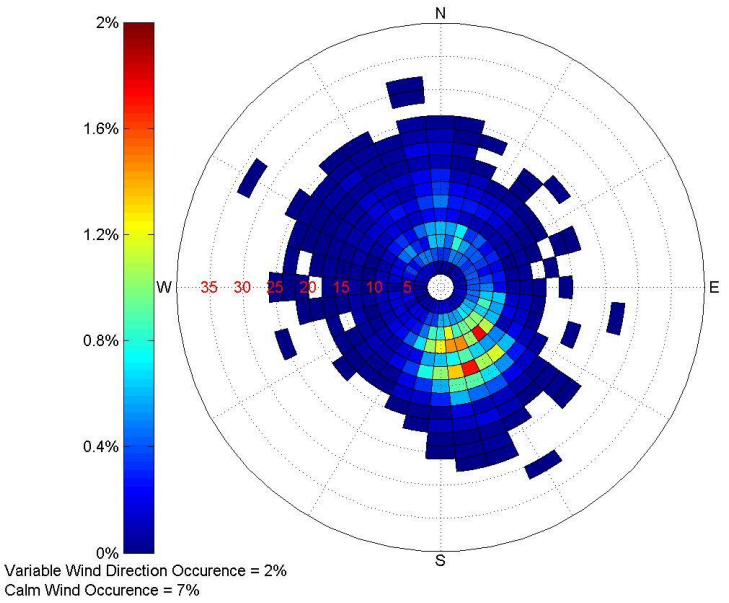

(b) Wind Density Graph

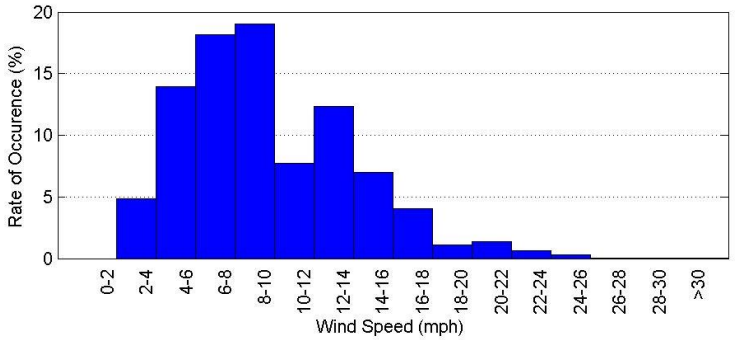

(c) Wind Speed Occurrence Rate

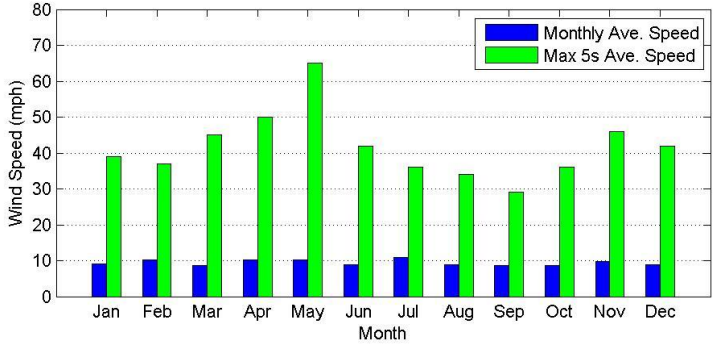

(d) Monthly Average Wind Speed

Figure 4.58: Wind Data Collected at the Fort Worth Meacham International Airport (13961) in the Year 2015

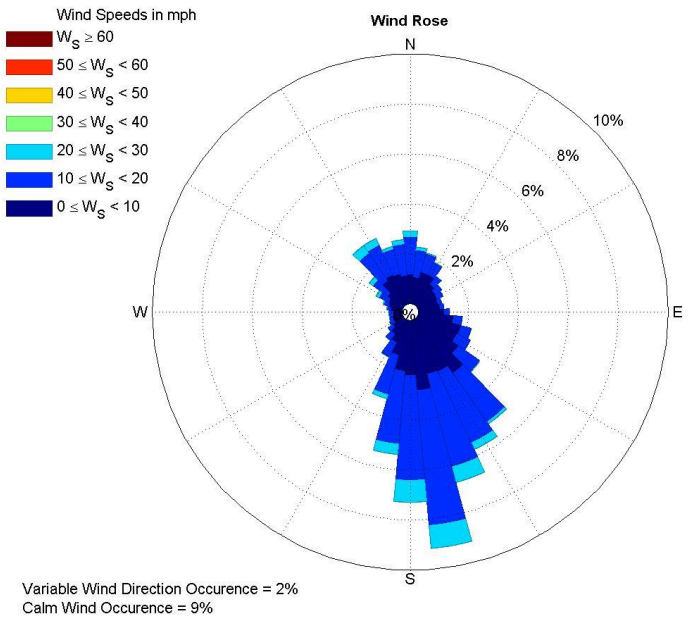

(a) Wind Rose Graph

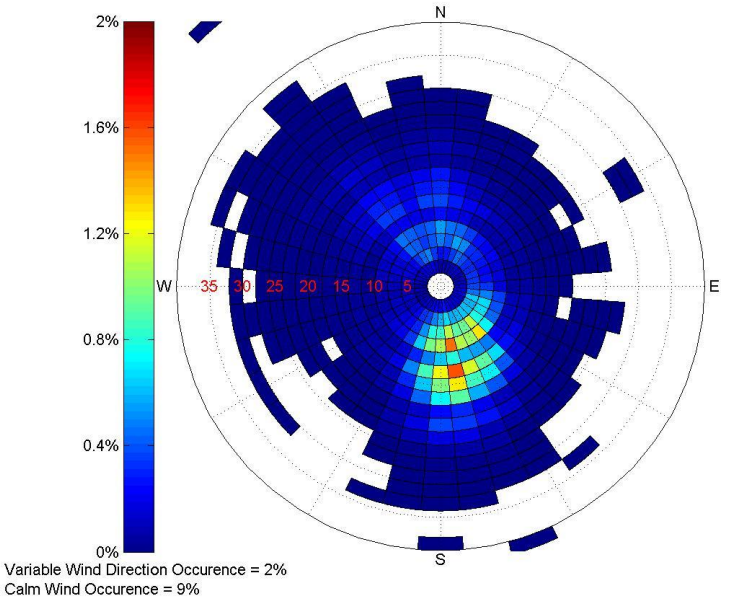

(b) Wind Density Graph

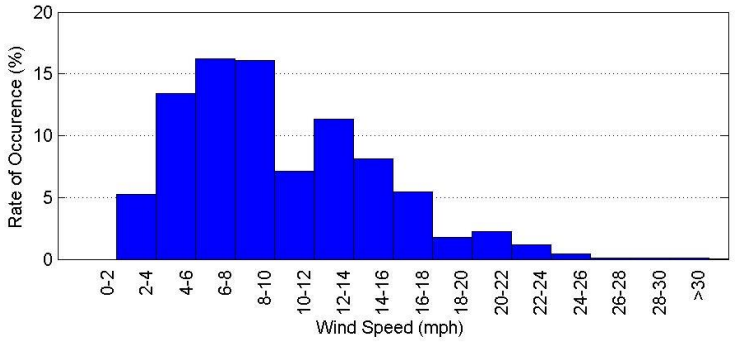

(c) Wind Speed Occurrence Rate

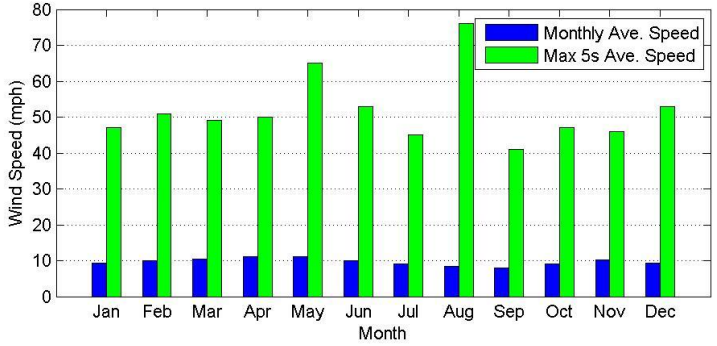

(d) Monthly Average Wind Speed

Figure 4.59: Wind Data Collected at the Fort Worth Meacham International Airport (13961) from 2008 to 2015

FORT WORTH NAVAL AIR STATION JRB/CARSWELL FIELD (13911)

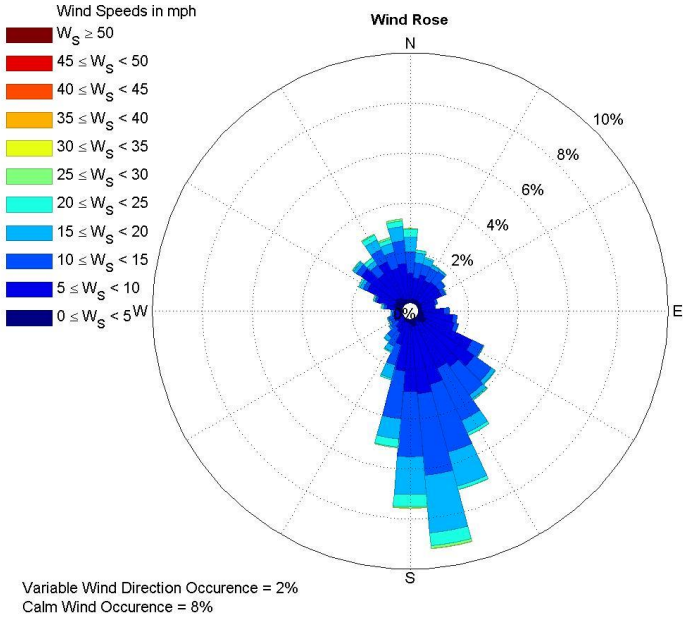

(a) Wind Rose Graph

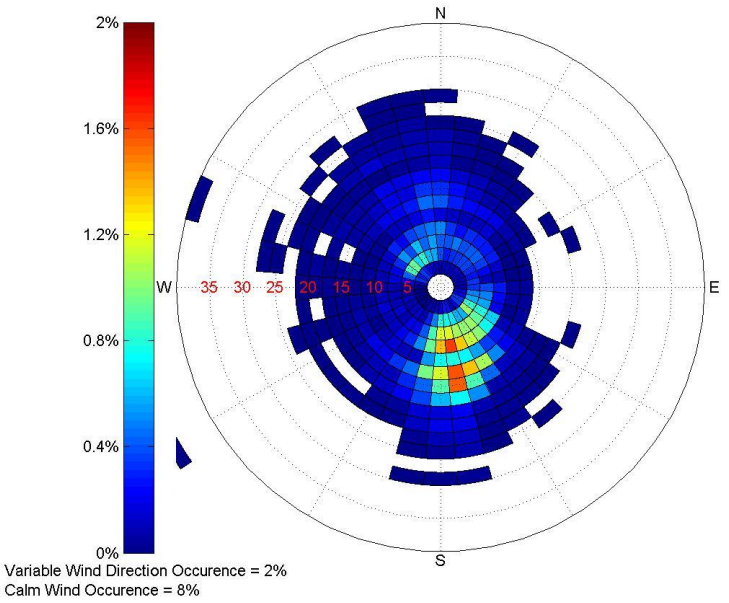

(b) Wind Density Graph

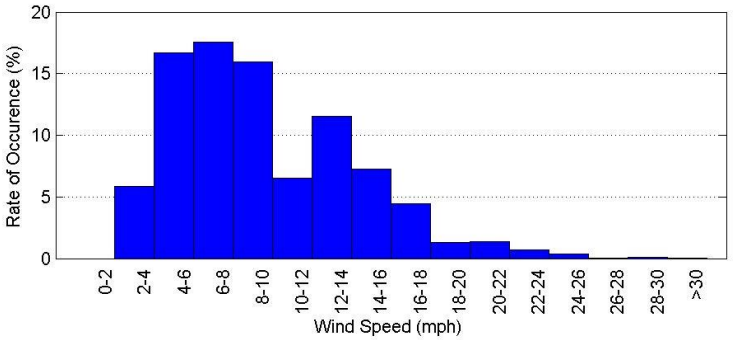

(c) Wind Speed Occurrence Rate

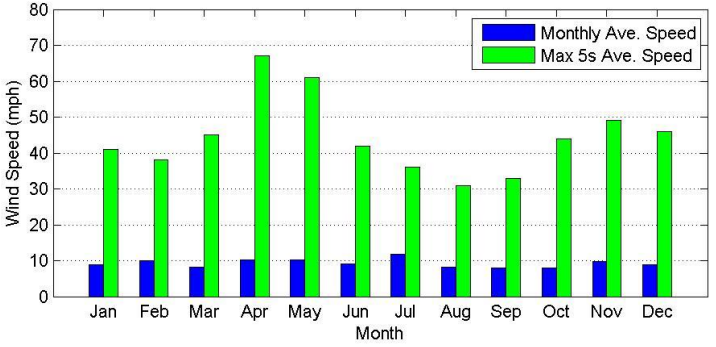

(d) Monthly Average Wind Speed

Figure 4.60: Wind Data Collected at the Fort Worth Naval Air Station JRB/Carswell Field (13911) in the Year 2015

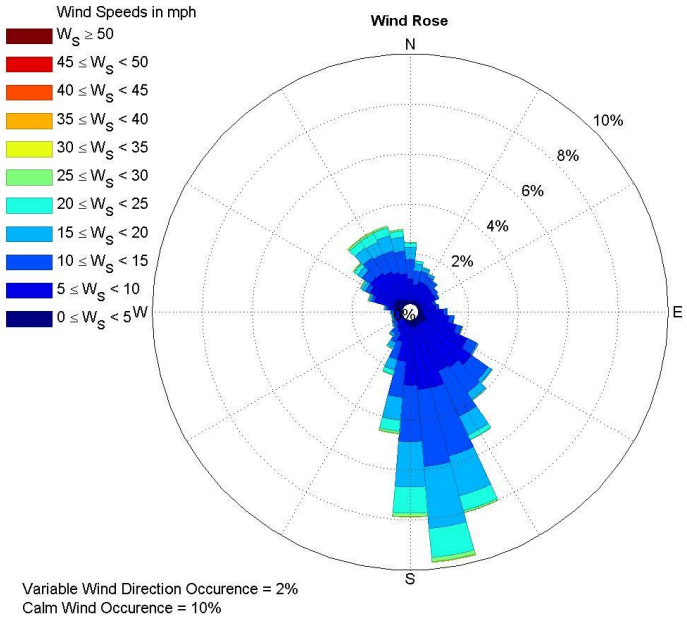

(a) Wind Rose Graph

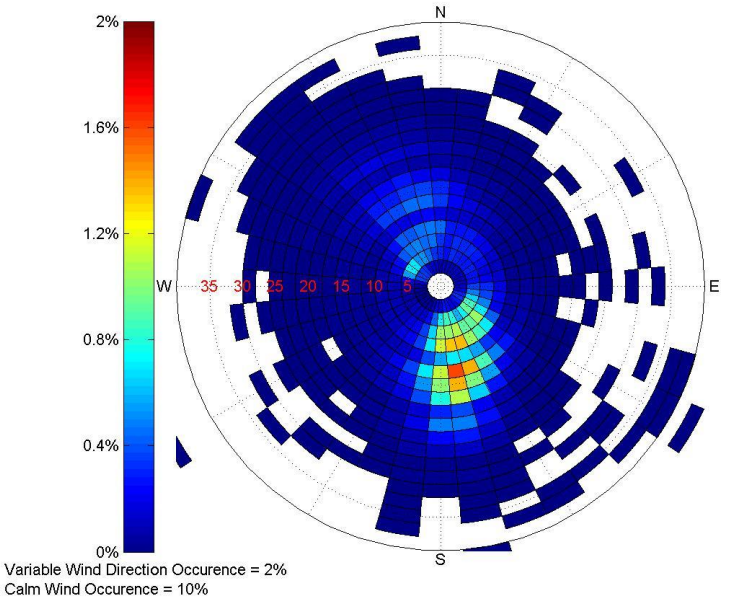

(b) Wind Density Graph

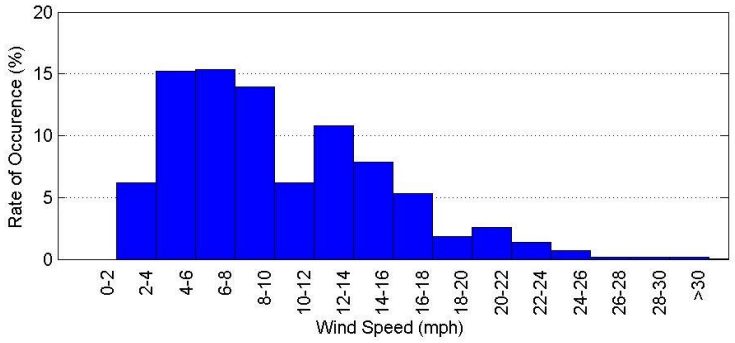

(c) Wind Speed Occurrence Rate

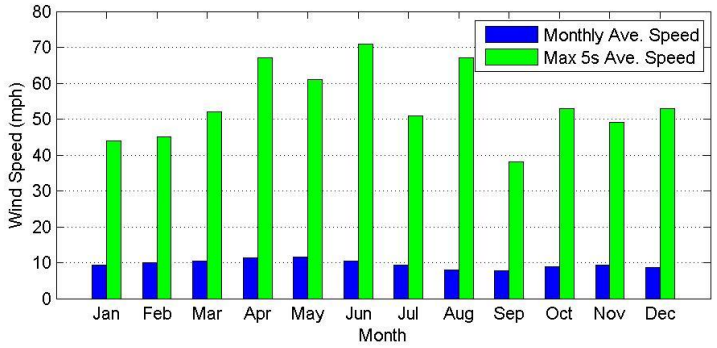

(d) Monthly Average Wind Speed

Figure 4.61: Wind Data Collected at the Fort Worth Naval Air Station JRB/Carswell Field (13911) from 2008 to 2015

GRANBURY MUNICIPAL ARPT (53977)

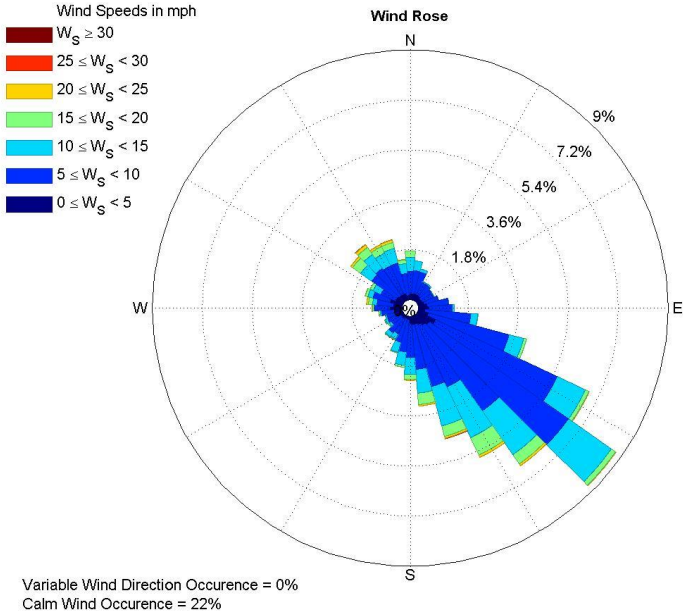

(a) Wind Rose Graph

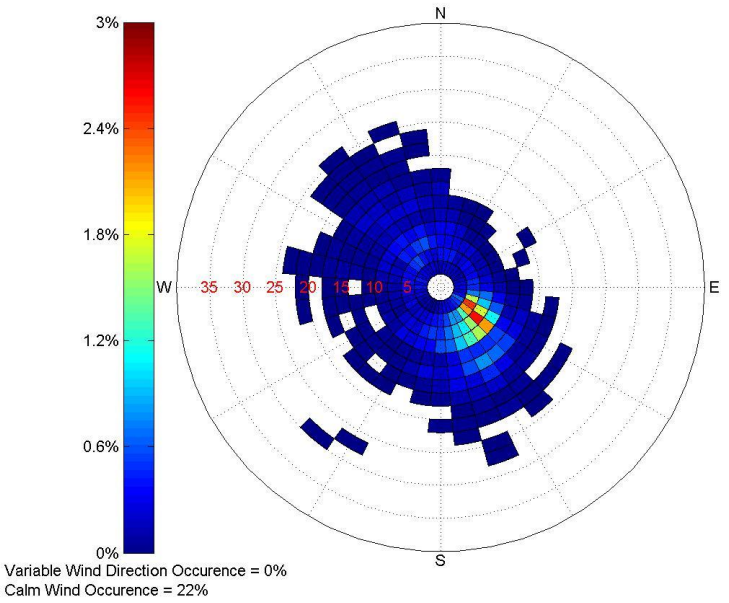

(b) Wind Density Graph

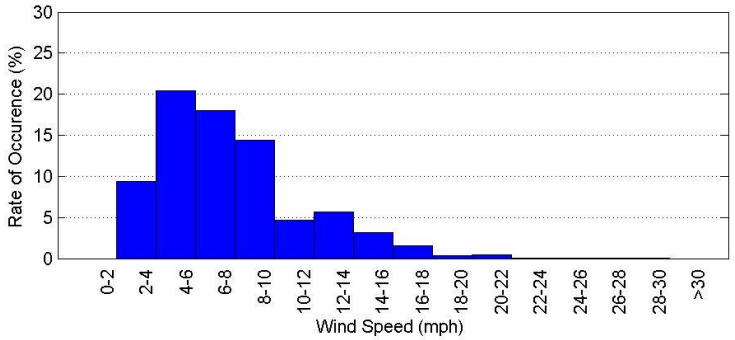

(c) Wind Speed Occurrence Rate

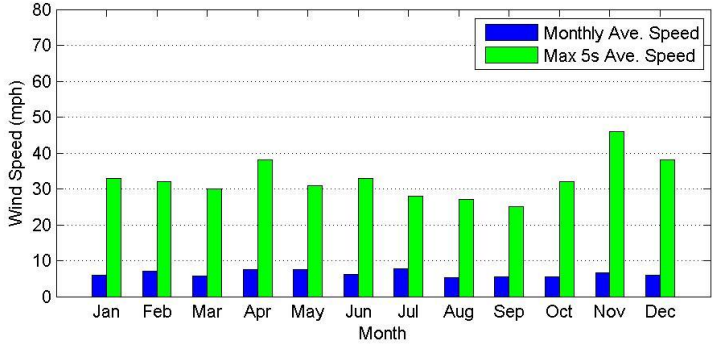

(d) Monthly Average Wind Speed

Figure 4.62: Wind Data Collected at the Granbury Municipal Airport (53977) in the Year 2015

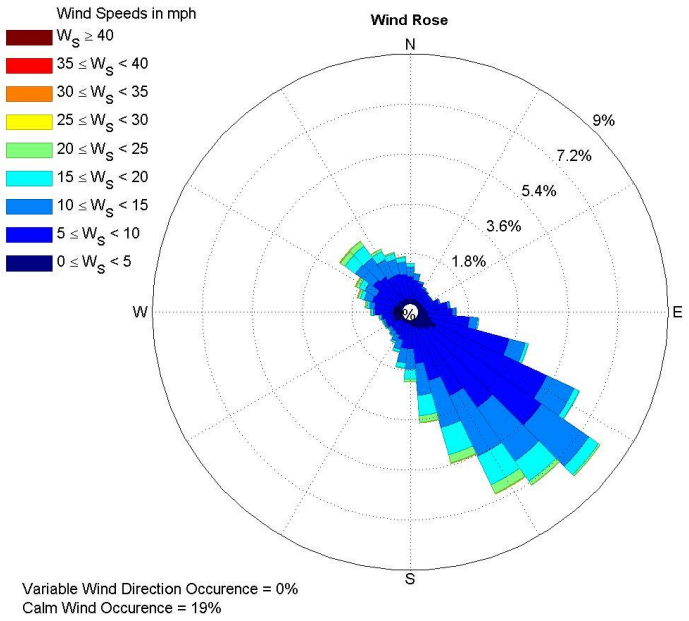

(a) Wind Rose Graph

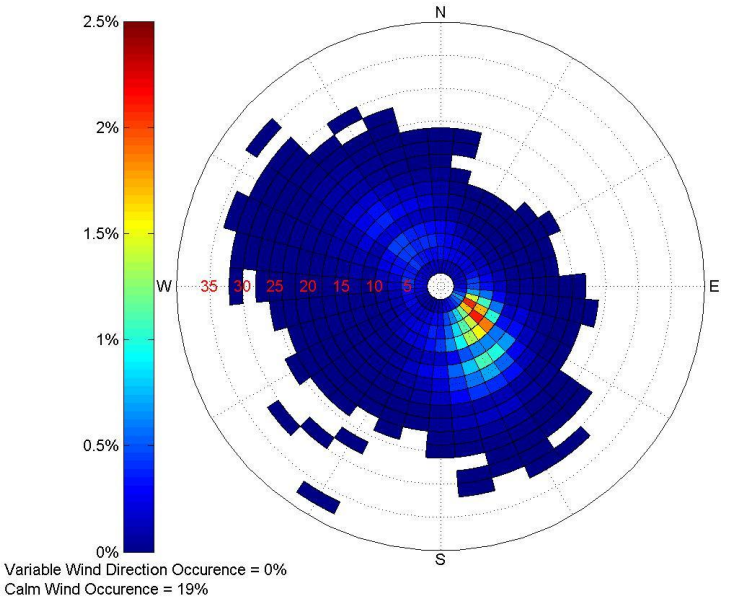

(b) Wind Density Graph

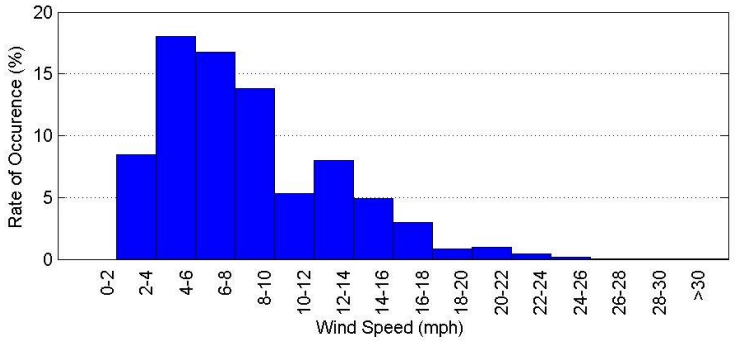

(c) Wind Speed Occurrence Rate

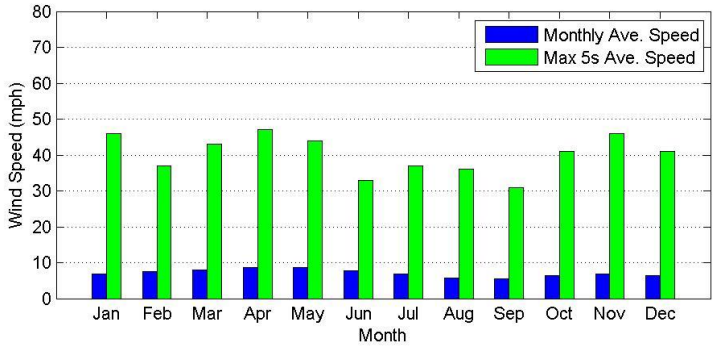

(d) Monthly Average Wind Speed

Figure 4.63: Wind Data Collected at the Granbury Municipal Airport (53977) from 2008 to 2015

MAJORS AIRPORT (13926)

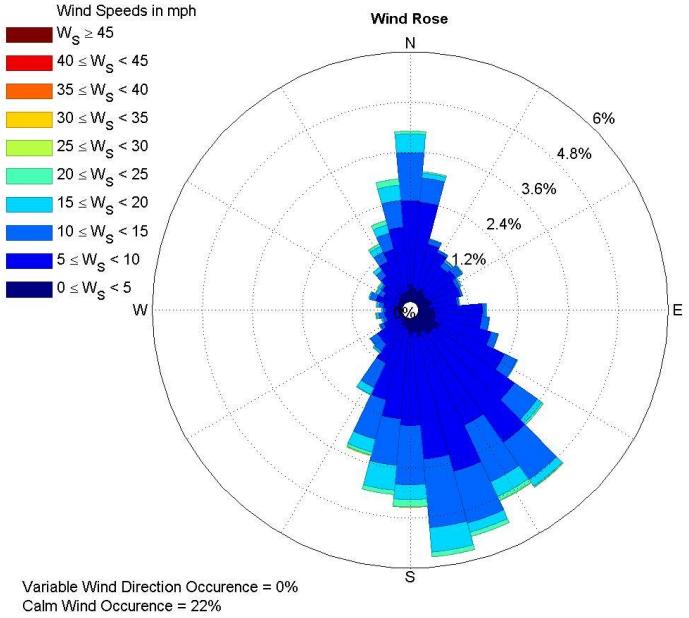

(a) Wind Rose Graph

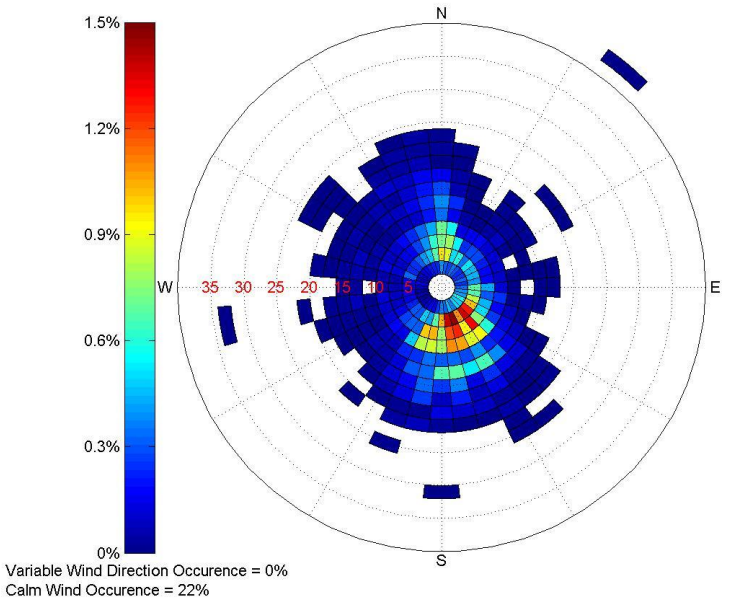

(b) Wind Density Graph

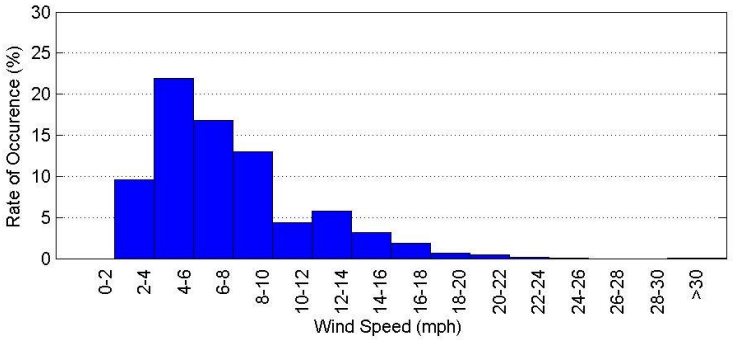

(c) Wind Speed Occurrence Rate

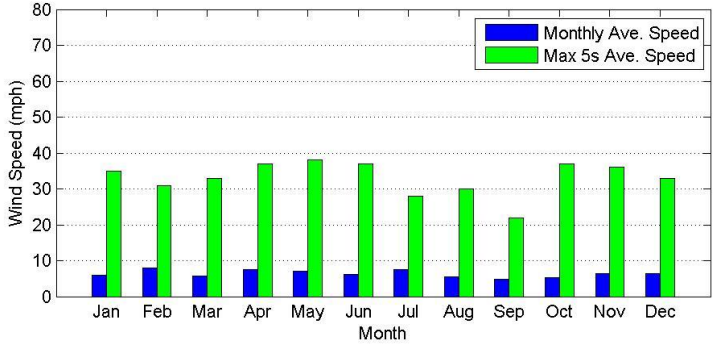

(d) Monthly Average Wind Speed

Figure 4.64: Wind Data Collected at the Majors Airport (13926) in the Year 2015

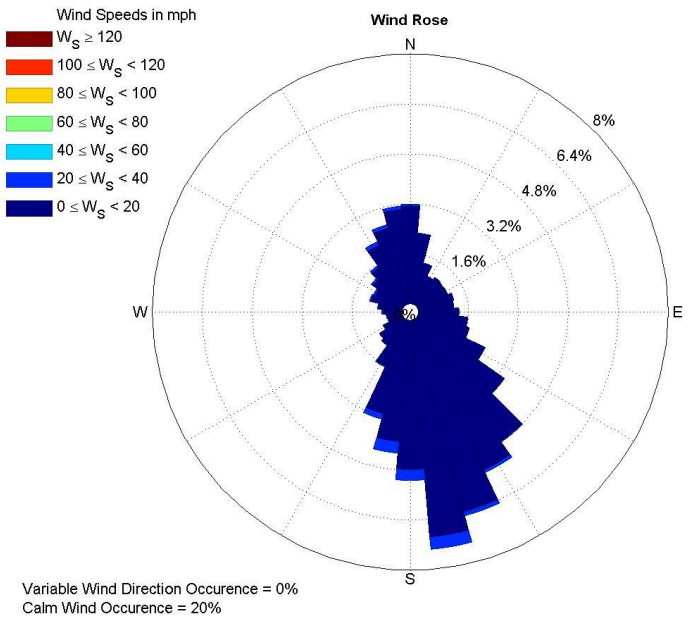

(a) Wind Rose Graph

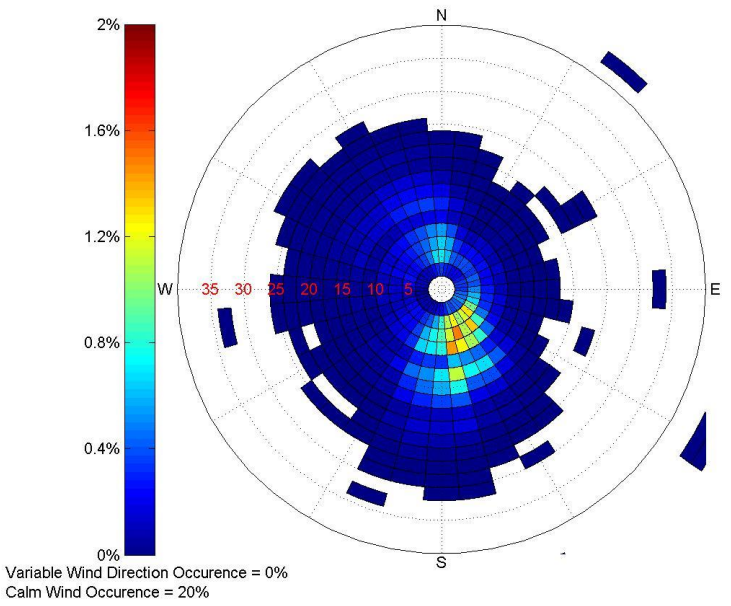

(b) Wind Density Graph

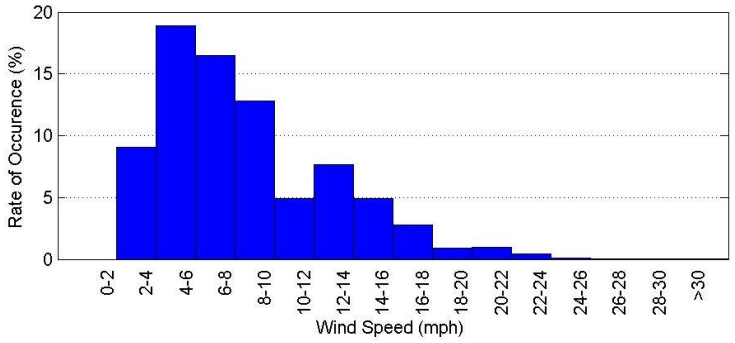

(c) Wind Speed Occurrence Rate

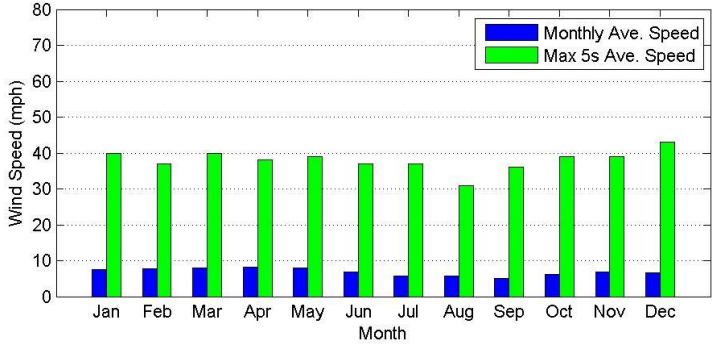

(d) Monthly Average Wind Speed

Figure 4.65: Wind Data Collected at the Majors Airport (13926) from 2008 to 2015

COX FIELD AIRPORT (93955)

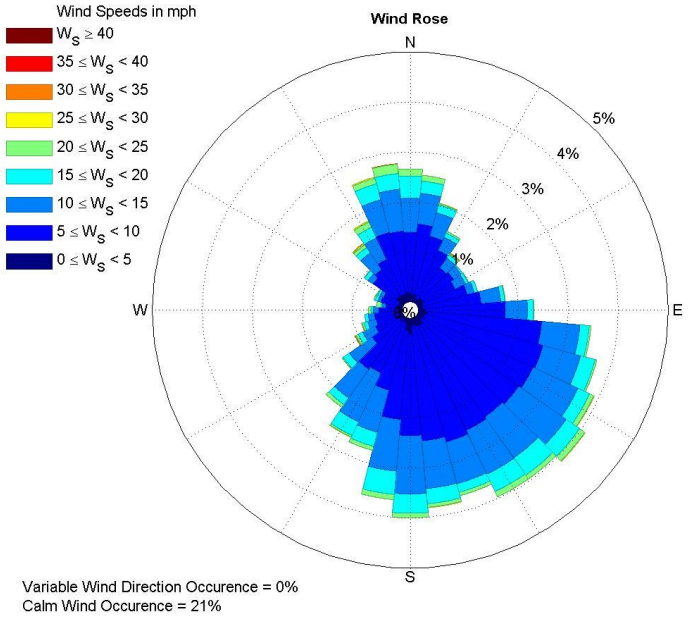

(a) Wind Rose Graph

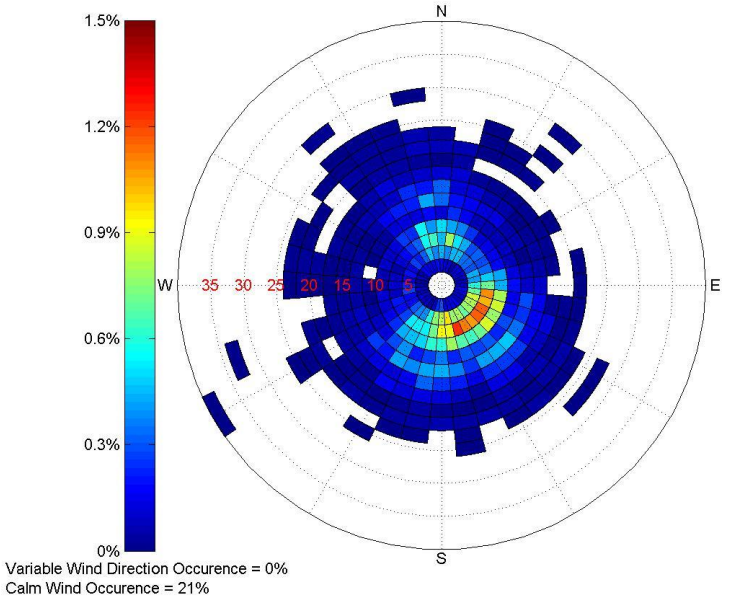

(b) Wind Density Graph

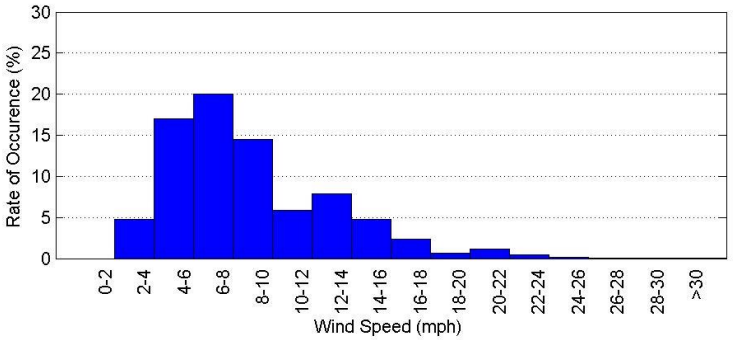

(c) Wind Speed Occurrence Rate

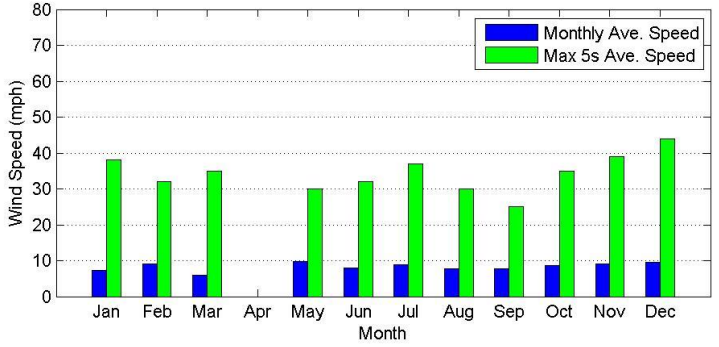

(d) Monthly Average Wind Speed

Figure 4.66: Wind Data Collected at the Cox Field Airport (93955) in the Year 2015

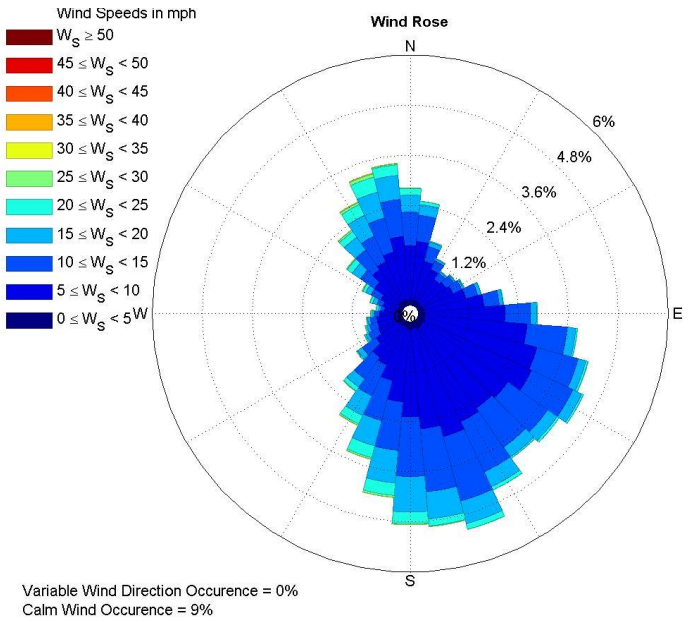

(a) Wind Rose Graph

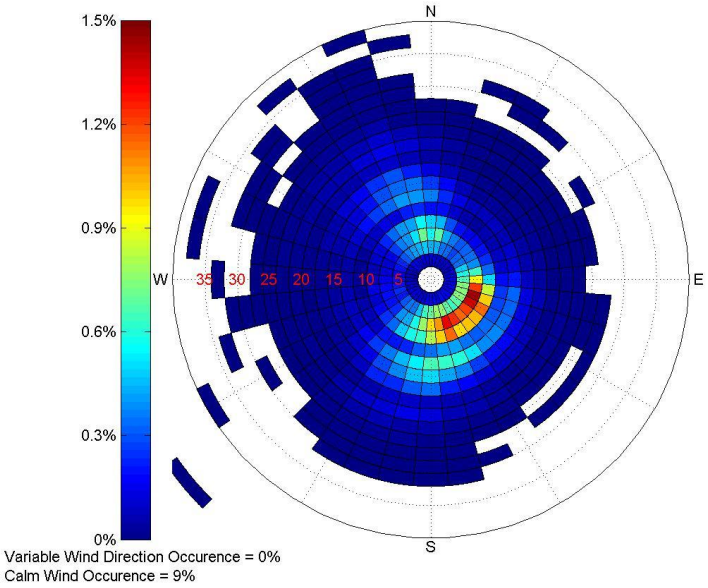

(b) Wind Density Graph

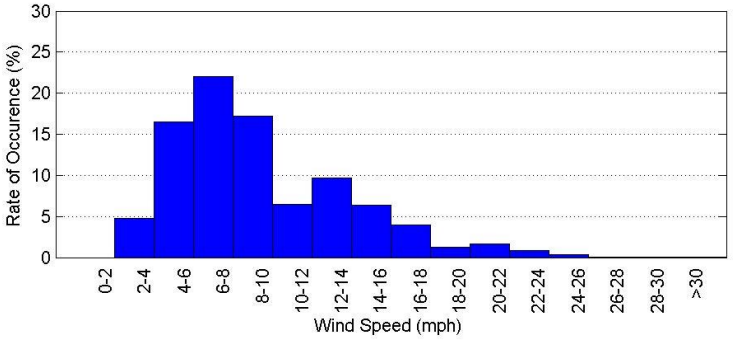

(c) Wind Speed Occurrence Rate

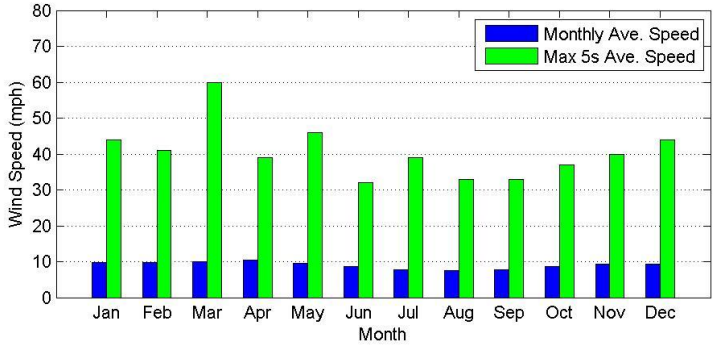

(d) Monthly Average Wind Speed

Figure 4.67: Wind Data Collected at the Cox Field Airport (93955) from 2008 to 2015

GRAYSON COUNTY AIRPORT (53967)

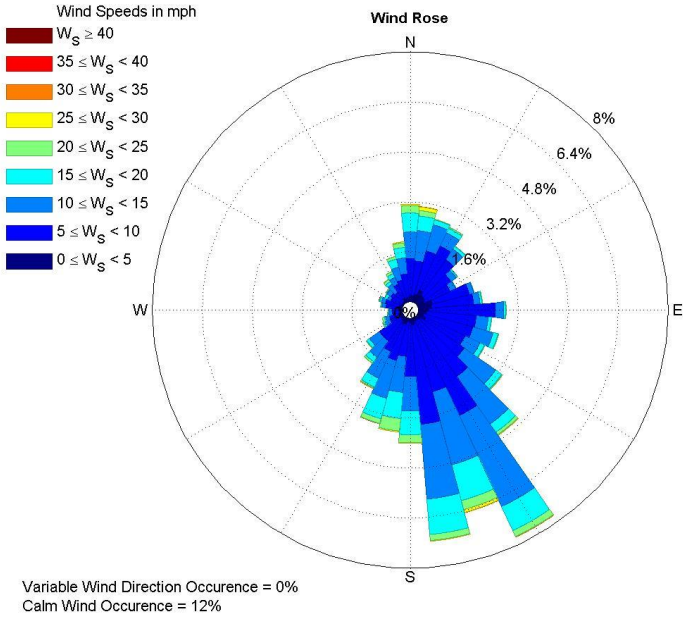

(a) Wind Rose Graph

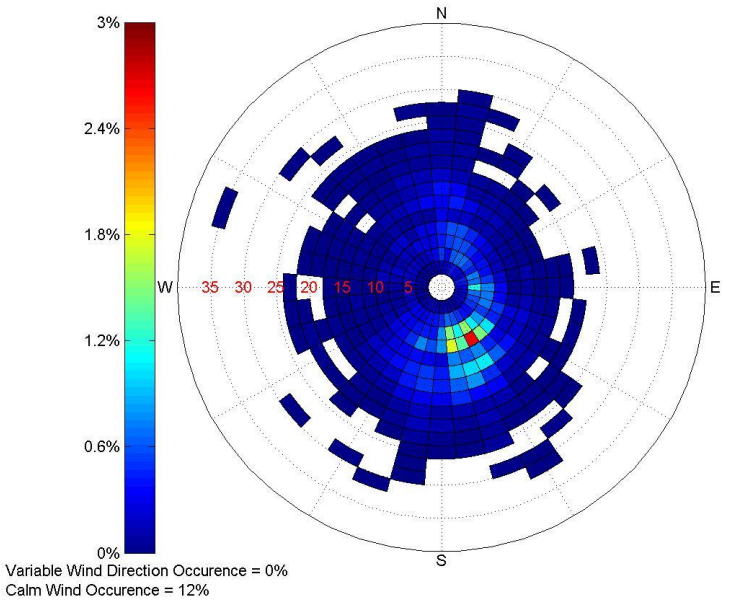

(b) Wind Density Graph

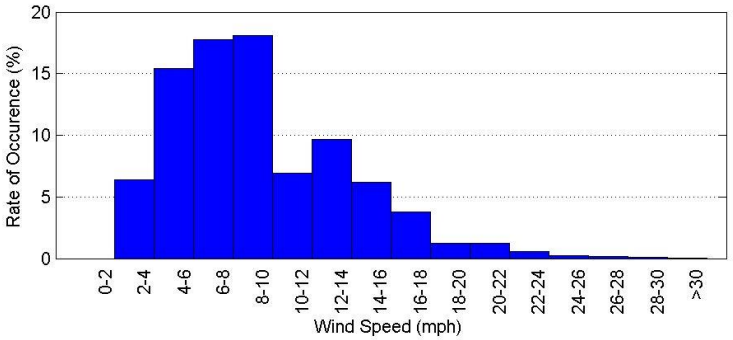

(c) Wind Speed Occurrence Rate

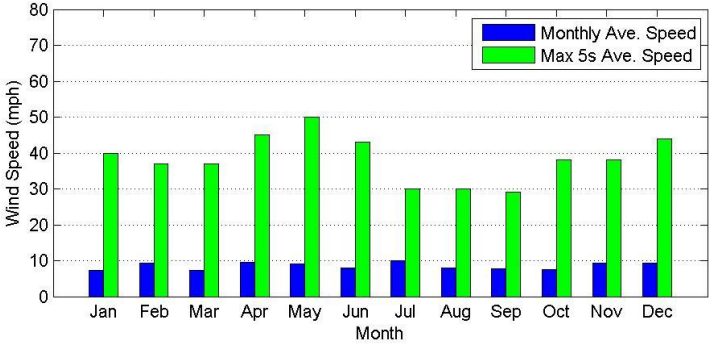

(d) Monthly Average Wind Speed

Figure 4.68: Wind Data Collected at the Grayson County Airport (53967) in the Year 2015

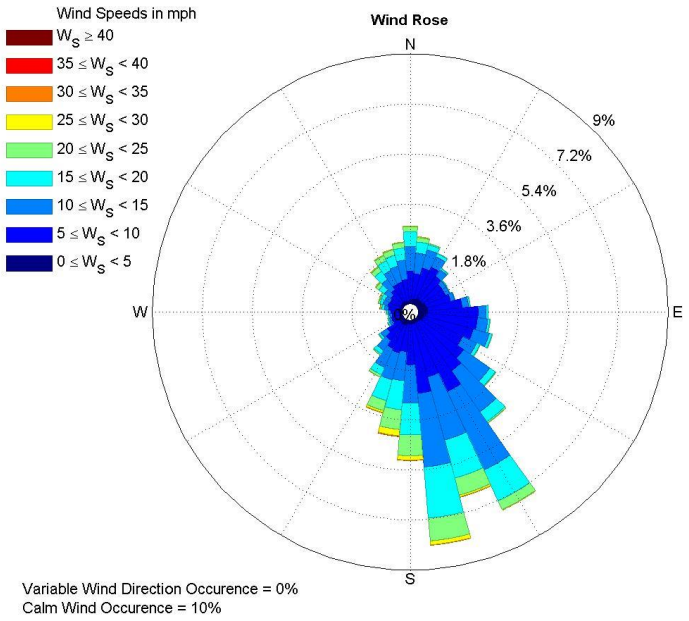

(a) Wind Rose Graph

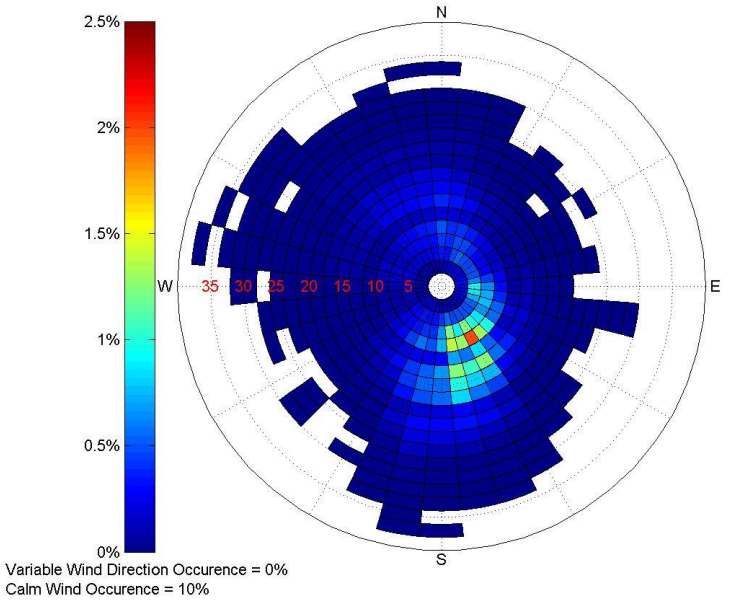

(b) Wind Density Graph

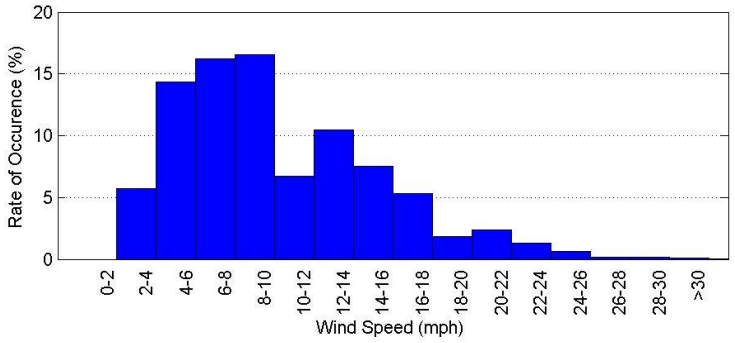

(c) Wind Speed Occurrence Rate

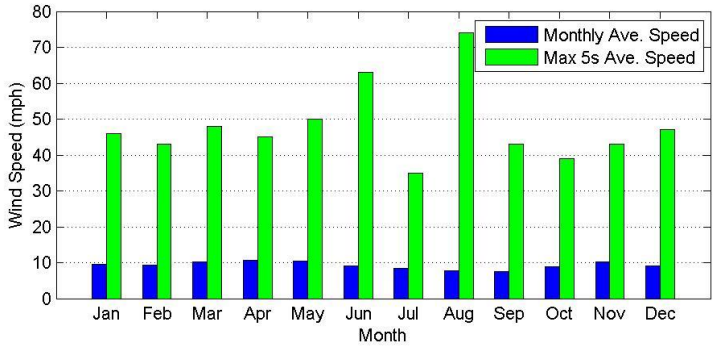

(d) Monthly Average Wind Speed

Figure 4.69: Wind Data Collected at the Grayson County Airport (53967) from 2008 to 2015

HILLSBORO MUNICIPAL ARPT (53972)

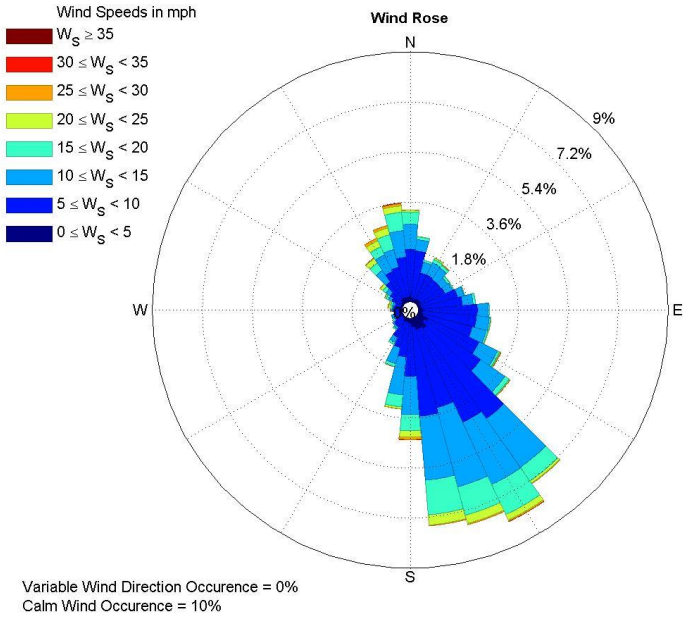

(a) Wind Rose Graph

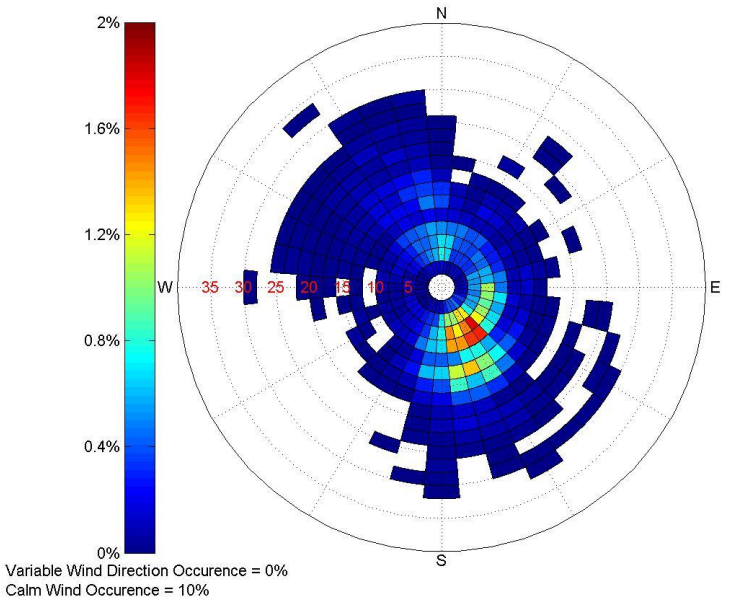

(b) Wind Density Graph

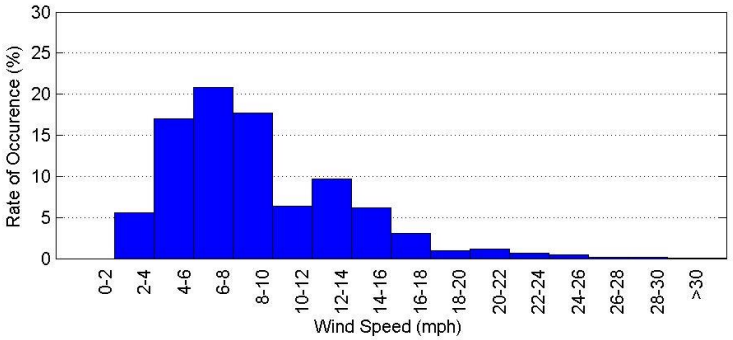

(c) Wind Speed Occurrence Rate

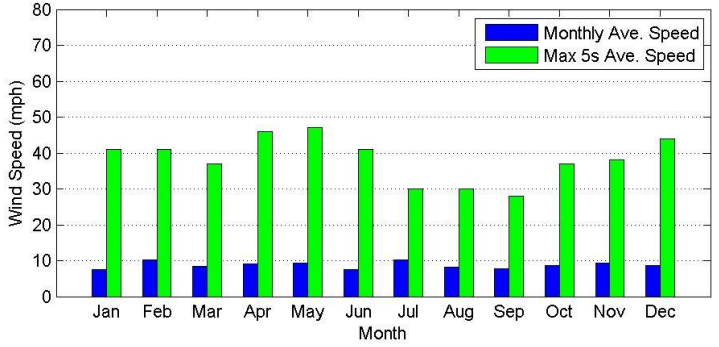

(d) Monthly Average Wind Speed

Figure 4.70: Wind Data Collected at the Hillsboro Municipal Airport (53972) in the Year 2015

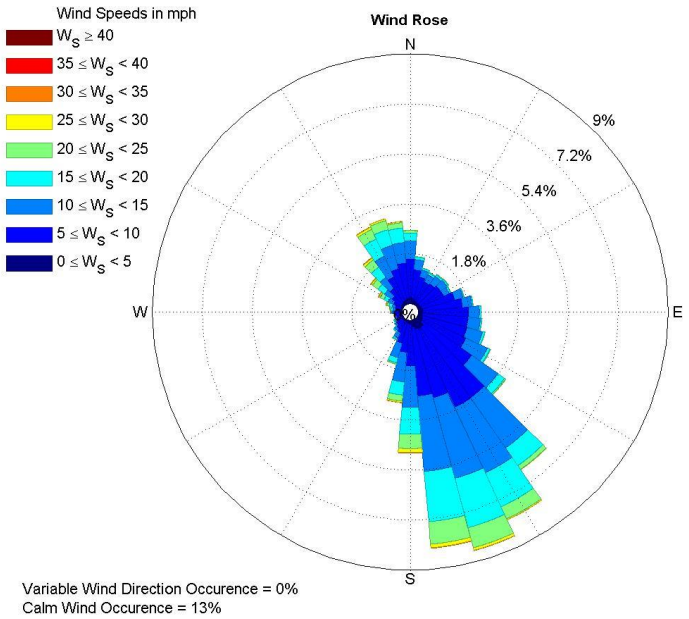

a) Wind Rose Graph

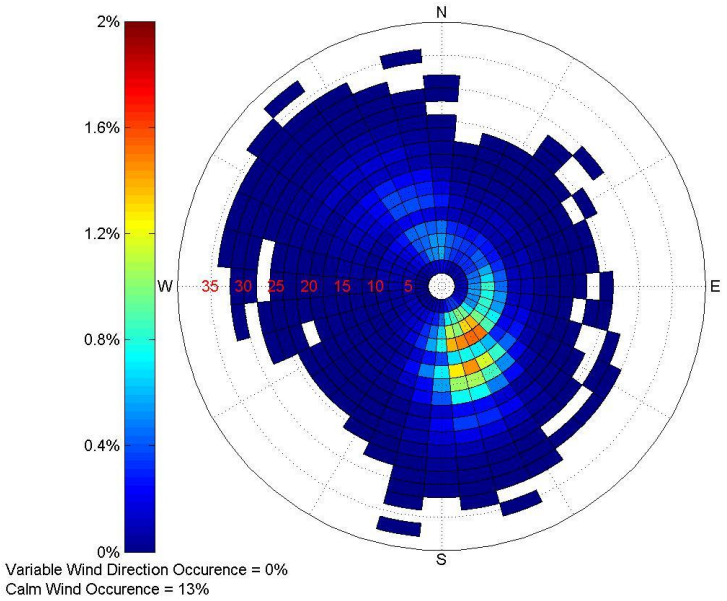

(b) Wind Density Graph

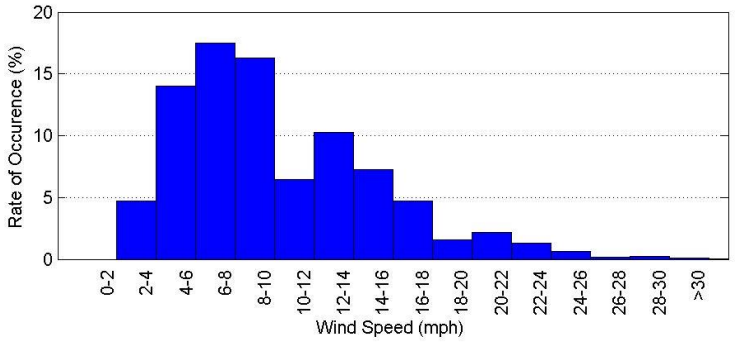

(c) Wind Speed Occurrence Rate

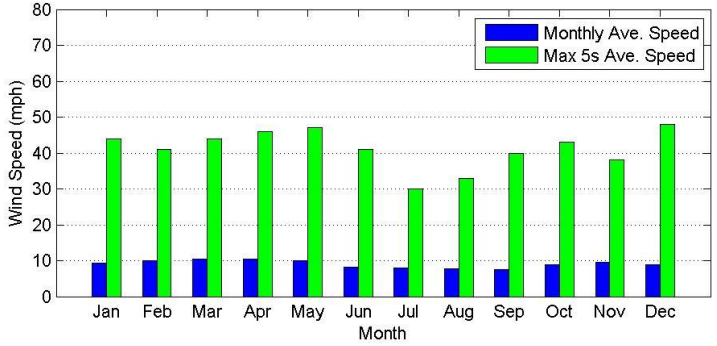

(d) Monthly Average Wind Speed

Figure 4.71: Wind Data Collected at the Hillsboro Municipal Airport (53972) from 2008 to 2015

WACO REGIONAL AIRPORT (13959)

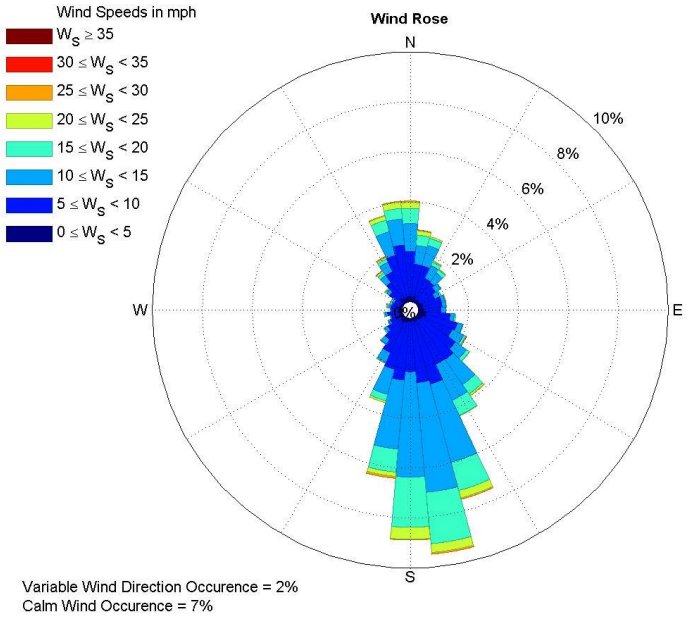

(a) Wind Rose Graph

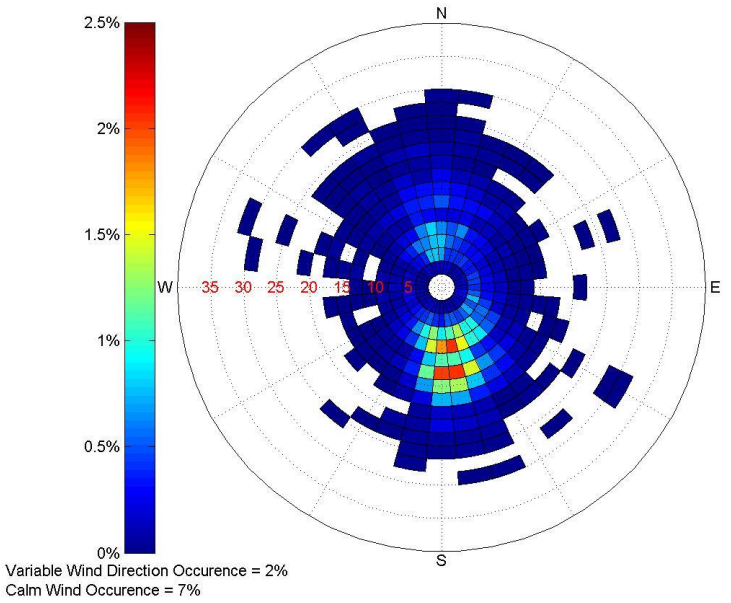

(b) Wind Density Graph

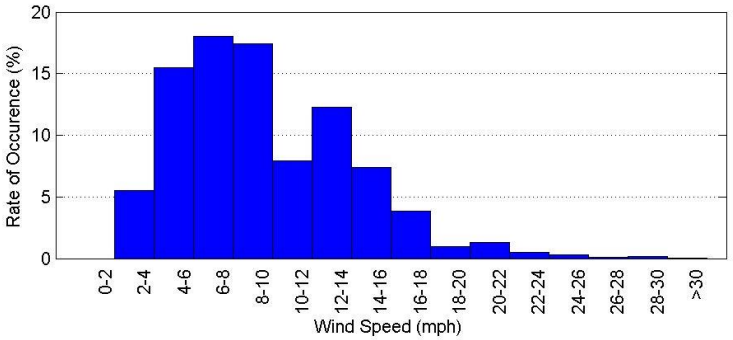

(c) Wind Speed Occurrence Rate

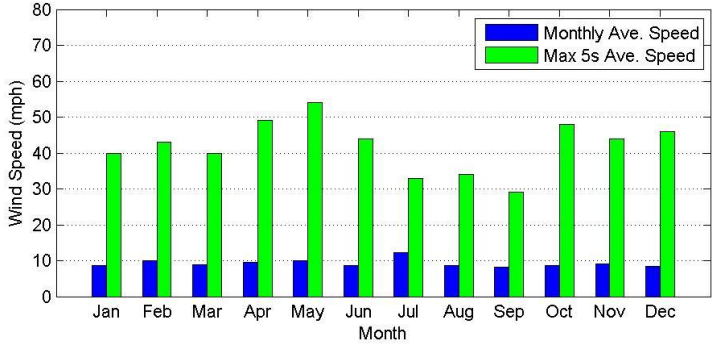

(d) Monthly Average Wind Speed

Figure 4.72: Wind Data Collected at the Waco Regional Airport (13959) in the Year 2015

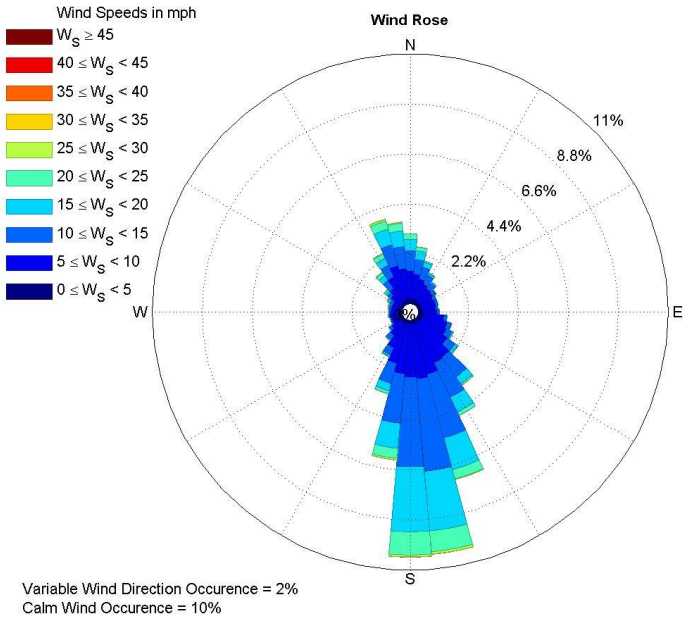

(a) Wind Rose Graph

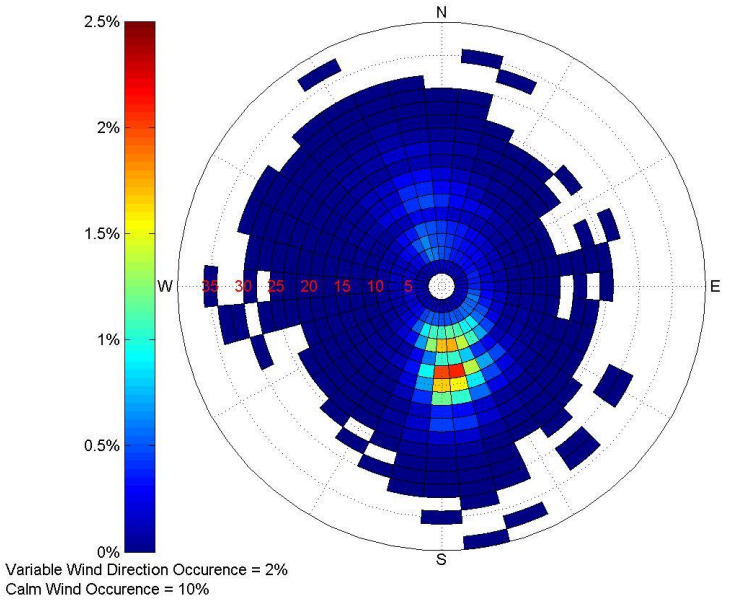

(b) Wind Density Graph

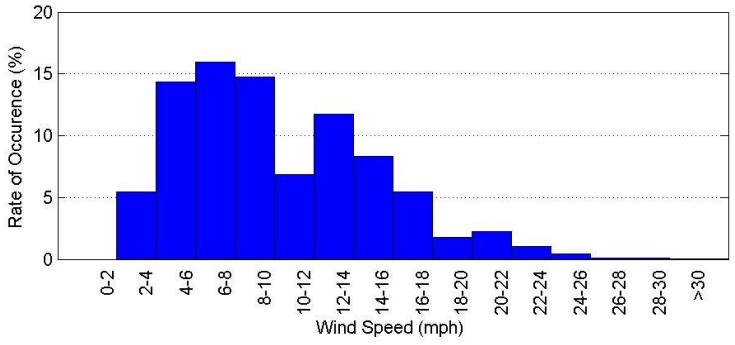

(c) Wind Speed Occurrence Rate

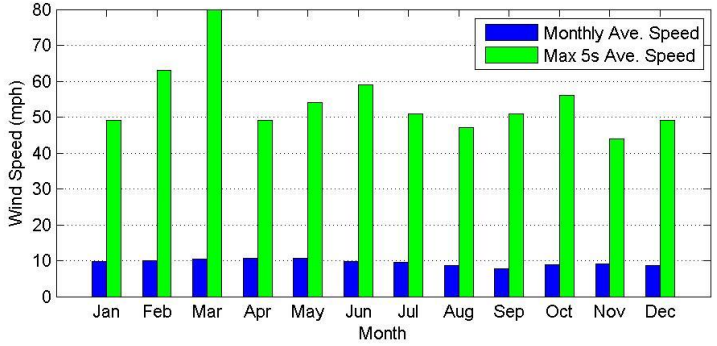

(d) Monthly Average Wind Speed

Figure 4.73: Wind Data Collected at the Waco Regional Airport (13959) from 2008 to 2015

MC GREGOR EXECUTIVE ARPT (53952)

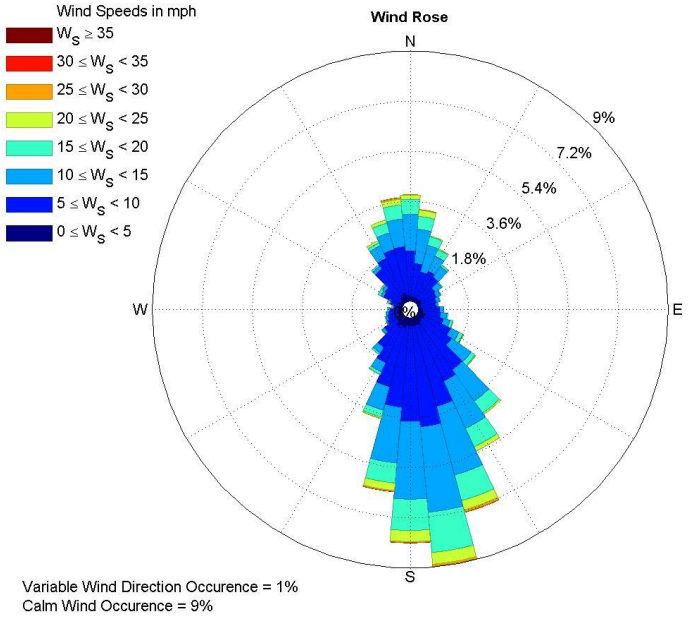

(a) Wind Rose Graph

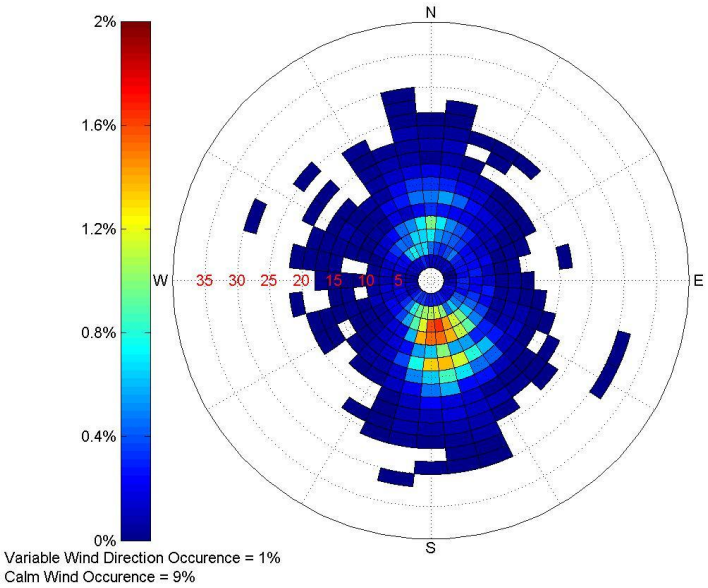

(b) Wind Density Graph

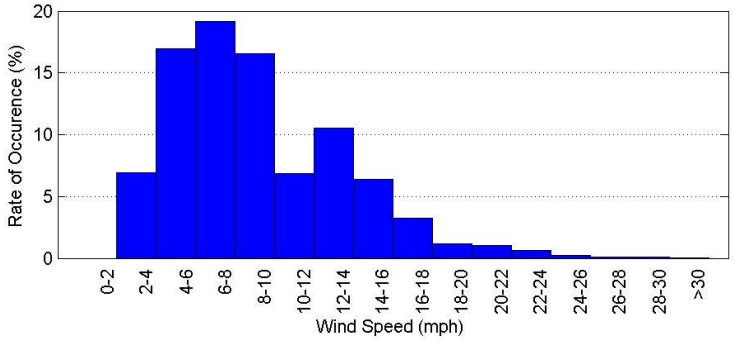

(c) Wind Speed Occurrence Rate

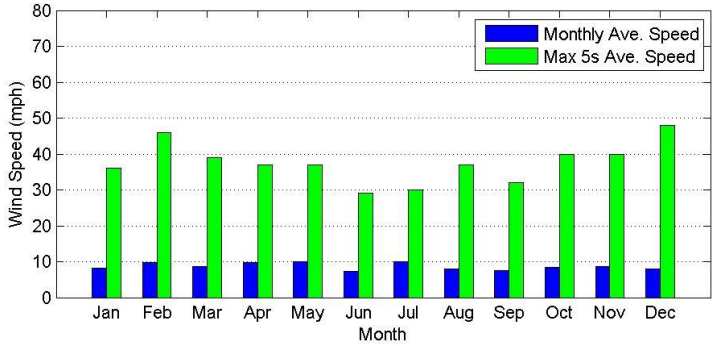

(d) Monthly Average Wind Speed

Figure 4.74: Wind Data Collected at the McGregor Executive Airport (53952) in the Year 2015

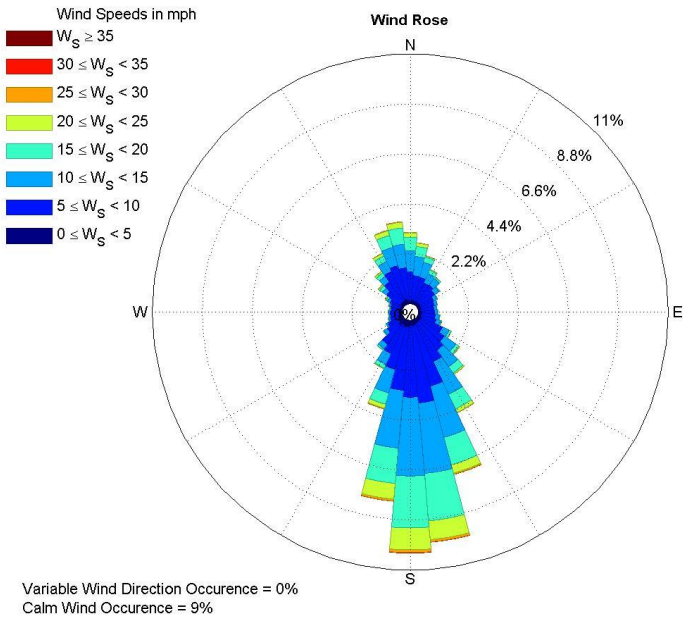

(a) Wind Rose Graph

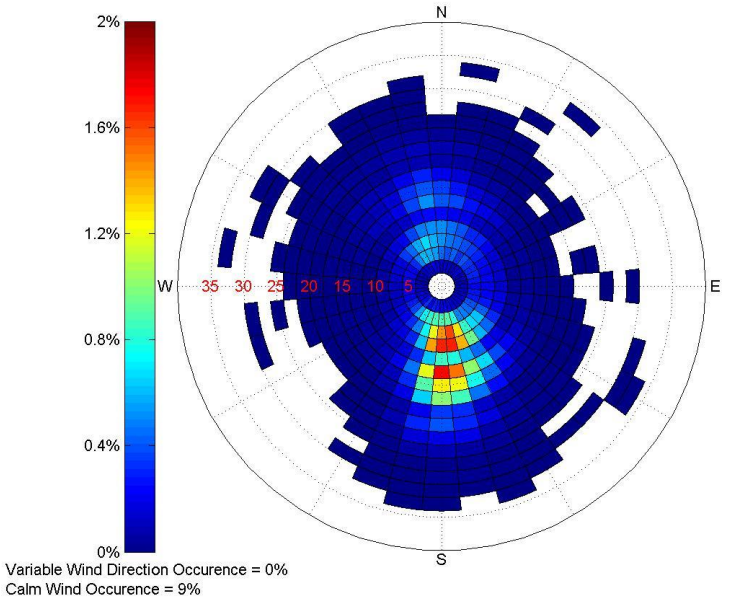

(b) Wind Density Graph

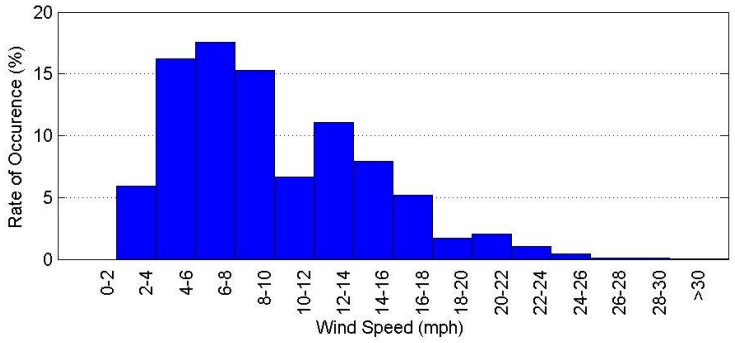

(c) Wind Speed Occurrence Rate

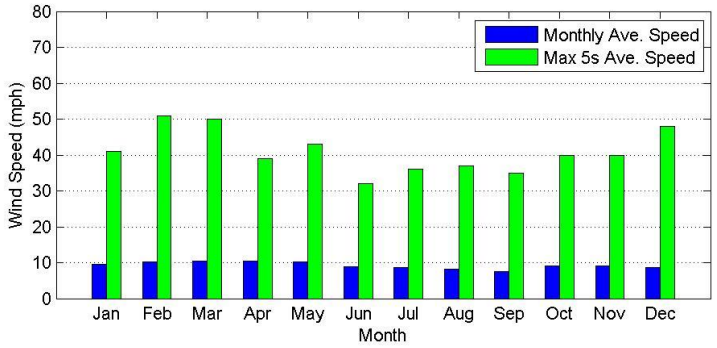

(d) Monthly Average Wind Speed

Figure 4.75: Wind Data Collected at the McGregor Executive Airport (53952) from 2008 to 2015

DRAUGHON-MILLER CNTRL TX RGNL ARPT (93984)

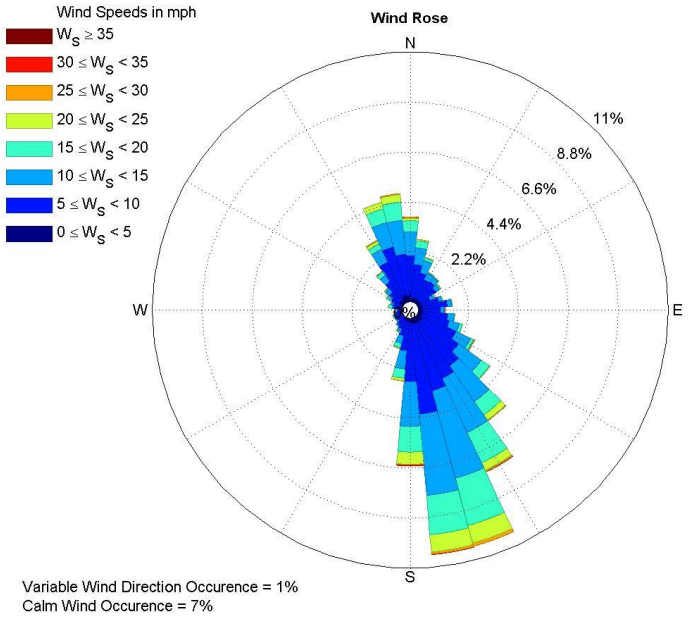

(a) Wind Rose Graph

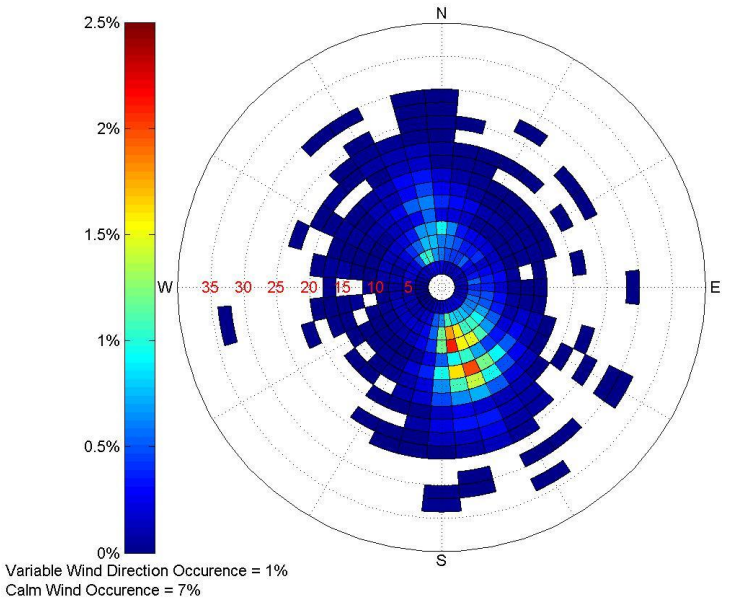

(b) Wind Density Graph

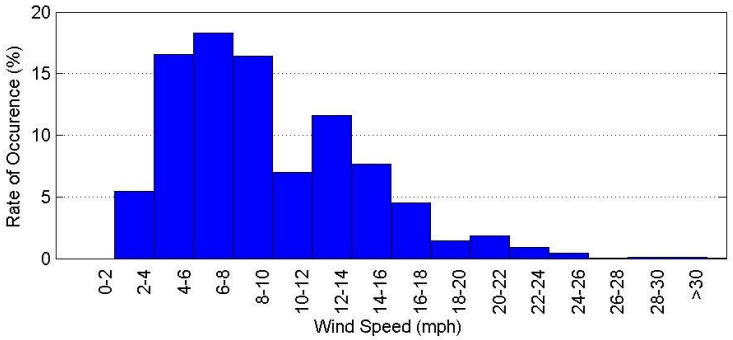

(c) Wind Speed Occurrence Rate

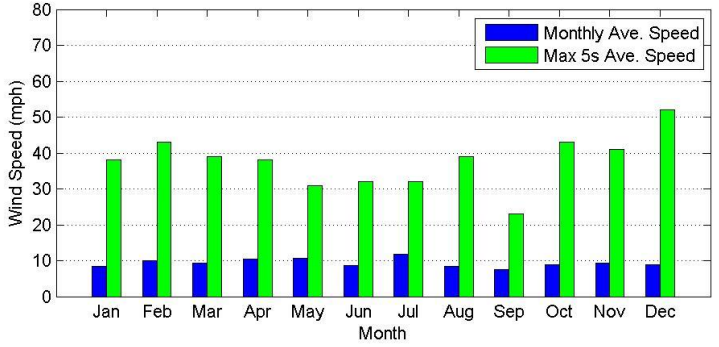

(d) Monthly Average Wind Speed

Figure 4.76: Wind Data Collected at the Draughon-Miller Central Texas Regional Airport (93984) in the Year 2015

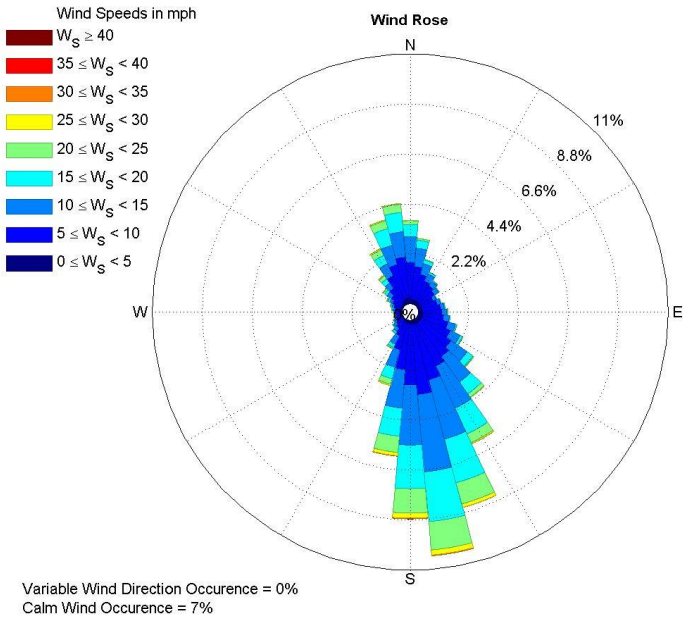

(a) Wind Rose Graph

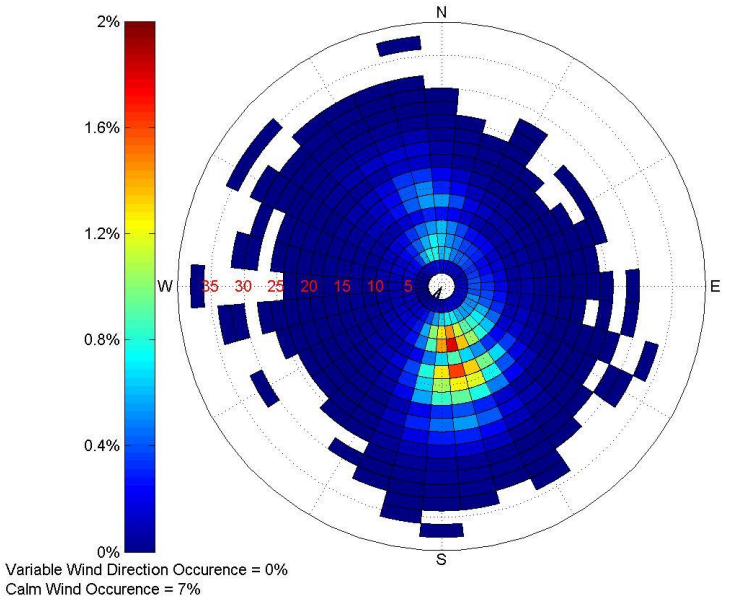

(b) Wind Density Graph

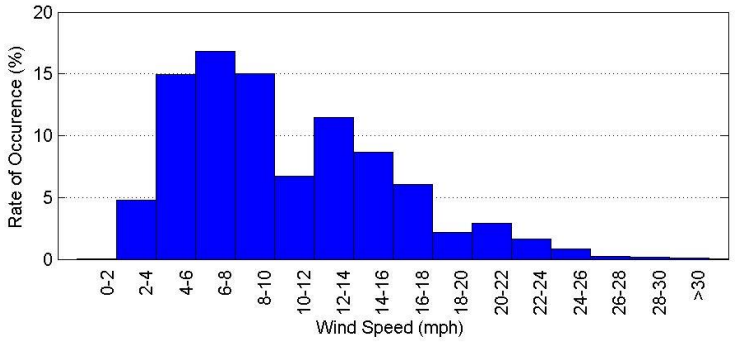

(c) Wind Speed Occurrence Rate

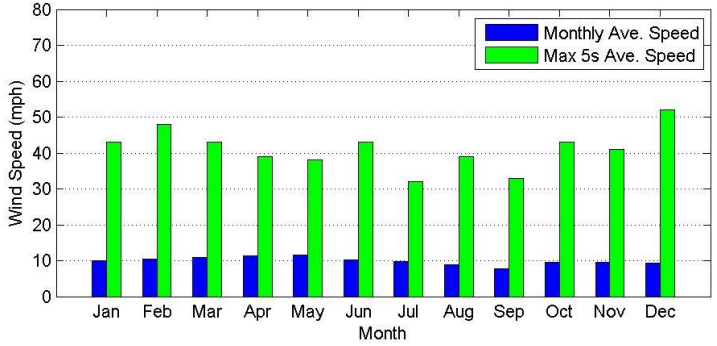

(d) Monthly Average Wind Speed

Figure 4.77: Wind Data Collected at the Draughon-Miller Central Texas Regional Airport (93984) from 2008 to 2015

ROBERT GRAY AFF AIRPORT (3902)

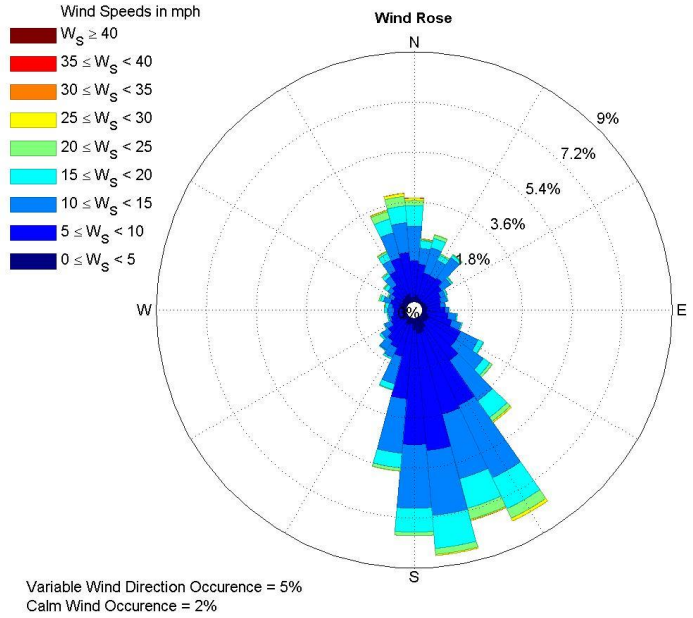

(a) Wind Rose Graph

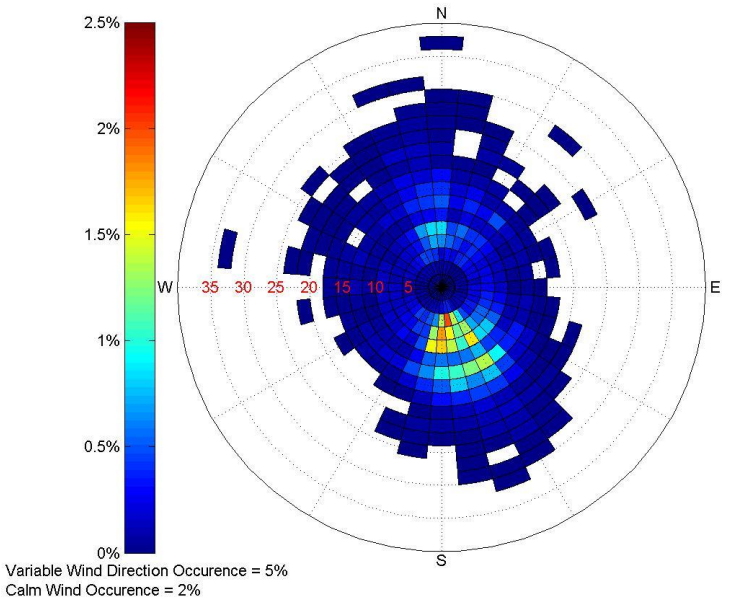

(b) Wind Density Graph

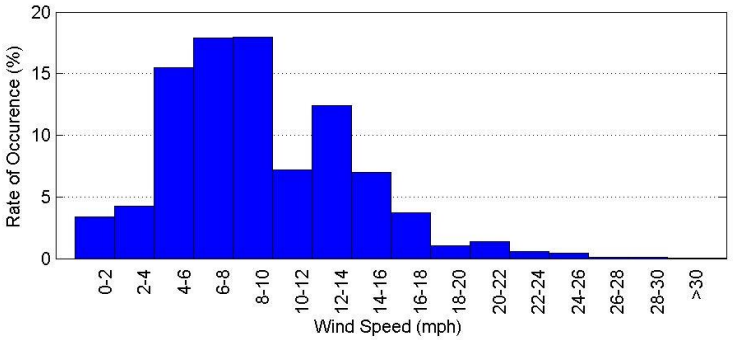

(c) Wind Speed Occurrence Rate

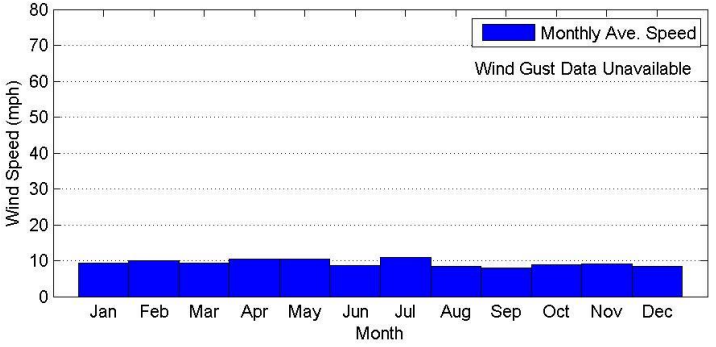

(d) Monthly Average Wind Speed

Figure 4.78: Wind Data Collected at the Robert Gray AFF Airport (3902) in the Year 2015

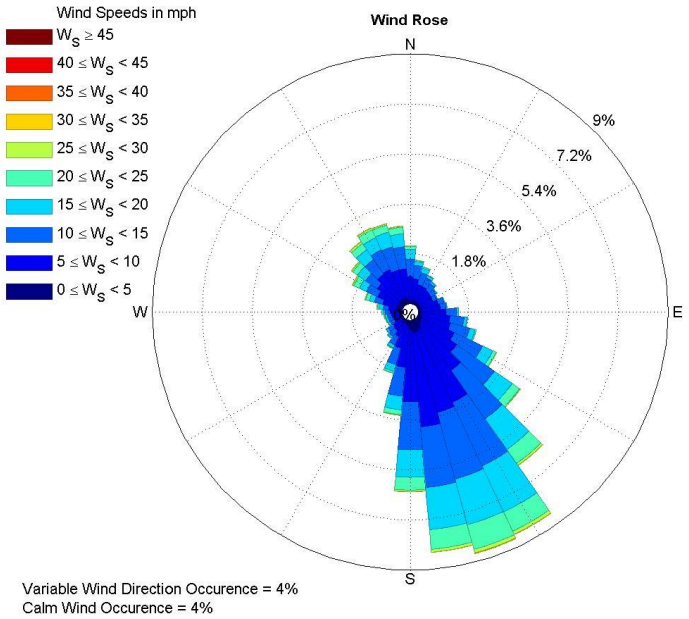

(a) Wind Rose Graph

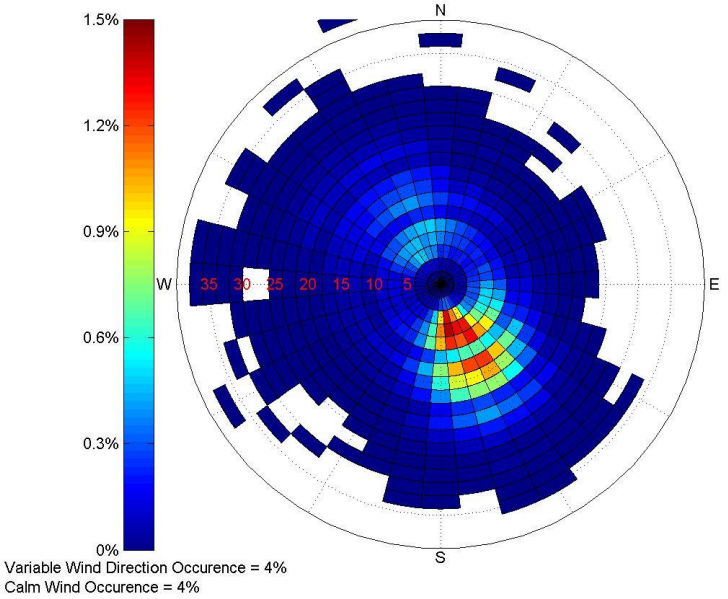

(b) Wind Density Graph

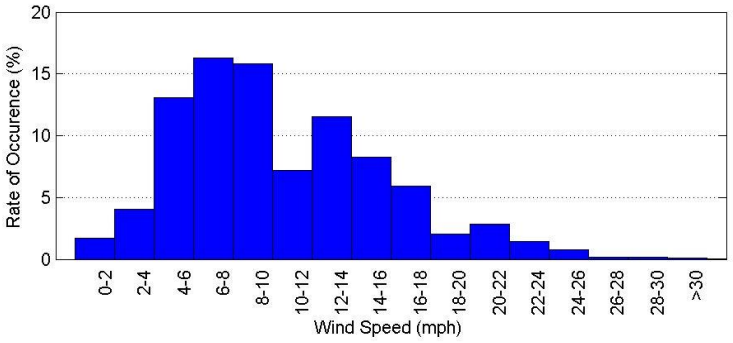

(c) Wind Speed Occurrence Rate

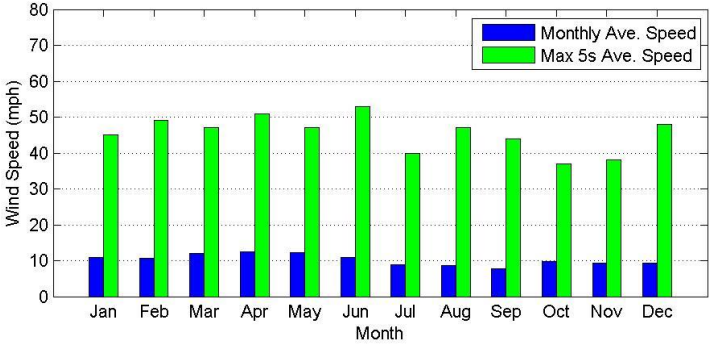

(d) Monthly Average Wind Speed

Figure 4.79: Wind Data Collected at the Robert Gray AFF Airport (3902) from 2008 to 2015

HOOD AAF AIRPORT (3933)

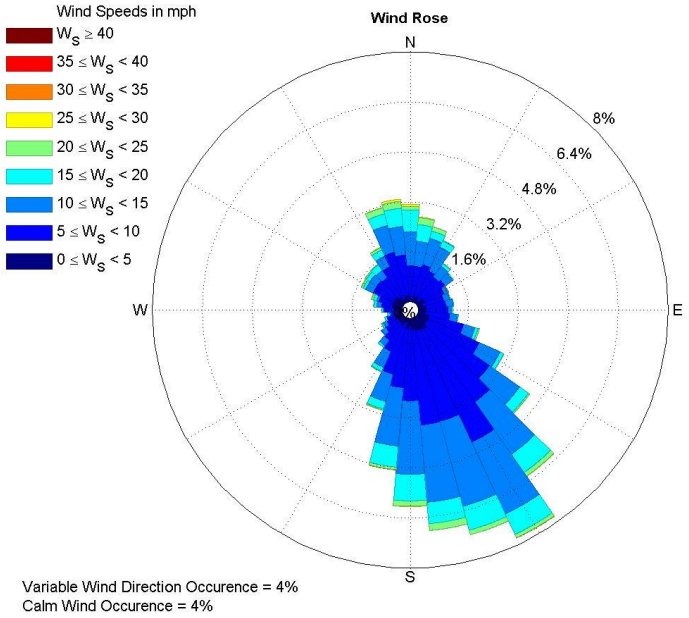

(a) Wind Rose Graph

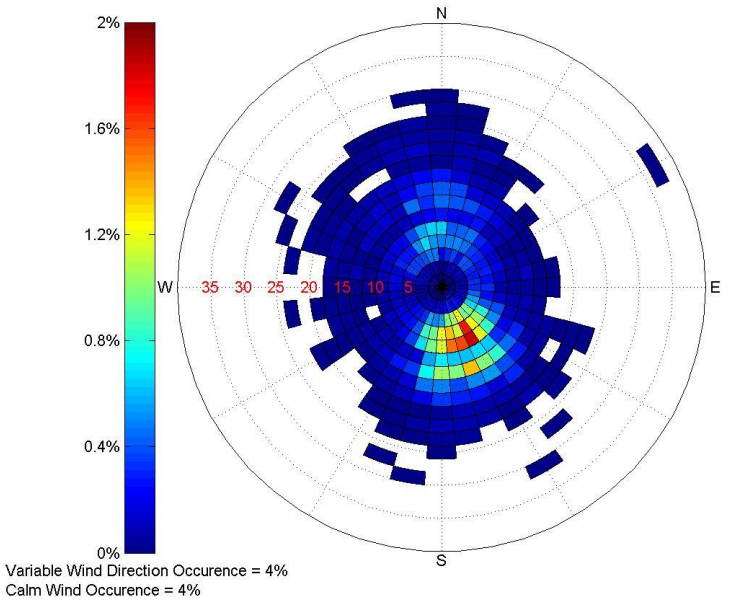

(b) Wind Density Graph

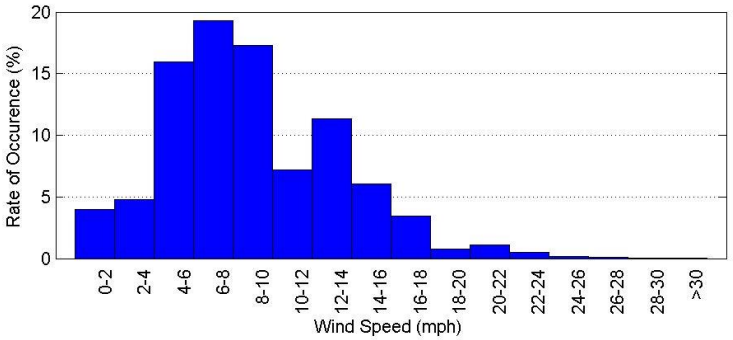

(c) Wind Speed Occurrence Rate

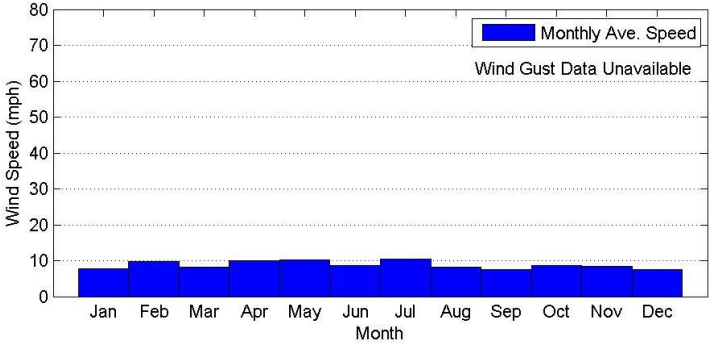

(d) Monthly Average Wind Speed

Figure 4.80: Wind Data Collected at the Hood AAF Airport (3933) in the Year 2015

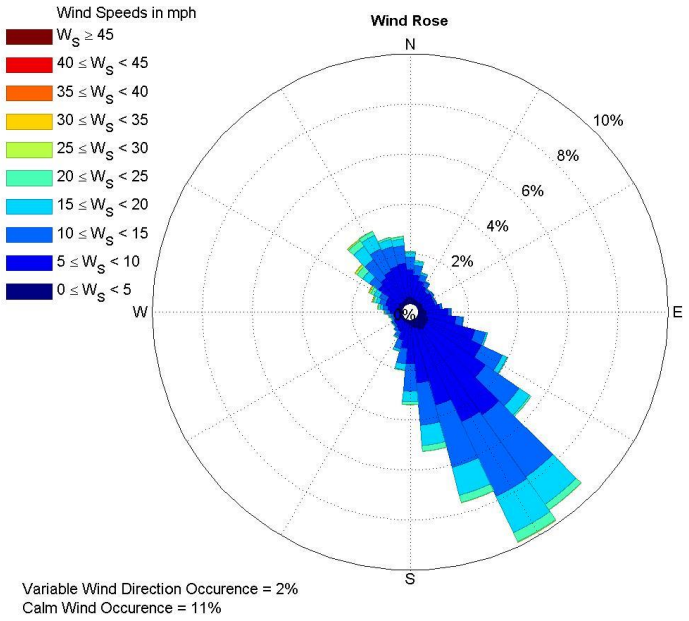

(a) Wind Rose Graph

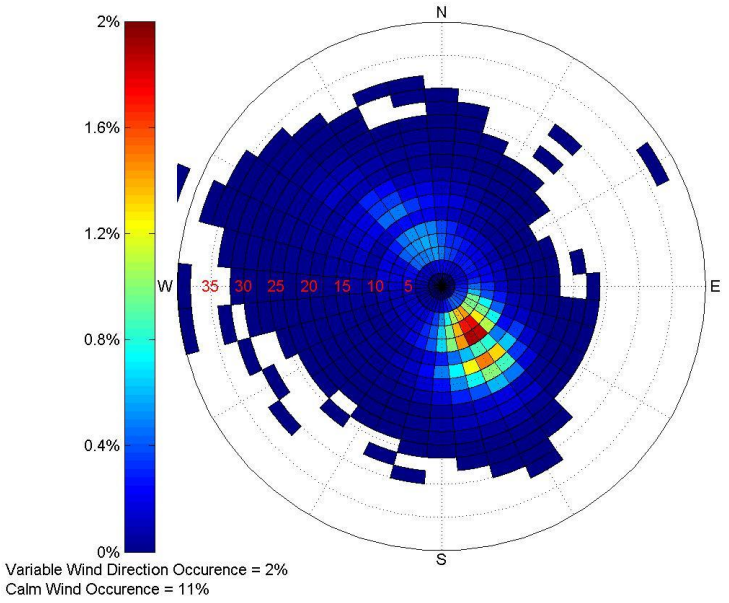

(b) Wind Density Graph

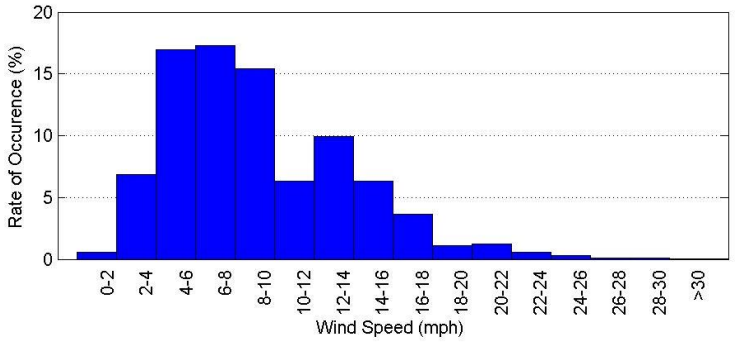

(c) Wind Speed Occurrence Rate

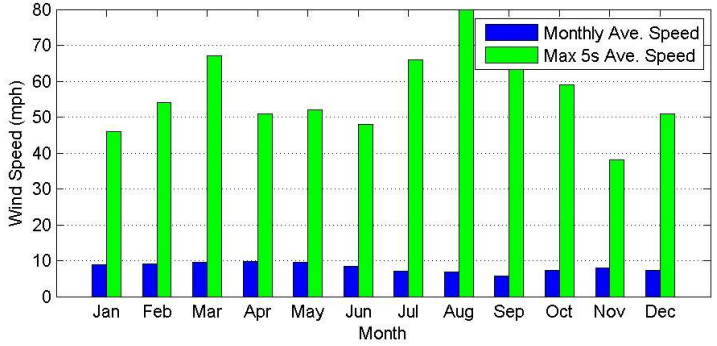

(d) Monthly Average Wind Speed

Figure 4.81: Wind Data Collected at the Hood AAF Airport (3933) from 2008 to 2015

KILLEEN MUNICIPAL AIRPORT (3972)

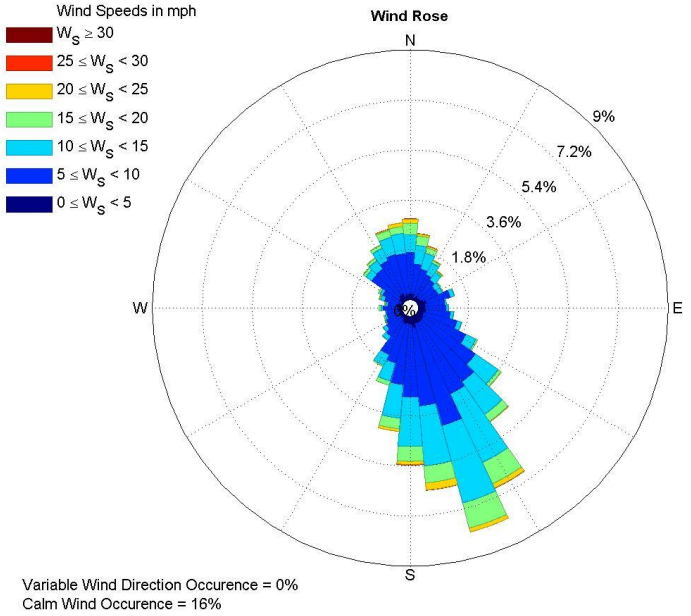

(a) Wind Rose Graph

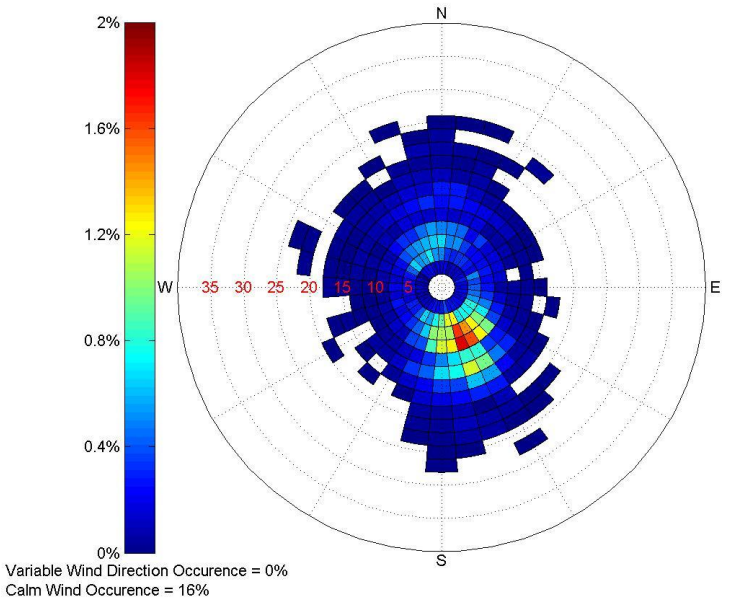

(b) Wind Density Graph

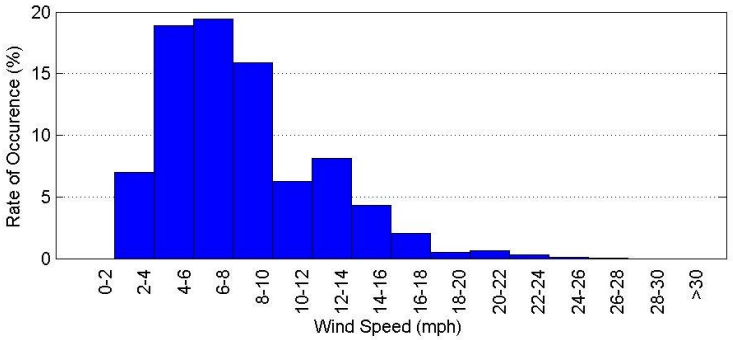

(c) Wind Speed Occurrence Rate

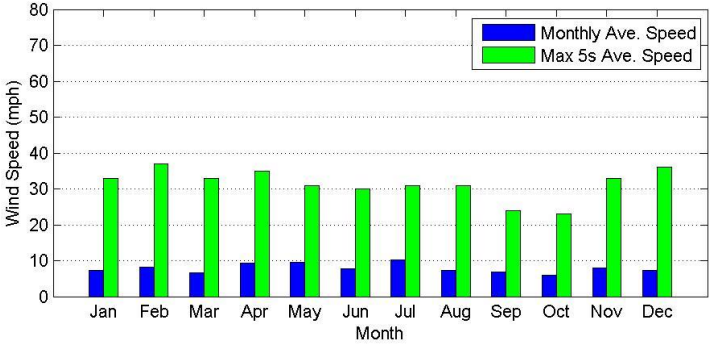

(d) Monthly Average Wind Speed

Figure 4.82: Wind Data Collected at the Killeen Municipal Airport (3972) in the Year 2015

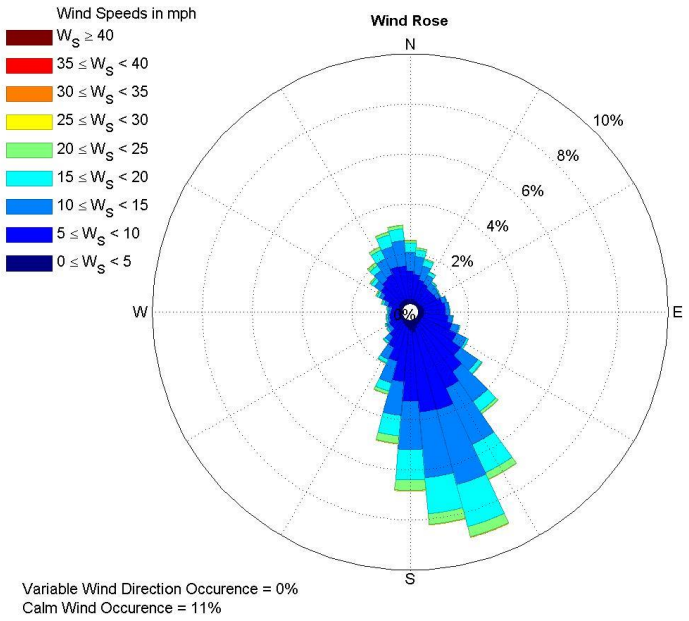

(a) Wind Rose Graph

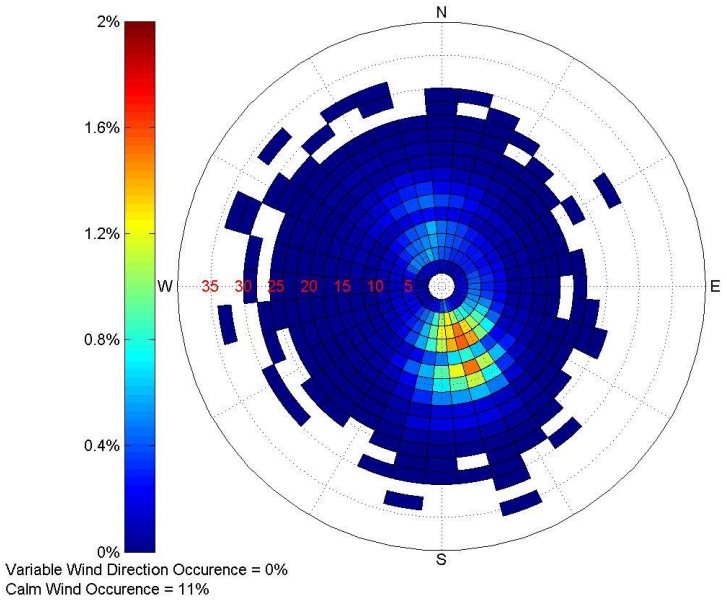

(b) Wind Density Graph

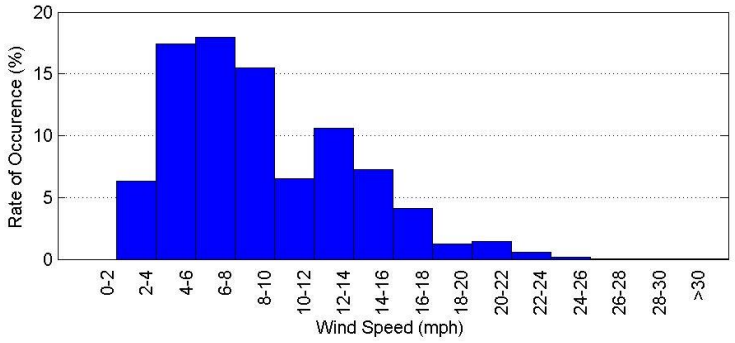

(c) Wind Speed Occurrence Rate

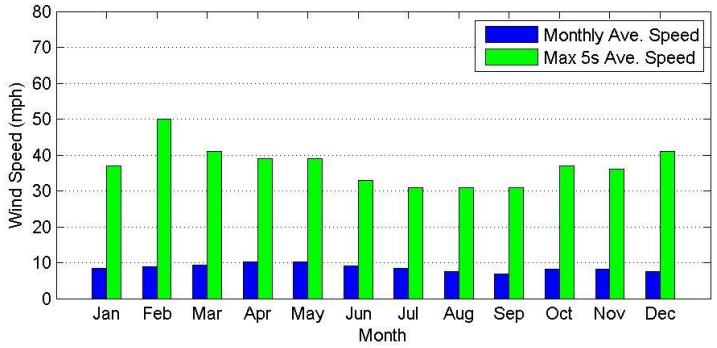

(d) Monthly Average Wind Speed

Figure 4.83: Wind Data Collected at the Killeen Municipal Airport (3972) from 2008 to 2015

STEPHENS COUNTY AIRPORT (176)

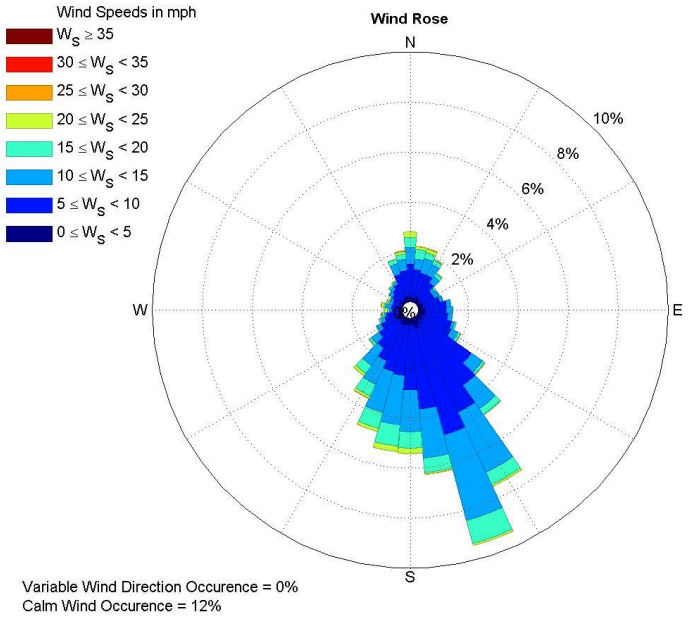

(a) Wind Rose Graph

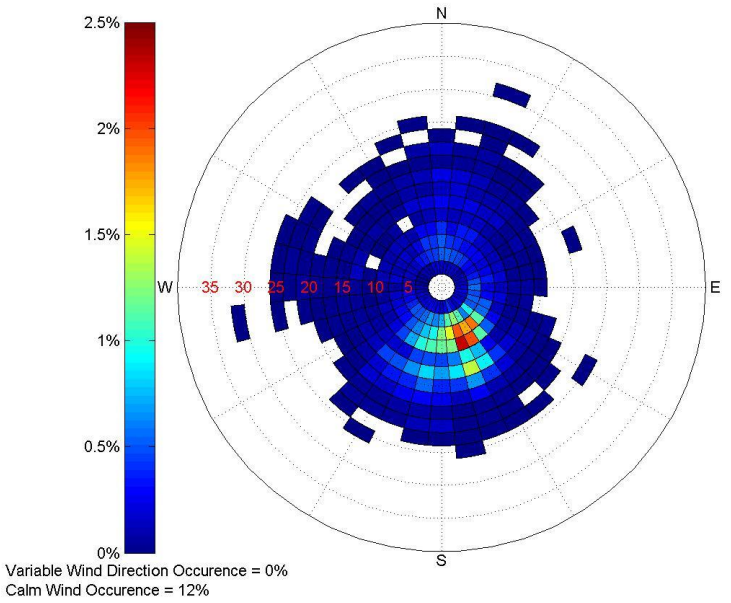

(b) Wind Density Graph

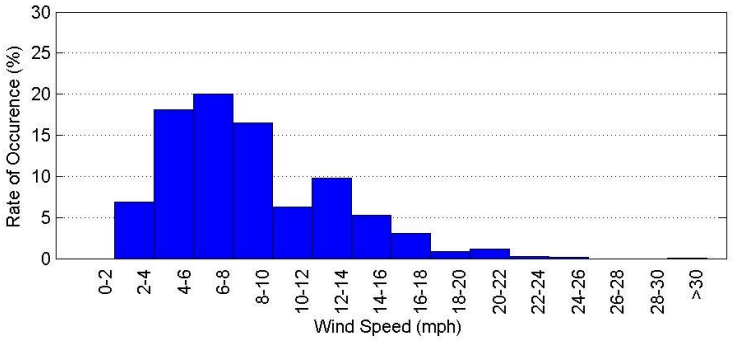

(c) Wind Speed Occurrence Rate

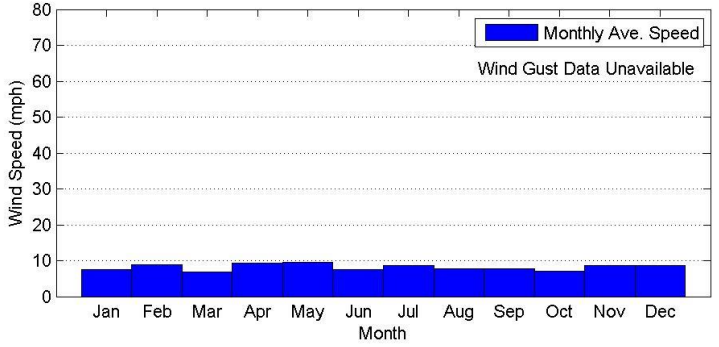

(d) Monthly Average Wind Speed

Figure 4.84: Wind Data Collected at the Stephens County Airport (176) in the Year 2015

KICKAPOO DOWNTOWN AIRPORT (134)

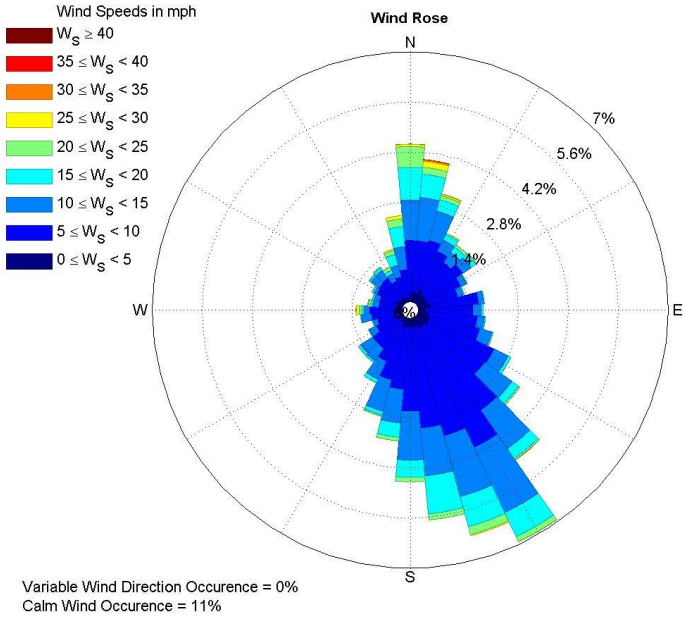

(a) Wind Rose Graph

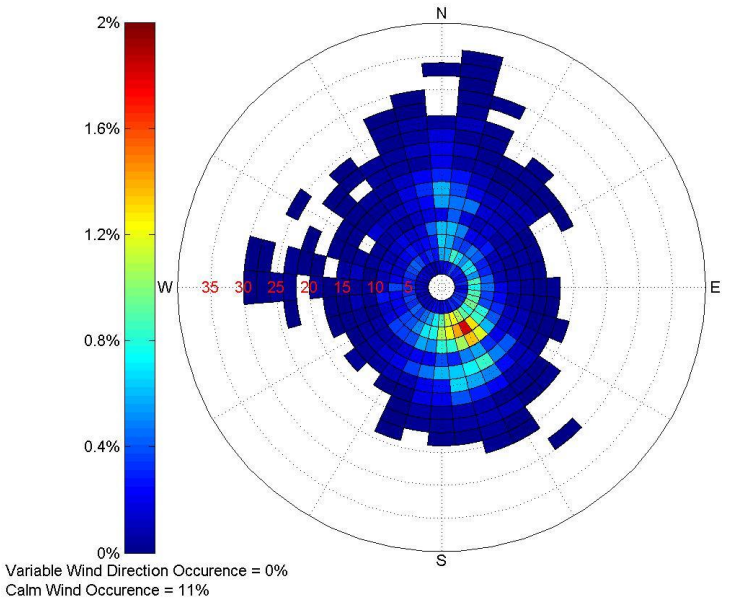

(b) Wind Density Graph

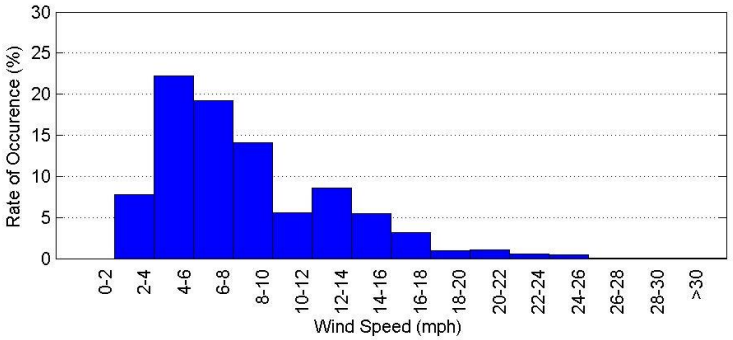

(c) Wind Speed Occurrence Rate

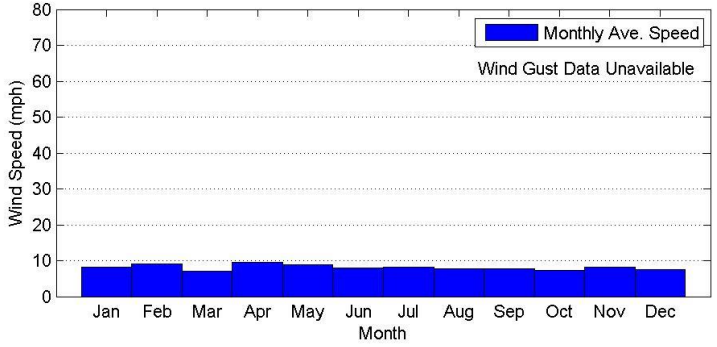

(d) Monthly Average Wind Speed

Figure 4.85: Wind Data Collected at the Kickapoo Downtown Airport (134) in the Year 2015

SHEPPARD AFB/WICHITA FALLS MUNI AP (13966)

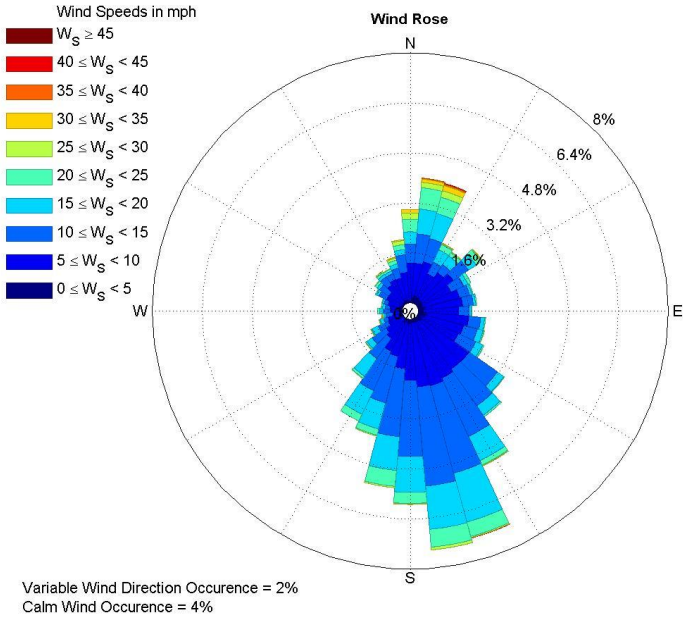

(a) Wind Rose Graph

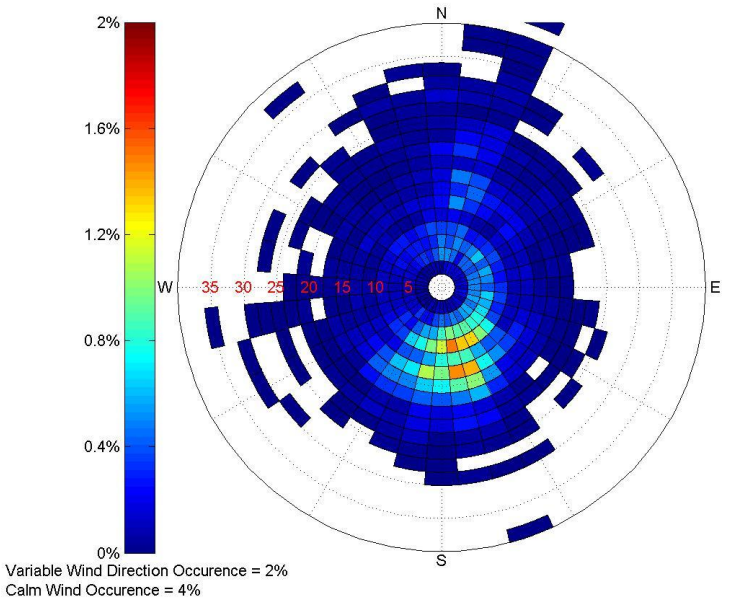

(b) Wind Density Graph

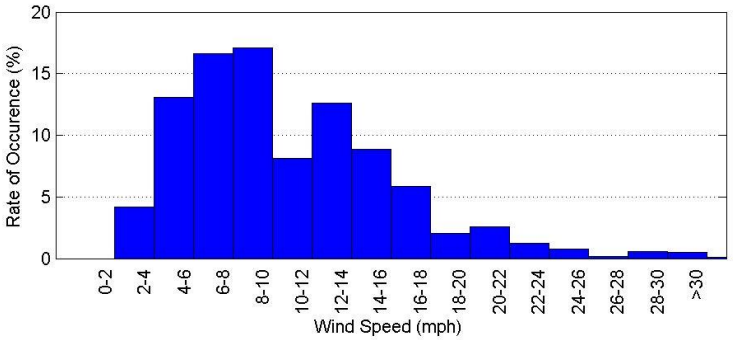

(c) Wind Speed Occurrence Rate

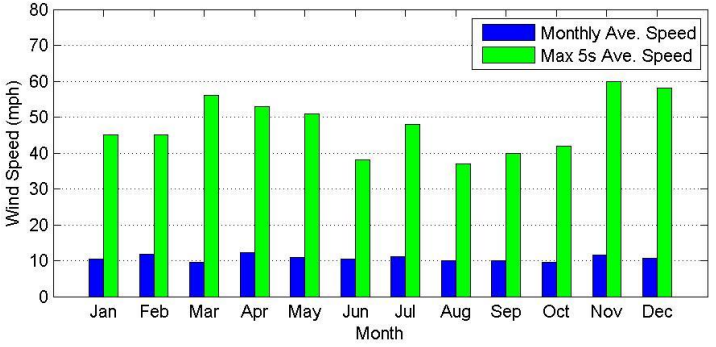

(d) Monthly Average Wind Speed

Figure 4.86: Wind Data Collected at the Sheppard AFB/Wichita Falls Municipal Airport (13966) in the Year 2015

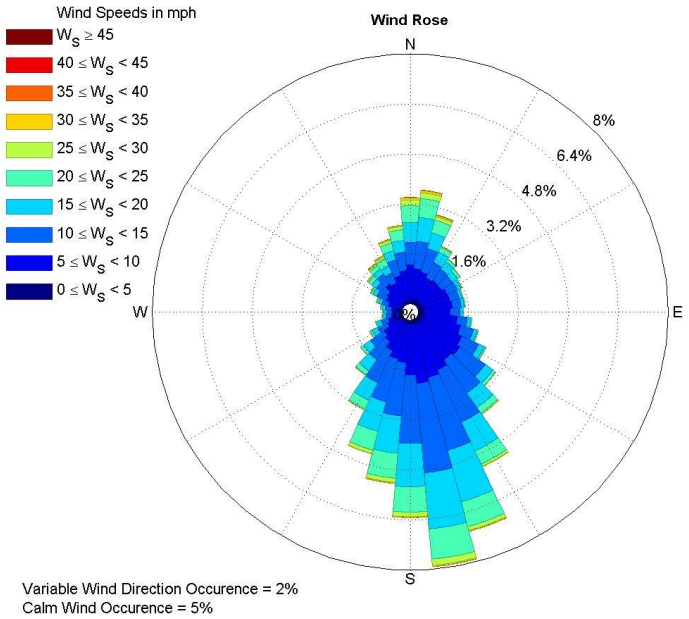

(a) Wind Rose Graph

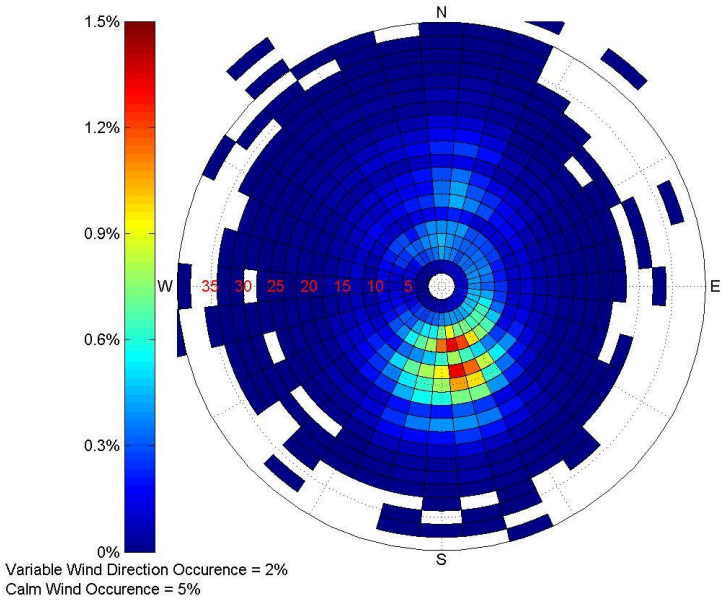

(b) Wind Density Graph

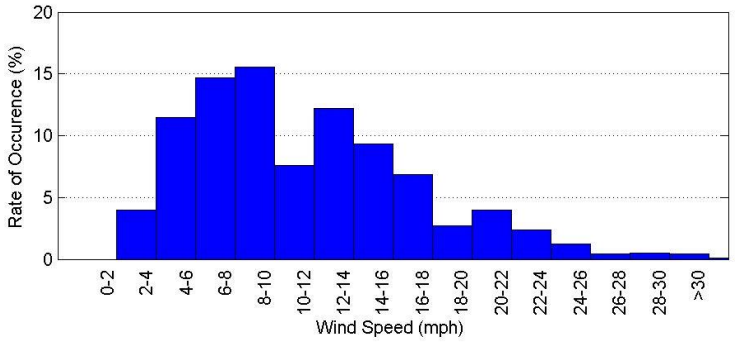

(c) Wind Speed Occurrence Rate

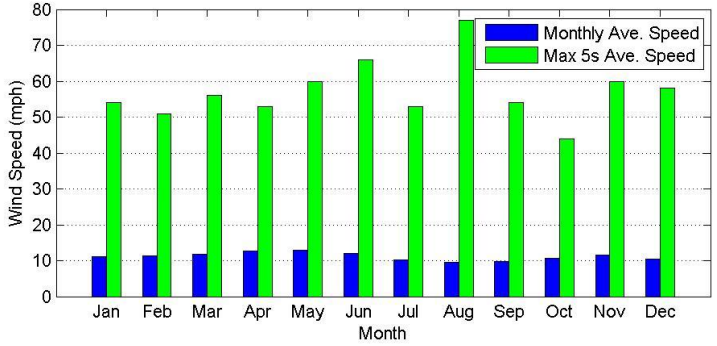

(d) Monthly Average Wind Speed

Figure 4.87: Wind Data Collected at the Sheppard AFB/Wichita Falls Municipal Airport (13966) from 2008 to 2015

GAINESVILLE MUNICIPAL ARPT (93929)

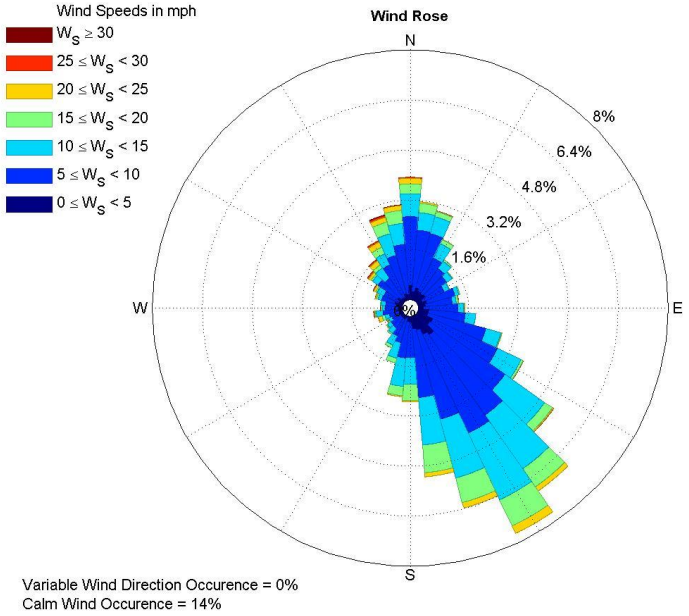

(a) Wind Rose Graph

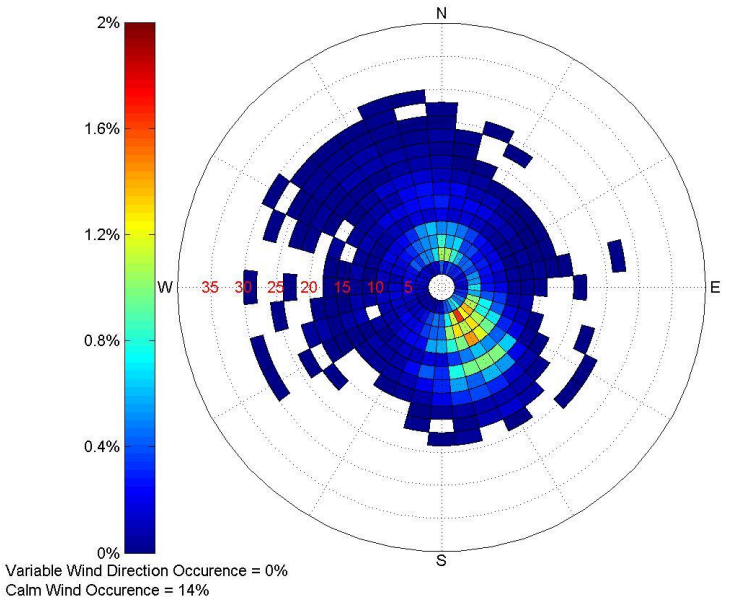

(b) Wind Density Graph

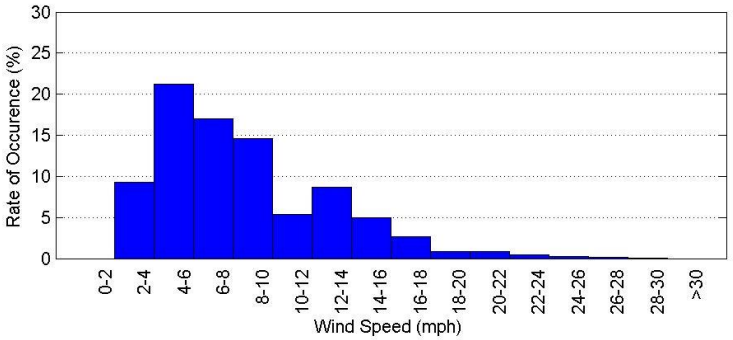

(c) Wind Speed Occurrence Rate

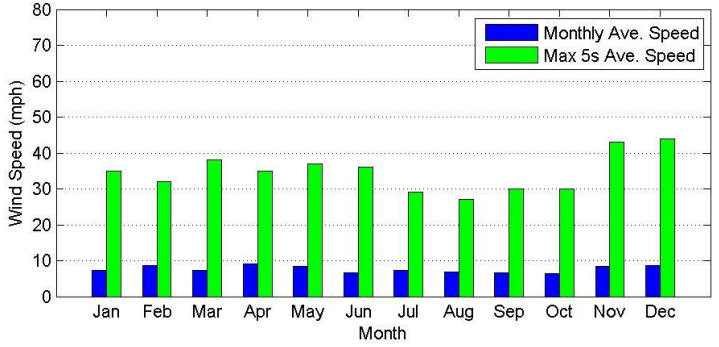

(d) Monthly Average Wind Speed

Figure 4.88: Wind Data Collected at the Gainesville Municipal Airport (93929) in the Year 2015

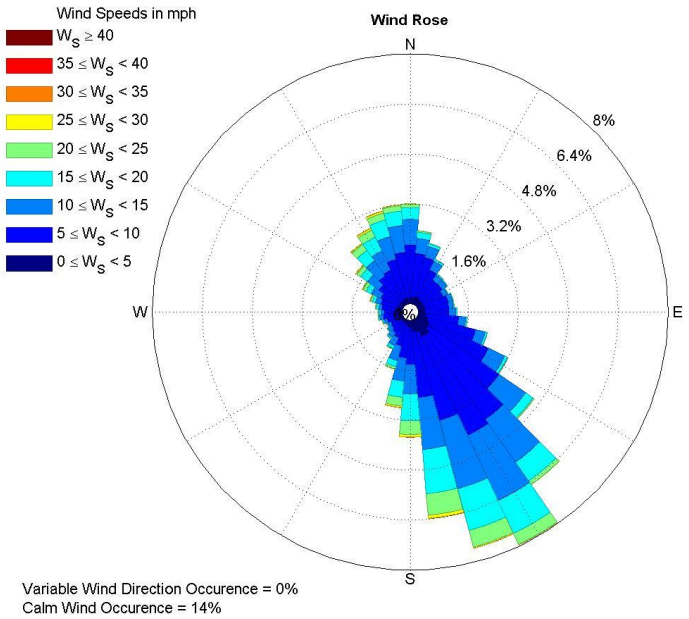

(a) Wind Rose Graph

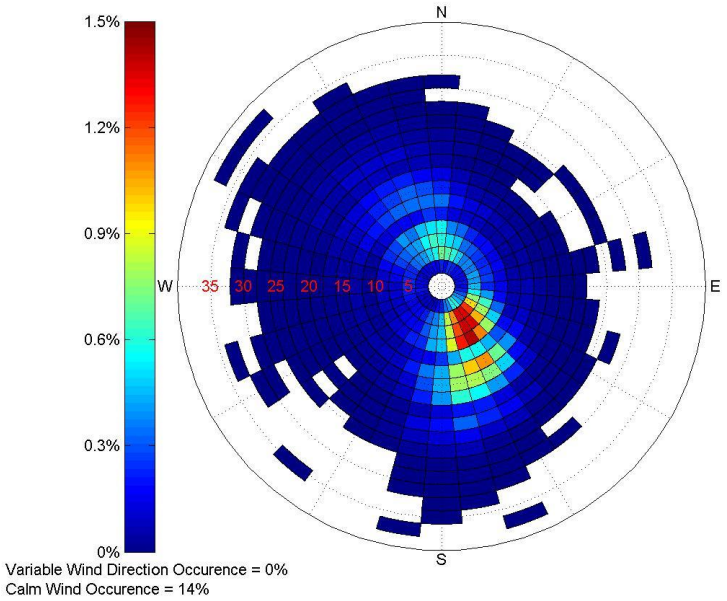

(b) Wind Density Graph

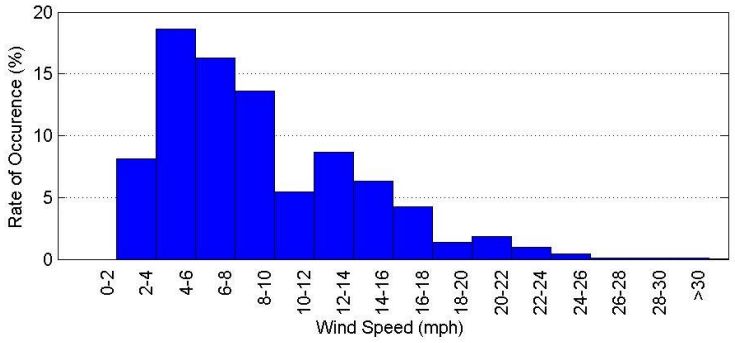

(c) Wind Speed Occurrence Rate

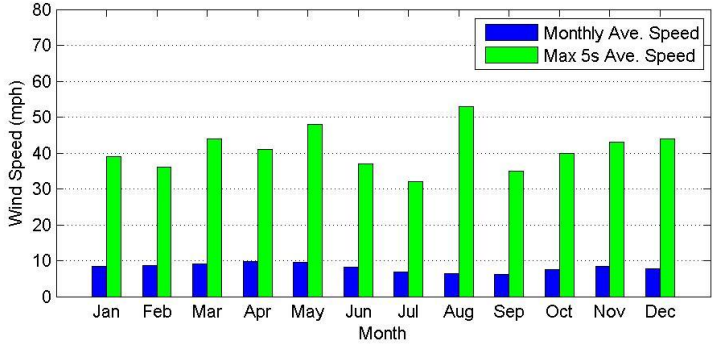

(d) Monthly Average Wind Speed

Figure 4.89: Wind Data Collected at the Gainesville Municipal Airport (93929) from 2008 to 2015

EASTERWOOD FIELD AIRPORT (3904)

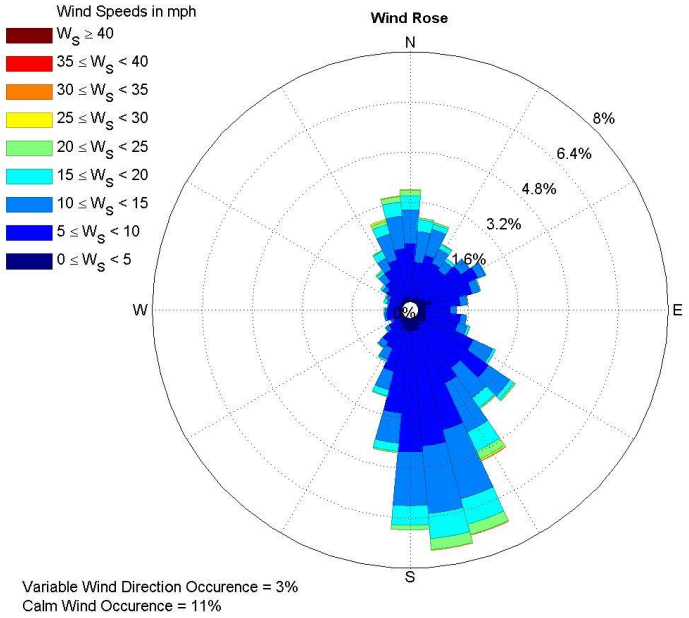

(a) Wind Rose Graph

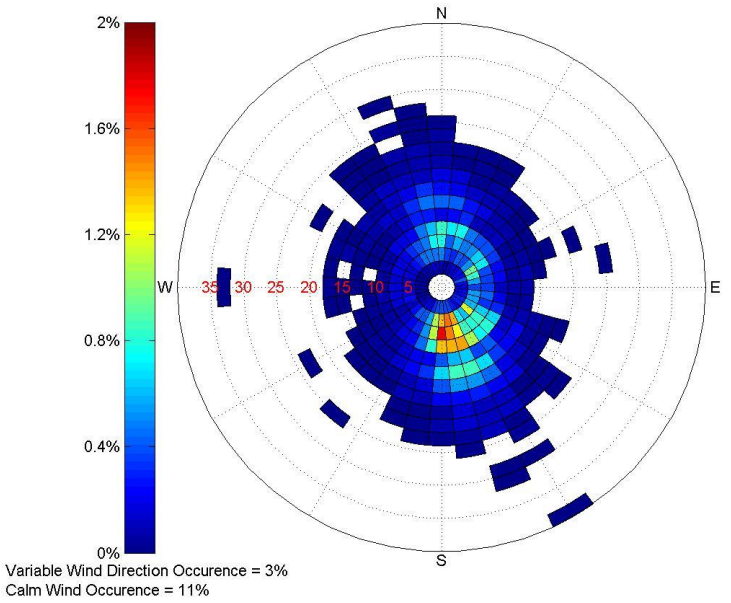

(b) Wind Density Graph

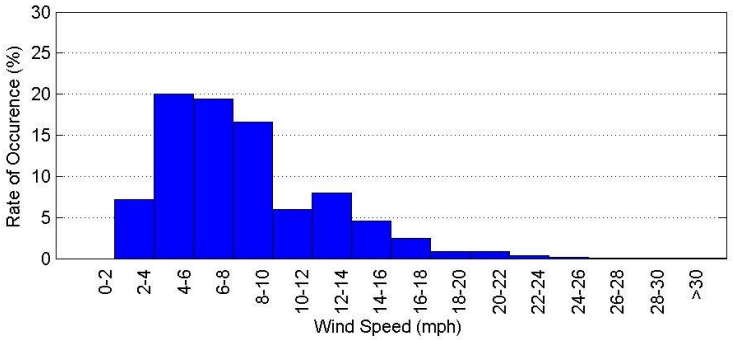

(c) Wind Speed Occurrence Rate

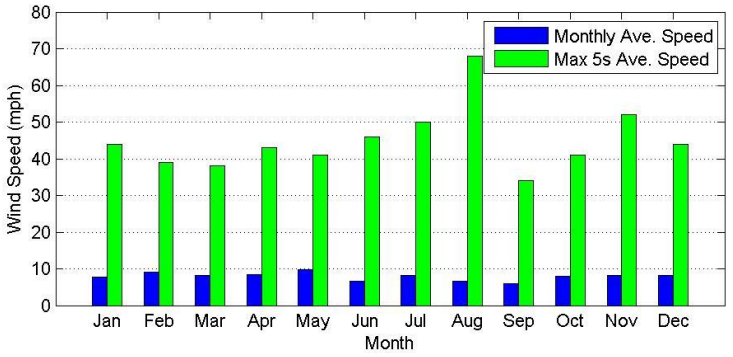

(d) Monthly Average Wind Speed

Figure 4.90: Wind Data Collected at the Easterwood Field Airport (3904) in the Year 2015

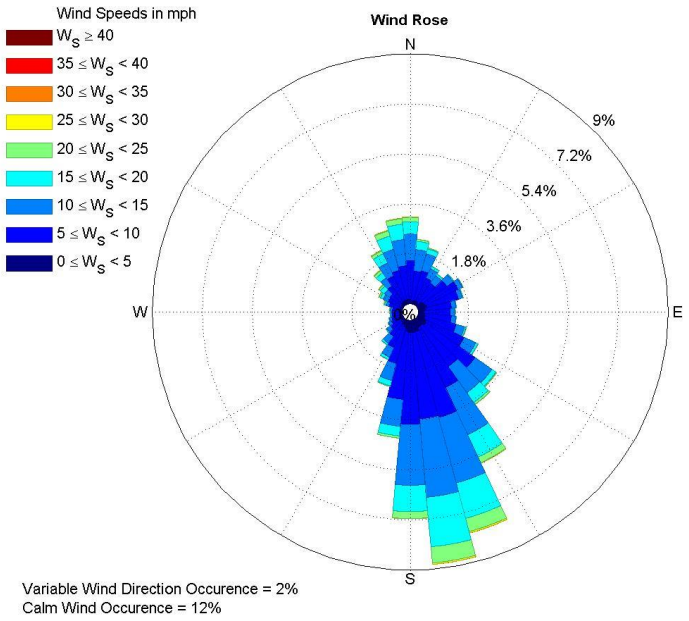

(a) Wind Rose Graph

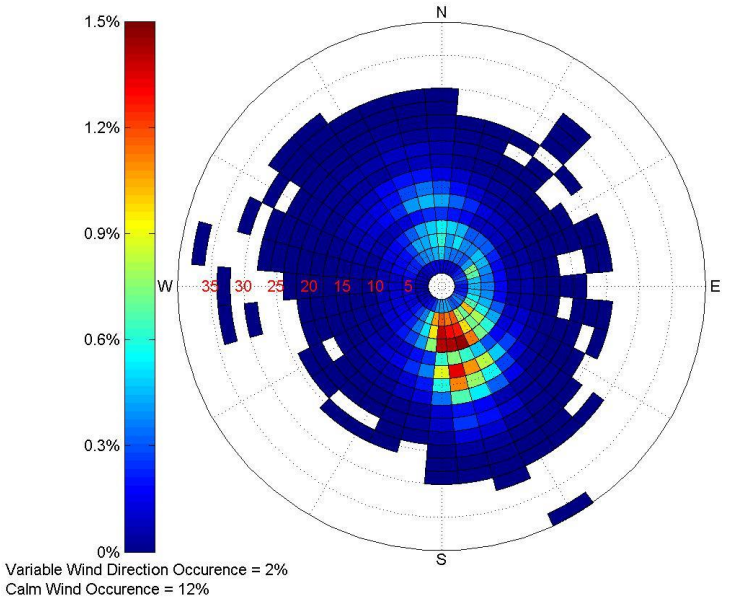

(b) Wind Density Graph

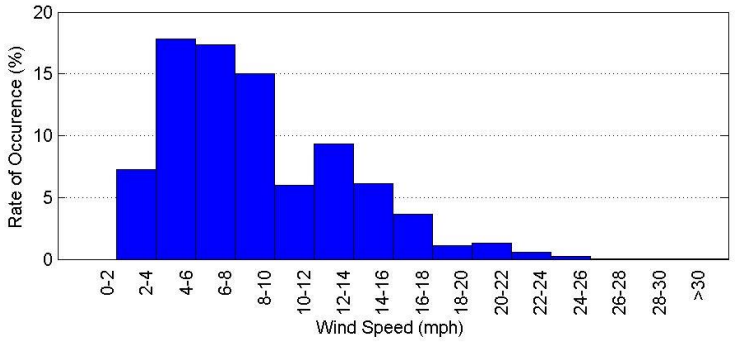

(c) Wind Speed Occurrence Rate

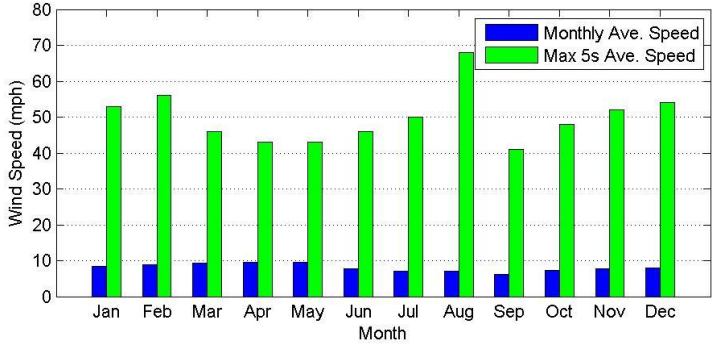

(d) Monthly Average Wind Speed

Figure 4.91: Wind Data Collected at the Easterwood Field Airport (3904) from 2008 to 2015

COULTER FIELD AIRPORT (438)

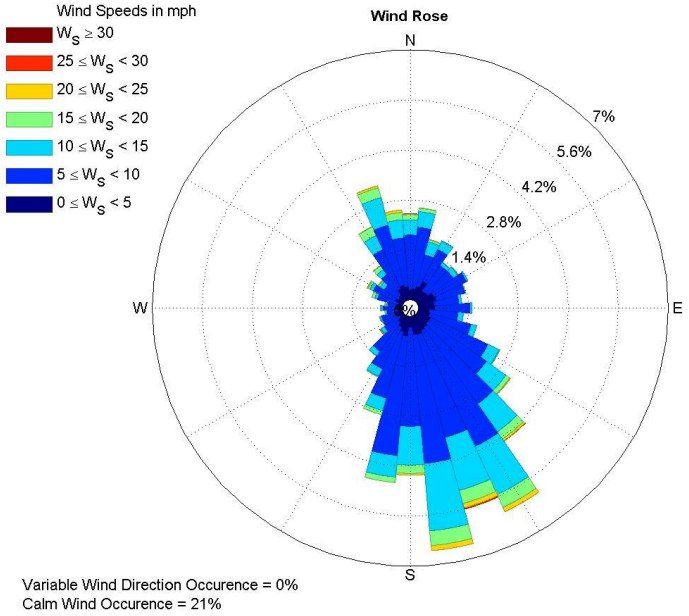

(a) Wind Rose Graph

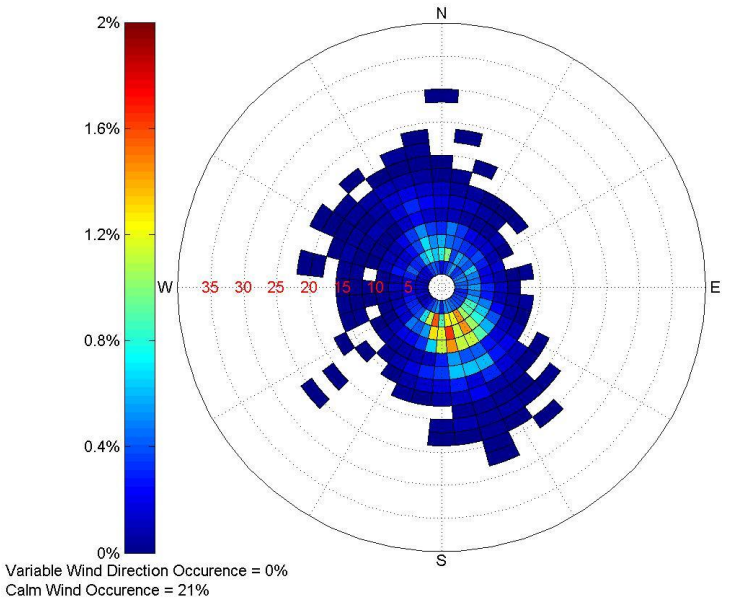

(b) Wind Density Graph

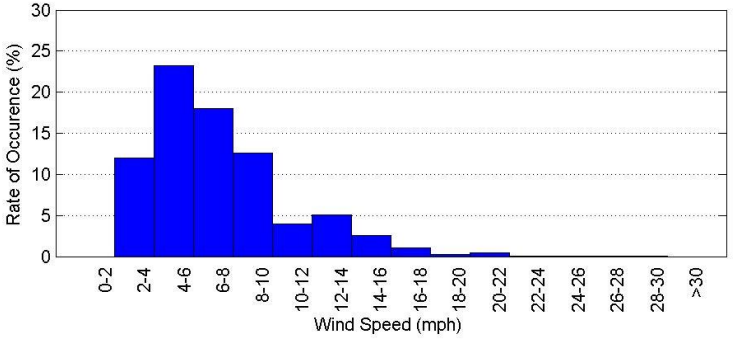

(c) Wind Speed Occurrence Rate

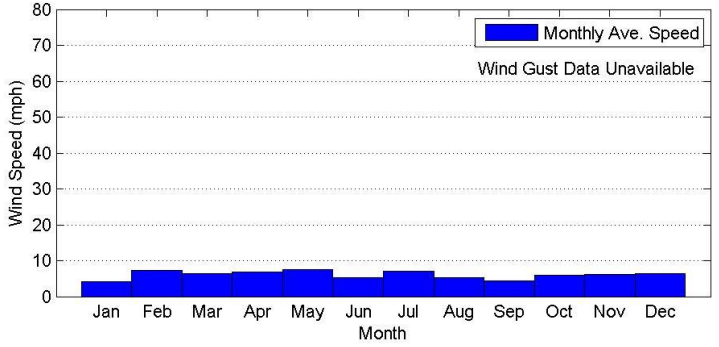

(d) Monthly Average Wind Speed

Figure 4.92: Wind Data Collected at the Coulter Field Airport (438) in the Year 2015

4.4 Historical Wind Data in Texas - Secondary Sites

4.4.1 Yearly Averaged Data

Yearly average wind speeds for secondary sites are listed in Table 4.8. Figure 4.93 further indicates if the wind speed at any location has any specific trend over the span of eight years from 2008 to 2015.

Table 4.8: Yearly Average Wind Speed for Secondary Sites

District	WBAN	2008	2009	2010	2011	2012	2013	2014	2015	Average
Houston	12923	10.89	10.97	11.12	11.87	10.54	11.06	11.59	10.76	11.10
	12918	7.64	7.71	7.40	8.10	7.02	7.55	7.54	7.05	7.50
	188	N/A	N/A	N/A	N/A	N/A	N/A	N/A	7.58	7.58
	12960	8.17	7.42	7.23	8.16	6.80	7.56	7.34	6.83	7.44
	12977	7.94	7.75	7.33	8.33	6.98	7.56	8.00	7.54	7.68
San Antonio	12909	8.28	8.35	8.16	8.97	7.45	8.02	8.39	7.67	8.16
Pharr	12959	10.32	10.81	10.02	11.16	10.26	10.30	10.13	9.63	10.33
Beaumont	12917	8.74	8.30	8.10	8.73	7.55	8.11	8.38	7.83	8.22
Lubbock	23042	11.84	11.33	11.37	11.89	11.66	11.72	12.18	11.17	11.65
Tyler	13972	8.67	7.88	7.61	8.57	7.64	7.72	8.15	7.80	8.00
Corpus Christi	12924	11.36	12.35	10.83	12.37	11.28	11.96	11.69	11.24	11.63
Lufkin	93987	6.22	5.59	5.44	6.25	5.22	5.37	5.79	5.50	5.67
Abilene	13962	11.32	10.50	10.35	11.00	10.50	10.46	11.23	10.25	10.70
Amarillo	23047	13.66	12.75	12.80	13.20	12.79	13.13	13.29	12.16	12.97
Dallas	13960	10.21	9.50	9.21	9.78	9.05	9.16	10.04	9.12	9.51

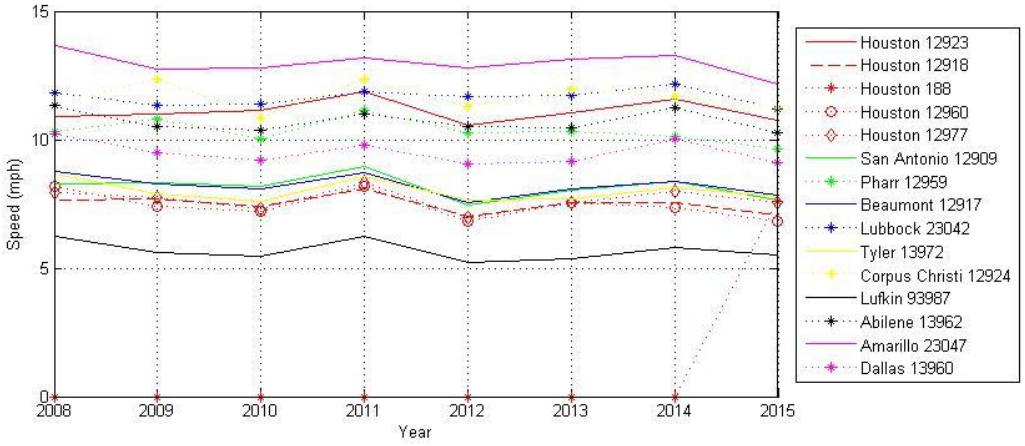

Figure 4.93: Yearly Average Wind Speed for Secondary Sites over the Span of 2008 to 2015

Average wind speeds for each month over the period of eight years from 2008 to 2015 are tabulated in Table 4.9. for the secondary sites. Seasonal variation can specifically be observed in Figure 4.94.

Table 4.9: Monthly Average Wind Speed from 2008 to 2015 for Secondary Sites

District	WBAN	Jan	Feb	Mar	Apr	May	Jun	Jul	Aug	Sep	Oct	Nov	Dec	Ave.
Houston	12923	11.37	11.82	11.57	12.65	12.70	11.31	9.87	9.23	9.93	10.29	11.35	11.12	11.10
	12918	8.43	9.01	8.66	9.08	8.25	6.65	5.80	5.57	6.07	6.68	7.57	8.37	7.51
	188	6.69	9.90	8.09	8.67	N/A	8.08	6.56	5.19	5.82	5.93	8.19	7.80	7.36
	12960	7.72	8.52	8.53	9.48	8.71	7.13	5.93	5.77	6.17	6.50	7.21	7.69	7.45
	12977	8.01	8.99	9.02	9.75	9.18	7.57	6.28	5.90	5.84	6.46	7.27	7.93	7.68
San Antonio	12909	7.21	8.42	9.11	9.61	9.73	9.51	8.47	7.73	6.92	7.46	6.98	6.88	8.17
Pharr	12959	8.88	10.48	11.51	12.28	12.57	11.80	11.91	10.19	7.61	8.85	8.94	8.92	10.33
Beaumont	12917	9.08	9.91	9.53	10.34	9.32	7.19	5.85	5.70	6.83	7.36	8.41	9.22	8.23
Lubbock	23042	11.32	12.21	13.11	14.52	13.22	13.42	10.41	9.56	9.37	10.62	11.22	10.88	11.65
Tyler	13972	8.29	9.11	9.40	9.88	8.83	7.89	7.04	6.65	6.04	7.12	7.83	8.05	8.01
Corpus Christi	12924	11.39	12.56	13.16	14.29	13.67	11.62	11.12	10.02	9.09	10.17	11.08	11.50	11.64
Lufkin	93987	5.71	6.63	6.86	7.36	6.51	5.30	4.63	4.66	4.34	4.99	5.44	5.71	5.68
Abilene	13962	10.14	11.17	12.17	13.37	12.05	12.21	9.63	8.74	8.59	9.82	10.57	10.07	10.71
Amarillo	23047	12.28	12.76	13.81	15.35	13.95	14.78	12.37	11.30	11.52	12.10	13.01	12.52	12.98
Dallas	13960	8.48	10.05	10.96	11.76	11.10	10.71	8.79	8.18	7.74	8.56	9.15	8.71	9.52

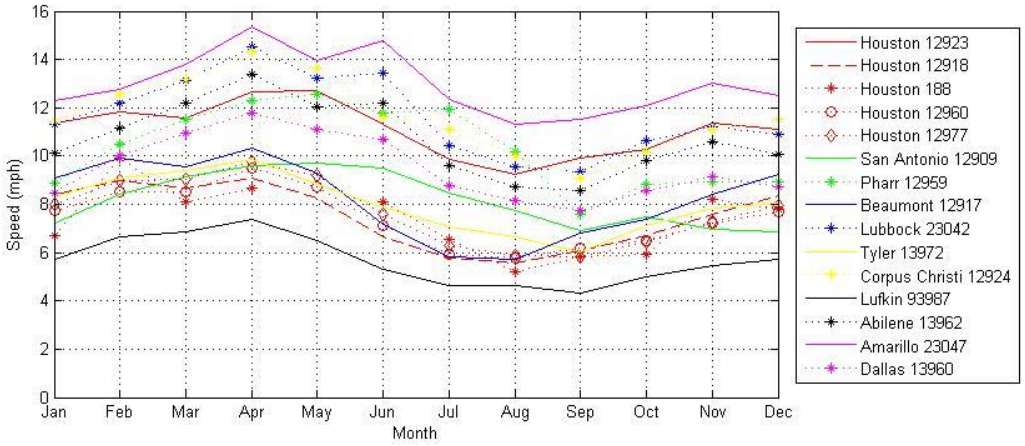

Figure 4.94: Monthly Average Wind Speed for Secondary Sites over the Span of 2008 to 2015

4.4.2 Site-Specific Wind Data from Secondary Sites

Historical data for the 15 secondary sites are presented with four graphs: wind rose graph, wind density graph, wind speed rate of occurrence, and monthly average wind speed and gust wind variation. Wind rose graph, wind density graph, and wind speed rate of occurrence all use the hourly wind data while monthly average wind speed uses the daily wind speed data. Each site is presented with a one-year short term data in 2015 and a long term data covering the span of eight

years at most. Data gap may occur in some of the sites. To illustrate this gap, the number of collection days in each year in percent are tabulated in Table 4.10.

4.5 Summary

This chapter has summarized historical wind data for locations representative of major wind environments in Texas. Information presented includes daily and monthly average wind speeds and maximum gusts, for various average periods. Wind data were presented in a variety of formats, including wind rose and wind density graphs. This data will be used as part of the reliability based evaluation of the fatigue behavior of HMIPs with pre-existing cracks, presented in Chapter 9 of this report.

Table 4.10: Number of Data Collection Days at Secondary Sites (in Percent)

District	WBAN	2008	2009	2010	2011	2012	2013	2014	2015
Houston	12923	98	99	100	100	100	100	100	100
	12918	100	100	100	100	100	100	100	100
	188	0	0	0	0	0	0	44	85
	12960	100	100	100	100	100	100	100	100
	12977	100	100	100	100	100	100	100	100
San Antonio	12909	97	99	100	100	100	100	100	100
Pharr	12959	100	100	100	100	100	100	100	100
Beaumont	12917	100	100	100	100	100	100	100	100
Lubbock	23042	100	100	100	100	100	100	100	100
Tyler	13972	100	100	100	100	100	100	100	100
Corpus Christi	12924	100	100	100	100	100	100	100	100
Lufkin	93987	100	100	100	100	100	100	100	100
Abilene	13962	100	100	100	100	100	100	100	100
Amarillo	23047	100	100	100	100	100	100	100	100
Dallas	13960	100	100	100	100	100	100	100	100

%

SCHOLES INTL AT GLSTON APT (12923)

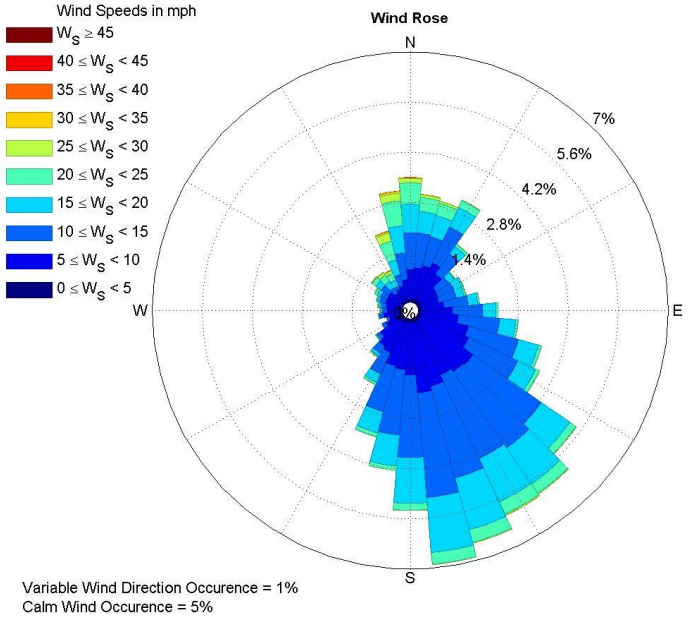

(a) Wind Rose Graph

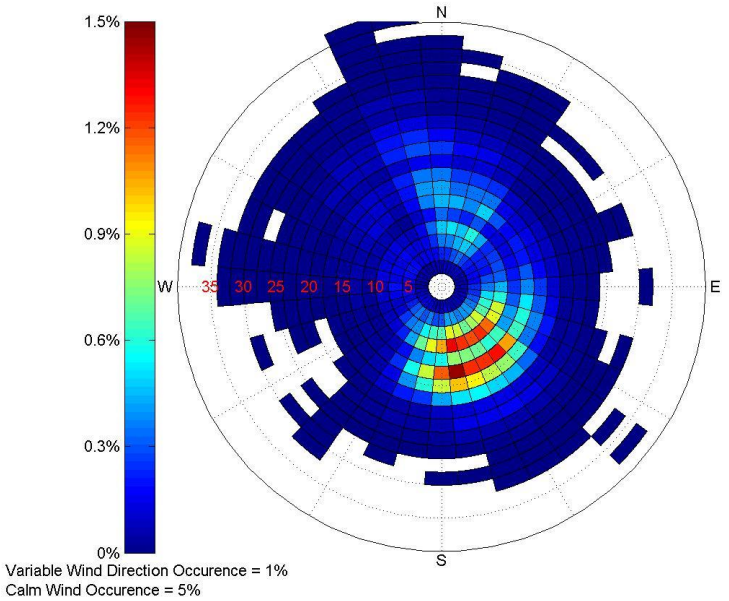

(b) Wind Density Graph

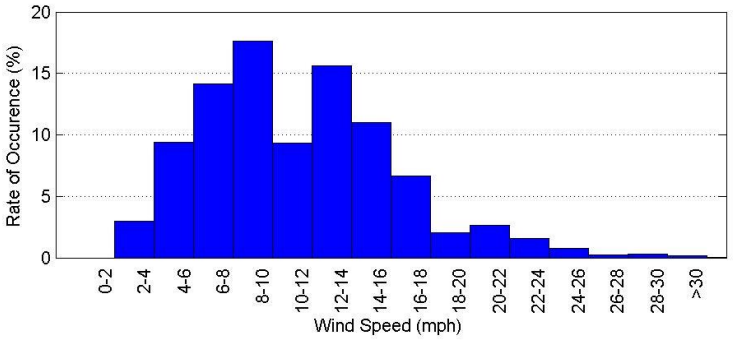

(c) Wind Speed Occurrence Rate

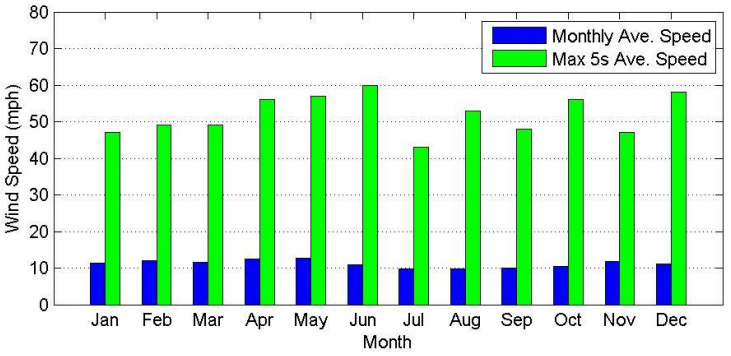

(d) Monthly Average Wind Speed

Figure 4.95: Wind Data Collected at the Scholes International Airport at Galveston (12923) from 2008 to 2015

WILLIAM P. HOBBY AIRPORT (12918)

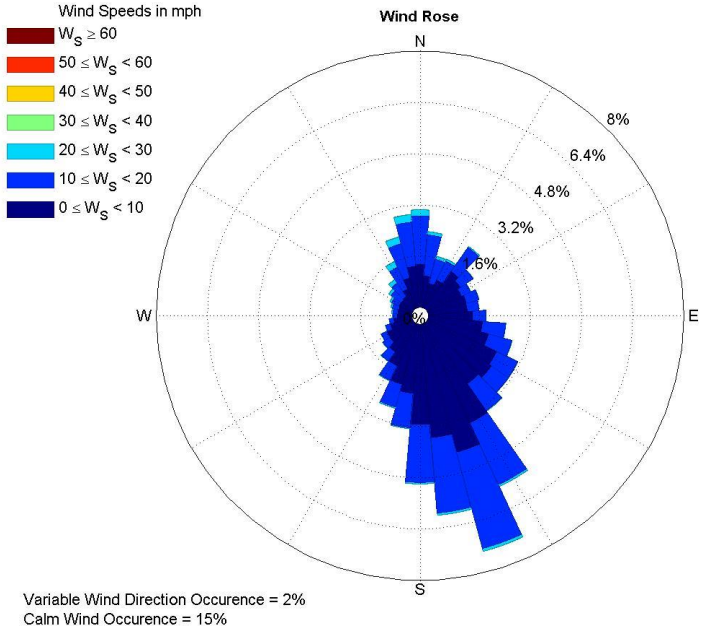

(a) Wind Rose Graph

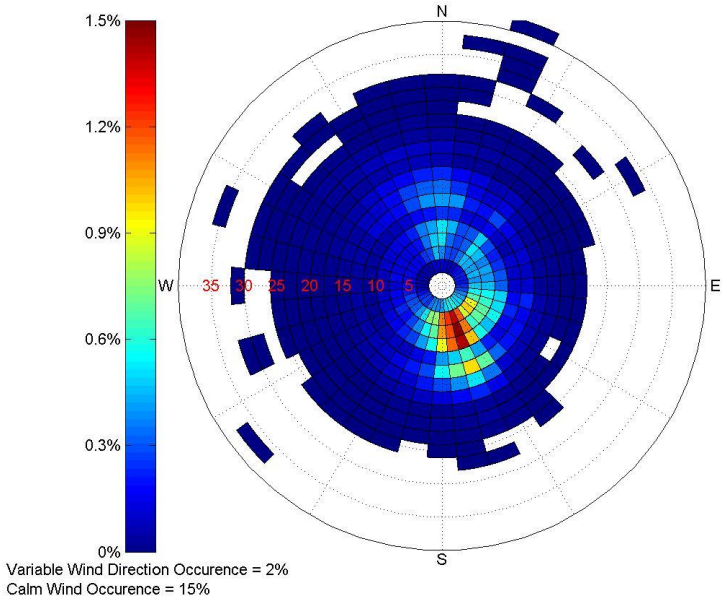

(b) Wind Density Graph

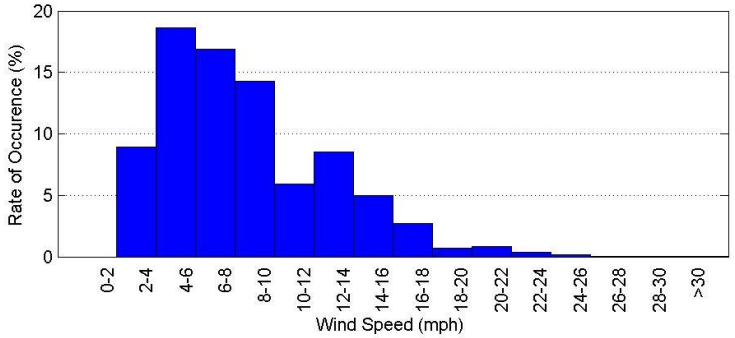

(c) Wind Speed Occurrence Rate

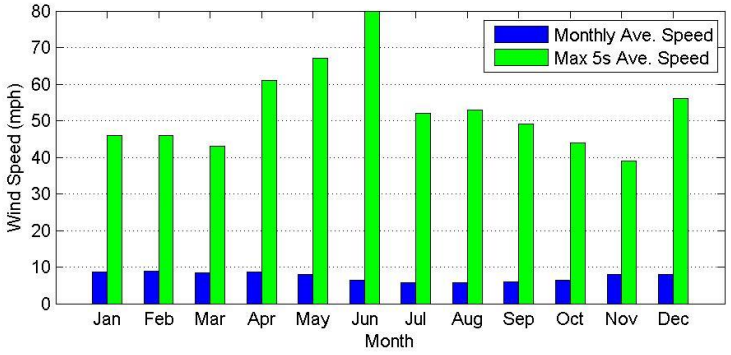

(d) Monthly Average Wind Speed

Figure 4.96: Wind Data Collected at the William P. Hobby Airport (12918) from 2008 to 2015

HOUSTON DUNN HELISTOP (188)

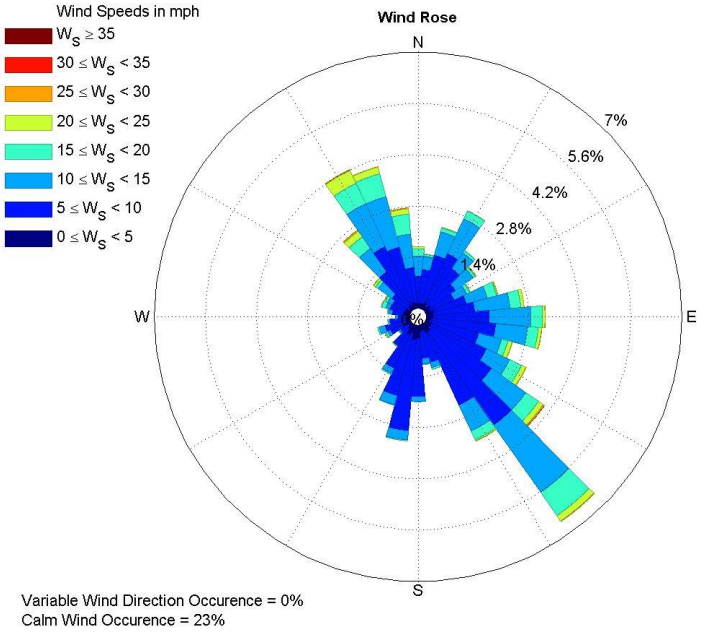

(a) Wind Rose Graph

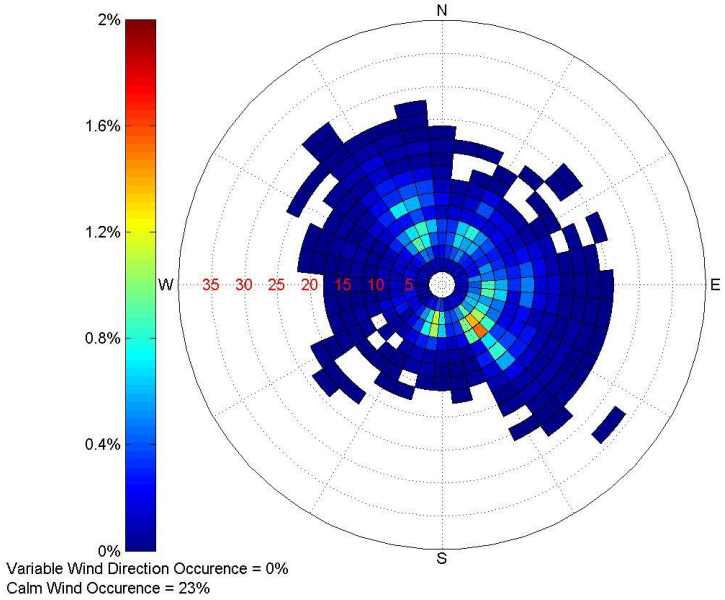

(b) Wind Density Graph

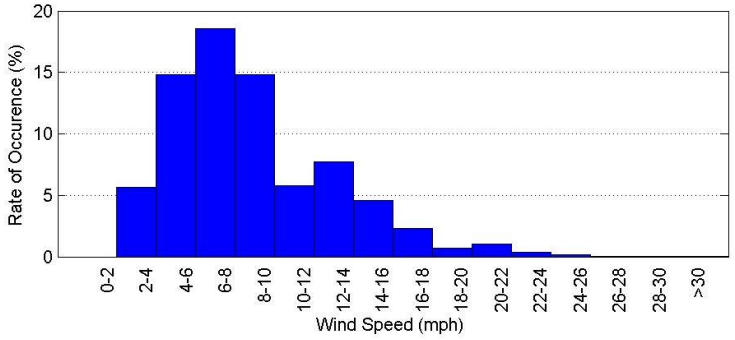

(c) Wind Speed Occurrence Rate

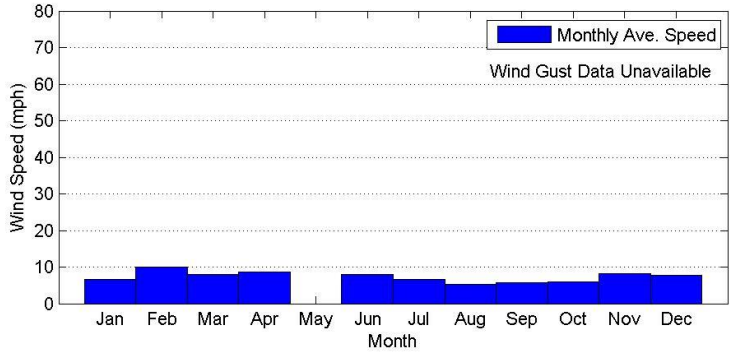

(d) Monthly Average Wind Speed

Figure 4.97: Wind Data Collected at the Houston Dunn Helistop (188) from 2008 to 2015

G BUSH INTERCONTINENTAL AP/HOUSTON AP (12960)

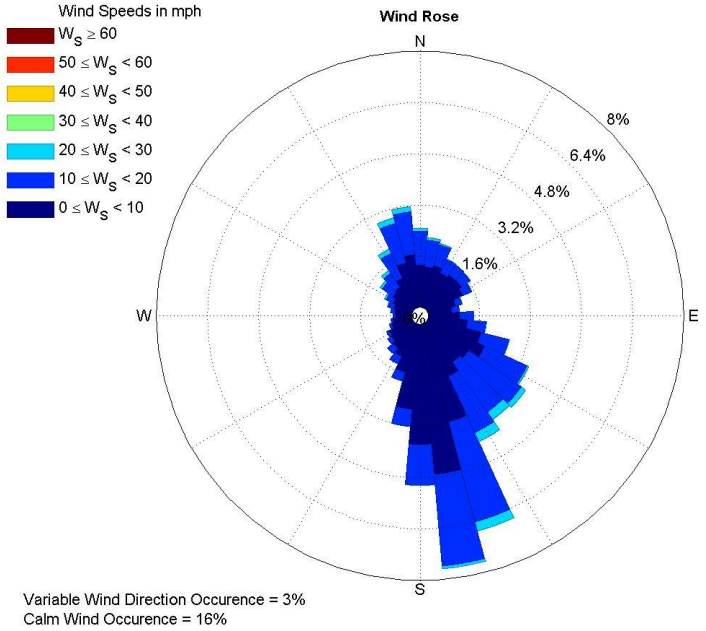

(a) Wind Rose Graph

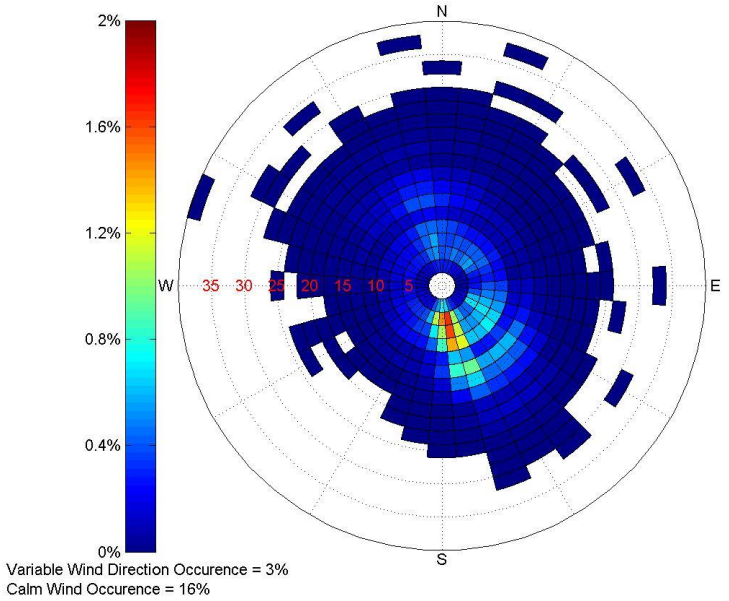

(b) Wind Density Graph

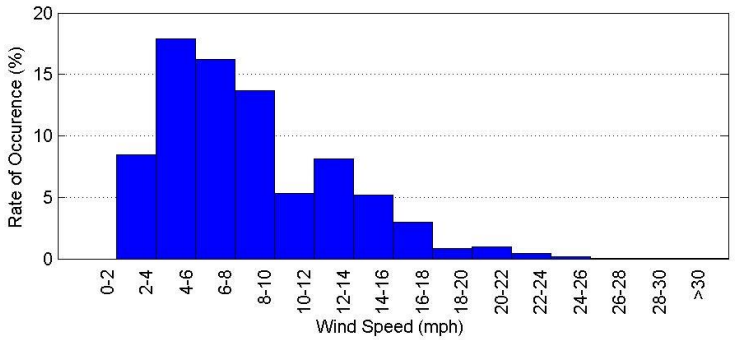

(c) Wind Speed Occurrence Rate

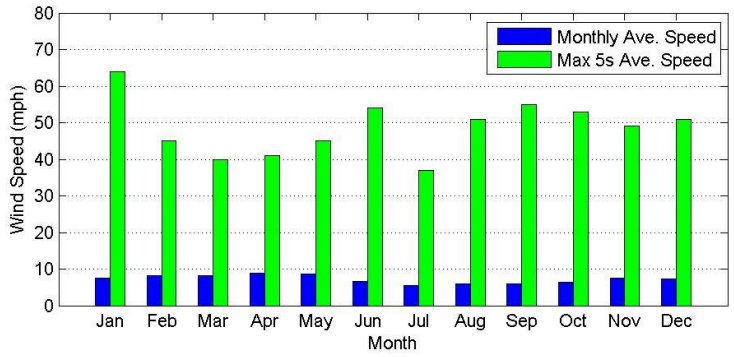

(d) Monthly Average Wind Speed

Figure 4.98: Wind Data Collected at the George Bush Inter-Continental Airport (12960) from 2008 to 2015

SUGAR LAND REGIONAL ARPT (12977)

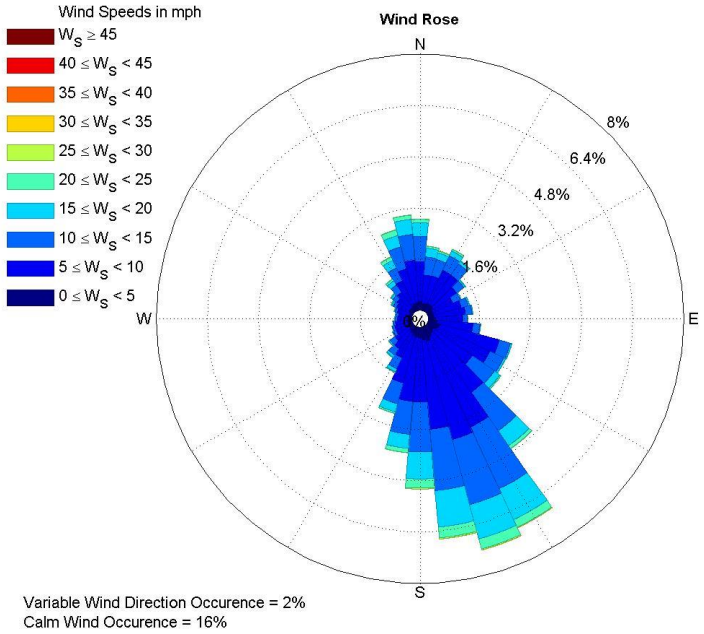

(a) Wind Rose Graph

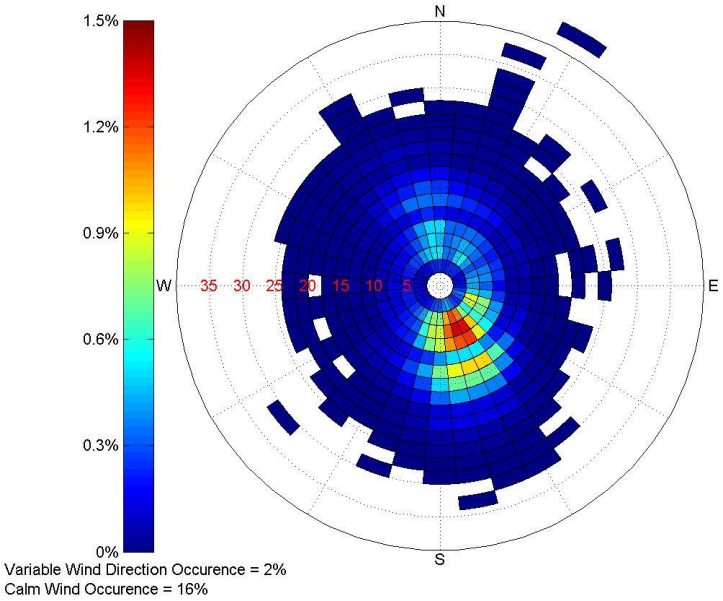

(b) Wind Density Graph

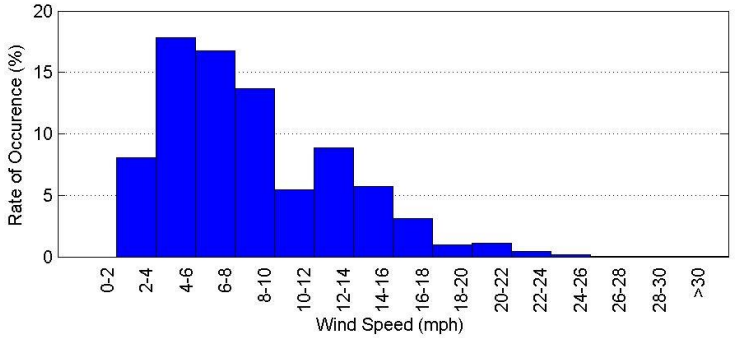

(c) Wind Speed Occurrence Rate

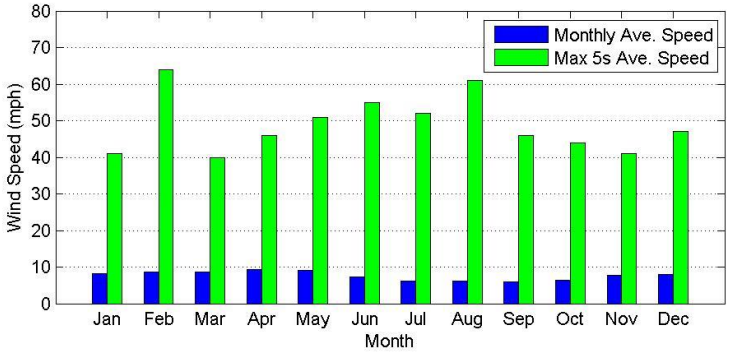

(d) Monthly Average Wind Speed

Figure 4.99: Wind Data Collected at the Sugar Land Regional Airport (12977) from 2008 to 2015

LACKLAND AIR FORCE BASE (KELLY FIELD ANNEX) (12909)

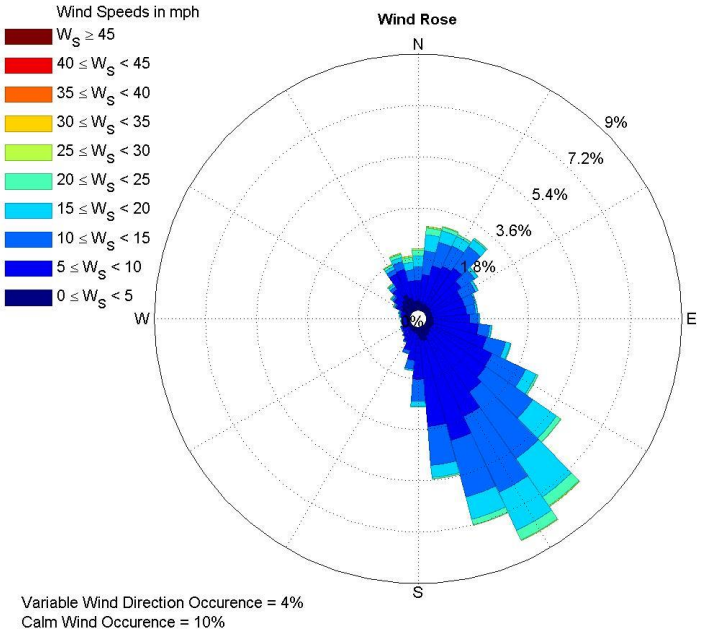

(a) Wind Rose Graph

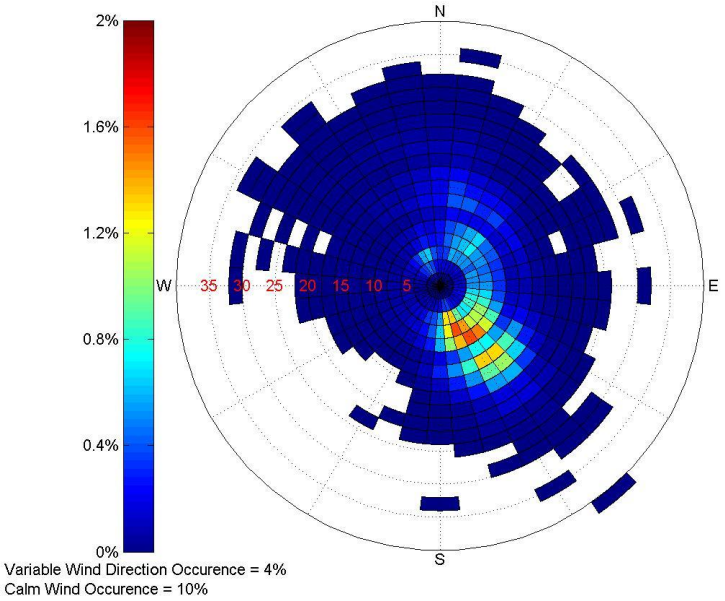

(b) Wind Density Graph

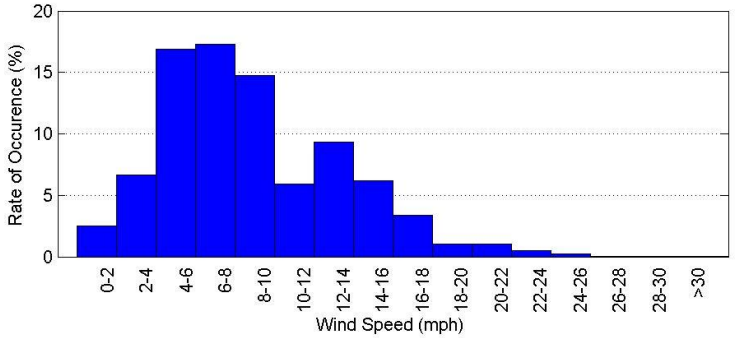

(c) Wind Speed Occurrence Rate

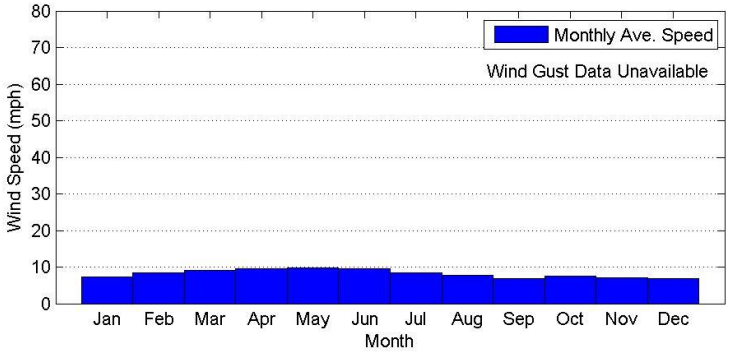

(d) Monthly Average Wind Speed

Figure 4.100: Wind Data Collected at the Lackland Air Force Base (12909) from 2008 to 2015

MC ALLEN MILLER INTL ARPT (12959)

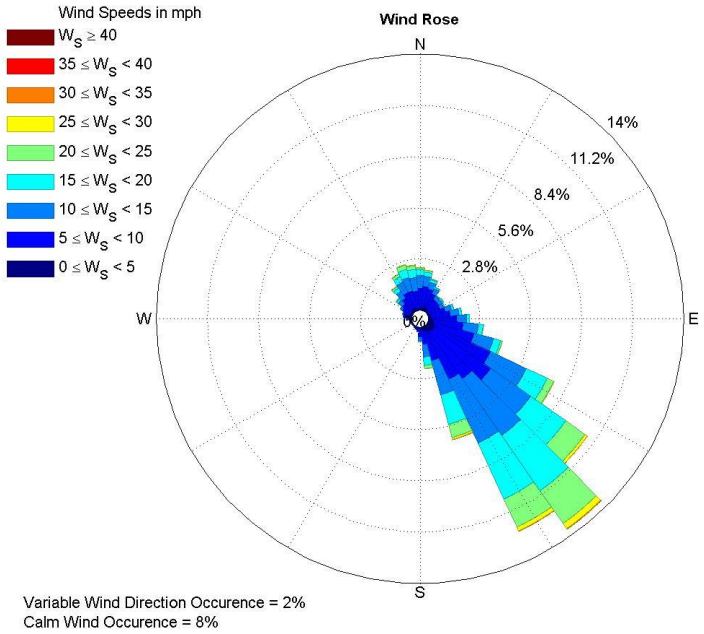

(a) Wind Rose Graph

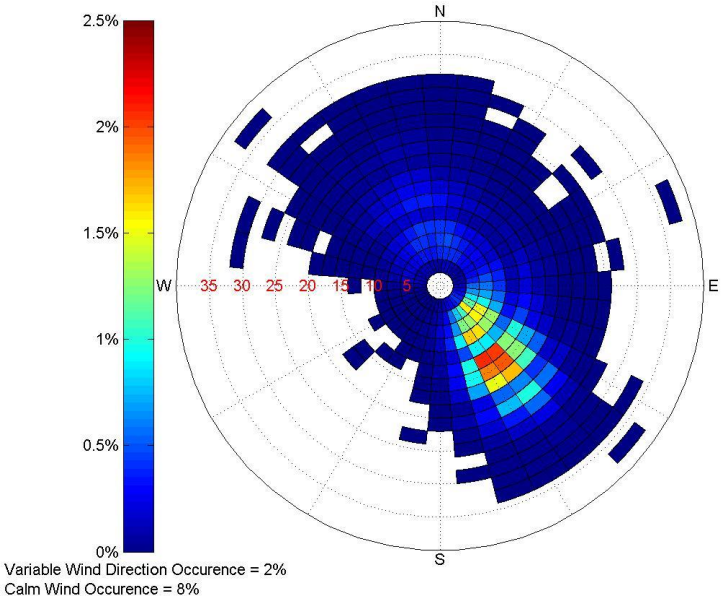

(b) Wind Density Graph

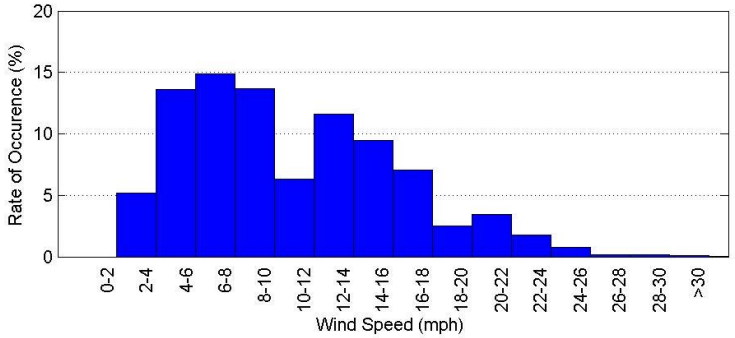

(c) Wind Speed Occurrence Rate

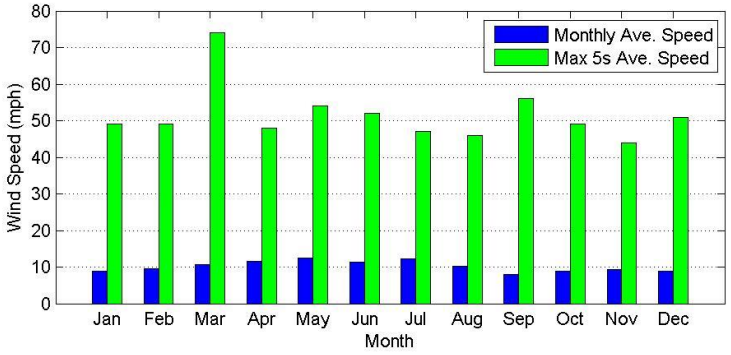

(d) Monthly Average Wind Speed

Figure 4.101: Wind Data Collected at the McAllen Miller International Airport (12959) from 2008 to 2015

SOUTHEAST TEXAS REGIONAL AIRPORT (12917)

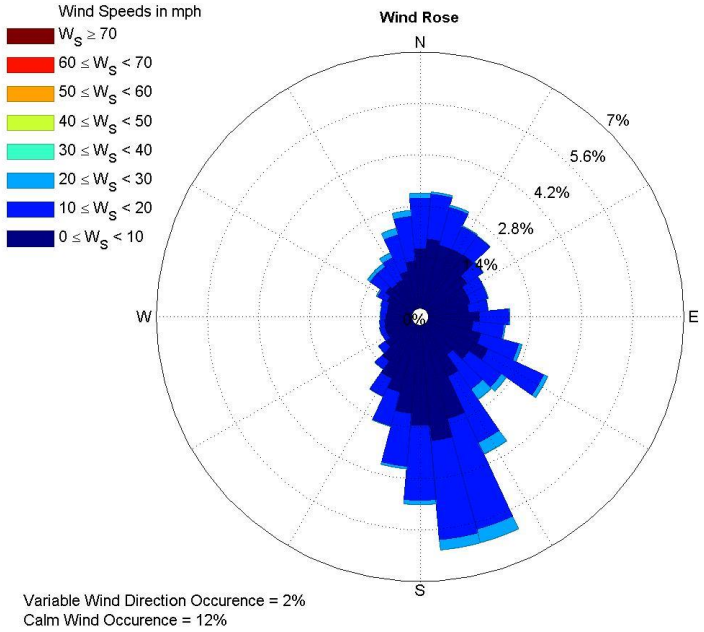

(a) Wind Rose Graph

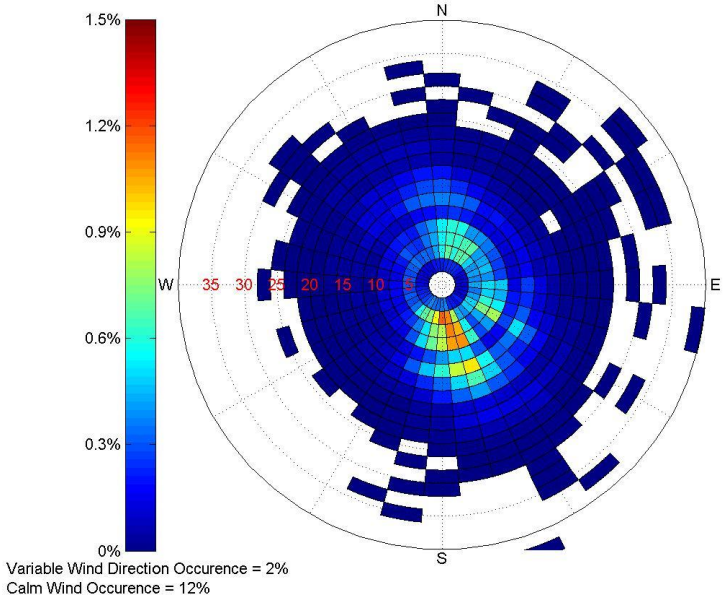

(b) Wind Density Graph

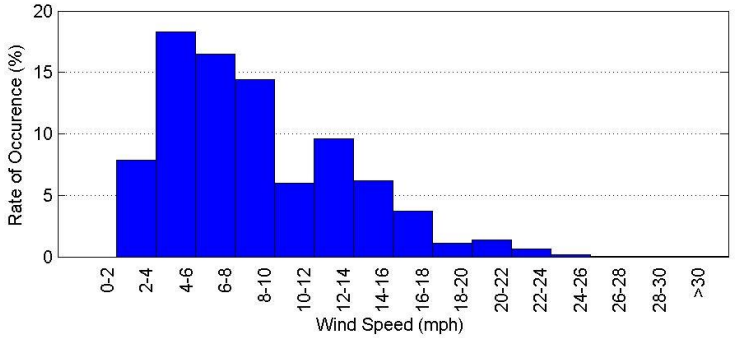

(c) Wind Speed Occurrence Rate

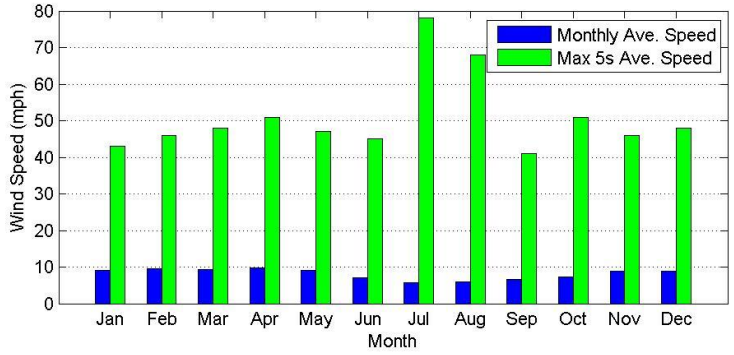

(d) Monthly Average Wind Speed

Figure 4.102: Wind Data Collected at the Southeast Texas Regional Airport (12917) from 2008 to 2015

LUBBOCK INTERNATIONAL AIRPORT (23042)

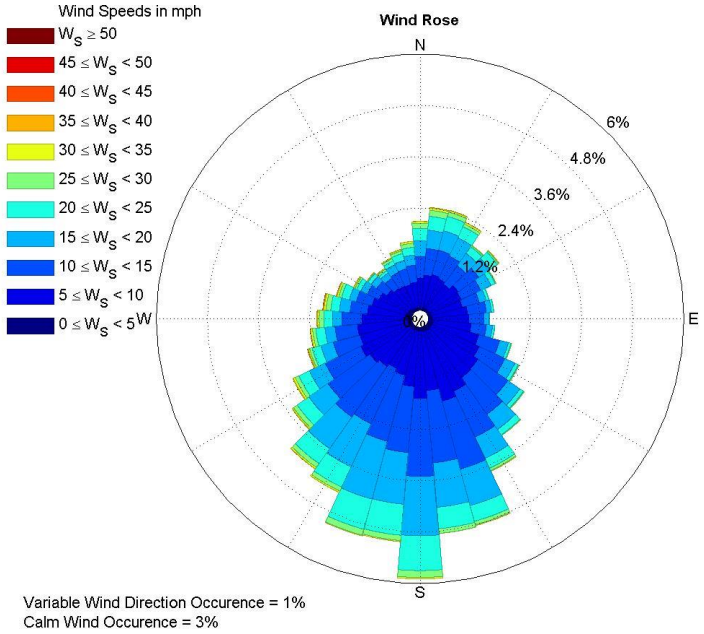

(a) Wind Rose Graph

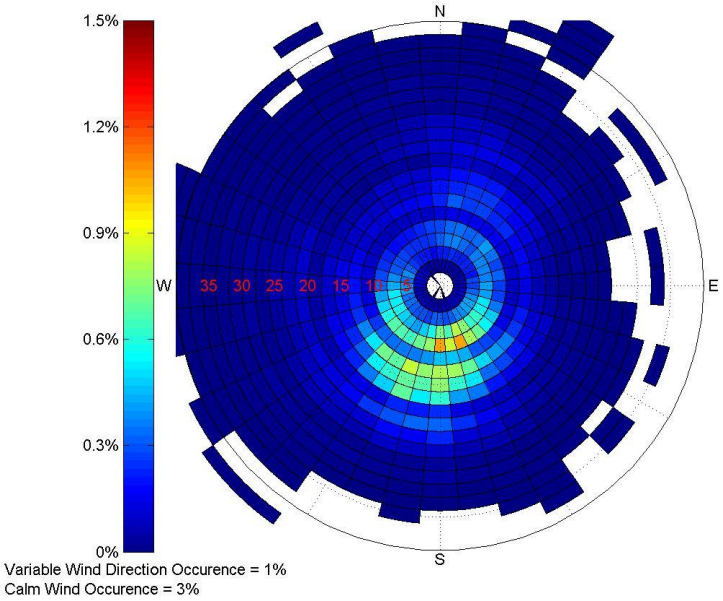

(b) Wind Density Graph

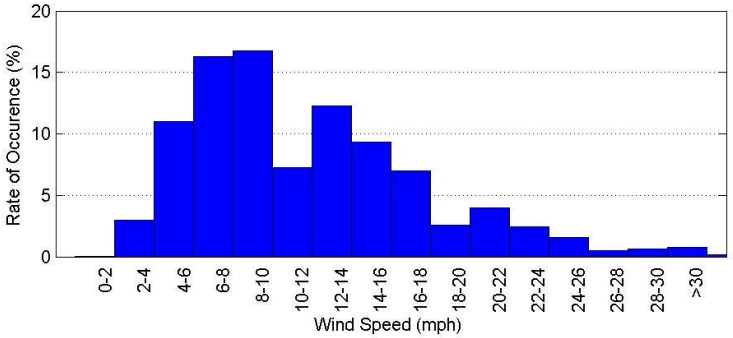

(c) Wind Speed Occurrence Rate

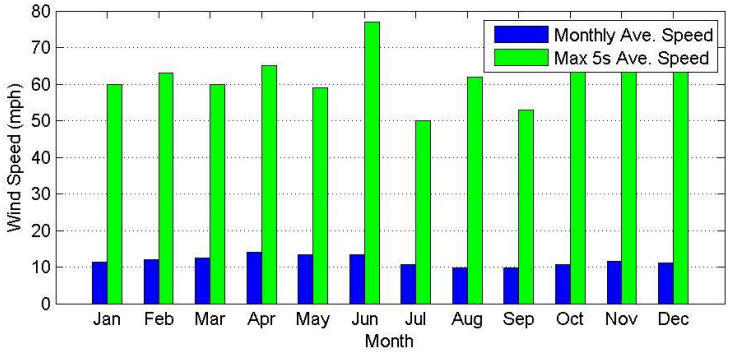

(d) Monthly Average Wind Speed

Figure 4.103: Wind Data Collected at the Lubbock International Airport (23042) from 2008 to 2015

TYLER POUNDS REGIONAL ARPT (13972)

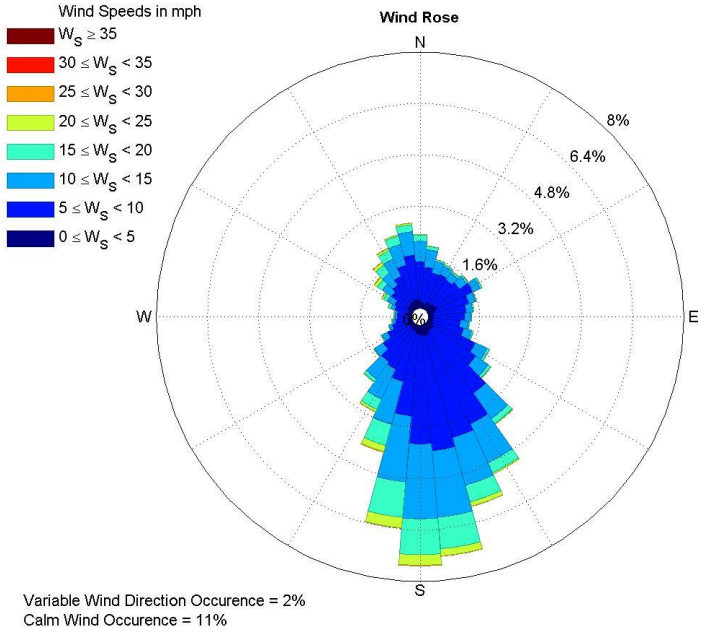

(a) Wind Rose Graph

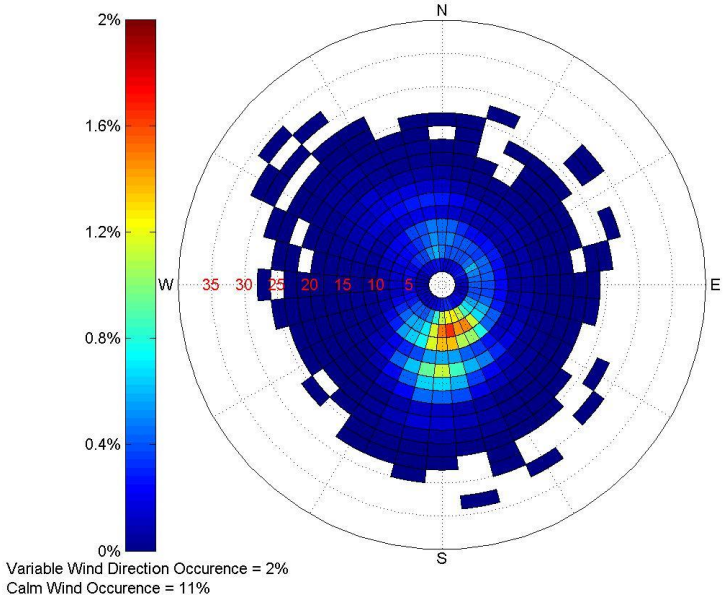

(b) Wind Density Graph

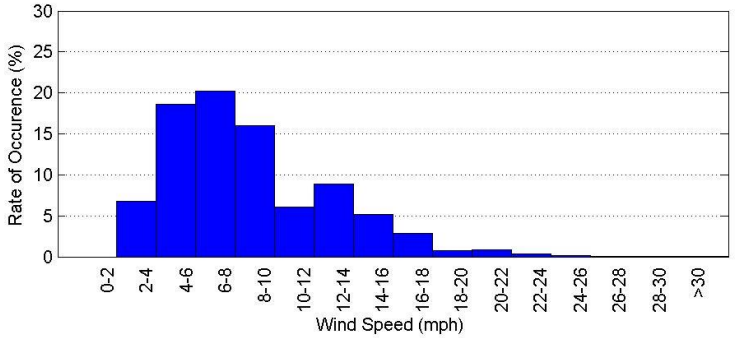

(c) Wind Speed Occurrence Rate

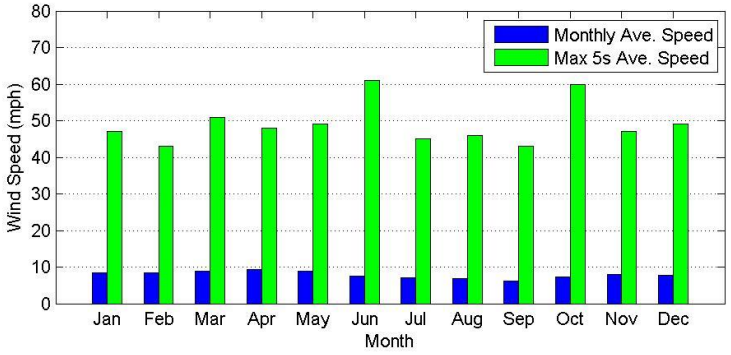

(d) Monthly Average Wind Speed

Figure 4.104: Wind Data Collected at the Tyler Pounds Regional Airport (13972) from 2008 to 2015

CORPUS CHRISTI INTERNATIONAL AIRPORT (12924)

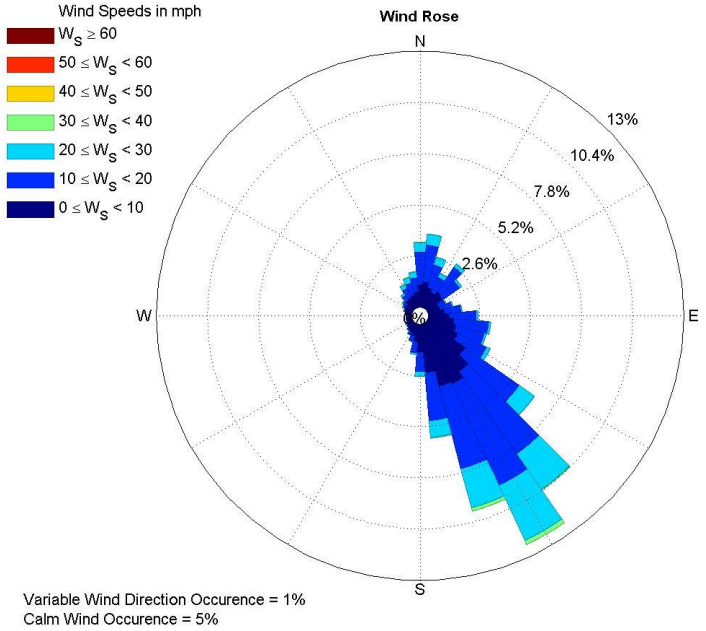

(a) Wind Rose Graph

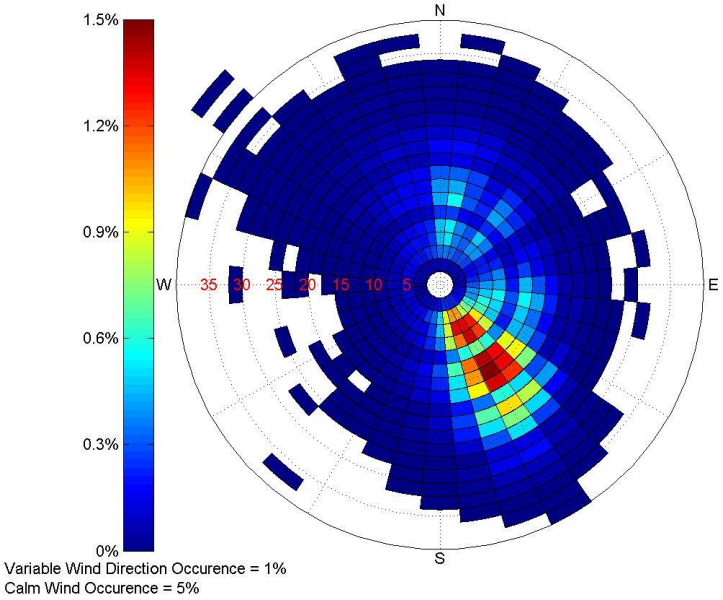

(b) Wind Density Graph

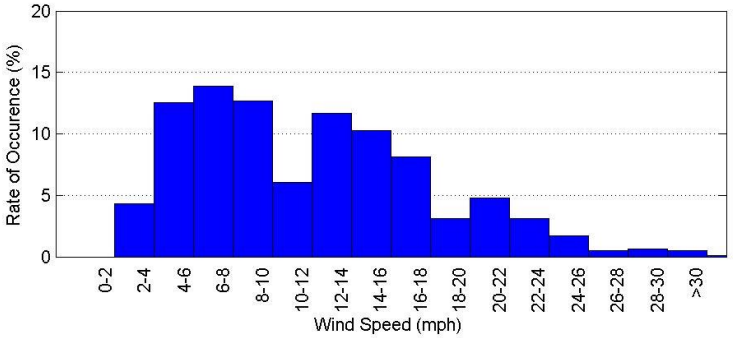

(c) Wind Speed Occurrence Rate

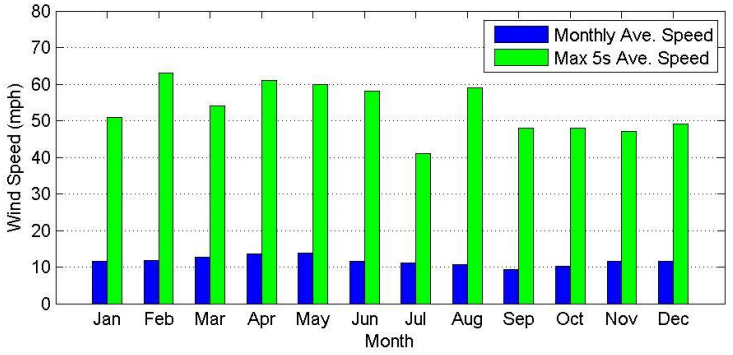

(d) Monthly Average Wind Speed

Figure 4.105: Wind Data Collected at the Corpus Christi International Airport (12924) from 2008 to 2015

ANGELINA COUNTY AIRPORT (93987)

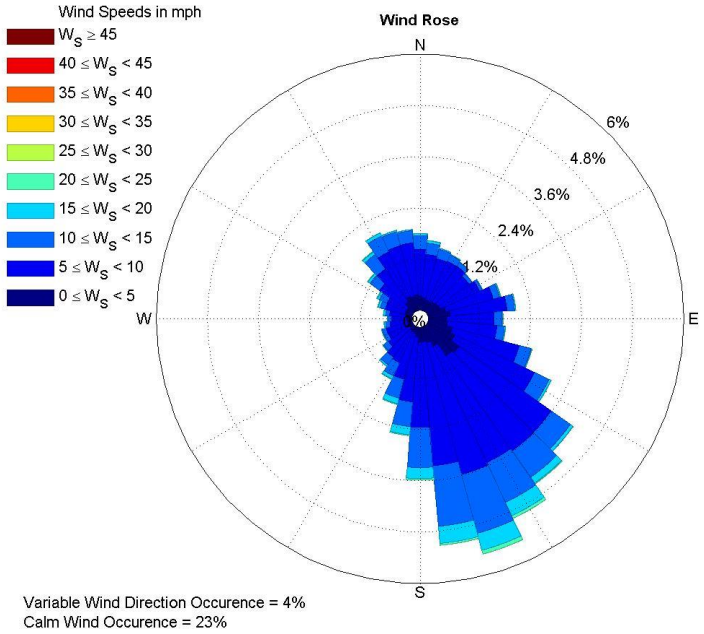

(a) Wind Rose Graph

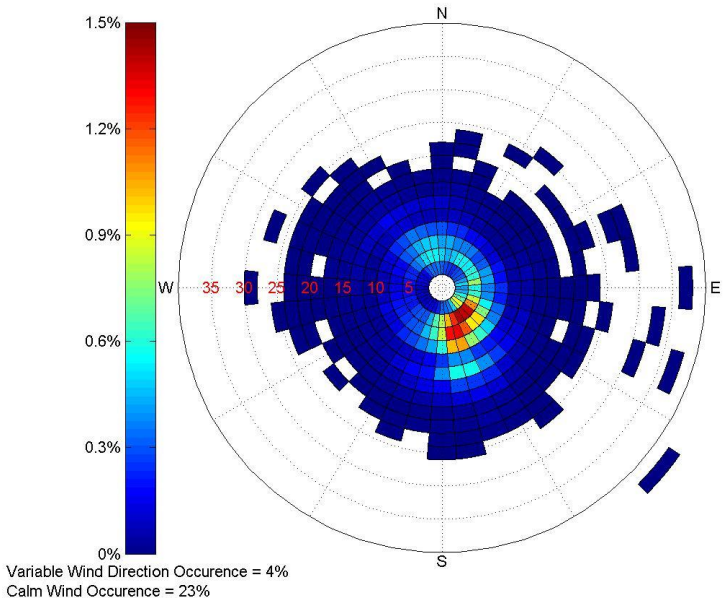

(b) Wind Density Graph

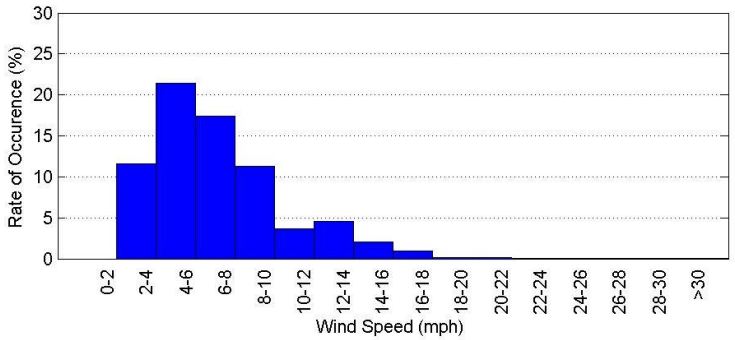

(c) Wind Speed Occurrence Rate

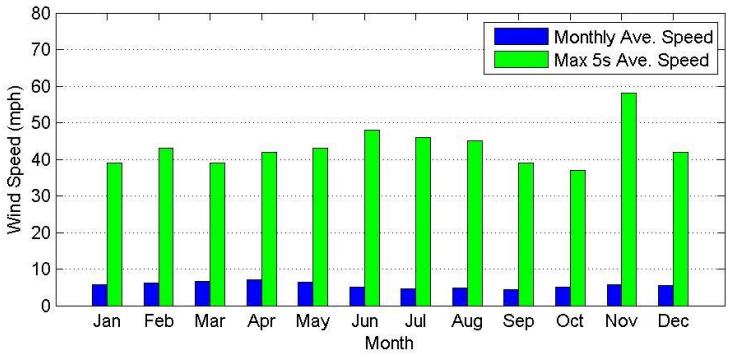

(d) Monthly Average Wind Speed

Figure 4.106: Wind Data Collected at the Angelina County Airport (93987) from 2008 to 2015

ABILENE REGIONAL AIRPORT (13962)

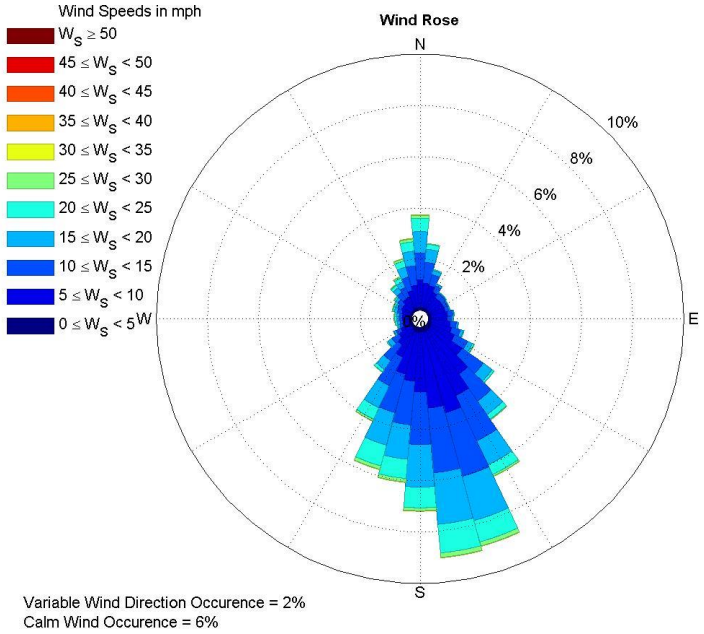

(a) Wind Rose Graph

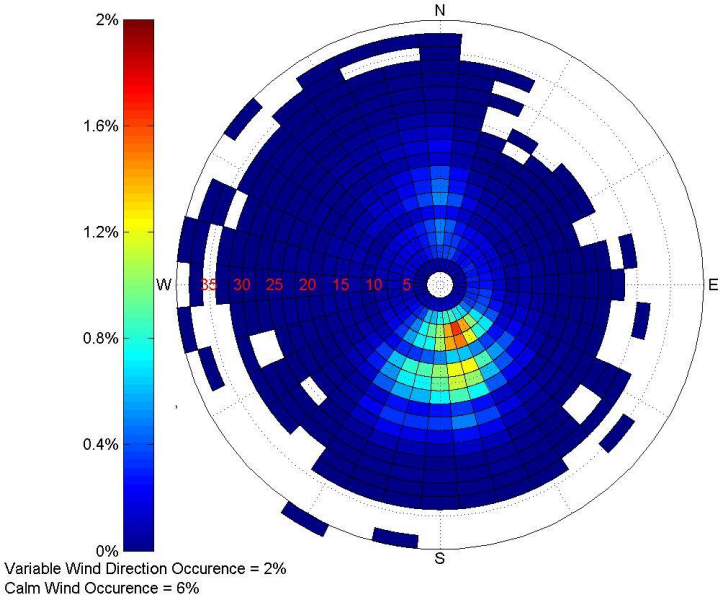

(b) Wind Density Graph

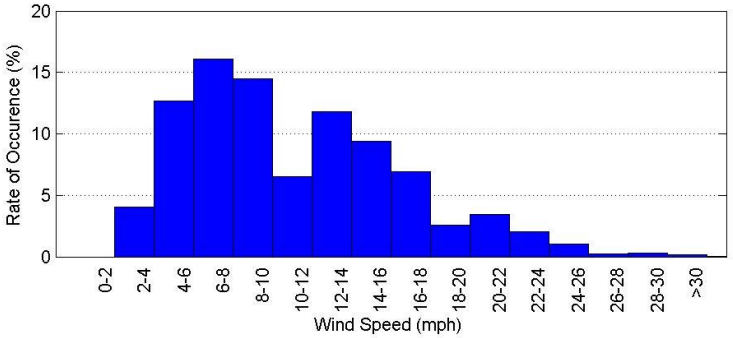

(c) Wind Speed Occurrence Rate

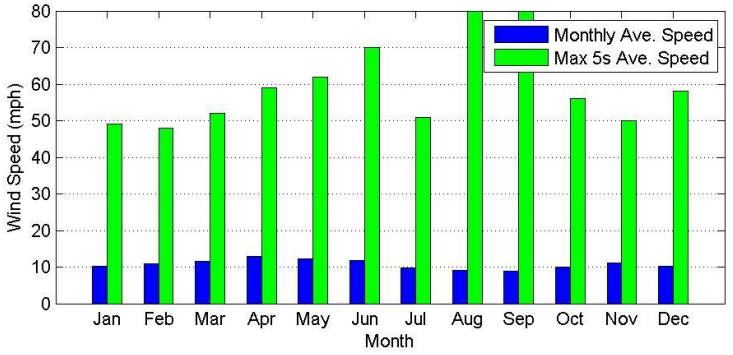

(d) Monthly Average Wind Speed

Figure 4.107: Wind Data Collected at the Abilene Regional Airport (13962) from 2008 to 2015

AMARILLO RICK HUSBAND INTL AIRPORT (23047)

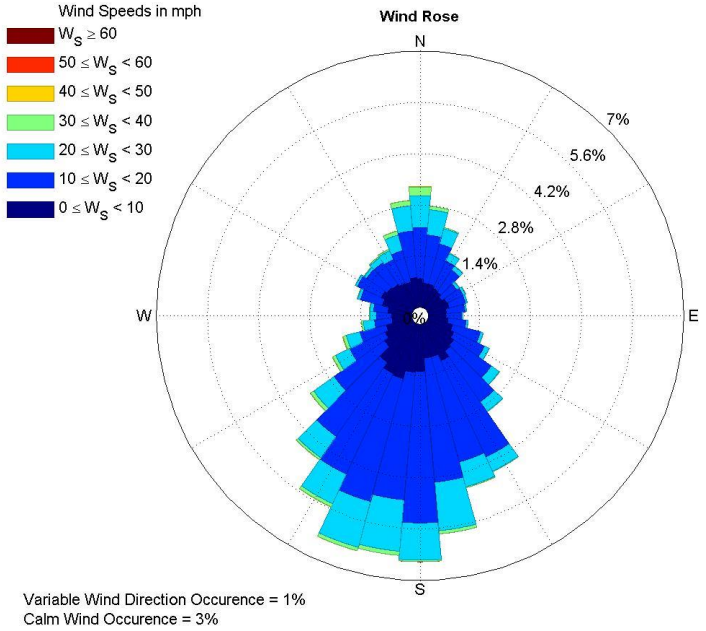

(a) Wind Rose Graph

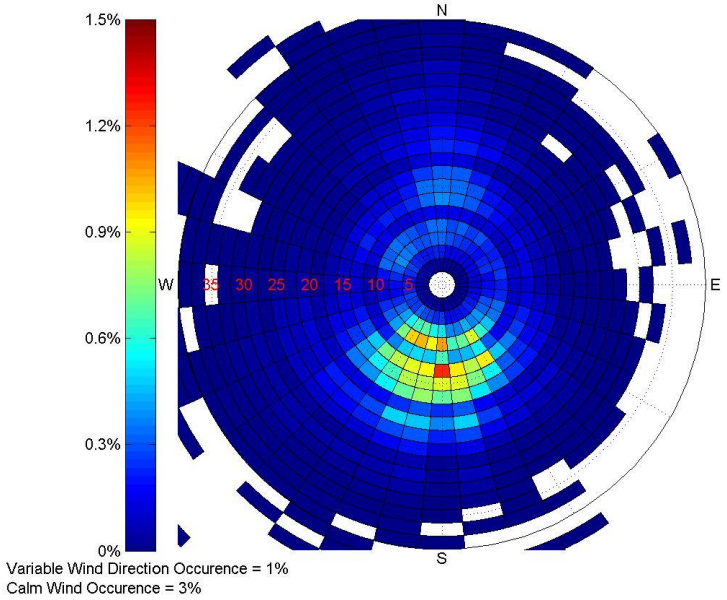

(b) Wind Density Graph

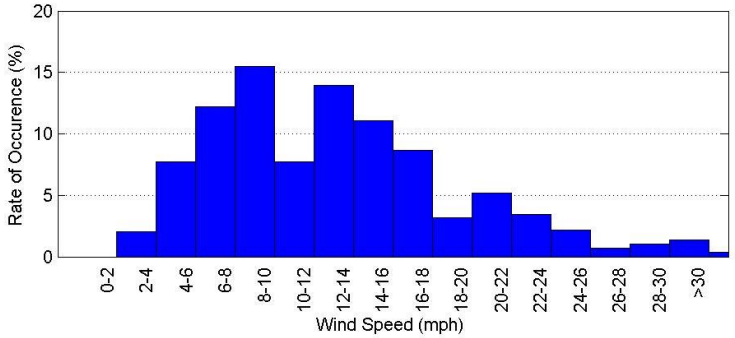

(c) Wind Speed Occurrence Rate

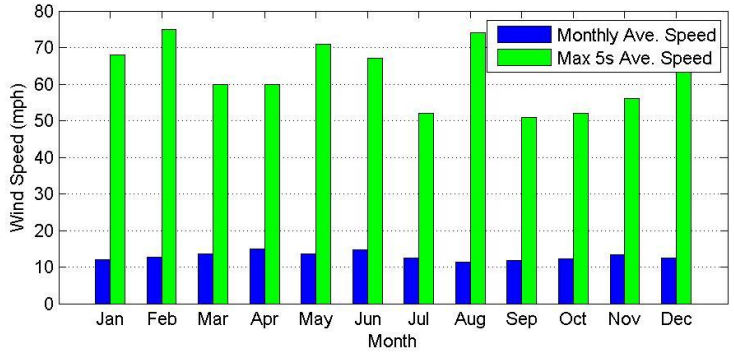

(d) Monthly Average Wind Speed

Figure 4.108: Wind Data Collected at the Amarillo Rick Husband International Airport (23047) from 2008 to 2015

DALLAS LOVE FIELD AIRPORT (13960)

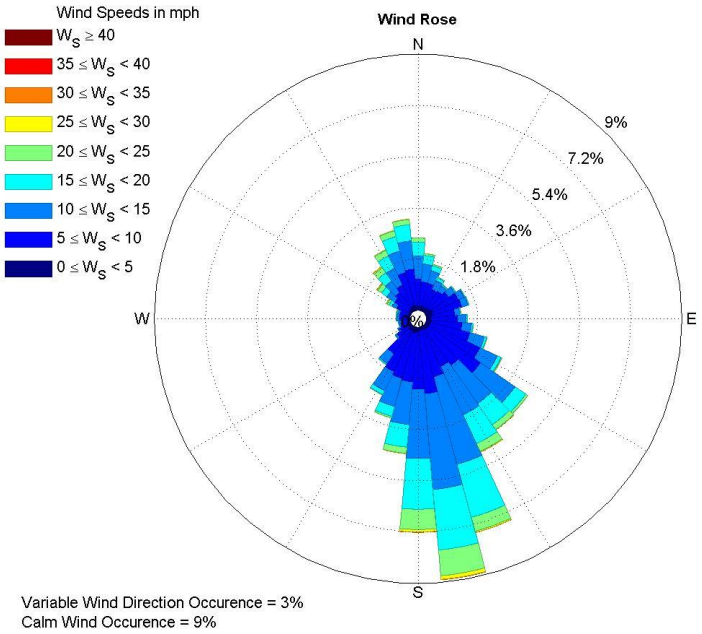

(a) Wind Rose Graph

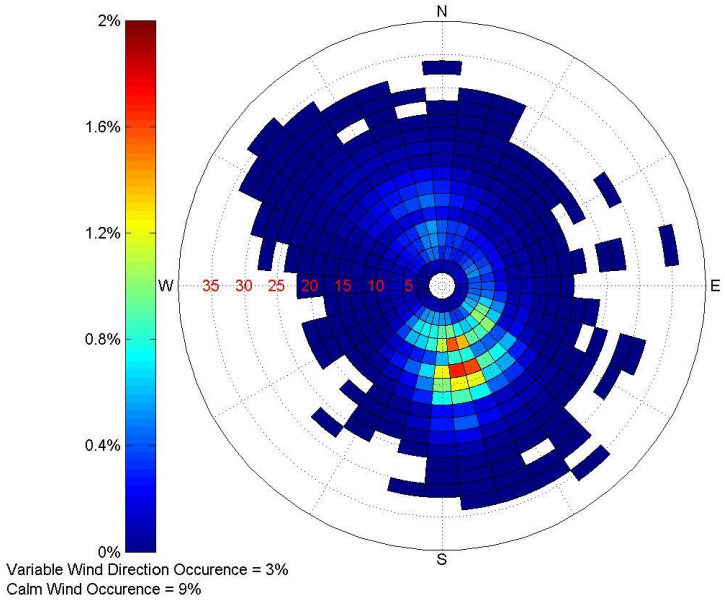

(b) Wind Density Graph

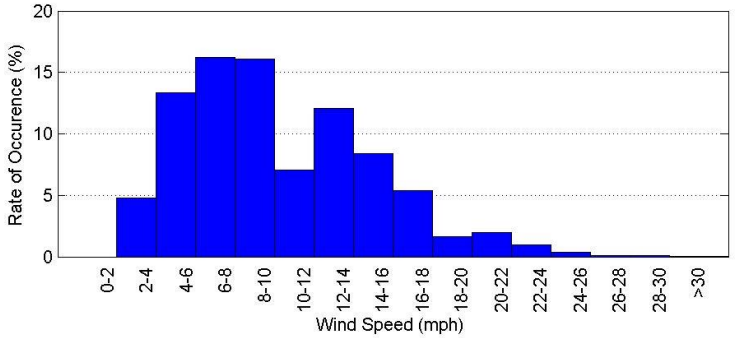

(c) Wind Speed Occurrence Rate

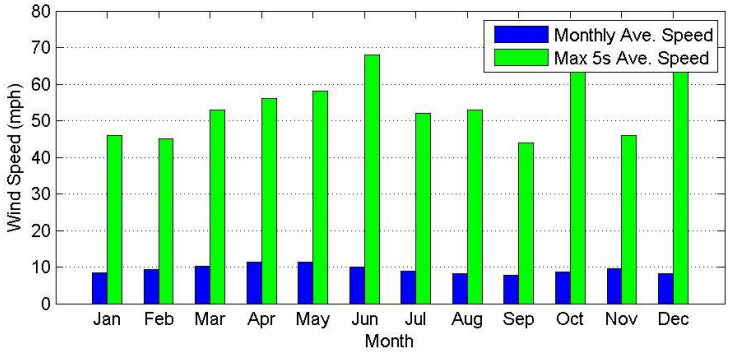

(d) Monthly Average Wind Speed

Figure 4.109: Wind Data Collected at the Dallas Love Field Airport (13960) from 2008 to 2015

Chapter 5. Laboratory Fatigue Tests

5.1 Overview

A major part of this research project involved conducting laboratory tests to assess the fatigue life of pre-cracked galvanized HMIP shaft-to baseplate connections. Through cyclic loading, these connections were tested at low stress ranges meant to emulate wind-induced stresses experienced by the HMIPs in service. This chapter provides details on the experimental fatigue program including specimen design, fatigue test setup and fatigue test procedure. A brief description of instrumentations utilized to acquire data during the fatigue tests is also included. Results of the fatigue tests are then presented and discussed. This chapter also presents the results of an ultimate strength test on an HMIP specimen with extensive cracking at the base connection.

5.2 Fatigue Tests on HMIP Specimens – Specimens Design

5.2.1 Pole Design: Geometry and Design Wind

The first step in conducting fatigue tests was to choose the pole design of interest. The research team worked in close collaboration with TxDOT to assure that the most important HMIP configurations were tested. Of all the HMIPs in service in Texas, poles having 12-sided, 150 ft tall shaft and considered design wind of 80 mph were selected for fatigue testing in this study. In addition, HMIP specimens without ground sleeves were selected for the first series of fatigue tests. This selection was particularly informed by the previous study reported by TxDOT (2008) indicating significant cracks in the shaft-to-base plate welds for HMIPs with this specific design. For reference, the results of the study reported by TxDOT (2008) in terms of the probability of observed cracks for HMIPs with different designs are summarized in Table 5.1.

Table 5.1: Probability of Observed Cracks (in percent) (TxDOT 2008)

		With Ground Sleeve				Without Ground Sleeve			
		100 ft	**125 ft**	**150 ft**	**175 ft**	**100 ft**	**125 ft**	**150 ft**	**175 ft**
8 sided	**80 mph**	N/A	0	0	N/A	N/A	0	0	N/A
	100 mph	0	0	0	5	N/A	0	0	N/A
12 sided	**80 mph**	57	100	50	50	67	33	**100**	44
	100 mph	20	38	0	63	N/A	0	57	13

In consultation and discussion with TxDOT engineers, it was later decided to consider HMIP specimens with the same design but with ground sleeves to further investigate the effectiveness of ground sleeves in improving the fatigue life of HMIPs. In this report, the specimens without ground sleeves are referred to as “specimens of primary interest”, while those with ground sleeves are called “specimens of secondary interest”.

5.2.2 Laboratory Specimens: Specimens of Primary Interest

The specimens referred to as the specimens of primary interest are based on the TxDOT design for an HMIP with a pole that is 12-sided, 150 ft tall, with a design wind speed of 80 mph, and without ground sleeves. The layout of HMIP test specimens in the first series of fatigue tests is shown in Figure 5.1. The specimens are each approximately 14.5 ft. in length. One end of the specimen is provided with the actual shaft-to-base plate connection detail of interest described above (left end of specimen in Figure 5.1). The design of this base plate along with the weld details are shown in Figures 5.2 and 5.4, respectively. Note that this design (as shown in Figures 5.2 and 5.4) conforms to the TxDOT Standard HMIP (1)-98. The other end is provided with a welded reaction plate that allows attachment to the reaction support fixtures, as will be described and shown in Section 5.3. The design of this reaction plate (end plate) along with the weld details are depicted in Figures 5.3 and 5.4, respectively. A picture of HMIP test specimen used in the first fatigue test is further shown in Figure 5.5.

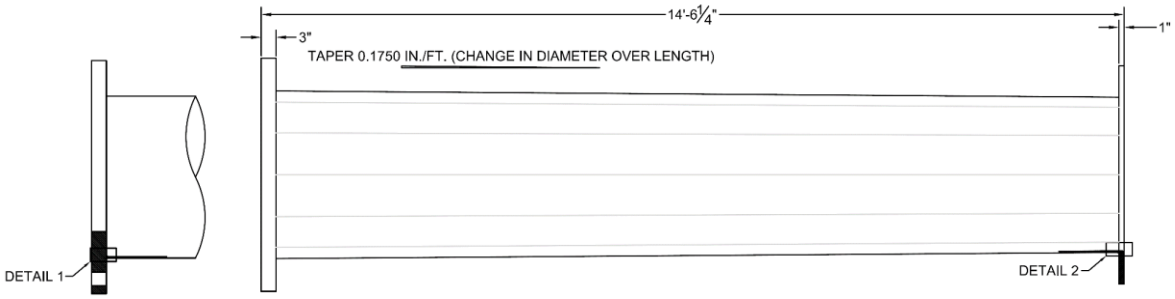

Figure 5.1: Layout of the HMIP Fatigue Test Specimens of Primary Interest

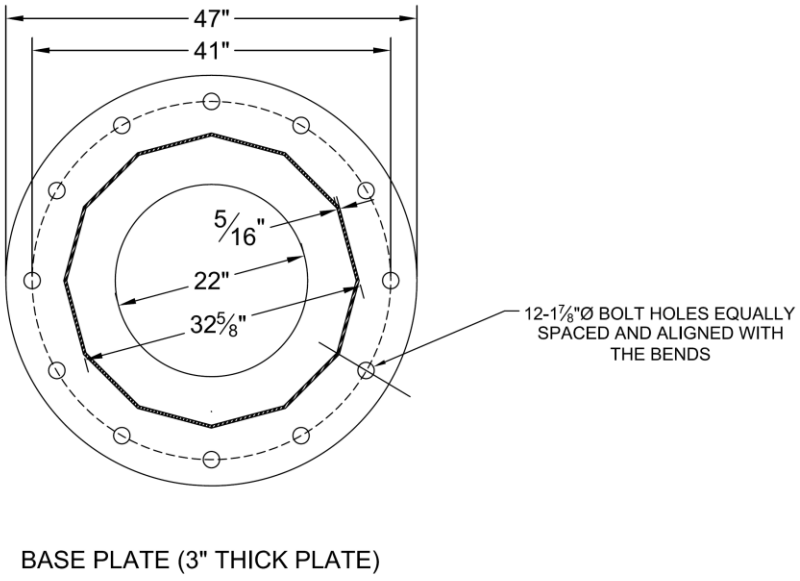

Figure 5.2: HMIP Fatigue Test Specimens of Primary Interest – Base Plate Details

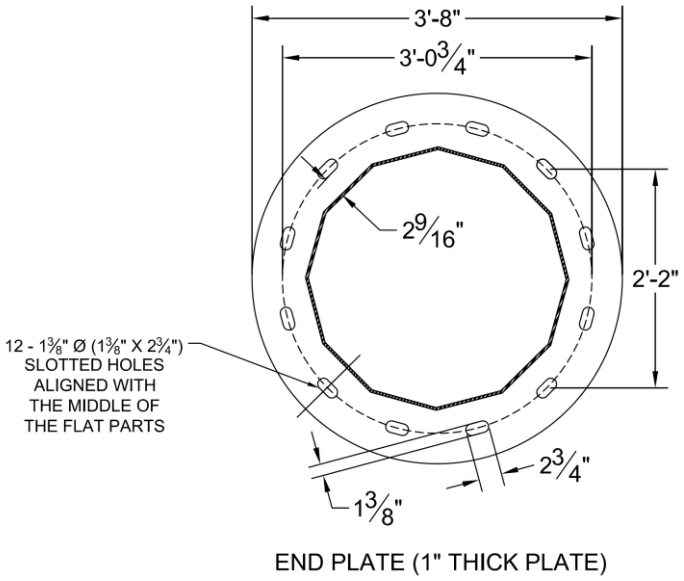

Figure 5.3: HMIP Fatigue Test Specimens of Primary Interest – End Plate (Reaction Plate) Details

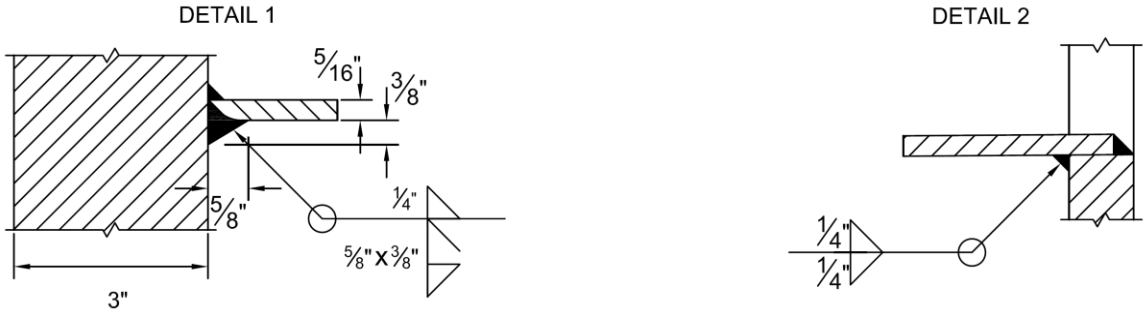

Figure 5.4: HMIP Fatigue Test Specimens of Primary Interest – Weld Details on Both Ends

Figure 5.5: HMIP Fatigue Test Specimen of Primary Interest being Fabricated at the Shop

5.2.3 Laboratory Specimens: Specimens of Secondary Interest

The specimens referred to as specimens of secondary interest are based on the TxDOT design for an HMIP with a pole that is 12-sided, 150 ft tall, with a design wind speed of 80 mph, and with ground sleeves. The layout of these HMIP test specimens is shown in Figure 5.6. The specimens are each approximately 14.5 ft. in length. One end of the specimen is provided with the actual shaft-to-base plate connection detail of interest described above (left end of specimen in Figure 5.6). The design of this base plate along with the weld details are shown in Figures 5.7 and 5.9, respectively. Note that this design (as shown in Figures 5.7 and 5.9) conforms to the TxDOT Standard HMIP (1)-98. The other end is provided with a welded reaction plate that allows attachment to the reaction support fixtures, as will be described and shown in Section 5.3. The design of this reaction plate (end plate) along with the weld details are depicted in Figures 5.8 and 5.9, respectively.

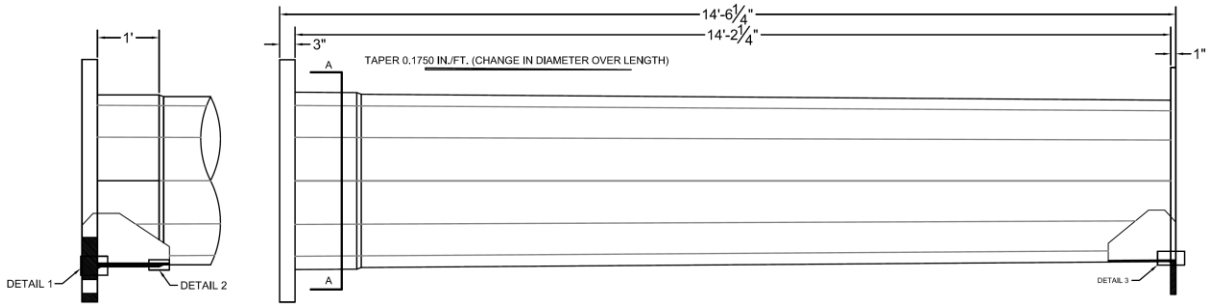

Figure 5.6: Layout of the HMIP Fatigue Test Specimens of Secondary Interest

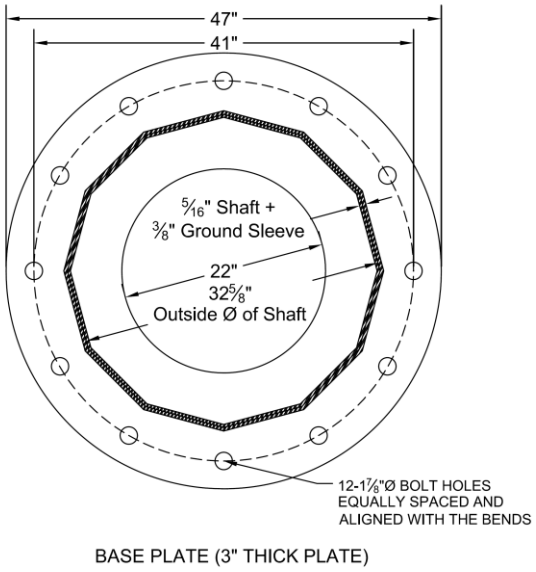

Figure 5.7: HMIP Fatigue Test Specimens of Secondary Interest – Base Plate Details

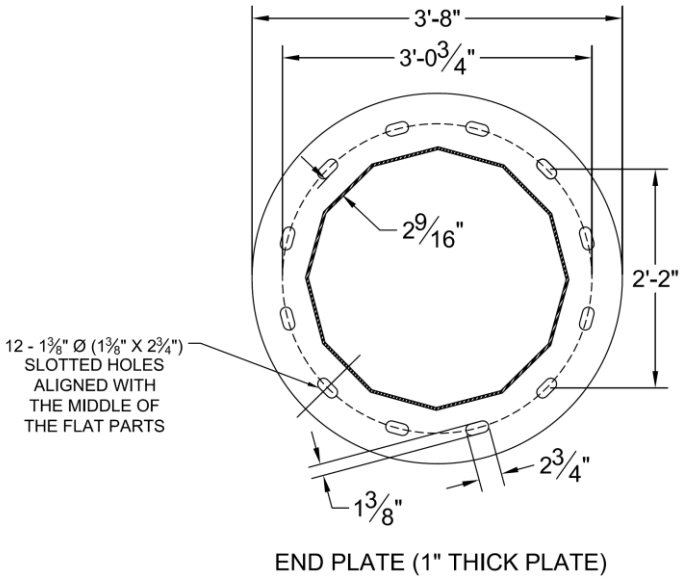

Figure 5.8: HMIP Fatigue Test Specimens of Secondary Interest – End Plate (Reaction Plate) Details

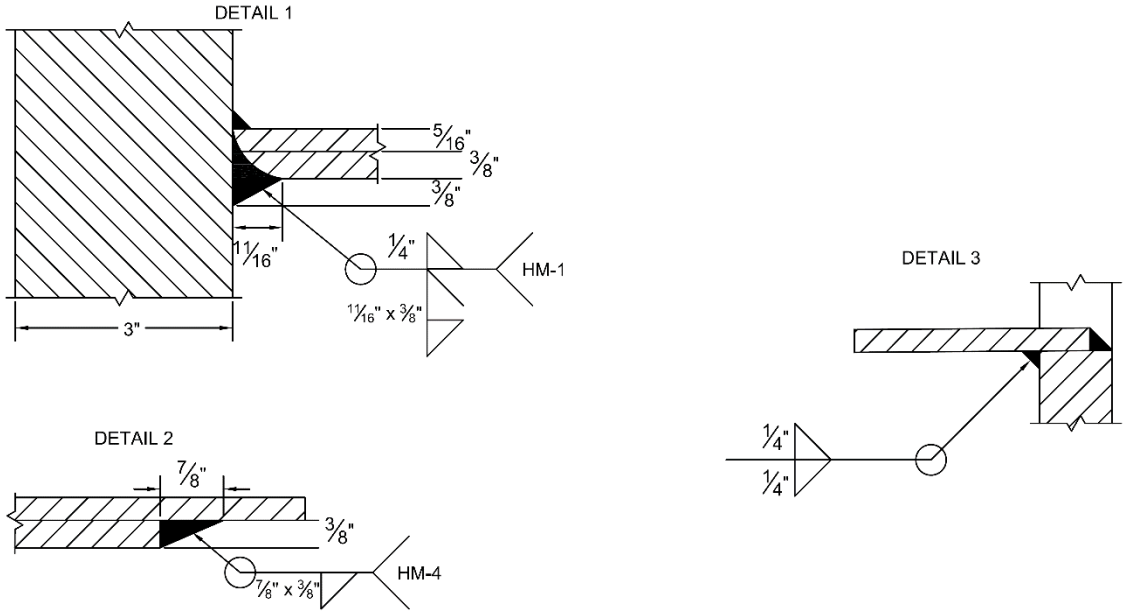

Figure 5.9: HMIP Fatigue Test Specimens of Secondary Interest – Weld Details on Both Ends

Pictures of HMIP test specimens of secondary interest are further shown in Figures 5.10 and 5.11.

Figure 5.10: HMIP Fatigue Test Specimens of Secondary Interest following Fabrication

Figure 5.11: A close-up of the Ground Sleeves (External Collars) of the HMIP Specimens of Secondary Interest

As shown above in presenting the details of the shaft-to-baseplate connections for both primary and secondary designs, the connection details for specimens with primary design (Figures 5.1, 5.2, and 5.4) and those with secondary design (Figures 5.6, 5.7, and 5.9) are virtually identical. The only differences stem from the addition of the ground sleeve, which

results in a larger weld at the baseplate and an additional weld at its termination to the pole. Neither of these is an issue for connections detailed in the primary design.

It should also be noted that the research team selected the fabricator and galvanizer used to produce the test specimens in consultation with TxDOT. The goal was to produce specimens having pre-existing cracks at the shaft-to-base plate connection. The research team also worked with TxDOT, pole fabricators, and galvanizers to design test specimens with a high likelihood of cracking during the galvanization process. More specifically, none of the welds in both primary and secondary designs were repaired after galvanization, a common practice with HMIPs today. This decision was made on the basis that the poles would be cracked similarly to those being monitored in the field when they were first installed.

5.2.4 Laboratory Specimens: Naming Scheme

The naming scheme used in this research was similar to that used in previous research on fatigue strength of HMIPs conducted at the Ferguson Structural Engineering Laboratory. This naming scheme provides a concise means of summarizing the critical geometric details for each specimen. The naming scheme used in the research reported in this document is shown in Figure 5.12. In total, eight specimens were utilized in fatigue studies of cracked HMIPs in the reported research. Six specimens designated as 33-3-12-TX-A1, 33-3-12-TX-A2, 33-3-12-TX-A3, 33-3-12-TX-A4, 33-3-12-TX-A5, and 33-3-12-TX-A6 were without ground sleeves (specimens of primary interest). The other two, Specimens 33-3-12-TXEC-A7, and 33-3-12-TXEC-A8, were with ground sleeves (specimens of secondary interest).

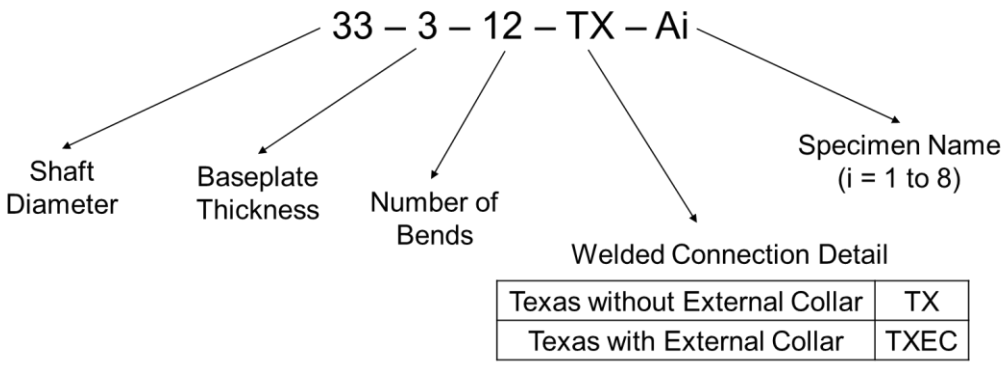

Figure 5.12: Naming Scheme for the HMIP Specimens

5.3 Fatigue Tests on HMIP Specimens – Test Setups and Test Procedures

5.3.1 Horizontal Test Setup and Test Procedure

Horizontal Test Setup: Details

The test setup used for the fatigue tests was a modified version of that used successfully in several past studies on the fatigue behavior of HMIPs at the Ferguson Structural Engineering Laboratory. The setup is shown schematically in Figure 5.13. In this setup, two specimens are tested simultaneously, in a back-to-back configuration with a stiff reaction box in the middle. As a result, the two specimens are essentially two cantilevers forming a simply supported beam.

Figure 5.14 further presents details of the end supports for this simply supported beam. The reaction support shown on the left in Figure 5.14 represents the pinned connection. This single degree of freedom reaction support restricts any lateral or vertical displacement and allows only rotation. The reaction support shown on the right in Figure 5.14 represents a roller support in the simply supported beam analogy. While restricting vertical displacement, the reaction support allows lateral displacement as well as rotation much like a roller. Details of the stiff reaction box (also referred to as the load box) are further depicted in Figure 5.15.

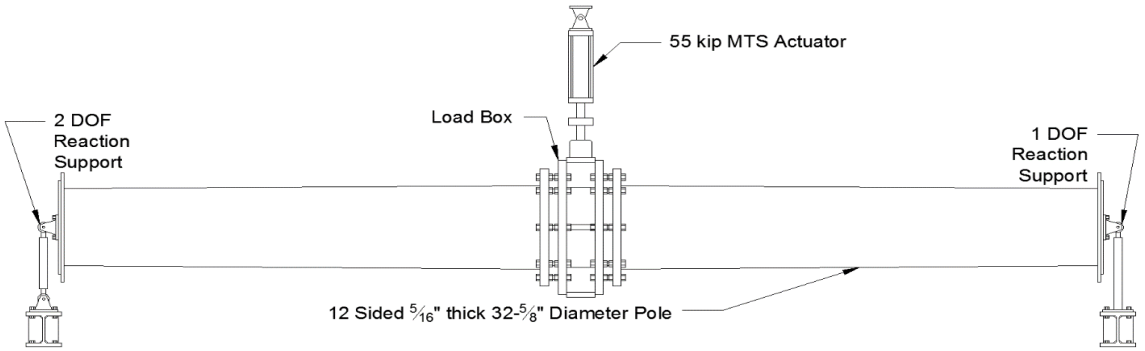

Figure 5.13: Schematics of the Setup for Fatigue Testing of HMIPs

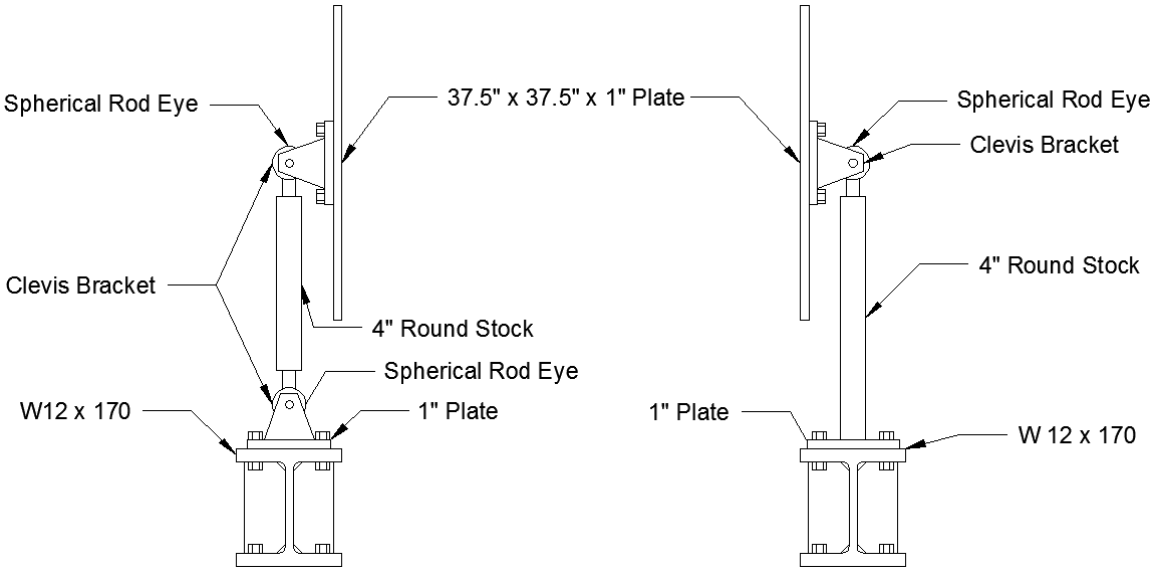

Figure 5.14: Schematics of the End Supports in Fatigue Testing of HMIPs

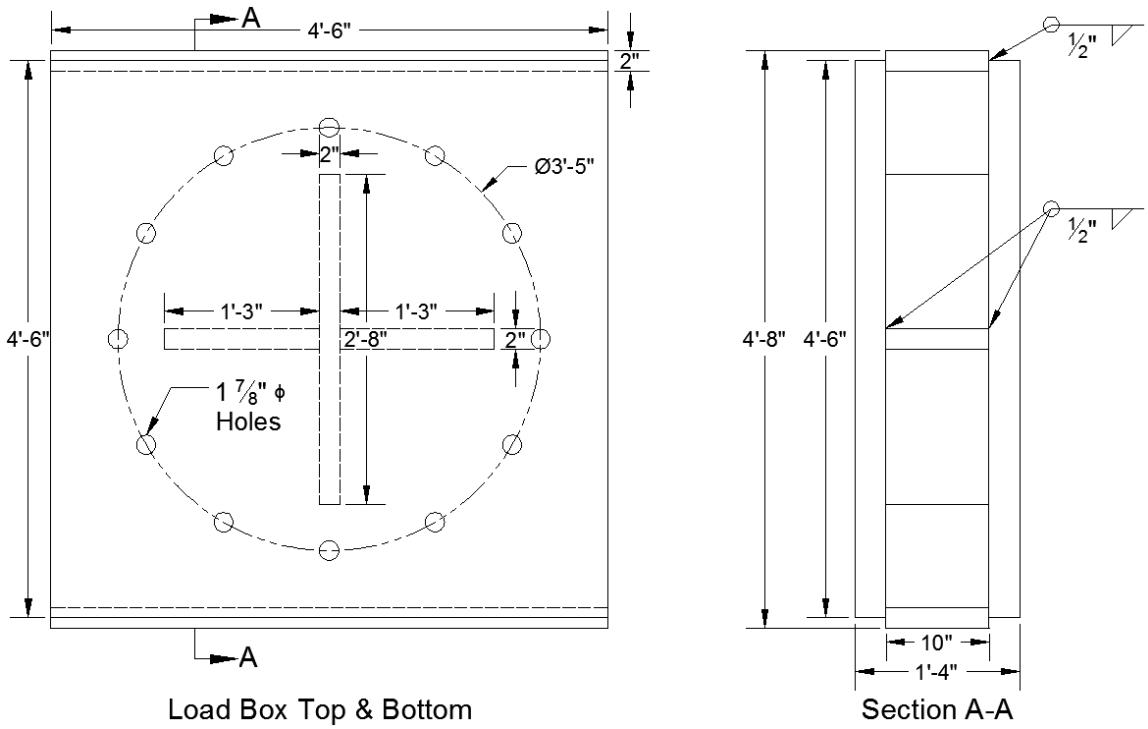

Figure 5.15: Schematics of the Stiff Reaction Box (Load Box) in Fatigue Testing of HMIPs

As also shown in Figure 5.13, the Fatigue loading was applied by a single 55-kip MTS actuator working in displacement control. The 55 kip capacity MTS hydraulic actuator was controlled by an MTS FlexTest SE Controller. Hydraulic pressure was supplied by an MTS SilentFlo HPU operating at 3000 psi with a 30 gpm capacity. Hydraulic pressure was regulated by an MTS 293 Hydraulic Manifold.

Pictures in Figures 5.16 to 5.19 provide more details of the fatigue test setup at the Ferguson Structural Engineering Laboratory, including the portal loading frame and lateral braces, the stiff reaction box, the hydraulic actuator, and the end support fixtures.

Figure 5.16: Portal Loading Frame Used in Fatigue Testing of HMIP Specimens at the Ferguson Structural Engineering Laboratory

Figure 5.17: MTS 55-kip Hydraulic Actuator and the Stiff Reaction Box (the Load Box)

Figure 5.18: Pin Support (1 DOF End) in the Horizontal Fatigue Test Setup

Figure 5.19: Roller Support (2 DOF End) in the Horizontal Fatigue Test Setup

Horizontal Test Setup: Installation of HMIP Specimens

As described above, the fatigue test setup used in this project was similar to that used in previous studies at the Ferguson Structural Engineering Laboratory. Like the test setup, the procedure used to install the HMIP specimens was similar to that incorporated in previous tests. Procedures were slightly modified to improve efficiency and to maximize data collection. The most important of these changes was to attach strain gauges to the specimens prior to testing. This allowed researchers to monitor the stresses induced in the specimens during installation. In doing this, the research team was able to ensure minimal residual stresses were locked into the specimen before testing.

While no specimen was instrumented before installation, researchers created analysis models to simulate loading conditions during installation. These models were made in a structural analysis program called Visual analysis (Figure 5.20). Two models were made to capture separate conditions: the specimen resting on the ground and the specimen being lifted by the crane. Each of these models was created using a continuous beam element. This element was discretized so that a node was created every six inches. Member self-weight was also considered in the models. Since the continuous beam element did not account for changes in the specimen's geometry, stresses reported by the program could not be used. Instead, the moment diagrams for each loading condition were exported and used with calculated moments of inertia to determine the specimen's stresses using classical beam theory equations for simple bending.

Small stresses were expected on the order of magnitude of 0.003 ksi near the base when the specimen was on the ground, and 0.007 ksi when the specimen was lifted by the crane. These small stresses were the result of specimen self-weight and were verified during the subsequent

specimen installation. The contribution of self-weight was accounted for when determining the nominal stress ranges at which the HMIP specimens were tested.

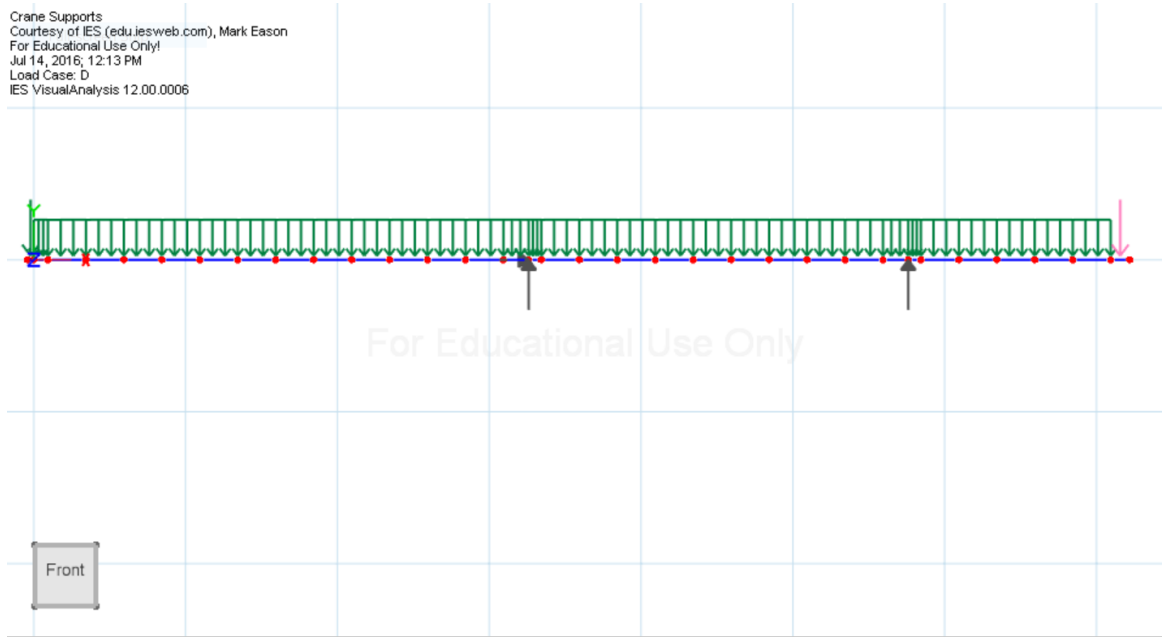

Figure 5.20: Crane Supported Loading Condition modeled using Visual Analysis Program.

As an example, representative pictures of the installation process are presented in Figures 5.21 to 5.23. The pictured specimen was tested until failure, removed from the setup, rotated, and reinstalled. Figures 5.21 and 5.22 were taken during the reinstallation of the specimen. Figure 5.21 shows a lab technician directing the specimen toward the loading box. Figure 5.22 shows this from another angle. Notice that the base-plate and the load box are in parallel planes. This was accomplished via a leveling process whereby the positions of the straps lifting the specimen were adjusted until the base-plate was level. This facilitated the process of installing the specimen, as it could be pushed straight on to the loading box's threaded rods. Figure 5.23 shows the specimen after reinstallation. At this point, the nuts on the threaded rods were tightened, but the roller support was yet to be reattached. Taking its place was an adjustable jack that prevented the specimen from becoming a cantilever. This jack was removed after the roller connection was reattached to the specimen and the testing frame.

Figure 5.21: Installation of an HMIP Specimen into the Horizontal Fatigue Testing Setup.

Figure 5.22: Attachment of a "leveled" HMIP specimen to the Load Box.

Figure 5.23: A specimen supported on a jack during Final Stages of installation.

Horizontal Test Setup: Test Procedure

Due to programming limitations, displacement control was used in lieu of force control for the fatigue tests. Displacement levels were chosen so that the target nominal stress ranges were met. To best match results of previous experiences, two methods of test management were employed.

The first method of test management was to adjust the displacement command gradually during the test. These adjustments were made throughout the test to maintain constant nominal stress range. Failure was defined as the point when the displacement command had to be increased by 10-percent, relative to the beginning command, to maintain the same force range. This method of test management was designed to emulate force control and was dubbed "Poor Man's Force Control".

The second method of test management was to set the displacement command and simply run the test without adjustments. This is pure displacement control. No adjustments were made to the control throughout the test unless changes to the testing frame required them. Failure was defined as a 10-percent reduction in the load.

Stress Ranges

In an effort to represent the loading conditions experienced by HMIPs in the field, the laboratory specimens were subjected to various stress ranges from 2 to 6 ksi. Specifically, the specimens were tested at the stress ranges of 6 ksi, 4 ksi, 3 ksi, and 2 ksi.

The first fatigue test was conducted at a stress range of 6 ksi to provide a benchmark to previous tests conducted at the Ferguson Structural Engineering Laboratory and those conducted at the Stress Engineering Laboratory by the research team from University of Houston. The next

three were conducted at smaller stress ranges. The specimens with ground sleeves were tested at a stress range of 6 ksi to provide a benchmark to previous tests performed at the Ferguson Structural Engineering Laboratory.

A positive mean tensile stress of 6 ksi was selected in all fatigue tests. Therefore, for example, in the test conducted at the stress range of 3 ksi, the minimum stress was 4.5 ksi and the maximum stress was 7.5 ksi. Similarly, in the test conducted at the stress range of 6 ksi, the minimum stress was 3 ksi and the maximum stress was 9 ksi. Keeping the mean stress at 6 ksi for all tests eliminated one source of uncertainty in the experiments.

Note that the nature of this testing method is that only the top bend experiences the specified targeted tensile stress range. The neighboring bends (one on each side) undergo similar but slightly smaller stress ranges. Stresses in the bends bellow the top three are significantly smaller than the specified tested stresses, as the stress declines when the neutral axis is approached. In addition, the bends above the neutral axis were in tension and were fatigued, while the bends below the neutral axis were in compression and were not fatigued. As a result, the HMIP specimens could be flipped 180 degrees after their first failure.

Instrumentation

Fourteen strain gages (Model FLA-6-350-11-3LT) (Figures 5.24 and 5.25) were installed on each HMIP specimen to monitor stresses during the fatigue tests.

To verify that the nominal stresses were applied to the shaft-to-base plate weld connection, the stresses at a section 6-inches away from the base plate were monitored with strain gages. In this way, the influence of local effects in the stress measurement was mitigated providing an accurate verification method of the nominal applied stresses.

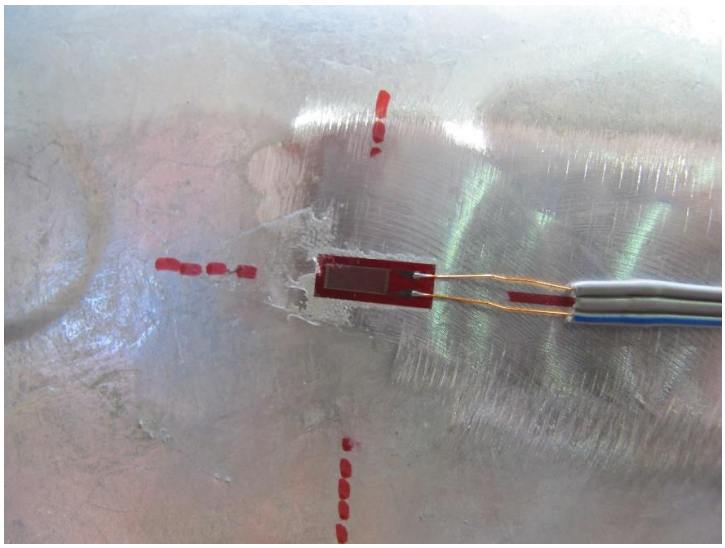

Figure 5.24: Strain Gauges Installed 6-inches away from the Base Plate to Monitor the Nominal Stress Ranges

As shown in Figure 5.25, strain gages were also installed in the vicinity of the welds to obtain a measure of the variation in the stresses near the welds.

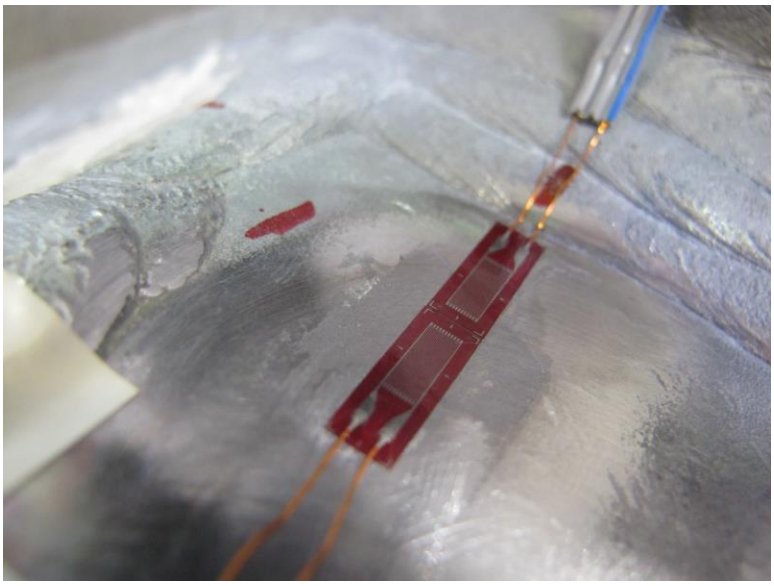

Figure 5.25: Strain Gauges for Monitoring the Stress Profile Near the Base Plate-to-Shaft Welds

Data Acquisition System

The data acquisition system, Compact RIO, from National Instruments (NI) was used to record and to analyze the fatigue test data. The Compact RIO consisted of the controller (Model cRIO-9024), an eight slot chassis (Model cRIO-9114), and a series of modules. Directly connected to MTS FlexTest SE Controller, One NI-9205 module was used to record forces and displacements from MTS actuator. Additionally, seven NI-9239 modules were used to record strain gauge data. A picture of the data acquisition system used in fatigue tests on HMIP specimens is presented in Figure 5.26. As further seen in Figure 5.26, an Airlink Raven X cellular modem from Sierra Wireless was also utilized to access the NI Compact RIO DAQ remotely through the GPRS/EDGE wireless network. The NI Compact RIO DAQ and the wireless modem were placed in a water-resistant enclosure box for better protection.

Figure 5.26: NI Compact RIO Data Acquisition System Used to Record Fatigue Test Data

National Instruments LabVIEW was used to program the NI Compact RIO DAQ, and to record the fatigue test data. The program was set to capture the data at a frequency of 50 Hz (samples per second). Figure 5.27 depicts a screenshot of the program showing the stresses monitored during fatigue tests on HMIP specimens.

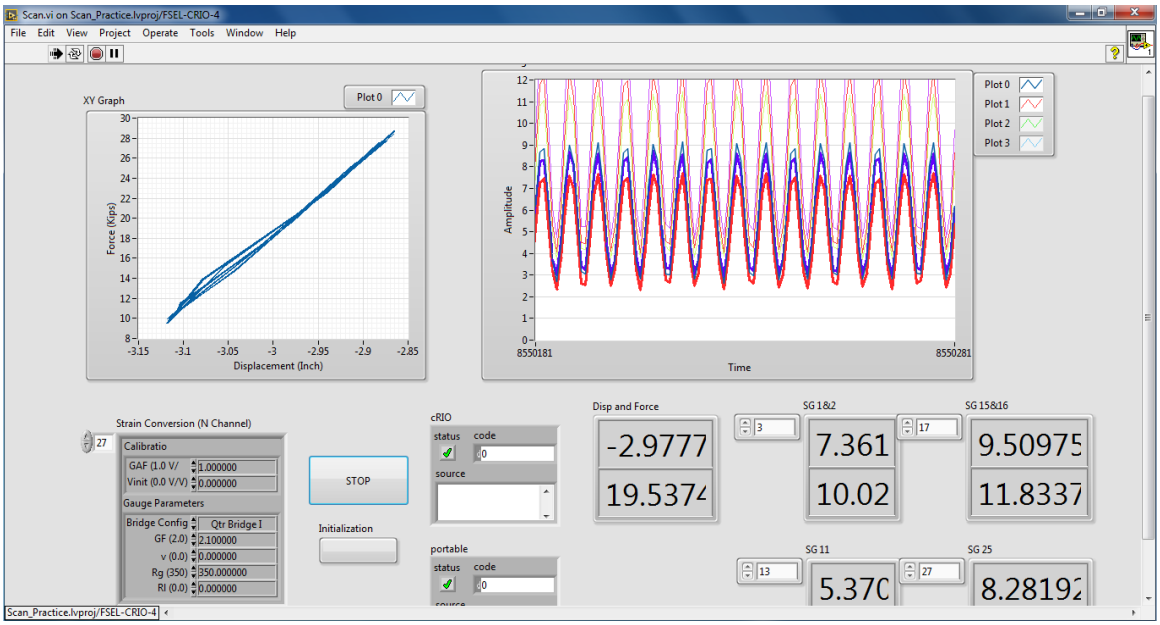

Figure 5.27: A Screenshot from the LabVIEW Program Showing the Stresses Monitored in a Fatigue Test

5.3.2 Vertical Test Setup for Conducting Static and Fatigue Tests

In addition to the first test setup (horizontal setup), a second test setup was designed and fabricated in later stages of the experimental fatigue studies. In this second setup, a single HMIP specimen could be tested in vertical position. Therefore, this second setup is referred to as the "vertical test setup" throughout this report.

The reason for fabrication of the vertical test setup was twofold. First, the fatigue testing of cracked HMIPs under low stress ranges was proved to be very time consuming, so the second fatigue test setup helped researchers to conduct more fatigue tests throughout the life of the project. Second, the second vertical setup was utilized to perform a static test to evaluate the ultimate strength of cracked poles. Development of the data on the ultimate strength of cracked poles was of interest since the collapse behavior of heavily cracked HMIPs in service as a result of sudden high wind gusts was a matter of concern to TxDOT.

In this section, this second vertical setup is introduced. The conduct of a static test on evaluating the ultimate strength capacity of a cracked HMIP is discussed in Section 5.5.

Vertical Test Setup: Details

A portrayal of the vertical test setup is displayed in Figures 5.28 and 5.29, where different elements of the setup are indicated. More details on the vertical and lateral support conditions are further provided in Figures 5.30 and 5.31. All materials needed for this setup, with the exception of nuts and bolts, was recycled from previous tests at the Ferguson Structural Engineering Laboratory. The setup consisted of two structural steel I-beams that were bolted to the strong floor. On top of these I-beams would rest the loading box that was previously used in fatigue tests on high-mast poles at the Ferguson Structural Engineering Laboratory. The testing specimen would then rest on top of the repurposed loading box. An actuator was bolted to the strong wall and connected to the specimen via a pinned connection. This actuator was utilized to apply forces to the specimen. Pictures of the vertical setup configured for both static and fatigue tests on cracked HMIP specimens along with more details on the actuators and on the force and displacement measurements are shown in Figures 5.32 through 5.36.

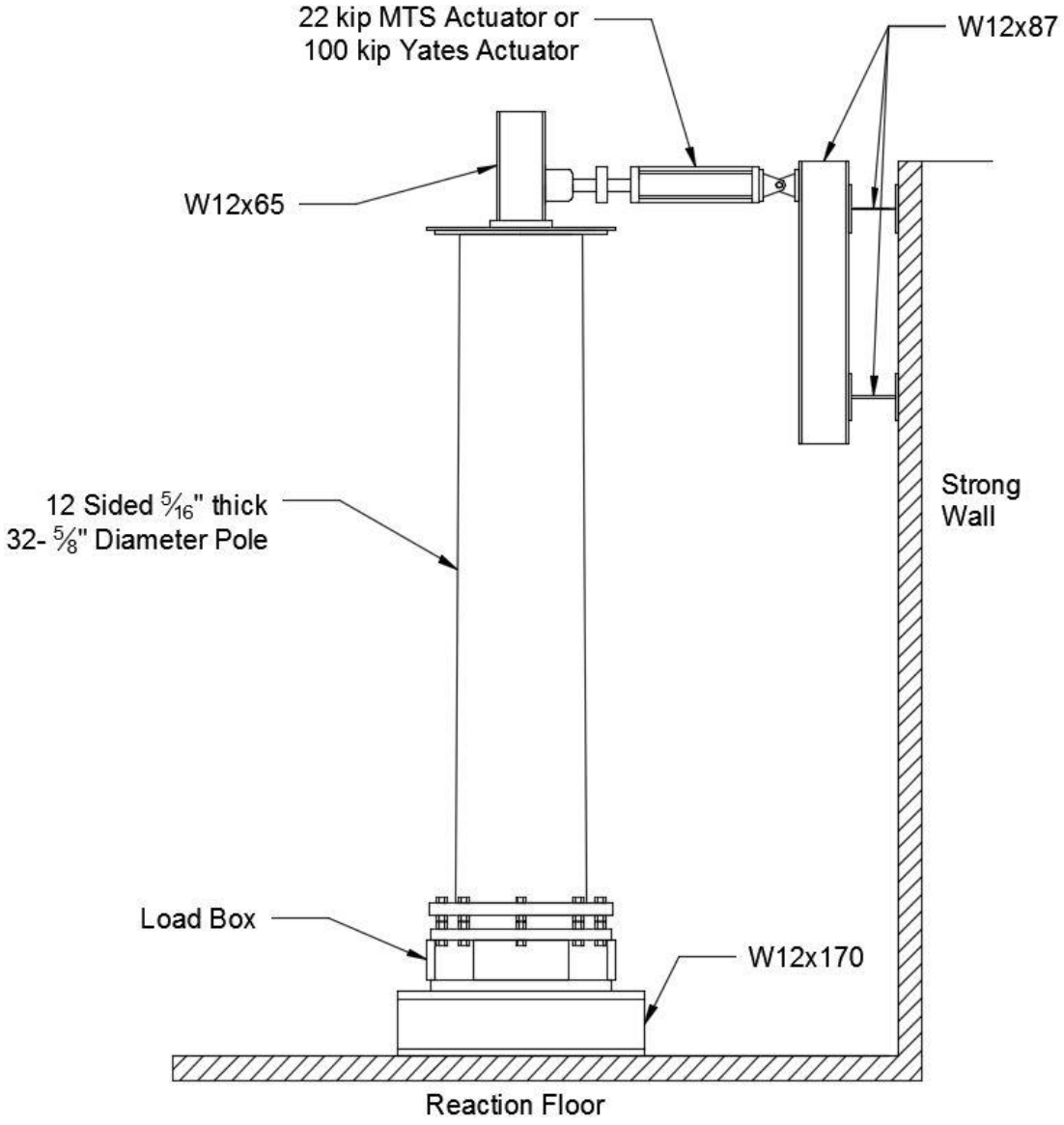

Figure 5.28: 2D Schematics of the Vertical Setup for Ultimate Strength and Fatigue Testing of HMIP Specimens

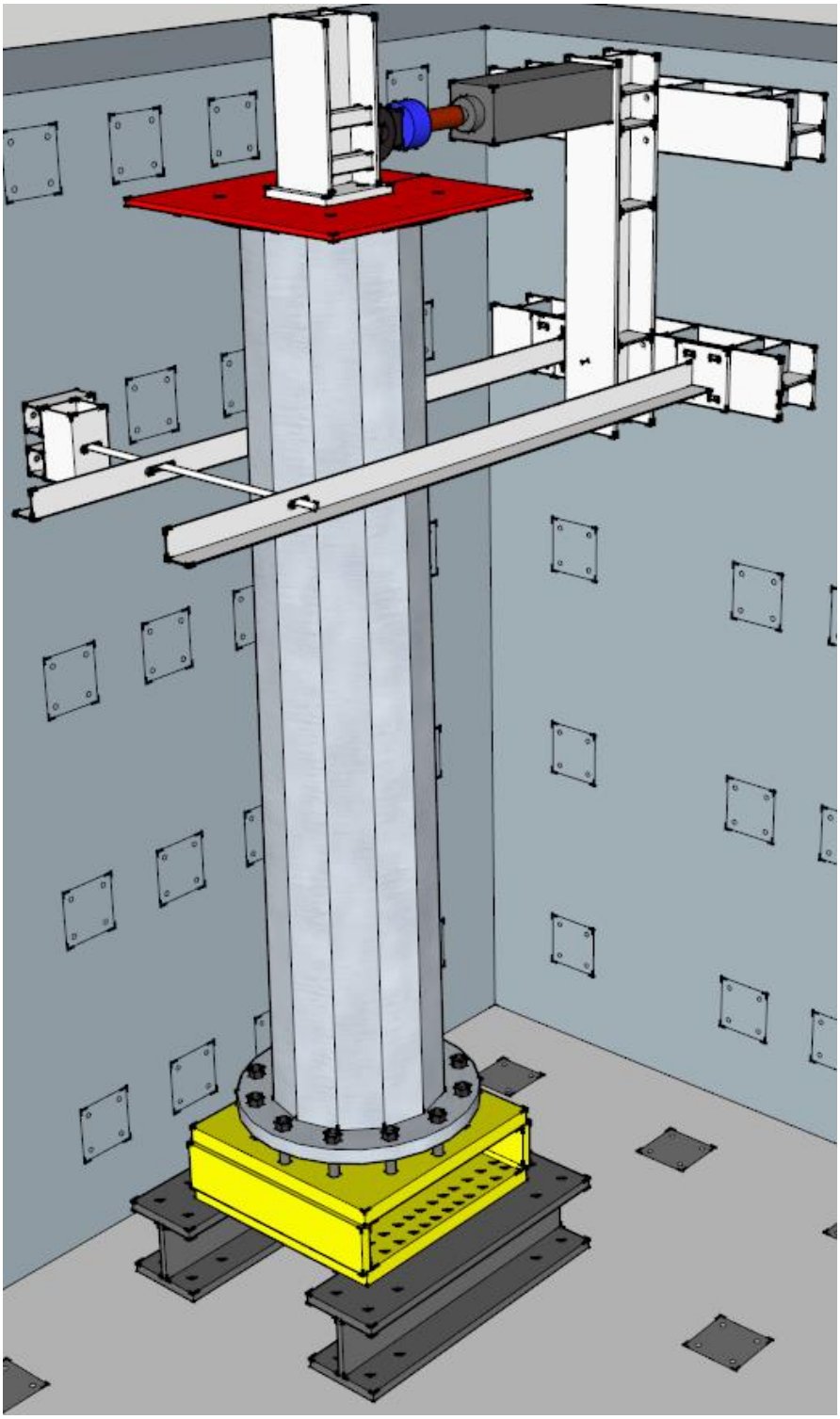

Figure 5.29: 3D Isometric Schematics of the Vertical Setup for Ultimate Strength and Fatigue Testing of HMIP Specimens

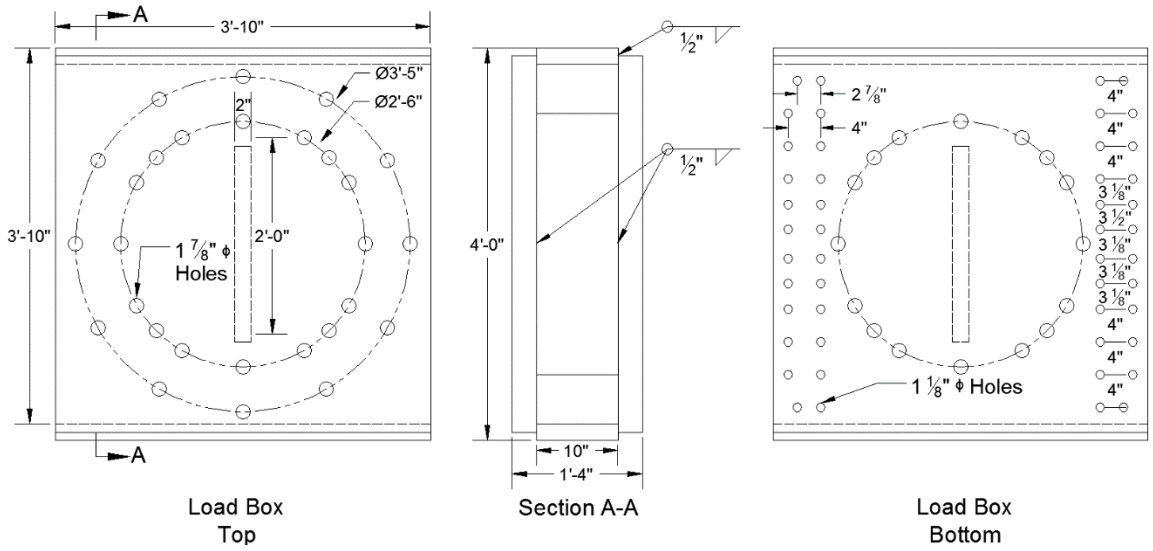

Figure 5.30: Details of the Vertical Setup: Modified Load Box

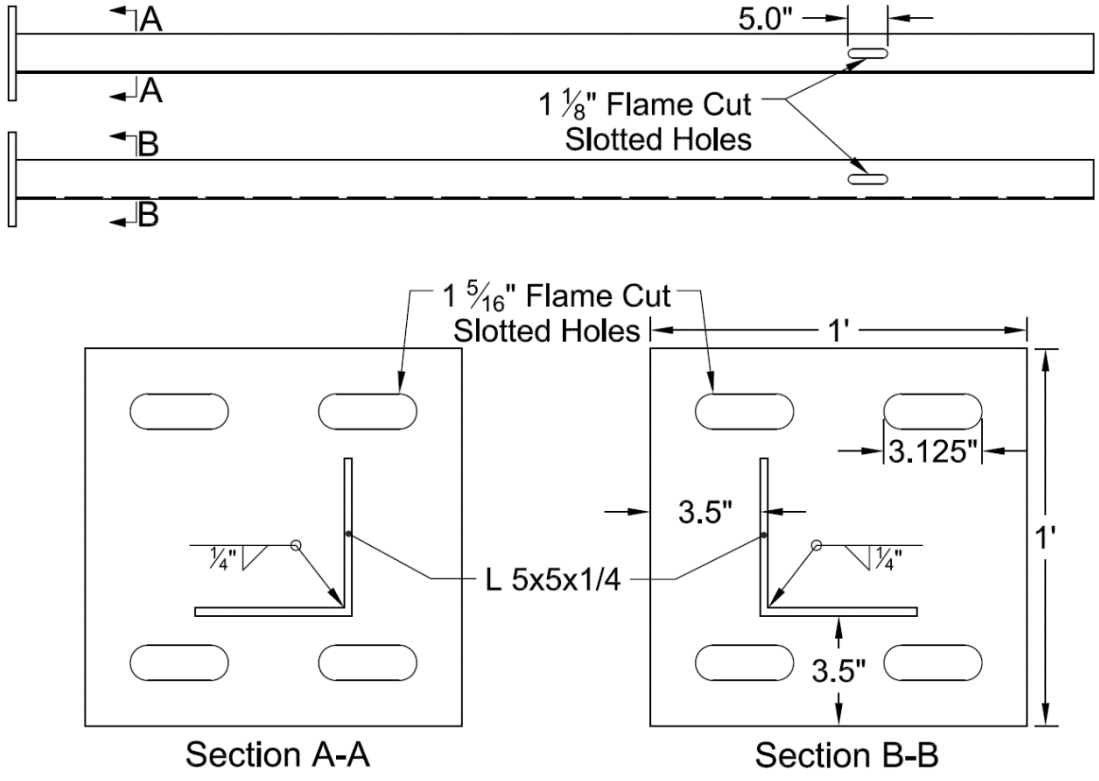

Figure 5.31: Details of the Vertical Setup: Lateral Restraints

Figure 5.32: Vertical Setup Configured to Perform Fatigue Tests on HMIP Specimens at the Ferguson Structural Engineering Laboratory

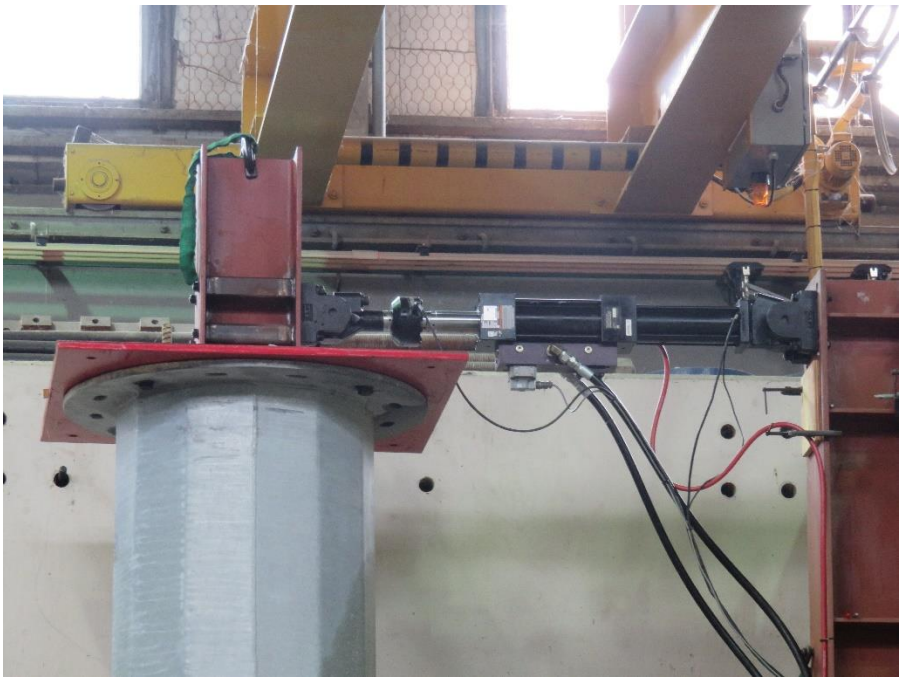

Figure 5.33: MTS 22-kip Hydraulic Actuator used in the Vertical Setup to Perform Fatigue Tests on HMIP Specimens at the Ferguson Structural Engineering Laboratory

Figure 5.34: Vertical Setup Configured to Perform Ultimate Strength Test on an HMIP Specimen at the Ferguson Structural Engineering Laboratory

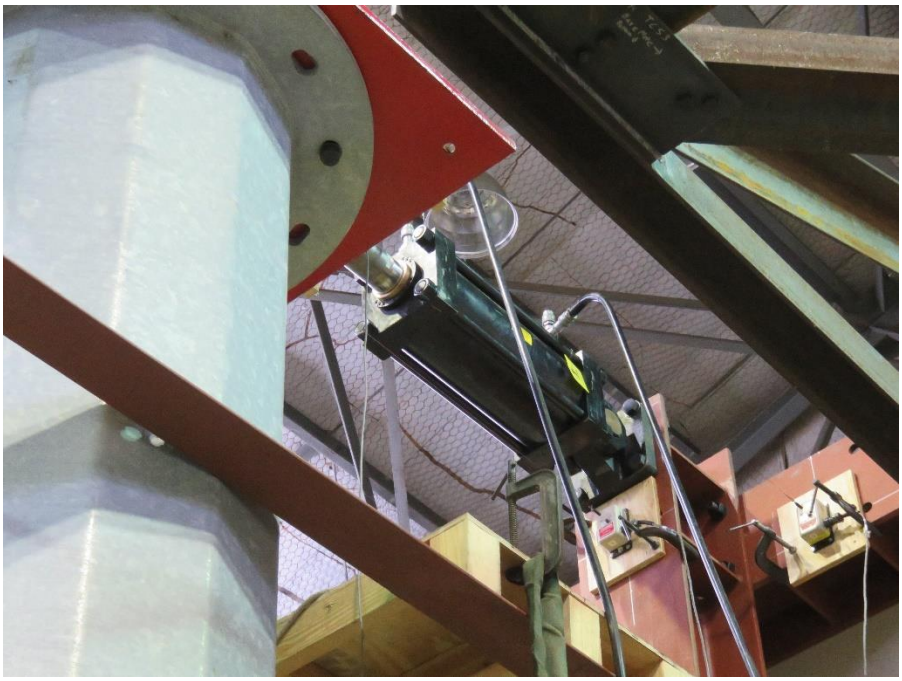

Figure 5.35: An Actuator in the Vertical Setup Used in Ultimate Strength Testing of an HMIP Specimen at the Ferguson Structural Engineering Laboratory

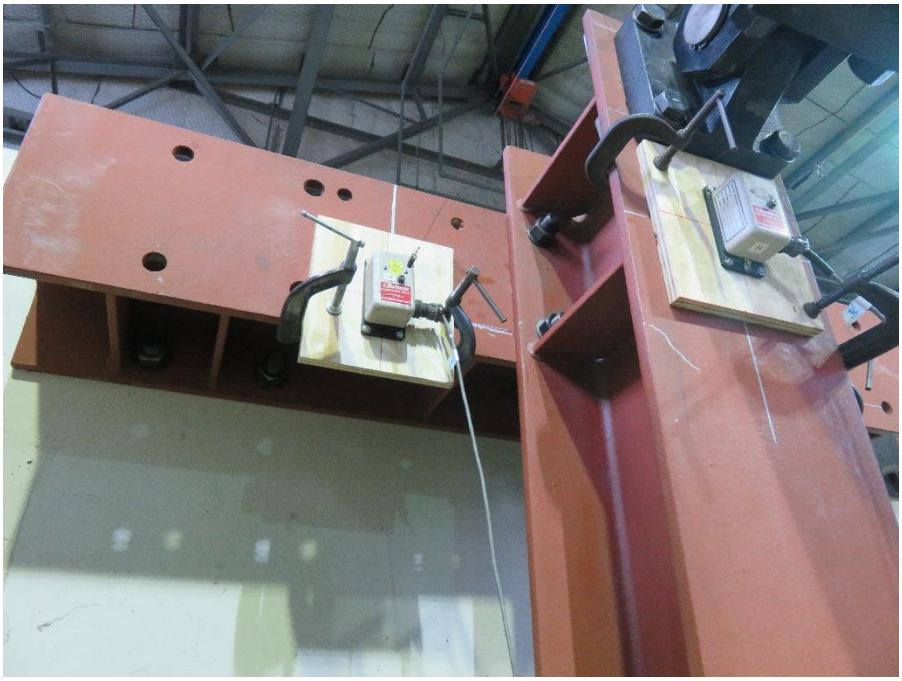

Figure 5.36: String Pods to Measure Lateral Displacements of an HMIP Specimen in the Ultimate Strength Testing at the Ferguson Structural Engineering Laboratory

5.3.3 Phased Array Ultrasonic Test (PAUT) Procedure to Characterize Cracks

Phased Array Ultrasonic Tests (PAUTs) have been conducted on every specimen tested in the Ferguson Structural Engineering Laboratory. Conventional ultrasonic tests (UTs) were initially performed by TxDOT on Specimens 33-3-12-TX-A1 and 33-3-12-TX-A2 used in the fatigue test at a stress range of 6 ksi. Crack length, but no crack depth data were obtained using UTs. Starting in mid-November of 2015 until the end of the project, tests had been performed by Reinhart & Associates, a nondestructive evaluation testing and engineering firm based in Austin, Texas. Reinhart & Associates developed a specific procedure to measure the length and depth of the cracks existed in the shaft-to-baseplate welded connections of the HMIP specimens of primary interest (Figures 5.37 to 5.39).

The crack lengths/depths were measured before the start of fatigue tests and periodically during the tests. Reinhart & Associates recorded the data from the ultrasonic tests and provided reports on the PAUTs. Samples of PAUT reports are shown in Figures 5.40 and 5.41. With the instruction of the research team from the University of Texas, Reinhart & Associates technicians also marked the beginning locations of the cracks, the ending locations of the cracks, and the length of the cracks on the HMIP specimens so that crack growth could be tracked throughout fatigue tests.

Figure 5.37: Hargang X-32 PAUT Instrument Used in Detecting Cracks in an HMIP Specimen

Figure 5.38: Sample of Crack Markings Indicating the Crack Locations, Lengths, and Depths Documented in a Fatigue Test

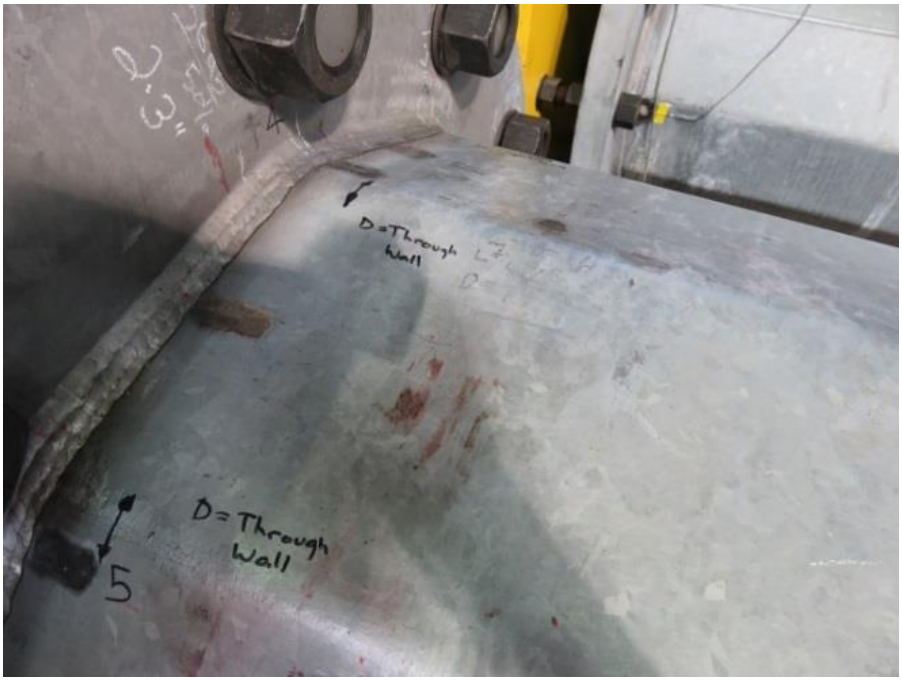

Figure 5.39: Sample of Crack Markings for a Specimen with Severe Cracking in a Fatigue Test

TABLE VI. PAUT sizing results in April 28, 2016 at FSEL.

POLE ID NUMBER	BEND NUMBER	LENGTH OF INDICATION	DEPTH OF INDICATION	DATE OF SCAN
A5	2	3.375"	0.071"	4/28/16
A5	1	2.125"	0.075"	4/28/16
A5	12	3.125"	0.075"	4/28/16
A5	11 (top)	3.375"	0.083"	4/28/16
A5	10	3.00"	0.051"	4/28/16
A5	9	0.50"	<.005"	4/28/16
A5	8	1.50"	<.005"	4/28/16
A6	8	1.735"	0.069"	4/28/16
A6	7	X	X	4/28/16
A6	6	X	X	4/28/16
A6	5 (top)	5.00"	0.117"	4/28/16
A6	4	3.125"	0.134"	4/28/16
A6	3	X	X	4/28/16
A6	2	X	X	4/28/16

Figure 5.40: Sample PAUT Results for Specimens 33-3-12-TX-A5 and 33-3-12-TX-A6 after 36.7 Million of Fatigue Cycles

TABLE VII. PAUT sizing results in July 14, 2016 at FSEL.

POLE ID NUMBER	BEND NUMBER	LENGTH OF INDICATION Before	After	DEPTH OF INDICATION	DATE OF SCAN
A5	1	1.125 "	1.0"	0.075"	7/14/16
A5	12	1.125 "	1.0"	0.075"	7/14/16
A5	11 (top)	1.375 "	2.0"	0.083"	7/14/16
A5	10	1.875 "	1.125"	0.051"	7/14/16
A5	9	X	0.5"	0.005"	7/14/16
A6	7	X	X	X	7/14/16
A6	6	X	X	X	7/14/16
A6	5 (top)	2.0" "	3.0"	0.117"	7/14/16
A6	4	1.5625 "	1.5625"	0.134"	7/14/16
A6	3	X	X	X	7/14/16

Figure 5.41: Sample PAUT Results for Specimens 33-3-12-TX-A5 and 33-3-12-TX-A6 after 54.9 Million of Fatigue Cycles

Crack-size data were used in the fatigue-testing program for several purposes. Most notably, this information was used before tests to determine which bend to be tested. The top bend was typically assigned to be the bend most critically cracked before the test commences.

This designation was made by analyzing PAUT results prior testing to see which bend had the longest and deepest cracks. Usually there was only one bend with significant cracking, but when there were multiple bends, the neighboring bends were also considered. In this situation, the bend with the most cracking between itself and its neighbors was deemed the top bend.

The procedure of testing the most cracked bend was done to capture the worst-case loading scenario and to obtain a lower bound on the S-N curve. The one exception to this procedure was the first fatigue test, in which one of the seam welds (bend 1) was placed on top and tested. It was initially believed that the seam-welded bends were weak due to the stress concentration, but the first test disproved this assumption. The first test lasted significantly longer than similar tests with a cracked bend on top, even those tested at a lower stress range. It showed that the measureable cracks were more critical than the presence of a seam weld.

Throughout each fatigue test, crack data, determined using the Phased Array Ultrasonic Tests, were recorded and analyzed to monitor crack growth. Results from these PAUTs conducted during each fatigue test are presented and discussed in Section 5.4.

Phased Array Ultrasonic Testing: Specimens of Secondary Interest

Due to their complex welded geometry, the external collar specimens posed a unique challenge for the detection of both crack length and crack depth using PAUTs. Further, since the initial crack propagation site for these specimens was unknown, researchers asked the Reinhart & Associates technicians to perform PAUTs at multiple locations. These locations were at the collar-to-baseplate weld and on each side of the collar-to-shaft fillet weld. Figure 5.42 below shows a technician performing a PAUT at collar side of the fillet weld. The other two locations are also highlighted in Figure 5.42.

Figure 5.42: Probe Locations in PAUTs Conducted on the Specimens of Secondary Interest

Figures 5.43, 5.44, and 5.45 show screen captures of the PAUT instrument during a phased array test. The figures were provided by Reinhart & Associates in their report to the Ferguson Structural Engineering Laboratory after their work was completed on Specimens 33-3-12-TXEC-A7 and 33-3-12-TXEC-A8. Each figure shows a screen capture from a PAUT conducted at each location discussed above.

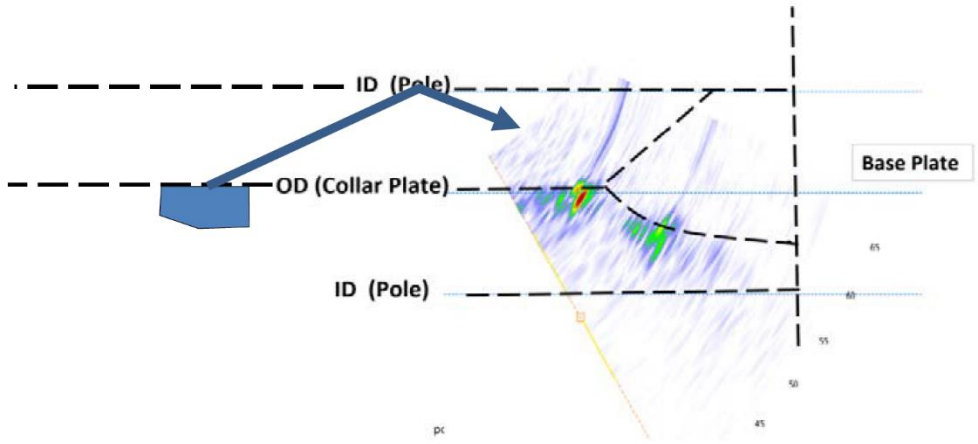

Figure 5.43: Scan of the Collar to Baseplate Weld

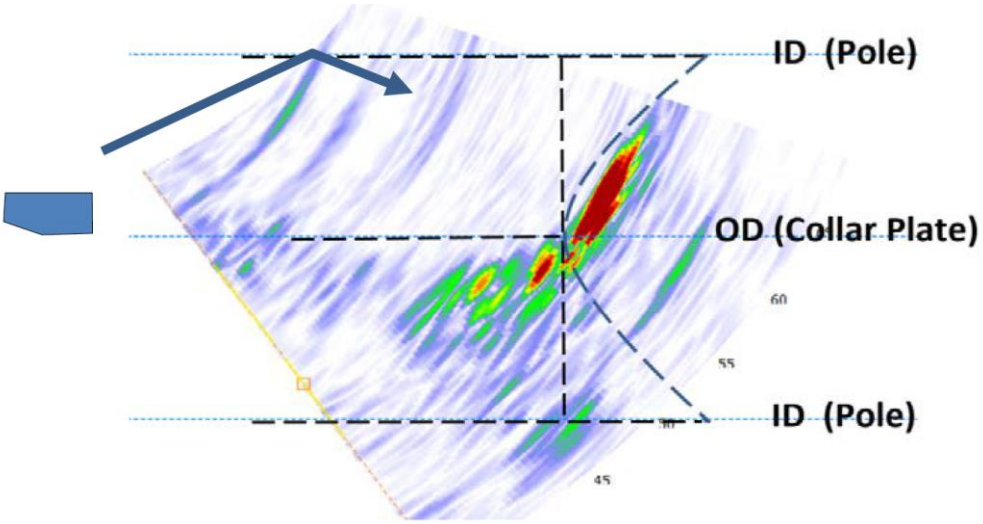

Figure 5.44: Scan of the Fillet Weld from the External Collar Side

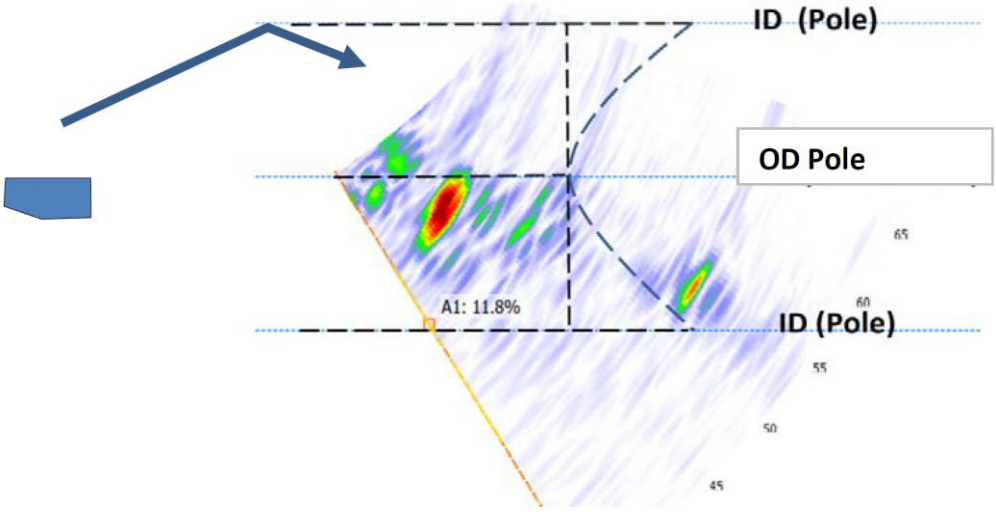

Figure 5.45: Scan of the Fillet Weld from the Shaft Side

Through their tests, the Reinhart & Associates technicians identified three bends on Specimen 33-3-12-TXEC-A7 that were cracked. The cracks were found in the fillet weld connecting the external collar to the shaft of the pole. These cracks were very small in size. While Reinhart & Associates technicians could identify the cracks, they could not determine any length or depth measurements. Screen captures from the PAUT instrument of these cracks can be seen in Figures 5.46, 5.47, and 5.48.

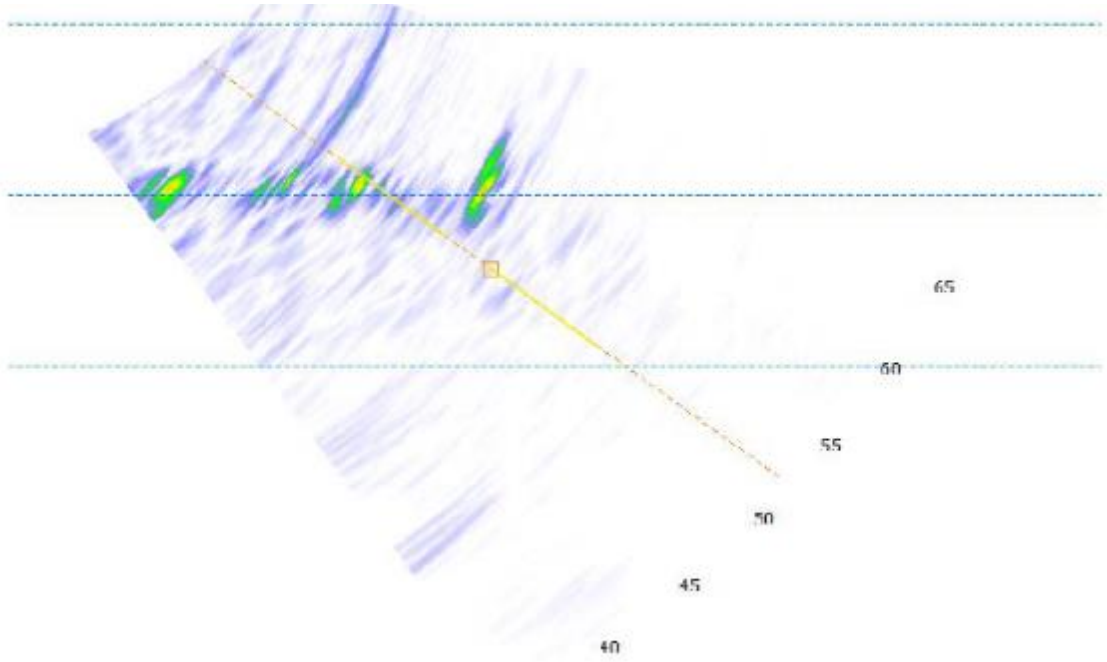

Figure 5.46: Cracks Found on Bend 2 of Specimen 33-3-12-TXEC-A7 while Scanning from the Collar Side

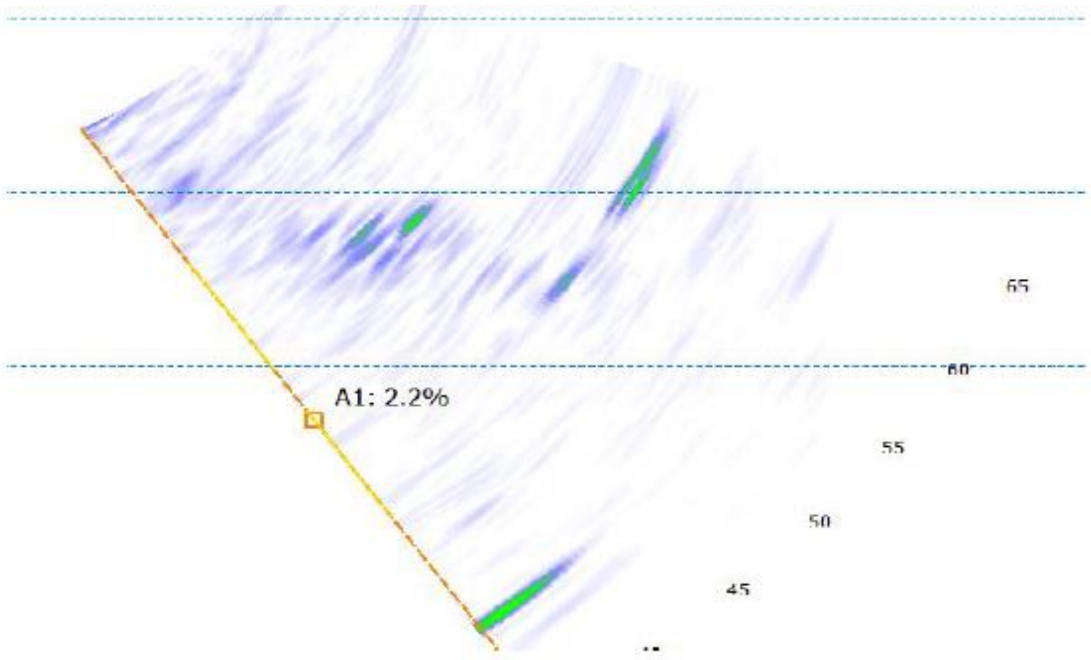

Figure 5.47: Cracks Found on Bend 9 of Specimen 33-3-12-TXEC-A7 while Scanning from the Collar Side

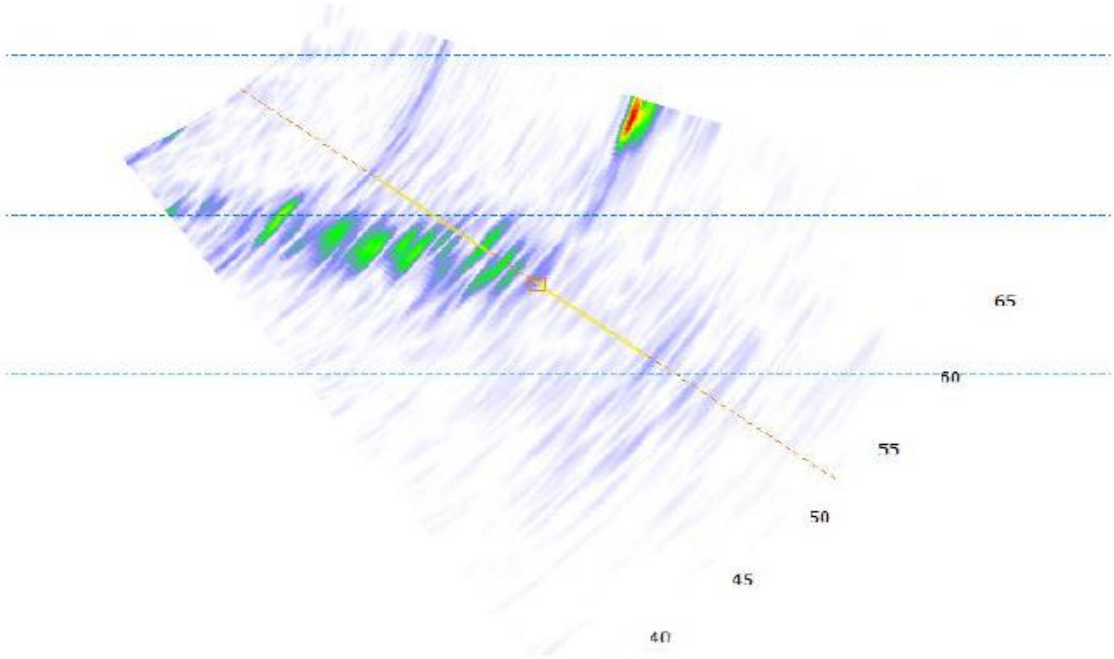

Figure 5.48: Cracks Found on Bend 9 of Specimen 33-3-12-TXEC-A7 while Scanning from the Collar Side

5.4 Fatigue Tests on HMIP Specimens – Test Results

5.4.1 Overview

As mentioned before, eight HMIP specimens were tested in this project. Six specimens designated as 33-3-12-TX-A1, 33-3-12-TX-A2, 33-3-12-TX-A3, 33-3-12-TX-A4, 33-3-12-TX-A5, and 33-3-12-TX-A6 were without ground sleeves (specimens of primary interest). The other two specimens, Specimens 33-3-12-TXEC-A7, and 33-3-12-TXEC-A8, were with ground sleeves (specimens of secondary interest). The fatigue tests were conducted on specimens of primary interest at stress ranges from 2 ksi to 6 ksi. Six data points were collected for the S-N curve, with one point coming from the fatigue test at 6-ksi stress range, three points coming from the ones conducted at 4-ksi stress range, one data point at 3 ksi, and one from a test at 2-ksi stress range. While these tests were running, Phased Array Ultrasonic Tests (PAUTs) were conducted at various intervals. As mentioned before, these tests allowed researchers to document the crack growth and provided a basis on which hypotheses could be made about the starting location and the direction of crack propagation.

In this section, results of fatigue tests in terms of number of cycles to failure are presented and discussed. Representative results from Phased Array Ultrasonic Tests (PAUTs) are further shown to document the progression of cracks, both in length and in depth, corresponding to fatigue cycles.

5.4.2 Fatigue Test 1 — Stress Range of 6 ksi: Specimens 33-3-12-TX-A1 and 33-3-12-TX-A2

The Specimens 33-3-12-TX-A1 and 33-3-12-TX-A2 were tested in the first fatigue test; test 1. These specimens were tested at the stress range of 6 ksi and at the mean stress of 6 ksi (minimum stress of 3 ksi and maximum stress of 9 ksi). The loading frequency was 0.5 Hz and 2.2 Hz. These specimens were fabricated with a full penetration welded connection and no external collar, as described in Section 5.2. The initial conditions in terms of the length and depth of the cracks existed in the shaft-to-baseplate welded connection of these cracked HMIP specimens were established at the beginning of the test. As a result of fatigue Test 1, one fatigue data point was obtained corresponding to the stress range of 6 ksi. This data point came from Specimen 33-3-12-TX-A1.

Results of Fatigue Test 1: Initial Conditions of the Tested Specimens

Prior to the fatigue Test 1, TxDOT technicians performed ultrasonic tests on the specimens to identify preexisting cracks. These tests showed that every bend had indications of initial cracking, with the exception of the bends that contained the longitudinal seam welds. Despite this finding, bend 1, a seam-welded bend, was designated as the top bend.

The initial crack measurements for Specimens 33-3-12-TX-A1 and 33-3-12-TX-A2 can be seen in Figure 5.49. While the depths of these cracks were not measured, their lengths were measured and recorded for future comparisons. Note that each of these specimens had approximately 10-percent of their 105-inch perimeters cracked before testing began.

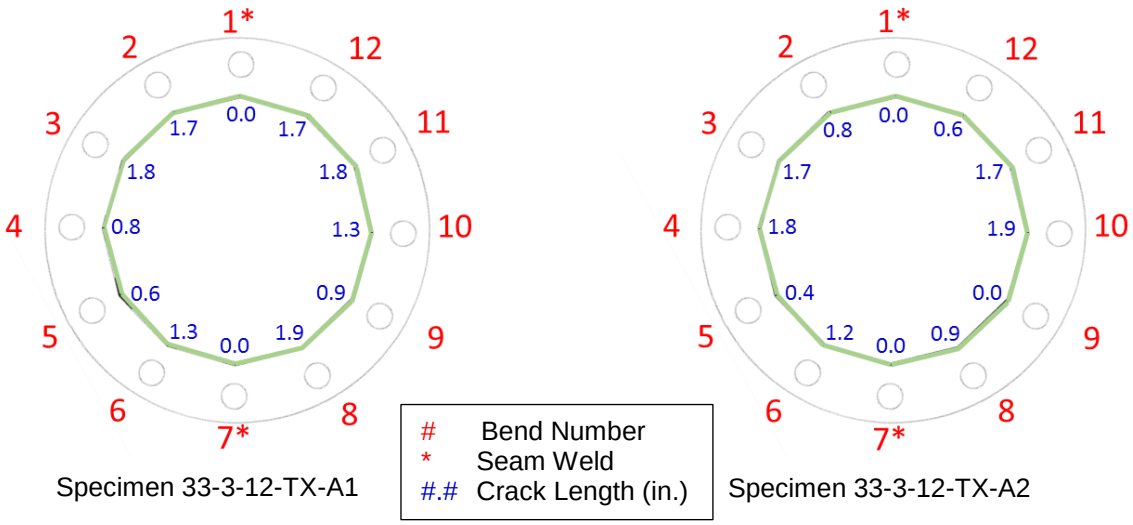

Figure 5.49: Specimens 33-3-12-TX-A1 and 33-3-12-TX-A2: Initial Cracks

Results of Fatigue Test 1: Observations

Figures 5.50 and 5.51 represent the state of cracks on the three top bends of Specimen 33-3-12-TX-A1 tested in Test 1 under the stress range of 6 ksi. As seen in these figures, severe cracking occurred at the end of Test 1; resulting in through-thickness cracks over more that 40% of the connection length between the base plate and the shaft. As further indicated in Figure 5.52, despite being at a lower stress range of 5 ksi, the adjacent bends (Bends 2 and 12) to the top bend failed first. The cracks propagated from these two bends towards the top bend (Bend 1) at later stages of the fatigue test and ultimately resulted in the failure of Bend 1 (the tested bend). This mode of failure was probably due to the fact that Bend 1 was crack free at the beginning of the Test 1 (Figure 5.49).

Figure 5.50: Specimen 33-3-12-TX-A1 following the Fatigue Test 1 at the Stress Range of 6 ksi (Fatigue Cracks after 19.4 Million Cycles)

Figure 5.51: Specimen 33-3-12-TX-A1 following the Fatigue Test 1 at the Stress Range of 6 ksi (Fatigue Cracks at Bend 1 [Tested Bend] after 19.4 Million Cycles)

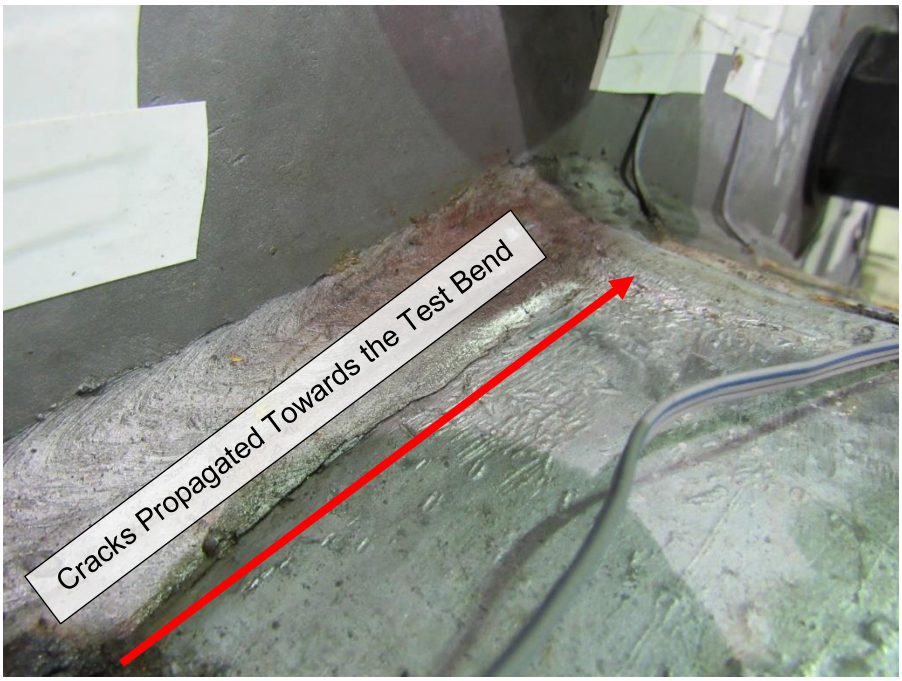

Figure 5.52: Specimen 33-3-12-TX-A2 following the Fatigue Test 1 at the Stress Range of 6 ksi (Fatigue-Crack Propagation after 19.4 Million Cycles)

Results of Fatigue Test 1: Crack Growth Information

Following the initial ultrasonic measurements of the crack state, Specimens 33-3-12-TX-A1 and 33-3-12-TX-A2 were periodically examined using ultrasonic testing to monitor the progression of cracks throughout the fatigue test, and to provide data on the increase in crack length/depth as a function of number of fatigue loading cycles. The successive ultrasonic test data for Specimens 33-3-12-TX-A1 and 33-3-12-TX-A2 can be seen below in Figures 5.53 through 5.57.

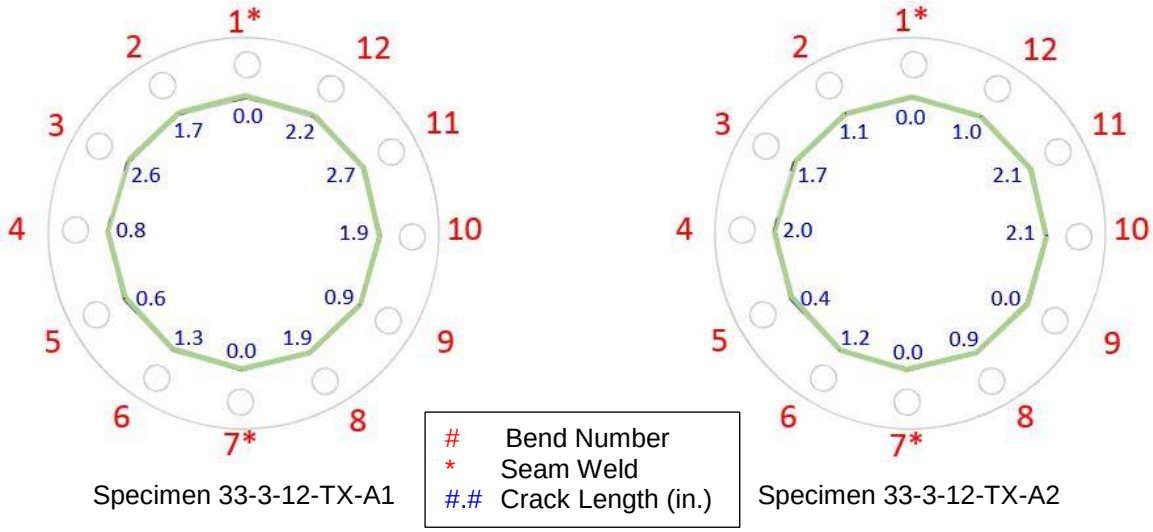

Figure 5.53: Specimens 33-3-12-TX-A1 and 33-3-12-TX-A2: Cracks after 1.6 Million Fatigue Cycles

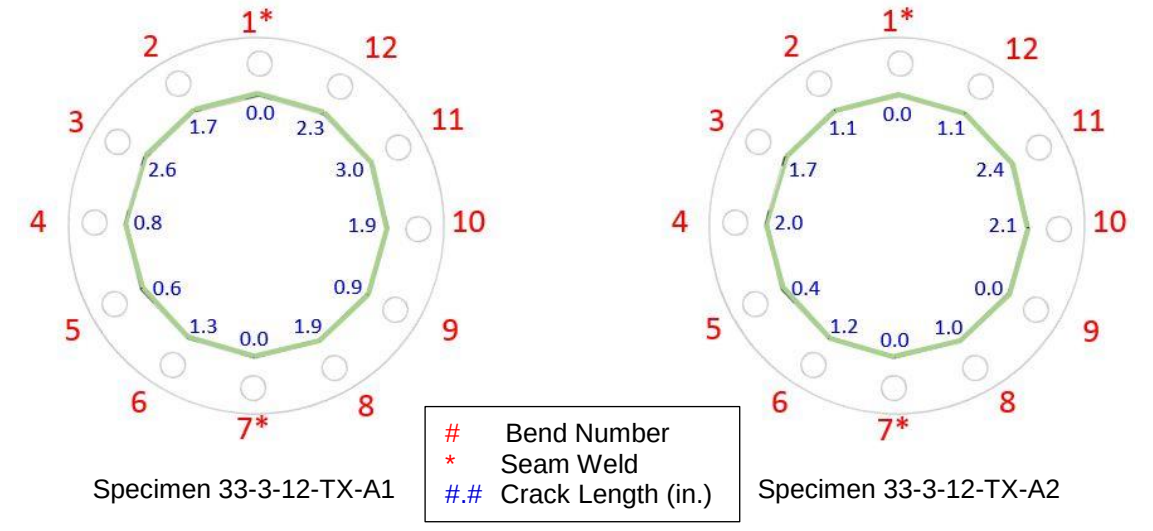

Figure 5.54: Specimens 33-3-12-TX-A1 and 33-3-12-TX-A2: Cracks after 4.0 Million Fatigue Cycles

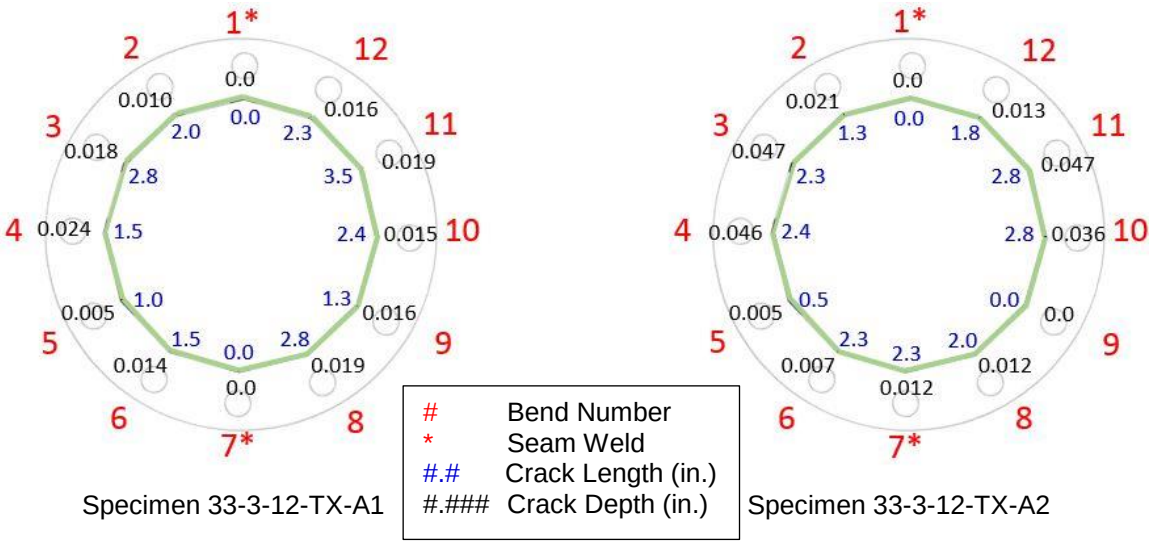

Figure 5.55: Specimens 33-3-12-TX-A1 and 33-3-12-TX-A2: Cracks after 11.9 Million Fatigue Cycles

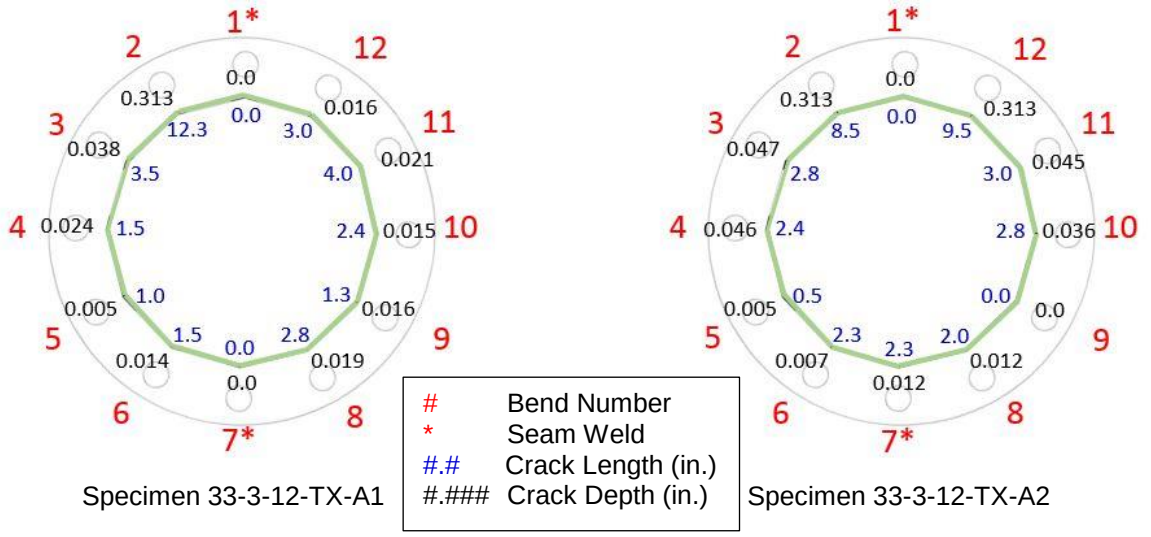

Figure 5.56: Specimens 33-3-12-TX-A1 and 33-3-12-TX-A2: Cracks after 16.8 Million Fatigue Cycles

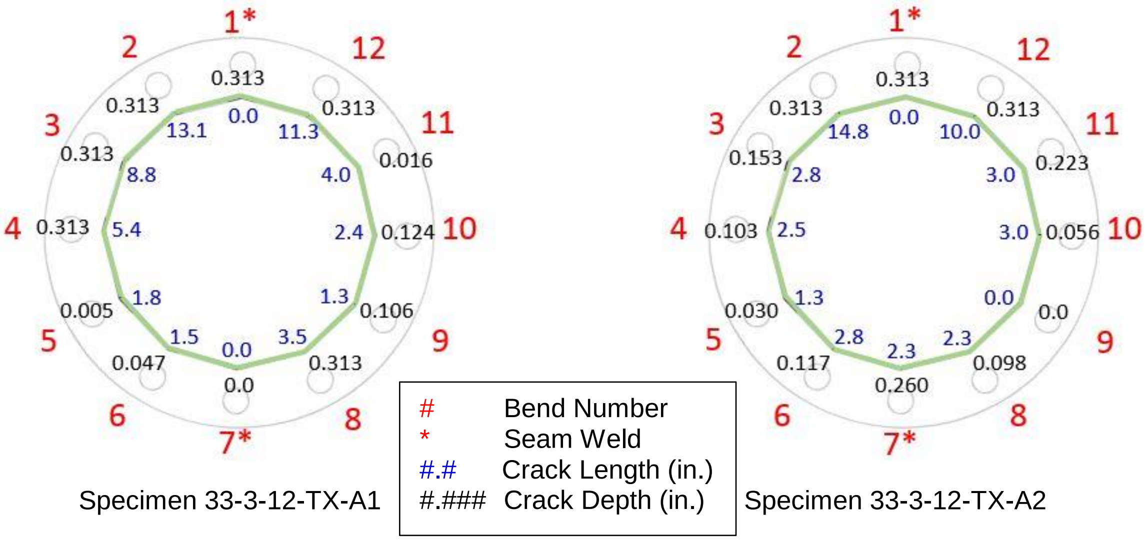

Figure 5.57: Specimens 33-3-12-TX-A1 and 33-3-12-TX-A2: Cracks after 19.4 Million Fatigue Cycles

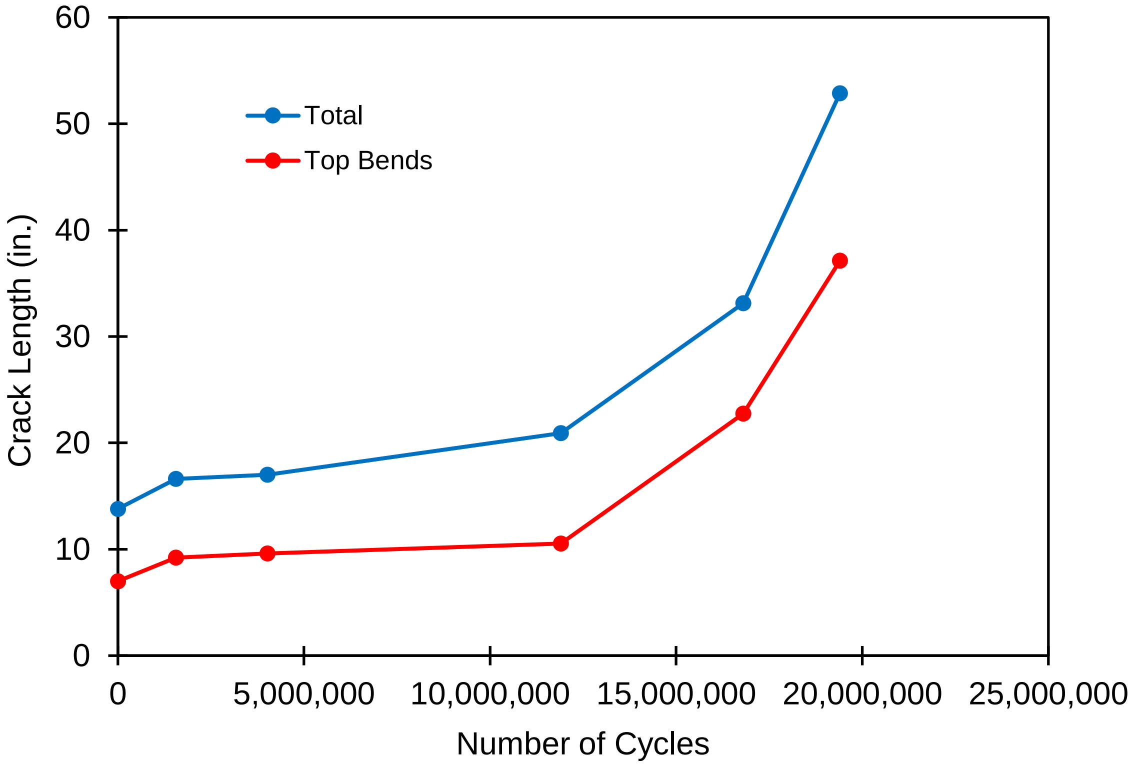

Figure 5.58: Crack Growth as a Function of Number of Cycles for Specimen 33-3-12-TX-A1

5.4.3 Fatigue Test 2 — Stress Range of 3 ksi: Specimens 33-3-12-TX-A5 and 33-3-12-TX-A6

The second fatigue experiment was conducted on Specimens 33-3-12-TX-A5 and 33-3-12-TX-A6. The specimens were tested at the stress range of 3 ksi and at the mean stress of 6 ksi

(minimum stress of 4.5 ksi and maximum stress of 7.5 ksi). The loading frequency was 3.5 Hz. The initial conditions in terms of the length and depth of the cracks existed in the shaft-to-baseplate welded connection of these cracked HMIP specimens were established at the beginning of the test. As a result of fatigue Test 2, one fatigue data point was obtained corresponding to the stress range of 3 ksi. This data point came from Specimen 33-3-12-TX-A6.

Results of Fatigue Test 2: Initial Conditions of the Tested Specimens

As with all other experiments, Test 2 began with the PAUTs of the specimens. These phased array tests marked the research team's first work with Reinhart & Associates, a nondestructive testing company based in Austin, Texas. The initial crack measurements for Specimens 33-3-12-TX-A5 and 33-3-12-TX-A6 can be seen in Figure 5.59.

The PAUT results were used to determine the top bend for each specimen. Unlike the fatigue test 1, the same top bend was not used for each specimen. For Specimen 33-3-12-TX-A5, the top bend was designated as bend 11. The top bend for Specimen 33-3-12-TX-A6 was selected to be bend 5. These selections were made based upon the initial PAUT readings shown in Figure 5.59. Notice that while the top bends were not the same, they were 180-degrees removed from one another. This left the seam welds in the same position for each specimen, meaning that their effect on each specimen's fatigue resistance were the same. Despite being arbitrarily labeled differently, the top bends of these specimens were subjected to similar external conditions. The same, however, cannot be said about the internal conditions of the specimens. As Figure 5.59 shows, Specimen 33-3-12-TX-A5 was notably more cracked than Specimen 33-3-12-TX-A6. Specimen 33-3-12-TX-A5 had cracks on nearly 25-percent of its perimeter at the beginning of the experiment. Specimen 33-3-12-TX-A6, on the other hand, only had about 8-percent of its perimeter cracked.

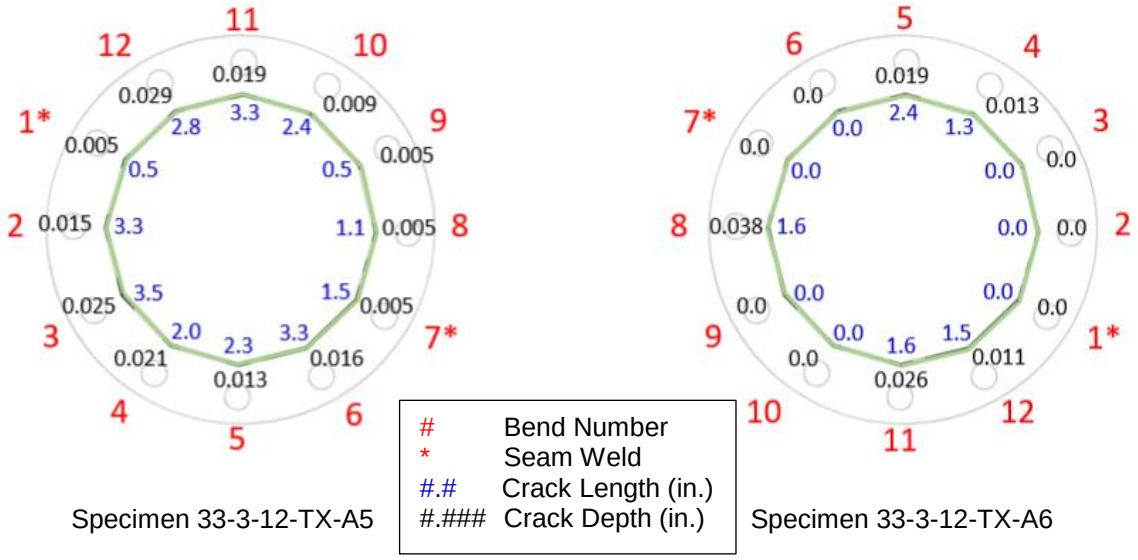

Figure 5.59: Specimens 33-3-12-TX-A5 and 33-3-12-TX-A6: Initial Cracks

Results of Fatigue Test 2: Observations

Figures 5.60 through 5.62 represent the state of cracks on the three top bends of Specimen 33-3-12-TX-A6 tested in Test 2 under the stress range of 3 ksi. As seen in these figures, sever cracking occurred at the end of Test 2; resulting in through-thickness cracks over more that 20% of the connection length between the base plate and the shaft. The top bend (Bend 5) failed first in Test 2 and the cracks propagated from this bend towards the two adjacent bends (Bends 4 and 6) at later stages of the fatigue test. A very important observation to make from Figures 5.60 through 5.62 is that when cracks approached irregularities on the weld path (at the shaft-to-baseplate weld toe), they started to propagate in the shaft away from the weld path. When cracks started to propagate in the shaft, the rate of change in their length increased very rapidly causing a very fast fatigue failure.

Figure 5.60: Specimen 33-3-12-TX-A6 following the Fatigue Test 2 at the Stress Range of 3 ksi (Fatigue Cracks after 169.0 Million Cycles)

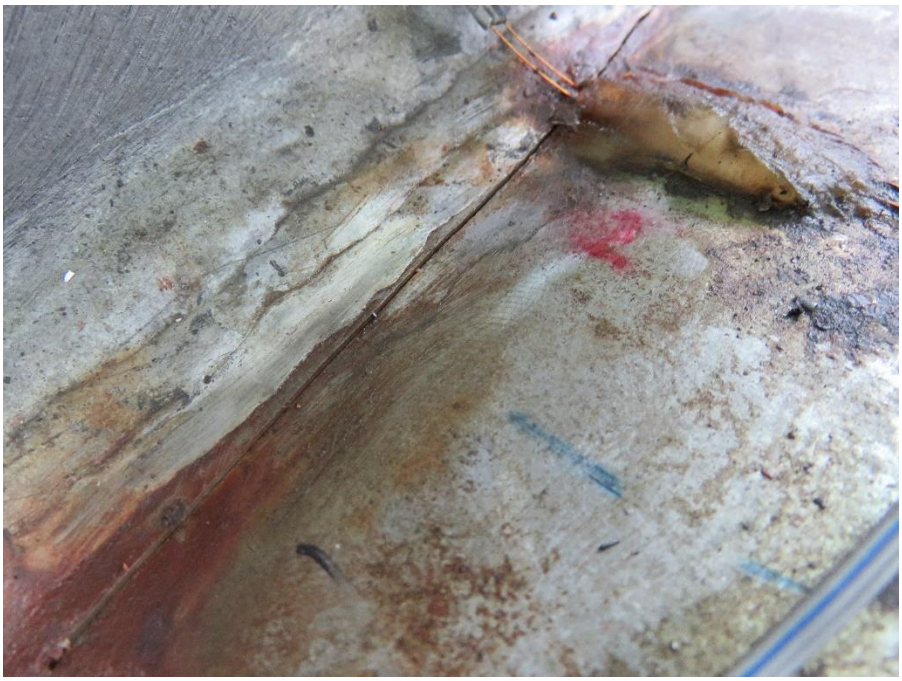

Figure 5.61: Specimen 33-3-12-TX-A6 following the Fatigue Test 2 at the Stress Range of 3 ksi (Fatigue Cracks Close to Bend 5 [Flat 5-6] after 169.0 Million Cycles)

Figure 5.62: Specimen 33-3-12-TX-A6 following the Fatigue Test 2 at the Stress Range of 3 ksi (Fatigue Cracks Close to Bend 5 [Flat 4-5] after 169.0 Million Cycles)

Results of Fatigue Test 2: Crack Growth Information

Following the initial ultrasonic measurements of the crack state, Specimens 33-3-12-TX-A5 and 33-3-12-TX-A6 were periodically examined using ultrasonic testing to monitor the progression of cracks throughout the fatigue test, and to provide data on the increase in crack length/depth as a function of number of fatigue loading cycles. The successive ultrasonic test data for Specimens 33-3-12-TX-A5 and 33-3-12-TX-A6 can be seen below in Figures 5.63 through 5.71. It should be noted that, at some point throughout the test, cracks stopped increasing in length and just propagated through the thickness of the shaft. This is unique under the conditions of small stress ranges like 3 ksi in Test 2. This behavior of cracks makes their in-service detections very challenging.

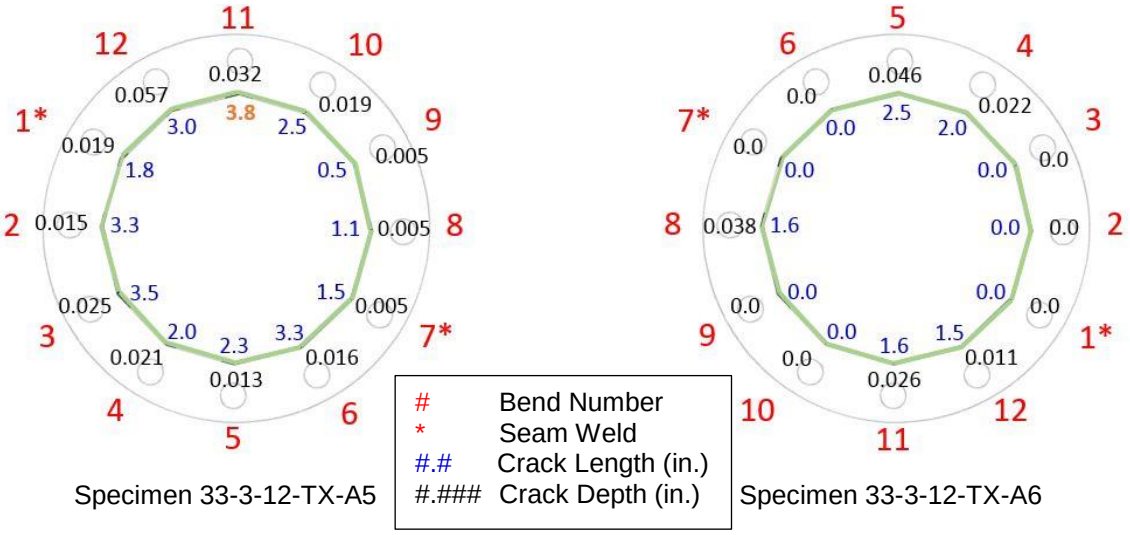

Figure 5.63: Specimens 33-3-12-TX-A5 and 33-3-12-TX-A6: Cracks after 4.4 Million Fatigue Cycles

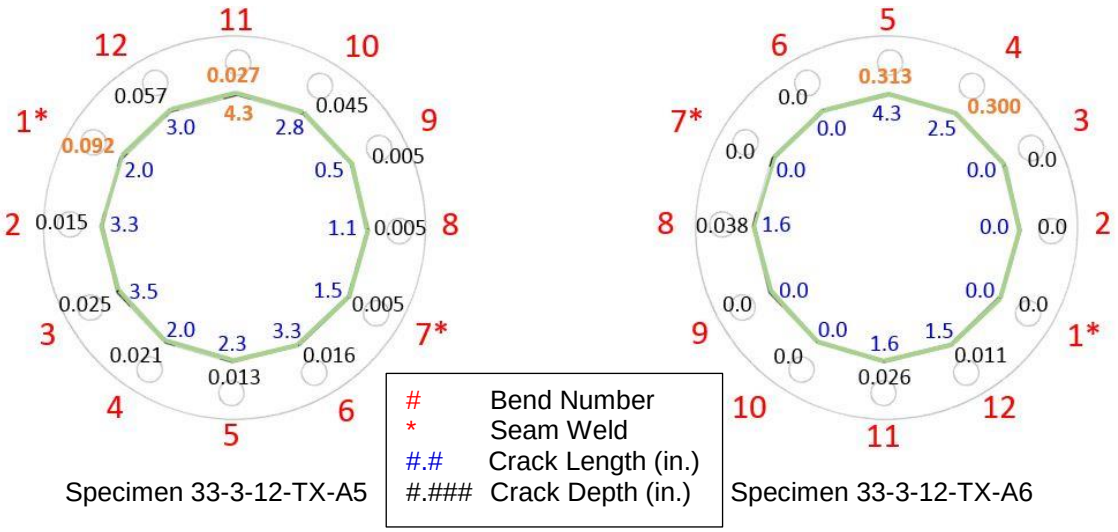

Figure 5.64: Specimens 33-3-12-TX-A5 and 33-3-12-TX-A6: Cracks after 7.8 Million Fatigue Cycles

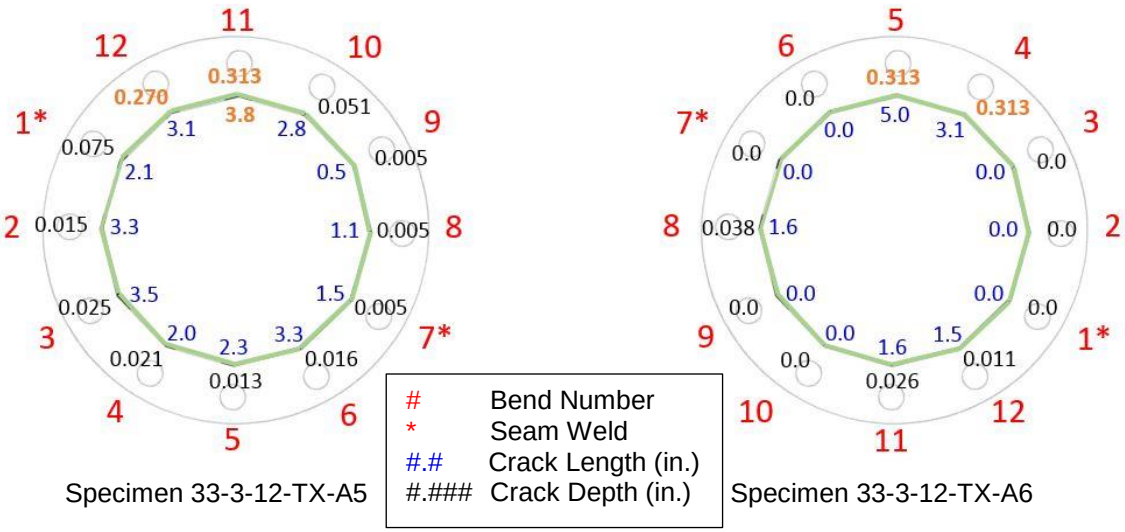

Figure 5.65: Specimens 33-3-12-TX-A5 and 33-3-12-TX-A6: Cracks after 16.8 Million Fatigue Cycles

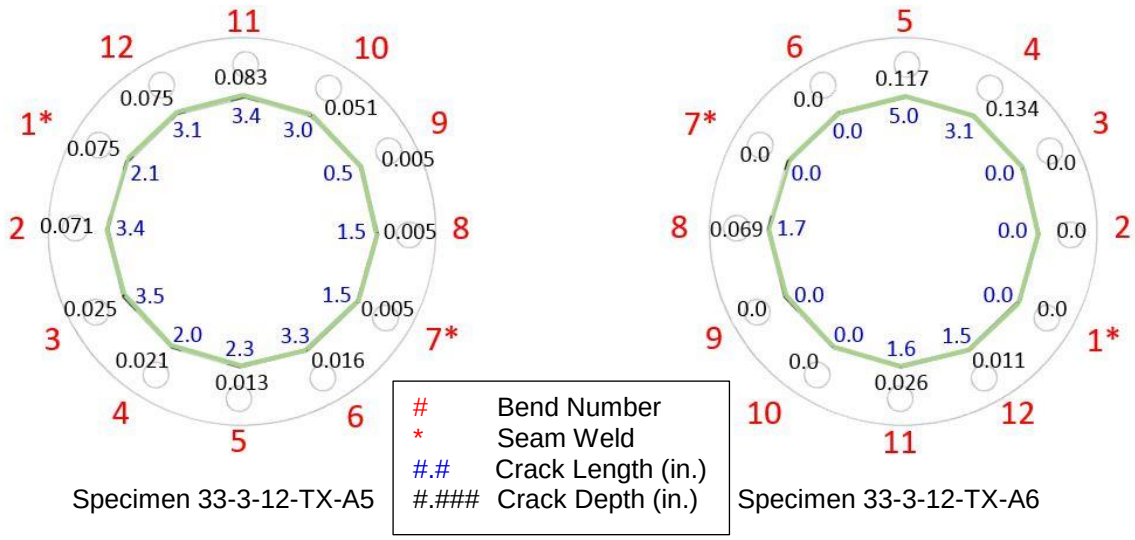

Figure 5.66: Specimens 33-3-12-TX-A5 and 33-3-12-TX-A6: Cracks after 37.7 Million Fatigue Cycles

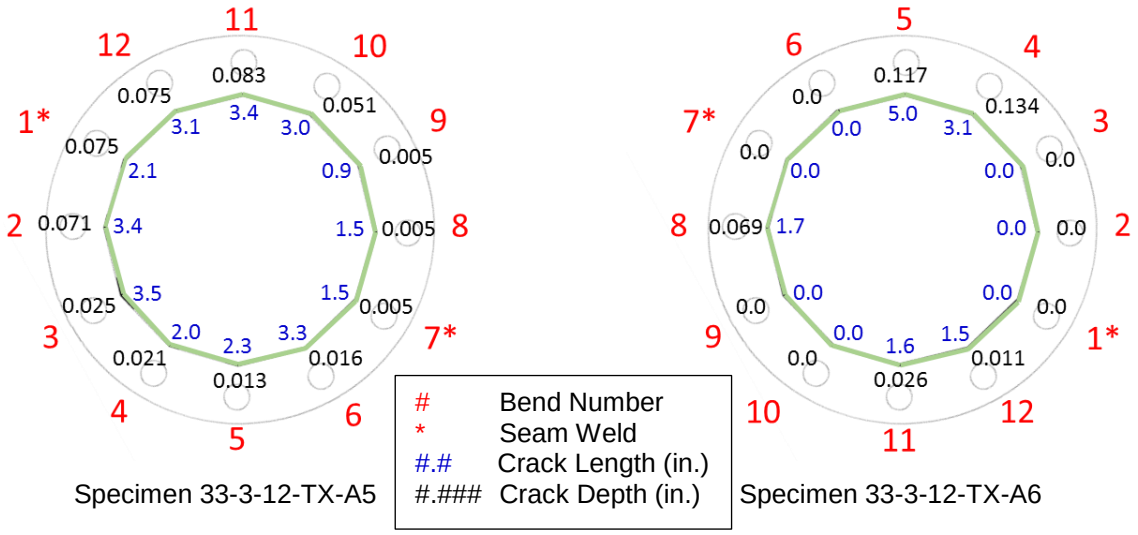

Figure 5.67: Specimens 33-3-12-TX-A5 and 33-3-12-TX-A6: Cracks after 54.7 Million Fatigue Cycles

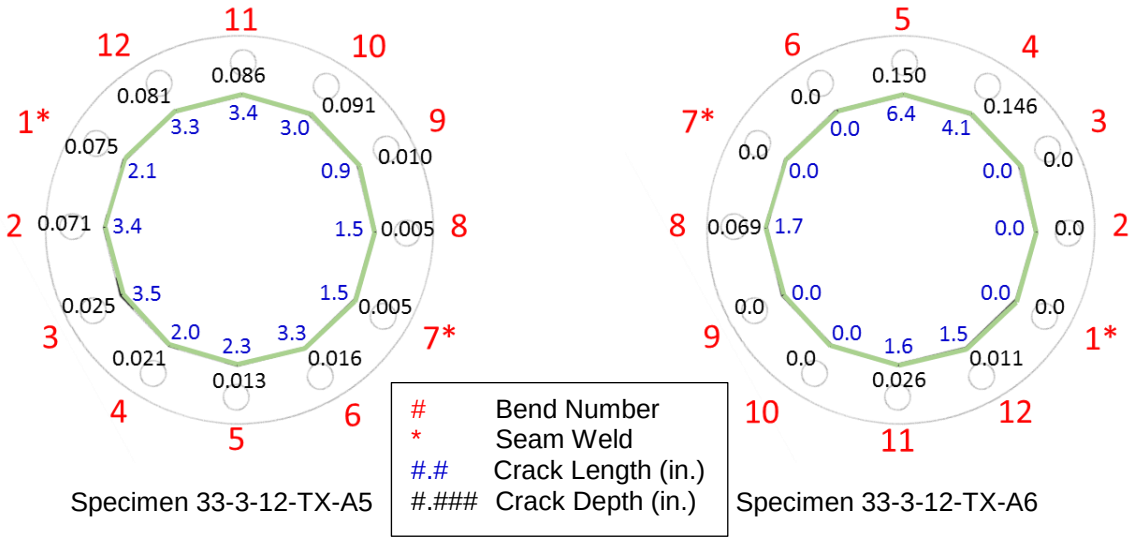

Figure 5.68: Specimens 33-3-12-TX-A5 and 33-3-12-TX-A6: Cracks after 79.2 Million Fatigue Cycles

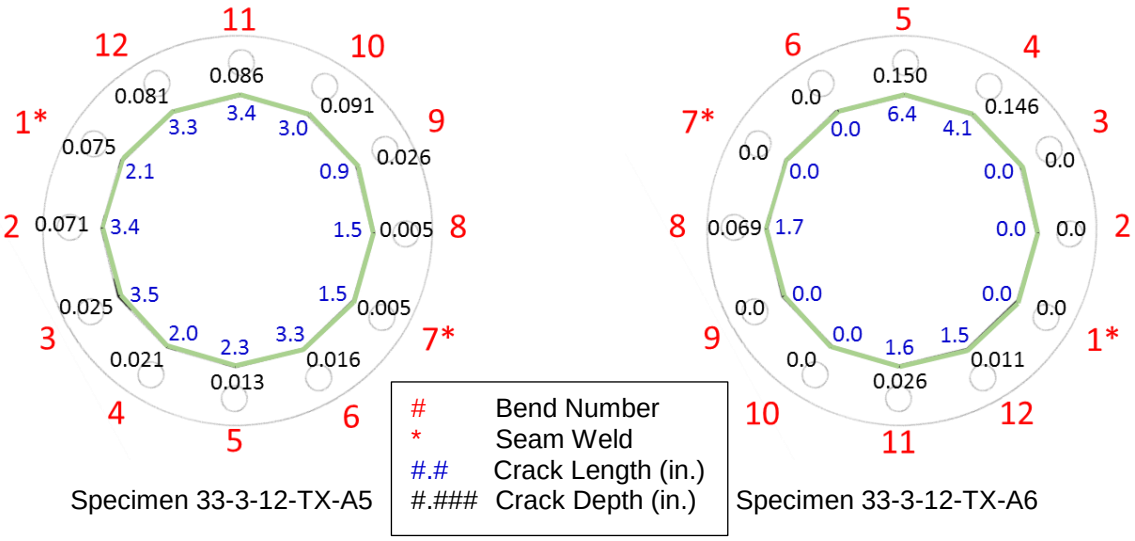

Figure 5.69: Specimens 33-3-12-TX-A5 and 33-3-12-TX-A6: Cracks after 94.1 Million Fatigue Cycles

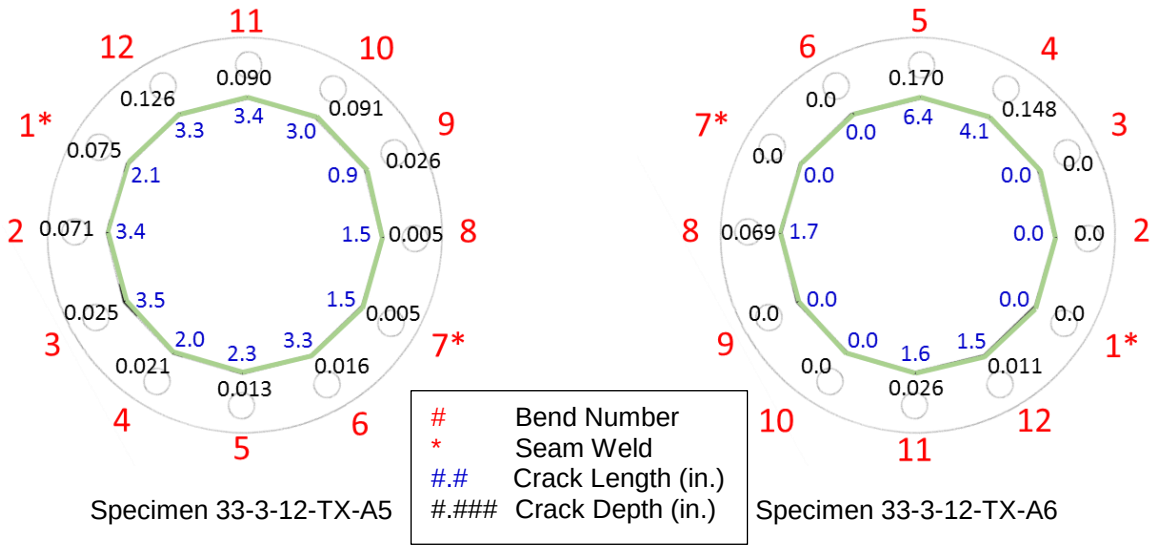

Figure 5.70: Specimens 33-3-12-TX-A5 and 33-3-12-TX-A6: Cracks after 129.7 Million Fatigue Cycles

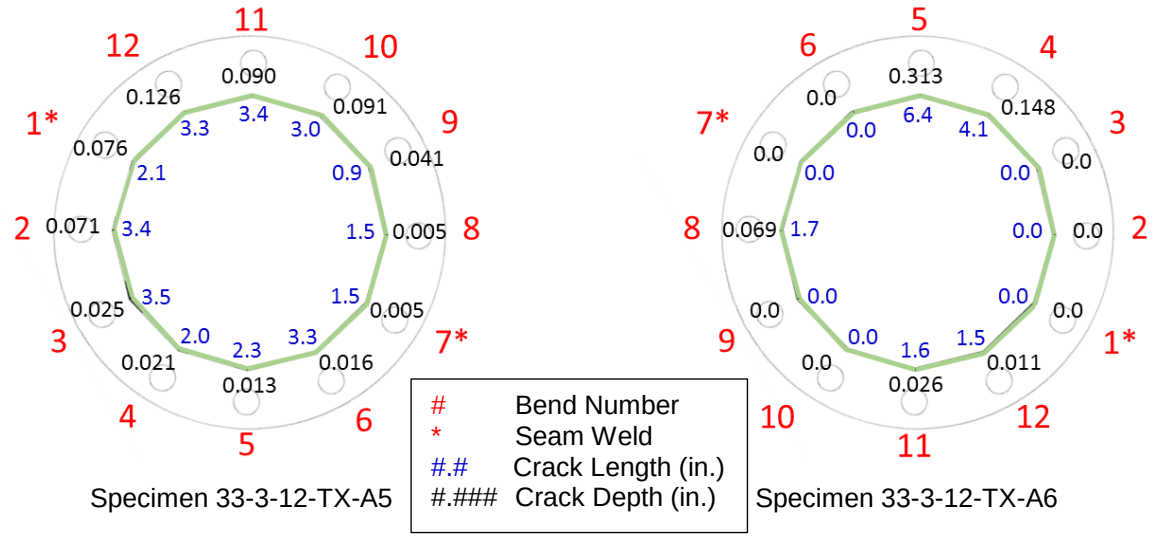

Figure 5.71: Specimens 33-3-12-TX-A5 and 33-3-12-TX-A6: Cracks after 148.9 Million Fatigue Cycles

Note that a few anomalies are bolded in orange text in Figures 5.63 through 5.71. After examining trends in the PAUT data for Specimens 33-3-12-TX-A5 and 33-3-12-TX-A6 across multiple tests, some measurements were determined to be anomalies. Through discussions with Reinhart and Associates technicians, it was determined that an error was likely made for these measurements.

5.4.4 Fatigue Test 3 — Stress Range of 4 ksi: Specimens 33-3-12-TX-A3 and 33-3-12-TX-A4

The third experiment of this research program was run on Specimens 33-3-12-TX-A3 and 33-3-12-TX-A4. These specimens were tested at the stress range of 4 ksi and at the mean stress of 6 ksi (minimum stress of 4 ksi and maximum stress of 8 ksi). The loading frequency was 2.7

Hz. These specimens were fabricated with a full penetration welded connection and no external collar, as described in Section 5.2. The initial conditions in terms of the length and depth of the cracks existed in the shaft-to-baseplate welded connection of these cracked HMIP specimens were established at the beginning of the test. As a result of fatigue Test 3, one fatigue data point was obtained corresponding to the stress range of 4 ksi. This data came from Specimen 33-3-12-TX-A4.

Results of Fatigue Test 3: Initial Conditions of the Tested Specimens

Prior to the fatigue Test 3, PAUTs were performed on the specimens to identify preexisting cracks. The initial crack measurements for Specimen 33-3-12-TX-A4 can be seen in Figure 5.72. These tests showed that every bend had indications of initial cracking, with the exception of the bend 10. Further, as seen in Figure 5.72, before testing commenced, Specimen 33-3-12-TX-A4 had nearly 16-percent of its perimeter cracked.

Based on the initial PAUT results, shown in Figure 5.72, it was decided to designate bend 4 as the top bend for this test. This bend was chosen because it was the most severely cracked (in terms of crack depth) before testing began.

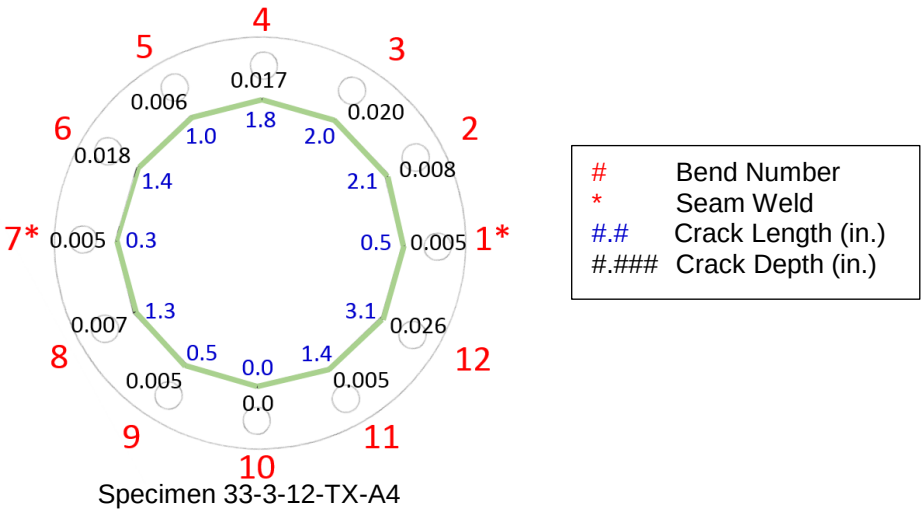

Figure 5.72: Specimen 33-3-12-TX-A4: Initial Cracks at the Beginning of Test 3

Results of Fatigue Test 3: Observations

Test 3 was completed after approximately one month of fatigue tests. Specimen 33-3-12-TX-A4 was deemed to have failed after it had developed sufficient cracking to reduce its stiffness by 10 percent. This reduction in stiffness occurred at 2.6 million cycles. The test was allowed to run to 3.8 million cycles before it was stopped. At that point, the stress range at the monitoring strain gauge dropped to 0 ksi. Pictures of Specimen 33-3-12-TX-A4 after failure can

be seen in Figures 5.73 and 5.74. At this point, cracks in the top bends had coalesced to form a nearly 31-inch long crack.

Figure 5.73: Specimen 33-3-12-TX-A4 following the Fatigue Test 3 at the Stress Range of 4 ksi (Fatigue Cracks after 3.8 Million Cycles)

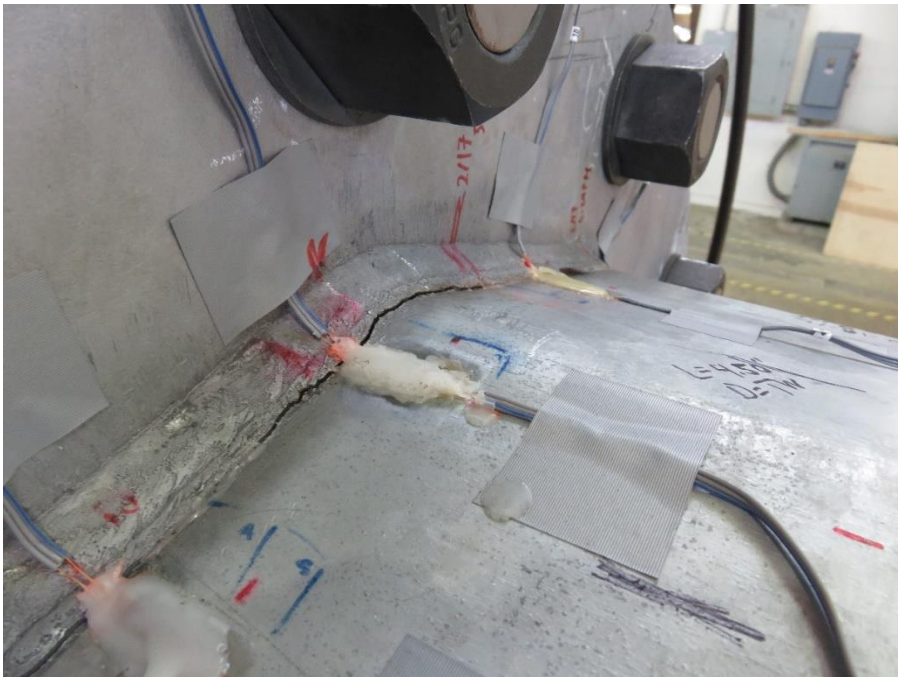

Figure 5.74: Severe Cracking on Bend 4 of the Specimen 33-3-12-TX-A4 following the Fatigue Test 3 at the Stress Range of 4 ksi (Fatigue Cracks after 3.8 Million Cycles)

Following the conclusion of Test 3, Specimen 33-3-12-TX-A4 was removed from the testing setup. It was then flipped 180-degrees and re-attached to the testing frame. Testing was then resumed as test 4.

Results of Fatigue Test 3: Crack Growth Information

Following the initial ultrasonic measurements of the crack state, Specimen 33-3-12-TX-A3 and 33-3-12-TX-A4 were periodically examined using ultrasonic testing to monitor the progression of cracks throughout the fatigue test, and to provide data on the increase in crack length/depth as a function of the number of fatigue loading cycles. The successive ultrasonic test data for Specimen 33-3-12-TX-A4 can be seen below in Figures 5.75 and 5.76.

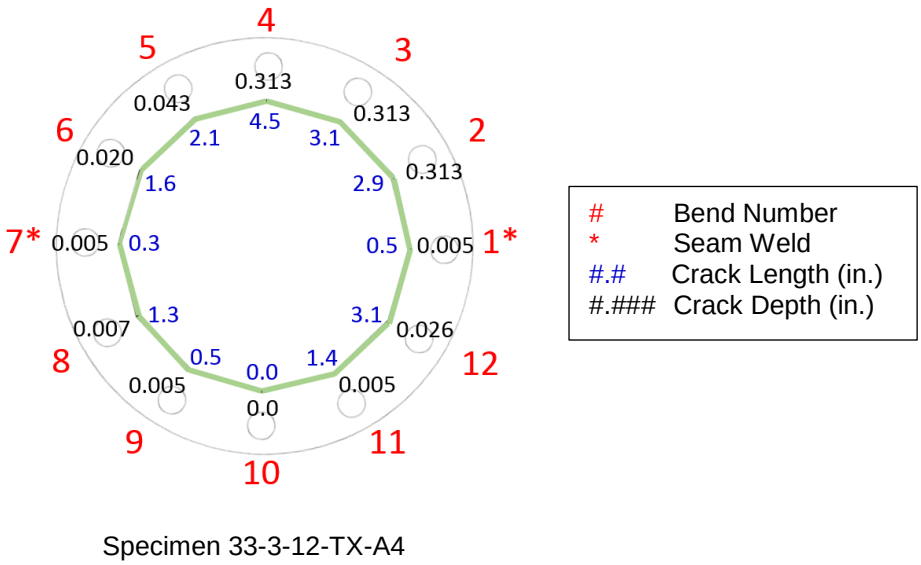

Figure 5.75: Specimen 33-3-12-TX-A4: Cracks after 1.7 Million Fatigue Cycles

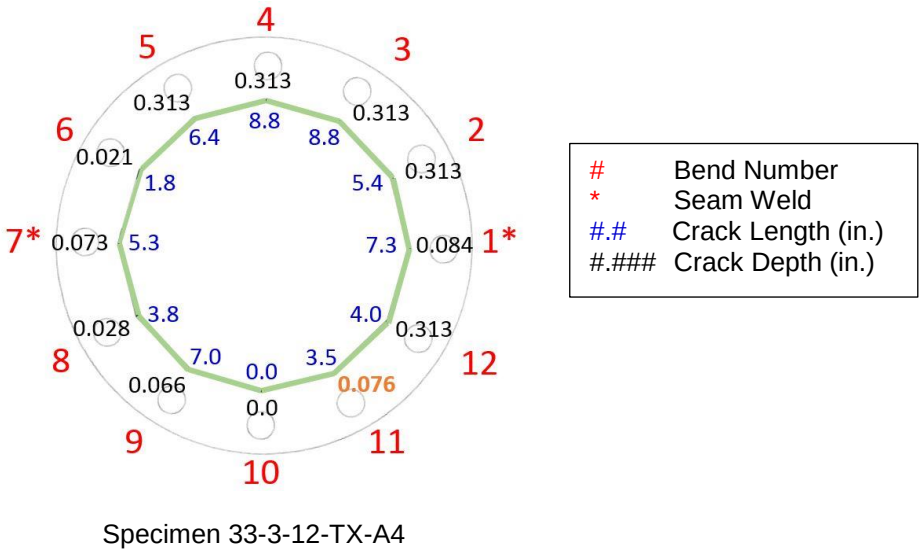

Figure 5.76: Specimen 33-3-12-TX-A4: Cracks after 3.8 Million Fatigue Cycles

5.4.5 Fatigue Test 4 — Stress Range of 4 ksi: Specimens 33-3-12-TX-A3 and 33-3-12-TX-A4

The forth fatigue test was run on Specimens 33-3-12-TX-A3 and 33-3-12-TX-A4. These specimens were tested at the stress range of 4 ksi and at the mean stress of 6 ksi (minimum stress of 4 ksi and maximum stress of 8 ksi). The loading frequency was 2.7 Hz. These specimens were fabricated with a full penetration welded connection and no external collar, as described in Section 5.2. The initial conditions in terms of the length and depth of the cracks existed in the shaft-to-baseplate welded connection of these cracked HMIP specimens were established at the

beginning of the test. As a result of fatigue Test 4, one fatigue data point was obtained corresponding to the stress range of 4 ksi. This data came from Specimen 33-3-12-TX-A3.

Results of Fatigue Test 4: Initial Conditions of the Tested Specimens

Prior to the fatigue Tests 3 and 4, PAUTs were performed on the specimens to identify preexisting cracks. The initial crack measurements for Specimen 33-3-12-TX-A3 can be seen in Figure 5.77. These tests showed that every bend had indications of initial cracking, with the exception of bend 7. Further, as seen in Figure 5.77, before testing commenced, Specimen 33-3-12-TX-A4 had nearly 16-percent of its perimeter cracked.

Based on the initial PAUT results, shown in Figure 5.77, it was decided to designate bend 4 as the top bend for this test. This bend was chosen because it was the most severely cracked (in terms of crack depth) before testing began.

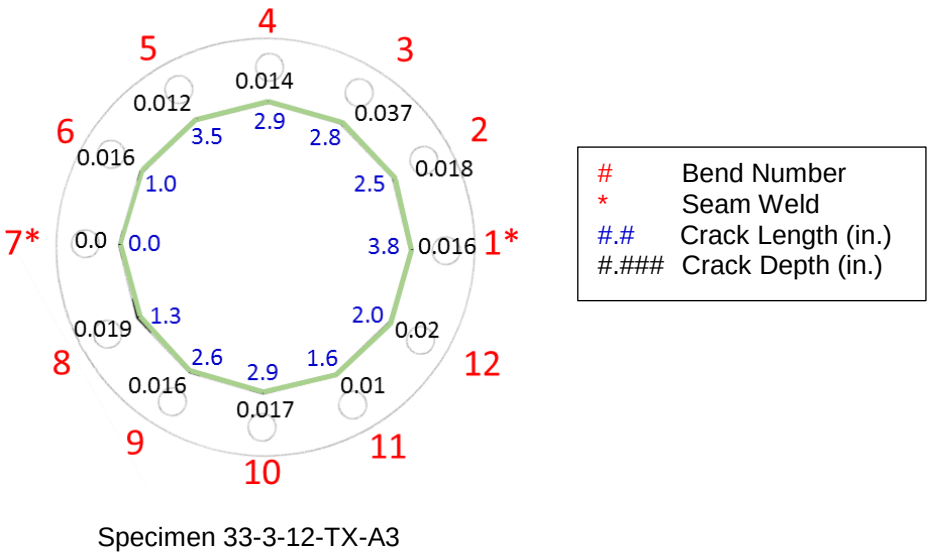

Figure 5.77: Specimen 33-3-12-TX-A3: Initial Cracks at the Beginning of Test 3

Results of Fatigue Test 4: Observations

A picture of Specimen 33-3-12-TX-A3 after failure in Test 4 is shown in Figure 5.78. Specimen 33-3-12-TX-A3 was deemed to have failed after it had developed sufficient cracking to reduce its stiffness by 10 percent. This reduction in stiffness occurred at 4.1 million cycles. The test was allowed to run to 5.5 million cycles before it was stopped. At that point, the stress range at the monitoring strain gauge dropped to 0 ksi.

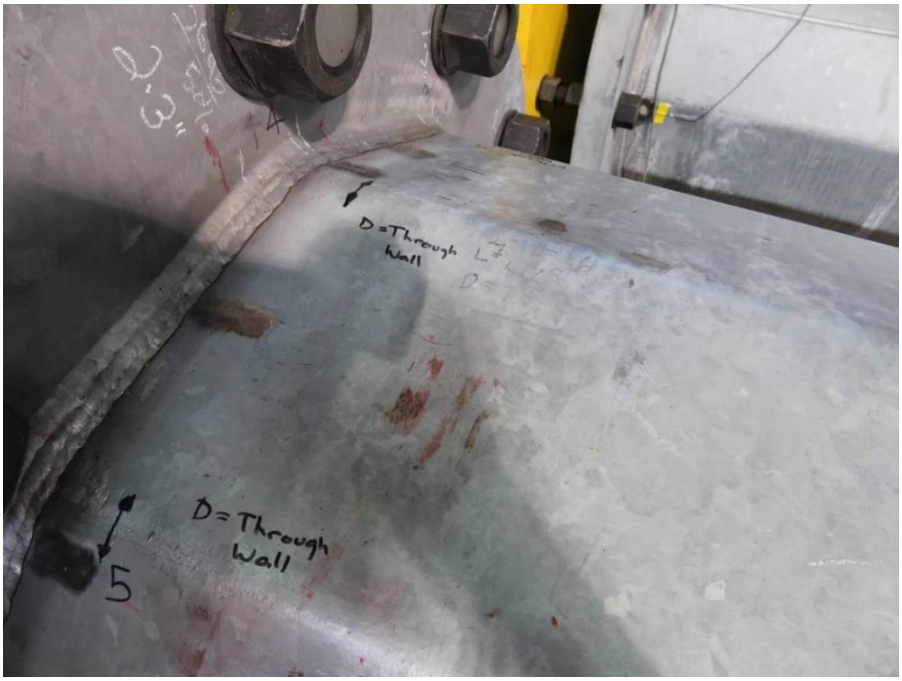

Figure 5.78: Specimen 33-3-12-TX-A3 following the Fatigue Test 4 at the Stress Range of 4 ksi (Fatigue Cracks after 5.5 Million Cycles)

Following the conclusion of Test 4, Specimen 33-3-12-TX-A3 was removed from the testing setup. It was then flipped 180-degrees and re-attached to the testing frame. Testing was then resumed as test 5.

Results of Fatigue Test 4: Crack Growth Information

Following the initial ultrasonic measurements of the crack state, Specimen 33-3-12-TX-A3 and 33-3-12-TX-A4 were periodically examined using ultrasonic testing to monitor the progression of cracks throughout the fatigue test, and to provide data on the increase in crack length/depth as a function of the number of fatigue loading cycles. The successive ultrasonic test data for Specimen 33-3-12-TX-A3 can be seen below in Figures 5.79 through 5.81.

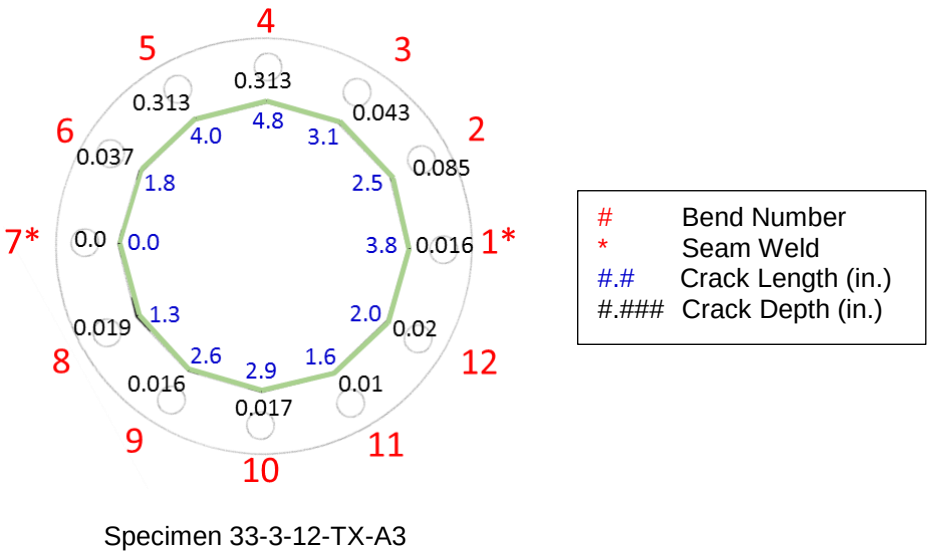

Specimen 33-3-12-TX-A3

Figure 5.79: Specimen 33-3-12-TX-A3: Cracks after 1.7 Million Fatigue Cycles in Test 3

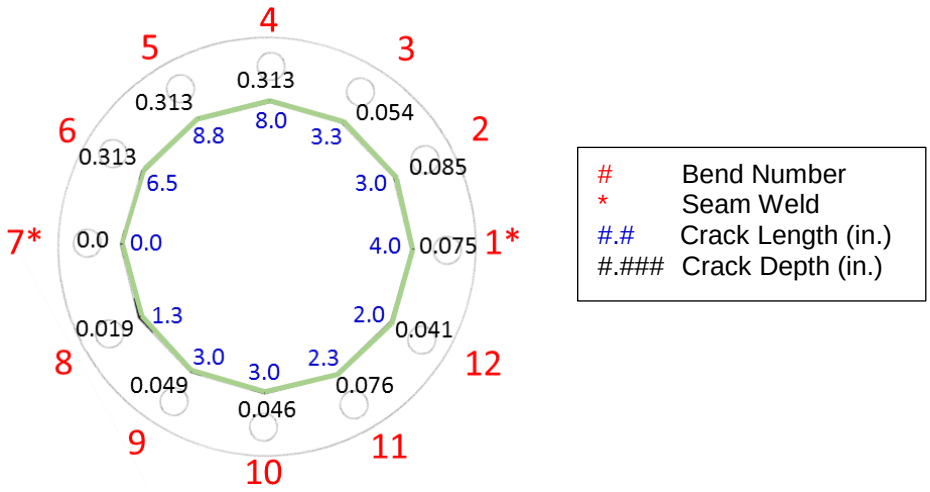

Specimen 33-3-12-TX-A3

Figure 5.80: Specimen 33-3-12-TX-A3: Cracks after 3.8 Million Fatigue Cycles in Test 3 (Initial Cracks at the Beginning of Test 4)

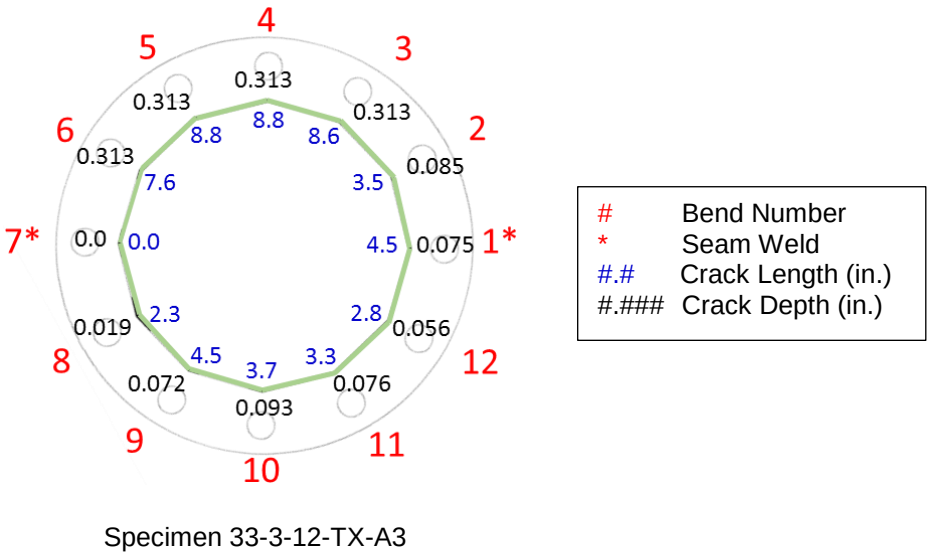

Figure 5.81: Specimen 33-3-12-TX-A3: Cracks after 5.5 Million Fatigue Cycles (3.8 Million Cycles during Test 3 and 1.7 Million Cycles during Test 4)

5.4.6 Fatigue Test 5 — Stress Range of 4 ksi: Specimens 33-3-12-TX-A3 and 33-3-12-TX-A4

The fifth fatigue test was run on Specimens 33-3-12-TX-A3 and 33-3-12-TX-A4. These specimens were tested at the stress range of 4 ksi and at the mean stress of 6 ksi (minimum stress of 4 ksi and maximum stress of 8 ksi). The loading frequency was 2.7 Hz. These specimens were fabricated with a full penetration welded connection and no external collar, as described in Section 5.2. The initial conditions in terms of the length and depth of the cracks existed in the shaft-to-baseplate welded connection of these cracked HMIP specimens were established at the beginning of the test. As a result of fatigue Test 5, one fatigue data point was obtained corresponding to the stress range of 4 ksi. This data came from Specimen 33-3-12-TX-A4. Note that following the failure of Specimen 33-3-12-TX-A4 in Test 3, it was removed from the test setup, flipped 180-degrees, and reinstalled. By flipping the specimen, the top bend was changed from bend 4 to bend 10. Therefore, Test 5 encompasses the test that was run on Specimen 33-3-12-TX-A4 in its flipped orientation.

Results of Fatigue Test 5: Initial Conditions of the Tested Specimens

Prior to the fatigue Tests 5, PAUTs were performed on the specimens to identify preexisting cracks. The initial crack measurements for Specimen 33-3-12-TX-A4 can be seen in Figure 5.82. Note that the initial conditions for Specimen 33-3-12-TX-A4 at the beginning of Test 5 was basically the condition of this specimen at the end of Test 4.

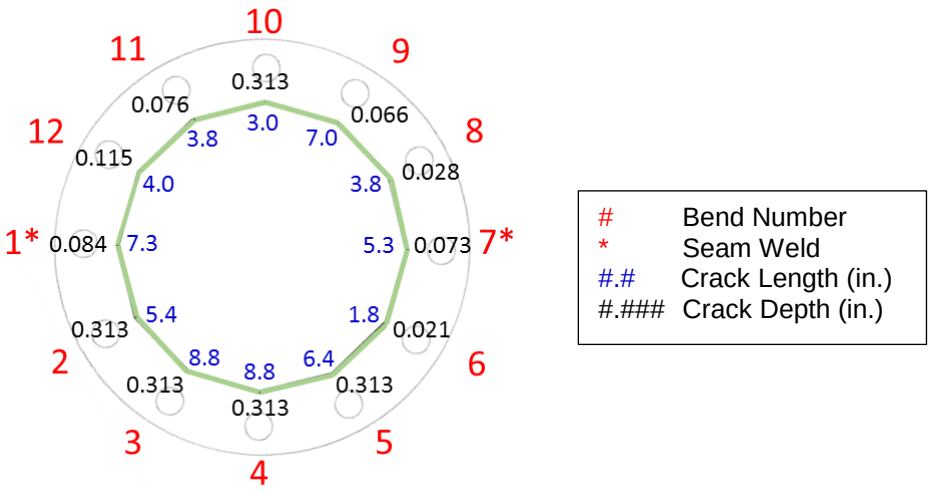

Figure 5.82: Specimen 33-3-12-TX-A4: Cracks after 1.7 Million Fatigue Cycles in Test 4 (Initial Cracks at the Beginning of Test 5)

Results of Fatigue Test 5: Observations

Figure 5.83 shows the state of cracks on the three top bends of Specimen 33-3-12-TX-A4 tested in Test 5 under the stress range of 4 ksi. As seen in this figure, sever cracking occurred at the end of Test 5; resulting in through-thickness cracks over more that 17% of the connection length between the base plate and the shaft. The top bend (Bend 10) failed first in Test 5 and the cracks propagated from this bend towards the two adjacent bends (Bends 9 and 11) at later stages of the fatigue test. A very important observation to make from Figure 5.83 is that when cracks approached to irregularities on the weld path (at the shaft-to-baseplate weld toe), they started to propagate in the shaft away from the weld path. When cracks started to propagate in the shaft, the rate of change in their length increased very rapidly causing a very fast fatigue failure.

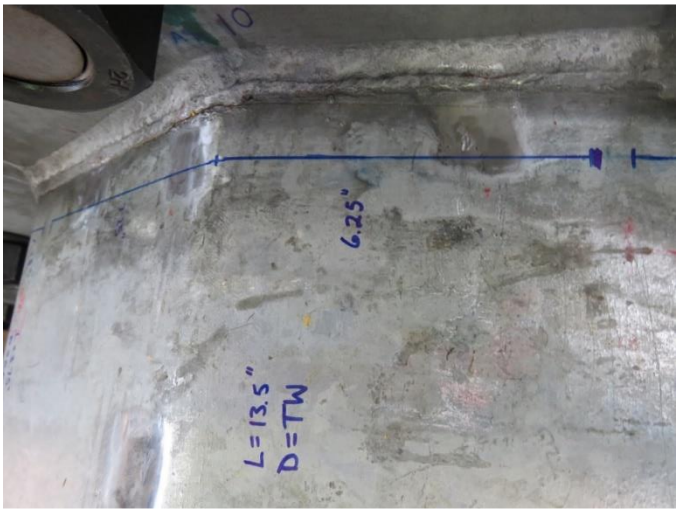

Figure 5.83: Specimen 33-3-12-TX-A4 following the Fatigue Test 5 at the Stress Range of 4 ksi (Fatigue Cracks after 6.5 Million Cycles)

Results of Fatigue Test 5: Crack Growth Information

Following the initial ultrasonic measurements of the crack state, Specimen 33-3-12-TX-A3 and 33-3-12-TX-A4 were periodically examined using ultrasonic testing to monitor the progression of cracks throughout the fatigue test, and to provide data on the increase in crack length/depth as a function of the number of fatigue loading cycles. The successive ultrasonic test data for Specimen 33-3-12-TX-A4 can be seen below in Figure 5.84.

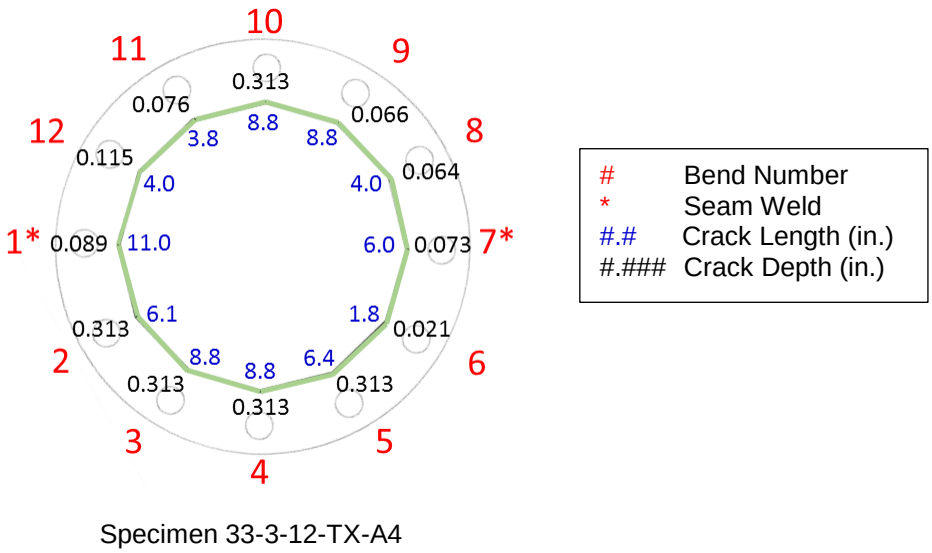

Figure 5.84: Specimen 33-3-12-TX-A4: Cracks after 6.5 Million Fatigue Cycles (1.7 Million Cycles during Test 4 and 4.8 Million Cycles during Test 5)

5.4.7 Fatigue Test 6 — Stress Range of 2 ksi: Specimens 33-3-12-TX-A3 and 33-3-12-TX-A4

The sixth fatigue test was run on Specimens 33-3-12-TX-A3 and 33-3-12-TX-A4. These specimens were tested at the stress range of 2 ksi and at the mean stress of 6 ksi (minimum stress of 5 ksi and maximum stress of 7 ksi). The loading frequency was 4.0 Hz. These specimens were fabricated with a full penetration welded connection and no external collar, as described in Section 5.2. The initial conditions in terms of the length and depth of the cracks existed in the shaft-to-baseplate welded connection of these cracked HMIP specimens were established at the beginning of the test. As a result of fatigue Test 6, one fatigue data point was obtained corresponding to the stress range of 2 ksi. This data came from Specimen 33-3-12-TX-A3.

It should be noted that Specimens 33-3-12-TX-A3 and 33-3-12-TX-A4 used in Test 6 had already experienced fatigue cracks during fatigue Tests 3, 4, and 5 conducted at the stress range of 4 ksi. The intent of Test 6 was to generate a fatigue data point at 2 ksi stress range using specimens with more sever cracking so that the test could be finished in the life of the project.

Results of Fatigue Test 6: Initial Conditions of the Tested Specimens

Prior to the fatigue Tests 6, PAUTs were performed on the specimens to identify preexisting cracks. The initial crack measurements for Specimens 33-3-12-TX-A3 and 33-3-12-TX-A4 can be seen in Figure 5.85. Note that the initial conditions for Specimens 33-3-12-TX-A3

and 33-3-12-TX-A4 at the beginning of Test 6 was basically the condition of these specimens at the end of Test 5. The orientation of the specimens shown in Figure 5.85 also represent the orientation at which these two specimens were tested in Test 6 under the stress range of 2 ksi.

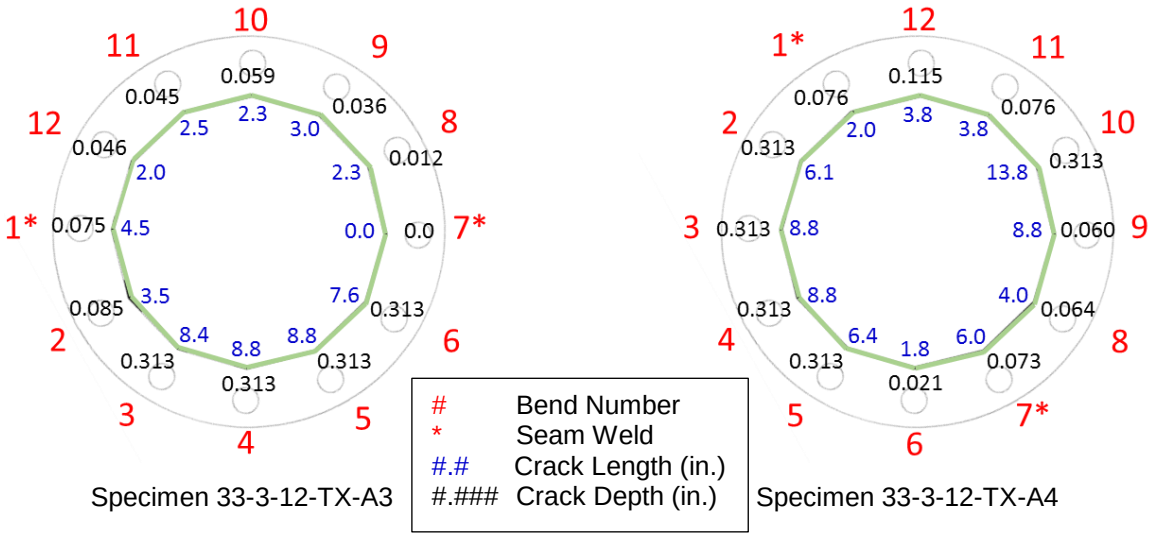

Figure 5.85: Specimens 33-3-12-TX-A3 and 33-3-12-TX-A4: Initial Cracks at the Beginning of Test 6

Results of Fatigue Test 6: Observations

Figure 5.86 represents the state of cracks on the Bend 11 of the Specimen 33-3-12-TX-A3 tested in Test 6 under the stress range of 2 ksi. As seen in this figure, the 10% drop in the stiffness of the specimen occurred without sever cracking. The Bend 11 (adjacent to the top Bend 10) failed first in Test 6 and the cracks propagated from this bend towards the two adjacent bends (Bends 10 and 12) at later stages of the fatigue test. It should be noted that, at some points throughout the test, cracks would stop increasing in length and just propagate through the thickness of the shaft. This is unique under the conditions of small stress ranges like 2 ksi in Test 6 (and 3 ksi as observed in Test 2). This behavior of cracks makes their in-service detections to be very challenging.

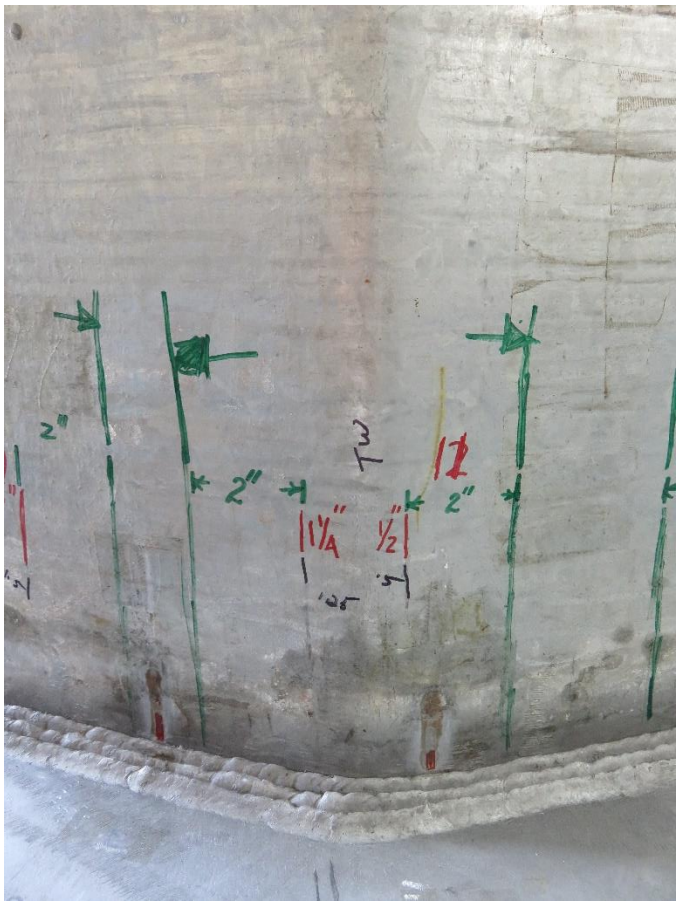

Figure 5.86: Specimen 33-3-12-TX-A3 (Bend 11) following the Fatigue Test 6 at the Stress Range of 2 ksi (Fatigue Cracks after 66.2 Million Cycles)

Results of Fatigue Test 6: Crack Growth Information

Following the initial ultrasonic measurements of the crack state, Specimens 33-3-12-TX-A3 and 33-3-12-TX-A4 were periodically examined using ultrasonic testing to monitor the progression of cracks throughout the fatigue test, and to provide data on the increase in crack length/depth as a function of the number of fatigue loading cycles. The successive ultrasonic test data for Specimens 33-3-12-TX-A3 and 33-3-12-TX-A4 can be seen below in Figures 5.87 through 5.90. It should be noted that, at some points throughout the test, cracks would stop increasing in length and just propagate through the thickness of the shaft. This is unique under the conditions of small stress ranges like 2 ksi in Test 6 (and 3 ksi as observed in Test 2). This behavior of cracks makes their in-service detections to be very challenging.

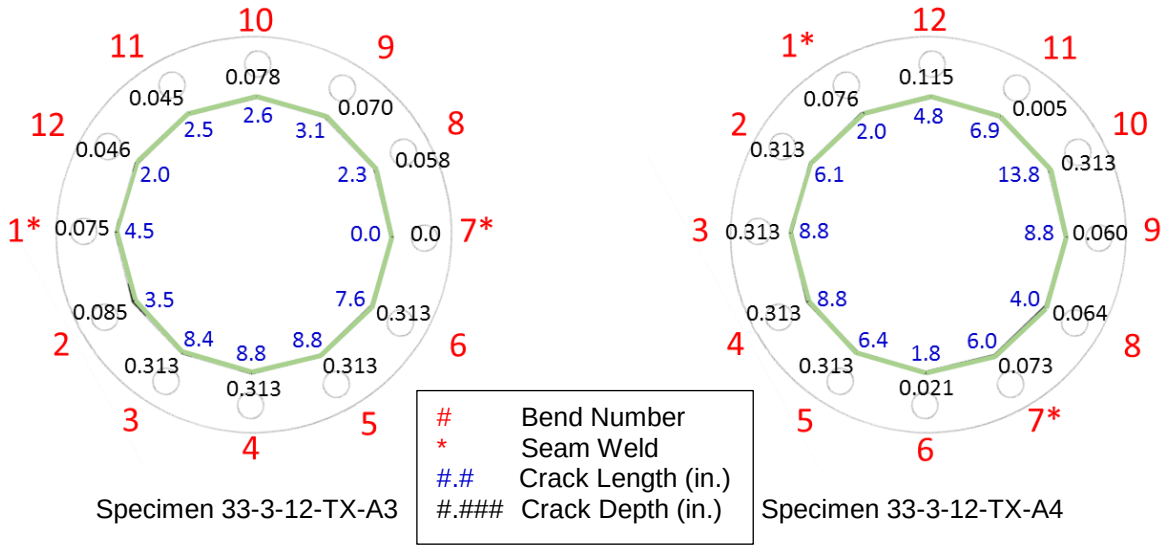

Figure 5.87: Specimens 33-3-12-TX-A3 and 33-3-12-TX-A4: Cracks after 22.6 Million Fatigue Cycles in Test 6

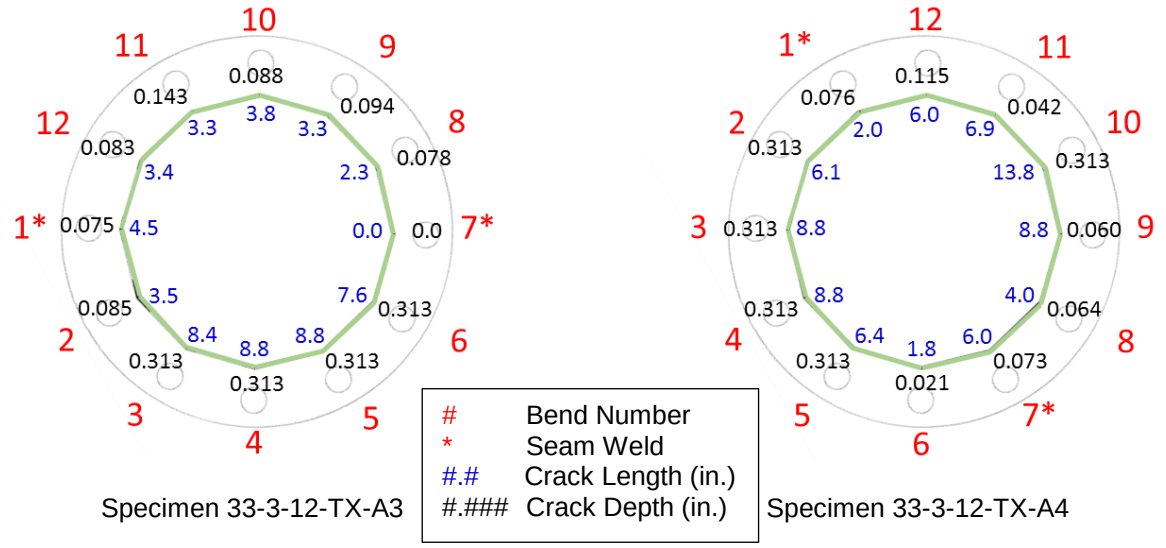

Figure 5.88: Specimens 33-3-12-TX-A3 and 33-3-12-TX-A4: Cracks after 43.0 Million Fatigue Cycles in Test 6

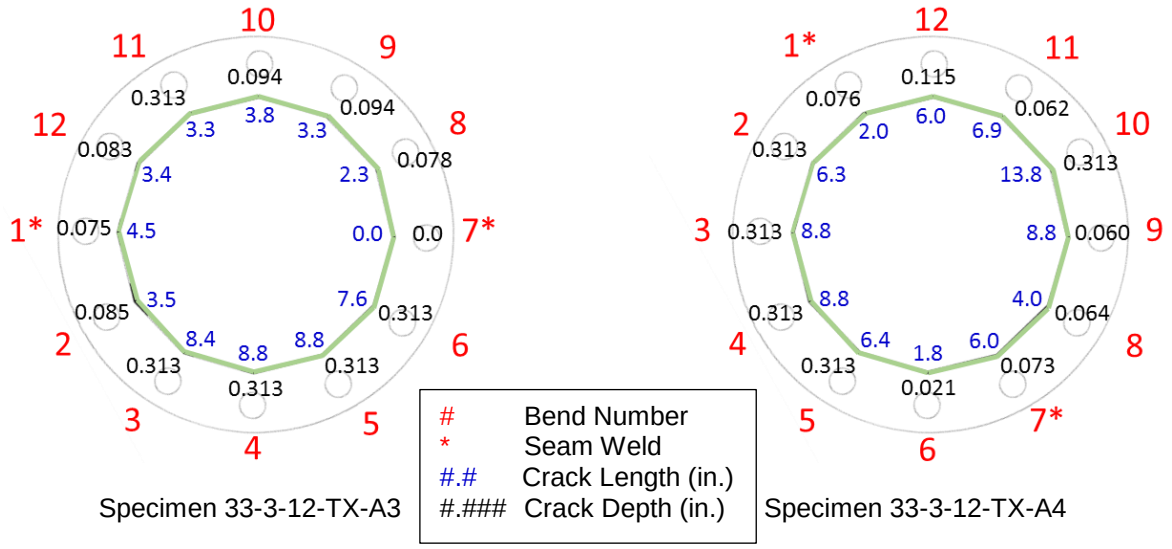

Figure 5.89: Specimens 33-3-12-TX-A3 and 33-3-12-TX-A4: Cracks after 57.6 Million Fatigue Cycles in Test 6

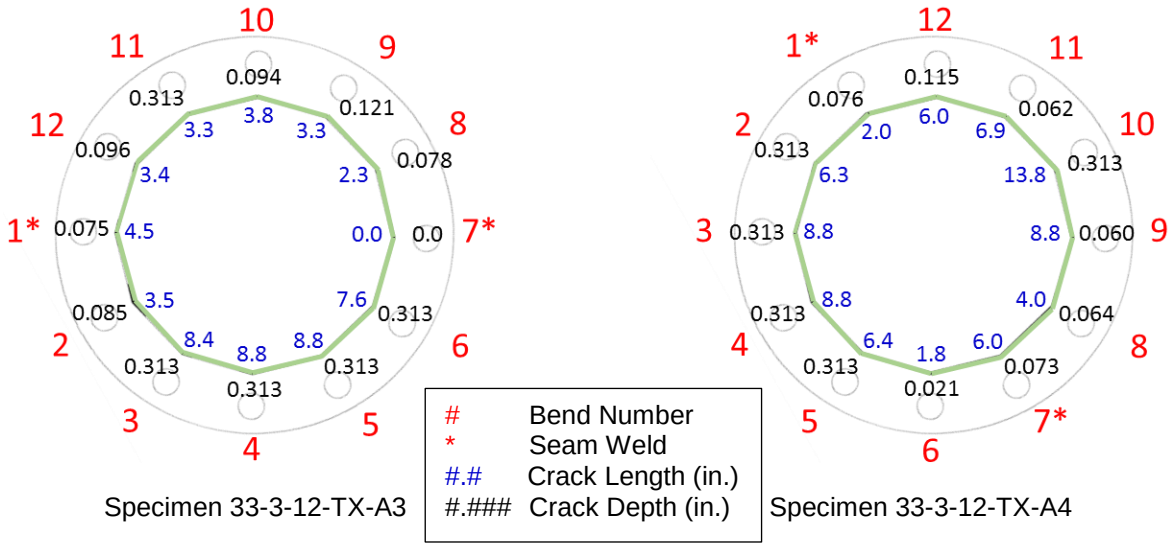

Figure 5.90: Specimens 33-3-12-TX-A3 and 33-3-12-TX-A4: Cracks after 66.2 Million Fatigue Cycles in Test 6

5.4.8 Fatigue Test 7 — Combined Stress Ranges of 6 ksi and 10 ksi: Specimens 33-3-12-TXEC-A7 and 33-3-12-TXEC-A8

The seventh fatigue test was run on Specimens 33-3-12-TXEC-A7 and 33-3-12-TXEC-A8. These specimens were tested at the combined stress ranges of 6 ksi and 10 ksi and at the mean stress of 6 ksi (minimum stress of 3 ksi and maximum stress of 9 ksi for the 6-ksi test and minimum stress of 1 ksi and maximum stress of 11 ksi for the 10-ksi test). The loading frequency was 0.5 Hz. These specimens were fabricated with a full penetration welded connection with external collar, as described in Section 5.2. The initial conditions in terms of the length and depth

of the cracks existed in the shaft-to-baseplate welded connection as well as the fillet weld connection at the top of the ground sleeve were established at the beginning of the test. As a result of fatigue Test 7, one fatigue data point was obtained corresponding to the combined stress ranges of 6 ksi and 10 ksi. This data came from Specimen 33-3-12-TXEC-A7. The failure happened at the fillet weld location at the top of the ground sleeve.

Results of Fatigue Test 7: Initial Conditions of the Tested Specimens

Prior to the fatigue Test 7, PAUTs were performed on the specimens to identify preexisting cracks. Using PAUTs, three bends on Specimen 33-3-12-TXEC-A7 were identified to have cracks. The cracks were found in the fillet weld connecting the external collar to the shaft of the pole. These cracks were very small in size. While Reinhart & Associates technicians could identify the crack, they could not determine any length or depth measurements. Screen captures from the PAUT instrument of these cracks can be seen in Figures 5.91, 5.92, and 5.93. No cracks were found on Specimen 33-3-12-TXEC-A8.

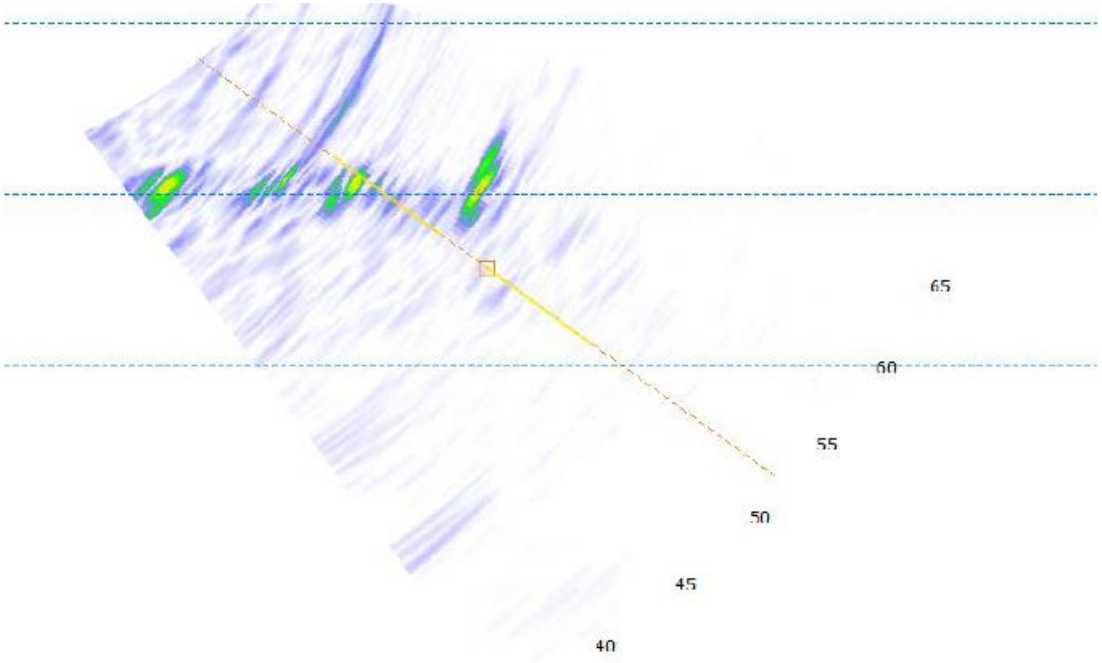

Figure 5.91: Cracks Found on Bend 2 of Specimen 33-3-12-TXEC-A7 while Scanning from the Collar Side

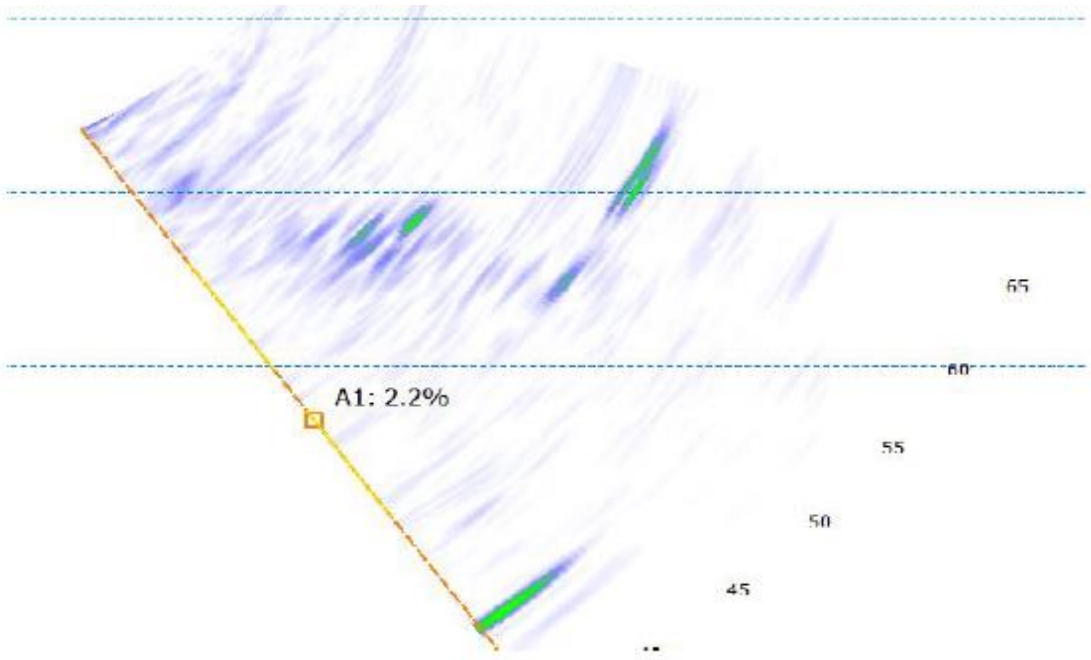

Figure 5.92: Cracks Found on Bend 9 of Specimen 33-3-12-TXEC-A7 while Scanning from the Collar Side

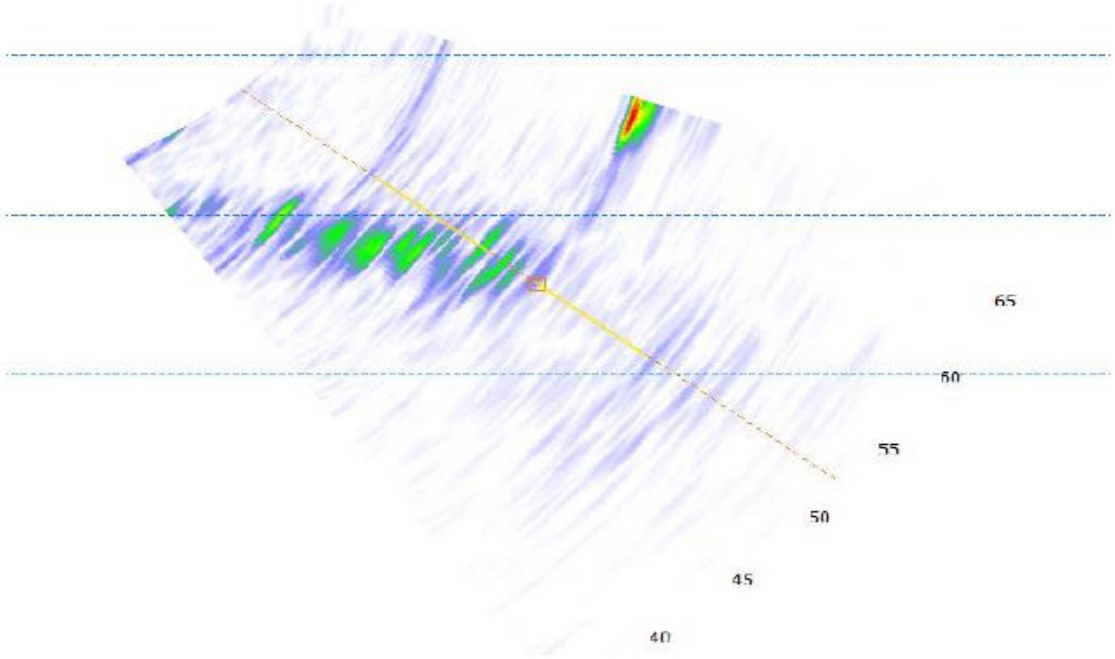

Figure 5.93: Cracks Found on Bend 9 of Specimen 33-3-12-TXEC-A7 while Scanning from the Collar Side

Results of Fatigue Test 7: Observations

Figures 5.94 through 5.96 represent the state of cracks on the three top bends of Specimen 33-3-12-TXEC-A7 tested in Test 7 under the combined stress ranges of 6 ksi and 10

ksi. As seen in these figures, severe cracking occurred at the end of Test 7; resulting in through-thickness cracks over more that 20% of the connection length between the base plate and the shaft. It can also be observed that failure occurred at the location of fillet welds at the top of the ground sleeve. The top bend (Bend 10) failed first in Test 7 and the cracks propagated from this bend towards the two adjacent bends (Bends 9 and 11) at later stages of the fatigue test. A very important observation to make from Figures 5.94 through 5.96 is that when cracks approached to irregularities on the weld path (at the shaft-to-baseplate weld toe), they started to propagate in the shaft away from the weld path. When cracks started to propagate in the shaft, the rate of change in their length increased very rapidly causing a very fast fatigue failure.

Figure 5.94: Specimen 33-3-12-TXEC-A7 (Bend 10) following the Fatigue Test 7 at the Combined Stress Ranges of 3 ksi and 5 ksi (Fatigue Cracks after 4.2 Million Cycles)

Figure 5.95: Specimen 33-3-12-TXEC-A7 (Bends 10 and 11) following the Fatigue Test 7 at the Combined Stress Ranges of 3 ksi and 5 ksi (Fatigue Cracks after 4.2 Million Cycles)

Figure 5.96: Specimen 33-3-12-TXEC-A7 (Bends 10 and 11) following the Fatigue Test 7 at the Combined Stress Ranges of 3 ksi and 5 ksi (Fatigue Cracks after 4.2 Million Cycles)

Results of Fatigue Test 7: Crack Growth Information

Following the initial ultrasonic measurements of the crack state, Specimens 33-3-12-TXEC-A7 and 33-3-12-TXEC-A8 were periodically examined using ultrasonic testing to monitor the progression of cracks throughout the fatigue test, and to provide data on the increase in crack length/depth as a function of the number of fatigue loading cycles. The successive ultrasonic test data for Specimens 33-3-12-TXEC-A7 and 33-3-12-TXEC-A8 can be seen below in Figures 5.97 and 5.98.

Date	5/24/2017					
Weld	Base			Pole Filet)		
Knuckle	Before	After	Depth	Before	After	Depth
1						
2						
3						
4						
5						
6						
7						
8	0.250	0.000	0.007	x	x	x
9	x	x	x	1.500	1.500	TW
10	2.000	0.000	TW	2.000	→	TW
11	x	x	x	→	6.875	TW
12	0.875	0	0.127	x	x	x

Figure 5.97: Specimen 33-3-12-TXEC-A7: Cracks after 4.2 Million Fatigue Cycles in Test 7

Date	5/24/2017					
Weld	Base			Pole (Filet)		
Knuckle	Before	After	Depth	Before	After	Depth
1						
2						
3						
4						
5						
6						
7	x	x	x	x	x	x
8	x	x	x	x	x	x
9	x	x	x	0.000	0.375	0.005
10	x	x	x	0.000	0.500	0.032
11	x	x	x	x	x	x
12						

Figure 5.98: Specimen 33-3-12-TXEC-A8: Cracks after 4.2 Million Fatigue Cycles in Test 7

5.4.9 Fatigue Test 8 — Stress Ranges of 5 ksi: Specimens 33-3-12-TXEC-A7 and 33-3-12-TXEC-A8

The eighth fatigue test was run on Specimens 33-3-12-TXEC-A7 and 33-3-12-TXEC-A8. These specimens were tested at the stress range of 5 ksi and at the mean stress of 3 ksi (minimum stress of 0.5 ksi and maximum stress of 5.5 ksi). The loading frequency was 0.5 Hz. These specimens were fabricated with a full penetration welded connection with external collar, as described in Section 5.2. The initial conditions in terms of the length and depth of the cracks existed in the shaft-to-baseplate welded connection as well as the fillet weld connection at the top of the ground sleeve were established at the beginning of the test. As a result of fatigue Test 7, one fatigue data point was obtained corresponding to the stress range of 5 ksi. This data came from Specimen 33-3-12-TXEC-A7. The failure happened at the shaft-to-baseplate location.

Results of Fatigue Test 8: Observations

Figure 5.99 represents the state of cracks on the Bend 4 of the Specimen 33-3-12-TXEC-A7 tested in Test 8 under the stress range of 5 ksi. As seen in this figure, the 10% drop in the stiffness of the specimen occurred without sever cracking. The top Bend 4 failed first in Test 8 and the cracks propagated from this bend towards the two adjacent bends (Bends 3 and 5) at later stages of the fatigue test. It should be noted that, at some points throughout the test, cracks were developing through the thickness of the shaft, but not through the thickness of the collar (10% drop in stiffness observed with apparent cracks from outside). This crack propagation phenomenon is unique to the specimens with ground sleeves. This behavior of cracks makes their in-service detections to be very challenging.

Figure 5.99: Specimen 33-3-12-TXEC-A7 (Bend 4) following the Fatigue Test 8 at the Stress Range of 5 ksi (Fatigue Cracks after 1.8 Million Cycles)

Results of Fatigue Test 8: Crack Growth Information

Following the initial ultrasonic measurements of the crack state, Specimens 33-3-12-TXEC-A7 and 33-3-12-TXEC-A8 were periodically examined using ultrasonic testing to monitor the progression of cracks throughout the fatigue test, and to provide data on the increase in crack length/depth as a function of the number of fatigue loading cycles. The successive ultrasonic test data for Specimens 33-3-12-TXEC-A7 and 33-3-12-TXEC-A8 can be seen below in Figures 5.100 and 5.101.

Date	5/24/2017						8/18/2017					
Weld	Base			Pole Fillet			Base			Pole Fillet		
Knuckle	Before	After	Depth	Before	After	Depth	Before	After	Depth	Before	After	Depth
1												
2							0.375	0.375	0.037	X	X	X
3							X	X	X	X	X	X
4							1.500	1.250	0.251	X	X	X
5							X	X	X	X	X	X
6							X	X	X	X	X	X
7												
8	0.250	0.000	0.007	X	X	X						
9	X	X	X	1.500	1.500	TW						
10	2.000	0.000	TW	2.000	→	TW						
11	X	X	X	→	6.875	TW						
12	0.875	0.000	0.127	X	X	X						

Figure 5.100: Specimen 33-3-12-TXEC-A7: Cracks after 1.3 Million Fatigue Cycles in Test 8

Date	5/24/2017						8/18/2017					
Weld	Base			Pole Fillet			Base			Pole Fillet		
Knuckle	Before	After	Depth	Before	After	Depth	Before	After	Depth	Before	After	Depth
1												
2												
3												
4												
5												
6												
7	X	X	X	X	X	X	X	X	X	X	X	X
8	X	X	X	X	X	X	X	X	X	X	X	X
9	X	X	X	0.000	0.375	0.005	X	X	X	0.000	0.375	0.005
10	X	X	X	0.000	0.500	0.032	X	X	X	X	X	X
11	X	X	X	X	X	X	0.500	0.000	0.129	X	X	X
12												

Figure 5.101: Specimen 33-3-12-TXEC-A8: Cracks after 1.3 Million Fatigue Cycles in Test 8

5.4.10 Fatigue Test Results: Summary and Discussions

Results from fatigue tests on specimens without ground sleeves (specimens of primary interest) and on specimens with ground sleeves (specimens of secondary interest) are summarized in Tables 5.2 and 5.3, respectively. Fatigue test results from tests on specimens without ground sleeves are further presented on an S-N plot in Figure 5.102. In addition to data gathered in this project, fatigue data generated previously during experimental studies at the Ferguson Structural Engineering Laboratory as well as data created by researchers from University of Houston (TxDOT Project 0-6830) are also shown in Figure 5.102. Therefore, Figure 5.102 depicts all the available data on the fatigue behavior of tested specimens without ground sleeves (specimens of primary interest).

Several important observations should be made from Figure 5.102. First, there are two data points indicated as hollow circles in this figure. These fatigue data are representing runout tests at 3ksi and 1 ksi. Second, the two data points circled around by a rectangular shape indicate test results on specimens fabricated by different fabricator than Structural and Steel Products. Third, the two data points circled around by a triangular shape indicate test results on specimens without initial cracks. Therefore, as seen from Figure 5.102, almost all the fatigue data points are below Category E'. No specific conclusions can be made for the fatigue behavior of these specimens at small stress ranges (below 2 ksi) due to the lack of available data.

Table 5.2: Result Summary of Fatigue Tests on HMIP Specimens without Ground Sleeves

Stress Range (ksi)	Specimen	Cycles to 10% Reduction in Stiffness	Cycles to Failure
6	A1	17.7×10^6	19.5×10^6
	A2		
4	A4	2.6×10^6	3.8×10^6
	A3	4.1×10^6	5.5×10^6
	A4	3.5×10^6	6.2×10^6
2	A3	53.0×10^6	$66.2 \times 10^{6\#}$
	A4	$--^{\dagger}$	
3	A5	$--^{\dagger}$	$169.1 \times 10^{6\#}$
	A6	160.5×10^6	

†No failure $^{\#}$Test Stopped

Table 5.3: Result Summary of Fatigue Tests on HMIP Specimens with Ground Sleeves

Stress Range (ksi)	Specimen	Cycles to 10% Reduction in Stiffness	Cycles to Failure
Combined 6 and 10	A7	0.2×10^6 @ 10 ksi	$4.4 \times 10^{6\#}$
		4.1×10^6 @ 6 ksi	
	A8	$--^{\dagger}$	
5	A7	1.1×10^6	$1.3 \times 10^{6\#}$
	A8	$--^{\dagger}$	

†No failure $^{\#}$Test Stopped

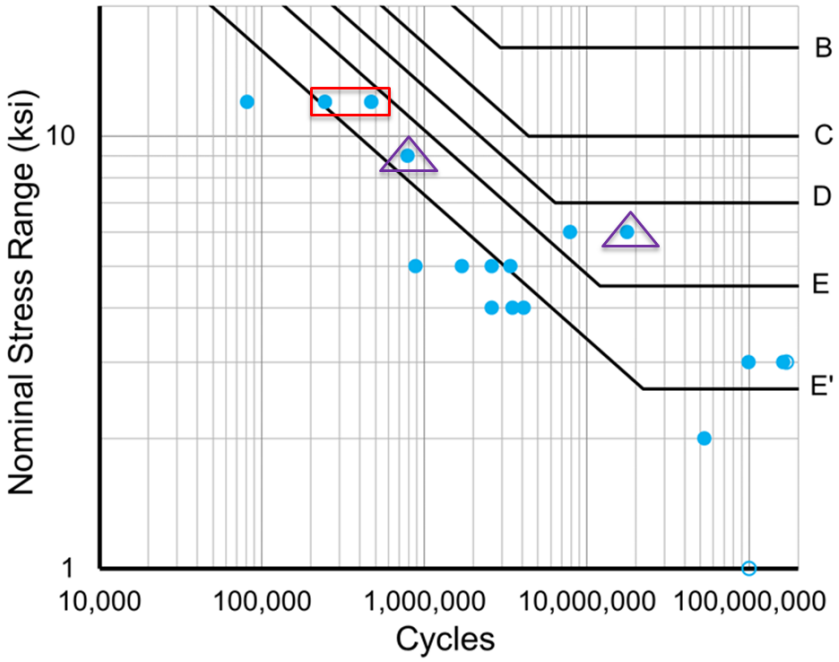

Figure 5.102: All Available Fatigue Test Data on the HMIP Specimens with the Design of Interest (Specimens of Primary Interest)

As a final note on the data summarized in Table 5.3, it should be pointed out that the specimen with ground sleeves failed at around 1.1 million cycles at the stress range of 5 ksi. This makes this specimen below the fatigue Category E′. Although this represents only a single data point on specimens with ground sleeves, it clearly indicates the need for further investigation of the fatigue behavior of these specimens (secondary design).

5.5 Ultimate Strength of Cracked HMIPs

While the main objective of the laboratory experiment was to perform fatigue tests to assess the remaining fatigue life of cracked HMIP specimens, development of the data on the ultimate strength of cracked poles was also of interest. This was specifically the case since the collapse behavior of heavily cracked HMIPs in-service as a result of sudden high wind gusts was a matter of concern to the TxDOT. To address this concern, an ultimate strength test on a damaged HMIP specimen was planned and performed at the Ferguson Structural Engineering Laboratory. In performing this test, researchers were able to study and quantify the strength of an HMIP specimen with extensive damage due to the prior fatigue loading history. Details of ultimate strength tests and their representative results are provided and discussed in this section.

5.5.1 Conduct of the Ultimate Strength Test

To assess the ultimate strength of a damaged specimen, a moment equal to the ultimate moment (plastic moment) of the specimen must be applied at the base of the HMIP specimen. This moment was applied via the application of a force at the free end of the specimen. More specifically, this lateral force created an overturning moment at the base leading to the failure of the shaft-to-baseplate weld detail. Because the exact ultimate moment of damaged section was

difficult to quantify, the lateral force was applied in various steps until the ultimate capacity was reached and the specimen failed.

Specimen 33-3-12-TX-A1, with extensive damage from a fatigue test at the stress range of 6 ksi, was selected for the ultimate strength test. As indicated in Figure 5.103, this specimen was extensively instrumented with strain gages to evaluate the stresses generated in the specimen during the ultimate strength test. The ultimate strength test started by pulling on the specimen first to straighten the specimen. The test was then followed as a pushover test that moved the specimen laterally to failure. The pushover test halted at increments of 0.5-in. to monitor the behavior of the specimens and to do careful measurements and documentations.

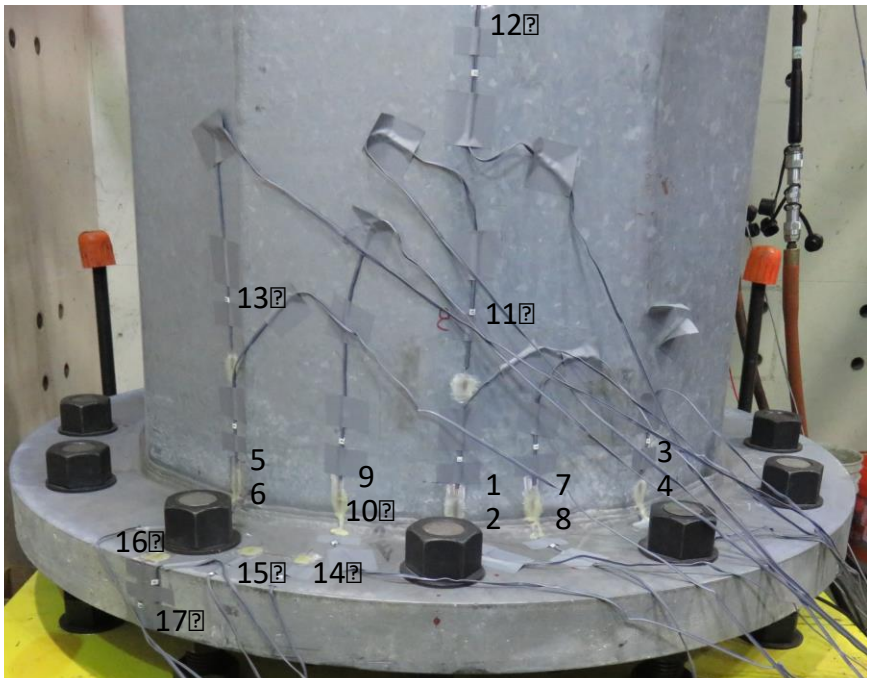

Figure 5.103: Strain Gages Installed on the Compression Side of the HMIP Specimen in the Ultimate Strength Test

5.5.2 Results of the Ultimate Strength Test

Results from an ultimate strength test on a cracked HMIP specimen are presented in Figures 5.104 through 5.111. As can be observed from Figures 5.104 through 5.111, during the ultimate strength test, cracks were propagating from the bends towards the flats nearly symmetrical on both sides of the specimen. This made the behavior of the severely damaged HMIP specimen very ductile in the test. As further shown in load-displacement plots in Figures 5.104 and 5.111, the specimen achieved 80% of its calculated capacity based on the plastic moment of undamaged specimen (lateral force of 100 kips was calculated as the plastic strength of the specimen).

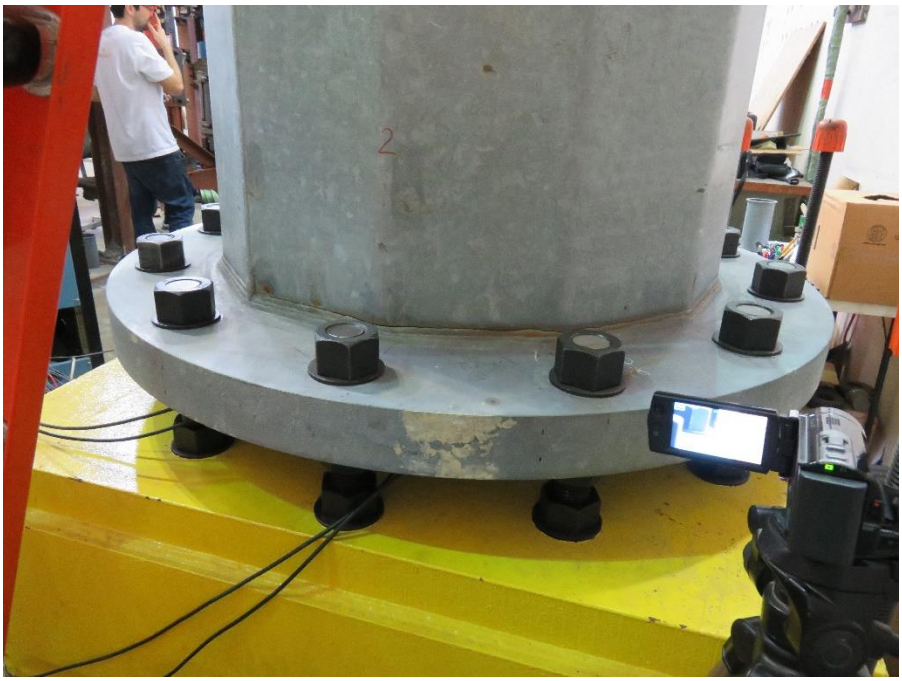

Figure 5.104: Tension Side of the Damaged Specimen 33-3-12-TX-A1 Prior to the Ultimate Strength Test

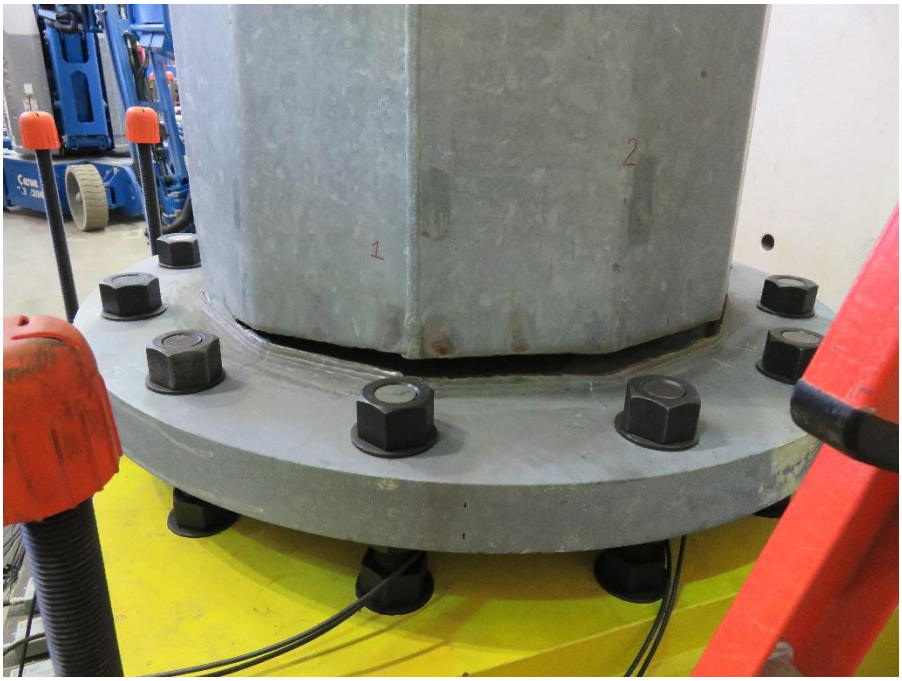

Figure 5.105: Tension Side of the Damaged Specimen 33-3-12-TX-A1 Following the Ultimate Strength Test

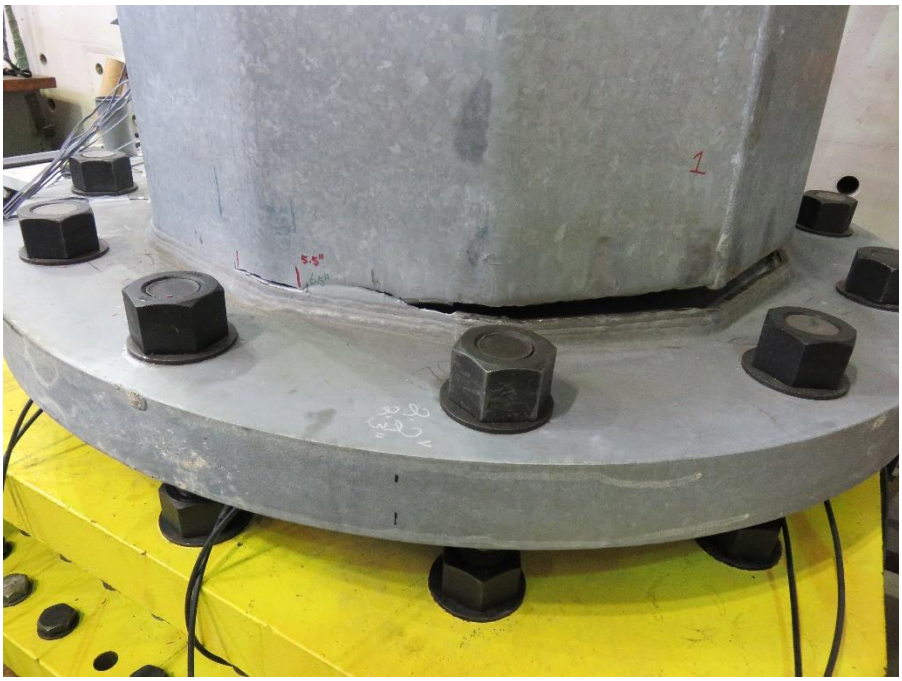

Figure 5.106: Propagation of Cracks in the Damaged Specimen 33-3-12-TX-A1 Following the Ultimate Strength Test

Figure 5.107: Propagation of Cracks from Bends 12 and 11 towards the flat Following the Ultimate Strength Test on the Damaged Specimen 33-3-12-TX-A1

Figure 5.108: Propagation of Cracks from Bends 3 and 4 towards the flat Following the Ultimate Strength Test on the Damaged Specimen 33-3-12-TX-A1

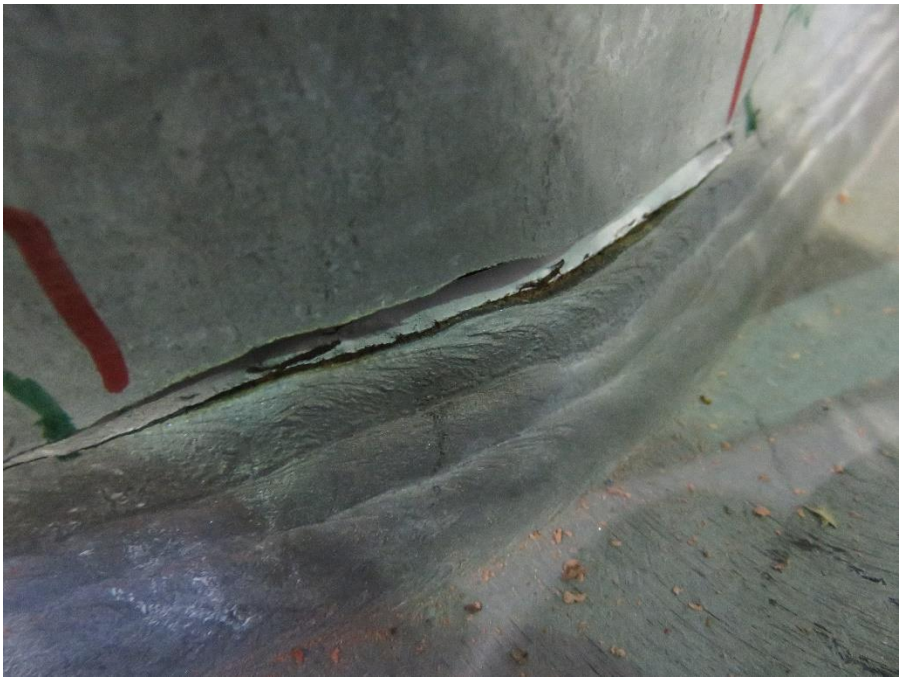

Figure 5.109: Close-up of Cracks on Bend 11 of the Damaged Specimen 33-3-12-TX-A1 – Cracks from a Fatigue test at a stress range of 6 ksi and from the Ultimate Strength Test

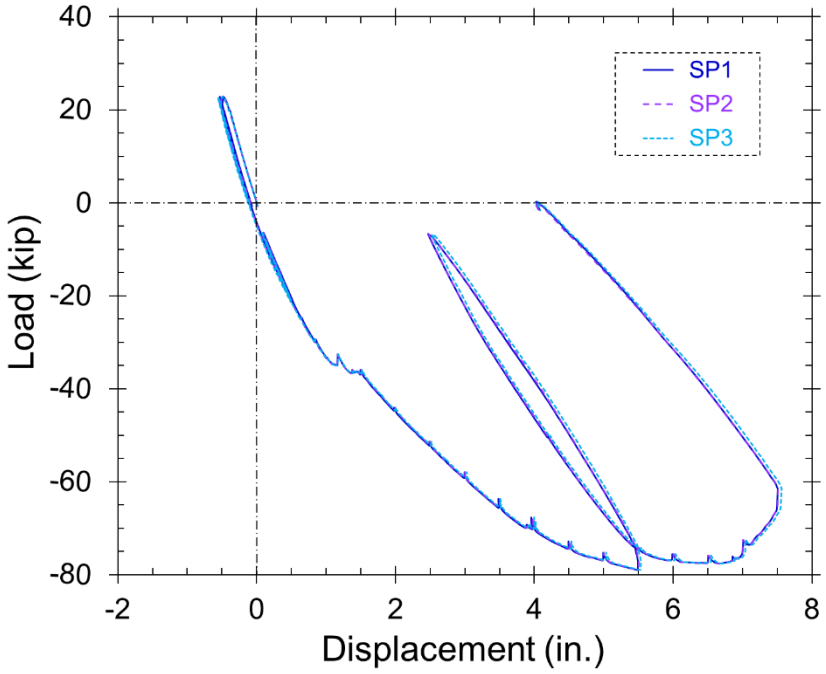

Figure 5.110: Load-Displacement Behavior of the Damaged Specimen 33-3-12-TX-A1 During the Ultimate Strength Test

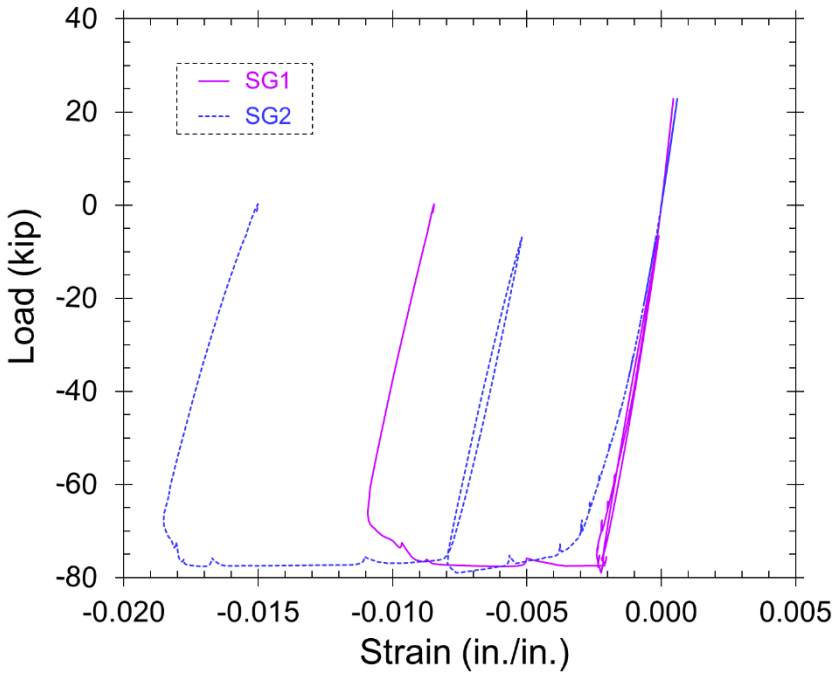

Figure 5.111: Load-Strain Behavior Obtained Using the Strain Gages 1 and 2 Located at the uttermost Compression Bend of the Damaged Specimen 33-3-12-TX-A1 During the Ultimate Strength Test

5.6 Summary

This chapter has described a fatigue testing program conducted on HMIP test specimens with pre-existing cracks. Included in this chapter was a description of the test set-up, test specimens, instrumentation, and test results. Monitoring of cracks in the HMIP specimens using phased array ultrasonic testing was also described. In addition to the fatigue tests, a single HMIP specimen, after completion of fatigue testing, was loaded statically to failure to evaluate the residual strength of an HMIP with extensive cracking at its base. Some of the key observations from data presented in this chapter are as follows:

- A number of HMIP specimens were tested to failure under fatigue loading, at a variety of stress ranges. Fatigue failure was defined to occur when the stiffness of the test specimen was reduced by 10-percent. Although this is a somewhat arbitrary definition of failure, the cracking of the specimens at this defined point of failure was normally quite extensive, with cracks extending through the full thickness of the shaft wall.

- All HMIP specimens tested in this program were designed and fabricated to TxDOT standards, by a commercial fabricator and galvanizer experienced in producing HMIPs for TxDOT. All of the specimens had pre-existing cracks at their base, of varying degrees of severity, when delivered to the laboratory for fatigue testing. Consequently, the specimens were considered to be representative of typical in-service HMIPs with pre-existing cracks, for the specific designs of interest in this research program.

- The majority of specimens tested in this program were representative of HMIPs with poles that are 12-sided, 150 ft. tall, with a design wind speed of 80 mph, and without ground sleeves (referred to in this report as specimens of primary interest). All of these specimens showed poor fatigue behavior, with failure occurring on an S-N plot below AASHTO fatigue category E′. Thus, this testing program confirmed the poor fatigue performance of these poles.

- Only one specimen was tested in this program that was representative of HMIPs with poles that are 12-sided, 150 ft. tall, with a design wind speed of 80 mph, and with ground sleeves (referred to in this report as specimens of secondary interest). This specimen also failed below AASHTO fatigue category E′. Although this represents only a single data point on specimens with ground sleeves, it clearly indicates the need for further investigation of the fatigue behavior of these specimens (secondary interest).

- The initial condition of the HMIP specimens in terms of both crack length and crack depth was found to significantly affect the fatigue life of the cracked HMIPs.

- The fatigue behavior of cracked HMIP specimens under lower stress ranges (at 3 ksi and lower) was different from that under higher stress ranges. The crack depth appeared to play a major role in the fatigue life predictions at low stress ranges.

- Cracks were observed to propagate in the shaft away from the weld as a result of irregularities on the weld toe. When cracks started to propagate in the shaft, the rate of change in their length increased very rapidly causing a very rapid fatigue failure. This

suggests that if cracks are seen in the shaft of an in-service pole that are growing away from the weld toe, repair or replacement should be undertaken.

- One of the specimens of the primary interest, after completion of fatigue testing, was subjected to static loading to complete failure. Since this specimen was already deemed to have failed under fatigue loading, it had extensive cracking at its base, prior to the application of static loading. The purpose of this static test was to assess the residual static strength of a pole with extensive fatigue cracking, and to assess the degree of ductility exhibited during failure under static loading. The results of this test showed that this pole with extensive fatigue cracking retained approximately 80-percent of its full static strength, based on the estimated plastic moment capacity of the shaft at the base of the pole. Further, the failure under static loading showed considerable ductility. Although based on a single test, this result suggests that an in-service pole with extensive fatigue cracking may exhibit a ductile failure under a large wind gust.

- Phased array ultrasonic testing (PAUT) was used to detect and characterize the length and depth of cracks in many of the HMIP specimens tested in this research program. PAUT appears to be capable of characterizing cracks more accurately than conventional ultrasonic testing, and it is recommended that TxDOT employ PAUT for future inspections of HMIPs, both for shop and field inspections. However, even with PAUT, there is uncertainty in crack detection. The depths of cracks appears to be particularly difficult to measure accurately.

- Crack-size detection using both conventional ultrasonic and phased array ultrasonic methods proved to be dependent on the orientation of the HMIP specimens. More specifically, accurate detection of crack sizes was more challenging when the specimens were positioned vertically rather than horizontally. This suggests greater care in ultrasonic inspection may be needed for in-service poles, which will be in a vertical orientation, as compared to the test specimens ultrasonically examined in a horizontal position in this research program.

- Accurate crack-size detection using both conventional ultrasonic and phased array ultrasonic methods proved to be challenging for more complex weld details such as the seam weld to baseplate detail, and the shaft-to-baseplate weld detail for the specimens with ground sleeves.

Chapter 6. Field Monitoring of In-Service HMIPs

6.1 Overview

As part of this project, field data were collected to characterize wind response of Texas HMIPs at five sites in Texas. This chapter first describes the considerations that went into selecting and locating the candidate HMIPs. A description of the instruments utilized to acquire data during the field monitoring is then presented. The data processing procedures used to analyze the field data are then introduced and explained in detail. Finally, analyses of field data together with their interpretation are presented and discussed.

6.2 Field Monitoring Locations

6.2.1 Key considerations in selecting monitored poles

Pole Design: Geometry and Design Wind

The first step in selecting the poles for monitoring was to choose the pole design. Of all the HMIPs in service in Texas, poles having 12-sided, 150 ft-tall shaft and considered design wind of 80 mph were selected for field monitoring in this study. Only poles without ground sleeves were considered. This selection was informed by the previous study reported by TxDOT (TxDOT 2008) indicating significant cracks in the shaft-to-base plate welds for HMIPs with this specific design (as discussed in Chapter 3, Section 3.4, Table 3.9).

Location by District

After choosing the specific HMIP design for monitoring, the second step was to identify districts in Texas where the poles with the design of interest were located. There are seven districts having the largest number of poles of interest. As indicated in Table 3.10 in Chapter 3, these districts include Austin, Laredo, Atlanta, El Paso, Odessa, Fort Worth, and Paris. Of all these districts, Austin, Laredo, El Paso, and Dallas (Fort Worth) were selected for field monitoring in this study. In addition to these districts, the Houston district was also chosen for field monitoring since it has a very large number of HMIPs.

Wind Characteristics: Wind-Induced Vibrations

The third and last step in selecting the poles for field monitoring was to consider the wind characteristics. This is particularly important since the primary loading on in-service HMIPs is due to wind. Wind affects HMIPs in three different modes; buffeting, vortex shedding and galloping. Of all these vibration modes, vortex-induced vibration was shown to have major impact on the fatigue life of HMIPs due to the relatively large amplitudes and large number of cycles (Dawood et al. 2014). Therefore, poles prone to vortex-shedding excitation were specifically selected for field monitoring. To better represent the major wind environments in Texas, some poles located in regions with significant wind gusts were also proposed for field monitoring studies.

The selection of HMIPs based on wind characteristics was informed using the historical wind data for Texas provided by the National Oceanic and Atmospheric Administration (NOAA), as described in Chapter 4. Wind data collected at different weather stations provide hourly wind velocity and direction as well as wind gust speed.

6.2.2 List of Poles Selected for Field Monitoring

The selected HMIPs for field monitoring in this study are listed in Table 6.1. The research team first started instrumenting/monitoring the pole in Austin in mid-December 2015 and continued monitoring that pole for about 5 months to evaluate and adjust the instrumentation setup and data acquisition system. They then started instrumenting/monitoring poles in El Paso, Dallas, Houston/Galveston and Laredo. All poles were monitored for a period of about twelve (12) months.

Table 6.1: Location and Design of Selected Poles for Field Monitoring

		Location			Design			
			Latitude	Longitude	Speed (Mph)	Height (ft)	Side	GS
UT Selected Locations	Austin	SH45 EB	30.4769	-97.69618	80	150	12	No
	Dallas	I 635	32.9135	-96.73925	80	150	12	No
	Houston	IH 45	29.3295	-94.9324	100	150	12	No
	Laredo	IH 35	27.6057	-99.4942	80	150	12	No
	El Paso	US-54 @ Fred Wilson	31.8253	-106.4386	80	150	12	No

In the following, more specific information on the poles selected for the field monitoring will be provided. For each pole, reasons for the selection are also briefly discussed and reviewed.

HMIP in Austin District

The Austin District was selected since it has a large number of poles with the design of interest (195 HMIPs of 12 sided, 150-ft poles designed for 80 mph winds), and its potential of having winds in the speed ranges causing vortex shedding vibrations. Austin was also selected for convenience in evaluating the monitoring system.

The location of the selected pole and a wind monitoring site in the Austin district, representative wind data from a wind monitoring station in Austin district, and the satellite and street views of the pole for monitoring in the Austin district are shown in Figures 6.1, 6.2 and 6.3, respectively. Additionally, the pole was selected based on accessibility and the small blockage of wind from the south, the major wind direction throughout the year.

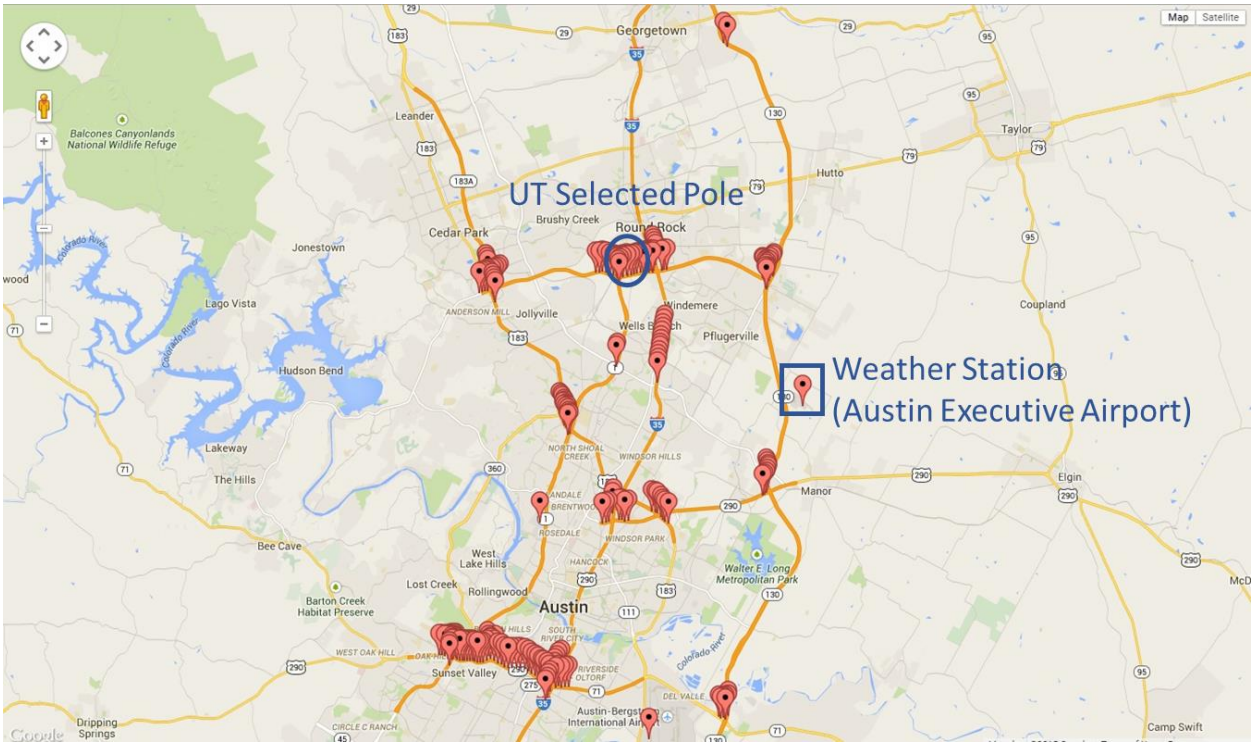

Figure 6.1: Location of the Selected HMIP and a Wind Monitoring Site in Austin District

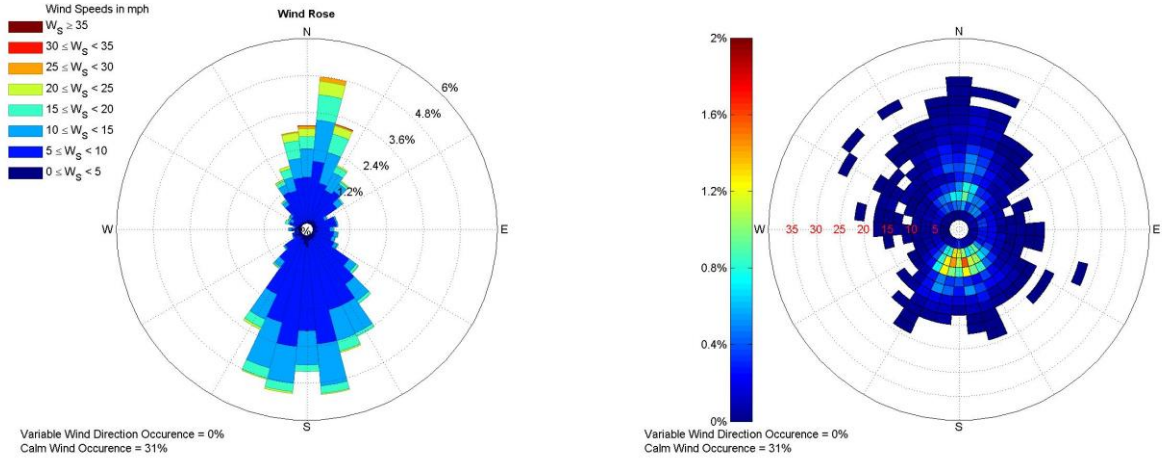

(a) Wind Rose (Austin) (b) Wind Density (Austin)

Figure 6.2: Wind Data from a Wind Monitoring Station at the Austin Executive Airport

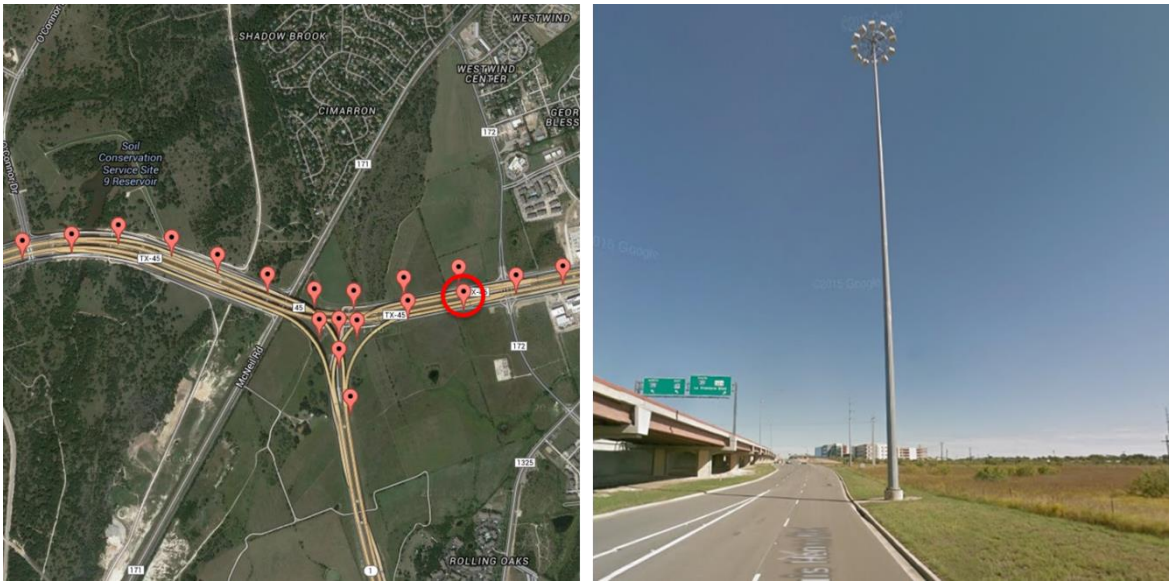

Figure 6.3: Pole for the Field Monitoring in Austin District

HMIP in Houston District

The Houston District was selected due to its proximity to the Texas coast. The location of the selected pole and a wind monitoring site in the Houston district, representative wind data from a wind monitoring station in the Houston district, and the satellite and street views of the pole are shown in Figures 6.4, 6.5 and 6.6, respectively. Additionally, the pole was selected based on accessibility and the steady wind near the coast of Galveston that may potentially cause vortex-shedding response.

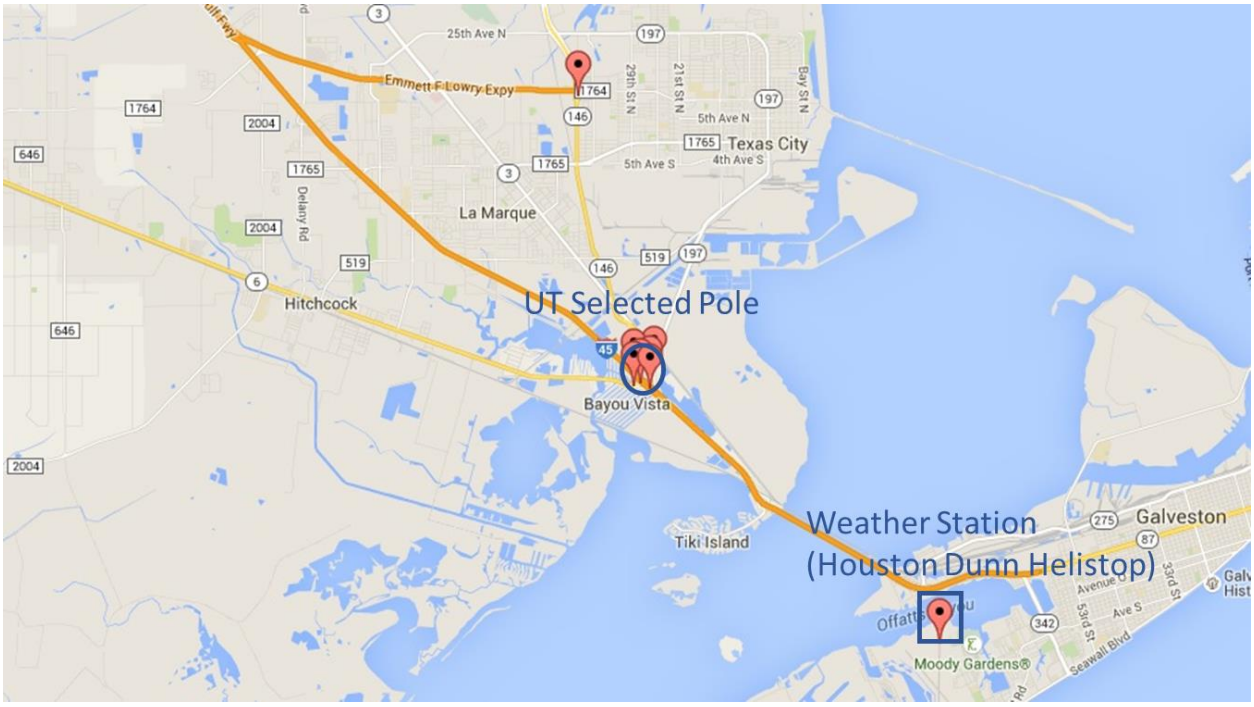

Figure 6.4: Location of the Selected HMIP and a Wind Monitoring Site in Houston District

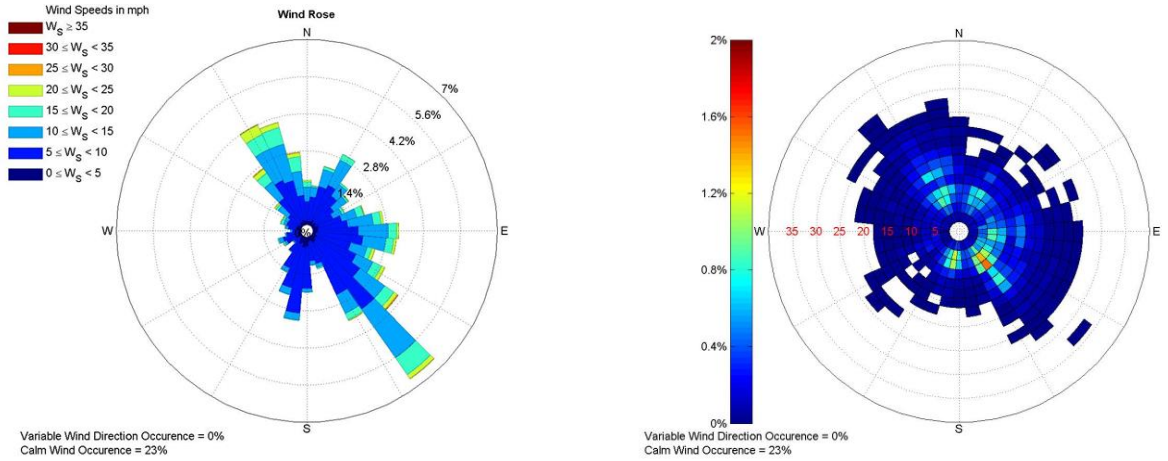

(a) Wind Rose (b) Wind Density

Figure 6.5: Wind Data from a Wind Monitoring Station in Houston (Houston Dunn Helistop)

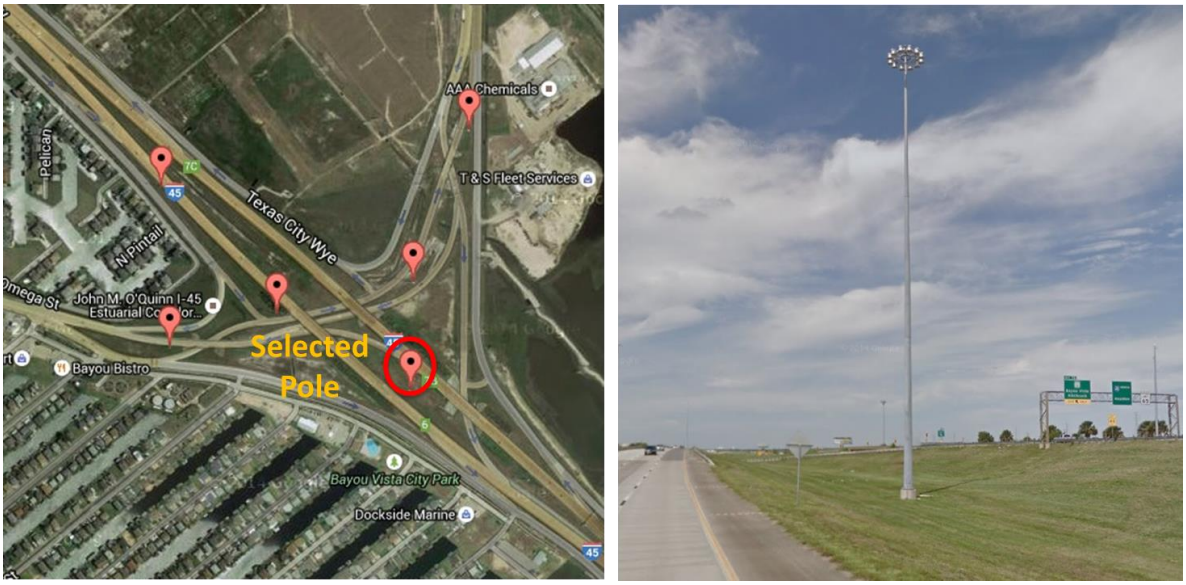

Figure 6.6: Pole for the Field Monitoring in Houston District (Galveston Coast)

HMIP in Dallas District

The Dallas District was selected since it has a large number of poles with the design of interest (51 HMIPs of 12 sided, 150-ft poles designed for 80 mph winds). It also represents an urban terrain with the potential of having winds causing turbulence.

The location of the selected pole and a wind monitoring site in the Dallas district, representative wind data from a wind monitoring station in the Dallas district, and the satellite and street views of the selected pole for monitoring in the Dallas district are shown in Figures 6.70, 6.80 and 6.90, respectively. Additionally, the proposed pole was selected based on accessibility and unsteady wind near big cities that potentially causes wind gust events to occur.

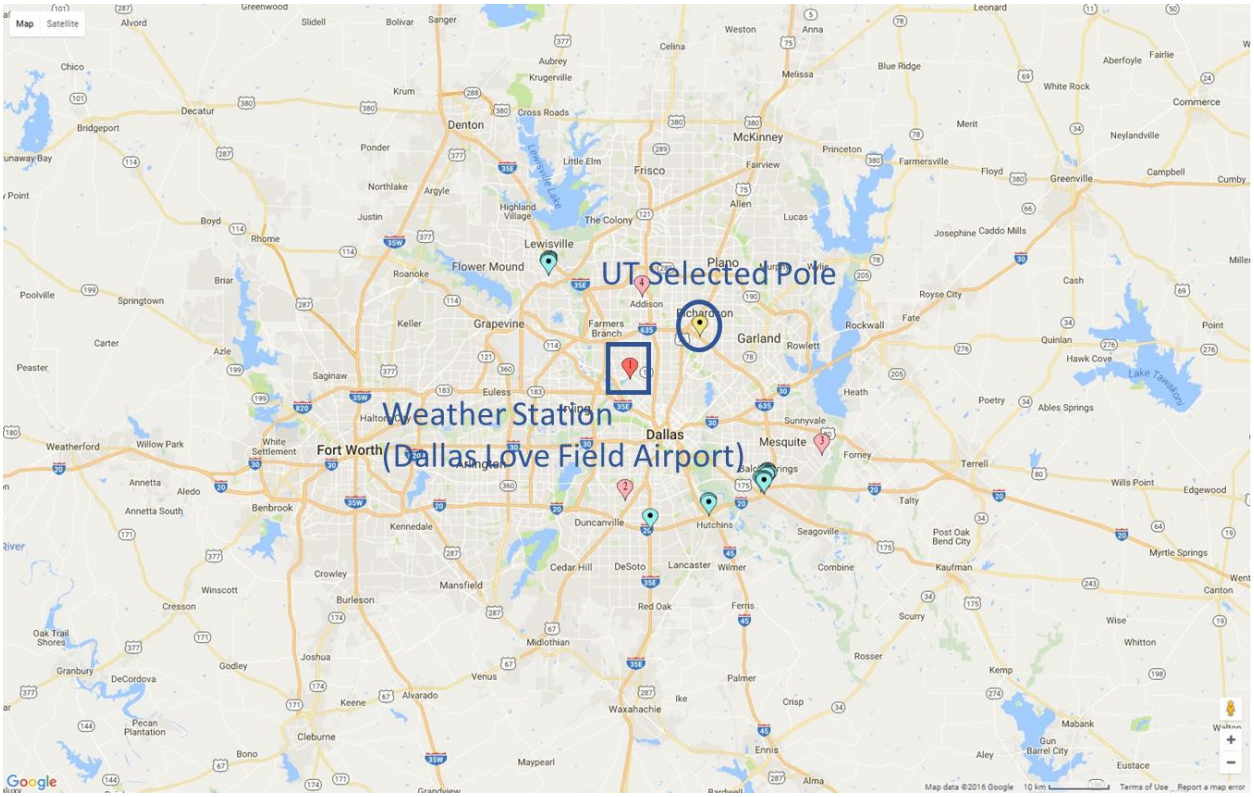

Figure 6.7: Location of the Selected HMIP and a Wind Monitoring Site in Dallas District

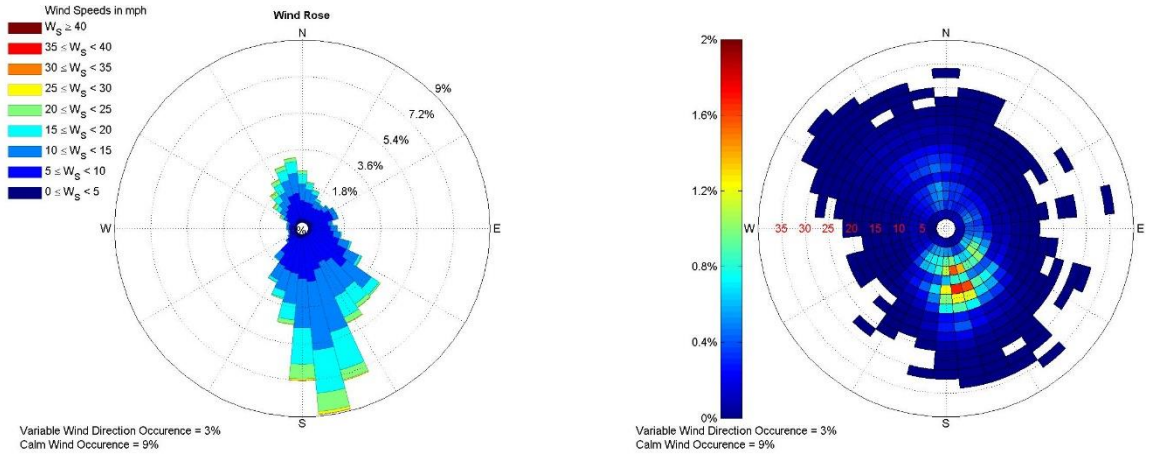

(a) Wind Rose (b) Wind Density

Figure 6.8: Wind Data from a Wind Monitoring Station at the Dallas Love Field Airport

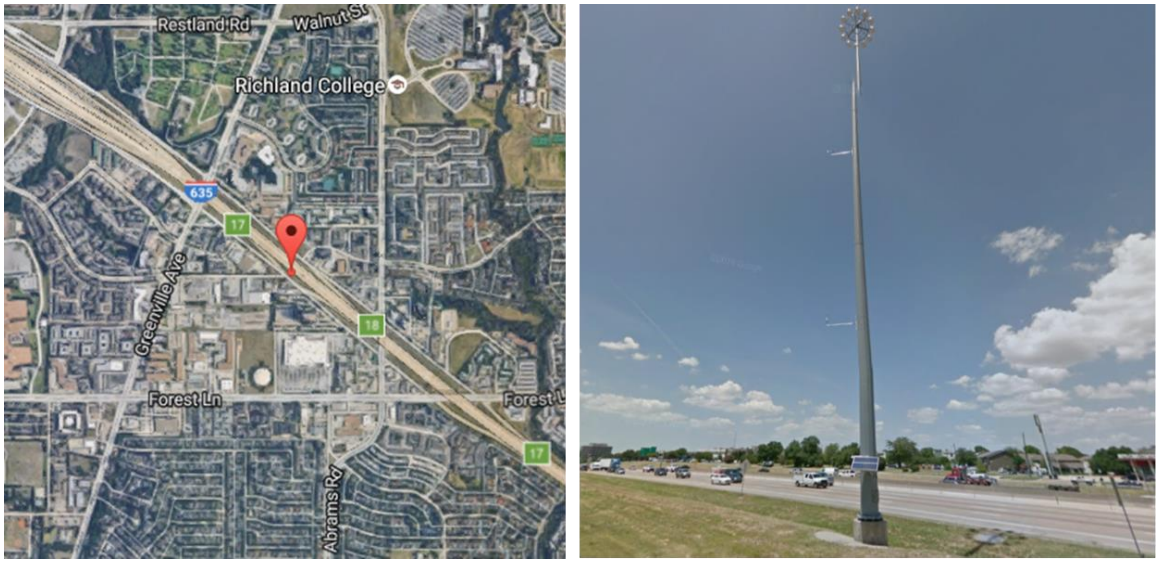

Figure 6.9: Pole for the Field Monitoring in Dallas District

HMIP in Laredo District

The Laredo District was selected because it has the second largest number of poles with the design of interest (101 HMIPs of 12 sided, 150-ft poles designed for 80 mph winds).

The location of the selected pole and a wind monitoring site in the Laredo district, representative wind data from a wind monitoring station in Laredo district, and the satellite and street views of the monitored pole in the Laredo district are shown in Figures 6.10, 6.11 and 6.12, respectively. Additionally, the pole was selected based on accessibility.

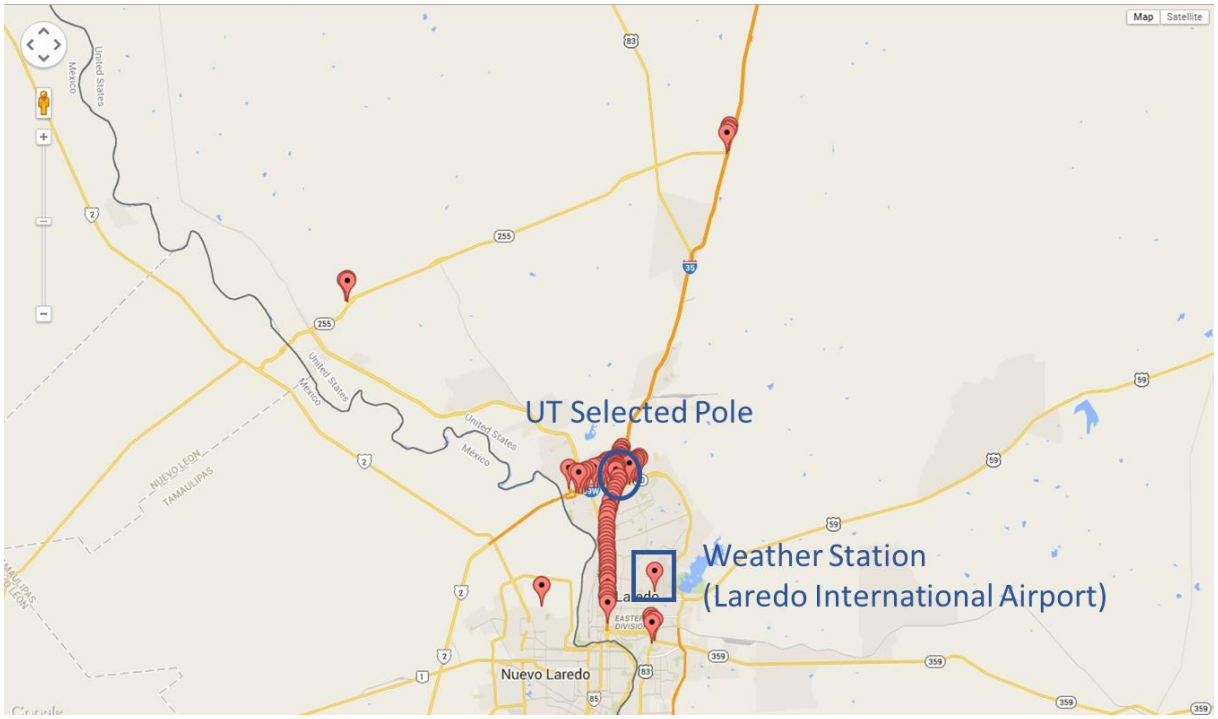

Figure 6.10: Location of the Selected HMIP and a Wind Monitoring Site in Laredo District

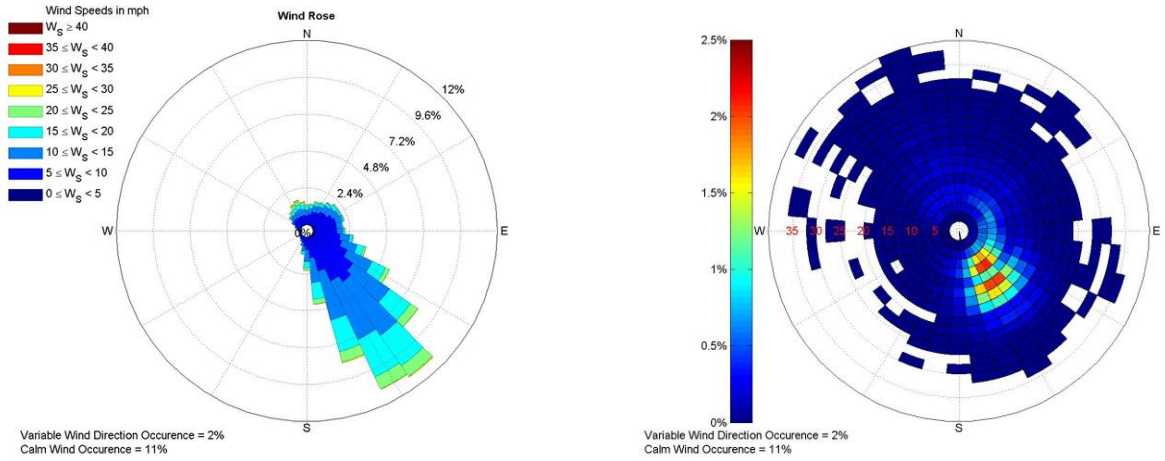

(a) Wind Rose (b) Wind Density

Figure 6.11: Wind Data from a Wind Monitoring Station at the Laredo International Airport

Figure 6.12: Pole for the Field Monitoring in Laredo District

HMIP in El Paso District

The El Paso District was chosen since it has very unique wind condition with no fixed dominant wind direction, and its potential for turbulence.

The location of the selected pole and a wind monitoring site in the El Paso district, representative wind data from a wind monitoring station in the El Paso district, and the satellite and street views of the selectedpole for monitoring in the El Paso district are shown in Figures 6.13, 6.14 and 6.15, respectively. Additionally, the pole was selected based on accessibility and the gusty wind near the mountains, which potentially causes large buffeting response.

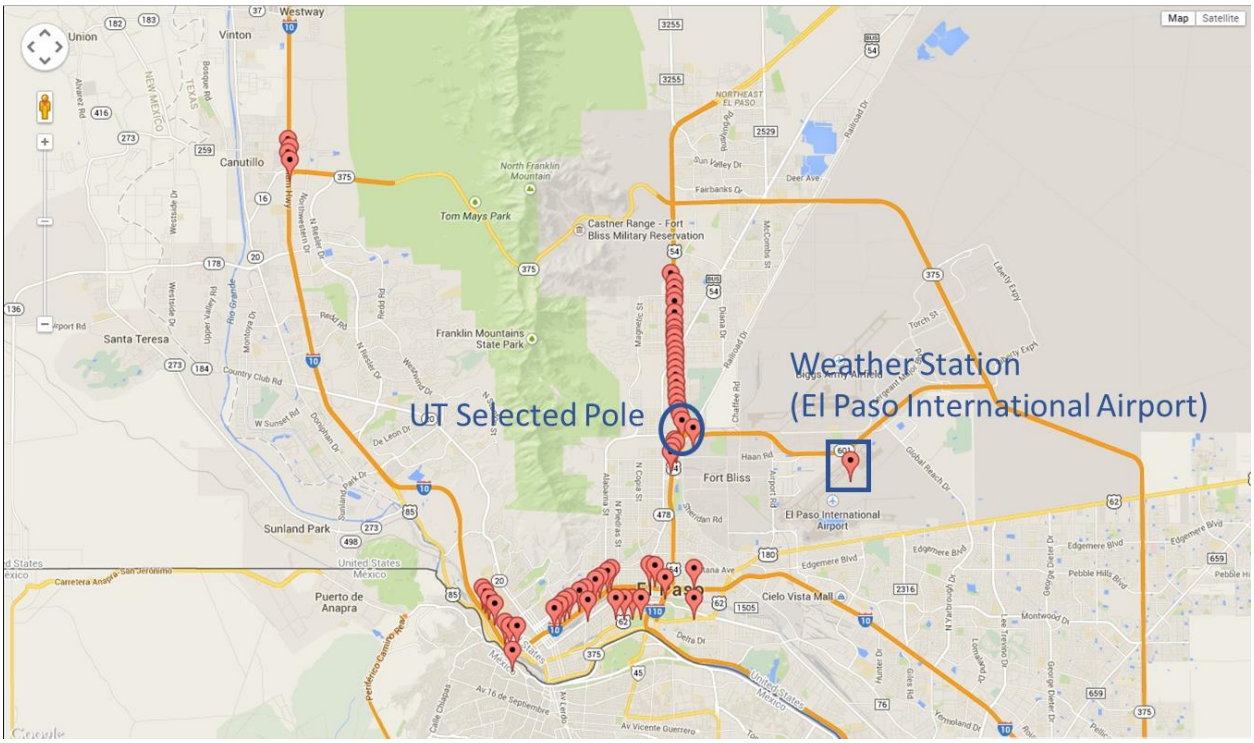

Figure 6.13: Location of the Selected HMIP and a Wind Monitoring Site in El Paso District

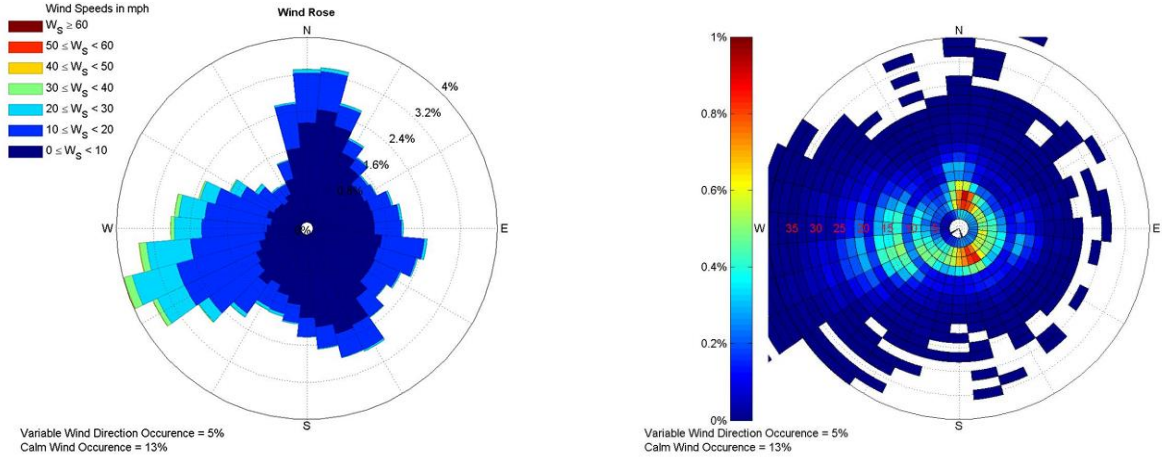

(a) Wind Rose (b) Wind Density

Figure 6.14: Wind Data from a Wind Monitoring Station at the El Paso International Airport

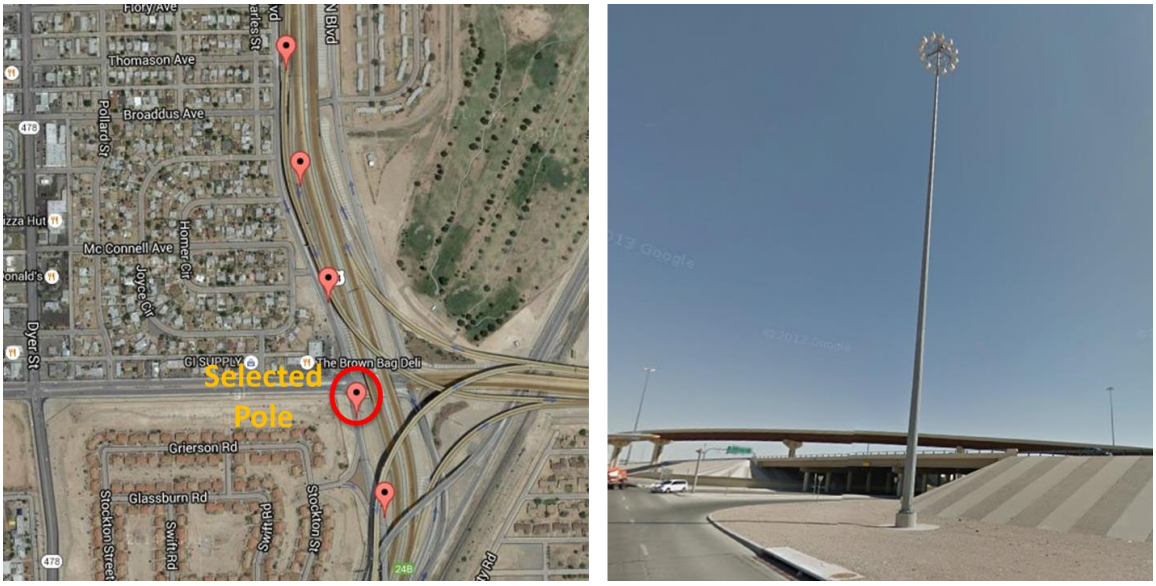

Figure 6.15: Pole for the Field Monitoring in El Paso District

6.3 Field Instrumentation

6.3.1 Instrumentation Setup

This section provides a brief overview of the instrumentation used in the field monitoring of HMIPs in Texas. The instrumentation includes different sensors, data acquisition, and a power system.

Sensors

Two anemometers were installed on each pole to gather wind data. A propeller anemometer (Model Young 05103) (Figure 6.16a) was used to gather data on wind speed and direction. An ultra-sonic anemometer (Model Young 81000) (Figure 6.16b) was used to monitor wind speed and direction as well as wind turbulence. These anemometers have a frequency range that is broad enough to capture gust events. Further, having two anemometers installed over the height of each pole provides useful data on the variation of wind velocity with height.

(a) Propeller Anemometer (b) Ultra-Sonic Anemometer

Figure 6.16: Anemometers to Monitor Wind Environment

In addition to anemometers, three accelerometers (PCB Model 3713B1110G) were used to monitor the vibrations of the HMIP structure. The accelerometers manufactured by PCB were three-axis accelerometers with a measuring range of 10 G. Accelerometers were installed over the height of each HMIP to evaluate the dynamic characteristics of the poles in their first three modes of vibration. Moreover, as shown in Figure 6.17, accelerometers were positioned inside small enclosures, and secured to the HMIPs using hose clamps.

Figure 6.17: Accelerometer shown in a small enclosure

Four strain gages (Model WFLA-6-11-3LT as shown in Figure 6.18) were installed on each orthogonal face of the HMIPs near the base. The strain gages were used to monitor the stresses caused by the wind-induced vibrations of the HMIPs. Strain data were collected using a rainflow cycle-counting algorithm that allows counting the number of cycles of loading at various strain levels over the full monitoring period. Strain data were continuously recorded to make sure that the stresses caused by pole vibrations due to high winds, and vortex shedding winds were captured.

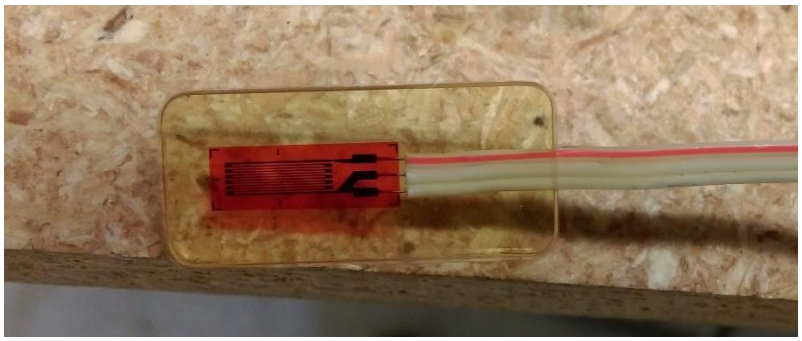

Figure 6.18: Strain Gage to Monitor Wind-Induced Stresses

Power System

The power system for the field instrumentation consisted of solar panels, batteries and charge controllers. The solar panels were selected/designed to generate power required by the data acquisition system and by the sensors based on the shortest daylight in a year. The demand of the power load was approximately 42 W, which required 1088 W-hrs. The shortest daylight in a year was approximated to last 7 hours thereby requiring 156 W solar panels. As shown in Figure 6.19, two 90 W solar panels (Model 90J) from Campbell Scientific were used to generate power for monitoring system. Figure 6.19 further shows the mounting frame used to attach the solar panels to the poles.

(a) Two 90J Solar Panels (b) Solar Panel Frames

Figure 6.19: Solar Panels and their Installation

Two AGM batteries from Duracell (Model DURHR 12-540, shown in Figure 6.20) with the capacity of 155 AH (Amperage-Hours) were used to power the monitoring system. With no sunlight, a total of 310 AH provided power to the system for approximately 3.5 days.

Figure 6.20: AGM Batteries from Duracell

An MPPT charge controller from SunSaver (Model SS-MPPT-15L, shown in Figure 6.21) was used to maximize the usage of solar power. The charge controller saves the power collected from the solar panels to the batteries and provides a stable load current for the sensors and data acquisition system.

Figure 6.21: MPPT Charge Controller from SunSaver

Wireless System

As shown in Figure 6.22, a wireless modem (Model Raven X) from Sierra was used for remote control of the data acquisition system. The modem was also powered by the power system described above. The modem was connected to an antenna to transfer signals to the data acquisition system through an Ethernet cable.

Figure 6.22: A Raven X Wireless Modem

Data Acquisition System

The data acquisition system, Compact RIO, from National Instruments (NI) was utilized to record and to analyze the field data. The Compact RIO (Figure 6.23) consisted of the controller (Model cRIO-9024), an eight slot chassis (Model cRIO-9114), and a series of modules. One NI-9237 module was used to record data from strain gages, three NI-9239 modules were used to record data from accelerometers and from the ultra-sonic anemometer, and one NI-9219 module was used to record data from the propeller anemometer.

Figure 6.23: NI Compact RIO Data Acquisition System

As depicted in Figure 6.24, the data acquisition system, the charge controller, and the modem were all installed on a panel and connected to each other using electric wires and terminals. In Figure 6.24, the sensors were connected to the terminals on the left. The terminals on the right functioned as the load and signal terminals.

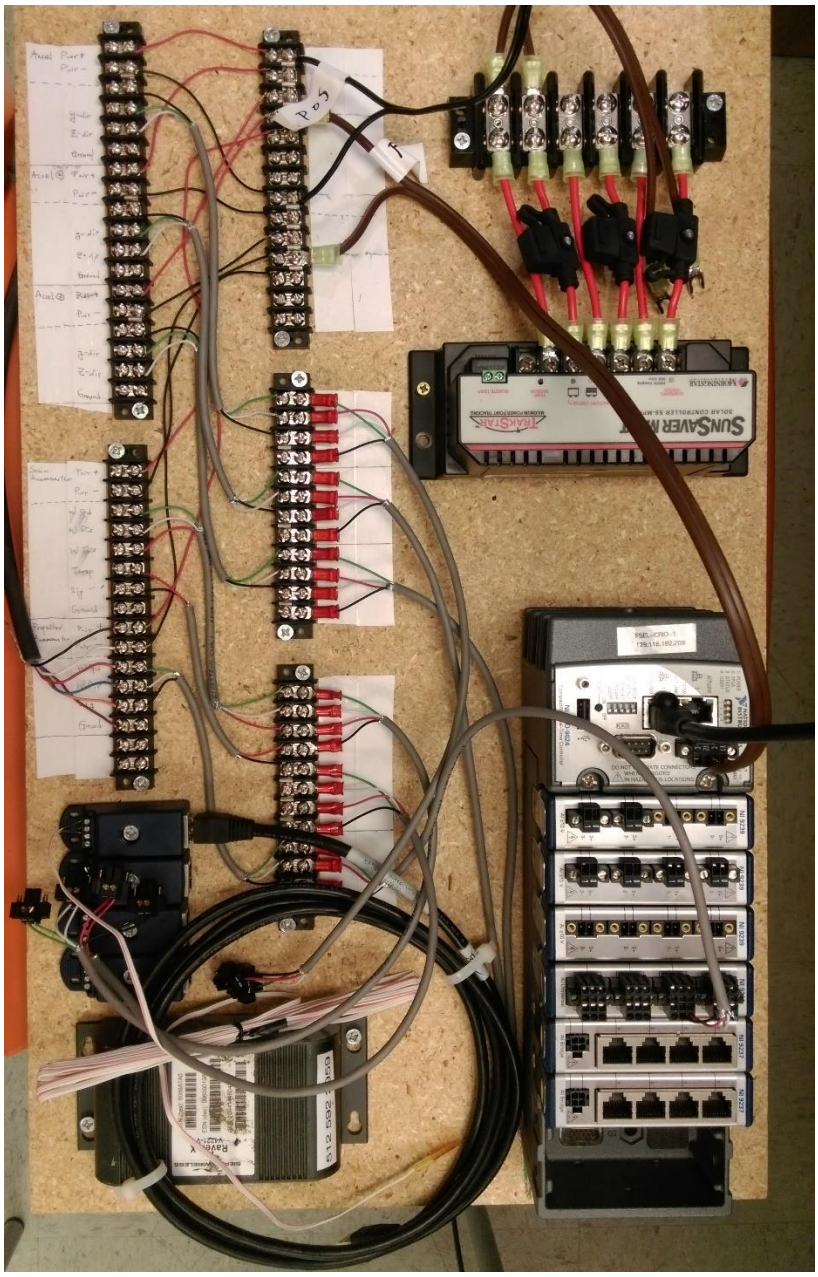

Figure 6.24: Instrumentation Panel

To protect the instrumentation panel shown in Figure 6.24 from direct exposure to the outside environment, the panel was positioned inside an enclosure at the site of each pole (Figure 6.25).

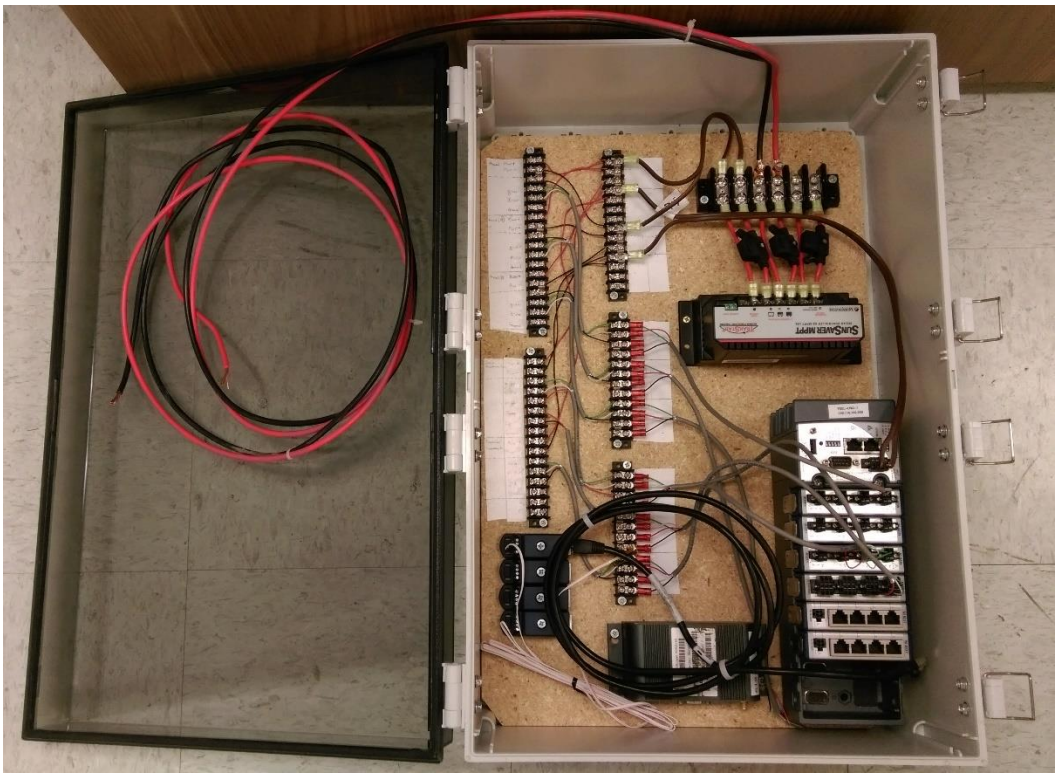

Figure 6.25: Instrumentation Panel inside an Enclosure

Installment and Evaluation of the Monitoring Systems

To evaluate the monitoring system and to practice different methods of installation of sensors, the research team setup a mock-up pole outside the Ferguson Laboratory at the University of Texas at Austin. As shown in Figure 6.26, one ultra-sonic anemometer, one propeller anemometer, one accelerometer, and two 90 watt solar panels were mounted on the mock-up pole. All these sensors were attached to the pole shaft using hose clamps.

Figure 6.26: Anemometers and Solar Panel Installed on a Mock-up Pole

6.3.2 On-Site Instrumentations

In this section, details of the instrumentation setup and equipment for each individual HMIP selected for field monitoring studies are illustrated.

HMIP in Austin

The instrumentation scheme for the selected HMIP in Austin is shown in Figure 6.27. As seen in Figure 6.27, to characterize the wind environment at the pole site, one ultra-sonic anemometer was installed at the height of 30 feet, and two propeller anemometers were installed at the heights of 80 and 105 feet above the base plate. Four accelerometers, installed at the heights of 30, 50, 80, and 105 feet above the base plate, were utilized to monitor the motion of the pole. Four strain gauges were installed at 76-inches above the base plate in North, East, South and West directions to record the wind-induced stresses. Solar Panels were installed at approximately the same locations as the strain gauges. One battery and two data acquisition boxes were set on a wooden support inside the HMIP shaft.

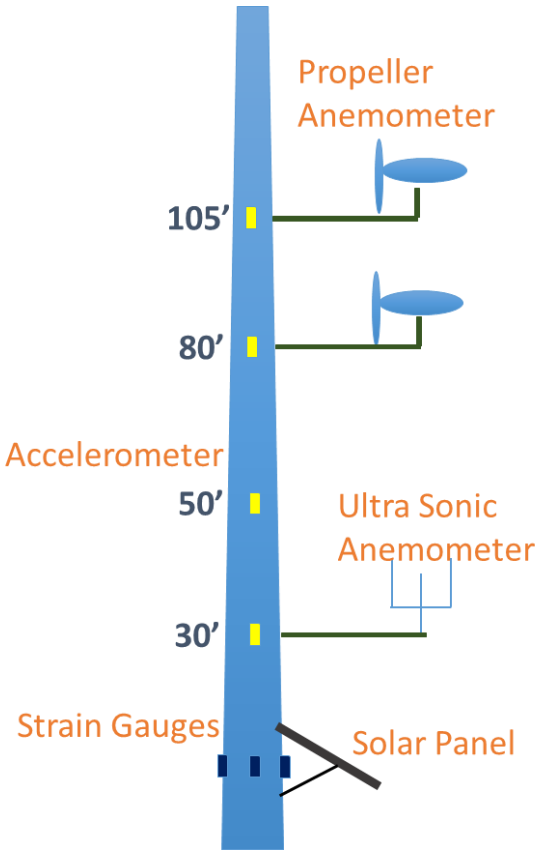

Figure 6.27: Instrumentation Scheme in the Field Monitoring Studies in Austin

Figure 6.28 shows the boom lift used to install sensors at different locations along the height of the pole. The boom lift was a JLG Ultra Boom model 1500SJP. Traffic control was provided by TxDOT as shown in Figure 6.29.

Figure 6.28: JLG Ultra Boom Lift used to Instrument the Selected HMIP in Austin

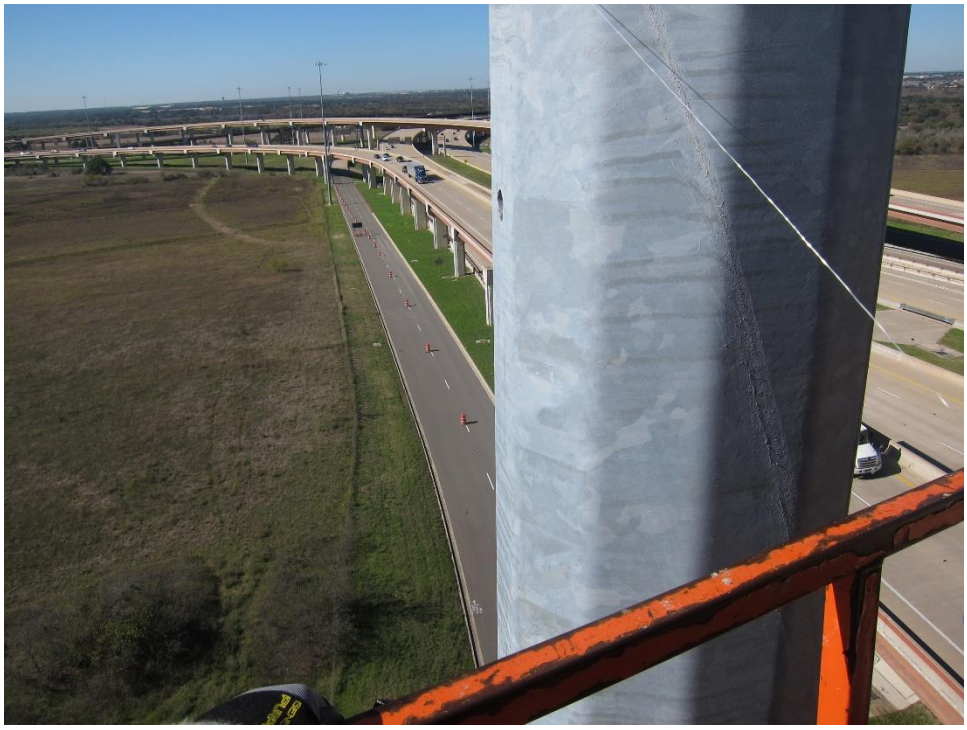

Figure 6.29: Traffic Control Cones Provided by TxDOT during Instrumentation in Austin

Details of Sensor Installation

The aluminum arms for the anemometers were clamped with four adjustable hose clamps as shown in Figure 6.30. The arms were clamped on the East side of the HMIP to avoid wind blockage by the HMIP. The selection of this direction was informed by the historical wind data indicating North and South as the most dominant wind directions. The anemometers were connected to the arms with hose clamps in the direction where the zero degree output direction aligned with the North direction (Figure 6.31). The socket screws on the clamped part of the arm frame were adjusted to ensure the arms were level. The accelerometers were clamped to the HMIP with two hose clamps on the North side of the HMIP as shown in Figure 6.32.

Figure 6.30: Attachment Details for the Anemometer Arms

Figure 6.31: Ultra-Sonic Anemometer Installed on the Pole in Austin

Figure 6.32: Accelerometer Clamped on to the HMIP in Austin

To run the accelerometer and anemometer cables inside the pole shaft, 0.75-inch diameter holes were drilled through the HMIP wall with a slugger drill at 30 and 80 feet (Figure 6.33). Cables at 50 and 105 feet were dropped through the existing holes in HMIP near 50 and 100 feet elevations. Fishing wires connected to a small screw were threaded in the holes first to ensure the wires could reach the bottom of the HMIP (Figure 6.34). After the fishing wires reached to the bottom of the pole, the sensor cables were connected to the other end of the fishing wires. The cables were then threaded through the holes while the personnel on the ground started pulling on the fishing wires until the cables also reached the bottom of the HMIP.

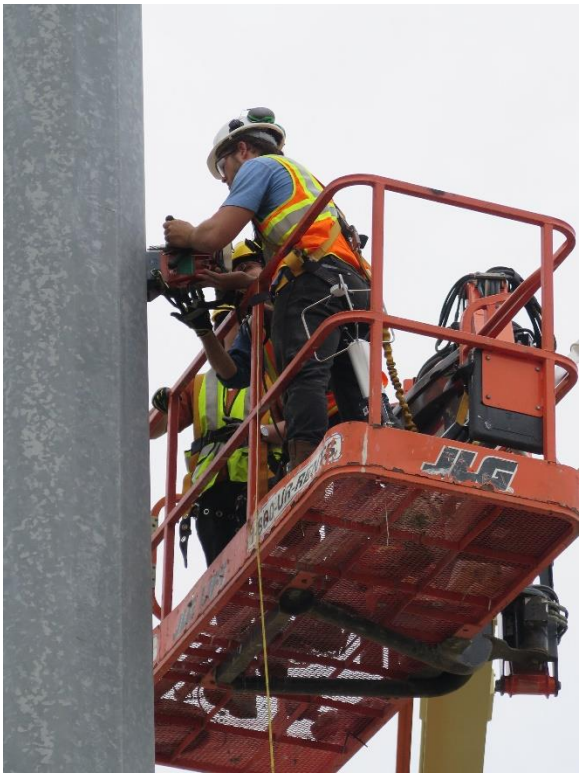

Figure 6.33: Drilling Holes through the HMIP Shaft

Figure 6.34: Threading the Fishing Wire inside the HMIP

Installing strain gauges on the HMIP consisted of multiple steps as follow:

- Grinding the steel surface at target locations (Figure 6.35)
- Cleaning the grinded surface with acetone
- Applying the adhesive on the prepared surfaces and catalyst on the back surface of the strain gauges (Figure 6.36)
- Pressing and holding the strain gauges on the targeted surfaces for several seconds for proper attachment
- Applying silicon coatings over the attached strain gauges (Figure 6.37)
- Applying protective wax coatings over the strain gauges (Figure 6.38)

Figure 6.35: Preparation of the Surface to Install Strain Gages

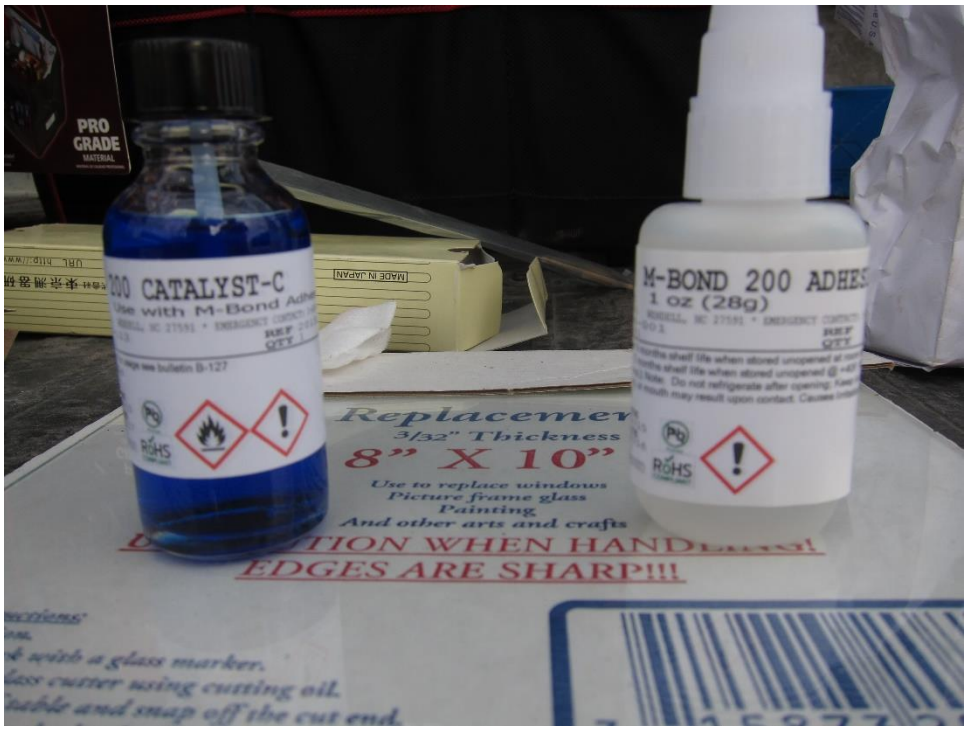

Figure 6.36: The Adhesive and Catalyst for Attaching Strain Gauges

Figure 6.37: Silicon Epoxy to Protect the Strain Gages from Environment

Figure 6.38: Wax to Protect the Strain Gages from Humidity

Solar Panel and Battery

The solar panel was installed on the south face of the HMIP (Figure 6.39). Two rectangular box tubes were attached to the HMIP with four hose clamps. The frame of the solar panels were connected to the two rectangular tubes. The two 90-Watts solar panels connected by two aluminum angles were attached to the frames. The wires of the two solar panels were connected in series to achieve higher voltages. The battery was set on two steel plates resting on top of a wooden support inside the HMIP shaft (Figure 6.40).

Figure 6.39: Solar Panel Installed on the South Side of the HMIP in Austin

Figure 6.40: Battery Situated inside the HMIP

Data Acquisition System

The sensor cables were connected to the acquisition box first as shown in Figure 6.41. The fuses for the charge controller were installed after the solar panel and battery were connected to the system. The system was switched on following the installation of fuses, and the preliminary check of the data acquisition system (NI Compact RIO) as well as the wireless modem. After the strain gauges were connected to the Compact RIO as shown in Figure 6.42, the data acquisition program was tested (Figure 6.43). Once the data acquisition program was running, holes on the enclosure box for cables were sealed (Figure 6.44). After the two enclosure box were sealed and set on the wooden stool inside the HMIP, the hand hole was closed and the field instrumentation was finished (Figure 6.45). The instrumentation of the selected HMIP in Austin was completed on December 7, 2015.

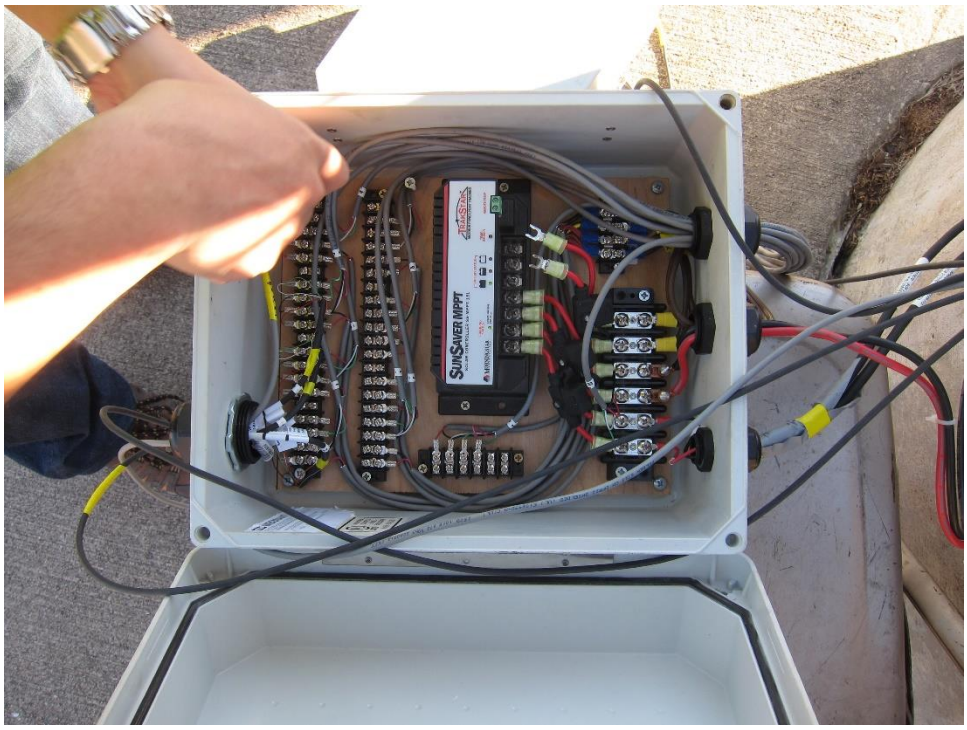

Figure 6.41: Connections for Sensor Cables inside an Enclosure Box

Figure 6.42: Connecting Strain Gauge Cables to the Data Acquisition System

Figure 6.43: Testing of Data Acquisition Program

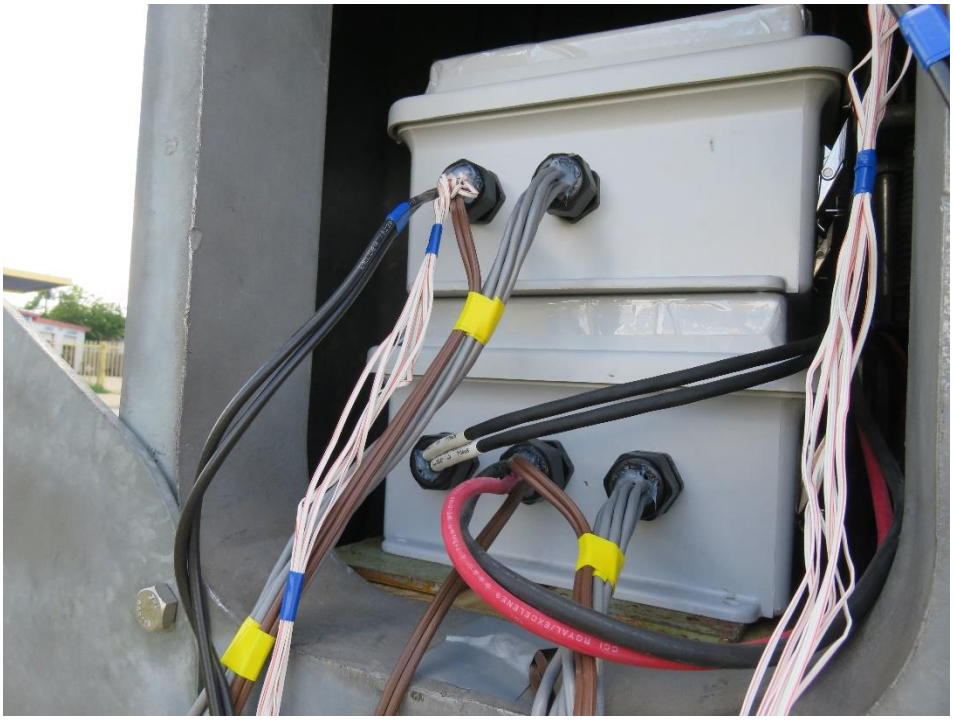

Figure 6.44: Cable Holes Sealed with Silicon Epoxy

Figure 6.45: Instrumented HMIP in Austin

HMIP in El Paso

The instrumentation plan for the El Paso location is shown in Figure 6.46. One sonic anemometer at 30 feet above the base plate, and one propeller anemometers at 80 feet above the base plate were installed to study the wind environment. Three accelerometers located at 30, 50 and 80 feet were used to monitor motions of the HMIP. Eight strain gauges were installed at 76 inches above the base plate in North, East, South, West and other four flats on the East side of the HMIP to record the wind-induced stresses. Solar Panels were installed at approximately the same locations as the strain gauges. A battery and two data acquisition enclosure boxes were set on a wooden support inside the HMIP.

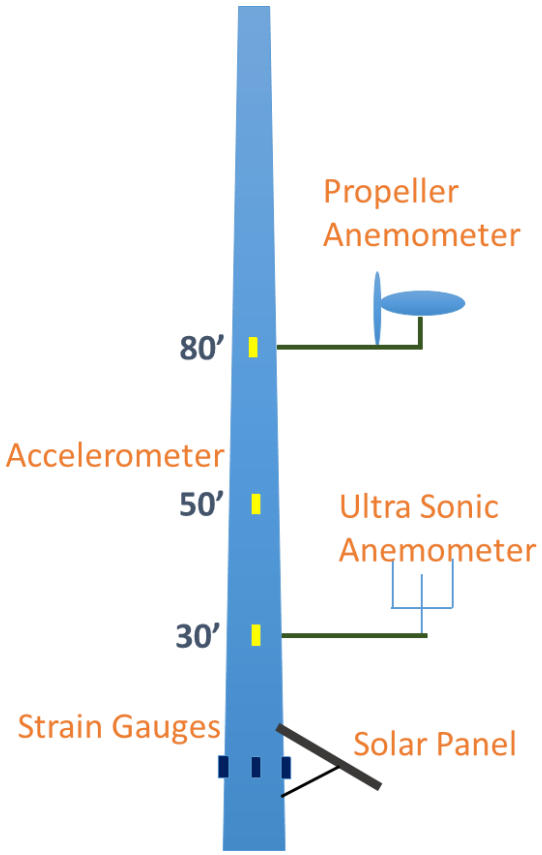

Figure 6.46: Instrumentation Scheme in the Field Monitoring Studies in El Paso

Figure 6.47 shows the boom lift used to install sensors at different locations along the height of the pole. The boom lift was a JLG Ultra Boom model 1200SJP. No traffic control was needed for this specific site. The general procedure for installing instruments and sensors on the selected HMIP in El Paso was the same as that for the pole in Austin. The major difference was in the direction of the arm that was changed to the West direction, a more frequent wind direction in El Paso. A picture of the instrumented HMIP in El Paso is shown in Figure 6.48. The instrumentation of the selected HMIP in El Paso was completed on June 18, 2016.

Figure 6.47: JLG Ultra Boom Lift used to Instrument the Selected HMIP in El Paso

Figure 6.48: Instrumented HMIP in El Paso

HMIP in Dallas

The instrumentation scheme for the Dallas pole was the same as that for the pole in El Paso. The boom lift used in Dallas was a Genie telescopic 120 feet capacity model (Figure 6.49). No traffic control was needed for this specific site. A picture of the instrumented HMIP in Dallas is shown in Figure 6.50. The instrumentation of the selected HMIP in Dallas was completed on June 28, 2016.

Figure 6.49: Genie Ultra Boom Lift used to Instrument the Selected HMIP in Dallas

Figure 6.50: Instrumented HMIP in Dallas

HMIP in Galveston

The instrumentation plan for the Galveston location was the same as that for the pole in El Paso. The boom lift used in Galveston was a JLG Ultra Boom model 1200SJP (Figure 6.51). No traffic control was needed for this specific site. A picture of the instrumented HMIP in Galveston is shown in Figure 6.52. The instrumentation of the selected HMIP in Galveston was completed on July 21, 2016.

Figure 6.51: JLG Ultra Boom Lift used to Instrument the Selected HMIP in Galveston

Figure 6.52: Instrumented HMIP in Galveston

HMIP in Laredo

The instrumentation plan for the Laredo location was the same as that for the pole in El Paso. The boom lift used in Galveston, shown in Figure 6.53, was a JLG Ultra Boom model 1250AJP. Traffic control (lane closure) was provided by TxDOT. A picture of the instrumented HMIP in Laredo is shown in Figure 6.54. The instrumentation of the selected HMIP in Laredo was completed on August 15, 2016.

Figure 6.53: JLG Ultra Boom Lift used to Instrument the Selected HMIP in Laredo

Figure 6.54: Instrumented HMIP in Laredo

6.4 Methodology for Data Processing

This section illustrates the processing and analyzing of the data collected in the field study. To analyze and process the data, the continuous data streams consisting of wind conditions (data from anemometers), motion response (data from accelerometers), and induced-stress response (data from strain gauges) were broken down into 5-minute segments.

The dynamic properties of the HMIP structure such as natural frequencies, mode shapes, and damping ratios were first extracted based on the motion and strain response. Different wind characteristics such as wind speed, wind direction, and wind turbulence were later determined for each time-segment. Next, the vibrating motion of the HMIP and the corresponding amplitudes and frequencies were obtained for each time-segment. Last, the induced fatigue damage based on the sustained stress ranges in each time-segment was evaluated using the concept of the Equivalent Fatigue Load (EFL). The processed data from each site are presented in Section 6.5.

6.4.1 Dynamic Properties of In-service HMIPs

Natural Frequencies

Natural frequencies of high-mast poles were determined based on a simple peak picking method from the power spectrum of the collected acceleration or strain time histories. The power spectra from each 5-minute segment were averaged to obtain a smoother and more representative power spectrum to capture the natural frequencies. The frequencies corresponding to the peaks represent the natural frequencies of the structure. Shown in Figure 6.55: is an example of a power spectrum extracted from the Austin site using the strain history obtained from the strain gauge located on the South side of the HMIP. Seen from the power spectrum in Figure 6.55: are peaks at the first three modal frequencies: 0.28 Hz, 1.2 Hz, and 3.14 Hz, respectively. Natural frequencies obtained using this method for each in-service HMIPs at different sites are presented and compared in Section 6.5.

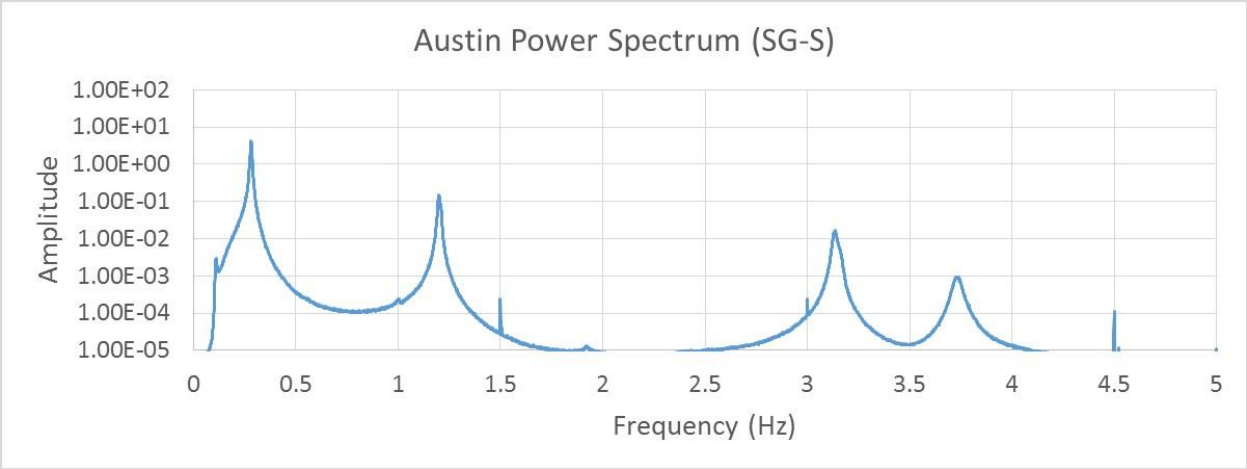

Figure 6.55: Averaged Power Spectrum (Austin - South Strain Gauge)

Structural Damping Ratios

Damping ratios can be extracted from log-decrement method or the Ibrahim Time Domain method(ITD) using a free decaying response in the time domain or a half-power bandwidth method in the frequency domain (Connor et al. 2012). Both methods in the time domain require a free decaying response time history, which can be recorded by deploying a pluck test on the structure or can be extracted using ambient data through Random Decrement Technique (RDT) (Ibrahim 1977). The half-power bandwidth method in the frequency domain can be used with both free decaying response and ambient data. Since pluck tests were not implemented in this study and only ambient data were available, the half-power bandwidth method in the frequency domain was used to extract the structural damping ratios.

From the averaged frequency response spectrum, a frequency band was established between two frequencies f_1 and f_2 as illustrated in Figure 6.56. These two frequencies were chosen to correspond to an amplitude equal to the peak amplitude divided by $\sqrt{2}$. The two frequencies, f_1 and f_2, referred to as half-power points, were used to determine the damping ratio using Equation 6.1.

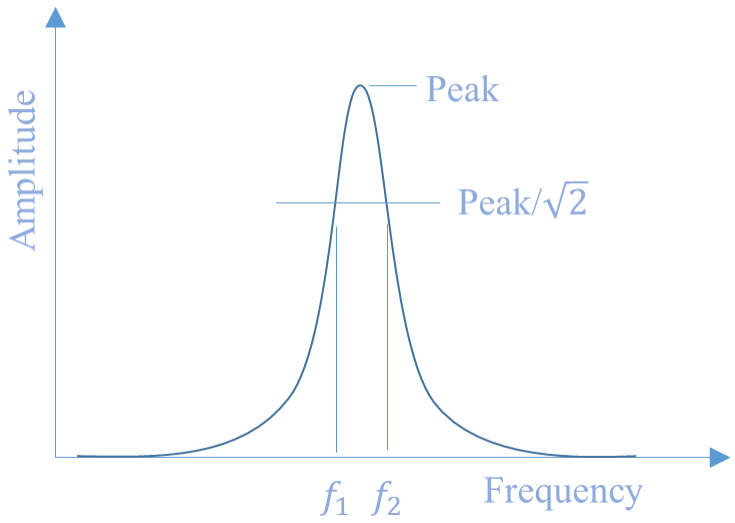

Figure 6.56: Half-power Bandwidth Method

$$\xi = \frac{f_2 - f_1}{f_1 + f_2} \qquad \textit{Equation 6.1}$$

Since the half-power bandwidth method uses ambient data where all sorts of excitations due to natural effects such as wind gusts or vortex shedding are included, the damping ratio most likely consists of structural damping and the aerodynamic damping caused by natural wind as well. To obtain the structural damping alone, the aerodynamic effects from the wind are excluded by avoiding segments in low wind speeds where vortex shedding is more likely to be dominant as reported in past studies (Chang 2009). However, if the total damping effect caused by vortex shedding is of interest, segments for which vortex-shedding is dominant can be extracted individually to investigate the effect of aerodynamic damping.

Modal Shapes and Modal Contributions

The contribution of each mode was estimated using Spectral Proper Transformation (SPT) or Proper Orthogonal Decomposition (POD) implemented in the frequency domain (Srivilairit and Manuel 2009). The cross-power spectral density function matrix ($S(n)$) for frequencies (n) of interest (Equation 6.2) was estimated using displacement time histories calculated from acceleration time histories at 30, 50, and 80 feet above the base plate. Eigenvalues ($\lambda(n)$) of these matrices represent the variance contributed to the mode described by the corresponding eigenvectors ($\psi(n)$) at that frequency (Equation 6.3). Since the second and third eigenvalues are relatively small compared to the first (largest) eigenvalue, the contributions at each frequency are represented by the largest eigenvalues in a 0.3 Hz frequency band centered on the three modal frequencies. The eigenvector ($\psi(n)$) corresponding to the largest eigenvalue at the three modal frequencies represents the vibrating mode shape of the structure. Figure 6.57 shows an example of the estimated eigenvectors obtained for the in-service HMIP in Austin. As seen in Figure 6.57, mode shapes obtained from field data match closely with the corresponding ones derived using the structural analysis software, SAP2000.

$$S(n) = \begin{bmatrix} S_{11}(n) & S_{12}(n) & S_{13}(n) \\ S_{21}(n) & S_{22}(n) & S_{23}(n) \\ S_{31}(n) & S_{32}(n) & S_{33}(n) \end{bmatrix} \qquad \textit{Equation 6.2}$$

$$\lambda(n) = \begin{bmatrix} \lambda_1(n) \\ \lambda_2(n) \\ \lambda_3(n) \end{bmatrix} \qquad \psi(n) = \begin{bmatrix} \psi_{11}(n) & \psi_{12}(n) & \psi_{13}(n) \\ \psi_{21}(n) & \psi_{22}(n) & \psi_{23}(n) \\ \psi_{31}(n) & \psi_{32}(n) & \psi_{33}(n) \end{bmatrix} \qquad \textit{Equation 6.3}$$

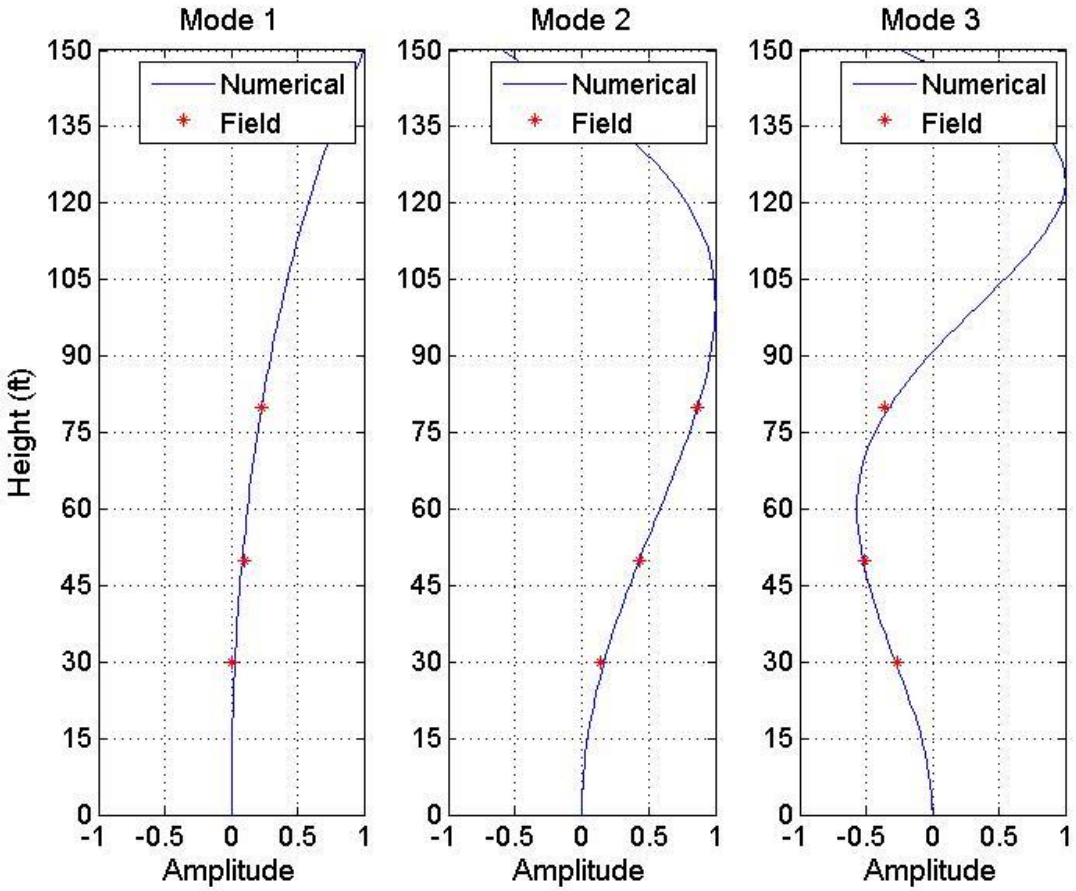

Figure 6.57: Modal Shapes for In-Service HMIPs - Field versus Simulation

6.4.2 Wind Environment

Wind Speed and Direction

The propeller anemometer instrumented at 80 feet above the base plate outputs the wind speed and wind direction at a frequency of 1 Hz. The representative wind speed and direction during the 5-minute period is determined using the resultant direction and amplitude which views

the wind speed ($U(t)$) and direction ($\theta(t)$) as a vector in Cartesian coordinates ($x(t), y(t)$) (Equation 6.4). The subtraction from π/2 is to rotate the axis that defines zero degrees from North to East to be consistent with the Cartesian coordinates. The summation of the wind vectors gives a resultant direction of the wind (θ_{ave}) where the amplitude divided by the number of data points (N) represents the mean wind speed (U_{ave}) as illustrated in Equations 6.50 and 6.60.

$$x(t) = U(t) \cdot \cos(\frac{\pi}{2} - \theta(t))$$
$$y(t) = U(t) \cdot \sin(\frac{\pi}{2} - \theta(t))$$

Equation 6.4

$$\theta_{ave} = \frac{\pi}{2} - atan2(\sum x(t), \sum y(t))$$

Equation 6.5

$$U_{ave} = \sqrt[2]{(\frac{\sum x(t)}{N})^2 + (\frac{\sum y(t)}{N})^2}$$

Equation 6.6

The ultrasonic anemometer instrumented at 30 feet above the base plate outputs the absolute wind speed, the horizontal angle ($\theta(t)$), and the vertical angle ($\gamma(t)$) in a spherical coordinate system defined in Figure 6.58. Data from ultrasonic anemometer were acquired at the rate of 50 Hz to be consistent with the acquisition rate for strain gauges and accelerometers. The horizontal wind speed was determined using the vertical angle ($\gamma(t)$) as indicated in Equation 6.7.

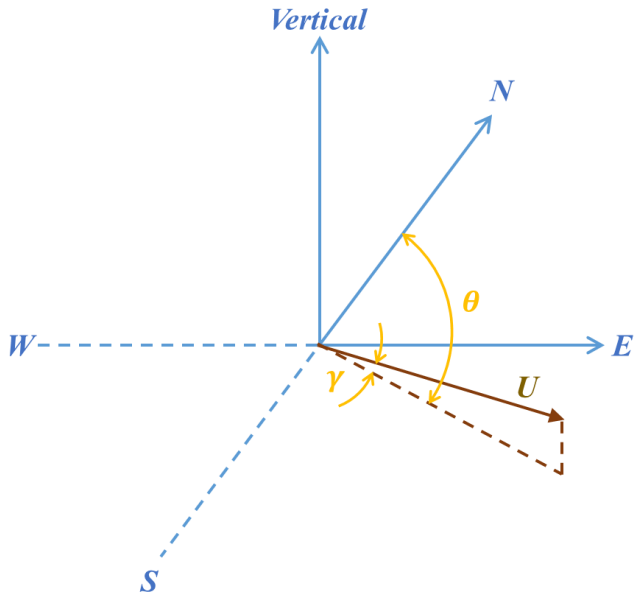

Figure 6.58: Coordinate Definition for the Output Data from Ultrasonic Anemometers

$$U_h(t) = U(t) \cdot \cos(\gamma(t)) \qquad \textbf{Equation 6.7}$$

The calculation of the resultant wind speed and direction follows the same procedure as for the propeller anemometers by replacing the wind speed ($U(t)$) in Equation 6.4 with the horizontal wind speed ($U_h(t)$).

Wind Profile

The wind profile (wind shear) parameter (α) is determined assuming the wind speed distribution along the height of the pole follows the power law (Equation 6.8). The parameter (α) is determined from the average wind speed at 30 feet and 80 feet. Larger α indicates larger wind variations along the height of the pole. Figure 6.59 shows an example of different wind profiles (α) while sustaining the same wind speed at 30 feet.

$$\frac{U}{U_r} = \left(\frac{Z}{Z_r}\right)^{\alpha} \qquad \textbf{Equation 6.8}$$

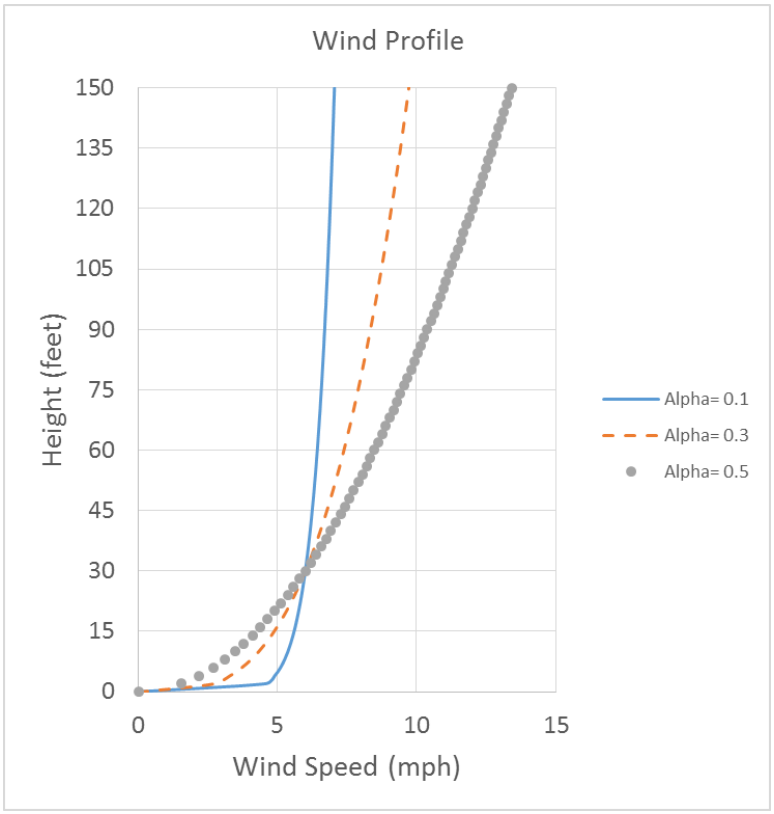

Figure 6.59: Wind Profile Affected by the Value of Parameter α

Turbulence Intensity

Turbulence intensity in along-wind (I_u), across-wind (I_v), and vertical-wind (I_w) directions can be determined at 30 feet above the base plate using the ultrasonic anemometer. Turbulence

intensity is defined as the standard deviation of the fluctuating wind speed ($u(t), v(t), w(t)$) divided by the mean wind speed or the resultant wind speed (U_{ave}), during the 5-minute duration, in the along wind direction (Equation 6.9).

$$I_u = \frac{\sigma_u}{U_{ave}}, I_v = \frac{\sigma_v}{U_{ave}}, I_w = \frac{\sigma_w}{U_{ave}} \qquad \textbf{Equation 6.9}$$

The fluctuating wind speed history for along-wind direction ($u(t)$) was calculated based on the wind speed difference of the horizontal instant wind speed component in the resultant wind direction and the mean wind speed (U_{ave}) as shown in Equation 6.10.

$$u(t) = U_h(t) \cdot \cos(\theta(t) - \theta_{ave}) - U_{ave} \qquad \textbf{Equation 6.10}$$

The fluctuating wind speed history for across-wind direction ($v(t)$) was calculated based on the horizontal instant wind speed component in the direction perpendicular to the resultant wind direction as shown in Equation 6.11.

$$v(t) = U_h(t) \cdot \sin(\theta(t) - \theta_{ave}) \qquad \textbf{Equation 6.11}$$

The fluctuating wind history in the vertical-wind direction ($w(t)$) was calculated based on the instant wind speed component in the vertical direction shown in Equation 6.12, where γ is the vertical angle defined in Figure 6.58.

$$w(t) = U(t) \cdot \sin(\gamma(t)) \qquad \textbf{Equation 6.12}$$

6.4.3 Wind-Excited Response – Pole Movements

The motion response of high mast poles was calculated using a similar method employed in a research study of a cantilevered mast arm for traffic signal structures (Zuo and Letchford 2010). According to the method employed, it is necessary to extract displacements contributed by different participating modes of vibration. The data processing flow chart is presented in Figure 6.60.

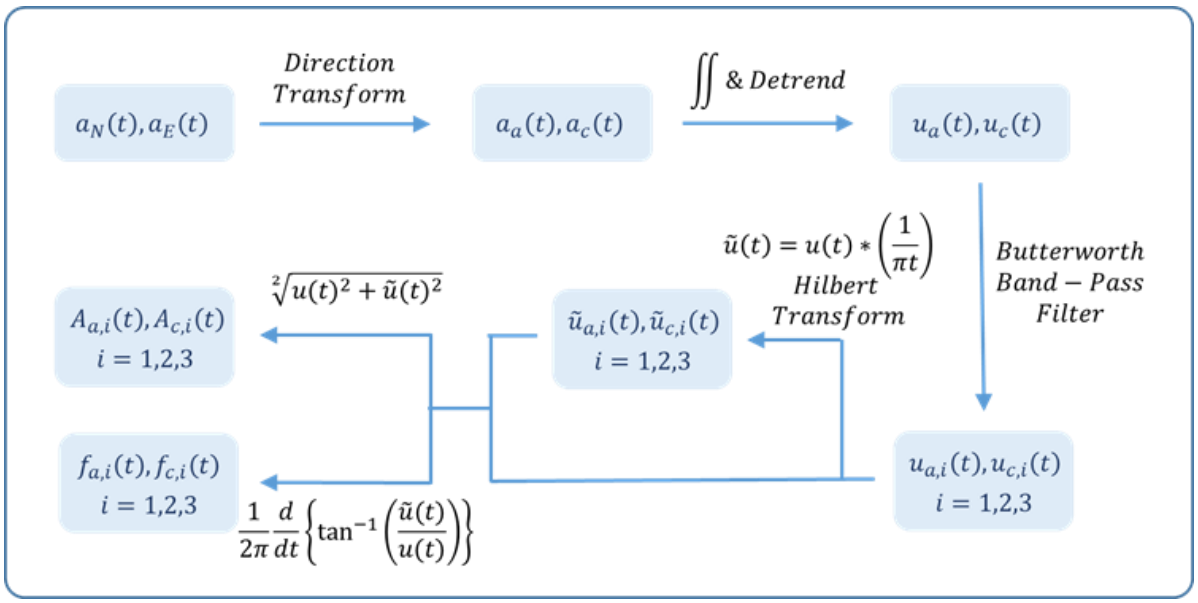

Figure 6.60: A Flowchart Summarizing the Field Data Processing

First, the acceleration time series recorded in the N-S and E-W directions were transformed into along-wind and across-wind directions using Equation 6.13.

$$a_\theta(t) = a_N(t) \cdot cos\theta + a_E(t) \cdot sin\theta \qquad \textbf{Equation 6.13}$$

where θ is the clockwise angle from North to the along-wind direction. Second, both the along-wind and across-wind acceleration time series were numerically integrated twice to obtain displacement time series. A wavelet detrend process (db10 - level 7) was implemented after each integration to remove any resulting offset and slowly varying trend. Third, the displacement time series data were band-passed (fifth order) using a 0.3 Hz frequency band with a Butterworth filter applied around the first three natural frequencies identified by peak picking from the power spectra of the acceleration data. Fourth, the Hilbert transform (Bendat 2002) of the displacement time series was obtained to construct the envelope of the peak displacements and instantaneous frequencies for each mode. The average displacement of the envelope process and the average frequency for each mode in the along-wind and across-wind directions at all three locations of the accelerometers were obtained in this manner.

Figure 6.61 shows a sample 5-minute acceleration time series that is processed to generate displacement time series for the three primary modes. Identified frequencies for the three modes are consistent with the natural frequencies from the power spectral of the transformed displacement record.

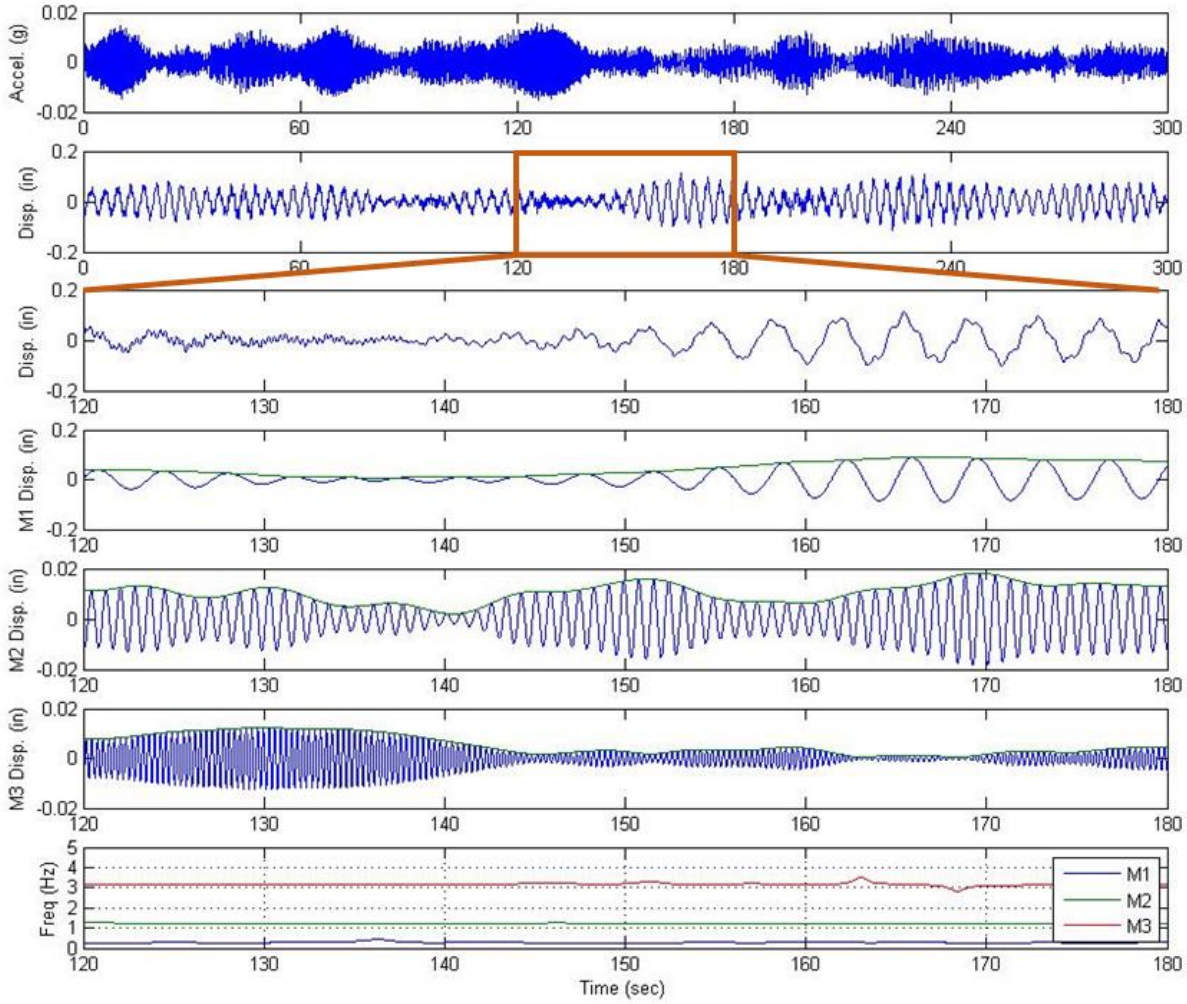

Figure 6.61: 5-Minute Displacement Time Histories in Three Primary Modes Derived from Acceleration Data

6.4.4 Wind-Excited Response – Pole Stresses

The continuously measured strain data were used to calculate the induced fatigue damage. The strain time histories from perpendicular directions were also rotated into the along-wind and across-wind directions in a manner as was indicated for accelerations using Equation 6.13. If more than one pair of orthogonal strain histories were available, the strain histories were averaged for the along- and across-wind directions, respectively. The derived strain histories were subsequently used to obtain stress range histograms using the rainflow-counting algorithm and in turn to determine the "equivalent" fatigue load (EFL) representing the fatigue demand.

Rainflow Counting

A cycle-counting method is needed to determine the variable-amplitude stress range cycles from the strain-time histories in order to apply the Palmgren-Miner's rule (Miner 1945). Numerous counting methods for fatigue analysis have been developed and standardized in ASTM E1049 (2011). The simplified rainflow-counting method included in ASTM E1049 and developed by

Downing and Socie (1982) is a simple method that resolves the stress-time histories into full cycles. The algorithms of the simplified rainflow-counting method can be found in Downing and Socie 1982. This simplified rainflow-counting method has been implemented in fatigue analysis of steel bridges (Fasl 2013), and of HMIPs (Magenes 2011) in the past, and is also selected for the purpose of this study.

Equivalent Fatigue Load (EFL)

Equivalent fatigue load (EFL) is a constant-amplitude stress range that essentially results in the same amount of damage from the variable-amplitude stress ranges. The concept of equivalent fatigue load (EFL) was successfully used in the past for fatigue analysis of wind turbines (Sutherland 1999, Nguyen 2012). The concept of equivalent fatigue load (EFL) is very similar to the commonly known concept of effective stress range (S_{RE}), which is often used in estimating fatigue loads for steel bridges (Fasl 2013). The effective stress range is defined in Equation 6.14, which corresponds to a slope (m) of three as proposed by the AASHTO (AASHTO 2013).

$$S_{RE} = \sqrt[3]{\frac{\sum S_{R,i}^3}{n}} \qquad \textit{Equation 6.14}$$

In Equation 6.14, $S_{R,i}$ are the stress ranges determined from the strain-time histories using rainflow-counting method and *n* is the corresponding number of stress cycles. Similarly, the EFL is determined using Equation 6.15 with the same $S_{R,i}$ determined from the same strain-time histories, but with a fixed cycle number (N_0) instead of the actual number of cycles, *n*.

$$EFL = \sqrt[3]{\frac{\sum S_{R,i}^3}{N_0}} \qquad \textit{Equation 6.15}$$

The EFL can be interpreted as a constant amplitude load (stress range), applied for a fixed number of cycles (N_0), and results in the same damage as that of the actual number of variable-amplitude stress cycles in the stress-time histories. N_0 is determined using Equation 6.16 assuming that the pole vibrates in the first mode with the frequency (f_1) during the time of interest (T). The time of interest is the length of the analyzed stress-time histories used to calculate EFL. The selection of the frequency does not affect the method as long as all EFLs are calculated based on the same frequency where N_0 is only dependent on T.

$$N_0 = T \cdot f_1 \qquad \textit{Equation 6.16}$$

The benefit of using a fixed number of cycles over a fixed duration rather than the actual number of cycles is that it is more convenient to compare the resulted damage between two stress-time histories since a higher EFL reflects larger damage. Note that a higher effective stress range does not necessarily indicate larger damage because the corresponding number of cycles might be low resulting in smaller damage. The actual number of cycles a pole is exposed to is extremely scattered and hard to predict due to the uncertainty in vibrating modes. In addition, the effective stress range has been reported to be very sensitive to the truncation point of stress range in the

rainflow-counting algorithm (Fasl 2013) whereas the EFL is not affected much. Further, since the interest is in the correlation between the wind speed and the induced damage, using EFL omits the need to predict the number of cycles, while providing the indication of induced damage under different wind speed.

EFL Calculations Using Two-Slope S-N Curves

The EFL presented in the previous section is determined assuming that the fatigue behavior of HMIPs is described with a single-slope S-N curve. However, according to past studies and recommendations (Lassen and Rẻcho 2006 and EN1993 2002), the S-N curve in the low stress region is represented by a second line with shallower slope (m = 5). This is justified by the fact that smaller stress ranges cause less fatigue damage, and therefore a single-slope S-N line extended from high stress ranges results in over estimation of fatigue damage under low stress ranges (Figure 6.62).

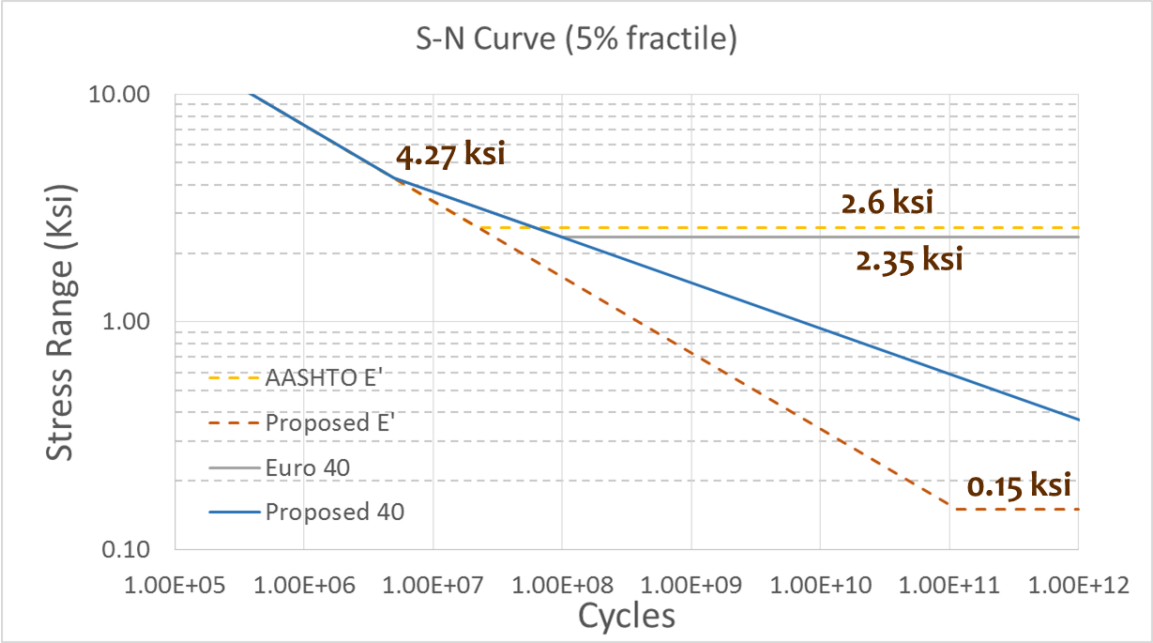

Figure 6.62: Comparison between One-Slope and Two-Slope Representations of the S-N Curves for HMIP Specimens

Figure 6.62 shows four S-N curves that represent the AASHTO E′ category and Eurocode 3 category 40 with or without (labeled as "proposed" in the figure) a constant amplitude fatigue limit (CAFL). Since most of the stress cycles experienced by HMIPs fall below the CAFL, this study conservatively neglects the CAFL to account for the damage caused by low stress cycles. However, there is still a limiting threshold at 0.15 ksi to remove the noise in data caused by acquisition system. The S-N curves for AASHTO category E′ and Eurocode 3 category 40 are essentially the same for stress ranges above 4.27 ksi, and follow the same Equation (Equation 6.17).

$$A = S_R^3 \cdot N \qquad \textbf{Equation 6.17}$$

The Eurocode 3 S-N curve diverges from that of the AASHTO for stress ranges below 4.27 ksi and it is represented by a second line with different slope, m = 5, as indicated in Equation 6.18.

$$B = S_R^5 \cdot N \qquad \textbf{Equation 6.18}$$

To calculate the EFLs using two-slope S-N curves (hereafter referred to as two-slope EFLs), Miner's rule was applied to equate the damage from a second-slope S-N curve to that from a one-slope S-N curve. According to Miner's rule, the fatigue damage caused by a specific stress range cycle under two-slope S-N curve can be determined using Equation 6.19.

$$D_i = \begin{cases} \frac{S_{R,i}^3}{A}, & when\ S_{R,i} \geq S_{RT} \\ \frac{S_{R,i}^5}{B}, & when\ S_{R,i} < S_{RT} \end{cases} \qquad \textbf{Equation 6.19}$$

where D_i is the damage resulted from a specific stress range cycle, A and B are the fatigue constants, $S_{R,i}$ is the corresponding stress range and S_{RT} is the stress range where the slope changes. The damage from variable-amplitude stress ranges when applying two-slope S-N curves can be determined using Equation 6.20.

$$\begin{aligned} D &= \frac{\sum_i S_{R,i}^3}{A} + \frac{\sum_j S_{R,j}^5}{B} \\ &= \frac{\sum_i S_{R,i}^3 + \sum_j S_{R,j}^5 \cdot \frac{A}{B}}{A} \end{aligned} \qquad \textbf{Equation 6.20}$$

As seen from Equation 6.20, for stress ranges below S_{RT}, an adjustment factor of A/B is considered. This adjustment factor can be determined with a given S_{RT} (Equation 6.21).

$$\frac{A}{B} = (S_{RT})^{(3-5)} = (S_{RT})^{-2} \qquad \textbf{Equation 6.21}$$

The two-slope EFL is defined similar to the single-slope EFL, as indicated in Equation 6.22. It is important to acknowledge that although the damage was accumulated based on a two-slope S-N curve, the damage from the second slope was adjusted as an equivalent damage under the first curve so that the representative EFL can be calculated using the slope of the first curve which is equal to 3.

$$EFL = \sqrt[3]{\frac{\sum_i S_{R,i}^3 + \sum_j S_{R,j}^5 \cdot \frac{A}{B}}{N_0}} \qquad \textbf{Equation 6.22}$$

Compared to one-slope S-N curves, two-slope S-N curves result in lower predicted fatigue damage. This is due to the presence of the second line with shallower slope in the region of small stress ranges. This prediction aligns with the fact that low stress-range cycles result in much less

fatigue damage. Since most of the stress ranges experienced by in-service HMIPs are small and below S_{RT}, using two-slope S-N curves results in more realistic predictions of fatigue damage. In addition, while the Eurocode 3 considers a CAFL for different fatigue categories, the two-slope S-N curve proposed in this study accounts for the damage below the suggested CAFL and therefore ignores the presence of a CAFL. The omission of the CAFL results in relatively more conservative fatigue life predictions.

6.5 Field Results

Field monitoring of the selected HMIPs started in December 2015 and finished early in August 2017. Data were continuously collected at each pole site. However, occasional interruptions due to insufficient sunlight or equipment malfunction resulted in some data loss during October 2016 to January 2017. The number of days of available data in each month are shown in percent in Figure 6.63:.

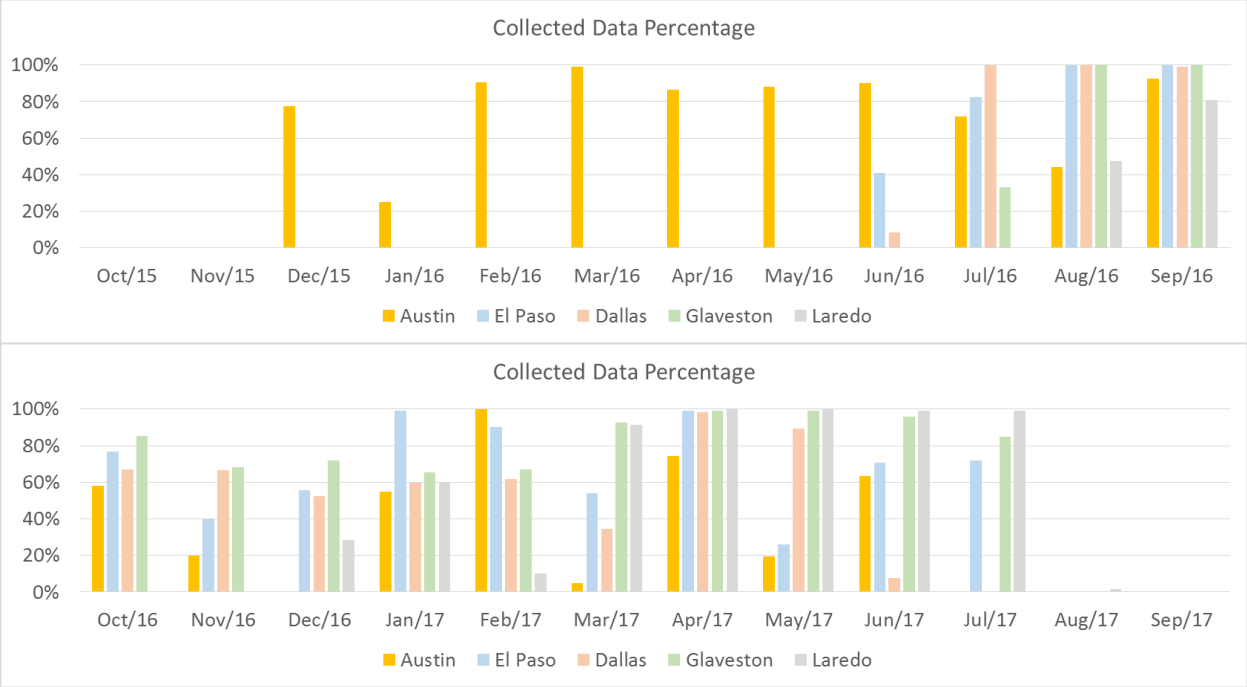

Figure 6.63: Field Data Collected at each Pole Site

Since the monitoring duration for each site is different, the number of 5-minute segments analyzed at each site, excluding erroneous segments, is documented in Table 6.2. The equivalent days indicating number of days with available data are also listed in Table 6.2. Note that, even though field data are not available for a full year, the collected data are assumed to be sufficient to represent the wind regimes of interest.

Table 6.2: 5-Minute Segments and Their Equivalent Days Representative of Duration of Analyzed Data

	Austin	El Paso	Dallas	Galveston	Laredo
Number of 5-Minute Segments	100938	88022	74104	93241	63269
Number of Days	350	306	257	324	220

6.5.1 Dynamic Properties of Monitored Poles

As discussed in section 6.4, the natural frequencies of in-service poles were determined from the frequencies at the peaks in the power spectrum, whereas the damping ratios were determined based on the half-power bandwidth method illustrated in the previous section. Since a power spectrum from a single time history does not result in a smooth curve, thereby making it difficult to identify the frequencies corresponding to the half-power amplitude, an averaged power spectrum (using all 5-min segments) was used. The averaged power spectrum is also more representative since it represents the entire data set. Since the calculated damping ratios would be erroneous if data collected under vortex-shedding vibration was included (Connor et al. 2012), 5-min segments were selected only when the average wind speeds were higher than 12 mph when vortex-shedding response was not expected to occur.

The power spectrum of the accelerations (at 80 feet) and the strain-time histories in N-S and E-W directions were extracted and averaged individually. Since accelerations and strain time histories resulted in the same natural frequencies and damping ratios, only the averaged power spectrum from the strain time histories are presented here (Figure 6.64). As seen in Figure 6.64 and Table 6.3, HMIPs located in Austin, Dallas, and Laredo showed very similar behavior in the first three natural frequencies while the HMIP in Galveston showed slightly higher frequencies due to having a thicker shaft (100 mph wind design). A numerical model for both designs built in SAP2000 showed similar natural frequencies to the observed values (Table 6.3) except for the pole in El Paso. Additionally, although the design for the El Paso HMIP and the Austin HMIP is the same, only the first mode frequency is matched. This mismatch between observed first mode frequencies is most probably related to the different soil conditions at the two pole sites that is not considered in the numerical models. The damping ratios for each mode are further determined using half-power bandwidth method and are listed in Table 6.3. The lowest damping ratio in the second mode is seen from the HMIPs in Laredo and Galveston. Note that low damping ratios may result in higher vibration responses in the second mode caused by vortex shedding.

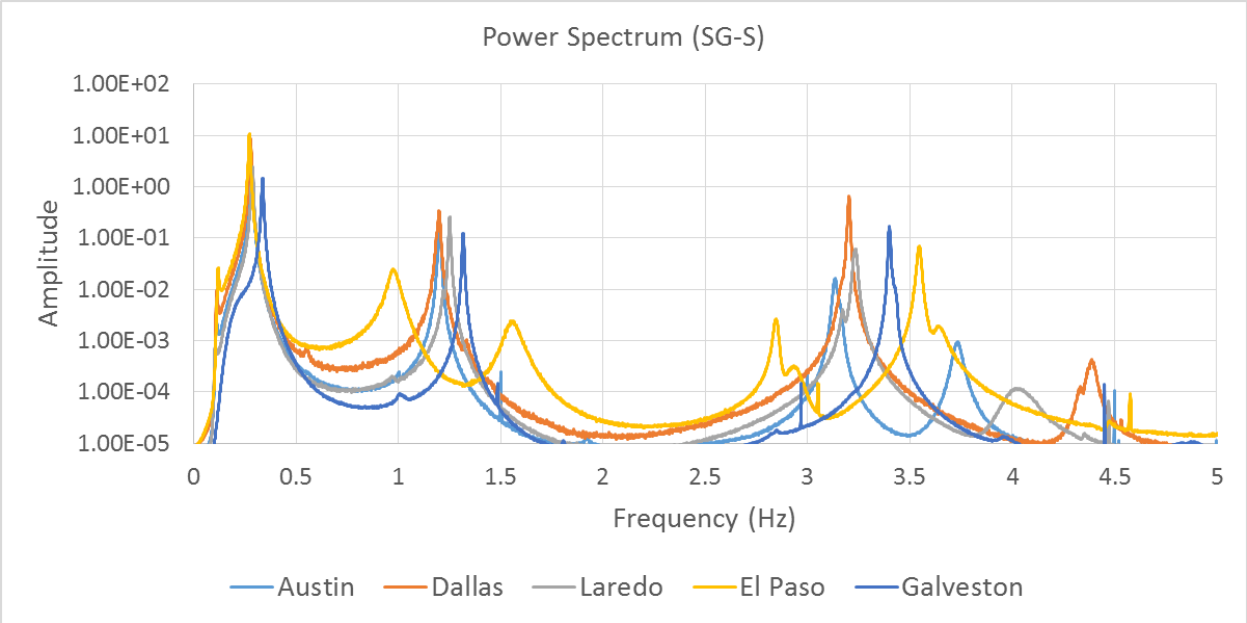

Figure 6.64: Averaged Power Spectrum for Instrumented Poles at Different Sites (From Strain Gauges Located at the South Side)

Table 6.3: Natural Frequencies and Damping Ratios for Instrumented Poles at Various Locations

		Modes	Numerical	Field				
				Austin	Dallas	Laredo	El Paso	Galveston
Natural Frequencies (Hz)	80 mph	M1	0.29	0.28	0.28	0.29 (0.28)	0.27 (0.28)	
		M2	1.23	1.2 (1.21)	1.2 (1.19)	1.25 (1.22)	0.98 (0.99)	
		M3	3.37	3.14 (3.16)	3.2	3.23 (3.17)	3.55	
	100 mph	M1	0.35					0.34
		M2	1.34					1.32
		M3	3.6					3.4 (3.43)
Damping Ratio (%)		M1		0.9 (0.7)	1	1.1 (1.0)	0.9	0.8 (0.7)
		M2		0.4	0.3 (0.5)	0.2 (0.3)	1.7	0.2 (0.3)
		M3		0.3	0.1	0.2	0.2	0.1 (0.2)

6.5.2 Wind Conditions at Each Monitored Pole Sites

For each 5-minute segment of data from all sites, mean wind speed and wind direction at 30 and 80 feet locations along the height of the HMIPs, wind profile parameter (α), and wind turbulence intensity in both along-wind and across-wind directions are determined and documented. Visual representation of the data in the form of wind rose graphs, wind density

graphs, wind speed histograms, and turbulence intensity graphs are constructed to help better understand the wind environment at each pole site.

Wind Speed Histogram

The calculated 5-minute mean wind speeds for each site, based on the entire monitoring period for each site, were binned in 2-mph intervals to obtain the occurrence rate for different wind speed ranges. Figure 6.65 shows the wind speed histogram from all sites. Dallas and El Paso experience a high percentage of low wind speeds while Galveston indicates a higher occurrence for the higher wind speeds. The average wind speed and the maximum gust speed, which is a 5-sec average wind speed at 30 feet above the base plate, are listed in Table 6.4. It is interesting to note that the highest average wind speed and the lowest maximum gust speed are observed at the pole site in Galveston. On the contrary, the highest maximum gust wind speed is observed at the pole site in El Paso where the second lowest average wind speed from all five sites was recorded.

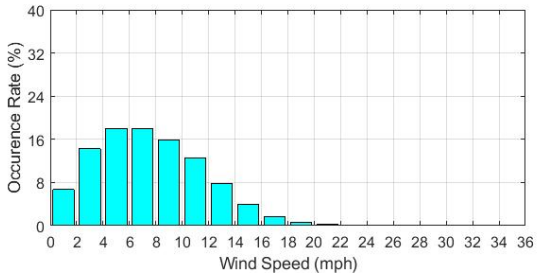

(a) Austin

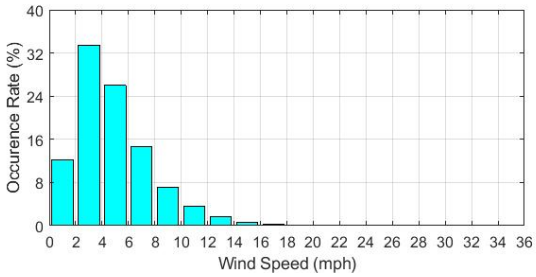

(b) Dallas

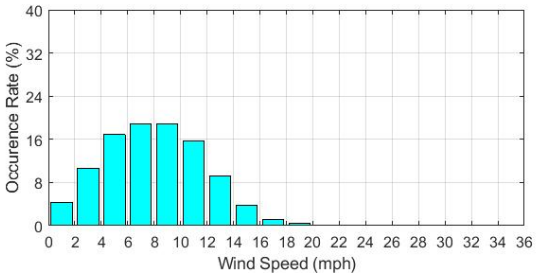

(c) Laredo

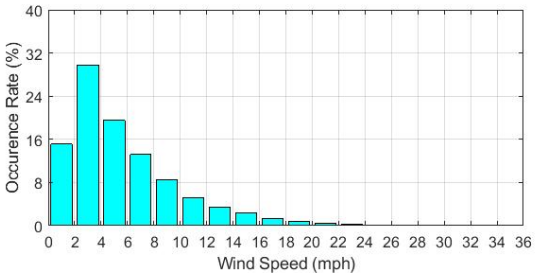

(d) El Paso

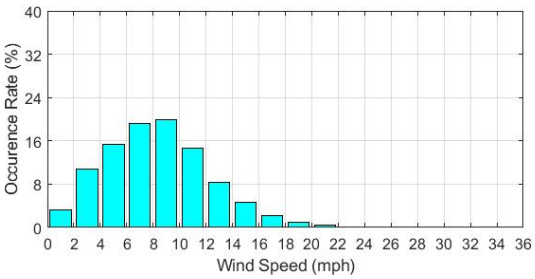

(e) Galveston

Figure 6.65: Wind Speed Histogram for the Monitored Pole Sites

Table 6.4: Average Wind Speed and Maximum Gust Speed for Monitored Pole Sites

	Austin	El Paso	Dallas	Galveston	Laredo
Average Wind Speed (mph)	7.6	5.7	4.9	8.4	8.0
Maximum Gust Speed (mph)	42.5	54.8	40.3	38.6	52.4

Wind Rose and Wind Density Graphs

As described in Chapter 2, the occurrence rate for wind speed and wind direction is often visualized using wind rose graphs, which are radial plots with the length of each radius representing the probability of occurrence and the radial direction representing the wind direction. Additionally, different color segments represent different wind speed ranges where longer segments represent higher occurrence rates. Wind rose graphs were constructed for each pole site and are plotted in Figure 6.66:. As further mentioned in Chapter 2, another way to visualize the occurrence rate for wind speed and wind direction is to construct wind density graphs. In wind density graphs, radii represent wind speed and radial directions represent wind direction. The occurrence rate is represented by different colors so that the highest occurring wind speed and wind direction can be easily identified. The wind density graphs constructed for each pole site are also shown in Figure 6.66.

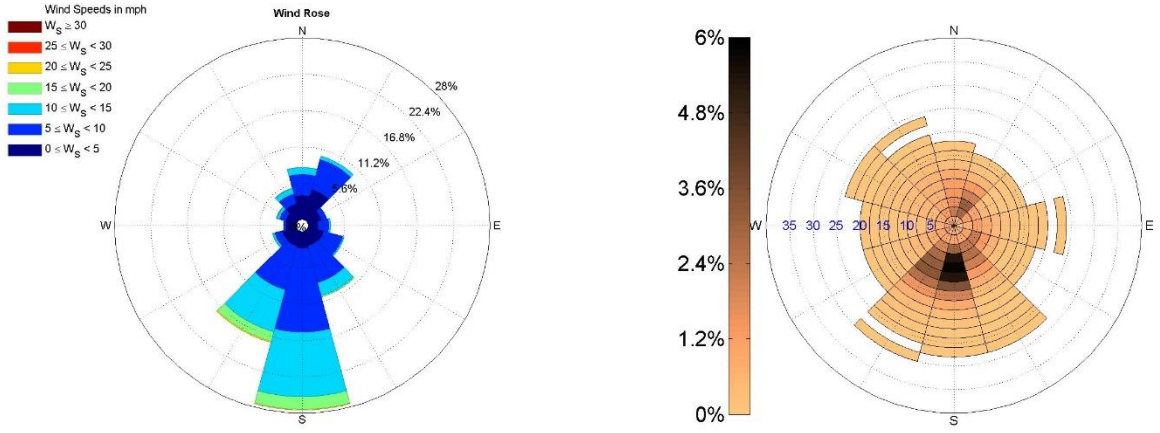

(a) Austin

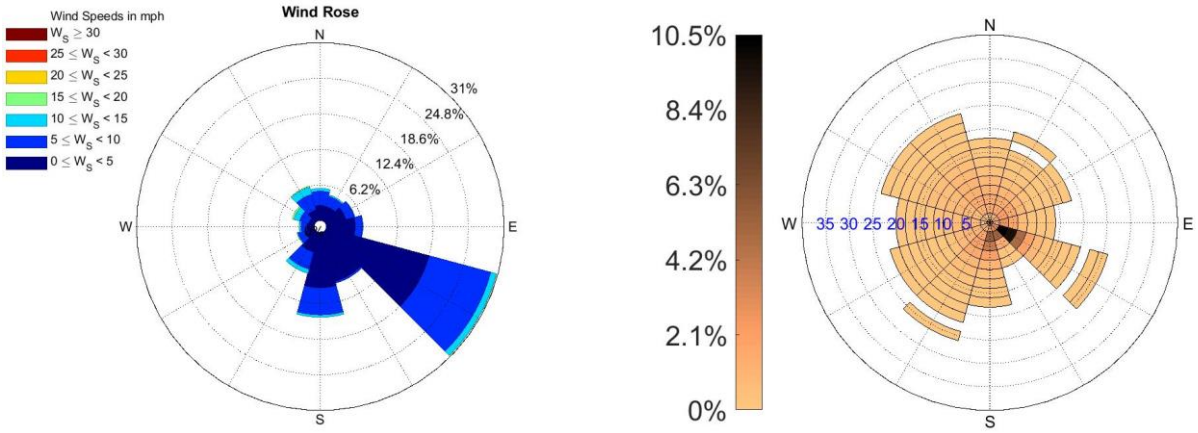

(b) Dallas

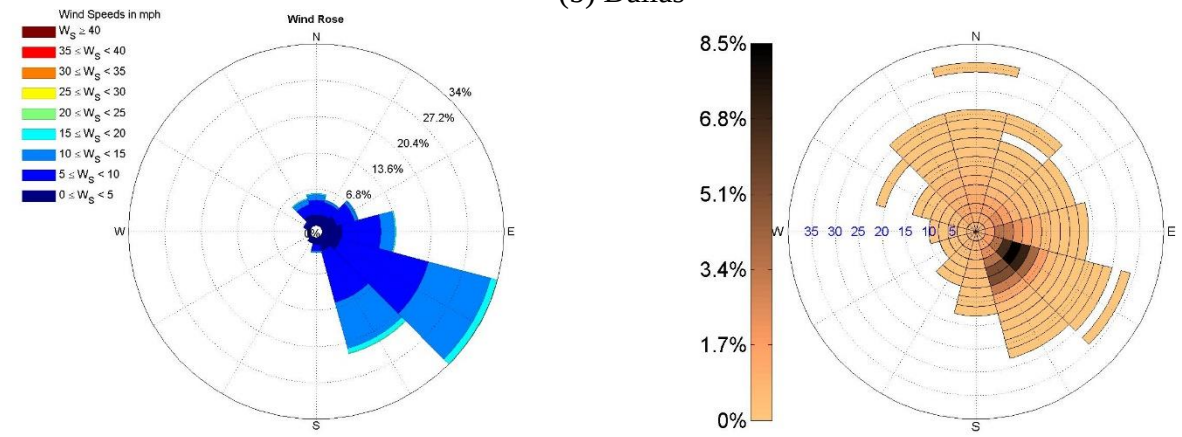

(c) Laredo

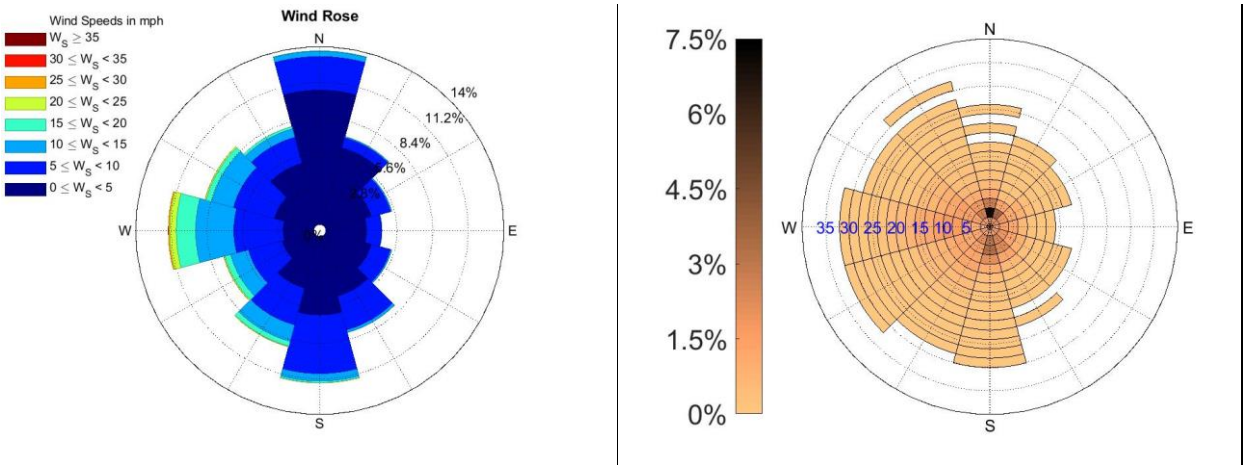

(d) El Paso

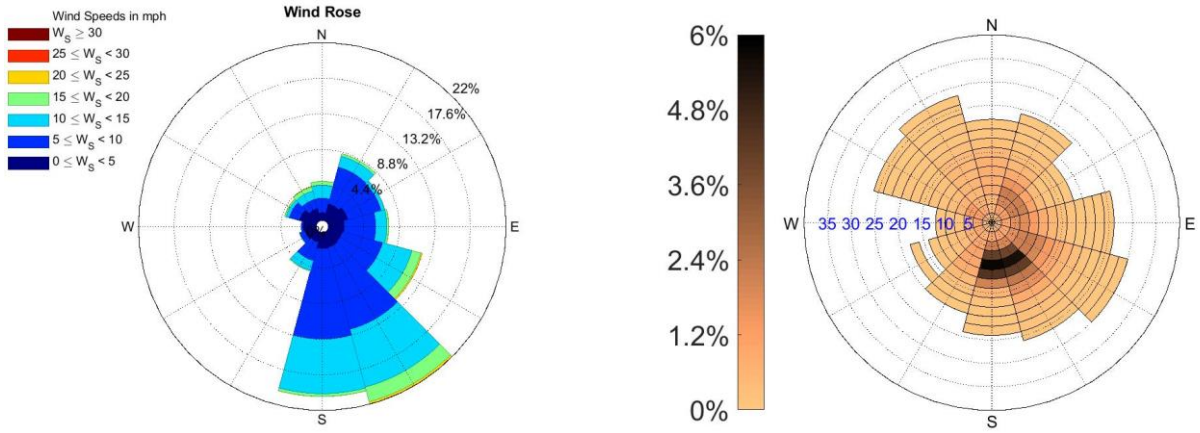

(e) Galveston

Figure 6.66: Wind Rose and Wind Density Graphs for Monitored Pole Sites

Wind data from the pole site in Austin (Figure 6.66a) suggest similar wind conditions compared with results gathered from weather stations around Austin. The dominating wind speed is also around 8 to 10 mph, which may result in lesser occurrences of vortex-induced vibrations. However, the dominance in one direction is expected to induce damage in a certain direction.

Wind data from the pole site in Dallas (Figure 6.66b) indicate a lack of wind information in the direction of 150 degree indicating the wind in that direction is particularly low or that there is a blockage effect which is the case shown in the latter section when turbulence intensity is plotted with wind direction. Although it seems that the majority of speed is in the low wind speed region in the 120 degree direction, it is hard to say if the blockage effect also affects the wind speed.

Wind data from the pole site in Laredo (Figure 6.66c) are similar to the results gathered from the weather station in Laredo where the majority of wind is in approximately the South-East direction with a dominating wind speed of 8 to 10 mph. The dominance in wind direction also predicts damage accumulating in the same location around the HMIP.

Wind data from the pole site in El Paso (Figure 6.66d) are similar to the results gathered from the weather station in El Paso where the wind speed and direction scatter from the West side of the HMIP. However, there is a high occurrence rate in the low wind speed range (2 to 4 mph) in the North direction which may be prone to vortex-induced vibrations if the wind is smooth with low turbulence intensity.

Wind data from the pole site in Galveston (Figure 6.66e) are similar to the results gathered from the weather station in Galveston where most of the wind is from the South with a higher dominating wind speed around 10 to 12 mph. Since the dominant wind speed is higher compared to other sites, lower occurrence of vortex-induced vibrations is expected from this site.

Turbulence Intensity

In order to understand the smoothness or roughness of the incoming wind, the calculated along-wind turbulence intensity (σ_u) is plotted with the wind direction to evaluate the distribution of turbulence wind around the monitored poles. The turbulence intensity is calculated from each 5-minute segment (excluding low mean wind speed under 2 mph to avoid unreasonable high values) using methods illustrated in previous section. Figures 6.67 to 6.71 presents the turbulence

intensity to wind direction and the geographic picture as well as the orientation of the supporting arm for the ultra-sonic anemometer for each monitored pole site. In each graph, radii represent the turbulence intensity and radial directions represent the wind direction.

The surroundings of the pole in the Austin site is shown in Figure 6.67:. As seen in this figure, a highway bridge was in close proximity of the pole resulting in a wind shielding effect and introducing a more turbulent wind environment. This phenomenon can be observed from the lack of low turbulence intensity from the North. Figure 6.67: also indicates lack of low turbulence in the West direction due to the orientation of the supporting arm for the ultrasonic anemometer on the East side of the HMIP. To avoid the local effect from the surrounding built environment, the data from 0° to 90° and 210° to 360° directions were excluded in the analysis of wind data presented later in this chapter.

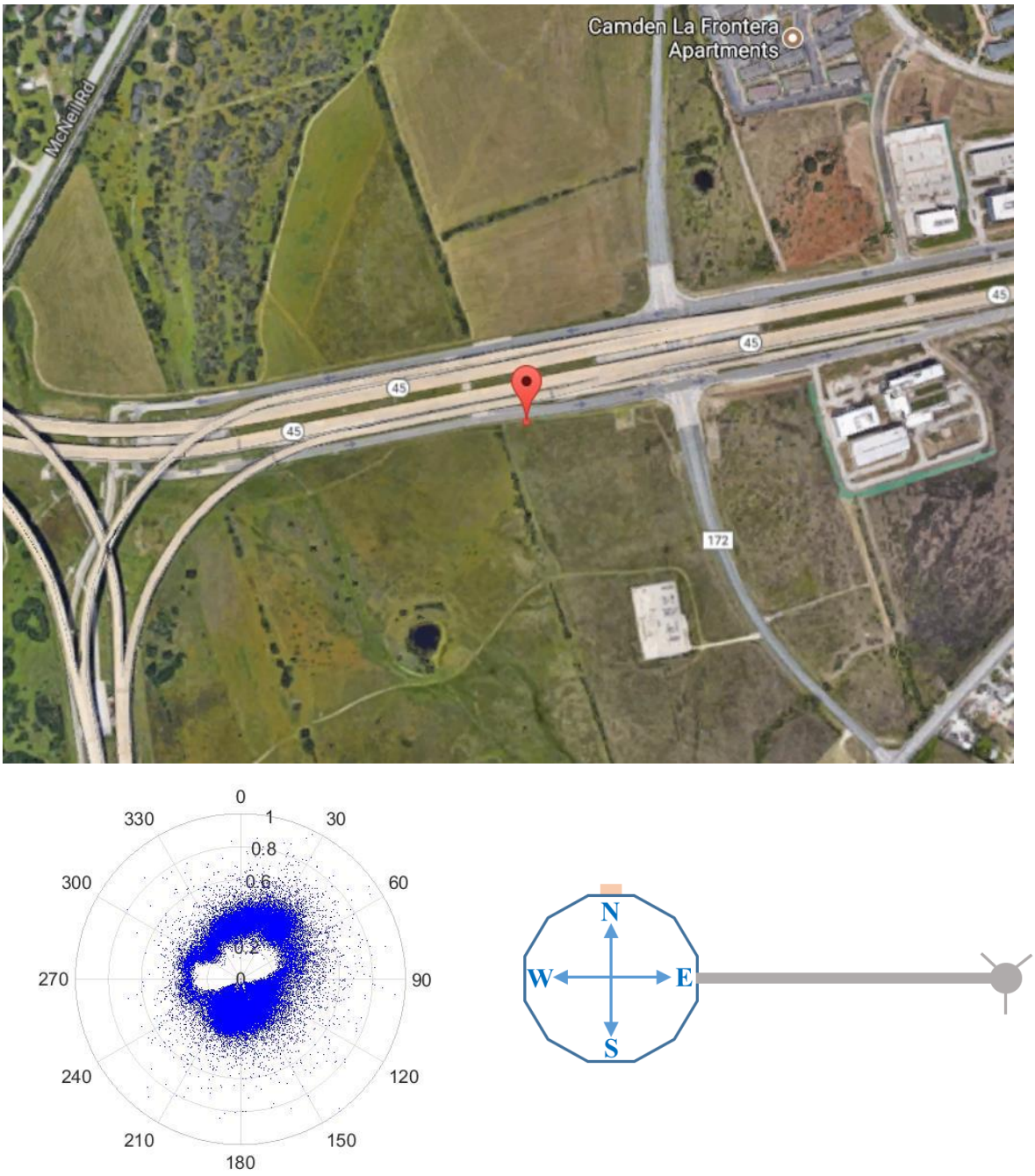

Figure 6.67: Topography, Orientation of the Ultrasonic Anemometer, and Turbulence Intensity at the Pole Site in Austin

The turbulence intensity graph for the pole site in Dallas (Figure 6.68) indicates a large jump from 120° to 180° directions, caused by a nearby tall building located at the South of the HMIP as seen in the satellite map. Since South is the predominant wind direction, most of the wind is hindered by the building and therefore no wind data are present in the wind rose and wind density graphs in the 150° direction. The orientation of the supporting arm for the ultrasonic anemometer is on the West side of the pole where the lack of low turbulence can also be observed in the

turbulence graph. To avoid the local effect from the surrounding built environment, the data from 30° to 210° directions were excluded in the analysis of wind data presented later in this chapter.

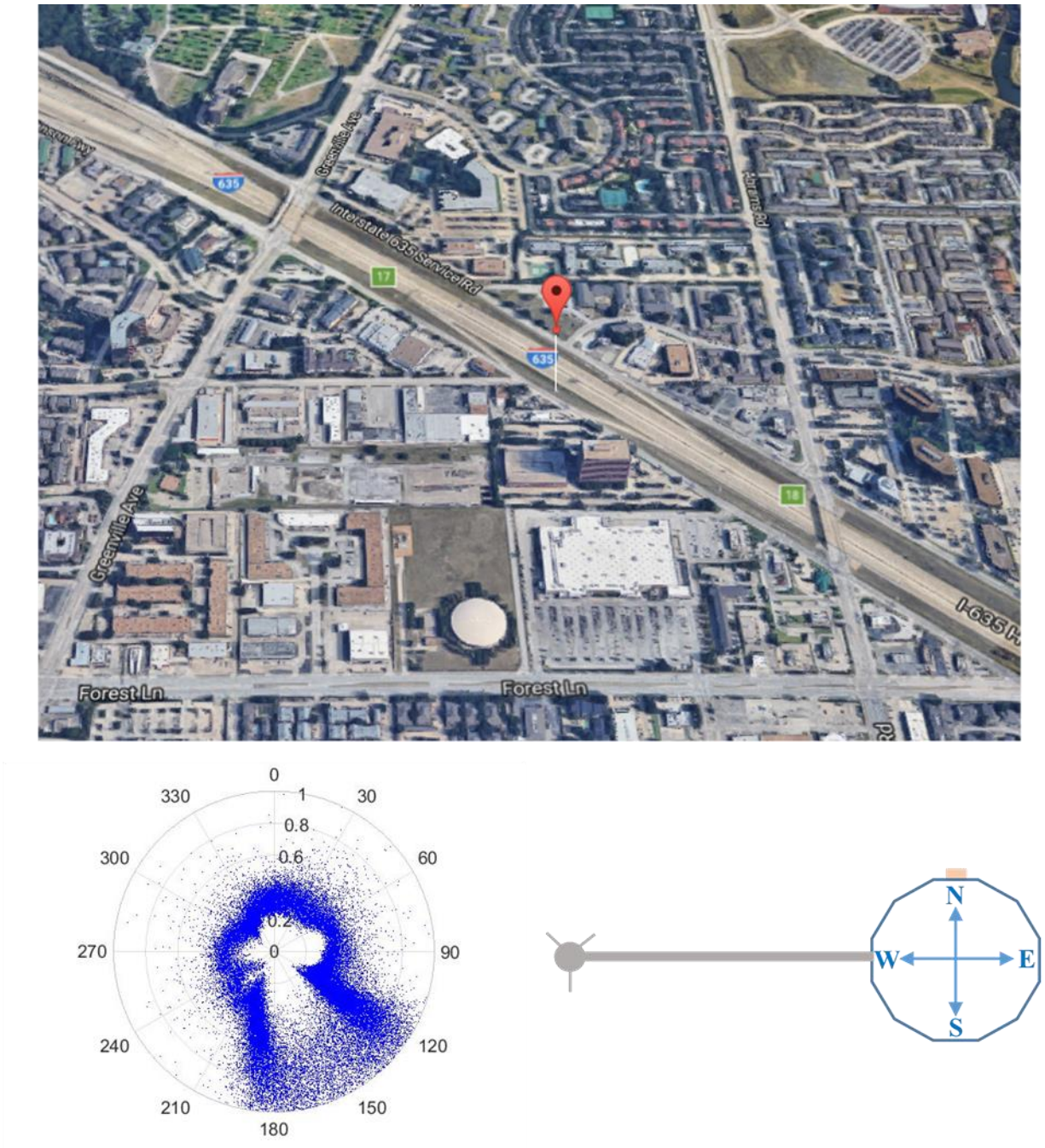

Figure 6.68: Topography, Orientation of the Ultrasonic Anemometer, and Turbulence Intensity at the Pole Site in Dallas

The turbulence intensity graph for the pole site in Laredo (Figure 6.69) indicates a more uniform distribution where most of the values are in the lower range as seen in the South-East side of the HMIP which is also the predominant wind direction. The lack of low turbulence intensity in

the North-East direction may be due to some low rise buildings in that direction as shown in the satellite map. Since the orientation of the supporting arm for the ultrasonic anemometer and a highway bridge is on the West side of the pole, a lack of low turbulence can also be observed. To avoid the local effect of the surrounding structures, the data from 0° to 90° and 180° to 360° directions were excluded in the analysis of wind data presented later in this chapter.

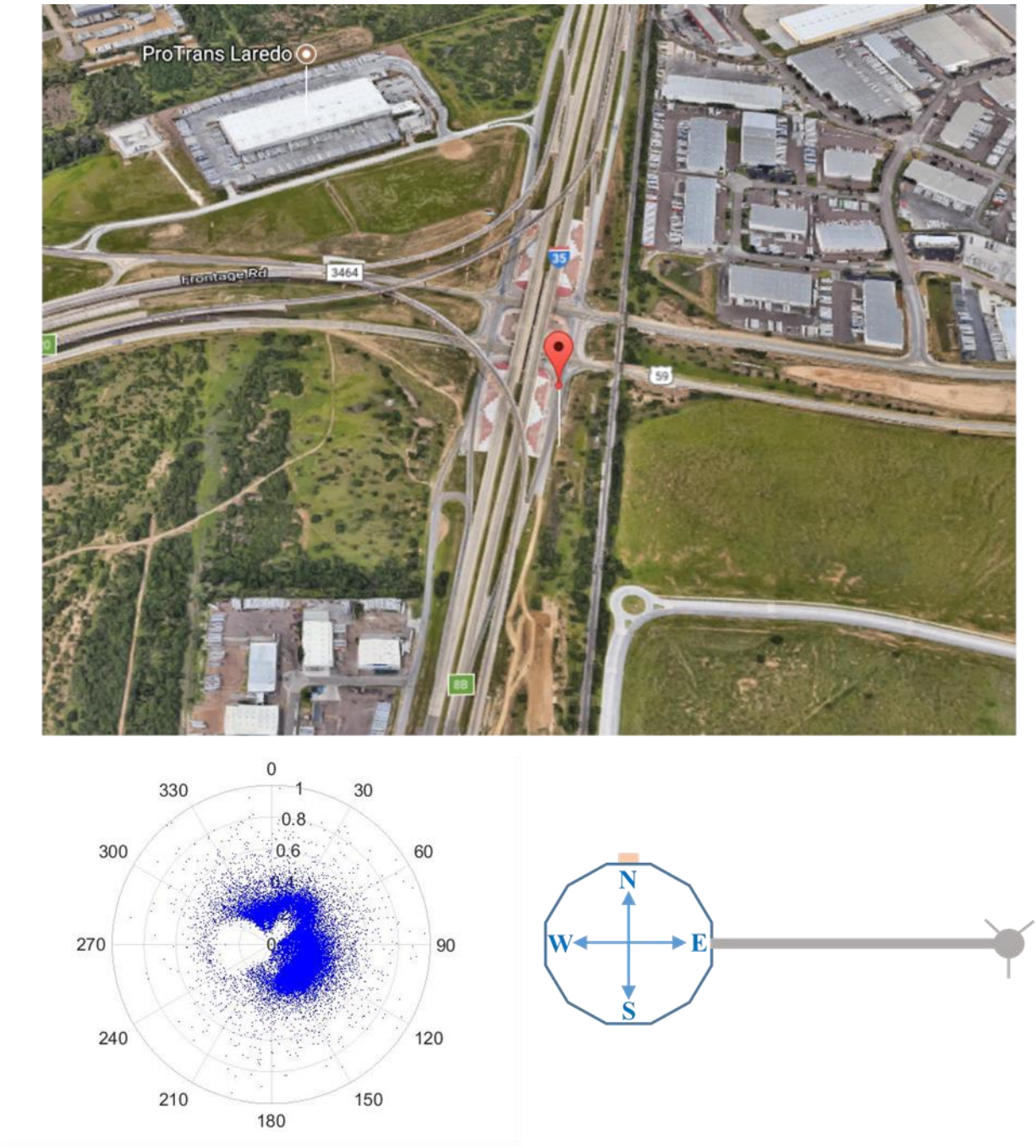

Figure 6.69: Topography, Orientation of the Ultrasonic Anemometer, and Turbulence Intensity at the Pole Site in Laredo

The turbulence intensity graph for the pole site in El Paso (Figure 6.70) indicates a highly scattered distribution where high turbulence wind is seen in almost every direction. Since the orientation of the supporting arm for the ultrasonic anemometer and a highway bridge is on the East side of the pole, a lack of low turbulence wind data can be observed on the East side as shown in the figure. To avoid the local effect of the HMIP itself, the data from 30° to 150° directions were excluded in the analysis of wind data presented later in this chapter.

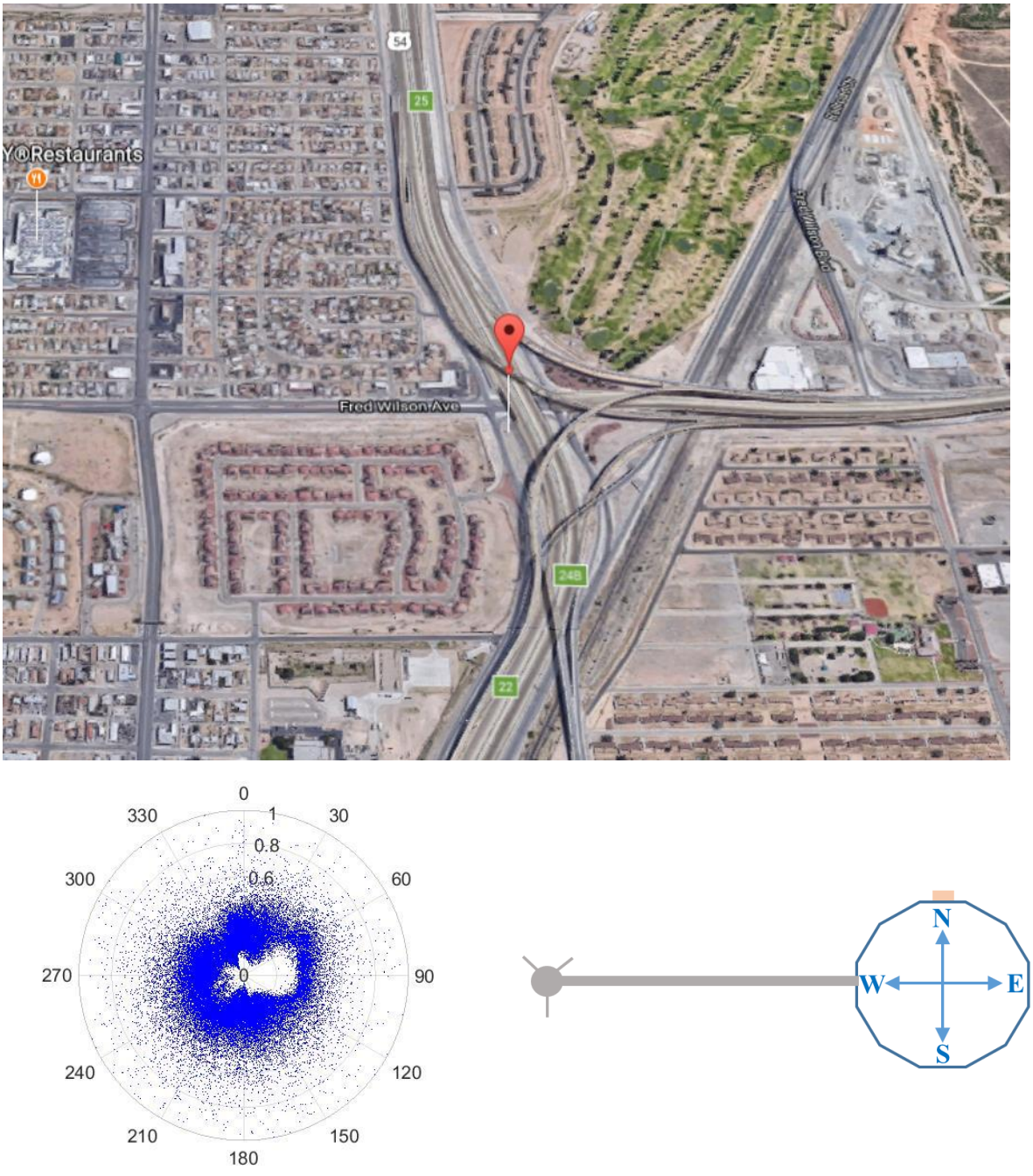

Figure 6.70: Topography, Orientation of the Ultrasonic Anemometer, and Turbulence Intensity at the Pole Site in El Paso

The turbulence intensity graph for the pole site in Galveston (Figure 6.70) indicates higher turbulence in the North and South directions while the West direction shows a large gap in the low turbulence intensity data due to the orientation of the supporting arm for the ultrasonic anemometer. There were no buildings near the pole site (seen in the satellite map) to cause any local effect of high turbulence seen in Austin or Dallas. To avoid the local effect of the HMIP itself, the data from 210° to 330° directions were excluded in the analysis of wind data presented later in this chapter.

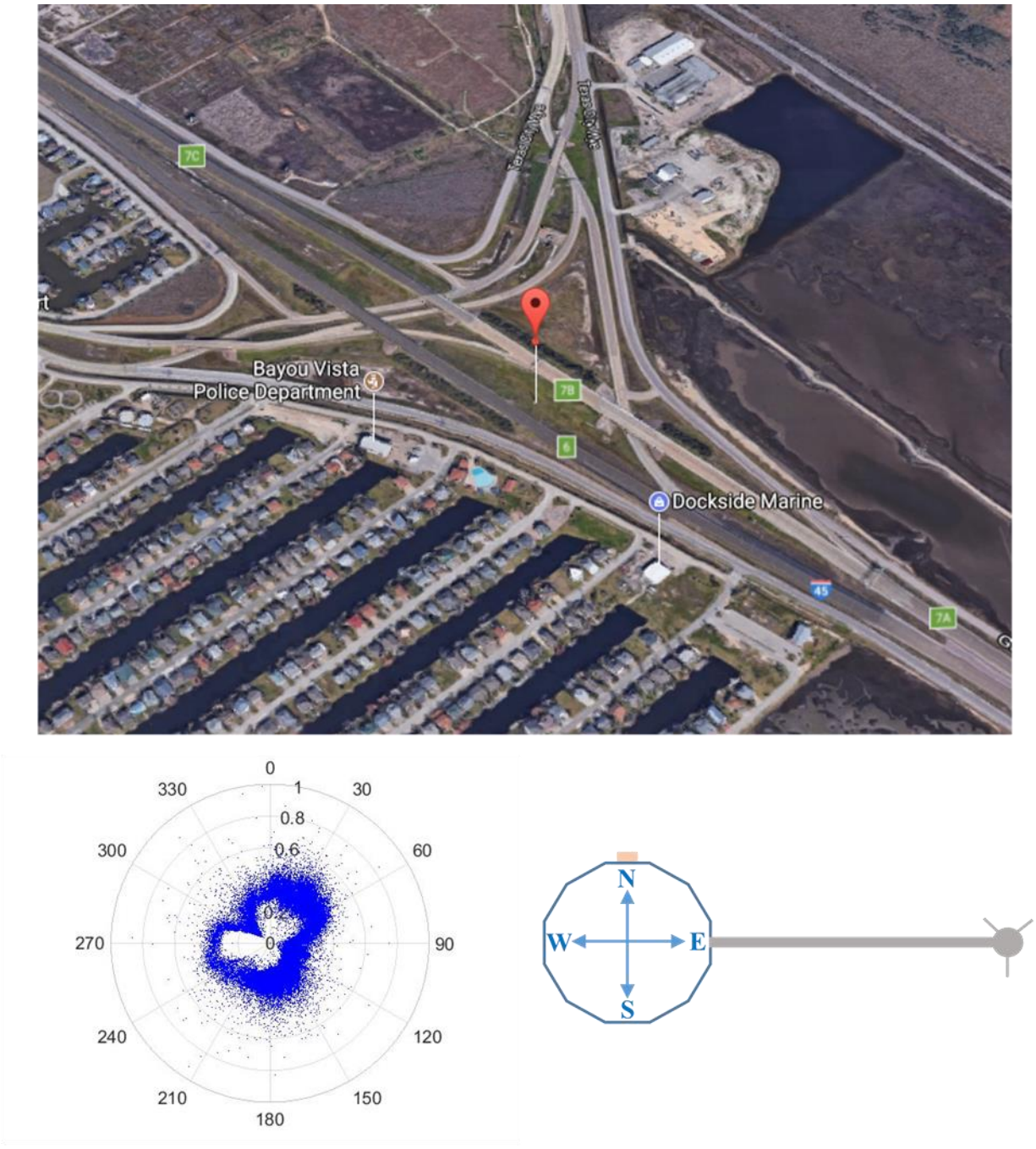

Figure 6.71: Topography, Orientation of the Ultrasonic Anemometer, and Turbulence Intensity at the Pole Site in Galveston

6.5.3 Stress-Range Histogram

Fatigue damage caused by variable-amplitude stress ranges is often represented by stress-range histograms, where the cycles under different stress-range bins are obtained by applying the rainflow-counting algorithm to the collected stress-time histories. Stress-range histograms generated for each pole site using the collected strain-time histories from strain gauges located on

the South and West flats of each pole are presented here. The histogram gives a general view of how many cycles corresponding to specific stress ranges are experienced by an HMIP without any specific reference to the wind environment.

Figure 6.72 shows the stress-range histogram normalized by cycles-per-day for all the instrumented poles at different locations. As seen from Figure 6.72, most of the observed stress ranges from all sites are below 2 ksi, which is smaller than the constant amplitude fatigue limit (CAFL) of 2.6 ksi for the AASHTO fatigue category E′ (the lowest CAFL in the AASHTO fatigue categories). Figure 6.73 further shows the stress-range histograms compared at different pole sites. As seen in Figure 6.73, the stress-range histogram for the pole in Laredo shows the highest number of cycles for all stress ranges, while the stress-range histogram for the pole in El Paso shows the lowest. Figure 6.73 also indicates that poles at both Laredo and Galveston experience high cycles in the low stress ranges, while high stress ranges are not observed in Galveston due to the different HMIP design. To better compare the sustained cycles, Figure 6.74 compares the number of cycles from each site under the same stress-range bins. The South side of the HMIP in Laredo clearly shows higher cycles in all stress-range bins where the damage is expected to be the worst. Although the number of cycles for low stress ranges are relatively small for the pole in El Paso, the cycles in the higher stress ranges can be seen to be relatively higher than other locations (Figure 6.74); except for the pole in Laredo possibly due to the higher turbulence seen in the area.

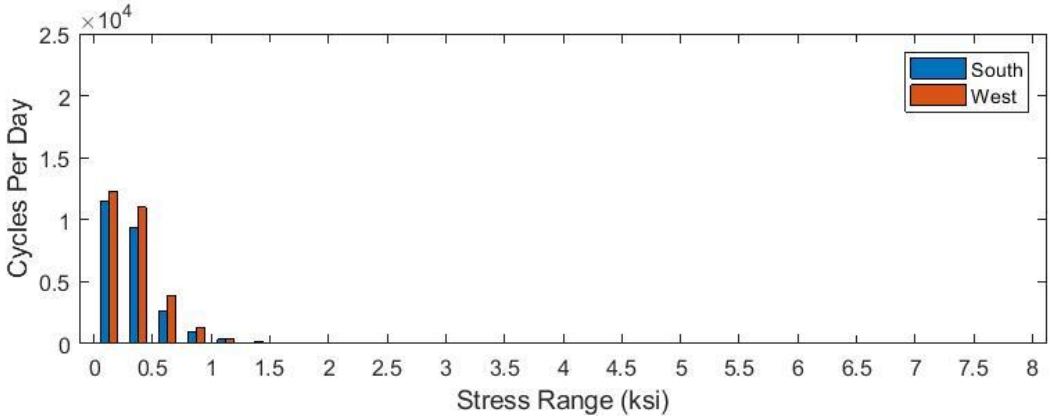

(a) Austin

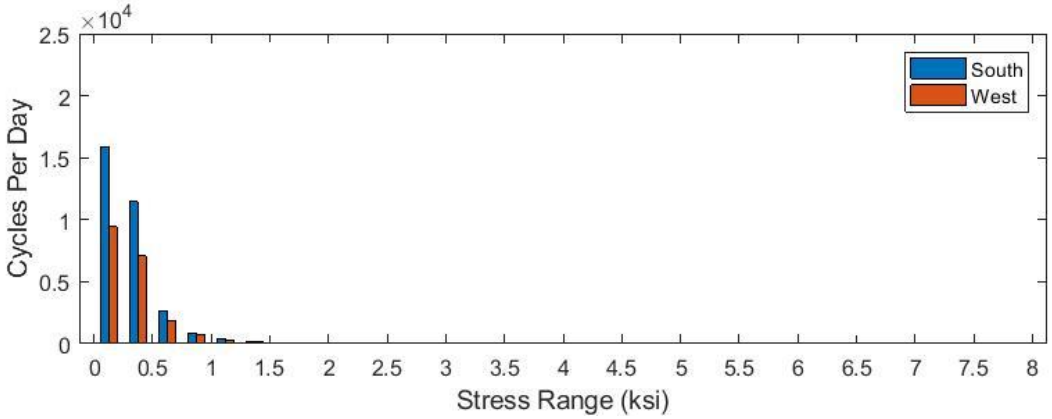

(b) Dallas

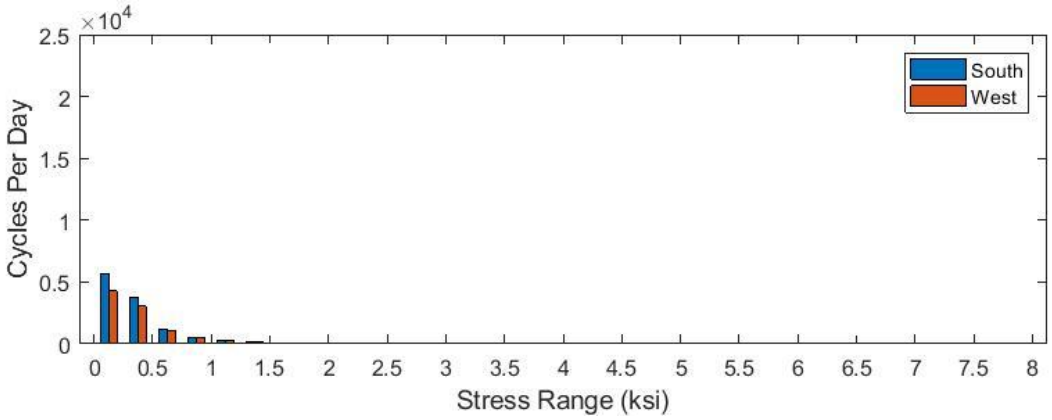

(c) El Paso

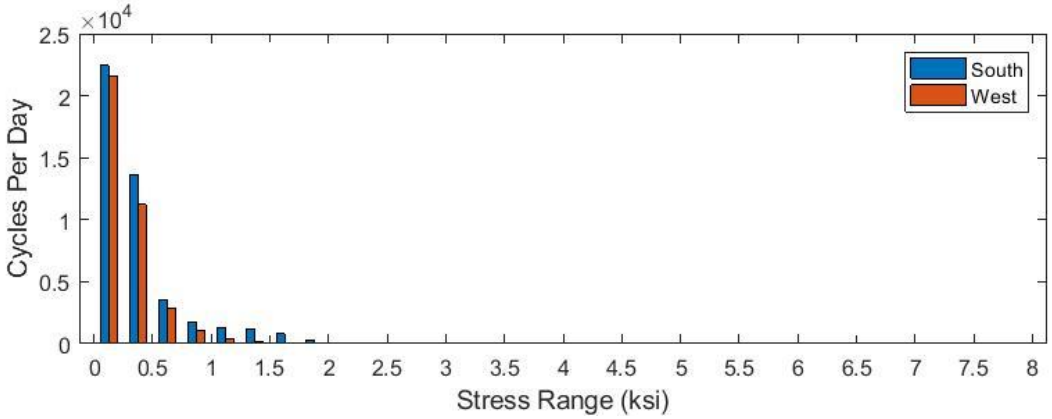

(d) Laredo

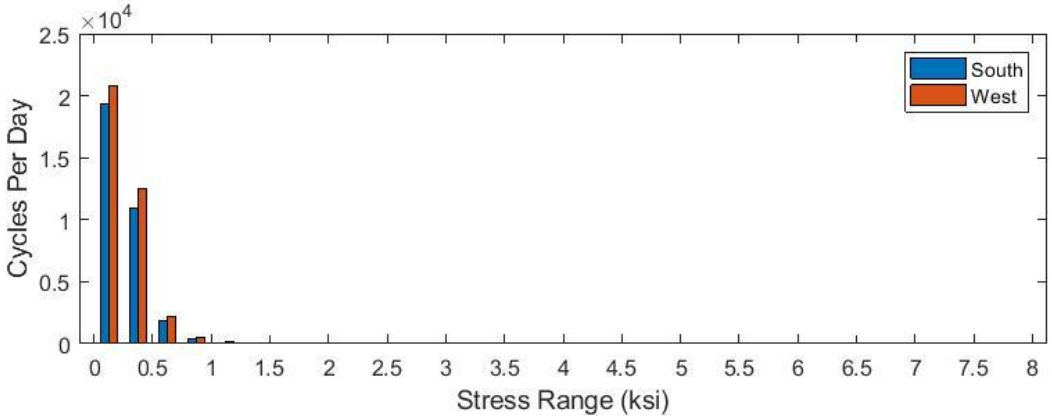

(e) Galveston

Figure 6.72: Stress-Range Histogram Normalized as Cycles-Per-Day for the Monitored Poles

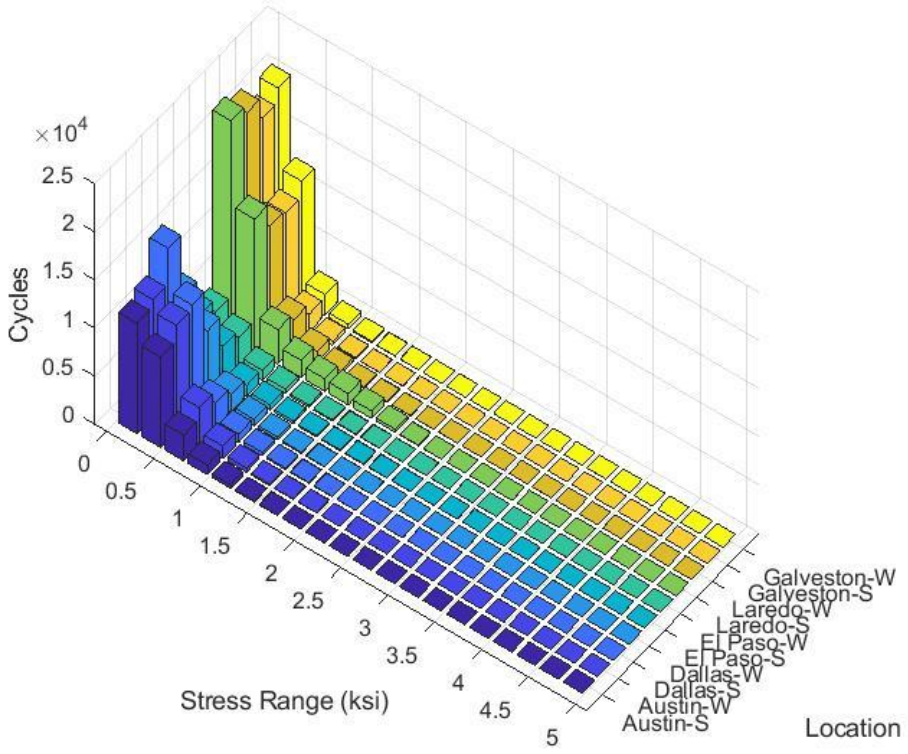

Figure 6.73: Stress-Range Histogram Normalized as Cycles-Per-Day for the Monitored Poles

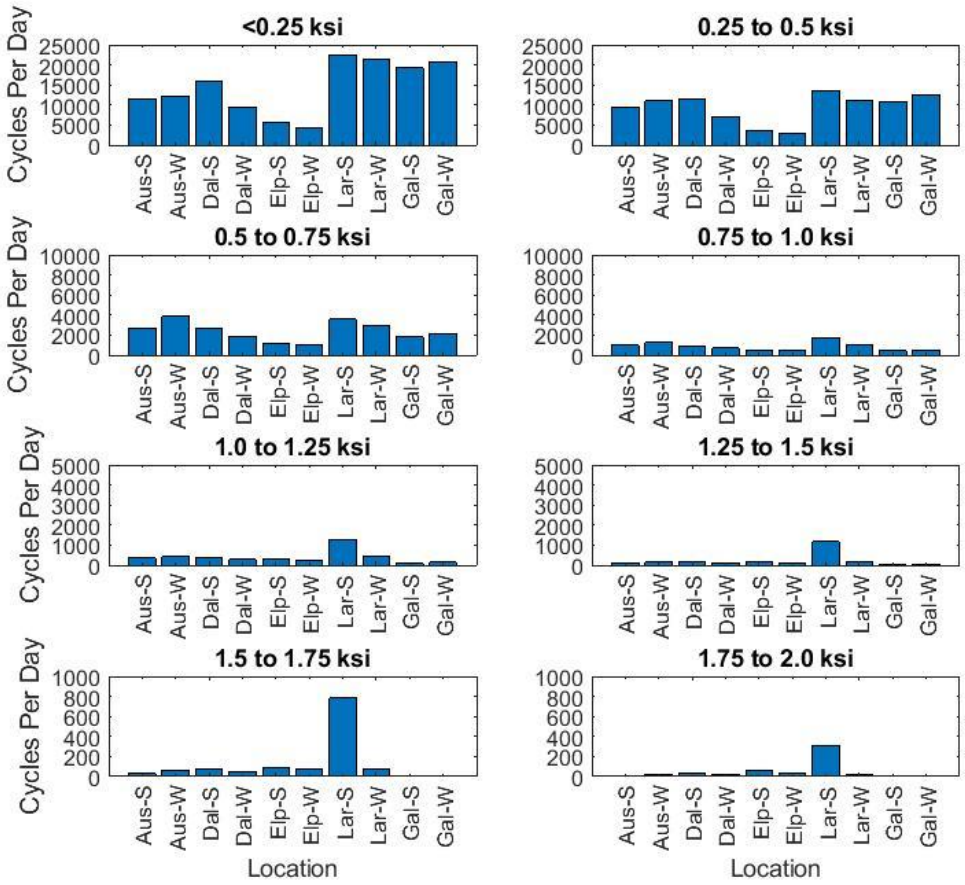

Figure 6.74: Stress-Range Histogram for Specific Stress Bins at Different Pole Sites

To have a more complete picture of the stresses experienced by each pole at different locations, maximum stress ranges observed for each pole during the monitoring period are summarized in Table 6.5.

Table 6.5: Maximum Stress Ranges Observed for Monitored Poles at Different Locations

Maximum Stress Range (ksi)

	Austin	**Dallas**	**Laredo**	**El Paso**	**Galveston**
South	8	8.5	5.9	10.5	4.2
West	9	7.8	6.6	9.2	3.1

Although the fatigue damage from each site can be assessed using the stress range histograms presented in this section, a more comprehensive method to assess the induced-fatigue damage under different wind environments is needed. Development of this method requires an understanding of the relation between the induced-stress ranges and the wind characteristics such as wind speed, wind direction, and wind turbulence. A proposed method, which considers the wind

conditions at each pole site and predicts the induced-damage for a given wind environment under a given duration, is introduced in the following sections.

6.5.4 Responses under Different Governing Modes

The power spectrum of the time histories indicates that the motion of the pole is mainly dominant in either of the first three natural frequencies or combinations of them. Examples of 5-minute response, dominant in the first three natural frequencies, are presented here for the monitored pole in Austin to study how the pole vibrates under different dominant modes.

Figure 6.75a-c show a sample first-mode dominant strain time series obtained from strain gauges attached to the South and West flats of the HMIP monitored in Austin. The average wind speed at 30 feet above the base plate is 8.3 mph from the North (0°) and is aligned with the higher response levels in the North-South direction (Figure 6.75c). As seen in the zoomed graph of a few strain cycles (Figure 6.75b), the dominant frequency in the along-wind direction (South) is close to the first modal frequency whereas the across-wind direction (West) exhibits some small-amplitude vibrations at higher frequencies.

Figure 6.75d-f show a sample second-mode dominant strain time series from the same strain gauges. The average wind speed at 30 feet above the base plate is 3.1 mph from the North-East (45°), which is perpendicular to the vibrating direction (Figure 6.75f). As seen from the zoomed graph of a few strain cycles (Figure 6.75e), the vibrating frequencies for both strain gauges correspond to the second mode frequency, which is presumably related to vortex shedding.

Figure 6.75h-i show a sample third-mode dominant strain-time series from the same strain gauges. The average wind speed at 30 feet above the base plate is 3.1 mph from the South-West (225°) which is perpendicular to the vibrating direction (Figure 6.75i). As seen from the zoomed graph of few strain cycles (Figure 6.75h), the vibrating frequency from both strain gauges is close to the third mode frequency.

Figure 6.76 shows stress-range histograms that result from rainflow cycle counting based on the strain-time series presented in Figure 6.75. The stress-range histograms for first-mode dominant time series indicate a greater number of occurrences of higher stress-range bins for the South direction, which is consistent with direction of the larger vibrating amplitudes indicated in Figure 6.75c. The second- and third-mode dominant time series also bring about larger vibrating amplitudes (and stress ranges) in the South direction, which can be confirmed by studying Figure 6.76. The number of stress cycles generally increases with higher mode; this is a result of the higher vibrating frequencies. However, as seen from Figure 6.76, stress-range amplitudes for the third mode are relatively small. Most of the cycles are confined to low stress range bins and thus relatively little fatigue damage will result from the third-mode dominant stress data compared to the second-mode dominant data.

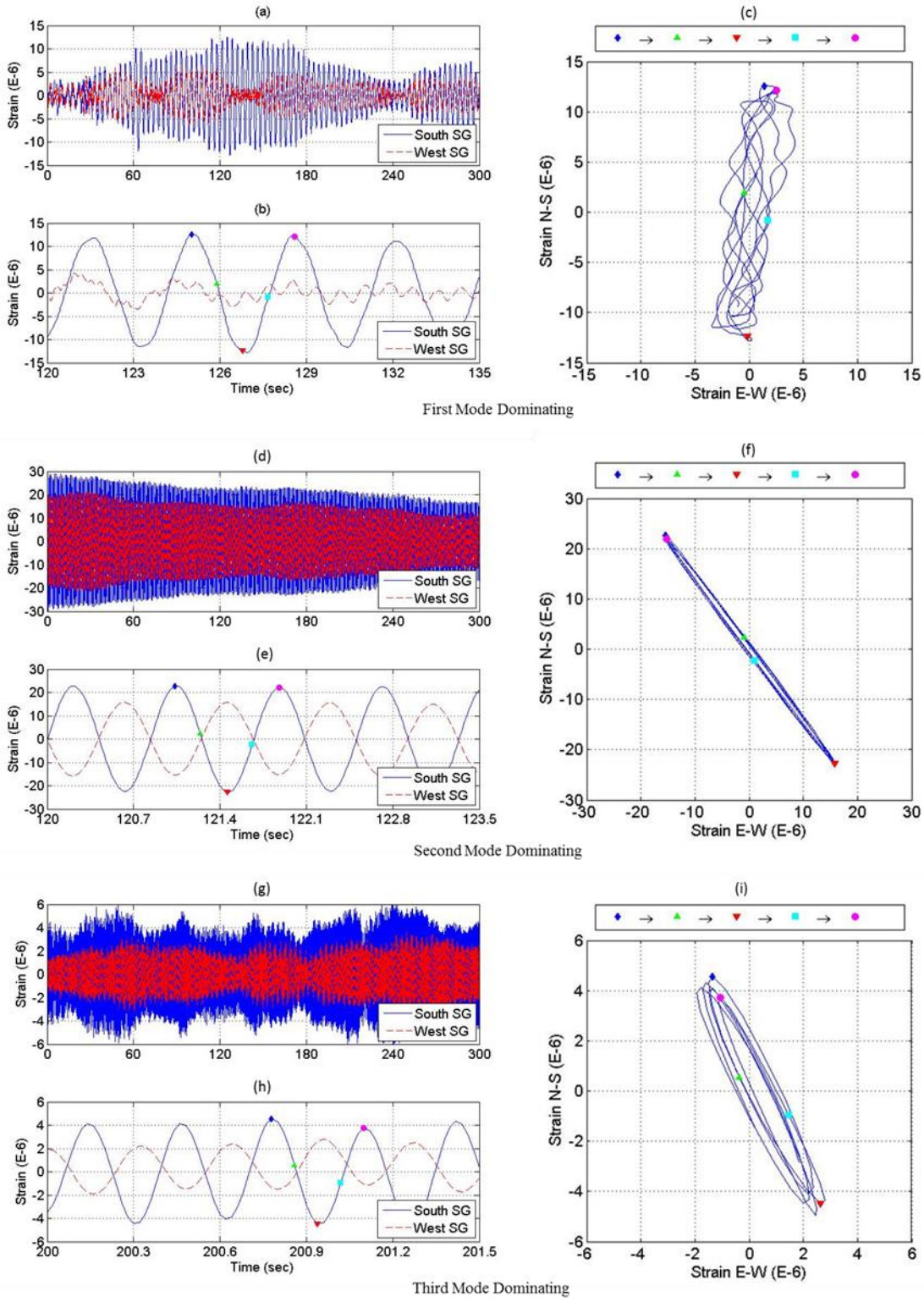

Figure 6.75: Strain-Time Series Corresponding to Different Dominating Vibration Modes

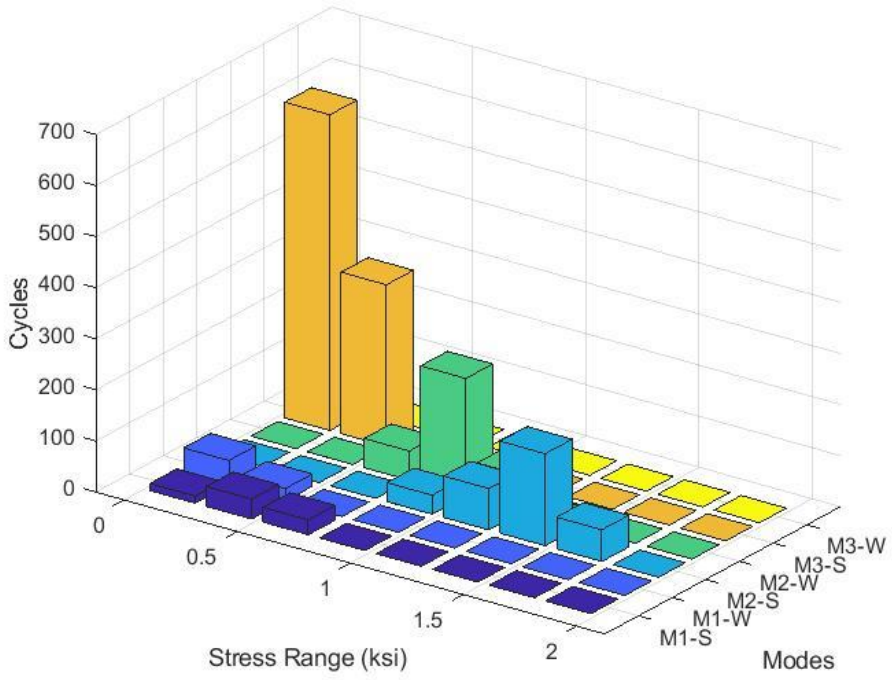

Figure 6.76: Stress-Range Histograms from Strain-Time Series with Different Dominant Modes (5-min Duration)

6.5.5 Responses Due to Different Wind Conditions

To identify and categorize different HMIP responses, the HMIP motion is presented in this section under different wind conditions to observe the effect of wind speed and turbulence intensity. The main purpose of this section is to observe and identify vortex-induced vibration and the corresponding wind conditions and vibrating mode. The data from the Austin site (5-minute segments data) is used here to illustrate the effect of wind conditions. A comparison of results from each site was conducted to show how the response varies while excluding known wind effects.

Wind Speed Effect

Figure 6.77 shows HMIP along-wind and across-wind displacements 80 feet above the base plate decomposed into the first three modes for different wind speeds recorded at 30 feet above the base plate. It is seen that Mode 1 displacements generally increase with increasing speed in both the along-wind and cross-wind directions. This response is attributed mostly to turbulence that typically increases with increasing wind speed in both directions as has been observed in previous studies (Chang 2009). Mode 2 displacements indicate a clear peak in the low wind speed range that is thought to be due to vortex shedding since the amplified dynamic response only occurs in a specific narrow wind speed range. Although Mode 3 vortex shedding is also reported in other studies (Dawood 2014), the observed Mode 3 contributions indicated in Figure 6.77 are relatively small compared to those from the two other modes and can therefore be neglected.

In order to clearly identify HMIP response that is associated with vortex shedding, displacements for dominating modes among the collected data are plotted against the reduced velocity (Ur) (Figure 6.78), which is the reciprocal of the Strouhal number (*St*); i.e., Ur = 1/St = U/fs·D, where U and D are taken to be the wind velocity and pole diameter, respectively, at 100 feet above the base. Since both the wind velocity and the diameter of the pole vary with height, the 100 feet location was selected to represent the whole pole since the maximum displacement in the second mode occurs at that height. The wind speed at 100 feet is estimated using a power law with the wind speed measurements at 30 feet and 80 feet. The mode with the highest contribution to the displacement variance is regarded as the dominating mode. The average frequency (fs) of the dominating mode is estimated using the Hilbert transform illustrated in the previous section.

The significant peak over a relatively narrow band that corresponds to a reduced speed around 5, as seen in Figure 6.78, is close to the vortex-shedding lock-in reduced speed reported in the literature (Chang 2009). Higher response levels in the cross-wind direction over the lock-in speed range are also an indication of vortex shedding and vortex-induced vibration (VIV). From the figure, we can see that the lock-in response is only coming from the second mode. Mode 1 is influenced by turbulence and greater response levels are seen only at higher wind speeds. Mode 3 does not contribute significantly to either cross-wind or along-wind response.

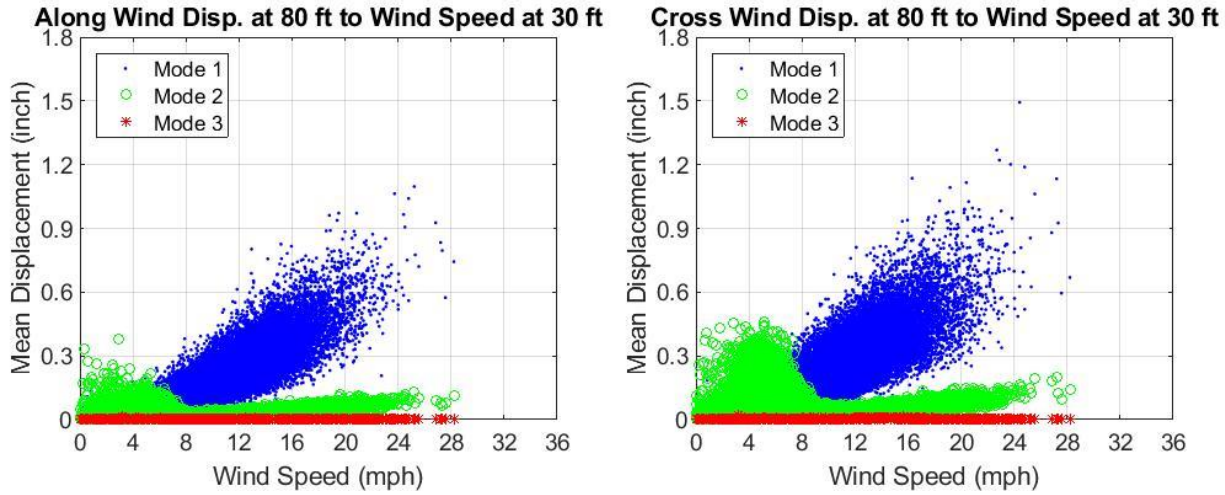

Figure 6.77: Along- and Across-Wind Displacements at 80 Feet for Various Wind Speeds Measured at 30 Feet

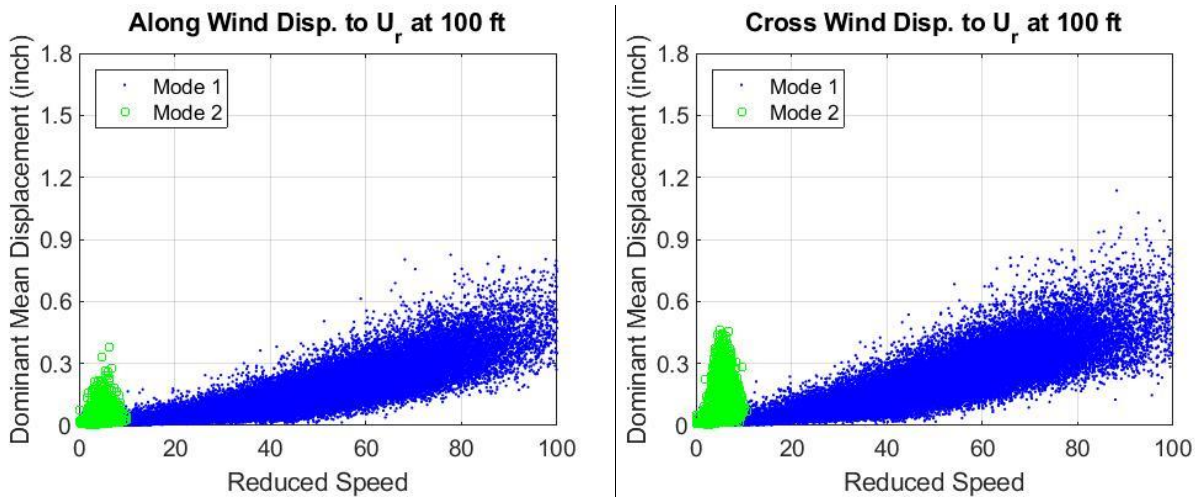

Figure 6.78: Along- and Across-Wind Response at 80 feet to Reduced Speeds at 100 feet

Wind Turbulence Effect

Smooth winds with low turbulence intensity provide favorable conditions for vortex-induced vibration of cantilevered mast arms for traffic signals (Zuo and Letchford 2010). Upon examining turbulence data at the monitored site for this HMIP study, it was found that due to the orientation of the arm that supports the ultrasonic anemometer, a shielding or blockage effect from the pole itself is observed. This leads to the absence of low turbulence intensity levels in the 270° direction (West) as can be seen in Figure 6.67. A highway bridge is in close proximity due North of the pole and this also leads to additional blockage for some directions. In order to study the effect of atmospheric turbulence on HMIP motions and to avoid drawing incorrect conclusions, winds coming from behind the pole and in the direction of the bridge are neglected leaving only data with wind directions between 90° and 240° for analysis.

Figure 6.79 shows plots of the along-wind maximum stress ranges versus the cross-wind maximum stress ranges for low wind speeds (4 to 6 mph) and higher wind speed (18 to 20 mph). At the low wind speeds (Figure 6.79a), data for the time series with higher turbulence intensity levels are seen to result in low induced stress ranges in both the along-wind and cross-wind directions while with lower turbulence intensity levels, higher induced stress ranges are seen particularly in the cross-wind direction due to vortex shedding. At the higher wind speeds (Figure 6.79b), the recorded stress ranges show no preferential magnitude variation in either the along- or cross-wind directions. The response in both directions show a tendency to increase with increasing turbulence intensity which is a characteristic of buffeting response.

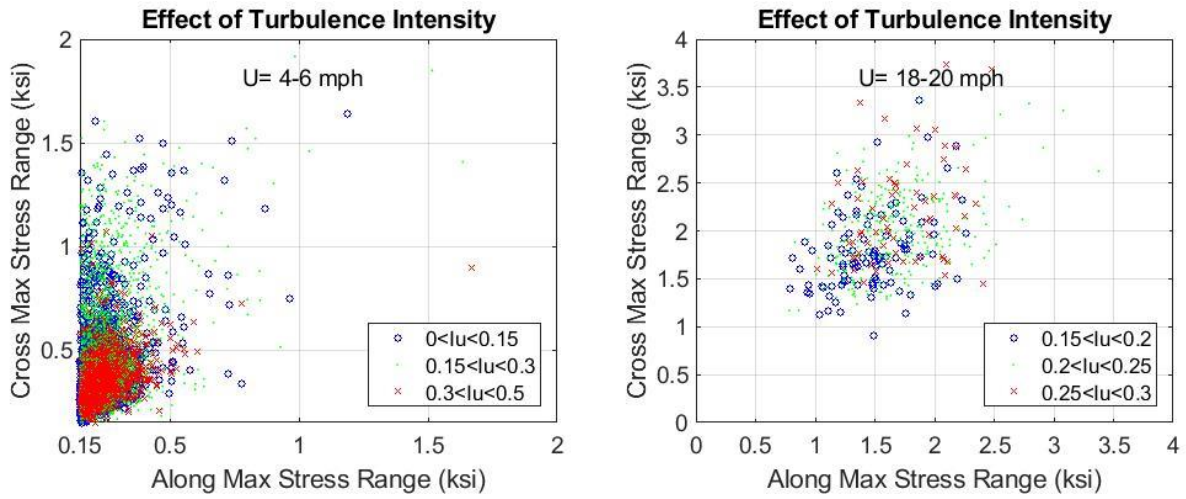

Figure 6.79: Along- and Across-Wind Maximum Stress Ranges for Different Turbulence Intensities

Comparison among Different Sites

Since data segments with high turbulence due to nearby structures have been excluded in the graphs, the comparison of the graphs presents the response due to the geographical terrain from the collected sites. Figure 6.80 indicates that the largest observed VIV response is from Laredo followed by Galveston and Austin; Dallas has relatively small response where El Paso shows none. Turbulence intensities from the analyzed directions in each site under low wind speed (2 to 6 mph) were pooled individually where the median is used to present the turbulent condition at low wind speed at different sites (Table 6.4). The reason for Laredo and Galveston having larger VIV response while experiencing more turbulence than Austin may be due to the lower structural damping ratio in the second mode reported from both sites (Table 6.3). The second mode structural damping ratio from the El Paso HMIP is also high which may also be the reason why there is almost no VIV response from El Paso. Although the second mode damping ratio is approximately the same between Dallas and Austin, the lower VIV response is due to the high turbulence intensity in that region (Table 6.4).

The inconsistencies among sites indicate that other factors contribute to the VIV response besides wind speed and turbulence intensity. Although the majority of vortex-induced response occurs in the same wind speed range, the response amplitude and the occurrence rate of the VIV differ among sites. However, it is important to recognize that all sites shows no significance in the third mode VIV which was assumed to dominant in high wind speeds in past studies (Dawood 2014).

Higher responses in the first mode under higher wind speed ranges are observed in Dallas and El Paso where turbulence intensity is higher. The response is contributed by buffeting response where past studies (Chang 2009) suggests that the first mode and higher turbulence results in higher response. Based on the knowledge of the mechanics behind these responses, the induced fatigue damage resulting from these responses are introduced in the following section.

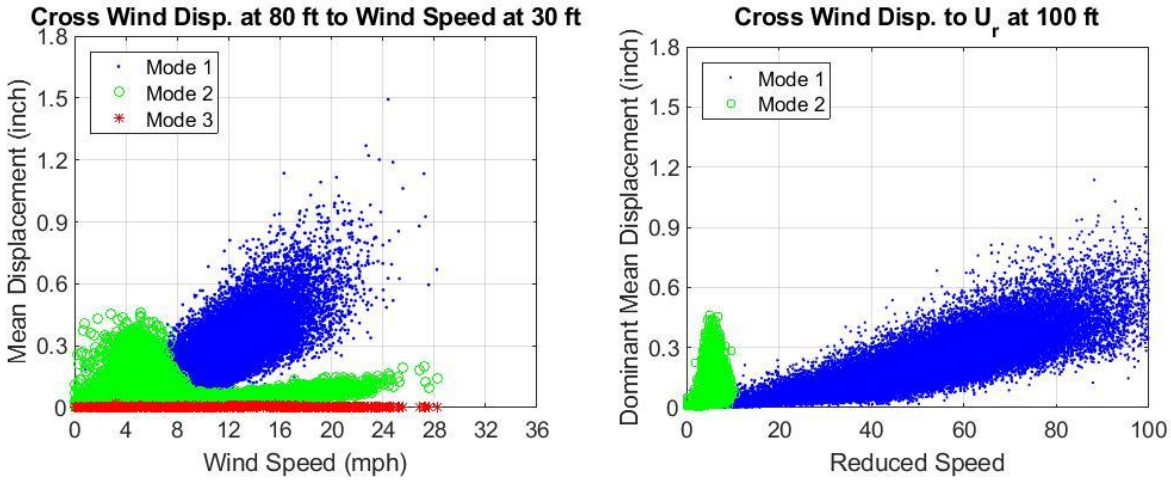

(a) Austin

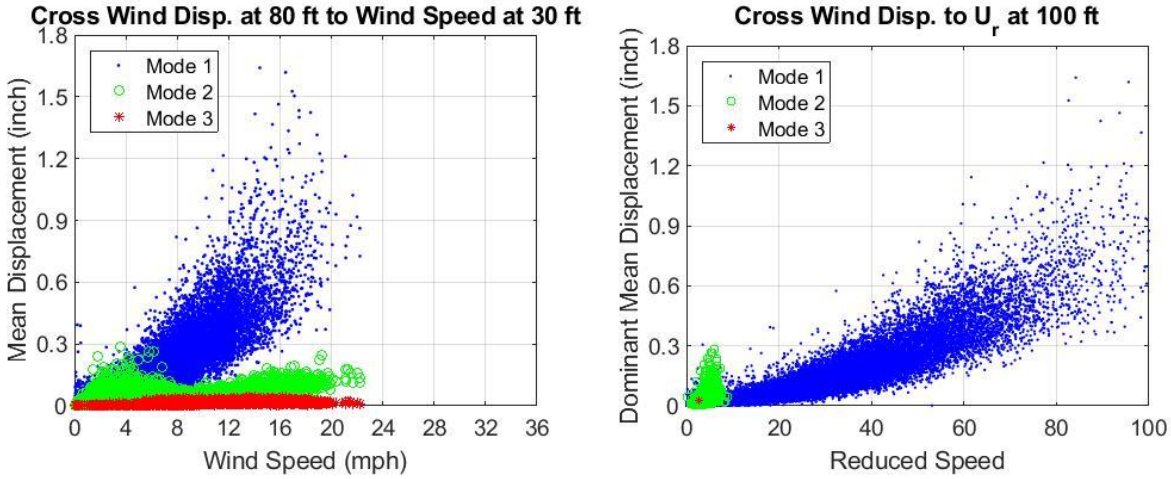

(b) Dallas

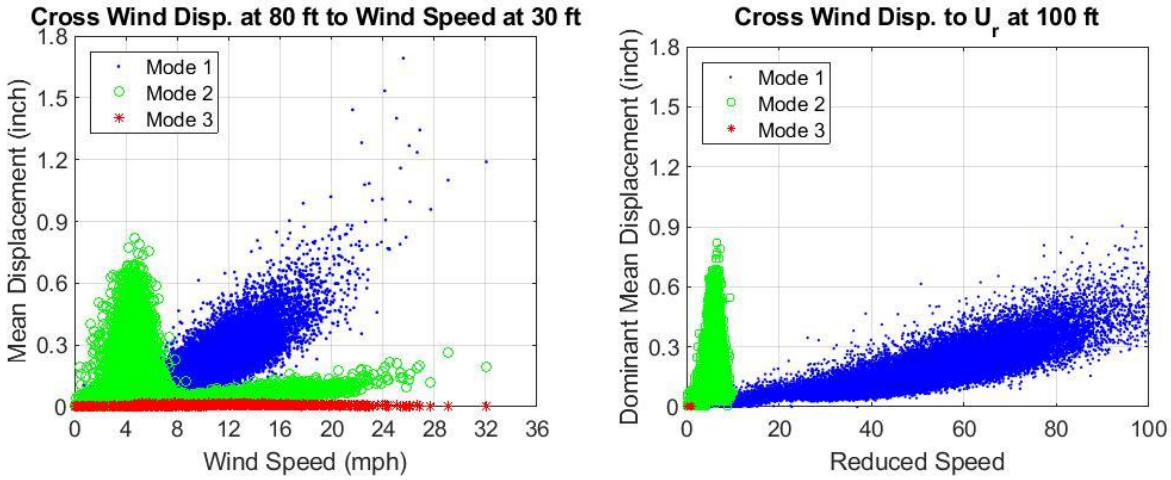

(c) Laredo

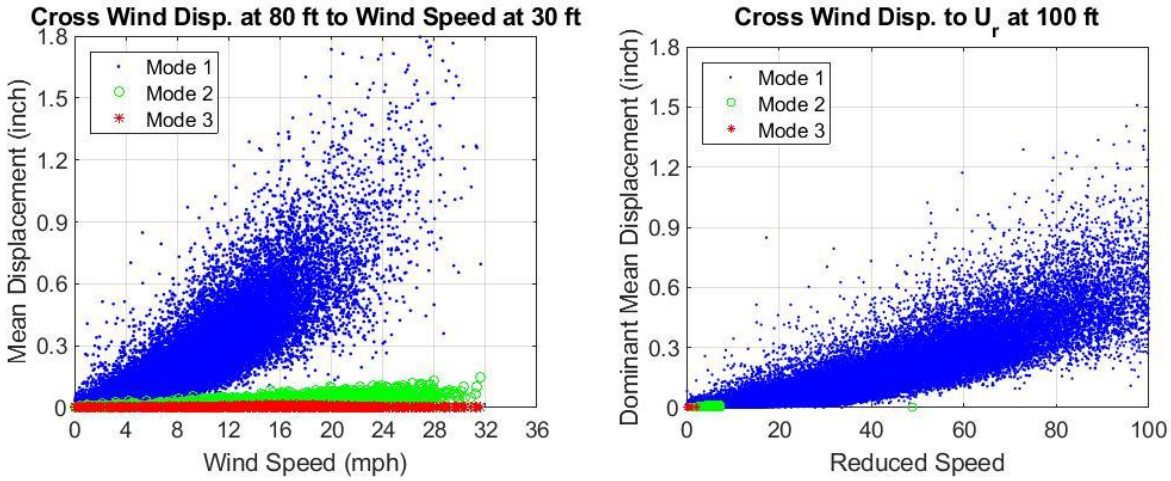

(d) El Paso

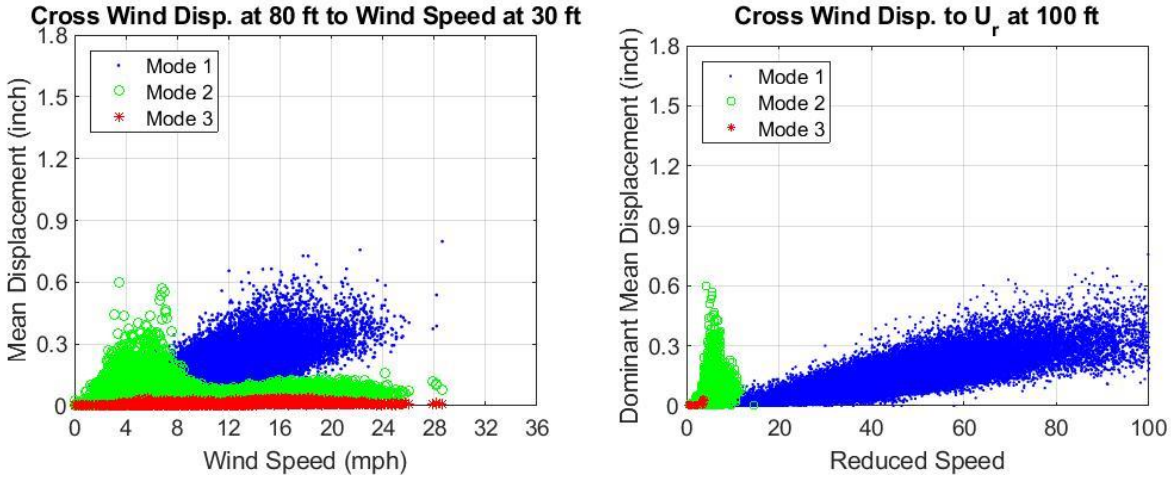

(e) Galveston

Figure 6.80: Comparison of Across-Wind Response from All Sites

Table 6.6: Turbulence Intensity (Median) for Monitored Pole Sites

	Austin	El Paso	Dallas	Galveston	Laredo
Turbulence Intensity (Median)	0.21	0.27	0.31	0.25	0.25

6.5.6 Induced Fatigue Damage

In addition to recognizing the higher response in low wind speed range due to VIV in the second mode, the induced fatigue damage due to this response is of great interest. The fatigue damage presented as EFL illustrated in Section 6.4.4 is determined in along- and across-wind directions and plotted with wind speed to show how much damage is expected with respect to the wind speed. An "expected" EFL ($E(EFL)$) is also determined, using Equation 6.23, to represent the scattered EFL (denoted by EFL_k in Equation 6.23) under different wind speed ranges.

$$E(EFL) = \frac{\sum_k^N EFL_k}{N}$$ ***Equation 6.23***

The EFL in directions other than along- and across-wind directions were also determined to establish an "expected" EFL table that can easily account for all wind directions and wind speeds. To account for two-slope S-N curves as illustrated in Section 6.4.4, EFL based on the S-N curve from Eurocode 3 fatigue category 40 without CAFL (Constant Amplitude Fatigue Limit) is also determined and presented in this section.

Equivalent Fatigue Load (EFL)

The EFL according to a one-slope S-N curve under along- and across-wind directions is plotted with wind speed at 30 feet above the base plate (Figure 6.81). Each dot in the EFL graph represents the induced damage from the 5-minute strain series in along and cross wind directions while the color represents the dominating mode of the segment. Note that the EFL is not calculated based on strain series separated into each mode like in the motion analysis (Figure 6.80).

The EFL figure shows similar trends to the 80 feet motion response to wind speeds where Laredo exhibits the largest observed second mode VIV. However, the EFL values dominant in the second mode with respect to those dominant in the first mode is relatively higher when compared to the motion response shown in Figure 6.80. One reason for this is due to the different mode shapes (Figure 6.57), where same displacements at 80 feet above the base plate would result in higher stresses at the bottom of the pole if vibrating in the second mode. Another reason is the higher frequency in second mode results in higher number of cycles and in turn, higher EFLs. This results in some cases where the induced damage, or EFL, is actually higher in low wind speed ranges than in high wind speed ranges.

The EFL calculated for the pole in El Paso shows no peak in the low wind speed range, which is expected since no indication of VIV was seen in the motion responses. Despite the occasional second and third mode dominant series, the EFL is insignificant such that it does not need to be addressed. Although it is interesting to see a few high EFLs under the third mode from the Galveston Pole which are results of the high third mode frequency mentioned earlier, the wind speed for these cases are still in the low wind speed ranges similar to those dominant in the second mode. The advantage of using EFL to represent the damage is that it does not require information of the dominant mode in order to retrieve the induced damage. This allows the EFL in different dominant modes to group together while in the same wind criterion such as wind speed ranges. In other words, the EFL is still representative of the damage seen in this wind speed, which may consists of different mode combinations, regardless of the actual dominant mode.

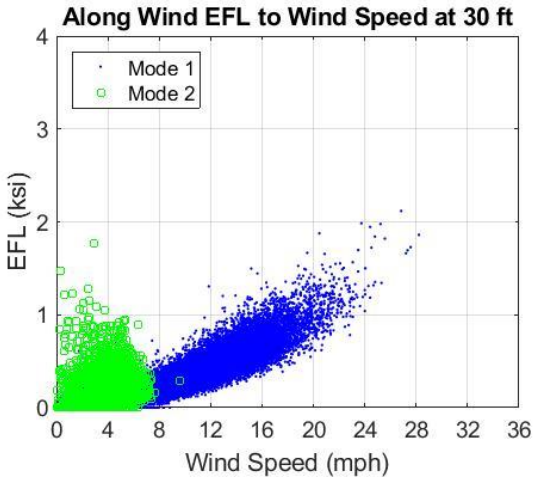

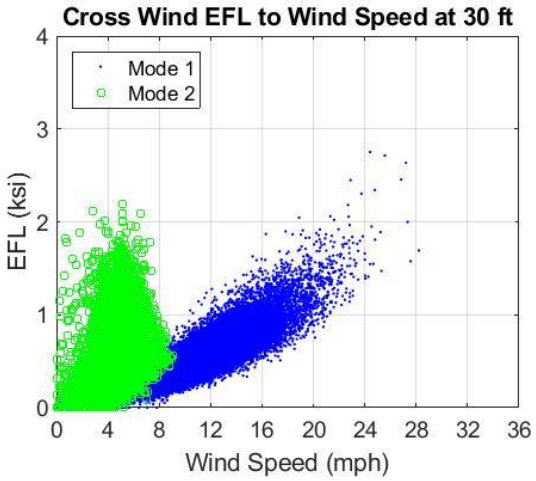

(a) Austin

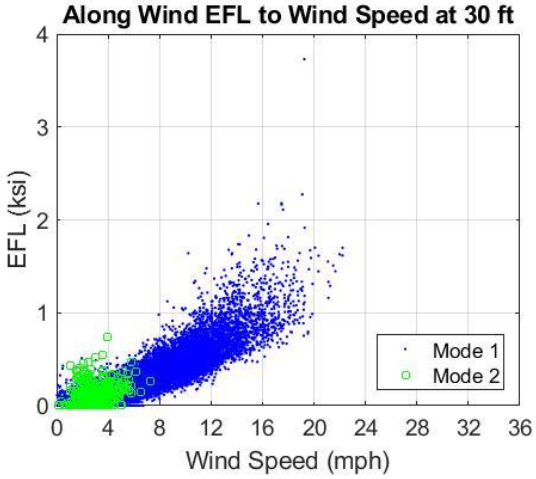

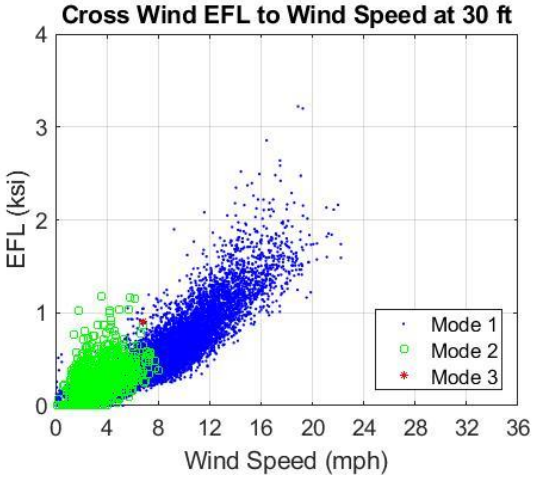

(b) Dallas

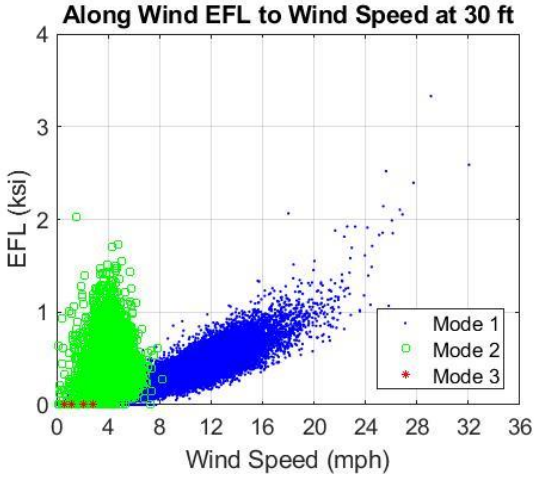

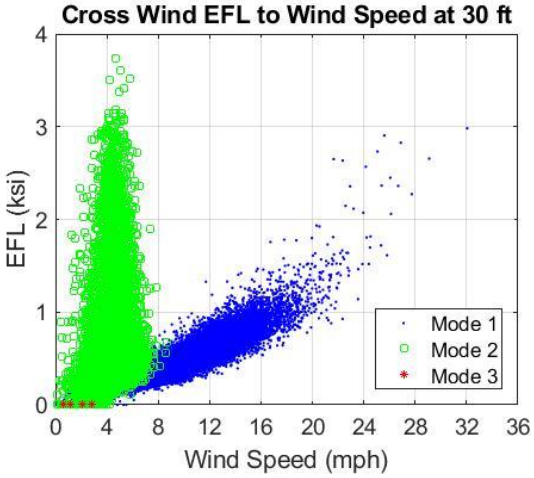

(c) Laredo

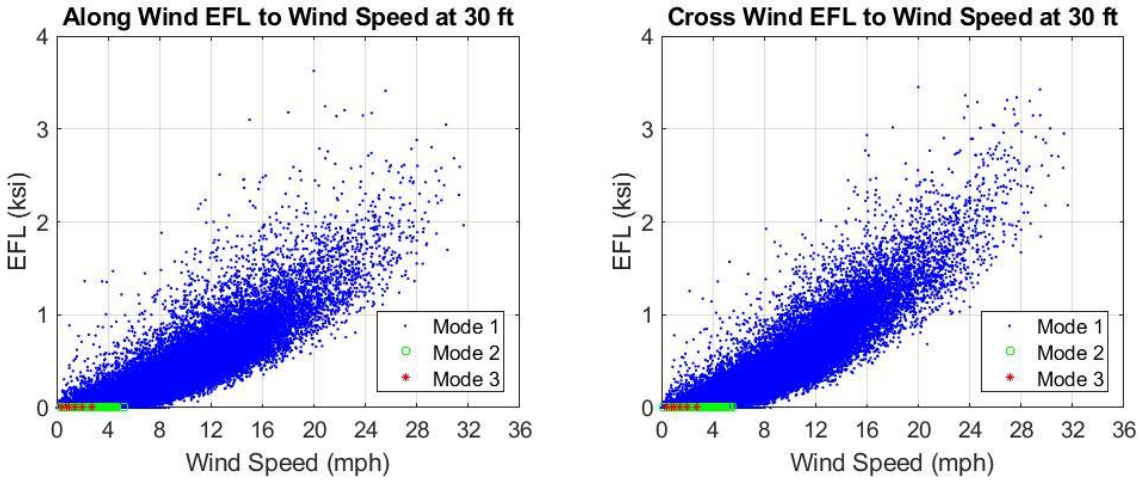

(d) El Paso

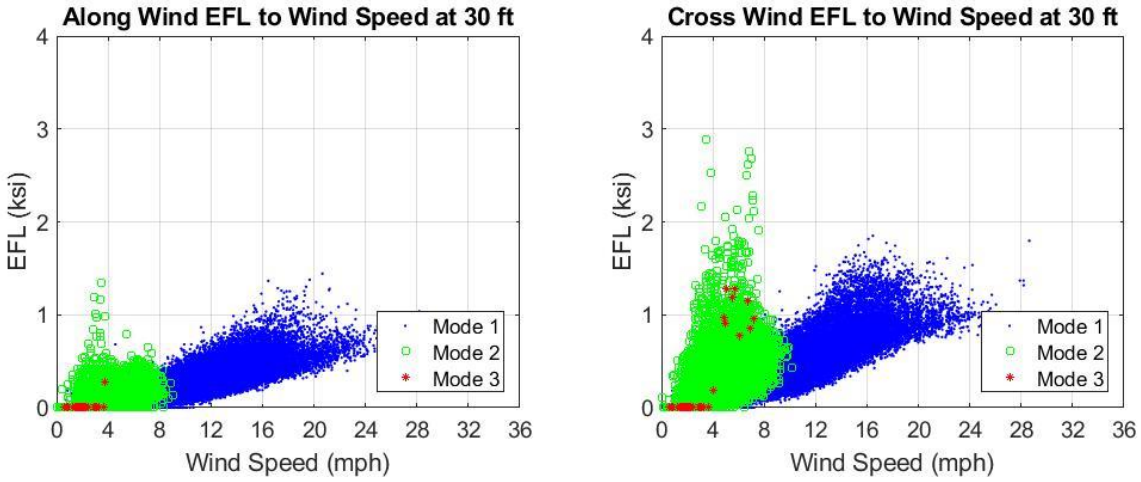

(e) Galveston

Figure 6.81: Along- and Across-wind EFLs for various Wind Speeds at 30 feet

Expected EFL (One-Slope S-N Curve)

With knowledge of the wind direction from each 5-minute data segment, one can recover, using Equation 6.13 applied to strains, strain-time series at any location, both in the along- and across-wind directions, and at around the perimeter of the HMIP. Accordingly, for 12 different angles (relative to the wind), θ_r, at 30° intervals, EFL values and the corresponding "expected" EFLs are computed for all pole sites. The database then conveniently yields an $EFL(U, \theta_r)$ matrix or table of fatigue damage information conditional on a wind speed bin, U, and for a direction of the wind relative to the detail of interest, θ_r. Only six different θ_r values need to be included in the important $EFL(U, \theta_r)$ table since $EFL(U, \pi + \theta_r) = EFL(U, \theta_r)$.

Figure 6.82a shows the computed $EFL(U, \theta_r)$ information derived using all the data from the Austin site. Higher EFL values implying greater fatigue demand in the across-wind direction (θ_r=90°) are clearly seen at lower wind speeds indicating the influence of VIV in fatigue damage there. Since the expected EFL accounts for all EFL and not only the peak values in the selected bins, the EFL peak from Figure 6.82 is not as significant as the peak shown in Figure 6.81 which indicates that not all EFLs in the low wind speed region are high and dominated by VIV. However,

the expected EFL is more representative of the damage in that wind speed than a peak EFL that is VIV dominated.

Both EFL results from Dallas and El Paso (Figure 6.82b and 85d) show no peak in the low wind speed range which suggests that the damage due to vortex-shedding can be neglected for these instrumented HMIPs. However, the EFL in high wind speed regions in Dallas and El Paso are relative higher than those from Austin which is assumed to be a result of lower wind turbulence condition at the Austin site. EFL from Laredo shows the largest peak in the low wind speed region which agrees well with the largest observed VIV response (Figure 6.82c) due to low structural damping and low wind turbulence conditions as previous discussed. Besides the larger hump seen in Laredo, similar EFL values at high wind speeds can be seen in Austin and Laredo.

Although not very significant, two EFL peaks, both in low and high wind speed ranges, are observed in Galveston (Figure 6.82e). The milder peak in the low wind speed range represents a slightly higher induced damage while indicating lower occurrence of VIV response compared to Laredo and Austin. The peak in the high wind speed range can only be observed in Galveston where the HMIP design is different. Since the EFL in the high speed region shown in Figure 6.81 does not indicate a third mode dominant response the cause of this relative peak requires further investigation. However, since the use of EFL does not require any prior information of which mode is dominant, the EFL just reflects the damage observed in the selected wind ranges as noted in the previous section.

A comparison among the EFLs from different sites is shown in Figures 6.82f and 6.82g. In the low wind speed range, poles in both Austin and Laredo show larger response compared to those in Dallas and El Paso, while high wind speed range shows otherwise due to lower wind turbulence exhibited in Austin and Laredo. The low EFL shown from Galveston is mainly due to the stiffer HMIP design. Since the wind turbulence is not measured in most weather stations, it is difficult to set wind turbulence as a parameter in the EFL table. As a result, an envelope EFL (Figure 6.82h) which gathers the largest value from all sites for each relative direction and wind speed is proposed as a comprehensive EFL that covers the worst cases (low turbulence in low wind speed region and high turbulence in the high wind speed region) representing the expected damage in a conservative manner.

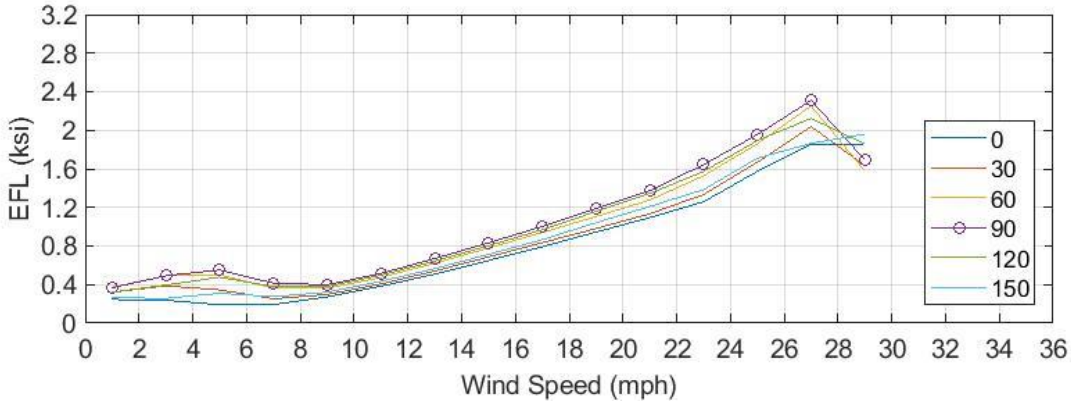

(a) Austin

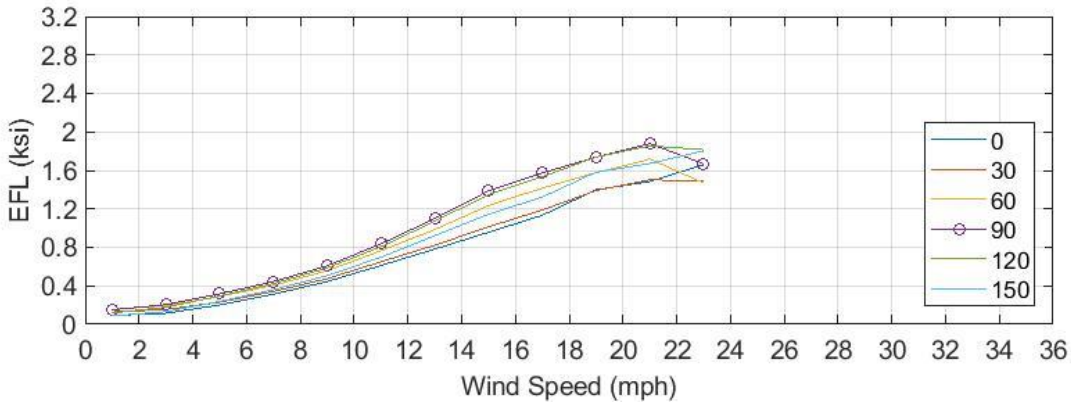

(b) Dallas

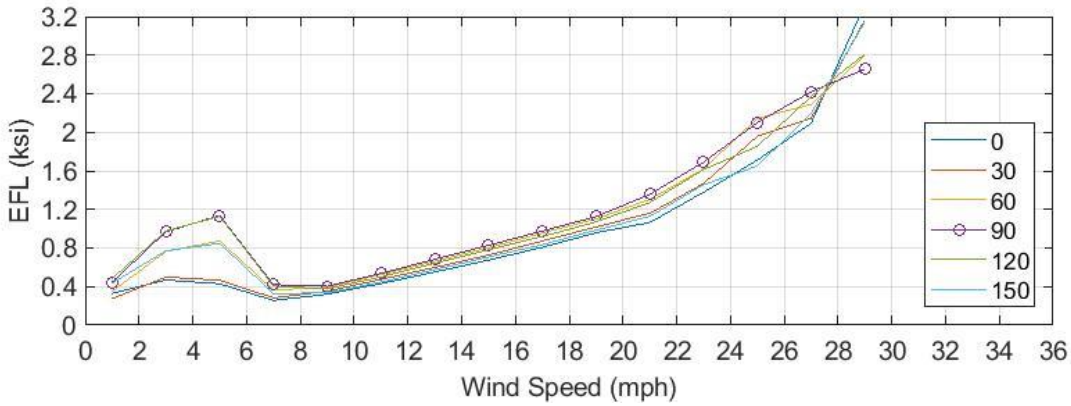

(c) Laredo

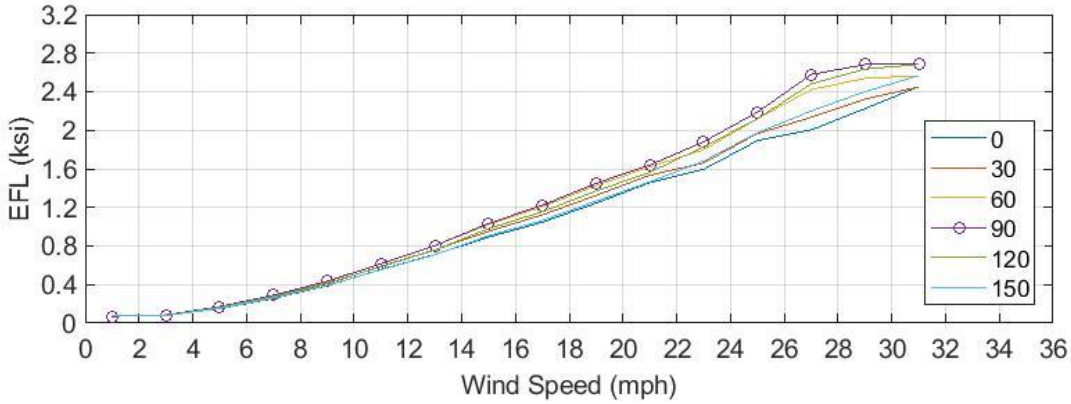

(d) El Paso

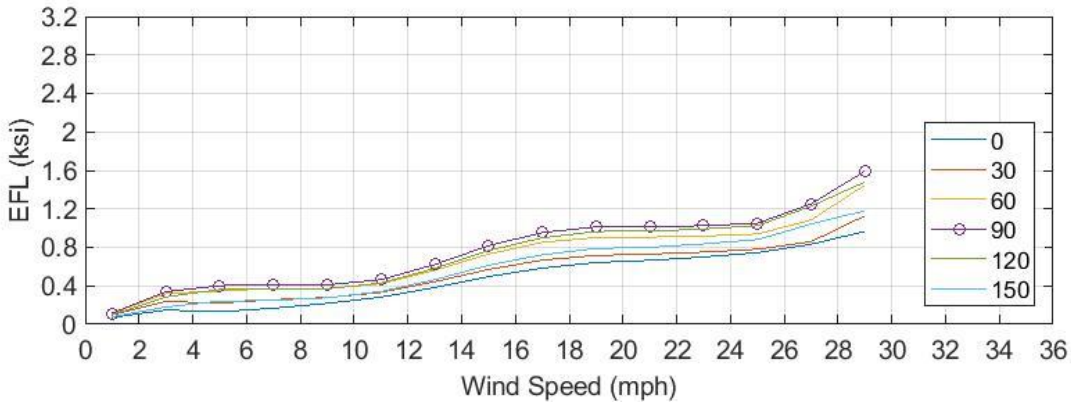

(e) Galveston

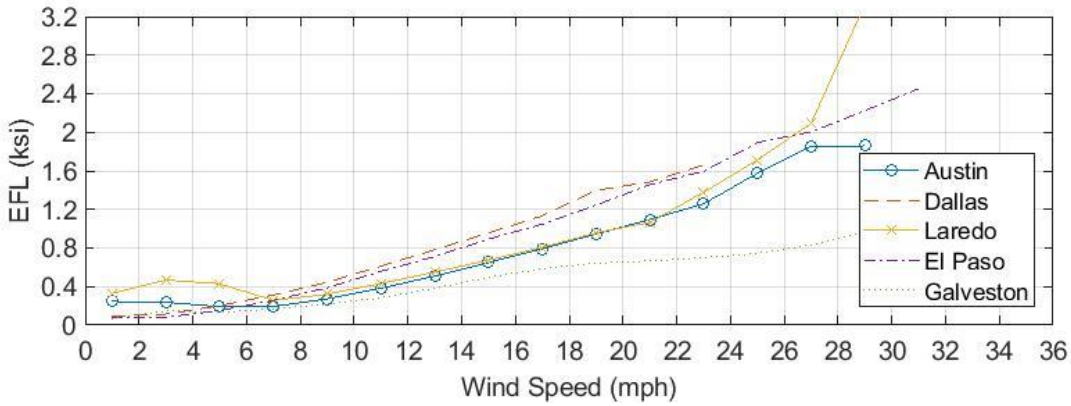

(f) Along-Wind Comparison

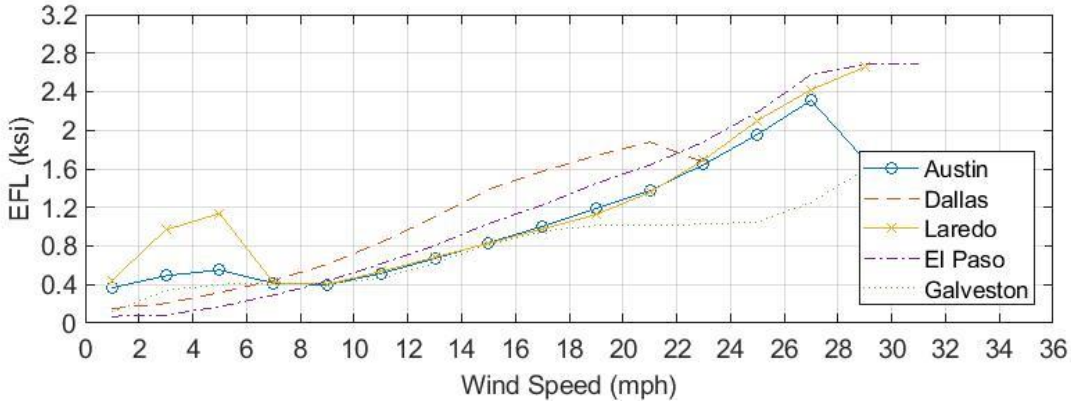

(g) Across Wind Comparison

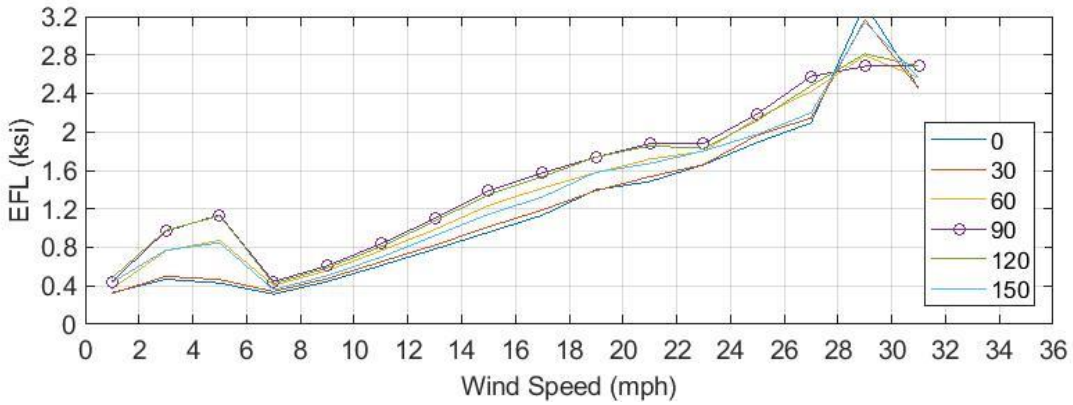

(h) Envelope EFL

Figure 6.82: Expected EFL Values for Different Wind Speeds (at Different Relative Angles to the Wind and based on the One-Slope S-N Curves)

Expected EFL (Two-Slope S-N Curve)

As illustrated in Section 6.4.4, according to past studies (Lassen and Rėcho 2006) and the Eurocode 3 structural design code (EN1993:2002), two-slope S-N curves are more representative of the actual induced damage for low stress-range cycles. The EFL based on Eurocode 3 category 40 S-N curve without CAFL is presented in this section (Figure 6.83). The new EFLs are smaller compared to the EFLs under one-slope S-N curves in general since all speed ranges may result in small stress ranges where the induced damage is significantly reduced. The trend in the EFL with respect to the speed is similar between the one- and two-slope S-N curve assumptions showing a small peak in the low wind speed region and increasing EFL as wind speed increases. The EFL under the two different S-N curves in Figure 6.83i shows less difference at high wind speeds since stress ranges are normally higher and mostly subjected to the same S-N slope.

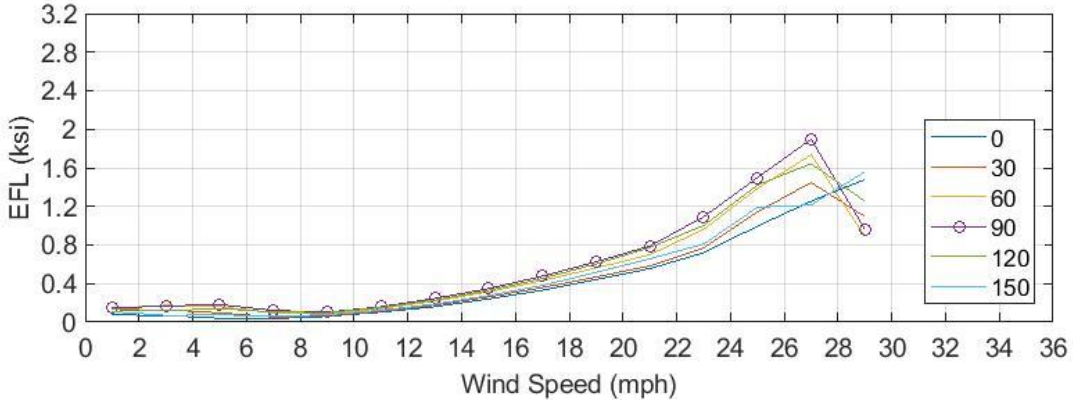

(a) Austin

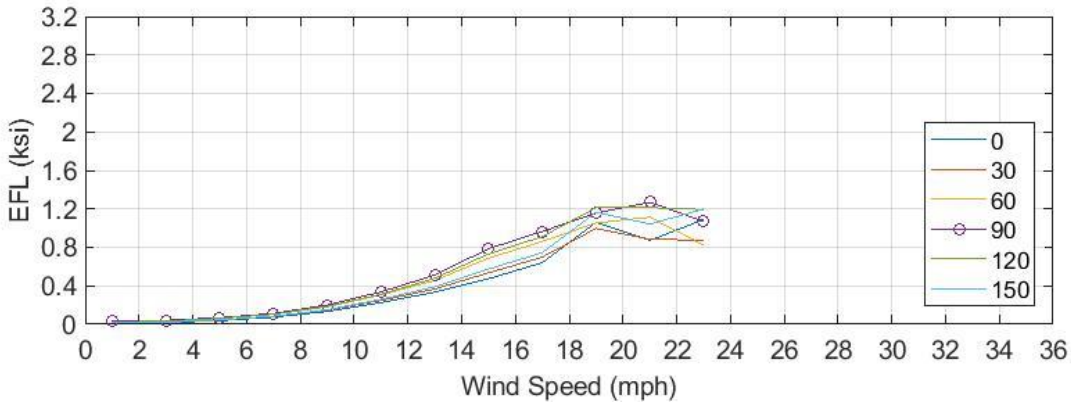

(b) Dallas

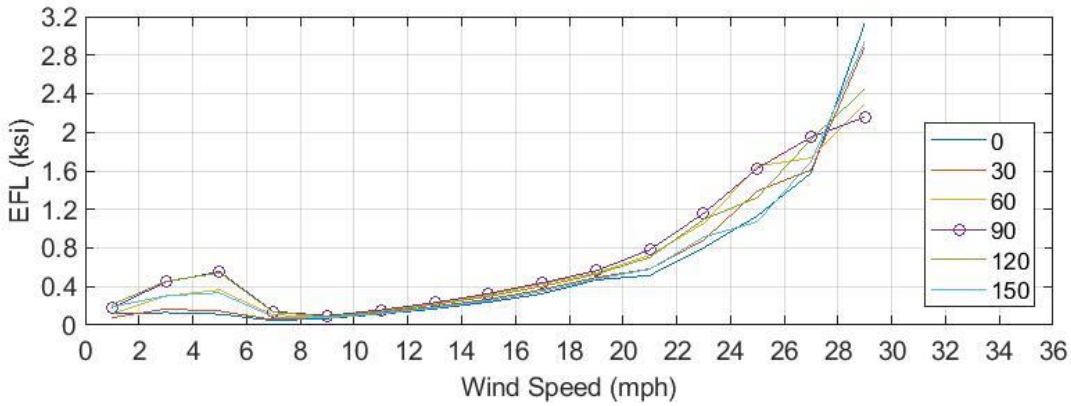

(c) Laredo

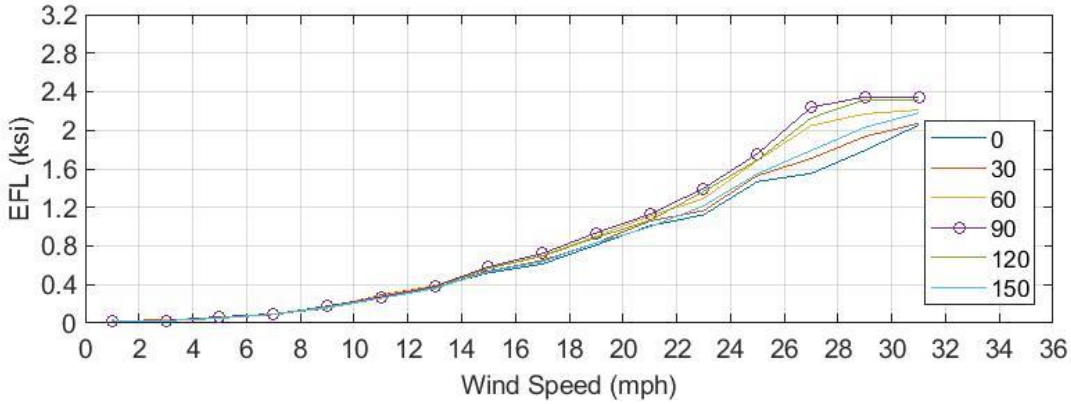

(d) El Paso

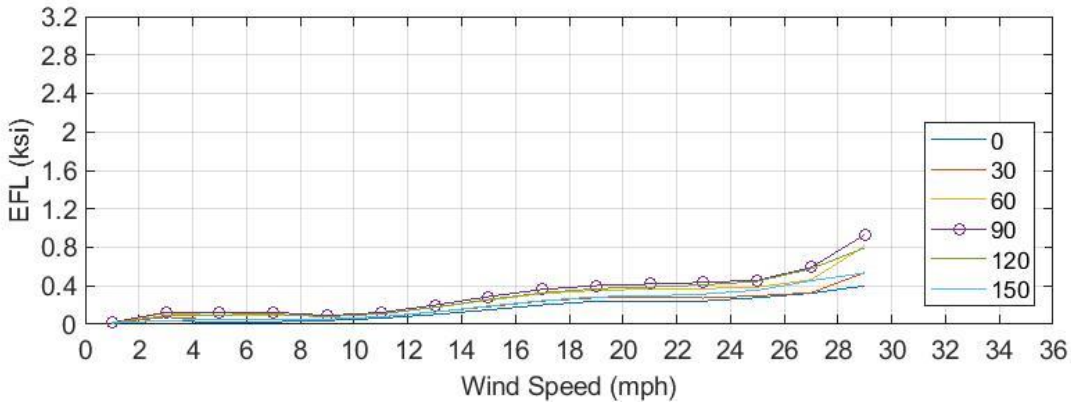

(e) Galveston

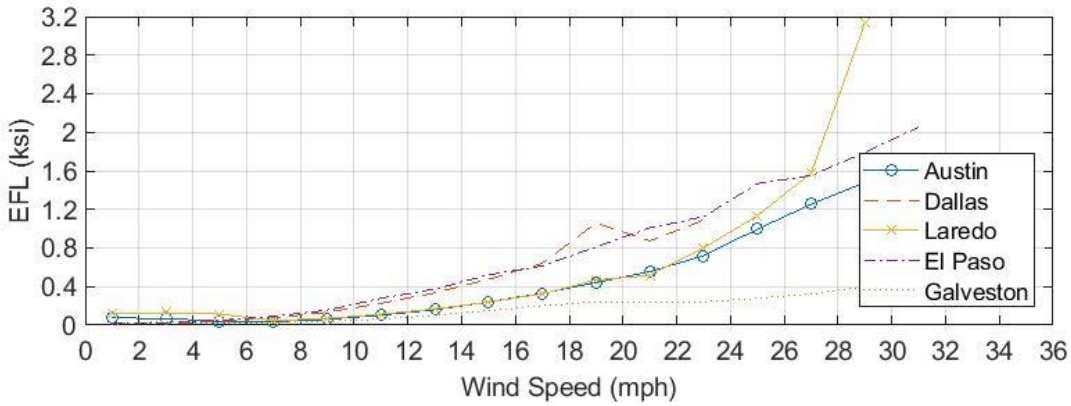

(f) Along-Wind Comparison

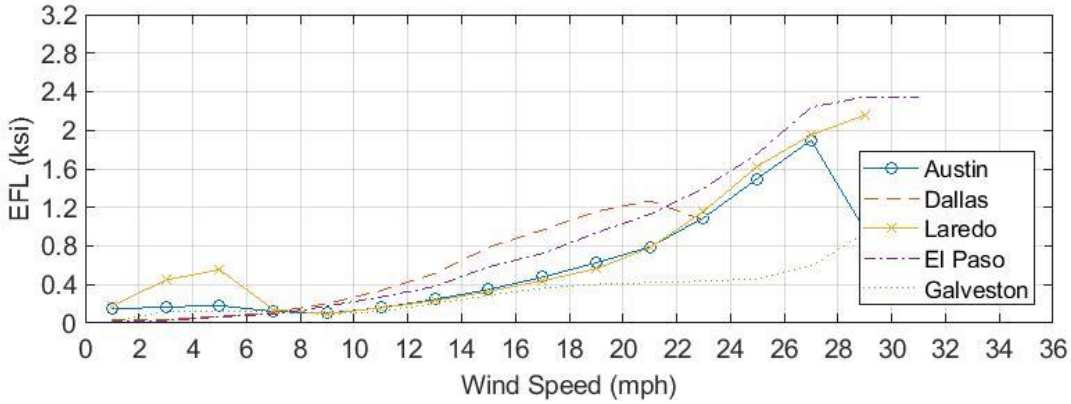

(g) Across-Wind Comparison

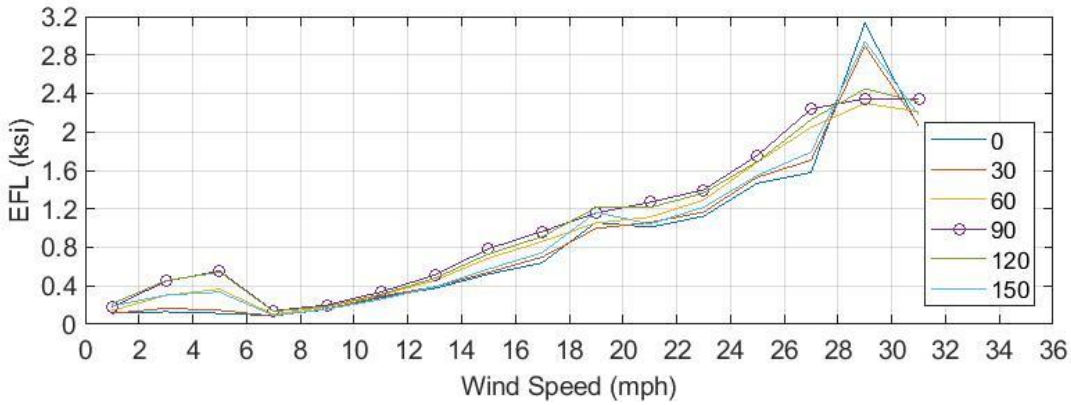

(h) Envelope EFL

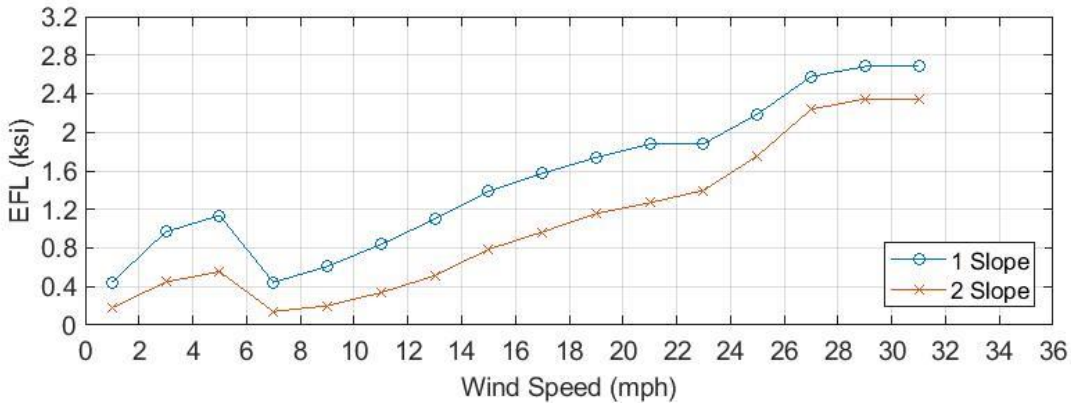

(i) One-Slope versus Two-Slope S-N Curve (Envelope in Cross Wind)

Figure 6.83: Expected EFL Values for Different Wind Speeds (at Different Relative Angles to the Wind and based on the Two-Slope S-N Curves)

6.6 Summary

Field monitoring studies and analysis of field data from HMIPs at five different locations in Texas were described in this chapter. The considerations that went into selecting and locating the candidate HMIPs were first described in this chapter. A description of the instruments utilized to acquire data during the field monitoring was then presented. Further, the data processing procedures used to analyze the field data were introduced and explained in detail. Finally, analyses of field data together with their interpretation were presented and discussed. Some of the key observations from the data and analyses presented in this chapter are as follows:

- Dynamic characteristics of HMIPs such as structural natural periods and mode shapes obtained from numerical models corresponded well with those measured in the field.

- Wind characteristics such as turbulence intensity, and wind speed and direction were all shown to be affected by the built and natural environment surrounding the monitored HMIPs.

- Large-amplitude, vortex-induced vibrations in the across-wind direction was observed for HMIPs at low wind speeds (at around 7 mph), confirming observations from previous studies.

- Vortex-induced phenomenon mainly influenced the second mode vibrations. The third mode vortex-induced vibrations were rarely observed for the monitored poles.

- Buffeting response was observed in the first mode vibrations for both the along-wind and across-wind directions.

- Turbulence was found to be more important at higher wind speeds where both the along-wind and across-wind vibrations in the first mode were significant.

- A method for quantifying the damage using the concept of Equivalent Fatigue Load (EFL) was used to directly assess the contributions of different wind conditions such as wind speed, direction, and turbulence intensity to the fatigue damage. The concept of EFL directly links the wind condition to the fatigue damage without the need to assume a dominant mode or to predict the response amplitude.

- Damage expressed in terms of EFL for low wind speeds exceeded that for high wind speeds due to the higher vibration frequencies and higher motion amplitudes resulting from vortex-induced vibrations.

- Different EFL results from different sites were observed due to different turbulence intensities from the wind and damping factors inherent in the structural properties.

- To better represent the EFL for fatigue-damage assessment at different locations in Texas, the averaged EFLs and envelope EFLs are proposed. The envelope EFL resulted in more conservative predictions of the fatigue damage.

- A modified EFL based on the two-slope S-N curve was suggested and implemented in the analysis of field data. Compared to the S-N curves with Constant Amplitude Fatigue Limit (CAFL) or single straight line S-N curves without CAFL, the two-slope S-N curves more realistically represented the fatigue strength at low stress ranges experienced by in-service HMIPs.

The field data described in this chapter was further used to develop a reliability-based framework for evaluation of the fatigue behavior of HMIPs with pre-existing cracks. Details of this reliability-based framework are presented in Chapter 9 of this report.

Chapter 7. Computational Studies of HMIPs

7.1 Overview

This chapter describes computational studies performed to extend the information collected in the laboratory test and the field monitoring programs, described previously in Chapter 5 and Chapter 6, respectively. More specifically, the main goal of the computational studies was to evaluate the capability of available computational tools to study the fatigue behavior of cracked HMIPs. Commercially available finite element software SAP2000, Abaqus, fe-safe, and AFGROW were utilized in these studies. Using these software packages, different analyses were performed to study the dynamic characteristics of in-service HMIPs, to evaluate the fatigue behavior of HMIP specimens tested in the laboratory, and to predict the fatigue-induced crack-growth observed in laboratory fatigue tests.

This chapter provides an overview of the detailed models of HMIPs developed using the above-mentioned finite element programs. The results of these computational studies are further presented and discussed. It should be pointed out that, of all the HMIPs in service in Texas, poles having 12-sided, 150-ft tall shaft and considered design wind of 80 mph were selected in the computational studies.

7.2 Dynamic Behavior of In-Service HMIPs

In this section, finite element models created to study the fatigue behavior of in-service HMIPs are introduced. Some details of these finite element models along with validation studies are briefly presented and discussed. The focus of these studies has been on the use of computational tools to evaluate the dynamic characteristics of in-service HMIPs. Structural analysis program SAP2000, and general-purpose finite element program Abaqus are used in the verification studies.

7.2.1 Free-Vibration Analysis Using SAP2000

As the first step in creating and validating finite element models of in-service HMIPs, frequency analyses are performed on models of the entire structure of the poles. Frequency analyses are fast to perform and therefore are not computationally expensive when running large finite element models like HMIPs with all the details.

The modal analysis of the in-service poles was first performed using SAP2000. A cantilever beam model was developed in SAP2000 to simulate the dynamic behavior of the poles. The section of the HMIPs was simply modeled as a tube section with tapered diameter. The geometry of the pole was discretized into 20 segments of 7.5-ft along the height. The bottom- and the top-end segments were further divided into three segments in order to increase the accuracies in capturing the bending moment at the base and lateral displacement at the top, respectively. In addition, the overlap between the three segments is neglected. The lighting apparatus was also modeled as a point mass of 1800 lbs (818 kg) at the top of the pole (1800 lbs was considered following the recommendation by Magenes). Figure 7.1 shows the geometry of the in-service HMIPs as modeled in the SAP2000. Table 7.1 further summarizes the dimensions used to model the high mast poles in SAP2000.

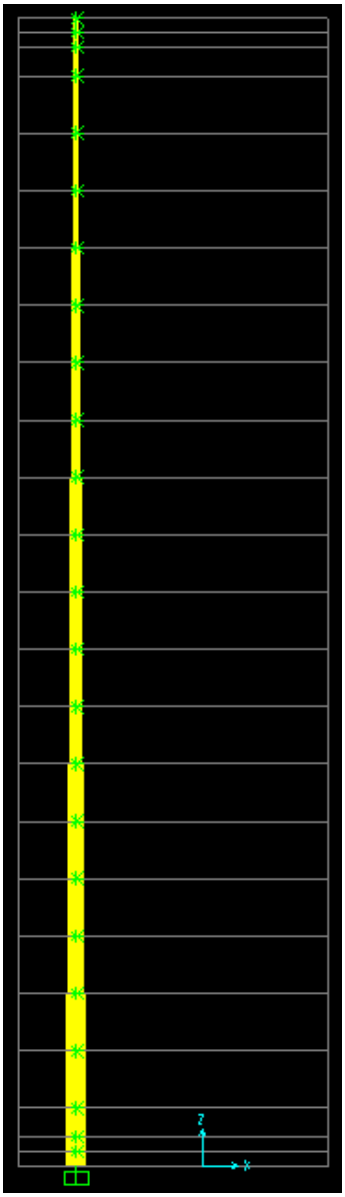

Figure 7.1: Models of the In-Service HMIPs in SAP2000

Table 7.1: Geometry of HMIPs Modeled in SAP2000 for Natural Frequency Calculations

		Dimensions			
Height	**H**	150	ft	45.72	m
Outer Diameter	**D_O**	32.625	in.	0.828675	m
Inner Diameter	**D_I**	32	in.	0.8128	m
Thickness	**t**	0.3125	in.	0.007938	m
Taper Ratio	**u**	0.175	in./ft	0.014583	m/m
Segments		20		20	
Segment Length	**S**	7.5	ft	2.286	m
		Illumination Fixture			
Mass				818	kg

Natural periods and frequencies for the first three modes of vibration calculated in modal analysis of in-service HMIPs in SAP2000 are tabulated in Table 7.2.

Table 7.2: Natural Frequencies and Periods of In-Service HMIPs Predicted in SAP2000

	Period T (Sec)	**Frequency f_n (Hz)**
Mode 1	3.57374	0.280
Mode 2	0.83527	1.197
Mode 3	0.31320	3.193

To verify the accuracy of the calculated natural periods and frequencies of free vibration of in-service poles, such values were also obtained from measurements in the field. In order to find the contribution of each mode and its corresponding mode shape, Proper Orthogonal Decomposition (POD) method was used. Using the acceleration-time histories at three locations along the height of the pole, the cross-power spectra were constructed resulting a three by three matrix at each frequency. The largest eigenvalue and the corresponding eigenvector of the matrix indicate the contribution (natural frequency) and the mode shape at a specific frequency, respectively. Results of such calculations for the instrumented pole in Austin are shown in Figure 7.2. As seen in Figure 7.2, high contributions corresponding to the first three frequencies match quite well with those calculated in the frequency analysis of HMIPs in SAP2000.

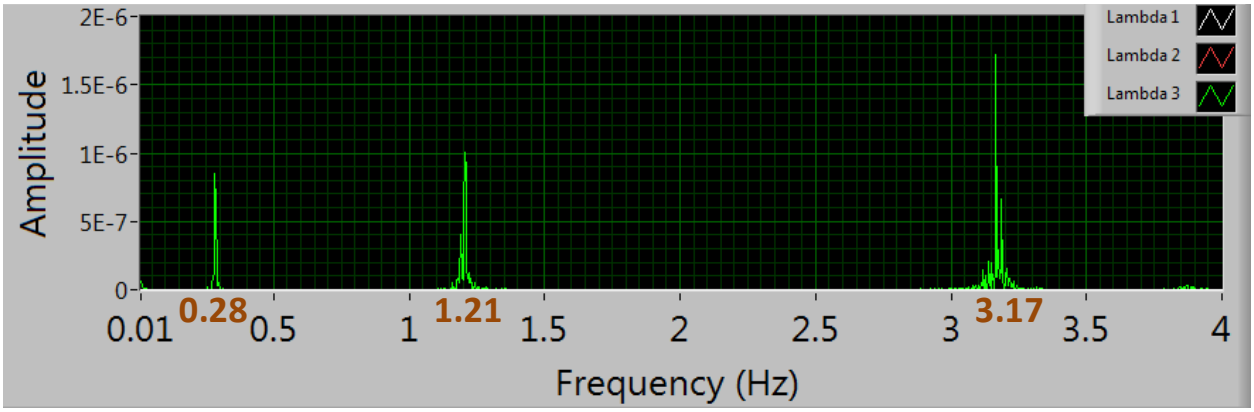

Figure 7.2: Field Measured Modal Frequencies of an In-Service HMIP in Austin

Results from modal analysis of in-service HMIPs in SAP2000 are further presented in Figure 7.3 in the form of vibration mode shapes for the first three modes. As expected, these mode shapes closely follow the form of theoretical mode shapes of a cantilever beam.

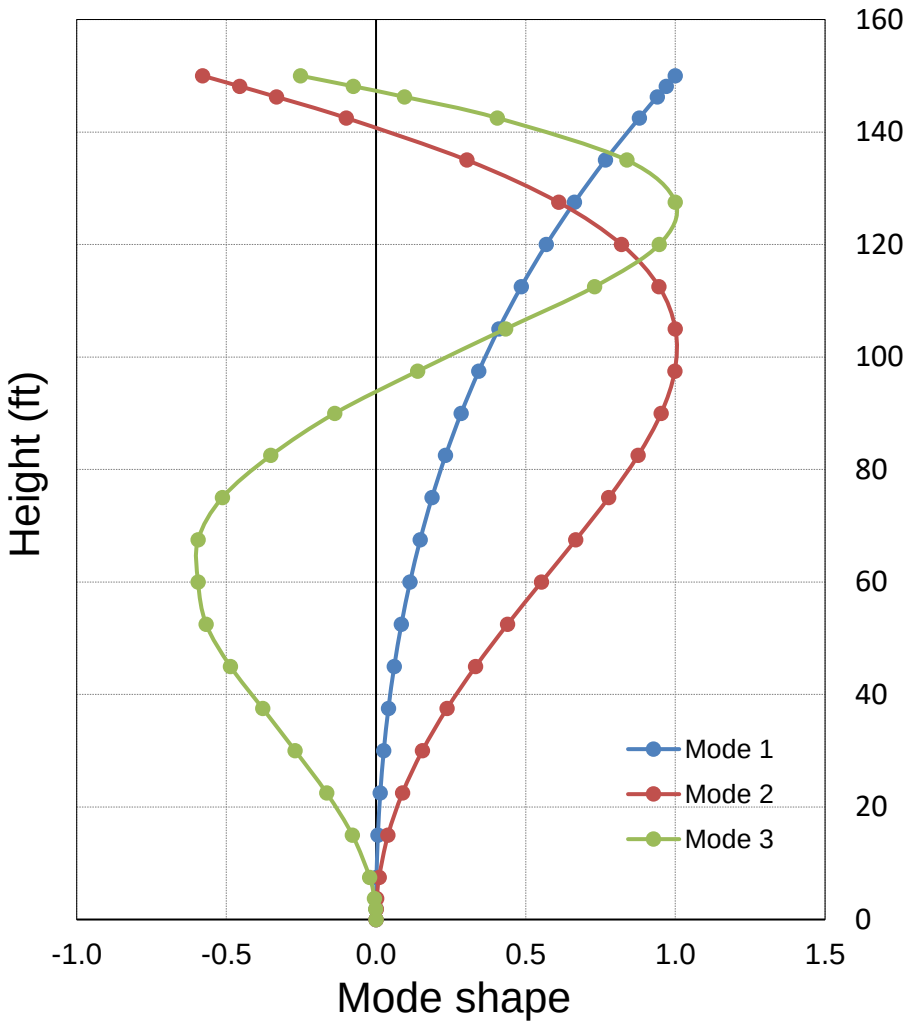

Figure 7.3: Vibration Mode Shapes of In-Service HMIPs Predicted in SAP2000

To verify the accuracy of the calculated vibration mode shapes, the eigenvector corresponding to the largest eigenvalue in the cross-power spectrum matrix at dominating frequencies are plotted in Figure 7.4 along with the corresponding ones from SAP2000 analyses. Although the three points from field measurements themselves cannot represent the entire mode shape, they very well match with the calculated mode shapes from the SAP2000 model, as can be seen in Figure 7.4.

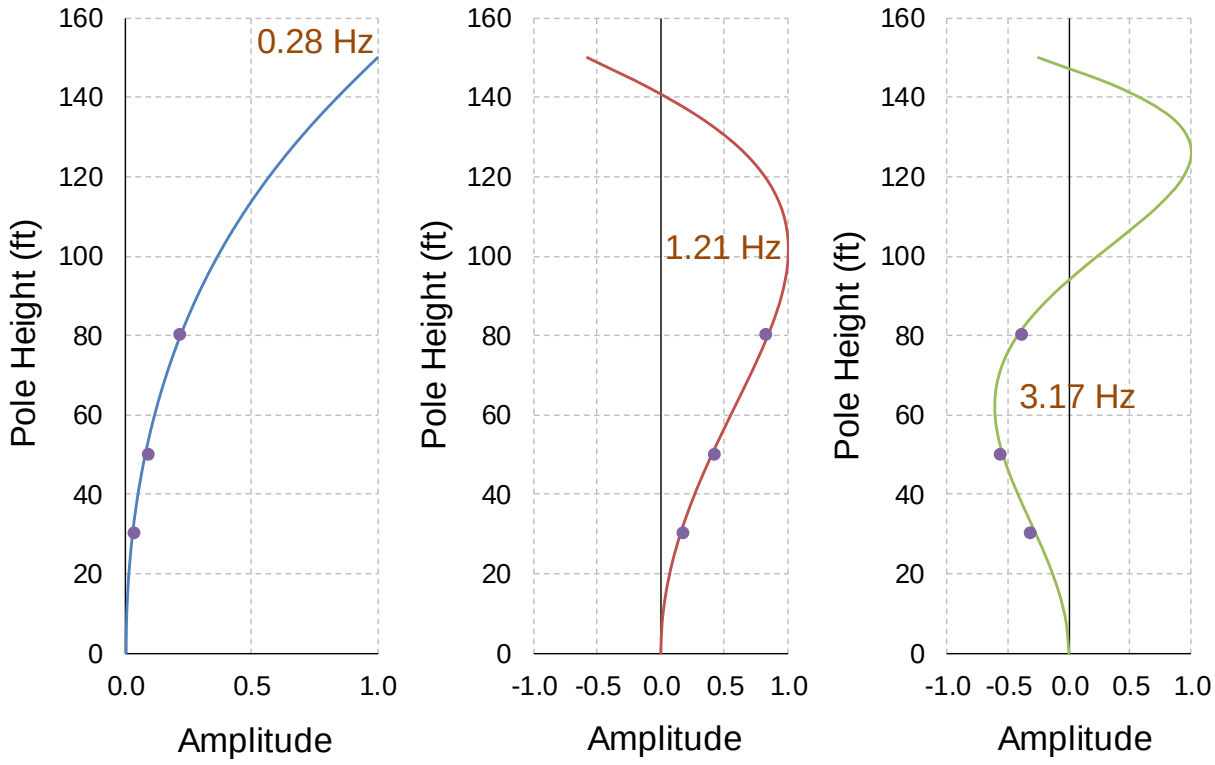

Figure 7.4: Vibration Mode Shapes of an In-Service HMIP in Austin: Comparison between Calculations and Measurements

7.2.2 Simulated Pluck Tests in SAP2000

To further evaluate the ability of the structural analysis software SAP2000 to study the vibration characteristics of HMIPs in service, a pluck test was simulated. In a pluck test, a static load is applied to the high mast pole and quickly removed. As a result, the HMIP is excited similar to a string plucked on a musical instrument. The action of plucking oscillates the pole and data are recorded until the pole vibration is damped out. The data collected from pluck tests are short-termed, and usually last less than 3 minutes.

In the simulated pluck test in SAP2000, the pluck location was set around 30 feet from the pole base. This location was selected according to the AASHTO Report 718, "Fatigue Loading and Design Methodology for High-Mast Lighting Towers" (Connor et al. 2012) There are no specifications as how large a pluck force should be, as long as the pole still oscillates in elastic range. Force resulting in stresses equal to one third of the yield stress at the bottom of the pole has been proposed in the literature. In the simulated pluck test, a pluck force of 50 kN was applied for about 2 seconds (Figure 7.5). Pole's accelerations were measured at three different locations, where each mode shape had its largest displacement amplitude along the height of the pole. These locations were at 67.5 ft, 105 ft, and 150 ft from the base of the pole. Figure 7.6 indicates the location of the pluck load and points along the height of the pole where accelerations were measured during the simulated pluck test in SAP2000.

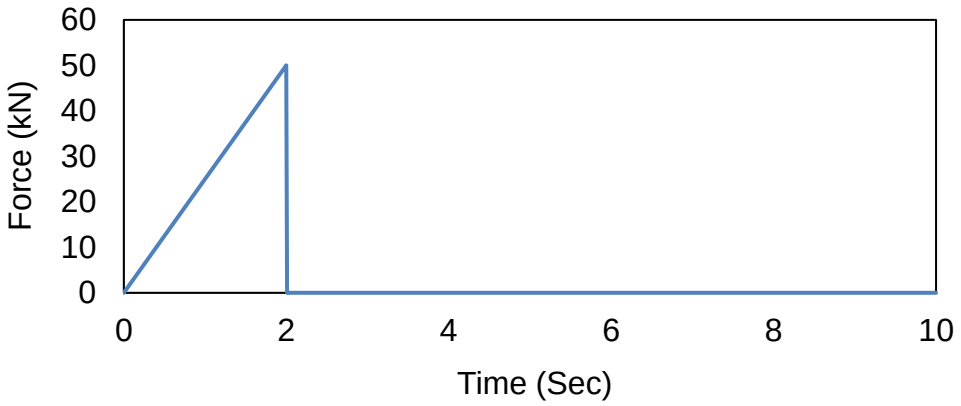

Figure 7.5: Force History in the Simulated Pluck Test on an In-Service HMIP in SAP2000

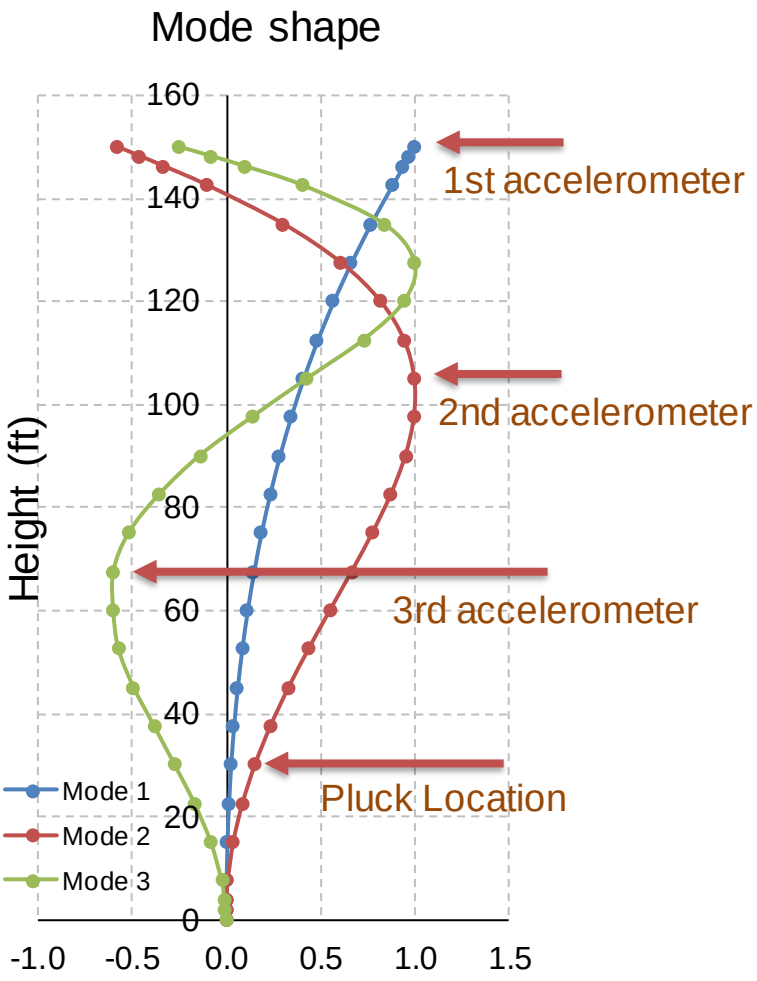

Figure 7.6: Locations of the Pluck Load and Acceleration Recordings in a Simulated Pluck Test on an In-Service HMIP in SAP2000.

The acceleration-time series recorded during the simulated pluck test are plotted in Figure 7.7. Fast Fourier Transform analyses were then performed on the acceleration data obtained at three different locations along the height of the HMIP (as plotted in Figure 7.7) to determine the first three natural frequencies of the simulated high mast pole in the pluck test in SAP2000. The Fourier transform of acceleration-time series are plotted in Figure 7.8. As can be observed from the frequency responses shown in Figure 7.8, the natural frequencies calculated during the pluck test are in good agreement with those measured in the field and obtained in frequency analysis in SAP2000 (Figure 7.2, and Table 7.2, respectively).

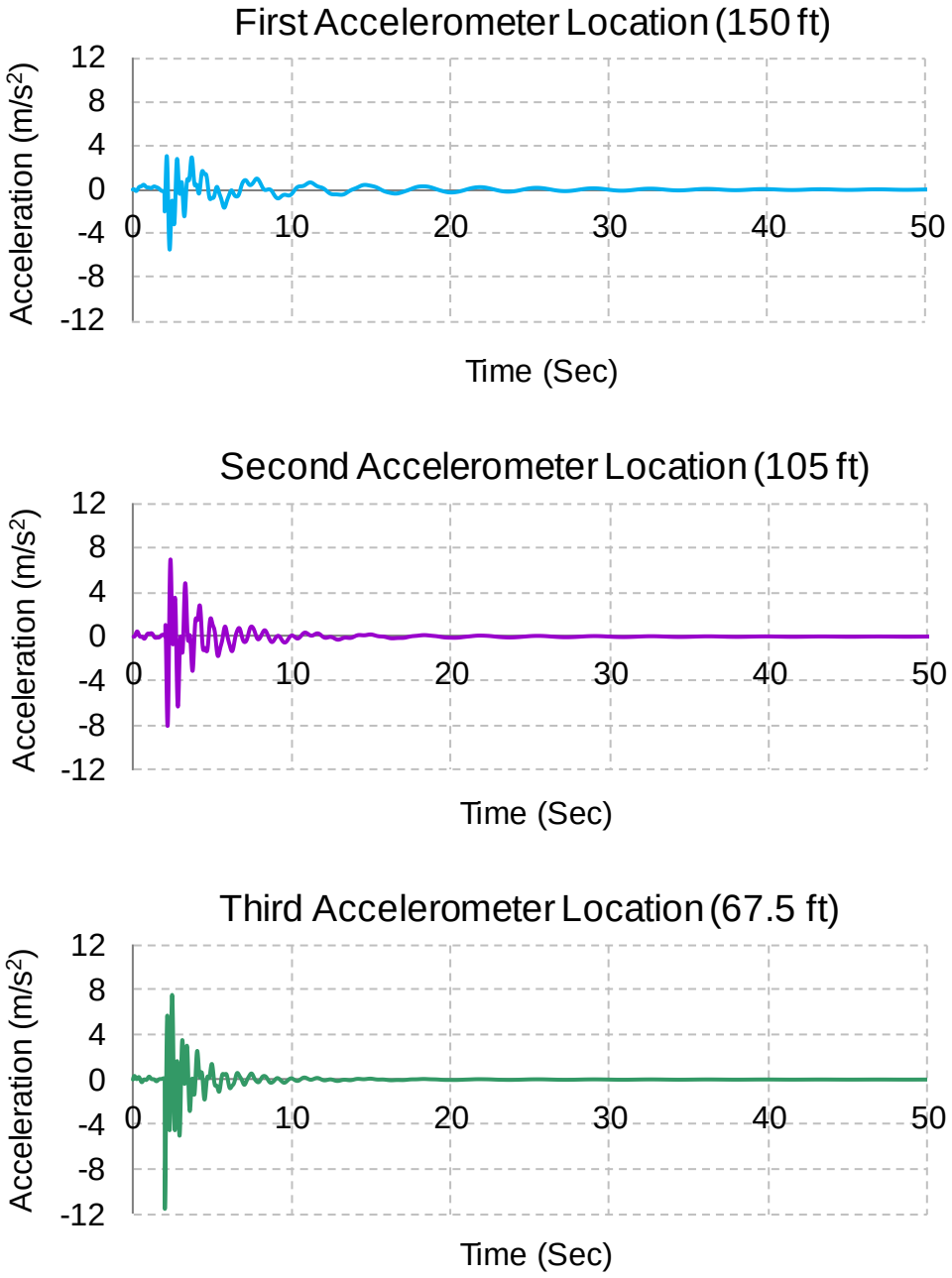

Figure 7.7: Results from a Simulated Pluck Test on an In-Service HMIP in SAP – Time Series Response

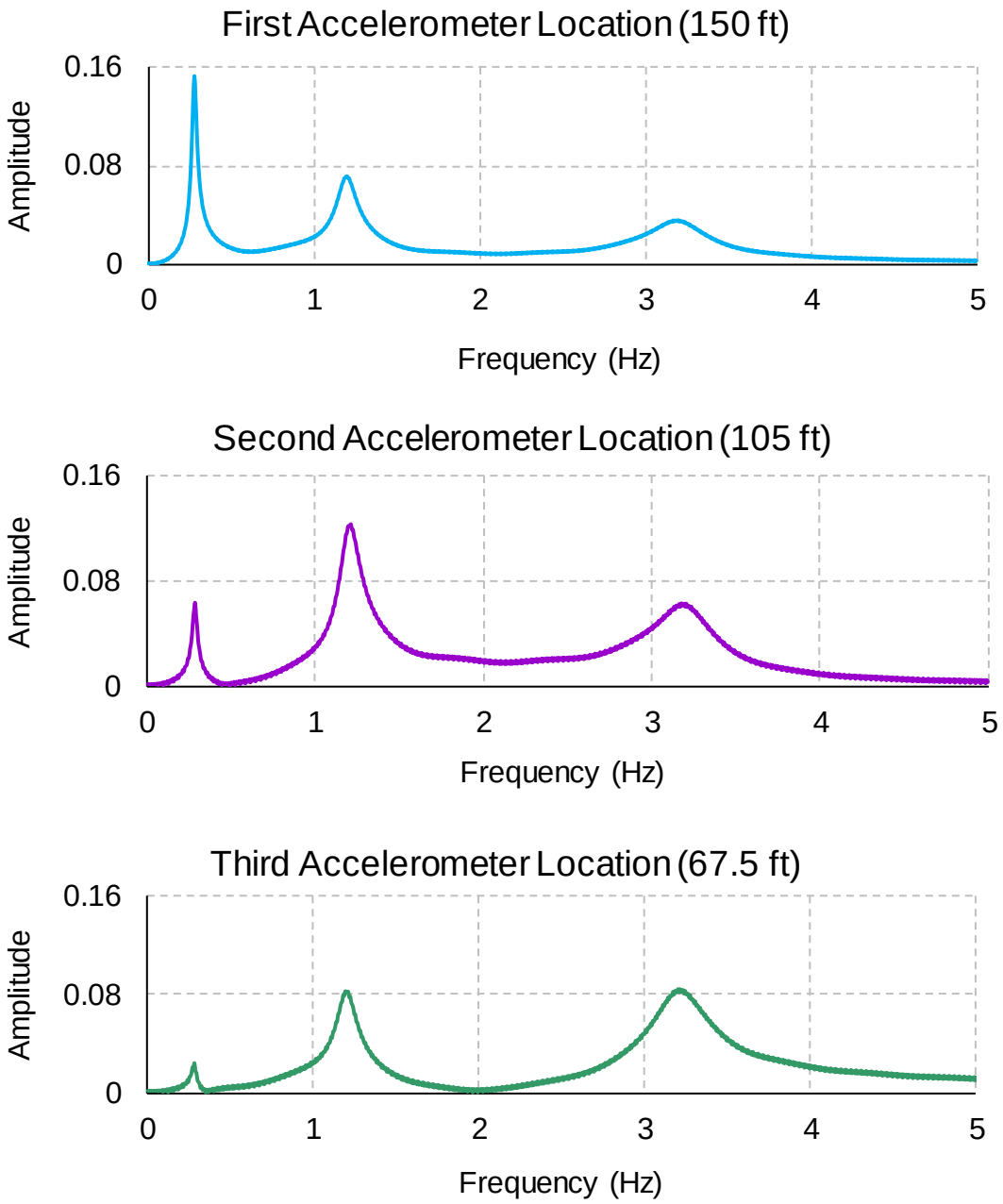

Figure 7.8: Results from a Simulated Pluck Test on an In-Service HMIP in SAP – Frequency Response

7.2.3 Free-Vibration Analysis in Abaqus

As mentioned previously, frequency analyses are fast to perform and therefore are not computationally expensive when running large finite element models like HMIPs with all the details. Therefore, frequency analyses were additionally performed on models of in-service HMIPs using the general-purpose finite element program Abaqus.

The entire structure of HMIPs following the dimensions given in the Texas HMIP(1)-98 design were modeled on Abaqus. In the first model, only the tapered shaft of the HMIP was modeled with shell elements. Overlaps (splices between the segments of the HMIP) were not

modeled. Four-node shell elements with reduced integration (S4R) were used to discretize the finite element model of the poles. A concentrated weight of 1800 lbs was included in the model to represent the lighting fixture at the top of the pole. The assumption of 1800 lbs for the weight of lighting fixture was based on a recommendation by Magenes (2011).

As seen in Figure 7.9, the first five natural vibration modes were considered in validation studies. Results of the frequency analyses are further summarized in Table 7.3. No significant changes in frequency predictions were observed when 6 elements or more were used to discretize each bend, as indicated in Table 7.3. Following the mesh-sensitivity study, 6 elements were used to discretize each bend for the rest of finite element analyses conducted in computational studies of HMIPs.

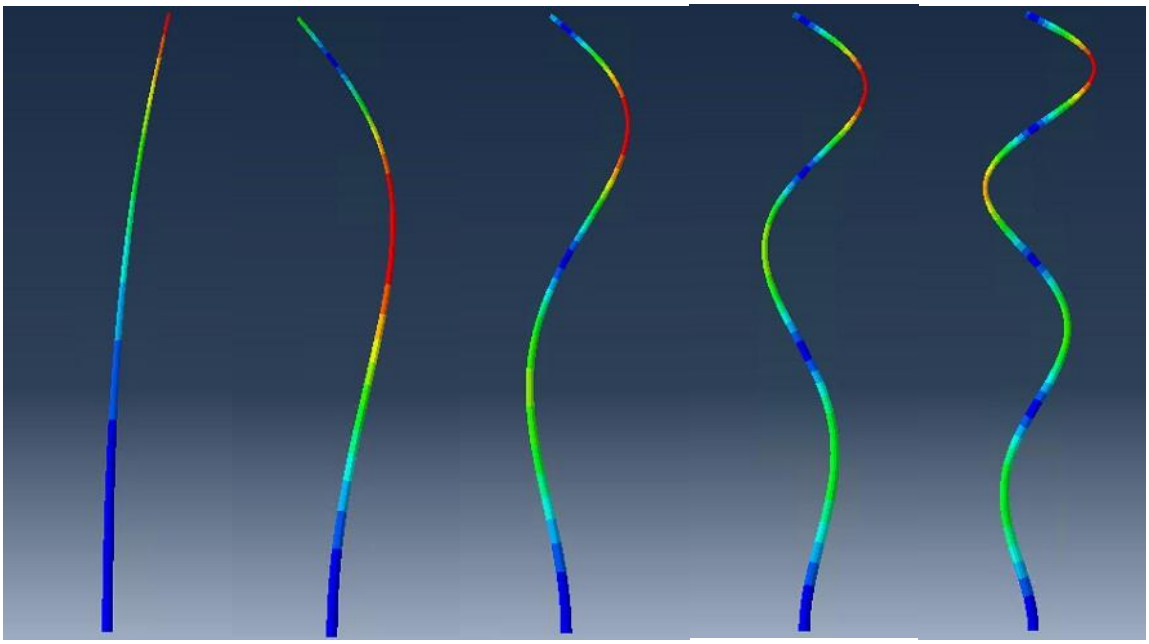

Figure 7.9: The First Five Modes Shapes of HMIPs with the Design of Interest

Table 7.3: Element-Size Dependency of the Computed Natural Frequencies

Number of Elements in Each Shaft Bend	Frequency (Hz)				
	1st Mode	2nd Mode	3rd Mode	4th Mode	5th Mode
2	0.29044	1.2798	3.5256	6.8880	11.534
4	0.29665	1.2880	3.5386	6.9090	11.564
6	0.29784	1.2896	3.5410	6.9128	11.569
8	0.29811	1.2900	3.5417	6.9140	11.571

The first finite element model of in-service HMIPs was further modified by including both the base-plate and anchor bolts in the model. The bottom part of this modified model is shown in Figure 7.10. Eight-node brick elements with reduced integration (C3D8R) were used to discretize the base-plate and anchor bolts. As anticipated, the addition of the base-plate decreased the stiffness at the bottom of the pole when compared with the fixed-end conditions in the first model. However, the changes in the natural frequencies of the pole structure were not significant. The first three natural frequencies were calculated as 0.30 Hz, 1.29 Hz, and 3.54 Hz, respectively.

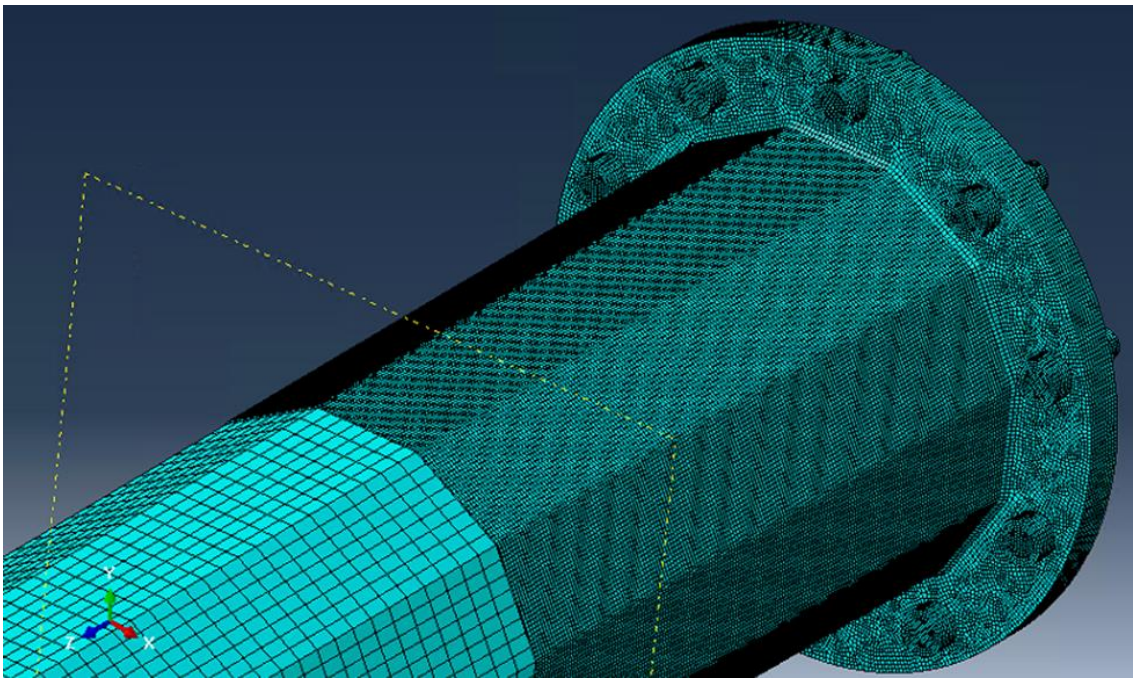

Figure 7.10: Finite Element Models of In-Service HMIPs including the Base-plate and Anchor Bolts

7.3 Development of Finite Element Models of HMIP Test Specimens

In addition to developing computational models for in-service HMIPs, finite element models were created for HMIP specimens used in the fatigue tests conducted at the Ferguson Structural Engineering Laboratory. These models were primarily developed to investigate stress concentration and fatigue performance of HMIP specimens and to verify observations in the fatigue tests. In this section, these models are introduced and analysis results are presented and discussed.

7.3.1 Finite Element Models – General Considerations

In order to develop more efficient finite element models of the HMIP test specimens and to decrease computational time, the bottom 4.5-ft of the pole, base-plate and bolts were modeled using solid elements (C3D8R elements) and the top 9.5-ft of the specimen was modeled with shell elements (S4R elements). The shell part is connected to the solid part using the shell-to-solid coupling constraint feature in Abaqus. The bolts were modeled as part of the base-plate for the same purpose. The average inside bend radius of 1.4-inches was modeled in the solid part. The finite element assembly can be seen in Figure 7.11.

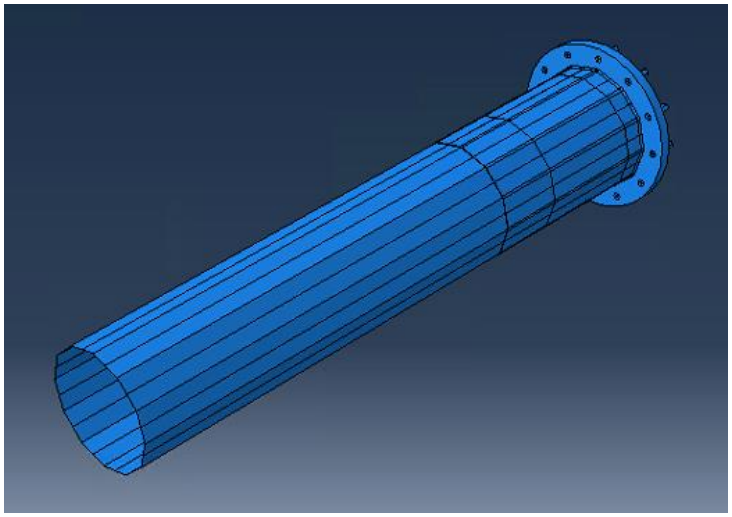

Figure 7.11: Finite Element Models of the HMIP Test Specimens

Finite element models of the HMIP test specimens were then analyzed to obtain an insight into the stress concentration. As an example of such analyses, resulting stresses when a unit force applied in the critical direction for crack-growth are shown in the Figure 7.12.

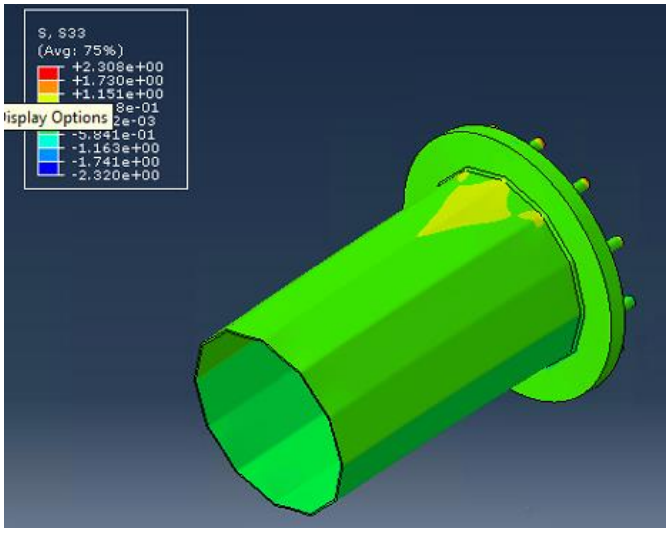

Figure 7.12: Evaluation of Stresses in Critical Sections (S33)

Models for HMIP test specimens were additionally created where anchor bolts were modeled as separate parts. In these models, anchor bolts and nuts were modeled as one part. In other words, the interaction between the anchor bolts and nuts was ignored in the finite element models of the HMIP test specimens. Figure 7.13 shows details of this model.

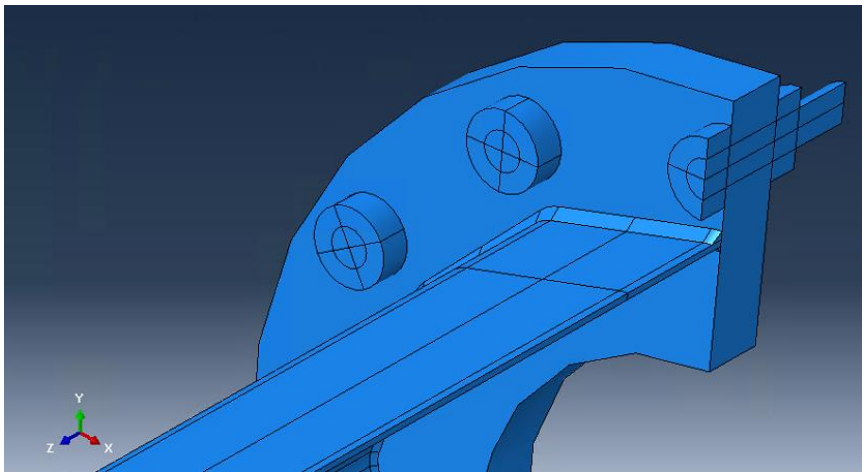

Figure 7.13: Details of the Models of HMIP Test Specimens including the Anchor Bolts and Nuts

To evaluate the effect of anchor bolts on the behavior of the HMIP test specimens, a unit force applied to the two finite element models. The results of these analyses are presented in Figure 7.14. As seen in Figure 7.14, the stresses away from the weld toe are not affected by the modelling approaches for the anchor bolts. However, stresses at locations 2-inches or closer to the weld toe are affected by modeling procedure. It can be seen that larger stresses are developed for the test models with separate anchor bolts. The reason might reside in the fact that the addition of anchor bolts results in increasing the stiffness of the base-plate.

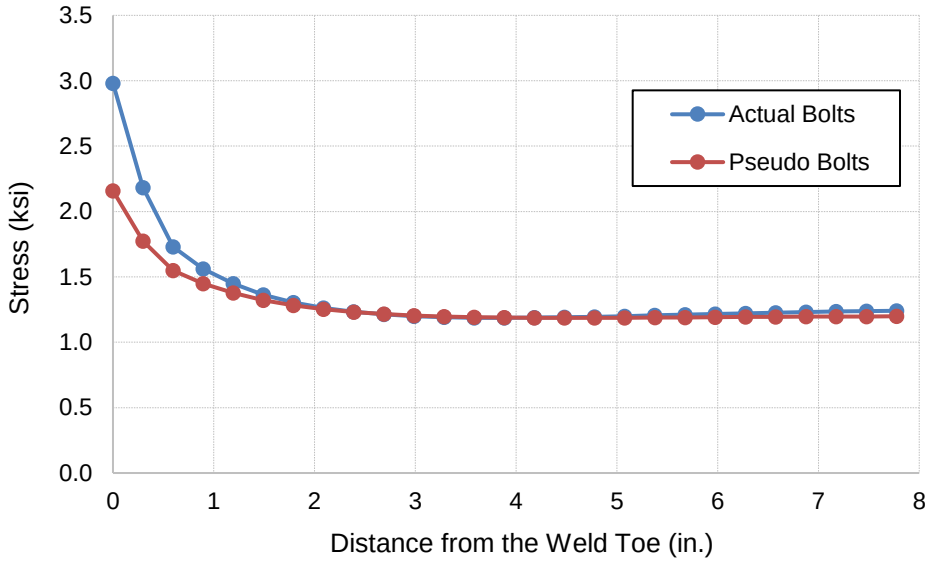

Figure 7.14: Stress Distribution along the Shaft of HMIP Test Specimens

It is further observed that modeling the anchor bolts as separate parts resulted in an increase in the stress concentration factor from 2.16 to 2.98.

7.4 Fatigue Analysis of HMIP Test Specimens

As the next step in verifying the capability of available computational tools to study the fatigue behavior of cracked high-mast poles, a finite element program called fe-safe was chosen to perform fatigue analysis of HMIP specimens tested in the laboratory.

Developed and maintained by a UK-based company called Safe Technology, fe-safe is basically a fatigue solver, serving as a post-processor for common finite element analysis packages like Abaqus. Therefore, models of HMIP specimens were first created in Abaqus, as explained in previous sections, and stress analyses were performed. Through a direct interface with Abaqus, fe-safe was then utilized to perform fatigue analysis on HMIP specimens. Fe-safe was specifically verified on its predictions of the locations where fatigue cracks occurred and of the number of cycles caused the fatigue cracks initiation.

The analysis process for conducting fatigue analysis on HMIP specimens closely followed the "Tutorial 106: Using fe-safe with Abaqus.odb files." A new project was created, and the Abaqus model was opened and scanned for datasets. The Abaqus model had stress and linear elastic strain outputs, which were used directly in the fatigue analysis. The stress response was from a unit load at the end of the HMIP experimental section. Units were then set for fe-safe. Figure 7.15 shows this information in the "Current FE Models" section.

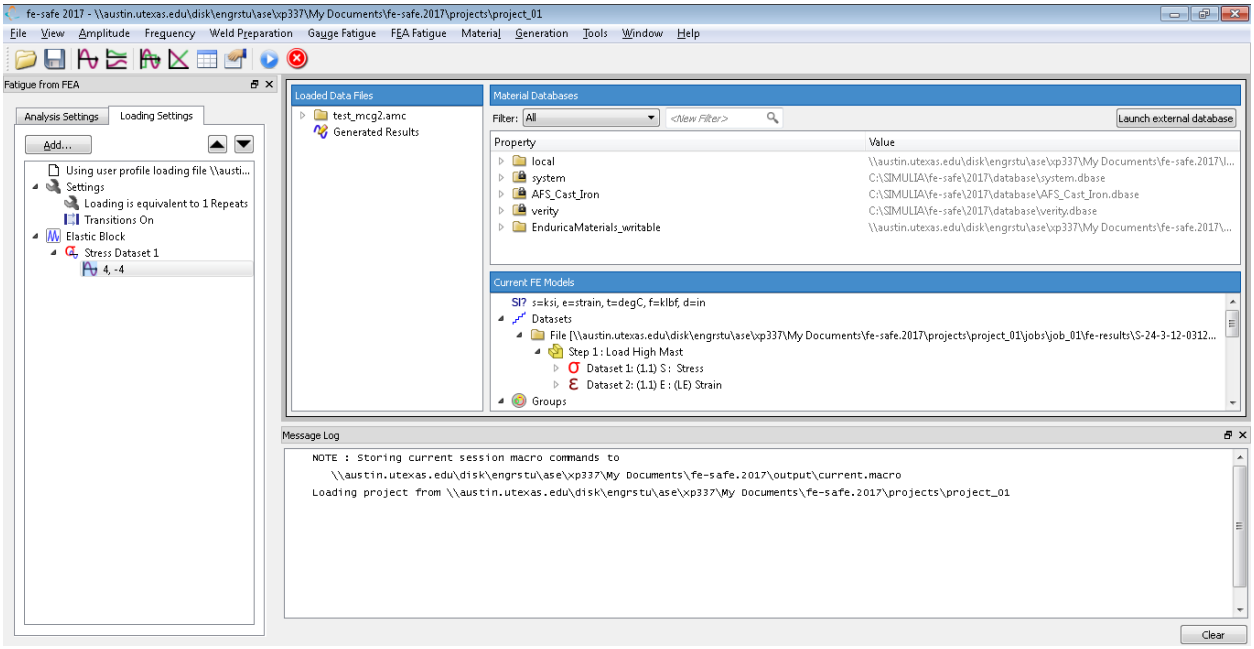

Figure 7.15: fe-safe Main Window

Clicking on available datasets provides information such as the direct stress range, shear range, the time steps from which they are loaded, and the number of elements for which the data are available. Group information from Abaqus can similarly be extracted.

Next, a uniaxial analysis was performed. Exercise 1 of Tutorial 106 briefly explains how the fatigue life is calculated for each node during a multiaxial analysis; the process shares some similarities with a uniaxial analysis.

The loading history (shown in Figure 7.15 "Loading Settings" section) was simply made up of a tension and compression cycle. Using only a tension (or compression) showed no

damage, so “compression + tension” was used. It can be specified that compression cycles cause no damage, so this would seem to match the experimental test.

The material for all elements was chosen to be ASTM-A715-G50 (from the fe-safe material database), as it had similar properties to ASTM A572-50 steel that the HMIP specimens were made of. The surface finish was left to the default (the mirror-polished finish), even though, it was most probably not a very representative of the actual surface of the HMIP specimens. The default analysis algorithm for this material was also used (Brown-Miller using Morrow mean-stress correction). The selection of the above-mentioned information is shown in Figure 7.16. No residual stresses were included in the model. As shown as an example in Figure 7.17, following the analysis, a summary is generated by fe-safe. Figure 7.18 shows the results of the analysis, including the minimum fatigue life and the node at which the fatigue has occurred. Figure 7.19 further shows a color plot of the results, indicating that the minimum fatigue life (and hence location of crack initiation) has been predicted to be at the weld toe.

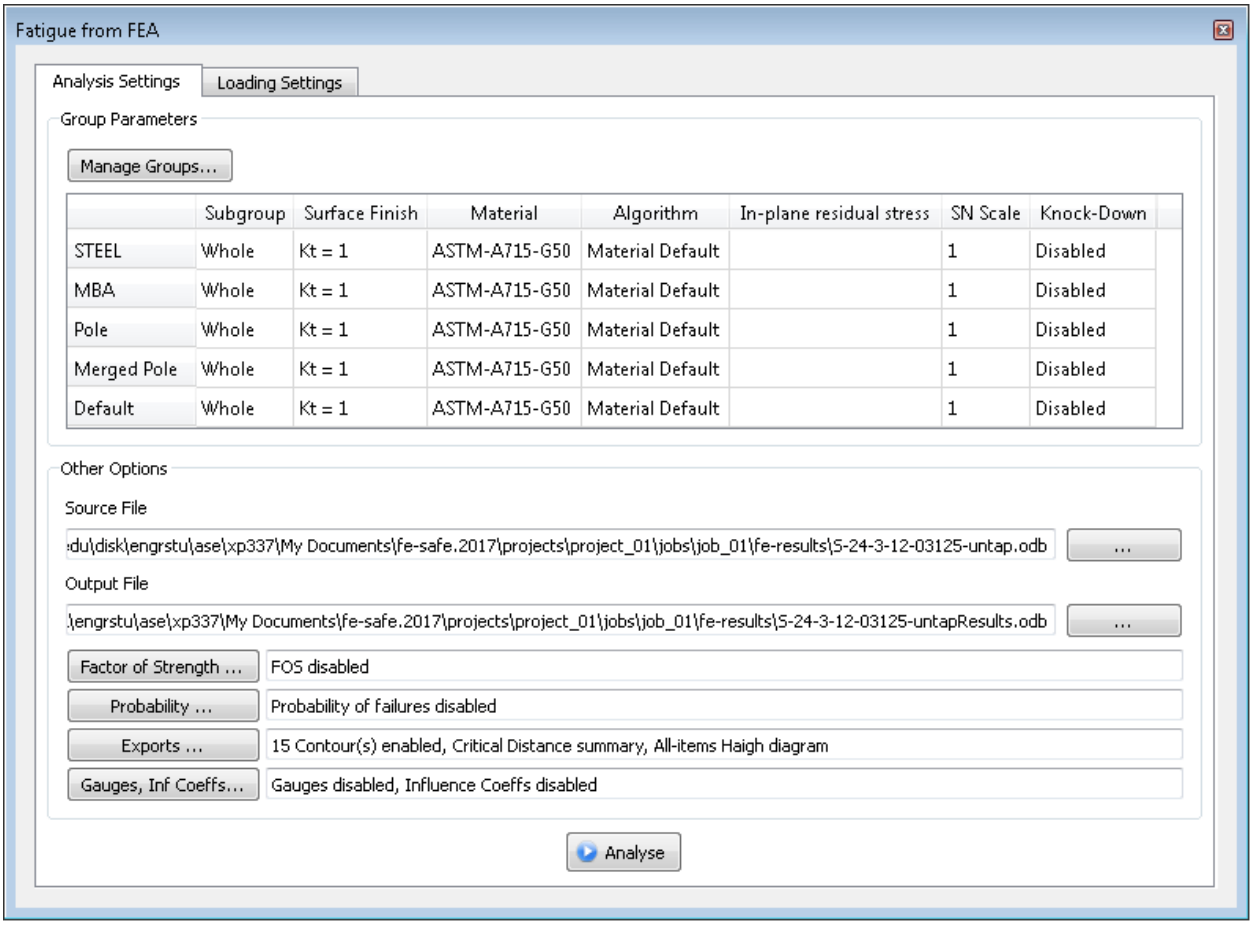

Figure 7.16: Element Groups and Properties in fe-safe

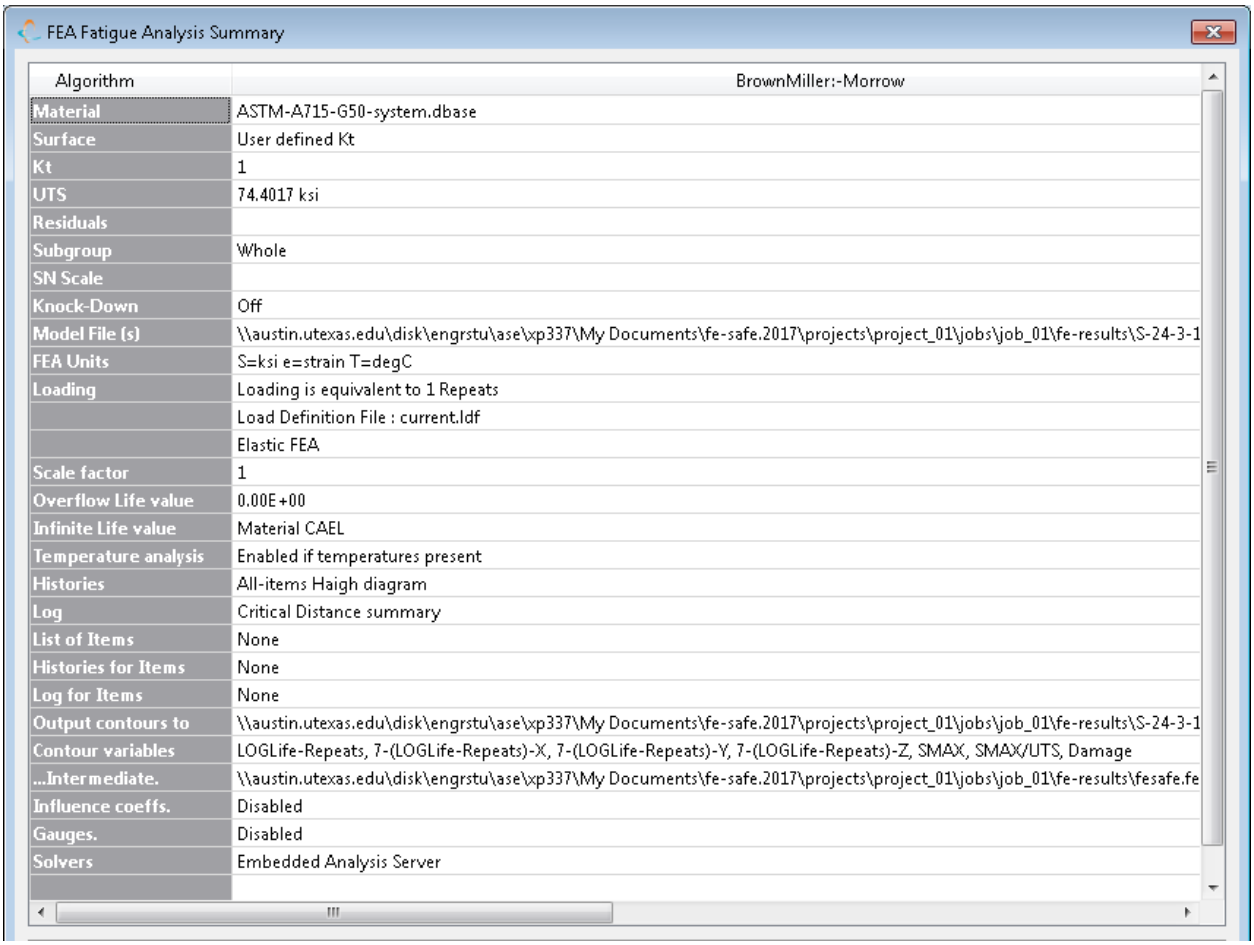

Figure 7.17: Analysis Summary in fe-safe

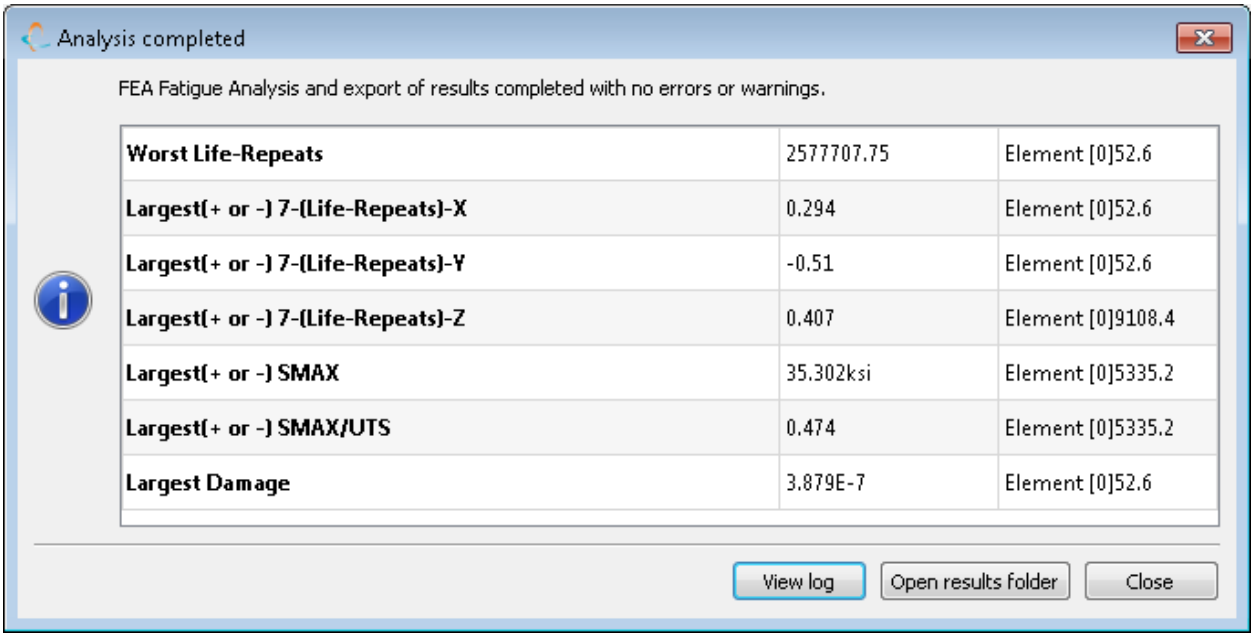

Figure 7.18: Results Summary in fe-safe

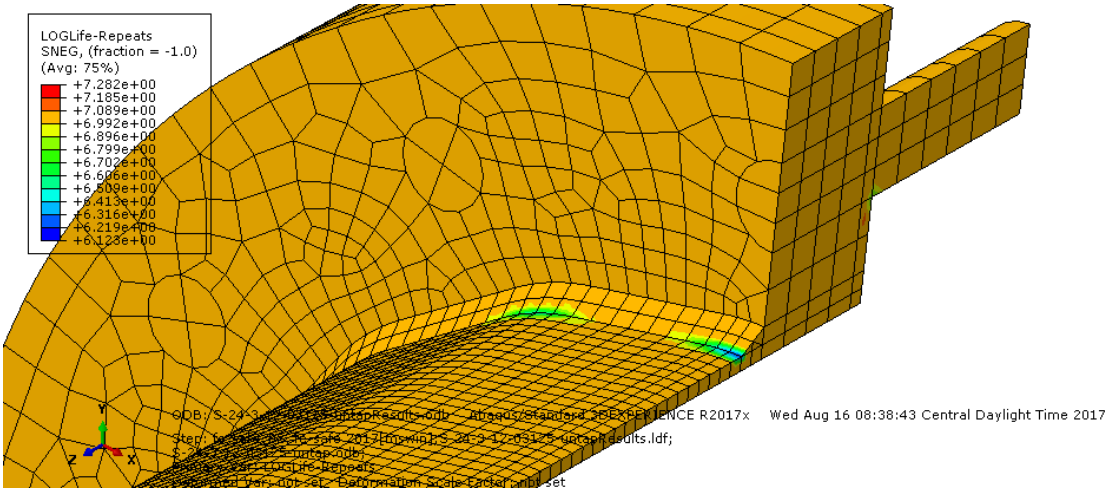

Figure 7.19: LOGLife-Repeats Predictions Indicating the Locations of Fatigue-Induced Fracture Initiation in fe-safe

As specifically indicated in Figure 7.19, the research team have successfully shown that the finite element program fe-safe is capable of predicting the locations of fatigue crack initiation.

7.5 Fatigue-Induced Crack-Growth Analysis of HMIP Test Specimens

As the final step in verifying the capability of available computational tools to study the fatigue behavior of cracked high-mast poles, a finite element program called AFGROW was chosen to perform fatigue-induced crack-growth analysis of HMIP specimens tested in the laboratory.

Developed by U.S. Air Force and currently owned and maintained by a US-based company called LexTech, AFGROW is a fracture mechanics-based finite element program utilized for crack-growth life predictions. Therefore, AFGROW is a stand-alone finite element program allowing both the model creation and analysis of HMIP specimens. In the following, the construction of models of HMIP specimens in AFGROW will be explained and sample results of crack-growth predictions using AFGROW will be briefly presented and discussed.

The first step is to create a geometry that resembles closely the geometry of HMIP test specimens. A pipe section was selected as it was the closest resemblance of multi-sided cross sections of the HMIP specimens. "Part Through Crack in Pipe" was further chosen to model the HMIP specimens with pre-existing cracks. The assumed geometry of the cracked HMIP specimens in AFGROW is summarized in Figure 7.20.

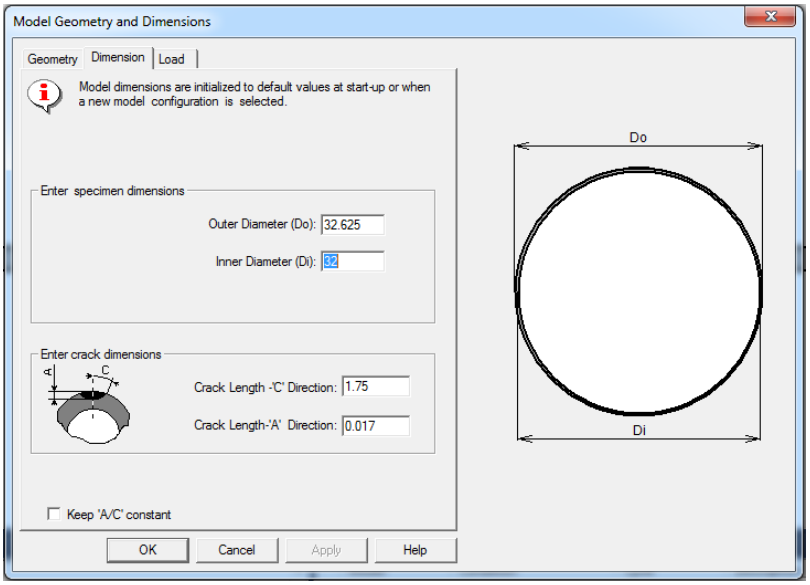

Figure 7.20: Assumed Geometry of the Cracked HMIP Specimens in AFGROW

Figure 7.21 further indicates the loading conditions assumed in AFGROW to conduct fatigue crack-growth analysis of HMIP specimens.

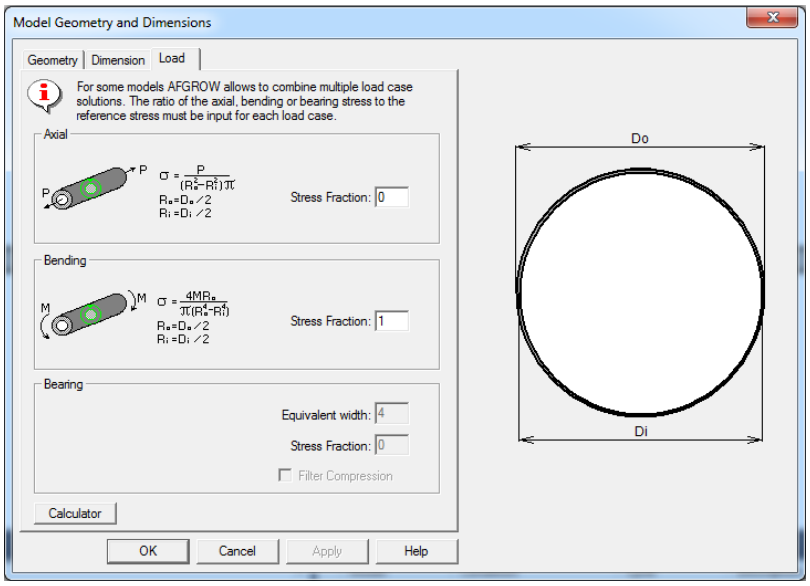

Figure 7.21: Defining Loading Conditions for Crack-Growth Analysis in AFGROW

Following the creation of the geometry of HMIP specimens in AFGROW, a proper material model needs to be defined to accurately represent the structural steel that the pole specimens are made of. It should be pointed out that the material properties are the backbone of the crack-growth analysis in AFGROW, and the accuracy of fatigue crack-growth predictions are highly dependent on the accuracy of the selected material model. Unfortunately, as will be seen and explained, the uncertainties in the material models result in high degrees of uncertainties in crack-growth predictions. For the fatigue crack-growth analysis of HMIP specimens, material models found in literature were used in the "Tabular LOOKUP Data" format provided by the AFGROW program. The selected material is shown in Figure 7.22. Moreover, Figure 7.23 specifically presents the assumed crack-growth rate model used for ASTM A572-50 Steel. Again, it should be emphasized that the AFGROW predictions of crack-growth are highly influenced by the assumed crack-growth rate model, like the one shown in Figure 7.23. Moreover, in the case of HMIP specimens, what makes the predictions of fatigue crack-growth using AFGROW more challenging is the fact that there are not any material data available for galvanized A572-50 steel (at least none were found by the research team).

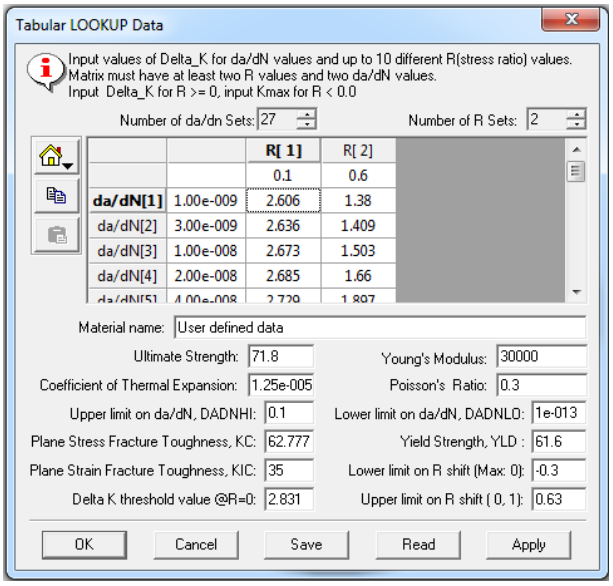

Figure 7.22: Defining Material Properties for Crack-Growth Analysis in AFGROW

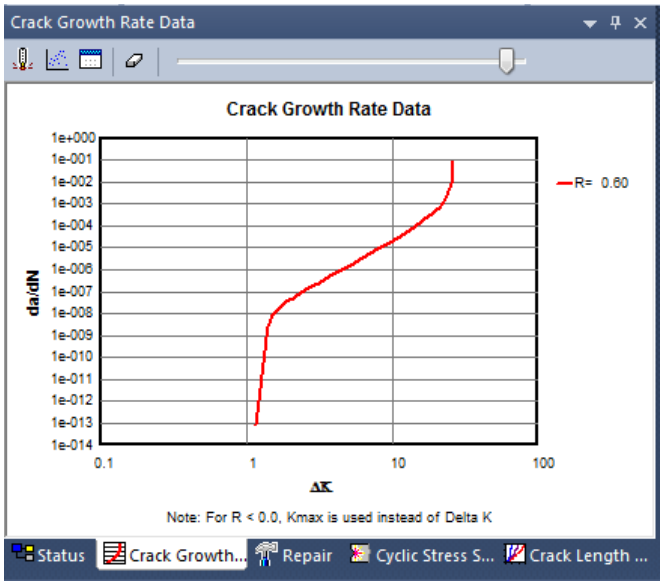

Figure 7.23: Assumed Crack-Growth Rate Model for ASTM A572-50 Steel

To predict the crack-growth observed in the fatigue tests in the laboratory, a fatigue loading spectrum in the form of constant amplitude loading was selected in AFGROW (Figure 7.24). One of the challenges in using AFGROW to performed fatigue crack-growth analysis is the proper selection/definition of the "Stress Multiplication Factor (SMF)" as shown in Figure 7.24. Unfortunately, no specific guidance exists on the proper selection values for SMF. For the analysis reported in this document, the maximum stresses measured at the weld toed during fatigue tests were used as SMF in AFGROW. For example, in a fatigue test conducted at the stress range of 4 ksi with the nominal mean stress of 6 ksi (minimum nominal stress of 4.5 ksi and maximum nominal stress of 7.5 ksi), the maximum stress measured at the weld toe was

about 15 ksi (mean stress of 12 ksi and minimum stress of 9 ksi). Therefore, to predict the results of this test, 15 ksi was selected as a starting point for SMF and slightly adjusted to get the closest matching results with the tests. Since the selection of SMF can significantly affect the crack-growth predictions using AFGROW, the blind predictions using AFGROW are very challenging and are subject to potentially enormous errors.

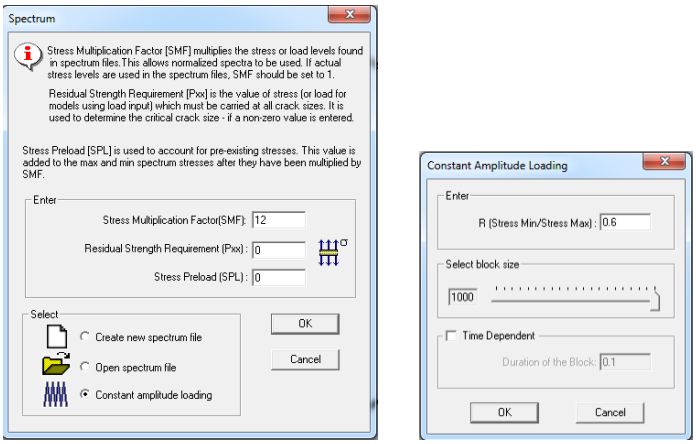

Figure 7.24: Defining Fatigue Loading Spectrum for Crack-Growth Analysis in AFGROW

Figure 7.25 shows the geometry of a crack following a fatigue crack-growth analysis in AFGROW. As can be observed in Figure 7.25, AFGROW assumes formation of a through crack along the entire length of the crack at failure. It should be clear that knowing this assumption is important in interpreting the results from AFGROW and their comparison with the actual test results.

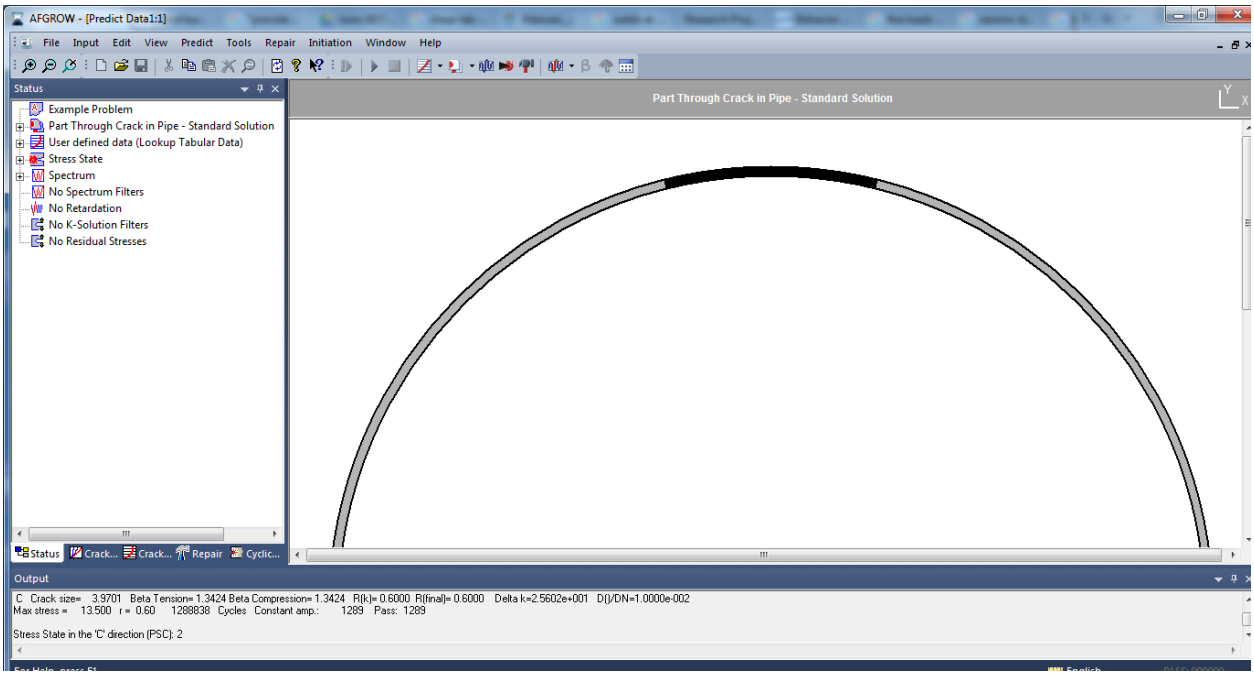

Figure 7.25: Geometry of a Crack following a Crack-Growth Analysis in AFGROW

Figures 7.26 to 7.37 present predictions of crack-growth using AFGROW for fatigue tests conducted at the nominal stress range of 4 ksi. Results from fatigue tests on HMIP specimens are also included in these figures as solid blue circles. As seen in Figures 7.26 to 7.37, there exist a significant scatter in predictions of fatigue-induced crack-growth between the tests and AFGROW analyses. Some of these discrepancies are due to the inherent uncertainty of the fatigue phenomenon of HMIPs. But, it can be also argued that much of the discrepancies if not most of them are due to the assumptions made in the material models and other analysis parameters used in AFGROW program.

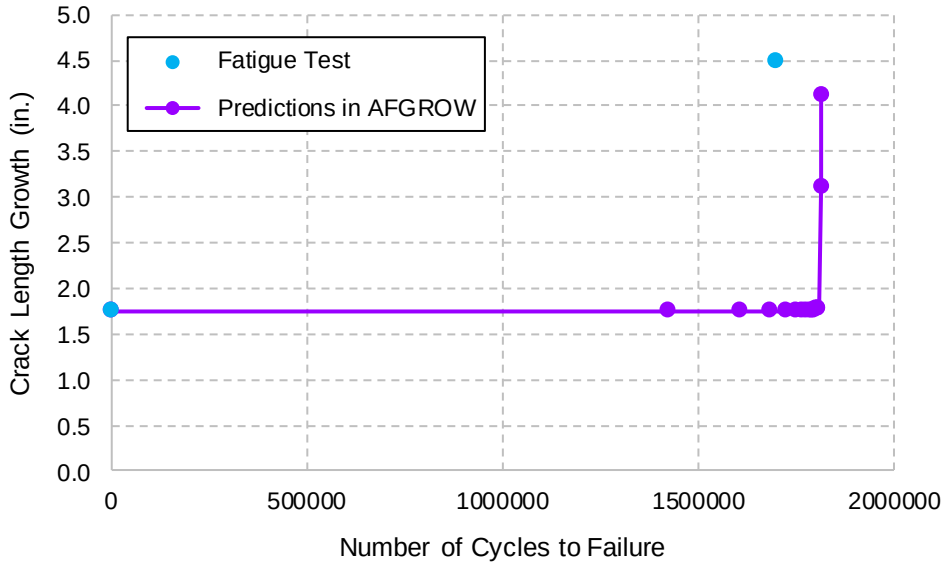

Figure 7.26: Predictions of Fatigue Crack Length Growth – Specimen A4: Bend 4

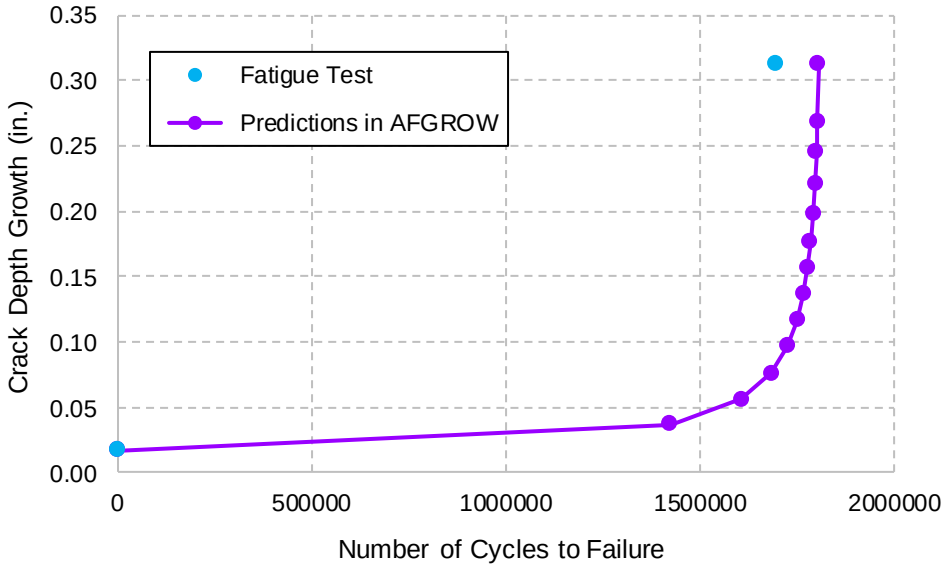

Figure 7.27: Predictions of Fatigue Crack Depth Growth – Specimen A4: Bend 4

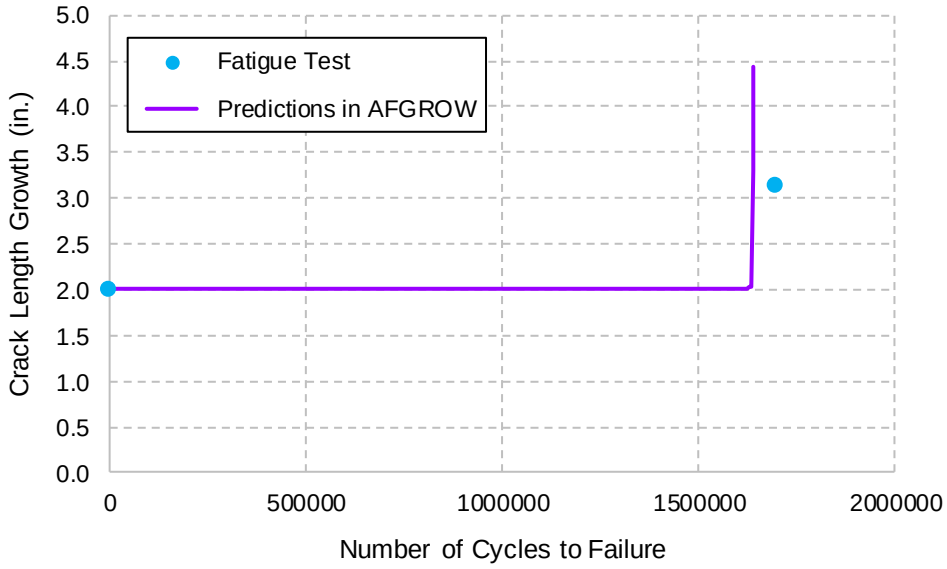

Figure 7.28: Predictions of Fatigue Crack Length Growth – Specimen A4: Bend 3

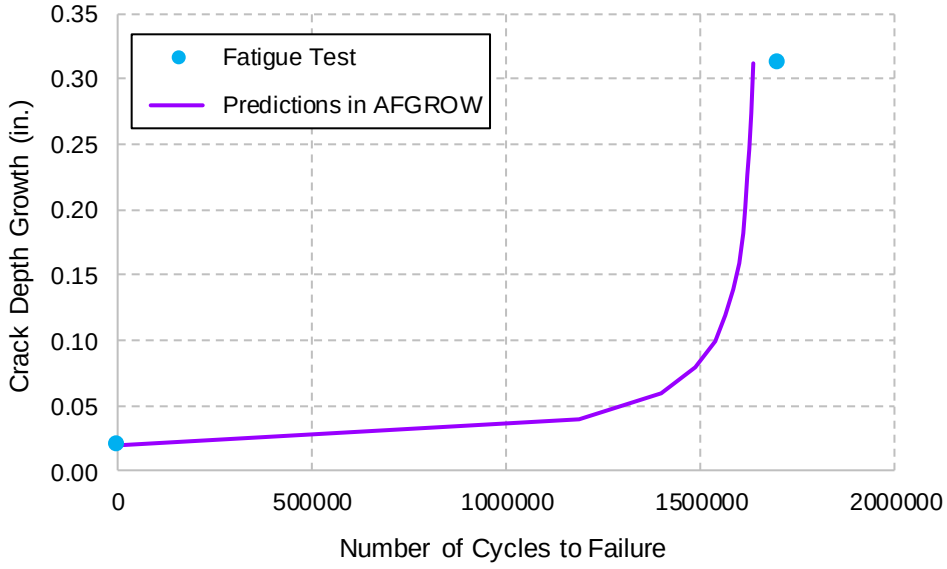

Figure 7.29: Predictions of Fatigue Crack Depth Growth – Specimen A4: Bend 3

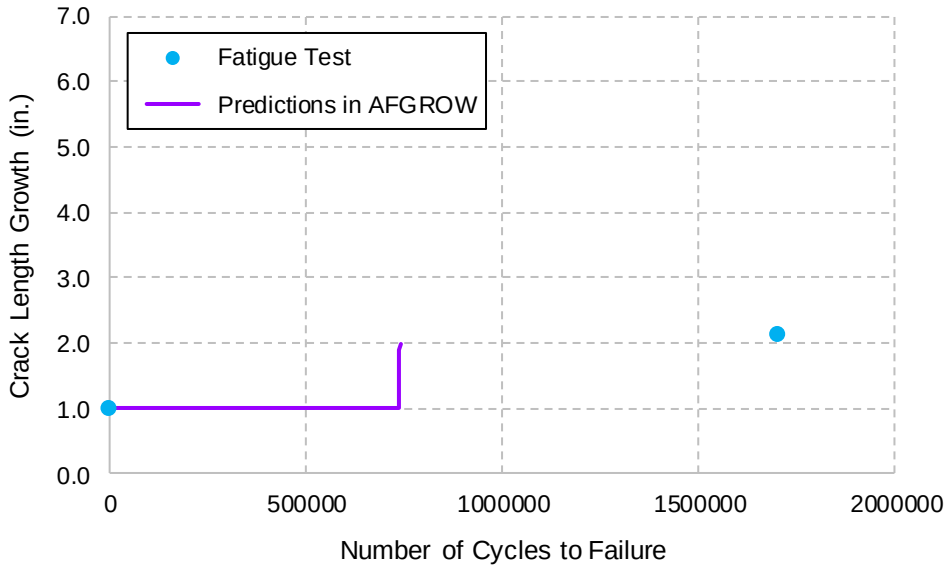

Figure 7.30: Predictions of Fatigue Crack Length Growth – Specimen A4: Bend 5

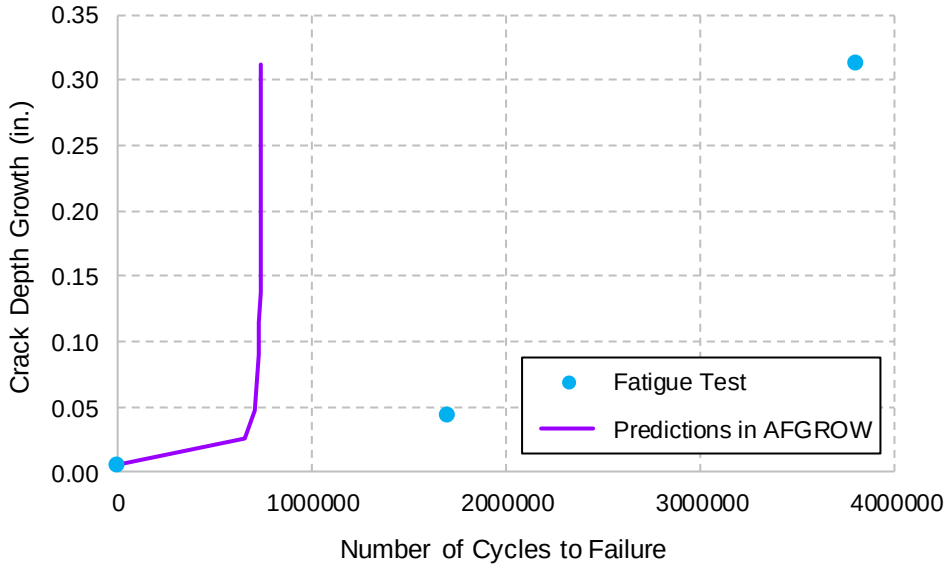

Figure 7.31: Predictions of Fatigue Crack Depth Growth – Specimen A4: Bend 5

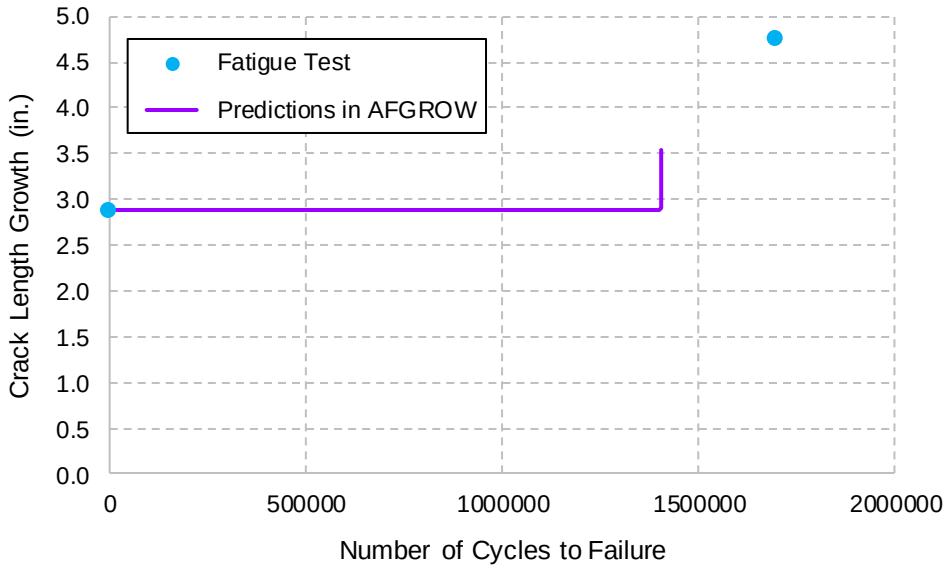

Figure 7.32: Predictions of Fatigue Crack Length Growth – Specimen A3: Bend 4

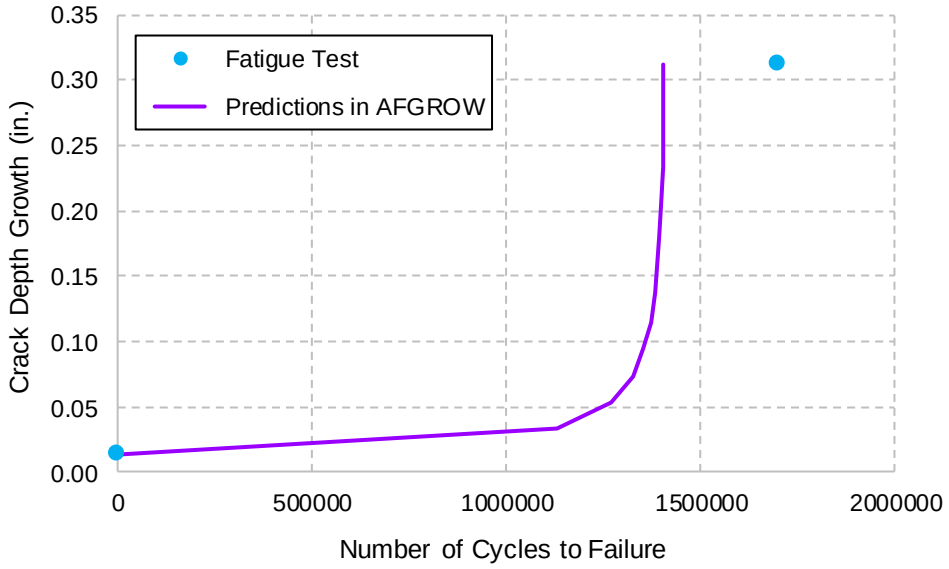

Figure 7.33: Predictions of Fatigue Crack Depth Growth – Specimen A3: Bend 4

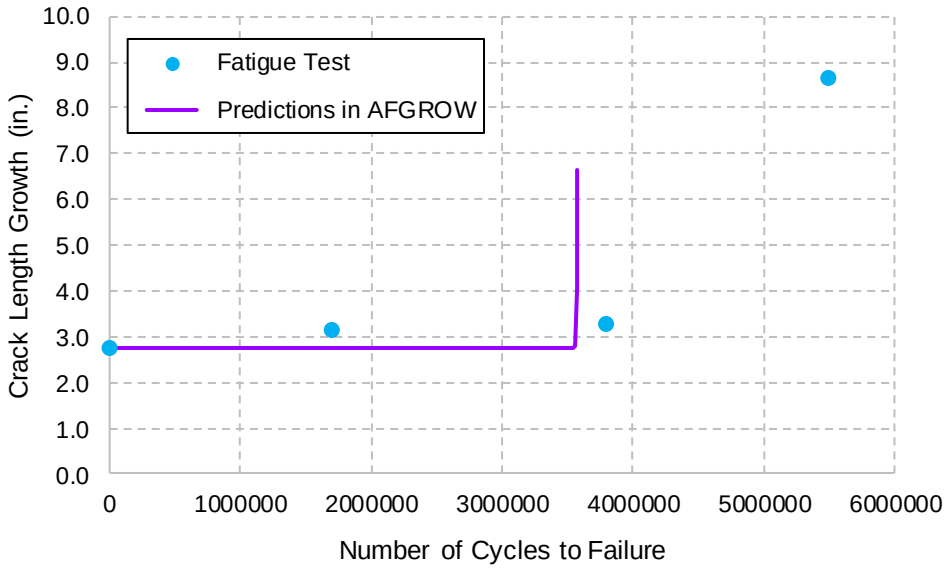

Figure 7.34: Predictions of Fatigue Crack Length Growth – Specimen A3: Bend 3

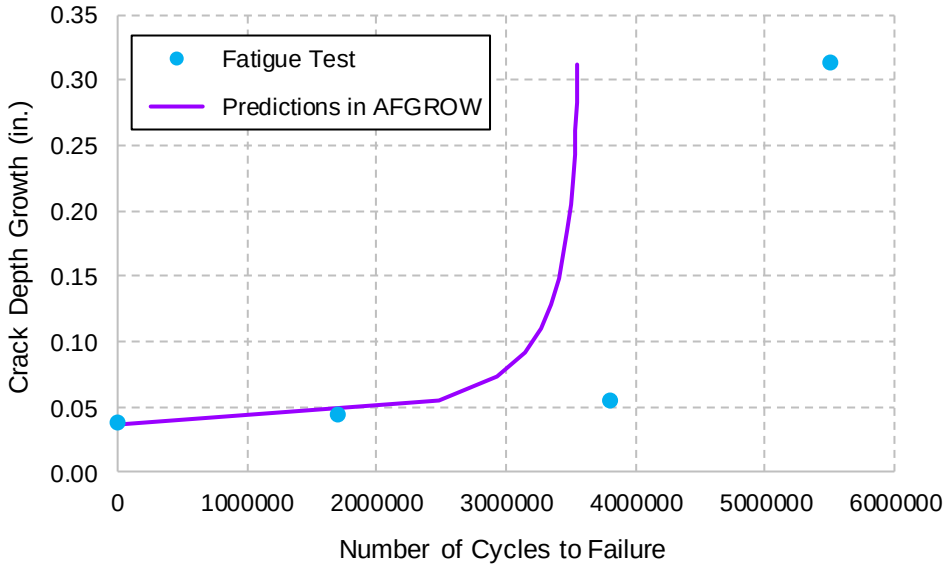

Figure 7.35: Predictions of Fatigue Crack Depth Growth – Specimen A3: Bend 3

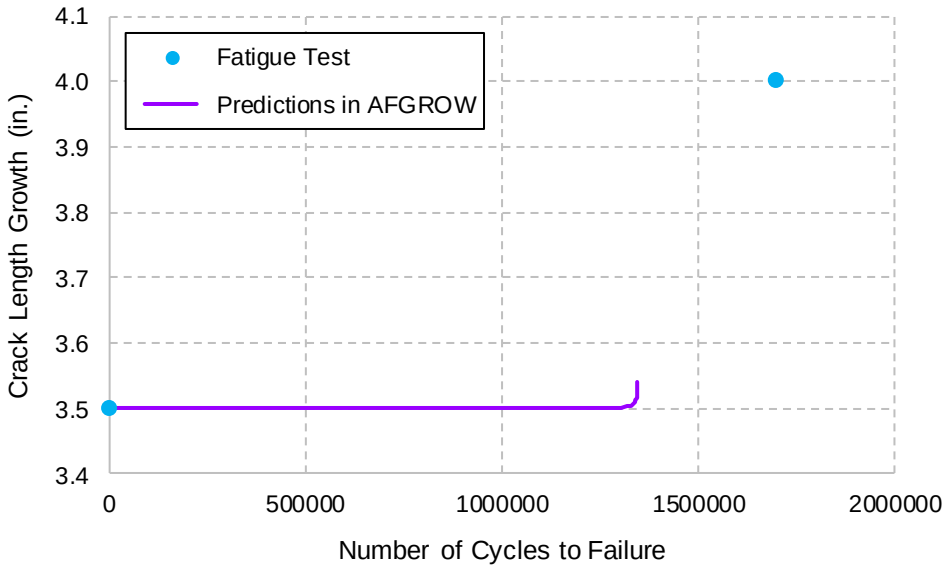

Figure 7.36: Predictions of Fatigue Crack Length Growth – Specimen A3: Bend 5

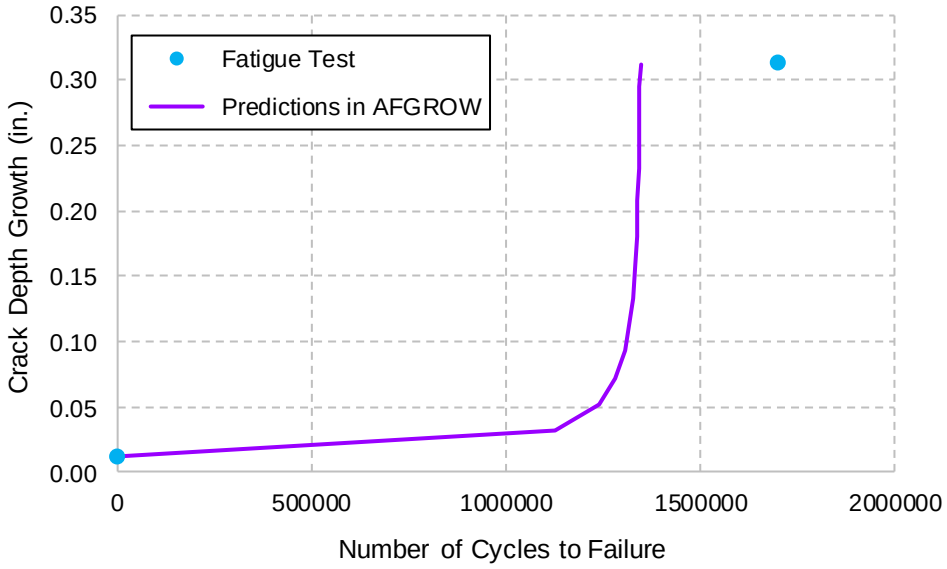

Figure 7.37: Predictions of Fatigue Crack Depth Growth – Specimen A3: Bend 5

As a final note on the fatigue crack-growth analysis using AFGROW, it should be noted that the program seems to have particular difficulty converging for very small crack depths (smaller than 0.01 in.), and as a result it cannot accurately perform crack-growth analysis for such small-depth cracks (Figures 7.30 and 7.31). This is partly due to the tolerances defined in the program solver, but certainly deserves closer attention.

7.6 Finite Element Studies of the Retrofitted HMIP Specimens

Finite element studies were conducted to evaluate a possible retrofit measure for HMIPs with cracks at their base. As shown in Figure 7.38, the retrofit that was considered involves the attachment of a bolted jacket (ring) to the shaft of the HMIP specimen. Threaded rods were inserted and bolted to the jacket. These rods were connected to the HMIP anchoring rods via a coupler. Following their installation, the rods were post-tensioned. The intent of this retrofit was that post tensioning of the rods would apply compressive stresses at the shaft-to-base-plate weld, thereby minimizing cyclic tensile stresses that produce fatigue damage.

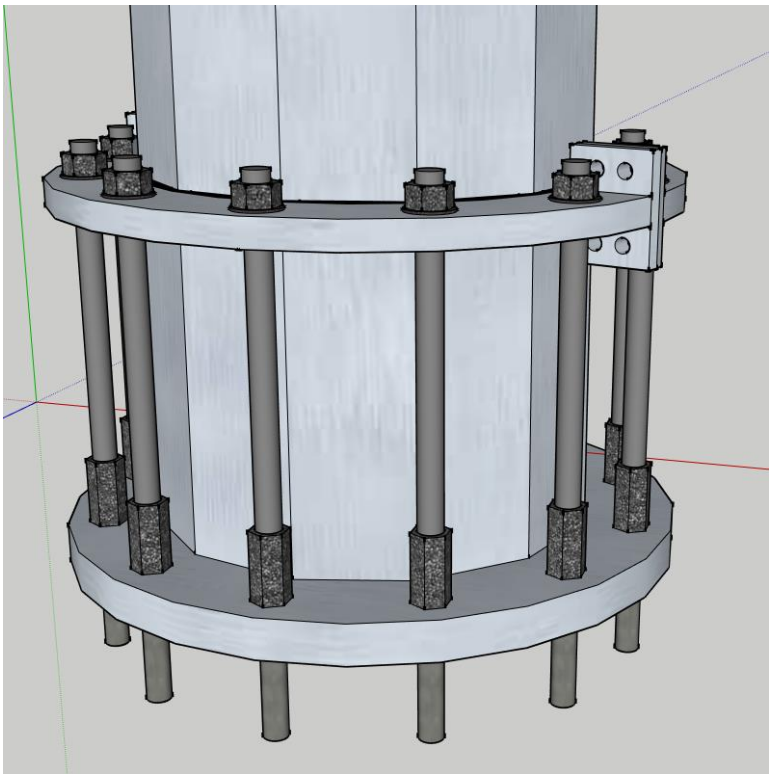

Figure 7.38: Post-Tensioned Rod Retrofit Schematic

A model of this retrofit scheme was created and tested in Abaqus to study different parameters that might impact the effectiveness of the retrofit. In the following, a brief overview of these finite element analyses along with preliminary results are provided and discussed.

7.6.1 Post-tensioned Rod Retrofit

To study the effectiveness of the proposed retrofit scheme, a ring was modeled identical to the details in stool-base connection (Stam 2009). More specifically, the ring was located 11-inch from the base-plate and had a thickness of 1.25-inches. The HMIP shaft modeled with taper following the design detailed in HMIP(1)-98 standard. To match the geometry of the ring and that of the HMIP's shaft, corners of the HMIP were modeled with 0-inch bend radii. The model is shown in Figure 7.39. As shown in Figure 7.39, models of the retrofit scheme were created with and without explicit modeling of anchor bolts. More details of the finite element model of the retrofit scheme are depicted in Figure 7.40.

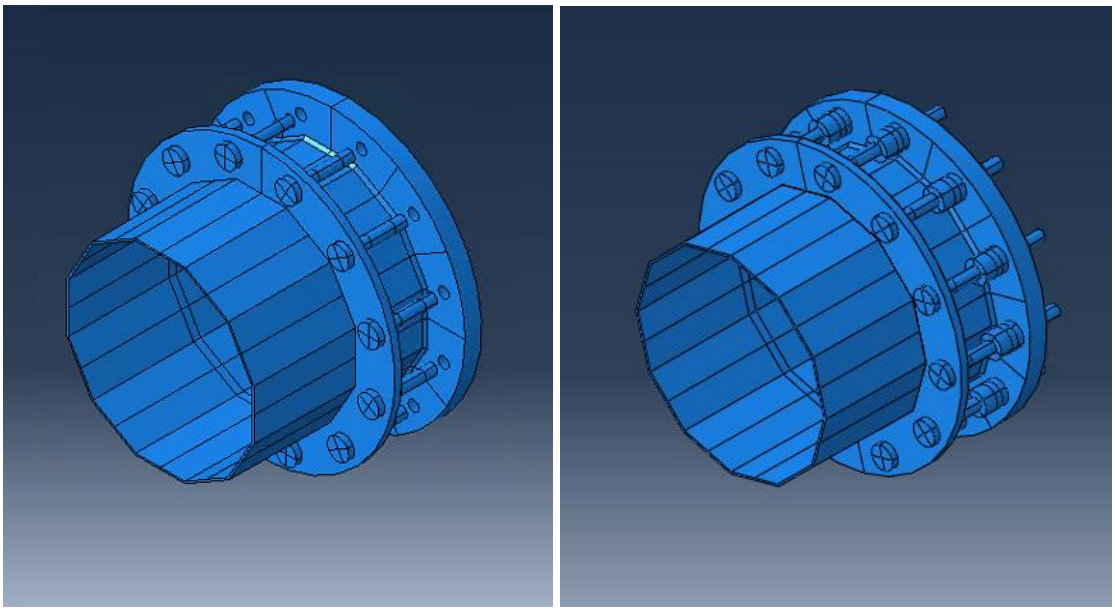

(a) Anchor bolts modelled as pins (b) Anchor bolts modelled as separate parts

Figure 7.39: Models of Post-Tensioned Rod Retrofit in Abaqus

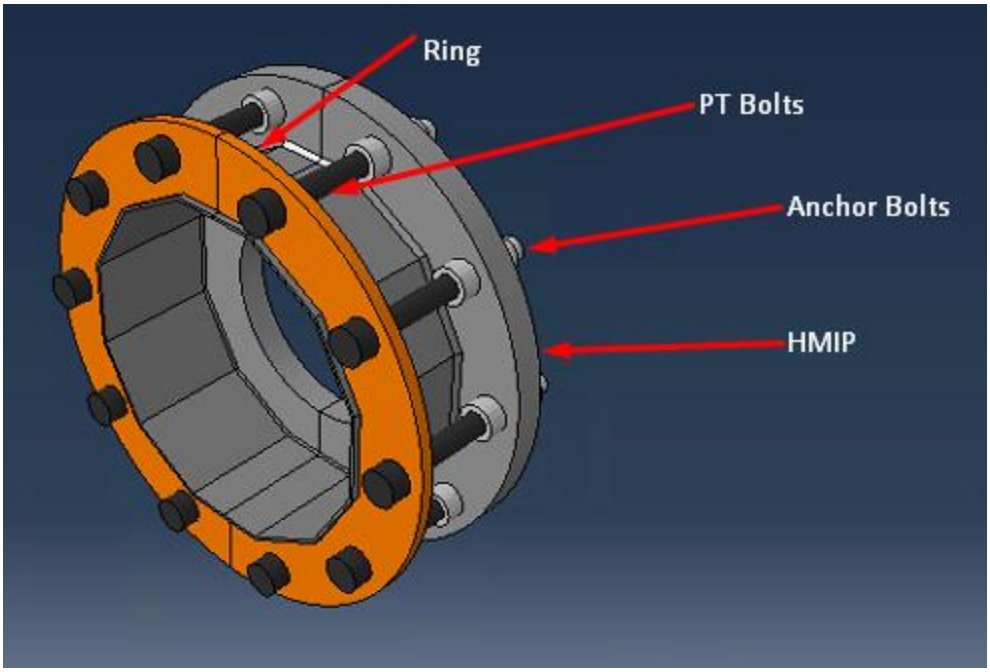

Figure 7.40: Details of the Model of the Retrofitted HMIP Test Specimen

Different considerations went to the development of the finite element models of the retrofit scheme to make them more efficient and to reduce the computational time. These include:

- only the bottom 13-inch of the shaft and base-plate were modeled

- anchor bolts and nuts were modeled as one part to decrease the number of defined contacts
- taking advantage of the symmetry, only half of the HMIP was modeled to manage the size of the model.

In addition, a very fine mesh was also used to investigate stresses developed in the shaft. More specifically, four elements were used through the shaft thickness. The base-plate and the shaft were modeled as separate parts and were tied together with surface constraint. The reason for this approach was to manage element sizes and to decrease the number of elements in the model. The contact between the ring and the shaft was defined with friction coefficient of 0.3. Post-tension rods were tied to the anchor bolts, which were constrained at their bottom.

A post-tensioning force equal to 1 kip was applied to each post-tensioning rod. As a result of post-tensioning, the ring went down for about 0.4 inches. Further, compressive stresses were developed on the shaft perimeter and along the weld toe as represented in Figure 7.41. As seen in Figure 7.41, stresses near the bends are larger than those over the flats. It can further be observed from Figure 7.41 that the minimum compressive stress developed at the weld toe is in the order of 0.45 ksi. The results of these analyses suggest the proposed retrofit scheme may improve the fatigue performance of existing HMIPs with pre-existing cracks.

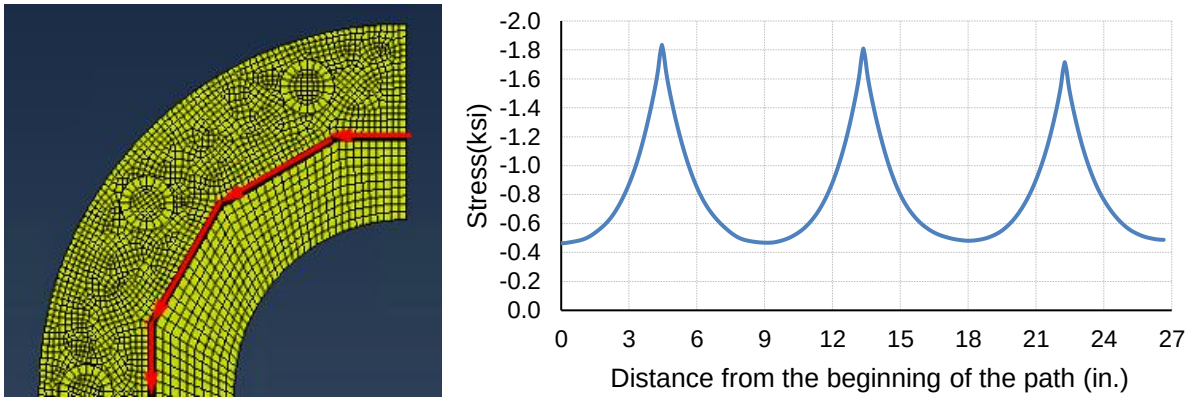

(a) Specified Path (b) Stress variations along the specified path

Figure 7.41: Compressive Stresses along the Specified Path on the Shaft Perimeter

7.7 Summary

The main goal of the studies reported in this chapter was to evaluate the capability of available computational tools to study the fatigue behavior of cracked HMIPs. Commercially available finite element software SAP2000, Abaqus, fe-safe, and AFGROW were utilized in the studies. Using these software packages, different analyses were performed to study the dynamic characteristics of in-service HMIPs, to evaluate the fatigue behavior of HMIP specimens tested in the laboratory, and to predict the fatigue-induced crack-growth observed in laboratory fatigue tests.

The finite element programs SAP2000 and Abaqus were capable of accurately modeling and predicting the dynamic behavior of in-service HMIPs. Further, the fatigue solver fe-safe was shown to be capable of predicting the location of fatigue crack initiation. Results from the AFGROW software in predicting crack-growth observed in fatigue tests on HMIP specimens have shown to be highly uncertain particularly due to uncertainties in material models.

Thus, while finite element software packages are capable of predicting the overall dynamic properties of HMIPs, the results of these studies suggest that reliable prediction of fatigue crack-growth and fatigue life of HMIPs with pre-existing cracks, using the evaluated software packages, may not be possible. Consequently, the prediction of fatigue life of HMIPs with pre-existing cracks in this study are based on the experimental fatigue data described in Chapter 5.

Chapter 8. Mitigation Strategies for In-Service HMIPs with Pre-Existing Cracks

8.1 Overview

This chapter describes mitigation strategies for HMIPs with pre-existing cracks. Two overall approaches to mitigation were considered. The first approach was to retrofit existing poles. The second approach was to repair the welds on existing poles. Based on input from TxDOT, the decision was made to focus this part of the study on development of a weld repair procedure. Specifically, a weld-repair procedure was developed, implemented, and examined to extend the fatigue life of cracked poles. Details of this weld-repair procedure along with experimental data collected on the repaired HMIP specimens through fatigue tests are documented in this chapter. It is important to emphasize here that the development and application of a weld-repair procedure was not the main purpose of the TxDOT research project 0-6829. Therefore, the weld-repair procedure developed and implemented in this research should not be construed as a comprehensive development. Devising a comprehensive and robust weld-repair procedure requires consideration of different governing factors and extensive fatigue testing. Such an endeavor was outside the scope of the current project.

8.2 Development of Mitigation Strategies for Cracked HMIPs

Different mitigation strategies in the forms of rehabilitation/retrofit and repair were explored during the course of this project. This section briefly presents some information about these strategies and introduces a weld-repair procedure ultimately adopted by the researchers to remove cracks from in-service HMIPs to extend their fatigue life.

8.2.1 HMIP Specimens Considered in Mitigation Studies

Like in the rest of this project, a 12-sided, 150 ft, 80 mph design without ground sleeve (specimen of primary interest) was the HMIP design of consideration for mitigation studies. The layout for HMIP test specimens following this design was shown previously in Chapter 5 (Section 5.2, Figures 5.1 to 5.5).

8.2.2 Rehabilitation/Retrofit Strategies

During the course of the research project, the researchers examined potential retrofits for damaged HMIP specimens. The rehabilitation/retrofit ideas explored are briefly reviewed and discussed in this section.

Retrofit Procedures Explored in Past Studies

Several studies in the past investigated different retrofit procedures as a remedial action to improve fatigue behavior of in-service high-mast poles. For instance, Suksawang et al. (2009) conducted an experimental study to investigate the effectiveness and feasibility of such retrofit schemes in enhancing the fatigue life of HMIPs in the state of Florida. These retrofit methods included welding plate stiffeners (Figure 8.1a), bolted stiffeners (Figure 8.1b), and steel jacket encasements (Figure 8.1c). Sherman et al. (2016) also explored more retrofit schemes in the form of short and long steel jacket encasements (Figure 8.1d).

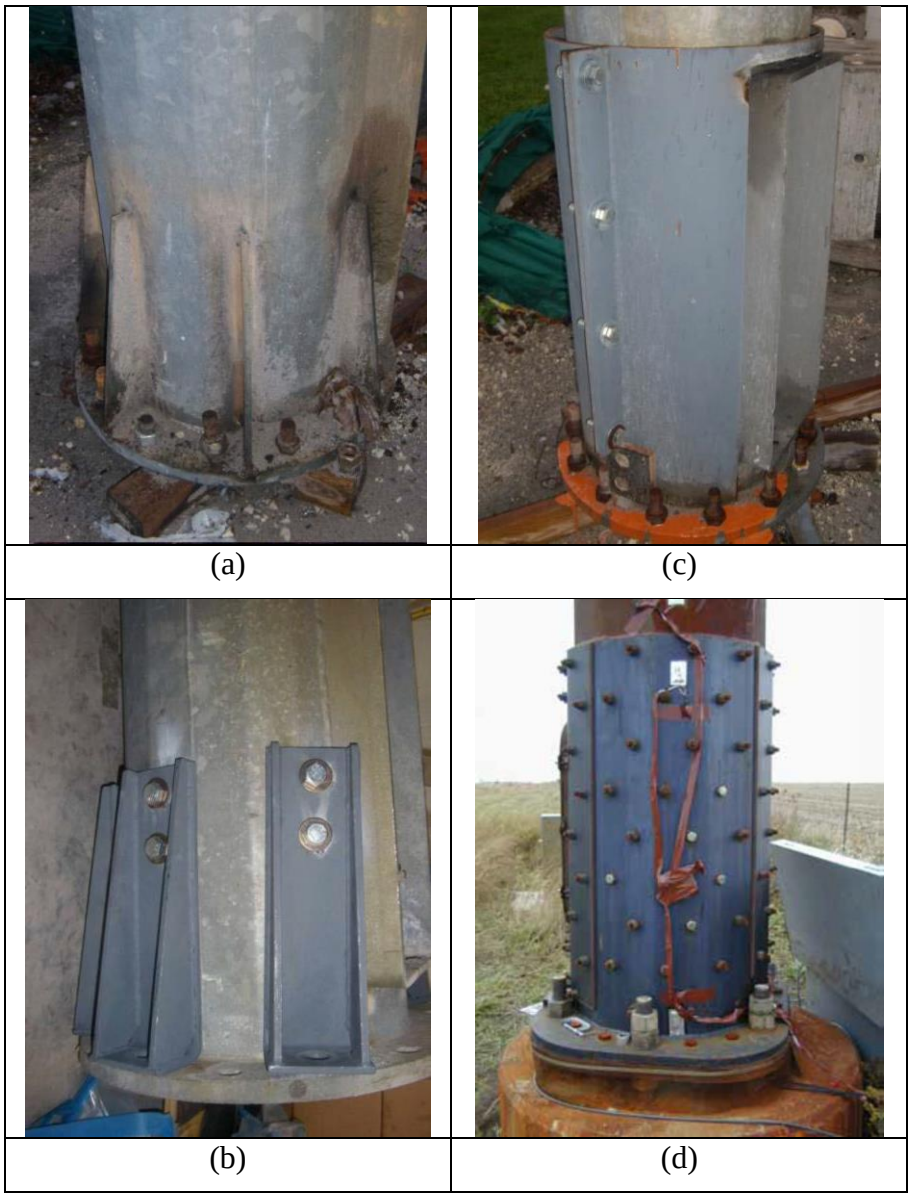

Figure 8.1: Different Retrofit Schemes Proposed and Implemented for In-Service HMIPs

Throughout these studies, it was indicated that steel jacket encasement was more effective than other mitigation strategies in enhancing the fatigue life of cracked poles. As indicated in Figure 8.2, even steel jacket encasements (especially short jackets) were not always very effective in improving the fatigue life of the shaft-to-base plate detail of in-service HMIPs. More importantly, the retrofit methods shown in Figure 8.1 appeared to be costly, and difficult-to-apply for in-service applications.

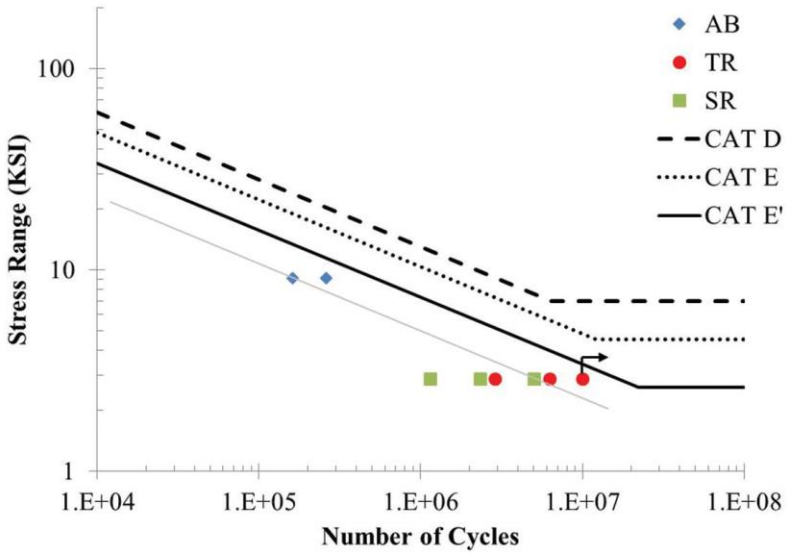

Figure 8.2: Fatigue Test Data on HMIP Specimens Retrofitted with Steel Jacket (Sherman et al. 2016)

Retrofit Procedures Explored in TxDOT Project 0-6829

In this project, the researchers explored different retrofit solutions to the problem of damaged HMIPs in service. Two ideas emerged as potential retrofit solutions. As displayed in Figure 8.3, one of these ideas involved the attachment of a bolted jacket (ring) to the shaft of the HMIP specimen. Threaded rods would be inserted and bolted to the jacket. These rods would be connected to the HMIP anchoring rods via a coupler. Following their installation, the rods would be post-tensioned. The theory of this retrofit was that post tensioning of the rods would alleviate stress in the shaft-to-baseplate weld.

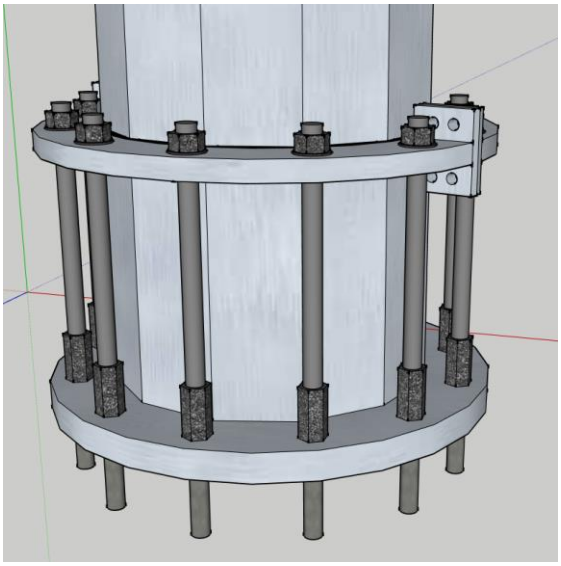

Figure 8.3: Post-Tensioned Rod Retrofit

The second potential retrofit idea involved welding triangular stiffener plates with semicircular attachments to the shaft and the baseplate (Figure 8.4). The purpose of these

stiffeners was to replace the stiffness lost through cracking of the shaft-to-baseplate connection. The stiffeners provided a simple way to increase serviceable life of HMIPs. Stiffeners could also simply be fillet welded in place, such that full penetration welds were not necessary. Their semicircular attachments, whose purpose was to reduce stress concentration points at the termination of the shaft-to-stiffener weld, could then be welded in a similar fashion. As mentioned in the previous section, similar retrofit strategies were employed in various research projects on other high mast lighting fixtures.

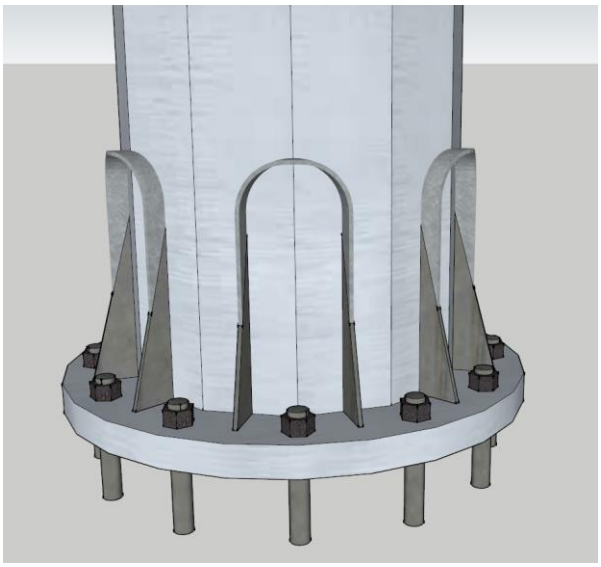

Figure 8.4: The U-shaped Triangular Stiffener Plate Retrofit

Following discussions, the first idea was chosen for further study. Therefore, a model of this retrofit scheme was created and tested in Abaqus to study different parameters that might impact the effectiveness of the retrofit. The results of this finite element study was described in Chapter 7. The finite element study indicated that this retrofit technique could potentially benefit the fatigue performance of the HMIP, although experimental verification would certainly be needed. However, after consultation with TxDOT, the decision was made to not further pursue the retrofit strategies described above. It was believed that repairing the existing welds would likely to be a more cost-effective mitigation strategy. Weld repair strategies are described below.

Repair Strategies

In addition to rehabilitation/retrofit procedures discussed in the previous section, the researchers explored repair solutions to the problem of damaged HMIPs in service. Specifically, the weld-repair procedure was considered. This section provides information about a weld-repair procedure previously developed at the Ferguson Structural Engineering Laboratory. Based on this previous experience, a weld-repair procedure was proposed/implemented/verified in the current study. The proposed weld-repair procedure will be explained in Section 8.2.4.

Repair Procedures Explored in Past Studies at Ferguson Lab

In a previous study on developing mitigation strategies for HMIPs in Texas, weld-repair methods were developed and tested at the Ferguson Structural Engineering Laboratory (Pool

2010). These weld-repair methods were developed for both the shop and field applications. These weld-repair strategies are presented in the following.

Shop-Repair Procedure

A "shop repair" weld procedure was developed to address poles that contain cracks after galvanizing but before installation, which means that this repair will replicate the repair of initial cracks found in the shop.

A flux core arc welding procedure (FCAW) was chosen as the shop repair procedure due to its ease of implementation in a fabrication shop. The ability of the shop to orient the high masts in the horizontal position as well as provide shielding gases makes FCAW a viable option. The advantages of using FCAW were that it provided better and more consistent weld quality, with fewer likely defects compared to other available weld processes, and it could also be done at a higher rate of speed than shielded metal arc welding.

The weld-repair procedure developed for the shop repair was specified as follows:
"Prior to any welding, specific surface preparations must be made to ensure the removal of all parts of the initial crack. First, cracks must be identified using ultrasonic testing with a seventy degree transducer to locate these shallow cracks. These cracks should be marked two inches past their extents for grinding. After ultrasonic testing, the specimen will need to be cleaned with acetone to remove any couplant, dirt, and grease. Once clean, the crack locations and two inches beyond their extents shall be ground out. The depth of the grind shall be one half of the pole wall thickness and shall have a radius of 1/4 inch. After grinding, the groove surface shall be inspected with magnetic particle testing to ensure the complete removal of the initial crack. If any indication is found, the indication shall be ground out. Then, any galvanic coating near the weld surface shall be removed with a flap wheel, or a comparable mechanical device to ensure no zinc gets into the weld. This will conclude weld preparations. The weld shall adhere to the following. The weld process shall be flux core arc weld and the filler metal shall be compliant with AWS classification E71T-1 and have a diameter of 1/8 inch. The current shall be between 170 and 370 amps, DC+, with a voltage falling between 21 and 28 volts. The shield gas shall be 25% carbon dioxide and 75% argon at a flow rate of 45 cubic feet per hour. The weld technique shall be a single stringer pass".

The repair was executed in a horizontal orientation with the high mast lying sideways on the ground. The circular base plate and end plate made rotating the specimen easy, and allowed for the easy use of the FCAW weld procedures on any bend, as it required a relatively flat, horizontal weld surface. This is similar to what would be encountered in a fabrication shop, where cranes and mandrels make manipulating the poles much easier. Welding in this orientation, and with the capability of rotation the specimen when necessary, contributed to relatively fast, and well controlled welds.

It was also helpful that this weld procedure only necessitated grinding down to one half of the wall thickness, comparatively less grinding than the field procedure. Having a larger root face enabled the welder to use more heat without fear of burning through to the other side, and to repair the weld in one pass. Figure 8.5 below is a picture of the FCAW shop-repair procedure performed on the specimen at the Ferguson Structural Engineering Laboratory.

Figure 8.5: FCAW Being Performed at the Ferguson Lab (Pool 2010)

Because only one broad pass was needed to repair the weld, the weld profile on the shop repair specimen resulted in a smooth broad parabolic shape. Previous research was indicated that this interface is critical to maintaining smooth stress flow between the stiff base plate, and relatively flexible pole wall (Stam 2009). This shape is advantageous due to the reduction of the notch effect at the transition between the toe weld and pole wall, which, in turn, leads to a lower stress increase.

Field-Repair Procedure

A "field repair" weld procedure was developed to address poles that were found with cracks in the field after the pole has been erected.

Shielded metal arc welding (SMAW) was the method chosen for the repairs of the field specimen. Like the shop specimen the location and ability to manipulate the pole governed which methods were viable. SMAW was chosen because of its general ease to perform on an in-situ pole with portable equipment and no need to reorient the pole.

The weld-repair procedure for the field specimens was described as follows:

"Surface preparations will be similar to those detailed in the flux core arc weld procedures. The only differences in procedure will be the amount of root face to be left after grinding, and the width and radius of the groove. The groove at indications, and two inches beyond, shall leave 1/16 inch root face, have a radius of 1/4 inch and leave a groove angle of 45 degrees. After grinding, magnetic particle inspection shall be conducted to verify the crack has been removed. After surface preparations, the welder shall use filler metal adhering to AWS classification E7018 for the repair. Two different sizes of electrode will be used—3/32 inch electrode for the root pass, and 1/8 inch electrode for the other necessary passes. The weld shall be executed with a current of between 80 to 100 amps, DC+. The weld technique shall be composed of four stringer passes, using the appropriate electrodes where specified above, and a wire brush shall be used for interpass cleaning".

To properly mimic in situ conditions, the field repair specimen was oriented vertically, elevated off the ground four inches, and mock anchor rods were inserted into bolt holes near the

site of welding. The orientation, anchor rods, as well as the significantly thinner root face significantly increased the amount of time necessary to complete these repairs compared to the shop repaired specimen.

The tight controls on the depth of the grinding also added additional time into the weld repair process. Not only was it necessary for the welder to be careful to maintain the correct root face, one sixteenth of an inch, but if too much was ground off, the welder ran the risk of blowing through the root material during welding. In fact, the welder did burn through and had to fill the location of the hole, further contributing to a longer repair time, as well as risking disruption to the continuity of the surface on the inside of the pole. The welder performing the SMAW repair is shown in Figure 8.6.

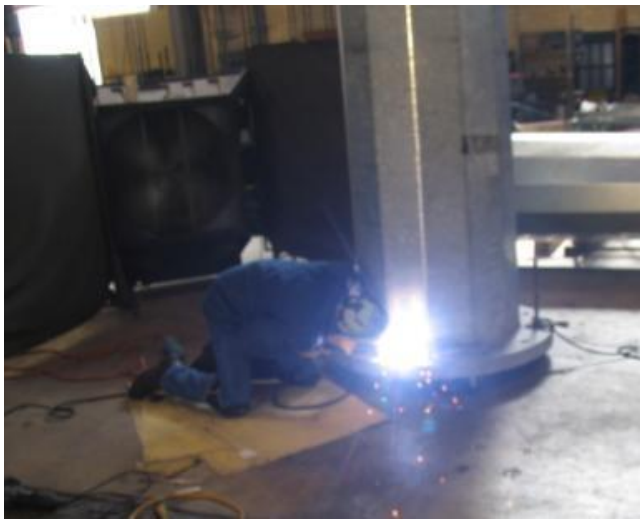

Figure 8.6: The Application of the Field-Repair Procedure at Ferguson Laboratory (Pool 2010)

To maintain the one sixteenth inch root face, the welder recommended using smaller electrodes, minimizing heat input into pole wall. This helped to maintain the root without burning through, but resulted in the larger number of passes to fill the ground opening. In doing so, the exterior of the weld had a noticeably rougher surface with many discontinuities.

Following the repair, a fatigue test was performed at a 12 ksi stress range with a 10 ksi mean stress. The field-repaired specimen failed due to a loss of stiffness. Additionally, instead of failing in the typical manner, where the toe of the weld meets the shaft of the pole, this specimen failed in the middle between two weld passes. Figure 8.7 shows this failure. Bends 10, 11, and 12 all had large fatigue cracks exhibiting this failure through the weld.

This failure occurred after 1,467,734 cycles, which places the Field Repair specimen in the D category, and showed a substantial improvement from the fatigue strength of the specimen prior to weld repair. This type of failure also progressed much slower than previous failures. The crack became visible after approximately 600,000 cycles, but no substantial loss in stiffness occurred until just before failure. The slow rate of propagation was attributed to the fatigue cracks progressing through the thicker weld profile instead of the thinner shaft. It was believed that this slow loss of stiffness highlighted another advantage to the use of the weld repairs: visible cracks can be found long before the system is likely to fail.

Figure 8.7: Bend 11 of the Field-Repaired Specimen with Failure through Weld

8.2.3 Proposed Repair Procedure for Cracked HMIPs

Based on previous experience with the weld-repair solution as a viable mitigation strategy, a welding procedure was proposed/implemented/verified to repair HMIP specimens by removing the cracks from the shaft and filling the excavation with weld material. Details on the development of this weld-repair procedure are provided in Section 8.3. Results from fatigue tests on weld-repaired specimens will be further described in Section 8.4.

8.3 The Proposed Weld-Repair Procedure: Development and Implementation

This section provides detail on the development and implementation of a welding procedure to repair HMIP specimens through the removal and rewelding of cracks. This weld-repair procedure is specifically proposed for the in-service application. Therefore, the goal is to remove cracks caused by both fatigue during service, and galvanization during construction.

8.3.1 Identification of Cracks

The first step of the proposed weld-repair procedure involves characterization of crack geometry in terms of both length and depth. It is recommended that cracks be identified using either conventional ultrasonic testing (in accordance with TxDOT procedure using a seventy degree transducer) or phased array ultrasonic testing (in accordance with UT-938 procedure developed by R&A) to find both crack length and depth. In addition, cracks should be marked two inches past their extents for grinding.

Based on crack detections using phased array ultrasonic testing (in accordance with UT-938 procedure developed by R&A) and in close coordination with TxDOT engineers, two HMIP specimens that were fatigue tested in the Task 4 of the research project (see Chapter 5) were selected for the weld-repair implementation. These were specimens 33-3-12-TX-A2 and 33-3-12-TX-A2. The state of cracks following previous fatigue tests are shown in Figures 8.8 and 8.9 for these two specimens. Figures 8.8 and 8.9 further show the orientation of these specimens for

studying their fatigue behavior after the weld-repair as well as evaluating effectiveness of the repair technique.

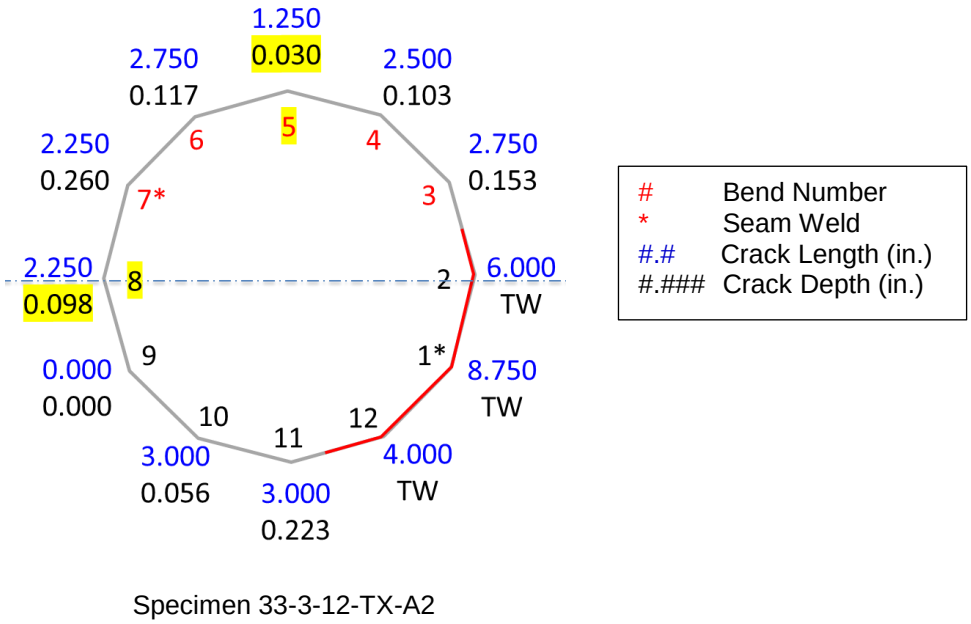

Specimen 33-3-12-TX-A2

Figure 8.8: Specimen 33-3-12-TX-A2: Candidate for Shallow Repair (10% Excavation Depth)

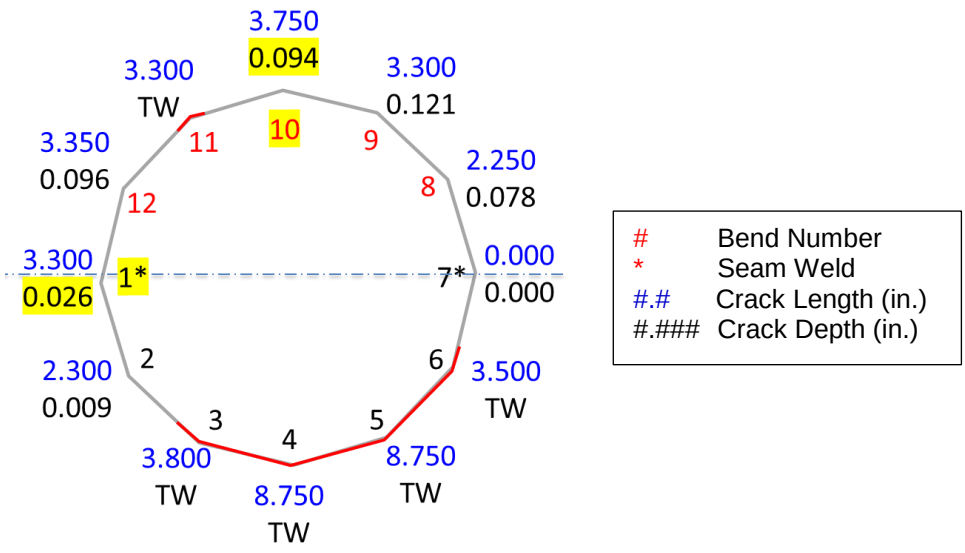

Specimen 33-3-12-TX-A3

Figure 8.9: Specimen 33-3-12-TX-A3: Candidate for Deep Repair (30% Excavation Depth)

Figures 8.10 through 8.22, and Figures 8.23 through 8.29 further depict the crack geometry at each specific bends of the Specimens 33-3-12-TX-A2 and 33-3-12-TX-A3, respectively. These figures specifically show the marks of 2-in. extension of cracks on both sides for grinding. More importantly, careful review of these figures reveals discrepancies in crack geometries between data shown in these figures and those shown in Figures 8.8 and 8.9. For most cases, larger values for both crack lengths and depths are reported in Figures 8.8 and 8.9. For example, for bend 10 on Specimen 33-3-12-TX-A3, the crack length is recorded as 3.750” in Figure 8.8, while it is indicated as 2.750” in Figure 8.27. The characterization of cracks by conducting PAUT testing on HMIP specimens in the horizontal versus vertical orientations is the main cause of the discrepancies in reported crack-geometry data. More specifically, detection of cracks when HMIP specimens are situated in the test setup (in horizontal orientation and displaced to the maximum stress in a fatigue test) results in higher values for both crack length and depth (values reported in Figures 8.8 and 8.9). This observation further justifies the extension of cracks beyond each ends for grinding to make sure the complete removal of cracks.

Figure 8.22 also shows a situation where a fatigue crack propagates away from the weld toe to the shaft wall during a fatigue test. When considered for weld-repair, cracks like the one shown in Figure 8.22 need more careful consideration in removing and rewelding of the shaft material.

Figure 8.10: State of Cracks: Specimen 33-3-12-TX-A2 – Bend 1

Figure 8.11: State of Cracks: Specimen 33-3-12-TX-A2 – Bend 2

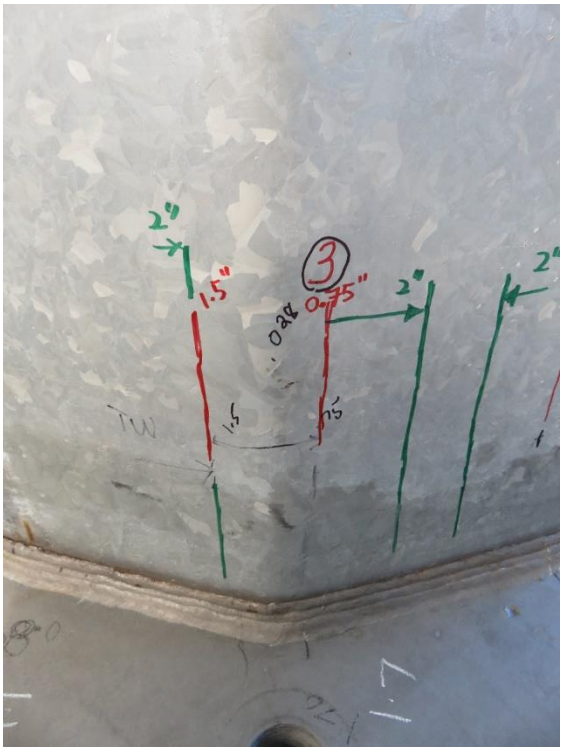

Figure 8.12: State of Cracks: Specimen 33-3-12-TX-A2 – Bend 3

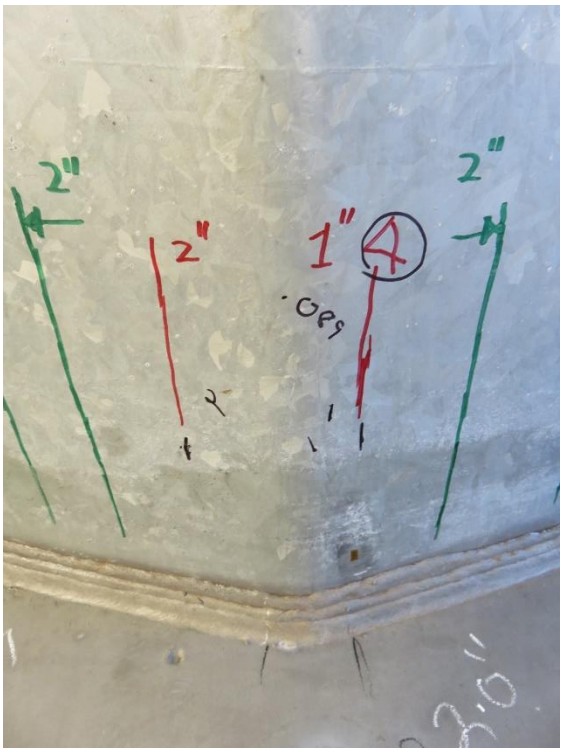

Figure 8.13: State of Cracks: Specimen 33-3-12-TX-A2 – Bend 4

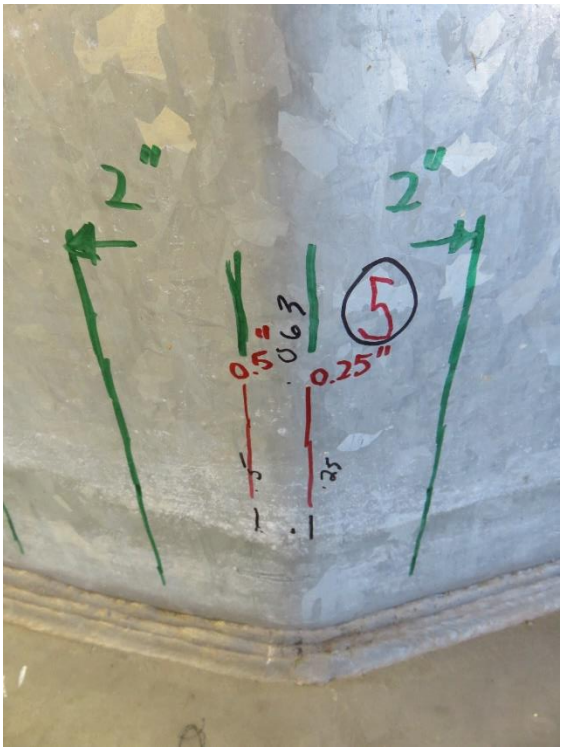

Figure 8.14: State of Cracks: Specimen 33-3-12-TX-A2 – Bend 5

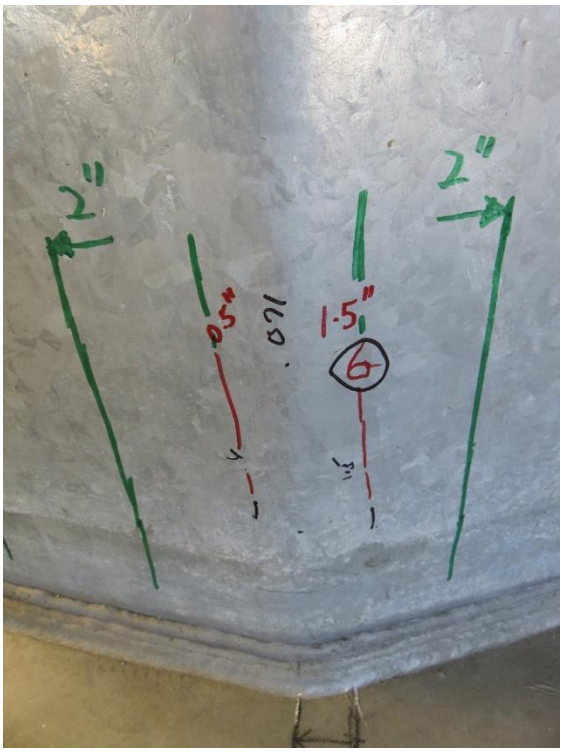

Figure 8.15: State of Cracks: Specimen 33-3-12-TX-A2 – Bend 6

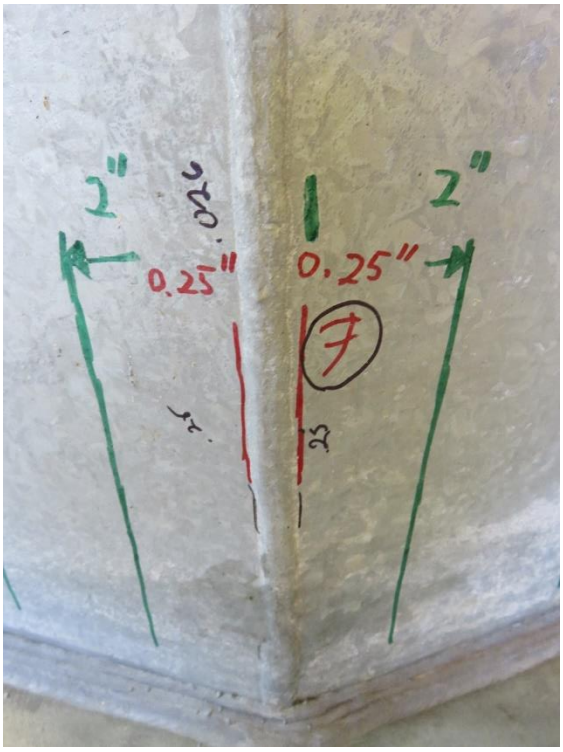

Figure 8.16: State of Cracks: Specimen 33-3-12-TX-A2 – Bend 7

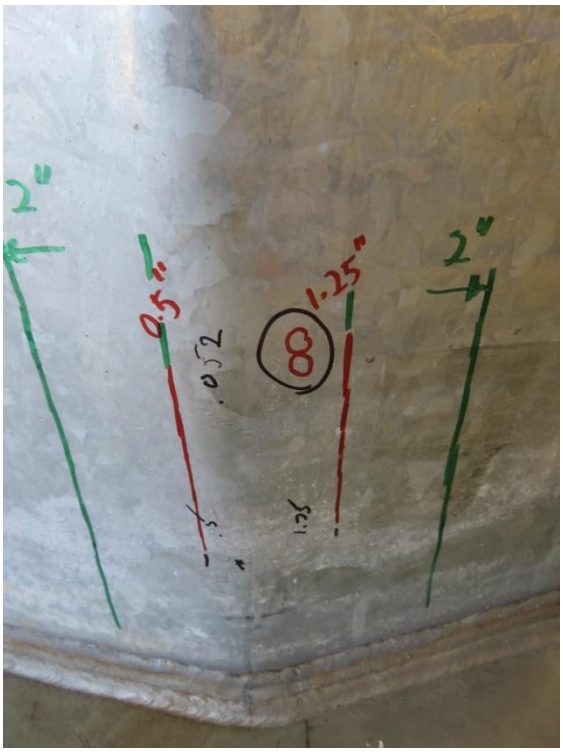

Figure 8.17: State of Cracks: Specimen 33-3-12-TX-A2 – Bend 8

Figure 8.18: State of Cracks: Specimen 33-3-12-TX-A2 – Bend 9

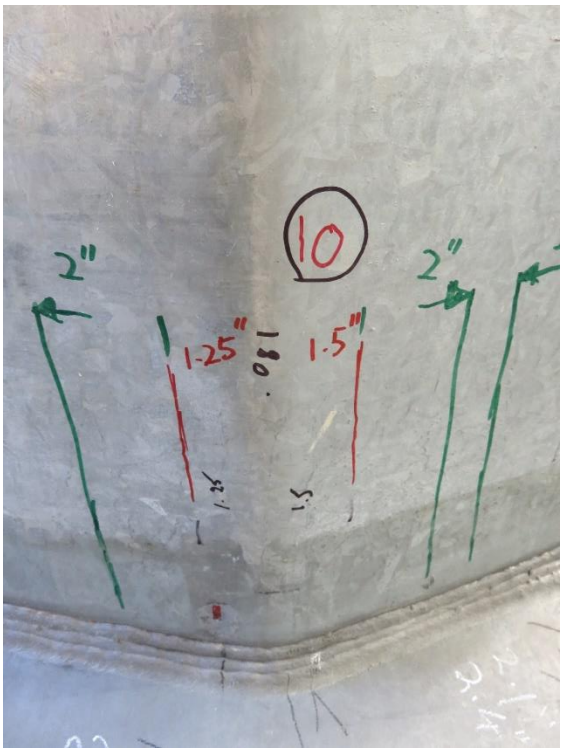

Figure 8.19: State of Cracks: Specimen 33-3-12-TX-A2 – Bend 10

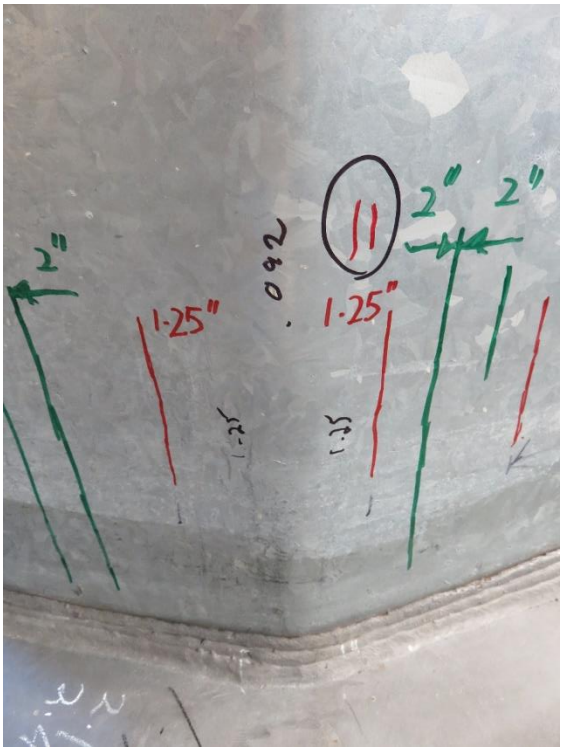

Figure 8.20: State of Cracks: Specimen 33-3-12-TX-A2 – Bend 11

Figure 8.21: State of Cracks: Specimen 33-3-12-TX-A2 – Bend 12

Figure 8.22: Cracks Propagating Away from the Weld Toe: Specimen 33-3-12-TX-A2 – Bend 2

Figure 8.23: State of Cracks: Specimen 33-3-12-TX-A3 – Bend 1

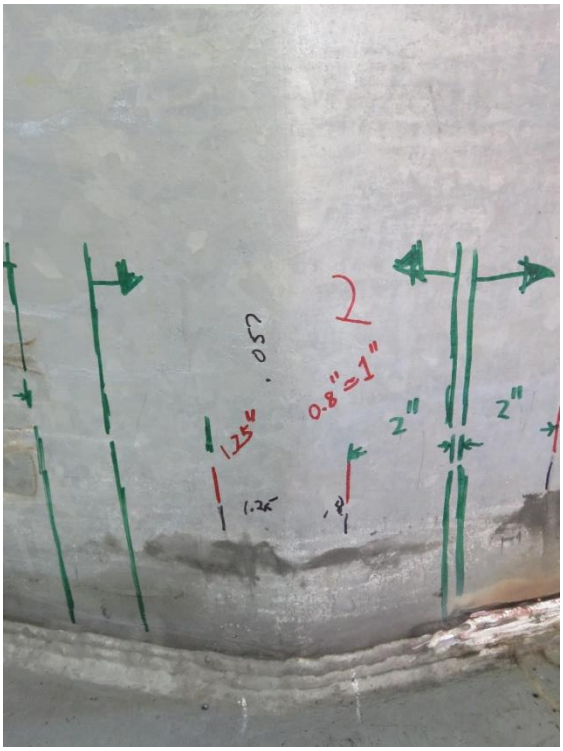

Figure 8.24: State of Cracks: Specimen 33-3-12-TX-A3 – Bend 2

Figure 8.25: State of Cracks: Specimen 33-3-12-TX-A3 – Bend 8

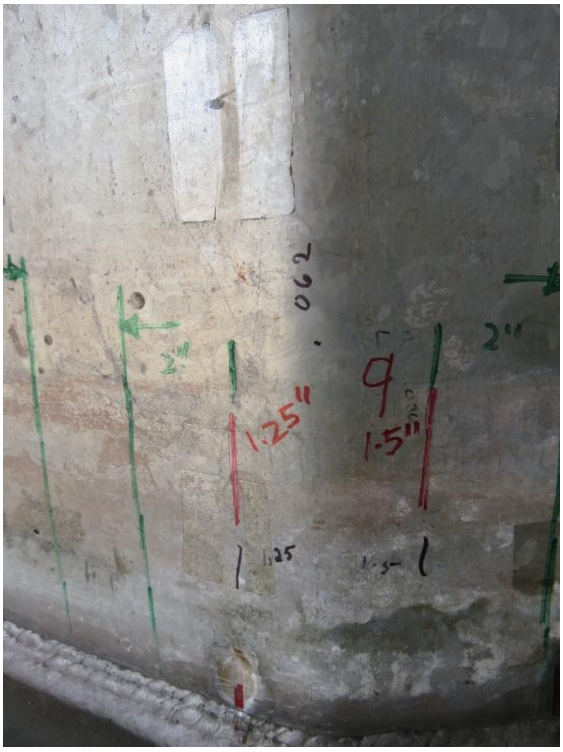

Figure 8.26: State of Cracks: Specimen 33-3-12-TX-A3 – Bend 9

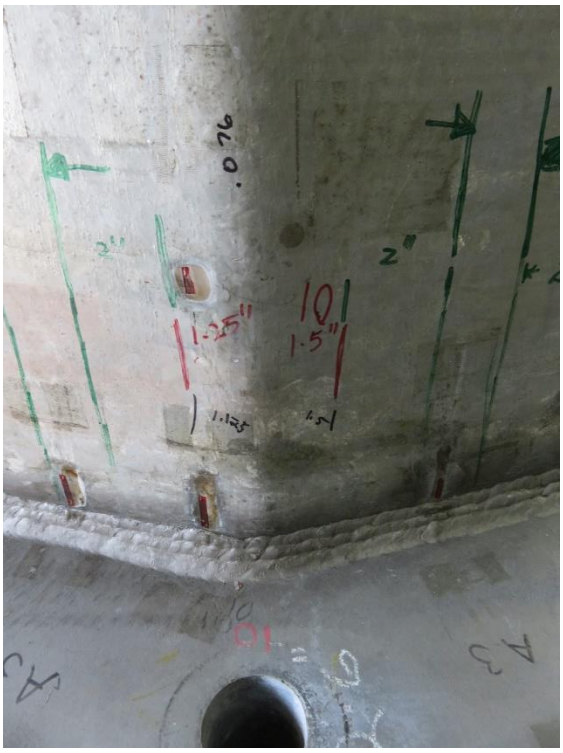

Figure 8.27: State of Cracks: Specimen 33-3-12-TX-A3 – Bend 10

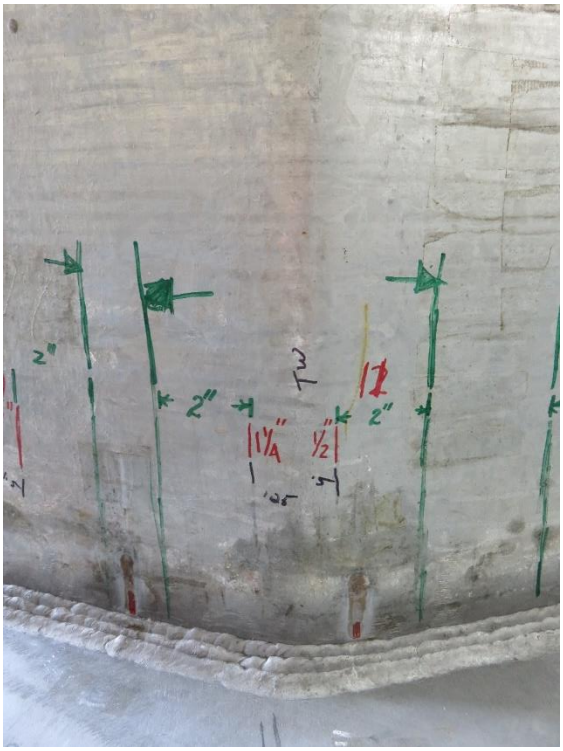

Figure 8.28: State of Cracks: Specimen 33-3-12-TX-A3 – Bend 11

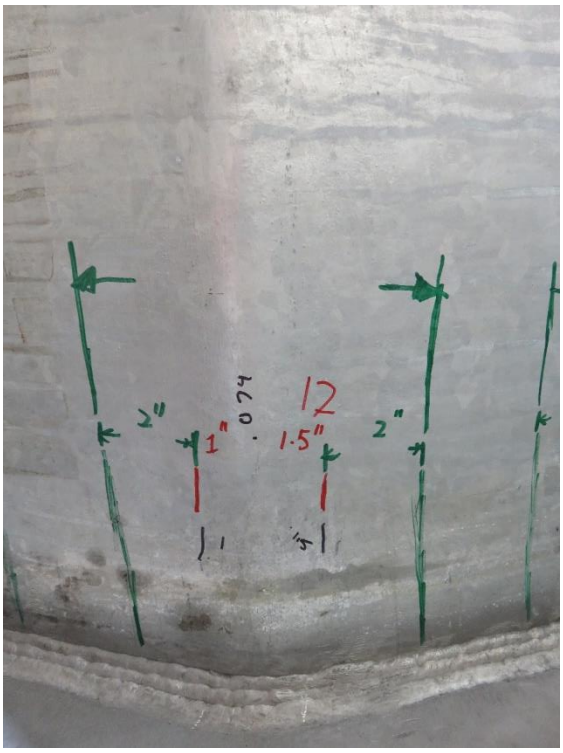

Figure 8.29: State of Cracks: Specimen 33-3-12-TX-A3 – Bend 12

8.3.2 Surface Preparation

To ensure an effective weld-repair implementation, the HMIP specimens were cleaned with acetone to remove any couplant, dirt, and grease remained from the ultrasonic testing. No further specific surface preparations like removal of the galvanized coating at the weld toe were made in this study.

8.3.3 Removal of Cracks

Two methods of crack removal were studied in the development of the weld-repair procedure: Gradual Removal, and Rapid Removal. These procedures are explained in the following through series of pictures depicting the removal procedure. Figures 8.30 through 8.32 presents some general aspects of the crack removal, including grinding orientation/technique, tools, etc.

Figure 8.30: Grinding the Shaft Wall Adjacent to the Weld Toe to Remove Cracks – Orientation of the Specimen

Figure 8.31: Grinding the Shaft Wall Adjacent to the Weld Toe to Remove Cracks – Grinding Technique

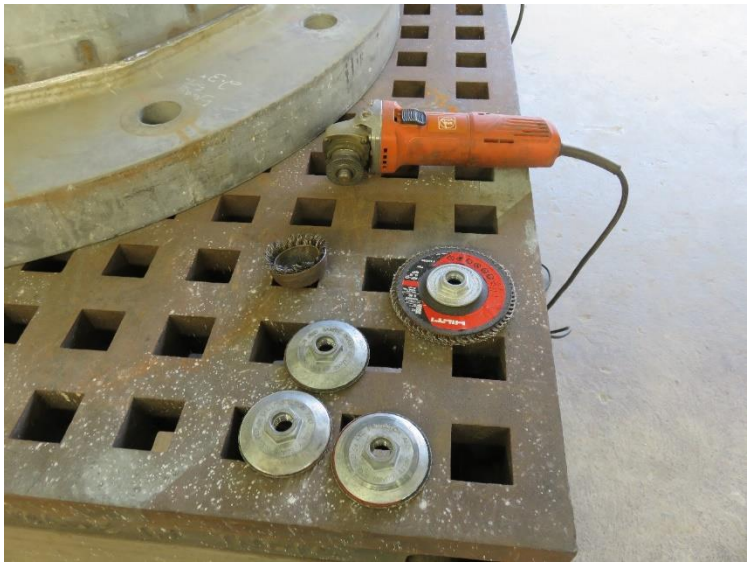

Figure 8.32: Grinding the Shaft Wall Adjacent to the Weld Toe to Remove Cracks – Grinding Tools

Gradual Removal – Specimen 33-3-12-TX-A3

In the gradual removal of cracks procedure, to expose the cracks, the cross-section of the HMIP specimen was slightly grinded over the identified crack length. Magnetic Particle Testing was then conducted to expose the cracks. The grinding was continued to remove magnetic evidence of the cracks. The gradual removal of cracks are shown in the following pictures for the Bend 10 of Specimen 33-3-12-TX-A3 (Figures 8.33 through 8.38). Since cracks are removed gradually, it is easier to observe, using Magnetic Particle Testing, if cracks are completely removed or not. The main disadvantage of the gradual removal procedure is that it is a long and tedious procedure.

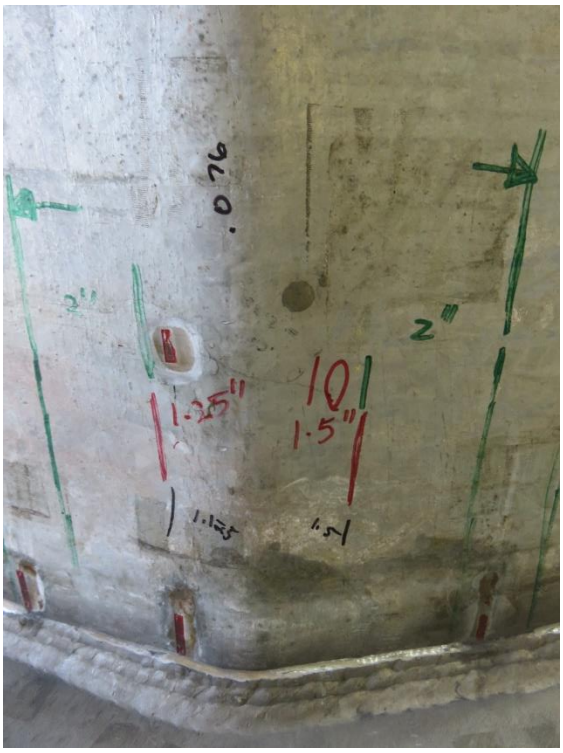

Figure 8.33: Slight Grinding of the Cross-Section to Expose the Cracks: Specimen 33-3-12-TX-A3 – Bend 10

Figure 8.34: Magnetic Particle Testing to Trace the Cracks: Specimen 33-3-12-TX-A3 – Bend 10

Figure 8.35: Grinding Continued to Remove Magnetic Particle Evidence of the Cracks: Specimen 33-3-12-TX-A3 – Bend 10

Figure 8.36: Grinding Continued to Remove Magnetic Particle Evidence of the Cracks: Specimen 33-3-12-TX-A3 – Bend 10

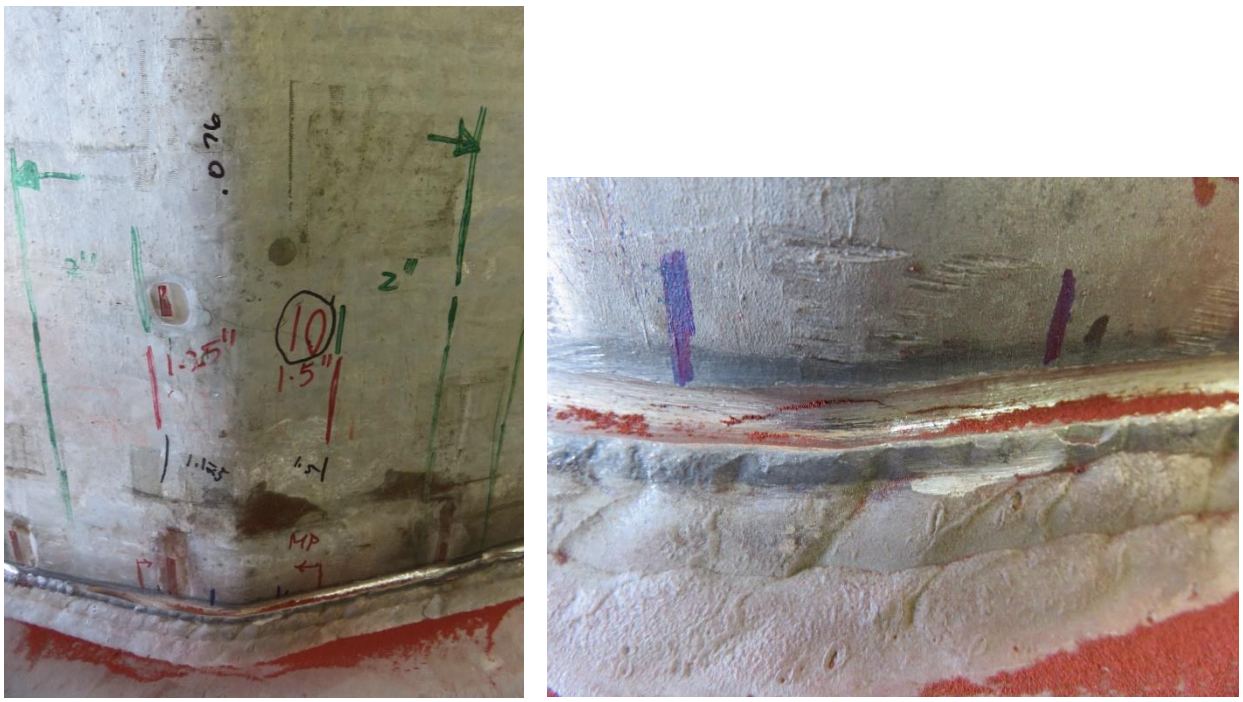

Figure 8.37: Grinding Continued to Remove Magnetic Particle Evidence of the Cracks: Specimen 33-3-12-TX-A3 – Bend 10

Figure 8.38: Grinding Continued to Remove Magnetic Particle Evidence of the Cracks: Specimen 33-3-12-TX-A3 – Bend 10

Rapid Removal – Specimen 33-3-12-TX-A2

In the rapid removal of cracks procedure, cracks were grinded in one single pass or two using the values of their depth predicted in a PAUT test. The rapid removal of cracks made it extremely difficult to identify if cracks are completely removed or not using Magnetic Particle Testing. The rapid removal of cracks were adopted in repairing the Specimen 33-3-12-TX-A2.

8.3.4 Rewelding of Cracks

Shielded Metal Arc Welding procedure (SMAW) was used to reweld the cracks. The filler metal adhering to the AWS classification E7018_was used for the repair. Two different sizes of electrode were utilized: 3/32 inch electrode for the root pass, and 1/8 inch electrode for the other necessary passes. The weld was executed with a current of between 80 to 100 amps, DC+. The weld technique was composed of several stringer passes, using the appropriate electrodes specified above, and a wire brush was used for inter-pass cleaning.

Figures 8.39 and 8.40 represent, respectively, the Bend 10 on Specimen 33-3-12-TX-A3, and Bend 5 on Specimen 33-3-12-TX-A2 following the application of the described weld-repair procedure. As can be seen from Figures 8.39 and 8.40, a slight modification in the grinding technique resulted in fewer weld passes as well as an improved weld profile for the Specimen 33-3-12-TX-A2. For the sake of this study, it was decided to leave the rough surfaces and welding profiles of the Specimen 33-3-12-TX-A3 as is and not to modify the welding profile by grinding.

Figure 8.39: Specimen 33-3-12-TX-A3 – Bend 10 Following the Weld-Repair

Figure 8.40: Specimen 33-3-12-TX-A2 – Bend 5 Following the Weld-Repair

8.4 The Proposed Weld-Repair Procedure – Verification

To verify the effectiveness of the proposed weld-repair procedure in enhancing the fatigue life of cracked HMIPs, fatigue tests were conducted on the repaired specimens. This section provides information about the fatigue tests and discusses results/observations from these tests. The experimental setup used for these fatigue tests was the same as that described in Chapter 5. Fatigue Test Procedure for Repaired HMIP Specimens

Fatigue tests of the developed weld-repair procedure were conducted at the stress range of 10 ksi and at the mean stress of 10 ksi (minimum stress of 5 ksi and maximum stress of 15 ksi). Two fatigue tests were conducted on weld-repaired Specimens 33-3-12-TX-A2 and 33-3-12-TX-A3. In the first test, Bend 5 of the Specimen 33-3-12-TX-A2 and Bend 10 of the Specimen 33-3-12-TX-A3 were fatigued. Rotating both specimens 90 degrees following the first test, in the second test, Bend 8 of the Specimen 33-3-12-TX-A2 and Bend 1 of the Specimen 33-3-12-TX-A3 were fatigued. Results from these fatigue tests are presented in the following.

8.4.1 Results of Fatigue Tests on Repaired HMIP Specimens

Figures 8.41 through 8.43 represent the state of cracks on the three top bends of Specimen 33-3-12-TX-A2 tested under the stress range of 10 ksi. As seen in these figures, severe cracking occurred at Bend 5. The top bend (Bend 5) failed first and the cracks propagated from this bend towards the two adjacent bends (Bends 4 and 6) at later stages of the fatigue test. A very important observation to make from Figures 8.41 through 8.43 is that when cracks approached to irregularities on the weld path (at the shaft-to-baseplate weld toe), they started to propagate in the shaft away from the weld path. When cracks started to propagate in the shaft, the rate of change in their length increased very rapidly causing a very fast fatigue failure.

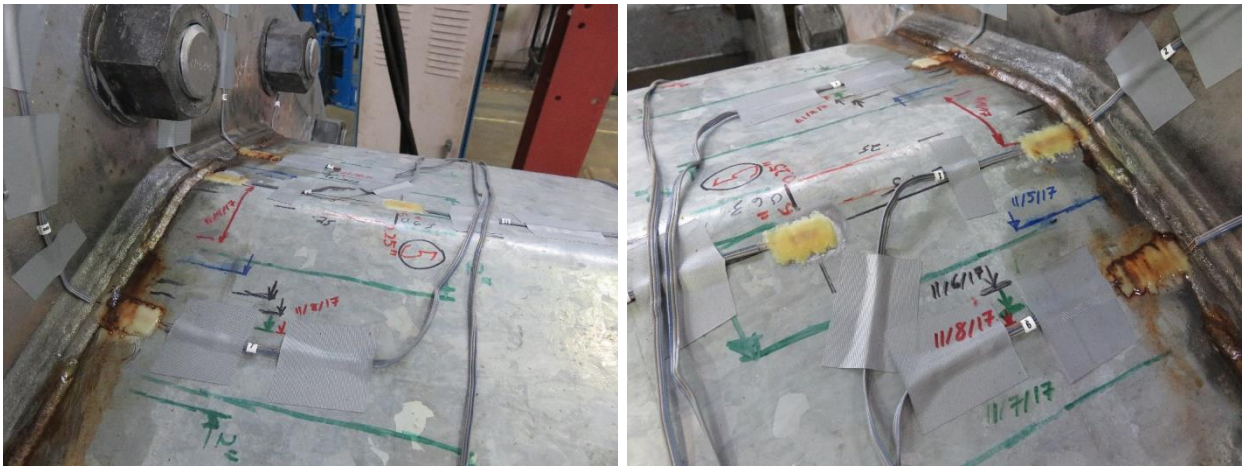

Figure 8.41: Weld-Repaired Specimen 33-3-12-TX-A2 – Bend 5 Following the Fatigue Test: General View

Figure 8.42: Weld-Repaired Specimen 33-3-12-TX-A2 – Bend 5 Following the Fatigue Test: Close-up View

Figure 8.43: Weld-Repaired Specimen 33-3-12-TX-A2 – Bend 5 Following the Fatigue Test: Close-up View

Figures 8.44 and 8.45 show the state of cracks on the top bend of Specimen 33-3-12-TX-A3 tested under the stress range of 10 ksi. As seen in these figures, sever cracking occurred at Bend 10. The top bend (Bend 10) failed first and the cracks propagated from this bend towards the two adjacent bends (Bends 9 and 12) at later stages of the fatigue test. A very interesting observation to make from Figures 8.44 and 8.45 is that following cracks appearance at the weld toe, cracks were also formed and propagated in between the passes of the original cracks.

Figure 8.44: Weld-Repaired Specimen 33-3-12-TX-A3 – Bend 10 Following the Fatigue Test: General View

Figure 8.45: Weld-Repaired Specimen 33-3-12-TX-A3 – Bend 10 Following the Fatigue Test: Close-up View

Figures 8.46 and 8.47 represent the state of cracks on the three top bends of Specimen 33-3-12-TX-A2 tested under the stress range of 10 ksi. As seen in these figures, sever cracking occurred at Bend 1. The top bend (Bend 1) failed first and the cracks propagated from this bend towards the two adjacent bends (Bends 2 and 12) at later stages of the fatigue test. A very important observation to make from Figures 8.46 and 8.47 is that when cracks approached to irregularities on the weld path (at the shaft-to-baseplate weld toe), they started to propagate in the shaft away from the weld path. When cracks started to propagate in the shaft, the rate of change in their length increased very rapidly causing a very fast fatigue failure.

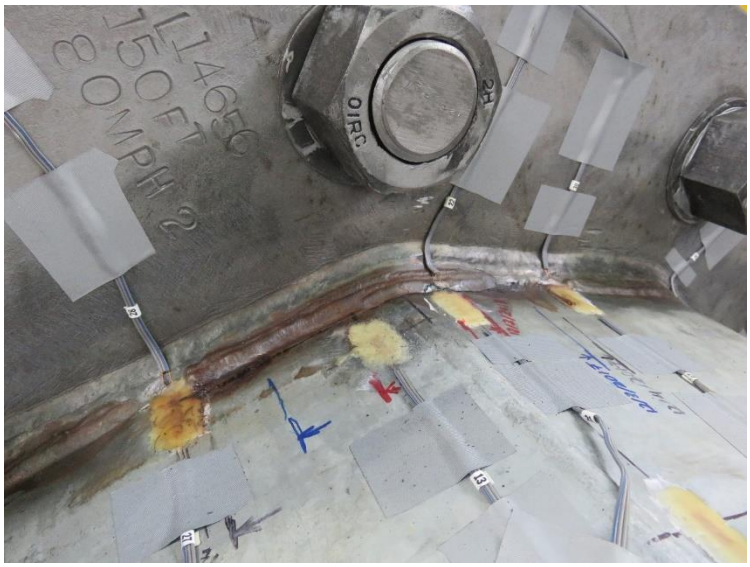

Figure 8.46: Weld-Repaired Specimen 33-3-12-TX-A3 – Bend 1 Following the Fatigue Test: Close-up View

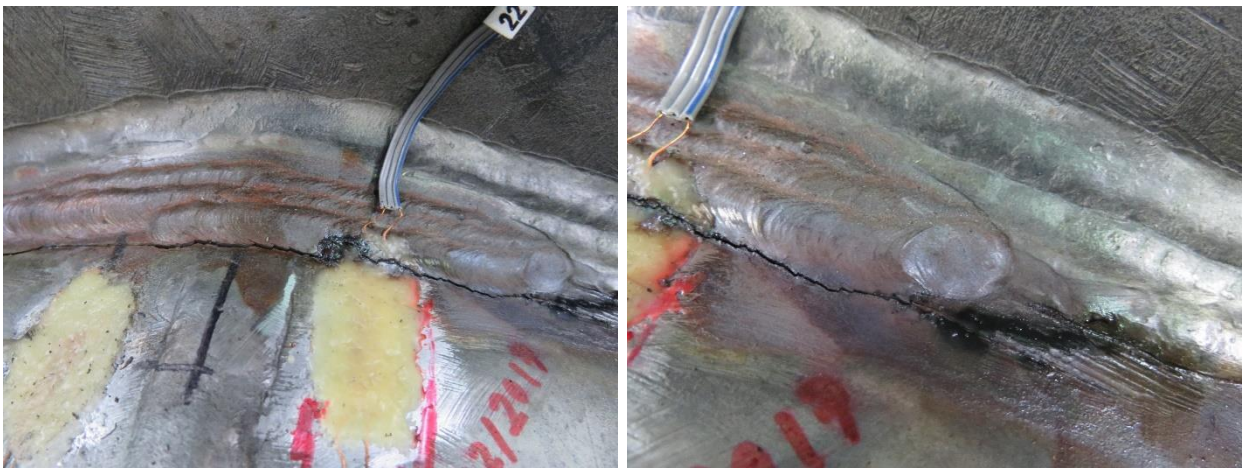

Figure 8.47: Weld-Repaired Specimen 33-3-12-TX-A3 – Bend 1 Following the Fatigue Test: Close-up View

Figures 8.48 and 8.49 represent the state of cracks on the three top bends of Specimen 33-3-12-TX-A2 tested under the stress range of 10 ksi. As seen in these figures, sever cracking occurred at Bend 8. The top bend (Bend 8) failed first (at the same time that Bend 9 failed) and the cracks propagated from this bend towards the two adjacent bends (Bends 7 and 9) at later stages of the fatigue test. A very important observation to make from Figures 8.48 and 8.49 is that when cracks approached to irregularities on the weld path (at the shaft-to-baseplate weld toe), they started to propagate in the shaft away from the weld path. When cracks started to propagate in the shaft, the rate of change in their length increased very rapidly causing a very fast fatigue failure. As seen in Figures 8.48 and 8.49, the significant propagation of cracks resulted in rapid failure of the weld seam Bend 7 as well.

Figure 8.48: Weld-Repaired Specimen 33-3-12-TX-A2 – Bend 8 Following the Fatigue Test: General View

Figure 8.49: Weld-Repaired Specimen 33-3-12-TX-A2 – Bend 8 Following the Fatigue Test: Close-up View

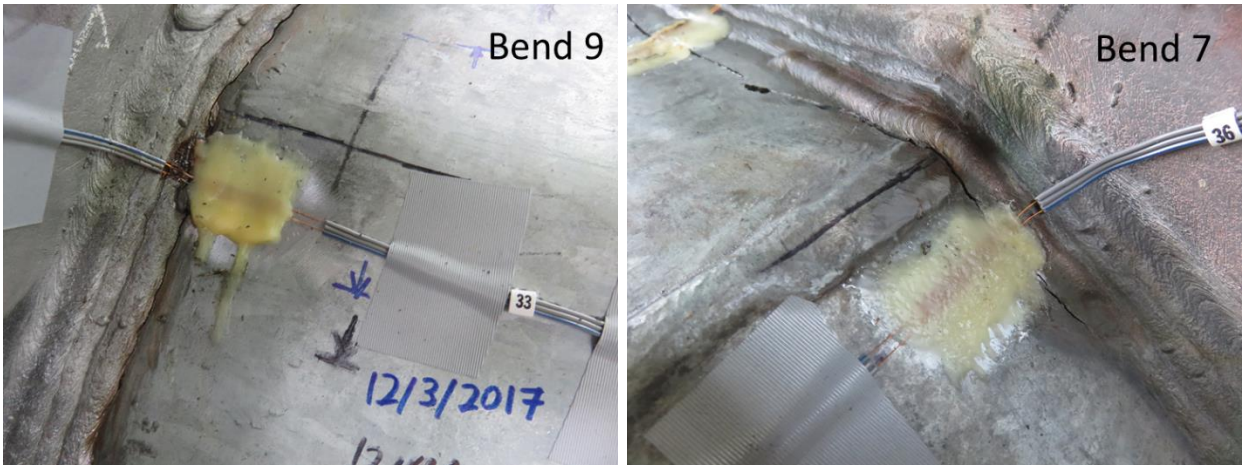

Figure 8.50: Weld-Repaired Specimen 33-3-12-TX-A2 – Adjacent Bends to Bend 8 Following the Fatigue Test

Results from fatigue tests on repaired specimens are summarized in Table 8.1. Fatigue test results from tests on repaired specimens are further presented on an S-N plot in Figure 8.51. In addition to data gathered in this project, a fatigue data point generated previously during experimental studies at the Ferguson Structural Engineering Laboratory is also shown in Figure 8.51. Therefore, Figure 8.51 depicts all the available data on the fatigue behavior of weld-repaired specimens.

Table 8.1: Results of Fatigue Tests on Repaired HMIP Specimens

Stress Range (ksi)	Specimen	Cycles to 10% Reduction in Stiffness
10	A3 – Bend 10	1,200,000
	A3 – Bend 1	510,000
10	A2 – Bend 5	930,000
	A2 – Bend 8	790,000
9	A2 – Bend 7	890,000

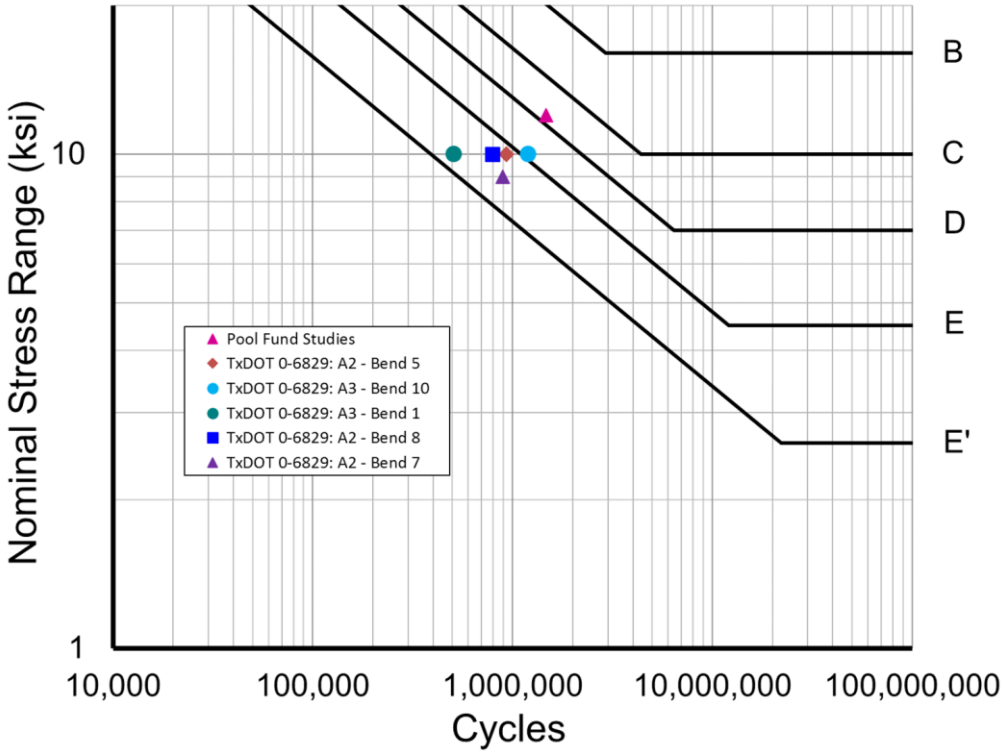

Figure 8.51: Fatigue Behavior of Repaired HMIP Specimens

The results from fatigue tests on repaired specimens are shown together with those from tests on cracked specimens on an S-N plot in Figure 8.52. As shown in this figure, the proposed weld-repair procedure was in general effective in enhancing the fatigue life of cracked poles.

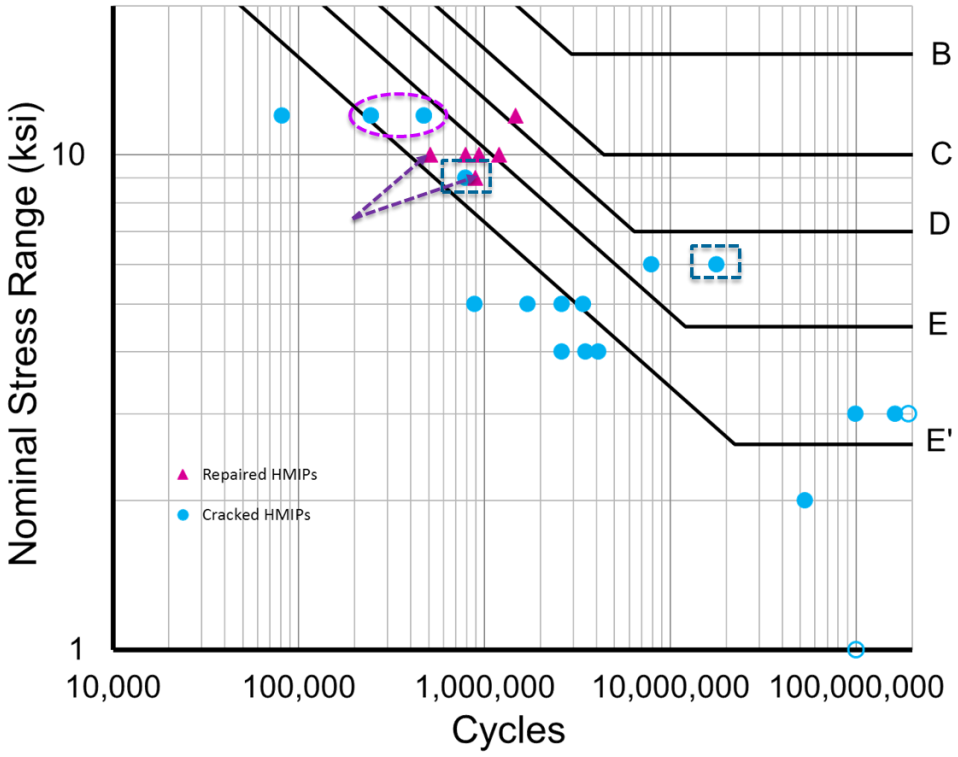

Figure 8.52: Fatigue Behavior of Repaired and Unrepaired HMIP Specimens

8.5 Summary

A weld-repair procedure was developed/implemented/verified to enhance the fatigue life of in-service HMIPs with pre-existing cracks. Fatigue testing on repaired HMIP specimens showed that this procedure was effective in increasing the fatigue life of cracked HMIPs. It is important to emphasize again that the development and application of a weld-repair procedure was not the main purpose of the TxDOT Research Project 0-6829. Therefore, the weld-repair procedure developed and implemented in this research should not be construed as a comprehensive development. Devising a comprehensive and robust weld-repair procedure requires consideration of different governing factors and extensive fatigue testing. Such an endeavor was outside the scope of the current project.

Chapter 9. Reliability-Based Evaluation of the Fatigue Behavior of HMIPs with Pre-Existing Cracks

9.1 Overview

This chapter describes the development of a reliability-based framework to extend the information collected in the laboratory test and during the field monitoring tasks to assess the safety of in-service HMIPs. Reliability-based evaluation of HMIPs under fatigue load incorporates the uncertainties in the wind loading (demand), the uncertainties in the fatigue behavior of HMIPs (resistance), and the accumulation of fatigue damage to predict the life expectancy under different target probabilities of failure. The concept of equivalent fatigue load (EFL) and fatigue life assessment techniques used in the past literature in assessing steel bridges (Chung 2004 and Fasl 2013) and offshore structures (Wirsching 1987), forms the backbone of the proposed reliability-based evaluation technique. This chapter introduces and describes the proposed reliability-based framework. The results of the study are then presented and discussed in detail.

9.2 Introduction

The purpose of this section is to introduce the concept of reliability and to provide a brief background on how fatigue analysis is incorporated into the reliability-based evaluation of HMIPs with and without pre-existing cracks.

9.2.1 Reliability Concept

Consider a structural element for which both the resistance (R) and the applied loads (S) are independent random variables with mean values of (μ_S, μ_R), and standard deviations of (σ_S, σ_R), respectively. Failure of the structural element occurs when the loading is greater than the resistance. In other words, the probability of failure is the chance or probability of the loading being greater than the resistance. Figure 9.1 shows the probability distribution of the resistance and the loading where the overlapping portion indicates failure.

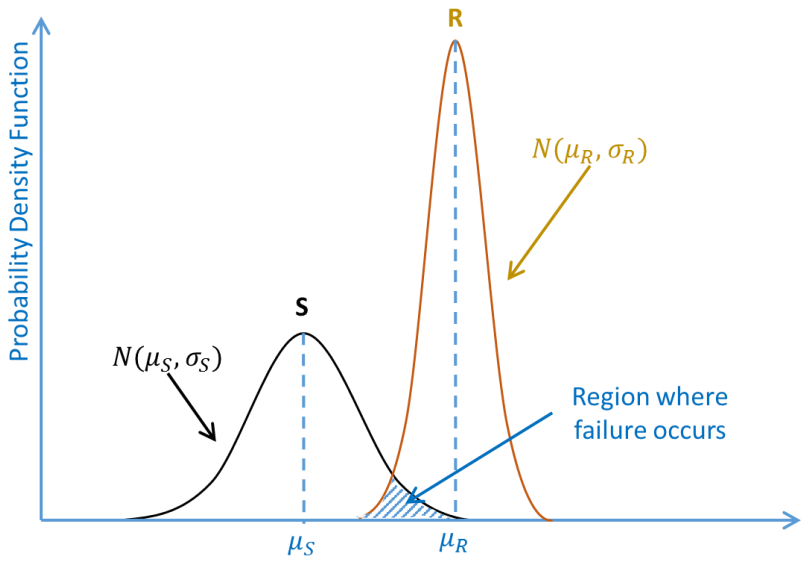

Figure 9.1: Probability Density Curves for R and S

The probability of failure is computed by first defining a limit state function, $g(\boldsymbol{X})$, which is a function of both the resistance (or capacity) and the loading (or demand) as defined in Equation 9.1. Failure occurs when the limit state function is smaller than zero.

$$g(\boldsymbol{X}) = g(R,S) = R - S \qquad \textbf{Equation 9.1}$$

In Equation 9.1, $g(\boldsymbol{X})$ is the limit state function described by a probability distribution model with mean value, μ_X, and standard deviation, σ_X.

If the resistance and the loading side are independent and normally distributed with mean values (μ_S, μ_R) and standard deviations (σ_S, σ_R), the limit state function would also result in a normally distributed random variable with mean value (μ_X) and standard deviation (σ_X) calculated using Equation 9.2. The probability distribution of the limit state function is shown in Figure 9.2 where the shaded area represents the probability of failure.

$$\mu_X = \mu_R + \mu_S$$

$$\sigma_X = \sqrt{\sigma_R^2 + \sigma_S^2} \qquad \textbf{Equation 9.2}$$

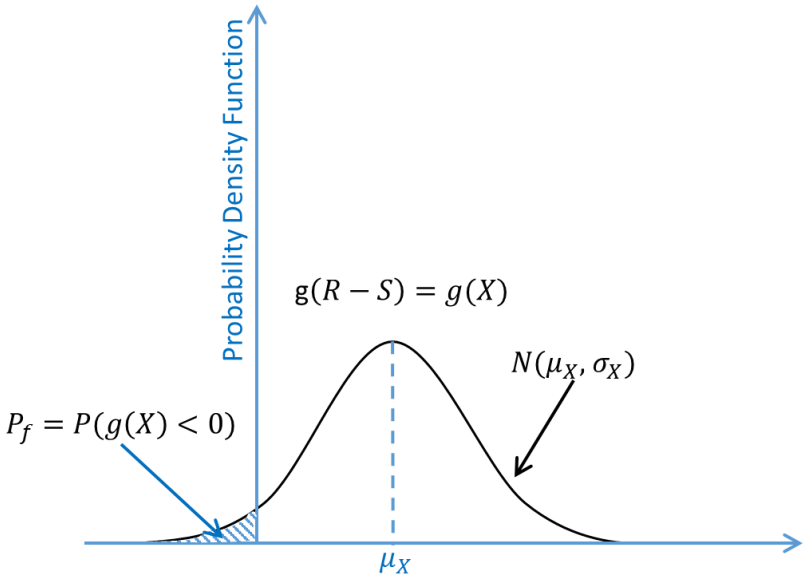

Figure 9.2: A Probability Density Curve for $g(X)$

If the limit state function is normally distributed with mean value (μ_X) and standard deviation (σ_X), the probability of failure, P_f, can be determined as shown in Equation 9.3.

$$P_f = P(g(\boldsymbol{X}) < 0) = \Phi\left(\frac{0 - \mu_X}{\sigma_X}\right) = \Phi\left(\frac{\mu_S - \mu_R}{\sqrt{\sigma_R^2 + \sigma_S^2}}\right) \qquad \textbf{Equation 9.3}$$

In Equation 9.3, $\Phi()$ is the cumulative distribution function of a standard normal random variable.

9.2.2 Fatigue Analysis

Fatigue analysis is used when structural components or connection details are subjected to cyclic or fluctuating loads. The demand in fatigue arises from fluctuating loads expressed using a strain/stress history or a strain/stress range histogram, which describes the distribution of the varying-amplitude stress/strain ranges. The fatigue resistance, on the other hand, can be characterized using a stress-based approach (S-N curves) or numerically using the linear elastic fracture mechanics (LEFM) procedure. The success of the LEFM method in determining the fatigue resistance (capacity) depends on the accuracy of information about initial flaw sizes and the fracture toughness. Both of these factors are not well known in the case of HMIPs with pre-existing cracks. Consequently, this study uses the stress-based approach where fatigue resistance is characterized by the number of constant-amplitude stress range cycles that a structure or design detail can sustain. The fatigue resistance using the stress-based approach is typically expressed by S-N curves developed using experimental results.

Fatigue Resistance (S-N Curves)

One of the common methods to characterize the fatigue resistance of a specific design detail is to test it in tension at a constant-amplitude stress range and determine the corresponding number of cycles to failure. The constant-amplitude stress range is defined as the difference between the constant peak and constant valley of the stress history. A specific design detail is

tested using various constant-amplitude stress ranges (S_R) to determine the corresponding number of cycles to failure (N_f) which is typically plotted on a log-log scale (e.g. Figure 9.3).

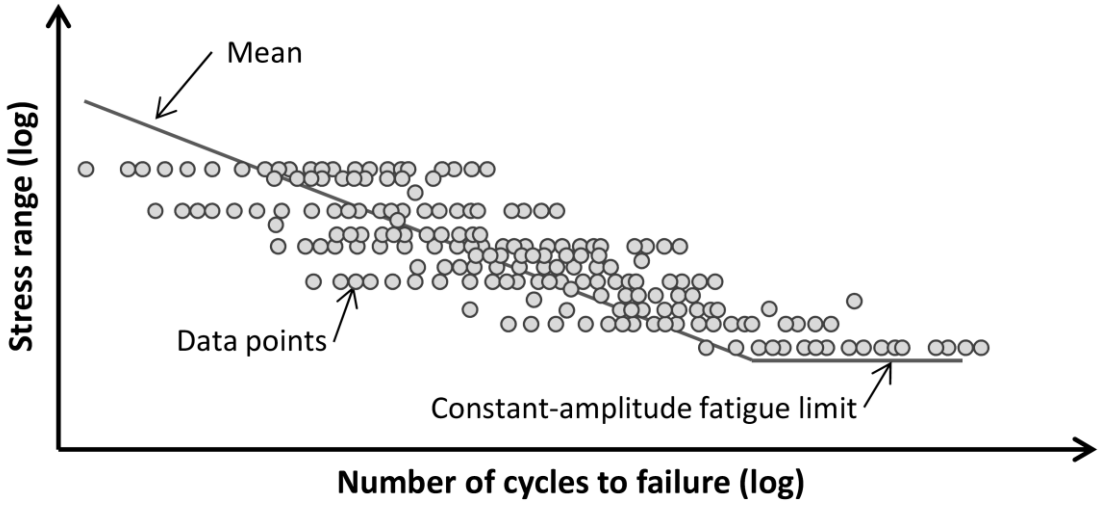

Figure 9.3: A Representative S-N Curve Constructed Using Fatigue Test Data (Fasl 2013)

The scatter in N_f at a fixed S_R is mainly due to uncertainty in the fatigue resistance. The median of N_f values and the corresponding fixed S_R are plotted on a log-log plot to find the best-fitting straight line or regression line (Figure 9.3). This straight line represents the S-N curve and has a general form represented in Equation 9.4.

$$N_f = A \cdot S_R^{-m} \qquad \textbf{Equation 9.4}$$

In Equation 9.4, *m* is the slope of the log-log curve and is a material constant, while *A* is also a material constant that further depends on the design detail under consideration.

Since S-N curves are determined based on the median of the scatter data, 50% of the structures with the same design detail are expected to fall under the line. S-N curves are usually shifted downward to target a lower probability of failure. In fact, AASHTO LRFD Specifications implemented this methodology in their proposed S-N curves (AASHTO 2014, AASHTO 2015). Details on the development of S-N curves for different design details suggested in AASHTO are provided in Section 9.3.1.

Palmgren-Miner Method

Since the stress ranges experienced by in-service structures are not of constant amplitude, Miner (1945) introduced a linear damage accumulation rule to account for the fatigue caused by variable-amplitude loading. The rule allows the damage caused by different level of stress ranges to be accumulated until it reaches failure. Miner's rule is expressed by Equation 9.5 (Miner 1945).

$$D = \sum_{i=1}^{k} \frac{n_i}{N_{f,i}} \qquad \textbf{Equation 9.5}$$

In Equation 9.5, D is the Miner's damage accumulation index and n_i are the number of cycles corresponding to a specific stress range, $S_{R,i}$. $N_{f,i}$ are the number of cycles until failure under a constant-amplitude stress range, $S_{R,i}$. Based on Miner's damage accumulation rule, failure occurs when $D \geq 1$.

The effective stress range (S_{RE}) is introduced as a constant-amplitude stress range that, if used with the same total number of cycles (N), would result in the same damage as if experienced under variable-amplitude stress ranges ($S_{R,i}$). By combining Equation 9.4 and Equation 9.5 and setting equal damage from using variable-amplitude stress ranges and from using the effective stress range (S_{RE}), the effective stress range (S_{RE}) can be derived as follow:

$$D = \sum_{i=1}^{k} \frac{n_i \cdot S_{R,i}^m}{A} = \frac{N \cdot S_{RE}^m}{A}$$

Equation 9.6

$$S_{RE} = \left(\sum_{i=1}^{k} \frac{n_i}{N} \cdot S_{R,i}^m \right)^{\frac{1}{m}} = \left(\sum_{i=1}^{k} \gamma_i \cdot S_{R,i}^m \right)^{\frac{1}{m}}$$

In Equation 9.6, γ_i is the ratio of n_i to the total number of cycles (N). With the use of the effective stress range, variable-amplitude loading may be used to estimate the number of cycles until failure according to any S-N curve that is associated with the design detail.

The uncertainty arising from using Miner's rule is accounted for in the critical damage accumulation index (Δ), which substitutes for the deterministic D value of 1. A survey of fatigue test data for offshore structures and steel structures conducted by Wirsching et al. (1987) showed that a lognormal distribution with a mean value (μ_Δ) of 1.0 and coefficient of variance (δ_Δ) of 0.3 is a reasonable model to describe Miner's critical damage accumulation index (Δ). The proposed model by Wirsching et al. (1987) has been extensively utilized in offshore and many other fatigue problems involving variable-amplitude stress ranges.

Rain-Flow Counting

The application of the Palmgren-Miner's rule requires a cycle-counting method to determine the variable-amplitude stress range cycles from the strain-time history. Numerous counting methods for fatigue analysis have been developed and standardized in ASTM E1049 (2011). The simplified rain-flow counting method included in ASTM E1049 (2011) and developed by Downing and Socie (1982) is a simple method that resolves the stress-time history into full cycles. The algorithms of the simplified rain-flow counting method can be found in Downing and Socie (1982). The simplified rain-flow counting method has been implemented in fatigue analysis of steel bridges (Fasl 2013) and of HMIPs (Magenes 2011) in the past, and is also selected in this study.

9.2.3 Fatigue Limit State Function

The conventional way to quantify the fatigue failure is to use the number of cycles to failure as a criterion to compare with the number of cycles anticipated in a target service life. The limit state function can then be expressed as shown in Equation 9.7.

$$g(N) = N_f - N_e(t) = 0 \qquad \textbf{Equation 9.7}$$

In Equation 9.7, $g(N)$ is the uncertainty model for the limit state function of both N_f and N_e. Representing the resistance or capacity side, N_f is the number of cycles to failure for a specific stress range. Representing the demand side, $N_e(t)$ is the number of expected cycles in service years (t). The number of cycles under a given stress range is determined using the S-N curve as shown in Figure 9.3. The S-N curve introduced in the previous section is described in the form of Equation 9.8.

$$A = S_{RE}^m \cdot N_f \qquad \textbf{Equation 9.8}$$

In Equation 9.8, S_{RE} is the effective stress range and N_f is the sustained cycles before failure. The Miner's rule introduced earlier allows variable-amplitude stress ranges to be transformed into a single effective stress range (S_{RE}) and a total number of cycles (N_f). Further, in Equation 9.8, m is the slope of the log-log S-N curves, which is again a material-dependent constant, while A is an empirical coefficient that describes the capacity of different design details. Note that the S-N curves used in AASHTO and their developments are described in more details in the following section.

By substituting Equation 9.8 into Equation 9.7, the limit state function can also be expressed in the form of Equation 9.9, which directly shows the parameters that affect the limit state.

$$g(A, m, S_{RE}, N_e) = A - N_e(t) \cdot S_{RE}^m = 0 \qquad \textbf{Equation 9.9}$$

Introducing the uncertainty in using Miner's rule in the Palmgren-Miner's critical damage accumulation index (Δ), the limit state function is expressed as Equation 9.10.

$$g(\Delta, N) = \Delta - D = \Delta - \frac{N_e(t)}{N_f} = 0 \qquad \textbf{Equation 9.10}$$

Similarly, submitting Equation 9.8 into Equation 9.10 results in a limit state function in the form of Equation 9.11, which directly shows the parameters that affect the limit state function including the Palmgren-Miner's critical damage accumulation index.

$$g(\Delta, A, m, S_{RE}, N_e) = \Delta \cdot A - N_e(t) \cdot S_{RE}^m = 0 \qquad \textbf{Equation 9.11}$$

9.2.4 Reliability Index and Probability of Failure

The reliability index, β, is often used to quantify the degree of reliability, which is related to the probability of failure through Equation 9.12.

$$\beta = \Phi^{-1}(1 - P_f) = -\Phi^{-1}(P_f)$$

$$P_f = \Phi(-\beta) \qquad \textbf{Equation 9.12}$$

Table 9.1 shows the reciprocal relationship between the reliability index and the probability of failure in that the probability of failure increases with decreasing reliability index. For civil engineering applications, the accepted probability of failure is in the order of 10^{-3} to 10^{-4}. This probability of failure corresponds to a reliability index ranging from 3.09 to 3.72.

Table 9.1: Equivalent Probability of Failure and the Corresponding Reliability Index

Probability of Failure, P_f	Reliability Index, β
10^{-1}	1.28
10^{-2}	2.33
10^{-3}	3.09
10^{-4}	3.72
10^{-5}	4.26

By combining Equation 9.3 and Equation 9.12, the reliability index, β, can be directly determined from the resistance and the loading probabilities using Equation 9.13 given that both the resistance and the loading are normally-distributed random variables.

$$\beta = \frac{\mu_R - \mu_S}{\sqrt{\sigma_R^2 + \sigma_S^2}} \qquad \textit{Equation 9.13}$$

9.3 Fatigue Resistance of HMIPs

As described in Section 9.2.2, the fatigue resistance of a certain design detail is typically defined by an S-N curve determined from numerous tests under different stress range amplitudes. AASHTO Specifications (AASHTO 2014, AASHTO 2015) provides S-N curves for different categories based on the structure or components design details. The groove-welded base detail without ground sleeves used by TxDOT is classified as an AASHTO Category E fatigue detail (AASHTO 2015, Stam et al. 2011). However, the fatigue resistance of the same design with galvanizing cracks has not been addressed in any of these AASHTO categories. Therefore, using results from laboratory fatigue tests, this study attempts to determine an S-N curve for HMIPs with pre-existing cracks. The methodology used in developing the S-N curve closely follows that of AASHTO Specifications (AASHTO 2014, AASHTO 2015).

This section first illustrates the AASHTO S-N curves (AASHTO 2014, AASHTO 2015), and provides a brief background on their development. The S-N curve proposed in this study for the fatigue predictions of galvanized HMIPs with pre-existing cracks is then introduced and discussed.

9.3.1 AASHTO S-N Curves

The current AASHTO fatigue categories and the corresponding design parameters, fatigue constant (A) and constant-amplitude fatigue limit (CAFL), are listed in Table 9.2 and graphed in Figure 9.4. The straight lines in Figure 9.4 are the design S-N curves proposed by AASHTO. These curves are defined using the formula illustrated in Equation 9.4 in section 9.2.2. The fatigue constant (A) of the design S-N curves can be determined as the intercept of the design S-N curve at unit stress range or the product of the number of cycles and the cube of the corresponding stress

range on the design S-N curve. The constant-amplitude fatigue limit (CAFL) represents the stress range threshold, below which no fatigue failure occurs.

Table 9.2: Fatigue Constant (*A*) and Constant-Amplitude Fatigue Limit (CAFL) for the Fatigue Detail Categories in AASHTO (AASHTO 2014)

Category	Fatigue constant, A (ksi^3)	CAFL (ksi)
A	250×10^8	24.0
B	120×10^8	16.0
B’	61×10^8	12.0
C	44×10^8	10.0
D	22×10^8	7.0
E	11×10^8	4.5
E’	3.9×10^8	2.6

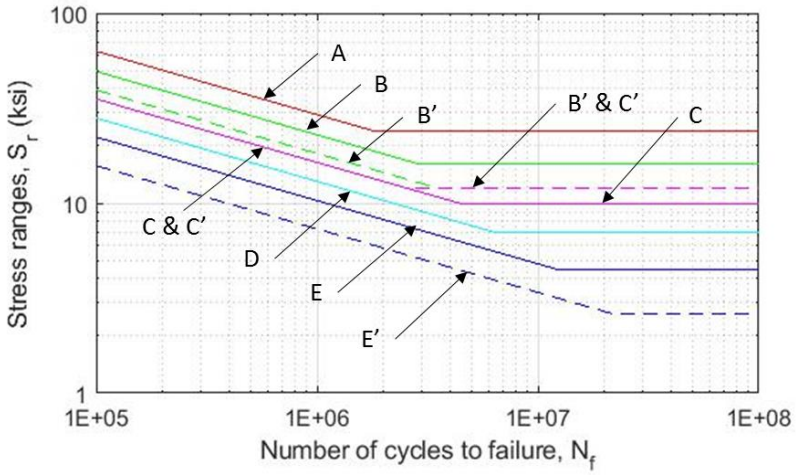

Figure 9.4: AASHTO S-N Curves Intended for Fatigue Design of Steel Bridges (AASHTO 2014)

The current design S-N curves in AASHTO have been developed using the results from more than 800 constant-amplitude fatigue tests (Keating and Fisher 1986). For each categorized data set, a linear regression analysis was performed on a log-log scale to obtain the “mean” S-N curve of the corresponding category. The “mean” S-N curve on the log-log scale is a line where 50% percent of the data are expected to lie on either side. To ensure most of the data (or failure points) lie above a design S-N curve, a lower bound of the regression line was suggested. Although the proposed design S-N curve was reported to be two standard deviation below the “mean” S-N curve that specifies a 95% exceedance (corresponding to a 95% probability of survival or a 5% probability of failure) by Moses et al. (1987), the actual distance between the “design” and “mean” is corrected to 1.64 times the standard deviation in a recent NCHRP report (Bowman et al. 2012). The corrected value actually corresponds better to the regression values documented by Moses et al. (1987) and is, therefore, adopted in this study. The slope of the “mean” S-N curve for each category was also found to have similar values close to -3.0, which was therefore proposed as the slope for the proposed design S-N curves. The design fatigue constant (A) of the design S-N curve

was determined from the product of 2 million cycles and the cube of the stress range intercept to the lower bound curve. The constant-amplitude fatigue limit (CAFL) was also verified against the collected fatigue test data (Keating and Fisher 1986) and it was shown that fatigue cracks did not propagate for stress ranges below the AASHTO's CAFLs.

In order to introduce uncertainty in the fatigue limit, a probability distribution of the S-N curves for each category is needed. In addition to the AASHTO proposed design S-N curves, the regression line (mean S-N curve) resulting from the original data is required to construct such a distribution. Although the regression values were determined in Keating and Fisher (1986), the actual values were not published in the corresponding NCHRP report (Keating and Fisher 1986). Nevertheless, the regression values presented in terms of the mean ($S_{R\mu}$) and design (S_{RD}) stress ranges at two million cycles for a slope of -3.0 were later presented in another NCHRP report (Moses et al. 1987). These values are provided in Table 9.3.

Table 9.3: Mean and Design Stress Ranges and the Corresponding Fatigue Constant, A (Moses et al. 1987)

Category	$S_{R\mu}$ at 2×10^6 Cycles (ksi)	S_{RD} at 2×10^6 Cycles (ksi)	A_m (ksi^3)	A_D (ksi^3)
A	33.0	23.2	718.7×10^8	249.7×10^8
B	22.8	18.1	237.0×10^8	118.6×10^8
B'	18.0	14.5	116.6×10^8	61.0×10^8
C	16.7	13.0	93.1×10^8	43.9×10^8
D	13.0	10.3	43.9×10^8	21.9×10^8
E	9.5	8.1	17.1×10^8	10.6×10^8
E'	7.2	5.8	7.5×10^8	3.9×10^8

The fatigue constants (A_m, A_D) in Table 9.3 are determined for each category using the mean and design stress ranges at two million cycles using Equation 9.4 with a slope (m) of -3.0 (Equation 9.14). It is important to note that A_m is the mean of $\ln A$.

$$A_m = 2\times10^6 \cdot S_{R\mu}^3$$

$$A_D = 2\times10^6 \cdot S_{RD}^3$$

Equation 9.14

The uncertainty is introduced in the fatigue constant (A) by assuming that it is a random variable with a log-normal distribution (Moses et al. 1987). Since a "mean" S-N curve represents the 50% mark in the physical scale, the fatigue constant determined from this S-N curve is actually the median value of the random variable (A). As such, the parameter (λ_A) of A in the log-normal distribution is determined as the natural log of A_m (Equation 9.15). Since A_D is set to have a 95% exceedance according to the design S-N curve, the natural log of A_D should be 1.64 times ζ_A, the standard deviation (SD) of $\ln(A)$, below λ_A, as presented in Equation 9.16 (Table 9.4). The coefficient of variation (COV), δ_A, of the random variable A can then be determined according to Equation 9.17. The calculated values of δ_A are also tabulated in Table 9.4. As will be shown in later sections, the derived values of A_μ and δ_A of the random variable A can be used in the fatigue reliability evaluation of the HMIPs with pre-existing cracks.

$$\lambda_A = \ln(A_m) \qquad \textit{Equation 9.15}$$

$$\zeta_A = \frac{\ln(A_m) - \ln(A_D)}{1.64} \qquad \textit{Equation 9.16}$$

$$\delta_A = \sqrt{e^{\zeta_A^2} - 1} \qquad \textit{Equation 9.17}$$

Table 9.4: Statistical Parameters for Fatigue Constant *A*

Category	$\ln(A_m) = \lambda_A$	$\ln(A_D)$	ζ_A (SD of $\ln(A)$)	δ_A (COV of A)
A	25.00	23.94	0.64	0.72
B	23.89	23.2	0.42	0.44
B′	23.18	22.53	0.40	0.41
C	22.95	22.2	0.46	0.48
D	22.20	21.51	0.43	0.45
E	21.26	20.78	0.29	0.30
E′	20.43	19.78	0.40	0.41

9.3.2 S-N Curves for Fatigue Tests

Defining the correct fatigue coefficient (A) for the HMIPs is essential in assessing the remaining fatigue life of in-service poles. The shaft-to-base plate connection detail used in the HMIPs of interest closely follows the fatigue detail defined by AASHTO as "full penetration groove welded tube-to-transverse plate connections welded from both sides (without backing ring)." This detail is fatigue rated as category E in the AASHTO specifications (AASHTO 2015). Therefore, category E represents the fatigue resistance for the un-cracked HMIPs under consideration. Micro-cracks due to galvanizing have been found to reduce the fatigue resistance of the HMIPs of interest (Pool 2010). Therefore, past studies either assumed fatigue category E′ (Dawood 2014) or established S-N curves based on the worst fatigue performance observed in tests (Magenes 2011) to represent the fatigue capacity of the galvanized HMIPs.

A more accurate estimate of the fatigue resistance can be developed by pooling the results of all cyclic load tests. A library of fifteen tests performed on 33-inch diameter, 12-sided poles is used to obtain a more representative curve (Pool 2010, Belivanis 2014, TxDOT project 0-6829, TxDOT project 0-6830). The S-N curves generated in this section would reflect the reduced fatigue capacity of the HMIP design subjected to micro-cracks both deterministically and probabilistically. The design S-N curve for deterministic method is obtained based on the 95% exceedance (following AASHTO method) of the fatigue constant (A) assuming it follows a log-normal distribution. The design fatigue constant (A_D) is determined as follows:

$$A_D = e^{(\lambda_A - 1.64\zeta_A)} \qquad \textit{Equation 9.18}$$

The design fatigue constant (A_D) defines the relationship between any stress range (σ_R) and the corresponding number of cycles to failure (N_f). This relationship is a straight line in log-log scale as defined in Equation 9.19.

$$A_D = \sigma_R^3 \cdot N_f \qquad \textbf{\textit{Equation 9.19}}$$

Additionally, the mean and the standard deviation of the natural log of experimental fatigue constant (A) are denoted as λ_A and ζ_A, respectively and are defined as,

$$\lambda_A = \mu_{lnA} \quad \text{and} \quad \zeta_A = \sigma_{lnA} \qquad \textbf{\textit{Equation 9.20}}$$

λ_A and ζ_A are also used in the probabilistic method of characterizing fatigue strength, in which the uncertainty of the fatigue constant *A* is introduced.

To develop the S-N curves for the HMIPs with pre-existing cracks, three different scenarios are considered. In the first scenario, all available fatigue data are used without any corrections for the effect of mean stress. In the second scenario, all available fatigue data are used, but corrections are made for the effect of mean stress. More specifically, using the method proposed by Goodman (1919), fatigue data are adjusted so that they all correspond to the same mean stress. In the third scenario, only selected fatigue data are used. These selected data represent fatigue data from tests conducted at the University of Texas at Austin. In addition, these selected data represent fatigue data from tests with initial cracks (test results from bends without initial cracks are not included). In the following, the developed S-N curves for these three scenarios are presented and discussed. The experiment-based S-N curves are also compared with the S-N curves from AASHTO (AASHTO 2015) and Eurocode 3 (EN1993 2002).

S-N Curves for Unadjusted Fatigue Data

The entire fatigue data set used in generating the S-N curve is listed in Table 9.5. These data include mean stress, stress range, and the number of cycles to failure. With the assumption of log-normal distribution for the fatigue constant (*A*) (Keating and Fisher 1986), the value of (*A*) (Equation 9.21) and its statistical parameters, λ_A and ζ_A (Equation 9.20) were determined.

$$A = \sigma_R^3 \cdot N \qquad \textbf{\textit{Equation 9.21}}$$

A probability plot is created for the grouped data to show the validity of the log-normal assumption when using limited available data (Figure 9.5). Additionally, a goodness-of-fit test known as Anderson-Darling Test (Anderson and Darling 1954) is performed to quantify how well the grouped test data fit the log-normal distribution. The Anderson-Darling Test indicates that the log-normal assumption cannot be rejected at a 95% significance level (Anderson and Darling 1954).

Table 9.5: Experimental Fatigue Data - Unadjusted

	Mean Stress (ksi)	Stress Ranges (σ_R) (ksi)	Number of Cycles (N)	Fatigue Constant (A) (10^8 ksi^3)
Project 0-6829 (UT)	6	6	17700000	38.2
	6	4	2600000	1.7
	6	4	4100000	2.6
	6	4	3500000	2.2
	6	2	53000000	4.2
	6	3	162500000	43.9
	9	9	790000	5.8
Pool (2010)	10	12	81326	1.4
	10	12	245746	4.2
	10	12	470711	8.1
Belivanis (2013)	6.5	5	885000	1.1
	6.5	5	1700000	2.1
	6.5	5	3400000	4.3
Project 0-6830 (UH)	0	6	8000000	17.3
	0	3	99000000	26.7

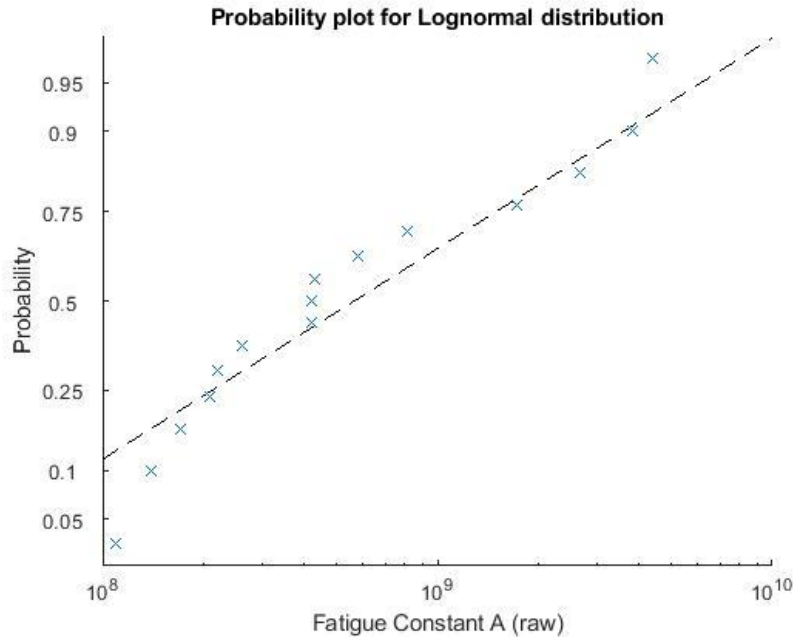

Figure 9.5: Log-Normal Probability Plot for Unadjusted Fatigue Data

According to Bowman (2012), the current AASHTO fatigue categories and their corresponding design fatigue constant (*A*) are determined based on the lower bound of the distribution indicating a 95% exceedance (i.e. 95% of the fatigue data points lie above each S-N curve). The distribution parameters for the fatigue constant (*A*) determined using the unadjusted fatigue test data and fatigue categories in AASHTO (AASHTO 2015) are presented in Table 9.6. As seen in Table 9.6, λ_A for the experiment is lowest compared to all categories under AASHTO which can be attributed to the known pre-cracked conditions. In addition, uncertainties, resulted from the initial conditions of HMIP specimens and variations in experimental procedures, contribute to higher values for ζ_A, and consequently lower values for the design fatigue constant (A_D). Although the design S-N curves in the current AASHTO code suggests a constant amplitude fatigue limit (CAFL) for each design category, the experiment results indicate otherwise showing signs of fatigue damage for stress ranges under the lowest CAFL in category E′. In the case of HMIPs, low stress range cycles are more important since the majority of the sustained stress ranges are well below the CAFL of the lowest fatigue category in AASHTO.

Table 9.6: Statistical Parameters for the Fatigue Constant A Using AASHTO and Unadjusted Fatigue Data

Category	λ_A ($\mu_{\ln(A)}$)	ζ_A ($\sigma_{\ln(A)}$)	$\ln(A_D)$	A_D ($\times 10^8$)
A	25	0.64	23.95	252.1
B	23.89	0.42	23.2	119.2
B′	23.18	0.4	22.52	60.5
C	22.95	0.46	22.2	43.6
D	22.2	0.43	21.49	21.6
E	21.26	0.29	20.78	10.6
E′	20.43	0.4	19.77	3.9
Experiment (unadjusted)	20.1	1.21	18.12	0.7

To better represent the fatigue behavior of HMIPs at low stress cycles, a two-slope S-N curve with no CAFL is constructed using the experimental results summarized in Table 9.5. The use of a second slope in the low stress range region is also suggested in past studies (Lassen and Rècho 2006) and in the Eurocode 3 (EN1993 2002). The second slope allows the damage from the low stress range cycles to be accumulated in a less aggravating way while still contributing to the damage of the HMIP. The fatigue damage is accumulated in a two-slope S-N relationship and represented as equivalent fatigue load (EFL) in a single-slope S-N relationship, which can be conveniently compared to the fatigue capacity represented in single-slope S-N curves. Following the format of the fatigue design categories in Eurocode, a threshold of 5 million cycles is selected as the transition from the first slope (m=3) to the second slope (m=5) in the experiment-based S-N curve.

Figure 9.6 shows the failure data points from Table 9.5 and the corresponding lower and upper bound S-N curve along with the lower bound S-N curves suggested by AASHTO code and

Eurocode. Category E in AASHTO is the design category of the target HMIP design while a lower category (E′) is assumed due to the pre-cracked conditions (Magenes 2011). The Eurocode category 40 was also included based on the same first slope level to category E′ in AASHTO while exhibiting a second slope and a different CAFL level. The data corresponds well falling between lower and upper bounds while the lower bound is relatively lower compared to category E and E′ from AASHTO as expected. The shaded area shows cycles above 5 million where Eurocode suggests a second slope S-N curve. As further illustrated in Figure 9.6, five experimental data points beyond the 5-million-cycle threshold were used to determine the 90% bound assuming a second slop of m=5. Adopting a two-slope S-N curve is justified since smaller stress ranges cause less fatigue damage than the extended single-slope S-N line from high stress ranges. The slope (m=5) and the 5-million-cycle threshold are recommended by past studies (Lassen and Rẻcho 2006 and EN1993 2002). The results indicate that the lower bound from the experiment represents the pre-cracked HMIPs well and that none of the categories in current codes are sufficient to represent the target HMIP of interest.

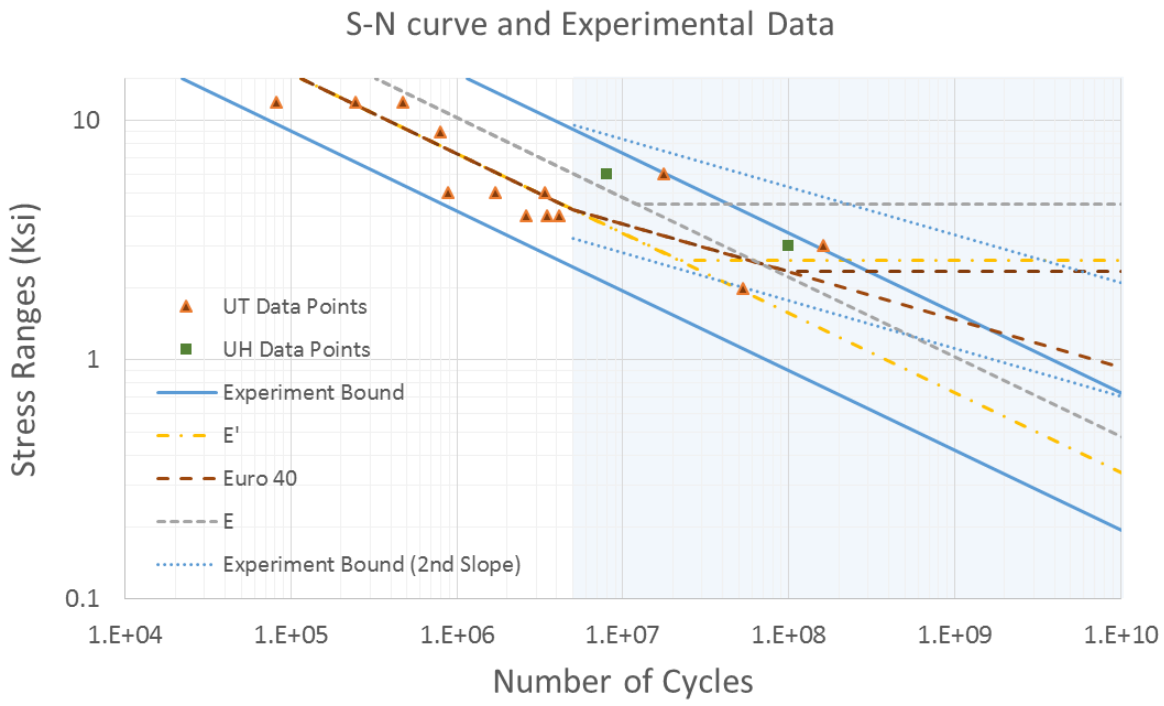

Figure 9.6: S-N Curves for Unadjusted Experimental Fatigue Data

S-N Curves for Adjusted Fatigue Data

According to Goodman (1919), the mean stress utilized in a fatigue experiment can have a significant impact on the test results in that higher mean stresses result in fewer number of cycles to failure at any specific stress range. To account for the different mean stresses used in the fatigue experiment, an adjustment equation (Equation 9.22) proposed by Goodman is introduced transforming the data points to the same mean stress of reference. σ_a is the stress cycle amplitude (stress ranges), σ_{aT} is the transformed alternating stress amplitude (stress ranges with zero mean),

σ_m is the actual mean stress in the fatigue test, and σ_{uts} is the material ultimate strength which is 71 ksi from the HMIP specimen.

$$\frac{\sigma_a}{\sigma_{aT}} = 1 - \frac{\sigma_m}{\sigma_{uts}} \qquad \textit{Equation 9.22}$$

Table 9.7 shows the adjusted data where all mean stresses are normalized to 6 ksi, which is the mean stress level utilized in fatigue experiments in this project. As a result of this adjustment, the stress ranges are increased for experiments with mean stresses higher than 6 ksi, and decreased for those with mean stresses lower than 6 ksi. In other words, to maintain the same level of fatigue damage, lowering mean stresses results in increasing stress ranges. The adjustment in stress ranges resulted in a different group of fatigue constants (*A*) which is plotted in a log-normal probability plot to show the validity of the distribution assumption (Figure 9.7). The adjusted data falls more closely to the theoretical straight line in the probability plot compared to using unadjusted data. A goodness-of-fit test (Anderson and Darling 1954) is also performed on the adjusted data showing the log-normal assumption is not rejected at a 95% significance level. The adjusted data resulted in a slightly different distribution for (*A*) (parameters are shown in Table 9.8). The adjusted parameters show a slightly smaller variation (ζ_A) with a narrower band and lower level of uncertainty, yet still high compared to parameters provided by AASHTO.

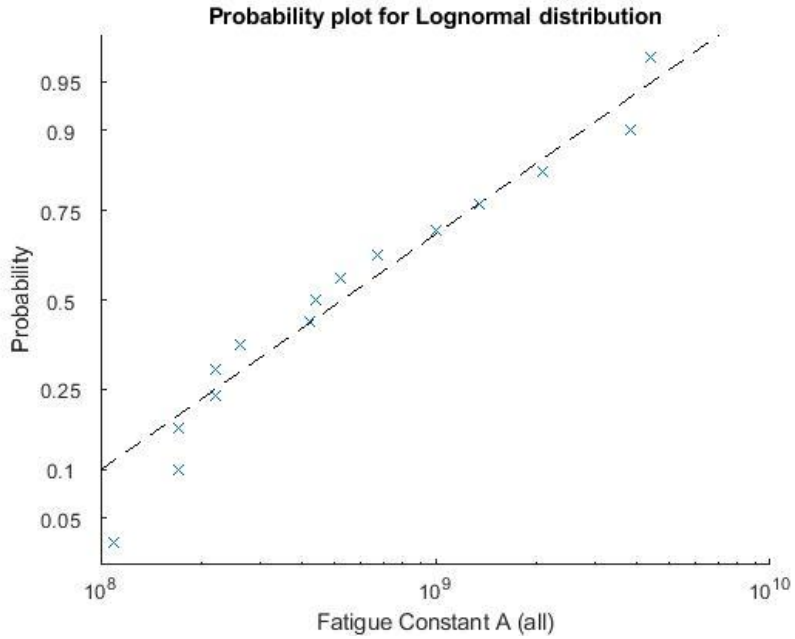

Figure 9.7: Log-Normal Probability Plot for Adjusted Experimental Fatigue Data

Table 9.7: Experimental Fatigue Data - Adjusted

	Mean Stress (ksi)	Stress Ranges (σ_R) (ksi)	Number of Cycles (N)	Fatigue Constant (A) (10^8 ksi^3)
Project 0-6829 (UT)	6	6	17700000	38.2
	6	4	2600000	1.7
	6	4	4100000	2.6
	6	4	3500000	2.2
	6	2	53000000	4.2
	6	3	162500000	43.9
	6	9.45	790000	6.7
Pool (2010)	6	12.84	81326	1.7
	6	12.84	245746	5.2
	6	12.84	470711	10
Belivanis (2013)	6	5.05	885000	1.1
	6	5.05	1700000	2.2
	6	5.05	3400000	4.4
Project 0-6830 (UH)	6	5.52	8000000	13.5
	6	2.76	99000000	20.8

Table 9.8: Statistical Parameters for the Fatigue Constant A Using Adjusted Fatigue Data

Category	λ_A ($\mu_{\ln(A)}$)	ζ_A ($\sigma_{\ln(A)}$)	$\ln(A_D)$	A_D (x10^8)
A	25	0.64	23.95	252.1
B	23.89	0.42	23.2	119.2
B'	23.18	0.4	22.52	60.5
C	22.95	0.46	22.2	43.6
D	22.2	0.43	21.49	21.6
E	21.26	0.29	20.78	10.6
E'	20.43	0.4	19.77	3.9
Experiment	20.12	1.15	18.23	0.8

The adjusted data points (filled markers) along with original data points (hollow markers) are plotted in Figure 9.8. The adjusted upper and lower bound are also plotted along with the lower bound S-N curves suggested by AASHTO and Eurocode. The difference of the adjusted data points may not seem to have a significant effect, however, the adjusted results is more realistic by taking the mean stresses into account. Therefore, the lower bound S-N curve and the corresponding distribution parameters of the fatigue constant (*A*) is proposed based on the adjusted data.

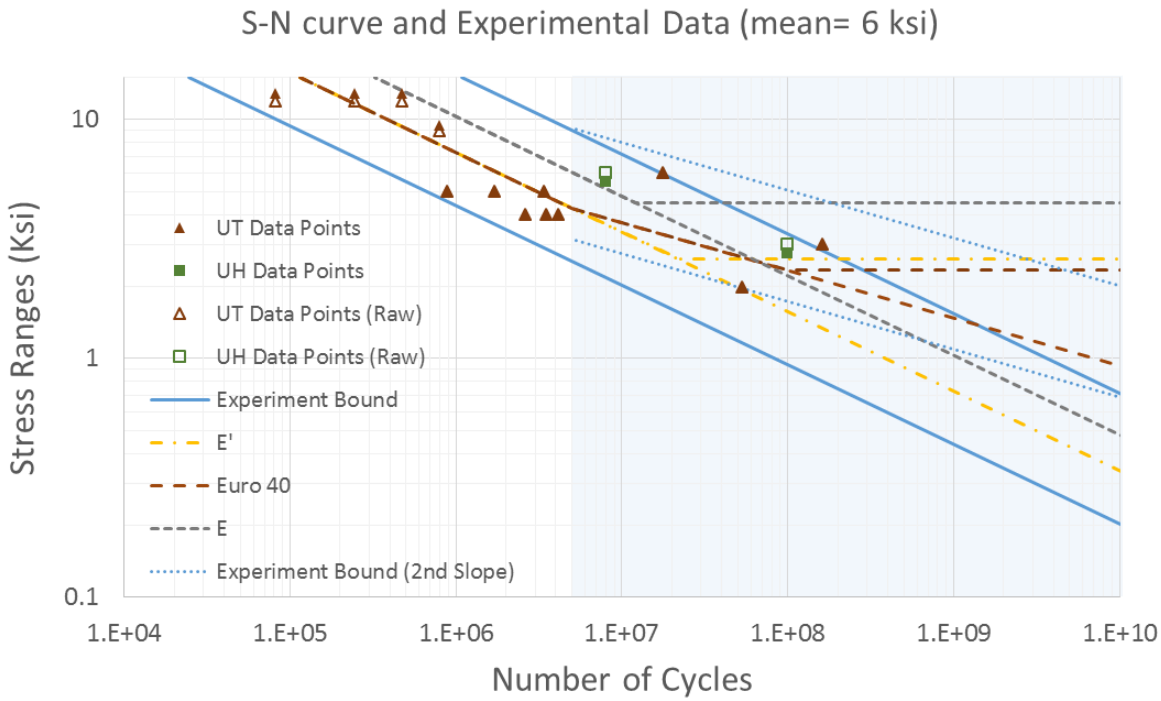

Figure 9.8: S-N Curves for Adjusted Experimental Fatigue Data

S-N Curves for Selected Fatigue Data

The results from the fatigue tests show that the fatigue capacity is largely affected by the initial condition of the tested bends around the HMIP at the base. Two data points in Table 9.7 (first and sixth row) showing a relatively higher fatigue parameter (A) is a result of test specimens orientated in a way where the bends with the least cracks are being tested. To more accurately represent the capacity of pre-cracked HMIPs, the data resulting from initially uncracked bends are neglected. Since the experimental setup and the loading protocol from the UH fatigue tests are different from tests carried out at UT, UH data points are also neglected to ensure consistency. A probability plot is created for the selected data to show the validity of the log-normal assumption (Figure 9.9) which shows a good fit. A goodness-of-fit test (Anderson and Darling 1954) is also tested on the selected data showing the log-normal assumption is not rejected at a 95% significance level.

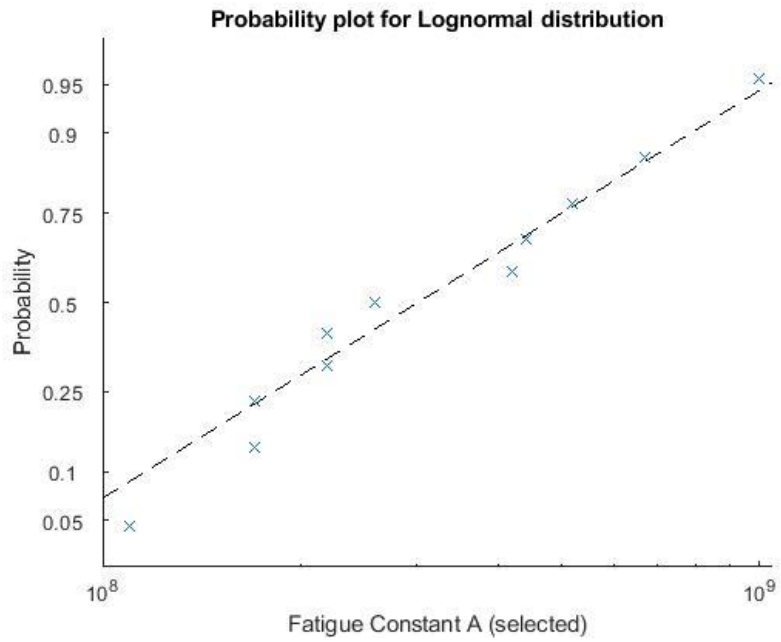

Figure 9.9: Log-Normal Probability Plot for Selected Fatigue Data

By only using selected fatigue data from tests at the University of Texas at Austin, the resulting parameters (Table 9.9) show a slightly lower λ_A and a smaller ζ_A indicating lower uncertainty when compared to the parameters using all fatigue data. The smaller ζ_A is consistent with the parameters provided by AASHTO which is expected, since considering the fatigue data from HMIPs with cracks and no cracks introduces more uncertainty. As a result, though the slightly lower λ_A reflects the lower mean fatigue capacity of the pre-cracked bends, the reduced uncertainty (characterized by ζ_A) from using selected fatigue data actually resulted in a higher design fatigue constant, A_D, compared to that when using all fatigue data (Table 9.8).

Table 9.9: Statistical Parameters for the Fatigue Constant A Using Selected Fatigue Data

Category	λ_A ($\mu_{\ln(A)}$)	ζ_A ($\sigma_{\ln(A)}$)	$\ln(A_D)$	A_D ($\times 10^8$)
A	25	0.64	23.95	252.1
B	23.89	0.42	23.2	119.2
B'	23.18	0.4	22.52	60.5
C	22.95	0.46	22.2	43.6
D	22.2	0.43	21.49	21.6
E	21.26	0.29	20.78	10.6
E'	20.43	0.4	19.77	3.9
Experiment	19.56	0.67	18.46	1

Figure 9.10 shows the bandwidth between the upper and lower bound of the fatigue constant A resulting from using selected fatigue test data. Compared to the bandwidths shown in Figure 9.6 and Figure 9.8 where all fatigue data are used, this bandwidth is significantly smaller

and is more similar to the bandwidth provided by AASHTO for other categories. Although the center of the band is higher for all-data results than for selected-data results, the narrower band actually results in a higher lower bound for design as discussed in the previous paragraph. The resulted parameters from selected data, representing the pre-cracked conditions, are suggested in this study to reflect the more severe poles that is in TxDOT's prime interest. Also, the parameters are more consistent with those from AASHTO. More importantly, since the selected fatigue test data are not sufficient to determine a bound for the second slope region, the assumption proposed by Eurocode is adopted where the second slope initiates at 5 million cycles.

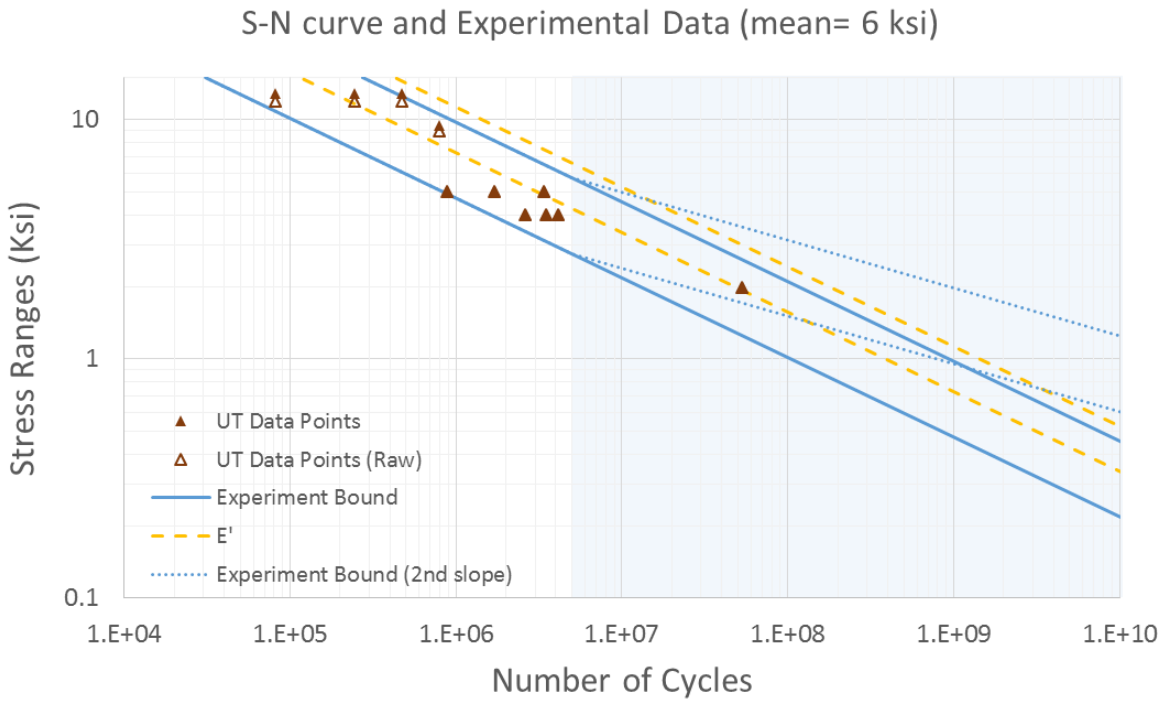

Figure 9.10: S-N Curves for Selected Experimental Fatigue Data

Uncertainty in Distribution Parameters

The sample distribution parameters of the fatigue constant A, (λ_A and ζ_A), is only an estimation of the true distribution parameters. The limited data samples of A from the experiment results in high uncertainties estimating the true distribution parameters. The uncertainty of the parameters is addressed based on the known distribution of the sample parameters with respect to the true parameters. It is known that the distribution of the sample mean with true standard deviation unknown follows the Student's t-distribution (or simply the *t*-distribution) as follow

$$T = \frac{\mu_{\ln A} - \lambda}{\sigma_{\ln A}/\sqrt{n}} \qquad \textbf{\textit{Equation 9.23}}$$

where T is a Student's t- distribution random variable with n-1 degree of freedom. With the sample mean (λ_A) and standard deviation (ζ_A) of ln(A) known, the distribution of the true parameter λ can be determined by simulating T. Similarly, the distribution of the true standard deviation is known to follow the Chi-square distribution as follow:

$$C = \frac{(n-1)\sigma_{\ln A}{}^2}{\zeta^2} \qquad \textbf{\textit{Equation 9.24}}$$

where C is a Chi-square distribution random variable with n-1 degree of freedom. With the sample standard deviation of ln(A) known, the distribution of the true parameter ζ can be determined by simulating C.

To illustrate the influence of the uncertainty of distribution parameters, a 95% confidence interval for the design S-N curve is determined using Monte-Carlo simulation of the true parameters λ and ζ. 100,000 simulations of the two parameters resulted in 100,000 realization of design fatigue constant A_D using equation

$$A_D = e^{(\lambda - 1.64\zeta)} \qquad \textbf{\textit{Equation 9.25}}$$

where the 2.5 and 97.5 percentile of A_D is determined as 0.5×10^8 (ksi^3) and 1.6×10^8 (ksi^3) respectively whereas the A_D obtained assuming sample parameters as true parameters is 1.0×10^8 (ksi^3). The uncertainty of the design S-N curve (experimental lower bound) is presented with a bound in dotted green lines (Figure 9.11). Although the width of the band due to parameter uncertainty does not seem wide in the log-log graph, the high uncertainties can be seen directly since the upper bound A_D is almost three times as large as the lower bound A_D. However, if the number of samples from the experiment is increased, the uncertainty represented by the green dotted lines may be reduced. The fatigue life analysis carried out throughout this study assumes the sample parameter reflects the true parameters neglecting the uncertainties due to small sample size. However, the effect on the analyzed results is illustrated in Section 9.5.4 to show the wide range of results when uncertainty of parameters are considered. The 95% confidence interval specified by the 2.5 and 97.5 percentile of the distribution of A_D is determined respectively (0.5 and 1.6 ($\times10^8$ksi^3)) where the A_D that considers no uncertainty in the distribution parameters results in between (1.0 ($\times10^8$ksi^3)).

The fatigue life analysis in this study utilizes the sample parameters resulted from the experiment without including the uncertainty from sample sizes. In other words, the sample parameters are assumed to be close to the true parameters and are sufficient to represent the whole population which neglects the effect of sample size. The effect of sample size to analyzed fatigue life is discussed and illustrated in Section 9.5.4.

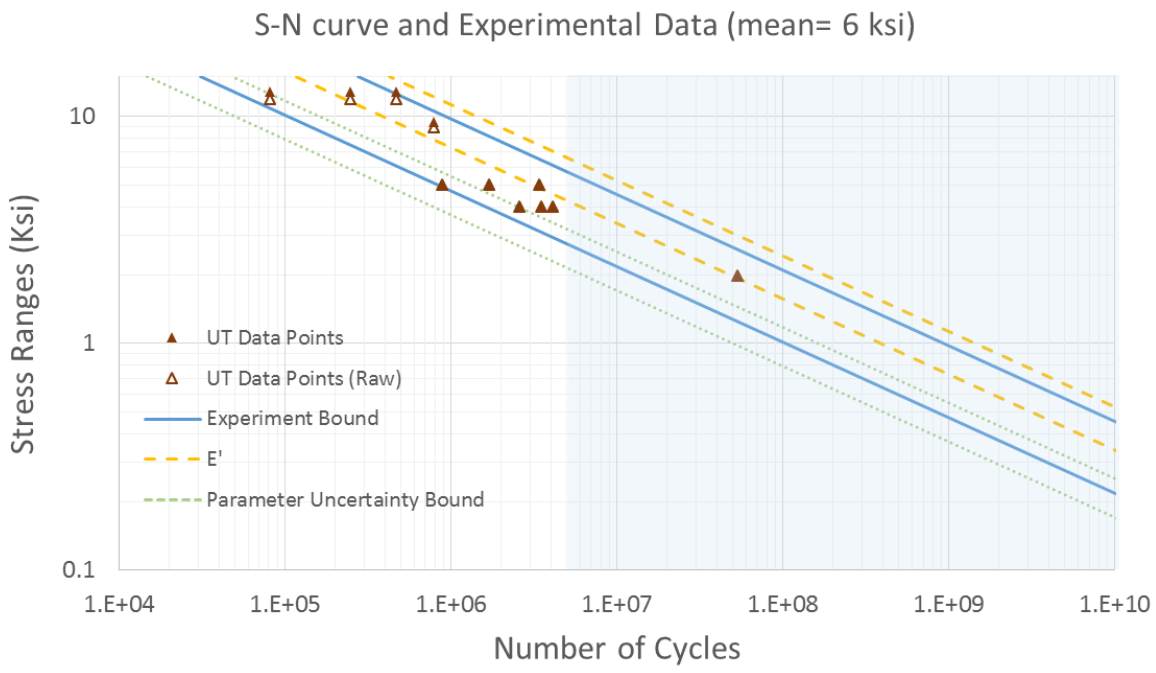

Figure 9.11: Uncertainty in Fatigue Parameters due to Limited Experimental Fatigue Data

9.4 Wind-Induced Fatigue Loading

Wind-induced vibration is the main cause of the fatigue loading experienced by HMIPs in service. Therefore, the fatigue behavior of in-service HMIPs is influenced by their surrounding wind environment in addition to their structural design details.

Efforts have been made in the past to estimate the fatigue damage of HMIPs under different wind environments. Chang (2007) attempted to construct a structural model that uses wind force histories derived from simulated wind histories to simulate the HMIP response. The simulated response has similar trend to the average response observed from the field, however, the scatter of the observed field data is difficult to address in the model. Also, assumptions such as a fixed wind profile or a fixed turbulence intensity do not truly reflect the complexity of the wind environment in the field. Magenes (2011) conducted a field study attempting to find the relation between the collected wind speed and the measured response. The histogram of the collected stress ranges are used to calculate the accumulated fatigue damage using the Miner's rule (Miner 1953). However, the histogram is basically related to the wind distribution (wind speed and wind direction) at the measured location and it may not be valid for other locations.

This study proposes a method, similar to the method used by Magenes (2011) but more comprehensive, to relate the vibration-induced damage to the wind speed and wind direction measured in the field. Specifically, the proposed method allows the information collected from a given site to be used at other sites for the same HMIP design and different wind distribution. In addition, the proposed method can be used to calculate the expected damage on any location around the circumference of the HMIP. To introduce the proposed method, it will be shown first how strain/stress time histories are created around the circumference of the pole in order to determine the fatigue damage resulting from stress ranges around the perimeter of the HMIP. The

introduction of the use of equivalent fatigue load (EFL) instead of effective stress ranges (S_{RE}) is illustrated next. Following, the EFL calculation based on two-slope S-N curve assumption is introduced. The calculated two-slope EFLs around the perimeter of the HMIP are later categorized into different wind speeds and wind directions. Further, a method to determine the cumulative damage using the EFLs and a given wind distribution is introduced along with the determination of expected life. Using both deterministic and probabilistic procedures, a reliability-based framework for assessing the fatigue life of in-service HMIPs with pre-existing cracks is developed and presented. The reliability assessment based on the observed wind data from the field and the collected wind information from NOAA documented in Chapter 4 is illustrated and compared. The uncertainties resulting from different aspects are discussed in the end to address how sensitive the concluded results are to various assumptions.

9.4.1 Transformation of Strain-Time Histories

The strain-time histories measured from strain gages are used to determine the fatigue load and in-turn to calculate the fatigue damage over a specified period. Since the measured strain-time histories are related to the incoming wind directions relative to the locations where the strain histories are measured, strain histories around the pole are needed to correlate with the wind directions. However, due to the limited number of installed strain gages, a method should be adopted to create the strain histories around perimeter of the pole (Ahern and Puckett 2010). Strain-time histories anywhere around the circumference of the pole can be created with any pairs of strain histories that are measured on perpendicular faces at the same height around the pole using Equation 9.26 with an orientation shown in Figure 9.12. If there are more than one pair of perpendicular strain histories, the time histories determined from each pair are averaged.

$$\varepsilon_\theta(t) = \varepsilon_N(t) \cdot \cos\theta + \varepsilon_E(t) \cdot \sin\theta \quad \text{or}$$

Equation 9.26

$$\varepsilon_\theta(t) = \varepsilon_S(t) \cdot \cos(\pi + \theta) + \varepsilon_W(t) \cdot \sin(\pi + \theta)$$

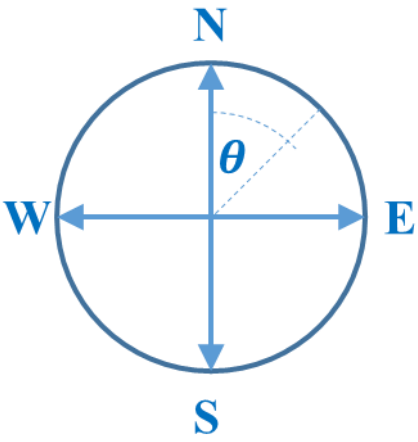

Figure 9.12: Transformation of Strain-Time Histories

9.4.2 Equivalent Fatigue Load (EFL)

Refer to Chapter 6 (Section 6.4.4)

9.4.3 EFL Calculations Using Two-Slope S-N Curves

Refer to Chapter 6 (Section 6.4.4)

9.4.4 EFL with Respect to Wind Direction

With knowledge of the wind direction in each 5-minute data segment and using Equation 9.26, strain-time series can be generated at any location around the perimeter of the HMIPs. In this study, EFL values in different directions relative to the wind, θ_r, are determined by dividing the perimeter of the HMIPs to 12 slices, each making a 30° angle. Although EFL for all 12 directions can be obtained, only six different θ_r values are need since $EFL(U, \pi + \theta_r) = EFL(U, \theta_r)$. Figure 9.13 shows how the EFLs around the pole are categorized into bins of wind speed and relative wind direction.

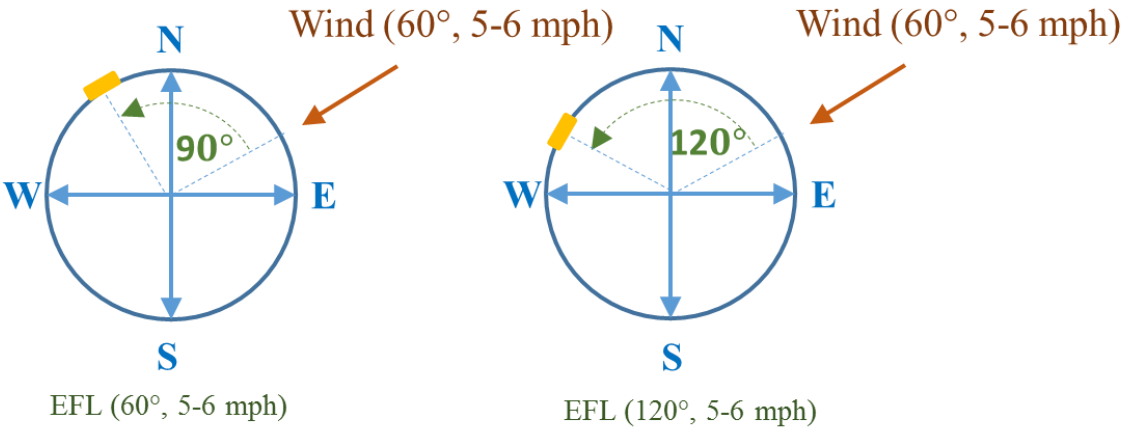

Figure 9.13: EFLs at Different Locations Relative to a Specific Wind Direction and Wind Speed (Wind Direction Fixed)

By grouping the calculated EFLs based on the wind speed and relative wind direction, the effect of wind speed and relative wind direction can be easily observed as shown in Chapter 6. Since the grouped EFLs are scattered in nature, the expected EFL is determined using Equation 9.27 to represent the EFL for any specific bin.

$$E(EFL) = \frac{\sum_k^N EFL_k}{N} \qquad \textit{Equation 9.27}$$

In Equation 9.27, N is the number of EFLs in the selected wind speed and relative direction bin and EFL_k are the scattered EFLs in that same bin. The database then conveniently yields an expected $EFL(U, \theta_r)$ matrix or table of fatigue damage information conditional on a wind speed bin, U, and for a direction of the wind relative to the location of interest, θ_r. Note that the EFL described above can either be determined using one-slope or two-slope S-N curves described in the previous section.

Figure 9.14 shows the computed $EFL(U, \theta_r)$ data for the pole monitored in Austin. The higher EFLs at lower wind speed and in the cross-wind direction, indicated by the 90 line in the figure, reflects the higher fatigue damage caused by VIV responses. Furthermore, the higher EFLs at higher wind speed region are caused by buffeting responses which are significant in all directions. The EFL data allows the fatigue damage of HMIP at any specified location around the perimeter of the pole to be evaluated with a specific wind distribution (probability of different wind speeds and directions) from any HMIP location. However, factors other than wind speed and relative wind direction may affect the EFL results in different areas or locations as discussed in Chapter 6. To address the different EFL results from all monitored sites, an average EFL (Figure 9.15) is used as a representative EFL for a more general result. An envelope EFL (Figure 9.16), which represents the highest EFL from all sites for all respective wind speed and wind direction is also proposed for a more conservative result.

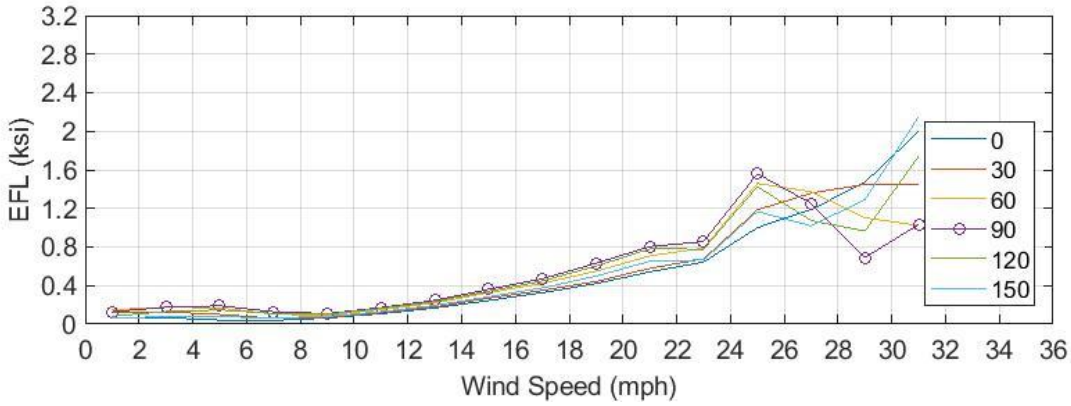

Figure 9.14: Two-Slope EFLs Calculated for the Monitored Pole Site in Austin

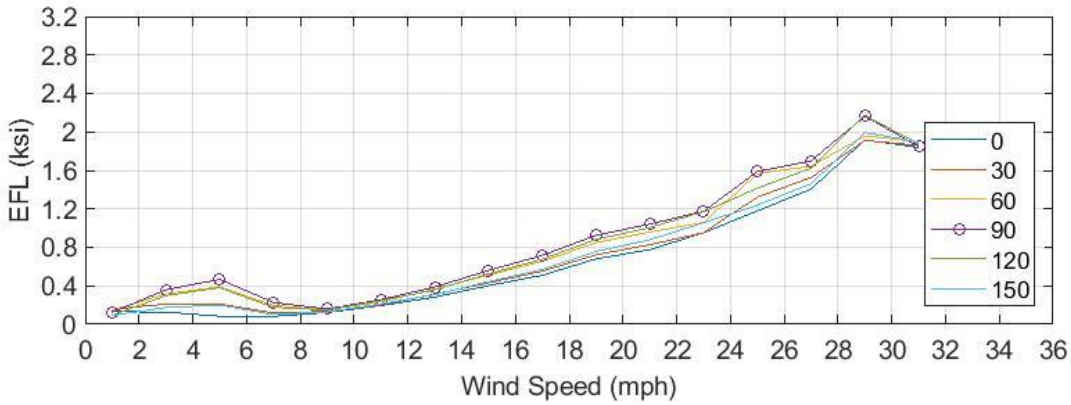

Figure 9.15: Average Two-Slope EFLs for all Monitored Pole Sites

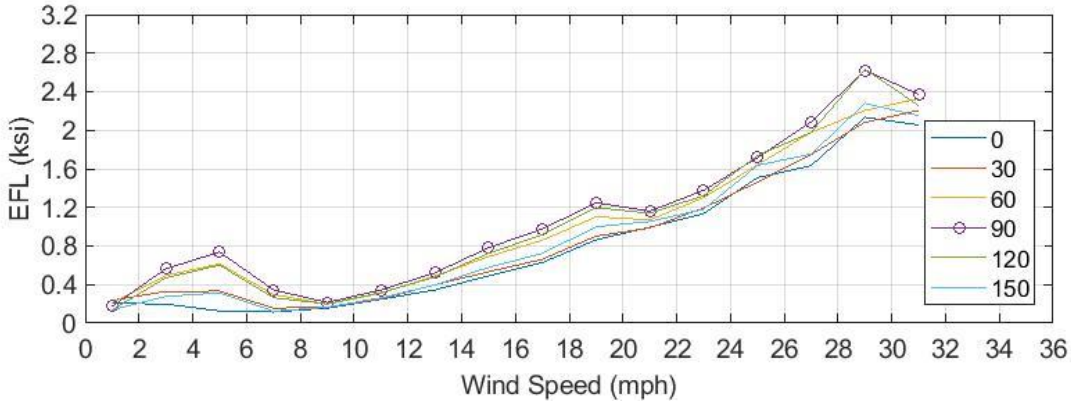

Figure 9.16: Envelope Two-Slope EFL for all Monitored pole sites

9.4.5 Cumulative Fatigue Damage for a Given Wind Distribution

The cumulative fatigue damage at any location around the perimeter of the pole can be calculated using the values of the two-slope EFL and the wind probability distribution. As an example, Table 9.10 presents the probability of occurrence for wind speeds and directions, $P(U, \theta_w)$ or denoted as α_{ij}, in Austin. The probability of wind speeds and directions is generally presented graphically using wind roses (Chapter 6). Note that although the wind probability here is the same as the one used in determining the EFLs for the monitored pole site in Austin, any other wind distribution can be utilized in calculating the cumulative fatigue damage. Moreover, 2-min average instead of 5-min average wind information is used hereafter to correspond to the average duration used in NOAA sites. The EFLs calculated previously in Chapter 6 are also adjusted using a 2-min duration to maintain consistency.

Table 9.10: Probability of Occurrence for Different Wind Speeds and Directions, $P(U, \theta_w)$ (%)

P(U, θw) %		2-min Average Wind Speed, U (mph)															
		1-2	3-4	5-6	7-8	9-10	11-12	13-14	15-16	17-18	19-20	21-22	23-24	25-26	27-28	29-30	31-32
2-min Average Wind Direction, θw	0° (N)	0.77	2.09	1.53	1.36	1.07	0.66	0.34	0.08	0.01	0.00	0.00	0.00	0.00	0.00	0.00	0.00
	30°	0.55	2.71	2.92	2.03	1.23	0.53	0.11	0.02	0.00	0.00	0.00	0.00	0.00	0.00	0.00	0.00
	60°	0.32	1.21	0.88	0.35	0.12	0.04	0.00	0.00	0.00	0.00	0.00	0.00	0.00	0.00	0.00	0.00
	90° (E)	0.24	0.69	1.06	0.80	0.42	0.19	0.09	0.03	0.01	0.01	0.00	0.00	0.00	0.00	0.00	0.00
	120°	0.36	1.07	2.13	1.32	0.63	0.21	0.08	0.02	0.00	0.00	0.00	0.00	0.00	0.00	0.00	0.00
	150°	0.40	0.93	2.18	2.46	2.00	1.31	0.68	0.31	0.10	0.02	0.01	0.00	0.00	0.00	0.00	0.00
	180° (S)	0.43	0.99	2.96	5.29	5.63	5.02	3.49	1.96	0.94	0.38	0.11	0.03	0.01	0.00	0.00	0.00
	210°	0.61	0.94	2.02	2.75	3.08	3.22	2.46	1.41	0.69	0.34	0.15	0.06	0.01	0.00	0.00	0.00
	240°	0.88	0.94	0.77	0.55	0.33	0.24	0.14	0.05	0.03	0.01	0.00	0.00	0.00	0.00	0.00	0.00
	270° (W)	0.75	0.59	0.27	0.16	0.09	0.05	0.01	0.00	0.00	0.00	0.00	0.00	0.00	0.00	0.00	0.00
	300°	0.75	0.80	0.41	0.45	0.34	0.24	0.18	0.09	0.05	0.01	0.00	0.00	0.00	0.00	0.00	0.00
	330°	0.83	1.28	0.80	0.66	0.59	0.48	0.27	0.14	0.05	0.01	0.00	0.00	0.00	0.00	0.00	0.00

An example is presented here to illustrate how fatigue damage at a specific location around the perimeter of the pole is determined from a certain wind speed and direction bin. The fatigue damage at a specific location (e.g. 150°) around the perimeter of the pole resulting from a given wind speed and direction bin (e.g. $= 5\sim6, \theta_w = 240°$) is calculated as indicated in Equation 9.28.

$$\begin{aligned} &Damage(150°|U = 5\sim6, \theta_w = 240°) \\ &= P(U = 5\sim6, \theta_w = 240°) \cdot T \cdot f_1 \cdot EFL(U = 5\sim6, \theta_r = 90°)^3 \\ &= 0.0077 \cdot T \cdot 0.2804 \cdot EFL(U = 5\sim6, \theta_r = 90°)^3 \end{aligned} \qquad \textit{Equation 9.28}$$

Note that the target location is defined as the clockwise angle from North. As demonstrated in Section 9.4.2, T is the analyzed duration in seconds and f_1 is the predetermined first mode frequency used in determining the EFLs. The direction relative to the wind (θ_r) is 90 degrees since the wind direction relative to the target location is perpendicular as shown in Figure 9.17. With the probability of occurrence of wind from Table 9.10 and the EFL table taken from the corresponding bin, the fatigue damage can be calculated for an assumed duration, T. Note that fatigue failure is expected when the fatigue damage accumulated from all wind bins equals the fatigue constant (A) of the target design.

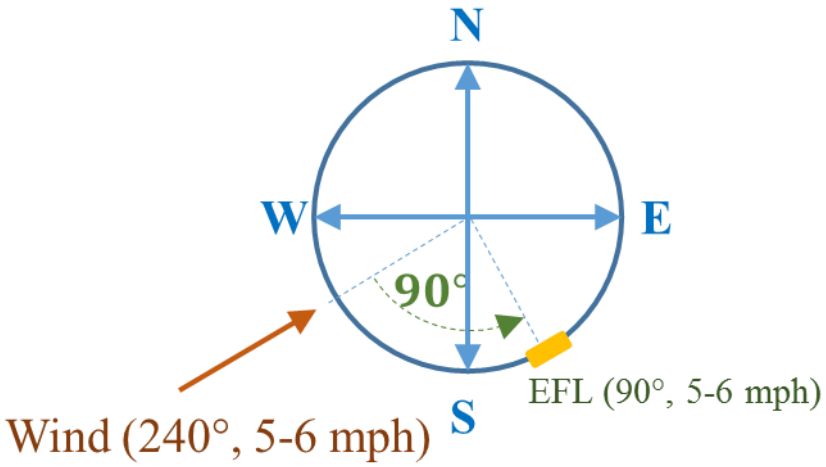

Figure 9.17: Evaluation of EFLs or Fatigue Damage Caused by a Certain Wind Speed and Direction

Figure 9.18 shows schematically how fatigue damage is accumulated for a target location (e.g., 150°) from different wind directions and their corresponding EFLs. First, the probability of wind in opposite directions are added since they correspond to the same EFL. Furthermore, the rows in the wind probability table are rearranged (Table 9.11), for a specified location around the pole (e.g. 150), such that the wind directions correspond to the relative directions in the EFL table (Table 9.12).

As explained in the previous section, the EFLs calculated on opposite sides of the pole results in the same value which means wind from opposite direction results in the same EFL. Thus, the wind probability table of interest is reduced to six directions by grouping wind probabilities in opposite directions together which results in the same number of rows to the EFL table. Also, by rearranging the rows in the wind table according to a target location around the pole, a new wind probability table (β_{ij}) is introduced (Table 9.11). The accumulated damage can then be easily determined by involving the adjusted wind probability table (β_{ij}) and the EFL table (Table 9.12).

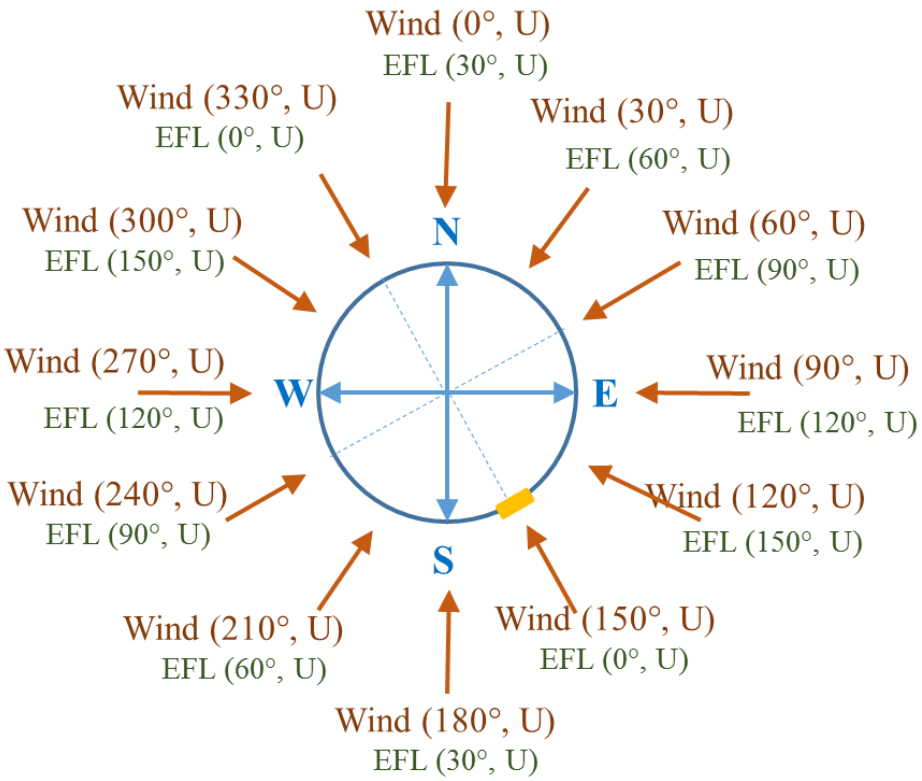

Figure 9.18: Accumulated Fatigue Damage at a Specific Location on the Perimeter of HMIPs Caused by Winds with different directions

Table 9.11: Grouped and Rearranged Probability of Occurrence (β_{ij}), $P(U, \theta_w)$ (%)

		2-min Average Wind Speed, U (mph)															
P(U, θ_w) %		**1-2**	**3-4**	**5-6**	**7-8**	**9-10**	**11-12**	**13-14**	**15-16**	**17-18**	**19-20**	**21-22**	**23-24**	**25-26**	**27-28**	**29-30**	**31-32**
Wind Direction	**150° 300°**	1.23	2.21	2.98	3.12	2.59	1.79	0.95	0.45	0.14	0.03	0.01	0.00	0.00	0.00	0.00	0.00
	0° 180°	1.20	3.08	4.49	6.64	6.70	5.67	3.83	2.04	0.95	0.39	0.11	0.03	0.01	0.00	0.00	0.00
	30° 210°	1.16	3.65	4.94	4.78	4.31	3.74	2.57	1.43	0.69	0.34	0.15	0.06	0.01	0.00	0.00	0.00
	60° 240°	1.20	2.15	1.65	0.89	0.45	0.29	0.14	0.06	0.03	0.01	0.00	0.00	0.00	0.00	0.00	0.00
	90° 270°	0.99	1.28	1.33	0.96	0.52	0.24	0.10	0.04	0.01	0.01	0.00	0.00	0.00	0.00	0.00	0.00
	120° 300°	1.11	1.87	2.53	1.77	0.97	0.45	0.26	0.11	0.05	0.01	0.01	0.00	0.00	0.00	0.00	0.00

Table 9.12: Expected EFLs (EFL_{ij}) for the Monitored Pole Site in Austin

EFL (ksi)		2-min Average Wind Speed, U (mph)															
		1-2	3-4	5-6	7-8	9-10	11-12	13-14	15-16	17-18	19-20	21-22	23-24	25-26	27-28	29-30	31-32
Relative Direction	0° (A)	0.07	0.07	0.04	0.04	0.06	0.11	0.17	0.25	0.33	0.42	0.54	0.64	1.00	1.19	1.47	2.00
	30°	0.12	0.13	0.10	0.06	0.07	0.12	0.18	0.27	0.35	0.44	0.58	0.68	1.19	1.36	1.45	1.45
	60°	0.15	0.18	0.17	0.10	0.09	0.15	0.22	0.33	0.42	0.55	0.71	0.79	1.46	1.37	1.10	1.02
	90° (C)	0.13	0.17	0.19	0.13	0.11	0.17	0.25	0.36	0.47	0.63	0.80	0.86	1.56	1.25	0.69	1.03
	120°	0.08	0.13	0.15	0.11	0.10	0.16	0.23	0.34	0.45	0.60	0.78	0.78	1.43	1.07	0.97	1.74
	150°	0.06	0.08	0.08	0.06	0.08	0.13	0.19	0.28	0.38	0.50	0.65	0.67	1.17	1.02	1.29	2.15

The accumulated damage for the specified location (e.g. 150) is determined by involving the rearranged wind probability table, represented by β_{ij}, and the EFL table, represented by EFL_{ij}, through Equation 9.29.

The cumulative damage at the target location (e.g., 150°) can then be determined using Equation 9.29.

$$Damage(150°) = \sum_{all\ U} \sum_{all\ \theta_r} Damage(150°|U, \theta_r),$$

$$\theta_r = 0, 30, 60, 90, 120, 150 \qquad \textit{Equation 9.29}$$

$$= \sum_{i=1}^{16} \sum_{j=1}^{6} \beta_{ij} \cdot T \cdot f_1 \cdot EFL_{ij}^3$$

In Equation 9.29, β_{ij} is the probability of occurrence listed in Table 9.11, EFL_{ij} is the equivalent fatigue load listed in Table 9.12, T is the total time of interest in seconds, and f_1 is the vibration frequency in first mode used in calculating the EFL in Section 9.4.

9.5 Assessment of Fatigue Life

The fatigue life of HMIPs can be estimated either deterministically or probabilistically. The deterministic method calculates the safe-life expectancy using the lower bound of the S-N curves (e.g. AASHTO suggested S-N curves) where a 5% probability of failure is inherent in the fatigue capacity. The probabilistic method, on the other hand, suggests a fatigue life according to a target probability of failure (or reliability index (β)) where uncertainties can be incorporated in the fatigue capacity, accumulated fatigue damage, and fatigue load. Both methods are first demonstrated with the field data from Austin as an example followed by a comprehensive assessment for other locations using wind information from NOAA documented in Chapter 4. The wide range of possible results and the uncertainty that is incorporated due to certain assumptions are discussed at the end.

By substituting the effective stress range (S_{RE}) with the equivalent fatigue load (EFL) and using the value of 3 as the slope of the S-N curve as suggested by AASHTO, the fatigue limit state function (Equation 9.11) can be rewritten as Equation 9.30. In addition, since the damage is accumulated from all wind speeds and wind directions, Equation 9.30 can be further refined into

Equation 9.31. The number of induced cycles from different wind speeds and directions (N_{ij}) can be calculated using the corresponding probability of occurrence and the assumed mode 1 vibration frequency. As such, the latter part of Equation 9.31 actually represents the accumulated damage illustrated previously in Section 9.4.5. The proposed fatigue limit state function in this study is then presented as Equation 9.32.

$$g(\Delta, A, EFL, N_e) = \Delta \cdot A - N_e(T) \cdot EFL^3 = 0 \qquad \textbf{\textit{Equation 9.30}}$$

$$g\left(\Delta, A, EFL_{ij}, N_{ij}\right) = \Delta \cdot A - \sum_{all\ \theta_r} \sum_{all\ U} N_{ij}(T) \cdot EFL_{ij}^3 = 0 \qquad \textbf{\textit{Equation 9.31}}$$

$$g\left(\Delta, A, EFL_{ij}, \alpha_{ij}\right) = \Delta \cdot A - \sum_{all\ \theta_r} \sum_{all\ U} \beta_{ij} \cdot T \cdot f_1 \cdot EFL_{ij}^3 = 0 \qquad \textbf{\textit{Equation 9.32}}$$

9.5.1 Deterministic Approach

The deterministic method assumes that the uncertainty resulting from the design fatigue constant (A_D) and the damage accumulation index are neglected. More specifically, in the deterministic method, a fixed "design" fatigue constant (A_D) is used to represent the fatigue resistance of the design detail. Although the fatigue constant is fixed and does not introduce any uncertainty, the "design" fatigue constant is set at a lower bound value corresponding to a 95% exceedance (5% probability of failure). The critical damage accumulation index (Δ) in the deterministic method is set to 1. The cumulative damage is calculated deterministically using Equation 9.29. The deterministic analysis is carried out by assuming various fatigue capacity described by the S-N curves, or design fatigue constant (A_D), and the wind induced fatigue demand described by the average or envelop two-slope EFL (EFL_{ij}) with wind distribution (α_{ij}) from Austin as an example. AASHTO Category E and E´ describing the fatigue capacity of the HMIPs are first analyzed to determine the fatigue life of assumed un-cracked and cracked HMIPs. The analysis are later performed by using the fatigue capacity determined experimentally, using all or selected data, to show the reduced fatigue life of pre-cracked HMIPs. Using average and envelop two-slope EFLs to describe the fatigue demand are both implemented in the deterministic analysis to show the influence of EFL assumptions.

AASHTO-Based S-N Curve

The groove-welded base detail without ground sleeves used by TxDOT is classified as AASHTO Category E fatigue detail (AASHTO 2015, Stam et al. 2011). However, due to the galvanization cracks, a lower capacity category, E′, is assumed for the in-service galvanized HMIPs. As shown in Table 9.2, the design fatigue constant (A) of Categories E and E′ are 10.6×10^8 and 3.9×10^8 ksi^3, respectively. Since the critical damage accumulation index (Δ) in the deterministic method is set to be equal to 1, the life expectancy can be estimated by rearranging Equation 9.32 into Equation 9.33. The assumed first-mode frequency (f_1) is used to calculate the EFLs is 0.2805 Hz and the T is the expected fatigue safe life in seconds.

$$T = \frac{A}{f_1 \cdot \sum_{all\ \theta_r} \sum_{all\ U} \beta_{ij} \cdot \left(EFL_{ij}\right)^3} \qquad \textit{Equation 9.33}$$

The wind probability distribution (α_{ij}) collected at the pole site in Austin (Table 9.10) is used here as an example to calculate the life expectancy in Austin for different locations (0°, 30°, 60°, 90°, 120°, 150°) around the perimeter of the HMIP (Figure 9.19). Only half of the locations around the pole are needed since the symmetric shape of the pole results in the same EFLs on opposite side of the pole. Besides the proposed average two-slope EFLs (Figure 9.15), the results from the more conservative envelop two-slope EFLs (Figure 9.16) is also presented here to show how different EFLs affect the fatigue safe life. In order to calculate the accumulated damage, the rows in the wind probability distribution are rearranged such that the wind direction in each row corresponds to the relative wind direction in the EFL table for a given target location around the pole. This new wind probability distribution (β_{ij}) can be easily seen as a function of the actual wind probability distribution ((α_{ij}) and the specified location.

The estimated life expectancy for each location around the pole are determined using the fatigue parameters from category E and E′ in AASHTO and the fatigue demand described by the average two-slope EFL and the envelop two-slope EFL (Table 9.13). Since the wind direction in North-South (0°) predominates at the monitored site in Austin, shorter life expectancy results in the East-West side of the pole is as observed due to the higher fatigue damage resulting from VIV in the cross wind direction.

The estimated life expectancy suggest that the lowest fatigue safe life for Austin poles near the monitored HMIP is around 350 years when assuming an AASHTO category E′ design and using an envelope EFL to represent the wind induced damage. The expected fatigue life increases to 952 years when category E, which is originally classified for un-cracked poles, is assumed. Furthermore, using the average two-slope EFL to represent the more general wind induced demand instead of envelop two-slope EFL that represents a more severe wind induced demand results in even longer fatigue life (2660 years if category E assumed). Note that the expected life determined deterministically incorporates a probability of failure of 5% from the proposed S-N curve.

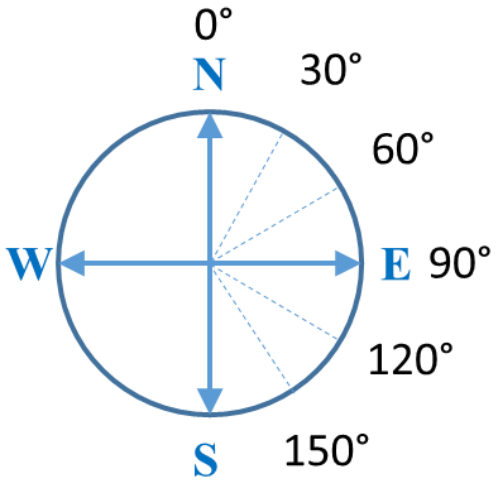

Figure 9.19: Locations Around the Perimeter of HMIPs Used to Determine the Accumulated Damage and the Corresponding Fatigue Safe Life

Table 9.13: Deterministic Estimation of the Fatigue Safe Life Using Fatigue Categories E and E′ (Years)

Location	Envelope EFL		Average EFL	
	Category E	Category E′	Category E	Category E′
0°	2029	747	5123	1885
30°	1713	630	4527	1666
60°	1202	442	3295	1212
90°	952	350	2660	979
120°	1030	379	2826	1040
150°	1514	557	3914	1440

Experiment-Based S-N Curve

Although fatigue categories E and E′ seem to show reasonable life performances in fatigue life as suggested in the previous section, the actual fatigue capacity of the galvanized, pre-cracked HMIPs have been found to significantly reduce the fatigue capacity below E′ category in AASHTO.

The capacity of pre-cracked HMIPs are determined through experiments performed in this study (Chapter 5). The fatigue capacity parameters are determined in Section 9.3.2 and listed in Table 9.8 and Table 9.9 in comparison with E and E′ categories in AASHTO. As illustrated in Section 9.3.2, due to variations in initial condition of bends and flats subjected to testing, all experimental data and selected experimental data are used in determining the distribution parameters of the fatigue constant (A). All experimental data include all the data from University of Texas at Austin (UT) and the data from University of Houston (UH) which uses a different experimental setup. The selected data excludes the experimental data that tested specimens with no initial cracks from UT. The selected data also excludes the experimental data provided by UH to avoid any uncertainties associated with different setup and testing methods.

The deterministic fatigue life is determined assuming the critical damage accumulation index (Δ) is 1 and the design fatigue constant (A_D) is resulting from experiments. Using Equation 9.33 and the wind probability distribution (α_{ij}) from Austin field data, the expected fatigue life for six different locations around the pole are determined. The estimated life expectancy for each location around the pole are determined using the design fatigue constant (A_D) resulting from the experiments (all experimental data and selected experimental data) and the fatigue demand described by the average two-slope EFL and envelop two-slope EFL. The results in Table 9.14 shows a significant decrease in expected life compared to those assuming AASHTO category E and E′ due to the lower design fatigue constant (A_D). Similarly, the shortest fatigue safe life at the East-West site of the pole (Location 90 in the table) results from the VIV response caused by the higher occurrence of wind direction in North and South. Longer fatigue safe life predicted from the selected experimental data which has a higher design fatigue constant due to the lower variability, described by ζ_A, of experiment conditions. Similar to Table 9.13, the use of envelope two-slope EFL representing a more severe wind induced fatigue demand resulted in a shorter life than when using an average two-slope EFL representing a more general wind induced fatigue demand. A 251 years of fatigue safe life is suggested for HMIPs near the monitored site in Austin, using the selected experimental data for the fatigue capacity and average two-slope EFL for the induced fatigue demand. Although the shortest fatigue safe life is 72 years, using all experimental data for the fatigue capacity and envelop two-slope EFL for the induced fatigue demand is considered too conservative. Including all experimental data introduces too much unnecessary uncertainties arising from the testing procedures and the initial state of the specimen which may not accurately reflect the pre-cracked poles. Using envelop two-slope EFL considers the highest induced fatigue damage observed from all monitored locations which may be too conservative. Though relatively shorter than the 2660 years of fatigue safe life when assuming AASHTO category E for the HMIP design detail, 251 years of fatigue safe life, assuming pre-cracked conditions, still exceeds the expected service life of 75 years. However, it should be noted that the example is based on the wind condition near the monitored pole in Austin, and that different wind conditions (occurrences of different wind speeds and directions) would result in different estimated fatigue safe life. Also, since the expected life is determined deterministically, it is important to understand that a probability of failure around 5% is incorporated.

Table 9.14: Deterministic Estimation of the Fatigue Safe Life Using Experimental Data (Years)

Location	Envelope EFL		Average EFL	
	All Data	Selected Data	All Data	Selected Data
0°	153	191	387	483
30°	129	162	342	427
60°	91	113	249	311
90°	72	90	201	251
120°	78	97	213	267
150°	114	143	295	369

9.5.2 Probabilistic Approach

The uncertainties in the S-N curves and in using the Miner's damage accumulation rule are included in the probabilistic determination of expected fatigue life. Instead of using fixed "design"

S-N curves or design fatigue constant (A_D), the probability distribution of the S-N curves, represented by the probability distribution of the fatigue constant (A) resulting from experiments, are used (Section 9.3.1). The fatigue constant (A), as illustrated in Section 9.3.1, follows a log-normal distribution with parameters λ_A and ζ_A. The uncertainty resulting from using the Miner's rule is encapsulated in the critical damage accumulation index (Δ), which is also found to fit a log-normal distribution with a mean value (μ_Δ) of 1.0 and coefficient of variance (δ_Δ) of 0.3. By including the distribution parameters of both the fatigue constant (A) and the critical damage accumulation index (Δ) into the fatigue limit state function (Equation 9.11 and Equation 9.32), expected fatigue safe life under various target reliability index (β) are determined.

The probabilistic analysis is carried out by assuming various fatigue capacities described by the S-N curves, or fatigue parameters (λ_A and ζ_A), and the wind induced fatigue demand described by the average or envelop two-slope EFL (EFL_{ij}) with wind distribution (α_{ij}) from Austin as an example. AASHTO Category E and E´ describing the fatigue capacity of the HMIPs are first analyzed to determine the fatigue life of un-cracked HMIPs. The analysis are later performed by using the fatigue capacity determined experimentally, whether using all or selected data, to show the reduced fatigue life of pre-cracked HMIPs. Using average and envelop two-slope EFLs to describe the fatigue demand are both implemented in the deterministic analysis to show the influence of EFL assumptions. Six different reliability indices (β) corresponding to different failure probabilities (P_f) are presented in this section to show how the expected lives varies significantly according to different target probabilities of failure. Although a reliability index (β) of 3.5 is inherited in the Strength I Limit State in AASHTO LRFD design, reliability index for fatigue limit state is not provided for HMIP structures and therefore a table including results under different reliability indices are provided in this study. (AASHTO 2013, ASCE 7 2016).

AASHTO-based S-N curve

As mentioned before, the groove-welded base detail without ground sleeve used by TxDOT is classified as AASHTO Category E fatigue detail (AASHTO 2013; Stam et al. 2011). However, due to the galvanization cracks, a lower capacity (fatigue category E′) was originally assumed for the HMIPs. Predictions of the fatigue life of in-service HMIPs using both fatigue categories E and E′ will be provided in this section for comparison. To introduce the uncertainty in the fatigue constant A, and the critical damage accumulation index Δ, the deterministic accumulated damage is moved to the right-hand side of the Equation 9.32. Taking the natural log of both sides will then result in a new limit state function presented in Equation 9.34.

$$\ln(\Delta \cdot A) = \ln\left(T \cdot f_1 \cdot \sum_{all\ \theta_r} \sum_{all\ U} \beta_{ij} \cdot \left(EFL_{ij}\right)^3\right)$$

Equation 9.34

$$\ln(\Delta) + \ln(A) - \ln(T) - \ln\left(f_1 \cdot \sum_{all\ \theta_r} \sum_{all\ U} \beta_{ij} \cdot \left(EFL_{ij}\right)^3\right) = 0$$

Since A and Δ are both random variables with lognormal distribution, their natural logs ($\ln(A)$ and $\ln(\Delta)$) will result in a normal distribution. With the accumulated damage being deterministic, the left-hand side of the limit state function in Equation 9.34 is also a normally

distributed random variable (X) with mean (μ_X) and standard deviation (σ_X). The parameters μ_X and σ_X can be determined from the distribution parameters for A and Δ as follow:

$$\mu_X = \lambda_\Delta + \lambda_A - \ln(T) - \ln\left(f_1 \cdot \sum_{all\ \theta_r} \sum_{all\ U} \beta_{ij} \cdot \left(EFL_{ij}\right)^3\right) \qquad \textbf{Equation 9.35}$$

$$\sigma_X = \sqrt{\zeta_\Delta^2 + \zeta_A^2}$$

In Equation 9.35, λ_Δ, ζ_Δ, λ_A and ζ_A are the parameters of the log-normal distribution of Δ and A, respectively. The mode-one frequency (f_1) used in calculating the EFLs is 0.2805 Hz, and the T is the expected fatigue life in seconds. The parameters λ_A and ζ_A for different fatigue categories in AASHTO were previously determined in Section 9.3.1 and listed in Table 9.4. Using Equation 9.36 and Equation 9.37, and the assumptions of the mean (μ_Δ) equal to 1 and coefficient of variance (δ_Δ) equal to 0.3, the parameters λ_Δ and ζ_Δ are determined as follows:

$$\lambda_\Delta = \ln(\mu_\Delta) - \frac{\zeta_\Delta^2}{2} = -0.019 \qquad \textbf{Equation 9.36}$$

$$\zeta_\Delta = \sqrt{\ln(1 + \delta_\Delta^2)} = 0.193 \qquad \textbf{Equation 9.37}$$

By combining Equation 9.3, Equation 9.12, and Equation 9.35, the relation between the reliability index (β) and the parameters for the limit state function can be presented as follows:

$$\beta = \frac{\mu_X}{\sigma_X} \qquad \textbf{Equation 9.38}$$

$$\beta = \frac{\lambda_\Delta + \lambda_A - \ln(T) - \ln(f_1 \cdot \sum_{all\ \theta_r} \sum_{all\ U} \beta_{ij} \cdot \left(EFL_{ij}\right)^3)}{\sqrt{\zeta_\Delta^2 + \zeta_A^2}}$$

By further rearrangement of Equation 9.38, the expected life of an HMIP associated with a target reliability index (β) can be determined using Equation 9.39.

$$T = \exp\left\{\lambda_\Delta + \lambda_A - \beta \cdot \sqrt{\zeta_\Delta^2 + \zeta_A^2} - \ln\left(f_1 \cdot \sum_{all\ \theta_r} \sum_{all\ U} \beta_{ij} \cdot \left(EFL_{ij}\right)^3\right)\right\} \qquad \textbf{Equation 9.39}$$

The wind probability distribution (α_{ij}) collected at the pole location in Austin (Table 9.10) is also used here as an example to calculate the life expectancy in Austin for different locations (0°, 30°, 60°, 90°, 120°, 150°) around the perimeter of the HMIP (Figure 9.19). Due to the symmetry of the pole's cross section, only half of the locations around the pole are used to estimate fatigue safe life. Both the proposed average two-slope EFL (Figure 9.15), and the envelop two-slope EFL (Figure 9.16) are used in the calculation of fatigue life. As mentioned in Section 9.4.5,

the row in the wind probability table is rearranged corresponding to the EFL table for a given target location to determine the fatigue safe life. Target reliability indexes in the range of 3.5 to 1.28 (corresponding to the probability of failure of 0.02% to 10%) are considered in determining the fatigue safe life.

The estimated life expectancies of the HMIP determined using the fatigue parameters from categories E and E′ in AASHTO with both the average two-slope EFL and the envelop two-slope EFL under different target reliability indices are listed in Table 9.15. Although various life expectancies for different locations around the pole can also be determined similar to the deterministic method, the fatigue life of the pole is controlled by the shortest fatigue life, therefore only the shortest expected life among all locations around the pole is presented here. For instance, the fatigue life presented in Table 9.15 is for the 90° location, which is the location with the shortest observed fatigue life for the monitored pole in Austin.

Table 9.15: Probabilistic Estimation of the Fatigue Safe Life Using Fatigue Categories E and E′ (Years)

		Envelope EFL		Average EFL	
		Category E	**Category E′**	**Category E**	**Category E′**
$P_f(\beta)$	**0.02% (3.5)**	347	113	970	316
	1% (2.33)	563	202	1572	564
	2% (2.05)	632	232	1765	648
	5% (1.64)	748	284	2090	795
	10% (1.28)	868	340	2424	950
	11% ()		350		979
	15% ()	952		2660	

Table 9.15 suggests that the expected fatigue safe life for the monitored pole in Austin is around 113 years when assuming an AASHTO category E′ design and using an envelope two-slope EFL at a target reliability index (β) of 3.5 (corresponding to a 0.02% probability of failure). The relatively short life span compared to the safe life obtained deterministically (350 years) is due to a conservative target of probability of failure set at 0.02%, meaning only one in 5000 is expected to fail or to experience significant cracks during the estimated life span. Setting a higher target probability of failure increases the estimated life span. The deterministic results, corresponding to probabilities of failure of 11% and 15%, are also listed in Table 9.15. The increase in probability of failure from the originally suggested 5% using the lower bound S-N curve is due to the additional uncertainty introduced by incorporating the critical damage accumulation index (Δ).

The probability method allows the liberty to choose any allowable probability of failure as a target to estimate the corresponding fatigue safe life or calculate the probability of failure for a given target life span. Most studies in the past (Magenes 2011, Chang 2007, Connor 2012) utilize the lower bound S-N curves provided by AASHTO to obtain the fatigue safe life which, according to the analysis, results in a range of 5% to 15% probability of failure which are not usually addressed. Dawood (2014) suggested adopting the 0.02% from the strength limit state provided in AASHTO LRFD to the fatigue limit state which yields a low expected life as seen also in this study. However, the target probability of failure purely depends on the allowable risk that TxDOT

is willing to take or incorporating the cost of failure and inspection to achieve a target failure probability while minimizing the total expected cost.

Although all the results, assuming categories E and E′, exceed the required service life of 75 years, the fatigue safe life is expected to decrease significantly due to the reduced fatigue constant (A) of the pre-cracked HMIPs determined from experiment. However, the results show that if the HMIP design were crack-free and is categorized as category E as designed, the expected fatigue life exceeds 300 years for the HMIP in Austin with the given wind probability distribution even under a conservative 0.02% probability of failure criteria.

Experiment-based S-N curve

The fatigue capacity of pre-cracked HMIPs are determined through experiments performed in this study (Chapter 5). The fatigue capacity parameters are determined and listed in Table 9.8 and Table 9.9 in comparison with categories E and E′. As discussed in Section 9.3.2, due to the variation of initial conditions of bends and flats subjected to testing, all experimental data and selected experimental data are used in determining the distribution parameters of the fatigue constant (A). All experimental data includes all the data from University of Texas at Austin (UT) and the data from University of Houston (UH) which uses a different experimental setup. The selected data excludes the experimental data for tested specimens with no initial cracks from UT. The selected data also excludes the experimental data provided by UH to avoid any uncertainties associated with different testing methods.

The probabilistic fatigue safe life is determined using the statistical parameters of the fatigue constant (A) using experimental data (Table 9.8 and Table 9.9) and introducing the uncertainty assuming the critical damage accumulation index (Δ) is a random variable of a log-normal distribution with mean (μ_Δ) of 1 and coefficient of variance (δ_Δ) of 0.3. The method and equation used is the same as previous section while subjecting to the fatigue constant () determined from using all or selected experimental data and the fatigue demand described by of the average and envelop two-slope EFL. Various target reliability indices (3.5 to 1.28) which correspond to probabilities of failure from 0.02% to 10% are used in determining the fatigue safe life.

The fatigue life expectancy of the HMIPs under different target reliability indices are listed in Table 9.16. The shortest fatigue life resulted from the location around the perimeter of the pole (90°) is presented since it controls the fatigue life of the pole. The results show a significant reduction in fatigue life from the results when design categories of E and E′ in AASHTO are assumed. A decrease from 347 years to 7 years of fatigue life is seen when the fatigue capacity resulting from selected experimental data is used instead of the un-cracked design described by category E′ in AASHTO. The results from selected experimental data excluding the non-cracked specimens and results from different testing procedure, reduces the uncertainty which in turn resulted in longer expected fatigue life. Also, by subjecting the average two-slope EFL instead of the envelope two-slope EFL to the assessment also extends the fatigue safe life. However, the increased fatigue life to 58 years is still considerably short compared to the 970 years if the HMIPs possess no pre-cracks and is considered AASHTO category E. The deterministic results (Section 9.5.1) are also listed in the table which corresponds to a probability of failure of 5.7% and 6.7%. The increase in probability of failure from the originally suggested 5% using the lower bound S-N curve is due to the additional uncertainty introduced by involving the critical damage accumulation index (Δ) as discussed in previous section.

As discussed previously, the target reliability affects the results significantly where the selected target is based on acceptable risk to TxDOT. However, as pointed out previously, if the

HMIP fatigue performance followed category E in AASHTO, the predicted fatigue safe life would be several hundred years for even the most conservative target probability of failure. The effect of the pre-cracked condition from the galvanizing process greatly reduces the fatigue life. The use of the selected experimental data, and the average two-slope EFL is recommended in determining the expected fatigue life as discussed in Section 9.5.1. The target reliability index is not suggested since it all depends on the degree of safety that is required for the HMIPs. Although only a few selected reliability indices are listed in the table, expected fatigue life for any reliability index can be determined from the reliability curves in Figure 9.20.

Table 9.16: Probabilistic Estimation of the Fatigue Safe Life Using Experimental Data (Years)

		Envelope EFL		Average EFL	
		All Data	**Selected Data**	**All Data**	**Selected Data**
$P_f(\beta)$	**0.02% (3.5)**	7	21	21	58
	1% (2.33)	30	49	83	137
	2% (2.05)	41	60	115	168
	5% (1.64)	67	81	188	226
	5.7% ()	72		201	
	6.7% ()		90		251
	10% (1.28)	103	105	288	294

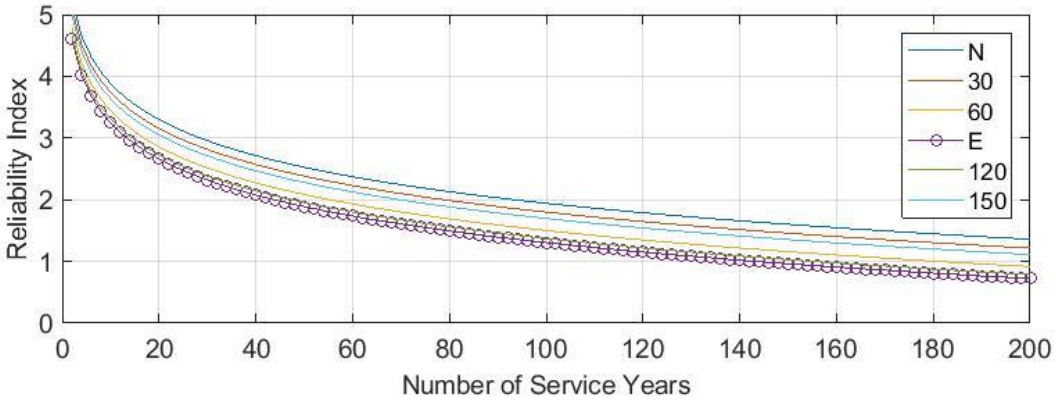

(a) Envelope Two-Slope EFL Using Unadjusted Experimental Data

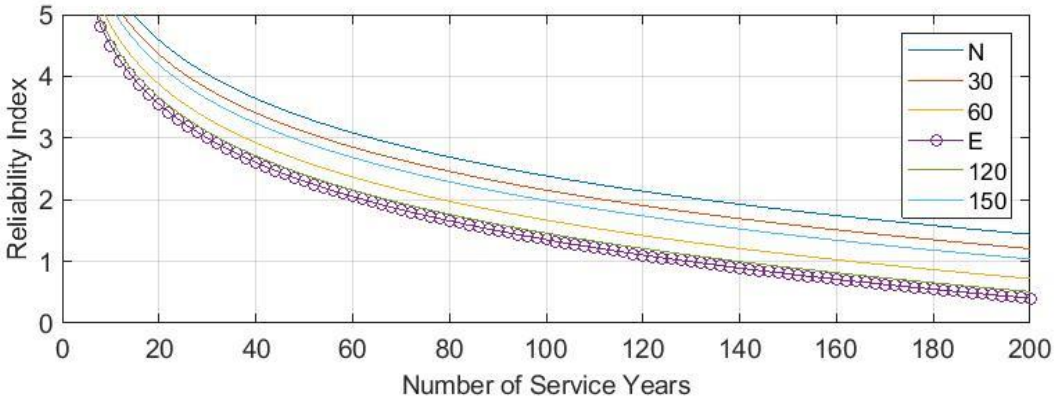

(b) Envelope Two-Slope EFL Using Selected Experimental Data

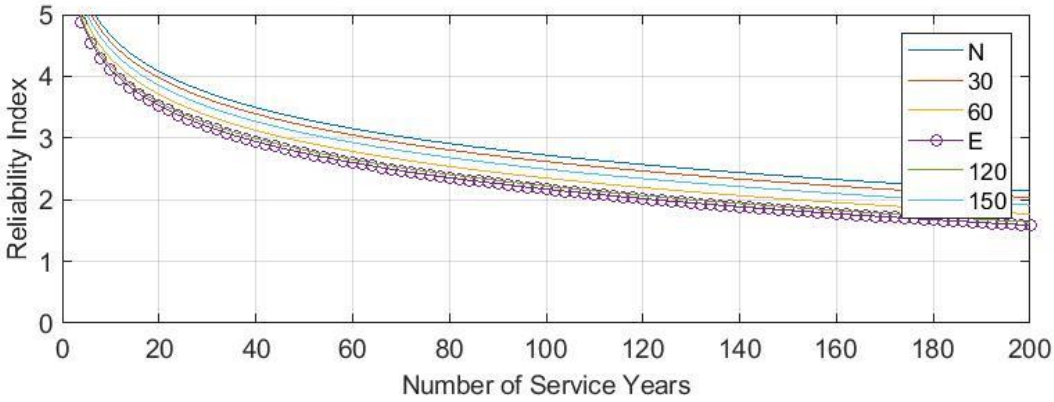

(c) Average Two-Slope EFL Using Unadjusted Experimental Data

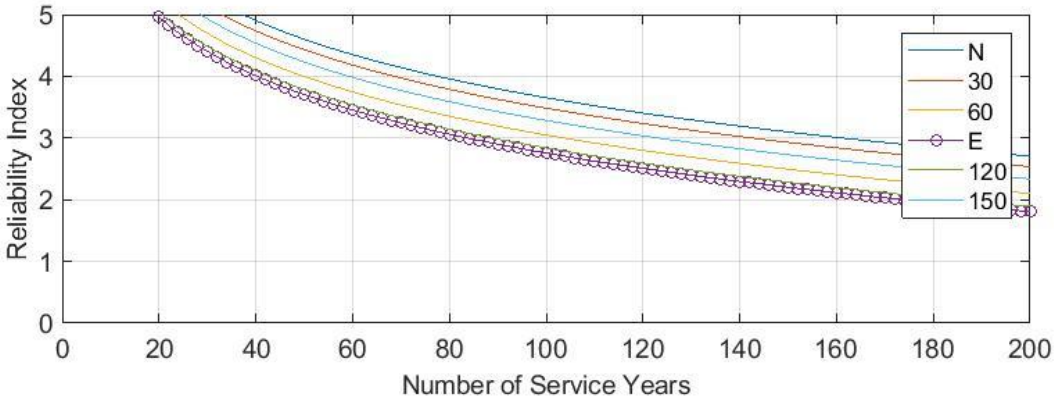

(d) Average Two-Slope EFL Using Selected Experimental Data

Figure 9.20: Reliability Index as a Function of Number of Expected Service Years before Failure

9.5.3 Fatigue Safe-Life Assessments Using Wind Data from the NOAA Sites

From the above discussion, the probabilistic fatigue safe life is dependent on the wind probability distribution (α_{ij}) (or β_{ij} for a specific location around the perimeter of the poles), the use of envelope or average two-slope EFL, the use of fatigue capacity from different sets of data, and the target reliability index (β). The use of average two-slope EFL is recommended which represents a general wind induce fatigue demand observed from the five monitored poles. Using fatigue parameters (λ_A and ζ_A) resulting from selected experimental data is also recommended to reflect the reduced fatigue capacity of pre-cracked poles more accurately. Wind probability distribution (α_{ij}) from various locations in Texas, provided by NOAA, are documented in Chapter 4 and are utilized with different target reliability indices (β) to assess the fatigue life of HMIPs at these locations.

EFLs Adjusted for High-Wind Speed

Since both average and envelope two-slope EFLs are calculated using actual field data, the EFL table is limited to the highest wind speed recorded in the field. However, the wind speed documented for sites in NOAA shows higher recorded wind speeds than field data gathered in this

study. In order to estimate the damage or EFL corresponding to the higher wind speed, individual EFL curves for different relative directions and for wind speed above 10 miles per hour are fitted to a second order polynomial function to produce smoother curves and obtain EFLs at higher wind speed. The EFLs at low wind speeds (below 10 miles per hour) due to vortex shedding is kept while substituting the EFLs in higher wind speed region with the fitted and extended EFLs. The EFL after fitting and extending is shown in Figure 9.21 where the wind speed bins are higher to accommodate locations with higher wind speeds.

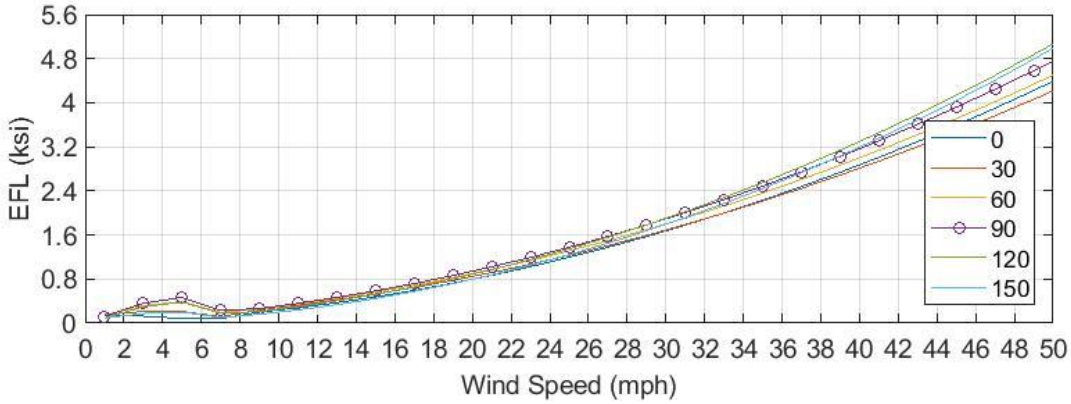

Figure 9.21: Fitted and Extended Average EFL

Expected Fatigue Safe-Life Using Experiment-Based S-N Curve

The fatigue life resulting from all sites from NOAA as well as the monitoring sites from this study is assessed in a probabilistic manner using the fatigue parameters established from selected experimental data and an extended average two-slope EFL as suggested. Similar to the probabilistic approach in Section 9.5.2, only the shortest fatigue life determined for locations around the perimeter of the pole is presented. Various target reliability index values are evaluated including the reliability index that corresponds to the probability of failure of the deterministic result which is 6.7%.

The assessed fatigue lives for all sites are listed in Table 9.17. Note that, as mentioned in Chapter 4, the selected districts are based on the number of the HMIPs with the target design in that area. The results show that for a target reliability index of 3.5, the expected life for most of the locations are alarmingly short. However, as pointed out previously, the proposed S-N curves in AASHTO are based on a 95% exceedance or a 5% probability of failure which is commonly used in fatigue design. If the deterministic method is applied, the fatigue safe life would increase from 58 to 251 years in Austin near the field monitoring site with a corresponding probability of failure of 6.7%.

If the allowable probability of failure is set to 5%, all sites in Austin including the monitored pole site in this study exceed 75 years showing no immediate concern. However, certain sites in certain districts such as El Paso, Odessa, Ft. Worth and Wichita Falls show relatively short expected life around 30 to 40 years suggesting the need for early attention. Due to the large geographic extent of a district, the wind condition (wind probability) varies from site to site even in the same district resulting in different estimated fatigue safe lives in the same district. The probability wind distribution can easily change due to the landscape or surroundings near the site.

However, if no wind information is available nearby, the probability wind distribution from the nearest NOAA site is suggested for assessing the fatigue life of the HMIPs.

It is important to note that the probability of failure at 5% should be interpreted as one out of 20 HMIPs in the region is "expected" to have considerable cracks which does not mean immediate collapse of HMIPs. Experiments have shown a certain amount of capacity reserve for poles after passing the failure point defined by a 10% stiffness loss in the HMIP. Table 9.17 provides information on the expected fatigue safe life of poles with pre-existing cracks located in different districts in Texas. This information is intended to be used by TxDOT engineers as a guideline in assessing mitigation strategies for HMIPs.

Table 9.17: Expected Fatigue Safe-Life for Different Target Probabilities of Failure

District	Name	WBAN	Location	Probability of Failure (%)					
				0.02	1	2	5	6.7	10
Austin	AUSTIN	Field	90	58	137	168	226	251	294
	PFLUGERVILLE	230	90	34	81	99	134	148	174
	AUSTIN/CITY	13958	90	101	238	292	395	438	514
	AUSTIN/BERGSTROM	13904	90	21	48	59	80	89	104
	GEORGETOWN	53942	90	23	54	66	89	99	116
Laredo	LAREDO	Field	60	53	125	153	207	268	270
	LAREDO	12907	60	14	34	41	56	62	72
Atlanta	TEXARKANA	13977	120	54	126	155	209	232	272
	LONGVIEW	3901	90	35	83	102	137	152	178
El Paso	EL PASO	Field	90	51	121	149	201	222	261
	EL PASO	23044	150	9	20	25	34	37	44
Odessa	ODESSA	3031	90	13	31	38	51	57	66
	MIDLAND	23023	90	9	22	27	36	40	47
	MIDLAND	3071	90	19	44	54	73	81	95
Ft. Worth	DALLAS-FORT WORTH	3927	90	9	21	26	35	39	46
	FORT WORTH	13961	90	15	35	43	58	64	75
	FORT WORTH	13911	90	12	29	36	49	54	63
	GRANBURY	53977	60	29	69	85	115	127	149
Paris	GREENVILLE	13926	90	26	62	76	103	114	133
	PARIS	93955	90	20	47	57	78	86	101
	SHERMAN/DENISON	53967	90	14	32	40	54	59	70
Waco	HILLSBORO	53972	60	14	33	41	55	61	72
	WACO	13959	90	15	35	43	58	64	75
	WACO	53952	90	16	38	47	63	70	82
	TEMPLE	93984	90	12	27	33	45	50	59
	FORT HOOD/KILLEEN	3902	60	12	28	34	46	51	60
	FORT HOOD (KILLEEN)	3933	60	21	49	60	81	90	106
	KILLEEN	3972	90	23	54	66	89	99	116
Brownwood	BRECKENRIDGE	176	90	31	74	91	123	136	159
Wichita Falls	WICHITA FALLS	134	90	25	59	72	97	108	126
	WICHITA FALLS	13966	90	7	17	21	29	32	38
	GAINESVILLE	93929	60	18	42	52	70	77	91
Bryan	COLLEGE STATION	3904	90	24	56	68	92	103	120
	BRYAN	438	90	61	144	176	238	264	310
Dallas	DALLAS	Field	30	88	206	253	341	378	444
	DALLAS	13960	90	16	39	48	64	71	84

9.5.4 Uncertainties from Experiment-Based Parameters

As discussed in Section 9.3.2, the statistical parameters of the fatigue constants (λ_A and ζ_A) used in introducing the uncertainties of the fatigue capacity have their own uncertainty due to limited experimental results. To incorporate the uncertainties from the two parameters (λ_A and ζ_A),

Monte Carlo simulation is implemented based on the known Student's t and Chi square distribution described in Equations 9.23 and 9.24. An example using the wind conditions from the monitored site in Austin, averaged two-slope EFL, and selected experimental data is presented to show the effect of experimental sample sizes to parameter uncertainties. The determination of expected life deterministically or probabilistically utilizes the same equations (Equations 9.33 and 9.39) by substituting the sample parameters (λ_A and ζ_A) with simulated parameters (λ and ζ).

The 100,000 design fatigue constants (A_D) are realized using the simulated parameters (Equation 9.25) which in-turn are used to determine the expected life deterministically (Equation 9.33). The resulted distribution of expected life is shown in Figure 9.22 where the 2.5 and 97.5 percentile is 101 and 448 years respectively indicating a 95% confidence interval. The wide range of expected lives is due to the limited experiment data where significant uncertainties are introduced when determining the parameters of the fatigue capacity distribution. The suggested 251 years of expected life that does not consider the uncertainty of the parameters lies between the confidence interval which can be seen as an estimate whereas the true fatigue life can vary significantly.

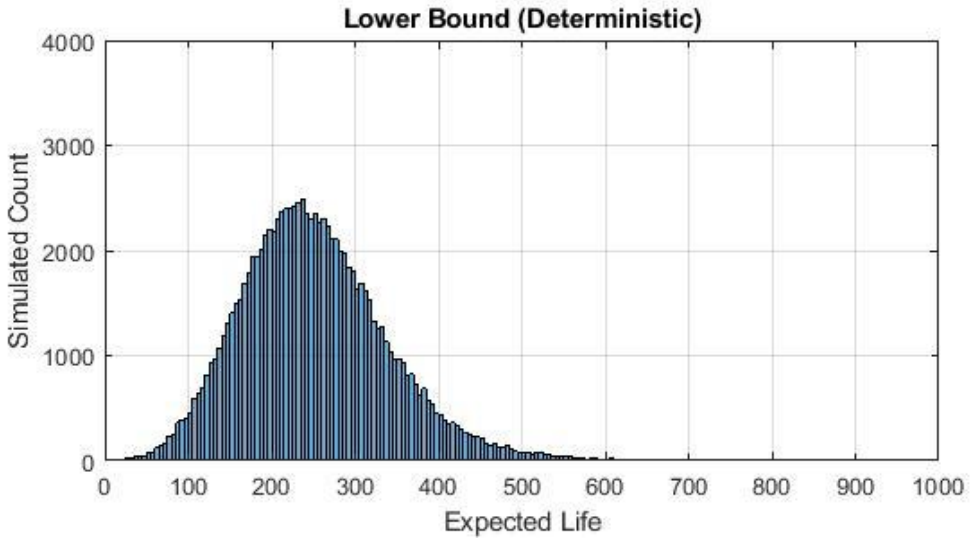

Figure 9.22: Distribution of Expected Fatigue Life (Deterministic Method)

The simulated parameters can also be utilized in the probabilistic method (Equation 9.39) to obtain a series of expected fatigue lives under different target reliability indices (β). The resulting distribution of expected life at a reliability index of 3.5 is presented in Figure 9.23 where 95% confidence interval is resulted between 10 and 124 years. The expected life is 58 years when no uncertainty from the parameters are considered which lies within the intervals as expected.

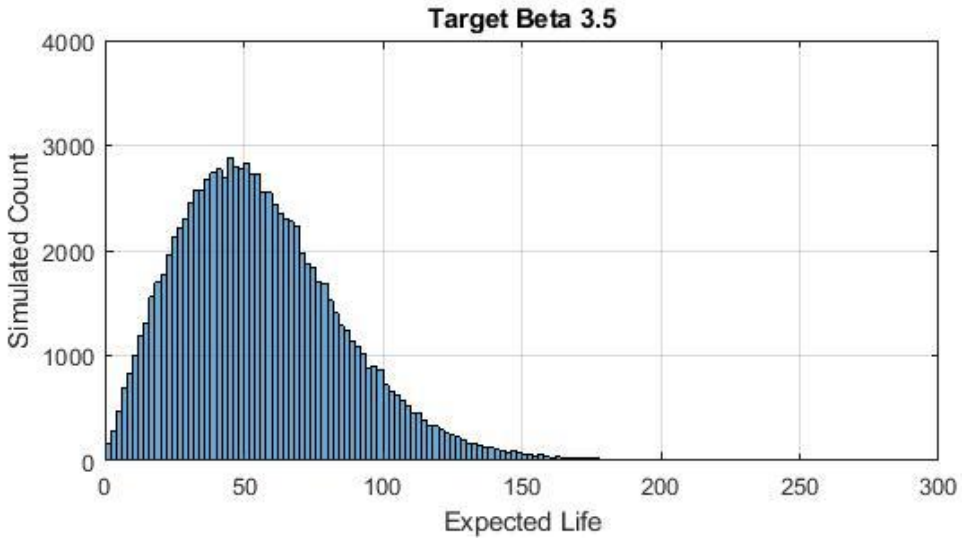

Figure 9.23: Distribution of Expected Fatigue Life (Probabilistic Method with β = 3.5)

The example presented is to illustrate the underlying uncertainties of the expected life when uncertainties due to limited experimental data are accounted for. Since the experimental data are limited in this study, the uncertainties are relatively high. However, if more available experimental data are provided, the uncertainty may be reduced significantly. All in all, it is important to note that the proposed expected life is a best estimate with high underlying uncertainty due to the limited experimental data.

9.6 Reliability-Based Inspection Scheduling

The development of a reliability-based inspection scheduling that takes into account both the economy and the safety aspects of maintaining and repairing in-service HMIPs is presented and explained in this section. The concept of reliability-based inspection scheduling has been applied in the past to the fatigue condition assessment of offshore structures (Thoft-Christensen and Sorensen 1987, Madsen 1989), reinforced concrete bridge structures (Frangopol et al. 1997), and steel bridge structures (Chung et al. 2003). The general idea is to find an optimal inspection schedule that minimizes the cost while meeting certain safety constraints. A scheduled inspection and a repair protocol based on the damaged condition of in-service HMIPs is believed to prevent conditions that are beyond repair or near collapse. Similar to the 2-year inspection frequency for bridges required by Federal Highway Administration (FHWA), a fixed time interval for inspection of HMIPs is proposed in this study. Specifically, an optimal or a preferable inspection schedule is determined to minimize a cost function consisting of the cost of inspection, repair, and failure/replacement during the service life of HMIPs. Optimization of this cost function requires information on the frequency of inspections and intervention strategies in the form of repair or replacement. To optimize the cost and consequently provide a guideline for inspection of in-service HMIPs, an event tree analysis is proposed and constructed. The reliability-based framework for fatigue analysis of in-service HMIPs, developed and presented in previous sections, is applied in the event tree analysis.

9.6.1 Event Tree Analysis

Event tree analysis is a modeling technique that explores all the possible outcomes of a series of decisions. For the problem of inspection scheduling for in-service HMIPs, the decision is whether a repair is required after an inspection. After every inspection, "Repair" or "No Repair" actions are possible. These two actions grow into an event tree that consists of all possible scenarios after each inspection over the planned service life of HMIPs. Figure 9.24 shows an example of an event tree, which is proposed and developed to find an optimum inspection interval for in-service HMIPs. This event tree analysis is the same as the one previously developed to establish an optimal inspection schedule for fracture critical bridges (Chung et al. 2003).

d

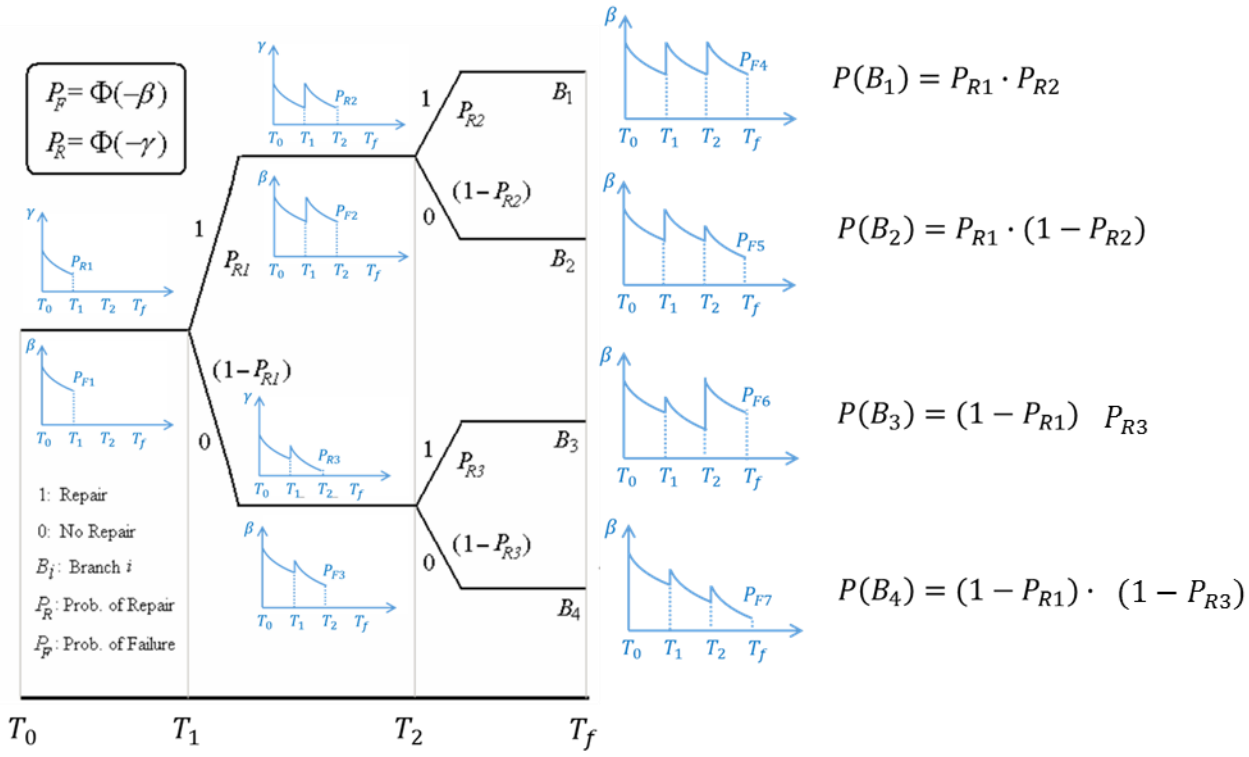

Figure 9.24: An Event Tree Model for all Inspection and Repair Realizations throughout the Planned Service Life of an HMIP (Similar to Chung at al. 2003)

The horizontal axis of the event tree in Figure 9.24 represents the time (T), that starts at T_0 indicating the installation of an HMIP in service, and ends at T_f indicating the planned service life of the HMIP. In addition, T_1 and T_2 indicate the time for the two inspections conducted throughout the service life of an HMIP. After each inspection, the tree branch bifurcates into "Repair" and "No Repair" cases denoted by "1" and "0", respectively. Whether to repair or not at the i-th bifurcation point in the event tree is represented by a repair probability (P_{Ri}) suggesting the chance of going through the "Repair" branch. The chance of going through the "No Repair" branch is then $(1 - P_{Ri})$. With the known probabilities of "Repair" actions at all bifurcation points (Section 9.6.2), the probability of j-th branch ($P(B_j)$) at the time T_f is the product of the branch probabilities at every inspection as illustrated in Figure 9.24.

One objective of the event tree analysis is to obtain an expected reliability curve ($E[\beta(t)]$) accounting all possible outcomes of inspections (Section 9.6.3). The expected reliability curve ($E[\beta(t)]$) is then used in determining the probability of failure over the service life ($P_{F-years}$) and in-turn determining the expected cost of replacement of an HMIP (Section 9.6.4). The expected reliability curve ($E[\beta(t)]$) is determined based on all reliability curves, shown at the end of each branch in Figure 9.24, weighted by their corresponding branch probabilities ($P(B_j)$). To obtain the reliability curves for all branches, the "Repair" or "No Repair" decisions at all inspections for each branch are considered. How an inspection affects the reliability index (β) (or probability of failure (P_F)) is illustrated in Section 9.6.2.

Another objective of the event tree analysis is to obtain the expected number of repairs at each inspection point ($E[R_i]$) accounting all possible outcomes of inspection (Section 9.6.3). The expected number of repairs ($E[R_i]$) is then used in determining the expected cost of repairs (Section 9.6.4). The expected number of repairs ($E[R_i]$) at i-th inspection point is determined based on the probability of repairs at i-th inspection and j-th branch ($P_{R_i}^{j}$) weighted by the corresponding branch probabilities ($P(B_i^j)$). The probability of repair at the bifurcation points, similar to the probability of failure (P_F), is affected by an inspection illustrated in Section 9.6.2.

9.6.2 Probability of Failure and Repair after Inspections

Updated Probability of Failure

The probability of failure (P_F) or the reliability index (β) is updated after each inspection. The reliability index (β) for the HMIP of interest, based on the fatigue constant determined from experiment and the fatigue demand based on the two–slope EFL from observed field data, is a decreasing function that is greatly affected by whether a "Repair" or "No Repair" action is being taken after inspection. Note that both actions increase the reliability of an HMIP and are discussed separately in the following.

For the purpose of this study, the condition of an HMIP after a "Repair" action is assumed to be crack-free, and therefore can be set to AASHTO category E or E′ based on the repair design, both considerably higher than the cracked condition of the current HMIPs. After a repair, the fatigue constants (Δ_A and λ_A) used in the reliability curve (Equation 9.38) is substituted with the fatigue constants from AASHTO category E or E′, and is then evaluated based on the time period following the repair. In other words, the reliability curve after a repair is replaced with a new curve based on the HMIP condition and the elapsed time since the repair. As a result, the fatigue reliability increases to a level representative of a "new" pole immediately after a repair action, (indicated by "1" at each bifurcation point in the event tree analysis in Figure 9.24). For instance, the reliability (β) after T_1, in Figure 9.24, shows an immediate increase to its original value at T_0 after a repair. If "No Repair" action is taken after the inspection, the reliability (β) after T_1, in Figure 9.24, shows an immediate but smaller increase. Note that an inspection itself increases the reliability of the HMIP against fatigue failure even though "No Repair" action is taken. This is the case because inspection that does not warrant a repair also implies that the HMIP is not near a failure state and the probability of failure after inspection needs to be updated conditioned on the fact that no failure has occurred before the inspection point. As an example illustrated in Figure 9.25, if "No Repair" action is taken after inspection at T_1, the probability of failure before T_2 is updated as follows,

$$P_f(t < T_2 | t > T_1) = \frac{P_f(T_1 < t < T_2)}{P_f(t > T_1)} = \frac{\int_{T_1}^{T_2} f_T(t)dt}{\int_{T_1}^{\infty} f_T(t)dt} \qquad \textbf{Equation 9.40}$$

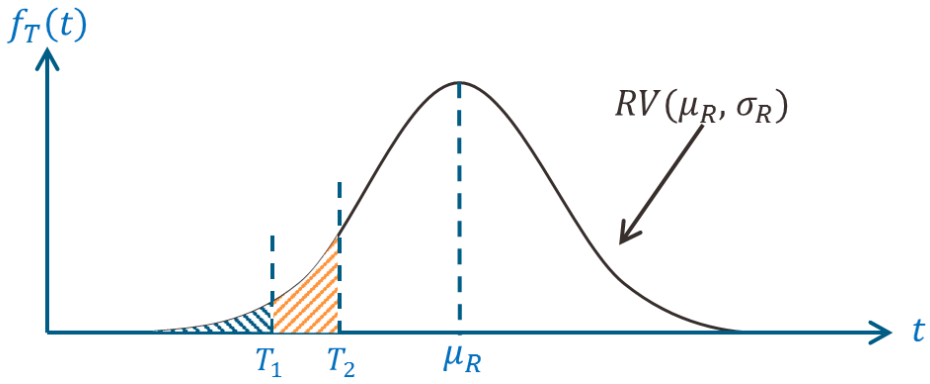

Figure 9.25: Probability Density Function of Failure as a Function of Time

As such, the reliability of an HMIP against fatigue failure immediately increases after an inspection whether or not a "Repair" action is taken. By updating the reliability curve based on the various combination of repair decisions at each inspection, the fatigue reliability curve for all branches in the event tree can be determined (as qualitatively shown in Figure 9.24).

Updated Probability of Repair

The probability of repair (P_R) also depends on the condition of the HMIP and is characterized by a decreasing function (γ) similar to that of a reliability curve (β). As observed in the fatigue experiments (Chapter 5), the fatigue failure defined by a 10% loss in stiffness results in a condition where HMIPs are beyond repair. More importantly, no through-thickness cracks are observed for fatigue cycles fewer than 75% of the total cycles to failure. Therefore, a criterion for the repairable condition is defined to correspond to a number of sustained cycles near 75% of the total cycles to failure. The 75%-limit for reparability was also reported in a study by Chung et al. (2003), where the first observation of cracks in a weld detail of bridge connections was found to be near 75% of the cycles to failure. The 75% limit for reparability was further found acceptable in a separate study on fatigue behavior of steel bridges conducted by Fisher et al. (1970).

Since the fatigue constant is directly proportional to the number of cycles, it can be reduced by 75% in the limit state function for the probability of repair as follows:

$$h(\Delta, A, EFL_{ij}, \alpha_{ij}) = \Delta \cdot 0.75A - \sum_{all\ \theta_r} \sum_{all\ U} \beta_{ij} \cdot T \cdot f_1 \cdot EFL_{ij}^3 = 0 \qquad \textbf{Equation 9.41}$$

where the only difference between the limit state function for the probability of failure (Equation 9.32), and the limit state function for probability of repair (Equation 9.41) is the factor 0.75 in front of the fatigue constant, A. By taking natural log of both sides of Equation 9.41, a new limit state function is formed,

$$\bar{h}\left(\Delta, A, EFL_{ij}, \alpha_{ij}\right) = \ln(\Delta) + \ln 0.75 + \ln(A) - \ln(T) - \ln\left(\sum_{all\ \theta_r}\sum_{all\ U} \beta_{ij} \cdot f_1 \cdot EFL_{ij}^3\right) = 0 \qquad \textit{Equation 9.42}$$

The left hand side of the limit state function can be seen as a random variable (Y) with a normal distribution since the fatigue constant (A), and the critical damage accumulation index (Δ) are both random variables with log-normal distribution. The probability of repair can then be related to an index (γ) and evaluated as:

$$P_R = P\left(\bar{h}\left(\Delta, A, EFL_{ij}, \alpha_{ij}\right) \leq 0\right) = \Phi(-\gamma) \qquad \textit{Equation 9.43}$$

where the index γ is determined as:

$$\gamma = \frac{\mu_Y}{\sigma_Y}$$

$$\gamma = \frac{\lambda_\Delta + \lambda_A + \ln 0.75 - \ln(T) - \ln\left(\sum_{all\ \theta_r}\sum_{all\ U} \beta_{ij} \cdot f_1 \cdot EFL_{ij}^3\right)}{\sqrt[2]{\zeta_\Delta^2 + \zeta_A^2}} \qquad \textit{Equation 9.44}$$

Similar to the probability of failure, the probability of repair is also updated after each inspection. The condition of an HMIP after a "Repair" action is assumed to be crack-free, and therefore can be set to AASHTO category E or E′ based on the repair design. As a result, the statistical parameters of the fatigue constant (Δ_A and λ_A) used in the repair index (Equation 9.44) is substituted with the fatigue constants from AASHTO category E or E′ after a repair which is then evaluated based on the time since the repair. In other words, the repair index (γ) after a repair is continued with a new repair index based on the repaired HMIP condition and the elapsed time since the repair. As a result, the repair index (γ) after T_1, in Figure 9.24, shows an immediate increase after a repair action , indicated by "1" at the bifurcation point in the event tree. Similar to the updated failure probability after an inspection without a repair action, the repair index (γ) increases less significantly as shown in Figure 9.24. As such, the probability of repair at every bifurcation point, considering all prior repair decisions, is determined. The probability of each branch is then determined based on the probabilities at each inspections. Note that a repaired HMIP, though assumed category E or E′ with a higher fatigue capacity, still holds a certain probability of failure and repair. A repaired HMIP or a new constructed HMIP only suggests a higher reliability or lower failure probability compared to a pre-cracked HMIP where zero probability of failure is not guaranteed.

9.6.3 Expected Reliability Curve and Expected Number of Repairs

Considering all different combinations of "Repair" and "No Repair" decisions after each inspection, an expected reliability curve ($E[\beta(t)]$) can be constructed. The expected reliability curve, $E[\beta(t)]$, is determined based on all individual reliability curves (β_j(t)) from the branches

in the event tree weighted by their corresponding probability. The reliability index for branch j is first transformed into failure probability as

$$P_{F,j}(t) = \Phi(-\beta_j(\mathrm{t})) \qquad \textbf{Equation 9.45}$$

Next, the expected probability of failure is calculated based on the weight (or probability) of each branch ($P(B_j)$) in the event tree as follows:

$$E[P_F(t)] = \sum_{j=1}^{2^n} \Phi(-\beta_j(\mathrm{t})) \cdot P(B_j) \qquad \textbf{Equation 9.46}$$

where n is the number of inspections resulting in an event tree with 2^n branches. Finally, the expected reliability curve ($E[\beta(t)]$) is determined by transferring the probability of failure back to reliability index as:

$$E[\beta(t)] = -\Phi^{-1}\left(\sum_{j=1}^{2^n} \Phi(-\beta_j(\mathrm{t})) \cdot P(B_j)\right) \qquad \textbf{Equation 9.47}$$

In order to estimate the repair cost throughout the service life of HMIPs, information on an expected number of repairs ($E[R]$) is needed. The expected number of repairs at the i-th inspection ($E[R_i]$) is determined based on the sum of all repair probabilities from all branches (denoted by j) at the i-th inspection ($P_{R_i}^{\ j}$) weighted by their branch probability at the i-th inspection ($P(B_i^j)$). Note that the probability of repair at the same i-th inspection point but different j-th branch is different due to the different event path. Thus the expected repair at i-th inspection, $E[R_i]$, can be specified as,

$$E[R_i] = \sum_{j=1}^{2^{j-1}} P_R(T_i \cap B_i^j) = \sum_{j=1}^{2^{i-1}} P_{R_i}^{\ j} \cdot P(B_i^j) \qquad \textbf{Equation 9.48}$$

where B_i^j is the j-th branch at the i-th inspection.

9.6.4 Cost of Maintenance

The cost of maintenance over the service life consists of the cost of inspection (C_I), the cost of repair (C_R), and the cost of replacement (C_F). The expected cost of the inspection (C_I), over the service life is determined using information about the number of inspections (n) and the cost of each inspection (K_I),

$$C_I = \sum_{i=1}^{n} K_I \qquad \textbf{Equation 9.49}$$

The expected cost of repair (C_R) over the service life is determined using information about the expected number of repairs at each inspection point, $E[R_i]$, and the cost of each repair for a specific weld detail (K_R). The total cost of repair over the service life can then be expressed as,

$$C_R = \sum_{i=1}^{n} K_R \cdot E[R_i] \qquad \textbf{\textit{Equation 9.50}}$$

Note that the expected number of repairs at the i-th inspection point can be understood as the probability of a "Repair" action at the i-th inspection point.

The cost of replacement (C_F) is determined based on the probability of failure over the service life and the cost to replace a single HMIP (K_F). Although referred to as a failed specimen in fatigue experiments (Chapter 5), the HMIP after the 10% stiffness loss still possess considerable resistance to immediate collapse. HMIPs with 10% loss in stiffness, however, are not repairable due to the presence of through-thickness cracks. Therefore, the failure probability in this study is associated with the replacement cost and not the cost of a collapse, which is suggested in other inspection scheduling studies (Chung et al. 2003).

The probability of failure over the service life is determined based on the expected reliability curve ($E[\beta(t)]$) determined from the event tree analysis discussed in Section 9.6.1. If no inspections are scheduled, the reliability index of the HMIP decreases monotonically with time where the probability of failure is determined from the reliability index at the end of service life. However, if a reliability curve is not a monotonic decreasing curve, such as the expected reliability curve ($E[\beta(t)]$), the probability of failure over the service life is controlled by the minimum reliability index during the service years. Therefore, the cost of replacement is calculated as follow,

$$C_F = K_F \cdot \Phi(-\min(E[\beta(t)])) \qquad \textbf{\textit{Equation 9.51}}$$

The total expected cost (C_T) over the service life of an HMIP is the sum of the cost of inspection, repair, and replacement as shown,

$$C_T = C_I + C_R + C_F \qquad \textbf{\textit{Equation 9.52}}$$

$$C_T = \left\{\sum_{i=1}^{n} K_I\right\} + \left\{\sum_{i=1}^{n} K_R \cdot E[R_i]\right\} + \{K_F \cdot \Phi(-\min(E[\beta(t)]))\} \qquad \textbf{\textit{Equation 9.53}}$$

The equation of total expected cost can further be simplified if the costs of inspection, repair and replacement (K_I, K_R and K_F) do not change over the service life of an HMIP as indicated in the following equation,

$$C_T = K_I \cdot n + K_R \cdot E[R] + K_F \cdot P_{F-years} \qquad \textbf{\textit{Equation 9.54}}$$

where the expected number of repairs throughout the service life ($E[R]$) is,

$$E[R] = \sum_{i=1}^{n} E[R_i] \qquad \textbf{Equation 9.55}$$

and the failure probability throughout the service life ($P_{F-years}$) is,

$$P_{F-years} = \Phi(-\min(E[\beta(t)])) \qquad \textbf{Equation 9.56}$$

Different inspection schedules result in different total expected costs. The schedule that yields the least expected cost is regarded as the optimal schedule as discussed in the following section.

9.6.5 Suggested Inspection Schedules

With the total cost equation formulated, several inspection schedule scenarios can be evaluated for their expected cost. The inspection schedule yielding the minimum total cost is considered as the optimal schedule. To simplify the complexity of the calculations, and to reduce the trouble of inspections with different intervals over the service life, a fixed inspection interval as adopted in bridge inspections is suggested where the duration of the interval is of main interest. An analysis for different inspection intervals from 3 to 30 years is carried out for a pole location in El Paso as an example. Furthermore, different optimal scheduling based on different cost scenarios (cost of inspection, repair, and replacement) is discussed. Lastly, the total cost for inspection interval from 3 to 30 years using a suggested cost scenario is assessed for all the locations assessed for fatigue life in Section 9.5.3.

El Paso Example

Ten different inspection intervals from 3 years to 30 years are evaluated for El Paso with a suggested cost of inspection, repair, and replacement. The cost of inspecting a single HMIP is roughly estimated at $500 whereas the cost of repairing and replacing a single HMIP is estimated by TxDOT at $6000 and $20,000 respectively. Although the actual cost may differ depending on various circumstances, the proposed cost herein is presented as an example to illustrate the optimal scheduling concept. The initial fatigue capacity of the HMIP used in the event tree analysis utilizes the fatigue parameters (Δ_A and λ_A) based on the selected experimental data illustrated in Section 9.5.2. The fatigue capacity after a repair is assumed to perform at an AASHTO category E′ level assuming a near-new condition. The fatigue demand utilizes the two-slope average EFL (Section 9.4) and the wind probability in El Paso provided by NOAA (weather station: WBAN23044).

Ten different event tree analyses are performed using the ten inspection schedules resulting in ten sets of number of inspections (n), expected number of repairs ($E[R]$) and failure probability ($P_{F-years}$) tabulated in Table 9.18. A service life of 75 years is assumed and analyzed for this study. The number of inspections is based on how many inspections can be done in 75 years using the given inspection interval. The expected number of repairs ($E[R]$) is determined using Equation 9.55 in Section 9.6.4. The failure probability is the maximum expected probability of failure in 75 years determined using Equation 9.56 in Section 9.6.4. Table 9.18 shows the number of inspections decreases with increasing inspection interval as expected. The expected number of repairs range from 0.27 to 0.42 indicating a 27% to 42% of a repair action over the service life of 75 years depending on the inspection intervals. An increasing trend of failure probability with increasing inspection intervals is as expected since an inspection improves the reliability as suggested in

Section 9.6.2. Note that the failure probability without any inspections over the service years is around 29%. With two inspections at 30th and 60th year, the failure probability is reduced to 15.43%, whereas 24 inspections at an interval of 3 years reduces the failure probability to 1.61%.

Table 9.18: Number of Inspection, Repair, and Probability of Failure under Different Inspection Intervals (El Paso 23044)

Inspection Interval (Years)		3	6	9	12	15	18	21	24	27	30
El Paso (23044)	No. of Inspection	24	12	8	6	4	4	3	3	2	2
	No. of Repairs	0.42	0.42	0.42	0.42	0.32	0.42	0.35	0.42	0.27	0.32
	Failure Prob. (%)	1.61	3.25	4.90	6.53	8.16	9.85	11.49	13.31	12.93	15.43

Utilizing the suggested cost of inspection, repair and replacement ($500, $6000 and $20,000), the total cost from the ten different inspection schedules are determined using Equation 9.54 and displayed in Figure 9.26. As inspection interval increases reducing the number of inspections, the cost of inspections decreases. However, the reduced inspection results in a higher probability of failure which increases the cost of replacement. The optimal inspection schedule, is to balance the cost from inspections, repairs, and replacement minimizing the total expected cost. The minimum total cost around $5,200 is found at a 27-year inspection interval. The reliability index (β) shows a decreasing trend due to the reduced inspections from long intervals. If TxDOT wishes to keep the safety (or reliability) above a certain level, a minimum reliability index can be selected resulting in shorter inspection intervals. However, shorter inspection intervals result in increased total cost.

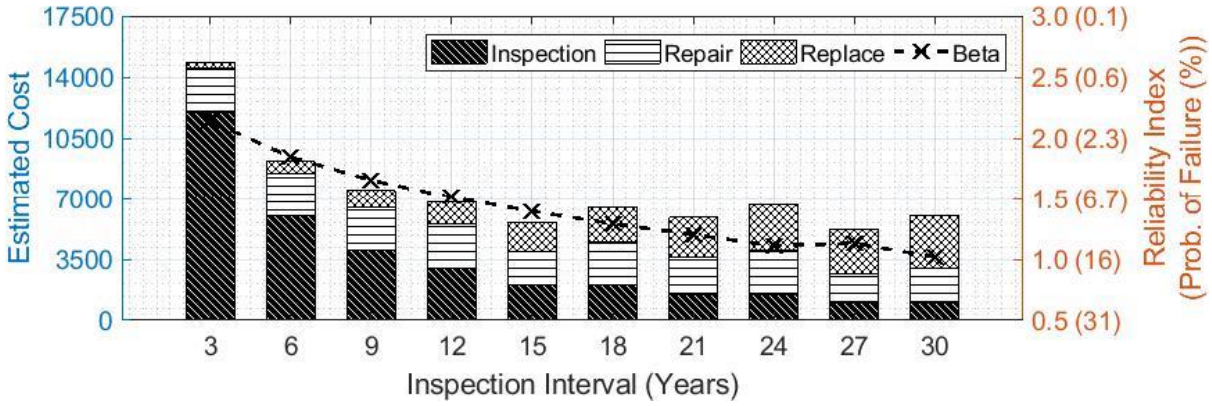

Figure 9.26: Relationship between Maintenance Cost and Inspection Interval for the Cost Scenario of ($K_I : K_R : K_F = 500 : 6000 : 20000$)

To show how different costs to inspect, repair and replace an HMIP affect the resulting optimal scheduling inspections, three scenarios of cost combinations are introduced (Table 9.19). An increased cost to replace an HMIP ($80,000) is introduced in the second scenario, which considers the monetary loss for an HMIP collapse. A reduced cost to inspect an HMIP ($300) is introduced in the third cost scenario assuming less costly inspection. Figures 9.27 and 9.28 show the expected cost with respect to the ten inspection intervals for the second and third cost scenarios. The second scenario resulted in an optimal inspection interval at 9 years and a minimum estimated total cost of $10,400. The increased total cost is due to the increased cost to replace a single HMIP.

Note that the estimated cost over the 75-year service life exceeds the cost to repair a single HMIP which makes more sense in repairing the HMIP without scheduling any inspection. The third scenario resulted in an optimal inspection interval at 6 years where the cost to replace a single HMIP is even more significant in the total estimated cost. However, the estimated cost still exceeds the cost to repair a single HMIP which would make more sense to repair an HMIP without any inspections. Note that the scenarios presented are intended to show the significance of the assumed cost. The actual costs to inspect, repair and replace of a pole can be modified based on more accurate cost estimations by TxDOT engineers.

Table 9.19: Cost Scenarios Considered in Finding an Optimal Inspection Schedule for In-Service HMIPs

	Inspection	Repair	Replacement
First	$500	$6,000	$20,000
Second	$500	$6,000	$80,000
Third	$300	$6,000	$80,000

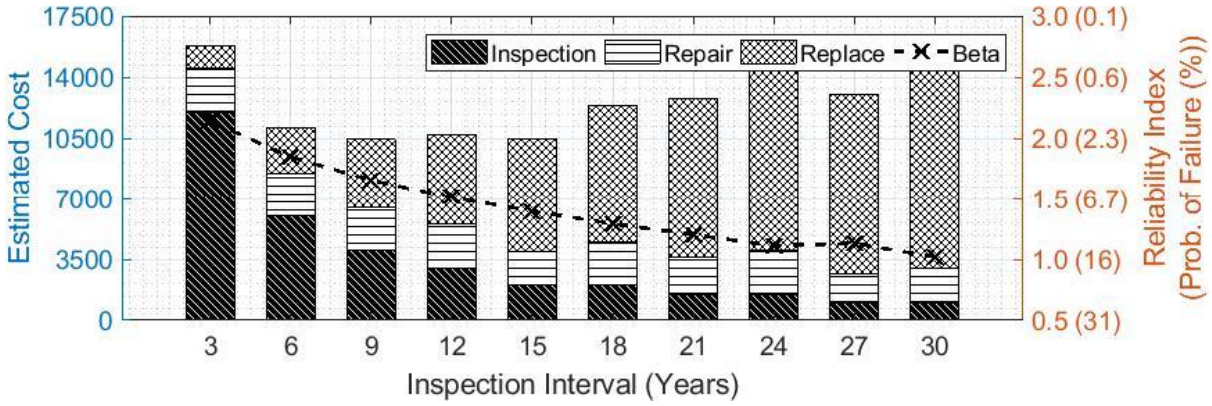

Figure 9.27: Relationship between Maintenance Cost and Inspection Interval for the Cost Scenario of ($K_I : K_R : K_F = 500 : 6000 : 80000$)

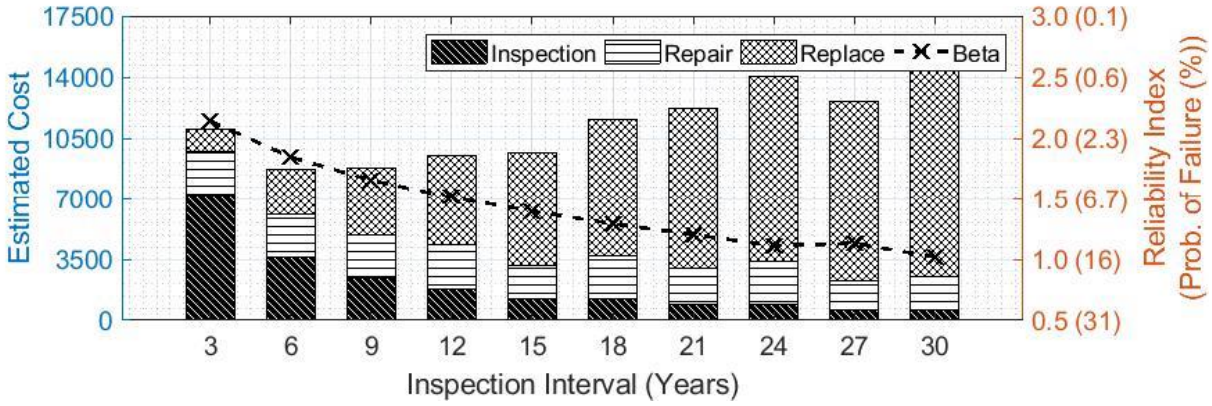

Figure 9.28: Relationship between Maintenance Cost and Inspection Interval for the Cost Scenario of ($K_I : K_R : K_F = 300 : 6000 : 80000$)

An Optimal Inspection Interval for Other Pole Sites

The cost assessment using the first cost scenario are analyzed for other locations based on the reliability curves analyzed from Section 9.5.3 and are shown in Figures 9.29 to 9.62 for reference. Locations where expected fatigue life exceeds 75 years with a 0.02% probability of failure tolerance are regarded as safe for the whole service life which are not analyzed for optimal inspection intervals. The number of inspections (n), expected number of repairs ($E[R]$), and probability of failure over the service years ($P_{F,years}$) for different inspection interval are also analyzed for all location of interests and tabulated in Table 9.20. Any cost scenario (Equation 9.54) can then be used in accordance with Table 9.20 to determine the optimal inspection intervals.

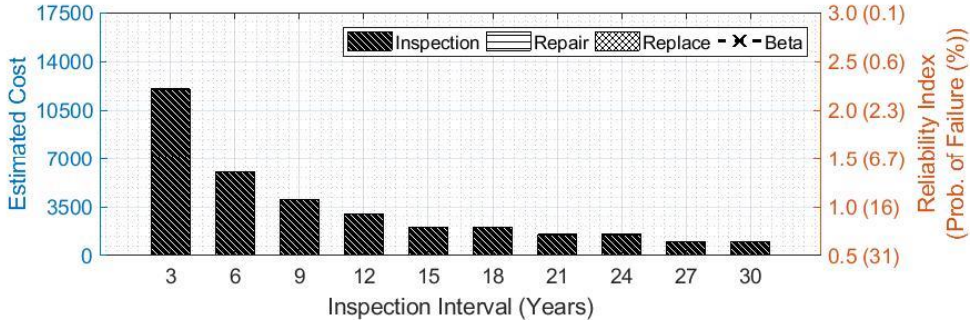

Figure 9.29: Austin (Field) - Relationship between Maintenance Cost and Inspection Interval for the Cost Scenario of ($K_I : K_R : K_F = 500 : 6000 : 20000$)

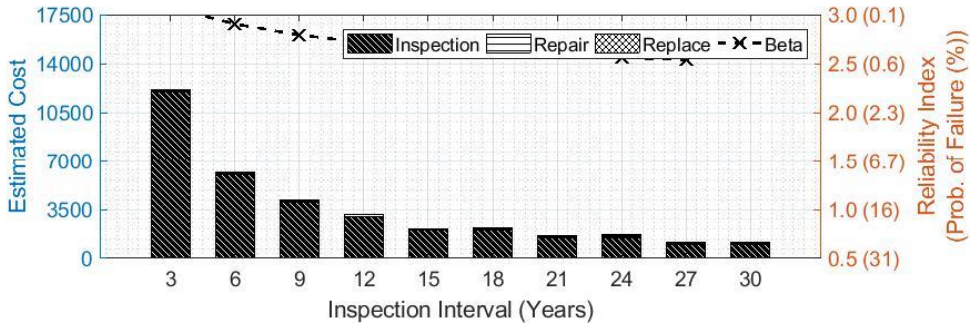

Figure 9.30: Austin (230) - Relationship between Maintenance Cost and Inspection Interval for the Cost Scenario of ($K_I : K_R : K_F = 500 : 6000 : 20000$)

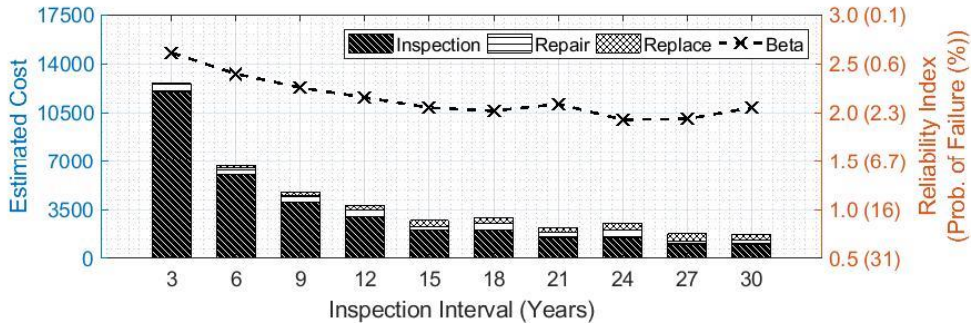

Figure 9.31: Austin (13904) - Relationship between Maintenance Cost and Inspection Interval for the Cost Scenario of ($K_I : K_R : K_F = 500 : 6000 : 20000$)

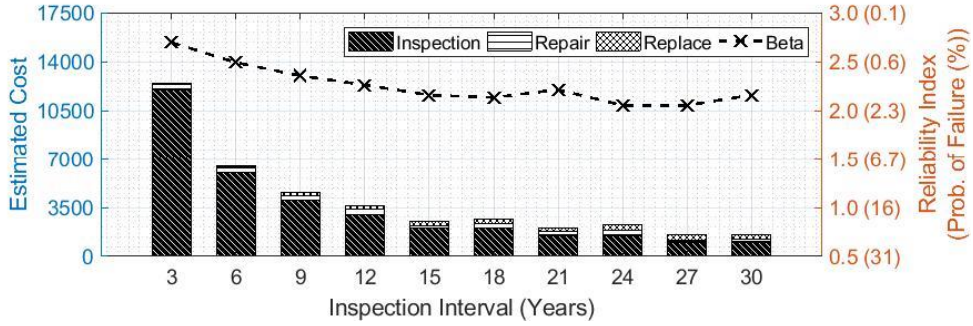

Figure 9.32: Austin (53942) - Relationship between Maintenance Cost and Inspection Interval for the Cost Scenario of ($K_I : K_R : K_F = 500 : 6000 : 20000$)

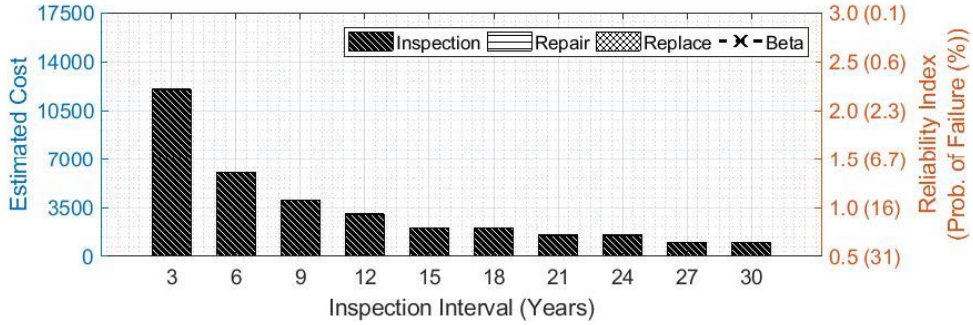

Figure 9.33: Laredo (Field) - Relationship between Maintenance Cost and Inspection Interval for the Cost Scenario of ($K_I : K_R : K_F = 500 : 6000 : 20000$)

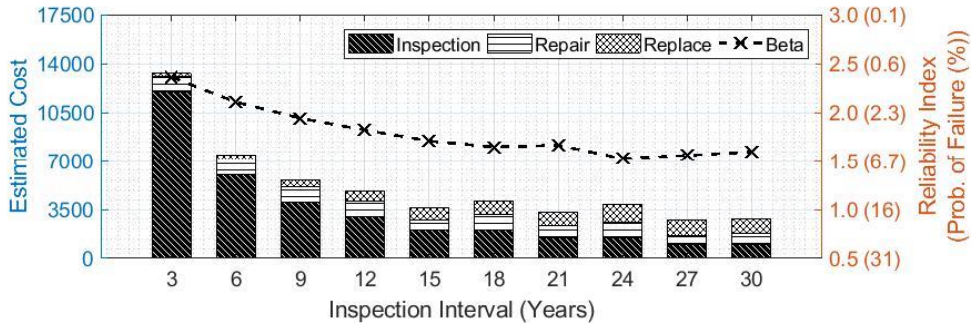

Figure 9.34: Laredo (12907) - Relationship between Maintenance Cost and Inspection Interval for the Cost Scenario of ($K_I : K_R : K_F = 500 : 6000 : 20000$)

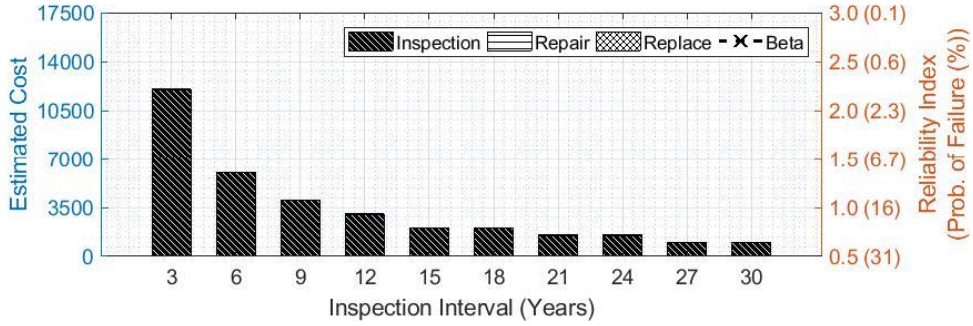

Figure 9.35: Atlanta (13977) - Relationship between Maintenance Cost and Inspection Interval for the Cost Scenario of ($K_I : K_R : K_F = 500 : 6000 : 20000$)

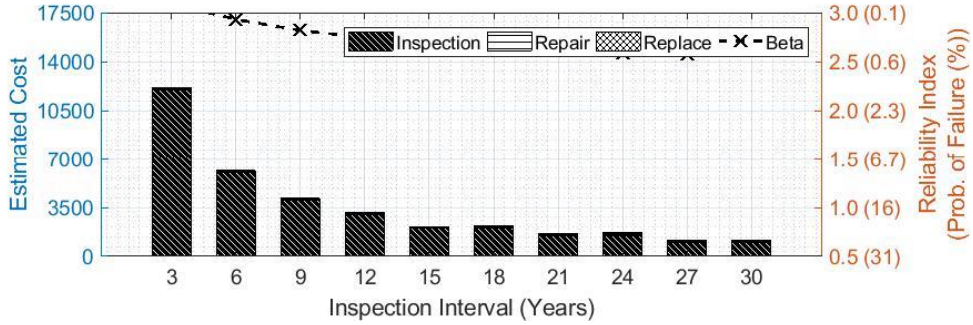

Figure 9.36: Atlanta (3901) - Relationship between Maintenance Cost and Inspection Interval for the Cost Scenario of ($K_I : K_R : K_F = 500 : 6000 : 20000$)

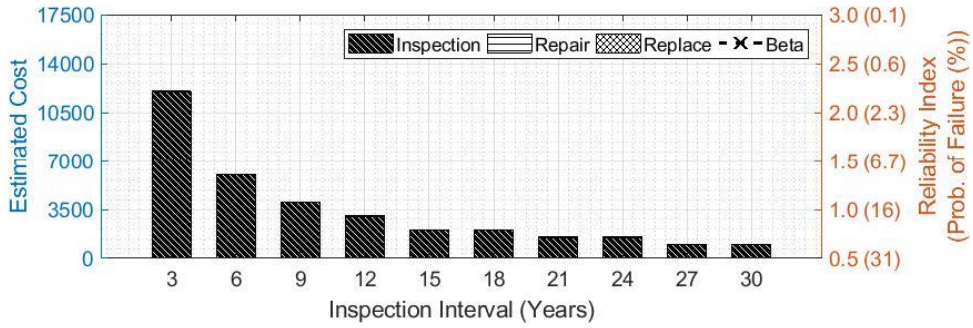

Figure 9.37: El Paso (Field) - Relationship between Maintenance Cost and Inspection Interval for the Cost Scenario of ($K_I : K_R : K_F = 500 : 6000 : 20000$)

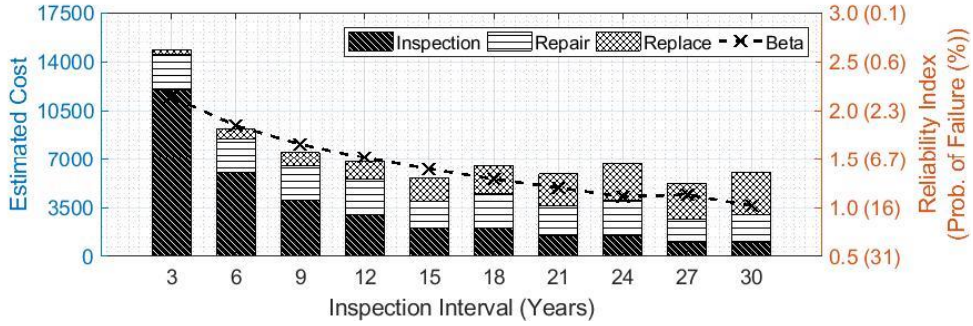

Figure 9.38: El Paso (23044) - Relationship between Maintenance Cost and Inspection Interval for the Cost Scenario of ($K_I : K_R : K_F = 500 : 6000 : 20000$)

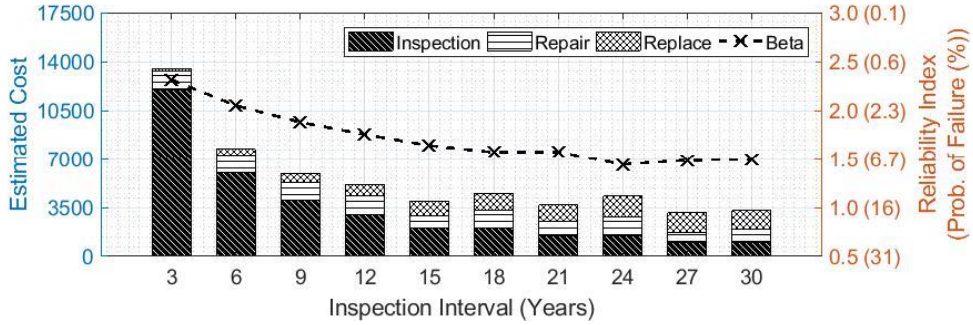

Figure 9.39: Odessa (3031) - Relationship between Maintenance Cost and Inspection Interval for the Cost Scenario of ($K_I : K_R : K_F = 500 : 6000 : 20000$)

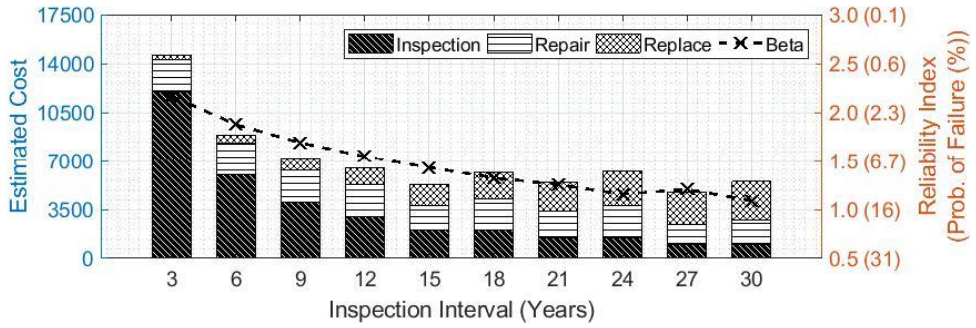

Figure 9.40: Odessa (23023) - Relationship between Maintenance Cost and Inspection Interval for the - Cost Scenario of ($K_I : K_R : K_F = 500 : 6000 : 20000$)

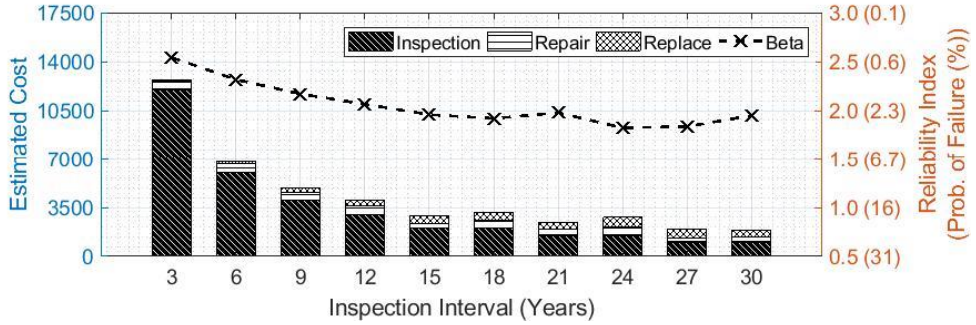

Figure 9.41: Odessa (3071) - Relationship between Maintenance Cost and Inspection Interval for the Cost Scenario of ($K_I : K_R : K_F = 500 : 6000 : 20000$)

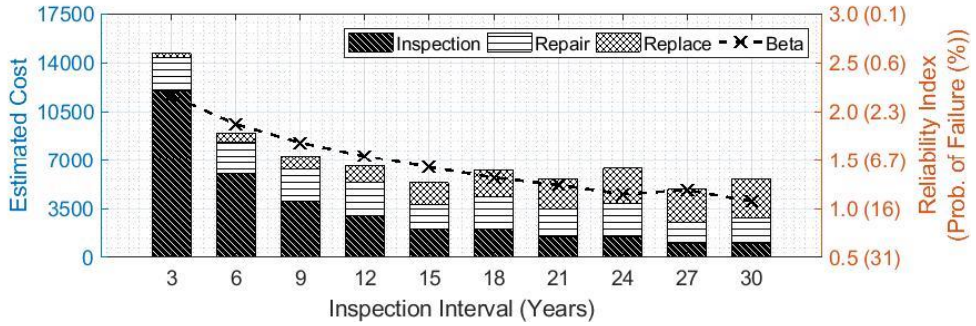

Figure 9.42: Ft. Worth (3927) - Relationship between Maintenance Cost and Inspection Interval for the Cost Scenario of ($K_I : K_R : K_F = 500 : 6000 : 20000$)

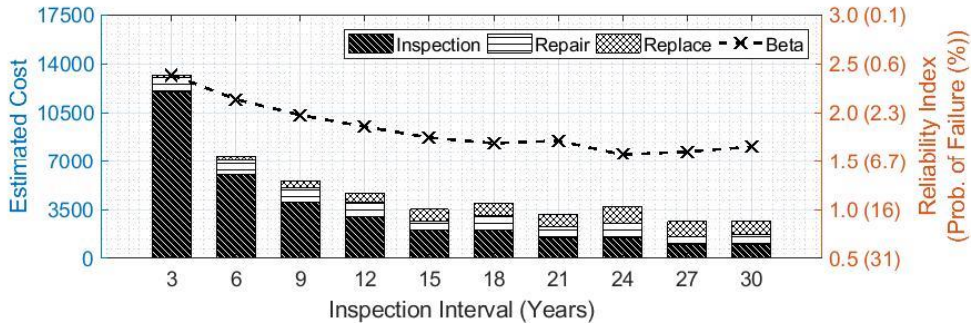

Figure 9.43: Ft. Worth (13961) - Relationship between Maintenance Cost and Inspection Interval for the Cost Scenario of ($K_I : K_R : K_F = 500 : 6000 : 20000$))

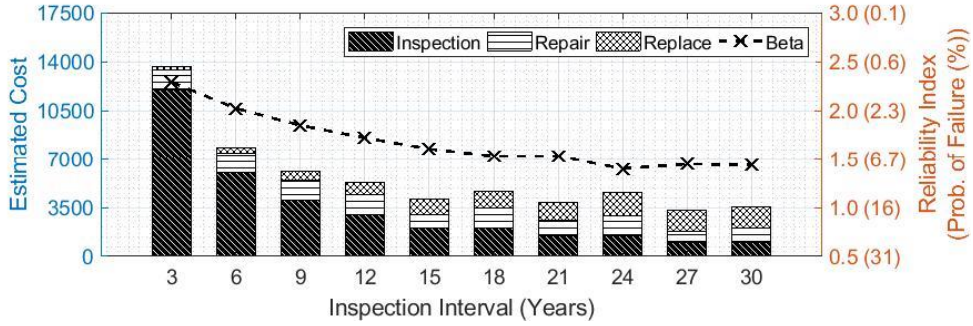

Figure 9.44: Ft. Worth (13911) - Relationship between Maintenance Cost and Inspection Interval for the Cost Scenario of ($K_I : K_R : K_F = 500 : 6000 : 20000$)

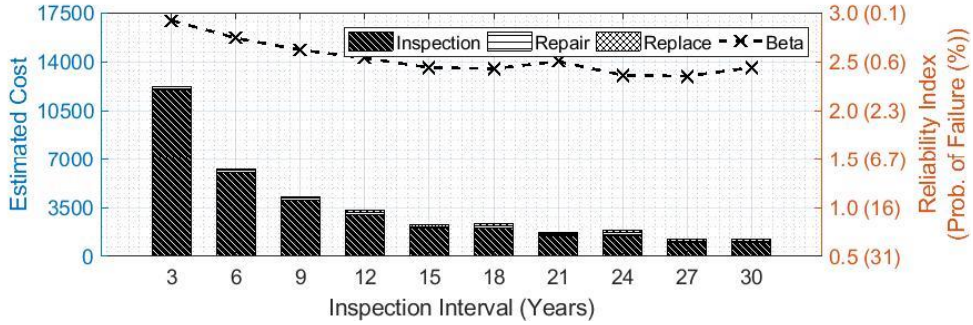

Figure 9.45: Ft. Worth (53977) - Relationship between Maintenance Cost and Inspection Interval for the Cost Scenario of ($K_I : K_R : K_F = 500 : 6000 : 20000$)

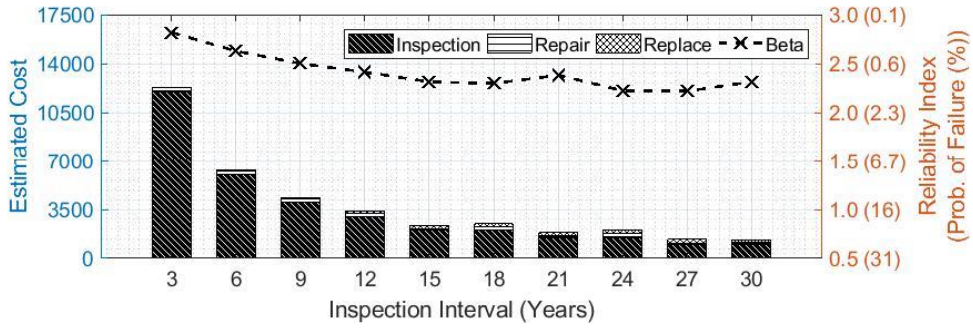

Figure 9.46: Paris (13926) - Relationship between Maintenance Cost and Inspection Interval for the Cost Scenario of ($K_I : K_R : K_F = 500 : 6000 : 20000$)

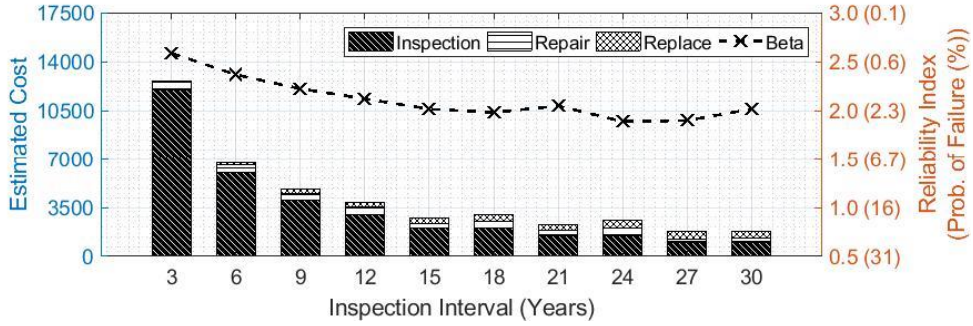

Figure 9.47: Paris (93955) - Relationship between Maintenance Cost and Inspection Interval for the Cost Scenario of ($K_I : K_R : K_F = 500 : 6000 : 20000$)

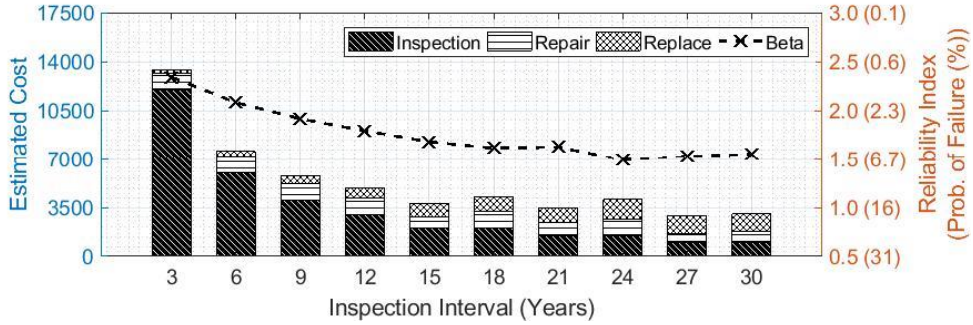

Figure 9.48: Paris (53967) - Relationship between Maintenance Cost and Inspection Interval for the Cost Scenario of ($K_I : K_R : K_F = 500 : 6000 : 20000$)

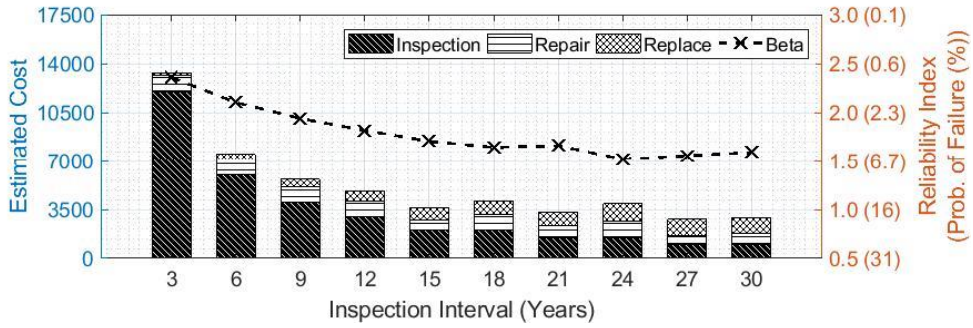

Figure 9.49: Waco (53972) - Relationship between Maintenance Cost and Inspection Interval for the Cost Scenario of ($K_I : K_R : K_F = 500 : 6000 : 20000$)

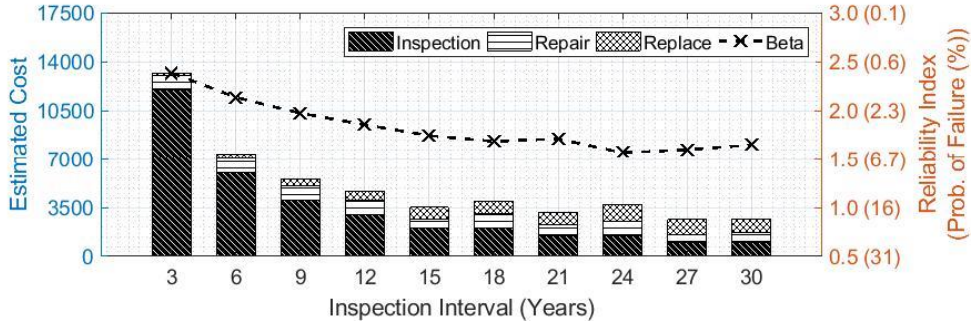

Figure 9.50: Waco (13959) - Relationship between Maintenance Cost and Inspection Interval for the Cost Scenario of ($K_I : K_R : K_F = 500 : 6000 : 20000$)

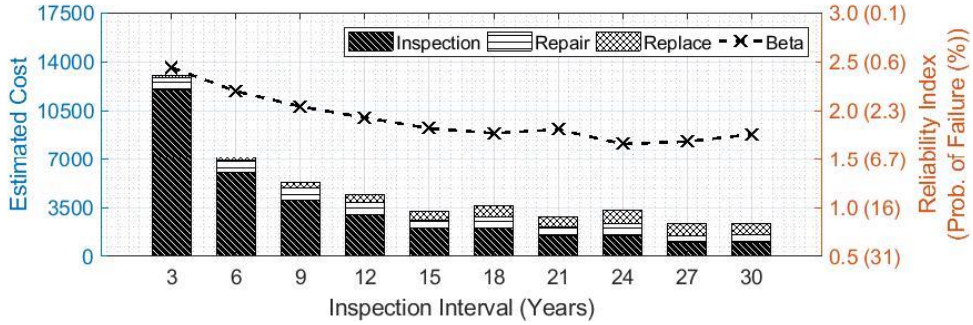

Figure 9.51: Waco (53952) - Relationship between Maintenance Cost and Inspection Interval for the Cost Scenario of ($K_I : K_R : K_F = 500 : 6000 : 20000$)

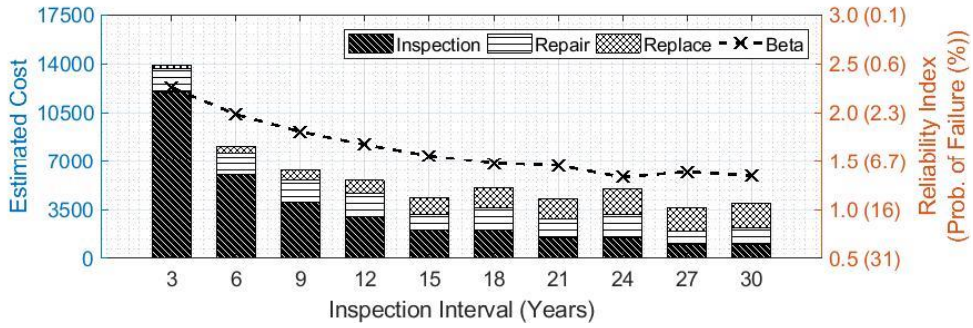

Figure 9.52: Waco (93984) - Relationship between Maintenance Cost and Inspection Interval for the Cost Scenario of ($K_I : K_R : K_F = 500 : 6000 : 20000$)

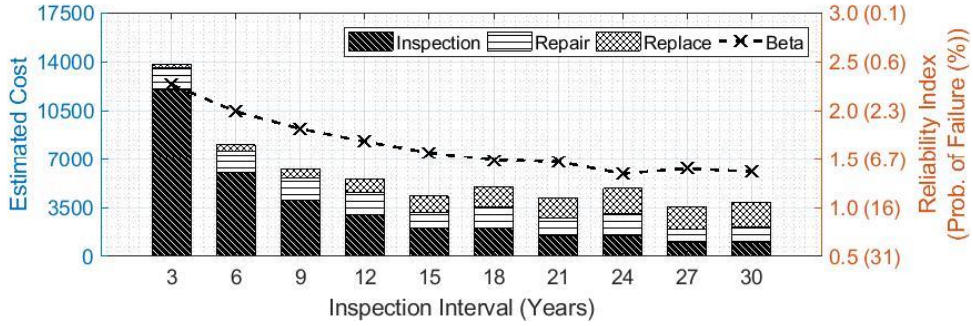

Figure 9.53: Waco (3902) - Relationship between Maintenance Cost and Inspection Interval for the Cost Scenario of ($K_I : K_R : K_F = 500 : 6000 : 20000$)

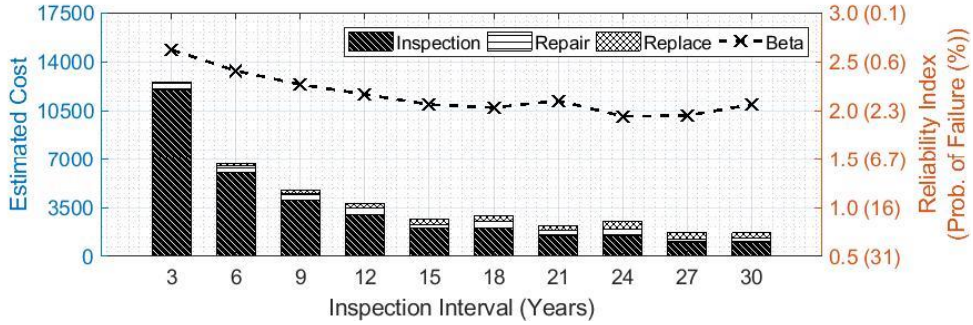

Figure 9.54: Waco (3933) - Relationship between Maintenance Cost and Inspection Interval for the Cost Scenario of ($K_I : K_R : K_F = 500 : 6000 : 20000$)

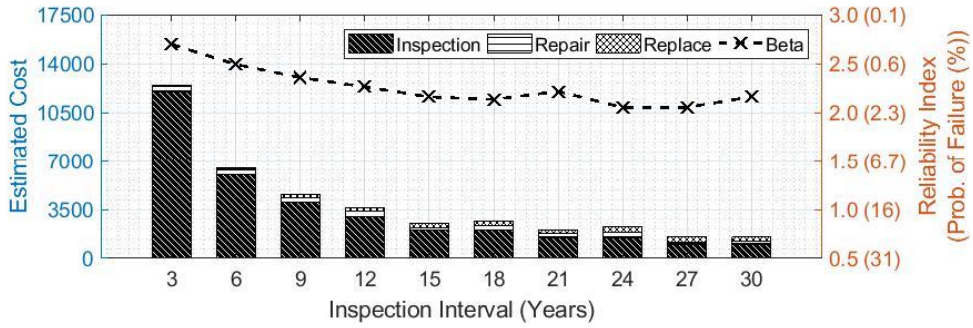

Figure 9.55: Waco (3972) - Relationship between Maintenance Cost and Inspection Interval for the Cost Scenario of ($K_I : K_R : K_F = 500 : 6000 : 20000$)

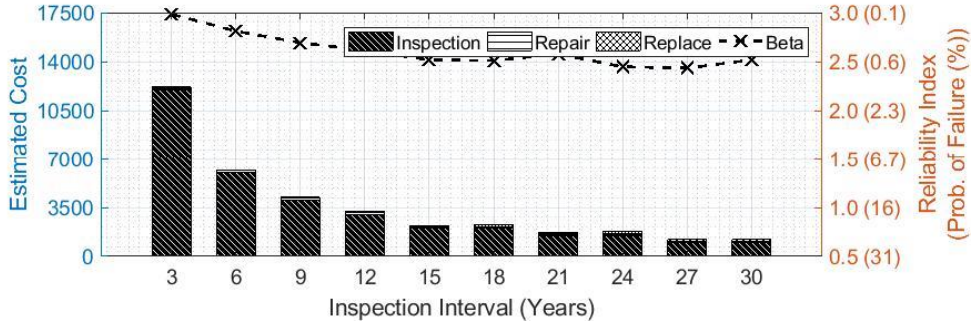

Figure 9.56: Brownwood (176) - Relationship between Maintenance Cost and Inspection Interval for the Cost Scenario of ($K_I : K_R : K_F = 500 : 6000 : 20000$)

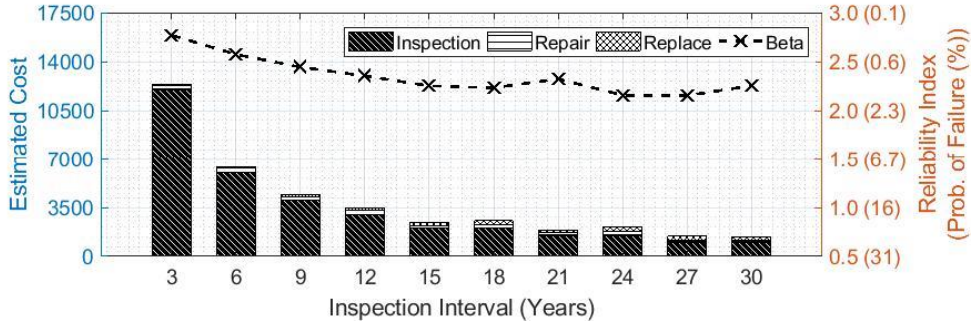

Figure 9.57: Wichita Falls (134) - Relationship between Maintenance Cost and Inspection Interval for the Cost Scenario of ($K_I : K_R : K_F = 500 : 6000 : 20000$)

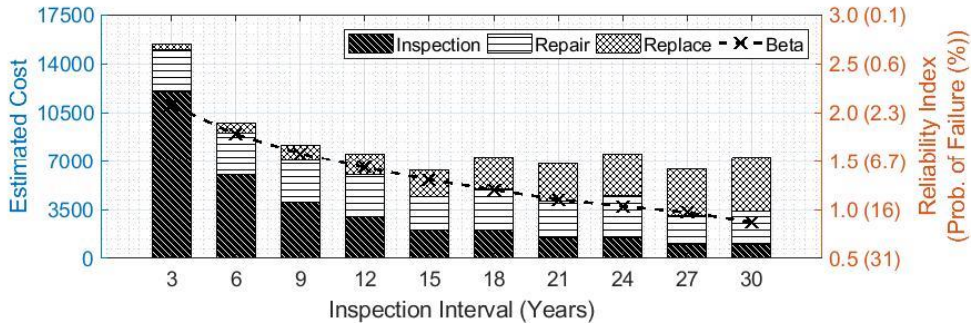

Figure 9.58: Wichita Falls (13966) - Relationship between Maintenance Cost and Inspection Interval for the Cost Scenario of ($K_I : K_R : K_F = 500 : 6000 : 20000$)

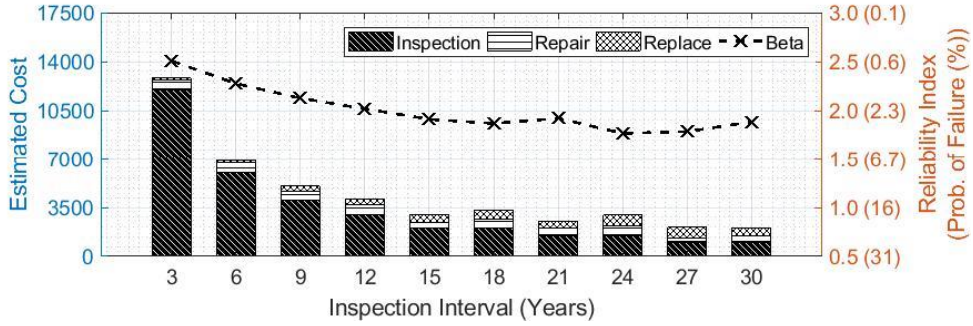

Figure 9.59: Wichita Falls (93929) - Relationship between Maintenance Cost and Inspection Interval for the Cost Scenario of ($K_I : K_R : K_F = 500 : 6000 : 20000$)

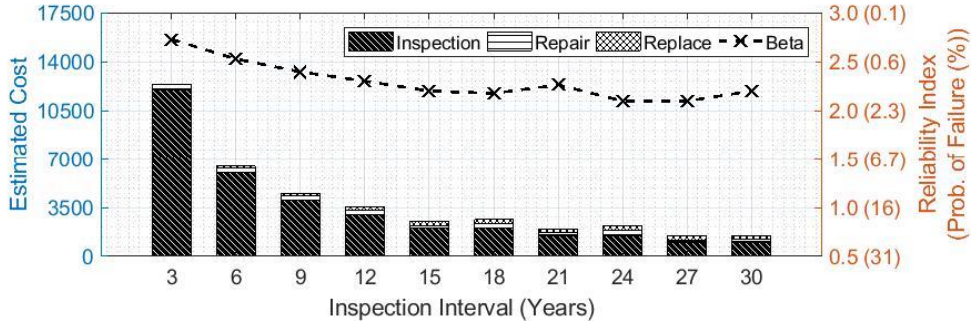

Figure 9.60: Bryan (3904) - Relationship between Maintenance Cost and Inspection Interval for the Cost Scenario of ($K_I : K_R : K_F = 500 : 6000 : 20000$)

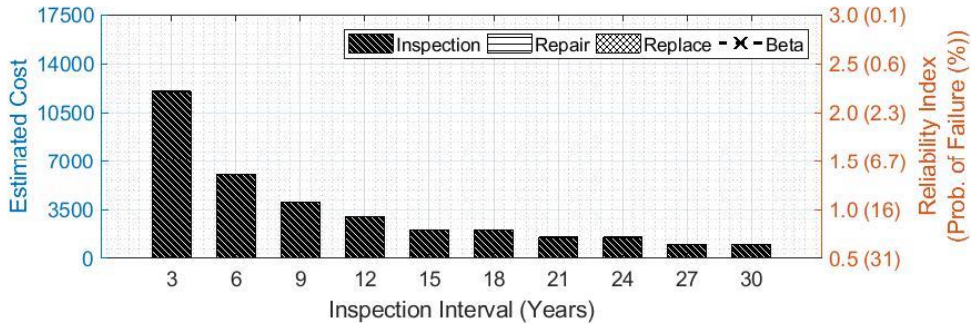

Figure 9.61: Bryan (438) - Relationship between Maintenance Cost and Inspection Interval for the Cost Scenario of ($K_I : K_R : K_F$ = 500 : 6000 : 20000)

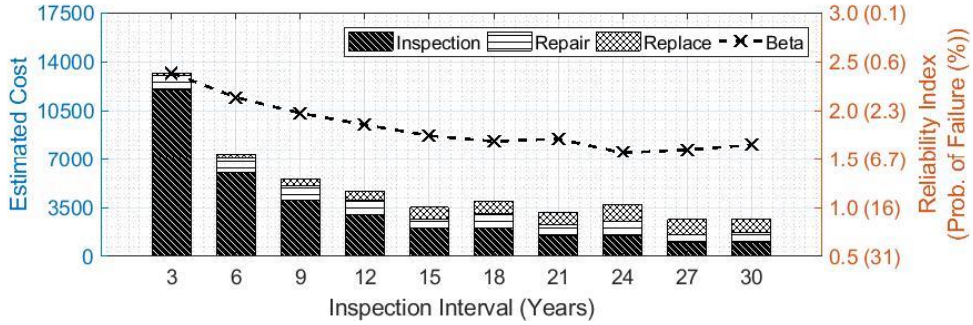

Figure 9.62: Dallas (13960) - Relationship between Maintenance Cost and Inspection Interval for the Cost Scenario of ($K_I : K_R : K_F$ = 500 : 6000 : 20000)

Table 9.20: Number of Inspections, Repairs, and Probability of Failure under Different Inspection Intervals

Inspection Interval (Years)		3	6	9	12	15	18	21	24	27	30
Austin (Field)	No. of Inspections	24	12	8	6	4	4	3	3	2	2
	No. of Repairs	0.00	0.00	0.00	0.00	0.00	0.00	0.00	0.00	0.00	0.00
	Failure Prob. (%)	0.01	0.02	0.03	0.04	0.05	0.05	0.05	0.06	0.07	0.05
Austin (230)	No. of Inspections	24	12	8	6	4	4	3	3	2	2
	No. of Repairs	0.02	0.02	0.02	0.02	0.01	0.02	0.01	0.02	0.01	0.01
	Failure Prob. (%)	0.11	0.18	0.26	0.33	0.44	0.44	0.37	0.52	0.55	0.44
Austin (13904)	No. of Inspections	24	12	8	6	4	4	3	3	2	2
	No. of Repairs	0.08	0.08	0.08	0.08	0.05	0.08	0.06	0.08	0.04	0.05
	Failure Prob. (%)	0.45	0.83	1.21	1.56	2.02	2.18	1.84	2.69	2.65	2.02
Austin (53942)	No. of Inspections	24	12	8	6	4	4	3	3	2	2
	No. of Repairs	0.06	0.06	0.06	0.06	0.04	0.06	0.04	0.06	0.03	0.04
	Failure Prob. (%)	0.35	0.64	0.92	1.19	1.54	1.65	1.34	2.01	2.00	1.54
Laredo (Field)	No. of Inspections	24	12	8	6	4	4	3	3	2	2
	No. of Repairs	0.00	0.00	0.00	0.00	0.00	0.00	0.00	0.00	0.00	0.00
	Failure Prob. (%)	0.02	0.03	0.05	0.06	0.08	0.08	0.07	0.09	0.10	0.08
Laredo (12907)	No. of Inspections	24	12	8	6	4	4	3	3	2	2
	No. of Repairs	0.19	0.19	0.19	0.19	0.13	0.19	0.14	0.19	0.10	0.13
	Failure Prob. (%)	0.91	1.76	2.61	3.43	4.37	4.97	4.79	6.35	5.93	5.51
Atlanta (13977)	No. of Inspections	24	12	8	6	4	4	3	3	2	2
	No. of Repairs	0.00	0.00	0.00	0.00	0.00	0.00	0.00	0.00	0.00	0.00
	Failure Prob. (%)	0.02	0.03	0.05	0.06	0.08	0.07	0.07	0.08	0.09	0.08
Atlanta (3901)	No. of Inspections	24	12	8	6	4	4	3	3	2	2
	No. of Repairs	0.02	0.02	0.02	0.02	0.01	0.02	0.01	0.02	0.01	0.01
	Failure Prob. (%)	0.10	0.17	0.24	0.30	0.40	0.41	0.34	0.48	0.51	0.40
El Paso (Field)	No. of Inspections	24	12	8	6	4	4	3	3	2	2
	No. of Repairs	0.00	0.00	0.00	0.00	0.00	0.00	0.00	0.00	0.00	0.00
	Failure Prob. (%)	0.02	0.04	0.05	0.07	0.09	0.09	0.08	0.10	0.11	0.09
El Paso (23044)	No. of Inspections	24	12	8	6	4	4	3	3	2	2
	No. of Repairs	0.42	0.42	0.42	0.42	0.32	0.42	0.35	0.42	0.27	0.32
	Failure Prob. (%)	1.61	3.25	4.90	6.53	8.16	9.85	11.49	13.31	12.93	15.43
Odessa (3031)	No. of Inspections	24	12	8	6	4	4	3	3	2	2
	No. of Repairs	0.22	0.22	0.22	0.22	0.15	0.22	0.17	0.22	0.12	0.15
	Failure Prob. (%)	1.03	2.02	3.00	3.96	5.03	5.80	5.76	7.47	6.88	6.80
Odessa (23023)	No. of Inspections	24	12	8	6	4	4	3	3	2	2
	No. of Repairs	0.38	0.38	0.38	0.38	0.29	0.38	0.31	0.38	0.24	0.29
	Failure Prob. (%)	1.51	3.03	4.56	6.09	7.62	9.25	10.51	12.40	11.40	13.79
Odessa (3071)	No. of Inspections	24	12	8	6	4	4	3	3	2	2
	No. of Repairs	0.10	0.10	0.10	0.10	0.06	0.10	0.07	0.10	0.05	0.06
	Failure Prob. (%)	0.55	1.03	1.50	1.95	2.51	2.75	2.39	3.41	3.31	2.57

Table 9.20: Number of Inspections, Repairs, and Probability of Failure under Different Inspection Intervals (Continued)

Inspection Interval (Years)		3	6	9	12	15	18	21	24	27	30
Ft. Worth (3927)	No. of Inspection	24	12	8	6	4	4	3	3	2	2
	No. of Repair	0.39	0.39	0.39	0.39	0.30	0.39	0.32	0.39	0.25	0.30
	Failure Prob. (%)	1.53	3.08	4.64	6.17	7.72	9.40	10.74	12.61	11.75	14.17
Ft. Worth (13961)	No. of Inspection	24	12	8	6	4	4	3	3	2	2
	No. of Repair	0.17	0.17	0.17	0.17	0.11	0.17	0.13	0.17	0.09	0.11
	Failure Prob. (%)	0.85	1.64	2.42	3.18	4.05	4.58	4.34	5.83	5.47	4.94
Ft. Worth (13911)	No. of Inspection	24	12	8	6	4	4	3	3	2	2
	No. of Repair	0.24	0.24	0.24	0.24	0.17	0.24	0.19	0.24	0.13	0.17
	Failure Prob. (%)	1.10	2.16	3.22	4.27	5.40	6.27	6.35	8.12	7.43	7.59
Ft. Worth (53977)	No. of Inspection	24	12	8	6	4	4	3	3	2	2
	No. of Repair	0.03	0.03	0.03	0.03	0.02	0.03	0.02	0.03	0.01	0.02
	Failure Prob. (%)	0.18	0.31	0.44	0.56	0.74	0.76	0.62	0.91	0.94	0.74
Paris (13926)	No. of Inspection	24	12	8	6	4	4	3	3	2	2
	No. of Repair	0.04	0.04	0.04	0.04	0.02	0.04	0.03	0.04	0.02	0.02
	Failure Prob. (%)	0.24	0.43	0.62	0.79	1.03	1.08	0.86	1.31	1.33	1.03
Paris (93955)	No. of Inspection	24	12	8	6	4	4	3	3	2	2
	No. of Repair	0.09	0.09	0.09	0.09	0.06	0.09	0.06	0.09	0.04	0.06
	Failure Prob. (%)	0.49	0.90	1.31	1.70	2.19	2.38	2.03	2.94	2.88	2.19
Paris (53967)	No. of Inspection	24	12	8	6	4	4	3	3	2	2
	No. of Repair	0.20	0.20	0.20	0.20	0.14	0.20	0.15	0.20	0.11	0.14
	Failure Prob. (%)	0.96	1.87	2.78	3.66	4.65	5.32	5.19	6.82	6.33	6.04
Waco (53972)	No. of Inspection	24	12	8	6	4	4	3	3	2	2
	No. of Repair	0.19	0.19	0.19	0.19	0.13	0.19	0.14	0.19	0.10	0.13
	Failure Prob. (%)	0.92	1.78	2.63	3.46	4.41	5.02	4.84	6.41	5.98	5.58
Waco (13959)	No. of Inspection	24	12	8	6	4	4	3	3	2	2
	No. of Repair	0.17	0.17	0.17	0.17	0.12	0.17	0.13	0.17	0.09	0.12
	Failure Prob. (%)	0.85	1.64	2.43	3.18	4.06	4.59	4.36	5.84	5.48	4.96
Waco (53952)	No. of Inspection	24	12	8	6	4	4	3	3	2	2
	No. of Repair	0.14	0.14	0.14	0.14	0.09	0.14	0.11	0.14	0.07	0.09
	Failure Prob. (%)	0.74	1.40	2.06	2.69	3.45	3.85	3.54	4.85	4.62	3.94
Waco (93984)	No. of Inspection	24	12	8	6	4	4	3	3	2	2
	No. of Repair	0.27	0.27	0.27	0.27	0.20	0.27	0.21	0.27	0.16	0.20
	Failure Prob. (%)	1.20	2.38	3.57	4.74	5.99	7.03	7.31	9.17	8.29	8.94
Waco (3902)	No. of Inspection	24	12	8	6	4	4	3	3	2	2
	No. of Repair	0.26	0.26	0.26	0.26	0.19	0.26	0.21	0.26	0.15	0.19
	Failure Prob. (%)	1.18	2.33	3.49	4.63	5.85	6.85	7.08	8.92	8.09	8.61
Waco (3933)	No. of Inspection	24	12	8	6	4	4	3	3	2	2
	No. of Repair	0.08	0.08	0.08	0.08	0.05	0.08	0.06	0.08	0.04	0.05
	Failure Prob. (%)	0.44	0.81	1.17	1.52	1.96	2.12	1.78	2.61	2.57	1.96

Table 9.20: Number of Inspections, Repairs, and Probability of Failure under Different Inspection Intervals (Continued)

Inspection Interval (Years)		3	6	9	12	15	18	21	24	27	30
Waco (3972)	No. of Inspection	24	12	8	6	4	4	3	3	2	2
	No. of Repair	0.06	0.06	0.06	0.06	0.04	0.06	0.04	0.06	0.03	0.04
	Failure Prob. (%)	0.35	0.64	0.92	1.18	1.54	1.64	1.34	2.00	2.00	1.54
Brownwood (176)	No. of Inspection	24	12	8	6	4	4	3	3	2	2
	No. of Repair	0.02	0.02	0.02	0.02	0.01	0.02	0.02	0.02	0.01	0.01
	Failure Prob. (%)	0.14	0.25	0.35	0.45	0.59	0.60	0.50	0.72	0.75	0.59
Wichita Falls (134)	No. of Inspection	24	12	8	6	4	4	3	3	2	2
	No. of Repair	0.05	0.05	0.05	0.05	0.03	0.05	0.03	0.05	0.02	0.03
	Failure Prob. (%)	0.28	0.50	0.73	0.93	1.21	1.28	1.01	1.55	1.56	1.21
Wichita Falls (13966)	No. of Inspection	24	12	8	6	4	4	3	3	2	2
	No. of Repair	0.50	0.50	0.50	0.50	0.40	0.50	0.43	0.50	0.35	0.40
	Failure Prob. (%)	1.88	3.79	5.72	7.61	9.60	11.48	13.56	15.06	16.59	19.19
Wichita Falls (93929)	No. of Inspection	24	12	8	6	4	4	3	3	2	2
	No. of Repair	0.11	0.11	0.11	0.11	0.07	0.11	0.08	0.11	0.06	0.07
	Failure Prob. (%)	0.61	1.14	1.67	2.18	2.80	3.08	2.73	3.85	3.71	2.97
Bryan (3904)	No. of Inspection	24	12	8	6	4	4	3	3	2	2
	No. of Repair	0.06	0.06	0.06	0.06	0.03	0.06	0.04	0.06	0.02	0.03
	Failure Prob. (%)	0.32	0.58	0.83	1.07	1.39	1.48	1.19	1.80	1.80	1.39
Bryan (438)	No. of Inspection	24	12	8	6	4	4	3	3	2	2
	No. of Repair	0.00	0.00	0.00	0.00	0.00	0.00	0.00	0.00	0.00	0.00
	Failure Prob. (%)	0.01	0.02	0.03	0.03	0.04	0.04	0.04	0.05	0.05	0.04
Dallas (13960)	No. of Inspection	24	12	8	6	4	4	3	3	2	2
	No. of Repair	0.17	0.17	0.17	0.17	0.12	0.17	0.13	0.17	0.09	0.12
	Prob. of Failure	0.85	1.64	2.43	3.18	4.06	4.59	4.36	5.84	5.48	4.96

9.7 Summary

A comprehensive reliability-based framework for estimating remaining fatigue life of in-service HMIPs with pre-existing cracks is developed in this chapter. The HMIP design of interest (80 mph, 150 feet, 12 sided, without ground sleeve) identified in previous parts of the research was chosen as the target for the reliability study. In addition to the predicted safe life for the HMIPs of interest, an inspection scheduling procedure was further developed to extend the service life of cracked HMIPs. Optimal inspection schedules were proposed based on minimal expected cost and corresponding reliability against failure.

Major findings/observations from the work presented in this chapter are summarized as follows:

- Analyzing results from fatigue experiments using the method proposed by AASHTO in determining the fatigue capacity and introducing the two-slope S-N curves suggested by Eurocode, a lower bound value for the fatigue capacity of cracked HMIPs is established.
- Experimental fatigue results obtained from specimens with different initial conditions and different testing procedures greatly increase the uncertainties in fatigue strength

predictions. Carefully selected results obtained from the same testing protocol yields less scattered results. The lower uncertainties from selected tests yields similar uncertainties observed in the AASHTO fatigue design categories.

- The different mean stresses in the fatigue testing are accounted for and corrected to provide more representative strength results from fatigue tests.
- The fatigue demand characterized by the equivalent fatigue load (EFL) is utilized with different wind data to obtain fatigue demands at different locations in Texas.
- Expected life based on an envelope EFL is more conservative compared to the one based on average EFL. Average-EFL is suggested to better represent the demand in the field.
- Expected life of in-service HMIPs with pre-existing cracks are determined based on the acceptable probability of failure from 0.02% to 10%. Ultimately, a probability of failure of 5% or 6.7% is suggested in this study to provide consistency with the lower bound S-N curve proposed by AASHTO. Key results are presented in Table 9.17.
- A wide range of expected safe lives are seen from all analyzed locations, even ones located in the same district. This scatter in predicted expected fatigue life for cracked HMIPs is mainly affected by the wind characteristics at each location.
- Taking account of the parameters uncertainty due to limited experimental data increases the range of expected life even more. The proposed expected life is a best estimate assuming the sample parameters determined from the experiment are close to the true values.
- Using an allowable probability of failure at 5% results in the predicted remaining fatigue life of around 30 to 40 years for the HMIPs located in El Paso, Odessa, Ft. Worth, and Wichita Falls districts. This prediction suggests the need for more immediate attention to HMIPs located in these districts. A failure probability of 5% implies that one out of twenty poles at any location would experience failure. A failure defined in this study is based on an unrepairable condition that warrants the pole replacement, and does not indicate collapse of the pole.
- The proposed inspection scheduling procedure is found to increase the service fatigue life of the HMIPs considering different costs involved including the costs of inspection, repair, and replacement.
- Different cost combinations result in different optimal inspection intervals. More specifically, high inspection costs yield longer optimal intervals, while high replacement or failure costs result in shorter optimal intervals.
- The proposed inspection scheduling procedure, taking into account different probabilities of failure over the service life of HMIPs and their associated costs, provides TxDOT with a method to schedule inspections according to the accepted probability of failure or maintenance cost.

Chapter 10. Summary, Major Findings, and Recommendations

10.1 Summary

TxDOT Project 0-6829 generated data and information to support a probabilistic-based assessment of the remaining life of pre-cracked HMIPs. As part of this project, laboratory fatigue tests were conducted on pre-cracked galvanized HMIPs. In addition, field data was collected and additional analyses were performed to characterize wind response of Texas HMIPs. Field and laboratory studies were supplemented by finite element studies simulating the global and local response of pre-cracked HMIPs. The results of the laboratory data, field studies, and analytical studies were combined in a reliability-based framework to provide a probabilistic assessment of the fatigue life of in-service pre-cracked HMIPs. Finally, additional information was developed in this project on options for mitigating risk associated with cracked HMIPs, such as increased inspection and monitoring, and repair techniques. This chapter presents major findings from this project, along with conclusions and recommendations.

10.2 Major Findings

The following subsections provide a summary of major findings from the TxDOT Project 0-6829 on Fatigue Resistance and Reliability of High Mast Illumination Poles (HMIPs) with Pre-Existing Cracks.

10.2.1 Survey of Texas HMIPs

- The research team has compiled and reported the most complete available Texas HMIP inventory in Chapter 3. Based on this inventory, it is estimated that there are approximately 1000 cracked HMIPs currently in-service in the state of Texas.

- The data collected in the survey showed that of all the HMIPs in-service in Texas, poles that are 12-sided, 150 ft. tall, with a design wind of 80 mph, and without ground sleeves are more prone to cracks at the shaft-to-base plate welds. The survey also showed that districts that have the largest number of these poles are Austin, Laredo, Atlanta, El Paso, Odessa, Fort Worth, and Paris. This information was used to guide the research efforts on the experimental and field investigations of the fatigue behavior of HMIPs with pre-existing cracks.

10.2.2 Fatigue Tests on Galvanized HMIPs

- A number of HMIP specimens were tested to failure under fatigue loading, at a variety of stress ranges. Fatigue failure was defined to occur when the stiffness of the test specimen was reduced by 10-percent. Although this is a somewhat arbitrary definition of failure, the cracking of the specimens at this defined point of failure was normally quite extensive, with cracks extending through the full thickness of the shaft wall.

- All HMIP specimens tested in this program were designed and fabricated to TxDOT standards, by a commercial fabricator and galvanizer experienced in producing HMIPs for TxDOT. All of the specimens had pre-existing cracks at their base, of varying degrees of

severity when delivered to the laboratory for fatigue testing. Consequently, the specimens were considered to be representative of typical in-service HMIPs with pre-existing cracks, for the specific designs of interest in this research program.

- The majority of specimens tested in this program were representative of HMIPs with poles that are 12-sided, 150 ft. tall, with a design wind speed of 80 mph, and without ground sleeves (referred to in this report as the primary design). All of these specimens showed poor fatigue behavior, with failure occurring on an S-N plot below AASHTO fatigue category E′. Thus, this testing program confirmed the poor fatigue performance of these poles.

- Two specimens were tested in this program that were representative of HMIPs with poles that are 12-sided, 150 ft. tall, with a design wind speed of 80 mph, and with ground sleeves (referred to in this report as the secondary design). One specimen failed below AASHTO fatigue category E′. Although this represents only a single data point on specimens with ground sleeves, it clearly indicates the need for further investigation of the fatigue behavior of HMIPs with ground sleeves.

- The initial condition of the HMIP specimens in terms of both crack length and crack depth was found to significantly affect the fatigue life of the cracked HMIPs.

- The fatigue behavior of cracked HMIP specimens under lower stress ranges (at 3 ksi and lower) was different from that under higher stress ranges. The crack depth appeared to play a major role in the fatigue life predictions at low stress ranges.

- Cracks were observed to propagate in the shaft away from the weld as a result of irregularities on the weld toe. When cracks started to propagate in the shaft, the rate of change in their length increased very quickly causing a very rapid fatigue failure. This suggests that if cracks are seen in the shaft of an in-service pole that are growing away from the weld toe, repair or replacement should be undertaken as soon as possible.

- One specimen of the primary design, after completion of fatigue testing, was subject to static loading to complete failure. Since this specimen was already deemed to have failed under fatigue loading, it had extensive cracking at its base, prior to the application of static loading. The purpose of this static test was to assess the residual static strength of a pole with extensive fatigue cracking, and to assess the degree of ductility exhibited during failure under static loading. The results of this test showed that this pole with extensive fatigue cracking retained approximately 80-percent of its full static strength, based on the estimated plastic moment capacity of the shaft at the base of the pole. Further, the failure under static loading showed considerable ductility. This result suggests that an in-service pole with extensive fatigue cracking may exhibit a ductile failure under a large wind gust; however as noted above, this observation is based upon a single static test.

- The results of the fatigue tests conducted as part of this project were combined with fatigue test results from other researchers. This combined data was used to develop fatigue S-N curves for HMIPs with pre-existing cracks. Even with the fatigue data collected at low

stress ranges in this test program by researchers at the University of Texas at Austin (TxDOT Research Project 0-6829) and at the University of Houston (TxDOT Research Project 0-6830), there is still considerable uncertainty on the fatigue life of HMIPs with pre-existing cracks at very low stress ranges that are representative of the stress ranges expected under vortex induced vibration.

- Phased array ultrasonic testing (PAUT) was used to detect and characterize the length and depth of cracks in many of the HMIP specimens tested in this research program. PAUT appears to be capable of characterizing cracks more accurately than conventional ultrasonic testing, and it is recommended that TxDOT employ PAUT for future inspections of HMIPs, both for shop and field inspections. However, even with PAUT, there is uncertainty in crack detection. The depths of cracks appears to be particularly difficult to measure accurately.

- Crack-size detection using both conventional ultrasonic and phased array ultrasonic methods proved to be dependent on the orientation of the HMIP specimens. More specifically, accurate detection of crack sizes was more challenging when the specimens were positioned vertically rather than horizontally. This suggests greater care in ultrasonic inspection may be needed for in-service poles, which will be in a vertical orientation, as compared to the test specimens ultrasonically examined in a horizontal position in this research program. The specimens tested in the laboratory only consisted of a single base sections. Field specimens will have added dead load of the upper segments of the pole as well as the luminaries, which may further complicate the ability to measure crack sizes.

- Accurate crack-size detection using both conventional ultrasonic and phased array ultrasonic methods proved to be challenging for more complex weld details such as the seam weld to baseplate detail, and the shaft-to-baseplate weld detail for the specimens with ground sleeves.

10.2.3 Field Studies of In-Service HMIPs

- Dynamic characteristics of HMIPs such as structural natural periods and mode shapes obtained from numerical models corresponded well with those measured in the field.
- Wind characteristics such as turbulence intensity distribution, wind speed and direction distribution are all affected by the built and natural environment surrounding the HMIPs.
- Large-amplitude vortex-induced vibration response in the cross-wind direction occurred for HMIPs at low wind speeds (around 7 mph) as was seen in previous studies.
- Vortex-induced vibration response mainly accompanied vibration in the second mode while the third mode was rarely excited significantly.
- Buffeting response vibrates in the first mode in both along-wind and cross-wind directions.
- Turbulence was found to be more important at higher wind speeds where both the along-wind and cross-wind responses in the first mode were significant.

- A method for quantifying the damage using the concept of Equivalent Fatigue Load (EFL) was used to directly assess the contributions of different wind conditions such as wind speed, direction, and turbulence intensity to the fatigue damage.
- The concept of EFL links the wind condition directly to the fatigue damage without the need to assume a dominant mode and without the need to predict the response amplitude.
- Damage expressed in terms of EFL for low wind speeds exceeds that for high wind speeds due to the higher vibration frequencies and higher motion amplitudes resulting from vortex-induced vibration.
- Variability in EFL results from different sites was observed due to different turbulence intensities from the wind and damping factors inherent in the structural properties.
- To better represent the EFL for fatigue-damage assessment in different locations in Texas, averaged EFLs and envelope EFLs were proposed. The envelope EFL results in more conservative predictions of the fatigue damage.
- A modified EFL based on a two-slope S-N curve was suggested and implemented. Compared to the S-N curves with Constant Amplitude Fatigue Limit (CAFL) or single straight line S-N curves without CAFL, the two-slope S-N curves more realistically represents the fatigue strength at low stress ranges experienced by in-service HMIPs.

10.2.4 Computational Studies of Cracked HMIPs

- The finite element programs SAP2000 and Abaqus were capable of accurately modeling and predicting the global dynamic behavior of in-service HMIPs.
- The fatigue solver *fe-safe* was shown to be capable of predicting the locations of fatigue crack initiation.
- Results from AFGROW software in predicting crack growth observed in fatigue tests on HMIP specimens were shown to be highly uncertain particularly due to uncertainties in material models.

10.2.5 Mitigation Strategies for Cracked HMIPs

- The weld-repair procedure implemented in this project to enhance the fatigue life of in-service HMIPs with preexisting cracks, was shown to be effective in increasing the fatigue life of cracked HMIPs to fatigue category E′ or better. However, it is important to note that this observation is based on a relatively limited number of tests.
- The development and application of a comprehensive weld-repair procedure was not the main purpose of the TxDOT Project 0-6829. Therefore, the weld-repair procedure developed and implemented in this research should not be construed as a comprehensive development. Devising a comprehensive and robust weld-repair procedure requires consideration of different governing factors and extensive fatigue testing. Such an endeavor was outside the scope of the current project.

10.2.6 Reliability-Based Evaluation Studies of Cracked HMIPs

- A lower bound value for the fatigue capacity of cracked HMIPs was established by analyzing results from fatigue experiments using the method for determining fatigue

capacity proposed by AASHTO and also introducing the two-slope S-N curves suggested by the Eurocodes.

- Experimental fatigue results obtained from specimens with different initial conditions and different testing procedures greatly increase the uncertainties in fatigue strength predictions. Carefully selected results obtained from the same testing protocol yields less scattered results. The lower uncertainties from selected tests yields similar uncertainties observed in the AASHTO design categories.
- The different mean stresses in the fatigue testing are accounted for and corrected to provide more representative strength results from fatigue tests.
- The fatigue demand characterized by the Equivalent Fatigue Load (EFL) is utilized with different wind data to obtain fatigue demands at different locations in Texas.
- Expected life based on an envelope EFL is more conservative compared to the one based on average EFL. Average-EFL is suggested to better represent the demand in the field.
- Expected life of in-service HMIPs with pre-existing cracks are determined based on the acceptable probability of failure from 0.02% to 10%. Ultimately, a probability of failure of 5% or 6.7% is suggested in this study to provide consistency with the lower bound S-N curve proposed by AASHTO. Key results are presented in Table 9.17.
- A wide range of expected fatigue lives are seen from all analyzed locations, even ones located in the same district. This scatter in predicted expected fatigue life for cracked HMIPs is mainly affected by the wind characteristics at each location.
- Using an allowable probability of failure of 5% results in the predicted remaining fatigue life of approximately 30 years for the HMIPs located in the El Paso, Midland, Dallas, Ft. Worth, and Wichita Falls TxDOT Districts. This prediction suggests the need for more immediate attention to HMIPs located in these TxDOT Districts. A failure probability of 5% implies that one out of twenty poles at any location would experience failure. A failure defined in this study is based on an unrepairable condition that warrants the pole replacement, and does not necessarily indicate collapse of the pole.
- The proposed inspection scheduling procedure was developed to increase the service fatigue life of the HMIPs considering different costs involved including the costs of inspection, repair, and replacement.
- Different cost combinations result in different optimal inspection intervals. More specifically, high inspection costs yield longer optimal intervals, while high replacement or failure costs result in shorter optimal intervals.
- The proposed inspection scheduling procedure, taking into account different probabilities of failure over the service life of HMIPs and their associated costs, provides TxDOT with a method to schedule inspections according to the accepted probability of failure or maintenance cost.

10.3 Conclusions and Recommendations

The main objective of Project 0-6829 was to develop a probabilistic-based assessment of the remaining life of HMIPs with pre-existing cracks in Texas. It is estimated that there are likely more than 1000 such HMIPs in Texas. The results of this study show a wide range in the predicted

lives of HMIPs with pre-existing cracks at different locations throughout the state. Based on a probability of failure of 5-percent, the predicted fatigue life at a number of locations analyzed throughout the state varied from approximately 30 years to over 300 years. The variation in predicted fatigue lives is mainly affected by differing wind characteristics at each location.

Fatigue failure, in the context of this study, was defined as the condition where the severity of cracking at the pole base was sufficient to cause a 10-percent reduction in the pole's stiffness. Although this is a somewhat arbitrary definition of failure, based on laboratory fatigue tests, the cracking of the pole at this defined point of failure is normally quite extensive, with cracks extending through the full thickness of the shaft wall. For this condition, the pole base likely cannot be repaired, due to the difficulty in repairing a through-thickness crack. However, this definition of failure does not necessarily correspond with collapse of the pole.

While the predicted fatigue life of HMIPs with pre-existing cracks, based on a 5-percent probability of failure, varied from about 30 years to more than 300 years for various locations around the state, there were a number of locations where the fatigue life was on the order of 30 to 40 years. Considering that a number of poles at these locations have already been in-service a number of years, the remaining fatigue life is likely less than 30 to 40 years. The research identified certain TxDOT districts with more severe wind conditions, and therefore shorter predicted fatigue lives. However, within any given district, the wind conditions can vary widely from one location to another. Consequently, HMIPs with rather short predicted fatigue lives can occur in any district. As a result, the research team recommends that TxDOT develop a program of inspection to identify HMIPs with significant cracking at the base, and consider repairing these poles before the cracks extend through the full thickness of the shaft wall. For poles with cracks that extend through the full thickness of the shaft wall, the research team recommends replacement of the poles.

This research study also investigated a relatively inexpensive weld repair procedure for HMIPs with cracks at the shaft to baseplate weld. The repair procedure involves mapping the length and depth of cracks using ultrasonic testing, carefully grinding out the cracked areas, and re-welding the excavated areas. A small number of poles were repaired in this study, and the repaired poles were subject to fatigue tests. These tests showed that the repairs improved the fatigue life of the poles. The repaired poles showed a fatigue performance corresponding to AASHTO fatigue category E′ or better. While these results are promising, it is important to note that the observations are based upon a relatively small number of tests. Consequently, the research team does not recommend implementing this repair procedure on in-service poles until more thorough testing is conducted. Additional work is needed to more fully examine how the many details involved in the repair procedure affect the fatigue life, and thereby identify a well-vetted procedure that can be used with confidence.

References

AASHTO 2015, LRFD *Specifications for Structural Supports for Highway Sign, Luminaires and Traffic Signals*, 7th edition, American Association of State Highway and Transportation Officials, Washington, DC.

AASHTO 2009, *Standard Specifications for Structural Supports for Highway Signs, Luminaires and Traffic Signals*, 5th edition, American Association of State Highway and Transportation Officials, Washington, DC.

AASHTO 2010, *AASHTO LRFD Bridge Design Specifications*, 5th edition, American Association of State Highway and Transportation Officials, Washington, DC.

AASHTO 2013, *Standard Specifications for Structural Supports for Highway Signs, Luminaires and Traffic Signals*, 6th edition, American Association of State Highway and Transportation Officials, Washington, DC.

AASHTO 2014, *AASHTO LRFD Bridge Design Specifications*, 7th edition, American Association of State Highway and Transportation Officials, Washington, DC.

AFGROW Users Guide and Technical Manual, Version 5.02.05.19, December 2015.

Ahearn, EB & Puckett, JA 2010, *Reduction of Wind-Induced Vibrations in High-Mast Light Poles*, Research report no. FHWA-WY-10/02F, Wyoming Department of Transportation.

AISC 2011, *Steel Construction Manual*, 14th edition, American Institute of Steel Construction, Chicago, Illinois.

Albrecht, P & Yazdani, N 1986, Risk Analysis of Extending Bridge Service Life, Research report no. FHWA/MD. 84/01, Department of Civil Engineering, University of Maryland, College Park, Maryland.

Anderson, TH 2007, *Fatigue Life Investigation of Traffic Signal Mast-Arm connection Details*, M.S. Thesis, University of Texas at Austin, Austin, Texas

ASCE 2010, Minimum Design Loads for Buildings and other Structures, Reston, Virginia.

ASTM 2011, *E1049: Standard Practices for Cycle Counting in Fatigue Analysis*, West Conshohocken: ASTM International

Basquin, OH 1910, "The exponential law of Endurance Tests" *American Society for Testing and Materials Proceedings*, Vol, 10, pp. 625-630.

Materials Proc, Vol, 10, pp. 625-630.

Bauschinger, J. 1886, Mitt. Mech-Tech, Lab Munchen, Vol.13, No.1 1886.

Belivanis, K 2013, *Assessment of Remaining Fatigue Life of High Mast Illumination Poles*, M.S. Thesis, University of Texas at Austin, Austin, Texas

Bendat, JS, Piersol, AG 2002, *Random data analysis and measurement procedures*, 3rd edition, John Wiley and Sons, New York, NY

Bowman, MD, Fu, G, Zhou, EY, Connor, RJ & Godbole, AA 2012, Fatigue Evaluation of Steel Bridges. Washington, DC: Transportation Research Board.

British Standard Institution 2002, EN1993, Eurocode 3: Design of Steel Structures, London

Brooks, CR, and Choudhury, A 2002, *Failure Analysis of Engineering Materials*, McGraw-Hill Book Company.

Canadian Standards Association (CSA) 2006, *Canadian Highway Bridge Design Code, Mississauga*, Ontario.

Chang, B 2007, *A Time-Domain Model for Predicting Aerodynamic Loads on a Slender Support Structure for Fatigue Design*, PhD Dissertation, Iowa State University, Ames, Iowa.

Chang, B, Phares, BM, Sarkar, PP & Wipf, TJ 2009, 'Development of a Procedure for Fatigue Design of Slender Support Structures Subjected to Wind-Induced Vibration', *Journal of the Transportation Research Board*, no. 2131, pp. 23-33.

Chung, H 2004, *Fatigue Reliability and Optimal Inspection Strategies for Steel Bridges*, PhD Dissertation, University of Texas at Austin, Austin, Texas

Chung, H, Manuel, L & Frank, KH 2003, 'Reliability-Based Optimal Inspection for Fracture-Critical Steel Bridge Members,' *Journal of the Transportation Research Board*, no. 1845, pp. 39-47.

Chung, H, Manuel, L & Frank, KH 2003, *Optimal Inspection of Fracture-Critical Steel Trapezoidal Girders*, Research report no. 0-2135-1, Center for Transportation Research, Austin, Texas

Chung, HY, Manuel, L & Frank, KH 2006, 'Optimal Inspection Scheduling of Steel Bridges using Nondestructive Testing Techniques', *Journal of Bridge Engineering*, ASCE, vol. 11, no. 3, pp. 305-319.

Connor, RJ & Hodgson, RH 2006, 'Field Instrumentation and Testing of High-Mast Lighting Towers in the State of Iowa', Final Report, Iowa Department of Transportation, Ames, Iowa.

Daniel Pereira 2014, Wind Rose (https://www.mathworks.com/matlabcentral/fileexchange/47248-wind-rose), MATLAB Central File Exchange. Retrieved Jan 15, 2015.

Dawood, M, Goyal, R, Dhonde, H & Bradberry, T 2014, 'Fatigue Life Assessment of Cracked High-Mast Illumination Poles', *J. Perform. Constr. Facil.*, vol. 28, no. 2, pp. 311-320.

Downing, S, & Socie, D 1982, 'Simple Rainflow Counting Algorithms,' *International Journal of Fatigue*, 4(1), 31-40

Dyrbye, C & Hansen, SO 1997, *Wind Loads on Structures*, John Wiley & Sons, New York, New York.

Fasl, J 2013, *Estimating the Remaining Life of Steel Bridges Using Field Measurements*, PhD Dissertation, University of Texas at Austin, Austin, Texas

Fe-safe User Manual, Safe Technology, 2013.

Foley, CM, Fournelle, RA, Ginal, SJ & Peronto, JL 2004, *Structural Analysis of Sign Bridge Structures and Luminaire Supports*, Research report no. 0092-00-0016, Wisconsin Department of Transportation.

Frangopol, DM, Lin, KY & Estes, A 1997, 'Life-Cycle Cost Design of Deteriorating Structures', *Journal of Structural Engineering*, ASCE, vol. 123, No. 10, pp.1390-1401.

Goode, J & Lindt, J 2007, 'Development of a Semiprescriptive Selection Procedure for Reliability-Based Fatigue Design of High-Mast Lighting Structural Supports,' *Journal of Performance of Constructed Facilities*, 21(3), pp.193-206

Goodman, J, 1919, *Mechanics Applied to Engineering*, Longmans, Green and Co., London

Goyal, R, Dhonde, H & Dawood, M 2012, *Fatigue Failure and Cracking in High Mast Poles*, Research report no. 0-6650-1, Center for Transportation Research, Austin, Texas

Ibrahim, SR1977, 'Random Decrement Technique for Modal Identification of Structures', *Journal of Spacecraft and Rockets*, vol. 14, no. 11, pp. 696-700.

Jancauskas, ED & Melbourne, WH 1986, 'The Aerodynamic Admittance of Two-Dimensional Rectangular Section Cylinders in Smooth flow', *Journal of Wind Engineering and Industrial Aerodynamics*, vol. 23, pp. 395-408.

Jeng, MC, Doong, JL & Liu, WC 1993, 'Finite Element Analysis of Crack Growth Life Prediction under Complex Load History', *Engineering Fracture Mechanics*, vol. 46, no. 4, pp. 617-616.

Keating, P, & Fisher, J 1986, Evaluation of Fatigue Tests and Design Criteria on Welded Details. Washington, DC: Transportation Research Board.

Kleineck, J 2011, *Galvanizing Crack Formation at Base Plate to Shaft Welds of High Mast Illumination Poles*, M.S. Thesis, University of Texas at Austin, Austin, Texas

Koenigs, M 2003, *Fatigue Resistance of Traffic Signal Mast-Arm Connection Details*, M.S. Thesis, University of Texas at Austin, Austin, Texas

Krishna, K, Verma, PE, Statnikov, ES & Theini, L 2004, 'Improving Service Life of Steel Bridges, Light Poles and Sign Structures Through the Use of Ultra Sonic Treatment (UIT)', *Bridge Maintenance, Safety, Management and Costs*, Taylor and Francis Group, London.

Lassen, T, Rěcho, N 2006, Fatigue Life Analyses of Welded Structures, 1st edition, ISTE Ltd., Newport Beach, CA

Madsen, HO, Krenk, S & Lind, NC 1985, *Method of Structural Safety*, Prentice-Hall Inc., Englewood Cliffs, New Jersey.

Magenes, L 2011, *Fatigue Assessment of High Mast Illumination Poles Using Field Measurements*, M.S. Thesis, University of Texas at Austin, Austin, Texas

Miner, MA 1945, 'Cumulative Damage in Fatigue', *Journal of Applied Mechanics*, vol. 12, no. 3, pp. 159-164.

Moses, F, Schilling, C & Raju, K 1987, *Fatigue Evaluation Procedures for Steel Bridges*, Washington, DC: Transportation Research Board.

National Cooperative Highway Research Program (NCHRP) 1978, *Fatigue of Welded Steel Bridge Members under Variable-Amplitude Loadings*, Research report no. 188 prepared by Schilling, CG, Klippstein, KH, Barsom, JM & Blake GT, Transportation Research Board, Washington, DC.

National Cooperative Highway Research Program (NCHRP) 1986, *Evaluation of Fatigue Tests and Design Criteria on Welded Details*, Research report no. 286 prepared by Keating, PB & Fisher, JW, Transportation Research Board, Washington, DC.

National Cooperative Highway Research Program (NCHRP) 1987, *Fatigue Evaluation Procedures for Steel Bridge*, Research report no. 299 prepared by Moses, F, Schilling, CG & Raju, KS, Transportation Research Board, Washington, DC.

National Cooperative Highway Research Program (NCHRP) 2002, *Fatigue-Resistant Design of Cantilevered Signal, Sign, and Light Supports*, Research report no. 469 prepared by Dexter, RJ & Ricker, MJ, Transportation Research Board, Washington, DC.

National Cooperative Highway Research Program (NCHRP) 2012, *Fatigue Loading and Design Methodology for High-Mast Light Towers*, Research report no. 718 prepared by RJ Connor, SH Collicott, AM DeSchepper, RJ Sherman, JA Ocampo, Transportation Research Board, Washington, DC.

Nguyen, H 2012, *The Influence of Thunderstorm Downbursts on Wind Turbine Design*, PhD Dissertation, University of Texas at Austin, Austin, Texas

Ocel, JM 2006, *The Behavior of Thin Hollow Structural Section (HSS) to Plate Connections*, PhD Dissertation, University of Minnesota, Minneapolis, Minnesota.

Onoufriou, T 1999, 'Reliability Based Inspection Planning of Offshore Structures", *Marine Structures*, vol. 12, pp. 521-539.

Palmatier, AH 2005, *Ultrasonic Impact Treatment of Traffic Signal Mast Arm Welds*, M.S. Thesis, University of Texas at Austin, Austin, Texas

Paris, PC and Erdogan, F 1963, 'A Critical Analysis of Crack Propagation Laws', *Journal of Basic Engineering*, ASME, vol. 85, pp. 528-534.

Pool, CS 2010, *Effect of Galvanization on the Fatigue Strength of High Mast Illumination Poles*, M.S. Thesis, University of Texas at Austin, Austin, Texas

Richman, NB 2009, *Fatigue Life Inspection of High Performance Mast Arm Base Plate Connections*, M.S. Thesis, University of Texas at Austin, Austin, Texas

Rios, CA 2007, *Fatigue Performance of Multi-Sided High-Mast Lighting Towers*, M.S. Thesis, University of Texas at Austin, Austin, Texas

Rippling, ER & Crosley, PB 1983, *Narrative Summary on Fracture Control in Relation to Bridge Design*, Federal Highway Administration, Washington, DC.

Roy, S, Park, YC, Sause, R & Fisher, JW 2012, 'Fatigue Performance of Stiffened Pole-to-Base Plate Socket Connections in High-Mast Structures', *Journal of Structural Engineering*, ASCE, vol. 138, no. 12, pp. 1203-1213.

Scanlan, RH 1993, 'Problematics in Formulation of Wind-Force Models for Bridge Decks', *Journal of Engineering Mechanics*, vol. 119, no. 7, pp. 1353-1375.

Schutz, W 1996, "A History of Fatigue", *Engineering Fracture Mechanics*, vol. 54, no. 2, pp. 263-300.

Simiu, E and Scanlan, RH 1996, *Wind Effects on Structures, Fundamentals and Applications to Design*, 3rd edition, John Wiley & Sons, New York, New York.

Srivilairit, T, & Manuel, L 2009, 'Vortex-Induced Vibration and Coincident Current Velocity Profiles for a Deepwater Drilling Riser,' *Journal of Offshore Mechanics and Arctic Engineering*, 131(2), 021101

Stam, A 2009, *Fatigue Performance of Base Plate connections Used in High-Mast Lighting Towers*, M.S. Thesis, University of Texas at Austin, Austin, Texas

Stam, A, Richman, N, Pool, C, Rios, C, Anderson, T & Frank, K 2011, *Fatigue Life of Steel Base Plate to Pole Connections for Traffic Structures*, Research report no. FHWA/TX-11/9-1526-1, Center for Transportation Research, Austin, Texas

Starnater, E 2009, *Sam Rayburn Tollway – HMIP Repair and Ultrasonic Impact Treatment*, NTTA, Inspection and Repair Report prepared by Lamb-Star Engineering, L.P., Plano, Texas

Suksawang, N, Mintz, B & Mirmiran, A 2009, Remedial Actions for Failed Pole/Base Plated Weld on High Mast Lighting Pole (HMLT), Final Research Report no. BD-015-23, Florida International University, Florida Department of Transportation.

Sutherland, H 1999, *On the Fatigue Analysis of Wind Turbines*, Technical Report SAND99-0089, Sandia National Laboratory, Albuquerque, New Mexico

TxDOT 2008. High Mast Illumination Poles: Cracking Issue. TXDOT Report Presentation

Thoft-Christensen, P & Sorensen, JD 1987, 'Optimal Strategy for Inspection and Repair of Structural Systems', *Civil Engineering Systems*, vol. 4, pp. 94-100.

Wirsching, PH & Chen, YN 1988, 'Consideration of Probability-Based Fatigue Design for Marine Structures', *Marine Structures*, vol. 1, pp. 23-45.

Yazdani, N 1984, *Risk Analysis of Extending Bridge Service Life*, PhD Dissertation, University of Maryland, College Park, Maryland.

Yazdani, N and Albrecht, P 1989, 'Crack Growth Rates of Structural Steel in Air and Aqueous Environments', *Engineering Fracture Mechanics*, vol. 32, no. 6, pp. 997-1007.